Radiation and Temperature Effects on the Harmonic and Intermodulation Performance of Mach-Zehnder Optomodulator

Muhammed Taher Abuelma'atti
King Fahd University of Petroleum and Minerals, Box 203, Dhahran 31261, Saudi Arabia

Abstract— This paper presents closed-form expressions for the amplitudes of document and intermodulation products resulting from driving a Mach-Zehnder optomodulator by a multisinusoidal RF voltage. These expressions are functions of the DC bias, ϕ_{BIAS}, and the voltage, V_π, required to change the output light intensity from its maximum value to its minimum value. Since ϕ_{BIAS} and V_π are strongly dependent on the radiation intensity and the temperature, these expressions can be used to study the variation of the harmonic and intermodulation performance of Mach-Zehnder optomodulator with irradiation intensity and/or temperature. Using the results obtained in this paper, a data base can be established for the variation of the harmonic and intermodulation performance of the Mach-Zehnder optomodulators with the irradiation intensity and/or temperature. This would be interesting for any space applications using Mach-Zehnder optomodulators.

1. INTRODUCTION

The Mach-Zehnder optomodulator [1–4], is a basic building block used in designing analog amplitude-modulated optical communication links. Since the output-intensity/input-voltage characteristic of the Mach-Zehnder modulator has a cosine shape, a multi-tone input signal will generate sums and differences of the multiples of the input frequencies. These intermodulation products will cause degradation in the signal-to-noise ratio as part of the output power will go to unwanted output components. In order to improve its intermodulation performance, the Mach-Zehnder modulator is usually operated with 50% optical bias. This "operation at quadrature" eliminates the even-order unwanted output products and provides the minimum odd-order unwanted output products [5].

On the other hand, optical fiber modulators, based on the Mach-Zehnder interferometric modulator are of great interest to space flight projects [6] and in high energy physics applications [8, 9]. Due to the harsh environments of these applications, space flight and high energy physics applications have a unique set of demands for the Mach-Zehnder-based photonic parts. Of particular interest here are the studies reported on the effect of radiation and temperature on the Mach-Zehnder-based photonic parts; see for example [7–11]. However, there is no study available in the open literature to investigate the effect of radiation on the harmonic and intermodulation performance of the Mach-Zehnder-based photonic parts. The major intention of this paper is, therefore, to present such a study.

2. ANALYSIS

Figure 1 shows the schematic of a Mach-Zehnder interferometeric modulator comprising a splitter at the entrance, to split the input light into two branches, a combiner at the output to combine the two lights after passing through the two electrodes. The first electrode is used to apply a DC voltage to select the bias point and the second electrode is used to apply the RF modulating voltage. The transfer function of the Mach-Zehnder interferometric modulator shown in Fig. 1 can be modeled by Equation (1).

$$P_{out} = P_{in}(1 + \cos\phi) \tag{1}$$

In Equation (1), P_{in} is the optical input intensity, P_{out} is the output optical intensity, $\phi = \phi_{BIAS} + \phi_{RF}$ where ϕ_{BIAS} is the phase shift caused by the DC bias voltage V_{BIAS} and $\phi_{REF} = \pi V_{REF}/V_\pi$ is the phase shift caused by the modulating RF voltage, V_{REF}, and V_π is the voltage required to change the output light intensity from its maximum value to its minimum value. Equation (1) can be rewritten in the form

$$P_{out} = P_{in}\left(1 + \cos\left((\pi V_{REF}/V_\pi) + \phi_{BIAS}\right)\right) \tag{2}$$

Results reported in Figs. 1 and 2 and Table 1 of [11] show that the temperature coefficient of ϕ_{BIAS} is of the order of few tens of thousands ppm/deg.C and for V_π is of the order of few hundreds ppm/deg.C. The results reported in Figs. 3 and 4 of [10] show that ϕ_{BIAS} and V_π are strongly

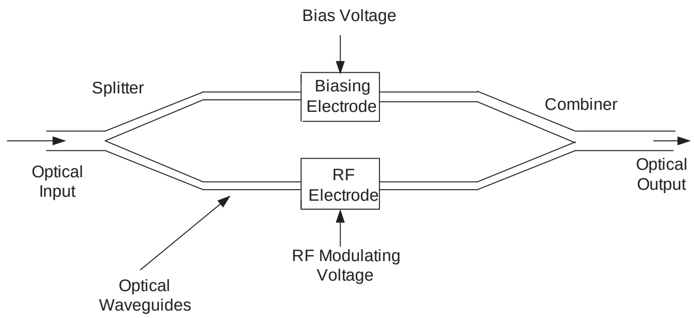

Figure 1: Mach-Zehnder interferometric modulator.

dependent on radiation but do not follow a specific pattern. Thus, the effect of temperature and radiation on the harmonic and intermodulation performance of the Mach-Zehnder interferometer of Fig. 1 can be investigated by studying the variation of harmonics and intermodulation products with ϕ_{BIAS} and V_π.

Assuming that the RF voltage comprises a multisinusoidal of the form

$$V_{RF}(t) = \sum_{m=1}^{M} V_m \sin \omega_m t \tag{3}$$

where V_m is the amplitude of the input sinusoid with frequencies ω_m, then combining Equations (2) and (3) yields

$$P_{out} = P_{in} \left(1 + \cos \left(\frac{\pi}{V_\pi} \left(\sum_{m}^{M} V_m \sin \omega_m t\right) + \phi_{BIAS}\right)\right) \tag{4}$$

Using the trigonometric identities

$$\begin{aligned}
\cos(x+y) &= \cos x \cos y - \sin x \sin y \\
\sin(x+y) &= \sin x \cos y + \cos x \sin y \\
\cos(z \sin x) &= J_0(z) + 2\sum_{n=1}^{\infty} J_{2n}(z) \cos(2nx)
\end{aligned}$$

and

$$\sin(z \sin x) = 2\sum_{n=1}^{\infty} J_{2n-1}(z) \sin((2n-1)x)$$

where $J_{|\alpha_m|}(z)$ is the ordinary Bessel function of order $|\alpha_m|$, it is easy to show that the amplitude of an output component can be expressed by

$$P_{out(\alpha_1,\alpha_2,\alpha_3,\ldots,\alpha_M)} = 2\cos\phi_{BIAS} \prod_{m=1}^{M} J_{|\alpha_m|}\left(\pi V_m/V_\pi\right) \quad \text{for} \quad \sum_{m=1}^{M} |\alpha_m| = \text{even integer} \tag{5}$$

$$P_{out(\alpha_1,\alpha_2,\alpha_3,\ldots,\alpha_M)} = 2\sin\phi_{BIAS} \prod_{m=1}^{M} J_{|\alpha_m|}\left(\pi V_m/V_\pi\right) \quad \text{for} \quad \sum_{m=1}^{M} |\alpha_m| = \text{odd integer} \tag{6}$$

Using Equations (5) and (6), the amplitude of any output frequency component can be obtained. For example, the amplitude of an output component of frequency $k\omega_r$ can be expressed as

$$P_{out(k\omega_r)} = 2\cos\phi_{BIAS} J_k\left(\frac{\pi V_r}{V_\pi}\right) \prod_{\substack{m=1 \\ m\neq r}}^{M} J_0\left(\frac{\pi V_m}{V_\pi}\right) \quad \text{for} \quad k = \text{even integer} \tag{7}$$

$$P_{out(k\omega_r)} = 2\sin\phi_{BIAS} J_k\left(\frac{\pi V_r}{V_\pi}\right) \prod_{\substack{m=1 \\ m\neq r}}^{M} J_0\left(\frac{\pi V_m}{V_\pi}\right) \quad \text{for} \quad k = \text{even integer} \tag{8}$$

the amplitude of an output component of frequency $\omega_r \pm \omega_s$ can be expressed as

$$P_{out(\alpha_r \pm \omega_s)} = 2\cos\phi_{BIAS} J_1\left(\frac{\pi V_r}{V_\pi}\right) J_1\left(\frac{\pi V_s}{V_\pi}\right) \prod_{\substack{m=1 \\ m \neq r,s}}^{M} J_0\left(\frac{\pi V_m}{V_\pi}\right) \tag{9}$$

the amplitude of an output component of frequency $2\omega_r \pm \omega_s$ can be expressed as

$$P_{out(2\alpha_r \pm \omega_s)} = 2\sin\phi_{BIAS} J_2\left(\frac{\pi V_r}{V_\pi}\right) J_1\left(\frac{\pi V_s}{V_\pi}\right) \prod_{\substack{m=1 \\ m \neq r,s}}^{M} J_0\left(\frac{\pi V_m}{V_\pi}\right) \tag{10}$$

the amplitude of an output component of frequency $\omega_r \pm \omega_s \pm \omega_p$ can be expressed as

$$P_{out(\omega_r \pm \omega_s \pm \omega_p)} = 2\sin\phi_{BIAS} J_1\left(\frac{\pi V_r}{V_\pi}\right) J_1\left(\frac{\pi V_s}{V_\pi}\right) J_1\left(\frac{\pi V_p}{V_\pi}\right) \prod_{m=1, m\neq r,s,p}^{M} J_0\left(\frac{\pi V_m}{V_\pi}\right) \tag{11}$$

$$P_{out(2\omega_r \pm 2\omega_s)} = 2\cos\phi_{BIAS} J_2\left(\frac{\pi V_r}{V_\pi}\right) J_2\left(\frac{\pi V_s}{V_\pi}\right) \prod_{\substack{m=1 \\ m \neq r,s}}^{M} J_0\left(\frac{\pi V_m}{V_\pi}\right) \tag{12}$$

In a similar way, the amplitude of any output frequency component can be obtained from Equations (5) and (6).

3. SPECIAL CASE

If the RF modulating voltage is composed of two equal-amplitude sinusoids of the form

$$V_{RF}(t) = V(\sin\omega_1 t + \sin\omega_2 t) \tag{13}$$

then using Equations (7)–(12), it is easy to show that the amplitude of the fundamental output component of frequency ω_1 (or ω_2) can be expressed as

$$P_{out(1,0)} = 2\sin\phi_{BIAS} J_1(\pi V/V_\pi) J_0(\pi V/V_\pi) \tag{14}$$

the amplitude of the kth-harmonic output component of frequency $k\omega_1$ (or $k\omega_2$) can be expressed as

$$P_{out(k,0)} = 2\sin\phi_{BIAS} J_k(\pi V/V_\pi) J_0(\pi V/V_\pi) \quad \text{for} \quad k = \text{odd-integer} \tag{15}$$

$$P_{out(k,0)} = 2\cos\phi_{BIAS} J_k(\pi V/V_\pi) J_0(\pi V/V_\pi) \quad \text{for} \quad k = \text{even-integer} \tag{16}$$

the amplitude of the output component with frequency $\omega_1 \pm \omega_2$ can be expressed as

$$P_{out(1,1)} = 2\cos\phi_{BIAS} J_1(\pi V/V_\pi) J_1(\pi V/V_\pi) \tag{17}$$

and the amplitude of the output component with frequency $2\omega_1 \pm 2\omega_2$ can be expressed as

$$P_{out(2,2)} = 2\cos\phi_{BIAS} J_2(\pi V/V_\pi) J_2(\pi V/V_\pi) \tag{18}$$

$$P_{out(2,1)} = 2\sin\phi_{BIAS} J_2(\pi V/V_\pi) J_1(\pi V/V_\pi) \tag{19}$$

Using Equations (14)–(19), the relative second-harmonic distortion $HD2$, third-harmonic distortion $HD3$, fourth-harmonic distortion $HD4$, second-order intermodulation distortion $IMD2$, third-order intermodulation distortion $IMD3$ and fourth-order intermodulation distortion $IMD4$ can be expressed as the ratio between the amplitude of the respective output harmonic or intermodulation component and the amplitude of the fundamental output component.

Inspection of Equations (14), (15) and (19) clearly shows that the $HD3$ and $IMD3$ are independent of the bias voltage (ϕ_{BIAS}). Thus, $HD3$ and $IMD3$ will not be affected by the variation of ϕ_{BIAS} with radiation and/or temperature and will be affected only by the variation of V_π with the radiation and/or temperature variations. Inspection of Equations (14), (16)–(18) shows that $HD2$, $HD4$, $IMD2$ and $IMD4$ will be affected by the variation of both ϕ_{BIAS} and V_π with the radiation and/or temperature variations. Moreover, as expected, inspection of Equations (14), (16)–(18) shows that for $\phi_{BIAS} = \pi/2$, then all the even-order harmonics and intermodulation products will be equal to zero.

4. RESULTS

Using Equations (14)–(19) the harmonic and intermodulation performance of the Mach-Zehnder interferometer under radiation and/or temperature variations can be calculated by investigating the variation of $HD2$, $HD3$, $HD4$, $IMD2$, $IMD3$ and $IMD4$ with the bias voltage, ϕ_{BIAS}, and the voltage V_π. Samples of the results obtained with $V = 1.0V$ are shown in Figs. 2–4. It is worth mentioning here that $V = 1.0V$ was selected just to reveal the large signal performance of the Mach-Zehnder interferometer. Similar results were obtained for other values of V. Inspection of Figs. 2 and 3 for values of $\phi_{BIAS} = 1.2566$ and $\pi/2$ shows that the relative harmonics and intermodulation products decrease with the increase in the value of the parameter V_π. Since V_π decreases with the increase in irradiation intensity and/or temperature, then this means that increasing the irradiation intensity and/or temperature will result in increasing the relative harmonics and intermodulation products and degradation of the Mach-Zehnder interferometer performance. Moreover, inspection of Fig. 3 shows that the even-order harmonics and intermodulation products will vanish when $\phi_{BIAS} = \pi/2$ and that the third-order intermodulation is dominant. Furthermore, inspection of Figs. 2 and 3 show that for values of $\phi_{BIAS} = 1.2566$ the second-order intermodulation is dominant for a wide range of values of the parameter V_π. It appears, therefore, that as the value of ϕ_{BIAS} approaches $\pi/2$, then the third-order intermodulation starts to dominate the harmonic and intermodulation performance of the Mach-Zehnder interferometer. Otherwise, the second-order intermodulation is dominant. This observation is confirmed by the results shown in Fig. 4.

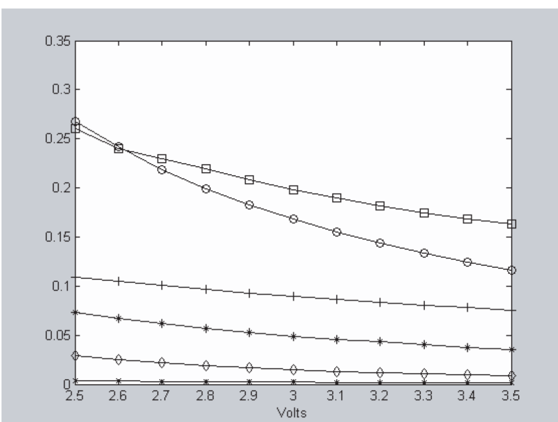

Figure 2: Variation of the relative harmonics and intermodulation products with the voltage V_π. $\phi_{BIAS} = 1.2566$ radians and $V = 1.0$ Volt. +: $HD2$; *: $HD3$; X: $HD4$; ○: $IMD3$; □: $IMD2$; ◊: $IMD4$.

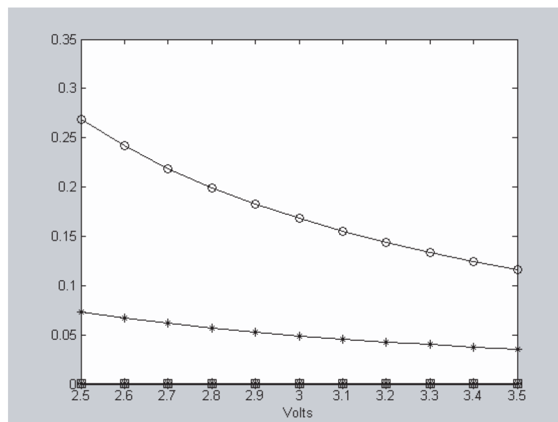

Figure 3: Variation of the relative harmonics and intermodulation products with the voltage V_π. $\phi_{BIAS} = 1.570795$ radians and $V = 1.0$ Volt. +: $HD2$; *: $HD3$; X: $HD4$; ○: $IMD3$; □: $IMD2$; ◊: $IMD4$.

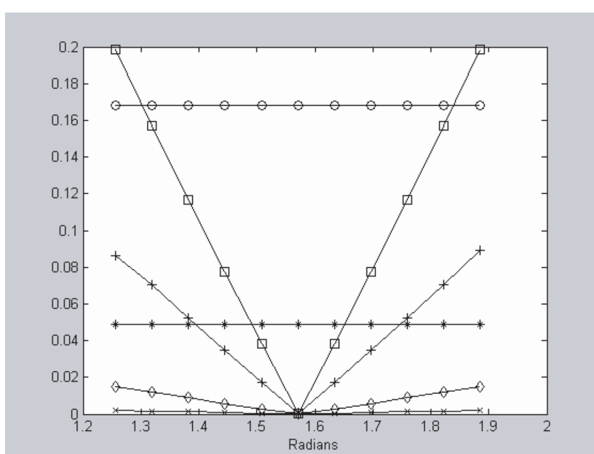

Figure 4: Variation of the relative harmonics and intermodulation products with ϕ_{BIAS}. $V_\pi = 3.0$ V and $V = 1.0$ Volt. +: $HD2$; *: $HD3$; X: $HD4$; ○: $IMD3$; □: $IMD2$; ◊: $IMD4$.

Inspection of Fig. 4 shows that the third-order harmonic and intermodulation are independent of the bias ϕ_{BIAS}. However, the second- and fourth-order harmonic and intermodulation performance is strongly dependent on the value of the bias ϕ_{BIAS} with the second-order intermodulation changing much faster with ϕ_{BIAS} than all the other even-order harmonic and intermodulation products. Moreover, it appears from Fig. 4 that for values of ϕ_{BIAS} far away from $\pi/2$, the second-order intermodulation is dominant. Since ϕ_{BIAS} is strongly dependent on temperature and irradiation intensity, then it appears that a high dose of irradiation and/or a large increase in temperature my result in a severe degradation of the harmonic and intermodulation performance of the Mach-Zehnder interferometer.

5. CONCLUSIONS

In this paper closed-form expressions are obtained for the amplitudes of the harmonics and intermodulation products resulting from a Mach-Zehnder interferometer driven by a multisinusoidal RF modulating signal. Using these expressions the variation of the relative harmonic and intermodulation performance of the Mach-Zehnder interferometer can be investigated as a function of the variations in the bias, ϕ_{BIAS} , and the parameter V_π. Since these two parameters are strongly dependent on the variation of irradiation intensity and/or temperature, then using the expressions obtained in this paper designers can establish a data base for the harmonic and intermodulation performance of Mach-Zehnder interferometer subjected to variations in irradiation intensity and/or temperature. This is specially important for Mach-Zehnder interferometers intended for space applications.

ACKNOWLEDGMENT

The author acknowledges with thanks the support of King Fahd University of Petroleum and Minerals under the internal project number IN090028.

REFERENCES

1. Becker, R. A., "Broad-band guided-wave electrooptic modulators," *IEEE Journal of Quantum Electronics*, Vol. QE-20, 723–727, 1984.
2. Kolner, B. H. and D. W. Dolfi, "Intermodulation distortion and compression in an integrated electrooptic modulator," *Applied Optics*, Vol. 26, 3676–3680, 1987.
3. Stephens, W. E. and T. R. Joseph, "System characteristics of direct modulated and externally modulated RF fiber-optic link," *Journal of Lightwave Technology*, Vol. LT-5, 380–389, 1987.
4. Cox III, C. H., G. E. Betts, and L. M. Johnson, "An analytic and experimental comparison of direct and external modulation in analog fiber-optic links," *IEEE Transactions on Microwave Theory and Techniques*, Vol. 38, 501–509, 1990.
5. Farwell, M. L., W. S. C. Chang, and D. R. Huber, "Increased linear dynamic range by low biasing the Mach-Zehnder modulator," *IEEE Photonic Technology Letters*, Vol. 5, 779–782, 1993.
6. Ott, M., J. Vela, C. Magee, and H. Shaw, "Reliability of optical fiber modulators for space flight environments, NASA Parts and Packaging Program Report," IPPAQ Task Report, 1–17, NASAGSFC Greenbelt, Maryland, October 2002.
7. Barnes, C. and R. Greenwell, "Radiation effects in photonic modulator structures," *Photonics for Space Environment III, SOIE Proceedings*, Vol. 2482, 48–83, 1995.
8. Wooten, E. L., K. M. Kissa, A. Yi-Yan, E. J. Murphy, D. A. Lafaw, P. F. Hallemeir, D. Maack, D. V. Attanasio, D. J. Fritz, G. J. McBrien, and D. E. Bossi, "A review of Lithium Niobate modulators for fiber-optic communications systems," *IEEE Journal of Selected Topics in Quantum Electronics*, Vol. 6, 69–82, 2000.
9. D'hose, C., E. Cassan, J. Baggio, O. Musseau, and J. L. Leray, "Electrical and optical response of a Mach-Zehnder electrooptical modulator to pulsed irradiation," *IEEE Transactions on Nuclear Science*, Vol. 45, 1524–1530, 1998.
10. Ohska, T. K., O. Sasaki, T. Murakami, K. Komenou, M. Seino, M. Doi, R. Hamatsu, M. Chiba, N. Yoshida, and H. Ishiyama, "Radiation resistance of a Mach-Zehnder optomodulator for analog signal transmission," *IEEE Nuclear Science Symposium and Medical Imaging Conference Record*, Vol. 1, 627–629, 1995.
11. Ohska, T. K., O. Sasaki, T. Murakami, M. Doi, and M. Seino, "A low temperature coefficient optomodulator for analog signal transmission," *IEEE Transactions on Nuclear Science*, Vol. 40, 805–808, 1993.

Experimental Investigation of the Shield Termination Effect on the Field-to-Cable Coupling Level

F. Üstüner[1], **N. Tarım**[2], **and E. Baran**[1]

[1]TUBITAK BILGEM UEKAE, Turkey
[2]Anadolu University, Turkey

Abstract— The functional and environmental requirements as well as the electromagnetic compatibility requirements are important in determining the types and installation of the cables used in platforms such as aircrafts. Interference problems related with field-to-cable type coupling mechanism is especially important. In this work, a typical cable connection between two avionic equipments is considered and investigated experimentally in order to assess the effect of shield termination on the field-to-cable coupling level. An experimental setup is developed and experiments are carried out on two different cables for several shield termination cases. Measurement results are given emphasizing the importance of the shielding integrity of the connectors in addition to the shield termination requirements.

1. INTRODUCTION

The functional and environmental requirements as well as the electromagnetic compatibility requirements are important in determining the types and installation of the cables used in platforms such as aircrafts. The high level electromagnetic field radiated from on-board and off-board RF transmitters induces currents on the cables installed in the aircraft and these currents result in interference voltages appearing at the victim equipment terminals. This type of coupling is known as the field-to-cable coupling and plays an important in the interference problems. The field-to-cable coupling constitutes one of the fundamental electromagnetic interference coupling mechanisms that plays a central role in evaluating the radiated immunity (or susceptibility) of the equipment under test. Assessment of the cable shield performance along with its connector terminations gives vital information for the proper design of the cable installation. The theory that explains the field-to-cable coupling is well established and useful in the evaluation of simple cable structures [1, 2].

The primary line of defense against this interference threat is to use shielded cables. If the surface transfer impedance of the cable is low (this is usually achieved with high optical coverage), then the interference voltage at the equipment terminal may be diminished. On the other hand, cable shield constitutes only one of the links of shielding chain. Other links of the shielding chain consist of chassis connectors, connector back-shells and the termination of the cable shield at the connector back-shells. Although the cable shield characteristic (surface transfer impedance) plays the most important role in the coupling level, the type of the shield termination at the connector back-shell is also important. A chain is only as strong as its weakest link. Therefore, the proper terminations of the cable shield at the connector back-shells are as important as the cable shield in decreasing the number of interference problems. To illustrate this fact, a typical cable connection between two avionic equipments is considered in this work and this cable connection is investigated experimentally in order to assess the effect of shield termination on the field-to-cable coupling level. This type of experimental approach is especially useful in assessing the shielding integrity of the overall cable structure.

2. FIELD-TO-CABLE COUPLING EXPERIMENTAL SETUP

A laboratory experimental setup is developed for investigating the effect of shielding structure and shielding terminations on the interference coupling. For comparison purposes, the shield of the cable under test is terminated in five different configurations as illustrated in Figure 1(a); no shield termination, 360° termination at one side, single pigtail termination at both sides, double pigtail termination at both sides, 360° termination at both sides. Two shielded boxes are connected to each other with a 2 m long cable under test and are installed on the floor of a GTEM Cell as seen in Figure 1(b). The coupling level is measured by a spectrum analyzer for each cable termination configuration. The first series of test was carried out on an RF coaxial cable of type RG-223. A second series of test was carried out on a MIL-STD-1553 data bus cable which comprises of a shielded twisted pair. The measurement was carried out between 1 MHz to 1 GHz. Measurement was repeated for different types of cable shield termination and cables.

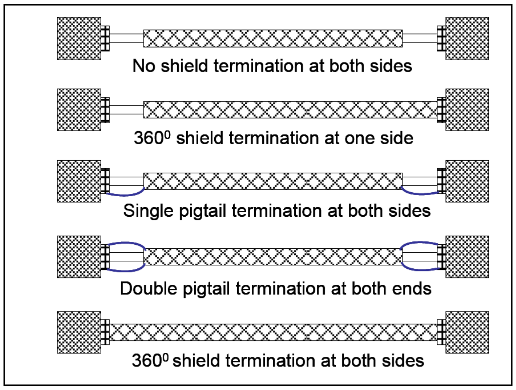

(a)

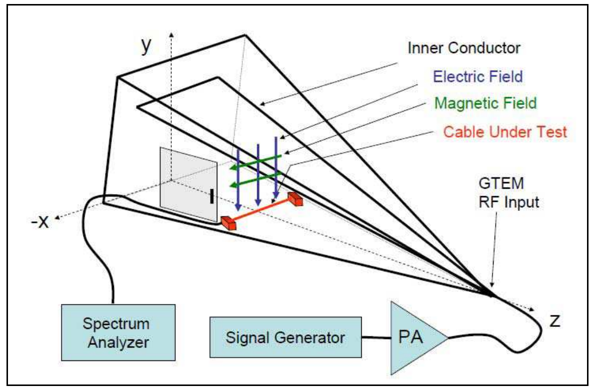

(b)

Figure 1: (a) Shield terminations and (b) test setup inside GTEM cell.

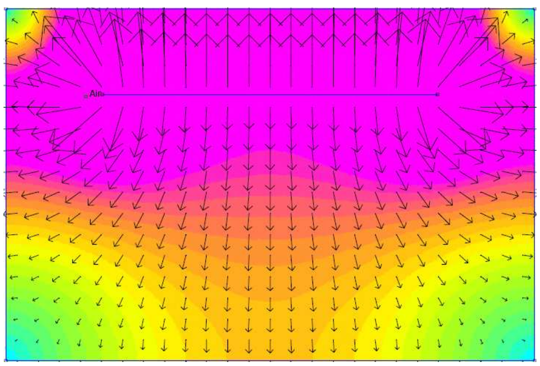

(a)

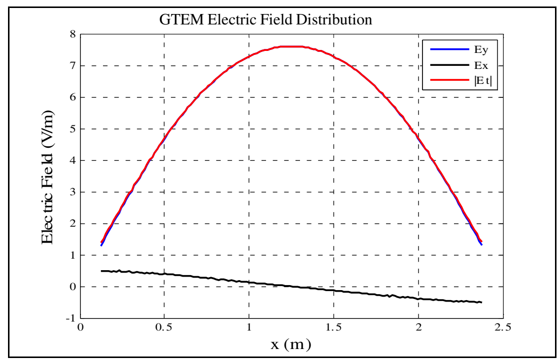

(b)

Figure 2: Electric field distribution (a) in the cross section of the GTEM cell and (b) on the x-axis.

In order to illuminate the cable with a plane wave, the GTEM cell environment is preferred. The boxes and the cable under test are placed on the bottom plate of GTEM cell in transverse position (see Figure 1(b)). A GTEM cell is basically a transmission line environment whose rectangular cross section increases towards its termination and an offset is present in the placement of the inner conductor. As in other TEM (transverse electromagnetic) wave guided structures, electric and magnetic field components in GTEM cells are perpendicular to the propagation direction. In order to evaluate the uniformity of the electric field over the cross section of the GTEM cell, it is estimated numerically using two dimensional finite element analysis. The length of the cable under test is approximately 2.1 m. A spacing of 5 cm is left between the cable and the floor of the GTEM cell. The distance between the floor and the inner conductor at the cross section where the cable under test is installed is equal to 1.28 m. In order to generate an electromagnetic field on the cable, a CW RF signal generator coupled with a power amplifier is used. The electrical field intensity distribution and its direction is illustrated in Figure 2(a). The variation in the x-direction of the electric field intensity to which the cable is exposed is given in Figure 2(b). As seen from the figure, the electrical field component which is perpendicular to the cable axis is dominant. In other words, the broadside coupling is dominant. In order to measure the voltage appearing on the cable termination impedance (50 ohm), a coaxial cable is connected and routed outside the GTEM cell to be connected to the spectrum analyzer. The chosen coaxial cable shielding effectiveness performance is much better than the cables under test and this is verified by the noise threshold measurement carried out before connecting the cable under test. The field-to-cable coupling experiments were carried on the following two cables:

- RG223 type double-shielded RF coaxial cable
- STM01-600 type MIL-STD-1553B data bus shielded twisted pair cable

3. MEASUREMENT RESULTS ON RG-223 COAXIAL CABLE

Although the final goal of the experiment is to evaluate the shielding effectiveness performance of regular multi-conductor shielded cables, it is first preferred to work with a well defined shielded cable; RF coaxial cable. Since it possesses only one inner conductor and the shield termination can clearly be identified, it constitutes the ideal structure. Since the characteristic impedance of the RG-223 cable is 50 ohm, termination impedances were chosen as 50 ohm. Measurements were taken for the above mentioned shield termination cases separately. Before doing these measurements on the cable under test, the susceptibility of the test setup was controlled because the coaxial cable routed to the outside of the GTEM Cell might also be susceptible to the RF field. For this purpose, a measurement was taken while no cable was present between the two boxes, and thereby the noise threshold of the test setup was determined. This threshold level (cyan curve) is illustrated in Figure 3 at the bottom of the graph around 5 to 10 dBuV level. In the figure, the red curve shows us the result with no shield case. As seen, it is increasing linearly with the increasing frequency showing a 20 dB/decade increase. At approximately 70 MHz, the first resonance occurs. This is expected since the resonance frequency corresponds to the frequency at which the cable length is equal to half wavelength ($\lambda/2$). After terminating one side of the cable with 360 degree at the connector back-shell, the black curve was obtained. Apart from a slight decrease at low frequencies (less than 10 MHz), almost the same response as in the no shield case was obtained. Whenever the cable shield was terminated with a piece of wire (pigtail) about 1 mm in diameter and 10 mm in length at both sides, the induced voltage decreased rapidly until the first resonance frequency (green curve). However, similar response was obtained at the first resonance point and afterwards. Adding another pigtail in parallel to the previous one at both sides, improved the situation (decreases the induced voltage) approximately 10 dB (blue curve). On the other hand, the real improvement came with the introduction of 360 degree termination at both sides (magenta curve). Apart from the resonance frequencies, the induced voltage is nearly the same as the noise threshold level. Moreover, the induced voltage is 50 dB less than the other cases at the first resonance frequency where the most severe induced voltages are obtained.

4. MEASUREMENT RESULTS ON MIL-STD-1553 DATA BUS CABLE

The second group of experiments was performed on the MIL-STD-1553 data bus cable. This cable has physically a shielded twisted pair structure and its characteristic impedance is 78 ohms [3]. MIL-STD-1553 data bus has balanced electrical terminations in real applications. Therefore a wideband balun transformer is used in order to measure the differential mode induced on the balanced termination load as a result of the common-mode current induced on the cable without distorting the balanced nature of the cable. The balanced side of the transformer is used to terminate the MIL-STD-1553 cable while the unbalanced output side of the transformer is connected to the spectrum analyzer via the coaxial cable.

First, the noise threshold level of the test setup was measured. This measurement was made for two different situations. In the first case, the box connector to which the balun transformer

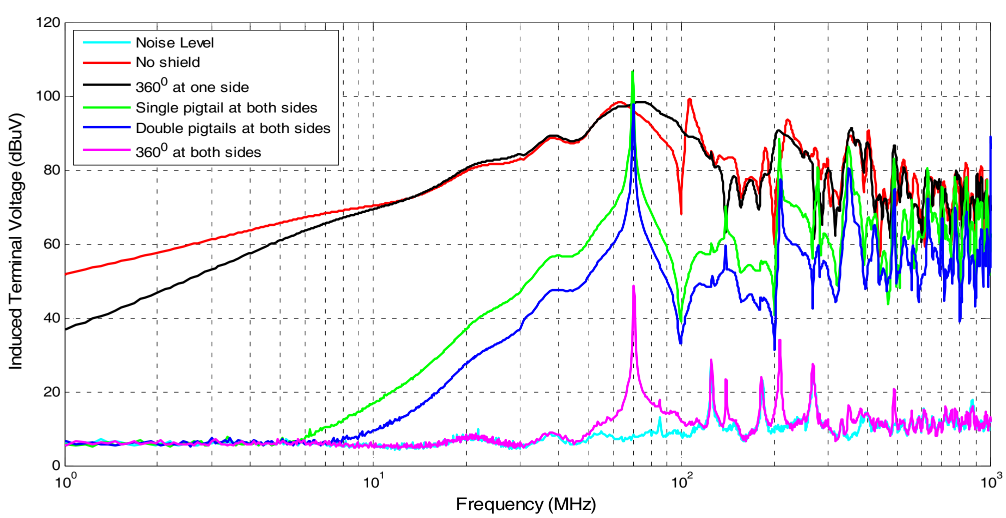

Figure 3: Measurement results on RG-223 coaxial cable for different shield terminations.

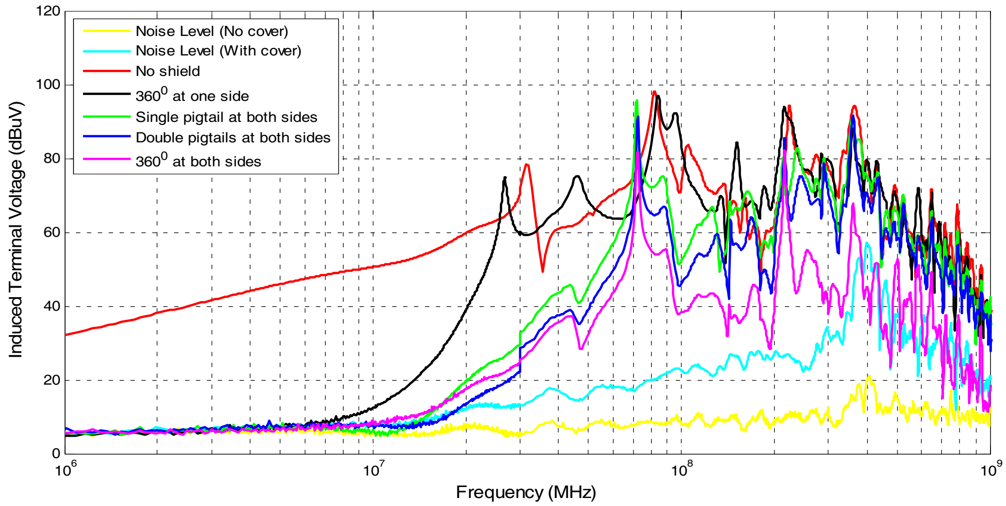

Figure 4: Measurement results on MIL-STD-1553 databus cable for different shield terminations.

is connected was left open and the cyan curve in Figure 4 was obtained. Since high levels were unexpectedly obtained especially at high frequencies, the connector was closed with a metal lid and the measurement was repeated. It is observed that the level was decreased (yellow curve). This experiment demonstrates the importance of the connector in the shield chain. Then it was passed to the experiments for different shield terminations. In no shield case, a linear increase in induced voltage with frequency (20 dB/decade) was observed until resonance region (red curve). In the next stage, the cable shield was terminated at one side of the cable with 360 degree. This time, it was observed that the level of interference (black curve) decreased 20 dB especially at the low frequencies (< 20 MHz). However, at high frequencies (> 30 MHz) a behavior identical to the "no shield" case was observed. In the third stage, the cable shield was terminated with one pigtail at both sides. This decreased the induced voltage significantly at lower frequencies (< 30 MHz) but the behavior at the resonance region remained the same (green curve). After adding a parallel pigtail at both sides, a slight (around 3 dB) improvement was obtained (blue curve). In the final stage, the cable shield on both sides were terminated with their connector back-shell in $360°$ (magenta curve). In this case, similar result to pigtail cases were obtained at lower frequencies while 15–20 dB improvement was obtained at higher frequencies (> 100 MHz).

5. CONCLUSION

In this work, a typical cable connection between two avionic equipments is considered and investigated experimentally in order to assess the effect of shield termination on the field-to-cable coupling level. The first series of experiment was carried out on a coaxial cable of type RG-223. These experiments show us clearly the importance of 360 degree shield termination at both sides of the cable. Moreover, they also show that the pigtail shield terminations are effective only at lower frequencies up to the first resonance frequency of the cable. A second series of experiments was carried out on a MIL-STD-1553 data bus cable which comprises of a shielded twisted pair. Although these experiments show similar results, an improvement similar to the one that is obtained in the RG223 cable has not been obtained in the case of $360°$ termination at both sides. The main reason behind this, is the failure in proper connection of the shield to the connector back-shell. In MIL-STD-1553 data bus cable, the connector back-shell constitutes the weakest link in the shield chain.

The use of GTEM cell for measuring the induced current on the cable (or voltage at the terminals) under plane wave excitation proves its usefulness in assessing the shielding integrity of the overall cable structure.

REFERENCES

1. Smith, Jr., A. A., *Coupling of External Electromagnetic Fields to Transmission Lines*, Interference Control Technologies, USA, 1989.
2. Paul, C. R., *Analysis of Multiconductor Transmission Lines*, Wiley, USA, 1994.
3. MIL-STD-1553B, "Aircraft internal time division command/response multiplex data bus," US DoD, 1978.

EMC in Malaysia: The First 10-Meter Semi-Anechoic Chamber (SAC) — Inception, Approach and Challenges

Lay Heng Chee and See See Cheng
EMC Testing Services and Solutions, Cisspr Sdn. Bhd., Malaysia

Abstract— In this paper, we provide an insight to the inception and approach used in the establishment of Malaysia's first public Electromagnetic Compatibility (EMC) Laboratory that is equipped with a 10-meter test range semi-anechoic chamber (SAC), and the challenges of EMC development in Malaysia. The PSDC EMC Laboratory, pioneered by Khazanah Nasional Berhad (a Government investment arm), PSDC (a non-profit society) and Cisspr Sdn. Bhd. (an entrepreneur enterprise), is a Malaysian government initiative to invest 30 million ringgit to establish a Shared Services Centre in Penang Skills Development Centre (PSDC). As the Electrical and Electronics (E&E) industry in Malaysia shifted from the lower value-added assembly and machining, to the higher value-added activities in test, manufacturing, and design and development (D&D), EMC test and measurement capability is vital to meet global regulatory compliance requirements in creating a situation of functional and safe operation in a common electromagnetic environment. A tri-partite approach was used to establish PSDC EMC Laboratory from concept to reality, based on well-defined objectives, voice of the industry, state-of-the-art test systems, competent people and internationally recognized ISO/IEC 17025 accreditation.

1. INTRODUCTION

Electrical and Electronics (E&E) sector is a significant contributor to Malaysia's national economy, accounting for 37 billion ringgit in gross national income (GNI) which is 6 percent of national GNI, 522,000 jobs and 41 percent of Malaysia's total exports in 2009 [1]. The E&E sector has been identified as one of the 12 National Key Economic Areas (NKEAs) as key growth engines of the nation's economic performance, under Malaysian government's New Economic Model as a comprehensive effort to transform Malaysia into a developed high-income nation by 2020.

In 1972, Malaysia's first Free Industrial Zone (FIZ) was set up in Penang to promote and facilitate the development of export-oriented electronics manufacturing. The first eight multinational corporations (MNC) in the E&E industry which set up offshore bases on the island in 1970s are Advanced Micro Devices Products, Agilent Technologies, Clarion, Fairchild Semiconductor, Hitachi Semiconductor, Intel, Osram Opto Semiconductor and Robert Bosch [2]. These anchor companies played a crucial role in seeding the growth and development of the nation's industry, by spurring local small and medium enterprises (SME) and acting as magnets for other major firms to invest in the country.

Malaysia has undergone intensive industrial and technological transformation over the past 40 years, from labor-intensive assembly and machining, into high technology, skilled, capital-intensive test and manufacturing operations, and design and development (D&D), which significantly contributes to the nation's technological enhancement and talent development. Today, Penang is known as the "Silicon Valley of the East" [3].

2. INCEPTION

The rapid growth of Malaysia's E&E industry and the necessity to enable global market access created the need for EMC test facilities that can fulfill global regulatory compliance requirements. Prior to this, there was no publicly available EMC test facility with a compliant 10-meter semi-anechoic chamber (SAC) in the country. Companies that require the test facility have to either send their products abroad for EMC testing or to build their own test facility. Sending their products abroad incurs extraneous transportation cycle time, high expenditure, loss of engineering design efficiency, while building their own test facility is simply too cost prohibitive.

In the effort to bridge this missing link, the Malaysian government took the initiative to invest 30 million ringgit to establish a Shared Services Centre in Penang Skills Development Centre (PSDC), which houses Malaysia's first public Electromagnetic Compatibility (EMC) Laboratory equipped with a 10-meter semi-anechoic chamber.

The objectives of setting up this EMC test facility are threefold. First, it is to strengthen the existing D&D ecosystem. Second is to support talent development for MNCs and local SMEs. Third is to provide state-of-the-art testing services to foster the growth of the nation's E&E industry. For local firms, the provision of this testing capability becomes an enabler for product design. For multinational companies, it is an extension of their in-house capacity.

By providing a locally accessible public test facility, this Malaysian government enabled project will boost business confidence, minimize outflow of currency abroad for EMC testing services, and attract more foreign investments into the nation. Malaysia stands to save on a potential outflow of at least RM3.2 million a year with the establishment of this test facility [4].

PSDC was selected for this mission due to its strategic role in promoting shared learning, accelerating talent development, strategic locality right in the heart of the Bayan Lepas Free Industrial Zone, and a large portfolio of members comprising of over 150 local and multinational companies.

3. APPROACH

3.1. Tripartite Approach

To pioneer this initiative, the Malaysian government took a tripartite approach, involving Khazanah Nasional Berhad (a Government investment arm), PSDC (a non-profit society) and Cisspr Sdn. Bhd. (an entrepreneur enterprise).

Khazanah Nasional Berhad is the investment holding arm of the government of Malaysia and is empowered to nurture the development of new industries and markets [5]. PSDC is a non-profit training and educational centre built on a tri-partied partnership model between the Government, Industry and Academia that embodies a dynamic and sustainable human capital development institution [6]. Cisspr Sdn. Bhd. is a premier test services and solutions provider in Malaysia, engaged to setup, operate and manage the daily operations of the PSDC EMC Laboratory and bring it to international recognition through ISO/IEC17025 accreditation [7].

This unique KHAZANAH-PSDC-CISSPR partnership fits seamlessly into the tripartite model, with KHAZANAH facilitating government capital funding, PSDC providing operational seed funding and laboratory building, and CISSPR offering EMC subject matter expertise and laboratory management.

3.2. Voice of the Industry

As this is an industry-driven initiative designed to serve the needs of the industry, a strong voice from the industry is crucial. To provide this voice, an EMC Expert Group was formed with representatives from diverse industries, ranging from audio-video, automotive, embedded systems, lighting, power tools, telecommunications to test and measurement. It includes MNCs and SMEs such as Aemulus, Affinex Technology, Agilent Technologies, Blaupunkt, Robert Bosch, Ceedtech Technology, Motorola Solutions and Sony. The Expert Group proved to be an effective steering committee that helps in defining appropriate specifications for the laboratory and ensures that industry requirements as well as national, regional and international standards are met.

3.3. Test Systems

3.3.1. Selection

In order to achieve a fine balance between the needs of the industry with the latest technical requirements of the standards and the constraints of the allocated budget, the laboratory engaged one competent, experienced and internationally recognized turn-key solutions provider with a reputable track record to provide a complete solution for the entire test systems, incorporating system integration, calibration and training.

Using this approach, an invitation was sent to several renowned professional EMC test solutions providers to submit their proposals for review and evaluation by the Expert Group. Selection was based on a number of criteria, such as technical specifications of the chambers, compliant test equipment and software, quality and reliability, calibration and maintenance, technical training, customer service and support, cost, delivery time, etc.

3.3.2. Setup

PSDC EMC Laboratory was setup to offer a comprehensive range of EMC testing to meet the requirements of various industries. It comprises of five main test systems designed to support over 50 national, regional and international standards. This is defined in Table 1.

3.3.3. Site Validation and System Verification

Upon completion of the construction of the anechoic chambers and shielded enclosures, a competent, experienced and internationally recognized site validation test provider was engaged to

Table 1: Types of test systems.

Test System	**Test Measurement**	**Industry**
10 m Semi-Anechoic Chamber (SAC)	Radiated Emissions	• Automotive Components • Broadcast Receivers and Associated Equipment • Electrical Equipment for Measurement, Control and Laboratory Use • Household Appliances • Industrial, Scientific, and Medical (ISM) • Information Technology Equipment (ITE) • Land Mobile Radio (LMR) • Lighting • Medical
3 m Compact Anehoic Chamber (CAC)	Radiated RF EM Field Immunity	
Electrostatic Discharge (ESD)	Electrostatic Discharge	
Conducted Emission (CE)	Conducted Emissions; Harmonic Current Emissions; Voltage Changes, Fluctuations & Flicker	
Conducted Immunity (CI)	Conducted RF Fields Disturbances; Electrical Fast Transient / Burst; Surge; Voltage Dips, Short Interruptions & Voltage Variations; Power Frequency Magnetic Field	

Table 2: Site validation measurements.

Measurement	**Standard**	**Frequency Range**
Shielding Effectiveness (SE)	EN 50147-1	10 kHz–40 GHz
Normalized Site Attenuation (NSA)	ANSI C63.4, CISPR 16-1-4	30 MHz–1 GHz
Site Voltage Standing Wave Ratio (SVSWR)	CISPR 16-1-4	1 GHz–18 GHz
Field Uniformity (FU)	IEC 61000-4-3	80 MHz–18 GHz

perform site validation for the laboratory as a test site qualification. System verification was conducted by proficient laboratory staff to ensure test equipment and software are capable to meet standard specifications as a complete test system. This includes ambient noise and reference source measurement, test pulse verification, as well as field calibration and verification. All test equipment are calibrated by competent ISO/IEC 17025 accredited calibration provider to assure test data accuracy and traceability. Site validation and system verification are crucial to ensure test results produced are valid and repeatable. Table 2 shows a list of validation measurements that were carried out.

3.4. People

Commissioning the first public EMC laboratory in Malaysia equipped with a 10-meter semi-anechoic chamber, furnished with hundreds of new equipment capable to support over 50 test standards, and bring it from ground zero to an internationally recognized level is tremendously challenging. Engaging the right people, with the right expertise, experience and dedication is the key to success.

To startup requires a highly competent Technical Manager with a team of Test Engineers and Specialists, well versed in the latest EMC test methods, systems and standards, including hardware, software, calibration, validation, verification and troubleshooting capabilities. This is crucial to overcome all the technical hurdles faced during the startup phase, and to keep laboratory up-to-date with the latest EMC requirements.

To bring it to the next level for international recognition the laboratory requires a proficient Quality Manager, well versed in the demand of ISO/IEC 17025 Quality Management System, with the experience, knowledge and skills of setting up a new quality system, managing document control, management reviews, audits, training, etc. and finally achieving ISO/IEC 17025 accreditation by an internationally reputable accreditation body.

The laboratory organization was structured with minimum hierarchy layers to reduce complexity, maximize learning and people development. Roles and responsibilities are clearly defined, covering both technical and quality areas. Figure 1 illustrates the laboratory organization structure.

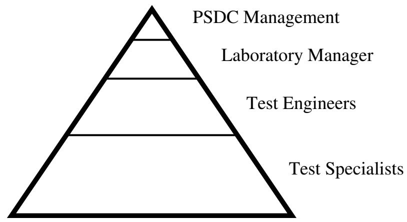

Figure 1: PSDC EMC laboratory organization structure.

- **PSDC Management:** Responsible to allocate sufficient funding and resources to ensure high quality, continuous improvement and an effective ISO/IEC 17025 laboratory management system.
- **Laboratory Manager:** Responsible to manage overall laboratory operations, and ensure laboratory remains in compliance with ISO/IEC 17025 standard requirements.
- **Test Engineers:** Responsible to understand customer requirements, to develop test plans and ensure testing performed fulfill standard and customer requirements.
- **Test Specialists:** Responsible to perform testing in accordance with test plan and laboratory procedures.

3.5. Accreditation

PSDC EMC Laboratory is ISO/IEC-17025 accredited by the American Association for Laboratory Accreditation (A2LA). The laboratory received the ISO/IEC-17025 accreditation certificate from A2LA on 5th January 2012, with certificate number 3185.01. Achieving accreditation to this international standard is proof that the laboratory has demonstrated its technical competency to produce valid and accurate test results. This allows the laboratory to provide compliance EMC testing for type approvals, and pre-compliance testing for prototype evaluations. The laboratory's accredited test reports are recognized worldwide for E&E products or components which are locally-designed and set for export to the European and US markets [8].

A2LA was chosen as the laboratory's accreditation body owing to its international recognition, high reputation and signatory to the International Laboratory Accreditation Cooperation (ILAC) Mutual Recognition Arrangement (MRA). These agreements facilitate the acceptance of test reports between various governmental and regulatory organizations on national, regional and international levels and ensure test results meet the same minimum standards for quality regardless of the laboratory's accreditation body.

4. CHALLENGES

While the rise of emerging technologies is desirable and essential to bring advancement to the modern world, it poses an increased challenge to the field of electromagnetic compatibility compliance. The following are the challenges faced by the EMC testing laboratories and design engineers in Malaysia.

Standard Requirements — One of the major challenges today for EMC laboratories is in managing and keeping up-to-date with the latest test standards. Changes are rapid, mainly driven by the accelerated development of E&E industry, in particularly multimedia and wireless technologies. The addition of new EMC requirements, stringent customer specifications and standard up-revisions, require tremendous efforts and financial resources to enhance laboratory test capabilities so that it always remains current.

Inter-laboratory Comparison — Inter-laboratory comparison is crucial to minimize site-to-site variation between laboratories. This is to ensure test results from different laboratories are comparable which in turn ease product design efforts and product quality control when multiple test sites are used. Inter-laboratory comparison activities between laboratories should be encouraged and conducted at regular interval.

Standards Harmonization — To date, EMC standards are still not fully harmonized in all regions of the world. This leads to a significant increase of time, effort and cost to perform multiple testing on the same product to cater for different standards in the effort to enable global market access. The process to achieve EMC compliance can be daunting and perplexing, especially for those who are new to EMC. Further standard harmonization efforts at international level will definitely benefit the industry.

EMC Community — An EMC Community comprises of various industry players in providing a common platform for EMC technical knowledge sharing and exchange will enhance EMC awareness, as well as to strengthen EMC expertise in the nation. Active involvements and strong commitments from diverse EMC industry players are indispensable for the realization and success of such community.

5. CONCLUSIONS

The tri-partite approach used proved to be very successful based on the laboratory's outstanding achievement to establish the laboratory from concept to reality in a mere two-year period, as depicted in the following roadmap. The realization of the PSDC EMC Laboratory as the country's first public EMC Laboratory furnished with a 10-meter semi-anehoic chamber represents a significant milestone in Malaysia's EMC development.

- **Mar 2009:** Industry roundtable held.
- **Apr 2009:** EMC Expert Group formed.
- **May 2009:** Grant of 30 million ringgit announced by Tan Sri Nor Mohamed Yakcop, Minister in the Prime Minister's Department.
- **Nov 2009:** Building construction began.
- **June 2010:** Building construction completed.
- **Aug 2010:** EMC anechoic chambers ready.
- **Oct 2010:** PSDC EMC Laboratory launching by Tan Sri Nor Mohamed Yakcop.
- **Nov 2010:** Laboratory started trial testing.
- **Jan 2011:** Laboratory started pre-compliance testing services to serve the industry.
- **Jan 2012:** PSDC EMC Laboratory obtained ISO/IEC-17025 accreditation and international recognition. Started offering compliance testing services to serve the industry.

ACKNOWLEDGMENT

The authors wish to express our most sincere appreciation and deepest gratitude to Tan Sri Nor Mohamed Yakcop (Minister in the Prime Minister's Department), Dato' Boonler Somchit (Chief Executive Officer of the PSDC), EMC Expert Group, all staff members of Khazanah Nasional Bernad, PSDC, A2LA, and Cisspr Sdn. Bhd. for their full support and contributions to the successful realization of the PSDC EMC Laboratory.

REFERENCES

1. "Electronics and electrical," Overview of the National Key Economic Areas, Performance Management and Delivery Unit (PEMANDU), n.d. Web. 01 Aug. 2011, http://etp.pemandu.gov.my/Overview_of_NKEAs_-@-Electronics_and_Electrical.aspx.
2. Singh, S., et al., "Lim Chong Eu — Penang's Father of Industrialisation," *News Straits Times*, The New Straits Times Press (Malaysia) Berhad, Nov. 24, 2010, Web. 10 Aug. 2011, http://e.nst.com.my/nst/articles/ChongEupassedaway/Article/art_print.
3. "Your investment destination for next-generation technology," *Opportunities in the Electronics Industry in Penang*, Invest-in-Penang Berhad, n.d. Web. 10 Aug. 2011, http://www.investpenang.gov.my/bs/eeoppor.php.
4. Emmanuel, M., "Country to save RM3m a year with EMC lab," *Business Times*, Oct. 30, 2010. *Penang Skills Development Centre Latest News*, Web. 10 Aug. 2011, http://www.psdc.org.my/WebLITE/Applications/news/uploaded/docs/BusinessTimes_301010.pdf.
5. "Khazanah at a glance," *Home*, The Khazanah Nasional Berhad, n.d. Web. 2 Sept. 2011, www.khazanah.com.my.
6. Dato, Somchit, B., "CEO's message," *About Us*, Penang Skills Development Centre, n.d. Web. 2 Sept. 2011, http://www.psdc.org.my/html/default.aspx?ID=9&PID=15.
7. "A place where innovation meets excellence," *About Us*, Cisspr Sdn. Bhd, n.d. Web. 2 Sept. 2011, http://www.cisspr.com/About.html.
8. "Penang's EMC lab poised to draw more foreign investments," *Business Times*, Penang Skills Development Centre Latest News, Jan. 26, 2012, Web. 26 Jan. 2012, http://www.psdc.org.my/html/news_details.aspx?ID=531&Type=News.

Electromagnetic Shielding of Expanded Polystyrene Doped with Copper, Zinc and Graphite

E. Wiese and M. Yarlequé
Pontificia Universidad Católica del Perú, Sección Telecomunicaciones
Av. Universitaria 1801, Lima-32, Lima, Perú

Abstract— The continuous growth of the telecommunications has brought up more connectivity as well as interference, mainly electromagnetic. One way to reduce it is by employing metallic enclosure, however, there are sceneries where metal shielding is not practical due to his weight, rigidity and proneness to corrosion. Conductive polymer has become a promising material to overcome these issues. In this work, a review of the conductive polymers principles is realized as well as the development and evaluation of expanded polystyrene (EPS) doped with copper, zinc and graphite at 9.6 GHz is presented.

1. INTRODUCTION

In the last decades, a new class of organic polymers, called synthetic metals, has been investigated and developed. These metals are capable of conducting electric current with the purpose of being a replacement to metal conductors for specific functions.

The research on this conductivity principle in non metal materials has caught the attention of scientist from different fields, such as chemists, physicists, electric engineers and matter scientists, who have decided to work towards a common goal: to control the electrical and metallic properties of these materials. As a result, the conducting polymers field has become an interdisciplinary one [1, 2].

Interestingly, this research started due to a laboratory error. In 1974, Hideki Hirakawa was preparing polyacetylene using a Ziegler-Nata polymerization catalyst when, due to an accident caused by the acetylene gas flow through an n-heptane solution and through the Ziegler $Ti(OC_4H_9)_4$ $/Al(C_2H_5)_3$ catalyst, which was already exceeding on substance in relation to the quantity normally used. This combination resulted in a film called polycrystalline, which showed conductivity traits. Later in 1977 [5], Shirakawa (Tokio Institute of Technology, Japan), A. Mac Diamid (University of Pennsylvania) and A. Heeger (University of California) discovered that the partial oxidation with iodine, or other reactive elements, makes the polyacetylene 109 times more conductive than the original. These studies earned the Nobel Prize of Chemistry.

This process is called doping, due to its similarity to semiconductors. In other words, it is when a material that is not conductive itself can acquire this quality through the inlay of chemical components, which should have certain characteristics in common.

2. GENERAL TERMS

Although conductivity in the conductive polymers can reach metallic values ($\sigma > 10^4$ S/cm), it is different from metallic conductivity. In the case of conductive polymers, it follows a complex process, which depends on the preparation and doping. Several mechanisms have been used to create such conductivity [5].

In a conductive material, the electric flow comes from the movement of electrons, which can move in and through discrete energy states, known as bands. Each band has a limited capacity for electrons, and the bands can also be empty. The movement of the electrons only occurs between partially full bands. The electric flow can neither happen in completely full bands, nor in empty bands, like in the case of isolators and semiconductors. On the other hand, metals have partially full bands. There are two types of bands that determine the electrical conductivity in a material. The band with the highest degree of occupation is called valence band, whereas the one above it is known as the conduction band [1, 3].

To be able to make a polymer with have an acceptable conductivity value, it must comply with two characteristics:

- **Type N Doping**: In which there should be a certain quantity of exceeding ions. This way, absence of π bonds will form inside the polymer parts, which in term an electron will be required to fill.

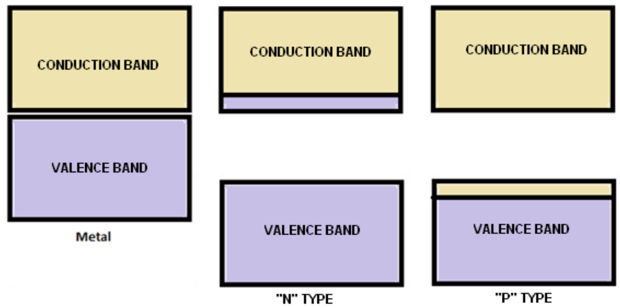

Figure 1: Comparison of metal, N-type doping and p-type doping.

- **Type P Doping**: In which there is a large number of ions, which will generate excess electrons inside the polymer, forcing them to find a place inside the polymer's chain where they can remain and form π bonds.

The diagram in Fig. 1 outlines the bands for each type of doping compared to metal.

3. TYPES OF SYNTHESIZING

Organic synthesis is a planned construction of organic molecules through chemical reactions. Organic molecules tend to be more complicated compared to basic inorganic compounds. As a result, organic compounds synthesis has become one of the most important aspects of organic chemistry [4].

In this work, two synthesis were used for creating a polymer:

Through the monomer's chemical oxidation: in a monomeric dissolution, an oxidant, whose oxidation potential is the same as the monomer's is added. By doing so, the monomer's Pi bond will be able to join one chain of monomers to another, consequently creating conductive polymers — thanks to the movement of the electrons inside them [2].

Through electro-chemical oxidation: this synthesis is similar to the previous one, with the only difference that in this case the process is heterogenic and it is produced on the anode of an electrochemical cell that contains a type of dissolvent. The cell allows the flow of the current and favors the polymer's oxidation.

4. EXPLANATION OF THE CONDUCTING POLYMER'S CONDUCTIVITY

The conductivity in conductive polymers can not be explained by the theory of bands because of the following reasons:

- The atoms are linked to one another covalently, forming polymeric chains that experience weak intermolecular interactions.
- The macroscopic conduction will require the electrons moving, not only through a chain but also from one to the other.
- This theory does not explain the fact that the charge carriers, generally electrons or holes, in polyacetylene and polypirrol, do not spin round the atom but on themselves.

Therefore, a different method should be found to detail the conduction process of a polymer. Some concepts used by physicists, such as solitons, polarones and bipolarones, are taken into account. We must turn to *Solid State Physics* to explain the procedure [6].

The movement of an electron from the maximum value of a conjugated polymer's valence band leaves a hole (or cation) in the conduction band; it's not relocated completely as it would be expected from the classic band theory. A partial relocation is produced, expanding over various monomeric units and causing a structural deformation. The energy level associated to this radical cation represents an unstable orbit and has more energy than the valence band, thus its energetic level lies in the barrier between bands.

This radical cation is partially relocated over a segment of the polymer, and it's defined as polaron. If another electron moves from the polymer with the polaron, another polaron can be formed in the polymer, thus forming a bipolaron.

There are some polymers that have a basic degenerated state, which means they are highly doped. At the moment of starting the doping function between two substances, the electrons will

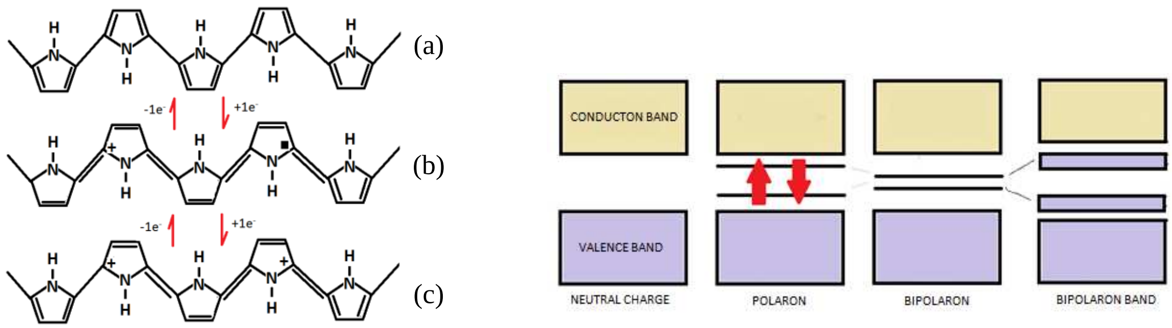

Figure 2: (a) Neutral charge, (b) polaron, (c) porripol bipolaron.

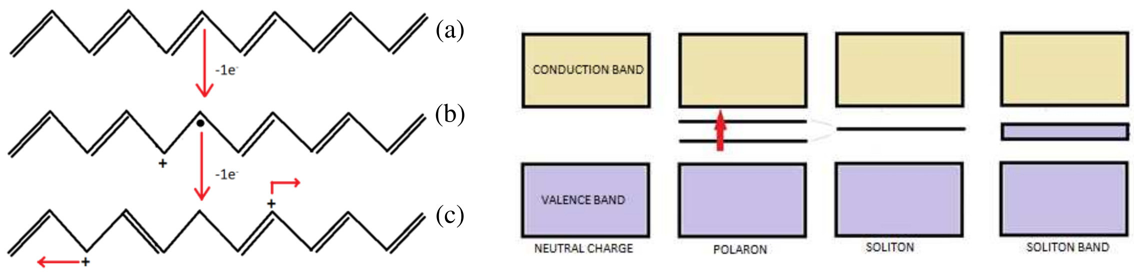

Figure 3: (a) Neutral charge, (b) polaron, (c) porripol soliton.

not follow a fixed direction (going up the Pi superior bond) but will have an electron transmission behavior of opposite phases; in other words, they will move into different directions, and the bipolaron will split in two independent cationic units without spin. These units are called solitons [1, 6].

The graphic in Fig. 2 represents an oxide-reduced synthesis of a conductive polymer.

The graphic in Fig. 3 shows the oxidant tuning of a soliton.

This way, it can be concluded that conductivity of a conductive polymer will be determined by three important points:

- The quantity of Carbon bonds: being C-C or C = C. The electrons will be able to move around the conductive polymer's chain thanks to how easily Carbon joins and separates covalent bonds [2, 6].
- The quantity of Pi bonds: If Pi bonds are created heterogenically, charge holes will be created too, which in term will give way to new bonds and will have conductivity properties.
- Range of the atom's covalent bonds: This will determine how far an electron can be from its nucleus at a time, so the higher the range of possible electron orbits, the simpler the polymer's doping will be.

5. IMPLEMENTATION

Expanded Polystyrene (EPS), was chosen to prove its doping. It was doped with graphite, zinc and copper. The process of the polymer synthesis was explained in Section 3. In Fig. 4, it is shown a guide for the process of oxidation.

This process permits to break pi bonds in the material, which allows storing charge and thus receiving electrons that are transmitted to the expanded polystyrene material used for doping. The dichloromethane solution act as a catalyst, creating voids of electrons in the conduction band The dissolution of the material, which will be seen as the number of pi bonds to break, measure the conductivity of doped material [4].

The laboratory procedure for the synthesis of conducting polymer is as follows:

1 A measure of Expanded Polystyrene is taken, according to the values indicated in Table 1, likewise, for the metal particles

2 The measure of expanded polystyrene is combined with 50 ml of dichloromethane.

3 The metal particles are placed in a 30×30 cm glass surface, which is lined with clay to prevent leakage of acid.

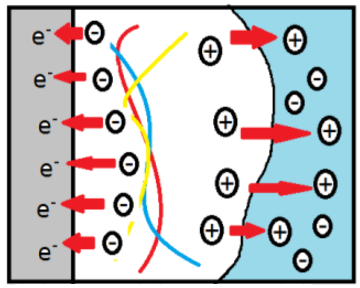

(a) (b) (c)

Figure 4: (a) Material used for doping, (b) expanded polystyrene, (c) diclurometane solution.

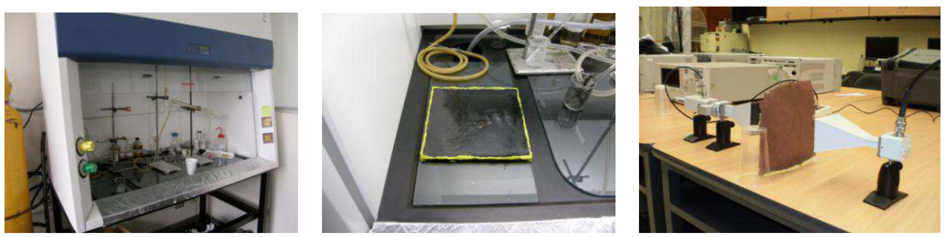

(a) (b) (c)

Figure 5: (a) ESCO fume hood, (b) EPS doped with graphite, (c) measurement of the EPS with copper.

Table 1: Measure of materials used for the process.

Used material	**Expanded polystyrene (g)**	**Metal (g)**
Zinc	1.92	23.18
Graphite	2.6	20.49
Copper	2.66	11.30

Table 2: Measurement equipment characteristics.

FRECUENCY	9.6 GHz
POWER SUPPLY	8.04 V a 472 mA
ANTENNA TYPE	horn antenna
SPECTRUM ANALYZER	Agilent 9 kHz to 26.4 GHz
SIZE OF THE POLYMER	30×30 cm

4 The dissolved polystyrene is added to the particles in the glass surface. This is realized inside an ESCO fume hood (see Fig. 5(a)), which will extract the gases that occur during the mixture.

5 The process is complete in about a couple of hours per sample (see Fig. 5(a)), and then is left in open air for one week.

A Lucas-Nulle module with their antennas and signal generator was employed for the tests together with an Agilent Spectrum Analyzer. The technical characteristics are specified in Table 2, and the measurement setup can be observed in Fig. 5, when the copper-doped polymer is measured.

The obtained results are reported in Table 3. Conventionally, we would expect that EPS doped with copper and zinc (high conductivity) would outperform the shielding features of the EPS doped with graphite (with lower conductivity). However, measurements show that the latter exhibits the best shielding characteristics at 9.6 GHz. EPS doped with graphite provides 10 dB more shielding than EPS with copper, and 16 dB more than EPS with zinc. This can be understood since the presence of the delocalized π orbital of the graphite improves conductivity, like it was a soliton. Similarly, the graphite double bonds improve the transport of the electrons in the polymer while copper and zinc do not provide further bonds in the polymer structure.

Table 3: Experiment results.

SIGNAL TYPE	RECEIVED POWER (dBm)	ATTENUATION
Free air	5.97	—
EPS with coope	−2.656	8.63
EPS with Zin	1.96	4.01
EPS with graphit	−13.96	19.9

6. CONCLUSION

In this paper, the principles of conductive polymer have been reviewed, the preparation of this employing expanded polystyrene doped with Copper, Zinc and Graphite has been shown and the performance at 9.6 GHz were measured and analyzed. Contrary to the conductivity behavior of the isolated doping material, high conductivity for the Copper and Zinc, and lower conductivity for graphite, when these materials are used as dopants, the resulting conductive polymer exhibit the highest conductivity and shielding with graphite.

REFERENCES

1. Armelin, J., I. Iribarren, J. Casanovas, F. Liesa, and C. Alemán, "Polímeros conductores con aplicaciones biomédicas y biotecnológicas," *Química e Industria*, Jul. 2004.
2. Inzelt, G., "Conducting polymers," *A New Era in Electrochemistry*, Berlin, Germany, 2008.
3. Dunne, D., *Electromagnetic Shielding Techniques for Inductive Powering Applications*, Galway, Ireland.
4. Fernandez, T., "Polimeros conductores: Sintesis, propiedades y aplicaciones electroquímicas," *Revista Iberoamericana de Polímeros*, Vol. 4, 2003.
5. Choy, M., "Polímeros conductores como alternativa tecnológica en la protección de nuestro ambiente," Universidad de los Andes, Merida, Venezuela, 2007.
6. Pratt, C., "Conducting polymers," Kingston University, London, 1996.

Computation of Coupled Voltage to an Unshielded Cable Due to Transient EM Fields Radiated by ESD

Rajashree Narendra[1], **M. L. Sudheer**[2], **V. Jithesh**[3], **and D. C. Pande**[3]

[1]BNMIT, Bangalore, India
[2]UVCE, Bangalore, India
[3]EMI/EMC Group, LRDE, Bangalore, India

Abstract— The increasing development of dispersed but highly interconnected systems of telecommunication centers, computers and control equipments leads to an extensive use of cables to avoid interference problems. When an external electromagnetic field interacts with an imperfectly shielded cable, the interconnecting cables act as collectors of energy and considerable amount of energy can be coupled into the systems. The induced current and voltage transients may then cause damage or malfunction of sensitive electronic circuits. Simulation of structural current due to an Electrostatic discharge (ESD) event involves passing large transient currents through the object under test. This causes radiation of transient electromagnetic fields in the environment and induced transient voltages into the cables and equipments. A coupling model is developed to estimate the extent of coupling of transient EM fields to cables.

A coupling model is presented to predict induced terminal voltages on an unshielded cable placed above a ground reference plane due to transient electromagnetic fields radiated by Electrostatic discharge (ESD). The unshielded cable is exposed to the free space-radiating field due to IEC 61000-4-2 ESD waveform. The transient current is represented by Hertzian dipole elements and the time domain expressions for the resultant electric field intensity at any point are obtained. The frequency spectrum of the electric field is obtained using Discrete Fourier Transform. Assuming that the incident transient electric field is parallel to the cable termination, the frequency spectrum of the coupled voltage at the terminations is computed. The time domain representation of the terminal induced voltage is determined using Inverse Discrete Fourier Transform (IDFT). Computed results are presented for the contact discharge IEC 61000-4-2 ESD current waveform at 8 kV and air discharge IEC 61000-4-2 ESD current waveform at 16 kV. The coupled voltage into an unshielded cable is computed for resistive termination and RC shunt termination. The coupled voltage reduces from 6.25 V for ESD air discharge and 625 V for ESD contact discharge for a resistive termination to 0.325 mV for ESD air discharge and 7.8 mV for ESD contact discharge for a RC shunt termination.

1. INTRODUCTION

The coupling of electromagnetic fields inside shielded cables is an important issue in EMC applications. Cables are widely used to connect electrical and electronic apparatus in order to reduce possible electromagnetic interference (EMI). Nevertheless, the cable can collect the electromagnetic disturbance produced by external fields and damage sensitive circuits and systems [1]. It is therefore important to develop software tools able to predict induced effects in various cable configurations.

This work is modeled on similar work [2] for fields at 1m distance from the ESD source and for a typical capacitive spark discharge current waveform. We have carried out the present work for the contact discharge IEC 61000-4-2 ESD current waveform at 8 kV and air discharge IEC 61000-4-2 ESD current waveform at 16 kV. The coupled voltages due to ESD induced transients for resistive and RC shunt termination are computed.

2. TRANSIENT CURRENT SOURCE

In the present model, standard IEC 61000-4-2 ESD waveform is used as the current waveform. Spline interpolation technique is used for computing the current values $i(t)$ from the standard IEC 61000-4-2 ESD waveform for contact discharge shown in Figure 1. The waveform has a 1 ns rise time and peak amplitude of 37.5 A at 8 kV (maximum value) for the case of contact discharge. Spline interpolation technique is used for computing the current values $i(t)$ from the air discharge waveform shown in Figure 2. The waveform has peak amplitude of 30 A at 35 ns. The analysis for both of these waveforms is carried out as the standard IEC 61000-4-2 ESD waveform holds good only for contact discharge and IEC has not defined the waveform separately for air and contact discharge. We have considered the waveforms from [3], which has the waveform for contact

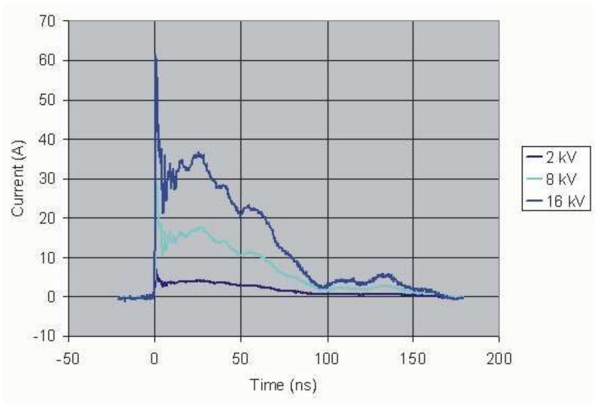

Figure 1: Contact discharge to IEC 61000-4-2 target.

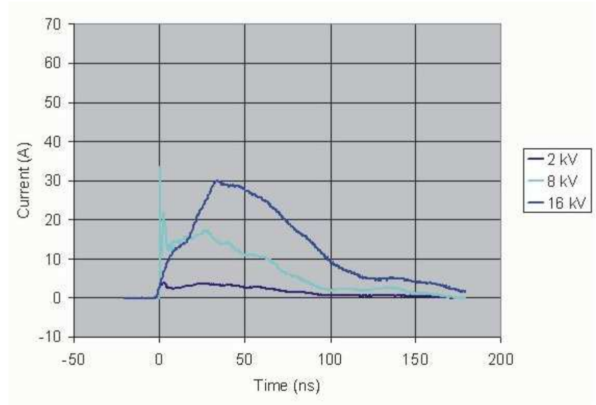

Figure 2: Air discharge to IEC 61000-4-2 target.

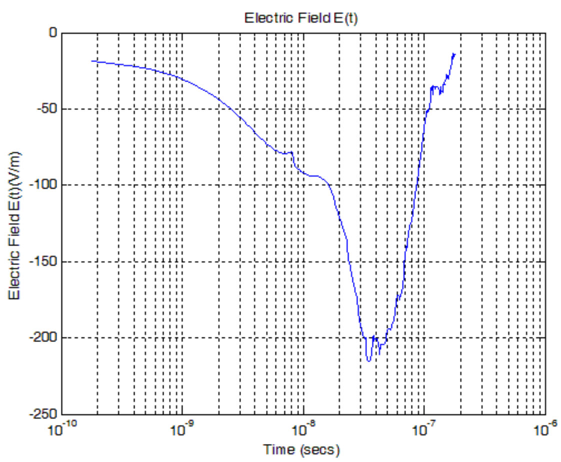

Figure 3: Electric field $E(t)$ for air discharge IEC current waveform.

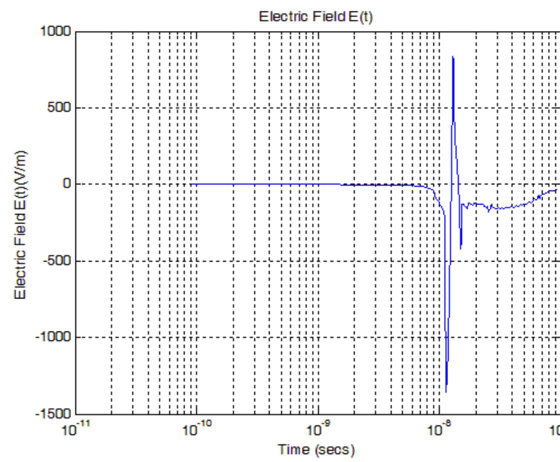

Figure 4: Electric field $E(t)$ for contact discharge IEC current waveform.

discharge as shown in Figure 1 same as the standard IEC 61000-4-2 ESD waveform and a different waveform for the air discharge as shown in Figure 2. We have considered the waveform for the worst cases being 8 kV for contact discharge and 16 kV for air discharge. The main difference between the contact and air discharge is the rise time of 1 ns during which the current overshoots to a high value of 37.5 A in the case of contact discharge. In case of the air discharge at 16 KV this overshoot does not exist.

3. RADIATED TRANSIENT FIELDS

The current elements have been modeled as Hertzian dipoles [4, 5]. The field components at any point $P(r, \theta, \varphi)$ of the dipoles expressed in terms of spherical coordinates r, θ, and φ are

$$E_r(t) = \frac{L\cos\theta}{2\pi}\left(\eta_0\frac{i(t)}{r^2} + \frac{\int i(t)\,dt}{\varepsilon_0 r^3}\right) \tag{1}$$

$$E_\theta(t) = \frac{L\sin\theta}{4\pi}\left(\frac{\mu_0}{r}\frac{d}{dt}i(t) + \eta_0\frac{i(t)}{r^2} + \frac{\int i(t)\,dt}{\varepsilon_0 r^3}\right) \tag{2}$$

$$H_\varphi(t) = \frac{L\sin\theta}{4\pi}\left(\frac{1}{rc}\frac{d}{dt}i(t) + \frac{i(t)}{r^2}\right) \tag{3}$$

where $\mu_0 = 4\pi \times 10^{-7}$ H/m = permeability of free space; $\varepsilon_0 = 1/(36\pi) \times 10^{-9}$ F/m = permittivity of free space; $c = 3 \times 10^8$ m/s, velocity of light in free space; $\eta_0 = 120\pi$ = intrinsic impedance of free space; L = length of the current element; $t = t' - (r/c)$ = time variable for retarded current; r = distance between the centre of current element $i(t)$ and point $P(r, \theta, \varphi)$.

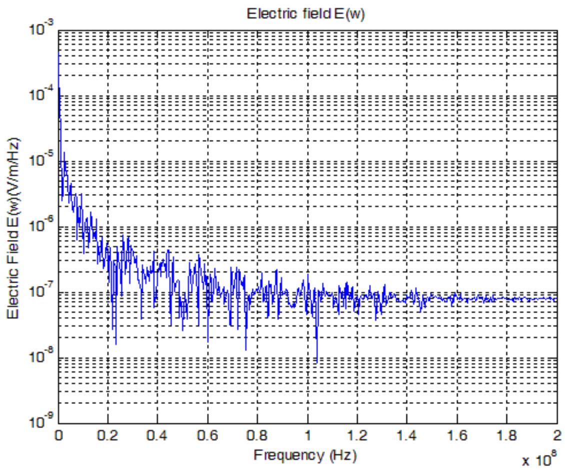

Figure 5: Frequency spectrum of the E-field $E(\omega)$ for air discharge IEC current waveform.

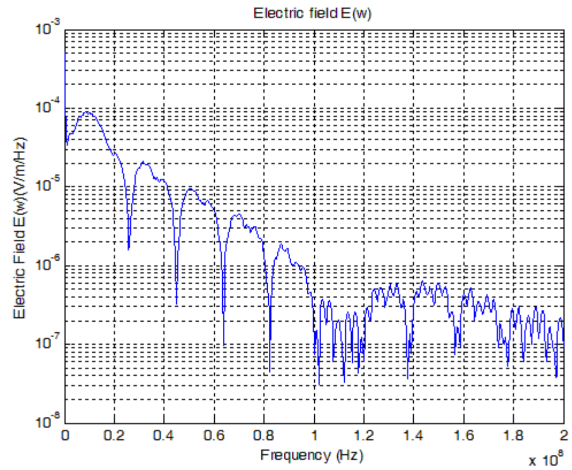

Figure 6: Frequency spectrum of the E-field $E(\omega)$ for contact discharge IEC current waveform.

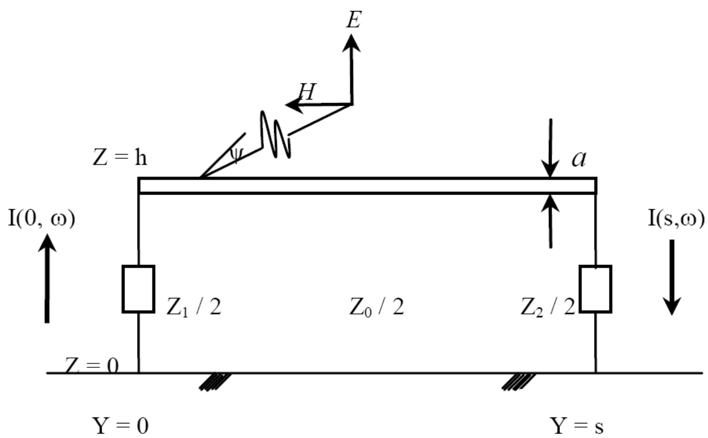

Figure 7: Field to unshielded cable coupling over a ground plane.

4. E-FIELD COMPONENT DUE TO ESD SIMULATION

The field intensities at any point on the x-y plane can be obtained from Equations (1) to (3) by substituting $\theta = \pi/2$. The E-field intensities along the x-direction are obtained in Figure 3 and Figure 4 for the ESD simulation current source with $L = 1\,\text{m}$. The frequency spectrum of the E-field $E(\omega)$ in Figure 5 and Figure 6 are obtained by taking discrete Fourier Transform (DFT) of the sample points of the Electric field time domain plot.

5. FIELD TO UNSHIELDED CABLE COUPLING

The coupling of transient E-field radiated by ESD simulation currents to an unshielded cable over a ground reference plane (x-y plane) is as shown in Figure 7. Assuming that the incident transient E-field is uniform and parallel to the termination, the induced currents at the left and the right terminations of an unshielded cable over a ground plane [6] are respectively given by

$$I(0,\,\omega) \;=\; \frac{4E(\omega)h}{D}\left[\{Z_o\cos\beta s + jZ_2\sin\beta s\} - Z_o\{\cos(\beta s\sin\psi) - j\sin(\beta s\sin\psi)\}\right] \qquad (4)$$

$$I(s,\,\omega) \;=\; \frac{4E(\omega)h}{D}\left[Z_o - \{Z_o\cos\beta s + jZ_1 sm\beta s\}\{\cos(\beta s\sin\psi) - j\sin(\beta s\sin\psi)\}\right] \qquad (5)$$

where $E(\omega) =$ Frequency spectrum of the incident E-field. $h =$ height of the cable over a ground plane in m; $a =$ diameter of the cable in m. $s =$ length of the cable in m; $Z_1/2$ and $Z_2/2 =$ left and right terminating impedances in ohms. $Z_0/2 =$ characteristic impedance of the line in ohms; $\psi =$ angle of incidence of E-field to the line; $\lambda =$ wavelength; $\omega = 2\pi f$, where f is frequency in Hertz; $\beta = 2\pi/\lambda =$ phase constant of the line.

The induced voltages at the left and right terminations respectively are then given by

$$\frac{Z_0}{2} = 138 \log 10 \left[\frac{2h}{a} + \sqrt{\frac{4h^2}{a^2} - 1} \right] \tag{6}$$

$$D = (Z_0 Z_1 + Z_0 Z_2) \cos \beta s + j(Z_0^2 + Z_1 Z_2) \sin \beta s \tag{7}$$

$$V(0, \omega) = I(0, \omega) \frac{Z_1}{2} \tag{8}$$

$$V(s, \omega) = I(s, \omega) \frac{Z_2}{2} \tag{9}$$

6. COUPLED VOLTAGE FOR RESISTIVE AND RC SHUNT TERMINATION

Using Equations (8) and (9) and the frequency spectrum of the transient E-field, the frequency spectrum of the coupled voltage at the termination of an unshielded cable over a ground plane has been computed for $s = 0.3\,\mathrm{m}$; $h = 0.01\,\mathrm{m}$; $a = 0.914 \times 10^{-3}\,\mathrm{m}$; $Z_1/2 = Z_2/2 = 10\,\mathrm{k\Omega}$; (resistive termination); $R = 10\,\mathrm{k\Omega}$; $C = 0.01\,\mu\mathrm{F}$ (RC Shunt).

The frequency spectrum of the coupled voltage are as shown in Figure 8 and Figure 9.

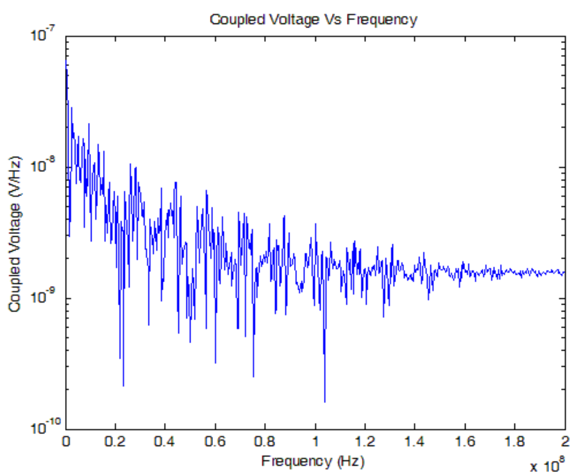

Figure 8: Frequency spectrum of the coupled voltage across resistive termination for air discharge IEC.

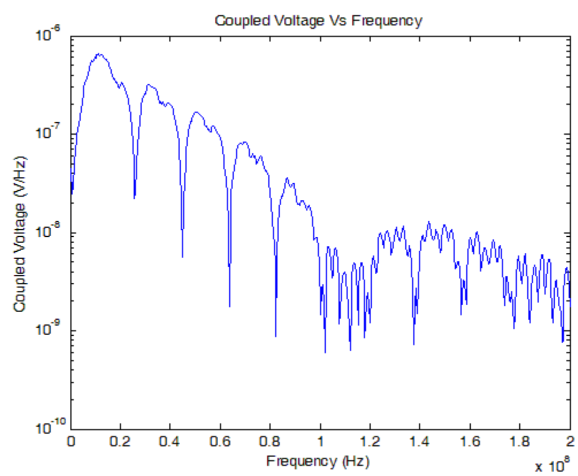

Figure 9: Frequency spectrum of the coupled voltage across resistive termination for contact discharge IEC.

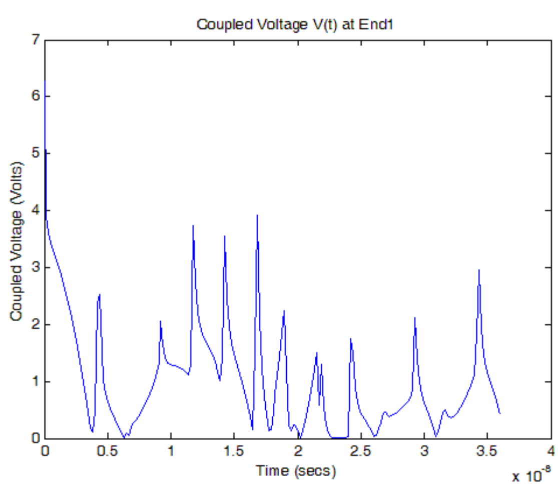

Figure 10: Time domain representation of the coupled voltage across resistive termination for air discharge IEC.

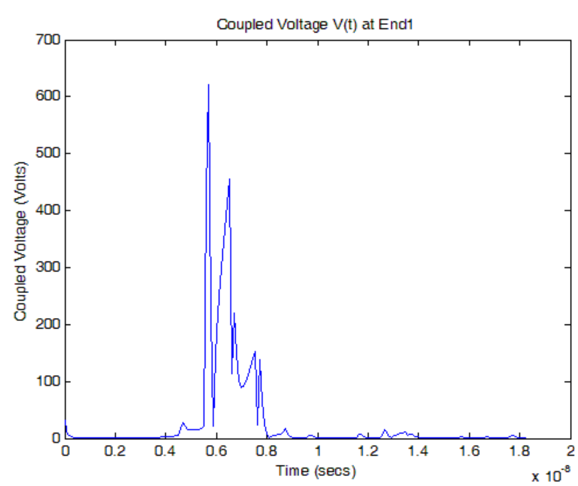

Figure 11: Time domain representation of the coupled voltage across resistive termination for contact discharge IEC.

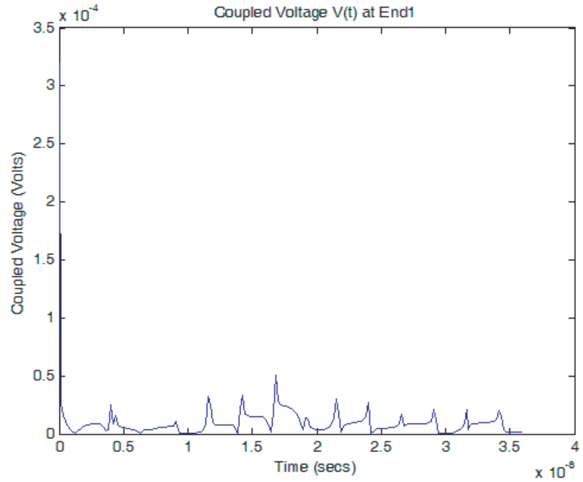

Figure 12: Time domain representation of the coupled voltage across RC Shunt termination for Air discharge IEC.

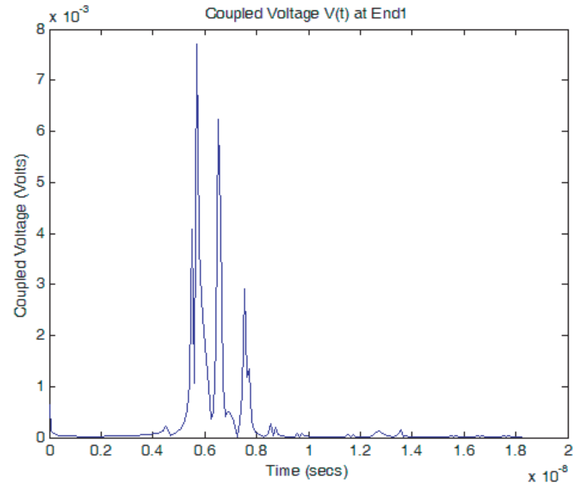

Figure 13: Time domain representation of the coupled voltage across RC Shunt termination for Contact discharge IEC.

The time domain representation of the coupled voltage for resistive termination shown in Figure 10 and Figure 11 is obtained by taking Inverse Discrete Fourier Transform (IDFT) of the sampled points. The time domain representation of the coupled voltage for RC Shunt termination is as shown in Figure 12 and Figure 13. The coupled voltage plots are same at both end 1 and end 2 of the unshielded cable for resistive and RC shunt termination. The coupled voltage is very small in magnitude for RC shunt termination compared to the resistive termination. The coupled voltage reduces from 6.25 V for air discharge and 625 V for contact discharge for a resistive termination to 0.325 mV for air discharge and 7.8 mV for contact discharge for a RC shunt termination.

7. CONCLUSION

The coupling of the transient electromagnetic fields generated by ESD currents to an unshielded cable over a ground plane has been modeled. The peak value of the coupled voltage for resistive termination being 600 V is very large compared to 7.8 mV for RC shunt termination for Contact discharge IEC ESD waveform at 8 kV whereas the coupled voltage for resistive termination is 4 to 6 V compared to 0.325 mV for Air discharge IEC ESD waveform at 16 kV. We conclude that RC shunt terminations are preferred compared to the resistive terminations as the coupled voltage is very small in magnitude for RC shunt termination. The use of shielded cables will also lead to significant reductions in the coupled voltage.

REFERENCES

1. Narendra, R., M. L. Sudheer, V. Jithesh, and D. C. Pande, "Mathematical analysis of ESD generated EM radiated fields on electronic subsystem," *Asia-Pacific International Symposium on Electromagnetic Compatibility*, 449–452, Beijing, China, Apr. 12–16, 2010.
2. Narendra, R., M. L. Sudheer, V. Jithesh, and D. C. Pande, "Coupling of transient electromagnetic fields radiated by ESD to unshielded cables," *INCEMIC, Proceedings of International Conference on EMI/EMC*, 493–498, Bangalore, India, Nov. 25–26, 2010.
3. Ashton, R. and O. N. Semiconductor, "Reliability of IEC 61000-4-2 testing on components," *EE Times Design Article*, 8/10/2008.
4. Shastry, S. V. K. and V. K. Hariharan, "Computer aided analysis of ESD effects in dual gate MOSFET VHF amplifier," *IEEE International Symposium on EMC*, 424–430, Aug. 1990.
5. Wilson, P. F., M. T. Ma, and A. R. Ondrejka, "Fields radiated by electrostatic discharges," *IEEE International Symposium on EMC*, 179–183, Aug. 1988.
6. Hariharan, V. K., S. V. K. Shastry, and V. R. Katti, "Coupling of transient electromagnetic field to unshielded cable," *INCEMIC*, 140–146, India, 1991.

Sampling Criterion for EMC Near Field Measurements

O. Franek[1], **M. Sørensen**[2], **H. Ebert**[1], **and G. F. Pedersen**[1]

[1]APNet Section, Department of Electronic Systems, Faculty of Engineering and Science
Aalborg University, Niels Jernes Vej 12, Aalborg 9220, Denmark
[2]Bang & Olufsen a/s, Peter Bangs Vej 15, Struer 7600, Denmark

Abstract— An alternative, quasi-empirical sampling criterion for EMC near field measurements intended for close coupling investigations is proposed. The criterion is based on maximum error caused by sub-optimal sampling of near fields in the vicinity of an elementary dipole, which is suggested as a worst-case representative of a signal trace on a typical printed circuit board. It has been found that the sampling density derived in this way is in fact very similar to that given by the antenna near field sampling theorem, if an error less than 1 dB is required. The principal advantage of the proposed formulation is its parametrization with respect to the desired maximum error in measurements. This allows the engineer performing the near field scan to choose a suitable compromise between accuracy and measurement time.

1. INTRODUCTION

In the research field of electromagnetic compatibility (EMC), there has recently been a considerable interest in near field measurements of electronic modules. The idea of being able to predict radiation levels of electronic devices without the need to use anechoic or semi-anechoic chambers seems certainly appealing. Another emerging application of near field measurements is characterization of electronic modules for the purpose of estimation of mutual coupling between the modules and/or a module and a chassis, which may result in unwanted radiation or intra-device electromagnetic interference [1–3].

In either case, we need to know the appropriate sampling density of the near field measurement in order to accurately extrapolate the fields outside of the measured perimeter. While too low sampling density (large spatial step) leads to inaccuracies in the extrapolated field, too high density (small spatial step) results often in impractically long measurement times. Sampling theorem for near field measurements of antennas is available, having been derived from the plane wave spectra, and can be directly applied to the problem of radiation prediction. Nevertheless, if we want to use the near field measurements as a source to estimate near field coupling, validity of the antenna-based sampling theorem may be limited, because we are now interested in field values very close to the source, i.e., in the reactive near field.

Instead, we focused on the scenario that is typical for EMC near field measurements — a thin trace on a printed circuit board (PCB). The near fields produced by such trace vary with distance to the trace. It is these variations which give rise to errors if the near fields are not sampled densely enough. We will make an attempt at expressing the fields over the trace analytically and quantify the influence of the field variations on measurement error with known sampling density. From here the sampling criterion will follow.

2. ELEMENTARY DIPOLE MODEL

In order to obtain an analytical expression for fields above the PCB trace, we have chosen to approximate the field produced by the trace with that of an infinitesimal electric dipole radiator (Fig. 1). This should represent the worst case in terms of field variations, as we expect conductors with larger volume (i.e., composed of many elementary dipoles) to produce smoother fields.

We also assume that it is the magnetic (H-) field that is dominant in this case and that it will be the H-field components that will be measured, in order to have the signal to noise ratio (SNR) as high as possible.

The H-fields around an elementary dipole are given by [4]:

$$H_\phi = \frac{I_0 h}{4\pi} \mathrm{e}^{-jkr} \left(\frac{jk}{r} + \frac{1}{r^2} \right) \sin\theta, \tag{1}$$

where $r = |\vec{r}| = \sqrt{x^2 + y^2 + z^2}$ is the total distance from the dipole to the point of observation (length of the position vector $\vec{r}$), $k = 2\pi f/c$ is the wavenumber, f is the frequency, c is the velocity

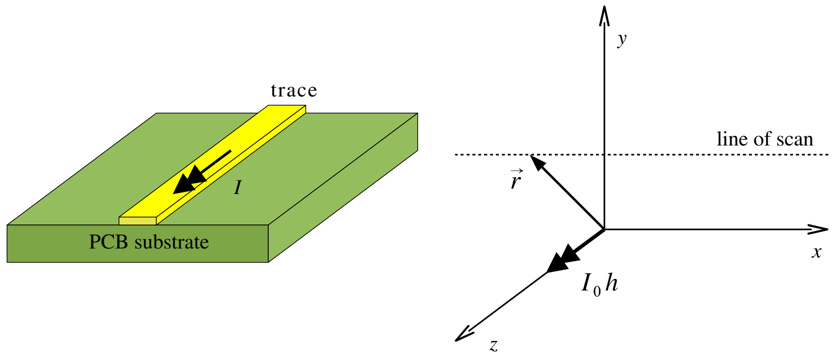

Figure 1: Schematic drawing of the PCB trace and its substitute, the elementary dipole, within the coordinate system. The dashed line denotes the scan trajectory.

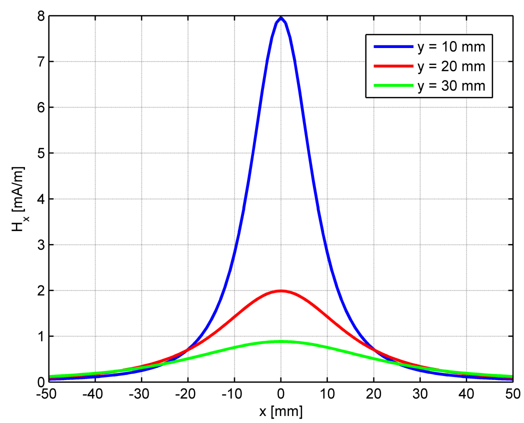

Figure 2: Profile of the H_x field parallel to the x-axis; the dipole moment is 10^{-5} Am.

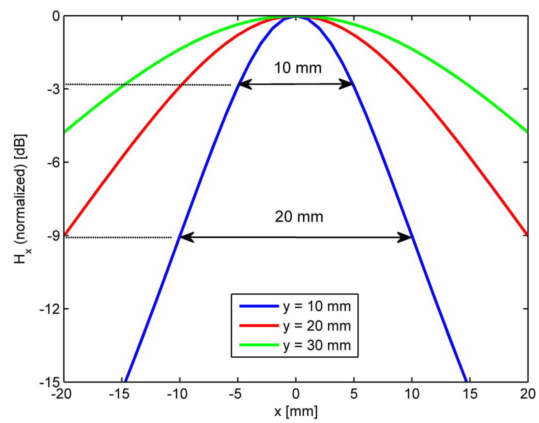

Figure 3: Profile of the H_x field parallel to the x-axis, normalized to the peak value.

of light, θ is the angle between $\vec{r}$ and the z-axis, and the term $I_0 h$ represents the dipole moment, with current I_0 and length of the dipole h.

Let us choose a scanning path perpendicular to the orientation of the dipole at height y over the dipole (denoted by the dashed line in Fig. 1). The dominant component in this case will be the H_x component:

$$H_x = \frac{I_0 h}{4\pi} \mathrm{e}^{-jkr} \left(-\frac{jk}{r^2} - \frac{1}{r^3} \right) y. \tag{2}$$

3. DISCUSSION

Figure 2 shows the magnitude of the H_x component parallel to the x-axis for $z = 0$ and in three different heights y, at frequency 100 MHz. Clearly, the intensity of the field is highest when the scan is performed close to the trace and the SNR will then be the maximum possible. On the other hand, it is the shape of the field profile that causes the errors if the size of the spatial sampling step is insufficient.

In Fig. 3, the H_x component is normalized and evaluated in dB with respect to the peak value occurring right above the trace. If there is no further interpolation of the measured near field samples, then the highest error occurs when the two adjacent samples are positioned symmetrically around the peak value — this is the worst case. The actual value of the peak is then missed by the measurement with an error corresponding to the field drop at half the sampling step from the peak.

Two such situations, for scan steps 10 mm and 20 mm, are displayed as examples in Fig. 3, denoting also the corresponding errors resulting from the respective scan steps at 10 mm height — approximately 3 and 9 dB, respectively. It is evident that there is a tradeoff between SNR of the measurement (following the height) and the sampling rate which influences the error in the peak field value.

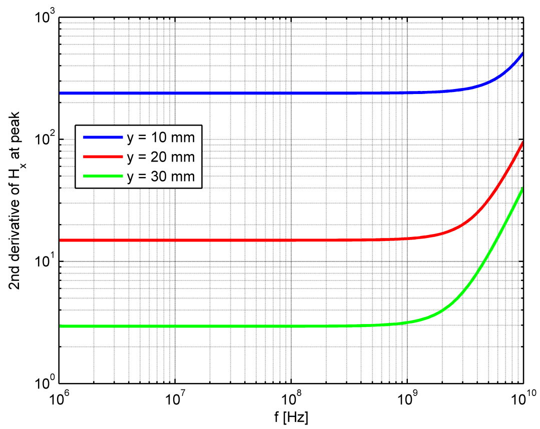

Figure 4: Frequency dependence of the second derivative of H_x at the peak point.

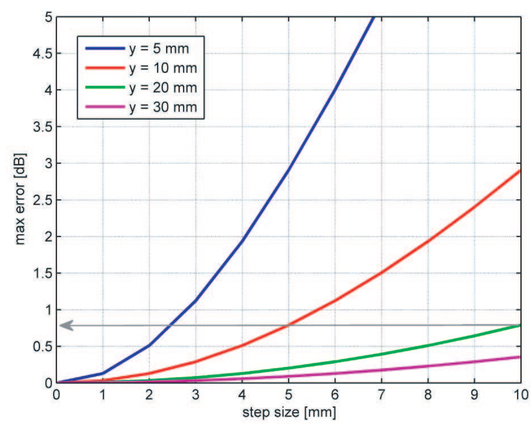

Figure 5: Maximum magnitude error achieveable for various sizes of scan steps; the gray arrow follows $d = 2$.

It is worth noting that the H_x component parallel to the z-axis has the same profile as in Fig. 3, and therefore the same error characteristics. The H_y component is lower in magnitude compared to H_x and its shape is more relaxed. The phase of the fields has been ignored entirely since it has only very smooth variations in the frequency band of interest. Also, in the present assumptions, the effective area of the near field probe is not taken into account, as well as its measurement and positioning accuracy.

The shape of the field is stable with frequency up to about 1 GHz, as documented by the second derivative of the field at the peak presented in Fig. 4. As a result, although Figs. 2 and 5 have been generated at 100 MHz, they would be practically identical in the entire 30 MHz–1 GHz band.

Since we are able to express the peak error resulting from the used scan step as

$$\text{error} = -20\log_{10}\left(\frac{|H_x(x = \Delta s/2)|}{|H_x(x = 0)|}\right), \tag{3}$$

where Δs is the scan step, it appears natural to perform an inverse task — to suggest optimal spatial scan step based on tolerated error level. This can be demonstrated using Fig. 5. If desired magnitude error is not to exceed 1 dB, for example, the spatial scan step should be approximately half the value of the distance from the PCB trace. Incidentally, this very criterion follows also from the widely accepted sampling theorem for near field scans of antennas [5]:

$$\Delta s = \frac{\lambda}{2\sqrt{1+\left(\frac{\lambda}{d}\right)^2}}, \tag{4}$$

where Δs is the scan step, d is the distance of the scanning surface from an antenna, and λ is the wavelength. In the frequency band of interest ($< 1\,\text{GHz}$), the ratio of the distance and the wavelength is very small, $d \ll \lambda$, which gives $\Delta s \approx d/2$. The gray arrow in Fig. 5 points to the error resulting from this criterion: approximately 0.8 dB. If time constraints on the duration of the scan dictate lower sampling density, this can be derived given any chosen acceptable error, as has been shown using Fig. 5.

4. CONCLUSION

In this paper, we have offered an alternative sampling criterion for EMC near field measurements based on worst case error in peak value of the fields. We argue that such criterion is well suited for EMC investigations in which the peak value is of greatest interest with respect to coupling and emission level conformance. It is possible to choose a suitable scan step dependent on the maximum tolerated error, making it flexible for various purposes. The criterion is derived by means of the elementary dipole, which is the least favorable emission source in terms of field variation. However, radiating elements of real PCBs (e.g., traces) have finite, nonzero sizes, and might produce smoother fields than elementary dipole, which opens the possibility for further relaxation of the scan step, provided that minimum size of these elements (e.g., width of a trace) is known. This is a subject for future work.

ACKNOWLEDGMENT

The present work has been supported by the Danish Agency for Science, Technology and Innovation. The authors also gratefully acknowledge the support from the Danish Center for Scientific Computing (DCSC) for the hybrid Linux Cluster "Fyrkat" at Aalborg University, Denmark.

REFERENCES

1. De Daran, F., J. Chollet-Ricard, F. Lafon, and O. Maurice, "Prediction of the field radiated at one meter from PCB's and microprocessors from near EM field cartography," *IEEE International Symposium on Electromagnetic Compatibility*, Vol. 1, 479–482, Istanbul, Turkey, May 2003.
2. Shi, J., M. A. Cracraft, J. Zhang, R. E. DuBroff, and K. Slattery, "Using near-field scanning to predict radiated fields," *IEEE International Symposium on Electromagnetic Compatibility*, Vol. 1, 14–18, Silicon Valley, CA, USA, Aug. 2004.
3. Baudry, D., A. Louis, and B. Mazari, "Overview of emission and susceptibility investigation and modeling with near-field measurements," *XXIX URSI General Assembly*, Chicago, IL, USA, Aug. 2008.
4. Ramo, S., J. R. Whinnery, and T. van Duzer, *Fields and Waves in Communication Electronics*, 3rd Edition, John Wiley & Sons, New York, 1994.
5. Yaghjian, A. D., "An overview of near-field antenna measurements," *IEEE Transactions on Antennas and Propagation*, Vol. 34, No. 1, 30–45, 1986.

Cryptography of the Medical Images

Cherif Moumen[1], **Malek Benslama**[1], **and Mekhilef Saad**[2]

[1]Laboratoire d'Electromagnétisme et de Télécommunication, Université de Constantine, Algérie
[2]Department of Electrical Engineering, University of Malaya, Kuala Lumpur, Malaysia

Abstract— This work presents a cryptography method that uses the properties of chaotic systems for medical images. A chaotic algorithm of 1-D proposed by Yen and Guo, is implemented using Bit Recirculation Image Encryption (BRIE) to control the pseudo-random operations of shift that is exerted on each pixels image. Testing results between the encrypted and decrypted image and their histogram have shown the algorithm effectiveness.

1. INTRODUCTION

Nowadays, digital exchanges of medical images are frequently used throughout the world in a fraction of a second via the Internet. These data can be read or modified during their transmission via a non-controlled channel [1]. Therefore, it becomes very important to protect this private information against unauthorized viewers [2] by using cryptography.

Cryptographic techniques can be divided into symmetric encryption (with a secret key) and asymmetric encryption (with private and public keys) [3].

In symmetric cryptosystems, the same key is used for the encryption or decryption and this key need to be secure and must be shared between the emitter and the receiver. These cryptosystems are very fast and easy to use [4].

In proposing specific algorithms for the transfer of medical data ensuring total privacy in parallel on the emission and receipt of data, by using 1D chaotic algorithms [5]: **BRIE** (Bit Recirculation Image Encryption), their basic ideas is the recirculation of bits (pixels) image in clear, so we resorted to study a simple logistic model: $\mathbf{x}_{n+1} = r\mathbf{x}_n(1 - \mathbf{x}_n)$ [6]. This chaotic system is a deterministic nonlinear dynamic system which has an unpredictable long-term [7]. This unpredictability is due to the sensitivity to initial conditions, the mixing property and the density of periodic points. This logistic model can generate chaotic binary sequences and pseudo-random, to manipulate of each pixels of the image, by the two properties "**confusion**" and "**diffusion**" in classical cryptography [8]. It is a natural idea to use chaos to conceive new cryptosystems [9, 10].

Indeed, the use of this new cryptosystems in the sector of the medical sciences, with evolves in the latter years in a remarkable way, generating applications related to the use of chaos in the security communication systems, for to realize the transfer of the medical data, is the object of this work.

2. LOGISTIC MODEL

There exists many mathematical models allowing to study the growth of a population, the term "**population**" is used here in the broad sense, it can be human populations, animals, plants, people infected by virus ... etc..

2.1. Logistic Function

New Population = growth factor (reproduction) **x** *old population* **x** (1− *old population).*

$$x_{n+1} = r \cdot x_n(1 - x_n) \tag{1}$$

To build a mathematical model, it is necessary to make hypotheses. These hypotheses play two roles [11].

1) To preserve certain essential characteristics of reality.
2) To simplify this reality sufficiently so that it can to be studied by mathematics.

Among these mathematical models, we will endeavour to define the logistic function f.

With $f\colon\ [0, 1] \to [0, 1]$.

$$\begin{cases} x_0 \in [0, 1], \\ x_{n+1} = f(x_n) \end{cases} \quad \text{with } f:\ x \to r.x(1 - x) \tag{2}$$

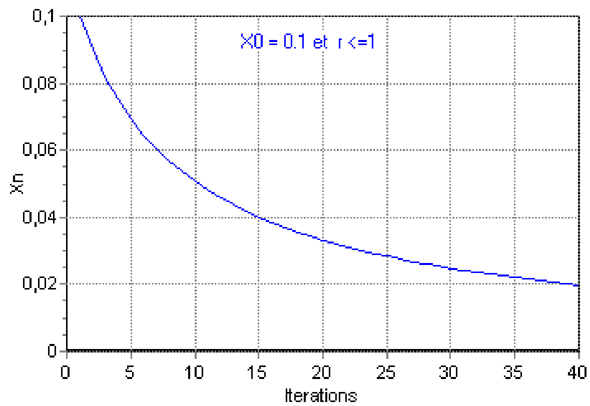

Figure 1: Evolution of the function logistic.

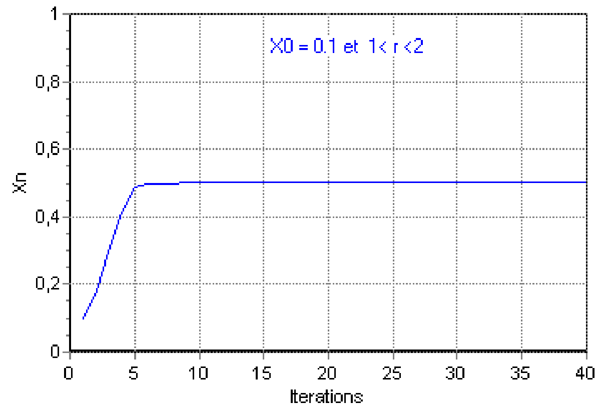

Figure 2: Evolution of the function logistic.

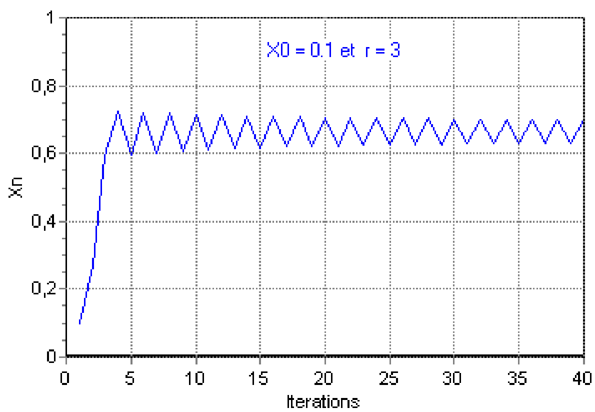

Figure 3: Evolution of the function logistic.

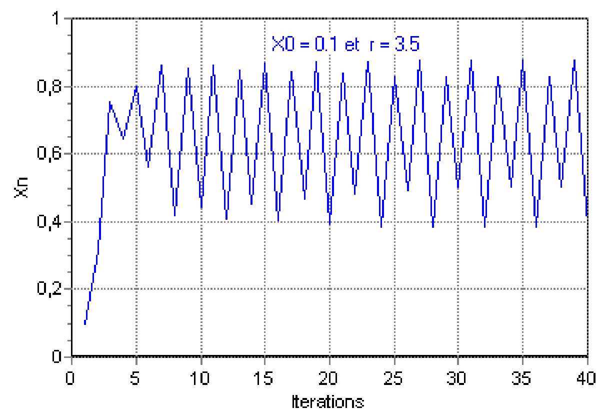

Figure 4: Evolution of the function logistic.

2.2. Interpretations of These Figures

Figure 1: When the rate of reproduction is weak (inferior or egal to 1), the population decreases and will tend towards zero.

Figure 2: When the rate of reproduction remains moderate (between 1 and 2), a significant population will be stabilized, around a number corresponding to half of the population that the territory could receive.

Figure 3: When the rate of reproduction egual the value 3, the number of individuals of this population starts to oscillate, between two distinct values (0.64 and 0.68).

Figure 4: When the rate of reproduction eguals the value 3.5, the population oscillates between four values: 0.39, then 0.83, then 0.49 and finally 0.87. The evolution of the double oscillation becomes quadruple.

Figure 5: When the rate reaches 4.00, the preceding regularity disappears to leave the place to chaos. The number of individuals of the populations of the successive periods seems to oscillate irregularly, in "chaotic" way between the two extremes: saturation when X_n tends towards 1, and the extinction when X_n tends towards 0.

3. CHAOTIC SYSTEMS

3.1. Properties of the Chaotic Systems

The chaotic system is a dynamic deterministic system which has an unforeseeable behavior in the long term. This unpredictability is due to the sensitivity to the initial conditions, but it is too a special nonlinear system. Such a system checks the following properties: The property of the sensitivity to the initial condition, the property of mixture and density of the periodic points [12].

3.2. The Sensitivity to the Initial Conditions

In a great number of dynamic systems, a small error on the initial conditions will lead to a controllable error on the following states of the system. An example is provided in Figure 6.

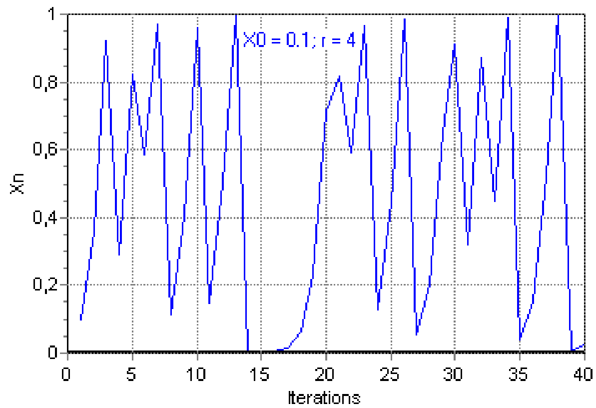

Figure 5: Evolution of the function logistic.

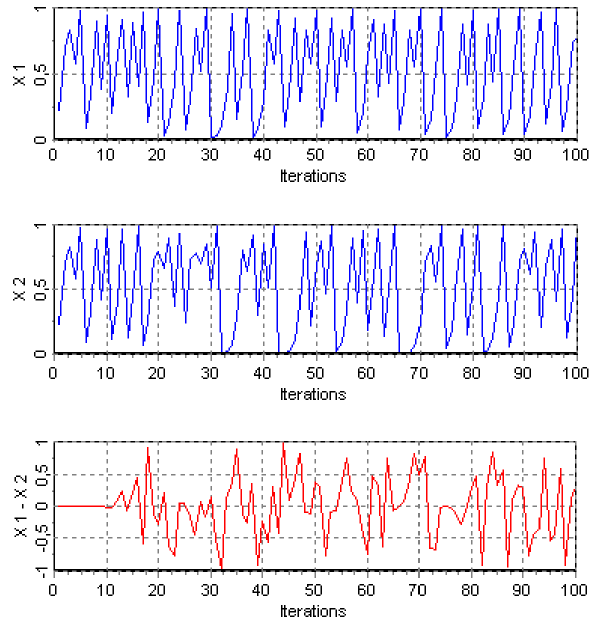

Figure 6: Represents the sensitivity to the initial conditions (Error of 0.00001).

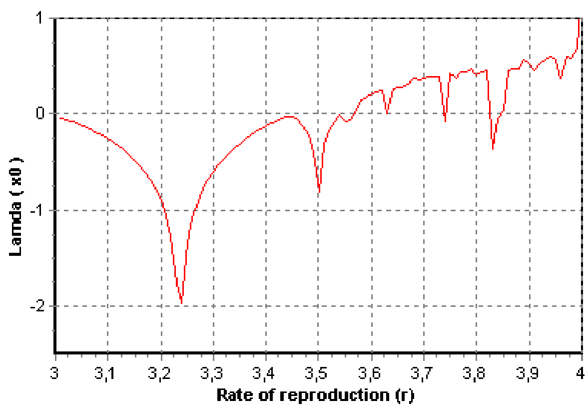

Figure 7: Diagram of Lyapounov.

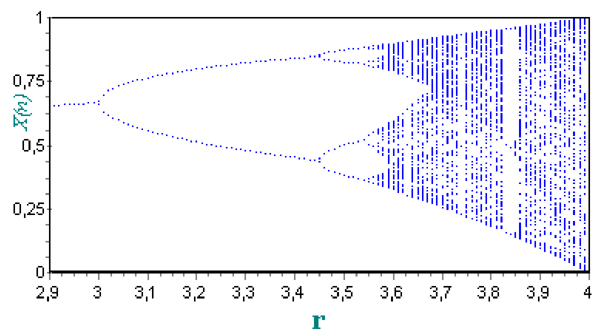

Figure 8: Diagram of Feigenbaum.

And for better quantification to the sensitivity to the initial conditions, we study the variations of the equation of Lyapounov (3), represented on the Figure 7:

$$\lambda(x_0) = \frac{1}{N}\sum_{k=1}^{n} \ln |r - 2rx_n| \tag{3}$$

The formula of Lyapounov thus makes it possible to quantify the sensitivity to the initial conditions, but it is capable of being separated by analysis, unstable behaviours and/or chaotic with stable behaviours and foreseeable, the diagram of Lyapounov is given in Figure 7:

If λ(x) is negative or egual to zero, we are in the presence of a stable phenomenon or periodical.

If λ(x) is positive, we are in the presence of an unstable phenomenon or chaotic.

3.3. The Capacity of Mixture

The definition of the capacity of mixture is as follows:

$$\forall]\alpha, \beta[,]\chi, \delta[\subset [0; 1], \exists x_0 \in]\alpha, \beta[, \exists n \in N, x_n \in]\chi, \delta[\tag{4}$$

The chaotic systems have the property of the capacity of mixture, which is that of the omnipresence of the points with ergodic orbit. An orbit is known as ergodic if the whole of its elements is dense in [0; 1], if under open interval from [0; 1] contains a point of this orbit. Omnipresence means that if one randomly takes a point in [0; 1], it is with ergodic orbit with a probability equal to 1.

3.4. Density of the Periodic Points

The diagram of **Feigenbaum** (Junction) allows to better visualize the evolution of a system towards chaos by **doubling of period**. Imagine Y capital letter, and then add to each higher point Y four times smaller, and so on. The structure which appears directly with the glance is that of a tree structure which indicates the qualitative changes in the dynamic behavior of the quadratic function. At the quantitative level, the diagram also tells us that the branches tend progressively to become increasingly short doubling of the period; it is to be shown with each division that it corresponds in fact a doubling of the mode period of the function.

Remarks on the Diagram of Feigenbaum

1. The dark zones filled of points represent a quasi infinity of states in which one can find the system.
2. Between 3.56999 and 3.7 the population fluctuates inside 4 zones of attraction, then of 2.
3. From 3.7 the population varies year by year in an irregular and unforeseeable way. Nevertheless, it is only when the rate of reproduction is equal to 4 that the totality of space is filled.
4. The dark lines which form parabolas inside the chaotic extent represent the values to which the probability of finding the system is higher
5. Around 3.8 appear windows of stability in the forms of vertical white bands.

4. THE CHAOTIC ENCODING OF THE IMAGES

Due to the enormous development of the communication networks, the security of digital image returns increasingly in a significant way and becomes necessary in several applications such as medical systems, military images and albums personals traditional techniques of encoding in real real time such as OF, RSA, IDE and Blowfish are not generally suitable because of their low speed Recently, the idea to use chaos in the encoding of the images was introduced and discussed, by several researchers [13].

Basically, there are two ways to use chaos in the field of coding images. One, it is used to produce pseudo-random bits with the desired statistical properties with coding,the other is used to make the permutation and substitution secret necessary to the coding image (the chaotic function in 1D, 2D or 3D)

This work use chaotic algorithms of 1-D, proposed by Yen and Guo. This algorithm use the logistic function $\mathbf{f(x) = rx(1 - x)}$, where the initial condition $\mathbf{x(0)}$ and the parameter of control $\mathbf{r}$ play the role of the secret key [14]. The encryption algorithm based on BRIE use the the following rules:

1. Execution of the logistic function to produce pseudo-random binary sequences $\{b(i)\}$, from a representation of n bits of each chaotic state $x(k)$ such as:

$$x(k) = b(n \cdot k)b(n \cdot k + 1) \dots b(n \cdot k + n - 1). \tag{5}$$

2. Use these chaotic binary sequences $\{b(i)\}$, to control the permutations and pseudo-random substitutions of each pixel of the image.

5. CHAOTIC ALGORITHMS

There are several chaotic algorithms which handle the image (operation of coding or decoding) in block or bit with bit. These algorithms in 1-D are the base of all other algorithms:

- **BRIE** (Bit Recirculation Image Encryption). $\{b(i)\}$ are used to control the pseudo-random operations of shift, exerted on each pixels image as seen in Figure 9 [15]. The version which improves BRIE is the TDCEA (The 2D Circulation Encryption Algorithm) [16].

There are several algorithms of chaotic encoding such as:

- **CKBA** (Chaotic Key-Based Algorithm).
- **HCIE** (Image Chaotique Hiérarchique Encryption).

In what follows, we try to describe and analyze algorithm (BRIE).

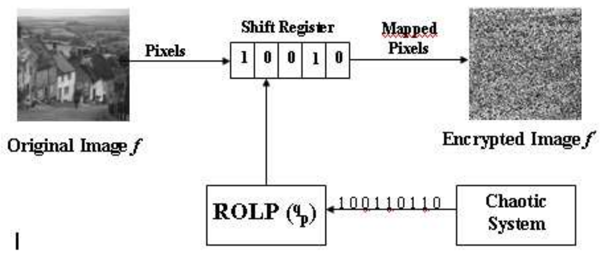

Figure 9: Structure of the algorithm BRIE.

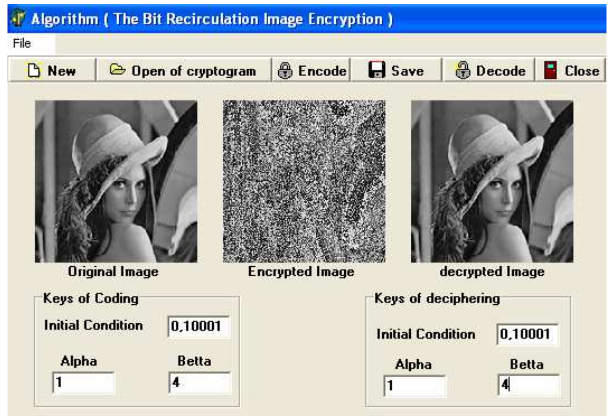

Figure 10: The interface of the software BRIE.

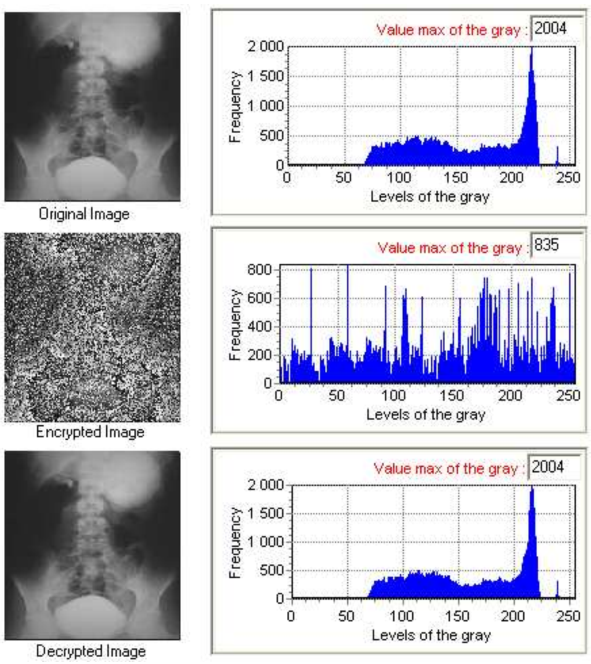

Figure 11: Encoding and decoding of the images.

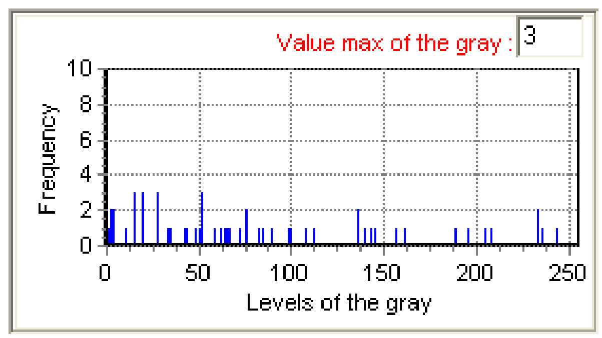

Figure 12: The difference between the histogram of the original image and the histogram of the image decoding in Fig. 11.

6. ALGORITHM BRIE

The basic idea of BRIE is the recirculation of bits of the image into clear, where, it is controlled by chaotic sequences binary and pseudo random in the Figure 9.

1- The secret key of BRIE is composed by the two entireties α, β and the condition initial $x(0)$ of a chaotic system [17]. Let us suppose that the clear image with a dimension of $M \times N$.

2- Execute the chaotic system to generate the chaotic orbits $\{x(i)\}_{i=0}^{MN/8-1}$.

3- Then, to generate the pseudo-random binary sequences (PRBS) $\{b(i)\}_{i=0}^{MN-1}$ from the binary representation with 8 bits of $x(i) = 0.b(8i+0)b(8i+1)\ldots b(8i+7)$.

For each pixel into clear $f(x,y)$ $(0 \leq x \leq M-1,\ 0 \leq y \leq N-1)$, their pixel encrypted corresponding $f'(x,y)$ is determined by the following rules and functions:

$$f'(x,y) = ROLP_p^q(f(x,y)), \tag{6}$$

where:

$$p = b(N \cdot x + y) \tag{7}$$
$$q = \alpha + \beta \cdot b(N \cdot x + y + 1) \tag{8}$$

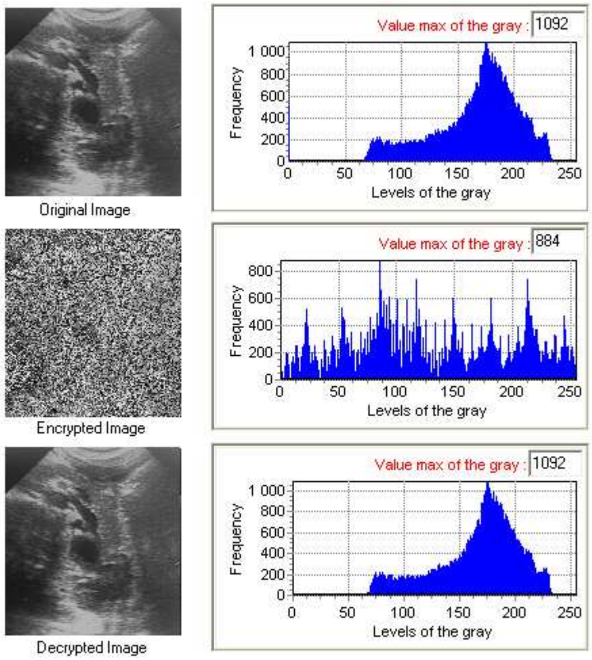

Figure 13: Encoding and decoding of the images.

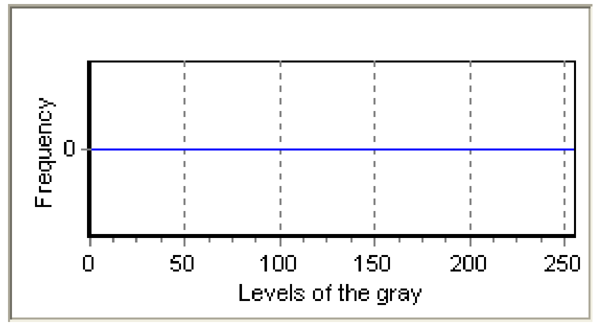

Figure 14: The difference between the histogram of the original image and the histogram of the image decoding in Fig. 11.

And $ROLP_p^q$ is it the *cyclique shift* by q bits in the direction controlled by p:

$$ROLP_p^q(x = b_7b_6\ldots b_0) = \begin{cases} \sum_{i=0}^{7} b_i \cdot 2^{(i-q+8) \bmod 8}, & p = 0 \\ \sum_{i=0}^{7} b_i \cdot 2^{(i+q) \bmod 8}, & p = 1 \end{cases} \tag{9}$$

The procedure of the decrypted will be:

$$f(x, y) = ROLP_{1-p}^q(f'(x, y)) = ROLP_p^{8-q}(f'(x, y)) \tag{10}$$

7. APPLICATIONS (ALGORITHM BRIE)

To check and clarify the analysis above, we provide some experimental results in this section. We use the logistic function like the chaotic system with the following key of encrypted: $\alpha = 1$, $\beta = 4$ and the initial condition $x_0 = 0.10001$.

Let us select the images of the Bmp type of 256×256 colors and 24 bits, this chaotic algorithm can be established in the form of an encrypted software with the key of encrypted which is identical to the key of decrypted Figure 10.

The Figures 11 and 13 represent the results of the chaotic software. The encrypted and decrypted images and their histograms show that:

The concentrations of the original images are different from one level of gray to another, and the frequency of appearance of the various levels of gray which compose them.

The decrypted images are identical by contribution to the original images, example in the Figure 11, the histogram of the original image is identical only to the decrypted image with the same maximum value of gray 2004, and the difference between them is negligible (represented by a maximum value of gray equals to 3 front 2004 Figure 12), and completely identical on the Figure 14.

The levels of gray for the original images are concentrated on places narrow and not on the range $(0, \ldots, 255)$.

8. CONCLUSION

A chaotic system is sensitive to the initial conditions, and it is thus a fundamental characteristic of chaos, and it magnifies even the smallest errors (ex: 0.00001). This signifies that: if one changes the starting state, one expects the general evolution of the system to be modified. Therefore this characteristic is exploited by: The cryptography in general and the chaotic cryptography in particular generate the keys of coding/deciphering, for example 0.1 and 0.10001 are two completely different keys.

Chaos with these characteristics found a very important applicability in cryptography, and created their own interval called: **Chaotic cryptography**.

We can start a chaotic phenomenon by a generator through respecting the properties of chaos.

Since the traditional algorithms are not recommended to encipher the medical images because they are slow, we can associate the properties of traditional cryptography which are substitution and transposition with the properties of a chaotic system to solve the problems of traditional cryptography. As we see in this paper.

Chaotic cryptography is a new method to encipher the medical data, and particularly medical imageries, where the data are voluminous, and cannot be enciphered with traditional algorithms such DES and RSA. Thus, the idea to make use of the chaotic systems became essential.

The complexity to keep the generation and the storage of the keys of encoding/decoding secretly in the traditional systems become useless in chaotic cryptography.

This software can be implemented in the medical systems for the filing and the transfer of the medical data.

REFERENCES

1. Jose Marconi, A. and M. Rodrigues, "Transfert securise d'images par combinaison de techniques de compression et cryptage," These de Doctorat de L'universite de Montpellier II, Oct. 2006.
2. Bruce, S., "Cryptographie appliquee," *Vuibert*, 2nd Edition, 2001.
3. Anane, N., M. Anane, H. Bessalah, M. Issad, and K. Messaoudi, "RSA based encryption decryption of medical images," Systems Signals and Devices (SSD), 2010.
4. Mollin, R. A., *RSA and Public-key Cryptography (Discrete Mathematics and Its Applications*, 1st Edition, Nov. 12, 2002.
5. Larger, L. and J. P. Goedgebuer, "Dynamiques chaotiques appliquées à la cryptographie," Laboratoire D'optique P. M., Université de France, Comté, 2003.
6. Moumen, C., "Etude d'un modèle logistique pour élaborer un algorithme de cryptage chaotique," Thèse de Magistère, Université de Constantine, 2005.
7. Raband, S. N., "Chaotic dynamics of nonlinear systems," Wiley, 1990.
8. Schneier, B., *Cryptographie Appliquée; Algorithmes, et Code Source en C*, 2nd Edition, 2001.
9. Vandewalle, D., "Le chaos politique," Thèse DEA, U.C.L Louvain la Neuve, Belgique, 1997.
10. Furht, B. and D. Kirovski, *Multimedia Security Handbook*, Feb. 5, 2004.
11. Kosmelj, K. and K. Vadnal, "Comparison of two generalized logistic regression models; a case studyInformation," Technology Interfaces, 2003.
12. Stork, M., "Digital chaotic systems examples and application for data transmission," *Electrical and Electronics Engineering*, 2009.
13. Wang, H., K. Ding, and C. Liao, "Chaotic watermarking scheme for authentication of JPEG images," *Biometrics and Security Technologies*, 2008.
14. Belkhouche, F. and U. Qidwai, "Binary image encoding using 1D chaotic maps," *IEEE Region 5, Annual Technical Conference*, 2003.
15. Sobhy, M. I. and A.-E. R. Shehata, "Chaotic algorithms for data encryption," *Acoustics, Speech, and Signal Processing*, 2001.

Expandable Multi-frequency EIT System for Clinical Applications

H. Wi, **T. E. Kim**, **T. I. Oh**, and **E. J. Woo**
Department of Biomedical Engineering, Kyung Hee University, Korea

Abstract— An electrical impedance tomography (EIT) system can visualize conductivity and permittivity distributions inside the human body from measured boundary voltages induced by externally injected currents. We have developed a fully parallel multi-frequency EIT system called the KHU Mark2.5. It is based on an impedance measurement module (IMM) comprising a current source, a voltmeter and a calibration circuit. Each IMM is independent and can calibrate its own current source and voltmeter through an automatic self-calibration procedure. We found that the output impedance values of all current sources are greater than $1\,\mathrm{M}\Omega$ at the chosen frequencies. The CMRR is around 96 dB and the voltmeter SNR is between 80 and 85 dB depending. To increase spatial resolution of conductivity and permittivity images, we can cascade multiple EIT systems to form a system with a larger number of channels. They are synchronized by clock synchronization circuits. Physiological events such as cardiac and respiratory functions alter electrical tissue properties. To correlate such events with EIT images, we can perform a biosignal-gated EIT imaging. We can improve interpretation of EIT images by incorporating real-time ECG and respiration signals into EIT images. This may allow us to separate fast cardiac events and slow respiratory events from reconstructed EIT images and also improve the SNR by signal-gated data averaging We present the performance of the KHU Mark2.5 system with experimental results of animal.

1. INTRODUCTION

EIT can produce functional images of conductivity variations associated with physiological events such as cardiac and respiratory cycles [1] After the first development of EIT was presented by Brown and Seagar, EIT has developed and clinical studies have been performed, but it still needs the breakthrough to apply EIT in clinic [2]. EIT system is required high performance and stability in order to be used in clinical application [3]. We can summary a few key points to improve the quality of the EIT images from previous studies. Images need to be acquired in a short time because of biological changes over the measurement time [4]. Measurement channels are directly related to the spatial resolution of reconstructed images and there is a need for three-dimensional data acquisition and imaging [5, 6]. A biosignal-gated imaging is useful to determine the relationship between the reconstructed impedance images and cardiac activity or respiration. It will allow us to capture fast cardiac events and may also improve the signal to noise ratio (SNR) using signal averaging methods. In a multi-channel EIT system, proper calibrations of current sources and voltmeters are essential to maximize its performance. For each current source, we need to maximize its output impedance above $1\,\mathrm{M}\Omega$ to get 0.1% accuracy to a maximum operating frequency. Since we inject currents with variable amplitudes from multiple current sources, we must carefully calibrate any small changes in their current amplitudes and phases. Within each voltmeter, all voltage gains at all measurement frequencies must be identical and this requires an intra-channel voltmeter calibration. Among multiple voltmeters, their gains must be matched and this requires an inter-channel voltmeter calibration [7] In this paper, we designed and evaluated a fast, multi-channel and expandable EIT system including biosignal gated imaging function and self-calibration.

2. METHOD

A fully parallel multi-frequency EIT system called the KHU Mark2.5 was developed by the above considerations as shown in Figure 1. It is based on an impedance measurement module (IMM) applying current to the subject, and measuring induced voltage independently. A high-capacity FPGA (EP3C10F256C8N, Altera, USA) controls all functions of the IMM. All IMMs in a system are operated synchronously by the control timing from intra-network controller. Distributed processing and pipeline structure in each IMM controller helps to increase the speed of the system for higher frame rates. External devices for acquiring biosignal such as ECG or respiratory signals can supply event trigger pulses synchronized with R-peak of ECG or intake time in respiration. Intra-network controller receives event trigger pulses and transmits the control timing signals to all IMM controllers to initiate data acquisition.

We may connect multiple KHU Mark2.5 EIT systems together to form a cascaded system with an increased number of channels. The cascaded system functions just like one system including all IMMs of the connected multiple systems. They have one master unit and several slave units using star connection. All information is transferred to each system by USB connections and timing was controlled by intra-network controller in master unit. Connected systems are resynchronized by the sync-out signal from master unit at regular intervals. Cascading method becomes an alternative method because it is very uncomfortable to develop, maintain and repair the multi-channel system.

To maintain the KHU Mark2.5 system at its maximal performance, we need to calibrate it occasionally. Though Oh et al. suggested an external calibrator for current sources and voltmeters, its use requires a manual operation by a trained personnel [8]. To facilitate the calibration process, we implemented an automatic calibration process by embedding the current source calibrator in each IMM and a resistor phantom inside the system. Oh et al. described how to perform the intra- and inter-channel calibrations of multiple voltmeters using a resistor phantom. In the KHU Mark2.5, we embedded a resistor phantom inside the system and adopted the same methods. We showed the automatic current source calibration circuit in Figure 2 where we adopted the droop method by Cook et al. [9]. We may initiate the automatic current source calibration in each IMM from the PC software. We connect the output of the current source to the calibrator with the switch setting A instead of a current-injection electrode. For given values of digital potentiometers in the Howland circuit and GICs, we measure the current twice at two different switch settings of C and D. The output of the current-to-voltage converter is connected to the voltmeter inside the same IMM with the switch setting E instead of a voltage-measuring electrode. Repeating the measurements for all possible combinations in settings of the digital potentiometers, we choose the best digital potentiometer settings that produced the largest output resistance and the smallest out capacitance thereby the largest output impedance. Automatic self-calibration helps to maintain the performance of system above the required level to be used in clinics.

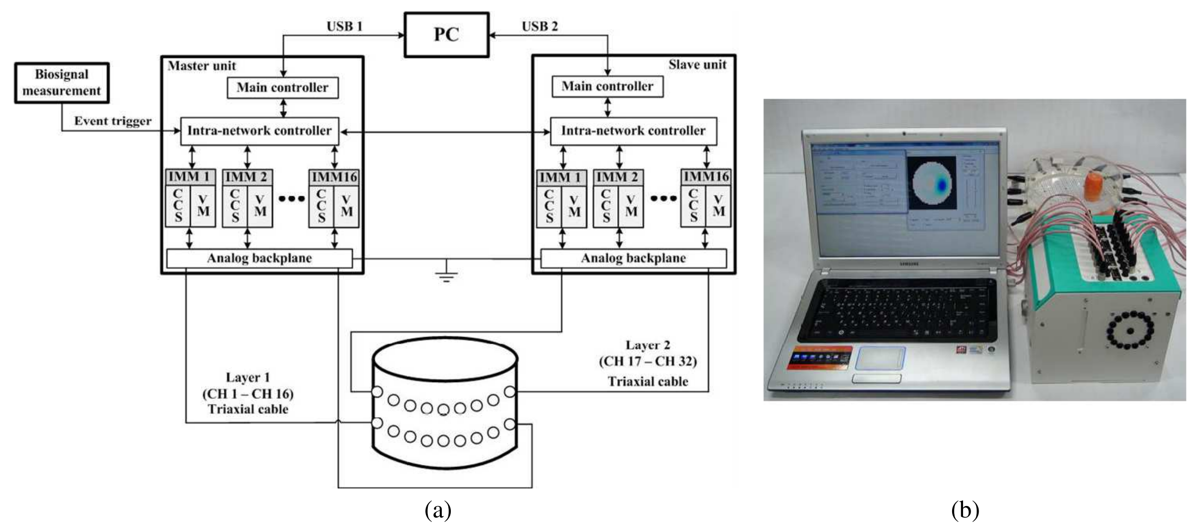

Figure 1: (a) The block diagram for expandable 32-channel EIT system, (b) developed KHU Mark2.5 system.

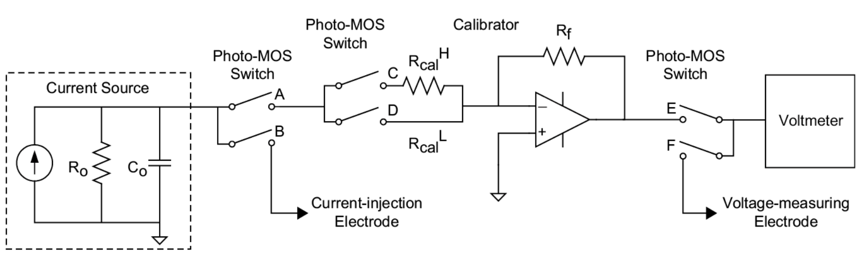

Figure 2: Schematic of the embedded current source calibrator using droop method and multiple GICs.

3. RESULTS

We chose ten operating frequencies of 0.01, 0.05, 0.1, 1, 5, 10, 50, 100, 250 and 500 kHz to evaluate the performance of the KHU Mark2.5 EIT system. The KHU Mark2.5 was tested the basic performance in terms of the current source output impedance variation along the time and DC offset on the calibration phantom. We found that output impedance at all operating frequencies except of 500 kHz were over 1 MΩ within 24 hours after calibrating. DC offset was calibrated at all operating frequencies within 1.5 μA. Figure 3 shows the performance results after calibration. The CMRR is around 96 dB and the voltmeter SNR is between 80 and 85 dB at tested frequencies.

We did animal experiments using biosignal gated imaging and fast imaging on canine chest. We monitored relative conductivity changes from −0.6 to 0.37 S/m due to respiration as like Figure 4. The speed of EIT system was 86 frames/s. Without using biosignal gated imaging, conductivity changes from cardiac function cannot be shown because it is smaller than one of respiration. Figure 5 shows the conductivity changes from cardiac function which were acquired at different time delay from R-peak by using biosignal gated imaging.

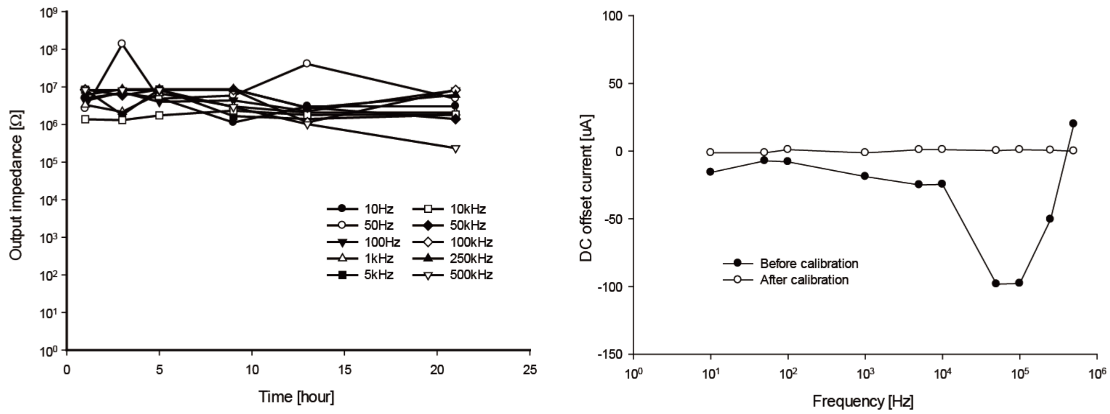

(a) (b)

Figure 3: (a) Output impedances over time, (b) DC offset current.

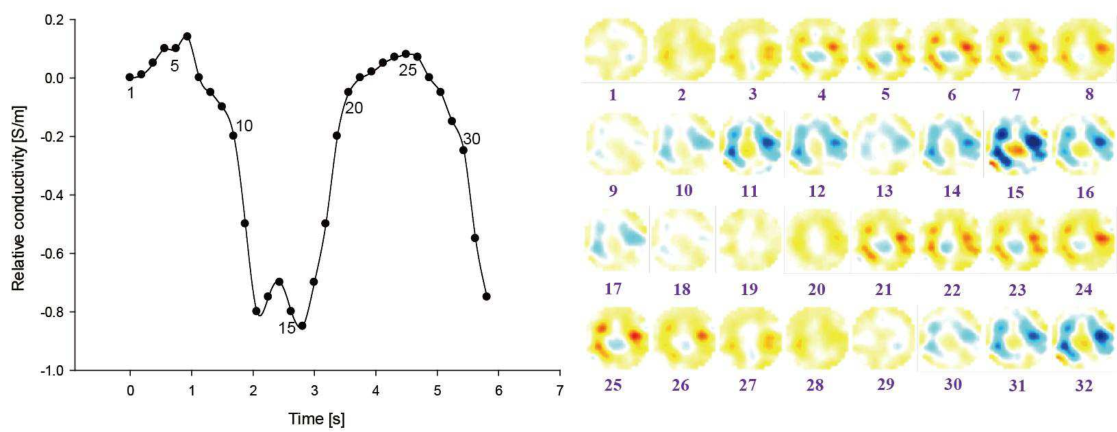

(a) (b)

Figure 4: (a) Relative conductivity changes on time, (b) EIT images during respiration.

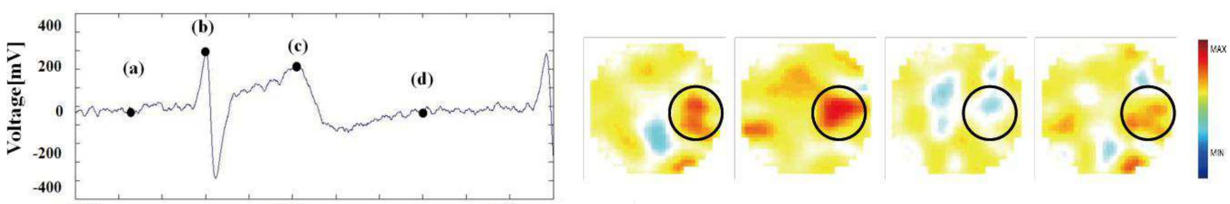

(a) (b) (c) (d)

Figure 5: Acquired corresponded EIT images with ECG signals at time (a), (b), (c) and (d).

4. CONCLUSIONS

We have developed a new multi-frequency parallel EIT system, the KHU Mark2.5 for spectroscopic conductivity imaging of the animal subject and evaluated its performance. All IMMs are operated synchronously and independently for flexible configuration and increasing the acquisition speed. Automatic self-calibration helps to maintain the performance of system above the designed level. Biosignal gated imaging was operated with a customized biosignal measurement unit for cardiac imaging and better interpretation for respiratory function. They can be connected together to build large number of channels EIT system for improving image quality.

The next version of our EIT system will acquire biosignal such as ECG or EEG together with EIT data. Integrated EIT system can show better interpretation for physiological variation and give an opportunity to overcome clinical uses for EIT.

ACKNOWLEDGMENT

This work was supported by the National Research Foundation of Korea (NRF) grant funded by the Korea government (MEST) (No. 20100018275).

REFERENCES

1. Holder, D. S., *Electrical Impedance Tomography: Methods, History and Applications*, IOP, Bristol, UK, 2005.
2. Brown, B. H. and A. D. Seagar, "The Sheffield data collection system," *Clin. Phys. Physiol. Meas.*, Vol. 8, 91–97, 1987.
3. Fabrizi, L., A. McEwan, E. Woo, and D. S. Holder, "Analysis of resting noise characteristics of three EIT systems in order to compare suitability for time difference imaging with scalp electrodes during epileptic seizures," *Physiol. Meas.*, Vol. 28, No. 7, S217–S236, 2007.
4. Eyuboglu, B. M., B. H. Brown, and D. C. Barber, "In vivo imaging of cardiac related impedance changes," *IEEE Eng. Med. Biol.*, Vol. 8, 39–45, 1989.
5. Metherall P., D. C. Barber, R. H. Smallwood, and B. H. Brown, "Three dimensional electrical impedance tomography," *Nature*, Vol. 380, 509–512, 1996.
6. Halter, R. J., A. Hartov, and K. D. Paulsen, "A broadband high-frequency electrical impedance tomography system for breast imaging," *IEEE Trans. Biomed. Eng.*, Vol. 55, No. 2, 650–659, 2008.
7. Oh, T. I, H. Wi, D. Y. Kim, P. J. Yoo, and E. J. Woo, "A fully parallel multi-frequency EIT system with flexible electrode configuration: KHU Mark2," *Physiol. Meas.*, Vol. 32, 835–849, 2011.
8. Oh, T. I., K. H. Lee, S. M. Kim, W. Koo, E. J. Woo, and D. S. Holder, "Calibration methods for a multi-channel multi-frequency EIT system," *Physiol. Meas.*, Vol. 28, 1175–1188, 2007.
9. Cook, R. D., G. J. Saulnier, D. G. Gisser, J. C. Goble, J. C. Newell, and D. Isaacson, "ACT3: a high-speed, high-precision electrical impedance tomograph," *IEEE Trans. Biomed. Eng.*, Vol. 41, No. 8, 713–722, 1994.

Conductivity Imaging of Animal and Human Body Using 3T Magnetic Resonance Electrical Impedance Tomography (MREIT)

W. C. Jeong[1], **Y. T. Kim**[1], **H. J. Kim**[1], **C. Y. Lim**[2], **H. M. Park**[2], **and E. J. Woo**[1]

[1]Department of Biomedical Engineering, Kyung Hee University, Gyeonggi, Korea
[2]Department of Veterinary Internal Medicine, Konkuk University, Seoul, Korea

Abstract— Magnetic resonance electrical impedance tomography (MREIT) aims to produce cross-sectional images of conductivity distributions inside animal and human subjects. In this study, we validate its feasibility by performing conductivity imaging experiments of animal and human bodies. We attached four carbon-hydrogel electrodes on the imaging area and placed the imaging object inside our 3T MRI scanner. We injected imaging currents in a form of short pulses into a chosen imaging area, of which timing was synchronized with an MRI pulse sequence. Obtaining images of induced magnetic flux density distributions inside the imaging object, we reconstructed conductivity images using the single-step harmonic B_z algorithm. Reconstructed conductivity images of the canine heart, kidney, prostate, and other organs exhibit unique contrast information which is hardly observed in other imaging modalities. The conductivity images of the human lower extremity well distinguished different parts of the subcutaneous adipose tissue, muscle, crural fascia, intermuscular septum and bone. Providing cross-sectional conductivity images, MREIT may deliver unique new diagnostic information in its future clinical studies.

1. INTRODUCTION

The electrical conductivity values of biological tissues may provide valuable diagnostic information that is not readily available from existing imaging modalities. Magnetic Resonance Electrical Impedance Tomography (MREIT) is a lately developed impedance imaging method that is expected to provide cross-sectional conductivity images of the human body with a spatial resolution of a few mm [1–3]. Injected current into an electrically conducting object including the human body induces internal distributions of current density, voltage, and magnetic flux density.

In MREIT, we use an MRI scanner with its main magnetic field pointing the z-direction to measure the induced magnetic flux density B_z that is the z-directional component. Multiple injection currents using at least two pairs of electrodes are adopted to produce multiple B_z data [3]. One may add a few voltage measurements to the data set. We apply a conductivity image reconstruction algorithm to the data set and produce multi-slice cross-sectional images of a conductivity distribution inside a chosen three-dimensional imaging domain [3]. The purpose of this study is to show the potential of the MREIT technique as a new clinically useful bio-imaging modality through whole body animal and human imaging experiments.

2. METHODS

2.1. MREIT System

MREIT imaging experiments are performed inside a 3T MRI scanner (Magnum 3, Medinus Co. Ltd., Korea) that is equipped with a constant current source. Figs. 1(a) and 1(b) show a MRI scanner and an MREIT current source Fig. 1(c) shows a carbon-hydrogel electrode (HUREV Co. Ltd., Korea) used in most MREIT experiments. It comprises the $80 \times 80\,\mathrm{mm}^2$ thin carbon electrode (1.6 S/m conductivity and black color), $80 \times 80 \times 5\,\mathrm{mm}^3$ hydrogel (0.17 S/m conductivity and blue color), and $80 \times 80 \times 0.7\,\mathrm{mm}^3$ hydrogel with adhesive (0.05 S/m conductivity and white color). By using large electrodes with a wide coverage of the circumference, we tried to induce a more uniform internal current density distribution.

2.2. Animal Experiment

Imaging objects were ten healthy laboratory beagles (4 males and 6 females, 2–3 years old, weighing 8–15 kg). To prevent dribbling, we injected 0.1 mg/kg of atrophine sulfate. Ten minutes later, we anesthetized the dog with intramuscular injection of 0.2 ml/kg Tiletamine and Zolazepam (Zoletil 50, Virbac, France). Twenty minutes later, we sacrificed it with an intravenous injection of 80 mg/kg KCL (Entobar, Hanrim Pharmacy, Korea). After clipping the hair, we attached four carbon-hydrogel electrodes around the imaging area (Fig. 2(a)). We placed the animal inside the bore

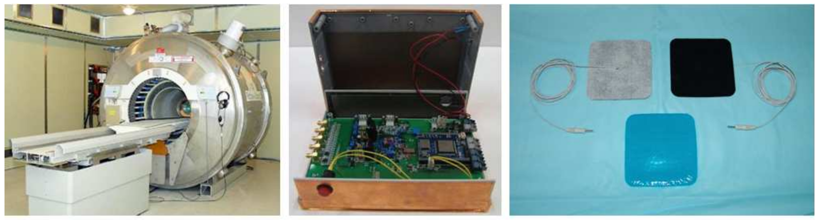

(a) (b) (c)

Figure 1: (a) 3T MRI scanner, (b) MREIT current source and (c) carbon-hydrogel electrode.

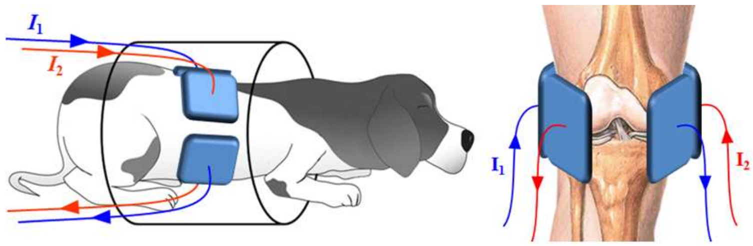

(a) (b)

Figure 2: MREIT imaging setup inside the bore for (a) animal and (b) human experiment.

of our 3T MRI scanner. This procedure was approved by the Institutional Animal Care and Use Committee (IACUC) of Konkuk University, Seoul, Korea.

We injected currents in two mutually orthogonal directions between two pairs of electrodes facing each other. The injection current amplitude ranged from 25 to 35 mA. We adopted multi-echo based ICNE pulse sequence [4]. The imaging parameters were as follows:

1. Chest and pelvis imaging: TR/TE $= 1000/30$ ms, FOV $= 240 \times 240\,\text{mm}^2$, matrix size $= 128 \times 128$, slice thickness $= 5$ mm, number of slices $= 8$, NEX $= 24$ and total imaging time $= 200$ min.

2. Abdomen imaging: TR/TE $= 1200/30$ ms, FOV $= 280 \times 280\,\text{mm}^2$, matrix size $= 128 \times 128$, slice thickness $= 4$ mm, number of slices $= 8$, NEX $= 10$ and total imaging time $= 100$ min.

2.3. Human Experiment

Six healthy volunteers (three for calf and three for knee imaging, 2530 years old) participated in the imaging experiments. The experimental protocol was the same as the one described by Kim et al. [5] and approved by the institutional review board (IRB). We attached four carbon-hydrogel electrodes around the knee or calf as shown in Fig. 2(b). We chose one pair of opposite electrodes to inject current. We gradually increased the current amplitude from zero mA to a pain threshold. We recorded current amplitudes at thresholds of sensation and pain. After repeating the same procedure for the other electrode pair, we determined the imaging current amplitude as 95% of the smaller pain threshold. After this setup, we placed the subject inside the bore of our 3T MRI scanner with the four electrodes connected to a custom designed MREIT current source [3].

2.4. Conductivity Image Reconstruction

We used the single-step harmonic B_z algorithm implemented in CoReHA for multi-slice conductivity image reconstructions [5]. All conductivity images presented in this paper should be interpreted as scaled conductivity images providing only contrast information.

3. RESULTS AND DISCUSSION

3.1. Animal Images

Figure 3(a) shows images of a canine chest. The reconstructed conductivity image reveals conductivity contrasts among the heart, longissimus thoracis muscle, and thoracic wall. Since MR signals from the lungs are weak, conductivity images of the lungs show peculiar noise patterns.

Figure 3(b) shows images of a canine upper abdomen. Conductivity images reveal different organs including the liver, stomach, gallbladder, and blood vessels. Fig. 3(c) shows images of a canine lower abdomen. Conductivity images distinguish organs including the spinal cord, peritoneal cavity, kidney, liver, large and small intestines, spleen, and stomach. The peritoneal cavity, which mainly consists of conductive fluids, shows a high conductivity value.

Figure 3(d) shows images of a canine pelvis. Conductivity images exhibit different contrasts for the prostate, sacrum, rectum, and surrounding muscles. Compared with the MR magnitude image of the prostate, the conductivity image shows a clear contrast between the central and peripheral zones which are closely related with the prostate cancer and benign prostatic hyperplasia.

3.2. Human Images

Figure 4 shows MR magnitude, magnetic flux density (B_z), and reconstructed conductivity images of the knee. In (b), we can see that signal void occurred at the outside of the bones. The conductivity image in (c) exhibits spurious noise spikes there. Reconstructed conductivity images well distinguish different parts of the subcutaneous adipose tissue, muscle, synovial capsule, cartilage and bone inside the knee. Conductivity images of the compact bone showed a comparable contrast with surrounding adipose tissues.

Figure 5 shows MR magnitude, magnetic flux density (B_z), and reconstructed conductivity images of the calf We can distinguish the skeletal muscle, adipose tissue, crural fascia, intermuscular septum, and yellow marrow. MR signal void has occurred in the ring-shaped cortical bone of the tibia primarily due to the lack of protons and we should expect noisy pixels within such a ring-shaped region in both B_z and conductivity images.

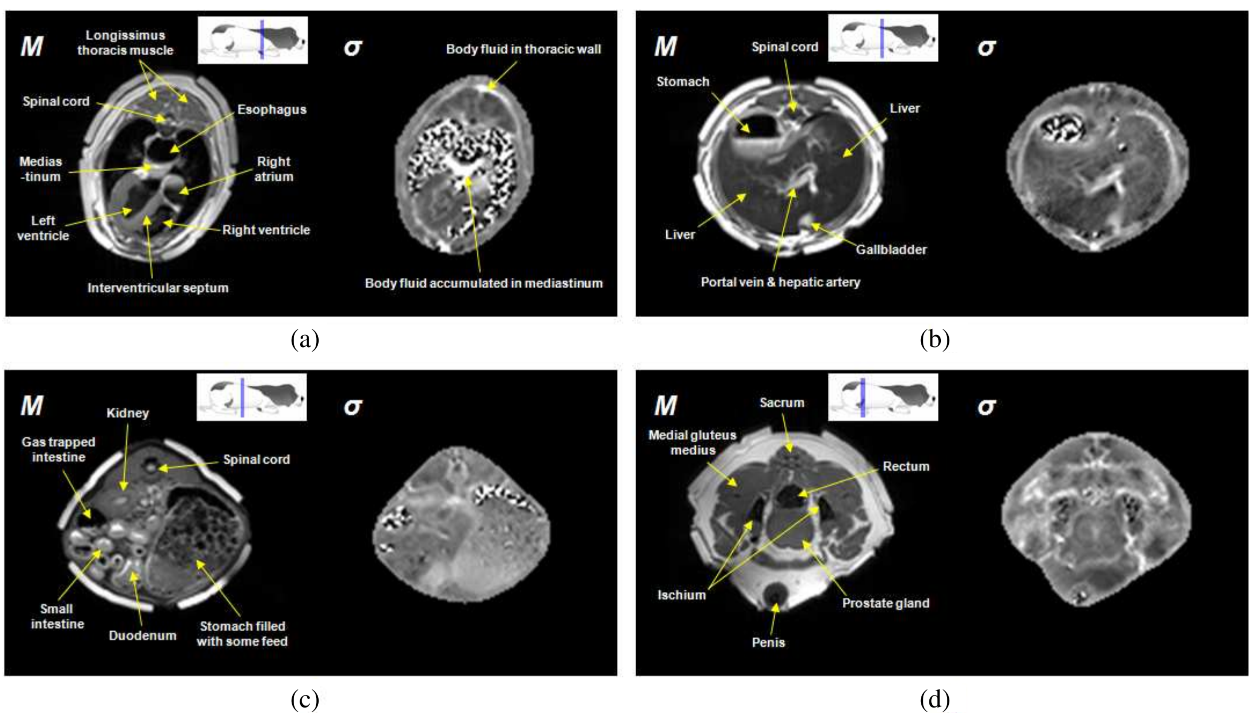

Figure 3: MR magnitude (M) and reconstructed conductivity image (σ) of canine whole body, (a) chest, (b) upper abdomen, (c) lower abdomen, and (d) pelvis.

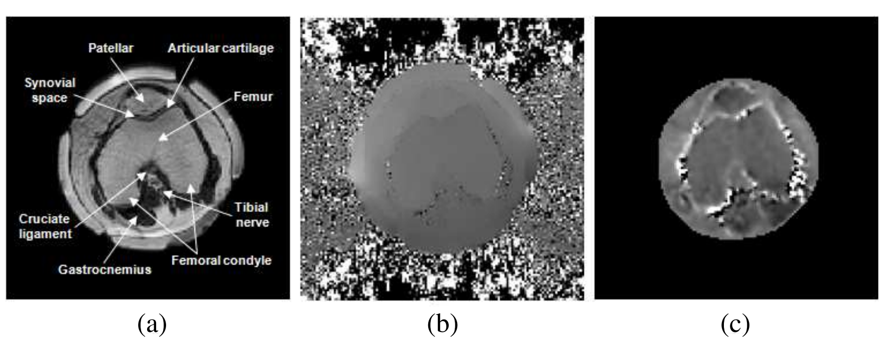

Figure 4: (a) MR magnitude, (b) magnetic flux density, and (c) reconstructed conductivity images of human knee. The typical anatomical structure of the knee is labeled in (a).

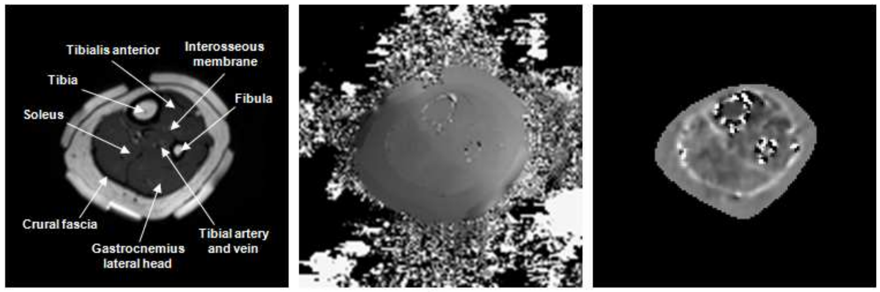

(a) (b) (c)

Figure 5: (a) MR magnitude, (b) magnetic flux density, and (c) reconstructed conductivity images of human calf. The typical anatomical structure of the calf is labeled in (a).

4. CONCLUSIONS

It is premature to affirm that MREIT is of clinical value. Imaging experiments of various disease animal models must be undertaken before clinical trials. We should identify clinical problems where conductivity images may add significant diagnostic values. These experimental validation studies demand technical progresses in terms of specialized MREIT pulse sequences and RF coils. Spin echo based pulse sequences have been widely used in MREIT and produced postmortem and *in vivo* conductivity images of animal and human subjects. The image quality depends on the SNR of measured magnetic flux density images. In order to reduce the scan time and current amplitude while keeping the image quality, we are developing fast pulse sequences for MREIT. MREIT must also be accompanied by recent technical advancement in general MRI technology. Providing cross-sectional conductivity images with a spatial resolution of a few millimeters, we expect MREIT to deliver unique new diagnostic information.

ACKNOWLEDGMENT

This work was supported by the National Research Foundation of Korea (NRF) grant funded by the Korea government (MEST) (No. 20100018275).

REFERENCES

1. Gabriel, S., R. W. Lau, and C. Gabriel, "The dielectric properties of biological tissues: II. Measurements in the frequency range 10 Hz to 20 GHz," *Phys. Med. Biol.*, Vol. 44, 2251–2269, 1996.
2. Grimnes, S. and O. G. Martinsen, *Bioimpedance and Bioelectricity Basics*, 93–124, Academic Press, London, UK, 2000.
3. Woo, E. J. and J. K. Seo, "Magnetic resonance electrical impedance tomography (MREIT) for high-resolution conductivity imaging," *Physiol. Meas.*, Vol. 29, R1-26, 2008.
4. Minhas, A. S., W. C. Jeong, Y. T. Kim, Y. Q. Han, H. J. Kim, and E. J. Woo, "Experimental performance evaluation of multi-echo ICNE pulse sequence in magnetic resonance electrical impedance tomography," *Magn. Reson. Med.*, Vol. 66, 957–965, 2011.
5. Kim, H. J., Y. T. Kim, A. S. Minhas, W. C. Jeong, E. J. Woo, J. K. Seo, and O. J. Kwon, "*In vivo* high-resolution conductivity imaging of the human leg using MREIT: the first human experiment," *IEEE Trans. Med. Imag.*, Vol. 28, 1681–1687, 2009.
6. Jeon, K., H. J. Kim, C. O. Lee, E. J. Woo, and J. K. Seo, "CoReHA: conductivity reconstructor using harmonic algorithms for magnetic resonance electrical impedance tomography (MREIT)," *J. Biomed. Eng. Res.*, Vol. 30, 279–287, 2009.

Dual Band Microstrip Antenna Working in the Frequency Bands 2.4 GHz and 5.8 GHz

R. Przesmycki, M. Wnuk, L. Nowosielski, K. Piwowarczyk, and M. Bugaj
Faculty of Electronics, Military University of Technology
Gen. S. Kaliskiego 2 Str., Warsaw 0-908, Poland

Abstract— The fast development technology of wireless internet access and the requirements to comply of the standards applied to the WLAN (Wireless Local Area Network) as well as the possibility of using the ISM (Industrial, Scientific, Medical) frequency bands in the ranges 2400–2500 MHz and 5725–5875 MHz has forced demand for dual-band antennas, which can be implemented in stationary and mobile devices. The paper shows the dimensional model of the antenna made in microstrip technology, working in two frequency bands −2.4 GHz and 5.8 GHz. This antenna can be used in mobile wireless networks. The paper show the results of simulation of radiation characteristics and electrical parameters of designed antenna made in the software CST Microwave Studio and the measurement results performed in anechoic chamber in the Electromagnetic Compatibility Laboratory in Military University of Technology in Warsaw, Poland.

1. INTRODUCTION

The fast development technology of wireless internet access and the requirements to comply of the standards applied to the WLAN (Wireless Local Area Network) as well as the possibility of using the ISM (Industrial, Scientific, Medical) frequency bands in the ranges 2400–2500 MHz and 5725–5875 MHz has forced demand for dual-band antennas, which can be implemented in stationary and mobile devices. Using antennas in mobile devices provides to requirement for unidirectional radiation patterns. This requirement, and additionally requirements on the size and electrical parameters of antenna meets mostly built antenna in microstrip technology.

One of the ways implementation of dual-band microstrip antenna is a double T antenna, which composed of two radiators in the shape of the letter T. In most of solutions radiating elements have different sizes. This allows antenna can work in two frequency bands. One of the ways implementation of dual-band microstrip antenna is a double T antenna, which composed of two radiators in the shape of the letter T. The double T antenna can be considered as two parts placed on one side of the laminate. They are supplied 50 Ω microstrip line placed on the same side of the laminate. On the second side dielectric is a ground plane (Figure 1(a)). One radiating element of antenna is operating in the lower frequency band. The second radiating element is designed for higher frequency band. Using different lengths of the horizontal line, and the thickness of the radiating elements allows for wider frequency bandwidth [2].

Double T antenna can be analyzed as two separate antennas working on individual frequency band.

Other interesting solution of dual band antenna is a structure which showed in Figure 1(b). The construction of this type antenna allows for a much larger frequency bandwidth than the antenna which is presented in Figure 1(a) [1].

2. THE MODEL AND SIMULATION RESULT OF DESIGNED ANTENNA

Figure 2 shows the analyzed antenna. It consists of two $\lambda/4$ monopolies shaped in T letter. Each of the two monopoles consists of two parts, orthogonal with each other. Element responsible for

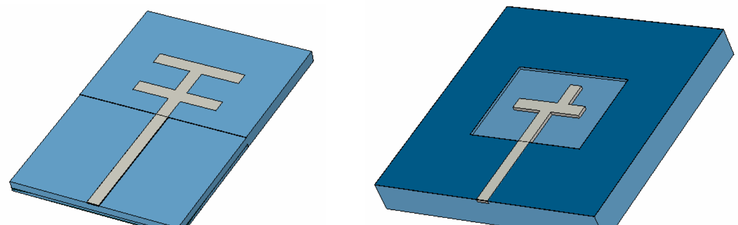

(a) (b)

Figure 1: Models of double T microstrip antenna.

the upper frequency range is a radiator in a T letter shaped, located in the central part of the antenna, while the radiator is responsible for the lower frequency range (2.4 GHz) is located above. Using the simulation environment — CST Microwave Suite, model of antenna was created, whose geometrical dimensions are shown in Figure 2.

As a result of the design process were finally selected dielectric: $h_2 = 1.524\,\mathrm{mm}$, $\varepsilon_2 = 2.6$ — Rogers — RT/ULTRALAM 2000.

Geometrical dimensions of the antenna shall be set at: $W_g = 72.98\,\mathrm{mm}$, $L_g = 29\,\mathrm{mm}$, $L_{de} = 24.33\,\mathrm{mm}$, $W_f = 4.83\,\mathrm{mm}$, $H_{tu} = 16.06\,\mathrm{mm}$, $H_{tl} = 9.245\,\mathrm{mm}$, $L_{tu} = 5.15\,\mathrm{mm}$, $W_{tu} = W_{tl} = 1.94\,\mathrm{mm}$, $L_{tl} = 7.26\,\mathrm{mm}$. For this model of the antenna using a simulation environment CST, electrical parameters and radiation patterns of the antenna was determined. Figure 3 shows the course of the VSWR and the antenna input impedance.

Figures 4 and 5 shows a radiation patterns of the antenna model in two polarization for 2.4 GHz and 5.8 GHz frequency obtained by the simulation. In the vertical polarization for both the frequency characteristics of the antenna are omnidirectional, which agrees with the assumptions posed design for the prepared antenna. The real part of input resistance of the designed model antenna for frequency 2.4 GHz is 39 Ω while for the frequency 5.8 GHz is 46 Ω (Figure 3(b)).

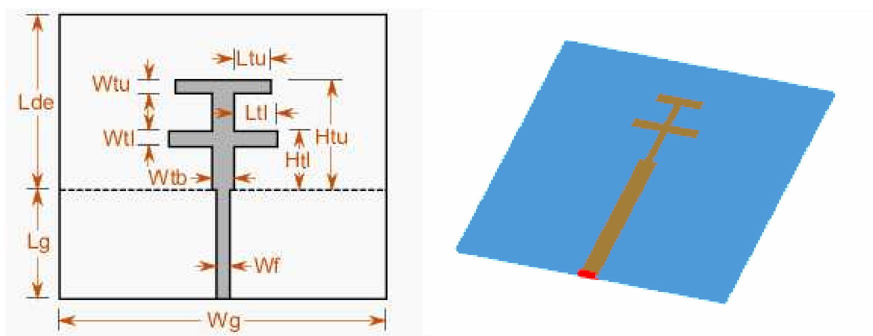

(a) (b)

Figure 2: The dimensioned model of analyzed antenna: (a) Construction of the radiator. (b) General view.

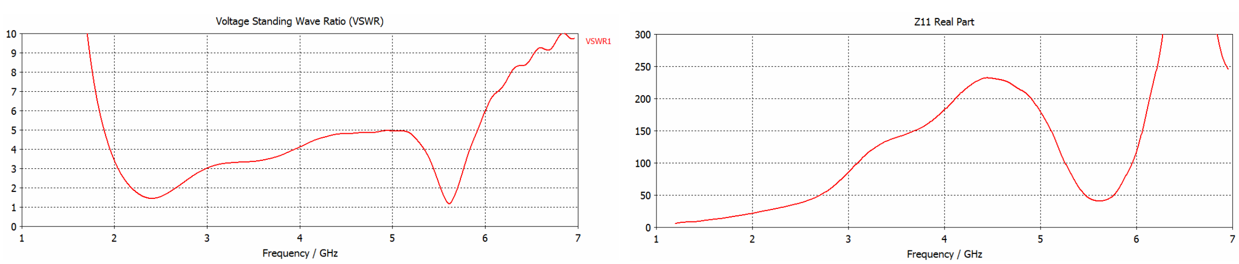

(a) (b)

Figure 3: (a) The simulation course of VSWR and (b) real part of input impedance as a function of frequency.

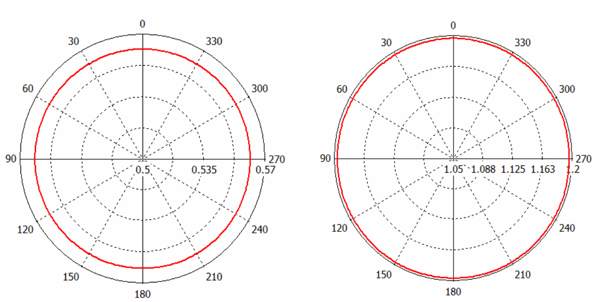

(a) (b)

Figure 4: The simulation of radiation patterns of the designed antenna model for vertical polarization for the frequency: (a) 2.4 GHz. (b) 5.8 GHz.

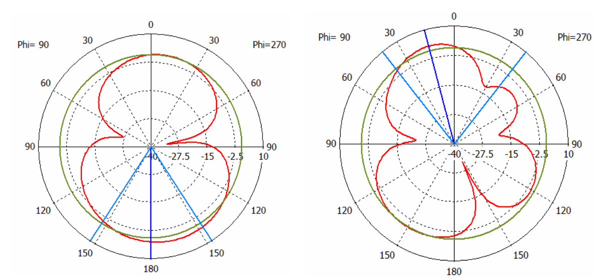

(a) (b)

Figure 5: The simulation of radiation patterns of the designed antenna model for horizontal polarization for the frequency: (a) 2.4 GHz. (b) 5.8 GHz.

Figure 6: Double T antenna during the measurements in anechoic chamber.

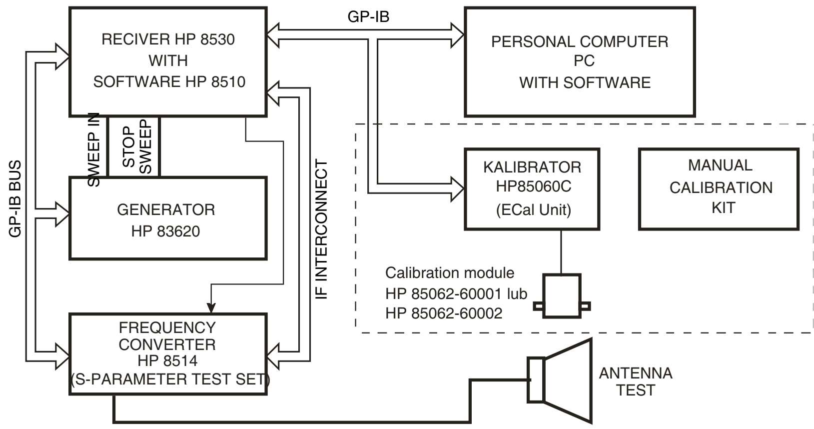

Figure 7: Block diagram of measuring position for VSWR testing and input impedance of antennas.

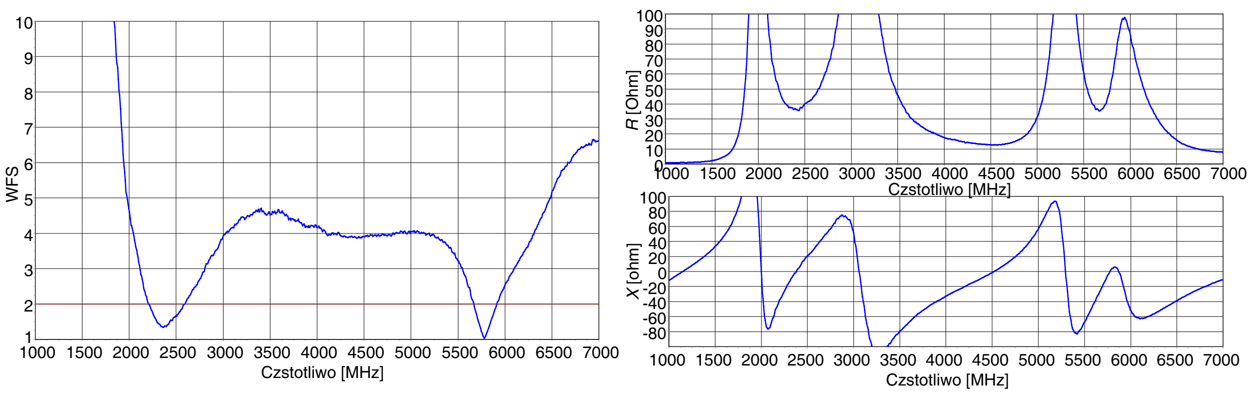

(a) (b)

Figure 8: (a) The measured course of VSWR and (b) input impedance (real and imaginary part) as a function of frequency.

3. THE MEASUREMENT RESULTS OF ELECTRICAL PARAMETERS AND RADIATION PATTERNS OF DOUBLE T ANTENNA

For the validate the analysis performed in the previous chapter, and verify the electrical parameters obtained in the final simulation model of the antenna were measured for the antenna made a physical model based on the results of the simulation. Figure 6 shows a designed model of double T antenna placed in the right place at the measurement positions of the radiation patterns and VSWR measurements in the anechoic chamber.

For measuring SWR and input impedance of antennas it is necessary to draw up measuring position in the configuration showed in Figure 7.

Measurement of VSWR and input impedance requires conducting calibration of measuring position. Calibration allows to minimize systematic errors which could appear during measurements. Because for SWR measurements and input impedance for various types of antennas there can be used different kinds of ducts, it is calibration that will provide elimination of influence of their parameters on the measurement result. After performing calibration of measuring position and verification of correctness of the performed calibration, to slotted line in the place of matched load it is necessary to connect the tested antenna. Connection should be made in such a way that measuring cable is connected directly to antenna input or by using minimum essential number of adapters necessary for change of connection standard.

Due to frequency band in which designed microstrip antenna operate, the measurements have been conducted in the range from 2 GHz to 6.4 GHz. The measurement results of VSWR and input impedance (real and imaginary part) of the discussed microstrip antenna in the function of frequency are showed in Figure 8.

Obtained by measuring the input resistance value is 39 Ω for a frequency 2.4 GHz and 39 Ω for a frequency 5.8 GHz (Figure 8).

For measuring antenna patterns it is necessary to draw up measuring position in the configuration shown in Figure 9.

Measuring of antenna patterns is performed in the below mentioned way. For initial position of rotary head desired power in the generator output is set and the first measuring frequency. Measurement of the power level of reference signal is conducted as well as test signal received by the tested antenna. After finishing measurement there comes retuning of the signal source and measuring both signals for next declared frequency. These measurements are carried out in turn until the last assigned frequency. According to the assigned step, rotary head performs rotation of the tested antenna to the next angular position and stops. Finishing measurements takes place after measuring power levels for the whole full rotation angle of the tested antenna.

On the basis of VSWR results and input impedance of the discussed microstrip antenna, the measurements of antenna characteristics have been made in the range of frequency of operating band of antennas, taking into account edges of frequency interval of operating band of antenna and mind-band frequencies. The measurement results of the discussed microstrip antennas in the angle

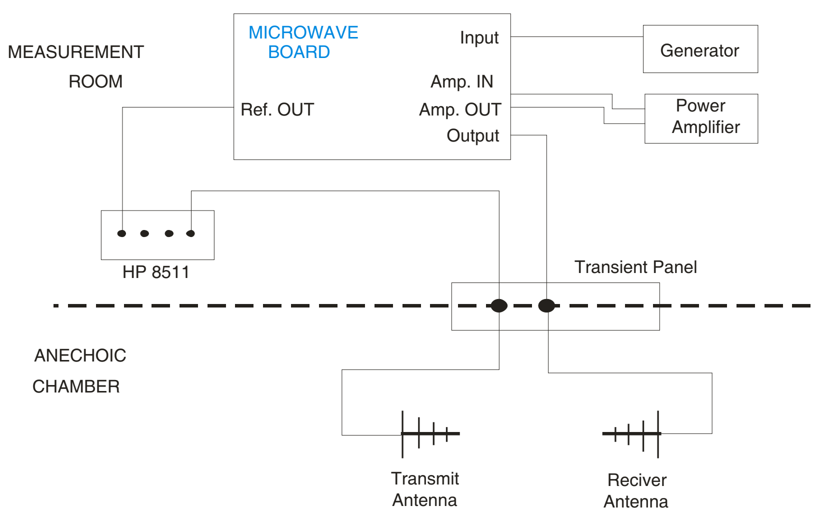

Figure 9: Block diagram of measuring position for antenna patterns measurements.

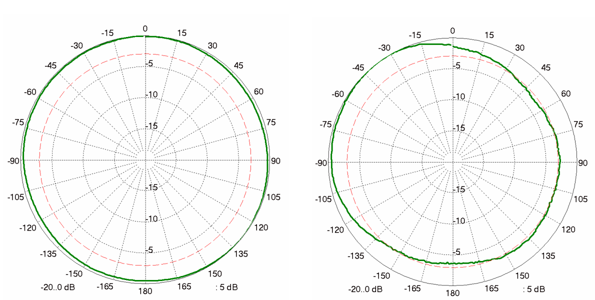

(a) (b)

Figure 10: Normalized antenna patterns of double T antenna in vertical polarization for frequencies: (a) 2400 MHz. (b) 5800 MHz.

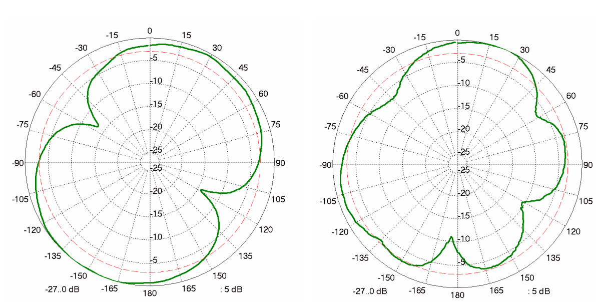

(a) (b)

Figure 11: Normalized antenna patterns of double T antenna in horizontal polarization for frequencies: (a) 2400 MHz. (b) 5800 MHz.

function for selected frequencies of the whole operating band are practically identical. Because of that, below there are presented normalized characteristics of the discussed microstrip antenna for the selected frequencies 2.4 GHz and 5.8 MHz in polar coordinates in vertical polarization (Figure 10) and horizontal polarization (Figure 11).

These results confirm the radiation patterns are omnidirectional shape in the vertical polarization, which is an advantage as an designed antenna for the possibility of using an designed antenna in mobile devices.

4. CONCLUSION

After analyzing the measurement results of the discussed microstrip antennas we can state that presented antennas are characterized by good mechanical and electrical parameters. Depending on needs, particular antennas can be used in various fields. The form of radiation characteristics is in accordance with theoretical assumptions.

The presented double T antenna model gives the possibility to work at the same time over the Wi-Fi 2.4 GHz and ISM frequencies from the range 2400–2500 MHz and 5725–5875 MHz range. The construction of the designed antenna made a modern solution to an antenna device for a compact form, which is especially important in a situation to use it on mobile devices. Omnidirectional radiation pattern in the plane of vertical polarization additionally increases usability of the designed double T antenna.

ACKNOWLEDGMENT

The research work financed from the financial funds assigned to the science in the years 2011/2013 as the development work. The research work is realized in Poland.

REFERENCES

1. Jang Large, Y.-W., "Bandwidth double-T shaped microstrip fed single layer single slot antenna," *Microwave and Optical Technology Letters*, Vol. 30, No. 3, Aug. 5, 2001.
2. Kuo, Y.-L. and K.-L. Wong, "Printed double-T monopole antenna for 2.4/5.2 GHz dual-band WLAN operations," *IEEE Transactions on Antennas and Propagation*, Vol. 51, No. 9, Sep. 2003.
3. Wnuk, M., R. Przesmycki, L. Nowosielski, and M. Bugaj, "Multilayer microstrip antenna on flat base in the X band (8.5 GHz–12 GHz)," *PIERS Online*, Vol. 7, No. 3, 216–220, 2011.
4. Bugaj, M., R. Przesmycki, L. Nowosielski, and K. Piwowarczyk, "Active microstrip antennas operating in X band," *PIERS Online*, Vol. 7, No. 3, 221–225, 2011.

Analysis Different Methods of Microstrip Antennas Feeding for Their Electrical Parameters

Marek Bugaj, **Rafal Przesmycki**, **Leszek Nowosielski**, **and Kazimierz Piwowarczyk**
Faculty of Electronics, Military University of Technology
Gen. S. Kaliskiego 2 Str., Warsaw 00-908, Poland

Abstract— The paper describes problems related to antenna technology. The paper shows the construction of different microstrip antennas on a dielectric substrate operating on 1.8 GHz. Microstrip antennas in antenna technology appeared relatively late, but in recent years has been a very large development of the design of these antennas and the huge interest in their capabilities. The article presents four models of single-layer microstrip antenna operating on the same 1.8 GHz frequency. Each of antennas was feed in other ways. For each of the antenna models designer set parameters such as VSWR, input resistance, input reactance and radiation pattern. Antenna model that characterized the best parameters was constructed. The article presents the results of measurements of the antenna built in the anechoic chamber. The results were compared with those obtained in simulation using CST software. Also presents the detailed design of the antenna, which has been built. The article also analyzes the results of computer simulations and measurements, thereby demonstrating the advantages and disadvantages of microstrip antennas with different feeding.

1. INTRODUCTION

The microstrip antennas have been one of the most innovative fields of antenna techniques for the last fifteen years. In high-performance spacecraft, aircraft, missile and satellite applications, where size, weight, cost, performance, ease of installation, and aerodynamic profile are constraints, low profile antennas may be required. Presently, there are many other government and commercial applications, such as mobile radio and wireless communications that have similar specifications. To meet these requirements, microstrip antennas can be used. These antennas are low-profile, conformable to planar and non-planar surfaces, simple and inexpensive to manufacture using modern printed circuit technology, mechanically robust when mounted on rigid surfaces, compatible with MMIC designs, and when particular patch shape and mode are selected they are very versatile in terms of resonant frequency, polarization, pattern, and impedance. In addition, by adding loads between the patch and the ground plane, such as pins and varactor diodes, adaptive elements with variable resonant frequency, impedance, polarization, and pattern can be adjusted [1]. Radiating patch may be square, rectangular, circular, elliptical, triangular, and any other configuration. In this work, rectangular microstrip antennas are the under consideration.

Millimeter wave printed antennas can take on many forms, including microstrip patch elements and a variety of proximity coupled printed radiators. The microstripline-fed printed slot and the aperture coupled patch are examples of the latter type and may be useful in certain planar array applications.

2. METHODS OF MICROSTRIP ANTENNA FEEDING

One of the most important issues is the wide operating band of the antenna, but is one of the weaker points of planar antennas, which are characterized by narrow-band operation. The work carried out in this regard, are intended to broaden a frequency band planar radiator work by increasing the number of dielectric layers and placing suitably located additional planar passive element, which in turn leads to a reduction in the goodness of the antenna.

There are several basic methods for microstrip antennas feeding, which are presented in Fig. 1.

3. ANALYSIS OF FEEDING METHODS

In the analysis of the impact of feeding on the parameters of the antennas will be considered work bandwidth antennas, impedance matching and shape of the radiation pattern. We try sought a solution that will give the wideband of work while maintaining a directional radiation patterns. From the numerical analysis was determined sequentially following parameters for presented models of antennas (Fig. 2): WFS, input impedance (resistance, reactance), radiation pattern.

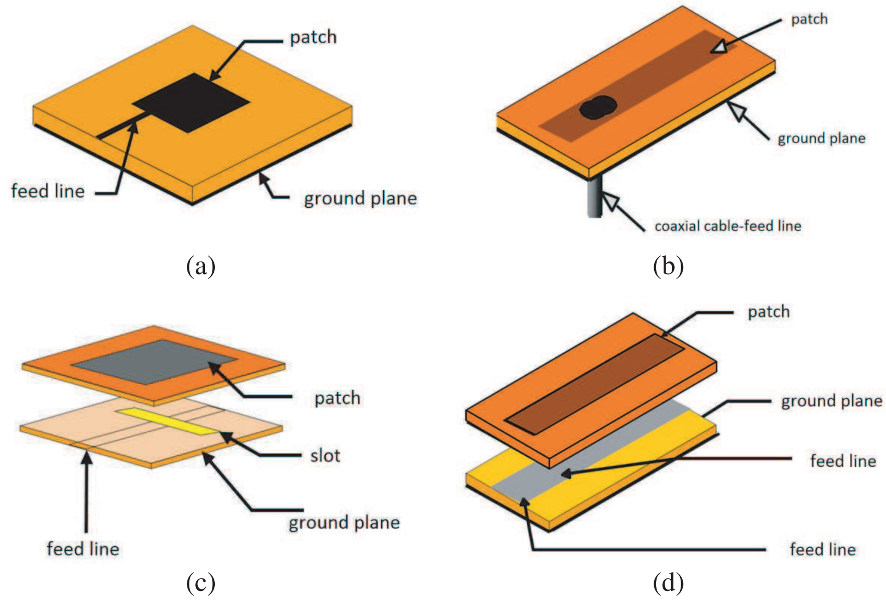

Figure 1: Methods of microstrip antennas feeding: (a) microstrip line, (b) coaxial line, (c) through the slot, (d) by coupling.

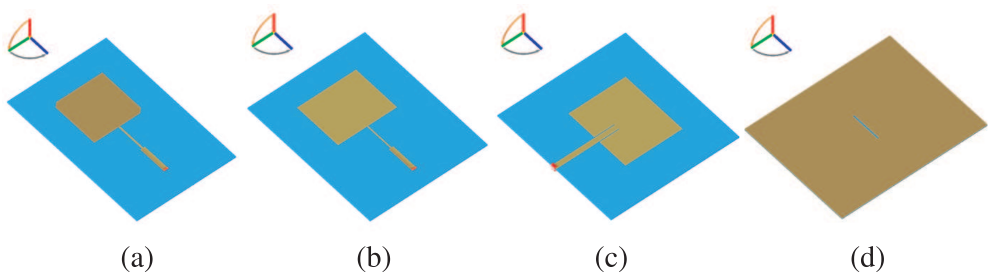

Figure 2: Analyzed models of microstrip antennas.

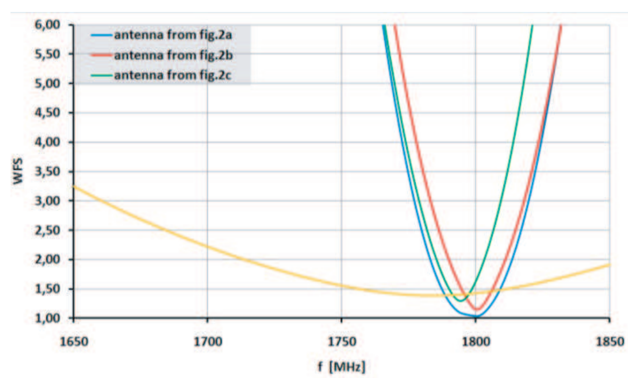

Figure 3: The VSWR course of tested antennas in the frequency function.

In Figs. 3, 4 and 5 are shown values of VSWR, input resistance and input reactance for the different models of antennas. The highest bandwidth is obtained for construction work fed slot, however, after taking into account the shape of the radiation pattern (antenna radiates symmetrically in two directions, a small gain directional $< 3\,\mathrm{dBi}$), this design was rejected and not taken into account in further considerations (Fig. 6).

After analyzing the results obtained in the simulation were selected antenna model shown in Fig. 7. It is a planar antenna fed by microstrip line of the radiator in the shape of a rectangle with beveled corners. To built antenna were used the ULTRALAM 2000 laminate from Rogers Corporation with a thickness $H = 1.524\,\mathrm{mm}$ and dielectric $\varepsilon_r = 2.6$, $\tan\delta = 0.0019$. Radiating element size is, respectively, $L = W = 50.65\,\mathrm{mm}$, the plurality of miter corners radiating element describes $L_t = 3.72\,\mathrm{mm}$. Dimensions of power line are as follows: $L_m = 29.45\,\mathrm{mm}$, $L_f = 28.42\,\mathrm{mm}$,

$W_m = 1.234\,\mathrm{mm}$, $W_f = 4.315\,\mathrm{mm}$.

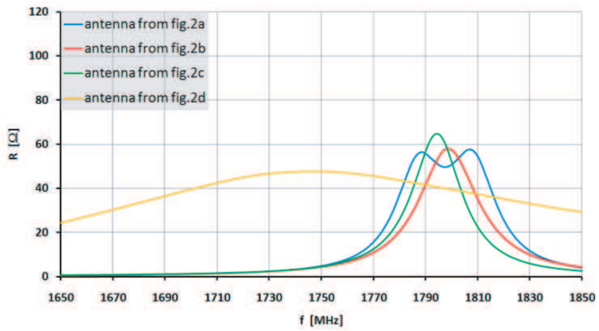

Figure 4: The input resistance course of tested antennas in the frequency function.

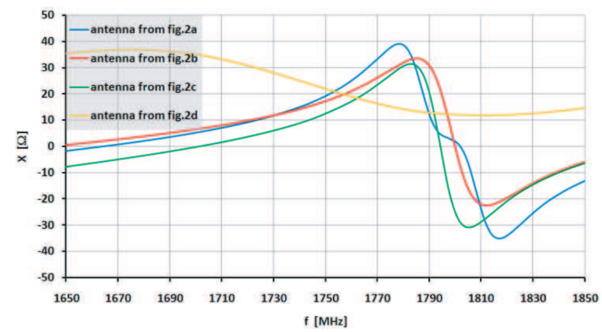

Figure 5: The input reactance course of tested antennas in the frequency function.

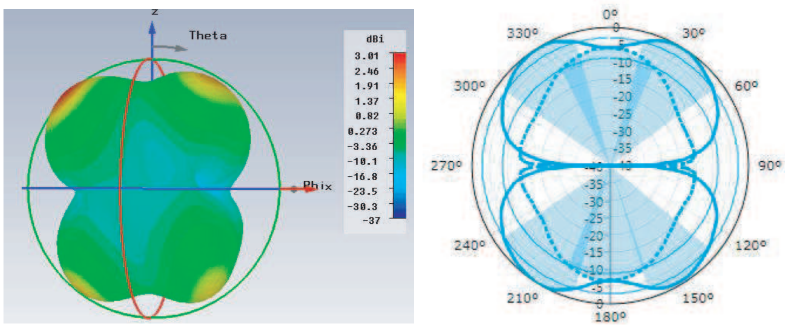

Figure 6: Radiations pattern for microstrip fed slot antenna.

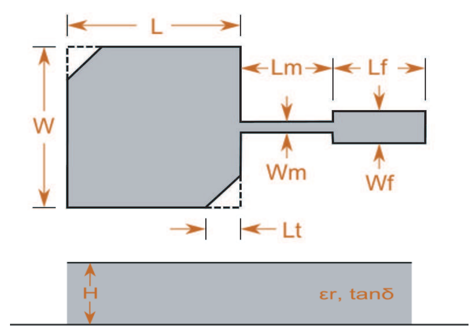

Figure 7: Construction of the antenna model chosen for the implementation.

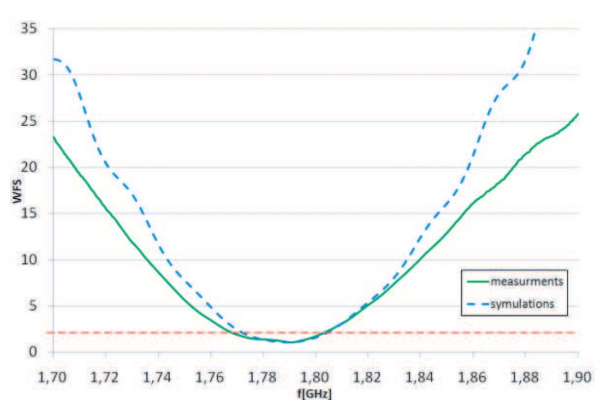

Figure 8: Summary of simulation results and measurements WFS.

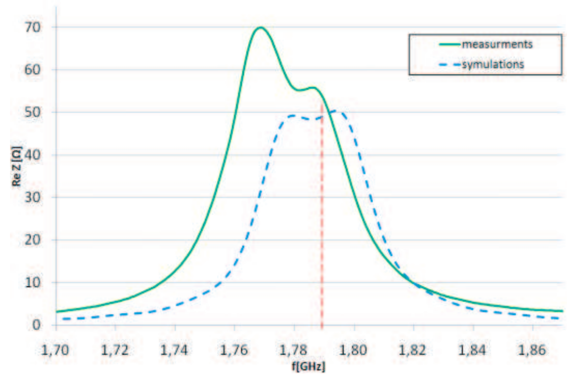

Figure 9: The input resistance course of tested antennas in the frequency fun.

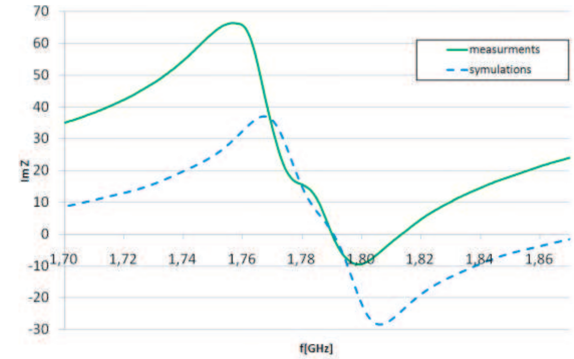

Figure 10: The input reactance course of tested antennas in the frequency function.

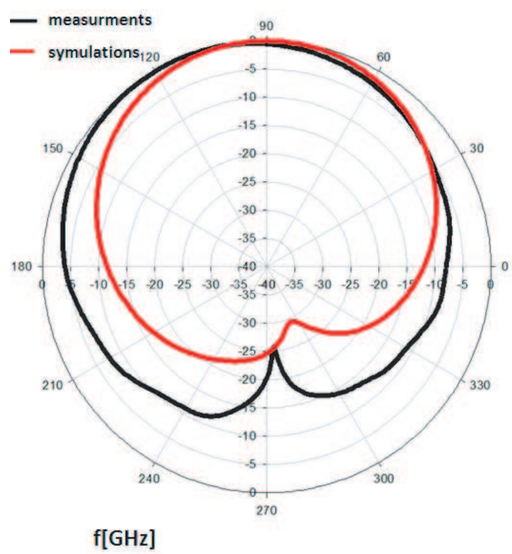

Figure 11: Radiation pattern in the plane V.

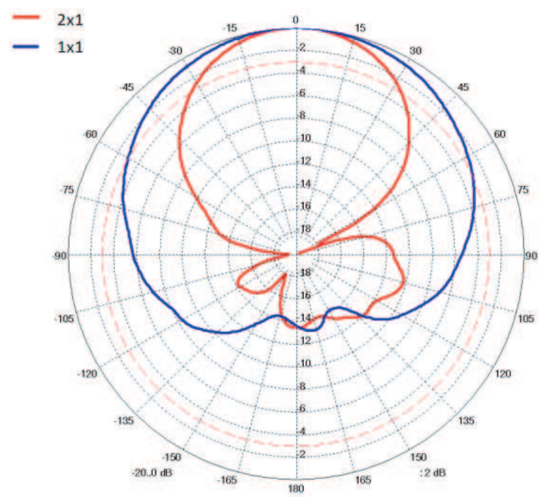

Figure 12: Summary of the characteristics of the radiation radiating a single element and two elements array (plane V).

4. THE MEASUREMENT RESULTS

In order to verify the results obtained in the simulation we performed measurements of electrical parameters and radiation characteristics of selected antnna. In order to investigate the antenna were measured the following parameters: VSWR, gain, radiation patterns and input impedance. The measurement of VSWR and input impedance (real and imaginary part) of the discussed microstrip active antennas in frequency domain are presented below(Figs. 6 and 7).

5. CONCLUSION

Considering the results of measurements of microstrip antenna can be stated that the selected antenna is characterized by good electrical parameters. The shape of the radiation characteristics is consistent with theoretical assumptions. Results of the simulation electrical parameters and characteristics of antenna has been confirmation by measurements. The measured operating band for the simulation results has shifted about 12 MHz in the range of lower frequencies. From the presented antennas the chosen antenna is characterized by the highest bandwidth of work while maintaining a directional radiation pattern shape.

Microstrip antennas are currently widely used in the construction of modern antennas, primarily in the so-called reported. antenna systems. Such technologies are used both in the construction of radar antennas, Wi-Fi and cellular sector antennas in UMTS.

ACKNOWLEDGMENT

The research work financed from the financial funds assigned to the science in the years 2011/2013 as the development work. The research work is realized in Poland.

REFERENCES

1. Bahl, I. J. and P. Bhartia, *Microstrip Antennas*, Artec House, 1980.
2. Bharatia, P., R. Garg, and I. Bahl, *Microstrip Antenna Design Handbook*, Artec House, 2001.
3. Wnuk, M., *Analiza Struktur Promieniującycych Położonych Na Wielowarstwowym Dielektryku*, Warszawa, WAT, 1999.
4. Szóstka, J., *Fale i anteny*, WKiŁ, Warszawa, 2006.

Wearable Antenna Constructed in Microstrip Technology

Marian Wnuk, **Marek Bugaj**, **Rafal Przesmycki**,
Leszek Nowosielski, **and Kazimierz Piwowarczyk**
Faculty of Electronics, Military University of Technology
Gen. S. Kaliskiego 2 Str., Warsaw 00-908, Poland

Abstract— Recently, the so-called body-centric communication (focused around the human body) has become a very big importance in the field of wireless communications. One of the key issues related to this type of communication is addressed by researchers wearable antenna. The paper presents the design of the wearable antenna made in microstrip technique working at a frequency of 1.8 GHz. The paper presents the results of discussed numerical analysis of antennas and the results obtained by experimental measurement.

1. INTRODUCTION

The term wearable antenna means literally dedicated antenna (or suitable) to wear. In simple terms it can be concluded that the wearable antenna serves as element of clothes, whose purpose is performing tasks directly related to telecommunications such as tracking and navigation, remote computing and communication tasks related to public safety.

Recently, the so-called body-centric communication (focused around the human body) has become a very big importance in the field of wireless communications. One of the key issues related to this type of communication is addressed by researchers wearable antennas. Typically, the requirements for this type of antennas used in modern solutions include small size and weight, low cost, virtually maintenance-free and no need for installation. Communications-type body-centric sphere of interest lies in areas such as medical emergency, fire-fighting and, above all military. However wearable antenna can also be used by athletes for example to monitoring.

2. DETERMINATION THE DIMENSIONS OF THE ANTENNA ELEMENTS

The main values characterizing the antenna radiator is a rectangular width W and length L of the patch. The width of radiating patch is fairly small effect on the shape of the antenna radiation pattern, but affect the input impedance and antenna operating band. Increasing the width of the radiator resulting in an increase in radiated power, expands bandwidth and increases efficiency. Critical parameter is the length of the radiator, because it determines the resonant frequency of the antenna. It is assumed that the ratio of emitter width to its length should be $1 < W/L < 2$. In the case of an antenna designed assumes that relationship. Through the parameterization values were assigned values of W and L satisfying the above condition on the basis of the following relationships (2 and 3):

$$L = \frac{c}{2f_r\sqrt{\varepsilon_{re}}} - 2\Delta L, \tag{1}$$

where ε_{re} is the effective dielectric constant, which is (for $W = 51,262\,\text{mm}$):

$$\varepsilon_{re} = \frac{\varepsilon_r + 1}{2} + \frac{\varepsilon_r - 1}{2}\left(1 + 12\frac{h}{W}\right)^{-1/2} = 2,487. \tag{2}$$

At the ends of the radiator are scattered fields that extend on both sides of the radiator with a value of extension. This size was determined as follows:

$$\Delta L = 0,412h\frac{\varepsilon_{re} + 0,300}{\varepsilon_{re} - 0,258}\frac{W/h + 0,264}{W/h + 0,813} = 0,773\,[\text{mm}]. \tag{3}$$

Hence, the final length of the the patch is:

$$L = W = 51,262\,[\text{mm}]. \tag{4}$$

3. MODEL ANTENY NASOBNEJ PRACUJĄCEJ W PAŚMIE 1.8 GHZ

Using a fixed antenna design in the previous section and simulation environment CST Microwave Studio was the final model was based on the physical antenna. As a result of the design process finally selected dielectric with parameters:

$$h_2 = 1.524\,\text{mm}, \quad \varepsilon_2 = 2.6\text{-Rogers-RT/ULTRALAM 2000}$$

Figure 2 shows the detailed dimensions of the created model. For such a set model, set the basic parameters and characteristics of the antenna. The lowest value of the VSWR was obtained at a frequency of 1.79 GHz (Fig. 3). This gives a deviation from the assumed antenna resonance frequency equal to 10 MHz, or approximately 0.56% f_r.

Figure 4 shows the radiation characteristics of the antenna model. Antenna directivity is 7.18 dB.

Input resistance of designed antenna for frequency 1.79 GHz is 49.25 Ω (Fig. 3(b)). Fig. 4 shows the radiation pattern of designed antenna. The radiation propagates along the Z axis, used the

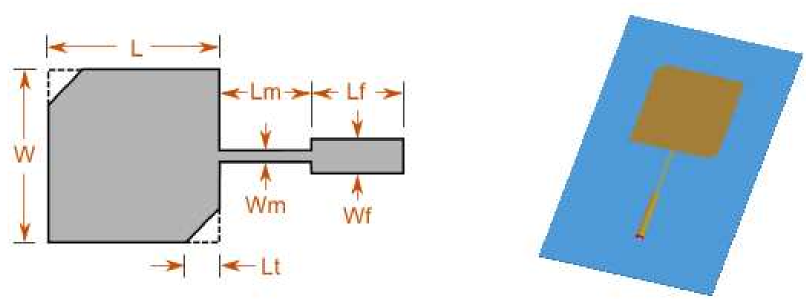

(a) (b)

Figure 1: Model of the proposed antenna. (a) Construction of the antenna. (b) General view.

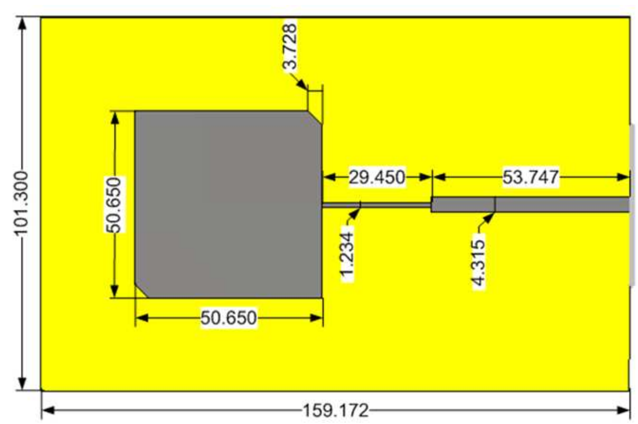

Figure 2: Dimensional model analyzed antenna.

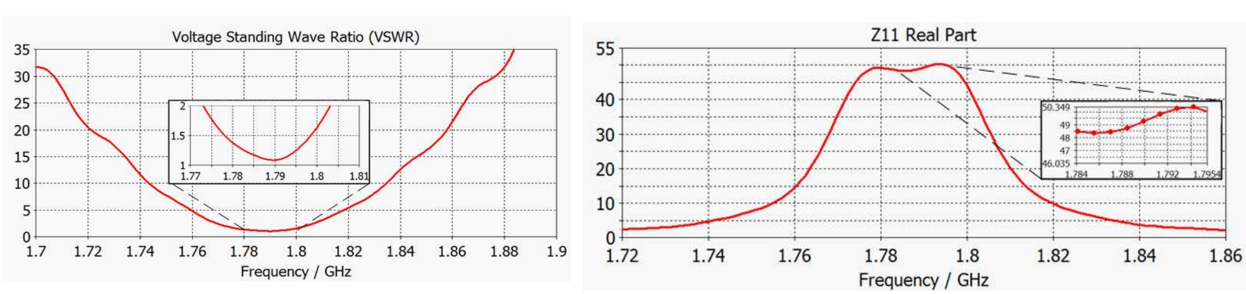

(a) (b)

Figure 3: The course of (a) VSWR and (b) real part of impedance as a function of frequency.

screen causes the radiation propagated in the direction of the human body is suppressed by about 15 dB.

4. MEASUREMENTS

In order to verify the results obtained in the simulation we performed measurements of electrical parameters and radiation characteristics of selected antenna. In order to investigate the antenna were measured the following parameters: VSWR, radiation patterns and input impedance. The measurement of VSWR and input impedance (real and imaginary part) of the discussed microstrip

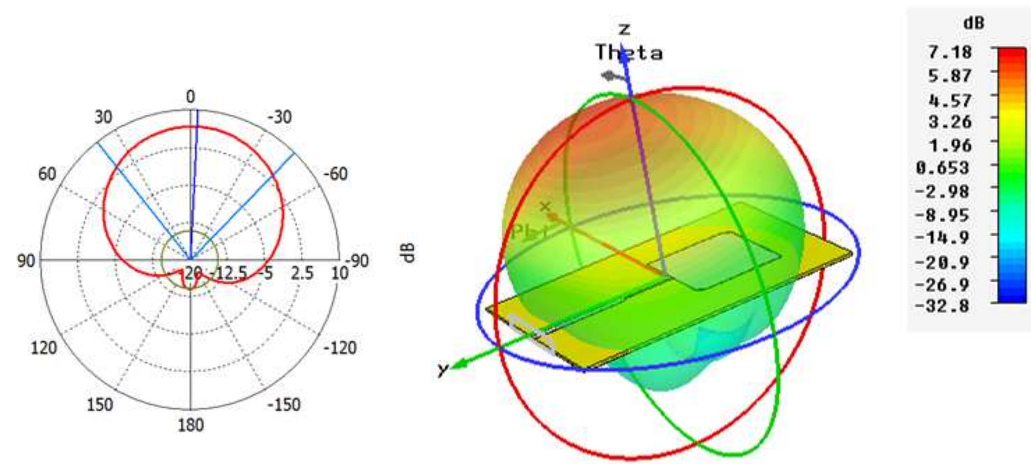

(a) (b)

Figure 4: Characteristics of the radiation model designed antenna polarization V at a frequency of 1790 MHz. (a) In polar coordinates. (b) Spatial.

Figure 5: Wearable antenna during the measurements in the anechoic chamber.

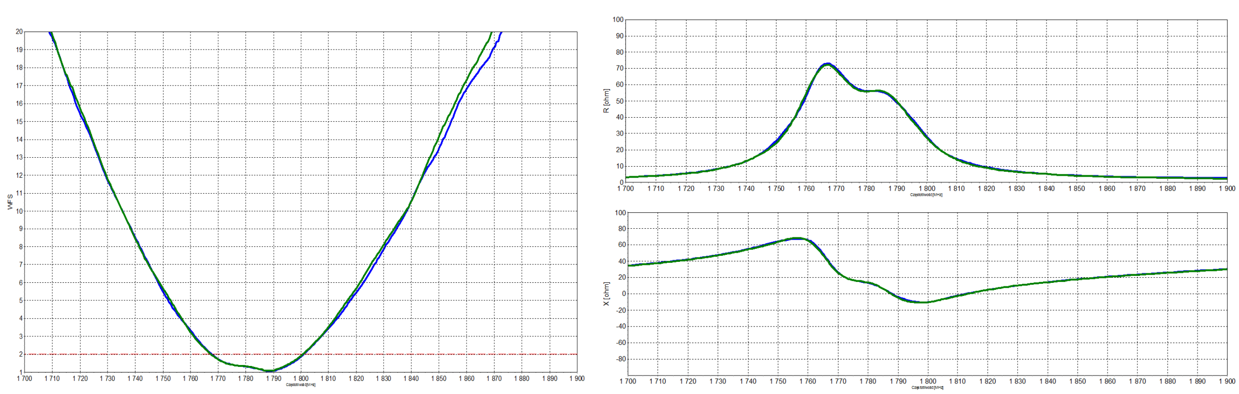

(a) (b)

Figure 6: The measured value parameters of the designed antenna as a function of frequency (green-measurement antenna positioned on soldier, blue-measurement in free space. (a) The VSWR. (b) Input impedance.

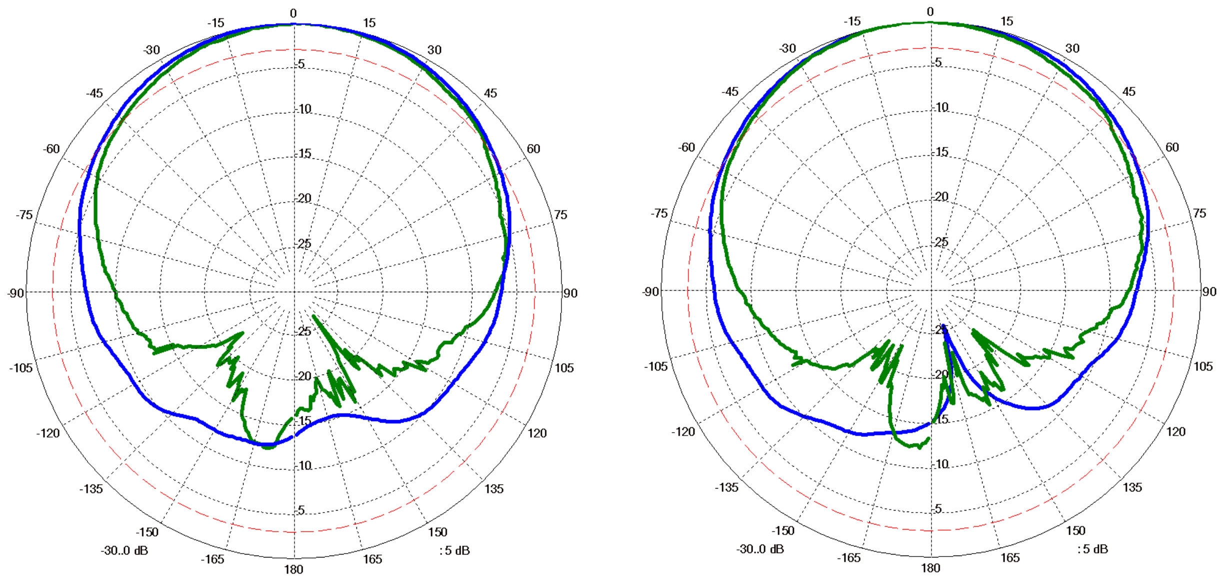

(a) (b)

Figure 7: The radiation pattern of antenna model in polarization V (green color-measurement of the antenna placed on a soldier, blue-measurement in free space). (a) 1780 MHz. (b) 1790 MHz.

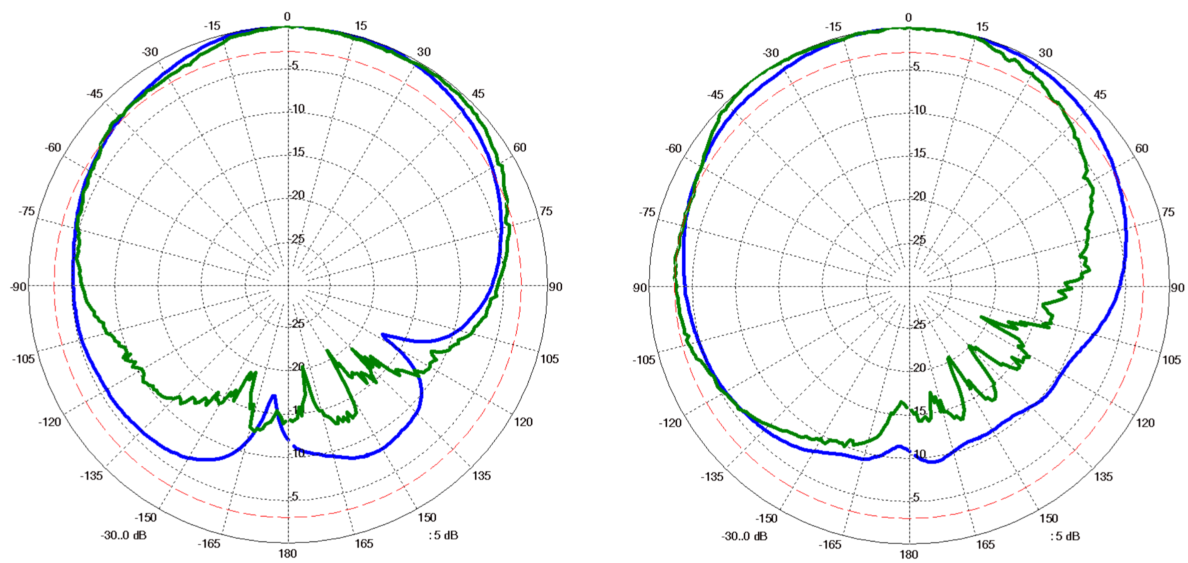

(a) (b)

Figure 8: The radiation pattern of antenna model in polarization H (green color-measurement of the antenna placed on a soldier, blue-measurement in free space). (a) 1780 MHz. (b) 1790 MHz.

active antennas in frequency domain are presented below (Fig. 7)

The measurements in anechoic chamber is shown in Fig. 6.

The results obtained by measuring confirm the correctness of performed simulations. Clearly show that the parameters associated with the antenna impedance matching in fact do not change (Fig. 6) without the insight of whether the antenna is in free space or close to the human body. This is a very desirable feature because the antenna during human movement changes its distance in relation to the human body.

In Figs. 7 and 8 shows the comparison of the characteristics of radiation in two planes of polarization measured in free space and near the body. The results obtained allow to conclude that the human body introduces additional damping in the reverse direction antenna. In the direction of the main stands no significant change, which is an advantage this construction of antenna.

5. CONCLUSIONS

Microstrip antennas are now widely used in the construction of modern aerials, primarily in the so-called reported. antenna systems. Such technologies are used both in the construction of radar antennas, Wi-Fi and cellular sector antennas in UMTS. Antenna design is a modern solution for a compact antenna device form, which is especially important in a situation to use it on moving objects. The results of measurements show that the designed and constructed antenna has a small influence on the human body and its performance characteristics. The measurement results fully confirm the possibility of using planar antenna constructed as wearable antenna.

ACKNOWLEDGMENT

The research work financed from the financial funds assigned to the science in the years 2011/2013 as the development work. The research work is realized in Poland.

REFERENCES

1. Rais, N. H. M., P. J. Soh, F. Malek, S. Ahmad, N. B. M. Hashim, and P. S. Hall *A Review of Wearable Antenna, Loughborough Antennas* & *Propagation Conference*, Loughborough, November 2009.
2. Garg, R., P. Bhartia, I. Bahl, and A. Ittipiboon, *Microstrip Antenna Design Handbook*, Artech House Inc., Norwood, 2001.
3. Białecki, M., *Bydgoski Biuletyn Mikrofalowy*, Bydgoszcz, Czerwiec 2005.

Coaxial Cables Shielding Efficiency Measuring Methodology

L. Nowosielski, M. Wnuk, R. Przesmycki, K. Piwowarczyk, and M. Bugaj
Faculty of Electronics, Military University of Technology
Gen. S. Kaliskiego 2 Str., Warsaw 00-908, Poland

Abstract— The article concerns problems connected with electromagnetic compatibility (EMC). Its aim is to present a sample application of measuring position and methodology of measuring shielding efficiency of coaxial cables in the frequency range from 30 MHz to 950 MHz. In the article a description of the position for measuring shielding efficiency of coaxial cables on the basis of the documents: PN-EN 50080-2 and CISPR 16-2-2 Ed.2 has been presented. The aim of these studies is to obtain measuring data essential for calculation of shielding efficiency of coaxial cables. In the article sample results from measurements of shielding efficiency of two coaxial cables (coaxial cable with a constant shield of the Heliax ETS1-50T type and coaxial cable with a shield in the form of copper braid with impedance $50\,\Omega$) in the frequency range from 30 MHz to 950 MHz have been shown. The above mentioned position is used for conducting research in the Laboratory of Electromagnetic Compatibility, Military University of Technology, which has accreditation granted by the Polish Accreditation Centre.

1. INTRODUCTION

During measuring shielding efficiency of small shielding chambers there is a necessity of connecting a measuring probe (sensor), placed inside the examined chamber, to input of a measuring receiver with the use of coaxial cable. Using small shielding chambers and coaxial cables with low shielding efficiency of mantle in the procedures for testing shielding efficiency results in adulteration of measurement results of shielding efficiency of the examined chamber. It results from the fact that during measuring attenuation of chamber shielding, a shield of measuring cable is extension of a shield of the examined shielding chamber and in case of a low quality shield used there it becomes the weakest link in the studied shielding structure. When efficiency of the examined shielding chamber is bigger than shielding efficiency of measuring cable, then the result of measuring shielding efficiency of the examined chamber will be a value close to shielding attenuation of measuring cable.

Because of that, during measuring shielding efficiency of small shielding chambers it is required to use measuring cables with shielding efficiency of mantle bigger than expected shielding efficiency of the examined chambers. It is forced by the need of monitoring shielding efficiency of measuring cables used in research procedures. The discussed procedure is based on the below mentioned standardization documents:

- PN-EN 50080-2 “Cable networks used for distribution of television & radio broadcasting signals and interactive services — Part 2: Electromagnetic compatibility of devices”,
- CISPR 16-2-2 Ed.2: “Specification for radio disturbance and immunity measuring apparatus and methods — Part 2-2: Methods of measurement of disturbances and immunity. Measurement of disturbance Power”.

2. PRINCIPLES OF RESEARCH METHOD

Measuring shielding efficiency of cables consists in testing which part of energy of the signal inputted into cable is emitted from the structure of its mantle. Test signal is given from a signal generator. Its frequency and amplitude must be contained in nominal operating ranges of the examined cable. For recording radiated energy we use absorbing clamp shifted along the whole tested cable. Change of measuring frequency should take place each time after a full shift cycle of absorbing clamp with a pitch allowing to examine the whole range of nominal frequency of a particular cable. Place of occurrence of maximal radiation is dependent on frequency and falls within the distance of $\lambda/2$ of wavelength of test signal from the beginning of the tested cable segment.

In order to measure the value of attenuation contributed by shield of the tested cable a measuring set is required which includes a measuring signal generator and a meter of signal level. The measuring set also includes software, which activated on operating computer allows for automation of measuring process and the measuring probe in the form of absorbing clamp cooperating with a slide bar. The rule of operation of the measuring set is described below.

Measurement of attenuation contributed by the cable shield comes to conducting two measurements of the test signal level for a particular probing frequency and amplitude. The first measurement is conducted as so called standardization measurement. With a determined value of the signal level generated by the probing signal generator connected to the input of the tested cable, the signal level is measured at the output of the tested cable with the use of a selective measuring receiver. Measurements can be carried out at discrete frequencies or in a set band with a determined step. The measured values of test signal at the output of the tested cable corresponding with particular measuring frequencies should be remembered. A simplified block diagram of a position for measuring shielding efficiency of cables used during standardization measurement has been shown in Fig. 1.

After conducting standardization measurement it is necessary to carry out basic measurement during which the output of absorbing clamp is being connected to the input of the selective measuring receiver. To the output of the tested cable, in the place of the selective measuring receiver attached during standardization measurement, matched load is being attached. The input of the tested cable is connected to the output of the test signal generator. With a determined value of the signal level generated by the test signal generator the signal level induced at the output of absorbing clamp is being measured. The absorbing clamp should be shifted along the whole length of the tested cable and record maximal values of cable radiation for a given frequency. The values measured with the use of selective measuring receiver should be corrected with the level values from calibration curve of absorbing clamp at particular frequency. Corrected power of radiation from the cable structure is expressed by formula:

$$P[\mathrm{dBm}] = P_m[\mathrm{dBm}] + K_m[\mathrm{dB}], \tag{1}$$

where: P — maximal power of radiation from the cable structure, P_m — indications of the meter, K_m — correction coefficient of absorbing clamp.

Basic measurement should be performed in the same way as standardization measurement at discrete frequencies or in a set band with particular step. The measured values at the output of absorbing clamp, corresponding with particular measuring frequencies, ought to be remembered. After subtracting recorded signal levels corresponding with particular frequencies of probing signal during standardization and basic measurement we obtain the difference of levels of received signals in [dB], which is the value of attenuation contributed by shield of the tested cable. In this way we can obtain characteristics of shielding efficiency in the function of frequency. A simplified block diagram of a position for measuring shielding efficiency of cables used during basic measurement has been presented in Fig. 2.

A very important stage of measuring procedure is checking correction of operation of a given measuring position. Test measurement consists in conducting standardization and basic measurement in the way described above and then repetition of basic measurement after previous connection of attenuator at the measuring output of absorbing clamp. A known value of attenuation of attached attenuator should be reflected in the increase of measured shield attenuation of the examined cable. In case when the above mentioned increase is equal to the attenuation value of the attached attenuator, one should recognize that the set measuring position works correctly. A simplified block diagram of a position for conducting test of correct operation of measuring position has been displayed in Fig. 3.

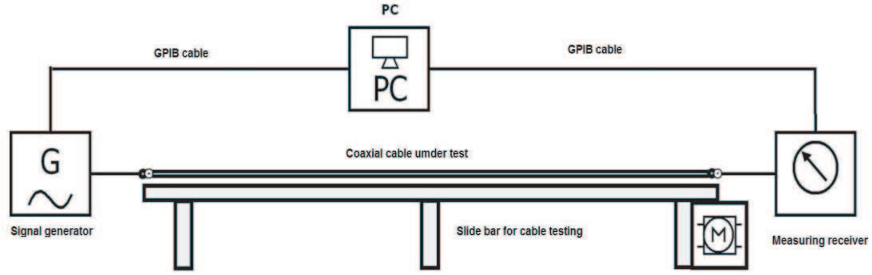

Figure 1: Block diagram of the position used during standardization measurement of testing shielding efficiency of coaxial cables.

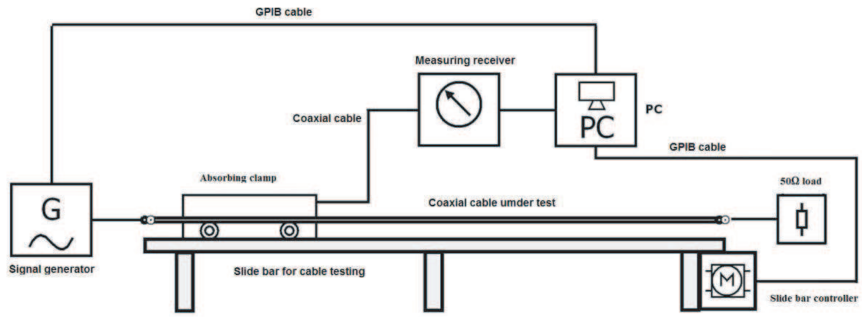

Figure 2: Block diagram of the position used during basic measurement of testing shielding efficiency of coaxial cables.

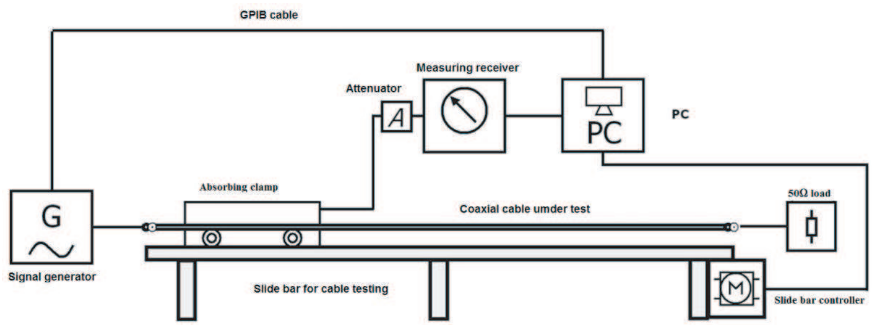

Figure 3: Block diagram of the position for conducting test of correct operation of the presented position.

Figure 4: Sample configuration of measuring position to measure shielding efficiency of cable.

3. MEASURING POSITION

Measurements are carried out with the use of measuring receivers equipped with peak detectors. A measuring place should allow to differentiate disorders caused by an examined object from the background of external disturbances. A photo of a sample configuration of measuring position is shown in Fig. 4.

In the discussed measuring position a spectrum analyzer E4407B by the Agilent company is being used as well as the signal generator SMB 100A by Rohde&Schwarz, absorbing clamp MDS-21 by Rohde&Schwarz, slide bar with the controller KMS 5300 by Rohde&Schwarz, controller CO2000 by INCO, adapter USB/GPIB 82357A by HP and PC computer. All equipment is remotely controlled by GPIB interface.

4. MEASUREMENT RESULTS

Using a designed methodology of measuring shielding efficiency of coaxial cables and measuring equipment provided by LAB KEM WEL WAT, measurements of two cables have been conducted: with constant shield and with shield in the form of copper wire braid, which are shown in Fig. 5 and Fig. 6. From the structure of both cables results that a bigger shielding efficiency should have the cable with constant shield in the form of copper tube. If measurement results of shielding efficiency of both cables reveal significant differences in favour of the cable with constant shield, it will be a proof for correct operation of the designed measuring position.

Figure 5: Coaxial cable with constant shield.

Figure 6: Coaxial cable with shield in the form of copper wire braid.

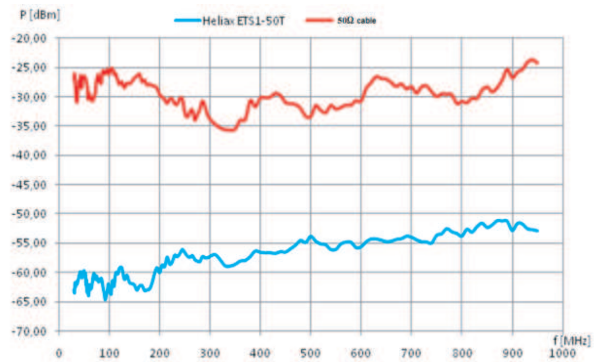

Figure 7: Comparison of maximal power for particular cables during basic measurement.

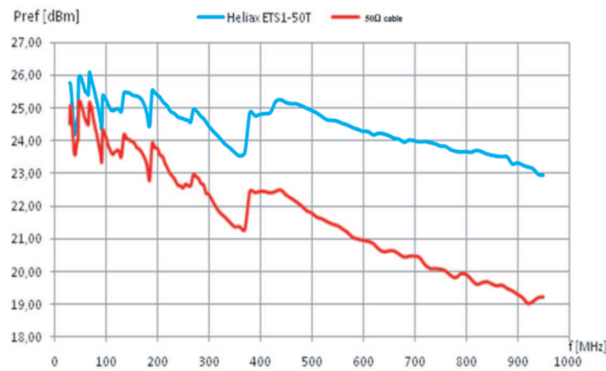

Figure 8: Comparison of maximal power for particular cables during reference measurement.

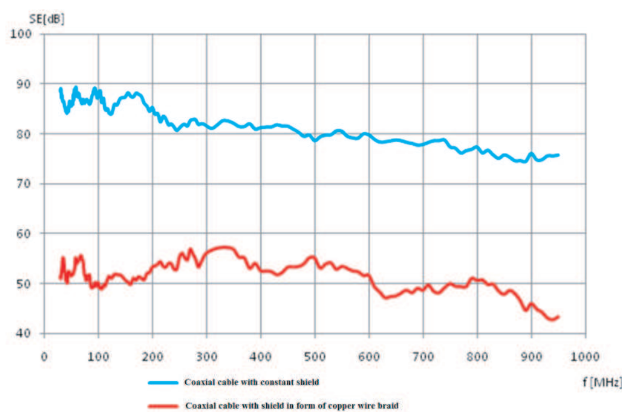

Figure 9: Shielding efficiency of cables with constant shield and in the form of copper wire braid.

Measurement results of maximal power radiated from the cable structure and maximal power received in standardization measurement for the examined coaxial cables have been presented in Figs. 7 and 8. Whereas calculated values of shielding efficiency of both cables have been shown in Fig. 9. From the presented diagrams one can see that the cable with constant shield is characterized by bigger shielding efficiency (of about 30 dB) compared to the cable with shield in the form of copper wire braid. It confirms initial assumptions and moreover it proves correctness of operation of the designed measuring position.

5. CONCLUSIONS

The designed measuring position is assigned for determining shielding efficiency of coaxial cables in the frequency range from 30 MHz to 950 MHz. The designed position has successfully gone through an internal technical audit conducted by experts from Military University of Technology. The studies carried out with the use of the presented position are included in an offer of the Laboratory of Electromagnetic Compatibility at the Faculty of Electronics of Military University of Technology.

ACKNOWLEDGMENT

The research work financed from the financial funds assigned to the science in the years 2010/2012 as the development work. The research work is realized in Poland.

REFERENCES

1. CISPR 16-2-2 Ed.2, "Specification for radio disturbance and immunity measuring apparatus and methods — Part 2-2: Methods of measurement of disturbances and immunity — Measurement of disturbance power," 2005.
2. CISPR 16-1, "Specification for radio disturbance and immunity measuring apparatus and methods — Part 1-1: Radio disturbance and immunity measuring apparatus — Measuring apparatus," 2008.

The Conducted and Radiated Emission Levels from IT Devices

Rafal Przesmycki, **Marian Wnuk**, **Leszek Nowosielski**,
Kazimierz Piwowarczyk, **and Marek Bugaj**
Faculty of Electronics, Military University of Technology
Gen. S. Kaliskiego 2 Str., Warsaw 00-908, Poland

Abstract— The article concerns problems of electromagnetic compatibility of contemporary IT devices. Particular attention was paid to undesirable emissions, which are by-products generated unintentionally during realization of basic functions of device. In the article the methodology of measuring conducted emission on supply terminals of IT devices according to the EN 55022:2006 standard in the frequency range from 0.15 MHz to 30 MHz has been presented as well as the methodology of measuring radiated emissivity of IT devices in accordance with the EN 5022:2006 standard in the frequency range from 30 MHz to 6000 MHz. Also the results of measurements conducted on particular number of central processing units have been demonstrated along with keyboards and mice produced in the years 2007–2011 and next their analysis has been made.

1. INTRODUCTION

Telecommunications and data communications devices are integral part of complex systems, which determine the correct functioning of economy. Efficiency and reliability of the functioning of electric and electronic devices decide about the functioning and development of national economy. To a large extent it depends on hazards and the level of disturbances occurring in the environment surrounding us. Thus it is necessary not only to study sensitivity of electric and electronic devices to electromagnetic fields but also to control the level of electromagnetic disturbances emitted to the surrounding environment through different ways.

The problem is important not only because of electromagnetic compatibility but also due to necessity of providing security of sent or processed information. Currently there are available devices which allow to reconstruct processed or sent information by using dispersed electromagnetic fields (unintentionally radiated). Therefore issues connected with the control of disturbance emissions become particularly significant.

In the article the measuring results of levels of radiated or conducted emission on supply terminals of contemporary IT devices including the measurement methodology have been presented.

2. ASSESSMENT OF THE DEVICE EMISSION

Each device is characterized by parameter ε determining emission ability. It is the function of emission direction φ, pulsation ω and time t,

$$\varepsilon = f(\varphi, \omega, \mathrm{t}). \tag{1}$$

Electromagnetic emissions to the environment can be divided into two large groups — namely: desirable and undesirable emissions. Desirable emissions are associated with the sending of signals carrying useful information. Disturbances in the device operation which are caused by desirable radiation are eliminated by appropriate assignment of frequency band or operating frequency.

In this study a particular attention was paid to undesirable emissions. They are by-products generated unintentionally during realization of basic function of the device. They are formed in electric circuits containing inductances and capacities in which there occur sudden changes of current or voltage, relatively fluctuating changes of density of electric charge carriers or in which there occurs positive back coupling.

Distribution of energy of electromagnetic disturbances in the frequency spectrum and their transient performances depend on the structure and electric parameters of the device generating them in the RF range, its transient response and impedance of loading circuits. Taking into account transient performances of desirable and undesirable emissions, we can divide generated disturbances into constant and impulse ones or due to frequency characteristic into: narrow and broad-band.

Because of different ways of energy emission of disturbances to the environment various parameters define the level of disturbances generated by one source or some set of sources. Usually the level of generated disturbances is determined by providing the value of power of emitted electromagnetic

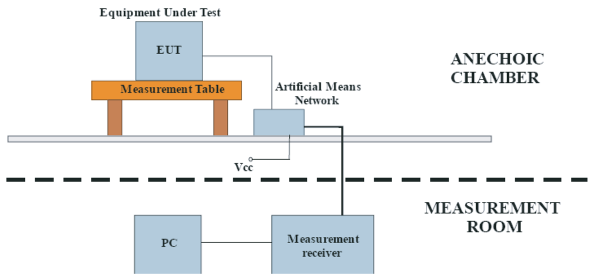

Figure 1: Block diagram of the measuring position for measuring conducted emissions.

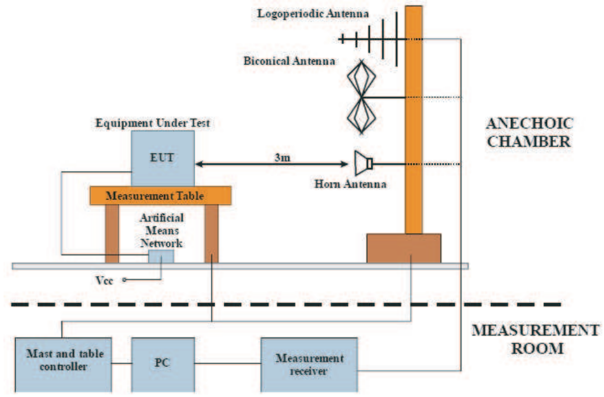

Figure 2: Block diagram of the measuring position for measuring radiated emissions.

field (P_z) or the value of electromagnetic field strength (electric component E_z or magnetic component H_z) within the determined distance from the source or the voltage value (U_z), or current (I_z) measured in an added to the source circuit loaded with known impedance. The values of these parameters are given in the frequency function i.e., in the form of spectral characteristics. Determined values of disturbances emitted to the environment are compared to admissible levels determined for a particular class of device during the process of supervising devices admitted to trade turnover.

In further part of the article the disturbances are defined, the methodology of measuring conducted and radiated emissivity of IT devices in accordance with the EN 55022:2006 standard is presented and the results of measurements carried out on particular number of samples consisting of central processing units produced in the years 2007–2011 are demonstrated. The measurements of conducted and radiated emissivity have been performed in the Electromagnetic Compatibility Laboratory at the Faculty of Electronics of the Military University of Technology in Poland.

3. MEASUREMENT OF CONDUCTED DISTURBANCES OF IT DEVICES IN THE RANGE FROM 150 KHz TO 30 MHz

The measurements of conducted disturbances emitted by IT devices have been performed in accordance with the EN 55022:2006 standard. They consist in measuring the level of electromagnetic field on supply terminals of device with the use of artificial mains network (AMN) line and measuring receiver in the frequency range from 0.15 MHz to 30 MHz.

Conducted disturbances are measured between phase circuit and reference ground and between neutral circuit and reference ground. Steering the measuring process (change of setting of measuring receiver and artificial network) is carried out by the software EMC32 of the Rohde&Schwarz company, installed on a computer which steers the measuring process.

To measure conducted disturbances it is necessary to set up a measuring position in the configuration as it is shown in Figure 1.

The measurements are performed in the frequency range from 0.15 MHz to 30 MHz, using the measuring receiver equipped with detectors of quasi-peak and average values and RBW filter of the frequency band equal to 9 kHz. Both detectors can be situated in one receiver and the measurements are carried out by turns for particular detectors. Due to the measurement automation, in the above mentioned measuring method the artificial means network ENV216 is used.

4. MEASUREMENT OF RADIATED DISTURBANCES OF IT DEVICES IN THE RANGE FROM 30 MHz TO 6000 MHz

Measurements of radiated disturbances emitted by IT devices have been performed in accordance with the EN 55022:2006 standard. They consist in measuring electromagnetic field strength within the distance of 3 m from the device with the use of measuring antennas and measuring receiver in the frequency range from 30 MHz to 6000 MHz. The measurements are conducted for vertical and horizontal polarization of measuring antennas and for particular combinations of location of the EUT. The EUT location towards measuring antenna is changed with the use of turntable and aerial mast automatically. It can be obtained due to using a suitable controller which steers the turntable and height of the aerial mast as well as computer steering the whole measuring process. To measure radiated disturbances it is necessary to set up the measuring position in the configuration as shown in Figure 2.

The measurements are made in the frequency range from 30 MHz to 6000 MHz, using measurement receiver with peak detector and RBW filter with frequency band equal to 120 kHz for the range 30 MHz–1000 MHz and 1 MHz for the range 1 GHz–6 GHz. Due to the measurement automation, in the above mentioned measuring method broad-band antennas have been used, which do not require adjustment of antenna's length to resonant length for particular measuring frequency. The biconical antenna SAS544 is used for measuring radiated disturbances in the frequency range from 30 MHz to 230 MHz, the log-periodic antenna 3147 is used in the frequency range from 230 MHz to 1000 MHz, whereas the horn antenna DRG-118/A — in the frequency range from 1 GHz to 6 GHz.

5. MEASURING RESULTS-LEVELS OF CONDUCTED EMISSION ON SUPPLY TERMINALS OF IT DEVICES IN THE RANGE FROM 0.15 MHz TO 30 MHz

The measurements of the disturbance levels of conducted emissions on supply terminals emitted by IT devices have been carried out on particular number of device items. On the basis of the obtained measuring results an analysis of levels of conducted emissivity of contemporary IT devices has been made. The measurements have been completed in the frequency range from 0.15 MHz to 30 MHz. Twenty items of PCs have been examined. In Figure 3 maximal and averaging levels of conducted emissions on supply terminals of contemporary IT devices are shown, taking into account all the tested devices.

6. MEASURING RESULTS-LEVELS OF RADIATED EMISSION OF IT DEVICES IN THE RANGE FROM 30 MHz TO 6000 MHz

The measurements of the disturbance levels of radiated emission emitted by IT devices have been carried out on particular number of device items within the distance of 3 m from the tested device. On the basis of the obtained measuring results an analysis of levels of radiated emission of contemporary IT devices has been made. The measurements have been performed in the frequency range from 30 MHz to 6000 MHz, using a peak detector, however because of measuring abilities of the laboratory and used measuring equipment (mainly antennas) the measurements have been divided into two sub-bands. The first frequency range spreads out from 30 MHz to 1000 MHz, the second frequency range is contained in the range between 1000 MHz and 6000 MHz. In the first frequency range 139 PCs have been examined while in the second frequency range 104 computers. In Figure 4 and Figure 5 maximal and averaging levels of measured values of electromagnetic field strength radiated by contemporary IT devices are showed, taking into account all the tested devices.

7. MEASURING RESULTS-ANALYSIS OF THE MEASURING RESULTS OF CONDUCTED AND RADIATED EMISSION OF IT DEVICES

Analyzing averaging values of conducted and radiated disturbances we can notice that for a few frequencies there occur much larger levels of emission when compared to others. For these frequencies an identification of components by the elimination method has been made. This method consists in consecutive disconnections of loads of interfaces in central processing units during the research

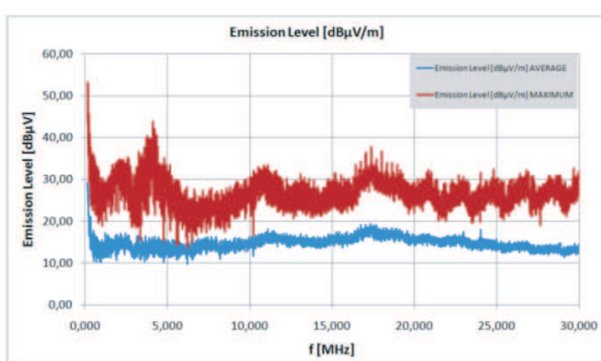

Figure 3: Maximal and averaging levels of conducted emissions of all EUT in the frequency range from 0.15 MHz to 30 MHz.

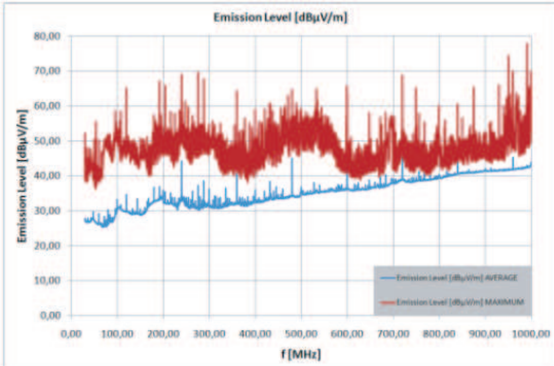

Figure 4: Maximal and averaging levels of radiated disturbances within the distance of 3 m from all EUT in the frequency range from 30 MHz to 1 GHz.

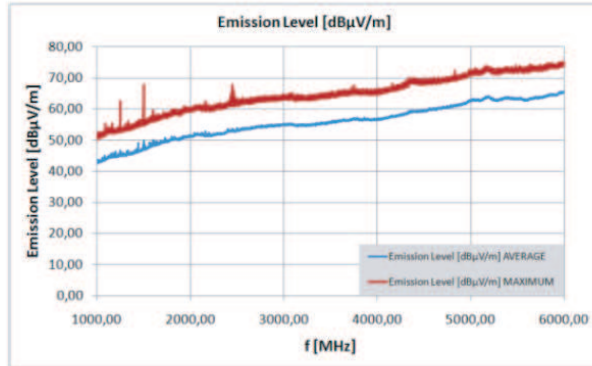

Figure 5: Maximal and averaging levels of radiated disturbances within the distance of 3 m from all EUT in the frequency range from 1 GHz to 6 GHz.

Table 1: Levels of electromagnetic field strength of the examined device deriving from components located in central processing unit.

Device/ type of interface	Frequency [MHz]	Emission level within the distance of 3 m from EUT [dBμV/m]	
		MAX	AVERAGE
USB	119.00	46.48	29.86
USB	120.00	65.26	35.11
Mouse / PS2	126.00	49.66	30.04
Printer / LPT	144.00	48.33	33.42
Mouse / PS2	166.00	39.58	30.54
USB	180.00	57.50	35.96
Keyboard / USB	200.00	48.31	35.37
USB	240.00	69.17	42.21
USB	480.00	55.56	42.34
Graphic card / DVI	720.00	68.89	44.96
USB	960.00	58.89	43.18

described in the above mentioned chapters. In Table 1 frequencies of occurrence of radiated emissions coming from particular components located in the CPU are presented as well as their levels measured in accordance with the methodology described in the EN 55022:2006 standard.

8. CONCLUSIONS

Every IT device from the European Union market should comply with particular standards concerning valid directives of new approach. Due to the necessity of conformity with the directive of electromagnetic compatibility of IT equipment, in the article the methodology of measuring conducted emissivity on supply terminals of IT devices in the frequency range from 0.15 MHz to 30 MHz has been presented as well as the methodology of measuring radiated emissivity of IT devices in the frequency range from 30 MHz to 6000 MHz in accordance with the EN 55022:2006 standard. Also the measuring results deriving from modern IT devices have been demonstrated.

The maximal levels of conducted and radiated undesirable emissions coming from contemporary IT equipment present in the EU market have been determined and estimated. Those emissions are by-products generated unintentionally during realization of basic function of the device, therefore it is necessary to strive to make their level as low as possible. Moreover the identification of particular components which are part of central processing unit has been made, based on spectra of radiated emissions of PC units. The determined levels can be fundamental at initial stages of designing electromagnetic securities of contemporary IT devices with striving to provide conformity with appropriate EMC standards valid in the European Union.

ACKNOWLEDGMENT

The research work financed from the financial funds assigned to the science in the years 2010/2012 as the development work. The research work is realized in Poland.

REFERENCES

1. EN 55022:2006 +A1:2007 standard, Information technology equipment, Radio disturbance characteristics, Limits and methods of measurement.

EMC Filters Attenuation Measuring Method

Kazimierz Piwowarczyk, **Marian Wnuk**, **Leszek Nowosielski**,
Rafal Przesmycki, and **Marek Bugaj**
Faculty of Electronics, Military University of Technology
Gen. S. Kaliskiego 2 str., 00-908 Warsaw, Poland

Abstract— The aim of this work is to present the attenuation measurement procedure measurement and laboratory stand for filters used to interference suppression in power and telecommunication lines. The procedure is based on the CISPR 17:2000 standard. The article describes the attenuation measurement system for filter with impedance different then $50\,\Omega$. The article presents the measured attenuation characteristics of set of EMC filters which are offered on the market. The calibration of measurement method is presented too.

1. INTRODUCTION

Electromagnetic compatibility (EMC) is the ability of an electronic system or subsystem to reliably operate in its intended electromagnetic environment without either responding to electrical noise or generating unwanted electrical noise. Electromagnetic interference (EMI) is the impairment of the performance of an electronic system or subsystem by an unwanted electromagnetic disturbance.

In general the public mains power supply voltage waveform is sinusoidal, which means that it includes only the fundamental frequency (50 or 60 Hz) without any harmonic multiples of this frequency. Purely resistive circuits such as filament lamps or heaters, when powered from the mains, draw a current that is directly proportional to the applied voltage, and do not create any extra harmonic components. By contrast, non-linear circuits do draw a non-sinusoidal current, despite the applied voltage being sinusoidal. All non-linear currents, however, will cause harmonics currents, i.e., currents with frequencies that are integer multiples of the supply frequency.

Traditionally, harmonic pollution was only a concern for larger installations, particularly for power generation and distribution and heavy industry. But the modern proliferation of small electronic devices, each drawing perhaps only a few tens or hundreds of watts of mains power, and usually single-phase (such as personal computers), has brought the problem of mains harmonics to the fore even in domestic and commercial applications. Of all the above examples, it is the electronic DC power supplies that are causing the most concern due to the increasing numbers of electronic devices such as TV sets in domestic premises, information technology equipment in commercial buildings and adjustable-speed drives in industry [1].

2. ELECTRICAL SPECIFICATIONS OF FILTERS

Where indicated, the component values in the datasheets are nominal values. The actual values can vary from the indicated ones based on the electrical tolerances given by the manufacturers. The test conditions for the components are listed below.

Current ratings of EMI filters are determined by the individual filter components. Since current flow leads to a temperature rise in passive components, the ambient temperature of the environment where the filter is to be used has a direct impact on the rated current. The nominal currents stated for our components refer to an ambient temperature of $0N = 40°\mathrm{C}$ or $0N = 50°\mathrm{C}$ as indicated on the component and in this catalog. The maximum operating current at any other ambient temperature Θ can be calculated by means of the formula (1).

$$I = I_N \cdot \sqrt{\frac{\theta_{\max} - \theta_{act}}{\theta_{\max} - \theta_N}} \tag{1}$$

where: I_N — rated current at θ_N, θ_{act} — actual ambient temperature, θ_N — temperature at which the rated current is defined, $\theta_{\max}$ — rated maximum temperature of the component,

Voltage. When looking at voltage ratings, care needs to be taken not to confuse the voltage rating of the filter with the nominal voltage of the power grid. The most common nominal voltages are defined in IEC 60038. A European power grid, for example, has a defined nominal voltage of $230\,\mathrm{V} \pm 10\%$. The maximum voltage at the terminals can therefore be $230\,\mathrm{V} + 10\% = 253\,\mathrm{V}$.

DC resistance. The DC resistance of the filter is the resistance measured at the relevant power network frequency, i.e., 50 Hz for European applications and at a defined temperature, such as 25°C.

3. MEASUREMENT METHODS

Generally, to suppress power line and signal line emission, some form of filtering is required. Filter attenuation is highly dependent upon source and load impedances. Manufacturers' data is generally published for 50 Ω source and load impedances while actual impedances are generally reactive and vary considerably over the frequency range of interest. While there are methods for determining the actual impedances, these values are usually unknown. Hence, the selection of filters through mathematical computation is usually impractical.

An alternative approach is that of impedance mismatch. That is, if a filter mismatches its source and load impedances, minimum transfer of signal (EMI) power will occur. If the source impedance is high, the filter input impedance should be low, or shunts capacitive. If the source impedance is low, the filter input impedance should be high, or series reactive. The same mismatch should exist between the load impedance and the filter's output impedance [2].

Another consideration is whether the EMI is common mode or differential mode, where common mode refers to noise voltages on two conductors referenced to ground, and differential mode refers to a voltage present on one conductor referenced to the other. In many cases both types of EMI must be attenuated. Virtually all off-the-shelf power line filters are designed to handle common mode noise, and many provide both common and differential mode filtering. Without conducted emission test data, it is generally difficult to determine the interference mode of the equipment and thus the type of filter required.

3.1. The Classic Method of Measuring

The method is based on measuring the efficiency of filters used to suppress disturbances in the supply lines and data lines. Measurement frequency range is in the band from 30 MHz to 950 MHz (the method is acceptable and correct to the frequency of 5 MHz). The measurement is carried out in an anechoic chamber. This allows get the most exact results without interference from other devices working.

Filters are generally described by their attenuation, also called insertion loss. In order to determine the attenuation, a defined source and load are connected and the signal from the source is measured. The filter is then inserted and the measurement repeated. The attenuation is then calculated from the two results by means of the formula (2).

$$n\,[\mathrm{dB}] = 20 \log \frac{E_1}{E_2} \tag{2}$$

where: n — attenuation [dB], E_1 — the results with the filter, E_2 — the results without the filter.

Interference accompanied current flowing in the circuit. It can be assumed that they have the same value but are in opposite phase relative to the second line. In the case of a symmetric measurement of attenuation is measured between two lines (L and N) through a symmetrical transformer. Wire mass (E) is not used during this measurement. In the asymmetrical attenuation

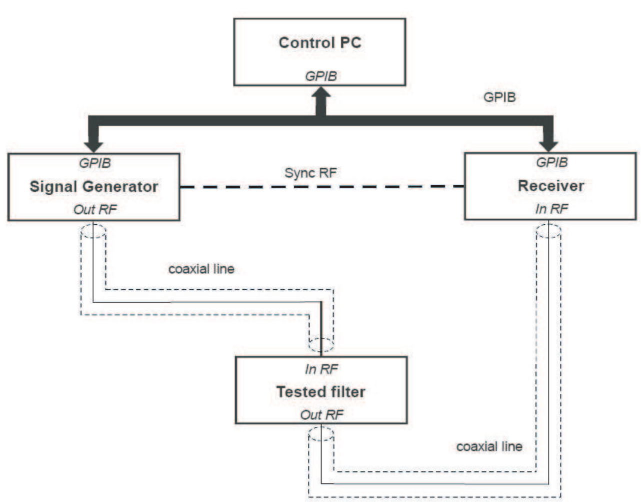

Figure 1: Classic laboratory stand.

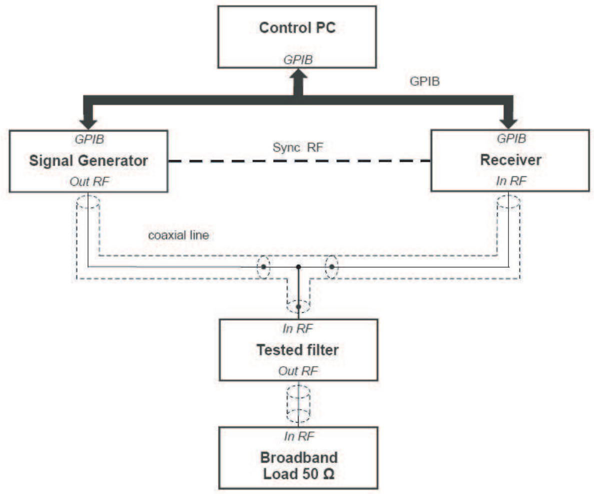

Figure 2: Block diagram of the test bench — standardization measurement.

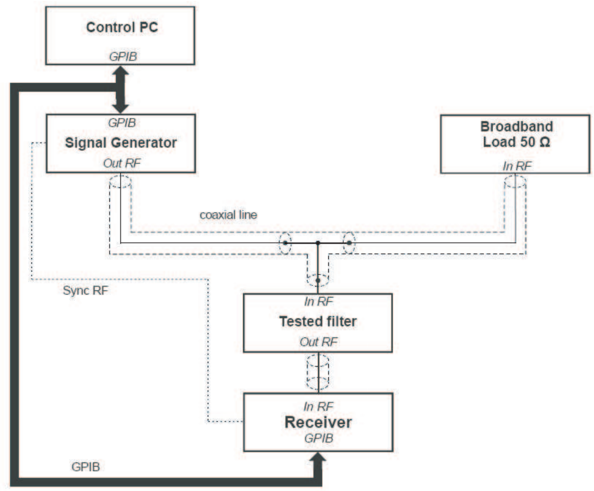

Figure 3: Block diagram of the test bench — proper measurement.

Figure 4: The measuring position prepared for conducting standardization measurement.

measurement method has the same phase as opposed to the line, but its value may be different depending on the output circuit. For this method the two lines (L and N) are connected together and the measurement is done in relation to the mass of the circuit (E) in the system. The concept of laboratory stand of shows the block diagram in Figure 1.

3.2. The Proper Method of Measuring

In to identify attenuation of individual power lines L and N well connected to them filters should be measured attenuation the individual circuits are installed on the destination solution design. Tests should be performed on the filters installed in the destination chamber shielding. Since it is not known input impedance tested power supply lines L and N, the measurements should be performed in the measurement system takes into account the differences in input impedance test circuit (impedances different from $50\,\Omega$) in relation to the input impedance of the measurement system used in devices like signal generator and receiver measurement (impedance equal to $50\,\Omega$). In Figure 2 and Figure 3 shows the proposed measurement systems to take account of differences in impedance.

Each of these configurations should be treated as a separate measuring circuit. After the measurement for standardizing the proper measurement should be done. In the place where during the standardization measurement the measurement receiver was connected the $50\,\Omega$ load must be connected. Filter attenuation is the difference between the measured signal levels in the function of frequency.

4. LABORATORY STAND

Constructed measuring stand should enable the measurement of attenuation filters. Measurements will be done according with the recommendations of the PN-CISPR 17:2000 in the frequency range from 10 kHz to 6 GHz. Table 1 shows the apparatus used for measuring the EMC filters. Figure 4 shows the measuring position prepared for conducting standardization measurement. Necessary the control software automates the measurement process.

5. MEASUREMENT RESULTS

In order to validate the work of the measuring system measured the attenuation of attenuator BN 745394 (Figure 4). Figure 5 shows the attenuation values obtained.

Figure 6 shows the measured values of attenuation power supply filter. Figure 7 shows the measured values attenuation of signal filters.

Table 1: List of equipment.

No.	Device Name	Manufacturer	Type	Serial Number
1	PC	HP	DV3600	-
2	Signal generator	Rohde & Schwarz	SMB 100A	100587
3	Reciver	Rohde & Schwarz	ESIB 26	-
4	Broadband load 50 Ω	Agilent	909F	51500
5	Attenuator	Spinner; HP	BN 745394	-
6	Filters	Schaffner Schaffner Schaffner Corcom Conec	FN 686-25-23 FN 700Z-20-03 FN 2070-3-06 F 7426-3 MAP1XAAAH02R	-
7	Converter USB/GPIB	Agilent	82357A	MY43457984

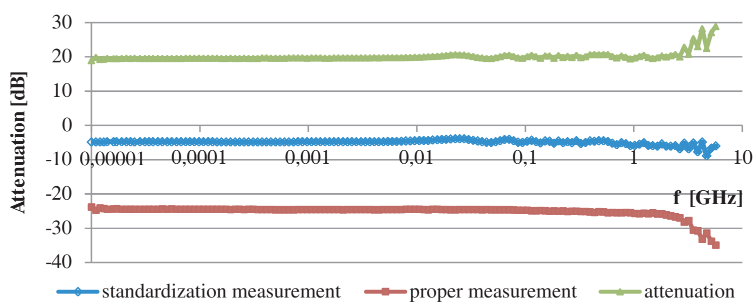

Figure 5: Attenuation attenuator BN 745394 (20 dB).

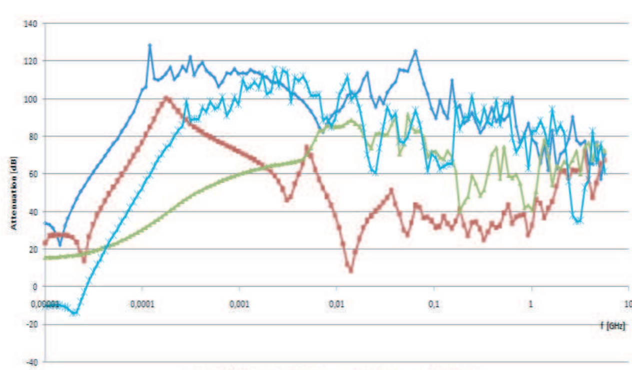

Figure 6: Attenuation power supply filters.

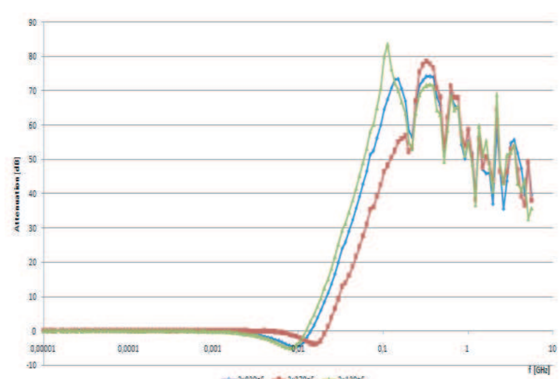

Figure 7: Attenuation signal filters.

6. CONCLUSIONS

Based on measurement results we can state that the laboratory stand built on the basis of Electromagnetic Compatibility Laboratory Military University of Technology equipment is working properly. The measured attenuation of attenuator and power supply and signal filters are similar to the manufacturer's specifications.

ACKNOWLEDGMENT

The research work financed from the financial funds assigned to the science in the years 2010/2011 as the development work. The research work is realized in Poland.

REFERENCES

1. "Basics in EMC and power quality," www.schafner.com.
2. "EMI shielding design guide," www.tecknit.com.
3. Ott, H. W., *Electromagnetic Compatibility Engineering*, A John Wiley & Sons, INC., 2009.
4. CISPR 17:2000, "Methods of measurement of the suppression characteristics of passive radio interference filters and suppression components," 2000.

NO and N_2O Detection with CEAS Method

J. Wojtas[1], **Z. Bielecki**[1], **T. Stacewicz**[2], **J. Mikolajczyk**[1], **R. Medrzycki**[1], **and B. Rutecka**[1]

[1]Institute of Optoelectronics, Military University of Technology
2 Kaliskiego Str., Warsaw 00-908, Poland
[2]Institute of Experimental Physics, University of Warsaw
69 Hoza Str., Warsaw 00-068, Poland

Abstract— The article describes an application of cavity enhanced absorption spectroscopy in nitric oxide and nitrous oxide sensors. For detection of both gases the vibronic molecular transitions were used. The wavelength ranges of these transitions are situated in mid-infrared spectra spectrum of radiation. To achieve optimal sensitivity and selectivity interferences by absorption lines from other gases commonly present in atmosphere (like H_2O or CO_2) should be minimised. The best results were obtained in the spectral regions of 5.23 µm–5.29 µm for NO and of 4.46 µm–4.54 µm for N_2O. A setup of the sensors consists of pulsed laser sources, optical cavities and photodetectors. As a radiation sources single mode quantum cascade lasers (QCL) were applied. Their narrow emission lines were precisely tuned to the wavelengths of interest. The optical cavities were built with spherical mirrors of high reflectance. The optical signal from the cavities outputs were registered with specially developed low noise detection modules. Thanks to this, the detection limits of single ppb were obtained.

1. INTRODUCTION

Nitric oxide (NO) and nitrous oxide (N_2O) are important compounds of the air. According to HITRAN database, in the standard atmosphere their concentrations are as follows: NO — 0.3 ppbv, N_2O — 320 ppbv [1]. However, in real ambient air the concentrations differ strongly due to influence of various emission sources (anthropogenic and natural). Both NO and N_2O are important greenhouse gases that have a large influence on environment, living organisms and human health. Acid rains occur due to reactions of these compounds with H_2O contained in the air. Moreover, NO and N_2O are produced during a decomposition process of specific explosive materials so these gases can be used as markers [2, 3]. Therefore these gases monitoring is of great importance for various applications: from routine air monitoring in industrial area and regions of intensive traffic, detection of explosives in airports, finally in medicine investigation, for health care, etc.

There are many techniques for NO and N_2O detection. For example, in the case of gas chromatography (GC) and mass spectrometry (MS), a detection limit of a few dozen ppb is reported [4, 5]. Detection methods using the photoacoustic phenomenon provide a sensitivity of about 20 ppb [6]. In gas detection applications, a special role is played by optoelectronic methods. They are characterized by both high selectivity and high sensitivity (low limit detection). In practice, cavity enhanced absorption spectroscopy (CEAS) belongs to the most sensitive sensors. In this technique, off-axis direction of laser beam to the optical cavity is applied (Figure 1). Inside the cavity the light is repeatedly reflected by the mirrors. In comparison to cavity ring-down spectroscopy (CRDS), the light spots on the mirrors surfaces are spatially separated and weak mode structure is occurred. It causes that the entire system is much less sensitive to instability in the cavity and to instability in laser frequencies. Additionally, due to off-axis illumination of the front mirror, the source interference by the optical feedback from the cavity is eliminated. The CEAS sensors can obtain a detection limit of about 10^{-9} cm^{-1} [7]. Therefore, this method makes the best opportunity to develop a portable optoelectronic sensor of nitrogen oxides.

In this technique determination of the concentration of the examined gas can be carried out during two-step process. In the frame of the first step, measurement of the signal decay time

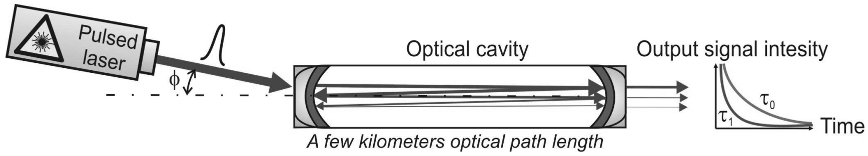

Figure 1: CEAS idea.

(τ_0) in the optical cavity not containing the absorber (tested gas) is performed. In the same way the signal decay time τ_1 in the cavity filled with the tested gas is also determined. Knowing the absorption cross section (σ) of the examined gas, its concentration can be calculated from the formula

$$C = \frac{1}{Nc\sigma}\left(\frac{1}{\tau_1} - \frac{1}{\tau_0}\right), \tag{1}$$

where N denotes the *Loschmidt's number*, c — the light speed, and

$$\tau_0 = \frac{L}{c\,(1-R)}. \tag{2}$$

2. SENSITIVITY ANALYSIS

The lowest concentration (concentration limit) of analyzed gas molecules (C_L), which causes a measurable change of the output signal, can be determined from the formula

$$C_L = \frac{1}{c\sigma\tau_0}\delta_\tau = \frac{1-R}{\sigma \cdot L}\delta_\tau, \tag{3}$$

where δ_τ is the relative measurement precision of the decay time (uncertainty). The relationship between uncertainty δ_τ and τ_0 can be described as

$$\delta_\tau = \frac{\tau_0 - \tau_L}{\tau_0} \cdot 100\%, \tag{4}$$

where τ_L denotes a decay time for the minimal absorber concentration.

In the other hand, C_L can be treated as the detection limit of the sensor. It is a function of two variables: the decay time for the empty cavity (τ_0) and measurement uncertainty ($\delta\tau$). Furthermore, the decay time τ_0, according to the formula (2), depends on the length of the resonator and the mirrors reflectivity. The increase in this time points growth of effective path of absorption. As results, the greater the sensitivity of the sensor and the lower concentrations of the absorber can be measured.

For the development of nitric oxide and nitrous oxide sensor, there could be applied both the electronic and vibronic transitions. In the case of ultraviolet wavelength range (UV) the gases absorption cross sections reach the value of $6 \times 10^{-18}\,\text{cm}^2$ for NO and value of $1.5 \times 10^{-19}\,\text{cm}^2$ for N_2O [8, 9]. In comparison with infrared spectrum (IR), these values of about $10^{-18}\,\text{cm}^2$ can be observed [1]. However, reflectivity of available UV mirrors does not exceed the value of 90%. Thus, higher sensitivity of the sensor can be obtained using IR absorption lines (Figure 2). Moreover, in the UV range, there are interferences of both investigated gases and oxygen (O_2), normally occurred in the atmosphere.

3. EXPERIMENT

The analysis shown, that application of CEAS method in the IR wavelength range provides possibility to develop NO and N_2O sensor, the sensitivity of which could reach the level of ppb. An

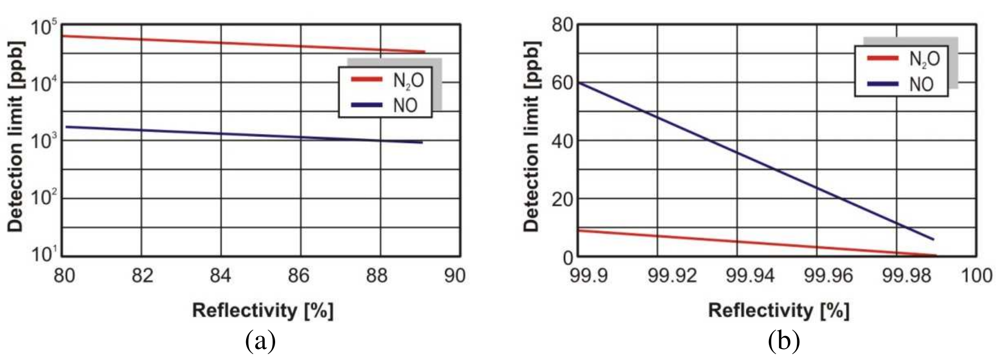

Figure 2: Detectable concentration limit vs. cavity mirrors reflectivity in the wavelength ranges of (a) UV, and of (b) IR.

experimental setup consists of two pulsed lasers with the control electronics, optical system and signal processing system (Figure 3). Two optical cavities were used, for detection of NO and N_2O respectively. Each cavity was built with highly reflective spherical mirrors (99.98%, Los Gatos Research, Inc.) characterized by curvature radius of 1 m. The distance between the mirrors was about 60 cm.

The main task of the laser electronics is to stabilize parameters of QCL's (power, lasing wavelengths). It was guaranteed with high quality power supplies (E3634A, Agilent) and thermoelectric cooling system with control unit TCU151 (Alpes Lasers SA). Laser wavelengths were precisely tuned to the selected absorption lines of NO and NO_2. Figure 4 shows selected tuning ranges of lasers spectrum.

The spectrum tuning was ensured with using temperature and power supply control. The pulsed modulations of the lasers were done using DG645 generator (Stanford Research Systems, Inc.) connected to laser drivers (LDD400, Alpes Lasers). For registrations of the optical signals from the cavity detection modules with HgCdTe (MCT) photodetectors were applied (VIGO System S.A.). Their spectral responsivity related to the selected nitrous and nitric oxides absorption lines are presented in Figure 4. The MCT modules use monolithic optical immersion technology and thermoelectric cooling. These photodetectors offer a high detectivity (about $10^{11}\,\mathrm{cm}\sqrt{\mathrm{Hz}}/\mathrm{W}$) and wide bandwidth (up to 1 GHz). The modules include special transimpedance preamplifiers that match output parameters of the photodetector to measuring circuits [10]. Signals from the detection modules were observed and analyzed using real-time oscilloscope DSA 70404 series (Tektronix, Inc.). Its software provided possibility to implement procedure of gas concentrations determination.

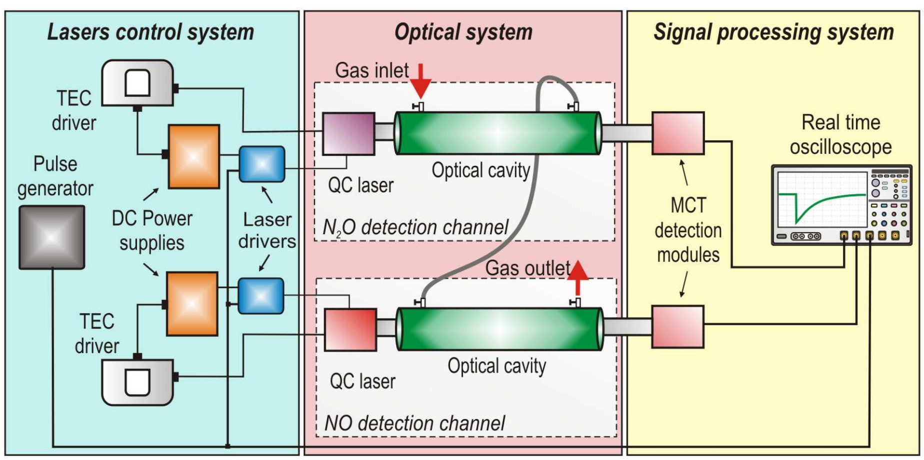

Figure 3: Simplified scheme of the experimental setup.

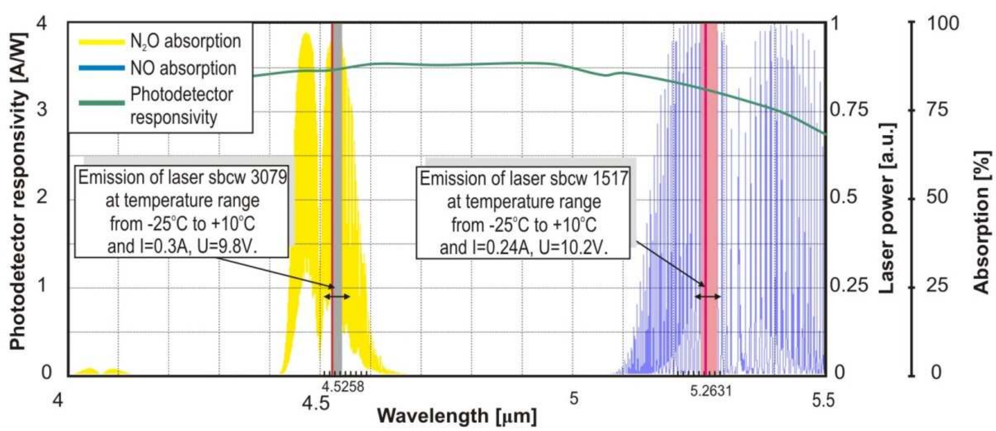

Figure 4: Characteristics of the selected QCL lasers spectra, NO and N_2O absorption lines, and photodetectors responsivity.

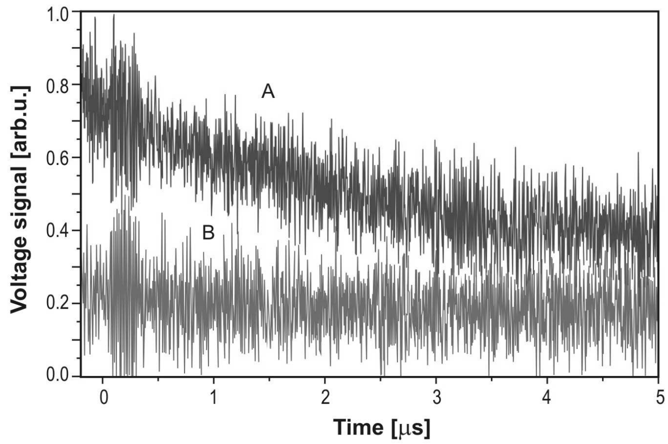

Figure 5: Example of output signals for the cavity filled with pure N_2 (A), and with N_2O (10 ppm) (B).

4. RESULTS AND DISCUSSION

During the measurements pure nitrogen (N_2) and different mixtures of NO-N_2 or N_2O-N_2 were used. The gases were let in optical cavities. Next decay times and specified gas concentration were measured at the output appropriate channel (NO or N_2O). Experiments showed that in the case of the cavity filled with nitrogen, so called reference gas, the determined decay time τ_0 was about of 2.2 μs for the NO channel and 1.6 μs for the N_2O channel. When the cavities were filled with NO and N_2O mixtures essential decrease in output signals levels was observed (Figure 5).

It should be pointed out that these compounds have no influence on measurement results in the second channel. Moreover, to improve precision of measurements, averaging procedure was applied. Thanks to this a lower uncertainty of decay time determination was obtained (uncertainty value of 0.1%).

Assuming optimal matching wavelengths of lasers radiations to respective nitric oxide and nitrous oxide absorption lines, high cross section factors can be reached: $0.7 \times 10^{-18}\,\mathrm{cm}^2$ for NO and $3.9 \times 10^{-18}\,\mathrm{cm}^2$ for N_2O. Using the formula (3) it can be noticed that the developed system provides the opportunity to detect N_2O at the level of 225 ppt, while sensitivity of NO channel is about 8 ppb.

5. CONCLUSIONS

The paper presents research of nitric oxide and nitrous oxide detection system based on cavity enhanced absorption spectroscopy. The best sensitivity was obtained at the wavelengths of 5.26 μm and of 4.53 μm respectively.

The constructed detection system is able to measure both NO and N_2O concentration at ppb level. Its sensitivity is comparable (or even better) with sensitivities of instruments basing on other methods, e.g., gas chromatography or mass spectrometry. The developed sensor can be applied to control the atmosphere quality. Using the sensor, detection of vapours from some explosive materials is also possible. Some successful research with nitro-glycerine, nitrocellulose, and TNT has been already performed.

ACKNOWLEDGMENT

The researches were supported from the Ministry of Science and High Education of Poland (Projects No. OR00002807, No. ON515216839).

REFERENCES

1. Hitran 2008 database, Ontar Corporation, http://www.ontar.com.
2. Schubert, H. and A. Kuznetsov, "Detection and disposal of improvised explosives," *NATO Security through Science Series*, Springer, 2006.
3. Yinon, J., *Forensic and Environmental Detection of Explosives*, John Wiley & Sons, Chichester, New York, Weinhein, Singapore, Toronto, 1999.
4. Shimadzu Scientific Instruments, 7102 Riverwood Drive, Columbia, MD 21046, http://www.mandel.ca.

5. Drescher, S. R. and S. D. Brown, "Solid phase microextraction-gas chromatographic-mass spectrometric determination of nitrous oxide evolution to measure denitrification in estuarine soils and sediments," *Journal of Chromatography A*, Vol. 1133, Nos. 1–2, 300–304, 2006.
6. Grossel, A., V. Zéninari, L. Joly, B. Parvitte, G. Durry, and D. Courtois, "Photoacoustic detection of nitric oxide with a Helmholtz resonant quantum cascade laser sensor," *Infrared Physics & Technology*, Vol. 51, 95–101, 2007.
7. Berden, G., R. Peeters, and G. Meijer, "Cavity ring-down spectroscopy: Experimental schemes and applications," *International Reviews in Physical Chemistry*, Vol. 19, No. 4, 565–607, 2000.
8. Merola, S. S., B. M. Vaglieco, and E. Mancaruso, "Multiwavelength ultraviolet absorption spectroscopy of NO and OH radical concentration applied to a high-swirl diesel-like system," *Experimental Thermal and Fluid Science*, Vol. 28, 355–367, 2004.
9. Rontu Carlon, N., D. K. Papanastasiou, E. L. Fleming, C. H. Jackman, P. A. Newman, and J. B. Burkholder, "UV absorption cross sections of nitrous oxide (N_2O) and carbon tetrachloride (CCl_4) between 210 and 350 K and the atmospheric implications," *Atmos. Chem. Phys. Discuss.*, Vol. 10, 11047–11080, 2010.
10. Piotrowski A., P. Madejczyk, W. Gawron, K. Klos, M. Romanis, M. Grudzien, J. Piotrowski, and A. Rogalski, "MOCVD growth of $Hg_{1-x}Cd_xTe$ heterostructures for uncooled infrared photodetectors," *Opto-Electron. Rev.*, Vol. 12, 453–458, 2004.

Estimation of Specific Attenuation Due to Scattering Points for Broadband PLC Channels

C. T. Mulangu, T. J. Afullo, and N. M. Ijumba
School of Electrical, Electronic and Computer Engineering
University of Kwazulu-Natal, Private Bag X54001, Durban 4000, South Africa

Abstract— The multipath propagation models in power-line communication channel (PLC) are some of the most successful models which are based mainly on scattering points located where the impedance mismatch occurs. In such models, not only the desired signal, but also one or more delayed and attenuated versions of it get to the receiver. The attenuation is basically due to different routes that the signal will take before getting to the receiver hence at the end there are many signals that reach the load at different times. In this submission, we investigate the number of branches and the numbers of reflections that occur at each node; the Mie scattering theory is applied to nodes in the network in order to determine the resulting specific signal attenuation in the network. The proposed model is compared to the theoretical model and the estimated error determined by root mean square and chi-square tests. Finally, a power law model is proposed where only the frequency range is needed to estimate the specific attenuation.

1. INTRODUCTION

The low voltage (LV) power network is a new option for providing access to high-speed communications. This supports the concept of broadband power line communications (PLC). With this system, it is possible to build an in-house communication network or access the Internet in a very cost-effective way.

The main problem of a PLC channel involves intersymbol inference, which is generated by multipath propagation effects and the resulting delay spread [1]. This indicates that not only the desired signal, but also one or more delayed and attenuated copies of it, arrive at the receiver [2, 3]. This is the result of several reflections caused at the joints of the network cables, connection boxes, serial connections of cables with different characteristic impedances, and in general, points of discontinuity, due to impedance mismatches that occur [4, 5]. Multipath propagation constitutes the principal broadband signal transfer mechanism over electric power network, by virtue of which the PLC links are characterized as strongly fading channels [4]. In the case of PLC channels, scattering-points are still discrete, located where the impedance mismatch occurs.

As we mentioned earlier, several reflections occurring at the joints of the network cables, connection boxes, serial connections of cables with different characteristic impedance, and at general points of discontinuity, due to impedance mismatches can be generally referred to as "scatterers". Therefore, each path is comprisedof scattering points that are reflected at a specific number of times at specific points of discontinuityalong its routes. Mulangu et al. [6] Haveproposed the lognormal distributionmodel for scattering points that involve nodes and numbers of reflections occurring at each node.

In this paper, we investigate the number of branches and the numbers of reflections that occur at each node; the Mie scattering theory is applied to the nodes in the network to determine the resulting specific signal attenuation in the network. The frequency of interest ranges between 10 MHz and 3 GHz.

2. MODEL AND OPTIMISATIONS

2.1. Transmission Line Characteristics

If we take into account the characteristics of the transmission line, the propagation constant p, and the characteristic impedance Z_0 are given by:

$$Z_0 = \sqrt{\frac{(R + j\omega L)}{(G + j\omega C)}} \tag{1}$$

$$p = \gamma + j\beta = \sqrt{(R + j\omega L)(G + j\omega C)} \tag{2}$$

and the attenuation coefficient is given by:

$$\gamma = real\,(p) \tag{3}$$

where, γ, is the attenuation constant, β is the phase constant, and cable's primary parameters, or the is resistance per unit length of Ohm/m, L is the inductance per unit length in Henry/m, G is conductance per unit length of Siemens/m, and C is the capacitance per unit length in Farads/m can be approximated as in [7].

2.2. Scattering Points Approximation

Consider a scattering point in transmission line as a spherical particle of radius a, complex electric permittivity $\varepsilon = m_1^2$ embedded in a dielectric medium of permittivity $\varepsilon_2 = m_2^2$. This scattering point is illuminated by a plane wave of angular frequency $\omega = 2\pi c/\lambda = kc/m_d$ and $k = 2\pi/\lambda$ is the wave number, λ the wavelength in the medium. The refractive index with respect to the medium, is given by:

$$m = \sqrt{\frac{\varepsilon_1 \cdot \mu_1}{\varepsilon_2 \mu_2}} \tag{4}$$

where, ε_1 and μ_1 are the permittivity and permeability of the spherical particle; and ε_2 and μ_2 are the permittivity and permeability of the medium.

The complex refractive index $m\,(f)$, being a function of frequency f, is related to the complex relative dielectric permittivity $\varepsilon(f)$ of metal at lower frequencies is given in [8] as:

$$m_1\,(f) = \sqrt{\sigma/2\varepsilon_0\omega}\,(1 - i) \tag{5}$$

where, σ is the electric conductivity of the conductor and ε_o is the permittivity of the free space.

At lower frequencies, from the Equation (17), It can be observed that the real and imaginary parts of refractive index $m\,(f)$, have the same magnitude. With such a large imaginary part of $m\,(f)$, the wave is rapidly attenuated in the metal [8]. In the case of copper, the frequencies less than 10^{12} Hz (Plasma frequency), $\sigma = 5.76 \times 10^7$ (ohm-meter)$^{-1}$ [8].

The efficiencies Q_i for the interaction of radiation with a sphere of radius a are cross sections σ_i normalized to the geometrical particle cross section, $\sigma_g = \pi a^2$ where i stands for extinction ($i = ext$), absorption ($i = abs$), scattering ($i = sca$), and backscattering. Energy conservation requires that [9–11]:

$$Q_{ext} = Q_{sca} + Q_{abs}, \text{ or } \sigma_{ext} = \sigma_{sca} + \sigma_{abs} \tag{6}$$

where,

$$Q_{sca} = \frac{2}{x}\sum_{n=1}^{\infty}(2n+1)\left(|a_n|^2 + |b_n|^2\right); \tag{7}$$

$$Q_{ext} = \frac{2}{x}\sum_{n=1}^{\infty}(2n+1)\mathrm{Re}\,(a_n + b_n); \tag{8}$$

The key parameters for Mie calculations are the Mie Coefficients a_n and b_n required to compute the amplitudes of the scattered field. The index n runs from 1 to ∞, but the infinite series occurring in Mie formulas can be truncated at a maximum $n_{\max}$, given in [11]:

$$n_{\max} = x + 4x^{1/3} + 2 \tag{9}$$

This value is used in this computation. The size parameter is given by $x = ka$.

2.3. Model Estimation

The amplitude of an electromagnetic wave travelling through a volume, containing N identical scattering particles with diameter D, at any distance l, decreases by the amount of $e^{-\gamma l}$. The attenuation coefficient $\gamma = NQ_{ext}(D)$.

The attenuation of the wave is then given in dB as follows

$$A_{\mathrm{dB}} = 10\log\frac{1}{e^{-\gamma l}} = 4.343\gamma l \tag{10}$$

and the specific attenuation in dB/km is given by:

$$A_s = 4.343\gamma \tag{11}$$

$$A_s\ [\mathrm{dB/km}] = 4.343 \times 10^3 \sum_0^{\infty} N\,(D)\,Q_{ext}\,(D)\,dD \tag{12}$$

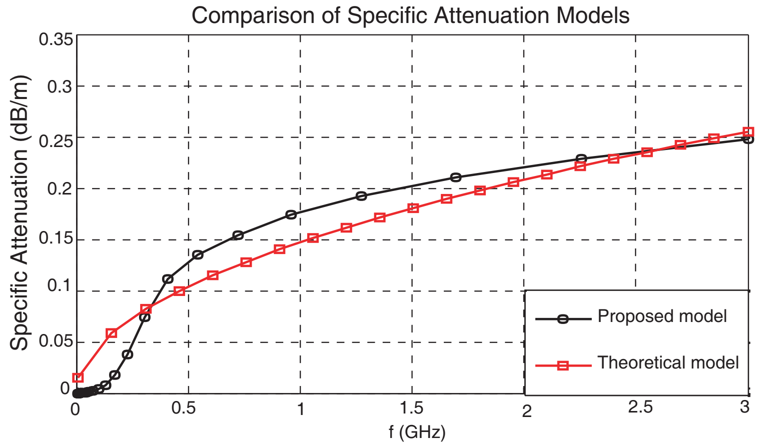

Figure 1: Comparison of estimated specific attenuation for PLC channel.

Mulangu et al. [9] and Mätzler [10] use the expression given by:

$$A_s\ [\mathrm{dB/km}] = 0.25\pi \sum_{0}^{\infty} D^2 N(D)\, Q_{ext}(D)\, dD \tag{13}$$

The computation of the proposed model as shown in Fig. 1, is performed by using the equation in (13) for different number of branches of the network. The numbers of branches are 1, 5, 10 and 15. The frequency range for this investigation is exclusively from 10 MHz to 3 GHz. The theoretical model uses the equations in (11) and in (3) in order to compare with the proposed model.As mention earlier, the selected diameters in our simulation range are: 0.9, 1.1, 1.3, 1.5, 1.6, 1.9, 2.25, 2.58 and 2.84 mm as in [6], while in the theoretical model, we have just selected one diameter of 1.6 mm as in [7].

2.4. Power Law Model

The scattering model can also be represented in power law form as:

$$A_s = \alpha f^{\beta} \tag{14}$$

where α and β are coefficients to be determined and f is the frequency range.

Figure 2 shows the regression fitting procedure employed in the estimation of α and β in the range span from 10 MHz to 3 GHz. It has been observed that the fitted model has a high coefficient of goodness (R^2) indicating a good fit to proposed model. We found $\alpha = 0.161$ and $\beta = 1.681$.

2.5. Optimization of Specific Attenuation Model

The root-mean-square error ($RMSE$) test and the chi-square χ^2 statistic test are used in this paper to optimize the proposed model.

$$RMSE = \sqrt{\frac{1}{n}\sum_{i=1}^{n}\left(x_i - x'_n\right)^2} \tag{15}$$

while chi-square (χ^2) statistic test is given by:

$$\chi^2 = \sum_{i=1}^{n} \frac{\left(x_i - x'_n\right)^2}{x'_n} \tag{16}$$

where $\{x_1, x_2, x_3, \ldots, x_n\}$ is the experimental data set; $\{x'_1, x'_2, x'_3, \ldots, x'_n\}$ is the theoretical model data set and N is the number of samples of x_i to x_n. In the case of χ^2, the $(N-1)$ degrees of freedom are applied to determine the significance level of the preferred model. The significance level used in this work is 1%. The $RMSE$ indicates the deviation of the proposed specific attenuation model from theoretical model. Therefore, the model with the least the error is the best the model

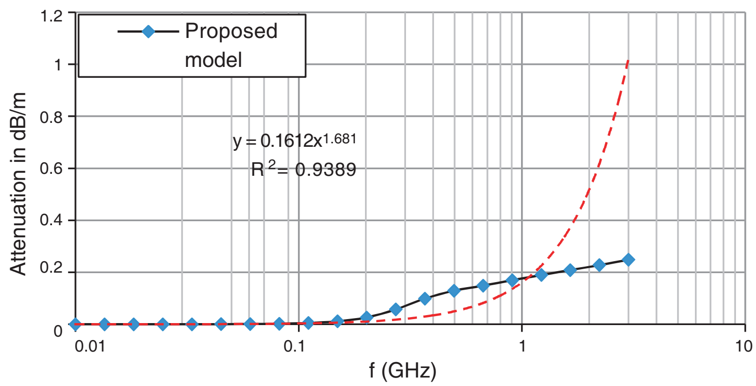

Figure 2: Regression fitting for specific attenuation.

that is fitted. On the other hand, χ^2 indicates the closeness of the proposed specific attenuation model with the theoretical model.

In this work, with 21 degrees of freedom, the χ^2 equals 1.57 with the threshold value given as 37.566 at 1% significance level. With the same degrees of freedom, the RMSE is 0.105.

3. CONCLUSION

In this paper, we present the results on specific attenuation of a power line network using scattering coefficients at the nodes where mismatches occur. The proposed model was estimated for four different numbers of branches. By using the frequency range of 10 MHz to 3 GHz, we compared the proposed model with the theoretical one. The results show that the proposed model underestimates the attenuation at the frequencies below 500 MHz and over estimates the attenuation value at the frequencies range from 500 MHz to 2 GHz before falling slightly down compare to the theoretical one. The approach included all different diameter sizes of the branches that are used in indoor PLC channels. Also, we developed a power law model that relies on the knowledge of frequency range and thus, the attenuation can be predicted.

ACKNOWLEDGMENT

This work was performed under the auspices of the HDVC Centre and Communications Centre of School of Electrical Electronic and Computer Engineering by University of KwaZulu-Natal.

REFERENCES

1. Papaleonidopoulos, I. C., C. G. Karagiannopoulos, N. J. Theodorou, C. E. Anagnostopoulos, and I. E. Anagnostopoulos, "Modelling of indoor low-voltage cables in the high frequency range," *Proc. ISPLC'97*, 267–271, 2002.
2. Pahlavan, K. and A. H. Levesque, *Wireless Information Networks*, 37–142, John Wiley & Sons, Inc., New York, 1995.
3. Papaleonidopoulos, I. C., C. N. Capsalis, C. G. Karagiannopoulos, and N. J. Theodorou, "Statistical analysis and simulation of indoor single-phase low voltage power-line communication channels on the basis of multipath propagation," *IEEE Trans. Consumer Electronics*, Vol. 49, No. 1, 89–99, February 2003.
4. Zimmermann, M. and K. Dostert, "A multi-path signal propagation model for the powerline channel in the high frequency range," *ISPLC'1999*, 45–51, Lancaster, UK, 1999.
5. Philips, H., "Modelling of powerline communication channels," *Proc. ISPLC'99*, 14–21, 1999.
6. Mulangu, C. T., T. J. Afullo, and N. M. Ijumba, "Scattering points size distribution for indoor broadband PLC channels," *Progress In Electromagnetics Research Symposium*, Kuala Lumpur, Malaysia, March 27–30, 2012,
7. Tsuzuki, S., T. Takamatsu, H. Nishio, and Y. Yamada, "An estimation method of the transfer function of indoor powerline channels for Japanese houses," *Proc. Int. Symp. Power-lines Comm.*, 55–99, Athens, Greece, 2002.
8. Richard, P. F., R. B. Leighton, and M. Sands, *The Feynman Lectures on Physics*, No. 2, Addison-Wesley, 1964.

9. Mulangu, C. T. and T. J. Afullo, "Variability of the propagation cofficients due to rain for microwave links in Southern Africa," *Radio Sci.*, Vol. 44, 2009.
10. Mätzler, C., "MATLAB functions for mie scattering and absorption," *IAP Res. Rep.*, Version 2, No. 2002-08, University of Bern, Switzerland, June 2002.
11. Bohren, C. F. and D. R. Huffman, *Absorption and Scattering of Light Particles*, John Wiley, Wienheim, 2004.

Transmission Analysis of Optical OFDMA-based Passive Optical Network Architecture Supporting Heterogeneous Services

Fan Bai, Peng Liu, and Mitsuji Matsumoto
Global Information and Telecommunication Studies, Waseda University, Japan

Abstract— The on-going surge in demand of high-speed broadband services such as Internet Protocol Television and High-Definition TV signals. For the next generation hybrid access networks, considering the increasing the bandwidth and data rate while keeping acceptable costs. Our research focus on orthogonal frequency division multiple access (OFDMA) technology over passive optical network (PON). In this paper, we propose a novel architecture for Optical OFDMA over PON. We present the performance of this O-OFDMA PON system using IM/DD (intensity modulation/direct detection). This architecture can supporting wireless signals combine with local band signals to transport to the OLT end. The simulation result shows that the BER (bit error rate), degradation trend of O-OFDM signal to optical signal-to-noise-ratio (OSNR) using 24/32/64-QAM.

1. INTRODUCTION

The next generation optical access networks are required to delivery heterogeneous services for multiple customers. Nowadays, with the users high demand in quality of data, supplying huge capacity, supporting the hybrid services become the hot point in the optical access networks. At present, two key technologies used in passive optical network are TDM PON such as EPON, GPON and WDM PON. Currently, TDM PON architecture need complex scheduling algorithms and framing technology to support a variety of services. On the other hand, WDM-PON assigns different high-speed data to the appoint wavelength. via arrayed-waveguide-grating (AWG) or optical filter distribute wavelengths to the correct receivers, which will increase both system cost and complexity [1].

In recent years, Orthogonal Frequency Division Multiplexing (OFDM) is used widely in wireless and wired communications since it provides immunity to interference cause by a dispersive channel. In addition, OFDM not only can be seen to a modulation, but also as a kind of multiple access technology be used in the access network-OFDMA (Orthogonal frequency division multiplexing access) [2]. OFDM assign one block (in time) to one user, and that OFDMA is a method that assigns different users to groups of orthogonal sub-carriers so they can access the air interface at the same time. The main advantages of OFDMA over TDMA/CDMA stem from its scalability, uplink orthogonality and the ability to take advantage of the channel frequency selectivity. Other advantages of OFDMA include its MIMO friendliness and ability to provide superior quality of service (QoS) [3–6]. At the same time, OFDMA signals through the DML (directly modulated laser) modulation thus generates the optical OFDMA signals. For such a new transceiver architecture design and performance of the system both are important emphases in our research.

In this paper, we propose a novel architecture for Optical OFDMA over PON. We present the performance of this O-OFDMA PON system using IM/DD (intensity modulation/direct detection). We setup the two ONUs at the user side, employ the SMF (single model fiber). ONU1 upstream data after directly optical modulation transports to OLT. The other ONU2's remote antenna receive the wireless signals from the base station, coupler combine with the local OFDMA signal and through DML, which data upload to OLT. The simulation result shows that the BER (bit error rate) and performance of optical-OFDMA PON system OSNR via a optical modulation.

The remainder of this paper is organized as follows. In Section 2, we describe the optical OFDMA PON architecture and integrated the wireless signal. In Section 3, we discuss the performance for optical OFDMA PON based on mathematical model. In Section 4, we ananlysis the optical OFDMA characteristics in PON via the simulation result. Finally, conclusion remarks are given in Section 5.

2. SYSTEM ARCHITECTURE

Optical-OFDM has been investigated within the last few years by extensive simulations and experiments. For the next generation passive optical network, adopt the optical-OFDMA in the passive optical networks become a new trend. Bringing the OFDMA signal into the optical domain thus generates several new transmitter and receiver architecture compared to the electronic or RF OFDMA [2]. In this section, we describe an optical-OFDMA PON transceiver architecture supporting the various services.

Optical-OFDMA PON transmission model (see Figure 1) connect multiple ONU's to the OLT via a passive optical distribution networks (ODN), which is connected to the OLT through a single mode fiber. Each ONU uses wavelength channels to convey upstream and downstream. Channels are further divided into synchronous time slots, called frames. The OFDM signals by occupying a separate frequency range. As to the signals passing downstream, the splitter in the ODN generates multiple signal from the OLT and bring the signals to each ONU through the splitter and single mode fiber. During the transmission, the sub-carriers and time slots allocation are controlled by the OLT. Sending the signals to the given sub-carriers, completes the modulation to generate an OFDM frames.

Figure 2 shows the detail of the Optical-OFDMA PON transceiver architecture. In the ONU1 system, a high-speed up-data is converted to parallel of multiple low-speed data stream. After a mapping modulation and insert the cyclic prefix, data stream are converted from frequency domain to time domain through the inverted fast Fourier transform (IFFT). We propose the architecture that using a directly modulated laser (DML) and optical modulator (OM) to convert the RF/electronic OFDMA signals into the optical domain. The OM include the optical filter Then, output the optical-OFDMA signals as wavelength $\lambda 1$ combined wavelength $\lambda 2$ at the optical coupler, detected by a photo-detector at the OLT receiver. On the other hand, we make the optical-OFDMA PON as an transmission particular platform to transmit various information and applications over same network contracture. What we design is to make wireless signal received from the remote antenna located at ONU2. Figure 2 illustrates how the wireless RF signals are integrated and overlaid with electronic OFDMA signals. In our proposal system, one RF signals are received by antenna and then transported via a bandpass filter (BPF). Then RF signal is combined with up-data stream, which is sent together by coupler to the directly modulated laser (DML). Finally, optical OFMDA signal is sent to the ODN (optical distributed network) as wavelength $\lambda 2$.

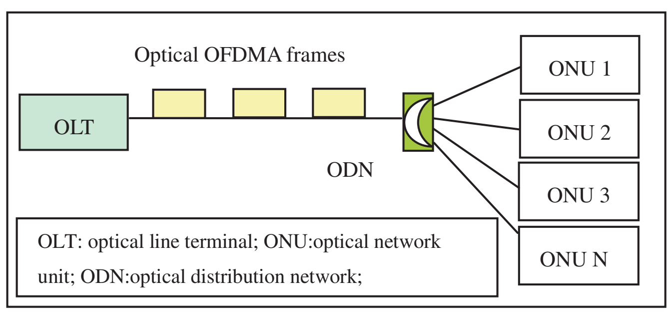

Figure 1: Optical-OFDMA PON transmission model.

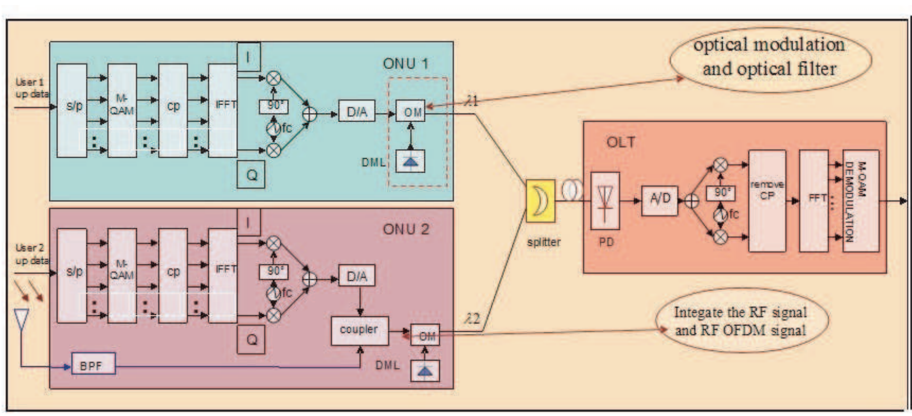

Figure 2: Optical-OFDMA PON transceiver architecture integrated wireless signals.

3. PERFORMANCE OF OPTICAL OFDMA PON

In this section, we study the bit error rate (BER) performance of optical-OFDMA signals over PON under a intensity modulation/direct detection (IM/DD) system. In the Figure 2, at the transmitter side, the up data-stream converts the serial data to parallel M-QAM symbols. Using the IFFT, the symbols are converted to frequency domain from time domain. The cyclic prefix is inserted to protect the ICI (inter-symbol-interference) form transmission link [8]. Electronic/RF-OFDMA signals after digital/analog convertor and bing the signals into the optical domain by optical modulation (Note that optical intensity modulation can be performance using the directly modulation laser and optical filter.). At the receiver side, we adopt a direct detection as a photo-detector. Then, through the A/D, remove the CP, and take the signals from the frequency domain to the time domain. At last, out of the sub-carriers signals by M-QAM demodulatior. We now analyze the performance of OFDMA signal with respect to the submit the OFDMA signal power before optical filter, P_o. X_n that denotes complex number representing M-QAM constellation point carried on the nth sub-carrier, P_o can be expressed as [8]:

$$P_o = P_{in}\left[1 + m\mathrm{Re}\left\{\sum_{n=1}^{N_s} X_n \exp\left(j2\pi f_n t\right)\right\}\right] \tag{1}$$

where P_{in} is the average optical power, N_s is the number of sub-carriers, m is the modulation depth per sub-carrier, and f_n is the nth sub-carrier's frequency. Thus the average signal power S of a single sub-carrier can be given by [8], where R is the responsivity of a photo-diode.

$$S = \left(P_{in}\cdot m\cdot R\right)^2 \Big/ 2 \tag{2}$$

As to DDO-OFDM, Optical spectrum of an optical OFDMA signal at the output of a transmitter is a linear copy of the RF OFDM spectrum plus an optical carrier as a direct-detection optical OFDM [7,8] , DC component that can be easily filtered out. Formally, this type of DDO-OFDM signals can be given

$$\begin{aligned} S_{DDO-OFDM}(t) &= A_c\left[1 + am_n(t)\right]\cos 2\pi f_c t \\ m_n(t) &= \sum_{n=1}^{N_s} X_n \exp\left(j2\pi f_n t\right) \end{aligned} \tag{3}$$

where $S_{DDO-OFDM}(t)$ is the transmit optical OFDM signal, A_c is optical carrier amplitude, f_c is the optical carrier frequency, $m_n(t)$ is OFDMA signals before optical filter, a is modulation index.

In an unamplified system as PON, the receiver noise is the greatest obstacle to system performance. The total receiver noise σ_{total} include both thermal noise σ_{th} and quantum shot noise are given by

$$\sigma_{total}^2 = \sigma_{th}^2 + \sigma_{sn}^2 \tag{4}$$

The shot-noise mean square value can be determined by

$$\sigma_{sn}^2 = 2qI \tag{5}$$

where q is the electron charge, I is photocurrent intensity. The thermal noise can be given by

$$\sigma_{th}^2 = \frac{4k_B\Theta}{R_L}B \tag{6}$$

where k_B is the the Boltzmann's constant, Θ is the absolute temperature, R_L is the load resistance, and B is the receiver bandwidth. Given the O-OFDMA signals optical power P_{in}, the optical signal-to-noise ratio for the optical OFDM signal, $OSNR_{OFDM}$ can be expressed as

$$OSNR_{OFDM} = \frac{P_{in}}{p_{ASE}} = \frac{P_{in}}{p_{\sigma_{total}^2}} = \frac{P_{in}}{\sigma_{th}^2 + \sigma_{sn}^2} \tag{7}$$

If the receiver's white noise is main source of signal degradation, the BER of the M-QAM can be given by [2]

$$BER = \frac{2\left(1 - \frac{1}{\sqrt{M}}\right) erfc\left(\sqrt{\frac{3OSNR_{OFDM}}{2(M-1)}}\right)}{\log_2(M)} \tag{8}$$

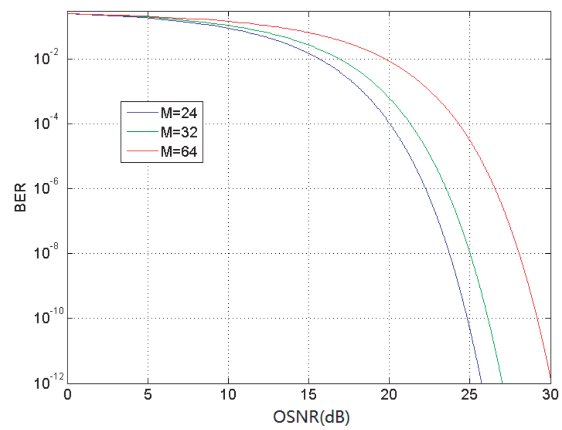

Figure 3: Performance of BER versus OSNR in optical-OFDMA PON under IM/DD.

Table 1: Optical OFDMA PON link parameters.

Parameter	Symbol	Value
FFT size		2048
Photo-diode responsivity	R	0.8 A/W
Absolute temperature	T	300 K
Load resistance	R_L	50 Ω
Modulation depth	m	15%
Modulation index	a	20%
Optical carrier frequency	f_c	100 MHz
Sub-carrier's frequency	f_n	0.3125 MHz

4. RESULTS AND DISCUSSION

In Figure 3, the optical OFDMA upstream BER versus received optical signal-to-noise ratio (OSNR) as measured in the optical domain is shown the single transmission using by 24-QAM, 32-QAM, and 64-QAM modulation. Using 24-QAM, the value of the BER has been achieve the 10^{-3} with an OSNR = 17 dB. The performance of system BER by 24-QAM is more better than 32/64QAM. The result mean that transmission performance is insensitive to M-QAM constellation point carried on the sub-carrier in PON system. In addition, via plus an optical carrier as a DDO-OFDM, DC component that can be easily filtered out and reduce the shot noise in system. Last, an optical filter is used to both decrease the influence of the fiber chromatic dispersion and at the same time adjust the power ratio of used optical carrier.

5. CONCLUSIONS

In this paper, we have propose a novel Optical OFDMA-PON architecture using IM/DD, as a DDO-OFDMA PON using optical filter. This system can integrates RF signals and optical OFDMA signals up to the OLT end. The obtained simulation results show that DDO-OFDMA PON can be easily filtered out the DC component. The RF signals robustness against OFDMA interference by simulation. In a word, it is feasible to use the architecture we proposed as the candidate for next-generation optical access networks.

ACKNOWLEDGMENT

This work is Grant-in-aid of High-tech Research Center Project by the Ministry of Education, Culture, Sports, Science and Technology, Japan.

REFERENCES

1. Cvijetic, N., "OFDM for next generation optical access networks," 2011.

2. Lin, Y.-M., "Next-generation OFDMA-based passive optical network architecture supporting radio-over-fiber," *Journal on Selected Areas Communications*, Vol. 34, No. 26, August 2010.
3. Qian, D., S.-H. Fan, N. Cvijetic, J. Hu, and T. Wang, "64/32/16QAM-OFDM using direct-detection for 40G-OFDMA-PON downstream," *OSA/OFC/NFOEC*, 2011.
4. Milosavljevic, M., P. Kourtessis, W. Lim, and J. M. Senior, "Next generation PONs with wireless backhauling," *ICTON*, 2011.
5. Cvijetic, N., D. Qian, J. Hu, and T. Wang, "Orthogonal frequency division multiple access PON (OFDMA-PON) for colorless upstream transmission beyond 10 Gb/s," *IEEE Journal on Selected Areas in Communications*, Vol. 28, No. 6, August 2010.
6. Armstrong, J., "OFDM for optical communications," *IEEE/OSA J. Lightwave Technol.*, Vol. 27, 189–204, Feb. 2009.
7. Chang, L., C. J. Chae, and A. Nirmalathas, "Selective delivery of DSB and SSB OFDM-based video signals over WDM PON," 2008.
8. Shieh, W. and I. Djordjevic, *OFDM for Optical Communications*, Academic Press, 2009.

Emerging Optical Broadband Access Networks from TDM PON to OFDM PON

Redhwan Q. Shaddad[1,2], **Abu Bakar Mohammad**[1], **Sevia M. Idrus**[1], **Abdulaziz M. Al-hetar**[2], **and Nasir A. Al-geelani**[3]

[1]Photonic Technology Center, InfoComm Research Alliance, Universiti Teknologi Malaysia, Malaysia
[2]Communication and Computer Engineering Department
Faculty of Engineering and Information Technology, Taiz University, Yemen
[3]Institute of High Voltage and High Current, Universiti Teknologi Malaysia, Malaysia

Abstract— The bandwidth requirements of the telecommunication network users increased rapidly during the last decades. The emerging optical access technologies must provide the bandwidth demand for each user. The passive optical access networks (PONs) support a maximum data rate of 100 Gbps by using the orthogonal frequency division multiplexing (OFDM) technique in the optical access network. In this paper, the enabling optical broadband access networks with many techniques are presented and compared. The architectures, advantages, disadvantages, and main parameters of these access networks are discussed and reported. A combination of different techniques in a hybrid PON network introduces a cost-effective, reliable and efficient access network. The hybrid optical broadband access technologies are presented which have many advantages to become next-generation broadband access networks. The concept and architecture of the hybrid optical broadband access networks are discussed.

1. INTRODUCTION

The high-speed broadband penetration and ongoing growth of the Internet traffic among customers have been placing a huge bandwidth demand on the telecommunication network. Next generation access networks are projected to support high data rate, broadband multiple services, scalable bandwidth, and flexible communications for manifold end-users. Optical broadband access networks have emerged to address two issues: (1) channel capacity sharing fairly to the customers, and (2) adequate capacity assignment according to service requirements.

The dominant broadband access network that is emerging from today's research and development activities is a point-to-multipoint (P2MP) optical network known as passive optical network (PON). In PON, the central office (CO) is connected to users by using one wavelength channel in the downstream direction [from optical line terminal (OLT) at CO to optical network units (ONUs)] and another wavelength channel in the upstream direction [from ONUs to OLT] [1]. The time division multiplexing technique is used in this PON, so it is called usually TDM PON. The existing PON architectures provide much higher bandwidth for data application but it has limited availability to end-users. 32 ONUs can be connected to one OLT over a single fiber. The fiber range is limited to 20 km [2].

The per-user cost of TDM PONs can be low as the bandwidth is shared among all the end users, so the wavelength division multiplexed PON (WDM PON) is used to solve this problem. A WDM-PON solution provides excellent scalability because it can support multiple wavelengths over the same fiber infrastructure, it is inherently transparent to the channel bit rate, depending on its architecture, and it may not suffer power-splitting losses [3]. WDM PON creates a point-to-point (P2P) link between the OLT and each ONU, so each ONU can operate at a rate up to the full bit rate of a wavelength channel. Moreover, different wavelengths may be operated at different bit rates, if necessary; hence, different types of services may be supported over the same network [1].

A code-division multiple-access (CDMA) PON is proposed as an optical access network system to satisfy the subscriber's increasing data traffic and get low cost [4]. To avoid the dispersion effects on the optical signal in the TDM PON and WDM PON, the future PONs are designed based on subcarrier multiplexing (SCM) and the optical orthogonal frequency division multiplexing (OFDM) techniques which are called SCM PONs and OFDM PONs respectively. These two types of PONs provide bandwidth efficient optical access networks [5]. The different PONs can be hybrid and integrated to get powerful PONs demand on the requirements as discussed later in this paper.

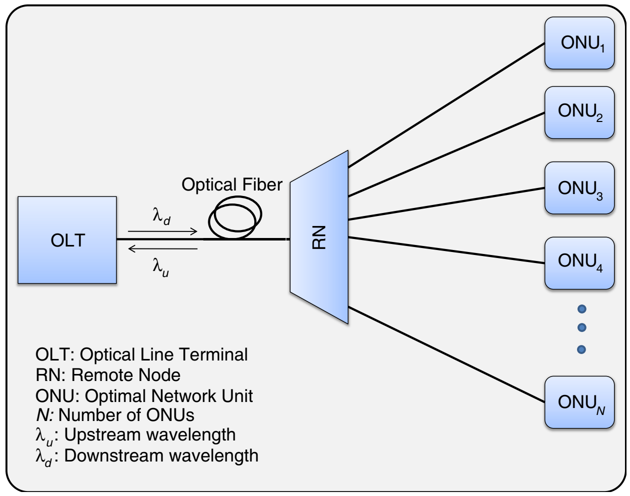

Figure 1: Passive optical network.

2. OPTICAL BROADBAND ACCESS TECHNOLOGIES

PONs offer a promising optical access solution for significantly enhancing the bandwidth of access networks. A PON basically consists of an OLT at the central office which transmits traffic received from the access network to the Internet and vice versa, an remote node (RN) which contains passive splitters/couplers for demultiplexing the downstream traffic received from the OLT and multiplexing the upstream traffic to the OLT, and multiple ONUs close to user's premises which receive the downstream traffic from the RN and generate the upstream traffic to the RN. Figure 2 illustrates the architecture of a passive optical network.

There are five main schemes of PON which can be summarized as using TDM, WDM, CDM, SCM, and OFDM. The only difference in the outside plant (OSP) between these five approaches is at the RN location. In TDM PONs, CDMA PONs, OFDM PONs and SCM PONs, passive power splitters are used to distribute the optical signal to manifold ONUs. The OLT and ONUs process the data according to the used technique. Passive wavelength splitters, such as an arrayed-Wavegauide-grating (AWG) router, is used to distribute the bandwidth among ONUs according to the assigned wavelengths in WDM PON [6].

3. TDM PON

In the TDM PON, the CO dedicates time slot to the multiple subscriber (ONU) connected to the PON. Each ONU can then use the full upstream bandwidth of the optical link for the duration of its assigned time slot. Since the TDM PON can typically service $N = 32$ or more subscribers, the average dedicated bandwidth to each ONU is usually only a few percent of the channel capacity. To connect the multiple ONUs to a single-feeder fiber, a passive optical power splitter (PS) is used at the RN. This PS couples $1/N$ of the power from each subscriber into the feeder fiber for transmission back to the OLT at the CO [6].

There are three standardized versions of the TDM-PON: Ethernet PON (EPON), broadband PON (BPON), and Gigabit PON (GPON). They all use one wavelength for downstream transmission (λ_d) and another wavelength for upstream transmission (λ_d) as illustrated in Figure 1. One important distinction between the three types of TDM-PON is operational speed. BPON is relatively low speed with 155 Mbps upstream/622 Mbps downstream operation. The EPON supports 1.0 Gbps symmetrical operation. The GPON promises 2.5/1.25 Gbps asymmetrical operation.

4. WDM PON

The straightforward approach to build a WDM PON is to employ separate wavelength channels from the OLT to the ONUs in the downstream direction which called downlink wavelengths (λ_{d1}, λ_{d2}, $\ldots$, λ_{dN}). In upstream direction, the uplink wavelengths (λ_{u1}, λ_{u2}, $\ldots$, λuN) pass from the ONUs to the OLT. Figure 2 shows generic network architecture of WDM PON. AWG router is used at the distribution node to separate and combine the downstream and upstream wavelengths respectively. This approach creates a P2P link between the OLT and each ONU. Since the optical

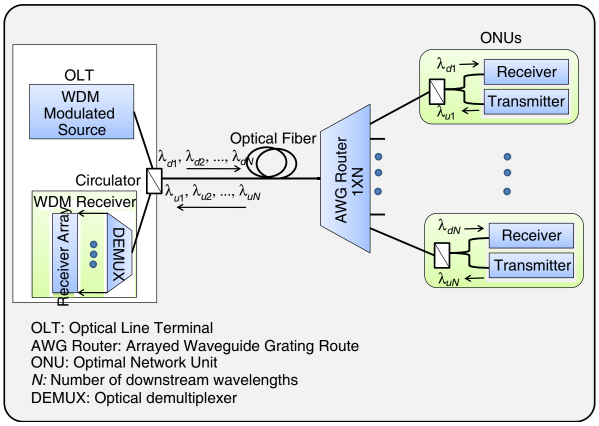

Figure 2: Typical WDM-PON access network.

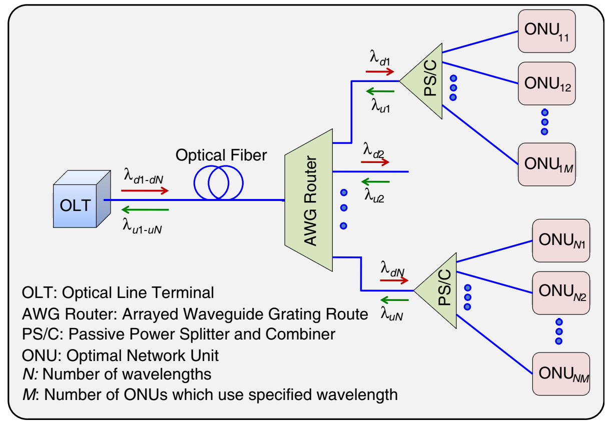

Figure 3: Network architecture of the hybrid TDM/WDM PON.

power is split for a smaller number of users, WDM PONs are less subject to optical power budget constraints and can support long reach to the ONUs [7].

An efficient bi-directional broadband optical networks using dense wavelength division multiplexing (DWDM) technology is proposed [8]. The proposed DWDM PON scheme is implemented using optical carrier suppression and separation (OCSS) technology to generate a down/uplink wavelength pair from a single laser source at the central office. This method enables the co-location of both upstream and downstream DWDM transmitters in the central office.

5. CDMA PON

Even though TDM PON has efficient bandwidth utilization, it has limitations in its increased transmission speed, difficulty in burst synchronization, low security, dynamic bandwidth allocation (DBA) requirement and inaccurate ranging. WDM PON becomes more favorable as the required bandwidth increases, but cost and wavelength tuning problems at remote units prevent its commercialization. In addition, the effect of statistical multiplexing is insignificant in multimedia communications environments. A CDMA PON, where each subscriber's channel is given its own code for spreading and dispreading, is a good alternative in view of cost and simplicity. Furthermore, the optical beat noise problem, which often arises in a system using several laser diodes (LDs) as in optical subcarrier multiplexing (SCM), does not have much effect on the CDMA PON system [4].

The CDMA PON has same architecture of the TDM PON. Downlink channels, from OLT to ONUs, are spectrum spread, combined, and then provided to an LD modulation part. After transmission, the signal is split at a splitter and spread at a receiver side. Since only one LD is used for the downlink, no optical beat noise exists. However, in the uplink case, each ONU uses its own LD whose wavelength is not unique unlike in the WDM PON [4]. Since CDMA PON uses an optical-power splitter at the RN, it suffers the same power-insertion-loss penalty as for the TDM PON case.

6. SCM PON

In SCM PON, one dedicated electrical subcarrier for each ONU is used, and it allows multiple users to share the same optical channel and its corresponding components. As compared to the conventional high-speed TDM systems, the SCM is less sensitive to fiber dispersion because the dispersion penalty is determined by the width of the baseband of each individual signal channel. As compared to the conventional WDM systems, it has been better optical spectral efficiency because much narrower channel spacing is allowed. Since it has a high bandwidth efficiency, it suffers the optical beat interference (OBI) especially when the number of nodes is large [9].

7. OFDM PON

Using OFDM format for PON is a subject of great interest for recent research works. OFDM signal has high spectral efficiency, high tolerance to the fiber chromatic dispersion and the high flexibility on both multiple services provisioning and dynamic bandwidth allocation. OFDM supports an effective solution to eliminate intersymbol interference (ISI) caused by dispersive channels [10]. The main disadvantages of OFDM are its high peak to average power ratio and its sensitivity to phase noise and frequency offset. These impairments are discussed and solved in [10].

There are two strategies for transmitting the optical OFDM signal: (1) Optical coherent detection OFDM (CO-OFDM) which is implemented by optical I-Q modulation in conjunction with coherent detection. CO-OFDM shows higher performance in terms of bandwidth efficiency and receiver sensitivity. By means of the choice of the modulation level, bandwidth efficiency and sensitivity can be balanced. (2) Optical direct detection OFDM (DD-OFDM): this method restricts to a real OFDM signal transmitted with intensity modulation and direct detection. DD-OFDM provides the advantages OFDM, like robustness toward fiber dispersion [10].

OFDM PON has same architecture of the conventional PON and uses one wavelength for downlink (λ_d) and another one for uplink (λ_u). In both the downlink and uplink traffics, the OFDM PON system divides the total OFDM bandwidth in N sub-bands, each containing a quantity of subcarriers required by each user. OFDM PONs can support huge data rates of 53 Gbps [5] and 100 Gbps [4].

8. HYBRID PONS

It is also possible to use mixed or hybrid approaches. The combination of TDM and WDM in a hybrid PON network (as shown in Figure 3) could be the most cost effective way of introducing TDM/WDM PON into the access network.

TDM-PONs limit each subscriber to a certain time interval and hence bandwidth per subscriber is reduced. Furthermore, the security of the transmission is not guaranteed since each subscriber on the TDM PON receives all the information sent to the other subscribers on the network. In contrast, DWDM PONs can solve the problems encountered in TDM PONs by allocating a specified wavelength to each subscriber. This provides a separate, secure P2P, and high data-rate channel between each subscriber and the CO. In addition to its efficient use of wavelengths, the WDM PON also has advantages in its use of optical-transmission power. The network management is much simpler than a TDM PON, and all future services can be delivered over a single network platform. In the case where allocating a single wavelength to each subscriber is not economical or impractical, DWDM can still be introduced in a hybrid TDM/DWDM PON as mentioned before.

If the user bandwidth demands are low or a small number of users can still share a single wavelength in the WDM PON, then a passive optical splitter following the wavelength division multiplexer is used to broadcast the downstream traffic and combine the upstream traffic as shown in Figure 3 [1]. In this case, multiple wavelengths separate a single PON into multiple logical TDM PONs: each PON runs on different wavelength, and a smaller number of users shares the bandwidth of a TDM PON.

To overcome relatively expensive cost of the WDM components in the WDM PON, the hybrid SCM/WDM PON is proposed [12]. In this proposed scheme, downstream signal modulated directly using a distributed-feedback laser diode (DFB-LD). In upstream transmission, the downstream signal is re-modulated using reflective semiconductor optical amplifiers (RSOA) with the SCM technique. No additional high cost devices are required such as external modulator and EDFA. To allow for higher data rates and higher number of users in the optical access network, the hybrid OCDMA/WDM PON is proposed [4]. It is a promising technology to realize soft capacity access network and high utilization of the bandwidth, as the subscribers of WDM PON can be multiplied. The proposed system supports 16,000–32,000 available subscribers.

A novel lightwave centralized hybrid bidirectional access network for integration of WDM/OFDM PON with radio-over-fiber (ROF) systems is proposed in [13] by employing multi-wavelength generation and the carrier-reuse technique. The proposed PON reduces Rayleigh backscattering (RB) in the bidirectional transmission. In this system, both 11.29 Gbps OFDM-16QAM downlink and 5.65 Gbps OFDM quadrature phase-shift keying (QPSK) uplink are investigated along 25 km single mode fiber (SMF).

9. CONCLUSION

This article has outlined the current and future generations of the optical broadband access technologies. The emerging optical broadband access technologies are reviewed and compared. While there are considerable differences between these technologies, there are also remarkable similarities. For broadband access services, there is strong competition among several technologies. Among the various emerging optical access technologies, the OFDM-based technologies are the most promising technologies because they provide the highest transmission capacity, the efficient bandwidth accesses, and the robust dispersion tolerance in the optical wireless links.

ACKNOWLEDGMENT

We greatly appreciate Universiti Teknologi Malaysia and Photonic Technology Center for providing the facilities which enable this work to be done. We would also like to thank the Ministry of Science, Technology and Innovation (MOSTI), Malaysia for sponsoring this work under the project vote number 73720.

REFERENCES

1. Sarkar, S., S. Dixit, and B. Mukherjee, "Hybrid wireless-optical broadband-access network (WOBAN): A review of relevant challenges," *J. Lightwave Technol.*, Vol. 25, No. 11, 3329–3340, 2007.
2. Shen, G., R. Tucker, and G. Chae, "Fixed mobile convergence architectures for broadband access: Integration of EPON and WiMAX," *IEEE Commun. Mag.*, Vol. 45, 4–50, 2007.
3. Banerjee, A., et al., "Wavelength-division multiplexed passive optical network (WDM-PON) technologies for broadband access: A review," *J. Opt. Netw.*, Vol. 4, 737–758, 2005.
4. Ahn, B. and Y. Park, "A symmetric-structure CDMA-PON system and its implementation," *IEEE Photonic. Tech. L.*, Vol. 14, 1381–1383, 2002.
5. Coura, D. J., J. Silva, and M. Segatto, "A bandwidth scalable OFDM passive optical network for future access network," *Photon. Netw. Commun.*, Vol. 18, No. 3, 409–4016, 2009.
6. Lee, C., W. Sorin, and B. Kim, "Fiber to the home using a PON infrastructure," *J. Lightwave Technol.*, Vol. 24, 4568–4583, 2006.
7. Kazovsky, L., et al., "Next-generation optical access networks," *J. Lightwave Technol.*, Vol. 25, 3428–3442, 2007.
8. Akanbi, O., J. Yu, and G. Chang, "A new scheme for bidirectional WDM-PON using upstream and downstream channels generated by optical carrier suppression and separation technique," *IEEE Photonic. Tech. L.*, Vol. 18, 340–342, 2006.
9. Hui, R., et al., "Subcarrier multiplexing for high-speed optical transmission," *J. Lightwave Technol.*, Vol. 20, 417–427, 2002.
10. Armstrong, J., "OFDM for optical communications," *J. Lightwave Technol.*, Vol. 27, No. 3, 189–204, 2009.
11. Kang, J. and S. Han, "A novel hybrid WDM/SCM PON sharing wavelength for up- and down-link using reflective semiconductor optical amplifier," *IEEE Photonic. Tech. L.*, Vol. 18, 502–504, 2006.
12. Kang, J. and S. Han, "A novel hybrid WDM/SCM PON sharing wavelength for up- and down-link using reflective semiconductor optical amplifier," *IEEE Photonic. Tech. L.*, Vol. 18, 502–504, 2006.
13. Hsueh, Y., et al., "A novel lightwave centralized bidirectional hybrid access network: Seamless integration of RoF with WDM-OFDM-PON," *IEEE Photonic. Tech. L.*, Vol. 23, 1085–1087, 2011.

Scattering Points Size Distribution for Indoor Broadband PLC Channels

C. T. Mulangu, T. J. Afullo, and N. M. Ijumba
School of Electrical, Electronic and Computer Engineering
University of Kwazulu-Natal, Private Bag X54001, Durban 4000, South Africa

Abstract— The multipath propagation of the power-line communication channel (PLC) arises from the presence of several branches and impedance mismatches that cause multiple reflections. Each path comprises of scattering points that are reflected at specific number of times at specific points of discontinuity along its routes. Scattering points located where impedance mismatch occurs and can be seen as spherical point with an approximation diameter size as for the branch. In such models, not only the desired signal, but also one or more delayed and attenuated versions of it get to the receiver. In [1], scattering points' spatial allocation, by which path amplitude distributions and path arriving time distributions are proposed to follow the lognormal distribution for different number of branches. Based on those findings in [1], in this submission, we investigate the number of branches and the numbers of reflections that occur at each node; the scattering point diameter density is derived in order to determine the scattering size distribution and the probability density distribution of the path. The proposed model shows that there are more contributions of branches with small diameters to the average attenuation in indoor PLC channel.

1. INTRODUCTION

However, the power cable structure of an electric power network is designed and optimized primarily for 50 or 60 Hz, and not as a communication medium at high frequency (HF). Furthermore, its transfer properties display considerable variation across the HF band [2, 3]. Firstly, wave-propagation techniques through the use of distributed-element transmission line models are required in order to explain HF signal propagation over power lines, as corresponding wavelengths are comparable to distances usually found within indoor grids [3]. Secondly, due to the variation of the loads, indoor electric power networks show certain time-variance, which is well dominated by wave propagation principles rather than those of classical circuit types [1].

Several reflections caused at the joints of the networks cables, connection boxes, serial connections of cables with different characteristic impedances, and in general, points of discontinuity, due to impedance mismatches that occur [4, 5]. Multipath propagation constitutes the principal broadband signal transfer mechanism over electric power network, by virtue of which the PLC links are characterized as strongly fading channels [4].

As we mentioned earlier, several reflections occurring at the joints of the network cables, connection boxes, serial connections of cables with different characteristic impedance, and at general points of discontinuity, due to impedance mismatches can be generally referred to as "scatterers". Therefore, each path comprises of scattering points that are reflected at specific number of times at specific points of discontinuity along its routes.

In this paper, we have proposed the lognormal distribution model for scattering points that involve nodes and numbers of reflections occurring at each node that will later use with, in our next, see our next paper submitted at this same conference, the Mie scattering theory is applied to the nodes in the network to determine the resulting specific signal attenuation in the network. The frequency of interest ranges between 10 MHz and 3 GHz.

2. MULTIPATH PROPAGATION MODEL

Papaleonidopoulos proposed appropriate assumptions in [1] based on indoor electric network's topology are adopted concerning scattering points' special allocation, by which path amplitudes are demonstrated to follow the lognormal distribution. Verification of statistical modeling is established, involving path inventory through simulation.

The path amplitude distribution within a group k is given as the function of the random variable τ_k that displays the normal distribution according to [1] and forming the arrival-time sequence set $(\tau = \tau_1, \tau_2, \ldots, \tau_{N_g})$, of the channel considered.

$$H_k(f) = |g_k| \cdot e^{-ac \cdot \tau_k} \tag{1}$$

where $|g_k|$ is a constant. As the path amplitude of each group is exponentially dependent on a normally distributed random variable, it therefore follows the lognormal distribution, having the mean parameter equal to $(\mu_k + \ln|g_k|)$, and the variance equal to σ_k^2. The corresponding probability density function (PDF) is given by:

$$P_k(x) = \frac{1}{\sigma\sqrt{2\pi}} \exp \frac{-(\ln x - (\mu_k + \ln|g_k|))^2}{2\sigma_k^2} \tag{2}$$

And forming the amplitude sequence set of the channel considered as in [4]:

$$H(F) = |H_1(f)|, |H_2(f), \ldots, |H_{N_g}(f)| \tag{3}$$

In this work, we proposed the scatterers size distribution in the channel of the transmission line using equation in (4) that requires both diameters of the main line and of branches connected to loads. In this work, D is in the range of 0.9 to 2.9 mm. Also, the number of branches in the network (K) required. In [1], in the estimation of the path amplitude distribution, the authors used $K = 5, 10$ and 15.

$$N(D_i) = \frac{N_t}{\sigma\sqrt{2\pi}} \exp \frac{-(\ln(D_i) - \mu_i)^2}{2\sigma_i^2} \tag{4}$$

where N_t is the scattering point 'diameter' density of reflection. The independent input, the 'mean diameter' of the scattering point, directly from the branch.

The input parameters N_t, μ, and σ are obtained by regression fitting procedures with corresponding branches' numbers K to yield:

$$\begin{aligned} N_t &= a_o K^{b_o} \\ \mu &= A_\mu + B_\mu \ln(K) \\ \sigma^2 &= A_\sigma + B_\sigma \ln(K) \end{aligned} \tag{5}$$

where $a_o, b_o, A_\mu, B_\mu, A_\sigma$, and B_σ all represent the regression coefficients of input parameters corresponding to the lognormal model.

The moment function generator for lognormal scattering point size distribution is given by:

$$M_n = N_t \exp \left| n\mu + \frac{1}{2}(k\sigma)^2 \right| \tag{6}$$

The third, fourth and sixth moment are considered sufficient to derive the input parameters N_t, μ, and σ for lognormal moment as suggested by [6]. The solutions to these three selected moments in (6) are:

$$N_t = \exp[(24L_3 - 27L_4 + 6L_6)/3] \tag{7}$$

$$\mu = \frac{-10L_3 + 13.5L_4 - 3.5L_6}{3} \tag{8}$$

$$\sigma^2 = \frac{2L_3 + 3L_4 + L_6}{3} \tag{9}$$

In the above equations, the values of L_3, L_4, and L_6 represent the natural logarithms of measured moments M_3, M_4, and M_6.

In this approach, we are based on the results made in [1], for $K = 5$, we are able to derive M_3, M_4, and M_6 from the path amplitude distribution developed in [1].

Table 1 shows the applied regression fittings for the lognormal proposed model according to their input parameters for N branches as described in (5). We note that the fitted results for the values N_t show dependency on the number of branches (K). Figures 1–5 show the average scattering point size distribution and probability density distribution models developed for the PLC channel for different number of branches (K): $K = 4, 10, 15$ and 20.

The scattering point size distribution and probability density distribution in the indoor single-phase networks show that there are more scattering points at lower diameter sizes of branches of indoor networks where the mean peak diameter is about 0.8 mm. That implies more reflections of signal in this range of diameters. The results show that the distribution is independent of the indoor network topology.

Table 1: Network parameters.

a_o	b_o	A_μ	B_μ	A_σ	B_σ
73.1	0.285	-0.479	0.003	0.072	0

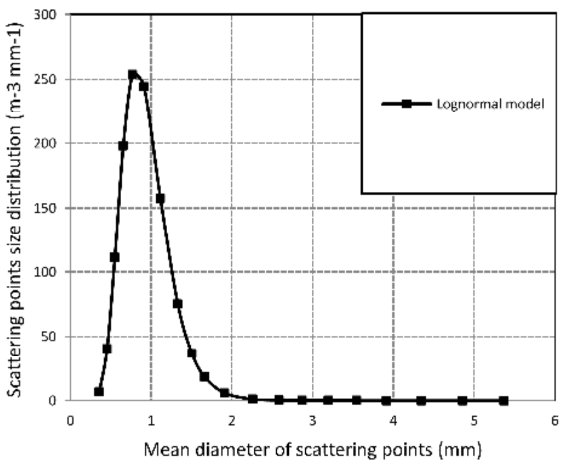

Figure 1: Scattering point size distribution for PLC channel with twenty branches.

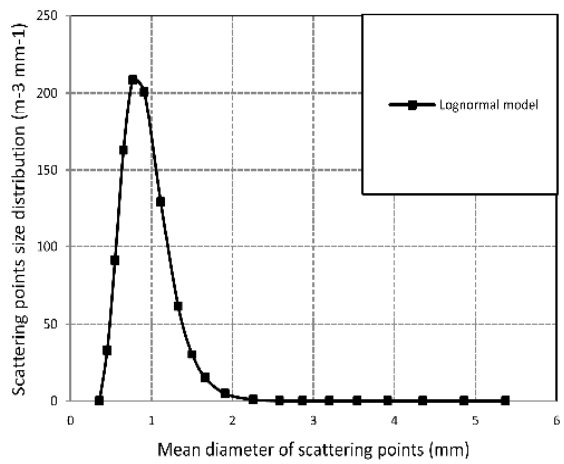

Figure 2: Scattering point size distribution for PLC channel with ten branches.

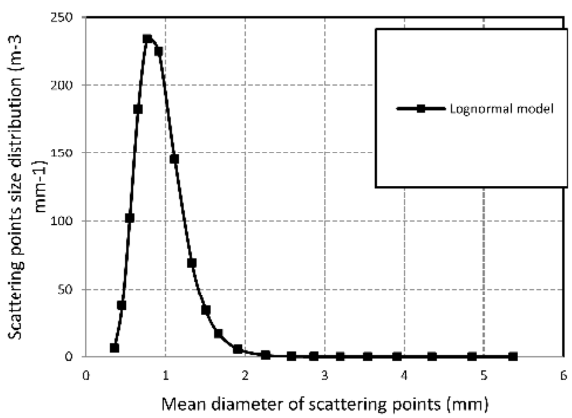

Figure 3: Scattering point size distribution for PLC channel with fifteen branches.

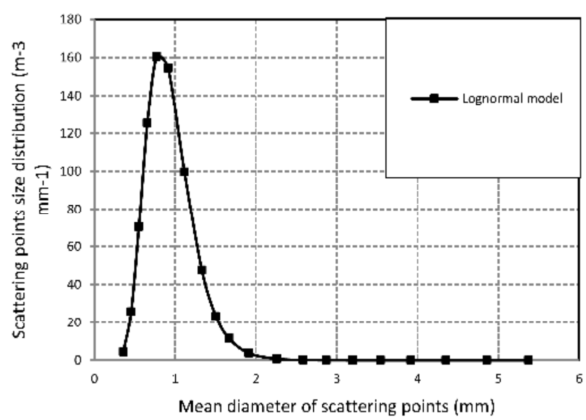

Figure 4: Scattering point size distribution for PLC channel with four branches.

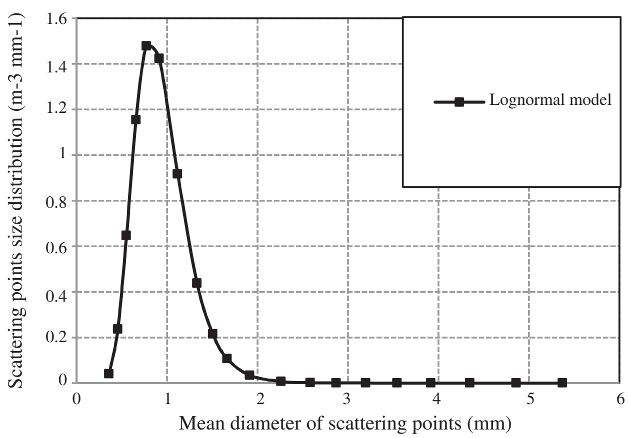

Figure 5: Probability density function of scattering points for PLC channel.

3. CONCLUSIONS

There are a lot of reasons that influence the reliable communication of high-speed data on single-phase networks LV. Among of these reasons, the distribution of scattering points that lead signal attenuation may be the essential one, which must be studied extensively. In this paper an analytical model of scattering size distribution and probability density distribution in broadband PLC channels are presented. The analysis performed show that there are more scattering points at lower diameter sizes of branches of indoor networks where the peak is reached at mean diameter 0.8 mm, that is implied more reflections of signal. In fact, there are extensively coupling and uncoupling of appliances connecting to branches of this mean diameter of indoor single-phase networks. But on the high diameter range (above 2 mm), scattering points are smaller and reflection is less. Also, the results show the independency of distributions toward to the indoor network topology. Measurements need to be conducted to confirm the results.

ACKNOWLEDGMENT

This work was performed under the auspices of the HDVC Centre and Communications Centre of School of Electrical Electronic and Computer Engineering by University of KwaZulu-Natal.

REFERENCES

1. Papaleonidopoulos, I. C., C. N. Capsalis, C. G. Karagiannopoulos, and N. J. Theodorou, "Statistical analysis and simulation of indoor single-phase low voltage power-line communication channels on the basis of multipath propagation," *IEEE Trans. Consumer Electronics*, Vol. 49, No. 1, 89–99, February 2003.
2. Papaleonidopoulos, I. C., C. G. Karagiannopoulos, N. J. Theodorou, C. E. Anagnostopoulos, and I. E. Anagnostopoulos, "Modelling of indoor low-voltage cables in the high frequency range," *Proc. ISPLC'97*, 267–271, 2002.
3. Malack, J. A. and J. R. Engstrom, "RF impedance of united states and european power lines," *IEEE Trans. Electromagnetic Compatibility*, Vol. 18, 36–38, February 1976.
4. Zimmermann, M. and K. Dostert, "A multi-path signal propagation model for the powerline channel in the high frequency range," *ISPLC'1999*, 45–51, Lancaster, UK, 1999.
5. Philips, H., "Modelling of powerline communication channels," *Proc. ISPLC'99*, 14–21, 1999.
6. Kozu, T. and K. Nakamura, "Rainfall parameter estimation from dual radar measurements combining reflectivity profile and path-integreted attenuation," *J. of Atmos. And Oceanic Tech.*, 259–270, 1991.

ONU Monitoring and Management Employing an In-band Ethernet Communication in FTTH/x System

Z. A. Manaf, **M. S. Salleh**, **K. Khairi**, **Z. Hamzah**, **M. N. Abd. Raman**, **D. A. M. Ssi**, **R. Mohamad**, **and Z. M. Yussof**
Next Generation Access Network Lab, TM Research & Development Sdn. Bhd.
Lingkaran Teknokrat Timur, Cyberjaya, Selangor 63000, Malaysia

Abstract— The FTTH/x is an emerging technology with the capability to deliver a high speed broad band services to the subscribers. Its flexibility and reliability are among major factors that drive the implementation world wide. In relation to this matter, the technique for monitoring and managing the element is a crucial subject to look into in order to ensure smooth operation as well as network survivability. In this paper, an enhancement to the existing ONU management system is proposed, developed and demonstrated as a proof of concept solution. An in-band management technique has been developed by integrating a microprocessor and data switching chip with the ONU in a single board. The main idea is to provide an Ethernet or IP based management link for remote management from the NOC office rather than MAC based only. With this unique solution, it serve as a complimentary features to the existing ONU management and monitoring function and additional external managed devices could be eliminated for a cost effective and simpler FTTH deployment and maintenance process.

1. INTRODUCTION

Fiber to the Home/x (will be referred as FTTH onwards) deployment is actively in progress around the world. Most of the telecommunication or internet service providers chose this type of access technology due to the nature of fiber optic cable that is capable to carry high bandwidth traffic. This solution is also made possible with the introduction of its components, namely Optical Line Terminal (OLT) which is placed in the Central Office (CO), Optical Network Unit (ONU) as the user's equipment and the optical splitter that will distribute the optical network from the OLT to multiple users.

Together with the deployment progress, researchers are also exploring various types of techniques to optimize this solution for a better service delivery as well as operational excellence. One of the main issues that could be look into is the monitoring and management process.

The monitoring and management method could vary from physical network, the network elements, or the service quality and status. One of the studies done is on in-service optical link monitoring using the Optical Time Domain Reflectometer (OTDR) [1]. Then there is also a significant application development for link surveillance and link faulty identification in the FTTH network [2]. However these studies are more towards the physical link aspect.

In this paper, a solution for Ethernet based ONU monitoring and management function is proposed. It could also be used for element (ONU) as well as link monitoring function.

2. DESIGN CONCEPT

The concept is based on the generic ONU architecture where its basic function is to convert the incoming optical to electrical signal and vice versa. In addition, the ONU is also communicating with the OLT for operational purposes, such as registration, provisioning as well as monitoring.

This is done through the Media Access Control (MAC) and Physical Media Dependant (PMD) layer in both OLT and ONU chipset. The service adaptation layer in the ONU will handle the appropriate signal format for each of the subscribed services by the users. These services will be sent to the user through the User Network Interface (UNI) port [3].

In FTTH architecture, the management function will be handled by the OLT chipset with a designated Operation Administration and Maintenance (OAM) or ONT Management Control Interface (OMCI) frames in EPON and GPON respectively. Theses frames are utilizing the same physical link as the user's traffic and usually have a proprietary message format defined by the chipset vendors.

Although the current defined command and protocol is sufficient for the provisioning of the FTTH-PON system, there is limitation should the operator require to mange the ONU through Ethernet based protocol. In fact, to archive this, an additional external Internet Protocol (IP)

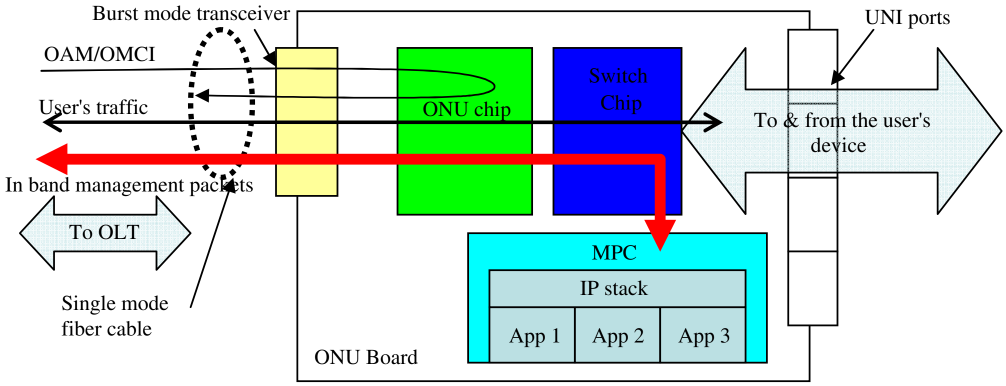

Figure 1: Conceptual design for in-band ONU management and monitoring function.

device, for instance, a router or monitoring PC is required to be installed at users' premises. The reason for this is because the existing communication method is based on Layer 2 or MAC based only. Thus, the monitoring application server could not recognize the ONU with this addressing scheme.

With this in mind, an enhancement has been proposed on top of the existing generic architecture. Apparently, in this project, the solution is derived on EPON technology. Although the communication method might differ, it is also applicable for GPON technology.

To archive this, two major components have been introduced together with the existing ONU chip. Firstly, a switch will distribute the user traffic to and from the ONU through the UNI port. Secondly, the microprocessor chip (MPC) will be used as the main management and processing module.

As shown in Figure 1, all of the management packet from the management or monitoring node will be diverted to the MPC by referring to its IP address. Other packets will be forwarded to the users based on the subscribed services through the UNI ports. On the other hand, the OAM or OMCI packets will be responded by the ONU chip to the OLT in the CO.

With this concept, not only the generic network application tool could be installed, but also a user customizable application could be ported with a specific management and monitoring functions and process.

3. DEVELOPMENT AND IMPLEMENTATION

The development idea is to integrate all of the three major chips (ONU, switch and MPC) in a single PCB board and enclosed with a 1U rack mounted casing.

In this project, the ONU chip used is TK3714 by Teknovus™ EPON solution, where it has a dual-speed (1.25/2.5 Gbps) and auto-sensing optical interface which will be connected to the burst mode transceiver and two UNI ports, i.e., Gigabit Ethernet (GE) and Fast Ethernet (FE) interface. Further more, it is a complete System-on-Chip (SoC) integrating an IEEE802.3ah-compliant EPON MAC, CPU, and memory [4].

The packet switching block consists of a Marvell 88E6095 chip, which has 8-port FE and 3-port GE interface [5]. Using this chip is an advantage to the development process due to the available firmware control provided by the Teknovus™ chip through the MDIO interface to control and manage the switch internally.

Finally the MPC or control processor block utilizes a Freescale™ MPC8349EA PowerQUICC II Pro integrated host processor. The processor is built with high-performance PowerPC e300 processor core operating at up to 667 MHz, as shown in the diagram below, and it features various peripheral interfaces sufficient for design requirements [6]. The firmware is based on Linux kernel 2.6 with a few additional drivers developed.

The network link for user's traffic from ONU chipset is connected to one of the GE port of the switch. Next, to enable the in-band management and monitoring function, another GE port of the switch is connected to the MPC's GE network interface. The interconnection could be seen in Figure 2 below.

Once the board has been fabricated and assembled, it has been put to test to prove its feasibility in FTTH network. An FTTH network has been setup in the laboratory emulating the actual deployment scenario starting with the GE switch as one of the Metro Ethernet node in the CO.

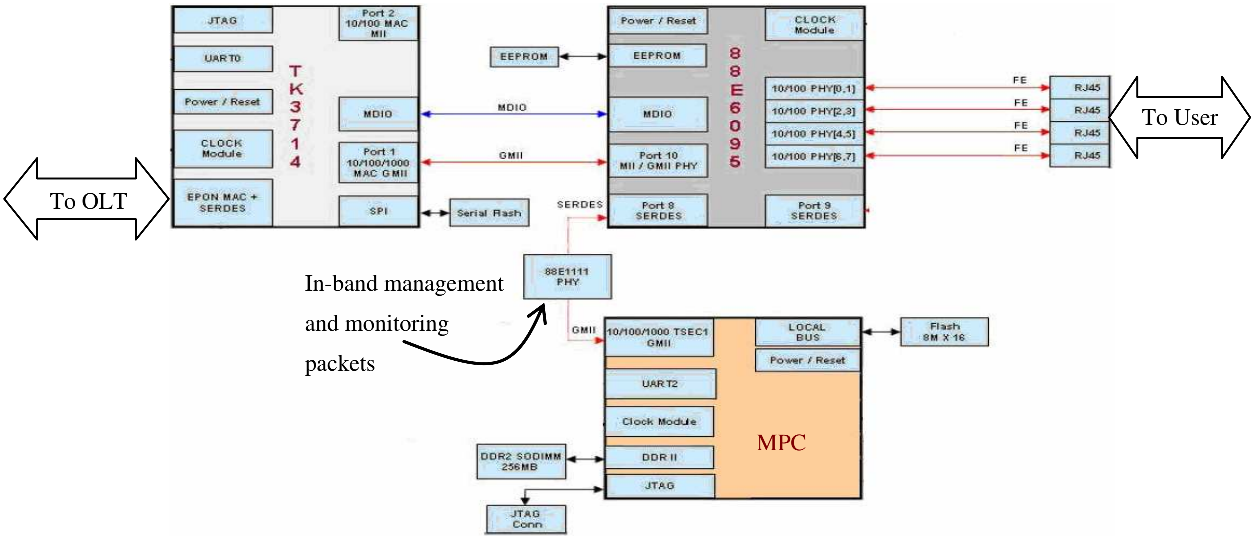

Figure 2: Final architecture for in-band monitoring and management.

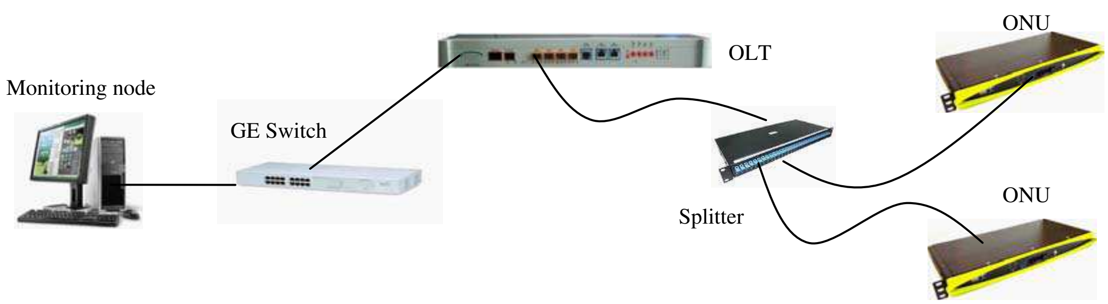

Figure 3: Experimental setup.

Then, the OLT is connected to the switch through its uplink GE port while the PON interface port is connected to the distribution splitter. Next, from the splitter, each port will be connected to this enhanced ONU optical port. On top of this, a monitoring and management workstation is connected to the GE switch, functioning as the Network Operation Center (NOC).

In order to enable the in-band feature, configuration has been made by defining a dedicated Virtual LAN (VLAN) ID for the monitoring and management packet. The affected devices for this configuration are the GE switch, OLT and ONU itself. Thus, these will provide a private virtual link from the monitoring and management node to the ONU.

Next, two network application tools are installed in the MPC chip for functionality test. The first is SNMP agent for management and monitoring using the Ethernet link, and the second one is the IXChariot by IXIA$^{\text{TM}}$ that could be used as a remote throughput or ONU data link speed testing tool. For both tools, the controlling and management is done remotely from the master application installed in the monitoring node. Figure 3 shows the experimental setup and the results will be discussed in the next section.

4. RESULT AND DISCUSSION

As described in the previous section, the developed device is tested on its capability to be managed through Ethernet communication using network application tools. Based from the network architecture defined in the previous section, each ONU will be pre-configured with a unique IP address (in the MPC chip). The result is captured by the monitoring node that is connected to the GE switch which is also being shared by the OLT for serving users' traffic.

Two tests being conducted to show the management function and its feasibility. The first one is to show the management function capability using SNMP by installing an SNMP agent in the MPC. The SNMP manager used is 'IReasoning MIB Browser' to emulate an actual network operation center monitoring application.

As shown in Figure 4(a), the monitoring node could send SNMP command to request or instruct the microprocessor to execute the desired operation. In this case, an SNMP get request command

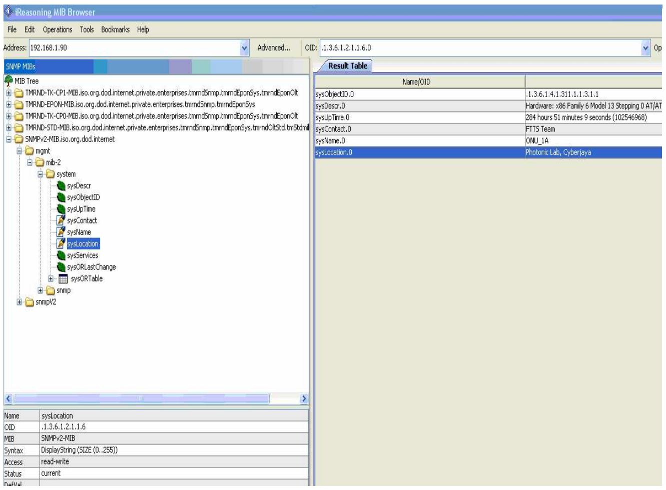

(a)

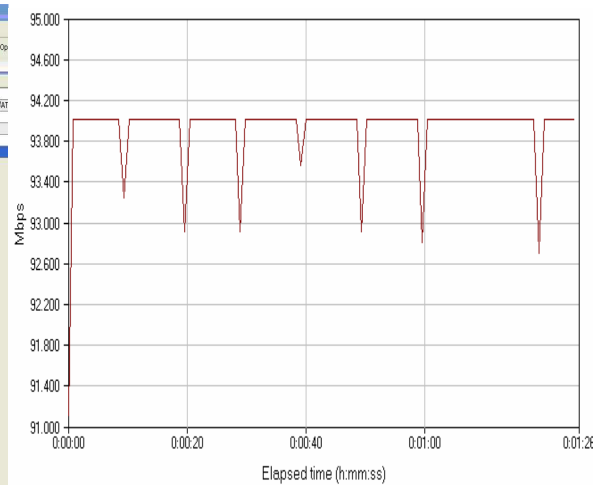

(b)

Figure 4: (a) MIB browser showing the received SNMP agent parameters. (b) Throughput test using IXChariot application.

has been sent to request the ONU information (as being defined in the SNMP agent in the MPC).

After that, a remote throughput test has been executed using IXChariot application to measure the ONU link speed. This could also be used as a diagnostic and verification tool to ensure link efficiency remotely. In this configuration, the bandwidth set for each of the ONU is 100Mbps. Hence, from the screen capture, the result shows that the actual ONU link speed is approximately 94 Mbps, which is acceptable taking into account the EPON packets overheads [7]. The result could be referred in Figures 4(a) and (b).

On the monitoring perspective, the ONU now could be seen as another IP node in the FTTH network and with this feature more monitoring and management flexibility could be archived.

5. CONCLUSION

The concept and method of in-band management for managing and monitoring the ONU in FTTH system has been demonstrated and explained in this paper. Apparently, the integration of a processor chip with the ONU could provide more space and flexibility for user defined network applications and various types of Ethernet based network application tools could be implemented in a single box. Hence, this approach could enhance the remote monitoring and management process in the FTTH system.

ACKNOWLEDGMENT

The authors would like to express their gratitude to GITN Sdn. Bhd. and Telekom Malaysia Berhad (TM) for the funding as well as co-operation and to TM Research & Development Sdn Bhd (TMR&D) management and Photonics Technology for the support and assistance on project execution.

REFERENCES

1. Gagnon, N., A. Girard, and M. Leblanc, "Considerations and recommendations for in-service out-of-band testing on live FTTH networks," *Optical Fiber Communication Conference, 2006* and *2006 National Fiber Optic Engineers Conference, OFC*, 2006.
2. Ng, B., M. S. Ab-Rahman, and K. Jumari, "FTTH network management software tool SANTAD ver 2.0," *2009 International Conference on Signal Acquisition and Processing*, 2009.
3. Cedric, L., *Passive Optical Networks — Principles and Practise*, Academic Press, 2007.
4. Teknovus — TK3714 Datasheet.
5. Marvell — 88E6095 Datasheet.
6. MPC8349EA, PowerQUICC$^{\text{TM}}$ II Pro Integrated Host Processor Family, Reference Manual.
7. Hajduczenia, M., H. J. A. da Silva, and P. P. Monteiro, "On efficiency of ethernet passive optical networks (EPONs)," *Proceedings of the 11th IEEE Symposium on Computers and Communications (ISCC'06)*, 2006.

Implementing Multiple WiFi Hotspots Using One Single Embedded Platform

Chun Yeow Yeoh
Lab Next Generation Access, TM Research & Development Sdn. Bhd., Malaysia

Abstract— To offer the mobility to existing fixed broadband customers, Telekom Malaysia (TM) has opted to deploy the WiFi hotspot using the 2.4 GHz ISM band. The WiFi hotspot is basically based on the IEEE 802.11 standard. 802.11 is an increasing popular standard that can be easily found in smart devices. Mobile service providers in Malaysia are also tried to offload their mobile data from 3G to WiFi due to the traffic growth. The common problem for WiFi deployment is site acquisition, a time-consuming and costly process. Usually, the suitable sites for WiFi deployment are public places, such as shopping malls, coffee shops, school, parks and etc. Technically, placing many Access Points (APs) within a site creates the interferences amongst the APs since there are only 3 non-overlapping channels in 2.4 GHz. Thus, a single AP which can allow more than one hotspot services is an interesting solution to the service provider. The service provider that owns the infrastructure can then "lease" it to other operators as well. In TM R&D, we have successfully found out a way to implement more than one hotspot services using one single embedded platform. This only requires the firmware update to the existing embedded platform either with 802.11 chipset or without 802.11 chipset. In this paper, we discuss the technical approach for providing multiple wireless hotspot services using one single embedded platform and also the experimental results.

1. INTRODUCTION

As a fixed broadband service provider, TM has taken the initiatives to offer its customers mobility or outdoor use via its Streamyx ZONE [1] or just recently rebranded as TM WiFi. "Wi-Fi", a trademark of the WiFi Alliance, utilizes IEEE802.11 standard and 2.4 GHz or 5GHz ISM band that are proliferated in many portable or smart devices. IEEE802.11 [2] is a specification for wireless local area network developed by IEEE working group. The most common standard nowadays is 802.11n which could offer high throughput up to 300Mbps utilizing Multiple Input Multiple Output (MIMO). The typical range of 802.11 is less than 30 meters for indoor usage and 100 meters for outdoor usage. The number of simultaneous clients per AP is probably less than 24. Since the coverage area is not wide and the capacity per AP is limited, the service providers are required to acquire a number of sites for their WiFi hotspot deployment.

Cellular operators in Malaysia are also looking to offload their 3G data to WiFi by launching their WiFi services, such as Maxis WiFi Hotspot [3] and DiGi Broadband Zone [4]. Currently, there are also WiMAX operators in Malaysia that tend to launch their own WiFi services. At the same time, WiFi hotspots are usually found at restaurant, train stations, airports, hotels, hospitals and other public establishments. So the service providers are actually looking for the same sites for their APs deployment. The ability to share the site using the same hardware by several providers will bring the benefit not only to the service providers but also to the users. Service providers can reduce the cost of network maintenance and operation. With less APs deployment, there will be less interference subsequently bringing better service for the users.

The major technical challenge for infrastructure sharing is to replicate the current WiFi hotspot services made available by respective service providers. In example, the service providers should able to maintain their own 802.11 service set identifier (SSID). Also, their subscribers should be able to be managed and controlled by their own authentication, authorization and accounting (AAA) system. We have successfully come out with the solution that can fulfill these two basic requirements. Although there are commercial solutions, such as [5], available in the market, our proposed solution is based on open source and no hardware limitation.

The rest of this paper is organized as follow. In Section 2, we discuss the details of our solution, including the technique used and method of implementation. The experimental results are presented in Section 3. We conclude our paper in Section 4 with some remarks regarding the technical issues on multiple WiFi hotspots in one single embedded platform.

2. MULTIPLE WIFI HOTSPOTS SOLUTION

Adoba has proposed the concept of virtual AP in [6]. Virtual AP is considered a logical entity that exists within a physical AP, but appears to stations (STAs) to be an independent physical AP. The multiple beacons, multiple Basic SSID (BSSID) approach has been identified as the best long term solution that able to mix the flexibility and compatibility. Beacon frame is one of the management frame defined by IEEE802.11 that periodically generated by the AP to announce the availability of the services. The beacon contains the information elements, such as SSID, supported rates, HT capabilities and etc. Figure 1 illustrates the concept of single AP with multiple BSSID and multiple beacons. In shared AP environment, the end users detect two BSSIDs similar to the case using two separate physical APs. The Linux wireless [7] that consists of various 802.11 drivers, soft-MAC/half-MAC, userspace/kernelspace communication transport and etc. has been a perfect choice for us. Open source community has done tremendous jobs and almost all the existing 802.11 drivers are able to support multiple BSSID. We have thus far verified that both Atheros chipset and Broadcom chipset are able to spawn multiple virtual APs in one single physical AP.

Captive portal technique, a technique that forces a client to go through a specified web page before he or she is able to access the Internet, is required for WiFi hotspot deployment. Refer to Figure 2 for the captive portal setup for WiFi hotspot. During the process, the client is required to submit the username and password for authentication purpose via web page obtained from the web server. He or she will be authorized with his or her subscribed service once successfully authenticated by the RADIUS [8] server. Both RADIUS server and web server can also be combined as one single entity. Access controller is the entity located between the AP and the Internet that implements captive portal mechanism. One of the open source access controllers is CoovaChilli [9]. For current TM WiFi deployment, we have integrated the CoovaChilli to our AP. Besides, our AAA system is based on open source RADIUS server known as FreeRadius [10]. By using open source, we have the flexibility to modify and customize our solution for TM requirements.

The *iw*, nl80211 based CLI configuration utility for wireless device, is used to create multiple virtual APs in our hardware platform. The execution of the CLI comman "*iw phy phy0 interface add wlan0 type managed*" creates the first virtual AP. For the second, third or fourth virtual APs, the syntax *wlan0* in the CLI command replace by *wlan1*, *wlan2* and *wlan3* respectively. CoovaChilli, software access controller is the userspace program that should be executed for supporting the

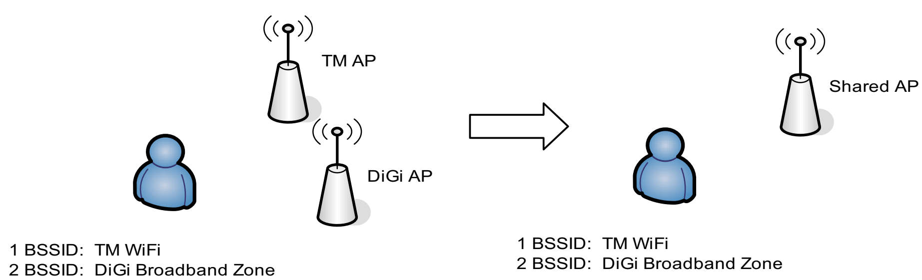

Figure 1: Virtual APs.

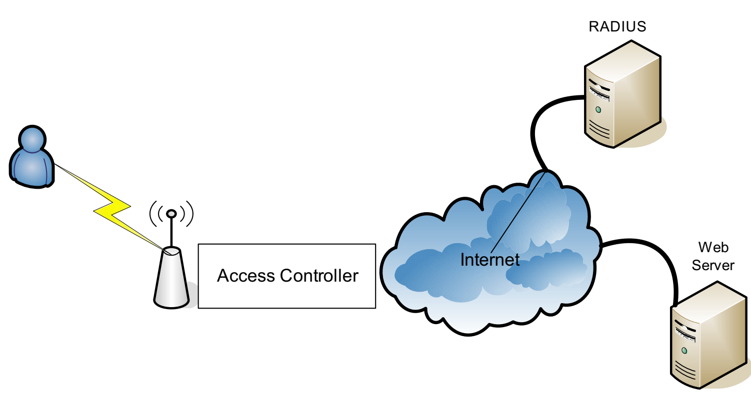

Figure 2: Captive portal setup for WiFi hotspot.

captive portal technique. The number of software access controller to be spawned in our system is based on the number of virtual APs. The correct interface of a particular SSID should be assigned during the startup of software access controller using the syntax *dhcpif*. In a case that the software access controller is not the entity resided in the physical AP, the AP is required to support Virtual LAN (VLAN) tagging in its wired interface. The VLAN port is then assigned as the *dhcpif* interface.

3. EXPERIMENTAL RESULTS

Two different experimental network setups, one with access controller resided in the AP as depicted in Figure 3(a) and another one with access controller located outside the AP as depicted in Figure 3(b), have brought up to verify our implementation. The hardware is the embedded platform known as UBNT RouterStation Pro featuring MIPS 680MHz CPU running Linux operating system. The user equipped with the 802.11 adapter cards is able to scan the SSIDs known as "TM WiFi" and "DiGi Broadband Zone". This is further proof using tcpdump. The beacons generated by the AP contain different BSSID and SSID name but both are operating in the same channel. The SSID name is actually specified using *hostapd*, an IEEE80211 AP and authenticator. The first requirement of having multiple SSIDs or virtual APs has been satisfied.

Spawning two access controllers in the Linux OS is by executing the CoovaChilli binary program twice with two separate configuration files. In Figure 5, the user is able obtain the landing page

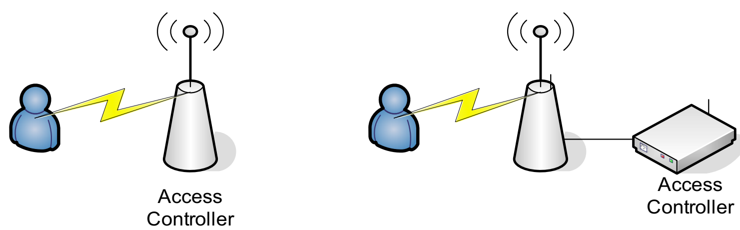

(a) (b)

Figure 3: Experimental setup for captive portal.

```
2011-11-18 15:54:25.939138 1.0 Mb/s 2462 MHz (0x00a0) -24dB signal -84dB noise antenna
5 [0x0000000e] BSSID:06:0b:6b:b6:5b:f6 DA:ff:ff:ff:ff:ff:ff SA:06:0b:6b:b6:5b:f6
Beacon (TM WiFi) [1.0* 2.0* 5.5* 11.0* 6.0 9.0 12.0 18.0 Mbit] ESS CH: 11
2011-11-18 15:54:25.956163 1.0 Mb/s 2462 MHz (0x00a0) -24dB signal -84dB noise antenna
5 [0x0000000e] BSSID:0e:0b:6b:b6:5b:f6 DA:ff:ff:ff:ff:ff:ff SA:0e:0b:6b:b6:5b:f6
Beacon (DiGi Broadband Zone) [1.0* 2.0* 5.5* 11.0* 6.0 9.0 12.0 18.0 Mbit] ESS CH:
11
```

Figure 4: Beacon captured by tcpdump.

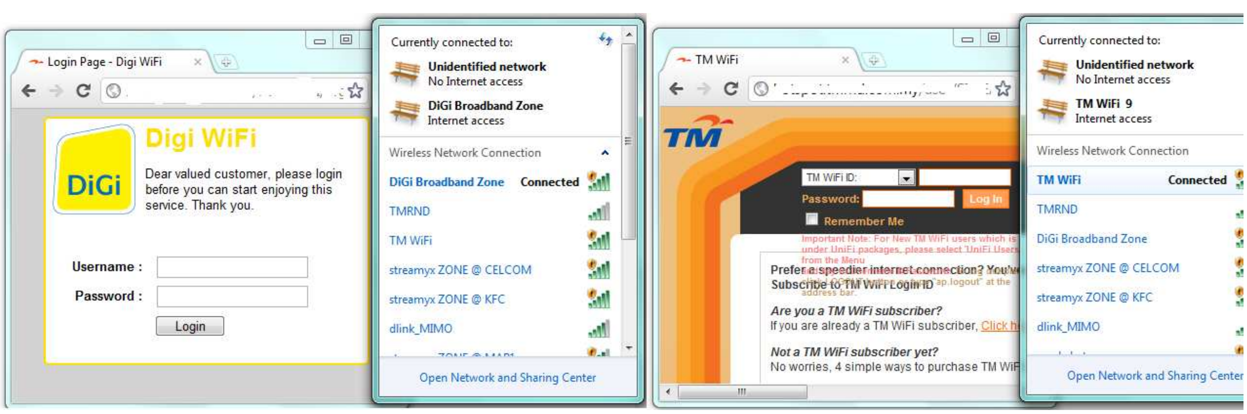

Figure 5: Different landing pages while connecting to different SSIDs.

```
# tcpdump -i eth0 -s 0 port 1812
tcpdump: verbose output suppressed, use -v or -vv for full protocol decode
listening on eth1, link-type EN10MB (Ethernet), capture size 65535 bytes
18:30:18.931345 IP 10.44.29.245.42151 > hotspot.tm.com.my.radius: RADIUS, Access Request (1), id: 0x08 length: 299
18:30:19.012512 IP hotspot.tm.com.my.radius > 10.44.29.245.42151: RADIUS, Access Accept (2), id: 0x08 length: 114
18:31:18.767149 IP 10.44.29.245.59012 > cds.tmrnd.com.my.radius: RADIUS, Access Request (1), id: 0x07 length: 296
18:31:19.783570 IP cds.tmrnd.com.my.radius > 10.44.29.245.59012: RADIUS, Access Reject (3), id: 0x07 length: 20
18:31:26.509510 IP 10.44.29.245.40445 > cds.tmrnd.com.my.radius: RADIUS, Access Request (1), id: 0x08 length: 296
18:31:26.522084 IP cds.tmrnd.com.my.radius > 10.44.29.245.40445: RADIUS, Access Accept (2), id: 0x08 length: 32
```

Figure 6: RADIUS packets captured by tcpdump.

according to the specified SSID. DiGi user obtains DiGi landing page while TM user gets TM landing page. Our access controllers are able to communicate with two separate RADIUS servers in our setup. The first RADIUS Access Request packet is sent to server named hotspot.tm.com.my and the second RADIUS Access Request packet is sent to server named cds.tmrnd.com.my as shown in Figure 6. Both of them are successfully authenticated. Thus, the second requirement is fulfilled.

4. CONCLUSIONS

In this paper, we have discussed the technical possibility of sharing the WiFi infrastructure by different service providers. We have demonstrated that it is possible to implement multiple WiFi hostpots in one single embedded platform by using open source solutions, namely the virtual AP concept supported by Linux wireless and CoovaChilli, a software access controller. The experimental results have verified that the basic requirements of having different BSSID and different AAA system can be both meet. However, there are further technical issues that we need to consider, such as how to ensure the end users' Quality of Service (QoS) from service provider A are not jeopardize due to domination of users from service provider B. Technique to load balance the end users between the APs must be further explored to cater this. However, the sharing of WiFi infrastructure is still a promising approach; especially when we consider it can further reduce the interference of ISM band. Besides, the difficulty of site acquisition can also be minimized if the service providers are able to share the infrastructure. Now, it is up to the service providers to reach an agreement on the business model to move this forward.

ACKNOWLEDGMENT

This work is conducted under the projects named Non Intrusive Universal Access Point Management Algorithm (NICE) and Back End System for WEB's AP (BEST) in TM R&D.

REFERENCES

1. TM Berhad, "Streamyx ZONE^{TM}," 2011 from http://streamyx.com.my/related_products/related_products.php?id=streamyx_hotspot.
2. IEEE P802.11n, Draft 2.0, "Part 11: Wireless LAN medium access control (MAC) and physical layer (PHY) specifications: enhancements for higher throughput," Feb. 2007.
3. Berhad, M., "Maxis WiFi hotspot," 2011 from http://www.maxis.com.my/personal/broadband/wifi/wifi.asp.
4. DiGi.com Berhad, "WiFi DiGi internet," 2011 from http://www.digi.com.my/internet/wifi/index.html.
5. BelAir Networks Inc., "BelAirOS carrier security module," *Data Sheet*, 2010.
6. Aboba, B., "Virtual Access Points," *IEEE 802.11-03/154r1*, March 2003.
7. Berg, J. M., "WiFi Overview," *Linux Wireless*, Feb. 2009.
8. Rigney, C., et al., "Remote authentication dial in user service (RADIUS)," *RFC2865*, Jun. 2000.
9. Bird, D., "CoovaChilli: Open-source software access controller," 2011 from http://coova.org/CoovaChilli.
10. Dekok, A., "The FreeRADIUS project," 2011 from http://freeradius.org/.

Particle Swarm Optimization Based Reception Diversity in Rayleigh Fading Channel

M. Riahi Manesh, **M. Akbari**, **S. A. Rafiei Taba Zavareh**,
P. Shahabi, **and Z. Pouladmast Ghadiri**
Faculty of Engineering, Multimedia University, Cyberjaya, Malaysia

Abstract— In the diversity concept, the maximal ratio combining (MRC) provides the best performance if the channel is perfectly estimated. However, channel estimation is scarcely perfect in practice which degrades the system performance. In this work, a diversity combining technique based on particle swarm optimization (PSO) algorithm is proposed to optimize the weighting coefficients vector of the system. Results indicate that the proposed method eliminates the need for estimating the channel and outperforms the MRC when channel estimation is imperfect. Nevertheless, it has almost the same performance as MRC when channel is perfectly estimated.

1. INTRODUCTION

Diversity, as an effective solution, is employed to overcome detrimental effects of channel fading and to improve the reliability of wireless communication systems [1]. In other words, having received multiple signals from multiple fading channels, diversity techniques are used to derive the information from received signals and consequently, enhance the received signal-to-noise ratio (SNR). Maximal ratio combining (MRC), equal gain combining (EGC), and selection combining (SC) are three commonly used diversity combining methods. The objective of these methods is to determine a set of weights $\vec{w} = [w_1, w_2, \dots, w_M]$ to combine the received signals, as illustrated in Figure 1. The mentioned techniques differ in the selection criteria of this weight vector.

These methods have been expansively investigated in the literature for their functionality in Rayleigh fading environment. Considering perfect channel estimation, it is shown in [1] that MRC can be applied to maximize the output SNR and minimize the bit error rate (BER). However, estimated channel is scarcely perfect in practice which degrades the system performance [2, 3]. The current enhancements in multiple-input-multiple-output communication systems have attracted the interests in discovering and diminishing the impact of imperfect channel estimation on diversity techniques [4–6]. Considering independent and identically distributed (i.i.d.) diversity paths, the performance of the MRC in Rayleigh fading channel has been examined in [3, 4]. For same scenario, the SNR distribution is investigated in [5]. In [6], the performance of the MRC in terms of BER has been studied when independent but not identically distributed (i.n.d.) paths were used. In this work, a diversity combining technique based on particle swarm optimization (PSO) algorithm is proposed in which the received signals are weighted based on PSO algorithm. The proposed PSO-based scheme opts for the best weighting coefficients vector, leading to improved performance of the system. The channel estimation error is considered as an additional source of noise with a parameter ρ, which is the normalized estimation error correlation coefficient. It is shown that the proposed diversity combining method does not require the channel estimation and outperforms the MRC when channel estimation is imperfect while it has almost the same performance as MRC when channel is perfectly estimated.

2. SYSTEM MODEL

Information symbols are assumed to be binary phase-shift keying (BPSK) modulated where the random variable $S = \pm\sqrt{E_s}$ presents the transmitted signal points with equal probability and E_s

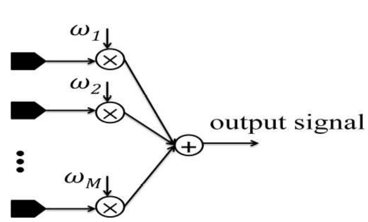

Figure 1: Diversity combining block diagram.

is the average symbol energy. It is assumed that the channel is frequency nonselective and slowly fading over the interval of the transmitted symbol. It is also presumed that the signals are received at M diversity paths at the receiver. The received signal at the ith path is then expressed by

$$r_i = g_i S + n_i \qquad i = 1, 2, \ldots, M \tag{1}$$

where g_i is the channel gain which is complex and its real and imaginary parts are uncorrelated and Gaussian distributed, each with zero mean and variance of σ_g^2. The complex additive white Gaussian noise (AWGN) random variable is denoted by n_i with zero mean and variance $\sigma_n^2 = \frac{N_0}{2}$. It is assumed that the channel gains g_i are identically distributed and uncorrelated at two different diversity branches. It is also assumed that there is no correlation between g_i and n_i. The receiver, then, linearly combines the received signals r_i with w_i which is the weighting coefficient of the ith path. The output r of the linear diversity combiner is given by

$$r = \sum_{i=1}^{M} w_i r_i = S \sum_{i=1}^{M} w_i g_i + \sum_{i=1}^{M} w_i n_i \tag{2}$$

Conditioned on the set $\vec{w} = [w_1, w_2, \ldots, w_M]$, the SNR at the output of the combiner (as per the definition of [3]) is expressed as

$$\gamma_s(\vec{w}) = \frac{E_s}{N_0} \frac{\left|\sum_{i=1}^{M} w_i g_i\right|^2}{\sum_{i=1}^{M} |w_i|^2} \tag{3}$$

Note that the SNR is greatly depending on w_i. As a result, the best possible solution is the weighting vector which maximizes $\gamma_s(\vec{w})$ in (3) as an objective function. In the ith diversity path, let p_i be the estimated channel gain and e_i be the estimation error with zero mean and variance of $\sigma_e^2 = \sigma_g^2(1 - \rho^2)$ where $\rho \in [0, 1]$ is the normalized estimation error correlation coefficient. Under Gaussian-error model, the relationship of g_i and p_i can be expressed as $g_i = p_i + e_i$ [7]. Based on the diversity combining rule for MRC method, the weights of the combiner adopt the values $w_i = p_i^*$ which, according to Cauchy-Schwartz inequality, maximize (3) if channel is perfectly estimated (i.e., $\rho = 1$). However, since channel is often imperfectly estimated in practice, the MRC is a suboptimal solution. In the next section, the PSO-based combining technique is described as a breakthrough to achieve the optimal weight vector $\vec{w}$.

3. PSO-BASED SOLUTION

PSO algorithm is taken from social behavior of flock of fishes and birds [8]. The behavior of these social organizations is emulated by PSO algorithm. In the PSO, each solution is referred to as a 'particle'. Each particle functions based on its own knowledge as well as group knowledge and has two primary operators: position and velocity. In this algorithm, each particle in the design space iteratively tries to find the best position, such as objective function's maximum value. The information about the best position is exchanged among the particles during many iterations. This information enables particles to update their position and velocity to achieve the best position. As such, after adequate number of iterations, the algorithm converges to the optimal solution of the objective function. In this section, the objective is to determine the set $\vec{w}$ which maximizes the objective function $\gamma_s(\vec{w})$ in (3). It is helpful to introduce additional constraint to reduce the search space on which the PSO works. The $\vec{w}$ used in this work satisfies the conditions $0 < w_i < 1$ and $\sum_{i=1}^{M} w_i^2 = 1$. The steps involved in the PSO algorithm to obtain the optimal weighting vector are shown in Table 1.

4. SIMULATION RESULTS

In this section, the performance of the proposed PSO-based technique is evaluated and compared with MRC, EGC and SC methods in two different environments of perfect and imperfect channel estimation using Monte-Carlo simulation. The average symbol energy is presumed to be $E_s = 1$ and the variance of the channel gain and AWGN at each dimension are $\sigma_g^2 = \sigma_n^2 = 0.5$. The parameters for the PSO algorithm are $N = 25$ and $c_1 = c_2 = 2$.

The normalized output SNR of PSO-based combining, MRC, EGC and SC techniques in terms of different number of diversity paths M in perfect channel estimation condition ($\rho = 1$) are shown in Figure 2. As it can be seen, the MRC provides the best SNR gain when channel state information

Table 1: Steps of the PSO algorithm to achieve optimal weight vector.

Step 1: Start the algorithm by randomly generating N numbers of $\vec{w}_s = [w_1, w_2, \ldots, w_M]$ ($s = 1, \ldots, N$) in the range of 0 and 1 where N is the number of particles. For simplicity, the position and velocity of particle s at iteration j are given by $\vec{w}_s^{(j)}$ and $\vec{v}_s^{(j)}$, respectively. Particle velocities are initially set to zero.
Step 2: Calculate the values of the objective function for the initial particle positions as $\gamma_s(\vec{w}_1^{(0)}), \gamma_s(\vec{w}_2^{(0)}), \ldots, \gamma_s(\vec{w}_N^{(0)})$.
Step 3: Determine the maximum value of the objective function in the step 2 and set its equivalent particle position as $P_{\text{best},\,0}$. Change the iteration number to $j = 1$.
Step 4: At the jth iteration, determine the velocity of the sth particle using $$\vec{v}_s^{(j)} = \vec{v}_s^{(j-1)} + c_1 r_1 \left[P_{\text{best},\,j} - \vec{w}_s^{(j-1)}\right] + c_2 r_2 \left[G_{\text{best}} - \vec{w}_s^{(j-1)}\right]$$ where c_1 and c_2 are the learning acceleration coefficients, r_1 and $r_2 \sim U(0,1)$ are uniformly distributed random numbers in the range of 0 to 1 which present stochastic components to the algorithm. $P_{\text{best},j}$ is the best value of experienced position of the particles at the jth iteration. Global best position (G_{best}) is the best value of experienced position among all iterations.
Step 5: Update the sth particle position at the jth iteration as follows: $$\vec{w}_s^{(j)} = \vec{w}_s^{(j-1)} + \vec{v}_s^{(j)}$$ Calculate the values of objective function corresponding to new particle positions as $\gamma_s(\vec{w}_1^{(j)})$, $\gamma_s(\vec{w}_2^{(j)}), \ldots, \gamma_s(\vec{w}_N^{(j)})$.
Step 6: Determine the maximum value of the objective function in the step 5 and set its equivalent particle position as the $P_{\text{best},j}$. If $P_{\text{best},j} \geq G_{\text{best}}$, replace G_{best} with $P_{\text{best},j}$.
Step 7: If the algorithm converged to a stable value, stop the procedure. Else, change the iteration number to $j = j + 1$ and jump to step 4.

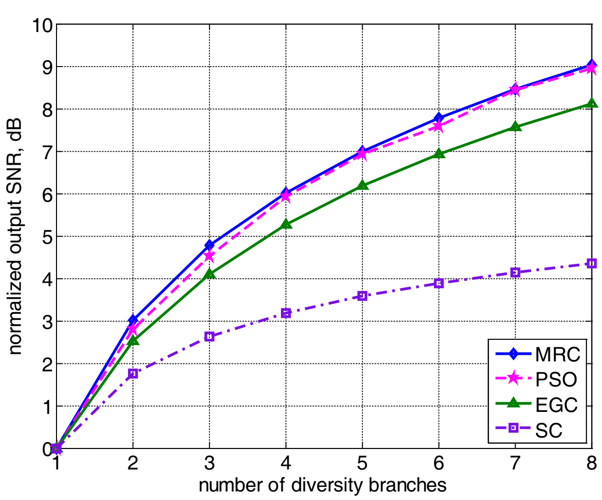

Figure 2: Comparison of normalized output SNR of PSO-based, MRC, EGC and SC methods when channel estimation is perfect.

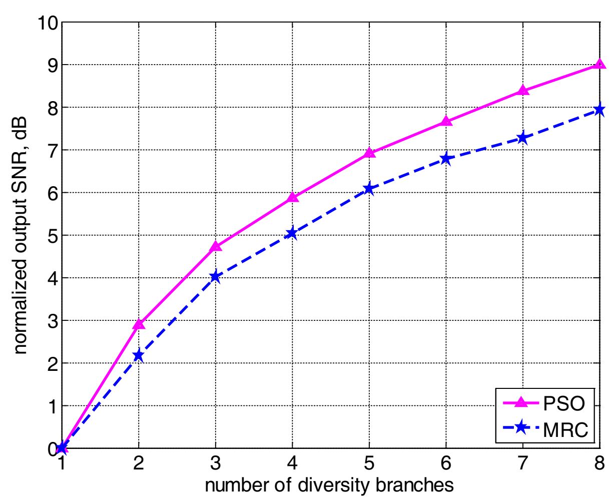

Figure 3: Comparison of normalized output SNR of PSO-based and MRC methods when channel estimation is imperfect.

is perfectly known at the receiver. However, the PSO-based solution demonstrates almost the same SNR improvement as MRC without the need of channel estimation which results in reduced complexity in the receiver.

Figure 3 shows the comparison between proposed PSO-based and MRC techniques in imperfect channel estimation environment ($\rho = 0$). It can be seen that the PSO-based method outperforms MRC when channel estimation is imperfect. The improvement achieved can be justified by ability of the PSO algorithm to thoroughly scrutinize the search space and appraise the objective function in (3) to maximize the output SNR.

5. CONCLUSION

A PSO-based diversity combining method is proposed to optimize the weighting vector which is used to combine the received signals at the receiver. Simulation results validate that the proposed PSO-based method provides higher output SNR gain than that of MRC when channel estimation is imperfect. On the other hand, in perfect channel estimation environment, the proposed method yields as much SNR gain as MRC.

REFERENCES

1. Proakis, J., *Digital Communications*, 4th Editon, McGraw-Hill, 2000.
2. Proakis, J., "Probabilities of error for adaptive reception of M-phase signals," *IEEE Transactions on Communication Technology*, Vol. 16, No. 1, 71–81, 1968.
3. Gans, M., "The effect of Gaussian error in maximal ratio combiners," *IEEE Transactions on Communication Technology*, Vol. 19, No. 4, 492–500, 1971.
4. Tomiuk, B. R., N. C. Beaulieu, and A. A. Abu-Dayya, "General forms for maximal ratio diversity with weighting errors," *IEEE Transactions on Communications*, Vol. 47, No. 4, 488–92, 1999.
5. Roy, S. and P. Fortier, "Maximal-ratio combining architectures and performance with channel estimation based on a training sequence," *IEEE Transactions on Wireless Communications*, Vol. 3, No. 4, 1154–64, 2004.
6. Thompson, J. S., "Antenna array performance with channel estimation errors," *Proc. ITG Workshop Smart Antennas*, 75–78, Munich, Germany, Mar. 2004.
7. You, R., H. Li, and Y. Bar-Ness, "Diversity combining with imperfect channel estimation," *IEEE Transactions on Communications*, Vol. 53, No. 10, 1655–62, 2005.
8. Kennedy, J. and R. Eberhart, "Particle swarm optimization," *Proc. IEEE Int. Conf.*, Vol. 4, 1942–1948, 1995.

Maximizing the Probability of Detection of Cooperative Spectrum Sensing in Cognitive Radio Networks

M. Akbari, M. Riahi Manesh, S. A. Rafiei Taba Zavareh, and P. Shahabi
Faculty of Engineering, Multimedia University, Cyberjaya, Malaysia

Abstract— To support the ever-increasing demand for radio spectrum, the cognitive radio (CR) is proposed as a solution to dynamically assign the spectrum based on certain observations. Weighting the coefficients vector is the principal factor influencing the detection performance of the system in soft-decision fusion (SDF-) based cooperative spectrum sensing. In this paper, the use of particle swarm optimization (PSO) algorithm as a significant method is proposed to optimize the weighting coefficients vector. The proposed technique investigates the best weighting coefficients vector. The performance of the proposed method is analyzed and compared with genetic algorithm (GA) based technique as well as other conventional SDF schemes through computer simulations. Simulation results validate the strength of the proposed method compared to all other SDF-based schemes.

1. INTRODUCTION

Cognitive radio (CR) [1], i.e., radio systems with adaptive intelligence, is attracting researchers to pass spectrum congestion bottlenecks in order to further increase the spectrum efficiency. In spite of cost issues, nowadays, communication systems are present everywhere and arising rapidly. Therefore, to overcome current spectrum paucity problem, they need to take advantage of CR.

Monitoring the radio spectrum at determined times, discovering the occupancy and finally utilizing identified spectrum holes, with negligible interference to licensed users or so called primary users (PUs), are three main stages in CR. CR receiver within the sharp sensing interval might not receive the PU transmitted signals due to hidden terminal problem and shadowing effect. Thus, at a special geographical location the sensing performance will be degraded [2]. This disadvantage is conquered by cooperative spectrum sensing [3] using CR's unlicensed users to leave the frequency band once present PU is detected. Unlicensed users in Cognitive Radio Network (CRN) are called secondary users (SUs).

Decision on the presence of PU is made by fusion centre (FC) based on the hard decision fusion (HDF) [3, 4], or soft decision fusion (SDF) [5, 6]. Detection performance of SDF-based schemes is superior in comparison with HDF-based schemes [7]. In [6], linear soft combination schemes for cooperative spectrum sensing in CRNs are investigated. In this paper, we focus on a scenario of cooperative spectrum sensing, in which a linear soft combination of basic measurements from individual SUs is performed at the fusion center using particle swarm optimization (PSO) algorithm to evaluate the optimal weighting vector.

2. SYSTEM MODEL

The block diagram of the cooperative spectrum sensing is shown in Figure 1. M numbers of SUs are acting as relays to amplify and forward (AAF) their individual perception of availability of PU to a common FC which works as a decision center. Usage of optimal weighting vector in the linear soft fusion eliminates the need for making a decision about optimal thresholds for each SU.

Each SU individually performs spectrum sensing to detect whether PU is present or absent. The formulation of binary hypothesis test of the spectrum sensing method is:

$$\begin{aligned} \text{Absence} \rightarrow H_0 &: X_i\,[n] = W_i\,[n] \\ \text{Presence} \rightarrow H_1 &: X_i\,[n] = g_i S\,[n] + W_i\,[n] \end{aligned} \tag{1}$$

where $X_i[n]$ is the received sampled signal at ith SU and $i = 1, 2, \ldots, M$, $n = 1, 2, \ldots, K$, K is the total number of samples of the received signal defined by $K = 2BT_s$ wherein B and T_s are, respectively, the bandwidth of the signal and sensing time, g_i is the channel gain of ith PU-SU link $S[n]$ is the PU transmitted signal which is presumed to be independent and identically distributed (i.i.d.) Gaussian random process with zero mean and variance σ_S^2, and $W_i[n]$ is additive white Gaussian noise (AWGN) with zero mean and variance $\sigma_{W_i}^2$. The measurements collected by the

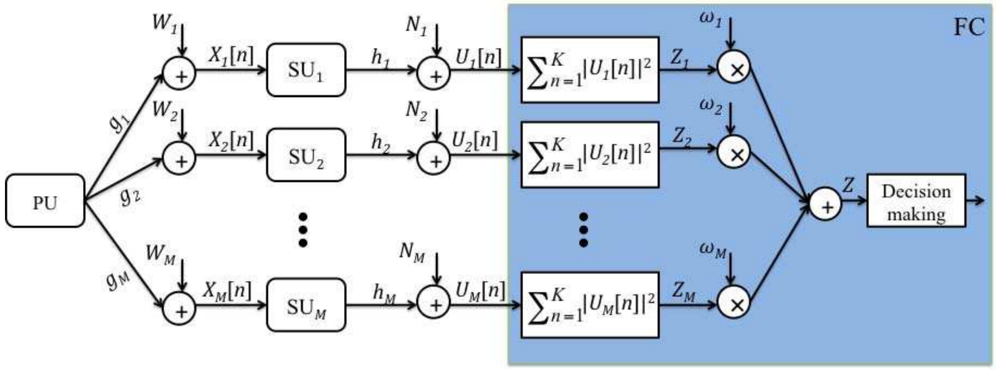

Figure 1: Block diagram of the cooperative spectrum sensing.

FC is given by $Z = \sum_{i=1}^{M} \omega_i Z_i$ where Z_i is the energy collected by FC from the ith SU signal and calculated by $Z_i = \sum_{n=1}^{K} |U_i[n]|^2$ and $U_i[n] = \sqrt{P_{R,i}} h_i X_i[n] + N_i[n]$ is the analogous signal received at FC wherein $P_{R,i}$ is the transmit power of each SU and h_i is the gain of the channel between FC and ith SU. $N_i[n]$ is assumed to be the AWGN in the SU-FC link with zero mean and variance δ_i^2, and lastly ω_i is the weighting coefficient of ith link. Under this frame work, probability of detection P_d in terms of the targeted probability of false alarm P_f, is concluded as fallows [5]:

$$P_d(\vec{\omega}) = Q\left(\frac{Q^{-1}\left(\bar{P}_f\right)\sqrt{\vec{\omega}^T \mathbf{\Phi}_{H_0}\vec{\omega}} - \vec{\omega}^T\vec{\theta}}{\sqrt{\vec{\omega}^T \mathbf{\Phi}_{H_1}\vec{\omega}}}\right) \tag{2}$$

where $Q(x) = \int_x^{+\infty} \frac{1}{\sqrt{2\pi}} e^{-t^2/2} dt$, $\Phi_{H_1} = \mathrm{diag}(2K(P_{R,i}|g_i|^2|h_i|^2\sigma_s^2 + \sigma_{0,i}^2)^2)$, $\Phi_{H_0} = \mathrm{diag}(2K\sigma_{0,i}^4)$, $\sigma_{0,i}^2 = P_{R,i}|h_i|^2\sigma_{W_i}^2 + \delta_i^2$, $\vec{\theta} = [\theta_1, \theta_2, \ldots, \theta_M]^T$, $\theta_i = KP_{R,i}|g_i|^2|h_i|^2\sigma_s^2$, $\vec{\omega} = [\omega_1, \omega_2, \ldots, \omega_M]^T$ is the weighting coefficients vector, T indicates the matrix transpose and $\mathrm{diag}(\cdot)$ is square diagonal matrix whose diagonal elements are the elements of a given vector. It is clear that the performance of detection is highly dependent on $\vec{\omega}$. Therefore, the optimal weighting vector maximizes P_d in (2). Additional limitation is necessary to reduce the search space on which PSO works because any real multiple value of $\vec{\omega}$ can be taken as an optimal solution. The $\vec{\omega}$ used in this paper fulfills the circumstances $0 < \omega_i < 1$ and $\sqrt{\sum_{i=1}^{M} \omega_i^2 = 1}$.

3. PARTICLE SWARM OPTIMIZATION-BASED WEIGHTING METHOD

Kennedy and Eberhart introduced PSO algorithm in 1995 [8], which is originally indicated as a model of social behavior of swarm of fishes and birds. Each particle in PSO algorithm functions based on its own knowledge as well as the group knowledge and has two main features: position and velocity. The particles exchange information about their best position among each other during many iterations.

Maximizing the objective function $P_d(\vec{\omega})$ in (2) is the goal of this paper and the steps of work are as follows:

Step 1: Considering the number of particles are N, initialize the algorithm by randomly generating N numbers of $\vec{\omega}_s = [\omega_1, \omega_2, \ldots, \omega_M]^T$: $(s = 1, \ldots, N)$ in the range of and 1. For simplicity, the position and velocity of particle s at iteration j are represented by $\vec{\omega}_s^{(j)}$ and $\vec{v}_s^{(j)}$, respectively. Particle velocities are initially set to zero.

Step 2: Evaluate the values of the objective function corresponding to initial particle positions as $P_d(\vec{\omega}_1^{(0)}) P_d(\vec{\omega}_2^{(0)}), \ldots, P_d(\vec{\omega}_N^{(0)})$.

Step 3: Find the maximum value of the objective function in the step 2 and set its equivalent particle position as the $P_{\text{best},0}$. Set the iteration number $j = 1$.

Step 4: At the jth iteration, find the velocity of the sth particle as follows:

$$\vec{v}_s^{(j)} = \vec{v}_s^{(j-1)} + c_1 r_1 \left[\mathbf{P}_{\text{best},j} - \vec{\omega}_s^{(j-1)}\right] + c_2 r_2 \left[\mathbf{G}_{\text{best}} - \vec{\omega}_s^{(j-1)}\right] \tag{3}$$

where c_1 and c_2 are the learning acceleration coefficients used to describe individual and social contributions of each particle, r_1 and $r_2 \sim U(0,1)$ are uniformly distributed random numbers in the range of 0 to 1 which present stochastic components to the algorithm. $P_{\text{best},j}$ is the best value of experienced position of the particles at the jth iteration. Global best position (G_{best}) is the best value of experienced position among all iterations.

Step 5: Update the sth particle position at the jth iteration using:

$$\vec{\omega}_s^{(j)} = \vec{\omega}_s^{(j-1)} + \vec{v}_s^{(j)} \tag{4}$$

Evaluate the values of objective function corresponding to new particle positions as $P_d(\vec{\omega}_1^{(j)})$, $P_d(\vec{\omega}_2^{(j)}), \ldots, P_d(\vec{\omega}_N^{(j)})$.

Step 6: Find the maximum value of the objective function in the step 5 and set its equivalent particle position as the $P_{\text{best},j}$. If $P_{\text{best},j} \geq G_{\text{best}}$, replace G_{best} with $P_{\text{best},j}$

Step 7: If the algorithm is converged to a stable value, stop the process. Otherwise, set the iteration number as $j = j+1$ and repeat from step 4.

4. SIMULATION RESULTS

In this work, PSO-based SDF technique is proposed and comprehensively evaluated and compared with genetic algorithm (GA-) based as well as conventional SDF methods such as normal deflection coefficient (NDC), modified deflection coefficient (MDC), maximal ratio combining (MRC) and equal gain combining (EGC). The number of users in CRN is $M = 20$, the bandwidth is $B = 6\,\text{MHz}$, sensing time $T_s = 25\,\mu\text{sec}$, SU transmit power $P_{R,i} = 32\,\text{dB}$, PU transmit power $\sigma_s^2 = 35\,\text{dBm}$, PU-SU channel noise $\sigma_{W_i}^2 = 0\,\text{dB}$, SU-FC channel noise $\delta_i^2 = 0\,\text{dB}$, number of particles is $N = 25$ and $c_1 = c_2 = 2$. To realize the excellent performance of the algorithm at low SNR conditions at SU and FC levels, the values of the $\{g_i\}$ and $\{h_i\}$ are randomly generated in the range of $-25 \leq g_i \leq -15\,\text{dB}$ and $-20 \leq h_i \leq -10\,\text{dB}$, respectively. Since the channel is assumed to be slow fading, $\{g_i\}$ and $\{h_i\}$ are assumed to be constant during the sensing time. The comparison of convergence between PSO- and GA-based SDF schemes for a given $P_f = 0.25$ are shown in Figure 2. This is obvious that PSO-based technique converges after the 30 iterations while the convergence for GA-based technique is attained after 44 iterations which imply the fast convergence of the PSO algorithm. The 32% improvement in convergence of PSO-based technique is observable compared to GA-based method.

The optimal weights obtained by PSO and GA algorithms in Figure 2 are used to plot the receiver operating characteristics (ROC) curve shown in Figure 3 which illustrates the probability of detection of PSO-based and GA-based scheme, as well as all other conventional methods for different given probabilities of false alarm. It is observable that PSO-based method outperforms all other methods with a large difference which validates the robustness of our proposed technique.

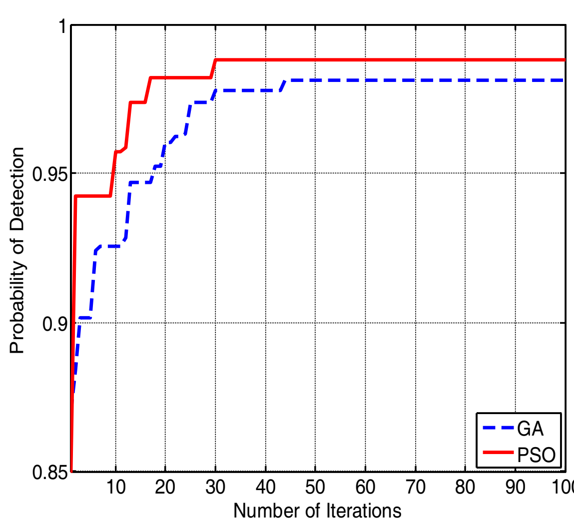

Figure 2: Comparison of probability of detection over 100 iterations for PSO and GA.

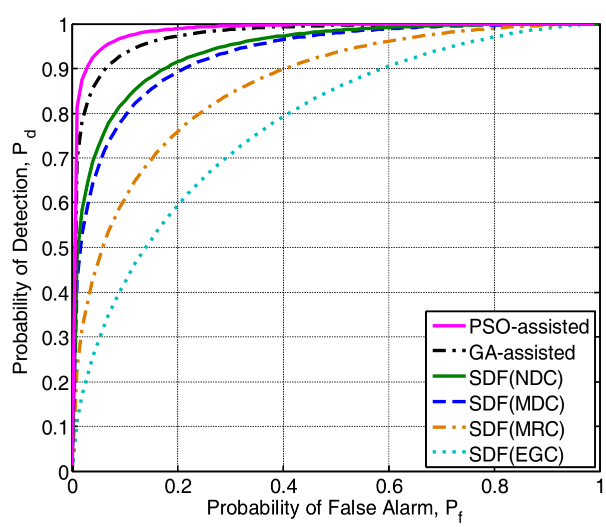

Figure 3: Comparison of probability of detection vs. probability of false alarm for PSO-assisted, GA-assisted and other SDF-based schemes.

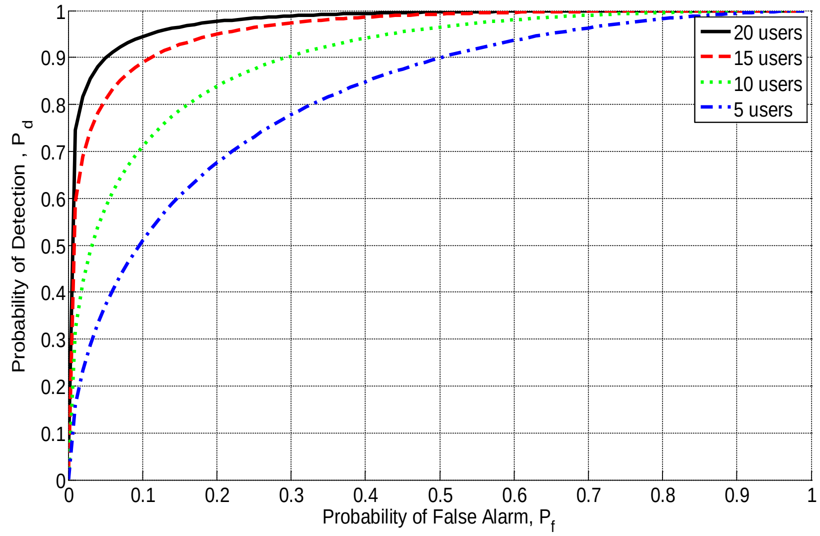

Figure 4: Probability of detection for different number of SUs.

For instance, for the fixed probability of false alarm $P_f = 0.1$, the probability of detection achieved by PSO is 97% which is the highest among all.

The effect of different number of cooperative SUs in CRN is also investigated on PSO-based scheme which is depicted in Figure 4. The detection performance of CRN for 5, 10, 15, and 20 SUs has been evaluated. It is obvious that by increasing the number of cooperative users, the performance is considerably improved. In fact, when $M = 5$, the ROC curve becomes closer to the discrimination line (the line where PU signal and noise cannot be discriminated which is often used as a bad detection indicator) than that when $M = 20$. Thus, as M increases, the separation between the hypotheses H_0 and H_1 increases and the performance of the ROC curve improves accordingly.

5. CONCLUSION

The appropriate choice of the weighting coefficients in CRN is a major challenge encountering cooperative spectrum sensing schemes and hence, methods to optimize these coefficients are crucial to the system detection performance. An enhanced SDF-based cooperative sensing using PSO algorithm has been proposed in this work. The proposed method has been expansively examined and compared with all other traditional techniques such as GA-, NDC- and MRC-based methods. Simulation results indicate that the proposed method provides higher probability of detection than those of all other SDF-based schemes with stationary convergence speed.

REFERENCES

1. Haykin, S. "Cognitive radio: Brain-empowered wireless communications," *IEEE J. Sel. Areas Commun.*, Vol. 23, No. 2, 201–220, Feb. 2005.
2. Ghasemi, A. and E. S. Sousa, "Collaborative spectrum sensing for opportunistic access in fading environments," *Proc. IEEE DySPAN 2005*, 131–136, Baltimore, MD, USA, 2005.
3. Ganesan, G. and Y. G. Li, "Cooperative spectrum sensing in cognitive radio, Part I: Two user networks," *IEEE Trans. on Wireless Communications*, Vol. 6, No. 6, 2007.
4. Zhang, W., R. K. Mallik, and K. Ben Letaief, "Cooperative spectrum sensing optimization in cognitive radio networks," *Proc. IEEE Int. Conf. Comm.*, 3411–3415, 2008.
5. Quan, Z., S. Cui, and A. H. Sayed, "Optimal linear cooperation for spectrum sensing in cognitive radio networks," *IEEE Journal of Selected Topics in Signal Processing*, Vol. 2, 28–40, 2008.
6. Shen, B. and K. S. Kwak, "Soft combination schemes for cooperative spectrum sensing in cognitive radio networks," *ETRI Journal*, Vol. 31, 263–270, 2009.
7. El-Saleh, A. A., M. Ismail, and M. A. M. Ali, "Genetic algorithm-assisted soft fusion-based linear cooperative spectrum sensing," *IEICE Electronics Express*, Vol. 8, 1527–1533.
8. Kennedy, J. and R. Eberhart, "Particle swarm optimization," *Proc. IEEE Int. Conf.*, Vol. 4, 1942–1948, 1995.

A Bandwidth Enhanced Elliptical Metamaterial Antenna

K. L. Sheeja[1], P. K. Sahu[1], and S. K. Behera[2]

[1]Department of Electrical Engineering, N.I.T. Rourkela, Orissa, India
[2]Department of Electronics and Communication Engineering, N.I.T. Rourkela, Orissa, India

Abstract— In this paper, an elliptical Zeroth Order Resonant (ZOR) antenna based on composite right/left handed (CRLH TL) is proposed. ZOR antennas suffer from a negative drawback of being narrow bandwidth. In this paper, an effort is made to circumvent this negative effect by implementing a coplanar waveguide (CPW) fed elliptical unit cells without vias. The bandwidth, gain and radiation efficiency of the proposed antenna is about 5%, 2.1054 dB and 65.937% respectively at 4.88 GHz ($n = 0$ mode). Simulated results are presented and discussed. The antenna consists of 2 elliptical unit cells flanked symmetrically on both sides by open ended spiral and anti-spiral inductors. The antenna was designed to operate from (4.715 to 4.945) GHz with a reflection coefficient of −24.2836 dB at the zeroth mode (4.88 GHz). The proposed elliptical ZOR antenna serves another purpose of being a very low profile one, exhibiting an omni-directional radiation pattern in H-plane (phi = 0 deg) and a dumb-bell shaped radiation pattern in E-plane (phi = 90 deg). Hence the proposed antenna is aptly suited for wireless applications (IEEE 802.11a standards). All simulations were carried out by using Ansoft HFSS.

1. INTRODUCTION

Low profile antennas with omni-directional radiation pattern are mostly suitable for modern day wireless communication systems. This requirement is met with the use of monopole and dipole antennas. However these devices being large couldn't meet the demands of compact, portable devices. Metamaterials comes into picture to solve this problem as metamaterials are popularly used to design low profile antennas and microwave devices [1, 2]. The composite right/left handed metamaterial transmission lines is an effective method to realize low profile,compact infinite wavelength zeroth order resonant antennas. But these ZOR antennas suffer from narrow bandwidth, low gain and low radiation efficiency [3, 4]. To circumvent all these negative effects a low profile elliptical ZOR antenna with symmetrically placed spiral and anti spiral inductors on both sides of each unit cell is designed and its performance studied.

In this paper, a low profile, extended bandwidth omni-directional antenna is designed with the foundation laid on CPW fed metamaterial CRLH TL concepts [5]. A high gain, monomode, single band antenna is achieved with 65.937% radiation efficiency. Simulated radiation pattern and 3D-gain using Ansoft HFSS are shown.

2. ZEROTH ORDER RESONANCE THEORY

ZOR phenomenon is based on infinite wave length with no dependence on its physical size at its zeroth order mode (fundamental mode). As shown below in Figure 1(a), a CRLH TL is composed of series capacitance C_L and inductance L_R as well as a shunt capacitance C_R and inductanceL_L.

The series and shunt resonant frequencies are given by

$$\omega_{se} = \frac{1}{\sqrt{L_R C_L}} \text{ rad/sec} \tag{1}$$

$$\omega_{sh} = \frac{1}{\sqrt{L_L C_R}} \text{ rad/sec} \tag{2}$$

By applying periodic boundary conditions (PBCs) related to the Bloch-Floquet theorem, the CRLH TL unit cell's dispersion relation is determined to be

$$\beta(\omega) = \frac{s(\omega)}{\Delta Z}\sqrt{\left[\omega^2 L_R C_R + \frac{1}{\omega^2 L_L C_L} - \frac{L_R C_L + L_L C_R}{L_L C_L}\right]} \tag{3}$$

where $s(\omega)$ and ΔZ are a sign function and the differential length, respectively.

For an unbalanced LC-CRLH TL, ω_{se} and ω_{sh} are unequal as shown in the dispersion diagram of Figure 1(b). At these resonant frequencies as $\beta = 0$, so an infinite wavelength can be supported and the resonance condition is independent of the size of the antenna (i.e.; the CRLH TL's length) while the shortest length of the conventional open ended resonator is one half of the wavelength. Thus, an antenna with a more compact size can be realized.

3. DESIGN METHODOLOGY

The proposed elliptical antenna implemented on a Rogers RT/Duroid 5880 substrate ($\varepsilon_r = 2.2$) with a size of $32\,\mathrm{mm} \times 30\,\mathrm{mm} \times 1.6\,\mathrm{mm}$ is presented. The antenna exhibits a high gain and antenna efficiency of about 2.1054 dB and 65.937% respectively at the zeroth mode of 4.88 GHz. The reflection coefficient achieved at this mode is about 24.2836 dB with a bandwidth of 5%.The antenna gives rise to an omni-directional radiation pattern in H-plane (phi = 0 deg) and a dumb-bell shaped radiation pattern in E-plane (phi = 90 deg). The ZOR antenna consists of 2 elliptical unit cells each of size ($6\,\mathrm{mm} \times 7.8\,\mathrm{mm}$) with coplanar waveguide feeding. Each unit cell is flanked symmetrically on both sides by a combination of short ended spiral and anti-spiral inductors. As the whole CRLH TL structure is excited by open circuiting, shunt resonance ω_{sh} initiates, with energy being stored in the shunt elements.

Therefore, in the open-ended CRLH resonator case, the fractional bandwidth is given by

$$B.W. = G\sqrt{\frac{L_L}{C_R}} \tag{4}$$

As bandwidth is directly proportional to the length of these spiral stub inductors (L_L) and inversely proportional to the overall area of the substrate (C_R). So by adopting this methodology of elliptical unit cells with spiral inductors, an extended bandwidth with high gain and radiation efficiency is achieved. As the spiral inductors are shorted at their ends to the CPW grounds so no vias are needed which simplifies the realization of this antenna.

4. ANTENNA DESIGN

The geometrical model of the proposed compact monomode, single-band ZOR antenna is shown in Figure 1 with two elliptical unit cells. The unit cells or the radiating patch is separated by a small gap of 0.2 mm. This gap provides the series LH capacitance C_L, while, the magnetic flux produced by the current flow along the radiating patch provides the parasitic series RH inductance L_R The short ended spiral inductors of width 0.4 mm introduce the LH inductance L_L. The gap between the spiral inductor strips is also equal to 0.4 mm. Figure 2 and Figure 3 shows the simulated reflection coefficients of −24.2836 dB and 3D-gain of 2.1054 dB at the zeroth mode respectively. Figure 4 shows the E-radiation pattern at x-y plane and H-radiation pattern at x-z plane at $n = 0$ mode. A dumb-bell shaped E-radiation pattern and an omni-directional based H-radiation pattern is obtained. Figure 5 shows that the VSWR of the antenna at $n = 0$ mode (freq = 4.88 GHz) is about 1.13 which is acceptable.

5. SIMULATION RESULTS

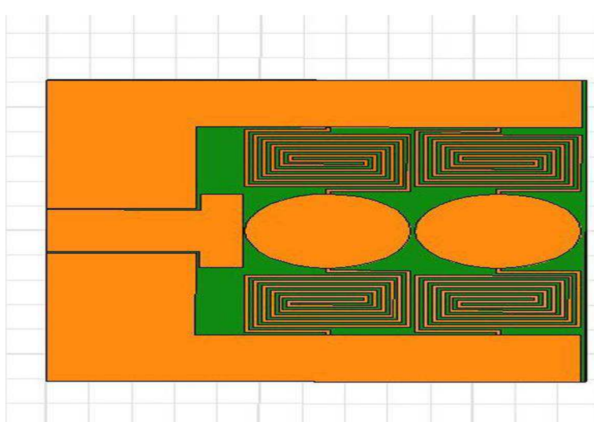

Figure 1: Geometrical model of the proposed single-band, monomode ZOR antenna (with two unit cells).

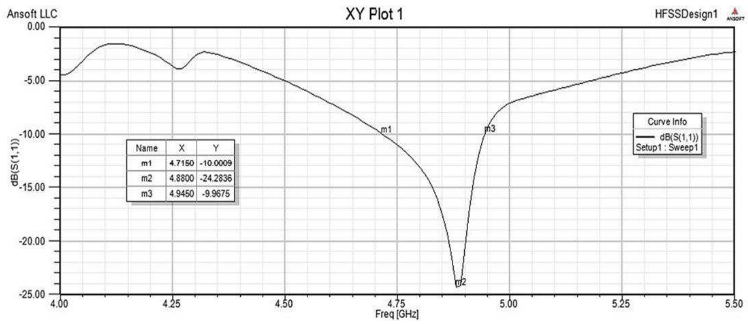

Figure 2: Simulated reflection coefficients of the proposed ZOR antenna.

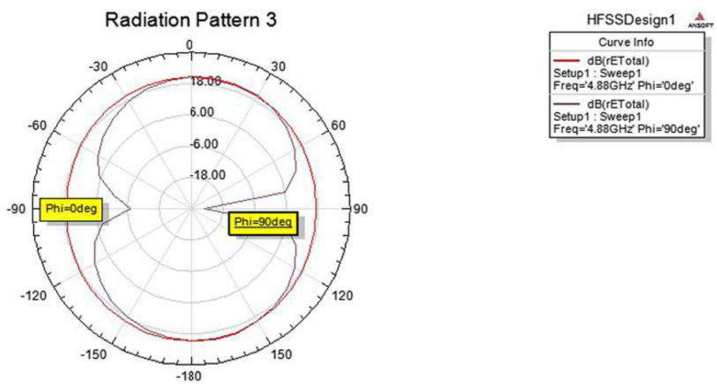

Figure 3: Simulated radiation pattern at $n = 0$ mode (freq = 4.88 GHz) [Phi = 0 deg (x-z plane) and Phi = 90 deg (y-z plane)].

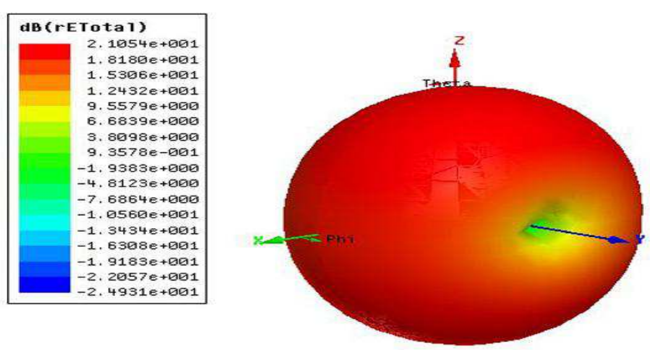

Figure 4: 3D-Gain of the proposed antenna at $n = 0$ mode (freq = 4.88 GHz).

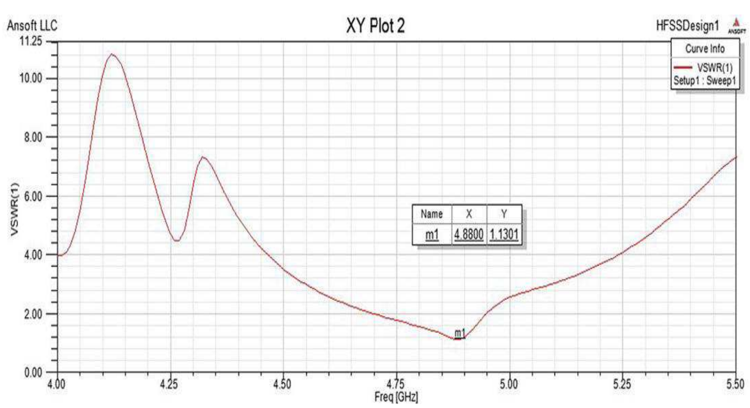

Figure 5: VSWR of the proposed antenna at $n = 0$ mode (freq = 4.88 GHz).

6. CONCLUSION

A new compact metamaterial based elliptical antenna built on a Rogers RT/duroid 5880 substrate is designed and presented. It radiates omni-directional waves in the horizontal plane. It is miniaturized by increasing the LH inductor by using a combination of spiral and anti-spiral stub inductors. This antenna, which exhibits a size of $0.158\_0 \times 0.07\_0$, shows a simulated gain of 2.1054 dB and a fractional bandwidth of 5%. with an antenna efficiency of 65.937%. Besides, the antenna gain of 2.11 dB and the efficiency of 65.937% were achieved.

ACKNOWLEDGMENT

The authors would like to thank Prof. D. R. Poddar, Jadavpur University, Kolkata, India for providing simulation facilities at his laboratory to carry out this work.

REFERENCES

1. Caloz, C. and T. Itoh, *Electromagnetic Metamaterials: Transmission Line Theory and Microwave Applications*, Wiley-IEEE Press, Hoboken-Piscataway, 2005.
2. Eleftheriades, G. V. and K. G. Balmain, *Negative Refraction Metamaterials: Fundamental Principles and Applications*, Wiley-IEEE Press, Hoboken-Piscataway, NJ, 2005.
3. Lai, A., K. M. K. H. Leong, and T. Itoh, "Infinite wavelength resonant antennas with monopolar radiation pattern based on periodic structures," *IEEE Trans. on Antennas and Propagation*, Vol. 55, No. 3, March 2007.
4. Lee, C. J., K. M. K. H. Leong, and T. Itoh, "Design of resonant small antenna using composite right/left-handed transmission line," *Antenna and Propagation Society Symposium*, July 2005.
5. Jang, T. and S. Lim, "A compact zeroth order resonant antenna on vialess CPW single layer," *ETRI Journal*, Vol. 32, No. 3, June 2010.

Determination of Effective Constitutive Parameters, Material Boundaries and Properties of SRR-rod and Fishnet Metamaterials by Drude/Lorentz Dispersion Models

Feng-Ju Hsieh[1], **Cheng-Ling Chang**[1], and **Wei-Chih Wang**[1,2,3]

[1]Department of Mechanical Engineering, University of Washington, Seattle, Washington, USA
[2]Department of Electrical Engineering, University of Washington, Seattle, Washington, USA
[3]Medical Device Innovation Center, National Cheng-Kung University, Tainan, Taiwan

Abstract— This paper presents two effective extraction methods to fully retrieve effective refractive indices (n), impedances (z), and material properties, such as dielectric permittivity (ε) and permeability (μ) of metamaterials (MMs). The first full extraction method based on the material continuity allows missing results in the strong resonant band where the imaginary part of permittivity or permeability is negative to be retrieved. The second method describes a genetic algorithm and optimization of properly defined goal functions to retrieve the parameters from Drude and Lorentz dispersion models for ε and μ, respectively. Proper initial values of the parameters of models and partial retrieved ε and μ are also derived for the second method in order to reduce the computation time and prevent the optimization solution from falling into local minimum. Finally, the refractive index, impedance, permittivity, and permeability of two slabs composed of SRR-based and fishnet MMs are retrieved and compared using the proposed methods.

1. INTRODUCTION

Metamaterials (MMs) [1, 2] operated in quasi-optical or Terahertz (THz) frequency range have been attracting attention over the past several years due to their unique phenomena, such as the negative refractive index and strong resonance in THz range, lacking in naturally occurring media. In order to utilize these phenomena of MMs in applications for bio-chemical sensing, spectroscopy, bio-imaging, security and communications,the effective boundaries of MMs must be determined first, before the constitutive parameters and frequency-dependent material properties of MMs are characterized. To meet this demand, we propose two optimization models to determine effective boundaries of MMs. The optimization models are defined based on the assumption of effective medium theory and characteristic of homogeneous media. The results are then compared with the traditional definition proposed by Kong [3].

Several methods [4–7] have been reported based on the assumption of effective medium theory, which means that the lattice size is much smaller than the operating wavelengths inside the medium.The common approach is to calculate effective refractive index (n) and impedance (z) from reflection (S_{11}) and transmission (S_{21}) coefficients of scattering parameters (S-parameters), and derive the effective constitute parameters ε and μ from n and z. There are known issues to this process that may fail the extraction, such as when either the magnitude of S_{11} or S_{21} is small or when the effective slab boundaries are not well estimated. The proposed methods will help to clarify the determination of effective boundaries of materials and simplify the determination of refractive index from the multiple-branch problem caused by the inverse of logarithm or arccosine operator.

Another major issue revealed by [3] indicates missing results in real part of n near resonant band where the imaginary part of ε or μ is negative. As a result, no constitutive parameters can be determined in the resonance band. However, there should be a value of ε and μ at any frequency to describe material properties, where transmission and reflection coefficients can also be derived or measured. Despite the controversy in considering whether negative ε and μ should exist or not, we propose two extraction methods for both sides to retrieve material properties of MMs. The first method allows the retrieval of constitutive parameters with negative imaginary part of ε or μ at resonant band, and the second method based on partial retrieved results and passive material dispersive Drude and Lorentz model allows to retrieve constitutive parameters with all positive imaginary parts of ε and μ.

2. SIMULATION MODELS

Two different types of MMs split ring resonator with a rod (SRR-Rod) and fishnet MMs as shown in Fig. 1, are simulated and used to calculate constitutive parameters and material properties. The dimensions of SRR-Rod unit cell are the lattice size $a = 50\,\mu\text{m}$, ring spacing $b = 5\,\mu\text{m}$, outer SRR height $h = 30\,\mu\text{m}$, strip width $w = 2.5\,\mu\text{m}$, and gap width $g = 5\,\mu\text{m}$. The dielectric material with 2.5μm thickness between SRR and rod, are characterized by $\varepsilon_r = 3.84$ and $\tan\delta = 0.018$. The slab thickness L_m is determined by the numbers of unit cell in $\hat{x}$ direction. A planar EM wave is incident from the side of the unit cell and propagating in $\hat{z}$ direction with simulation ports set originally $L1_o = L2_o = 75\,\mu\text{m}$ away from the slab/air interfaces. For the fishnet MM, dielectric is sandwiched between the two fishnet-shape conductors, and a planar EM wave propagates in $\hat{z}$ direction with $L1_o = L2_o = 150\,\mu\text{m}$ and impinges normal to the unit cell surface with the square lattice size $c = 150\,\mu\text{m}$, square conductive pad length $d = 104\,\mu\text{m}$, and $e = 10\,\mu\text{m}$. The slab thickness is the thickness of dielectric layer t_s plus the thickness of two conductive layers $2t_c$.

3. EXTRACTION METHODS

A partial extraction method with modifications in determining effective boundaries and real part of refractive index (n') from the well-known method [3] is shown in Fig. 2. Before n and z can be calculated from S_{11} and S_{21} using Equations (1)–(2), effective boundaries of a MM slab must be determined firstby proposed optimization models defined in (3)–(4). Since MMs are resonant in frequencies where n is negative, the characteristic of a homogenous material which means its impedance is independent of its slab thickness is adopted in defining the goal functions. By inspecting the impedance difference of two different slabs with different numbers of the unit cell layered

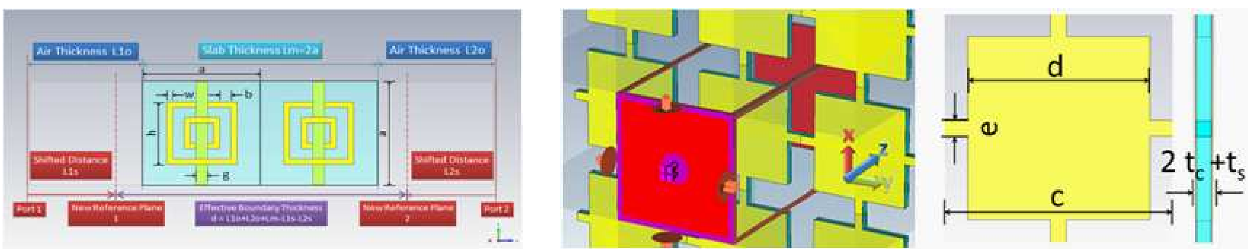

(a) (b) (c)

Figure 1: (a) Geometry of a two-cell SRR-Rod MM slab with effective boundaries set at new reference planes. For a single cell slab, the slab thickness L_m is a. For the two cells slab that has two unit cells stacked up together in z direction, the slab thickness $L_m = 2a$. (b) Single-layered fishnet MM array with dielectric sandwiched between the top and bottom fishnet-shaped conductors. (c) Geometry of a fishnet MM unit cell.

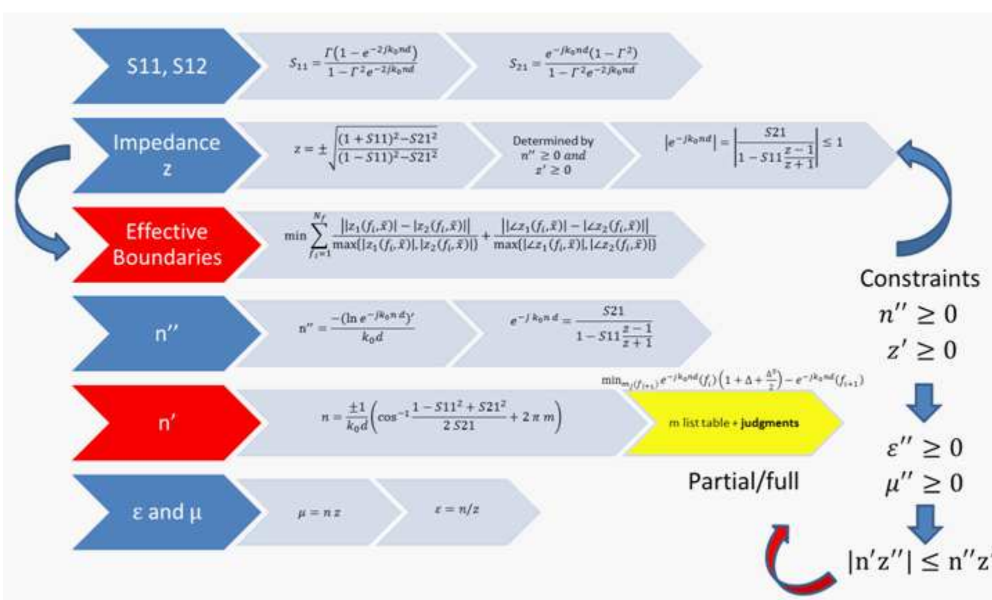

Figure 2: Flow chart of the proposed extraction method.

up in the wave propagating direction, we can define effective boundaries of the slabs at which the impedance difference of two slabs with different thickness is minimized. The original goal function of the optimization model defined in [3] is set up to find the locations of new reference planes of two slabs such that the mismatch of impedances of these two slabs at the effective boundaries is minimized, however, two new goal functions are set to find the effective boundaries where the mismatch of impedances at the investigated frequencies is minimized and equally weighted in magnitude and phase terms or real and imaginary parts of the impedance. Three goal functions are then used to generate the density plots of mismatch impedance within the searching range of $(L1_s, L2_s)$ set from $-80\,\mu\text{m}$ to $80\,\mu\text{m}$, as shown in Fig. 3. The darker zone represents smaller value of mismatch of the impedances. As a result, the original goal function gives three darker zones while the proposed goal functions give only one darker zone for the locations of effective boundaries at $L1_s = L2_s = -73\,\mu\text{m}$.

$$n = \frac{\pm 1}{k_0 d}\left(\cos^{-1}\frac{1 - S11^2 + S21^2}{2\ S21} + 2\pi m\right) \tag{1}$$

$$z = \pm\sqrt{\frac{(1+S11)^2 - S21^2}{(1-S11)^2 - S21^2}} \tag{2}$$

$$\min \int_{f_i=1}^{N_f} \frac{\left||z_1(f_i,\overline{x})| - |z_2(f_i,\overline{x})|\right|}{\max\{|z_1(f_i,\overline{x})|, |z_2(f_i,\overline{x})|\}} + \frac{\left||\angle z_1(f_i,\overline{x})| - |\angle z_2(f_i,\overline{x})|\right|}{\max\{|\angle z_1(f_i,\overline{x})|, |\angle z_2(f_i,\overline{x})|\}} \tag{3}$$

$$\min \int_{f_i=1}^{N_f} \frac{|z_1{}'(f_i,\overline{x}) - z_2{}'(f_i,\overline{x})|}{\max\{|z_1{}'(f_i,\overline{x})|, |z_2{}'(f_i,\overline{x})|\}} + \frac{|z_1{}''(f_i,\overline{x}) - z_2{}''(f_i,\overline{x})|}{\max\{|z_1{}''(f_i,\overline{x})|, |z_2{}''(f_i,\overline{x})|\}} \tag{4}$$

where N_f is the total number of samples of interesting frequencies and $z_j(f_i,\overline{x})$ is the impedance of slab j measured at frequency f_i with effective boundaries set at new reference planes $\overline{x} = (L1_s, L2_s)$. Positive signs of $(L1_s, L2_s)$ denote that the new reference planes are shifted outward from the slab while negative signs of $(L1_s, L2_s)$ denote that the new reference planes are shifted inward toward the slab from the original locations $(L1_0,\ L2_0)$.

The ambiguity of n' exists in the signs and the branch index m, and the first proposed method is to create table of m candidates at each frequency satisfying $|n'z''| \leq n''z'$. Then mathematical continuity of the n' can be applied to partially retrieve n' by examining Taylor series expansion of e^{-jk_0nd} at frequency f_i and f_{i+1} to determine the right branch index m at frequency f_{i+1} by the known value of m at frequency f_i, instead of solving the binomial equation proposed in [3]. By scanning the m value from all integers through all investigated frequencies using this algorithm, instead of the table of m candidates, n' can be fully retrieved.

The second method based on partial retrieved results of n and z, parameterized dispersive Drude/Lorentz models (5)–(6), can retrieve material properties with all positive ε'' or μ'' by proper defined optimization models (7)–(8). Proper initial search ranges for certain parameters, such as

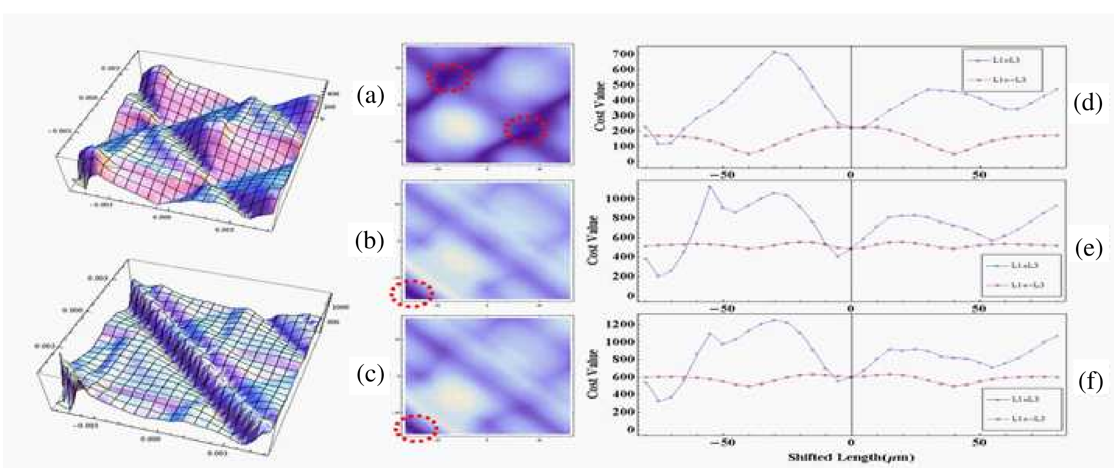

Figure 3: (a), (b) and (c) are 2D density graphs of original and the other two goal functions with x, y axes denote searching range of $L1_s$ and $L2_s$, respectively. (d), (e) and (f) are 1D graphs along diagonal and anti-diagonal direction of 2D density graphs of (a), (b), and (c), respectively.

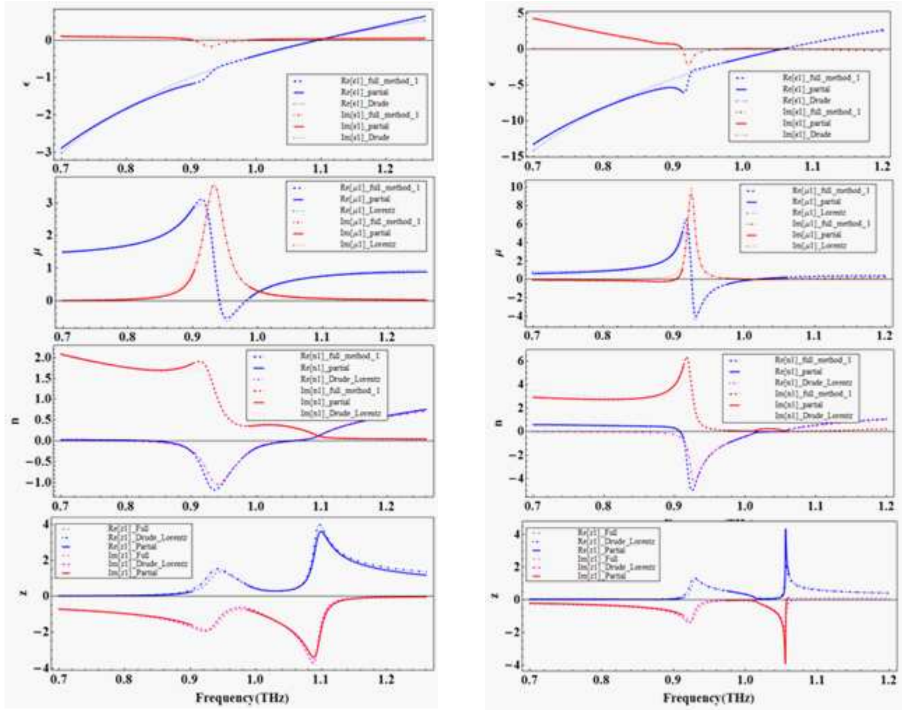

(a) (b)

Figure 4: (a), (b) are retrieved n, z, ε and μ of SRR-Rod and fishnet MMs, respectively.

ε_s, ε_∞, ω_0, μ_s and μ_∞, are necessary to speed up the calculation for the optimization and prevent the solution of optimal parameters to fall into the local minimum. The proper formulae considering the right phase terms of ε and μ are necessary to obtain n and z.

$$\varepsilon_{eff}(\omega) = \varepsilon_\infty - \frac{{\omega_p}^2}{\omega(\omega - j\omega_c)} \tag{5}$$

$$\mu_{eff}(\omega) = \mu_\infty + \frac{(\mu_s - \mu_\infty){\omega_0}^2}{{\omega_0}^2 + j\omega\delta - \omega^2} \tag{6}$$

where ε_∞ is the permittivity at the high frequency limit, ω_p is the radial plasma frequency, ω_c is the collision frequency, μ_s and μ_∞ is the permeability at the low and high frequency limit, respectively, ω_0 is the resonance frequency, and δ is the damping frequency.

$$\min G_\varepsilon = \min \sum_{f_i} Abs\left(|\varepsilon_{eff}(\omega_i)| - |\varepsilon_{ref}(\omega_i)|\right) + \min \sum_{f_i} Abs\left(\angle\varepsilon_{eff}(\omega_i) - \angle\varepsilon_{ref}(\omega_i)\right) \tag{7}$$

$$\min G_\mu = \min \sum_{f_i} Abs\left(|\mu_{eff}(\omega_i)| - |\mu_{ref}(\omega_i)|\right) + \min \sum_{f_i} Abs\left(\angle\mu_{eff}(\omega_i) - \angle\mu_{ref}(\omega_i)\right) \tag{8}$$

where $\varepsilon_{ref}(\omega)$ and $\mu_{ref}(\omega)$ are calculated from partial retrieved n and z.

Retrieval results including n, z, ε and μ of two simulation models, SRR-Rod and fishnet MMs, using different extraction methods are plotted in Fig. 4. Solid, dashed, dotted lines represent the data retrieved by partial extraction, first full extraction, and second Drude/Lorentz extraction methods, respectively. The first and second extraction methods can both retrieve the missing data with slightly difference in resonant band.

4. CONCLUSIONS

This paper presents two extraction methods to fully retrieve effective material properties and constitutive parameters of MMs based on continuity and dispersion models. Two types of MMs including SRR-Rod and fishnet MMs are designed and simulated in THz frequencies. The corresponding S parameters are investigated by two proposed methods to retrieve n, z, ε and μ. The retrieval resultsby two methods show good agreements over the investigated frequencies with a slightly difference in resonant band.

REFERENCES

1. Shelby, R. A., D. R. Smith, and S. Schultz, "Experimental verification of a negative index of refraction," *Science*, Vol. 292, 77–79, Apr. 6, 2001.
2. Pendry, J. B., "Negative refraction makes a perfect lens," *Physical Review Letter*s, Vol. 85, 3966, 2000.
3. Chen, X., T. M. Grzegorczyk, B.-I. Wu, J. Pacheco, and J. A. Kong, "Robust method to retrieve the constitutive effective parameters of metamaterials," *Physical Review E*, Vol. 70, 016608, 2004.
4. Nicolson, A. M. and G. F. Ross, "Measurement of the intrinsic properties of materials by time-domain techniques," *IEEE Transactions on Instrumentation and Measurement*, Vol. 19, 377–382, 1970.
5. Smith, D. R., S. Schultz, P. Marko, and C. M. Soukoulis, "Determination of effective permittivity and permeability of metamaterials from reflection and transmission coefficients," *Physical Review B*, Vol. 65, 195104, 2002.
6. Ziolkowski, R. W., "Design, fabrication, and testing of double negative metamaterials," *IEEE Transactions on Antennas and Propagation*, Vol. 51, 1516–1529, 2003.
7. Markos, P. and C. Soukoulis, "Transmission properties and effective electromagnetic parameters of double negative metamaterials," *Opt. Express*, Vol. 11, 649–661, 2003.

A Compact Hilbert Curve Fractal Antenna on Metamaterial Using CSRR

S. Suganthi[1], **S. Raghavan**[2], **D. Kumar**[3], **and S. Hosimin Thilagar**[4]

[1]Shri Angalamman College of Engineering and Technology, Trichy, India
[2]National Institute of Technology, Trichy, India
[3]Periyar Maniammai University, Thanjavur, India
[4]College of Engineering Guindy, India

Abstract— Recent advances in metamaterial (MTM) research in the microstrip antenna design for various wireless applications have been attracting researchers for further improvement in the performances. Though there have been many MTM based small antennas proposed so far, the use of MTM structures in fractal shaped antennas have been less attempted. This paper proposes a compact and novel MTM loaded Hilbert Curve Fractal Antenna (HCFA) design. The conventional HCFA has been designed using copper on a 20 mm × 20 mm × 1.6 mm FR4 substrate ($\varepsilon_r = 4.4$) and simulated. A complementary slip ring resonator (CSRR) for μ negative (MNG) along with a rectangular slot for ε negative (ENG) has been designed using copper, to exhibit MTM properties (negative μ and negative ε). Later this structure has been used as a defected ground plane for the HCFA. The complete design and simulation have been performed using HFSS 3D EM simulator software and the MTM properties have been verified by a separate MATLAB coding developed for Nicolson-Ross-Weir technique. The MTM HCFA appearing as a simple and compact structure with double side printed substrate and resonating at multiple frequencies are the novelties in this paper. In the CSRR loaded HCFA, the μ negative property is found predominating and the structure exhibits appreciable improvement in gain, directivity, shaped radiation and down shifted resonant frequencies.

1. INTRODUCTION

Despite recent advances in microwave integrated circuit technologies, a wide range of problems remain to be solved for both high-end and consumer applications, particularly within the scope of planar antenna design. For example simultaneous possibilities of miniaturization, cost reduction, multi-band or broadband resonance, radiation, gain and efficiency improvements remain key challenges whose solution depends upon continued research efforts focusing on the design of superior performance of the antenna. Challenges remain for antennas in the development of practical implementable solutions and new antenna materials including metamaterials. There have been investigators contributing to the successful coverage of these challenges.

Microstrip patch antennas have several popular advantages when compared to the other antennas because of their low profile, light weight, low cost and compatibility with other microwave integrated circuits. However narrow bandwidth and low gain are inherent limitations in these antennas. Multiple resonances or broad band of resonance with large gain in single patch is not directly attainable without the use of arrays of patches [1]. However, there is a limitation for such requirements because of the large physical size of the array and there have been continuous investigations on the size reduction [2]. Fractal antennas attract antenna designers because of their multi-resonant property with single antenna. The French mathematician B.B.Mandalbrot introduced the term fractal in 1970 after his interesting research on irregular and fragmented geometries. After him, several investigators reported many interesting fractal structures in miniaturized antenna designs and the iteration procedure of HCFA (Hilbert curve fractal antenna) is well discussed in [3–5] is much recognized here.

V. G. Veselago in 1968, provided a theoretical report [7] on the concept of metamaterial (MTM). Several contributions started emerging after Smith [8], Pendry [9] and Caloz and Itoh [10]. MTMs gain negative mu and negative epsilon properties from the engineered structures rather than directly from the material composition. These properties are not found in naturally existing materials [6, 13]. The existence of negative (single negative (SNG) or ε negative (ENG) or μ negative (MNG) or double (both ε and μ) negative (DNG)) properties in several new MTM structures and the use and applications of same are still being explored. It has been reported that the use of a LHM in near environment of patch antenna enhances antenna performances and the concept of SRR (slip ring resonator), MSSR (multiple slip ring resonator) and CSRR (complementary slip ring resonator) are well discussed in [11, 12, 15, 16]. There are four popular methods such as Nicolson-Ross-Wier (NRW), NIST iteration technique, new non-iterative technique and short circuit technique as reported in [11, 12, 14] for the verification of MTM property. In all these methods, the transmission and reflection S-parameters obtained from simulation or measurement results are required for verification.

In this paper an effort has been made to demonstrate the use of a small HCFA on a CSRR structure. The CSRRs are believed to exhibit negative μ whereas thin conductor to exhibit negative ε in some frequency regions. The possibility of multi-resonant property is focused in this new approach.

2. METHODS AND MATERIALS

In this paper, a modified miniaturized HCFA structure is designed using copper on a FR4 ($\varepsilon = 4.4$) substrate material of size 20 mm × 20 mm × 1.6 mm. The SRR and CSRR are duals and hence the conducting portion in SRR will appear as a slot in CSRR. Here, the desired MTM structure is CSRR which is derived from MSRR as shown in Figures 1(a) and (b). This structure is separately designed on another FR4 board of same type for verifying the MTM property. Finally the HCFA is placed on the top of the substrate whereas at the bottom side, the ground is replaced by CSRR. This CSRR is considered as a defected ground plane for the HCFA. The antenna is fed by a thin microstrip feed line. The dimensions of the HCFA, feed and CSRR are as depicted in Figures 1(c) to (e).

In this paper, the NRW parameter retrieval approach is used as it is straight forward involving simplest equations and fewer steps. The S_{11} and S_{21} parameters data from simulation are exported to MATLAB and the negative medium properties are obtained from a separate MATLAB coding developed for this. From these properties one can find whether the antenna resonates in negative medium region. The ε and μ of the medium are related to S-parameters by the Equations (1) and (2).

$$\varepsilon_r = \frac{2}{jk_0 d}\frac{1-V_1}{1+V_1} \tag{1}$$

$$\mu_r = \frac{2}{jk_0 d}\frac{1-V_2}{1+V_2} \tag{2}$$

where k_0 is a wave number equivalent to $2\pi/\lambda_0$, d is the thickness of the substrate and V_1 and V_2 are terms representing the composite of S_{11} and S_{21} as given in Equations (3) and (4). The term $k_0 d$ is expected to be very much less than unity for meeting the condition that the antenna must be smaller in size [11, 12, 14].

$$V_1 = S_{21} + S_{11} \tag{3}$$

$$V_2 = S_{21} - S_{11} \tag{4}$$

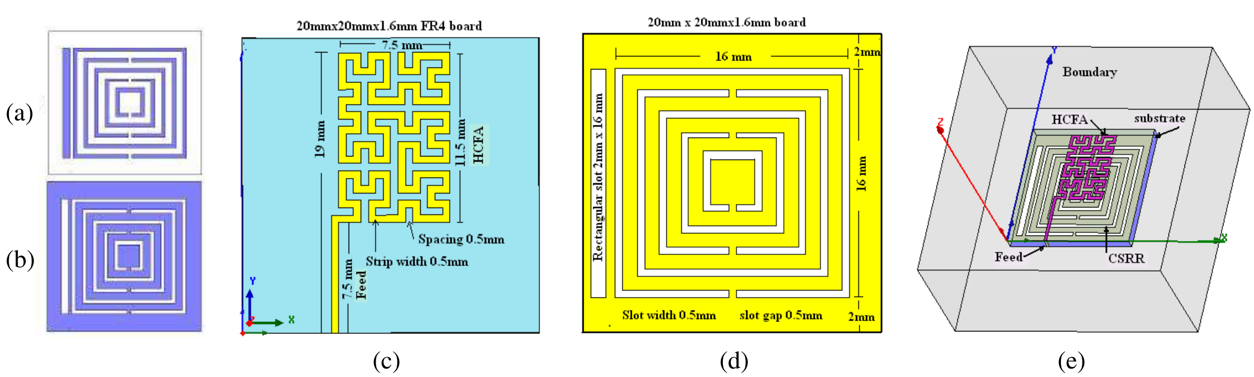

Figure 1: (a) Slip ring resonator (blue lines-conducting rings and white spacing-substrate). (b) Complementary slip ring resonator (white spacing-slots(substrate) and blue part-metallic portion). (c) Proposed Hilbert curve fractal antenna. (d) CSRR as defected ground plane. (e) CSRR loaded HCFA.

3. SIMULATION

For the design and simulation of the proposed HCFA, the CSRR structure (for obtaining required S-parameters) and the CSRR loaded HCFA, the HFSS 3D electromagnetic simulation software has been used. The simulation in all the three cases has been swept over a frequency range from 1 to 20 GHz. In the CSRR simulation, the PEC has been assumed on the left and right side of y-axis, PMC has been assumed on the top and bottom sides of z-axis and wave ports 1 and 2 are assumed on each face of the enclosed boundary in the x-axis.

4. RESULTS AND DISCUSSION

The proposed antenna resonates at multiple frequencies being fractal in shape. The return loss of the HFCA resonating at multiple frequencies and the 3D polar radiation pattern are shown in Figure 2. This antenna resonates at nine frequencies 6.3 GHz, 7.9 GHz, 9.3 GHz, 9.8 GHz, 11.6 GHz, 12.7 GHz, 13.9 GHz, 16.4 GHz, and 19.8 GHz with good return loss values varying between -10 dB (minimum) and -32 dB (maximum) as noted from the Figure 2(a). This antenna provides good matching which can be understood from the lower return loss values. As seen from the Figure 2(b), the gain of 0.396 dB and the directivity of 5.79 dB are only achievable with this antenna. The radiation pattern is not uniform in the ϕ direction. An overlapped view of reflection (S_{11}) and transmission (S_{21}) coefficients of the proposed CSRR structure over the swept frequency range are depicted in Figure 3(a). This resonates well at 11.8 GHz, 13.5 GHz and 19.3 GHz with return loss of -29 dB, -12 dB and -14 dB respectively. The relative μ and ε characteristics as obtained from the Equations (1) and (2) are plotted in Figure 3(b). The structure exhibits MNG property over large frequency ranges whereas the ENG property at some few frequency regions. It is because of the shape of CSRR, the μ negative property predominating. The frequencies where the MTM structure exhibits negative μ and/or negative ε can be identified from the characteristics.

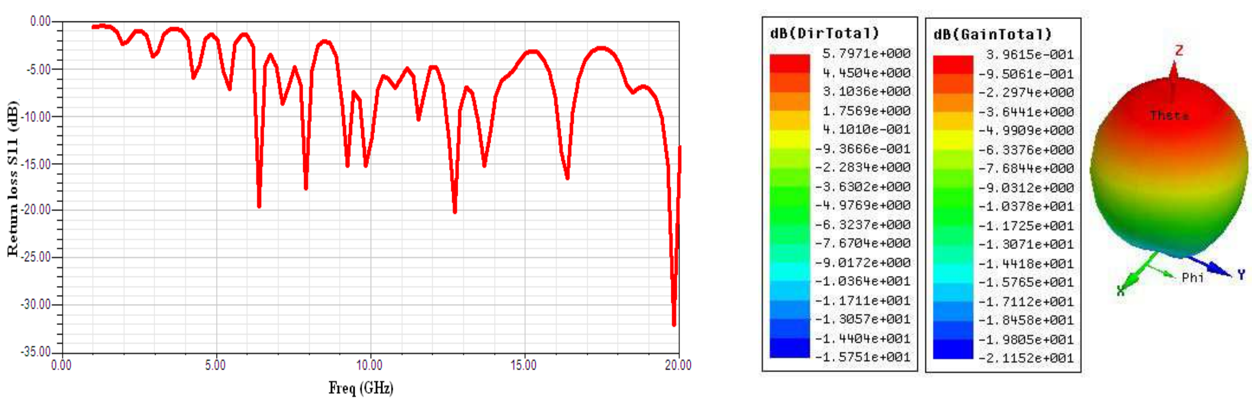

(a) (b)

Figure 2: HCFA Performance. (a) Return Loss. (b) Directivity, gain and 3D polar pattern.

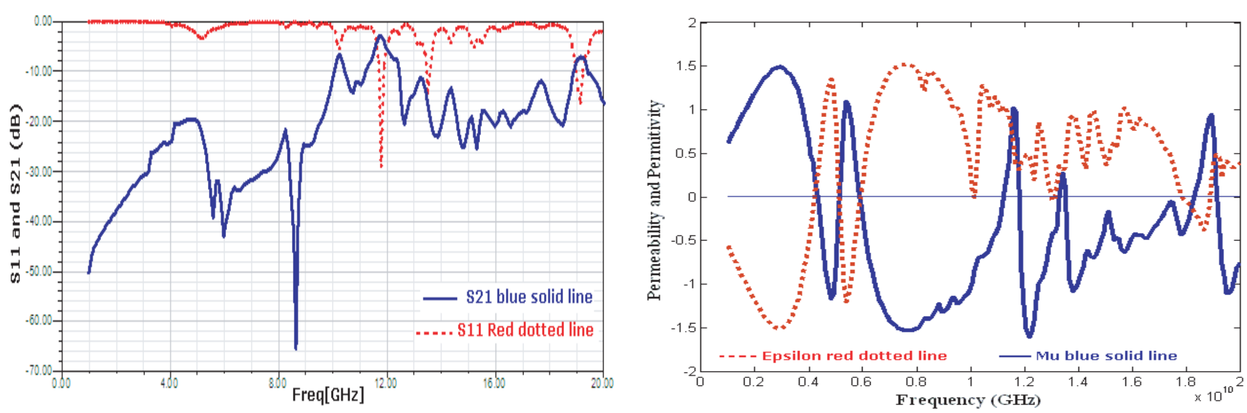

(a) (b)

Figure 3: CSRR performance (a).Reflection (S_{11}) and transmission (S_{21}) of CSRR (red line S_{11} and blue line S_{21}). (b) Retrieved negative medium properties (red line ε and blue line μ).

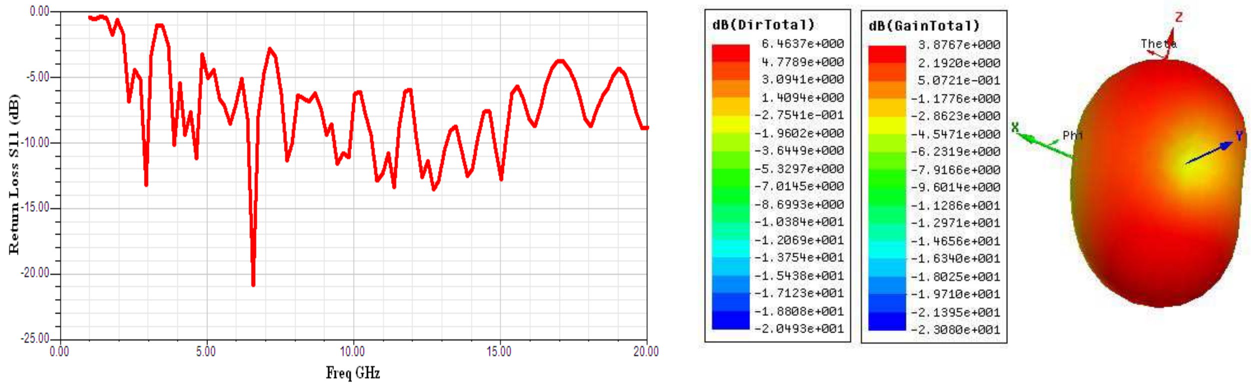

(a) (b)

Figure 4: CSRR loaded HCFA Performance. (a) Return Loss. (b) Directivity, gain and 3D polar pattern.

It is interesting to note that the MTM loaded HCFA also resonates at multiple frequencies 2.9 GHz, 3.9 GHz, 4.7 GHz, 6.6 GHz, 7.7 GHz, 9.4 GHz, 10.8 GHz, 11.4 GHz, 12.3 GHz, 12.7 GHz, 13.9 GHz and 15 GHz with return loss values varying between −10 dB (minimum) and −21 dB (maximum) as depicted in Figure 4(a). Since a minimum of −10 dB return loss itself provides matching, external tuning for this antenna is not required. The structure exhibits non-negative property at 4.2 GHz, 6 GHz, 11.2–11.8 GHz, 13.5 GHz and 19–19.3 GHz as observed from the Figure 3(b) The improved performances in terms of more resonant frequencies within the negative medium, improved gain (3.88 dB) and directivity (6.46 dB) and shaped radiation are satisfactorily achieved which can be seen in Figure 4(b).

5. CONCLUSION

The objective of design and simulation of HCFA on the CSRR structure for obtaining better performances has been satisfactorily noticed with the simulation results. The performances of the Hilbert curve fractal antenna with CSRR as a defected ground plane are appreciable in terms of more resonant frequencies, improved gain, directivity and shaped radiation. There is downshift in resonant frequencies with appreciable return loss values. This is because of the existence of the negative ε and negative μ properties in the prepared metamaterial. The future work would be to make efforts for further improving the return loss characteristics by applying suitable optimization algorithm. This kind of antenna can be of use in wireless applications requiring multiple resonances.

ACKNOWLEDGMENT

The technical facilities and expertise provided by authors 2, 3 and 4 for performing her research activity and her institution for the moral and financial supports are highly acknowledged by the author 1.

REFERENCES

1. Werner, D. H., R. L. Haupt, and P. L. Werner, "Fractal antenna engineering: The theory and design of fractal antenna arrays," *IEEE Ant. and Propgn. Magazine*, Vol. 41, No. 5, 37–59, 1999.
2. Werner, D. H. and S. Ganguly, "An overview of fractal antenna engineering research," *IEEE Antennas and Propagation Magazine*, Vol. 45, No. 1, 38–57, 2003.
3. Prombutr, N. and P. Akkaraaektharin, "Analysis and design hilbert curve fractal antenna feed with co-planar waveguide for multi-band wireless communications," *International Journal of Engineering*, Vol. 2, No. 3, 1–11, 2008.
4. Azad, M. A. and M. Ali, "A miniaturized implantable antennas for GPS application," *IEEE*, 1103–1106, 2006.
5. Huang, J.-T., J. H. Shiao, and J. M. Wu, " A miniaturized hilbert inverted-f antenna for wireless sensor network applications," *IEEE*, 3100–3103, 2010.
6. Shamonia, E. and L. Solymar, *Metamaterials: How the Subject Started*, 12–18, Elsevier, 2007.
7. Veselago, V. G., "The electrodynamics of substances with simultaneously negative values of ε and μ," *Soviet Physics Uspekhi*, Vol. 10, No. 4, 509–514, 1968.

8. Smith, D. R. and N. Kroll, "Negative refractive index in left-handed materials," *Physics Review Letters*, Vol. 85, No. 14, 2933–2936, 2000.
9. Pendry, J. B., "Negative refraction," *Contemporary Physics*, Vol. 45, No. 3, 191–202, 2004.
10. Caloz, C., A. Lai, and T. Itoh, "The challenge of homogenization in metamaterials," *New Journal of Physics*, Vol. 7, No. 167, 1–15, 2005.
11. Joshi, J. G., S. S. Pattnaik, S. Devi, and M. R. Lohokare, "Electrically small patch antenna loaded with metamaterial," *IEEE Journal of Research*, Vol. 56, No. 6, 373–378, 2010.
12. Pattnaik, S. S., J. G. Joshi, S. Devi, and M. R. Lohokare, "Electrically small rectangular microstrip patch antenna loaded with metamaterial," *IEEE*, 247–250, 2010.
13. Caloz, C. and T. Itoh, *Electromagnetic Metamaterials-transmission Line Theory and Microwave Applications*, Wiley, Hoboken, 2006.
14. Smith, D. R., D. C. Vier, T. H. Koschny, and C. M. Soukoulis, "Electromagnetic parameter retrieval from inhomogeneous metamaterials," *Physics Review*, E71, 036617-1-11, 2005.
15. Ouedraogo, R. and E. J. Rothwell, "Metamaterial inspired patch antenna miniaturization technique," *IEEE*, 2010.
16. Selvanayagam, M. and G. V. Eleftheriades, "A compact printed antenna with an embedded double-tuned metamaterial matching network," *IEEE Trans. on AP*, Vol. 58, No. 7, 2354–2361, 2010.

A Simultaneous Cooling and Dielectric Heating: An Advanced Technology to Improve the Yield of Lactides

Ani Idris[1], **Attaullah Bukhari**[1], **Noordin Mohd Yusof**[2], **and K. G. Tan**[3]

[1]Department of Bioprocess Engineering, Faculty of Chemical Engineering
Universiti Teknologi Malaysia, 81310 UTM Johor Bahru, Johor, Malaysia
[2]Department of Manufacturing and Industrial Engineering, Faculty of Mechanical Engineering
Universiti Teknologi Malaysia, 81310 UTM Johor Bahru, Johor, Malaysia
[3]Synotherm (SEA) Pte. Ltd., Malaysia

Abstract— Lactides with improved yield are prepared by depolymerization of oligo (lactic acid) under simultaneous cooling and microwave heating. The influence of microwave power input and its non-thermal effects on the yield of lactides are investigated. By increasing microwave power input, increased yield of lactides is obtained at 180–220°C at reduced pressure. Combined application of simultaneous cooling with microwave heating further increased the lactides yield. The removal of lactides during reaction shifts the equilibrium to the right. Simultaneous cooling enhances the absorbance of microwave irradiation into reactants; though increased yield of lactides is not only due to thermal effects of microwave irradiation. Maximum 85% yield of lactides is obtained at 500 W microwave power at 180–220°C and < 20 torr.

1. INTRODUCTION

Lactides are precursors for preparing high molecular weight, biodegradable polylactide acid by ring opening polymerization. In general, synthesis of lactides comprises of three stages (i) concentration of aqueous lactic acid (de-watering) (ii) oligomerization (dehydration) (iii) after the preparation of lactic acid oligomers of appropriate molecular weight lactide synthesis (depolymerization of oligomers) is performed.

Synthesis of lactides involved the back-biting reaction or transesterification. Lactides preparation can be performed in the presence of catalyst or without catalyst at elevated temperature. In 1932 Carothers reported linear polyesters are readily depolymerized due to high probability of close approach of atoms and consequently six atoms (cyclic ester) apart from the chain [1]. In back-biting reaction OH end group of oligomers attacks on the partially positive carbonyl carbon ($^{+\delta}C{=}^{\delta-}O$) [2] as shown in Figure 1.

Operating conditions and reaction time for preparing lactides influence the cost and quality of poly lactide acid intensively [3]. At present, the trend to replace the conventional mode of heating by microwave irradiation is rapidly increasing. However, when considering the interaction of microwaves with materials, microwave irradiation is not simply dielectric heating; rather a specific activation effect of microwaves are involved in the chemical reaction [4]. Microwave power input plays a critical role in the organic synthesis. 200 W microwave irradiation input has been reported as the most suitable microwave power input in depolymerization (lactide synthesis) of lactic acid oligomers to improve the yield. Increasing the microwave irradiation power input to more than 200 W results in carbonization of substrate and byproducts [5].

Unlike the direct heating (conventional heating where boiling of solvent start at the walls of container) dielectric heating causes hot spots that leads to superheating effect [6]. Microwave irradiation plays two roles in the synthesis reaction, which are known as thermal effect and non-thermal effect [7]. However, non-thermal effects in lactide synthesis is yet controversial [5, 8],

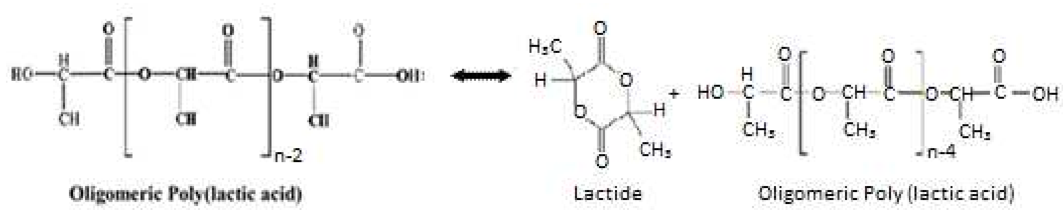

Figure 1: Schematic diagram of back-biting reaction of lactic acid Oligomers.

In lactides synthesis apparatus set up is very critical as the vapor pressure of lactides is very low. Therefore in order to enhance the yield of lactides, during synthesis, through vacuum distillation of lactides, it is very important to remove the gaseous product from reaction mixture as its formation tends to move the reaction to the right. However, it is difficult to use the oil bubbler as the optimum operating pressure required is very low.

Uneven microwave energy distribution and irregular increase in temperature are the problems encountered in pulsed mode microwave irradiation. To overcome the drawbacks of pulsed microwave irradiation a continuous microwave irradiation mode is preferred [5]. To date a few reports on microwave assisted synthesis of lactides have been found in literature. The potential of simultaneous cooling and microwave heating technology has not been explored yet in lactide synthesis. Simultaneous cooling and microwave heating allow for higher levels of microwave energy to be introduced into a reaction mixture. Up to 35% increment in product yield has been reported compared to microwave assisted synthesis without the use of both cooling and dielectric heating [9]. In this research work improved yield of lactides under the effects of simultaneous cooling and microwave irradiations is reported. In addition, lactide were synthesized by conventional methods under the same temperature and pressure so as to compare their yields thus explains for the differences in performances.

2. EXPERIMENTAL SECTION

2.1. Materials

L-lactic acid (88–92%) was purchased from Sigma-Aldrich. An analytical grade acetone was used to recover lactides. Toluene was used for recrystallization.

2.2. Preparation of Oligo (L-Lactic Acid) (OLLA)

OLLA was prepared by dehydrating 88–92 wt. % aqueous solution of L-Lactic acid first at 760 mm Hg for 2 hours, then at 100 mm Hg for 2 hours and finally at 30 mm Hg for another 4 hours. The final product obtained was a viscous liquid of oligo (L-lactic acid) (OLLA) [10]. This was the first step for the synthesis of L-lactides. The syntheses of L-lactides were performed using 3 different heating techniques: i) conventional heating, ii) microwave heating, iii) simultaneous cooling and microwave. Three different temperatures were used during the experiment ranging from 120, 150 and 180–220°C at a pressure of less than 20 torr. Upon obtaining the optimum temperature, experiments were performed at various pressures; atmospheric, 100 torr and less than 20 torr. Finally microwave power input was varied from 300 W to 500 W at optimum temperature and pressure.

2.3. Microwave Assisted Synthesis of L-lactide

60 g of OLLA was poured into a three-neck round bottom customized flask. The flask was placed in the cavity of the microwave. A condenser attached to the receiver, cold trap and vacuum system was connected to the reaction flask outside the reactor. Magnetic stirrer was used for stirring. The experiments were performed in MAS-II Microwave Synthesis Workstation. The reaction flask was specially fabricated so as to include cooling. Provision of cold air was made: whereby compressed air was passed through a cold air gun where subsequent cold-air at −10°C was used as a source of cooling. In this set up a 1 liter reaction volume was used. Temperature of condenser was maintained between 80–90°C. Temperature of reaction mixture was measured directly by using infrared (IR) thermocouple and was controlled by feed back mechanism. To optimize the effect of pressure on yield, experiments were performed at three different pressures; 760 torr, 100 torr and less than 20 torr. Reduced pressure was found to be influential on yields therefore <20 torr was selected for rest of experiments. Similarly 180–220°C temperature was found to be the optimum range for lactides synthesis. After achieving optimum temperature and pressure, three level of continuous microwave irradiation power were used: 300 W, 400 W and 500 W. Reaction temperature range was set at 180°C–220°C. Upon reaching the said temperature, reaction was allowed to continue until no more distillate was observed for each microwave input. Pressure was then reduced to 10 mm Hg. Lactide vapor phase was frequently stripped (flashed) by using compressed nitrogen. After approaching the temperature at 170°C unzipping reaction of OLLA started and crude lactide distillation commenced. Crude lactide was collected in the receiving flask. A little amount of crude lactides was also collected in the cold trap. Small quantities of lactides accumulated at adaptors, in condenser and at different connections were carefully collected by toluene. Crude lactide was

purified by recrystallization using the toluene. Percentage yield of lactides was calculated as:

$$\text{Yield of lactides (\%)} = \frac{\text{Amount of (D, L} - \text{Lactides, Meso lactides)}}{\text{Amount of Crude lactides}} \times 100$$

2.4. Simultaneous Cooling and Microwave Heating Assisted Synthesis of Lactides

In simultaneous cooling and dielectric heating, the similar setup as mentioned in Section 2.3 was used except that the reaction flask used is a jacketed type. The fabricated jacketed reaction flask used was a three-neck round bottom flask where compressed air via cold air gun was passed through the jacket of the flask.

2.5. Synthesis of L-lactide by Conventional Heating

60 g of OLLA was poured into a three-neck round bottom flask. The flask was clamped and placed on the hot plate, a condenser was attached to the receiver, cold trap and vacuum system was connected to the reaction flask. Magnetic stirrer was used for stirring. Temperature of condenser was maintained between 80–90°C. Temperature of reaction mixture was measured directly by using a thermocouple.

2.6. Analysis of Samples

For lactides analysis 1HNMR spectra were recorded by using Bruker AV300 spectrometer. Deuterium trichloromethane ($CDCl_3$) as solvent and tetramethylesilane (TMS) as internal standard were used. Three isolated doublet were detected at δ: 1.65–1.68, 1.70–1.75, and 1.45–1.64 as shown in Table 1.

3. RESULTS AND DISCUSSION

Reaction temperature and reduced pressure are very critical parameters in lactides synthesis. Lactides formation at 170°C under microwave irradiation was observed as reported in literature [8]. However, least yield (3.5%) was obtained at 170°C as it is the commencing temperature of back biting reaction of oligomers [8]. Figure 2 represents the results of lactide yields at the various temperatures at a constant pressure of 20 torr. Upon comparing the 3 methods, it was observed that the simultaneous cooling and microwave heating technique gave the highest yield at temperatures of 180–220°C. The lactide yields between the CH and MW heating technique were almost similar

Table 1: 1HNMR results.

Isolated doublet at δ:	Components
1.65–1.68	L/D lactides
1.70–1.75	Meso-lactides
1.45–1.64	Oligomers (PLA)

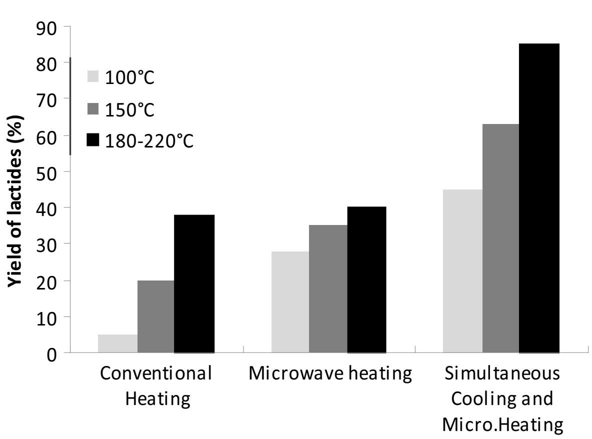

Figure 2: Effect of temperature on the yield of lactides at pressure <20 torr for the different depolymerization techniques of lactic acid oligomers.

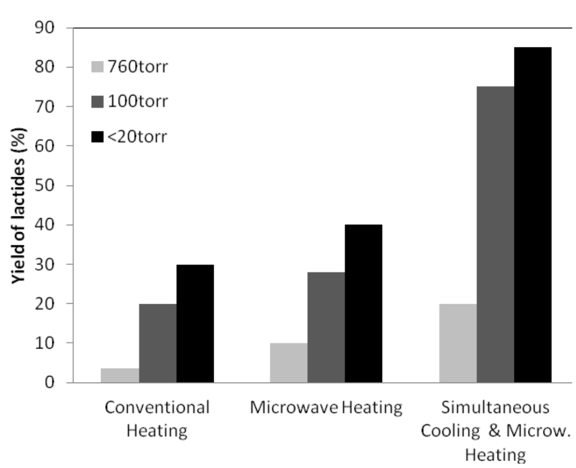

Figure 3: Effect of reduced pressure on the lactides yield at 180–220°C for the different depolymerization techniques of lactic acid oligomers.

except when it was performed at lower temperatures at 120 and 150°C where the MW technique seems to perform better giving slightly higher yields. The results also revealed that regardless of the technique used when reaction is performed at 180–220°C the yield obtained is the highest.

Figure 3 depicts the results of lactide synthesis performed at a temperature of 180–220°C but at reduced pressures of 760 torr, 100 torr and less than 20 torr. The results illustrated that an increased in yield occurred when pressure is reduced from 760 to pressures less than 20 torr. By lowering the pressure at optimum temperature, the yield was increased for all the different heating techniques. However the improvement in lactide yield was tremendous when simultaneous cooling and dielectric heating technique was applied (Figure 3).

Once the optimum temperature and pressure were ascertained, the influence of microwave input power on yield of lactides was assayed. Out of the three MW power inputs, 300 W, 400 W and 500 W maximum yield was observed at microwave energy level of 500 W (Figure 4). During the irradiation of different energy levels, temperature and pressure was maintained at 180–220°C and < 20 torr respectively. However for few seconds, deviations in the said temperature were observed as a result of change in the composition of reaction mixture (polarity of oligomers). In ^{1}HNMR spectrum of the products, three isolated doublets were detected at δ: 1.65–1.68, 1.70–1.75 and 1.45–1.64 which were assigned as methyl groups of L, D lactides, meso lactides and oligomers respectively, as reported by Yoo et al. 2006 [2] as shown in Table 1. However it was impossible to distinguish between the methyl group of L-lactide and D-lactide by ^{1}HNMR analysis. Reaction was continued until no more distillation was observed. Since very short time difference was found between post-distillation and carbonization, therefore the reaction was stopped just before carbonization. The carbonization of substrate at higher microwave power is more likely [5].

It should be noted that during all the operations, the gaseous lactides were removed from the microwave reactor by passing compressed nitrogen and this enhanced the yield of lactides and made recovery easier. Frequent removal of gaseous lactides shifts the equilibrium between oligomers and lactides to right [11]. Application of simultaneous cooling during microwave heating surprisingly increased the yields of lactides, under optimum conditions achieving maximum 85% yields of lactides (Figure 3). Since cooling allowed more microwave energy levels to penetrate the reaction mixture, simultaneous use of cooling and microwave heating can increase the yield of products [9, 12–14]. By increasing the microwave power input lactides yield was increased consequently, at optimum temperature and pressure. However, in parallel, such phenomenon was not observed in conventional synthesis under optimum temperature and pressure; yield cannot be increased and only 38% yield was observed.

Apparently it appeared that increased penetration of microwave irradiations under simultaneous cooling promoted the specific activation effects of microwave irradiation thus enhancing the rate of reaction. Increased yield of lactides was attributed to a specific activation effect of microwave irradiation induced by enhanced penetration of microwave irradiation under simultaneous cooling, in addition to thermal effect of microwaves. These results agreed with Bose et al. findings that reaction rate enhancement under microwave irradiation is not due to thermal heating [15].

Overall yield of lactides starting from the aqueous solution of lactic acid can be further increased by concentrating the aqueous distillate (containing lactic acid and low molecular weight oligomers) obtained during the oligomerization and by hydrolyzing the residue (polylactic acid, oligomers and lactic acids) in reaction flask for generation of oligomer feed.

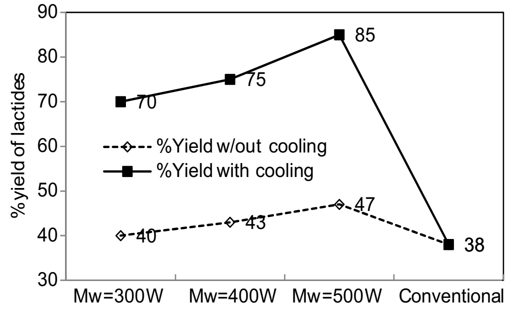

Figure 4: Effect of microwave power input under simultaneous cooling and heating, on the yield of lactides at 180–220°C and < 20 torr pressure.

4. CONCLUSION

A novel technique for preparing high yield of lactides was developed. It was concluded that employment of simultaneous cooling and microwave heating is a very influential technology to improve the yield of lactides. The technique is simple, saves energy and time, and can effectively reduce the production cost of precursors, lactides and subsequently of polylactides. Upon comparing the different techniques for lactides synthesis it can be concluded that improved yield of lactides was not only due to thermal effects but rather it was the result of combined effect of thermal and microwave specific effect. Simultaneous cooling along with microwave heating is advantageous over conventional and microwave heating for enhanced rate reaction and benign conditions. It is a potential novel route for lactides preparation.

ACKNOWLEDGMENT

The authors thanked the Ministry of Science, Technology and Environment for funding the research project (FRGS vote No. 77370).

REFERENCES

1. Carothers, W. H., G. L. Dorough, and F. J. van Natta, "Studies of polymerization and ring formation. X. The reversible polymerization of six-membered cyclic esters," *J. Am. Chem. Soc.*, Vol. 54, No. 2, 761–772, 1932.
2. Yoo, D. K. and D. Kim, "Synthesis of lactide from oligomeric PLA: Effects of temperature, pressure, and catalyst," *Macromol. Research*, Vol. 14, No. 5, 510–516, 2006.
3. Li, H., L. Liao, and L. Liu, "Kinetic investigation into the non-thermal microwave effect on the ring-opening polymerization of ε-caprolactone," *Macromol. Rapid Commun.*, Vol. 28, 411–416, 2007.
4. Jacob, J. and L. H. L. Chia, "Thermal and non-thermal interaction of microwave radiation with materials," *J. Mater. Sci.*, Vol. 30, 5321–5327, 1995.
5. Zhang, Y. M., P. Wang, N. Han, and H. F. Lei, "Microwave irradiation: A novel method for rapid synthesis of D, L-lactide," *Macromol. Rapid Commun.*, Vol. 28, 417–421, 2007.
6. Baghurst, D. R. and D. M. P. Mingos, "Superheating effects associated with microwave dielectric heating," *J. Chem. Soc. Chem. Commu.*, 674–677, 1992.
7. Haswell, S. J. and N. Howarth, "Development of a bi-functional silica monolith for electro-osmotic pumping and DNA," *Anal. Chim. Acta*, Vol. 387, 113–120, 1999.
8. Yang, X. G. and L. J. Liu, "Improved preparation of D, L-lactide from D, L-lactic acid using microwave irradiation," *Polym. Bullet.*, Vol. 61, 177–188, 2008.
9. Arvela, R. K. and N. E. Leadbeater, "Suzuki coupling of aryl chlorides with phenylboronic acid in water, using microwave heating with simultaneous cooling," *Orga. Lett.*, Vol. 7, 2101–2104, 2005.
10. Moon, S. I., C. W. Lee, M. Miyamoto, and Y. Kimura, "Melt polycondensation of L-lactic acid with Sn (II) catalysts activated by various proton acids: A direct manufacturing route to high molecular weight poly (L-lactic acid)," *J. Polym. Sci., Part A: Polym. Chem.*, Vol. 38, 16730–1679, 2000.
11. Hirao, K., K. Masutani, and H. Ohara, "Syntheis of L, lactides via depolymerization of oligo (L, lactic acid) by microwave irradiation," *J. Chem. Eng. Jap.*, Vol. 42, No. 9, 687–690, 2009.
12. Humphrey, C. E., M. A. M. Easson, J. P. Tierney, and N. J. Turner, "Solid-supported cyclohexane-1, 3-dione (CHD): A 'capture and release' reagent for the synthesis of amides and novel scavenger resin," *Org. Lett.*, Vol. 5, 849–852, 2003.
13. Chen, J. J. and S. V. Deshpande, "Rapid synthesis of ketoamides using microwave irradiation-simultaneous cooling method," *Tetrahedron Letters*, Vol. 44, 8873–8876, 2003.
14. Katritzky, A. R., Y. Zhang, S. K. Singh, and P. J. Steel, "1, 3-dipolar cycloadditions of organic azides to ester or benzotriazolylcarbonyl activated acetylenic amides," *Arkivoc*, Vol. 15, 47–64, 2003.
15. Bose, A. K., M. S. Manhas, M. Ghosh, V. S. Raju, K. Tabei, and L. Z. Urbanczyk, "Highly accelerated reactions in a microwave oven: Synthesis of heterocycles," *Heterocycles*, Vol. 30, 741–744, 1990.

A Coordinate Registration Technique for OTH Sky-wave Radars Based on 3D Ray-tracing and Sea-land Transitions

A. Cacciamano[1], **A. Capria**[1], **D. Olivadese**[1,2], **F. Berizzi**[1,2], **E. Dalle Mese**[1,2], **and F. Cuccoli**[1,3]

[1]CNIT National Lab of Radar and Surveillance Systems (RaSS), Pisa, Italy
[2]Department of Information Engineering, University of Pisa, Pisa, Italy
[3]Department of Electron. & Telecommun., University of Florence, Florence, Italy

Abstract— Target detection in Over-The-Horizon (OTH) radars is accomplished by tracking returns in slant range, Doppler and azimuth. Coordinate registration (CR) is the process of localizing the target by converting the slant coordinates to ground coordinates for all the frequencies used in transmission. The CR method uses a 3D ray-tracing algorithm which provides the ground range distance reached with a specific transmission frequency and elevation angle. The ray-tracing approach here adopted uses a 3D electron density model variable with height, latitude and longitude. The ray-tracing output is generally affected by errors due to numerical approximations of the 3D ionosphere model and discretization step used to integrate the differential equations of ray-tracing algorithm. Therefore the raw CR diagram suffers from an error which introduces as a consequence a degradation of target localization accuracy. Accordingly, we propose a coordinate registration technique for OTH sky-wave radars based on 3D ray-tracing that uses the sea-land transitions to mitigate the CR errors. The approach is based on the a priori knowledge of actual group delays relative to the sea-land transition within the area illuminated by the radar antenna beam. The method takes advantage of the geomorphological structure of the surveillance area. The errors introduced by the 3D ray-tracing software are then evaluated by using the actual group delay sat sea-land transitions.Afterwards, the estimated errors are used to correct the coarse CR diagram that was obtained straightforward from the ray-tracing output. Finally, the proposed correction method has been verified under the simplified assumption of a horizontally stratified ionosphere.

1. INTRODUCTION

Over-the-horizon (OTH) radars allow to reach distances well beyond the horizon by exploiting the effect of ionosphere refraction. In fact, in the 5–30 MHz frequency range (HF band), electromagnetic waves are gradually bended through the ionosphere until they are totally reflected back to the Earth [1]. In complex radar systems such as sky-wave OTH radars, the scenario modelization is a key task in order to assess the system performance. In particular, the ionospheric propagation modeling is required to fulfill the coordinate registration (CR) requirement. CR is the process of target localization which is obtained by converting the slant coordinates R_g to ground coordinates R_{gr}. There is no simple method for translating the radar coordinates into geographic coordinates (longitude and latitude), and the necessary relationships can only be found by characterizing the propagation over the radar area of interest. The CR method here presented is based on a 3D ray-tracing which provides the reached ground range distance R_{gr} and the relative time delay τ_g for a specific transmission frequency and elevation angle. In particular, the ray-tracing code is based on the numerical solution of a system of differential equations which was firstly proposed by Haselgrove [7]. The ray-tracing algorithm is applied to a 3D electron density data cube variable with height, latitude and longitude. The ionosphere characterization can be achieved by means of a network of ionosondes or by using a worldwide recognized long term ionospheric model such as the International Reference Ionosphere (IRI). Ionospheric abnormalities are difficult to model adequately during radar operation, furthermore the ray-tracing algorithm output is subject to errors due to the solver discretization step used to integrate the differential equations system, even though the latter has less impact than the former. Errors in the estimated down-range ionospheric parameters introduce, as a consequence, a degradation of the target localization accuracy. The inherent variability of the ionosphere and the inaccuracy of the related models bring to further degradation in the CR process [3–5]. The purpose of this paper is to provide a method able of achieving a coarse coordinate registration by means of a 3D ray-tracing and using sea-land transitions knowledge (geographic position and related radar time delay) for refining the final results. In [6], terrain features are used in order to determine position correction offsets, concluding that it can be used to provide coordinate registration benchmarks. The proposed technique has been tested by means of numerical simulations related to a reference scenario.

2. 3D RAY-TRACING TECHNIQUE

Ionospheric refraction makes possible the existence of the sky-wave OTH radar but at the same time it leads to very complex propagation phenomena that should be carefully handled. In order to model the HF radio propagation behavior, a ray-tracing technique must be developed. One of the most recognized approach to derive the ray paths is based on the numerical integration of Hamilton's equations. Haselgrove published for the first time [1] in 1954 the three dimensional version of the Hamilton's equations obtained in spherical polar coordinates. More precisely, the here developed code makes use of a modified version of Haselgrove's equations proposed in [2], rather than the original ones, using the group path as the independent variable. This choice allows to switch Hamiltonians and automatically adopt a smaller integration step nearby the reflection point, where the calculation of the derivatives are more critical. The implemented equations system (1) is the following:

$$\begin{cases} \dfrac{dr}{dP'} = -\dfrac{1}{c}\dfrac{\partial H/\partial k_r}{\partial H/\partial\omega} \\ \dfrac{d\theta}{dP'} = -\dfrac{1}{rc}\dfrac{\partial H/\partial k_\vartheta}{\partial H/\partial\omega} \\ \dfrac{d\varphi}{dP'} = -\dfrac{1}{rc\sin\theta}\dfrac{\partial H/\partial k_\varphi}{\partial H/\partial\omega} \\ \dfrac{dk_r}{dP'} = \dfrac{1}{c}\dfrac{\partial H/\partial r}{\partial H/\partial\omega} + k_\theta\dfrac{d\theta}{dP'} + k_\varphi\sin\theta\dfrac{d\varphi}{dP'} \\ \dfrac{dk_\theta}{dP'} = \dfrac{1}{r}\left(\dfrac{1}{c}\dfrac{\partial H/\partial\vartheta}{\partial H/\partial\omega} - k_\theta\dfrac{dr}{dP'} + k_\varphi r\cos\theta\dfrac{d\varphi}{dP'}\right) \\ \dfrac{dk_\varphi}{dP'} = \dfrac{1}{r\sin\theta}\left(\dfrac{1}{c}\dfrac{\partial H/\partial\varphi}{\partial H/\partial\omega} - k_\varphi\sin\theta\dfrac{dr}{dP'} - k_\varphi r\cos\theta\dfrac{d\theta}{dP'}\right) \end{cases} \tag{1}$$

where $P' = ct$ is the group path, t is the time, the variables r, ϑ, φ are the spherical coordinates of a generic point on the ray path, $(k_r,\, k_\varphi,\, k_\varphi)$ are the components of the propagation vector, $\omega = 2\pi f$ is the angular frequency of the wave, c is the light speed in free space and H is the Hamiltonian. The Hamiltonian can be defined in three different ways,however requiring only the real part of the dispersion relation to be satisfied, the following relation can be assumed (2):

$$H = \Re\left\{\frac{1}{2}\left(\frac{c^2}{\omega^2}(k_r + k_\vartheta + k_\varphi) - n^2\right)\right\} \tag{2}$$

The refractive index equation used in the ray-tracing program is based on the Appleton-Hartree formula. The squared value of the complex phase refractive index is given in the most general case (the formula takes into account the magnetic field and magneto ionic collisions) by (3):

$$n^2 = 1 - 2X\frac{1 - iZ - X}{2(1-iZ)(1-iZ-X) - Y_T^2 \pm \sqrt{Y_T^4 + Y_L^2(1-iZ-X)^2}} \tag{3}$$

where $X = f_N^2/f^2$, $Y = f_H^2/f^2$, $Z = v/2\pi f$, $Y_T = Y\sin\psi$, $Y_L = Y\cos\psi$, f_N is the plasma frequency, f_H is the electron gyro-frequency, v is the electron collision frequency, f is the wave frequency, ψ is the angle between the wave normal direction and the earth's magnetic field. The program needs the knowledge of the transmitter location (longitude, latitude and height above the ground), the frequency of the wave, the direction of transmission (elevation and azimuth), the 3D ionospheric model, the collision frequency and the earth's magnetic field values. Figures 1 and 2 show thegraphic output obtained for a radar located in Italy nearby Pisa (43.6°, 10.3°) and for a transmission azimuth angle equal to 135°. The input parameters used during the simulations are listed in Table 1.

Table 1: Ray-tracing simulations input parameters.

	Ionospheric Conditions	**Elevation angles** [°]	**Transmission frequency** [MHz]	**EM field**
Case A	16/2/2010, 9.00 AM	[5 : 3 : 20]	12	OFF
Case B	16/2/2010, 6.00 AM	7	[7 : 3 : 20]	ON

In details, Figure 1 represents the ray-tracing output for a fixed transmitted frequency and a set of elevation angles, neglecting the Earth magnetic field. On the contrary Figure 2 shows the ray-tracing output for a fixed elevation and a set of transmitted frequencies, taking into account the Earth magnetic field. It should be noted that the effect of the magnetic field mainly leads to azimuthal drifts on the ray-path which are not appreciable in this specific view. Finally, the color barre presents the plasma frequency value that is variable as a function of the height.

3. COORDINATE REGISTRATION BASED ON SEA-LAND TRANSITIONS

The ray-tracing program provides the relation between group delays and ground ranges. As the ray-tracing algorithm exploits a 3D ionospheric model in order to reconstruct the electron density profile, it will be certainly affected by errors, therefore the provided outputs need to be corrected. For this purpose, a number of known sea-land transitions must be identified on the Earth's surface within the surveillance area [8]. The choice of using coastal profiles for correction purposes simplifies the task of recognizing the relative radar echo associated with the sea-land transition [3].

Starting from the knowledge of the exact position of such points, the actual group delays from the radar site are directly estimated. For a fixed azimuth direction, N sea-land transitions are identified, therefore their group delays τ_{gi} and the relative ground range R_{gri} are calculated. Denoting with $\hat{\tau}_{gi}$ the group delay obtained through the ray-tracing program at the same reference ground range R_{gri}, the relative error can be assessed as the difference between the true and the estimated values ($\varepsilon_{\tau i} = \tau_{gi} - \hat{\tau}_{gi}$). Once the errors have been estimated, the relation between group delay and ground range can be corrected as well as the relative plot, as shown in Figure 3. Specifically, the mean value δ of the measured errors is evaluated and this correction factor is then applied to all the ground range points belonging to the same homogeneous ionospheric area, which implies a shift of the red curve of Figure 3.

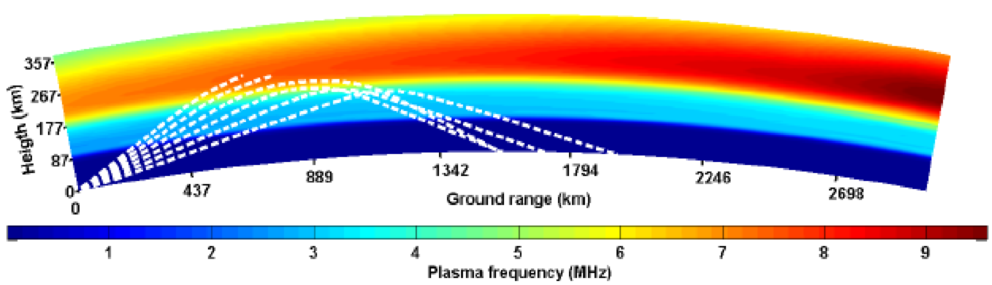

Figure 1: Ray paths obtained for CASE A of Table 1.

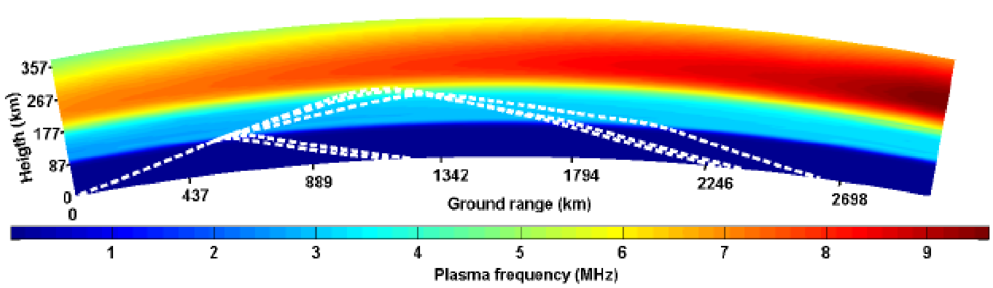

Figure 2: Ray paths obtained for CASE B of Table 1.

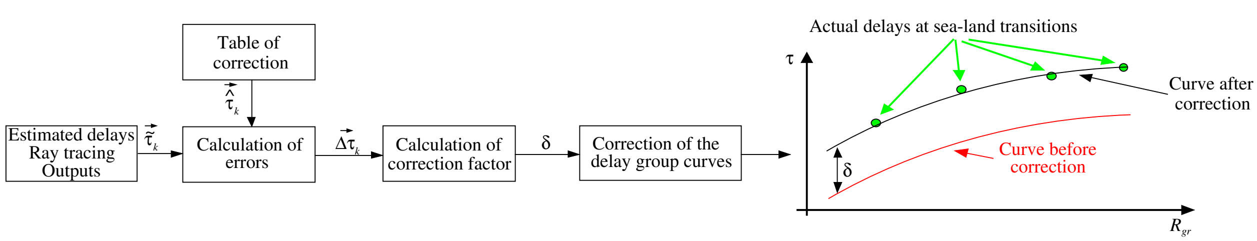

Figure 3: Block scheme of group delay correction technique.

4. NUMERICAL RESULT

In this section some numerical results are presented in order to show the application of the proposed method to an hypothetic scenario. It's should be noted that, because of the unavailability of real radar data, the method has been preliminary applied on simulated data obtained by means of a reference model. In details, the simulated scenario has been used to calculate the actual group delays relative to a set of sea-land transitions within the area illuminated by the radar antenna beam. Simulations have been carried out by using a real 3D ionospheric data cube, obtained by jointly exploiting a network of ionosondes [9] and the IRI model, by courtesy of INGV (National Institute of Geophysics and Volcanology). In order to obtain a useful case study, an ideal scenario (Figure 4) has been assumed as the reference radar data. The surveillance area is shown in Figure 5, where the geodetic coordinates of the radar site (OTHR) and of the coastal profile are visible.

Referring to the reference scenario of Figure 4, the projection of the virtual reflection point C on the Earth surface is at a distance $d_c = R_T(\theta/2)$ from the radar, and the height of such point h_v is known from the ionospheric model. Once the coordinates of the virtual reflection point are calculated, the angle of incidence in ionosphere can be easily derived. The critical frequency of the reflective layer f_v is also known from the ionospheric model, therefore the law of the secant can be applied to find the oblique frequency of transmission and the oblique virtual reflection point. After that, the elevation angle can be derived from the law of sines and the azimuth angle from a geometric relation. Therefore the equivalent virtual path (OTHR-C-B), represented in Figure 4 with a red line,is entirely defined and the group delay of the real path (green line) can be evaluated by applying the Breit & Tuve theorem and it is assumed to be the measured radar data.

The methodology has been numerically applied to a scenario characterized by a high number of sea-land transitions (Table 2). In particular, we have considered a radar site with latitude 43.6°, longitude 10.3°, and azimuth equal to 106°. The coverage area (Figure 5) ranges between [600–3000] km. In this specific scenario 11 sea-land transitions have been identified (Table 2). Figure 6 shows the curve of the CR obtained by applying the ray-tracing algorithm (red curve) and the calibrated version (black curve), obtained by means of the sea-land transitions delays.

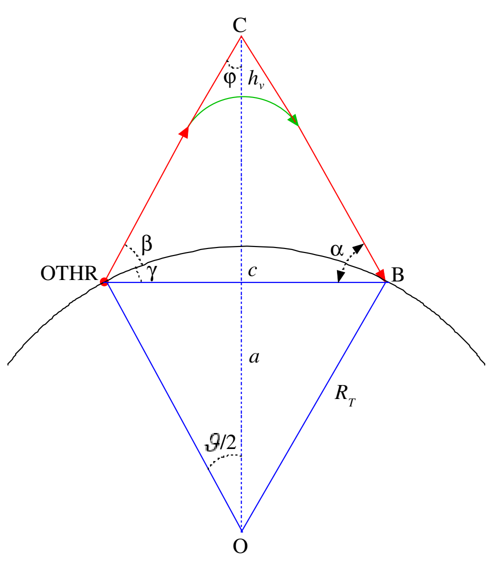

Figure 4: Geometry for the reference scenario.

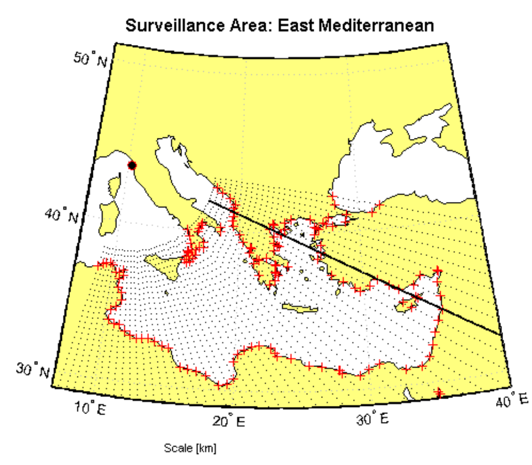

Figure 5: Surveillance area.

Table 2: Sea-land transitions of the simulated scenario.

Sea-land transition index	1	2	3	4	5	6	7	8	9	10	11
Latitude [°]	41.2	40.2	39.9	39.9	38.7	36.8	36.4	36.0	35.4	35.4	34.4
Longitude [°]	19.4	22.5	23.3	23.4	26.7	31.1	32.0	32.7	34.0	34.1	39.9
Distance [km]	797	1080	1155	1166	1475	1913	2007	2084	2217	2230	2423
Roup delay delays [ms]	3.26	4.04	4.25	4.29	5.37	6.76	7.06	7.31	7.74	7.78	7.78

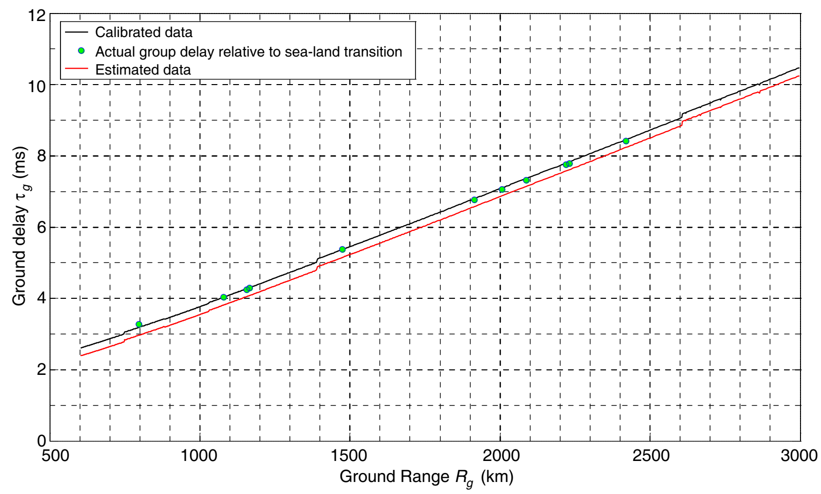

Figure 6: CR before (red line) and after (black line) calibration.

5. CONCLUSIONS

The CR process is affected by errors due to inherent approximations in the 3D ionosphere model and to the solver responsible of integrating the differential equations system which implements the ray-tracing algorithm. Such errors produce a degradation of target localization accuracy. In this paper, a coordinate registration correction technique making use of 3D ray-tracing and sea-land transitions has been proposed. Numerical results have proven the applicability of the technique to a realistic scenario. The performance of the method are strictly related to the morphology on the illuminated area, in fact the best results can be achieved when many sea-land transitions are available for the calibration.

ACKNOWLEDGMENT

The authors would like thank the National Institute of Geophysics and Volcanology (INGV) to have provided the 3D ionospheric data as well as for the useful advices. The work was partially funded by the Italian Ministry of Defence through the LOTHAR-FATT project.

REFERENCES

1. Headrick, J. M. and J. F. Thomason, "Application of high-frequency radar," *Radio Science*, Vol. 33, 1045–1054, Jul.–Aug. 1998.
2. Michael Jones, R. and J. J. Stephenson, "A versatile three-dimensional ray tracing computer program for radio waves in the ionosphere," *OT Rep.*, 75–76, US Dept. of Commerce, Office of Telecomunications, Oct. 1975.
3. C.C.I.R./I.T.U., "C.C.I.R. Interim method for estimating sky-wave field strength and transmission loss at frequencies between the approximate limits of 2 and 30 MHz," Report 252-2, 1970.
4. Headrick, J. M. and J. F. Thomason, "Application of high-frequency radar," *Radio Science*, Vol. 33, 1045–1054, Jul.–Aug. 1998.
5. Kelso, J. M., *Radio Ray Propagation in the Ionosphere*, McGraw-Hill, New York, 1964.
6. Barnum, J. R. and E. E. Simpson, "Over-the-horizon radar target registration improvement by terrain feature localization," *Radio Science*, Vol. 33, No. 4, 1077–1093, Jul.–Aug. 1998.
7. Haselgrove, C. B. and J. Haselgrove, *Twisted Ray Paths in the Ionosphere*, University of Manchester, 1960.
8. Cuccoli, F., L. Facheris, and F. Sermi, "Coordinate registration method based on sea/land transitions identification for over the horizon sky-wave radar: Numerical model and basic performance requirements," *IEEE Transactions on Aerospace and Electronic Systems*, Vol. 47, No. 4, 2974–2985, Oct. 2011.
9. http://roma2.rm.ingv.it/en/facilities/ionospheric_observatories.

Sea/Land Transition Identification for Coordinate Registration of OTH Sky Wave Radar: End to End Software Simulator and Performance Analysis

F. Cuccoli[1], **L. Facheris**[2], **and F. Sermi**[2]

[1]U.O. CNIT RaSS, c/o Dipartimento di Elettronica e Telecomunicazioni
Università di Firenze, via di Santa Marta, 3, Firenze 50139, Italy
[2]Dipartimento di Elettronica e Telecomunicazioni
Università di Firenze, via di Santa Marta, 3, Firenze 50139, Italy

Abstract— A software for the simulation of the coordinate registration technique for a pulse monostatic Over The Horizon Sky Wave Radar (OTH SWR) is presented. The main software features are described and the simulation results of a realistic propagation scenario are shown and discussed. The Sea/Land Transition Identification (SLTI) algorithm, developed by the same authors of this paper, has been applied assuming a 200 entries look-up table of ionospheric equivalent reflection height versus elevation angle. The SLTI algorithm performance is commented based on the error analysis of the ground range estimation of targets and the Sea/Land Transitions whose positions are known *a priori*.

1. INTRODUCTION

Recently, we introduced a Coordinate Registration (CR) method for an Over The Horizon Sky Wave Radar (OTH SWR) sensor based on the identification of Sea/Land transitions (SLTI) over the Earth surface [1]. The method was outlined, implemented and tested in a simplified reference scenario and the requirements for its applicability, in terms of minimum Clutter-to-Noise Ratio (CNR) and of Sea/Land backscattering coefficients difference, were highlighted [2].

The SLTI method is based on the *a priori* knowledge of the displacement of the sea-land transitions within the radar coverage area through which a geographic reference mask for the received radar echo is defined. The CR is then provided by maximization of a time domain cross-correlation function between the received single frequency radar echo and the time mask that is obtained transforming the geographic reference mask in a time signal through a parametric ionospheric transformation.

In order to analyze the performance of the proposed SLTI method in realistic scenarios, also a software tool for the simulation of the received echo of an OTH SWR in pulse mode has been developed [3]. The tool accounts for several models of the transmitted radar pulse, the antenna pattern, the electron ionospheric structure and the Sea/Land backscattering of the Earth's surface [4]. The tool is based on a numerical model of the OTH SWR monostatic equation that has been developed and already presented by the same authors of this work in [2].

In this paper, we assume that the parametric ionospheric transformation is based on a look up table of 200 profiles of ionospheric equivalent reflection height versus elevation angle, computed assuming 200 vertical profiles of electronic density. For a given frequency and a given elevation angle, the ionospheric equivalent reflection height is computed by means of a ray tracing procedure applied to the electron density profile.

We recall the main characteristics of the SLTI method and we present some details of the end to end software simulator related to the core of the cross-correlation algorithm applied to the look up table of ionospheric equivalent reflection heights.

Finally, we present some simulation results for the Mediterranean scenario and some specific radar setup in order to discuss the CR performance of the SLTI for different configurations of the Sea/Land mask jointly with the ionospheric behavior.

2. OTH SWR SOFTWARE SIMULATOR

The simulation software developed allows to compute the OTHR received signal through a complete model of the transmitting-propagation-backscattering-propagation-receiving chain (see Fig. 1) accounting for the geographical position of the radar and the antenna pattern (Radar model), the ionospheric propagation (ionospheric model) and the backscattering land/sea of the Earth's surface (clutter model). The following parameters and scenario features can be set:

- radar antenna: elevation and azimuth beamwidths assuming an elliptical beam or a complete antenna pattern;
- transmitter: frequency, pulse duration, power.
- ionospheric propagation: several models for the equivalent reflection height (constant, function of elevation, azimuth and frequency) or the possibility to select a 2D/3D ray tracing mode based on a ionospheric electronic density structure.
- Land/sea backscattering: several land/sea clutter models differing in statistics and spatial correlation can be selected. Also echoes from point targets can be generated, differing for amplitude and position;
- geographical scenario: radar position over the Earth's surface and pointing direction; elevation and azimuth scan mode.

The received signal is computed assuming that the received complex signal of a monostatic OTH SWR, after the transmission of a single pulse of duration T in the aiming direction (θ_0, φ_0), is given by the sum of the Ne × Na (Ne: # if elevation elements, Na: # if azimuth elements) signals obtained subdividing the -3 dB beam in Ne x Na propagation elements that propagate independently from each other.

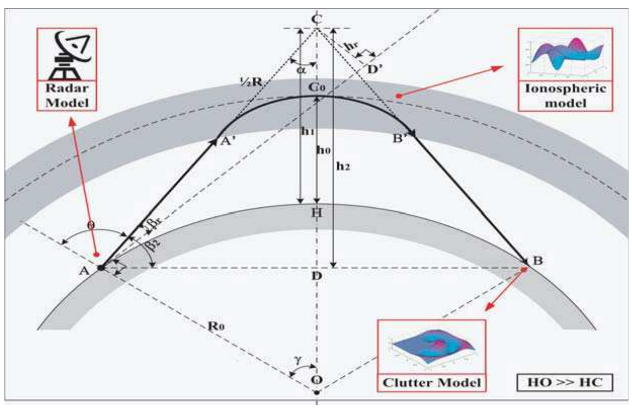

Figure 1: OTH SWR 2D geometry, parameters and the main simulation blocks.

Table 1: Main parameters for the OTH SWR scenario and signal simulation.

PARAMETER	VALUE
T : Radar pulse length	0.1 ms
f : Frequency	15 MHz
G: antenna gain	10 dB
θ_3 : -3 dB beamwidth in elevation	10°
φ_3: -3 dB beamwidth in azimuth	5°
θ_0: Elevation pointing angle	15°
φ_0 : Azimuth pointing angle	100°
σ_{S0} : Sea NRCS	-27 dB
σ_{L0} : Land NRCS	-34 dB
σ_{T0} : Target NRCS	0 dB
B_n : Noise bandwidth	$1/T$
TK : Noise Temperature	300°K
N_p: # time elements	1
N_e: # elevation elements	40
N_a: # azimuth elements	10

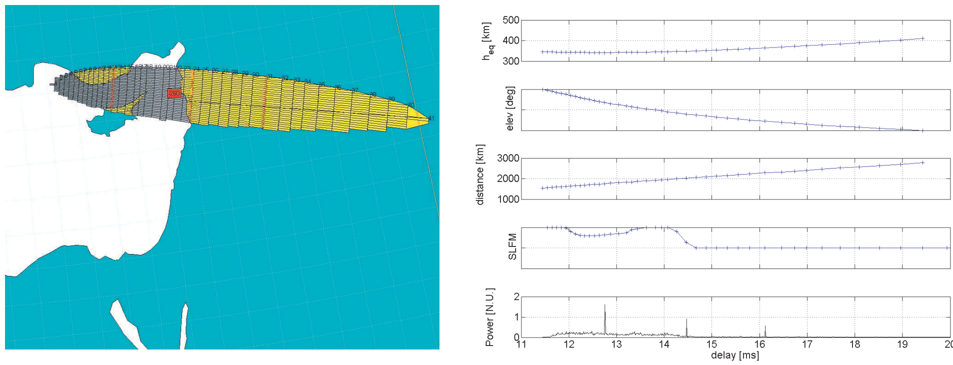

(a) (b)

Figure 2: (a) OTH SWR footprint. (b) Top down: the equivalent reflection height; the elevation propagation direction; the surface distance; the SLFM (percentage of sea with respect of land); the received signal power.

3. SIMULATION SCENARIO

In this work we assume that the OTH SWR site is in Sicily, with the antenna pointing towards Israel without any scanning (constant pointing direction (θ_0, φ_0)). The values of the main parameters used for the simulation are listed in Table 1.

As far as the propagation scenario is concerned, a constant electron density profile is assumed for the whole ionospheric area intercepted by the antenna beam. In this case, the equivalent reflection height is computed by a 2D raytracing mode separately for each propagation direction (θj, φk) within the antenna beam.

Three fixed point targets are located over the Earth's surface at the ground ranges of 1750, 2000 and 2250 km along the azimuth pointing direction φ_0 and a two values uncorrelated Gaussian model is assumed for both sea and land clutter [4]. Concerning the antenna pattern, we assumed an elliptical section defined by the -3 dB elevation and azimuth beamwidths. The overall system noise is assumed as a zero mean additive Gaussian process.

The sea and land clutter are modeled as Gaussian space-time processes, with given values of decorrelation distance and decorrelation time [4]. Different values of the backscattering coefficients σ_S and σ_L are assigned to sea and land as reported in Table 1.

4. SLTI METHOD WITH IONOSPHERE LOOK-UP TABLE

The SLTI method is a procedure aimed to the CR for a monostatic OTH SWR sensor and it is based on the identification of coastline profiles within the surveillance area. It is based on the *a priori* knowledge of the position of the sea/land transitions within the radar coverage area, employing the geo-morphological structure of the surveillance area to build a binary mask to be used as a geographic reference for the received radar echo. The SLTI method is based on the maximization of the cross-correlation between the received radar echo and the clutter signatures. In this work, we computed the clutter masks utilizing a 200 entries look-up table representing ionospheric equivalent reflection heights as a function of the elevation angles. The equivalent reflection heights of the look-up table are computed through a raytracing procedure, assuming 200 vertical profiles of electronic density of the Ionosphere. This set of electron density profiles has been generated accordingly with the International Reference Ionosphere (IRI-2007) by varying the Sun Spot Number (SSN).

Summarizing, the SLTI method provides a CR of the received radar signal by cross-correlating it with a clutter mask that depends on the vertical profiles of electronic density.

5. SIMULATION RESULTS

The left part of Fig. 2 shows the footprint of the antenna beam over eastern coast of the Mediterranean Sea, while the rights part of the figure shows five products of the simulation versus the radar echo time delay. The markers correspond to the 40 elevations. The simulation products are provided in terms of equivalent reflection height, elevation angle, distance computed over the Earth's surface and percentage of sea within each of the 40 surface elements. The plots must be read as in the following example: the signal power received with a delay of 14 ms is due to the propagation element with elevation 15° that – after being reflected with $h_{eq} = 345$ km - hits the

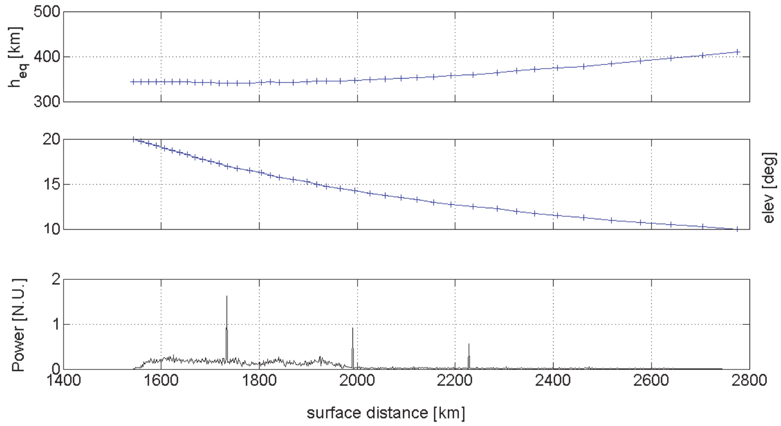

Figure 3: CR after SLTI method application to the received power signal of Fig. 2. Top down: the best equivalent reflection height line, the elevation propagation direction and the received radar signal.

surface element at 1950 km ground range, where only sea surface is present. Notice the presence of the three point targets at 1750, 2000 and 2250 km.

Figure 3 shows the products versus ground range after the application of the SLTI method as described in the previous section. The plot of estimated equivalent reflection heights is the one related to the vertical profile of electron density maximizing the cross-correlation between the received radar signal (bottom plot of Fig. 2, right) and the related entry of the look-up table. Such plot is used to convert the time delay to ground range. The three estimated target positions are 1730, 1990 and 2225 km, therefore the positioning error are −20, −10 and −25 km for the three targets, respectively.

6. CONCLUSIONS

An end to end software tool for the simulation of the pulsed OTH SWR signals and the implementation of the SLTI method has been presented. The SLTI method has been implemented using a 200 entries look-up table of ionospheric equivalent reflection heights. A first test of the software tool has been made in a Mediterranean scenario and the simulation products have been presented. The performance of the CR has been analyzed by simulating the received signals from three reference point targets. In the future, we foresee to proceed with an overall analysis of the SLTI method performance based on the look-up table of ionospheric equivalent reflection heights on a statistical basis by means of a Monte Carlo approach applied to the generation of all the random processes involved it the OTH SWR scenario.

REFERENCES

1. Cuccoli, F., L. Facheris, D. Giuli, and F. Sermi, "Over the horizon sky-wave radar: Coordinate registration by sea-land transitions identification," *PIERS Proceedings*, 21–25, Moscow, Russia, August 18–21, 2009.
2. Cuccoli, F., L. Facheris, and F. Sermi, "Coordinate registration method based on sea/land transitions identification for over the horizon sky-wave radar: Numerical model and basic performance requirements," *IEEE Transactions on Aerospace and Electronic Systems*, Vol. 47, No. 4, 2974-2985, October 2011.
3. Cuccoli, F., L. Facheris, and F. Sermi, "Over the horizon sky wave radar simulator for ionosphere and earth surface sounding," *IEEE International Proc. of Geoscience and Remote Sensing Symposium (IGARSS)*, *IEEE International on Geoscience and Remote Sensing Symposium (IGARSS)*, 277–280, 2011.
4. Cuccoli, F., L. Facheris, D. Giuli, and F. Sermi, "OTHR-SW coordinate registration method based on sea-land transitions: Clutter model definition," *Proceedings of the 7th European Radar Conference (EuRAD)*, 101–104, Parigi, France, September 30–October 1, 2010.

Investigation of the Transmittance in Superconducting Photonic Crystal

Arafa H. Aly[1, 3], **Walied Sabra**[1], **and Ehab Abdel-Rahman**[2, 3]

[1]Department of Physics, Faculty of Sciences, Beni-Suef University, Egypt
[2]Department of Physics, The American University in Cairo
P. O. Box 74, New Cairo 11835, Egypt
[3]YJ-STRC, The American University in Cairo
P. O. Box 74, New Cairo 11835, Egypt

Abstract— We will investigate the optical properties of the high temperature superconducting photonic crystals (HTScPC) in the ultra-violet region by using the ($YBa_2Cu_3O_7$) as a superconductor layer with the dielectric material strontium titanite ($SrTiO_3$) as a dielectric layer. Also we will see the effect of the thicknesses of both the superconductor layer and the dielectric layer on the width of the photonic band gaps (PBGs).

1. INTRODUCTION

The PCs have a photonic band gap (PBG) where electromagnetic waves are prohibited to propagate if there frequencies fall in the PBG. In a simple one-dimensional dielectric-dielectric photonic crystal (DDPC), it is known that the first and second bands can be widened considerably when the difference in dielectric permittivity of the constituent materials is increased [1]. There is no PBG below the first passband in a DDPC. In a metal-dielectric photonic crystal (MDPC), however, there is a low-frequency PBG called metallicity or plasmonic gap which is not related to the structural periodicity. Because it is of the order of the plasma frequency it is regarded as a modified effective plasma frequency [2]. In addition to the DDPCs and MDPCs, PCs made of superconducting materials are also of interest recent [3–7]. For a one-dimensional superconductor–dielectric photonic crystal (SDPC), it is seen like in an MDPC that there exists a low-frequency photonic band gap (PBG). This low frequency gap is not seen in a usual DDPC. This low frequency PBG is found to be about one third of the threshold frequency of a bulk superconducting material [3]. In this paper, based on the transfer matrix method, two fluid models, we investigate the effect of the different parameters on transmittance and PBG in a one-dimensional SDPCs. The purpose of this paper is to investigate the optical properties of the high temperature superconducting photonic crystals in the ultra-violet region and see the effect of the thicknesses of both the superconductor layer and the dielectric layer on the width of (PBGs).

2. THEORETICAL TREATMENT

In Fig. 1, an N-period superconductor-dielectric periodic multilayer structure in which the superconductor layer is layer one with thickness d_1 and the dielectric layer is layer two with thickness d_2 where the period is $d = d_1 + d_2$ the substrate is taken to be the free space with refractive index $n_s = 1$, and there is an electromagnetic wave incident on the structure. The refractive index of the

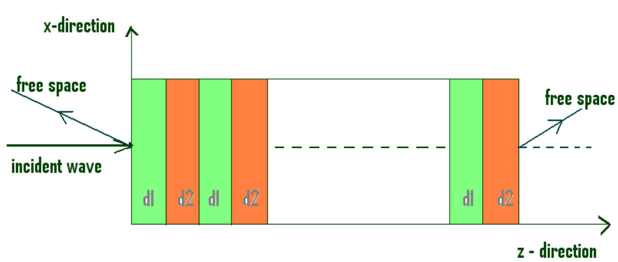

Figure 1: An N-period superconductor-dielectric periodic multilayer structure, in which layer one is the superconductor, layer two is the dielectric, The wave is incident in free space. The period is $d = d_1 + d_2$, where d_1 and d_2 are the thicknesses of layers one and two respectively. The vertical is x direction, while the z direction is in the horizontal.

superconductor layer is n_1 while the refractive index of the dielectric layer is n_2 and the refractive index of free space is taken to be $n_0 = 1$. From the two fluid model we find that the relative permittivity of the superconductor is

$$\varepsilon_r = 1 - (\omega_{th}^2/\omega^2) \tag{1}$$

where ω_{th} is the threshold frequency of the superconductor where it given by

$$\omega_{th}^2 = 1/\mu_0\varepsilon_0\lambda_L^2 \tag{2}$$

where λ_L is the temperature-dependent London penetration depth and it given by [7]

$$\lambda_L^2 = \lambda_0^2/(1 - (T/T_C)^4) \tag{3}$$

where λ_0 is the penetration depth at $T = 0\,\mathrm{K}$, T is operating temperature and T_C is the critical temperature of the superconductor. Then $n_1^2 = \varepsilon_{r1}$, $n_2^2 = \varepsilon_{r2}$ where ε_{r2} is the relative permittivity of the dielectric. We will use the transfer matrix method (TMM), in which the total transfer matrix is given by

$$M = \begin{pmatrix} M_{11} & M_{12} \\ M_{21} & M_{22} \end{pmatrix} = D_0^{-1} M_{cell}^N D_0 \tag{4}$$

where M_{cell} is the transfer matrix of a single period, and the elements of the matrix is appeared in Refs. [7, 8].

3. NUMERICAL RESULTS AND DISCUSSION

In our calculations we have investigated the optical properties of high temperature superconducting photonic crystal, $YBa_2Cu_3O_7$ with $T_c = 92\,\mathrm{K}^\circ$ and the penetration depth at $T = 0\,\mathrm{K}^\circ$is $\lambda_0 = 200\,\mathrm{nm}$. Also the operating temperature is $T = 4.2\,\mathrm{K}^\circ$ [9]. The temperature $4.2\,\mathrm{K}^\circ$, which is the boiling point of liquid helium, is frequently used in the community of superconductivity. The thickness of this layer is taken to be $d_1 = 40\,\mathrm{nm}$ and the refractive index in case of the superconductor is $n_1 = \sqrt{(1 - \omega_{th}^2/\omega^2)}$. The layer two is taken to be the dielectric layer ($SrTiO_3$) with a refractive index $n_2 = 2.437$ [10] and the thickness of the dielectric is taken to be $d_2 = 90\,\mathrm{nm}$, the nunber of periods is taken to be $N = 10$ and we suppose the normal incidence case $g_1 = 0^\circ$.

From the simulation program (MAT Lab) we have investigated the relation between the transmittance and the wavelength in the ultra-violet region for the TE-polarization wave and we have obtained that relation as in Figure 2.

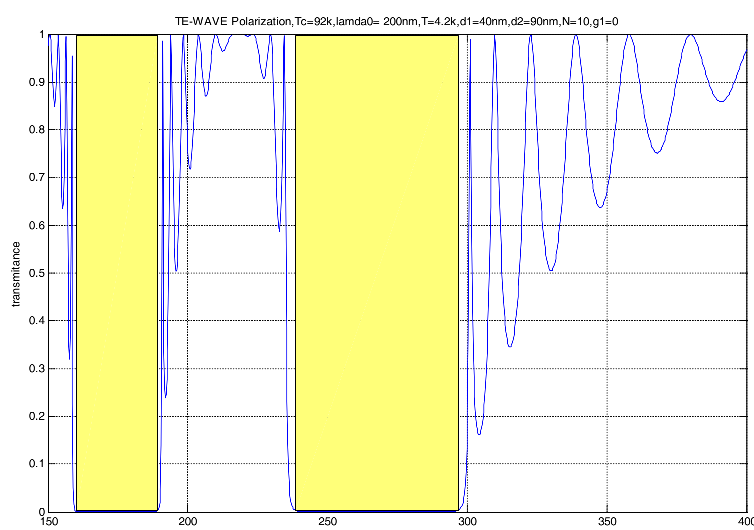

Figure 2: The transmittance versus the wave length in case of using the strontium-titanite ($SrTiO_3$) of the refractive index 2.437 as a dielectric layer with the ($YBa_2Cu_3O_7$) as a superconductor layer for TE-Polarization wave where $d_1 = 40\,\mathrm{nm}$ for the superconductor layer and $d_2 = 90\,\mathrm{nm}$ for the dielectric layer where in this case we have two PBGs.

In this figure, we have obtained two PBGs in the case of TE-polarization wave, where the width of the first PBG is $190-160\,\text{nm} = 30\,\text{nm}$, while the width of the second PBG is $295-240\,\text{nm} = 55\,\text{nm}$ First, in the case of increasing the thickness of the superconductor layer, two PBGs are created and shifted towards the long wave length range at $d_1 = 50\,\text{mm}$ with increasing the width of the second one and is equal 65 nm (Fig. 3). While in cases of $d_1 = 60\,\text{mm}$ and $d_1 = 70\,\text{mm}$, the width of the second band gap goes to 70 nm and 80 nm respectively as in Figs. 4 and 5. The width of the second PBG increased with increasing the superconductor layer thickness and become more enlarged at $d_1 = 70\,\text{mm}$, and we can be used this structure as a superconducting Bragg reflector. Finaly, we can say that the superconductor thickness is significance parameter in this structure.

Second, in the case of increasing the thickness of the dielectric layer, we found that the two PBGs are created and shifted towards the long wave length range where this shift is more noticeable than in the case of increasing the superconductor layer thickness. Also we noticed in the case of increasing the thickness of the dielectric layer that there is a slightly increasing in the width of the PBGs, where at $d_1 = 100\,\text{mm}$ the width of the first PBG is equal to $207 - 175\,\text{nm} = 32\,\text{nm}$, while the width of the second PBG is equal to $322 - 265\,\text{nm} = 57\,\text{nm}$ as shown in Fig. 6. For $d_1 = 110\,\text{mm}$,

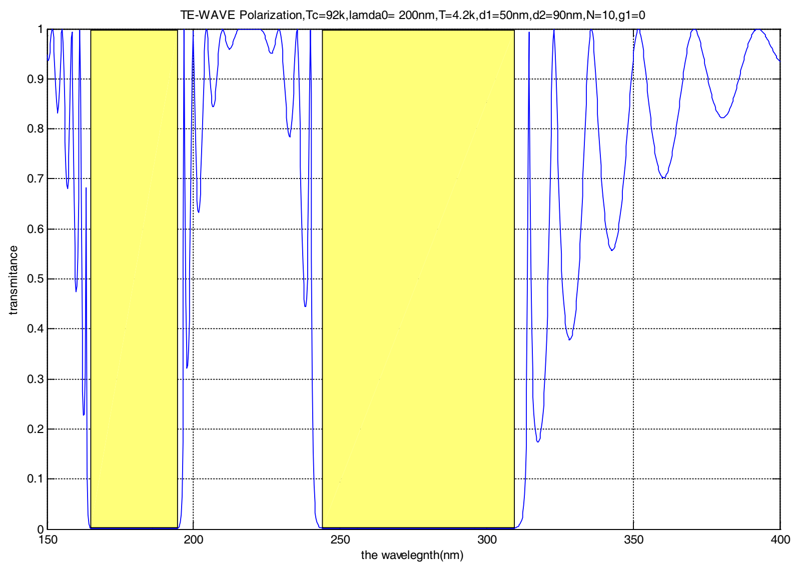

Figure 3: The shift of the two PBGs towards the long wave length range and the increasing of the width of the second PBG due to the increasing of the thickness of the superconductor layer to $d_1 = 50\,\text{nm}$.

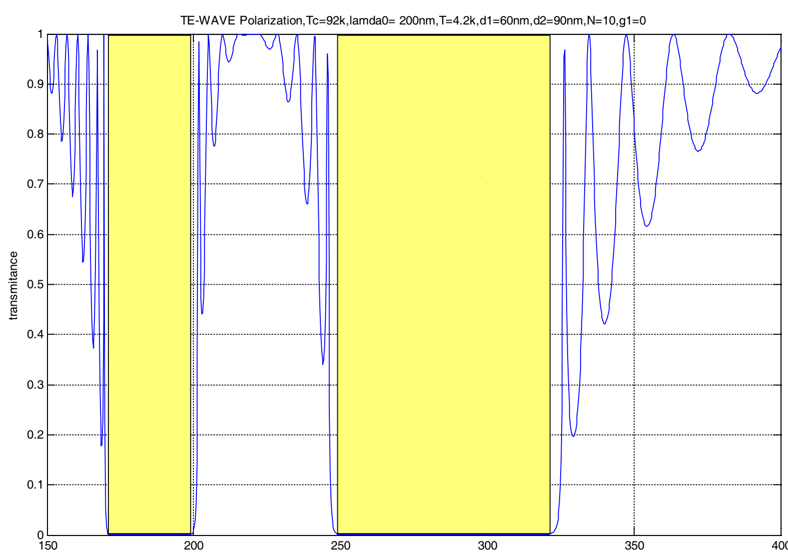

Figure 4: The shift of the two PBGs towards the long wave length range and the increasing of the width of the second PBG due to the increasing of the thickness of the superconductor layer to $d_1 = 60\,\text{nm}$.

the two PBGs are shifted and becoming from 192 nm to 225 nm with the width is 33nm and from 289 nm to 347 nm with the width 58 nm respectively. Also we notice that there is a newer PBG is created and its width equal to $163 - 150\,\text{nm} = 13\,\text{nm}$ as shown in Fig. 7.

For $d_1 = 120\,\text{mm}$, we have a new PBG created from 156 nm to 177 nm with width 21 nm and the first and second PBGs are becoming from 209 nm to 243 nm with width 34 nm and from 314 nm to 373 nm with width 59 nm respectively as shown in Fig. 8.

Based on theses resuclts, we can say that by increasing the thickness of the dielectric layer, there are new PBGs are created and we can control in the number of PBGs by varying the thickness of the dielectric layer as well as by increasing the thickness of the dielectric layer there is a slightly increasing in the width of the PBGs. So, we can say that the dielectric thickness is strong significance parameter in our structure.

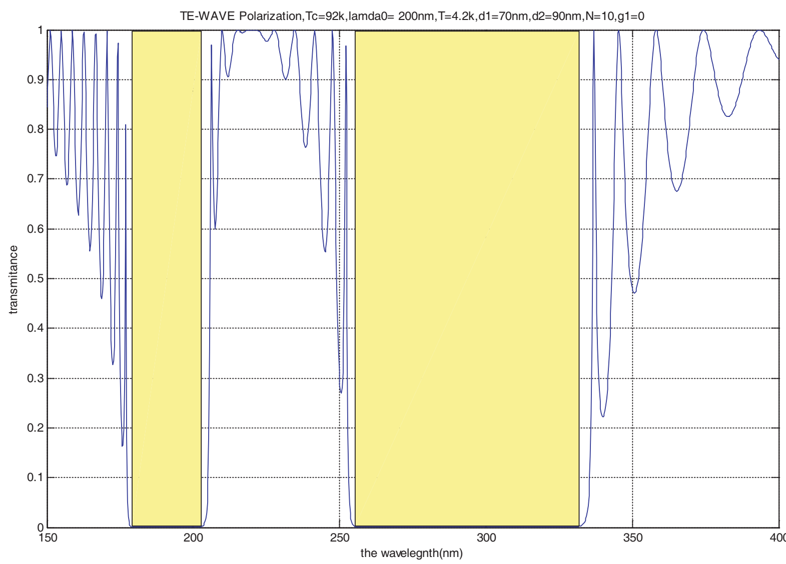

Figure 5: The shift of the two PBGs towards the long wave length range and the increasing of the width of the second PBG due to the increasing of the thickness of the superconductor layer to $d_1 = 70\,\text{nm}$.

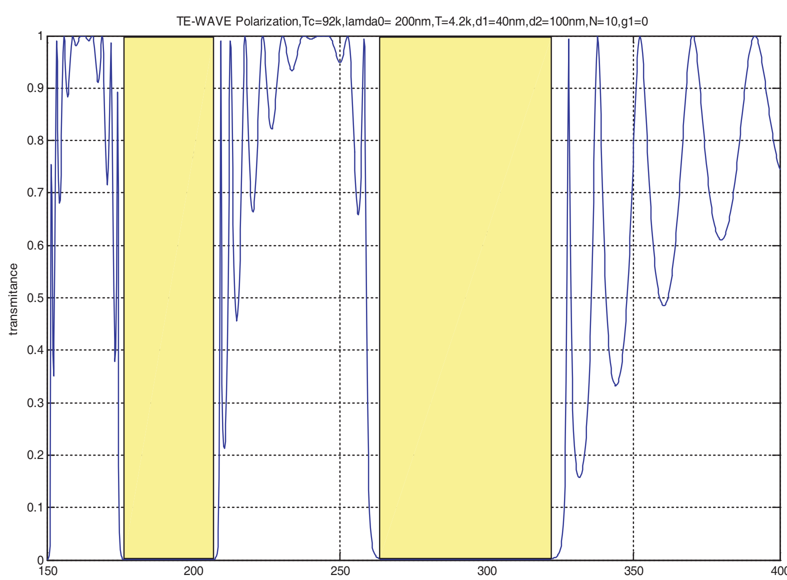

Figure 6: The shift of the two PBGs towards the long wave length range and a slightly increasing of the width of the second PBG due to the increasing of the thickness of the dielectric layer to $d_2 = 100\,\text{nm}$.

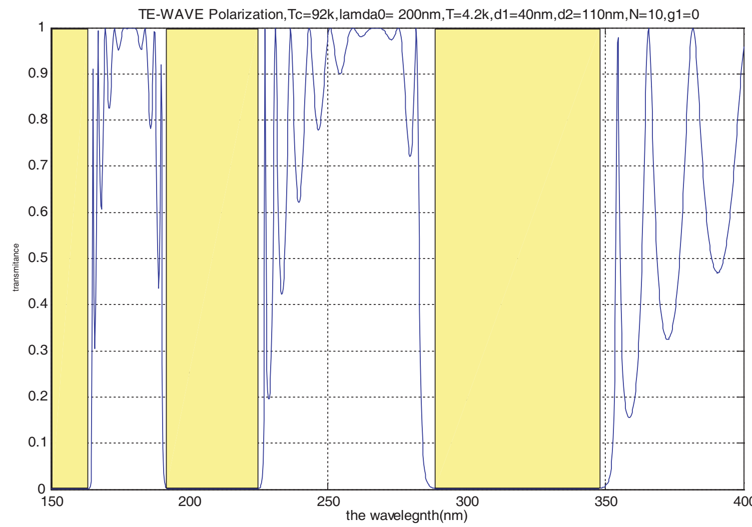

Figure 7: The shift of the two PBGs towards the long wave length range and a slightly increasing of the width of the second PBG due to the increasing of the thickness of the dielectric layer to $d_2 = 110$ nm, where in this case there is a newer PBG begin to appear in our UV range from 150 nm to 163 nm.

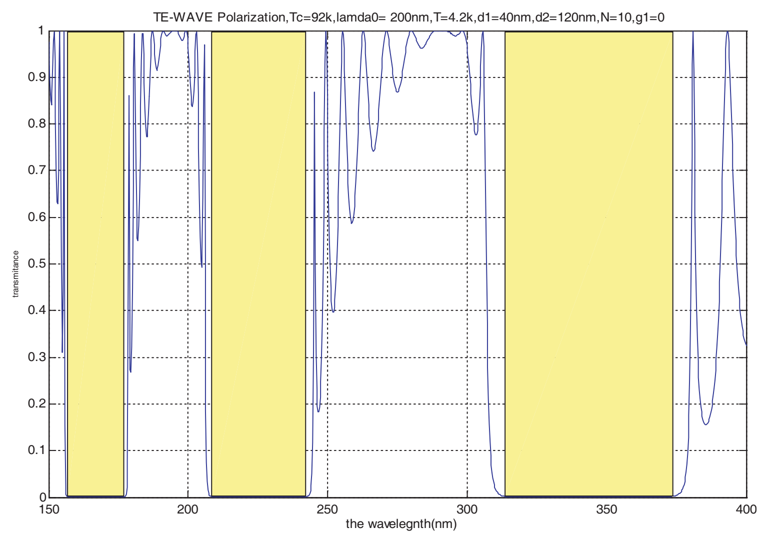

Figure 8: The shift of the two PBGs and the newer PBG 'towards the long wave length range and a slightly increasing of the width of the PBGs due to the increasing of the thickness of the dielectric layer to $d_2 = 120$ nm, where in this case there the newer PBG is created in our UV range from 156 nm to 177 nm.

4. CONCLUSION

From this numerical results and discussion we could investigated the optical properties of the HTScPC in the ultra-violet region by using ($YBa_2Cu_3O_7$) with dielectric materials such as $SrTiO_3$ where we found that the PBGs are created. The shift of the PBGs is more noticeable by varying the thickness of the dielectric layers than varying the thickness of the superconductor layers, also the number of PBGs can be controlled by increasing the thicknesses of the dielectric layers and the width of the PBGs is more sensitive to the thicknesses of the superconductor layers compared to the thicknesses of the dielectric layers.

REFERENCES

1. Joannopoulos, J. D., R. D. Meade, and J. N. Winn, *Photonic Crystals*, 41, Princeton University Press, New Jersey, 1995.
2. Soukoulis, C. M., *Photonic Band Gap Materials*, Kluwer, Dordrecht, 1996.
3. Raymond Ooi, C. H., T. C. Au Yeung, C. H. Kam, and T. K. Lim, *Phys. Rev. B*, Vol. 61, 5920, 2000.

4. Wu, C.-J., M.-S. Chen, and T.-J. Yang, *Physica C*, Vol. 432, 133, 2005.
5. Berman, O. L., Y. E. Lozovik, S. L. Eiderman, and R. D. Coalson, *Phys. Rev. B*, Vol. 74, 092505, 2006.
6. Wu, C.-J. and T.-J. Yang, "Anomalous microwave transmission in a superconducting periodic multilayer structure," *PIERS Online*, Vol. 4, 801–804, 2008.
7. Aly, A. H., H.-T. Hsu, T.-J. Yang, C.-J. Wu, and C. K. Hwangbo, *Journal of Applied Physics*, Vol. 105, 083917, 2009.
8. Yeh, P., *Optical Waves in Layered Media*, Chapter 5, Wiley, New York, 1988.
9. Lin, W.-H., C.-J. Wu, T.-J. Yang, and S.-J. Chang, "Terahertz multichanneled filter in a superconducting photonic crystal," *Optics Express*, Vol. 18, No. 26, 27155–27166, 2010.
10. Lyubchanskii, I. L., N. N. Dadoenkova, A. E. Zabolotin, Y. P. Lee, and T. Rasing, "A one-dimensional photonic crystal with a superconducting defect layer," *J. Opt. A: Pure Appl. Opt.*, Vol. 11, 114014 (4pp), 2009.

Optical Defect Modes in Spiral Media at Active Defect Layer

V. A. Belyakov
Landau Institute for Theoretical Physics, Russian Academy of Sciences
142432 Chernogolovka, Moscow Region, Russia

Abstract— An analytic approach to the theory of the optical defect modes (DM) in spiral media for the case of an active (i.e., transforming the light intensity or polarization) defect layer is developed. The chosen model allows one to get rid off the polarization mixing at the external surfaces of the defect structure (DMS) and to reduce the corresponding equations to the equations for light of diffracting in the spiral medium polarization only. The dispersion equation determining connection of the DM frequency with the layer parameters and other parameters of the defect structure is obtained. Analytic expressions for the transmission and reflection coefficients of the DMS are presented and analyzed. To be specific as the defect layers were considered birefringent, absorbing and amplifying defect layers in a perfect cholesteric structure. It is shown that the layer birefringence reduces the DM lifetime in comparison with the case of DM for an isotropic defect layer. Correspondingly, the effect of anomalously strong light absorption (and amplification) at the DM frequency are not so pronounced as in the case of the DMS with an isotropic defect layer. The case of DMS with low defect layer birefringence is studied in details. The effect of anomalously strong light absorption at the defect mode frequency for absorbing defect layer is discussed. It is shown that adjusting of the lasing frequency to the DM frequency for a DMS with an amplifying defect layer results in a significant lowering of the lasing threshold and the threshold gain is lowering with increase of defect layer thickness. The options of effectively influence at the DM parameters by changing the defect layer birefringence are discussed.

1. INTRODUCTION

Recently there was an intense activity in the field of mirrorless distributed feedback (DFB) lasing in structures consisting from many layers of chiral liquid crystals (CLC) mainly due to the possibilities to reach a low lasing threshold for the lasing [1–8]. The most part of the related theory is based at the numerical calculations [9] which results are not always interpreted in the frame work of a clear physical picture [8]. Several recent papers [10–13] showed that an analytic theoretical approach to the problem allows to create a clear physical picture of the linear optics and lasing in the mentioned structures. In particular, the physics and role of localized optical modes in the structures under consideration was clearly demonstrated. The most promising results in DFB lasing relates to defect modes (DM) [12, 13]. The DM existing at the structure defect as a localized electromagnetic eigen state with its frequency in the forbidden band gap were investigated initially in the three-dimensionally periodic dielectric structures [14]. The corresponding DM in spiral media, and more specific in chiral liquid crystals which will be studied below for the certainty, are very similar to the DM in one-dimensional scalar periodic structures. The qualitative difference with the case of scalar periodic media consists in the polarization properties. The DM in chiral liquid crystals is associated with a circular polarization of the electromagnetic field eigen state of the chirality sense coinciding with the one of the chiral liquid crystal helix. There are two main types of defects in chiral liquid crystals studied up to now. One of them is a plane layer of some substance differing from CLC dividing in two parts a perfect cholesteric structure and being perpendicular to the helical axes of the cholesteric structure [1]. Other one is a jump of the cholesteric helix phase at some plane perpendicular to the helical axes (without insertion any substance at the location of this plane) [2]. Recently, a lot of new types of defect layer were studied [15–21]. However, the consideration below will be limited by the first mentioned above type of defect, namely, a birefringent or absorbing (amplifying) layer inserted in a chiral liquid crystal. The reason for that is connected as with the experimental [20, 22] and theoretical [21, 23, 24] researches of the DFB lasing in CLC where a defect layer is birefringent or absorbing (amplifying) so with a general idea that the unusual properties of DM manifest themselves most clearly just at the middle of DMS, i.e., at defect layer where intensity of the DM field reaches its maximum. The analytic approach in studying of a DMS with a birefringent or absorbing (amplifying) defect layer is very similar to the previously performed DM studies for isotropic defect layer [12, 13], so we shell present below the final results of the present investigation sending the readers for the investigation details to references [12, 13].

In the present paper an analytical solution of the defect mode associated with an insertion of a birefringent or absorbing (amplifying) defect layer in the perfect cholesteric structure is presented for light propagating along the helical axes.

2. DEFECT MODE AT BIREFRINGENT DEFECT LAYER

To consider the DM associated with an insertion of a birefringent layer in the perfect cholesteric structure we have to solve Maxwell equations and a boundary problem for electromagnetic wave propagating along the cholesteric helix for the layered structure depicted at Fig. 1. Exploiting results obtained in [12, 13] (and using the same simplifications) one easily gets the results related a birefringent layer. For example, if one neglects the multiple scattering of light of nondifracting in CLC polarization the transmission $|T(d,L)|^2$ and reflection $|R(d,L)|^2$ intensity coefficients (of light of diffracting circular polarization) for the whole structure may be presented in the following form:

$$|T(d,L)|^2 = \left|[T_e T_d M(k,d,\Delta n)(\sigma_{\mathbf{e}}\sigma^*_{\mathbf{ed}})] \,/\, \left[1 - M^2(k,d,\Delta n)(\sigma_{\mathbf{r}}\sigma^*_{\mathbf{ed}})^2(R_d R_u\right]\right|^2, \quad (1)$$

$$|R(d,L)|^2 = \left|\left\{R_e + R_d T_e T_u M^2(k,d,\Delta n)\right|\sigma_{\mathbf{e}}\sigma^*_{\mathbf{ed}})\,|^2 /[1 - M^2(k,d,\Delta n)\left|\sigma_{\mathbf{r}}\sigma^*_{\mathbf{ed}})^2 R_d R_u]\right\}\right|^2, \quad (2)$$

where $R_e(T_e)$, $R_u(T_u)$ and $R_d(T_d)$ [12, 13] are the amplitude reflection (transmission) coefficients of the CLC layer (see Fig. 1) for the light of diffracting polarization incident at the outer (top) layer surface, for the light incidence at the inner top CLC layer surface from the inserted defect layer and for the light incidence at the inner bottom CLC layer surface from the inserted defect layer, respectively, $\sigma_{\mathbf{e}}$, $\sigma_{\mathbf{r}}$ and $\sigma_{\mathbf{ed}}$ are the polarization vectors of light exiting the CLC layer inner surface, reflected at the inner bottom CLC layer surface at the incidence from the inserted defect layer and of light whose some polarization vector $\sigma_{\mathbf{ed}}$ transforms to the polarization vector $\sigma_{\mathbf{e}}$ at crossing the birefringent defect layer of thickness d, respectively, Δn is the difference of two refractive indexes in the birefringent defect layer and $M(k,d,\Delta n)$ is the phase factor related to light single propagation in a birefringent defect layer. The corresponding polarization vectors may be found (see [23, 24]) as well as the polarization vector $\sigma_{\mathbf{ed}}$ may be easily calculated if the d, and Δn are known.

The calculation of the reflection and transmission coefficients according (1)–(2) is performable analytically in the general case, however, it is rather cumbersome. It is why below will be studied in details the case of a low birefringence.

Under the mentioned above simplification and the assumption that the refractive indexes of the DMS external media coincides with the average CLC refractive index and the average refractive indexes of defect layer the refractive indexes of defect layer may be given by the formulas

$$n_{\max} = n_0 + \Delta n/2, \quad n_{\min} = n_0 - \Delta n/2, \quad (3)$$

where n_0 coincides with the average CLC refractive index and Δn is small i.e., $\Delta n/n_0 < \delta$, where $\delta = (\varepsilon_{\shortparallel} - \varepsilon_\perp)/(\varepsilon_{\shortparallel} + \varepsilon_\perp)$ is the dielectric anisotropy. The phase difference of two beam component with different eigen polarization at the defect layer thickness is $\Delta\varphi = \Delta n k d/n_0$, $k = \omega n_0/c = \omega\varepsilon_0^{1/2}/c$, $\varepsilon_0 = (\varepsilon_{\shortparallel} + \varepsilon_\perp)/2$, and $\varepsilon_{\shortparallel}$, $\varepsilon_\perp$ are the local principal values of the LC dielectric tensor [25–29].

Finally, one gets the following expressions for reflection and transmission coefficients of light with a diffracting polarization for the incident beam with diffracting polarization in the case of low birefringence:

$$|T(d,L)|^2 = \left|[T_e T_d \exp[ikd]\cos(\Delta\varphi/2)] \,/\, \left[1 - \exp[i2kd]\cos^2(\Delta\varphi/2) R_d R_u\right]\right|^2, \quad (4)$$

$$|R(d,L)|^2 = \left|\left\{R_e + R_d T_e T_u \exp[i2kd]\cos^2(\Delta\varphi/2)/\left[1 - \exp[i2kd]\cos^2(\Delta\varphi/2) R_d R_u\right]\right\}\right|^2 \quad (5)$$

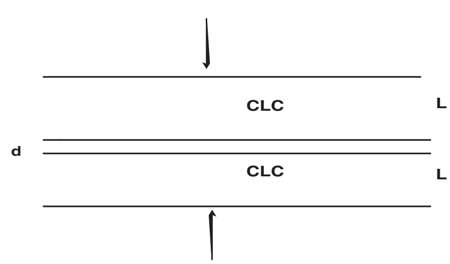

Figure 1: Schematic of the CLC defect mode structure with birefringent or absorbing defect layer of thickness d.

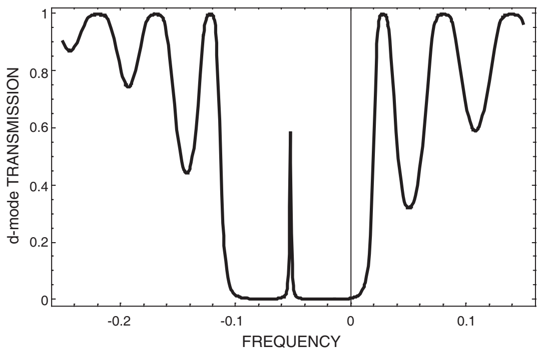

(a)

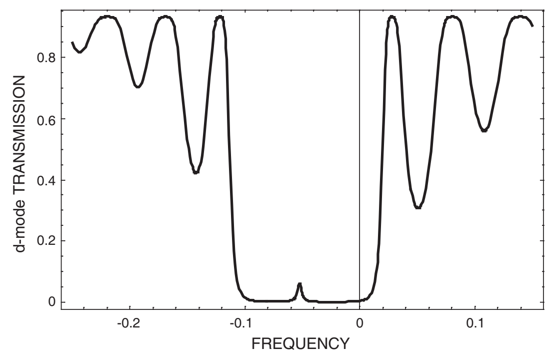

(b)

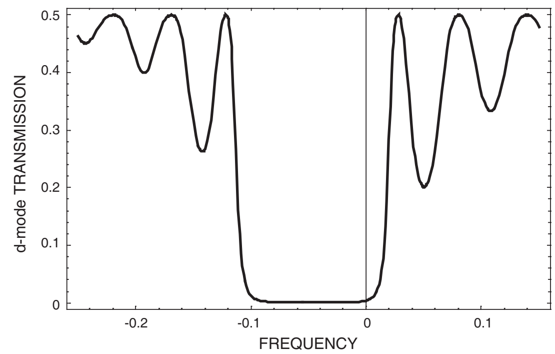

(c)

Figure 2: Calculated diffracting polarization intensity transmission coefficient $|T(d,L)^2|$ for a low birefringent defect layer versus the frequency ν (Here and at all other figures $\nu = \delta[2(\omega - \omega_B)/(\delta\omega_B) - 1)]$, $\delta = 0.05$ and $N = 33$ is the director half-turn number at the CLC layer thickness L.) for a diffracting incident polarization at the birefringent phase shift at the defect layer thickness (a) $\Delta\varphi = \pi/20$, at $d/p = 0.25$, (b) at $\Delta\varphi = \pi/6$, (c) at $\Delta\varphi = \pi/2$.

The calculations results for transmission $|T(d,L)|^2$ coefficients of light of diffracting polarization for the case of low birefringence are presented at Fig. 2 for various values of the birefringent phase factor $\Delta\varphi$. Fig. 2 shows that at low values of phase shift between eigen waves at their crossing the defect layer ($\Delta\varphi < \pi/2$) the shape of transmission curve is very similar to those for DMS with an isotropic defect layer. However, at approaching $\Delta\varphi$ to $\pi/2$ (see Fig. 2) typical for an isotropic defect layer increase of transmission at the defect mode frequency gradually disappears and at $\Delta\varphi = \pi/2$ (Fig. 2(c)) does not appear at all.

It is well known [9] that the position of the edge mode frequency in the stop band is determined by the frequency of the transmission (reflection) coefficient maximum (minimum) so the performed calculation of the transmission spectra (Fig. 2) determine a real component of the DM frequency. However because DM is a quasistationary mode an imaginary component of the DM frequency is not zero [12, 13]. A direct way to find the imaginary component of the DM frequency is a solving of the dispersion equation. The dispersion equation if the multiple scattering of nondifracting polarization light being neglected is presented by the following relationship:

$$\left\{M^2(k,d,\Delta n)\sin^2 qL - \exp(-i\tau L)[(\tau q/\kappa^2)\cos qL + i((\tau/2\kappa)^2 + (q/\kappa)^2 - 1)\sin qL]^2/\delta^2]\right\} = 0, \quad (6)$$

where $\tau = 4\pi/p$, p is the cholesteric pitch, and $q = \kappa\{1 + (\tau/2\kappa)^2 - [(\tau/\kappa)^2 + \delta^2]^{1/2}\}^{1/2}$.

3. AMPLIFYING AND ABSORBING CLC LAYERS

As the experiment [3] and the theory [12, 13] show unusual optical properties of DMS at the defect mode frequency ω_D may be effectively used for enhancement of the DFB lasing. It is quite naturally to study. For studying how the birefringent defect layer does influence anomalously strong amplification and absorption effects we assume, as was done in [12, 13], that the average dielectric constant of CLC has an imaginary addition, i.e., $\varepsilon = \varepsilon_0(1 + i\gamma)$ (Note, that at real situations $|\gamma| \ll 1$). The value of γ may be found from solution of the dispersion Equation (6). Another option (see [12, 13]) is studying of reflection and transmission coefficients (4)–(5) as a function of γ.

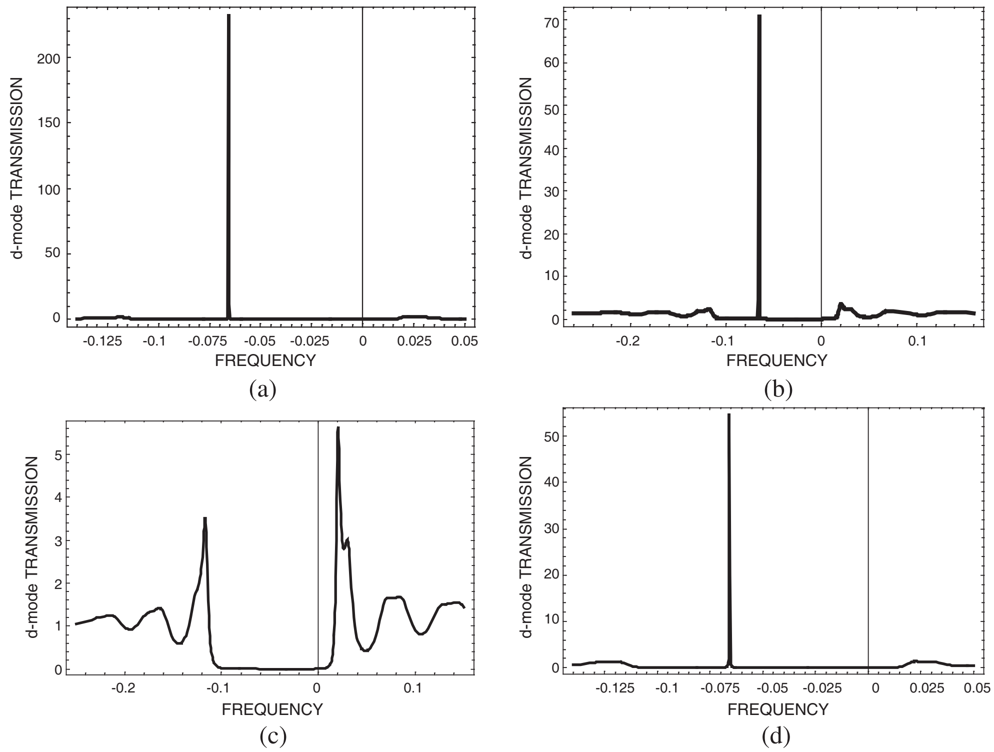

Figure 3: Calculated intensity transmission coefficients at a low birefringent defect layer for an amplifying CLC layer versus the frequency close to their divergence points for diffracting incident polarization (a) at $\Delta\varphi = \pi/8$, $\gamma = -0.00150$; $d/p = 2.25$, (b) at $\Delta\varphi = \pi/6$, $\gamma = -0.002355$, (c) at $\Delta\varphi = \pi/2$, $\gamma = -0.004500$, (d) at $\Delta\varphi = 0$, $\gamma = -0.000675$.

For amplifying CLC the value of γ corresponding to the divergence of DMS reflection and transmission coefficients just determines the solution of the dispersion Equation (6) and also determines the threshold DFB lasing gain in the DMS (see [12, 13]). So, there is an option to finding the threshold value of γ by calculating the DMS reflection and transmission coefficients at varying of γ and finding its value at the points of DMS reflection and transmission coefficients divergence.

According to the formulated approach Fig. 3 presenting values of DMS transmission coefficient close to their divergence points demonstrate growth of the threshold DFB lasing gain ($|\gamma|$) with increase of the birefringent phase factor $\Delta\varphi$ and even disappearance of the divergence at defect mode frequency at $\Delta\varphi = \pi/2$.

For absorbing CLC layers in DMS the anomalously strong absorption effect reveals itself at the value of γ ensuring a maximum of the total absorption in the DMS (see [12, 13]). For finite thicknesses of CLC layers L the DM frequency ω_D occurs to be a complex quantity which may be found by a numerical solution of Equation (6). For a very small values of the parameter γ the reflection and transmission spectra of MDS with absorbing (amplifying) CLC layers are similar to the studied in [12, 13] spectra (see Fig. 2). In particular, positions of dips in reflection and spikes in transmission inside the stop-band just correspond to $\mathrm{Re}[\omega_D]$ and this observation is very useful for numerical solution of the dispersion equation. What is concerned of the DM life-time it reduces for absorbing CLC layers compared to the case of nonabsorbing CLC layers [12, 13].

4. ABSORBING (AMPLIFYING) ISOTROPIC DEFECT LAYER

The studying of the defect mode associated with an insertion of an absorbing (amplifying) isotropic layer (Fig. 1) is performed in the same manner as above (see also [12, 13]). The transmission $|T(d, L)|^2$ and reflection $|R(d, L)|^2$ intensity coefficients (of light of diffracting circular polarization) for the whole structure may be presented in the following form:

$$|T(d, L)|^2 = |[T_e T_d \exp(ikd(1 + ig))] / [1 - \exp(2ikd(1 + ig))R_d R_u]|^2 , \tag{7}$$

$$|R(d, L)|^2 = |\{R_e + R_u T_e T_u \exp(2ikd(1 + ig))/[1 - \exp(2ikd(1 + ig))R_d R_u]\}|^2 , \tag{8}$$

where $R_e(T_e)$, $R_u(T_u)$ and $R_d(T_d)$ are determined above. The factor $(1+ig)$ is related to the defect layer only and corresponds to the dielectric constant of the defect layer having the form $\varepsilon_0(1 + 2ig)$

with a small g being positive for an absorbing defect layer and negative for an amplifying one.

The defect mode frequency ω_D is determined by the following dispersion equation:

$$\left\{\exp(2ikd(1+ig))\sin^2 qL-\exp(-i\tau L)[(\tau q/\kappa^2)\cos qL+i((\tau/2\kappa)^2+(q/\kappa)^2-1)\sin qL]^2/\delta^2]\right\}=0. \tag{9}$$

For finite thicknesses of CLC layers L ω_D occurs to be a complex quantity which may be found by a numerical solution of Equation (9). For very small values of the parameter g the reflection and transmission spectra of MDS with an active defect layer are similar to the studied in [12, 13] spectra. In particular, positions of dips in reflection and spikes in transmission inside the stop-band just correspond to $\mathrm{Re}[\omega_D]$. What is concerned of the DM life-time it reduces for absorbing defect layers compared to the case of nonabsorbing defect layer [12, 13].

As in the case of investigated DMs with absorbing CLC layers [12, 13] in DMS with an absorbing defect layer the effect of anomalously strong absorption takes place. The effect reveals itself at the DM frequency and reaches its maximum (maximum of $1-|T(d,L)|^2-|R(d,L)|^2$) for definite value of g which may be found using the expressions (7), (8). Fig. 4 demonstrate existence of the anomalously strong absorption effect. As follows from Fig. 4 the maximum values of the anomalous absorption [25, 30] are reached for $g == 0.04978$, $g = 0.00008891$ dependent on on the defect layer thickness d.

In the case of thick CLC layers ($|q| \gg L$) in the DMS the g value ensuring absorption maximum may be found analytically. For the defect mode frequency ω_D in the middle of stop-band the maximal absorption corresponds to

$$g_t = (2/3\pi)(p/d)\exp[-2\pi\delta(L/p)]. \tag{10}$$

As the calculations and the formulas (10) show the gain (g) corresponding to the maximal absorption is approximately inversely proportional to the defect layer thickness d.

In the case of DMS with amplifying defect layer ($g < 0$) at some value of $|g|$ divergences of reflection and transmission coefficients occur. The corresponding values of g are the gain lasing thresholds. Their values may be found numerically using the expressions (7, 8) for $|T(d,L)|^2$ and $|R(d,L)|^2$ or found approximately by plotting $|T(d,L)|^2$ and $|R(d,L)|^2$ at varying g. The second options is illustrated by Figs. 5–7 where "almost divergent" values of $|T(d,L)|^2$, $|R(d,L)|^2$ or absorption $(1-|T(d,L)|^2-|R(d,L)|^2)$ are shown. The used values of g at Figs. 5–7 are close to

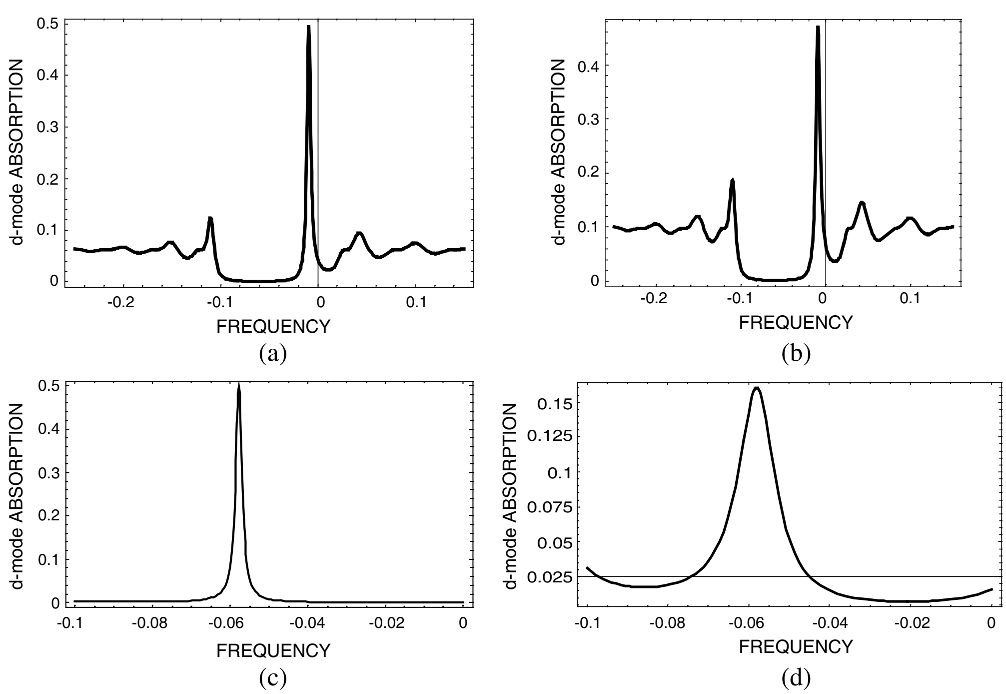

Figure 4: Total absorption versus the frequency for an absorbing defect layer and nonabsorbing CLC layers (a) at $g = 0.04978$ for $d/p = 0.1$, (b) at $g = 0.08$ for $d/p = 0.1$, (c) at $g = 0.00008891$ for $d/p = 22.25$, (d) at $g = 0.0008891$ for $d/p = 22.25$.

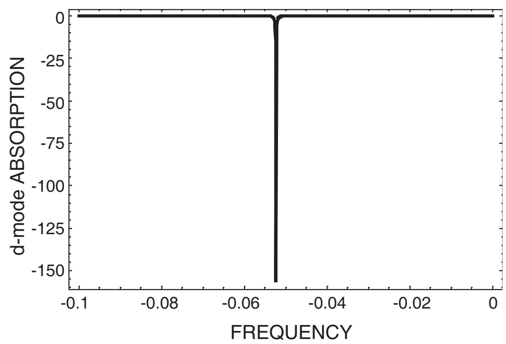

Figure 5: Total absorption versus the frequency for amplifying defect layer and nonabsorbing CLC layers at $g = -0.0065957$ for $d/p = 0.25$.

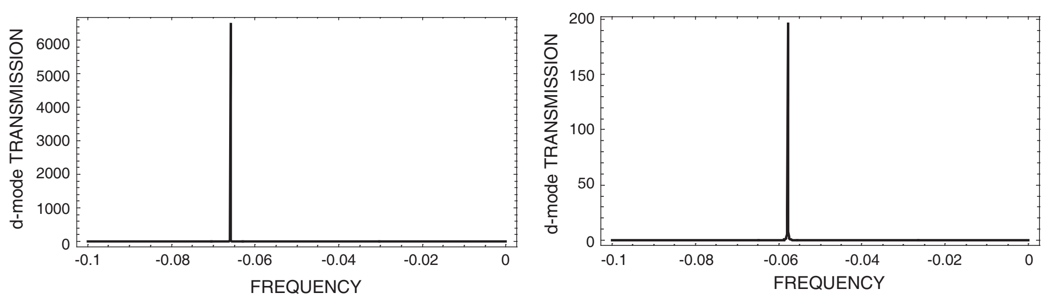

Figure 6: $T(d)$ versus the frequency for amplifying defect layer and nonabsorbing CLC layers (a) at $g = -0.001000$ for $d/p = 2.25$, (b) at $g = -0.00008891$ for $d/p = 22.25$.

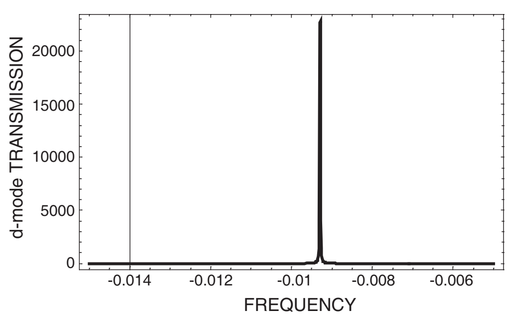

Figure 7: $R(d)$ versus the frequency for amplifying defect layer and nonabsorbing CLC layers at $g = -0.04978$ for $d/p = 0.1$.

the threshold ones ensuring divergence of $|T(d, L)|^2$ and $|R(d, L)|^2$. The calculation results show that the minimal threshold $|g|$ corresponds to location of ω_D just in the middle of the stop-band and $|g|$ is almost inversely proportional to the defect layer thickness. Really, the Figs. 5 and 6 correspond to location of the defect mode frequency ω_D close to the middle point of the stop band and demonstrate decrease of the lasing threshold gain with increase of the defect layer thickness. Fig. 7 correspond to location of the defect mode frequency ω_D close to the stop band edge and demonstrates increase of the lasing threshold gain with approaching the defect mode frequency ω_D to the stop band edge.

The analytic approach for thick CLC layers ($|q|L \gg 1$) results in the similar predictions, namely, for ω_D in the middle of the stop-band the threshold value of gain is given by (10) with a negative sign of the right hand side of the expression. So, as the formula (10) shows the thinner defect layer is the higher is threshold gain g. The same result, as was mentioned above, relates also to the absorption enhancement (formula (10)). The thinner defect layer is the higher is g value ensuring maximal absorption.

5. CONCLUSION

The performed analytical description of the defect modes at an active defect layer neglecting the polarization mixing at the boundaries of CLC in the structure under consideration allows one to reveal clear physical picture of these modes which is applicable to the defect modes in general. For example, more low lasing threshold and more strong absorption (under the conditions of anomalously strong absorption effect) for the defect mode frequency at the middle of stop-band compared to the defect mode frequency close to the stop-band edge are the features of any periodic media. For a special choice of the parameters in the experiment the obtained formulas may be directly applied to the experiment. However, in the general case one has take into account a mutual transformation at the boundaries of the two circular polarizations of opposite sense.

In the conclusion should be stated that the results obtained here for the defect modes with an active defect layer clarify the physics of these modes. An important result relating to the DFB lasing at DMS with active defect layer may be formulated as the following. The lasing threshold gain in defect layer decreases with the layer thickness decrease being almost inversely proportional to its thickness. The similar result relates to the effect of anomalously strong absorption phenomenon where the value of gain in the defect layer ensuring a maximal absorption is almost inversely proportional to the defect layer thickness. Note that the obtained above results are qualitatively applicable to the corresponding localized electromagnetic modes in any periodic media and may be regarded as a useful guide in the studies of the localized modes with an active defect layer in general.

ACKNOWLEDGMENT

The work is supported by the RFBR grants 11-02-90419-Ucr_f_a and 10-02-92103-Jp_a.

REFERENCES

1. Yang, Y.-C., C.-S. Kee, J.-E. Kim, et al., "Defect modes in chiral liquid crystals," *Phys. Rev. E*, Vol. 60, 6852, 1999.
2. Kopp, V. I. and A. Z. Genack, "Phase jump defect modes in chiral liquid crystals," *Phys. Rev. Lett.*, Vol. 89, 033901, 2003.
3. Schmidtke, J., W. Stille, and H. Finkelmann, "Observation of defect modes in chiral liquid crystals," *Phys. Rev. Lett.*, Vol. 90, 083902, 2003.
4. Shibaev, P. V., V. I. Kopp, and A. Z. Genack, "Studies of defect modes in chiral liquid crystals," *J. Phys. Chem. B*, Vol. 107, 6961, 2003.
5. Matranga, M. A., M. P. De Santo, G. Petriashvili, A. Chanishvili, G. Chilaya, and R. Barbery, "Lasing at multilayer liquid crystal structures," *Ferroelectrics*, Vol. 395, 1, 2010.
6. Yoshida, H., C. H. Lee, Y. Miura, A. Fujii, and M. Ozaki, "Optical mnipulation of photonic defect modes," *Thin Solid Films*, Vol. 516, 2358, 2008.
7. Takanishi, Y., Y. Ohtsuka, G. Suzaki, S. Nashimura, and H. Takezoe, "Low threshold lasing from multilayer structiures," *Optics Express*, Vol. 18, No. 12, 12909, 2010.
8. Shabanov, A. V., S. Yu. Vetrov, and A. Yu. Karneev, "Defect mode at spiral defect layer," *Pis'ma v Zhurnal Experimental'noi i Teoreticheskoi Fiziki,* Vol. 80, No. 3, 206, 2004; English translation, *JETP Letters*, Vol. 80, No. 3, 181, 2004.
9. Kopp, V. I., Z.-Q. Zhang, and A. Z.Genack, "Localized optical modes," *Prog. Quant. Electron.*, Vol. 27, No. 6, 369, 2003.
10. Becchi, M., S. Ponti, J. A.Reyes, and C. Oldano, "Analytic approach to defect modes," *Phys. Rev. B*, Vol. 70, 033103, 2004.
11. Schmidtke, J. and W. Stille, "Theory of defect modes in liquid crystals," *Eur. Phys. J.*, Vol. 90, 353, 2003.
12. Belyakov, V. A., "Analytic approach to defect modes theory," *MCLC*, Vol. 494, 127, 2008; *Ferroelectrics*, Vol. 364, 33, 2008.
13. Belyakov, V. A. and S. V. Semenov, "Defect modes in photonic liquid crystals," *JETP*, Vol. 112, 694, 2011.
14. Yablonovitch, E., T. J. Gmitter, R. D. Meade, et al., "Defect modes in solids," *Phys. Rev. Lett.*, Vol. 67, 3380, 1991.
15. Arkhipkin, V. G., V. A. Gunyakov, S. A. Myslovets, et al., "Electromagnetic swithcing of defect modes," *Zhurn. Eksperim. I Teor. Fiziki*, Vol. 139, 666, 2011.

16. Hodkinson, I. J., Q. H. Wu, K. E. Thorn, A. Lakhtakia, and M. W. McCall, "Spectral hole in transmission of chiral layer with phase defect," *Optics Communications*, Vol. 184, 57, 2000.
17. Wang, F. and A. Lakhtakia, "Defect modes in multisection structures," *Optics Express,* Vol. 13, No. 19, 7319, 2005.
18. Song, M. H., N. Y. Ha, K. Amemiya, B. Park, Y. Takanishi, K. Ishikaw, J. W. Wu, S. Nishimura, T. Toyooka, and H. Takezoe, "Defect mode lasing in a three-layered structure," *Adv. Mater.,* Vol. 18, 193, 2006.
19. Yoshida, H., C. H. Lee, A. Fuji, and M. Ozaki, "Tunable singlr photonic defect mode," *Appl. Phys. Lett.,* Vol. 89, 231913, 2006.
20. Yoshida, H., R. Ozaki, K. Yoshino, and M. Ozaki, "Effect of multiple chiral defects in optics of chiral liquid crystals," *Thin Solid Films*, Vol. 509, 197, 2006.
21. Gevorgyan, A. H. and M. Z. Harutyunyan, "Chiral photonic crystals with an anisotropic defect layer," *Phys. Rev. E*, Vol. 76, 031701, 2007.
22. Song, M. H., B. Park, Y. Takanishi, et al., *Jap. Jn. Appl. Phys.*, Vol. 44, 8165, 2005.
23. Gevorgyan, A. H., "Chyral photonic crystals with an anisotropic defect layer: Oblique incidence," *Optics Communications*, Vol. 281, 5097, 2008.
24. Gevorgyan, A. H. and M. Z. Harutyunyan, "Tuning of emission wavelength in chiral photonic crystals with an anisotropic defect layer," *J. Mod. Opt.*, Vol. 56, 1163, 2009.
25. Belyakov, V. A. and V. E. Dmitrienko, *Optics of Chiral Liquid Crystals (Soviet Scientific Reviews/Section A, Physics Reviews)*, Ed. I. M. Khalatnikov, Harwood Academic Publisher, Vol. 13, 54, 1–203, 1989.
26. Belyakov, V. A., *Diffraction Optics of Complex Structured Periodic Media*, Chap. 4, Springer Verlag, New York, 1992.
27. De Vries, H., "Optics of cholesteric liquid crystals," *Acta Crystallogr*, Vol. 4, 219, 1951.
28. Kats, E. I., "Theory of cholesteric liquid crystals optics," *Sov. Phys. JETP*, Vol. 32, 1004, 1971.
29. De Gennes, P. G. and J. Prost, *The Physics of Liquid Crystals*, Clarendon Press, Oxford, 1993.
30. Belyakov, V. A., A. A. Gevorgian, O. S. Eritsian, and N. V. Shipov, "Anomalous absorption," *Zhurn. Tekhn. Fiz.*, Vol. 57, 1418, 1987; English translation, *Sov. Phys. Technical Physics*, Vol. 32, No. 7, 843–845, 1987; *Sov. Phys. Crystalography*, Vol. 33, No. 3, 337, 1988.

Soliton Cryptography Using Dark-bright Conversion in a PANDA Ring Resonator

S. Songmuang[1], **X. Louangvilay**[2], **S. Mitatha**[3], **M. Yoshid**[4], **N. Komine**[4], **and P. P. Yupapin**[5]

[1]Faculty of Science and Technology, Kasem Bundit University, Bangkok 10250, Thailand
[2]International College, King Mongkut's Institute of Technology Ladkrabang, Bangkok 10520, Thailand
[3]Hybrid Computing Research Laboratory, Faculty of Engineering
King Mongkut's Institute of Technology Ladkrabang, Bangkok 10520, Thailand
[4]Department of Embedded Technology
School of Information Technology and Telecommunication Engineering, Tokai University, Japan
[5]Nanoscale Science and Engineering Research Alliance, Advance Research Center for Photonics
Faculty of Science, King Mongkut's Institute of Technology Ladkrabang, Bangkok 10520, Thailand

Abstract— We proposed a concept of cryptography using dark-bright soliton conversion behaviors within a nonlinear ring resonator, in which the orthogonal soliton is established among the soliton conversion. A new model of add/drop filters is modified which is known as a PANDA ring resonator is proposed. The orthogonal solitons can be formed randomly within the system and detected simultaneously at the output ports. The entangled solitons (photons) can be formed in the same way of the entangled photons, but in this case the entangled soliton pair is gained more power that gives the advantage of long distance communication.

1. INTRODUCTION

We use data and information in our live every day, so the security of data is considered first, therefore, there are a lot of techniques are used to protect the secret data or information. Communication security has become the popular technique in modern communication requirement. The dark soliton is one of the soliton properties where the soliton amplitude is vanished during the propagation in media; therefore, the dark soliton detection is extremely difficult. To date, several research works have investigated the dark soliton behaviors [1, 2], where one point of them has shown in teresting results, where the dark soliton can beconverted into bright soliton and finally detected. This means that we can use the dark soliton penalty to be the benefit, where the idea of using a dark soliton to be a communication carrier where the recovery can be retrieved by the dark–bright soliton conversion. Actually, we are looking for the simple technique that can be employed to detect the dark soliton.

Dark and bright soliton behaviors have been widely investigated in different forms [1, 3]. The use of soliton, i.e., bright solitonin long-distance communication link has been implemented for nearly two decades, however, the interesting works using bright soliton in communication remain, whereas the use of soliton pulse with in a micro-ring resonator for communication security has been studied [4]. The interesting results are when the technique could be implemented within a tiny device such as a micro-ring and a nano-ring resonators and could be implemented within the mobile hand-set [4, 5]. The dark soliton is one of the soliton properties, whereas the soliton amplitude is vanished or minimized during the propagation in media, therefore, the dark soliton detection is difficult. The investigation of dark soliton behaviors has been reported [6, 7], where one point of them has shown interesting results, where the dark soliton can be stabilized [8] and converted into bright soliton [9] and finally detected. This means that we can use the dark soliton penalty due to the low level of the peak power to be the benefit, where the promising idea is that a dark soliton can performed the communication transmission carrier where the recovery can be retrieved by the dark–bright so liton conversion. Actually, we are looking for the simple technique that can be employed to detect the dark soliton. Yupapin and Suwancharoen [10] have reported the interesting result so flight pulse propagating with in a non-linearmicro-ring device, where the transfer function of the output at the resonant condition is derived and used. They found that the broad spectrum of light pulse can be transformed to the discrete pulses.

In application, the device can be embedded within the computer processing unit with using to increase the capacity and the speed for internet, where the internet security can be provided. Furthermore, such a concept is also available for hybrid communications, for instance, wire/wireless, satellite. However, the theoretical background of correlated photon source generation is reviewed.

2. OPERATOR PRINCIPLE

A dark-bright soliton conversion system using a ring resonator optical channel dropping filter is composed with two sets of coupled waveguides, as shown in Fig. 1. The relative phase of the two output light signals after coupling into the optical coupler is $\pi/2$. This means that the signals coupled into the drop and through ports have acquired a phase of π with respect to the input port signal. In application, if we engineer the coupling coefficients appropriately, the field coupled into the through port on resonance would completely extinguish the resonant wavelength, and all the power would be coupled into the drop port. The input and control fields at the input and add ports are formed by the dark and bright optical solitons and described by Equations (1) and (2), respectively [20, 21].

$$E_{in}(t) = A_0 \tanh\left[\frac{T}{T_0}\right] \exp\left[\left(\frac{z}{2L_D}\right) - i\omega_0 t\right] \quad (1)$$

$$E_{in}(t) = A_0 \operatorname{sech}\left[\frac{T}{T_0}\right] \exp\left[\left(\frac{z}{2L_D}\right) - i\omega_0 t\right] \quad (2)$$

Here A_0 and z are the optical field amplitude and propagation distance, respectively. $T = t - \beta_1 z$, where β_1 and β_2 are the coefficients of the linear and second-order terms of Taylor expansion of the propagation constant. $L_D = T_0^2/|\beta_2|$ is the dispersion length of the soliton pulse. T_0 in equation is a soliton pulse propagation time at initial input (or soliton pulse width), where t is the soliton phase shift time, and the frequency shift of the soliton is ω_0. The optical fields of the system within the device as shown in Fig. 1 are obtained and expressed in following forms

$$E_1 = -j\kappa_1 E_i + \tau_1 E_4, \quad (3)$$
$$E_2 = \exp(j\omega T/2)\exp(-\alpha L/4)\, E_1, \quad (4)$$
$$E_3 = \tau_2 E_2 - j\kappa_2 E_a, \quad (5)$$
$$E_4 = \exp(j\omega T/2)\exp(-\alpha L/4)\, E_3, \quad (6)$$
$$E_t = \tau_1 E_i - j\kappa_1 E_4, \quad (7)$$
$$E_d = \tau_2 E_a - j\kappa_2 E_2, \quad (8)$$

Here E_i is the input field, E_a is the add (control) field, E_t is the through field, E_d is the drop field, $E_1, \ldots, E_4$ are the fields in the ring at points $1, \ldots, 4$, κ_1 is the field coupling coefficient between the input bus and ring, κ_2 is the field coupling coefficient between the ring and output bus, L is the circumference of the ring, T is the time taken for one round trip (roundtrip time), and α is the power loss in the ring per unit length. We assume that this is the lossless coupling, i.e., $\tau_{1,2} = \sqrt{1-\kappa_{1,2}^2}$, $T = Ln_{eff}/c$.

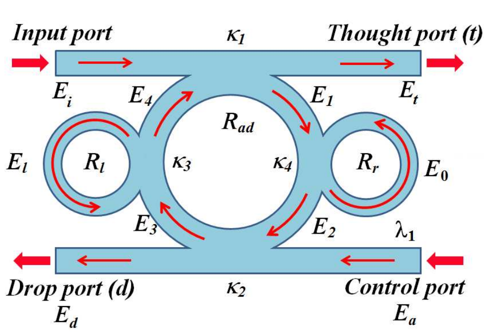

Figure 1: Schematic diagram if a proposed PANDA ring resonator.

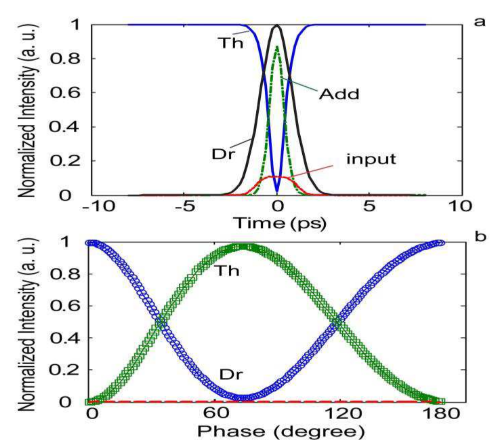

Figure 2: Shows the normalize intensity of a single dark-bright solition pair at the center wavelength by using the add-drop filter with the input dark soliton power (red) is 0.15 W.

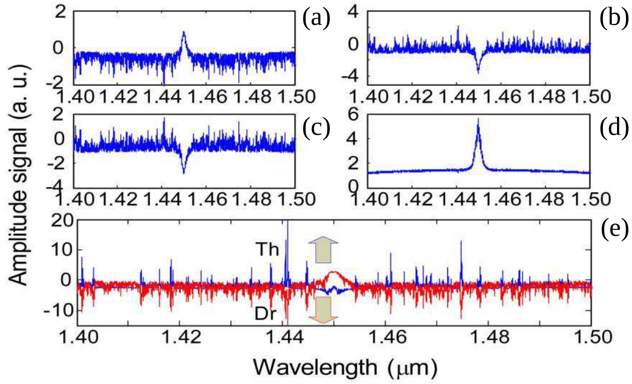

Figure 3: Orthogonal soliton pairs generated by a dark-soliton pump into a PANDA ring resonator at the center wavelength 1.45 μm.

3. DARK-BRIGHT CONVERSION

In Fig. 2(a), single dark-bright soliton pair is plotted at the center wavelength by using the add-drop filter with the input power is 0.15 W. The inversion of dark and bright soliton pulses is formed and detected by the through and drop ports as shown in Fig. 2(a), where the control field can be added via the Add port. The orthogonal solitons in terms of phase changes are plotted in Fig. 2(b), where we found that their behaviors can provide the similar manner of the entangled photon pair, which can be used in quantum information application, but in this case the advantage is that the long distance quantum communication link can be provided due to the soliton property of the generated entangled photon source.

Figure 3 shows the orthogonal soliton pairs generated by a dark soliton pump input into a PANDA ring resonator at the center wavelength 1.45 μm, where (a) a bright soliton at E_1, (b) a dark-soliton at E_2, (c) a dark soliton at E_3, (d) a bright soliton at E_4, and (e) the transmittance at through (Th) and reflectance at drop (Dr) ports, respectively.

In this paper, we present the multi-soliton dark and bright pule as shown in Fig. 3 which are available for high security. A dark-bright soliton pair is input as shown in Equations (1) and (2), where the coincidence dark and bright soliton pair is occurred and obtained by using a $(\pi/2)$ phase retarder (i.e., a beamsplitter), which means that bit "1" and bit "0" states represent the orthogonal dark and bright soliton pulses. The signals from through (Th) port are formed and transmitted to the transmission line and finally to the end user. The add/drop filter is used to separate (filter) the required signal form the transmission link, in which the Th and drop port signals are formed as transmitted and referencing signals, respectively. Moreover, because of the lack of phase of $(\pi/2)$ between dark and bright solitons, the use of such behaviors can form in the same way as the entangled photon behaviors, in which the use of dark-bright soliton pairs for bit states.

4. CONCLUSION

We have shown cryptography using dark-bright soliton conversion behaviors within a nonlinear ring resonator, in which the orthogonal soliton is established among the soliton conversion. A new model of add/drop filters is modified which is known as a PANDA ring resonator is proposed. The orthogonal solitons can be formed randomly within the system and detected simultaneously at the output ports. The entangled solitons (photons) can be formed in the same way of the entangled photons as shown in Figs. 2 and 3, but in this case the entangled soliton pair is gained more power that gives the advantage of long distance quantum communication. In application, the high capacity quantum communication is also available by using the multivariable entangled solitons that we purpose for a future work.

ACKNOWLEDGMENT

We would like to give our acknowledge to the AUN/SEED-Net for the fully ¯nancial support to Mr. Xaythavy LOUANGVILAY in higher education at International College, King Mongkut's Institute of Technology Ladkrabang (KMITL), Bangkok 10520, Thailand.

REFERENCES

1. Nakazawa, M., H. Kubota, K. Suzuki, E. Yamada, and A. Sahara, "Ultrahigh-speed long-distance TDM and WDM soliton transmission technologies," *IEEE J. Sel. Top. Quantum Electron.*, Vol. 6, No. 2, 363–396, 2000.
2. Zhao, W. and E. Bourkoff, "Propagation properties of dark solitons," *Opt. Lett.*, Vol. 14, No. 13, 703–705, 1989.
3. Kivshar, Y. S. and B. Luther-Davies, "Dark optical solitons: Physics and applications," *Phys. Rep.*, Vol. 298, No. 2–3, 81–197, 1998.
4. Pornsuwanchroen, N., S. Chaiyasoonthorn, and P. P. Yupapin, "Fast and slow lights generation using chaotic signals in the nonlinear micro ring resonators for communication security," *Opt. Eng.*, Vol. 48, No. 1, 2009.
5. Ngo, N. Q., "Proposal for a high-speed optical dark-soliton detector using a microring resonator," *IEEE Photon. Technol. Lett.*, Vol. 19, No. 17, 471–473, 2007.
6. Barashenkov, I. V., "Stability criterion for dark soliton," *Phys. Rev. Lett.*, Vol. 77, 1193, 1996.
7. Christodoulides, D. N., T. H. Coskun, M. Mitchell, Z. Chen, and M. Segev, "Theory of incoherent dark solitons," *Phys. Rev. Lett.*, Vol. 80, No. 23, 5113–5116, 1998.
8. Kim, A. D., W. L. Kath, and C. G. Goedde, "Stabilizing dark solitons by periodic phase-sensitive amplification," *Opt. Lett.*, Vol. 21, No. 2, 465–467, 1996.
9. Malomed, B. A., A. Mostofi, and P. L. Chu, "Transformation of a dark soliton into a bright pulse," *J. Opt. Soc. Am. B*, Vol. 17, No. 4, 507–513, 2000.
10. Yupapin, P. P. and W. Suwancharoen, "Chaotic signal generation and cancellation using a micro ring resonator incorporating an optical add/drop multiplexer," *Opt. Commun*, Vol. 280, No. 2, 343–350, 2007.

THz Switching Generation Using a PANDA Ring Resonator for High Speed Computer Communication

Suphanchai Punthawanunt[1], **Saysamone Soysouvanh**[2,3], **Khanthanou Luangxaysana**[2,3], **Somsak Mitatha**[3], **Masahiro Yoshida**[4], **Noriyuki Komine**[4], **and Preecha Yupapin**[5]

[1]Faculty of Science and Technology, Kasem Bundit University, Bangkok 10250, Thailand
[2]International College, King Mongkut's Institute of Technology Ladkrabang, Bangkok 10520, Thailand
[3]Hybrid Computing Research Laboratory, Faculty of Engineering
King Mongkut's Institute of Technology Ladkrabang, Bangkok 10520, Thailand
[4]School of Information and Telecommunication Engineering, Tokai University, Japan
[5]Nanoscale Science and Research Alliance (N'SEAR), Faculty of Science
King Mongkut's Institute of Technology Ladkrabang, Bangkok 10520, Thailand

Abstract— A novel design of Terahertz (THz) switching generation for high speed computer used is proposed. The dense wavelength division multiplexing (DWDM) can be obtained by using a Gaussian or Soliton pluses propagating within a modified add-drop filter know as a PANDA ring resonator. The THz devices can made contributions to promising applications in high-speed switching, demultiplexing, and wavelength conversion of optical signals. Effective THz control is also essential for the potential application to ultrahigh-speed wireless digital interconnects for computer chips of the ultrahigh clock rates (> 10 GHz). In principle, the high density frequency (wavelength) can be generated and used to form the radio frequency identification (RFID), Ad-Hoc network and ubiquitous applications, moreover, the tiny device system is the another advantage, which can be constructed incorporating the available currently used system. In this paper is organized as follow: introduction, theory and the use of such a system in all proposed applications.

1. INTRODUCTION

The Terahertz (THz) communication technology has become a part of communication system as an optical communication, wireless communication, and Radio over Fiber (RoF). The THz communication has effective data rate 1 Tbit/sec [1] i.e., communicate with a THz carrier wave, with frequency range from 200 GHz to 10 THz. THz are generated by quantum transition of light, which generates very high intensity for both the transition between the electric [2] and photonic [3] sources. THz is becoming of importance in high speed communication, one of them is RoF, where the fiber-wireless (WiFi) [4] network is incorporated with the optical communication and radio frequency with WDM and millimeter wave (mm wave) frequency. The architecture of a mm-wave fiber-wireless is central office (CO), which is connected to a large number of antenna or THz antenna [5] base station (BSs) via an optical fiber network such as RF-over-fiber, IF-over-fiber, and Baseband-over-fiber [6]. Optical fiber is an excellent medium for RF signal transmission due to the very high bandwidth (BW), low loss, light weight, small cross section, and low cost. In RoF system, a head-end (HE), which consists of an optical-to-electrical (O/E) and electrical-to-optical (E/O) modules, is connected to base station. The RoF systems are being applied many wireless applications such as fiber-to-the-home (FTTH), universal mobile telecommunication system (UMTS), vehicular ad-hoc network (VANET) [7] and microcellular system [8, 9]. The THz communication is one alternative technology to improve the performance of communication systems.

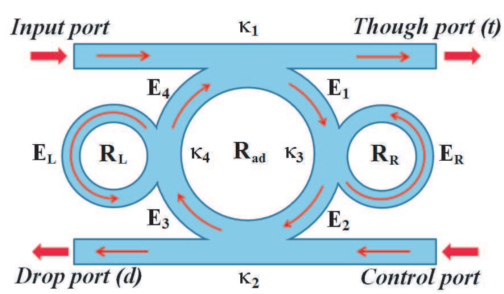

Figure 1: Schematic diagram of PANDA ring resonator.

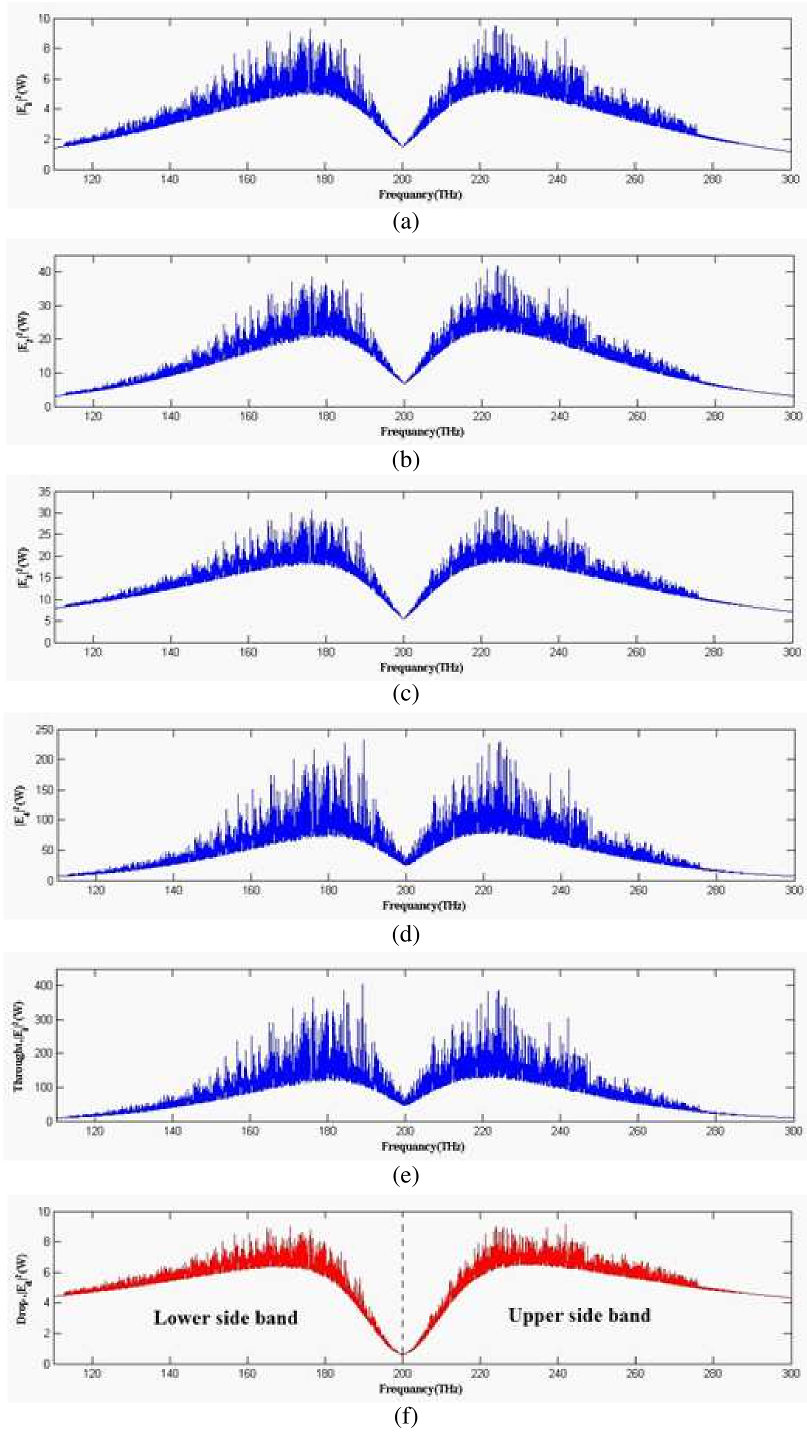

Figure 2: Simulation results of the light pulse generation by PANDA ring system with center wavelength $1.5\,\mu\text{m}$, where (a) $|E_1|^2$, (b) $|E_2|^2$, (c) $|E_3|^2$, (d) $|E_4|^2$, (e) $|E_t|^2$, and (f) $|E_d|^2$ are output powers inside the PANDA system.

2. THEORETICAL MODELING

In order to achieve a wide band frequency carrier, we propose a system consisting of microring resonators for applications in communication as a wireless terahertz communication system and faster data transfer which requires higher carrier frequencies. For the PANDA ears, the output optical fields from the right and left rings are express as

$$E_R = E_1 \left\{ \sqrt{(1-\gamma_3)(1-k_3)} - (1-\gamma_3) e^{-\frac{\alpha}{2}L_2 - jk_n L_2} / 1 - \sqrt{(1-\gamma_3)(1-k_3)} e^{-\frac{\alpha}{2}L_2 - jk_n L_2} \right\} \quad (1)$$

$$E_L = E_3 \left\{ \sqrt{(1-\gamma_4)(1-k_4)} - (1-\gamma_4) e^{-\frac{\alpha}{2}L_1 - jk_n L_1} / 1 - \sqrt{(1-\gamma_4)(1-k_4)} e^{-\frac{\alpha}{2}L_1 - jk_n L_1} \right\} \quad (2)$$

E_R and E_L are the outputs from the right and left rings of PANDA system. Inside the system E_1, E_2, E_3, and E_4, are the output of the optical fields that are shown in (3)–(6).

$$E_1 = \sqrt{1-\gamma_1}\left[\sqrt{1-k_1}E_4 + j\sqrt{k_1}E_{i1}\right] \quad (3)$$

$$E_2 = E_R e^{-\frac{\alpha}{2}\frac{L}{2} - jk_n\frac{L}{2}} \quad (4)$$

$$E_3 = \sqrt{1-\gamma_2}\left[\sqrt{1-k_2}E_2 + j\sqrt{k_2}E_{i2}\right] \quad (5)$$

$$E_4 = E_L e^{-\frac{\alpha}{2}\frac{L}{2} - jk_n\frac{L}{2}} \quad (6)$$

Therefore, the final equations for drop port and through port power are archived in (7)–(10).

$$E_t = \sqrt{1-\gamma_1}\left[\sqrt{1-k_1}E_{i1} + j\sqrt{k_1}E_4\right] \quad (7)$$

$$E_d = \sqrt{1-\gamma_2}\left[\sqrt{1-k_2}E_{i2} + j\sqrt{k_2}E_2\right] \quad (8)$$

$$P_t = (E_t)\cdot(E_t)^* = |E_t|^2 \quad (9)$$

$$P_d = (E_d)\cdot(E_d)^* = |E_d|^2 \quad (10)$$

here, P_t and P_d represent the output power of the through port and drop port respectively.

3. THz PULSE GENERATION

Here two types of input signals are obtained for different input signals which bright soliton pulse and Gaussian beam. With centre wavelength of 1.5 μm and pulse width 20 ns, power at 1 W is input into the PANDA ring. The parameters used are $R_L = R_R = 5\,\mu\text{m}$, $R_{ad} = 20\,\mu\text{m}$, $A_{eff} = 30\,\mu\text{m}^2$. The selected parameters of the system are fixed into, $n_0 = 3.34$ (InGaAsP/InP), and $\alpha = 0.2\,\text{dBmm}^{-1}$, the couple intensity loss is $\gamma = 0.1$. The coupling coefficient of the micro-ring resonator is change between 0.1–0.98. The nonlinear refractive index is $n_2 = 2.2 \times 10^{-17}$.

4. RFID APPLICATIONS

Radio-frequency identification (RFID) is a technology using communication through radio wave to transfer data between an electronic system and a reader. RFID systems consist of tiny integrated circuits (RFID tags) equipped with antennas, that communicate with their reading devices RFID readers using electromagnetic fields at one of several standard radio frequencies. RFID tags supported by a transparent optical radio frequency network can be used to sense, locale, and track an array of objects including luggage, mobile assets, and commercial goods, and can provide additional

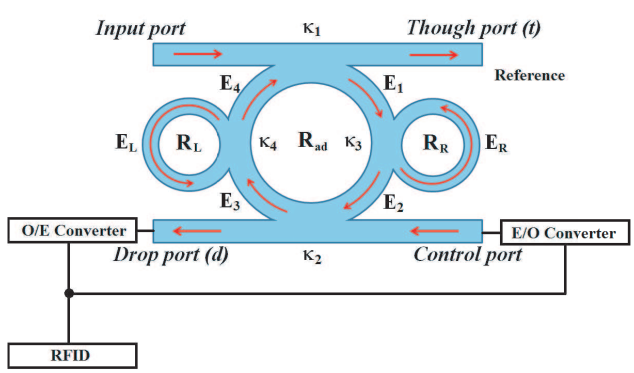

Figure 3: A multichannel RFID system, where R_s is ring radii, κ_s is coupling coefficients.

features such as boarding pass auto-tags, access control tags, and tagging support for airport commercial zoon. By using the proposed design as shown in Figure 3, the optical signal is converted to electrical signal by the O/E converter, in which the terahertz carriers can transmit many tags via the RFID link by a nano-antenna, where an up-to-dates 1 THz antenna is available for terahertz communication. The signal transmits throughout by antenna, where the receiver is operated to detect the incoming signals.

5. CONCLUSION

In this paper, a new design of PANDA ring resonator system has been introduced, which can improve the high channel capacity by using bright soliton and Gaussian pulses. The results have shown that the high channel capacity can be obtained in the range of 145 to 270 THz (Upper and Lower side bands). This enhancement of frequency bands can provide the reliable channels with high speed use between network and computers. It has been observed that the multi-frequency bands are generated by Gaussian beam pulse propagating within the PANDA ring, which can be simultaneously linked within a single device and available for the extended multi-switching application with the frequency center at the terahertz range.

ACKNOWLEDGMENT

We would like to thanks King Mongkut's Institute of Technology Ladkrabang (KMITL), Bangkok, Thailand for providing the excellent research facilities.

REFERENCES

1. Huang, K. C. and Z. Wang, "Terahertz terabit wireless communication," *IEEE Microw. Mag.*, Vol. 41, No. 3, 108–116, 2011.
2. Deal, W. R., X. B. Mei, V. Radisic, K. Leong, S. Sarkozy, B. Gorospe, J. Lee, P. H. Liu, W. Yoshida, J. Zhou, M. Lange, J. Uyeda, and R. Lai, "Demonstration of a 0.48 THz amplifier module using InP HEMT transistors," *IEEE Microw. Wirel. Compon. Lett.*, Vol. 20, No. 5, 289–291, 2010.
3. Blanchard, F., G. Sharma, L. Razzari, X. Ropagnol, H. Bandulet, F. Vidal, R. Morandotti, J. Kieffer, T. Ozaki, H. Tiedje, H. Haugen, M. Reid, and F. Hegmann, "Generation of intense terahertz radiation via optical methods," *IEEE J. Sel. Top. Quantum Electron.*, Vol. 17, No. 1, 5–16, 2011.
4. Ghazisaidi, N., M. Maier, and C. Assi, "Fober-wireless (FiWi) access networks: A survey," *IEEE Commun.*, Vol. 47, No. 2, 160–167, 2009.
5. Vourc'h, E., B. Della, D. L. Berre, and D. Herve, "Millimetter-wave power-fading compensation for WDM fiber-radio transmission using a wavelength-self-tunable single-sideband filter," *IEEE Trans. Microwave Theory Tech.*, Vol. 50, No. 12, 3009–3015, 2002.
6. Sharma, A. and G. Singh, "Rectangular microstirp patch antenna design at THz frequency for short distance wireless communication systems," *Springer Link J. Infra., Milli, and THz Wave,* Vol. 30, No. 1, 1–7, 2009.
7. Lin, C. T., J. Chen, P. C. Peng, C. F. Peng, W. R. Peng, B. S. Chiou, and S. Chi, "Hybrid optical access network integrating fiber-to-the-home and radio-over-fiber systems," *Photon. Technol. Lett.*, Vol. 19, No. 8, 610–621, 2007.
8. Kim, H. B., M. Emmelmann, B. Rathke, and A. Wolisz, "A radio over fiber network architecture for road vehicle communication systems," *IEEE Vehicle Technology Conference (VTC-2005)*, Vol. 5, 2920–2924, 2005.
9. Wu, J. S., J. Wu, and H. W. Tsao, "A radio-over-fiber network for microcellular system application," *IEEE Trans. Veh. Technol.*, Vol. 47, No. 1, 84–94, 1998.

All Optical Logic NAND Gate Using Dark-Bright Soliton Conversion Control

Saysamone Soysouvanh[1,2], Prapas Phongsanam[2], Khanthanou Luangxaysana[1,2], Somsak Mitatha[2], Komine Noriyuki[3], Masahiro Yoshida[3], and Preecha Yupapin[4]

[1]International College, King Mongkut's Institute of Technology Ladkrabang, Bangkok 10520, Thailand
[2]Hybrid Computing Research Laboratory, Faculty of Engineering
King Mongkut's Institute of Technology Ladkrabang, Bangkok 10520, Thailand
[3]School of Information and Telecommunication Engineering, Tokai University, Japan
[4]Nanoscale Science and Research Alliance (N'SEAR), Faculty of Science
King Mongkut's Institute of Technology Ladkrabang, Bangkok 10520, Thailand

Abstract— In this paper, we present a new concept of all-optical gates using Dark-Bright soliton conversion behaviors within a modified add/drop filter. The soliton can be used to generate logic data "1" and "0" using for optical gates. We have designed a photonic circuit for all-optical logic NAND Gate using dark-bright soliton conversion control within an optical add-drop multiplexer. The input and control logic '0', '1' are represented by dark (D) and bright (B) soliton pulses, respectively. We found that the simultaneous optical logic NAND Gate at the through port can be performed.

1. INTRODUCTION

The optical logic gates is one of the key techniques in all-optical signal processing and communication network, in which the implementation of all-optical logic gates can be used in various methods for processing signals with light. Many research have demonstrated various optical logic function using different schemes, such as including thermo-optic effect in two cascaded micro-ring resonators [1], quantum dot [2], semiconductor optical amplifier (SOA) [3–5], a terahertz optical asymmetric de-multiplex (TOAD) [6], nonlinear effects in SOI waveguide [7], nonlinear loop mirror [8], DPSK format [9], local nonlinear in MZI [10], photonic crystal [11]. Therefore, the searching for new design has become the interesting work. In this paper, we propose the one of the most important two logic gates namely NAND Gate based on dark-bright soliton conversion within the add/drop optical filter systems, which is a simple and flexible scheme for use as an arbitrary logic switching system. This can be used to form the advanced complex logic circuits, which will be detailed in the next section.

2. DARK-BRIGHT SOLITON CONVERSION

In operation, a ring resonator optical channel dropping filter (OCDF) is composed of two sets of coupled wave guides as shown in Figs. 1(a) and 1(b). For convenience, Fig. 1(a) is replaced by Fig. 1(b). The coupling equation outlined in the referenced in the previous section shows that there is a relative phase of $\pi/2$ between the signal coupled into the ring and the signal in the input bus. Similarly, the signal coupled into the drop and through ports, where both are acquired a phase of π with respect to the signal on the input port. This means that if we engineer the coupling

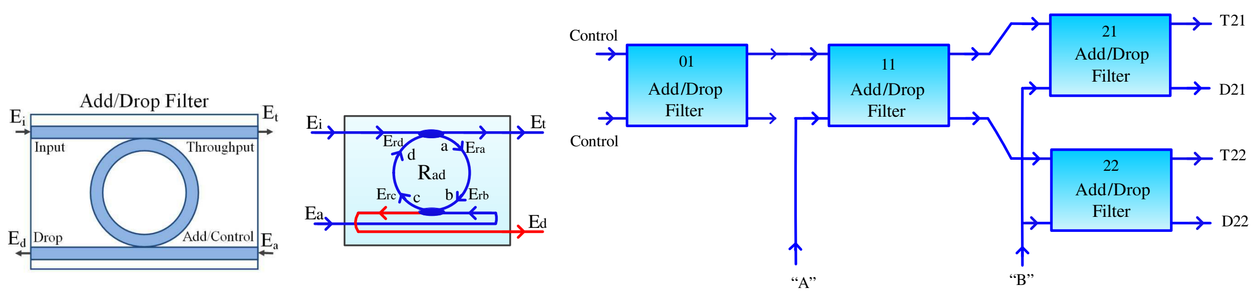

(a) (b) (c)

Figure 1: Schematic diagram simultaneous NAND Gate.

coefficients appropriately, the field coupled into the through port on resonance would completely extinguish the resonant wavelength, and all power would be coupled into the drop port field.

$$E_{ra} = -jk_1 E_i + \tau_1 E_{rd} \quad (1)$$
$$E_{rb} = \exp(j\omega T/2)\exp(-\alpha L/4) E_{ra} \quad (2)$$
$$E_{rc} = \tau_2 E_{rb} - jk2Ea \quad (3)$$
$$E_{rd} = \exp(j\omega T/2)\exp(-\alpha L/4) E_{rc} \quad (4)$$
$$E_t = \tau_1 E_i - jk_1 E_{rd} \quad (5)$$
$$E_d = \tau_2 E_i - jk_2 E_{rb} \quad (6)$$

here E_i is the input field, E_a is the added (control) field, E_t is the throughput field, E_d is the dropped field, $E_{ra} \ldots E_{rd}$ are the fields in the ring at the point $a \ldots d$, K_1 is the field coupling coefficient between the input and the ring, K_2 is the field coupling coefficient between the ring and the output bus, L is the circumference of the ring ($2\pi R$), T is the time taken for one round trip, $T{=}Ln_{eff}/c$, and α is the power loss in the ring per unit length. We assume that lossless coupling, i.e., The output power/intensities at the drop port and through port are given by π.

$$|E_d|^2 = \left| \frac{-\kappa_1 \kappa_2 A_{1/2} \Phi_{1/2}}{1 - \tau_1 \tau_2 A\Phi} E_i + \frac{\tau_2 - \tau_1 A\Phi}{1 - \tau_1 \tau_2 A\Phi} E_a \right|^2 \quad (7)$$
$$|E_t|^2 = \left| \frac{\tau_2 - \tau_1 A\Phi}{1 - \tau_1 \tau_2 A\Phi} E_i + \frac{-\kappa_1 \kappa_2 A_{1/2} \Phi_{1/2}}{1 - \tau_1 \tau_2 A\Phi} E_a \right|^2 \quad (8)$$

here $A_{1/2} = \exp(aL/4)$ (the half-round-trip amplitude); $A = (A_{1/2})^2$, $\Phi_{1/2} = \exp(j\omega T/2)$ (is the half-round-trip phase contribution), and $\Phi = (\Phi_{1/2})^2$. (The input and control fields at the input and add ports are formed by the dark-bright optical soliton [10] as shown in Equations (9)–(10).

$$E_{in}(t) = A_0 \tanh\left[\frac{T}{T_0}\right] \exp\left[\left(\frac{z}{2L_D}\right) - i\omega_0 t\right] \quad (9)$$
$$E_{in}(t) = A_0 \sec h\left[\frac{T}{T_0}\right] \exp\left[\left(\frac{z}{2L_D}\right) - i\omega_0 t\right] \quad (10)$$

here A and z are optical field amplitude and propagation distance, respectively. T is soliton pulse propagation time in a frame moving at the group velocity $T = t - \beta_1 - z$ where β_1 and β_2 are the coefficients of the linear and second-order terms of Taylor expansion of the propagation constant. $L_D = T_0^2/|\beta_2|$ is the dispersion length of the soliton pulse. T_0 in the equation is the initial soliton pulse width, where t is the soliton phase shift time, and the frequency shift of the soliton is ω_0. This solution describes a pulse that keeps its temporal width invariance as it propagates, and thus is called a temporal soliton. When a soliton peak intensity β/T_0^2 is given, then T_0 is known. For the soliton pulse in the nanoring device, a balance should be achieved between the dispersion length (L_D) and nonlinear length $L_{NL} = 1/\Gamma\phi_{NL}$, where $\Gamma = n_2 k_0$, is the length scale over which dispersive or nonlinear effects make the beam become wider or narrower. For a soliton pulse, there is a balance between dispersion and nonlinear lengths, hence $L_D = L_{NL}$.

When light propagates within the nonlinear material (medium), the refractive index (n) of light within the medium is given by

$$n = n_0 + n_2 I = n_0 + (n_2/A_{eff})P \quad (11)$$

here n_0 and n_2 are the linear and nonlinear refractive indexes, respectively. I and P are the optical intensity and optical power, respectively. The effective mode core area of the device is given by A_{eff}. For the micro/nano ring resonator, the effective mode core areas range from 0.50 to 0.10 μm^2. The resonant output of the light field is the ratio between the output and input fields [$E_{out}(t)$ and $E_{in}(t)$] in each round trip.

3. SIMULTANEOUS ALL-OPTICAL LOGIC GATES OPERATION

The proposed all-optical logic NAND Gate device is as shown in Fig. 1(b). The input and control light pulse trains are input in to the first add/drop optical filter (No. "01") using the dark-bright

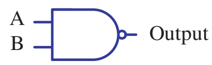

Input A	Input B	Output
0	0	1
0	1	1
1	0	1
1	1	0

Figure 2: Truth table NAND Gate.

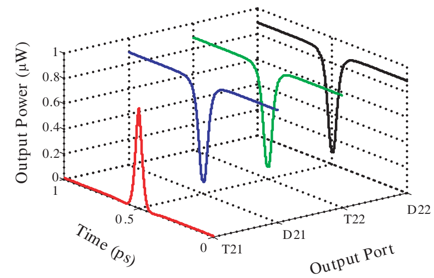

Figure 3: Show the output logic gates when the input logic stages 'DD'.

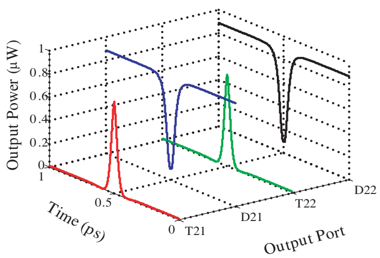

Figure 4: Show the output when the input logic stages 'DB'.

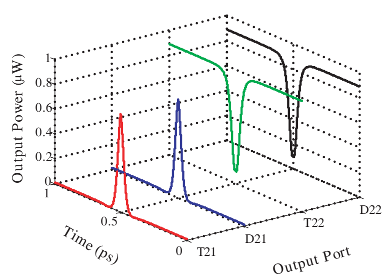

Figure 5: Show the output when the input logic stages 'BD'.

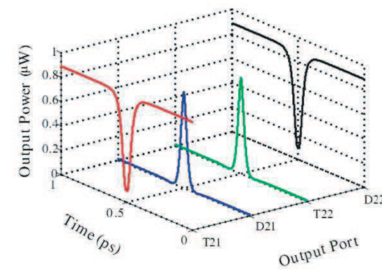

Figure 6: Show the output when the input logic stages 'BB'.

solitons, where firstly, the dark soliton is converted to be dark and bright solitons via the add/drop optical filter, which can be seen at the through and drop ports with π phase shift [12], respectively. By using the add/drop optical filters (No. "11", "12"), both input signals are generated by the first stage add/drop optical filter. Next, the input data "A" with logic "0" (dark soliton) and logic "1" (bright soliton) are added into both add ports. Secondly, the dark-bright soliton conversion with π phase shift is operated again. Finally, by using the add/drop optical filter (No. "21" to "22"), the input data "B" with logic "0" (dark soliton) and logic "1" (bright soliton) are seen at all the add ports. For large scale (Fig. 1(c)), results obtained are simultaneously seen by D21, D22, T22, T21 at the drop and through ports for optical logic gates, respectively. The truth table of NAND Gate is as shown in Fig. 2.

In simulation, the add/drop optical filter parameters are fixed for all coupling coefficients to be $K_s = 0.05$, $R_{ad} = 1.51\,\mu\text{m}$, $A_{eff} = 0.25\,\mu\text{m}^2$, $a = 0.05\,\text{dBmm}^{-1}$, $\gamma = 0.01$, $n_{eff} = 3.14\ (forGaAsP/InP)$ for all add/drop optical filters in the system. Result of the all-optical NAND gate is generated by using dark-bright soliton conversion with wavelength center at $\lambda_0 = 1.50\,\mu\text{m}$, pulse width 35 fs and input data logic "0" (dark soliton) and logic "1" (bright soliton). When the input data logic "00" is added, the obtained output optical logic is "1000" [Fig. 3]. When the input data logic "01" is added, the output optical logic "1010" [Fig. 4] is obtained. When the input data logic "10" is added, the output optical logic "1100" [Fig. 5] is obtained. When the input data logic "11" is added, we found that the output optical logic "0110" [Fig. 6] is seen.

We found that output data logic at the through port T21 is optical logic NAND Gate, the output data logic at drop port D21 and through port T22 are same with the input A and B respectively.

4. CONCLUSION

We have shown that the proposed photonic circuit can be used to create the logic NAND Gate. With the input data logic "0" (dark soliton) and logic "1" (bright soliton), the all-optical device can perform the optical logic NAND at the T21 output. This could be a potential key component in the all-optical signal processing, which is a simple and flexible scheme that can be used to perform the advanced logic switching system. This can be extended and implemented for any higher number of input digits by the proper incorporation of dark-bright soliton conversion control, based optical switches.

ACKNOWLEDGMENT

We would like to acknowledge to the Asian University Network (AUN/SEED-Net) for the financial support of one of the authors (Mr. Saysamone Soysouvanh) from National University of LAOS (NUOL), LAO PDR for his graduate study at King Mongkut's Institute of Technology Ladkrabang (KMITL), Thailand.

REFERENCES

1. Zhang, L., R. Ji, L. Jia, L. Yang, P. Zhou, Y. Tian, P. Chen, Y. Lu, Z. Jiang, Y. Liu, Q. Fang, and M. Yu, "Demonstration of directed XOR/XNOR logic gates using two cascaded microring resonators," *Opt. Lett.*, Vol. 35, No. 10, 1620–1622, 2010.
2. Ma, S., Z. Chen, H. Sun, and K. Dutta, "High speed all optical logic gates based on quantum dot semiconductor optical amplifiers," *Opt. Express*, Vol. 18, No. 7, 6417–6422, 2010.
3. Dong, J., X. Zhang, and D. Huang, "A proposal for two-input arbitrary Boolean logic gates using single semiconductor optical amplifier by picoseconds pulse injection," *Opt. Express*, Vol. 17, No. 10, 7725–7730, 2009.
4. Dong, J., X. Zhang, J. Xu, and D. Huang, "40 Gb/s all-optical logic NOR and OR gates using a semiconductor optical amplifier: Experimental demonstration and theoretical analysis," *Opt. Commun.*, Vol. 281, 1710–1715, 2008.
5. Han, B. C., J. L. Yu, W. R. Wang, L. T. Zhang, H. Hu, and E. Z. Yang, "Experimental study on all-optical half-adder based on semiconductor optical amplifier," *Optoelectron. Lett.*, Vol. 5, No. 3, 0162–0164, 2009.
6. Roy, J. N. and D. K. Gayen, "Integrated all-optical logic and arithmetic operations with the help of a TOAD-based interferometer device-alternative approach," *Appl. Opt.*, Vol. 46, No. 22, 5304–5310, 2007.
7. Khorasaninejad, M. and S. S. Saini, "All-optical logic gates using nonlinear effects in silicon-on insulator waveguides," *Appl. Opt.*, Vol. 48, No. 25, F31–F36, 2009.
8. Miyoshi, Y., K. Ileda, H. Tobioka, T. Inoue, S. Namiki, and K. I. Kitayama, "Ultrafast all-optical logic Gates using n nonlinear optical loop mirror based multi-periodic transfer function," *Opt. Express*, Vol. 16, No. 4, 2570–2577, 2008.
9. Wang, J., Q. Sun, and J. Sun, "All-optical 40 Gbit/s CSRZ-DPSK logic XOR gate and format conversion using four-wave mixing," *Opt. Express*, Vol. 17, No. 15, 12555–12563, 2009.
10. Wu, Y. D. and T. T. Shih, "New all-optical logic gates based on the local nonlinear Mach-Zehnder interferometer," *Opt. Express*, Vol. 16, No. 1, 248–257, 2008.
11. Zhang, Y., Y. Zhang, and B. Li, "Optical switches and logic gates based on self-collimated beams in two-dimensional photonic crystals," *Opt. Express*, Vol. 15, No. 15, 9287–9292, 2007.
12. Kokubun, Y., Y. Hatakeyama, M. Ogata, S. Suzuki, and N. ZaiZen, "Fabrication technologies for vertically coupled microring resonator with multilevel crossing busline and ultracompact-ringradius," *IEEE J. Sel. Top. Quantum Electron.*, Vol. 11, 4–10, 2005.

A New Novel GL Isotropic Invisible Cloak without Exceeding Light Speed Wave in Outer Layer of the Double Layer Cloak

Ganquan Xie, **Jianhua Li**, **Lee Xie**, **and Feng Xie**
GL Geophysical Laboratory, USA

Abstract— A more exciting breakthrough progress is that we discovered and propose a isotropic EM invisible cloak without exceeding light speed violation in this paper. The GL EM isotropic cloak is installed in outer layer of our double cloak. The GL isotropic invisible cloak in this paper and anisotropic invisible cloaks in our paper ArXiv 1050.3999 in May 2010 and paper in piers 2011 are complete new cloak and totally different from Pendry's cloak and Ulf's cloak in 2011. The dielectric and permeanbility of GL EM cloak in this paper are large than one. The refractive index of the GL cloak material, $n(r)$, is large than one or equal to one. The traditional geometry optical ray tracing method can not be used for explaining our GL isotropic and anisotropic cloak. When EM wave propagates in our GL cloak, an extensive Femate Principle is satisfied. Our GL isotropic cloak in this paper and anisotropic cloaks in ArXiv 1050.3999 in May 2010 are created from our unconventional GL EM cloak modeling and inversion that are proposed here. By searching in a distinctive class of the rational function of (h), $h = r - R_1$, the GL EM cloak modeling and inversion create GL EM isotropic invisible cloak class without exceeding light speed. The GL EM cloaks can be practicable by using conventional optical materials. The properties of our GL EM cloak and their proofs are presented by using GL modeling and inversion in this paper. The novel EM wave propagation and front branching in the GL cloak by GL EM modeling are presented in this paper. The EM wave front propagation in GL cloak is behind of the front in free space. At time steps $118dt$, in the GL cloak, the wave front is curved as a crescent like and propagates slower than the light in free space. At the time step $120dt$, the EM wave inside of the GL EM cloak propagates slower than light speed, moreover, its two crescent front peaks intersect at a front branching point. At the front branching point, the front is split to two fronts. The novel front branching and crescent like wave propagation are displayed in figures in this paper. All copyright and patent of the GL EM isotropic cloak in this paper and in piers 2011 and anisotropic cloaks in arXiv 1050.3999 and in piers 2011 and GL modeling and inversion methods are reserved by authors in GL Geophysical Laboratory.

1. INTRODUCTION

A more exciting breakthrough progress is that we discovered and propose a isotropic EM invisible cloak without exceeding light speed violation in this paper.The GL EM isotropic cloak is installed in outer layer of our double cloak. The new GL isotropic cloak without exceeding light speed in this paper and anisotropic cloak in [1] and [2] are complete new invisible cloak and are complete different from Ulf cloak in paper [3] in 2011 and Pendry cloak in ref. paper [14] of my paper [1]. The dielectric and permeability of GL EM cloak are large than one. The refractive index $n(r)$, is large than one or equal to one. In [3], Ulf Leonhardt refered almost all recent cloak publish papers, and wrote that "However, the realisation of electromagnetic cloaking suffers from a practical and a fundamental problem.". He cited our paper [1] "ArXiv 1050.3999v1" as his reference [35], and wrote that "the preprint [35] proposes a different method for cloaking without superluminal propagation.". The traditional geometry optical ray tracing method can not be used for explaining our GL isotropic and anisotropic cloak. When EM wave propagates in our GL cloak, an extensive Femate Principle is satisfied. The detailed full paper and references are presented our papers [2] and our GLGEO laboratory patent report. The all contents of this paper are new and patented by GLGEO laboratory, any colleague downloads and refers this paper in his research work and paper, please cite our paper as reference.

The isotropic dielectric and permeability cloaking material are proposed as (1)–(4) in this paper.

The GL EM isotropic cloak is installed in outer layer of our double cloak in Ref. [9] of [1]. The GL EM isotropic cloak in inner layer of our Double layer cloak will be presented in next PIERS 2012 in Moscow. In PIERS 2012 in MOSCOW, We will complete publish our GL isotropic EM double layer cloak. The traditional geometry optical ray tracing method can not be used for explaining our GL isotropic and anisotropic cloaks. Our GL isotropic cloak in this paper and anisotropic cloaks in ArXiv 1050.3999 in May 2010 are created from our unconventional GL EM cloak modeling and inversion that are proposed here. The GL isotropic dielectric and permeability cloaking material are proposed in this paper that is displayed in Figure 10. The electrioc wave propagation through the GL isotropic invisible cloaking without exceeding light speed are shown in Figures 1–6. The Figures 7, 8, and 9 show that the electric wave and its derivativewave are continuously propagating throught the outer boundary $r = R_2$ of the GL cloak in annular domain and have no any scattering from the cloak to disturb the the incident wave in the free space wave. All copyright and patent of the GL EM isotropic cloak in this paper and in piers 2011 and anisotropic cloaks in arXiv 1050.3999 and in piers 2011 and GL modeling and inversion methods are reserved by authors in GL Geophysical Laboratory.

The description order of this full paper is as follows: A new GL isotropic EM invisible cloak materials without exceeding light speed are proposed in Section 2. GL EM cloak modeling. and inversion and radial EM interal equations are proposed in Section 3 GL cloak properties are presented in Section 4. In Section 5, we give proof of the property 4. No scattering from GL cloak to disturb the exterior wave is proved in Section 6. In Section 7, by using GL EM modeling, we simulate full electromagnetic wave propagation through GL cloak and has no exceeding light speed propagation. The conclusion is presented in Section 8.

2. A NEW GL ISOTROPIC EM INVISIBLE CLOAK

2.1. GL EM Isotropic Cloak without Exceeding Light Speed Wave

In this paper, we propose a new class of GL cloak without exceeding light speed which is used as outer layer in our GL double layer cloak. The inner cloak of our GL double layer cloak does no exceed light speed in Ref. [9] of paper [1]. In ref. paper [10] of paper [1], we proved that there exist no Maxwell EM field can be excited by the source inside of the concealment, if the concealment is free space and cloaked by a single layer cloak. Therefore the double layer cloak is necessary for a normal EM environmental concealment. For overcoming the exceeding light speed difficulty, in this section, we propose a GL invisible cloak for outer layer of our double layer cloak [9] of [1]. In the concentric spherical annular $R_1 \leq r \leq R_2$ cloaking device, we propose an GL cloaking material which consist of the anisotropic dielectric diagonal matrix tensor $\bar{\varepsilon}$ and permeability $\bar{\mu}$ diagonal matrix tensor as follows:

$$\bar{\varepsilon} = \mathrm{diag}\left(\varepsilon_r, \varepsilon_r, \varepsilon_r\right)\varepsilon_0 \tag{1}$$

$$\bar{\mu} = \mathrm{diag}\left(\mu_r, \mu_r, \mu_r\right)\mu_0 \tag{2}$$

where ε_0 is the basic dielectric parameter in free space, ε_r is the relative isotropic dielectric in r, θ, and ϕ direction, we obtain a new class form of the GL EM isotropic invisible cloak without exceeding light speed, number. By GLGEO approving, we propose.

2.2. The GL Isotropic Invisible Cloak without Exceeding Light Speed Violation

By GL modeling, we are surprizing to discover a new GL isotropic invisible cloak without exceeding light speed violation. The isotropic dielectric and permeability are proposed in (4)–(5) and (7). When condition (23) is satisfied, the relative dielectric and permeability are large than one. The GL invisible cloak can be practicable made by the conventional isotropic optical materials.

2.3. The Isotropic Model GLM-2 EM Cloak

In this section, we propose a new GL EM isotropic invisibility GLM2 cloak as follows.

$$\varepsilon_r(r) = \mu_r(r) = \frac{R_2}{\sqrt{r-R_1}\sqrt{G_2\left(R_1,R_2,R_2-r\right)}} + \frac{4\left(R_2-2R_1\right)\sqrt{(r-R_1)}R_2}{\left(G_2\left(R_1,R_2,R_2-r\right)\right)^{\frac{3}{2}}F_2\left(R_1,R_2,\left(R_2-r\right)\right)}, \tag{3}$$

where

$$\begin{aligned} G_2(R_1,R_2,R_2-r) &= 3R_2-4R_1+\sqrt{R_2^2+16(R_2-R_1)(R_2-r)-8R_2(R_2-r)}, \\ F_2(R_1,R_2,R_2-r) &= \sqrt{R_2^2+16(R_2-R_1)(R_2-r)-8R_2(R_2-r)}, \end{aligned} \tag{4}$$

3. GL EM MODELING AND INVERSION IN SPHERICAL SYSTEM

Because the anisotropic dielectric and magnetic permeability electromagnetic parameters are radial dependence functions. In this section, we propose the three dimension and one dimension Maxwell equation in the spherical coordinate system with the anisotropic EM parameters.

3.1. Three Dimension Spherical Anisotropic Maxwell Equation

In this section, we propose the three dimension Maxwell equation in the spherical coordinate system with the anisotropic EM parameters that has been proposed in our paper [2], the following equations are patented by authors in GL geophysical Laboratory.

$$\begin{aligned}&\frac{1}{r^2}\frac{\partial}{\partial r}\frac{1}{(\mu_\theta)}\frac{\partial}{\partial r}\left(r^2\mu_r H_r\right)+\frac{1}{r^2}\frac{1}{\sin\theta}\frac{\partial}{\partial\theta}\sin\theta\frac{\partial}{\partial\theta}H_r+\frac{1}{r^2\sin^2\theta}\frac{\partial^2}{\partial\phi^2}H_r+\omega^2\varepsilon_\theta\mu_r H_r\\=&\ \frac{1}{\sin\theta}\left(\frac{\partial}{\partial\phi}(J_\theta)\right)-\frac{1}{\sin\theta}\frac{\partial}{\partial\theta}\sin\theta\,(J_\phi),\end{aligned}\tag{5}$$

$$\frac{1}{r^2}\frac{\partial}{\partial r}\frac{1}{(\varepsilon_\theta)}\frac{\partial}{\partial r}\left(r^2\varepsilon_r E_r\right)+\frac{1}{r^2}\frac{1}{\sin\theta}\frac{\partial}{\partial\theta}\sin\theta\frac{\partial}{\partial\theta}E_r+\frac{1}{r^2\sin^2\theta}\frac{\partial^2}{\partial\phi^2}E_r+\omega^2\mu_\theta\varepsilon_r E_r=S(J)\tag{6}$$

$$S(J)=(i\omega\mu_\theta)J_r-\frac{1}{r^2}\frac{\partial}{\partial r}\frac{1}{(i\omega\varepsilon_\theta)}\left(\frac{\partial}{\partial r}(r^2J_r)\right)-\frac{1}{r^2\sin\theta}\frac{\partial}{\partial r}\frac{\partial}{\partial\theta}\sin\theta\frac{rJ_\theta}{(i\omega\varepsilon_\theta)}-\frac{1}{r^2\sin\theta}\frac{\partial}{\partial r}\frac{\partial}{\partial\phi}\frac{rJ_\phi}{i\omega\varepsilon_\phi}.\tag{7}$$

$$\frac{1}{r}\frac{\partial}{\partial r}\frac{1}{(i\omega\mu_\phi)}\frac{\partial rE_\theta}{\partial r}-(i\omega\varepsilon_\theta)E_\theta=-\frac{1}{r\sin\theta}\frac{\partial}{\partial\phi}H_r+\frac{1}{r}\frac{\partial}{\partial r}\frac{1}{(i\omega\mu_\phi)}\frac{\partial E_r}{\partial\theta}+J_\theta,\tag{8}$$

$$\frac{1}{r}\frac{\partial}{\partial r}\frac{1}{(i\omega\mu_\theta)}\left(\frac{\partial}{\partial r}(rE_\phi)\right)-(i\omega\varepsilon_\theta)E_\phi=\frac{1}{r}\frac{\partial}{\partial r}\frac{1}{(i\omega\mu_\theta)\sin\theta}\left(\frac{\partial E_r}{\partial\phi}\right)+\frac{1}{r}\frac{\partial H_r}{\partial\theta}+J_\phi,\tag{9}$$

$$\frac{1}{r}\frac{\partial}{\partial r}\left(\frac{1}{(i\omega\varepsilon_\phi)}\frac{\partial}{\partial r}rH_\theta\right)-(i\omega\mu_\theta)H_\theta\frac{1}{r\sin\theta}\frac{\partial}{\partial\phi}E_r+\frac{1}{r}\frac{\partial}{\partial r}\left(\frac{1}{(i\omega\varepsilon_\phi)}\frac{\partial}{\partial\theta}H_r\right)+\frac{1}{r}\frac{\partial}{\partial r}\frac{rJ_\phi}{i\omega\varepsilon},\tag{10}$$

$$\frac{1}{r}\frac{\partial}{\partial r}\frac{1}{(i\omega\varepsilon_\theta)}\left(\frac{\partial}{\partial r}(rH_\phi)\right)-(i\omega\mu_\theta)H_\phi=\frac{1}{r}\frac{\partial}{\partial r}\frac{1}{(i\omega\varepsilon_\theta)\sin\theta}\frac{\partial}{\partial\phi}H_r-\frac{1}{r}\frac{\partial}{\partial\theta}E_r-\frac{1}{r}\frac{\partial}{\partial r}\frac{rJ_\theta}{(i\omega\varepsilon_\theta)},\tag{11}$$

where E_r is the radial component of the electric wave, E_θ is the θ component, E_ϕ is the ϕ component, H_r is the radial component of the magnetic wave, H_θ is the θ component, H_ϕ is the ϕ component.

3.2. One Dimensional Radial Maxwell Equation

In this section, we propose the one dimensional Maxwell equation in the spherical coordinate system with the anisotropic EM parameters. Suppose that the EM sources are located outside of the cloak, i.e., $r > R_2+\delta$, the $\delta > 0$, we consider the radial inhomogeneous Maxwell equations of the spherical Maxwell Equations (8)–(14). The following equations are patented by authors in GL geophysical Laboratory. The general solution of these equations, for example, is as follows,

$$H_r(r,\theta,\phi)=\sum_{l=1}^{\infty}h_l(r)\sum_{m=-l}^{l}Y_l^m(\theta,\phi).\tag{12}$$

Substitute (15) for H_r in the radial inhomogeneous Maxwell equations of the spherical Maxwell Equations (8)–(14), we have

$$\frac{1}{r^2}\frac{\partial}{\partial r}\frac{1}{(\mu_\theta)}\frac{\partial}{\partial r}\left(r^2\mu_r h_l\right)-\frac{l(l+1)}{r^2}h_l+\left(\omega^2\varepsilon_\theta\right)(\mu_r h_l)=0,\tag{13}$$

and

$$\frac{1}{r^2}\frac{\partial}{\partial r}\frac{1}{(\varepsilon_\theta)}\frac{\partial}{\partial r}\left(r^2\varepsilon_r e_l\right)-\frac{l(l+1)}{r^2}e_l+\left(\omega^2\mu_\theta\right)(\varepsilon_r e_l)=0.\tag{14}$$

3.3. New Radial EM Integral Equation

In this section, we propose a new radial electromagnetic integral equation as follows:

$$\begin{aligned}r^2\mu_r h_l(r)\ =&\ r^2\mu_{r,b}h_{l,b}+\omega^2\int_{R_1}^{R_2}r'^4(\mu_r\varepsilon_{\theta,b}\mu_{r,b}-\mu_{r,b}\varepsilon_\theta\mu_r)G_{l,b}h_l dr'-l(l+1)\int_{R_1}^{R_2}r'^2(\mu_r-\mu_{r,b})G_{l,b}h_l dr'\\&-\int_{R_1}^{R_2}\left(\frac{1}{\mu_{\theta,b}}-\frac{1}{\mu_\theta}\right)\frac{\partial}{\partial r'}\left(r'^2\mu_r h_l\right)\frac{\partial}{\partial r'}\left(r'^2\mu_{r,b}G_{l,b}\right)dr',\end{aligned}\tag{15}$$

and its dual integral equation,

$$r^2\mu_r h_l(r) = r^2\mu_{r,b}h_{l,b}(r)+\omega^2\int_{R_1}^{R_2} r'^4(\mu_r\varepsilon_{\theta,b}\mu_{r,b}-\mu_{r,b}\varepsilon_\theta\mu_r)G_l h_{l,b}dr' - l(l+1)\int_{R_1}^{R_2} r'^2(\mu_r-\mu_{r,b})G_l h_{l,b}dr'$$
$$-\int_{R_1}^{R_2}\left(\frac{1}{\mu_{\theta,b}}-\frac{1}{\mu_\theta}\right)\frac{\partial}{\partial r'}\left(r'^2\mu_{r,b}h_{l,b}\right)\frac{\partial}{\partial r'}\left(r'^2\mu_r G_l\right)dr'. \quad (16)$$

Similar integral equation and dual equation for the electric field e_l, $l = 1, 2, \ldots$. The equations are patented by authors in GL geophysical Laboratory.

3.4. New GL Modeling For Radial EM Wave Propagation

We propose a new GL modeling for radial electromagnetic wave propagation.

1 The interval $[R_1, R_2]$ is divided into sub intervals $\Omega_k = [r_k, r_{k+1}]$, such that

$$[R_1, R_2] = \bigcup_{k=0}^{N}\Omega_k = \bigcup_{k=0}^{N}[r_k, r_{k+1}]. \quad (17)$$

2 Let $h_{l,0}(r) = h_{l,b}(r), G_{l,0}(r', r) = G_{l,b}(r', r)$, by induction, suppose that $h_{l,k-1}$ and $G_{l,k-1}(r', r)$ are found in the $(k-1)$th step, we solve the triangle Green's function integral Equations (18)–(19) in the sub domain Ω_k to obtain $G_{l,k}(r', r)$.

3 Using the following new integral formula (19) in the sub domain Ω_k

$$r^2\mu_r h_{l,k}(r) = r^2\mu_{r,b}h_{l,k-1}(r)+\omega^2\int_{R_k}^{R_{k+1}} r'^4(\mu_r\varepsilon_{\theta,b}\mu_{r,b}-\mu_{r,b}\varepsilon_\theta\mu_r)G_{l,k}h_{l,k-1}dr'$$
$$-l(l+1)\int_{R_k}^{R_{k+1}} r'^2(\mu_r-\mu_{r,b})G_{l,k}h_{l,k-1}dr'$$
$$-\int_{R_1}^{R_2}\left(\frac{1}{\mu_{\theta,b}}-\frac{1}{\mu_\theta}\right)\frac{\partial}{\partial r'}\left(r'^2\mu_{r,b}h_{l,k-1}\right)\frac{\partial}{\partial r'}\left(r'^2\mu_r G_{l,k}\right)dr', \quad (18)$$

we calculate $h_{l,k}(r)$.

4 The steps (2) and (3) form a finite iterations, $k = 1, 2, \ldots, n$. The $h_{l,n}(r)$ is the solution of our GL method for radial magnetic Equation (16) with anisotropic EM material parameters. The GL method is used for solving radial electric wave Equation (17) and radial EM Equations (11)–(14). By using the new GL modeling for radial EM wave propagation,we calculated the radial electric sphere harmonic wave $E_{r,l}$ in Figures 9–11 and verified our GL cloak is invisible cloaking without exceeding light speed. New GL Modeling For Radial EM Wave Propagation is patented by GL Geopgysical Laboratory.

4. PROPERTIES OF GL INVISIBLE CLOAK

In previous section, we proposed the GL class of the EM invisible cloak without exceeding light speed wave. The GL cloak properties are presented in this section, uous.

Property 1: Assume that the GL relative cloak material $\varepsilon_r(r)$ and $\mu_r(r)$ are defined by (3) and (5) in the cloak, $\varepsilon_r(r) = 1$ and $\mu_r(r) = 1$ in the free space and concealment, then the relative radial dielectric parameter $\varepsilon_r(r)$ and magnetic permeability $\mu_r(r)$ are continuous in domain $r > R_1$, in particular, cross $r = R_2$, we have

$$\varepsilon_r(R_2) = \mu_r(R_2) = 1. \quad (19)$$

Property 2: Under the conditions in property 1 and if there is the additional assumption,

$$R_1 = 3R_2/8 \quad (20)$$

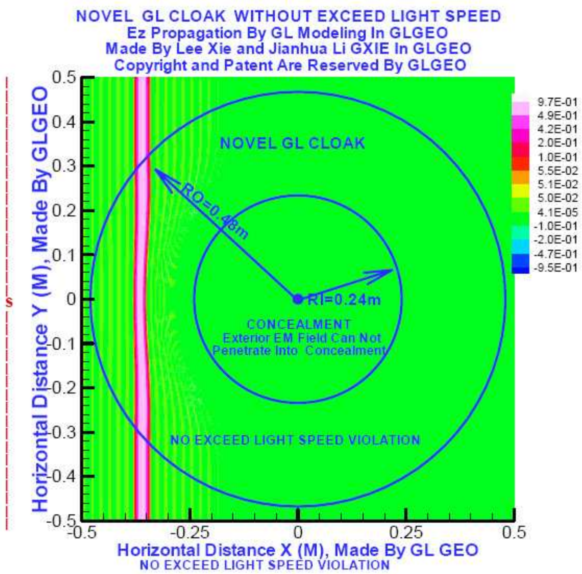

Figure 1: (color online) Electric wave E_z propagation at time step $48dt$.

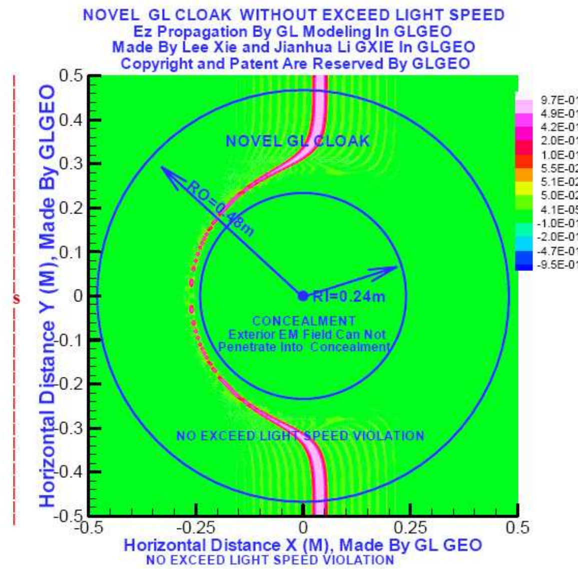

Figure 2: (color online) Electric wave E_z propagation at time step $88dt$.

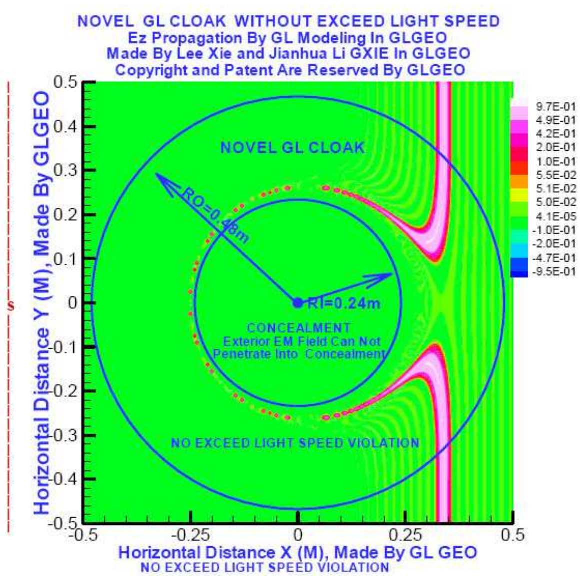

Figure 3: (color online) Electric wave E_z propagation at time step $118dt$.

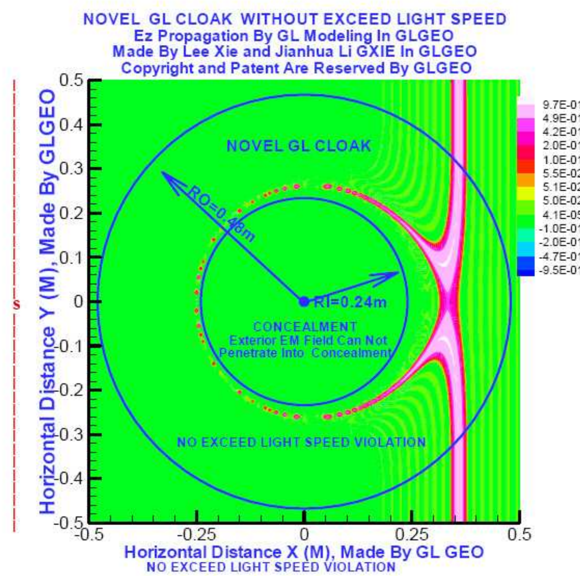

Figure 4: (color online) Electric wave E_z propagation at time step $120dt$.

then the first derivative of the dielectric and permeability are continuous in domain $r > R_1$, in particular, cross the outer boundary $r = R_2$,

$$\frac{d}{dr}\varepsilon_r(R_2) = \frac{d}{dr}\mu_r(R_2) = 0. \tag{21}$$

Property 3: Under the conditions in property 1 and if there is the additional assumption (21) is satisfied, then

$$\varepsilon_r(r) = \mu_r(r) = \geq 1, \quad \text{on } R_1 \leq r \leq R_2. \tag{22}$$

The radial dielectric and permeability are large than one.

Property 4: Under the conditions of the property 1 and 3, if there is the additional assumption (23), there exist EM wave $E(r,\theta,\phi)$ and $H(r,\theta,\phi)$ satisfy the Maxwell Equation (1), moreover, the grading $\nabla E(r,\theta,\phi)$ and $\nabla H(r,\theta,\phi)$ are continuous in the domain $r > R_1$, in particular, the exterior EM wave $E(r,\theta,\phi)$, $H(r,\theta,\phi)$ and their grading $\nabla E(r,\theta,\phi)$ and $\nabla H(r,\theta,\phi)$ are continuous

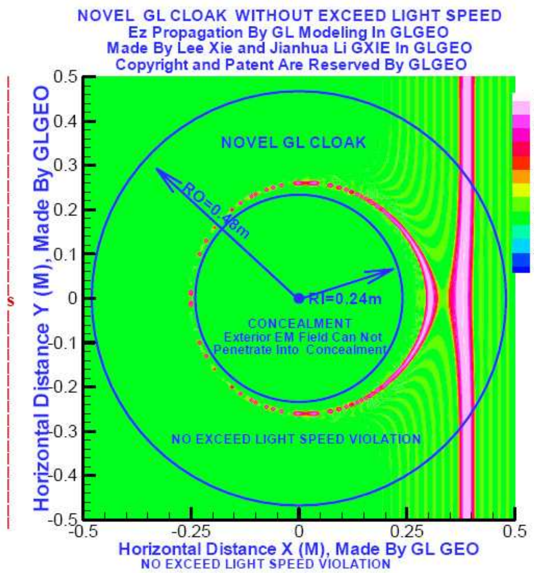

Figure 5: (color online) Electric wave E_z propagation at time step $123dt$.

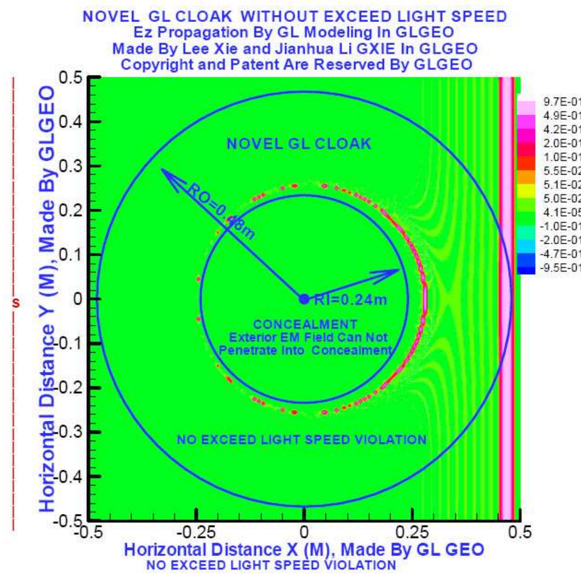

Figure 6: (color online) Electric wave E_z propagation at time step $131dt$.

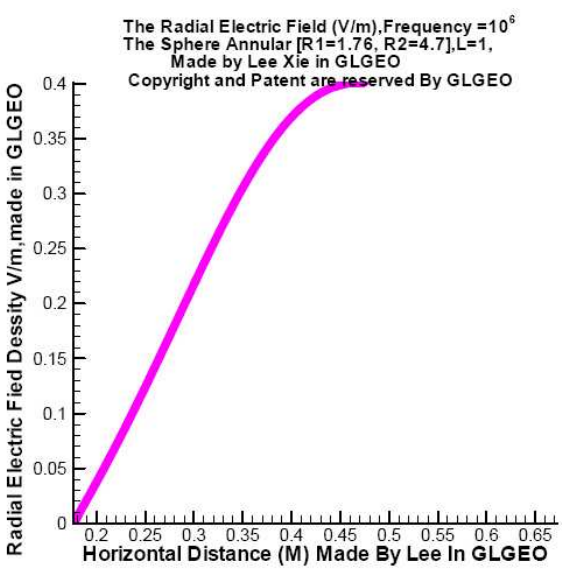

Figure 7: (color online) The Radial Electric Field (V/m), Frequency $=10^6$ Hz The Sphere Annular domain $[R_1 = 1.76,\ R_2 = 4.7]$, sphere harmonic number $L = 1$.

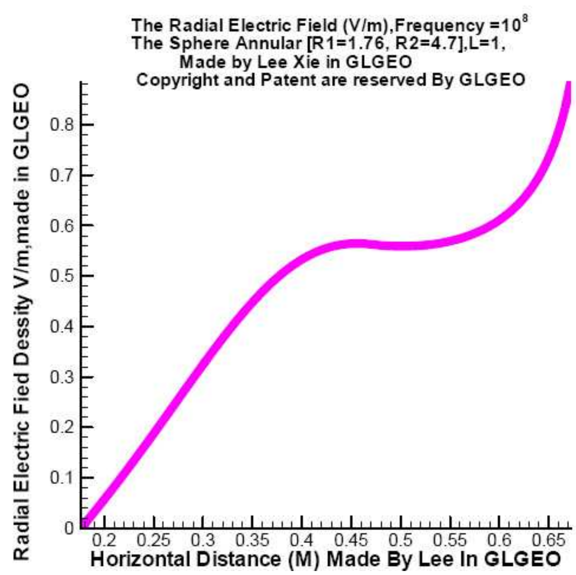

Figure 8: (color online) The Radial Electric Field (V/m), Frequency $=10^8$ Hz The Sphere Annular domain $[R_1 = 1.76,\ R_2 = 4.7]$, sphere harmonic number $L = 1$.

cross the outer boundary $r = R_2$. Therefore, there is no scattering wave from the cloak to disturb the exterior EM wave.

Property 5: Under the conditions of the property 4, then the EM wave propagation $E(r, \theta, \phi)$ and $H(r, \theta, \phi)$ can not penetrate into the concealment.

Property 6: Under the conditions of the property 4, we have the refractive index

$$N(r) = \sqrt{\varepsilon_r(r)\mu_r(r)} \geq 1, \tag{23}$$

in the all cloak domain $R_1 \leq r \leq R_2$.

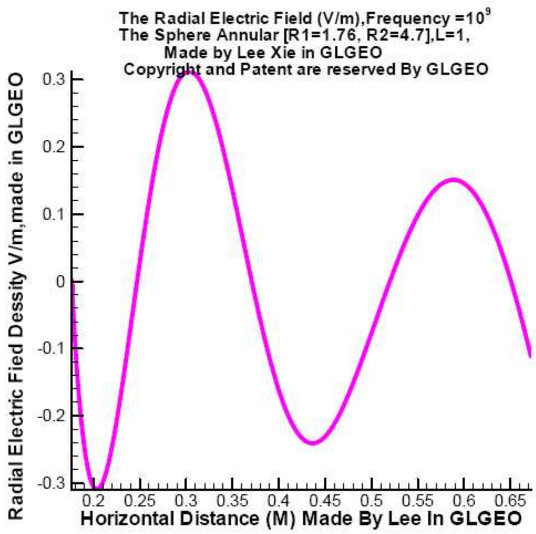

Figure 9: (color online) The Radial Electric Field (V/m), Frequency $=10^9$ Hz The Sphere Annular domain $[R_1 = 1.76,\ R_2 = 4.7]$, sphere harmonic number $L = 1$.

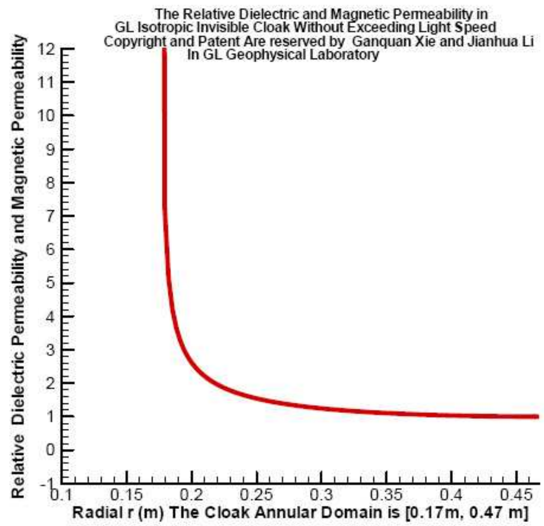

Figure 10: (color online) The isotropic GL invisible cloaking materials relative dielectric and magnetic permeability distribution in the sphere annular domain $[R_1 = 1.76,\ R_2 = 4.7]$.

Property 7: Under the conditions of the property 5, when the source and receiver are located outside of cloak, then

$$\omega^2 \int_{R_1}^{R_2} r'^4(\mu_r\varepsilon_{\theta,b}\mu_{r,b} - \mu_{r,b}\varepsilon_\theta\mu_r)G_{l,b}h_l dr' - l(l+1)\int_{R_1}^{R_2} r'^2(\mu_r - \mu_{r,b})G_{l,b}h_l dr'$$
$$-\int_{R_1}^{R_2}\left(\frac{1}{\mu_{\theta,b}} - \frac{1}{\mu_\theta}\right)\frac{\partial}{\partial r'}\left(r'^2\mu_r h_l\right)\frac{\partial}{\partial r'}\left(r'^2\mu_{r,b}G_{l,b}\right)dr' = 0, \tag{24}$$

i.e., there is no scattering wave from the GL EM cloak to disturb the incident EM wave in the free space

$$h_l(r) = h_{l,b} \tag{25}$$

when the source is located outside of cloak, and the receiver is located inside of the concealment then

$$r^2\mu_{r,b}h_{l,b} + \omega^2 \int_{R_1}^{R_2} r'^4(\mu_r\varepsilon_{\theta,b}\mu_{r,b} - \mu_{r,b}\varepsilon_\theta\mu_r)G_{l,b}h_l dr' - l(l+1)\int_{R_1}^{R_2} r'^2(\mu_r - \mu_{r,b})G_{l,b}h_l dr'$$
$$-\int_{R_1}^{R_2}\left(\frac{1}{\mu_{\theta,b}} - \frac{1}{\mu_\theta}\right)\frac{\partial}{\partial r'}\left(r'^2\mu_r h_l\right)\frac{\partial}{\partial r'}\left(r'^2\mu_{r,b}G_{l,b}\right)dr' = 0, \tag{26}$$

i.e., the exterior EM wave can not propagate penetrate into the concealment, the concealment is invisible room, inside of the concealment,

$$h_l = 0. \tag{27}$$

Therefore GL EM cloak is complete cloak,

The relative component $\varepsilon_r > 1$ and $\mu_r > 1$ are large than one in whole GL EM cloak domain. The refractive index $N > 1$ in the whole GL EM cloak. Therefore GL EM cloak is practiable complete cloak without exceeding light speed wave through it.

5. THE PROOF OF THE PROPERTY 4

To calculate $\frac{d}{dr}G_2(R_1, R_2, R_2 - R_2)$ and using condition (23), $-3R_2 + 8R_1 = 0$,, we have

$$\frac{d\varepsilon_r(R_2)}{dr} = \frac{d\mu_r(R_2)}{dr} = \frac{R_2}{(2(R_2 - R_1))^2}\left(-\frac{1}{2} + \frac{3}{16} + \frac{5}{16}\right) = 0 \tag{28}$$

The formula (33) is the formula (26) in property 4, therefore, we proved that the derivative of the transverse dielectric and magnetic permeability is continuous.

6. NO SCATTERING FROM GL CLOAK TO DISTURB THE EXTERIOR WAVE

6.1. The Continuous of the Solution of ODE with the Variable Coefficient

$$y'' + p(x)y' + q(x)y = 0, \tag{29}$$

$$\frac{d}{dx}\begin{bmatrix} y \\ y_1 \end{bmatrix} = \begin{bmatrix} & 1 \\ -q(x) & -p(x) \end{bmatrix}\begin{bmatrix} y \\ y_1 \end{bmatrix}, \tag{30}$$

Therefore, when $p(x)$ and $q(x)$ are continuous or integrable, the solution $y(x)$ of the second differential Equation (34) and its derivative function $y'(x)$ are continuous.

6.2. No Scattering from GL Cloak to Disturb the Exterior Wave

The radial magnetic Equation (16) and the radial electric Equation (17) can be translated to the second linear differential Equation (34).

$$p(r) = P(\varepsilon_r(r), \frac{d}{dr}\varepsilon_r(r), \mu_r(r), \frac{d}{dr}\mu_r(r)) \tag{31}$$

$$q(r) = Q(\varepsilon_r(r), \frac{d}{dr}\varepsilon_r(r), \mu_r(r), \frac{d}{dr}\mu_r(r)), \tag{32}$$

In our patent report in http://www.glgeo.com, we proved the GL EM cloak material components and their derivative $\varepsilon_r(r), \frac{d}{dr}\varepsilon_r(r), \mu_r(r), \frac{d}{dr}\mu_r(r)$ are continuous, from (37) and (38) we know the $p(x)$ and $q(x)$ are continuous. Therefore the radial magnetic wave h_l and radial electric wave e_l and their derivative functions are continuous. From the formula (15), we know that magnetic wave $H_r(r)$ and electric wave $E_r(r)$ and their derivative functions are continuous cross the outer boundary $r = R_2$. Therefore, no scattering wave from the GL EM cloak to disturb the exterior incident wave in free space. We can prove that when in the cloak, r going to R_1, the magnetic wave $H_r(r)$ and electric wave $E_r(r)$ and their derivative functions are continuous decay going to zero. The exterior EM wave can not be propagate penetrate into the concealment.

6.3. No Scattering from Coordinate Transform Cloak to Disturb the Exterior Wave

Assume that a cloak is made by coordinate transform, to substitute the coordinate transform $r = f(r')$ into the EM equations in the spherical system (10) and (11), immediately, we obtain the EM equation in cloak media with anisotropic permittivity and permeability $\varepsilon_r = \mu_r = (r'/r)^2 dr/dr'$, and $\varepsilon_\theta = \mu_\theta = dr'/dr$. However, blow up coordinate transform cloak has "exceeding light speed" physical difficulty.

7. FULL ELECTROMAGNETIC WAVE PROPAGATION THROUGH GL CLOAK AND HAS NO EXCEEDING LIGHT SPEED PROPAGATION

In this section, using the GL EM modeling method, we simulate full electromagnetic wave propagation through GL cloak and has no exceeding light speed propagation. The GL cloak materials dielectric and maganetic permeability are filling in the 3D sphere annular $R_1 \leq r \leq R_2$, the relative dielectric and maganetic permeability is shown in Figure 10, where $R_1 = 0.17625$ meter, $R_2 = 0.47$ meter. Let $E_{z,b}$ denote the background electric intensity plane wave at source plane $x = x_s$, $x = -0.83$ meter, in the left side outside of the cloak in free space.

$$E_{z,b}(x, x_s, t) = \delta(x - x_s)\delta(t). \tag{33}$$

The incident electric plane wave is denoted by vertical red line through red S in the figures in this paper. Figure 1, at time step $48dt$, Figure 2, at time step $88dt$, Figure 3, at time step

$118dt$,show than the electric wave E_z inside of the GL EM cloak $R_1 \leq r \leq R_2$ propagates slower than light speed. Figure 4 shows that at time step $120dt$, electric wave E_z inside of the GL EM cloak $R_1 \leq r \leq R_2$ propagates slower than light speed. The upside and downside parts of curved CRESCENT electric wave front are intersected at a branching point. These branching points form a 2D subsurface which depends on the source location. Figure 5 shows that at time step $123dt$, E_z electric wave front is split to two wave fronts, The outgoing front propagates forward to left and going to outer boundary $r = R_2$. The attractive front propagates and shrinks to the inner boundary.

The vertical red dashing line cross red S denotes the incident electric plane wave $E_{z,b}$ which is located in the left of the cloak. The front branching point is located in right of the concealment. In Figure 6, at time step $131dt$, the outgoing front of the electric wave E_z propagates on the outer boundary $r = R_2$, the attracting front rapid decay to zero and closes to the inner boundary of the cloak, $r = R_1$. Outgoing front propagates continuously forward to outer boundary $r = R_2$. The attractive front rapidly decay propagates to the inner boundary. The two wave front propagate without exceeding light speed. Using GL EM modeling, when frequency is 1.0^6, 1.0^8, 1.0^9 Hz and harmonic wave number $l = 1$, the electric radial sphere harmonic wave, $E_{z,l}$ is shown in Figure 9, Figure 10, and Figure 11, respectively.

8. THE CONCLUSION

By the GL invisible cloak class properties in Section 4 and full EM propagation through the GL EM cloak, our GL EM invisible cloak without exceeding light speed is verified. The Figures 7, 8, and 9 show that the electric wave and its derivativewave are continuously propagating through the outer boundary $r = R_2$ of the GL cloak in annular domain and have no any scattering from the cloak to disturb the the incident wave in the free space wave. These figures show that the electric wave and its derivative wave are continuously propagating decay to zero in the inner boundary $r = R_1$. "The EM wave can not propagate penetrate into the concealment" that cloaking property is verified. The all contents of this paper are new and patented by GLGEO laboratory, any colleague downloads and refers this paper in his research work and paper, please cite our paper as reference.

ACKNOWLEDGMENT

We wish to acknowledge the support of the GL Geophysical Laboratory.

REFERENCES

1. Xie, G., J. Li, L. Xie, and F. Xie, arXiv:1005.3999.
2. Xie, G., J. Li, L. Xie, and F. Xie, "A new GL anisotropic and isotropic invisible cloak without exceeding light speed violation," *PIERS Proceedings*, 870–877, Suzhou, China, September 12–16, 2011; *Progress in Some Fields of Mathematical Sciences*, 56–69, Chinese Sciences Press, ISBN 9758-7-03-032787-1.
3. Perczel, T. T. and U. Leonhardt, arXiv:1105.0164.

Lossy Gradient Index Metamaterial with General Periodic Permeability and Permittivity: The Case of Constant Impedance throughout the Structure

M. Dalarsson[1], **M. Norgren**[1], **and Z. Jaksic**[2]

[1]Division of Electromagnetic Engineering, School of Electrical Engineering
Royal Institute of Technology, Stockholm SE-100 44, Sweden
[2]IHTM — Institute of Microelectronic Technologies and Single Crystals
University of Belgrade, Njegoševa 12, Belgrade 11000, Serbia

Abstract— We utilize an exact analytical approach to investigate the electromagnetic wave propagation across an infinite metamaterial composite with general periodic gradient effective permittivity and permeability. A general analytic solution for the field distribution is obtained for an arbitrary periodic variation of complex refractive index across the structure. The calculation is done for the case of constant impedance across the structure. Arbitrary temporal dispersion and losses are allowed and the model is generally applicable to inhomogeneous and anisotropic media simultaneously containing positive and negative refractive index constituents as long as the effective medium approximation is valid.

1. INTRODUCTION

Electromagnetic metamaterials (MM) in electromagnetics and (nano)plasmonics are defined as artificial composites with electromagnetic properties not readily found in nature. A special class of MMs are the negative refractive index metamaterials (NRM or NIM), also known as the left-handed materials (LHM). They were theoretically described by Veselago in 1967 [1], but about three decades passed before their practical implementations were proposed by Pendry [2, 3].

LHM are typically produced using subwavelength "particles" or "atoms" with negative effective relative permittivity and permeability as their structural units. The first proposed LHM particles were split-ring resonators and nanowires, their composites simultaneously furnishing negative permeability and permittivity [3]. Split-ring resonators and wire media are still widely used in the microwave domain and are now well understood, but many other particles such as complementary split-ring resonators [4], cut-wire pairs and plate pairs [5] and double fishnets [6–8] have been investigated. The first experimental confirmation of a left-handed material was published in 2001 [9]. Until today, experimental fishnet-type LHM for the visible range have been fabricated and described [10].

The novel and often counter-intuitive properties of the LHM, which include negative index of refraction (and, hence, negative phase velocity), inverse Doppler effect, radiation tension instead of pressure, etc. [11, 12] resulted in numerous proposed applications. These applications include superlenses and hyperlenses that enable imaging far below the diffraction limit [13, 14], resonant cavities and waveguides with geometrical dimensions even orders of magnitude smaller than the operating wavelength [15], as well as invisibility cloaks and transformation optics [16].

A majority of cases consider structures with constant refractive index within the MM structure and abrupt interfaces with the surrounding positive index material ("right-handed" media, RHM). There is however a practical interest for metamaterials with spatially varying refractive index and with gradual transition from the RHM to LHM and vice versa, since many real-world applications would benefit from such structures. Graded refractive index is interesting for transformation optics and hyperlenses [17], and a class of the invisibility cloaks using spherically graded MM has been described [18]. Various other proposed applications of graded metamaterials include beam shaping and directing, enhancement of nonlinear effects [19], superlenses [20], etc..

As far as the authors are informed, the first paper dedicated to gradient refractive index LHM was published in 2005 [21]. Analytical approaches to graded index metamaterial structures are of special interest, since they ensure fast, simple and direct routes to the determination of the field distribution and the calculation of the scattering parameters within such materials. Some publications include [22–26]. In this paper, we present an exact analytical solution of Helmholtz equation for the propagation of electromagnetic waves through a lossy gradient metamaterial structure with periodic permeability and permittivity for the case of constant impedance throughout the structure.

2. PROBLEM FORMULATION

We start our analysis from Maxwell's equations, and we search for fields that are periodic in time according to an $\exp(i\omega t)$ dependency. Furthermore, we assume that the effective medium approximation can be made and that the materials are isotropic, so that their optical properties can be described by the effective dielectric permittivity and the effective magnetic permeability. For most metamaterials, the effective medium assumption is valid, because their constituent elements are on the subwavelength level.

The geometry of the problem can be found in Fig. 1 of [27]. An implementation of a periodic gradient index LHM metamaterial is shown in Fig. 2 of [27]. To this purpose a two-dimensional array of holes is drilled through a metal-dielectric-metal sandwich, furnishing a double fishnet medium with negative effective value of permittivity and permeability which may vary according to a suitably chosen periodic law.

The electric field is directed along the y-axis, $\mathbf{E}(\mathbf{r}) = E_y\mathbf{e}_y = E(x)\mathbf{e}_y$, whereas the magnetic field is directed along the z-axis, $\mathbf{E}(\mathbf{r}) = E_z\mathbf{e}_z = H(x)\mathbf{e}_z$. The propagation direction of the wave is along the x-axis. Since the fields depend only on the x-coordinate, the equations for $E(x)$ and $H(x)$ are given by [27]

$$\frac{d^2E}{dx^2} - \frac{1}{\mu}\frac{d\mu}{dx}\frac{dE}{dx} + \omega^2\mu\epsilon E(x) = 0, \qquad \frac{d^2H}{dx^2} - \frac{1}{\epsilon}\frac{d\epsilon}{dx}\frac{dH}{dx} + \omega^2\mu\epsilon H(x) = 0. \tag{1}$$

3. SOLUTIONS OF THE FIELD EQUATIONS

Let us consider an inhomogeneous medium for which the real parts of the effective permittivity and permeability vary according to an arbitrary periodic function $f(x)$. We use the functions

$$\epsilon(\omega, x) = -\epsilon_0\epsilon_R(\omega)f(x) - i\epsilon_0\epsilon_I(\omega), \qquad \mu(\omega, x) = -\mu_0\mu_R(\omega)f(x) - i\mu_0\mu_I(\omega). \tag{2}$$

Note that for the material to be passive, it follows that $\epsilon_I(\omega) > 0$ and that $\mu_I(\omega) > 0$. In order to obtain a constant wave impedance throughout the structure, we require that the real and imaginary parts of the effective permittivity and permeability satisfy the following condition

$$\frac{\epsilon_I(\omega)}{\epsilon_R(\omega)} = \frac{\mu_I(\omega)}{\mu_R(\omega)} = \beta. \tag{3}$$

Thus the functions (2) become

$$\epsilon(\omega, x) = -\epsilon_0\epsilon_R(\omega)[f(x) + i\beta], \qquad \mu(\omega, x) = -\mu_0\mu_R(\omega)[f(x) + i\beta]. \tag{4}$$

Except for the condition (3) our method allows for arbitrary temporal dispersion. Note that the wave impedance

$$Z = Z_0Z_R(\omega) = \sqrt{\frac{\mu_0\mu_R(\omega)}{\epsilon_0\epsilon_R(\omega)}} \quad \text{with} \quad Z_0 = \sqrt{\frac{\mu_0}{\epsilon_0}}, \; Z_R(\omega) = \sqrt{\frac{\mu_R(\omega)}{\epsilon_R(\omega)}}, \tag{5}$$

is constant throughout the entire structure. As a result, there is no reflection on the graded interfaces between the two materials. The two differential Eq. (1) allow for the remarkably simple exact solutions with appropriate boundary conditions, given by

$$E(x) = E_0e^{-k\beta x}\exp[-ikF(x)], \qquad H(x) = H_0e^{-k\beta x}\exp[-ikF(x)], \tag{6}$$

where

$$F(x) = \int^x f(\xi)d\xi. \tag{7}$$

In the solutions (6), E_0 and H_0 are the amplitudes of the electric and magnetic fields at $x = 0$, and $k^2 = -\omega^2\epsilon_0\mu_0\epsilon_R(\omega)\mu_R(\omega)$. We note here that for the simplest case of a periodic function $f(x) = \cos(\pi a/x)$, where a is the thickness of the individual RHM and LHM layers, the results (6) are reduced to the results in reference [27] as a special case. The field amplitudes are related by $E_0 = Z_0Z(\omega)H_0$. The choice of the periodic function $f(x) = \cos(\pi a/x)$ in [27] does not include the possibility to change the steepness of the transitions between the layers of RHM and LHM materials.

However, the present model allows for an arbitrary choice of the periodic function $-1 \le f(x) \le +1$, where we can vary the steepness of the transitions between the layers of RHM and LHM materials in an arbitrary way. However, for most practical applications the natural choice of the transition profile is a linear one. Furthermore we note that there are no restrictions on the thickness of RHM and LHM layers in the present model, i.e., they can be chosen as a and b respectively such that $a \neq b$. However, in this paper we assume that the periodic function $f(x)$ is an even function with period $2a$ (thickness of both LHM and RHM layers is equal to a), such that it can be represented by the Fourier series with cosine terms only

$$f(x) = \sum_{m=0}^{\infty} \alpha_m \cos\left(\frac{m\pi}{a}x\right). \tag{8}$$

The solutions (6) then become

$$\begin{aligned} E(x) &= E_0 e^{-k\beta x} \exp\left[-i\frac{ka}{\pi}\sum_{m=0}^{\infty}\frac{\alpha_m}{m}\sin\left(\frac{m\pi}{a}x\right)\right], \\ H(x) &= H_0 e^{-k\beta x} \exp\left[-i\frac{ka}{\pi}\sum_{m=0}^{\infty}\frac{\alpha_m}{m}\sin\left(\frac{m\pi}{a}x\right)\right] \end{aligned} \tag{9}$$

In an RHM layer, we obtain for $x \to 0$ that

$$E(x) = E_0 e^{-k\beta x} e^{-ikx}, \quad H(x) = H_0 e^{-k\beta x} e^{-ikx}, \tag{10}$$

where we used the property of the Fourier coefficients

$$\sum_{m=0}^{\infty} \alpha_m = 1, \tag{11}$$

valid for our assumptions on the periodic function $f(x)$. This results in the correct time-domain fields in the RHM layer

$$E(x) = E_0 e^{-k\beta x}\cos(\omega t - kx), \quad H(x) = H_0 e^{-k\beta x}\cos(\omega t - kx), \tag{12}$$

In an LHM layer, we obtain for $x \to (a/2)_+$ that

$$E(x) = E_0 e^{-k\beta x} e^{+ikx}, \quad H(x) = H_0 e^{-k\beta x} e^{+ikx}, \tag{13}$$

This results in the correct time-domain fields in the LHM layer

$$E(x) = E_0 e^{-k\beta x}\cos[\omega t - (-k)x], \quad H(x) = H_0 e^{-k\beta x}\cos[\omega t - (-k)x], \tag{14}$$

From the results (12) and (14), it follows that the asymptotic wavevector in the RHM layers is $\mathbf{k}_{RHM} = +k\mathbf{e}_x$, i.e., the wave propagates in the $+x$-direction. On the other hand the asymptotic wavevector in the LHM layers is, i.e., the wave propagates in the $-x$-direction. However, the energy flux (the Poynting vector) is still in the $+x$-direction in both media.

4. THE LINEAR TRANSITION PROFILE

Here we consider the case of the most general linear transition between the RHM and LHM layers. It can be described by the periodic function with the spatial period of $2a$, as follows

$$f(x) = \left\{ \begin{array}{ll} -1, & -a < x < -a/2 - d/2 \\ (2x+a)/d, & -a/2 - d/2 < x < -a/2 + d/2 \\ +1, & -a/2 + d/2 < x < +a/2 - d/2 \\ -(2x-a)/d, & +a/2 - d/2 < x < +a/2 + d/2 \\ -1, & +a/2 + d/2 < x < +a \end{array} \right\}, \tag{15}$$

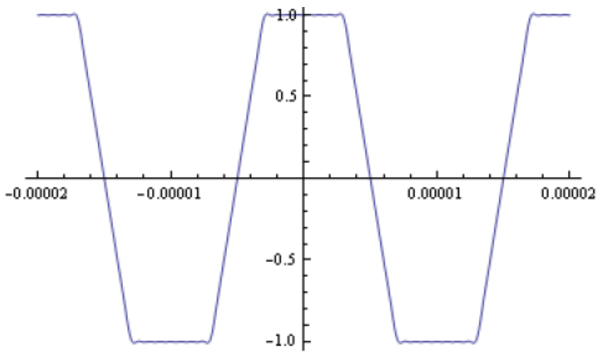

(a)

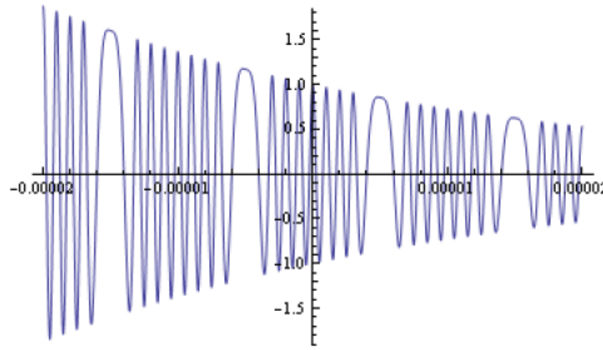

(b)

Figure 1: (a) Periodic profile with linear transition, as a function of x with $a = 10^{-5}$ m and $d = 4 \times 10^{-6}$ m. (b) Analytical results for the real part of the electric field $E(x)$ in a periodic profile with linear transition as a function of x, with $E_0 = 1$, $a = 10^{-5}$ m, $d = 4 \times 10^{-6}$ m, $k = 2\pi/(10^{-6})$ m and $\beta = 5 \times 10^{-3}$.

where d $(0 < d < a)$ is the width of the linear transition layer. This function can be represented by the Fourier series of the form

$$f(x) = \frac{8a}{\pi^2 d} \sum_{m=0}^{\infty} \frac{(-1)^m}{(2m+1)^2} \sin\left[(2m+1)\frac{\pi d}{2a}\right] \cos\left[(2m+1)\frac{\pi x}{a}\right]. \tag{16}$$

The first of the solutions (6) for the electric field $E(x)$ then becomes

$$E(x) = E_0 e^{-k\beta x} \exp\left[-i\frac{ka}{\pi}\frac{8a}{\pi^2 d} \sum_{m=0}^{\infty} \frac{(-1)^m}{(2m+1)^3} \sin\left[(2m+1)\frac{\pi d}{2a}\right] \sin\left[(2m+1)\frac{\pi x}{a}\right]\right], \tag{17}$$

with the analogous result for the magnetic field $H(x)$.

An example of the periodic profile function $f(x)$ with linear transition, as a function of x with $a = 10^{-5}$ m and $d = 4 \times 10^{-6}$ m, keeping the terms with $m \leq 12$ of the series in Eq. (16), is presented in Fig. 1(a). The exact analytical solution for the real part of the electric field $E(x)$ in the case of a linear transition profile, keeping the terms with $m \leq 7$ of the series in Eq. (17), is presented in the Fig. 1(b).

Using here

$$\lim_{d \to 0} \frac{2a}{(2m+1)\pi d} \sin\left[(2m+1)\frac{\pi d}{2a}\right] = 1, \tag{18}$$

we see that the results (16)–(17) are readily reduced to the corresponding results, for the abrupt transition. Thus, in the present model, we can vary the parameter d from very slow linear transitions $(d = a)$ to the abrupt transitions $(d = 0)$ without any approximations. The exact analytical result for $E(x)$ (17) and its analogous counterpart for $H(x)$ remain valid for all values of d $(0 \leq d \leq a)$.

5. CONCLUSION

We have presented an exact analytical solution to Helmholtz equation for a case of lossy periodic structure with graded permittivity and permeability profile changing according to an arbitrary periodic function along the direction of propagation. The general analytical solution is applicable in situations when the effective medium approximation is valid.

A special case of matched impedance throughout the structure was analyzed, with the effective permittivities and permeabilities having opposite signs and equal absolute values. Other than that, the model allows for arbitrary temporal dispersion and arbitrary losses and is thus usable to describe various inhomogeneous and anisotropic graded index metamaterial media. As an example, the case of linear transition profile between two materials (including the abrupt transition as a special case when $d \to 0$) has been studied. Important generalizations of the approach would include its expansion to various 2D and 3D dependencies and the case of arbitrary profiles for permittivity and permeability.

ACKNOWLEDGMENT

The work of Z. J. was funded by the Serbian Ministry of Science and Technology within the project TR-32008.

REFERENCES

1. Veselago, V. G., *Sov. Phys. Uspekhi*, No. 10, 509–514, 1968.
2. Pendry, J. B., A. J. Holden, D. J. Robbins, and W. J. Stewart, *J. Phys. Condens. Mat.*, No. 10, 4785–4809, 1998.
3. Pendry, J. B., A. J. Holden, D. J. Robbins, and W. J. Stewart, *IEEE T. Microw. Theory*, No. 47, 2075–2084, 1999.
4. Falcone, F., T. Lopetegi, M. A. G. Laso, J. D. Baena, J. Bonache, M. Beruete, F. Martiacute, and M. Sorolla, *Phys. Rev. Lett.*, No. 93, 197401, 2004.
5. Dolling, G., C. Enkrich, M. Wegener, J. F. Zhou, C. M. Soukoulis, and S. Linden, *Opt. Lett.*, No. 30, 3198–3200, 2005.
6. Zhang, S., W. Fan, N. C. Panoiu, K. J. Malloy, R. M. Osgood, and S. R. J. Brueck, *Phys. Rev. Lett.*, No. 95, 1–4, 2005.
7. Kafesaki, M., I. Tsiapa, N. Katsarakis, T. Koschny, C. M. Soukoulis, and E. N. Economou, *Phys. Rev. B*, No. 75, 235114, 2007.
8. Valentine, J., S. Zhang, T. Zentgraf, E. Ulin-Avila, D. A. Genov, G. Bartal, and X. Zhang, *Nature*, No. 455, 376–379, 2008.
9. Shelby, R. A., D. R. Smith, and S. Schultz, *Science*, No. 292, 77–79, 2001.
10. Xiao, S., U. K. Chettiar, A. V. Kildishev, V. P. Drachev, and V. M. Shalaev, *Opt. Lett.*, No. 34, 3478–3480, 2009.
11. Cai, W. and V. Shalaev, *Optical Metamaterials: Fundamentals and Applications*, Springer, Dordrecht, 2009.
12. Ramakrishna, S. A. and T. M. Grzegorczyk, *Physics and Applications of Negative Refractive Index Materials*, SPIE Press Bellingham, WA & CRC Press, Taylor & Francis Group, Boca Raton FL, 2009.
13. Pendry, J. B., *Phys. Rev. Lett.*, No. 85, 3966–3969, 2000.
14. Fang, N., H. Lee, C. Sun, and X. Zhang, *Science*, No. 308, 534–537, 2005.
15. Engheta, N., *IEEE Anten. Wirel. Propag. Lett.*, No. 1, 10–13, 2002.
16. Pendry, J. B., D. Schurig, and D. R. Smith, *Science*, No. 312, 1780–1782, 2006.
17. Jacob, Z., L. V. Alekseyev, and E. Narimanov, *Opt. Express*, No. 14, 8247–8256, 2006.
18. Cai, W., U. K. Chettiar, A. V. Kildishev, and V. M. Shalaev, *Nat. Photonics*, No. 1, 224–227, 2007.
19. Fung, T. H., L. L. Leung, J. J. Xiao, and K. W. Yu, *Opt. Commun.*, No. 282, 1028–1031, 2009.
20. Ramakrishna, S. A. and J. B. Pendry, *Phys. Rev. B*, No. 69, 115115, 2004.
21. Smith, D. R., J. J. Mock, A. F. Starr, and D. Schurig, *Phys. Rev. E*, No. 71, 036609, 2005.
22. Pinchuk, A. O. and G. C. Schatz, *J. Opt. Soc. Am. A*, No. 24, A39–A44, 2007.
23. Litchinitser, N. M., A. I. Maimistov, I. R. Gabitov, R. Z. Sagdeev, and V. M. Shalaev, *Opt. Lett.*, No. 33, 2350–2352, 2008.
24. Dalarsson, M. and P. Tassin, *Opt. Express*, No. 17, 6747–6752, 2009.
25. Dalarsson, M., Z. Jaksic, and P. Tassin, *J. Optoel. Biomed. Mat.*, No. 1, 345–352, 2009.
26. Dalarsson, M., Z. Jaksic, and P. Tassin, *Microwave Rev.*, No. 15, 1–5, 2009.
27. Dalarsson, M., M. Norgren, and Z. Jaksic, *J. Nanophoton.*, No. 5, 051804, 2011.

High Energy Particals and Nanostructures Physics

D. Bajalan
ret., Austria

Abstract— It is possible to produce nano-magnetic regions of magnetic nano- structures on thin film with high resolution lithography methods. The suitable selection of resist (positive or negative tone) is important, using anti reflection coat is essential to obtain well-defined nano mask structures on the thin film. Irradiation is the last fabrication stage to transport the nano mask structure to the magnetic layer of the thin films. The changes in the magnetic properties of the thin film multi-layer produces magnetic dots in the regions that were protected through the mask (with high H_c). The regions on the thin films which are irradiated do not show special magnetic properties. They offer themselves as gap between two dots only.

1. INTRODUCTION

Technology road maps are predicting minimum feature sizes in manufacturing approaching nm length [1]. Lithography is a technological process step in microelectronics, in which the patterns are drawn into a recording medium (resist) into which the desired device pattern is written (the mask) by using photons, electrons, or ions. Various methods such as electron beam lithography, X-ray lithography, and interference have been used to pattern magnetic nano-structures [2]. Lithography is a method for transferring a desired pattern into a thin film.Pattern transfer is achieved, for example, by using light exposure to change the chemical properties of a photosensitive material, called resist, which has been deposited on top of the device layer (thin film) to be patterned. (Advances in lithography have contributed significantly to the advancement of the integrated circuit technology, and the resolution-enhancement techniques (RET's) have become increasingly important as resolution has increased [3]. The interference lithography, uses the interference of two coherent laser beams to pattern a photo resist covered substrate. Conceptually, a grating is a simple pattern constituting periodic lines and spaces.

While non-optical next-generation lithography (NGL) solutions are being developed, optical lithography continues to be the work horse for high-throughput [3].

The use of lithography combined with an ion etching method like ion milling is one possible method to pattern nano-magnetic structures on thin film (a promising technique to produce ultra-high magnetic recording systems). An example is the use of He^+ ion to irradiate CoPt multi-layers through a silica mask obtained by a combination of high resolution lithography to produce an optical contrast-free, entirely planar, sub-50 nm magnetically patterned array [4–6].

2. INTERFERENCE LITHOGRAPHY

Interference lithography (IL) is the process of recording interference fringes. IL is presented as an optimal method for producing large-area arrays of magnetic structures; this technique of interference lithography is examined in the context of patterning 100 nm size features. Figure 1 shows using of positive and negative resist-tone to produce pattern on a given sample). Ion-beam, or ion milling is the method to etch the surface of the given thin film. In lithography, the stability of the beams position and angle is one of many factors affecting the accuracy of produced patterns [8].

2.1. Principle IL

The principle of interference lithography is simple; it uses the standing wave pattern (the interference of coherent light forms a standing wave pattern) formed between two interfering beams of light to expose a radiation sensitive material (recording on photo-resist). In traditional IL systems, the pattern is defined by the interference of spherical waves; hence the fringes produced by the spherical waves [5].

The period (Λ) of the standing wave, given in Equation (1) [8], is dependent on the wavelength of the light (λ) and the half-angle at which the two beams intersect (θ),

$$\Lambda = \frac{\lambda}{2\sin\theta} \tag{1}$$

Through additional exposures, or the interference of more than two beams, the possible patterns increase from simple gratings to a wide variety of periodic structures. Interference lithography is

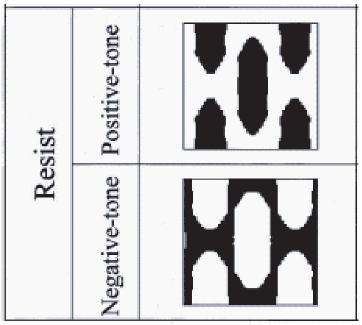

Figure 1: Resist profile white areas represent absorber of the mask and the black areas represent resist that remains after development (from) [7].

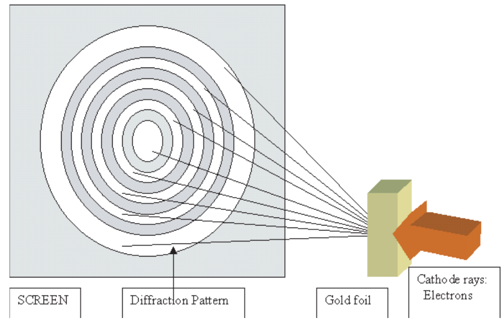

Figure 2: Thomas Diffraction electron by using a thin polycrystalline gold foil to produce a diffraction pattern on a screen (redrawn).

Table 1: Nano pattern production with various λ.

λ Wave length	[nm]	10	12	13	14
θ Angle	[deg]	80	80	80	80
$\sin\theta$	[1]	0.9848	0.9848	0.9848	0.9848
Λ Period length	[nm]	5.0771	6.0925	6.6002	7.1079
θ Angle	[deg]	45	45	45	45
$\sin\theta$	[1]	0.7071	0.7071	0.7071	0.7071
Λ Period length	[nm]	7.0710	8.4852	9.1923	9.8994

used commonly because of its simplicity. IL is used to produce only periodic patterns, this could be taken as a limitation factor for producing the images on the thin film. However, in patterned media applications large area periodic patterns are precisely the desired result, so this limitation is of little concern for this reason. Combination scanning beam interference lithography SBIL or of extreme ultraviolet lithography (EUVL) could be ideal to produce large area ultra nano-meter fine patterns on a given thin film to produce the mask for magnetic structure relief (see Table 1).

By supplying the Equation (1) with different wave length at constant trigger angle (hitting angle); assuming $\theta = 80$. The production of nano pattern could be calculated and archived as in the following two examples. Let us assume that the light is from an Ar-ion laser with a wavelength $\lambda = 351\,\text{nm}$. With the help of a beam splitter the given wave will be divided and rotated to each arm of the interferometer [9]. Hence, $\Lambda = 178.2$ nm pattern period length. On the other hand, let us assume that the light is from a source of UV with a wavelength $\lambda = 12\,\text{nm}$ (or 10–14 nm). Hence, $\Lambda = 6.092\,\text{nm}$ pattern period length.

3. ELECTRON BEAM LITHOGRAPHY

Although invented over 40 years ago, modern electron beam lithography (EBL) systems are still state of the art in the patterning of *nano-structures*, and they are extensively used in the production of masks for integrated electronic circuit fabrication. EBL technology has been suggested to be used in next-generation lithography [9] and it has been used to fabricate arrays of rectangular and triangular shaped dots. For technology nodes of sub-100 nm feature sizes, the International Technology Road-map for Semiconductors (ITRS) identifies NGL techniques employing both photons of significantly shorter wavelength and charged particles [9]. EBL systems expose patterns in one of three ways:

1. The system scans a focused e-beam over the target substrate
2. The system projects simple shapes formed by an aperture
3. The system projects an entire pattern formed by a mask (electron-projection lithography requires a mask made by one of the other two techniques).

EBL is based on an electron beam microscope, in which a focused beam of fast electrons are directed towards a resist-covered substrate (no mask is involved since the position of the electron beam can be controlled directly from a computer through electromagnetic lenses). To obtain resolutions better than the few μm of photolithography it is necessary to use either X-ray lithography or EBL (see Figure 2).

4. CONCLUSIONS

Lithography is a method for transferring a desired pattern into a thin film. Pattern transfer is achieved for example, by using light exposure to change the chemical properties of a photosensitive material, called resist, which has been deposited on top of the device layer (thin film) to be patterned. Advances in lithography have contributed significantly to the advancement of the integrated circuit technology. In using traditional interference lithography IL to pattern a grating, one splits a laser beam in two and spatially filters them to produce two spherical waves. The waves interfere and the resulting fringes are recorded in photo-resist. Conceptually, a grating is a simple pattern constituting periodic lines and spaces. On the way for information density increasing per given area of magnetic thin film, the industry have to create very small nano-magnetic structures on the top of the thin film magnetic recording media (essential procedure for the industry of ultra high magnetic devices. Currently, the tool of choice for achieving nano-scale resolution is electron beam lithography, which provides 10 nm resolution and arbitrary pattern generation. Electron beam lithography and the other types of lithography is the industry branch, that gives future hopes to create nano-magnetic structures. It is crucial to realize that the physics on the nano-meter scale tends to become dominated by quantum physics, in the nano-world one must always be prepared to take strange quantum phenomena into account and hence give up on an entirely classical description.

REFERENCES

1. Schattenburg, M. L., C. Chen, P. N. Everett, J. Ferrera, P. Konkola, and H. I. Smith, *J. Vac. Sci. Technol. B*, Vol. 17, 2692–2697, 1999.
2. Li, S. P., M. Natali, A. Lebib, A. Pepin, Y. Chen, and Y. B. Xu, *J. Magn. Magn. Mater.*, Vol. 241, 447–452, 2002.
3. Liebmann, L. W., S. M. Mansfield, A. K. Wong, M. A. Lavin, W. C. Leipold, and T. G. Dunham, *IBM J. Res. Develop.*, Vol. 45, 651–665, 2001.
4. Chen, C. G., "Beame alignment and imige metrology for scanning beame interference lithography," Ph.D. Thesis, MIT, 2003.
5. Chen, C. G., P. T. Konkola, R. K. Heilmann, G. S. Pati, and M. L. Schattenburg, *J. Vac. Sci. Technol. B*, Vol. 19, 2335–2341, 2001.
6. Devolder, T., C. Chappert, Y. Chen, E. Cambril, H. Launois, H. Bernas, J. Ferre, and J. P. Jamet, *J. Vac. Sci. Technol. B*, Vol. 17, 3177, 1999.
7. Toyota, E. and T. Hori, *J. Vac. Sci. Technol. B*, Vol. 19, 2428–72433, 2001.
8. Konkola, P. T., C. G. Chen, R. K. Heilmann, and M. L. Schattenburg, *J. Vac. Sci. Technol. B*, Vol. 16, 3282–3286, 2001.
9. Dhaliwal, R. S., W. A. Enichen, S. D. Golladay, M. S. Gordon, R. A. Kendall, J. E. Lieberman, H. C. Pfeiffer, D. J. Pinckney, C. F. Robinson, J. D. Rockrohr, W. Stickel, and E. V. Tressler, *IBM J. Res. Develop.*, Vol. 45, 615–638, 2001.

Research on Potential Use of Nanomaterials and Properties in Astrophysics

D. Bajalan
ret., Austria

Abstract— It is concluded that hydrogenation of polycyclic aromatic hydrocarbon followed by exposure to ultraviolet radiation in the presence of oxygen is a chemical route to the formation of nanodiamond material in interstellar clouds [1]. When the physical dimensions of a system become comparable to the interatomic spacing, strong modifications of the intrinsic magnetic properties (ordering temperature, magnetic anisotropy, spontaneous magnetization) are expected. Micromagnetic modeling of the behavior of a nanostructured film beautifully describes the magnetization process, but requires a high calculational effort and long computation times. Furthermore, it is difficult to predict changes of the macroscopic physical behaviour due to variation of parameters. Phenomenological models, on the other hand, are very useful to simulate the behaviour of the magnetic material under the influence of varying parameters, especially when the parameters are based on physical constants. Manufactured nanomaterials may bring significant innovation and advances to society and benefits for human health and the environment. They are also expected to provide a new competitive edge to European industry and to the European economy as a whole, and to contribute to job creation. At the same time, it will be necessary to ensure their safety for humans and the environment and to avoid negative impacts on society. Nanomaterials are manufactured for their specific properties providing possibilities for new uses and products. These specific properties may lead to different interactions with the physiology in humans and the environment and to effects that significantly differ from those known of materials without such properties. Within the context of REACH, the main issue pertaining to the development of nanotechnologies and nanomaterials is to ensure their safety to the human health and the environment covering the whole lifecycle. This is a prerequisite for the sustainable use of nanotechnologies and for the success of nanotechnologies in terms of market uptake and societal acceptance [2].

1. INTRODUCTION

Nanofabrication, offering unprecedented capabilities in the manipulation of material structures and properties, opens up new opportunities for engineering innovative magnetic materials and devices, developing ultra-high-density magnetic storage, and understanding micromagnetics. Most magnetic devices used today are based on the properties of thin-film or bulk materials; that is changing drastically, due to the advent of nanofabrication technology[1]. The magnetic properties of thin films are strongly influenced by their structure [9]. So small changes in the way a thin film is produced often give rise to large changes in some of the magnetic properties of the thin film. This is best understood by observing how the micro-structure of the film changes with processing and then correlating the micro-structure directly with the properties of the thin film [10]. Polymer-layered silicate (often referred as nanoclays) nanocomposites have proven to be an effective method of improving the physical properties of many different polymers [6]. Ionizing radiation such as gamma radiation and electron beam has been used widely in industry for crosslinking of polymer, polymer blend and composites. This technology can be well extended to the crosslinking of nanopolymeric materials or nanocomposites [7].

Characterizing grain surfaces and grain composition is a key in understanding grain chemistry and processing in different environments such as the outflows of evolved stars, the diffuse interstellar medium, molecular clouds and proto-planetary disks. Interplanetary and meteoritic dust the picture shows a GEMS particle, Glass with Embedded Metals and Sulfides attest to the complexity of dust chemistry in space and at the same time provide only a single tiny piece in the whole lifecycle of dust. Moving beyond the simple picture of bare silicates and graphite grains and identifying the complexity of dust chemistry requires a multidisciplinary approach [5].

Nano-fabrication allows us to achieve unique magnetic properties that do not exist in a thin-film or bulk material and gives us new freedom in controlling magnetic material properties, leading to innovative magnetic materials and devices, new ultra-high-density magnetic storage, and better understanding of micromagnetics. Use of nano structured perpendicular media in magnetic devices

[1] www.intel.com/research/silicon/nanotechnology, (2004).

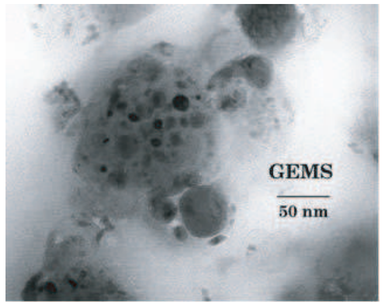

Figure 1: Interplanetary and meteoritic dust, glass with embedded metals and sulfides. Graphite grains and identifying the complexity of dust chemistry requires a multidisciplinary approach [5].

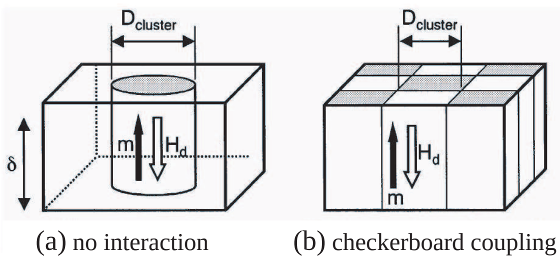

Figure 2: Schematic models of magnetic clusters; (a) isolated cluster; (b) checkerboard magnetization pattern [3].

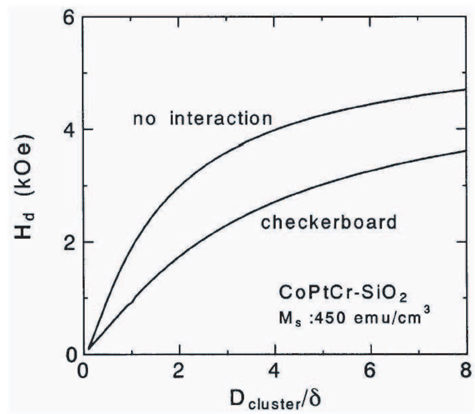

Figure 3: The values of H_d as a function of $D_{Cluster}/\delta$ calculated with an assumption of no interaction and checkerboard interaction, respectively [3].

is one of the hopes to increase the areal density of recording information storage; because perpendicular recording media has been proposed as a possible candidate for high data storage density [4]. Applications of nano-structures in electrical devices is ongoing also in cases like nano-structure-compatible computation paradigm, quantum-dot cellular automata (QCA) [8][2].

2. NANOMATERIALS IN ASTROPHYSICAL ENVIRONMENTS

There is growing evidence from astronomical observations that metallic Fe nano-particles form and become incorporated into chemically inhomogeneous dust grains. These observations are

1. infrared spectroscopy of dust surrounding evolved stars,
2. X-ray absorption and scattering measurements of interstellar dust in the galaxy, chemical sensitivity, etc.) of materials at the nano scale,
3. laboratory studies of Interstellar Dust. Particles that contain the most primitive material in the solar system, the so-called GEMS (Glass with Embedded Metals and Sulphides) [5].

3. EXAMPLE OF EFFECTS IN MANUFACTURED NANO-STRUCTURED

There are also some unwanted effects as well in nano-structured perpendicular recording media like:

Media Noise The media noise in the perpendicular media is a serious issue, the cluster size for example in perpendicular recording media, which is a main factor in media noise, is likely to be a

[2]QCA is a nanostructure-compatible computation paradigm that uses arrays of quantum-dot cells to implement digital logic functions, and hence quantum-dot cellular automata have also received significant attention. In this transistorless approach to computation, logic levels are represented by the configurations of single electrons in coupled quantum-dot systems. Like the quantum-dot systems also nanocomposite materials contain clusters, grains, or dots with characteristic dimensions in the 3–100 nm range.

function of the activation diameter and the strength of inter-granular exchange coupling, and both should be reduced to reduce the noise value [3, 4]. In other words, track edge effects might cause this noise; one solution to avoid such an issue is to physically separate each track with grooves or nonmagnetic materials [4].

Exchange Coupling In perpendicular recording, a small amount of exchange coupling may be required to reduce the noise caused by the reversal of grains due to the presence of a large demagnetization field.

It has become clear that magnetic structures designs are essential for new practical materials and devices in the data storage, spin-electronics, field sensors, memory devices and high-performance magnetic materials [9].

4. ADVANTAGES OF NANOTECHNOLOGY

From various sources on processing technologies, its expect that processing accuracy will reach the order of nano-meters in the twenty-first century. This speaks strongly for an urgent need to develop nanotechnology methods in several branches of the industry specially in our case magnetic storage and other essential computer network devices. The field of nano-structure science and technology has been growing very rapidly in the past few years, since the realization that creating new materials and devices from nano-scale building blocks could access new and improved properties and functionalities. While many aspects of the field existed well before nano-structure science and technology became a definable entity in the past decade, it has only become a coherent field of endeavor through the confluence of three important technological streams[3]:

1. New and improved control of the size and manipulation of nano scale building blocks.
2. New and improved characterization (spatial resolution, chemical sensitivity, etc.) of materials at the nano scale
3. New and improved understanding of the relationships. between nano-structure and properties and how these can be engineered.

Hence using nano-technology in electronic devices may solve some of problems like:

1. + The size of the devices.
2. + The performance of the devices.
3. + The fabrication problems of the devices.
4. + The price problems.
   + Fabrication.
   + Marketing.

Nano-technology was initially proposed to provide a concrete target accuracy for fabrication processes which involve ultra-precision surface and finishing (ultra- fine mirror cutting, various kinds of energy beam processing using photon electron, and ion beams). Materials-processing in nanotechnology thus consists mainly on:

1. + High-precision cutting with diamond tools of low wear.
2. + Fine lapping and fine polishing using fine abrasives.
3. + Physical and chemical processing using high-energy elementary particles such.
   + Photons.
   + Electrons.
   + Ions.
   + Chemically reactive atoms.
   + Soon atom craft technology could come into use.

[3]www.wtec.org/loyola/pdf/, (2005).

5. CONCLUSIONS

Nano technology could be one of the big hopes to produce cheaper, smaller computer and data storage systems without loosing system performance. Nano technology will affect almost every aspect of our lives, from the medicines we use, to the power of our computers, the energy supplies we require. Nano-technology will increase its influence in electrical engineering and electrical materials strongly.

Magnetic nanostructures are subjects of growing interest because of their potential applications in high density magnetic recording media and their original magnetic properties [11]. The rapid development of magnetic recording leads to a large increase of the bit density. Multilayer thin films with a perpendicular magnetic anisotropy devices may play an active role in the development and establishment of future storage technologies. Patterning magnetic media is a potential solution for ultrahigh density magnetic recording [14]. The superparamagnetic limit is encountered when the magnetic energy of the grain is comparable to thermal energy. The number of grains per bit can be reduced somewhat by advances in signal processing, but it is unlikely that this can continue at a sustainable pace [12]. Thermal stability is one of the serious issues for developing high density recording, and thus much effort has been made to overcome this issue [13]. Both of these theories result, under suitable conditions, in a logarithmic dependence of the magnetisation on time in a fixed external field, which is the form of dependence observed experimentally in a wide range of magnetic materials.

REFERENCES

1. Duley, W. W. and V. I. Grishko, *The Astrophysical Journal*, 2001.
2. Follow-up to the 6th Meeting of the REACH Competent Authorities for the Implementation of Regulation (EC) 1907/2006 (REACH), 2008.
3. Shimatsu, T., T. Oikawa, Y. Inaba, H. Muraoka, Y. Nakamura, and B. Lengsfield, *IEEE Trans. Magn.*, Vol. 39, 2335, 2003.
4. Haratani, S., A. Kaizu, and I. Sato, "Micromagnetic modeling of discrete patterned perpendicular media," *IEEE Transaction on Magnetics*, Vol. 39, 2326–2328, 2003.
5. *NWO Astrochemistry Programme*, Apr. 12, 2010.
6. Dillon, D. R., K. K. Tenneti, C. Y. Li, F. K. Ko, I. Sics, and B. S. Hsiao, *Polymer*, Vol. 47, Elsevier, 2006.
7. "IAEA-TECDOC-1438 Emerging applications of radiation," *Nanotechnology Proceedings of a Consultants Meeting*, Bologna, Italy, 2004.
8. Amlani, I., A. O. Orlov, G. Toth, G. H. Bernstein, C. S. Lent, and G. L. Snider, *Science*, Vol. 284, 289–291, 1999.
9. Sellmyer, D. J., C. P. Luo, and Y. Qiang, *Handbook of Thin Film Devices Magnetic, Vol. 5, Nanomaterials and Magnetic Thin Films*, 337–373, Academic Press, 2000.
10. Laughlin, D. E., L. L. Lee, and D. N. Lamberth, *IEEE Trans. Magn.*, Vol. 30, 3951, 1994.
11. Jamet, M., W. Wernsdorfer, C. Thirion, D. Mailly, V. Dupuis, P. Mélinon, and A. Pérez, *Phys. Rev. Lett.*, Vol. 86, 4676, 2001.
12. Walsh, M. E., *Degree in Electrical Engineering*, 29–75, MsC, MIT, 2000.
13. Mochidaa, M. and T. Suzuki, *J. Appl. Phys.*, Vol. 91, No. 10, 8644–8646, 2002.
14. Devolder, T., C. Chappert, Y. Chen, E. Cambril, H. Launois, H. Bernas, J. Ferre, and J. P. Jamet, *J. Vac. Sci. Technol. B*, Vol. 17, 3177, 1999.

Nano Particle Thermal Stability and Natural Subnanostructures

D. Bajalan
ret., Austria

Abstract— In the past decade, polymer-layered silicate (often referred as nanoclays) nanocomposites have proven to be an effective method of improving the physical properties of many different polymers. Even at very low nanoclay loadings, these nanocomposites have achieved higher moduli, improved thermal properties, and better barrier properties for both thermoplastic and thermoset polymers. They have also found commercial uses in such diverse applications as automobile engine components and plastic beverage containers. While many polymernanoclay systems have been studied extensively, polyvinylidene fluoride (PVDF) composites have received relatively little attention. PVDF is a semicrystalline thermoplastic with applications in such diverse fields as paint for skyscrapers, transducers for sensitive scientific instruments, and pipes for caustic chemical byproducts [1].

Multi-Layer devices like Co/Pt may play an active role in the developments and establishment of future storage technologies. We have prepared several samples of the Co/Pt onto silicon oxide, nitride, and glass substrates with different layer thickness and sequences to study thoroughly and investigate into the physics and magnetism of these materials.When the physical dimensions of a system become comparable to the interatomic spacing, strong modifications of the intrinsic magnetic properties (ordering temperature, magnetic anisotropy, spontaneous magnetization) are expected.The Co/Pt films were produced through sputtering from solid Co/Pt targets onto the Si substrates. The process of coating and measuring of thickness of the substrate-coating were repeated until the proper thin film of Co/Pt which has high anisotropy was reached. The sputtering process was established through the Triod Sputter System by using the "Triod Sputter Equipment" (consolidated vacuum corporation: type CV 18-AST 100).

1. INTRODUCTION

Nanomaterials like nanoclays occur widely in nature. The use of nanomaterials as immobilization support improves enzymatic stability and catalytic activity against other materials [2]. When the physical dimensions of a system become comparable to the interatomic spacing, strong modifications of the intrinsic properties (physical properties like: ordering temperature, magnetic anisotropy, spontaneous magnetization, etc.) are expected. Nano structures are subjects of growing interest in nearly all sinces. Their are suggestion that planetary materials incorporated different amounts of nanoparticles, possibly due to late injection by a nearby supernova. And over the past several decades, amorphous and more recently nano-crystalline materials have been investigated for applications in magnetic devices (the benefits found in the nano-crystalline alloys is from their chemical and structural variations on a nano-scale which are important for developing optimal magnetic devices with high properties). Polymer-layered silicate (often referred as nanoclays) nanocomposites have proven to be an effective method of improving the physical properties of many different polymers [1].

Ionizing radiation such as gamma radiation and electron beam has been used widely in industry for crosslinking of polymer, polymer blend and composites. This technology can be well extended to the crosslinking of nanopolymeric materials or nanocomposites [3]. Important industrial development is go on to integrate magnetic memory cells (magnetic RAM or MRAM) directly onto silicon chips for high-performance, low-power, and nonvolatile memory applications [8]. The subject of magnetism and applications of nanocomposite films is one of significant interest from both basic and technological view points [9]. The behaviour of magnetic nanoparticles has fascinated materials scientists for decades [13]. Magnetic nanostructures have become centre of great interest in the scientific community and in industry as the core technologies behind magnetic recording devices [7]. The computer industry will benefit largely from the size change in magnetic structures, which are used in technologies of hard disk drives (HDDs) or magnetic random access memories (MRAMs), and other hardware of computer systems parts. The cost per data bit will decrease year by year. The bit price decrease will give larger chances to store data onto magnetic recording media. With the advent of thin films and lithography techniques it is now possible to prepare nano-structured objects with a well controlled geometry, and the ability of modern lithography to produce arbitrary nano-scaled images on a given substrate [20].

Other applications of nanostracure in electrical devices like QCA which is a nanostructure-compatible computation paradigm that uses arrays of quantum-dot cells to implement digital logic functions [4], because quantum-dot cellular automata has received significant attention [5]. In this transistorless approach to computation, logic levels are represented by the configurations of single electrons in coupled quantum-dot systems [5]. Nanocomposite materials contains closters, grains, or dots with characteristic dimensions in the 3–100 nm range [9]. It has become cleare that such structures are essential for new practical materials and devices in the data storage, spin-electronics, field sensors, memory devices and high-performance magnetic materials [9]. Magnetic multilayers (like Co/Pt or Co/Pb), which are artificially grown periodic layered structures of alternating Co and Pd materials, have been one of the most prospective candidates for the next generation of high-density magneto-optical recording media, due to their novel magnetic and magneto-optical properties [6]. The thermal stability of the recorded bits becomes critical when the ultimate bit size is close to the limit of conventional methods [10]. Below a critical dimension of tens of nanometres the formation of magnetic domains becomesenergetically unfavourable and the particles behave as giant moments of ferromagnetically coupled atomic spins [13]. These can be thermally excited across the particles anisotropy barrier in timescales varying from nanoseconds to aeons or the giant moment can form a superposition by quantum mechanical tunnelling through the barrier [13]. The investigation of the properties of magnetic systems on the nanometre scale has lead to a better understanding of the fundamental physics of magnetism and the improvement of technological materials used in magnetic recording devices [7]. Still it is very important to understand the magnetic phenomenon since size has become smaller as it is in nanostructures, like the phenomenon of the superparamagnetic, and thermal stability of grains.

2. THE MAGNETIC PROPERTIES AND GRAIN SIZE

The magnetic properties of thin films are strongly influenced by their structure [9]. Structure change of thin film may cause change the grain per volume and so the bit, because increase the number of bits in a given area, either the number of grains per bit must decrease or the grain size itself must decrease. Therefore it is useful to describe the manner in which they grow before discussing their magnetic properties [7]. The idea to use a regular array of physically isolated grains/dots promises an improvement in thermal stability of the recorded bits [10].

3. SUPER PARA MAGNETIC LIMIT AND THERMAL STABILITY

The issue of stability itself simply requires physical isolation of the recording bits, the competition with the present media involves necessity of a nanoscale resolution in pattern fabrication [10]. With nanomagnetic resolution there is SPML, this limit, which to be considered when the grain become smaller, so that the stored magnetic energy compared to the thermal energy of the particle, still larger that the stored information keep on the media so that the thermal energy do not delete it. Hence SPML can be understood by considering the behavior of a single particle as the medium is scaled thinner [12]. As an important example of how the properties of magnetic particles can differ from those of the bulk material, a sufficiently fine particle consists of a single domain, whose magnetic moment, can rotate due to thermal agitation, surmounting the magnetic-anisotropy potential barriers [14].

The relation between the magnetic energy and the thermal energy has to be taken in consideration to make it possible going on in direction of secure information on the nano-magnetic data storage. Regarding some important variables as (V m^3 volume of a given nano magnetocrystalline, ΔE_{aniso} [Jule] magnetic-anisotropy potential barriers, K_0 [Jule/m^3] direction independent constant, and K_1 [Jule/m^3] cubic magnetocrystalline anisotropy constant, and E_{therm} [Jule] thermal energy of a given nano magnetocrystalline) we could write a simple equation which explains the relation between storage time of an information on to a magnetic particle as the following,

$$\tau = 10^{-10} \exp \frac{K_1 V}{k_B \cdot T} \tag{1}$$

$$\Delta E_{aniso} = K_1 V \tag{2}$$

$$E_{therm} = K_B T \tag{3}$$

and hence the Eq. (1) will be simple as,

$$\tau = 10^{-10} \exp \frac{\Delta E_{aniso}}{E_{therm}} \tag{4}$$

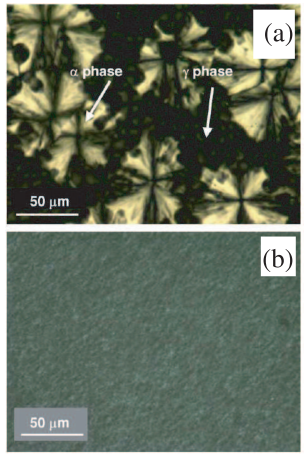

Figure 1: PLM images of PVDF and PVDF-layered silicate nanocomposites: (a) pristine PVDF spherulites after 6 h at 152 8C, (b) PVDF15A nanocomposite after 5 h at 162 8C [1].

It is very important to have a large ratio of of magnetic to thermal energy, because If the ratio of magnetic to thermal energy is too low, the magnetization state of the grain can spontaneously reverse, leading to random and uncontrollable data loss. In modern data storage media, by continuing increasing recording density, keeping the thermal stability has become one of the first issues in recording media development and research. There is several researches to test the best alloys with very good property. for example: It appears that NiAl can provide potential benefits over the Cr underlayer due to its small grain size, good thermal conductivity, high stiffness and good environmental corrosion resistance. The thermal stability factor $KV = kBT$ becomes < 100, even if K is increased beyond $10^6\,\mathrm{erg/cm^3}$ [7]. It is concluded that the first problem will arise from the storage medium, whose grain size cannot be scaled much below a diameter of ten nanometers without thermal self-erasure [12].

k_B Boltzmanns constant[1], T temperature, K uniaxial magnetic anisotropy[2], V particle volume[3].

4. CONCLUSIONS

Nano fabrication offers capabilities in patterning materials and in manipulating the size, shape, orientation, and composition of the structures. Perpendicular recording media could be a way to produce ultra-high-density magnetic data-storage media. Discrete perpendicular recording media with single domain dots which have vertical anisotropy, are the future hope for the industry to produce ultra height density magnetic recording media, and each magnetic pillar is a single domain magnetic particle, magnetized perpendicular to the template surface and, in principle, can store one bit of information. It is possible to achieve the perpendicular media through magnetic nanostructured patterns and so to produce patterned magnetic media. Patterned magnetic media is advanced to satisfy limitations in HDD. To increase the capacity it would be very important to increase the density of the magnetic structures on the recording surface. It is very important to thoroughly understand and find solutions for problems like thermal stability, self demagnetization, magnetic media transition.

Nano technology could be one of the big hopes to produce cheaper, smaller computer and data storage systems without loosing system performance. Nano technology will affect almost every aspect of our lives, from the medicines we use, to the power of our computers, the energy supplies we require. Nano-technology will increase its influence in electrical engineering and electrical materials strongly.

REFERENCES

1. Dillon, D. R., K. K. Tenneti, C. Y. Li, F. K. Ko, I. Sics, and B. S. Hsiao, *Polymer*, Vol. 47, Elsevier, 2006.
2. Calabia, M., A. Jarab, J. Bendallc, M. Wellandc, and M. de la Luz Morad, 1*9th World Congress of Soil Science, Soil Solutions for a Changing World*, Brisbane, Australia, Aug. 2010.

[1] 1.38×10^{-6} [j/deg].
[2] magnetic anisotropy of grains.
[3] the activation volume or grain volume.

3. "IAEA-TECDOC-1438 emerging applications of radiation," *Nanotechnology Proceedings of a Consultants Meeting*, Bologna, Italy, 2004.
4. Amlani, I., A. O. Orlov, G. Toth, G. H. Bernstein, C. S. Lent, G. L. Snider, *Science*, Vol. 284, 289–291, 1999.
5. Amlani, I., A. O. Orlov, R. K. Kummamuru, G. H. Bernstein, C. S. Lent, and G. L. Snider, *Appl. Phys. Lett.*, Vol. 77, No. 5, 738–740, 2000.
6. Choe, S.-B. and S.-C. Shin, *Physical Review B*, Vol. 57, No. 2, 1085–1089, 1998.
7. Mathuna, D. M., "Surface studies of nanomagnetic systems," 3, A Thesis Submitted to the University of Dublin, Trinity College, Physics Department, 2002.
8. CNS, Center for Nanoscale Systems, "Impacting and hastening the development of future information technologies charles," 6–14, 2002.
9. Sellmyer, D. J., C. P. Luo, and Y. Qiang, *Handbook of Thin Film Devices Magnetic, Vol. 5, Nanomaterials and Magnetic Thin Films*, 337–373, Academic Press, 2000.
10. Lapicki, A., K. Kang, and T. Suzuki, *IEEE Trans. Magn.*, Vol. 38, 2589–2589, 2002.
11. Walsh, M. E., "Degree in electrical engineering," 29–75, MsC., MIT, 2000.
12. Thompson, D. A. and J. S. Best, *Ibm J. Res. Develop.*, Vol. 44, No. 3, 321–321, 2000.
13. Binns, C. and M. J. Maher, *New Journal of Physics*, Vol. 4, 85.185.15, 2002.
14. Garcia-Palacios, J. L. and F. J. Lazaro, *Phys. Rev. B*, Vol. 55, No. 2, 1997.
15. Yamada, Y., T. Suzuki, H. Kanazawa, and J. C. Osterman, *J. Appl. Phys.*, Vol. 85, 5094, 1999.
16. Lapicki, A., K. Kang, and T. Suzuki, *IEEE Trans. Magn.*, Vol. 38, 2589, 2002.
17. Papusoi, C. and T. Suzuki, *J. Magn. Magn. Mater.*, Vol. 240, 568, 2002.
18. Kirk, K. J., J. N. Chapman, and C. D. W. Wilkinson, *J. Appl. Phys.*, Vol. 85, 5237, 1999.
19. Kisker, H., N. Abarra, Y. Yamada, P. Glijer, and T. Suzuki, *J. Appl. Phys.*, Vol. 81, 3937, 1997.
20. Noziéres, J. P., M. Ghidini, N. M. Dempsey, B. Gervais, D. Givord, G. Suran, and J. M. D. Coey, "Nucl. instr. and meth.," *Phys. Res. B*, Vol. 146, 250–259, 1998.

Variation in Wireless-sensing of UHF-RFID Antennas with Insertion of Dielectric Material

S. D. Nawale[1] **and N. P. Sarwade**[2]

[1]Sinhgad Institute of Technology, Lonavala, Pune (MH), India
[2]Veermata Jijabai Technological Institute, Mumbai (MH), India

Abstract— This work presents UHF RFID passive tag designed at 870 MHz, with the insertion of sensitive dielectric material placed at different portions of tag. Variation in position of dielectric, changes electric properties of the tag whose consequence results in variation of tag response. The change in tag impedance and realized gain also can be remotely monitored. The proposed device of the credit card size is simple in construction with folded planar antenna. Radiating H-shaped slot helps for impedance matching of antenna with the microchip. The integration of dielectric in open slot of antenna and even overlapping the slot is able to vary the read range 5–10 m. The idea of changing the material and its dielectric constant leads to develop RFID tag as a wireless sensor. Set of experiments are performed, with the purpose to sense the variation of realized gain. Measurement is done with turn-on power method where minimum transmitted reader power is scattered back by the designed tag. The results are compared with sizes of the overlapped dielectric. It shows that tag becomes more sensitive and provides improved realized gain by 2 dB, when dielectric Teflon with size variation is overlapped on the H-slot. Dielectric constant variation of material also results in change in realized gain by 7 dB.

1. INTRODUCTION

Radiofrequency identification (RFID) is growing technology in replacement of barcodes and optical character recognition. Wide range of applications including logistics, intelligent traffic, security, tale health made wireless RFID more popular. A passive tag, comprising of an antenna and a microchip transponder, is remotely interrogated by a reader [1]. The contents stored in the internal memory of the tag are communicated to interrogator by modulated backscattering of the signal. The short range radio communication technology shares the digital information of tag having Unique Identification Number (UIN). The exchange of information takes place due to magnetic or electromagnetic coupling between reader and a tag.

The applications of RFID technology are available in different standardized unlicensed frequency bands. The Low-frequency (LF, 125–134 kHz) and high-frequency (HF, 13.56 MHz) applications are most matured and world wide accepted. These applications are based on magnetic flux coupling between the reader's and tag's coils. RFID systems at Ultra-high frequency (UHF, 860–960 MHz) and microwave (2.4 GHz and 5.2 GHz) involves electromagnetic coupling between antennas and establish a communication link at longer distance [2]. These are the emerging applications and have increased the interest of the researchers.

Passive RFID tags have advantages over active tags in cost, size and complexity. Overall performance of RFID system depends on design of tag. The size of tag, read range, sensing capability and compatibility with the tagged objet decides are the deciding factors. As microchip's capacitive reactance makes it power sensitive, the goal of antenna designer is to provide conjugate inductive impedance match which improves tag's response. At UHF, printed dipole micro-strip antennas having Omni-directional pattern are preferred. Several methods are suggested for reduction in size, impedance matching and improvement in read range [3].

Passive sensor RFID technology is the emerging area of research. Integration of sensing and identification technologies enables the wide range of applications in environment monitoring and tale-health [4–7]. Adding the sensing capability, varies tag's parameters such as impedance, realized gain and read range. The idea of passive tag as a sensor has been recently investigated for wireless observations of change of liquids and powders as well as some of human body pathologies [8, 9].

Within this scenario, this work explores the results of integration of UHF (870 MHz) RFID passive tag with sensitive dielectric materials placed at different portions of the tag. Variation in position of dielectric, changes electric properties of the tag whose consequence results in variation of tag response. The change in tag impedance and realized gain also can be remotely monitored. A Computer Simulation Technology (CST) Microwave studio is used to simulate H-shaped folded antenna. Variation in the read range, realized gain and antenna impedance are well observed and experimentally validated. The results are given here to prove the sensitivity of the passive tag.

2. VARIATION IN SENSITIVITY OF PASSIVE TAG

A typical RFID system uses the principle of modulated back-scatter as shown in Figure 1. When Reader to tag communication establishes, the tag placed on target object is first activated by reader energy with transmission of continuous wave. This energy is being used to charge the capacitor of the microchip for required operation. This system transfers digital information in the form of UIN of microchip to the interrogating reader. Microchip has the fixed impedance with capacitive reactance as $Z_{Mc} = R_{Mc} - jX_{Mc}$. For maximum power transfer the antenna impedance $Z_{An} = R_{An} + jX_{An}$ has to be matched to Z_{Mc} ($Z_{An} = Z^*_{Mc}$). Major operational parameters such as maximum read range ($d_{\max}$) and realized gain (G_{Rg}) depends upon proper impedance matching in tag. To have feasibility of low cost device, instead of inserting external matching lumped networks, the mechanism have to be embedded within tag's antenna layout.

Adding sensing material to the tag can vary the antenna impedance ($Z^{\#}_{An} = R^{\#}_{An} + jX^{\#}_{An}$), which depends upon type of sensing material. This ultimately causes change in maximum read range ($d^{\#}_{\max}$) and realized gain ($G^{\#}_{Rg}$) of the tag which are given as (assuming there is no polarization mismatch)

$$d^{\#}_{\max} = \frac{c}{4\pi f}\sqrt{G_R G_T \tau^{\#} \frac{P_{in}}{Ptx}} \tag{1}$$

where, f is the frequency of operation, G_R is the gain of reader antenna given in dB, P_{in} is the total input power provided to reader from the system, G_T is the gain of the tag antenna placed on the target object (this gain can be increased by proper impedance matching) and $\tau^{\#}$ is power transmission coefficient of the tag and this is given as

$$\tau^{\#} = \frac{4R_{MC}R^{\#}_{An}}{\left[Z_{MC} + Z^{\#}_{An}\right]^2} \tag{2}$$

$G_T\tau^{\#}$ is called as realized gain ($G^{\#}_{Rg}$) which is given as

$$G^{\#}_{Rg} = \frac{P_{Tx}}{\left(\frac{c}{4\pi f d^{\#}_{\max}}\right)^2 G_R P_{in} X} \tag{3}$$

where, P_{Tx} is the transmitted power and X is polarization mismatch factor between antennas.

Expressions (1) to (3) helps to understand the variation in tag parameters and its sensitivity. The maximum distance at which the backscattered power can be detected by reader depends upon the realized gain of the tag antenna and in respect to antenna impedance.

3. INSERTION OF DIELECTRIC MATERIAL

The proposed rectangular tag of the credit card size with folded planar antenna working at UHF (870 MHz) is shown in Figure 2. The microchip impedance is assumed to be $Z_{Mc} = 12 - j\,175\Omega$.

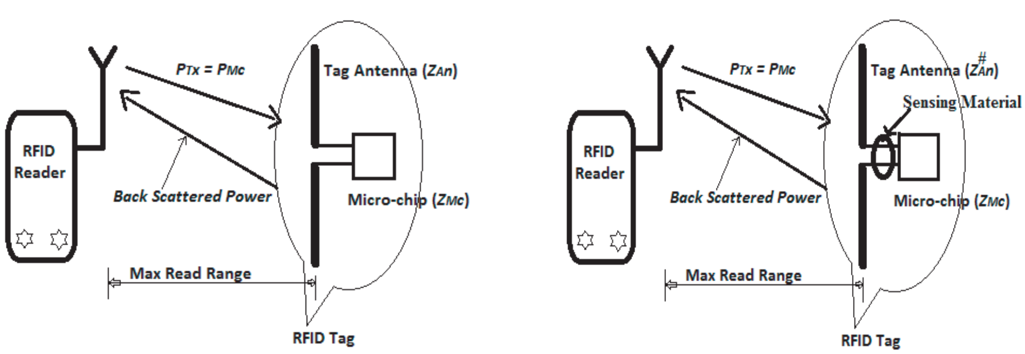

(a) (b)

Figure 1: Reader-tag scenario (a) without and (b) with sensing material inserted in tag.

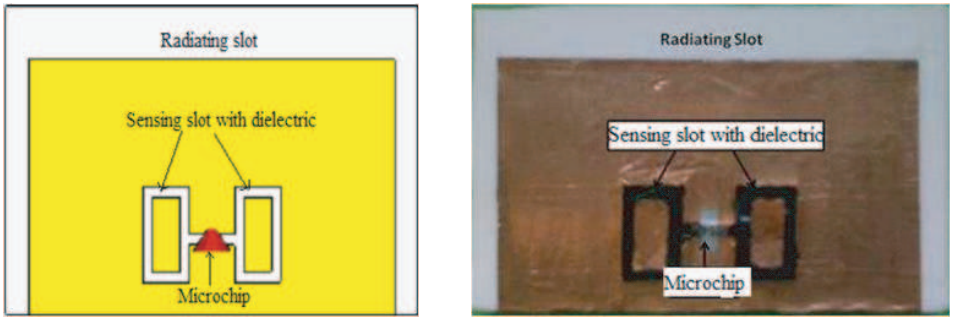

(a) (b)

Figure 2: Rectangular H-shaped folded planer antenna (a) simulation structure; (b) fabricated structure.

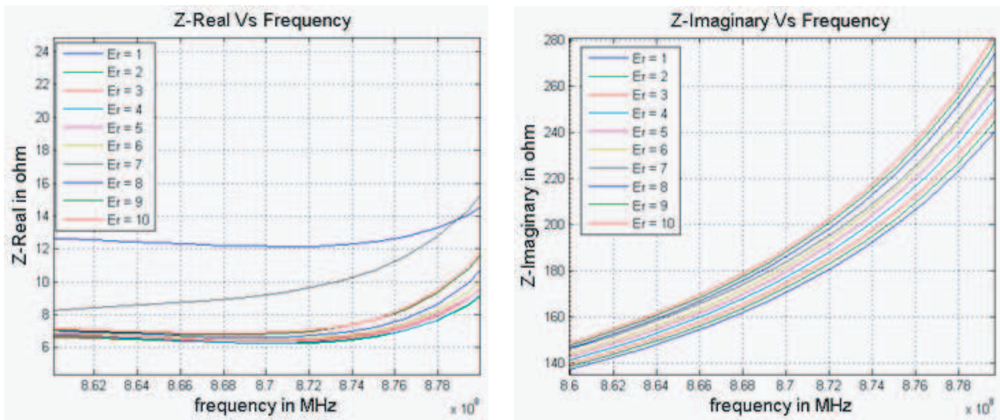

(a) (b)

Figure 3: Variation in antenna impedance w.r.t. frequency (a) $R_{An} = 12\,\Omega$; (b) $X_{An} = 175\,\Omega$ at 870 MHz.

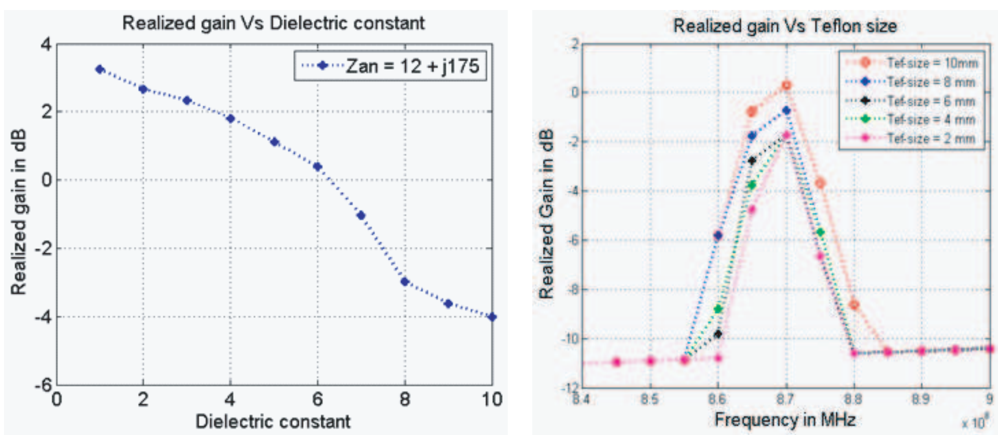

(a) (b)

Figure 4: Variation in realized gain (a) simulated result w.r.t.; (b) experimental result w.r.t. Teflon size @ 870 MHz.

Radiating H-shaped antenna impedance is matched with the microchip as shown in Figure 3. The final antenna design has been refined by CST Microwave studio simulator.

To validate mathematical expressions, the material with changing dielectric constant (ϵ_r) is inserted in the symmetrical open slot. The results are estimated by simulator. It gives the variation in the Realized gain by 7 dB (3 dB to −4 dB) with ϵ_r as shown in Figure 4(a).

4. EXPERIMENTATION AND RESULTS

Sensitivity of tag is observed through experiments like overlapping the area of H-shaped slot by the dielectric Teflon ($\epsilon_r = 2.08$) of different sizes whose results are shown in Figure 4(b). These readings are taken at 6 meter distance from the reader antenna (read range = 6 meter) by using turn on power method. Graph shows that there is improvement in realized gain by 2 dB with respect to (w.r.t.) Teflon size from 2 mm to 10 mm. Maximum read range observed is 10 meters with the Teflon of 10 mm size.

Tag sensitivity is also being observed by placing the dielectric material at different portions of the open slot. It is observed that the realized gain of the tag is higher if the dielectric material is placed at all open gaps of H-slot as shown in Figure 2(b).

5. DISCUSSION AND CONCLUSION

Integration of Dielectric material into RFID tag has been reported with the aim to design and test the passive sensor, without modifying the original structure. Simple structure with folded PIFA is being used for analysis purpose. Theory behind backscattering and change in tag parameters w.r.t. impedance is explained. To validate theoretical proof the tag is fabricated and experiments are carried over.

Purpose of this paper is to demonstrate the idea of inserting a material with the tag whose, electrical and chemical properties can vary in accordance with the change in the environmental parameters or tagged objects. The tag and the measurement results are suited for sensing of different kind of gas provided that specific dielectric polymers are used. The readings are taken by considering the possibilities of variation in dielectric inside the tag and overlapped to the tag. The realized gain and the read range have shown the variation in accordance with impedance variation.

ACKNOWLEDGMENT

The authors would like to thank Board of Colleges and University Department (BCUD), University of Pune, MH, India, for supporting this research with funding. (Reference No. BCUD/OSD/390, Dated: 26/10/2010).

REFERENCES

1. Finkenzeller, K., *RFID Handbook: Fundamentals and Applications in Contactless Smart Cards and Identification*, 3rd Edition, John Wiley and Sons Inc, New York, 2010.
2. Stockman, H., "Communication by means of reflected power," *Proceedings of the IRE*, Vol. 36, No. 10, 1196–1204, October 1948.
3. Marrocco, G., "The art of UHF RFID antenna design: Impedance-matching and size reduction techniques," *IEEE Antenna and Propagation Magazine*, Vol. 50, No. 1, 66–79, February 2008.
4. Calabrese, C. and G. Marrocco, "Meandered slot antennas for sensor RFID tags," *IEEE Antenas and Wireless Propogation Letters*, Vol. 7, 5–8, 2008.
5. Nambi, S., S. Nyalamadugu, S. M. Wentworth, and B. A. Chin, "Radio frequency identification sensors," *Proc. 7th World Multiconf. Systematics, Cybernetics and Informatics (SCI 2003)*, 386–390, 2003.
6. Marrocco, G., L. Mattioni, and C. Calabrese, "Multiport sensor RFID's for wireless passive sensing of objects-basic theory and early results," *IEEE Transactions on Antennas and Propogation*, Vol. 56, No. 8, 2691–2702, August 2008.
7. Marrocco, G., "RFID antennas for uhf remote monitoring of human subjects," *IEEE Transactions on Antenna and Propagations*, Vol. 55, No. 6, 1862–1870, June 2007.
8. Occhiuzzi, C., S. Cippitelli, and G. Marrocco, "Modeling, design and experimentation of wearable RFID sensor tag," *IEEE Transactions on Antennas and Propogation*, Vol. 58, No. 8, 2490–2498, August 2010.
9. Potyrailo, R. A., C. Surman, W. G. Morris, S. Go, Y. Lee, J. Cella, and K. S. Chichak, "Selective quantization of vapors and their mixtures using individual passive multivariable RFID sensors," *IEEE RFID*, 22–28, 2010.

Reflection Technique for the Determination of Moisture Content in Hevea Rubber Latex

Farizah Ansarudin[1,2], **Zulkifly Abbas**[1], **Ali Hamad Ali**[1], **and Mohamad Aliff Ismail**[1]

[1]Department of Physics, Faculty of Science, Universiti Putra Malaysia, Serdang 43400, Selangor, Malaysia
[2]Department of Electrical, Electronic and Systems Engineering
Faculty of Engineering and Built Environment
Universiti Kebangsaan Malaysia, Bangi 43600, Selangor, Malaysia

Abstract— This paper presents a new technique for the determination of moisture content in hevea rubber latex using an insulated monopole antenna. The antenna was fabricated from a coaxial SMA stub contact panel. The reflection measurements of hevea rubber latex were carried out using an Agilent Professional Network Analyzer N5230A (PNA) in the frequency range from 0.1 to 4 GHz. The variations in magnitude and phase shift with moisture content were analyzed using regression analysis at several selected frequencies. These in turn were used to establish the relationship in magnitude and phase shift with moisture content. The actual moisture content was determined by the standard oven drying method and compared with predicted values of moisture content. The mean relative errors in the determination of moisture content range from 36.95% to 87.51% using magnitude and phase shift techniques were 0.0505 and 0.0144, respectively.

1. INTRODUCTION

Accurate determination of moisture content in agricultural product at microwave frequencies is necessary for application such as to maintain its quality and biological effects of natural or raw materials. Natural rubber latex is complex biological product containing 50–80% of water, 15–45% of rubber hydrocarbon and approximately 2–4% of non-rubber constituents [1]. This composition is varied with weather, soil condition, clone, tapping system, season etc. The amount of water content is very important in latex industries in order to produce a wide range of rubber products since the production is increased dramatically over the years. Moreover, hevea rubber latex is one of the important consumption producing the national export contribution exceed RM33.99 billion in December 2010 especially for natural rubber [2]. The dielectric properties of hevea rubber latex have been reported by previous researcher at high frequency range with different temperature variations [3, 4]. As to the authors' knowledge, no detailed study on determining the moisture content of hevea rubber latex at low frequency, accurate, rapid, flexible and economical for rubber industries based on reflection method.

2. MATERIALS AND METHODS

The antenna is fabricated from a stub contact that consists of an inner conductor and insulated with a PTFE material. The sample used in this study is freshly tapped latex that was obtained from Universiti Putra Malaysia Research Park. The mass of fresh and diluted latex samples were recorded using electronic balance and dried into microwave laboratory oven at 70°C for 24 hours [4]. The dried samples were kept at room temperature before weighing again until it reaches a constant value. The insulated monopole antenna was connected to a computer controlled Professional Network Analyzer N5230A (PNA) to measure its magnitude and phase of reflection coefficient (S_{11}) for reflectivity measurement. PNA is connected with coaxial semi-rigid cable with characteristic impedance ($Z_o = 50\,\Omega$) and calibration was performed in open, short and load using the Calibration Kit 85052D. The cable is then connected to the insulated monopole antenna to measure the S_{11} in free space, distilled water and rubber latex samples with different percentages of moisture content. The actual moisture content of hevea rubber latex in percentage was obtained using the conventional oven drying method and it was calculated specifically as:

$$mc(\%) = \frac{m_w - m_d}{m_w} \times 100 \tag{1}$$

where the m_w and m_d is the mass of wet and dry samples, respectively [4–6].

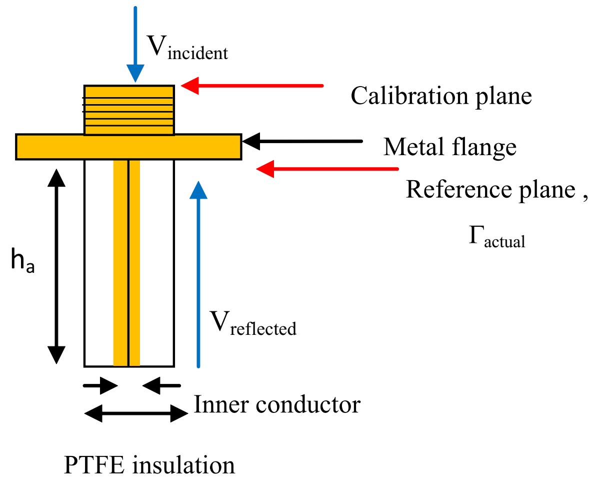

Figure 1: Physical dimension of insulated monopole antenna.

Figure 2: Reflection measurements set-up.

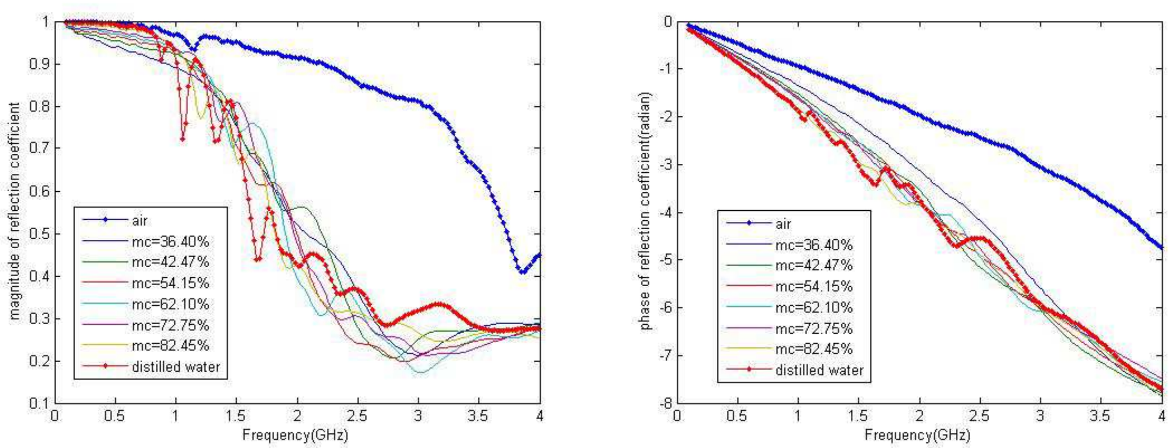

(a) (b)

Figure 3: Reflection measurement results with frequency (a) magnitude of reflection coefficient (b) phase of reflection coefficient (radian).

3. RESULTS AND DISCUSSION

The values of magnitude ($|\Gamma|$) and phase (Φ) of reflection coefficient that were obtained via reflection measurement has been observed at the frequency range from 0.1 to 4 GHz with different percentages of moisture content (mc) of hevea rubber latex starts from 36.40% to 82.45% are shown in Figures 3(a) and 3(b), respectively. The reflection method is widely used in the measurement of permittivity and permeability of low conductivity materials [7]. From the Figure 3(a), it was clearly seen that the $|\Gamma|$ of free space was not accurately 0 dB because of the calibration effect and mismatch impedance. The figure also suggests that the magnitude of reflection coefficient were decreased at 1.2 GHz until 3 GHz. A similar frequency range also has shown multiple reflections for $|\Gamma|$ due to conductive losses in the liquid material. However, the $|\Gamma|$ was almost constant after 3 GHz and overlapping each other for all mc of rubber latex including water. According to [3], any moist material will contain water molecules bound with different strength as well as free water depending on the moisture. Hence, the important factor which affects the dielectric properties of latex under this study are the dipole effects due to water molecules and it can be clearly seen at approximately below 3 GHz.

Figure 3(b) shows that Φ is frequency dependence for different mc of hevea rubber latex. Nevertheless, the different percentages of mc do not affect the values in phases. Therefore, the shift in phase was taking into account to establish the parameter under study with different percentages of mc. About 50 samples were prepared for reflection measurement to establish the empirical equations that was attained from the relationship between mc with $|\Gamma|$ and mc with phase shift ($\Delta\Phi$).

There were latex concentrate (mc = 36.4%), freshly tapped latex (mc = 42.47%) and diluted fresh latex (mc = 54.15% to 82.45%). Both correlations were found high regression (R^2) at 0.52 GHz as shown in Figures 4(a) and 4(b). Empirical equations were developed at 0.52 GHz for $|\Gamma|$ and $\Delta\Phi$

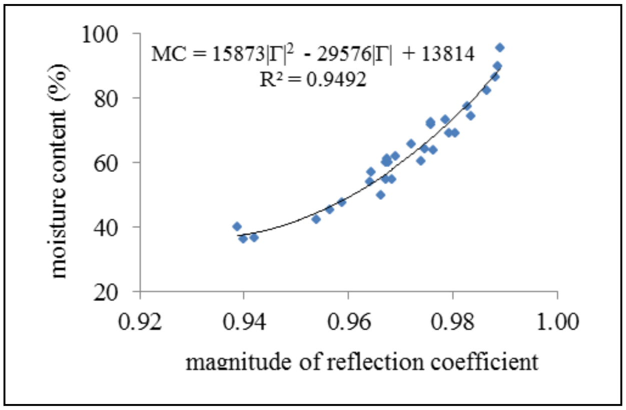

(a)

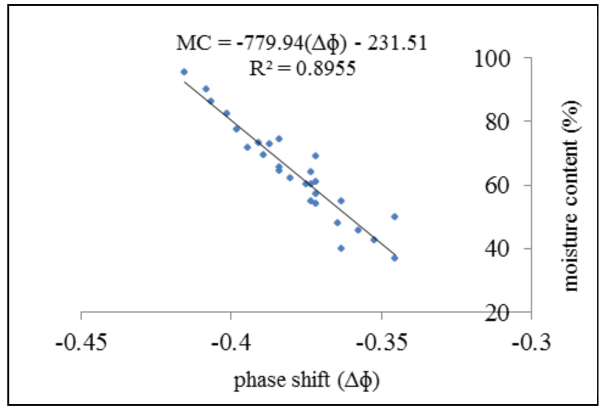

(b)

Figure 4: The relationship between moisture content and (a) magnitude of reflection coefficient (b) phase shift at 0.52 GHz.

Table 1: Standard method and predicted values of moisture content in hevea rubber latex at 0.52 GHz based on magnitude of reflection coefficient.

Sample	MC (%) Standard Method	Measured $\vert\Gamma\vert$	MC (%) Predicted	Relative Error
1	36.95	0.9404	38.05	0.0298
2	50.85	0.9658	55.31	0.0878
3	55.26	0.9715	62.00	0.1221
4	62.29	0.9748	66.45	0.0667
5	67.17	0.9780	70.98	0.0568
6	72.44	0.9817	76.55	0.0568
7	77.33	0.9850	81.97	0.0600
8	80.57	0.9866	84.83	0.0529
9	82.92	0.9869	85.21	0.0276
10	87.51	0.9903	91.50	0.0456

Mean relative error = 0.0505

Table 2: Standard method and predicted values of moisture content in hevea rubber latex at 0.52 GHz based on phase shift.

Sample	MC (%) Standard Method	Measured ($\Delta\Phi$-rad)	MC (%) Predicted	Relative Error
1	36.95	−0.3421	35.31	0.0445
2	50.85	−0.3613	50.28	0.0112
3	55.26	−0.3683	55.74	0.0087
4	62.29	−0.3770	62.53	0.0038
5	67.17	−0.3822	66.58	0.0087
6	72.44	−0.3892	72.04	0.0055
7	77.33	−0.3944	76.10	0.0159
8	80.57	−0.3979	78.83	0.0216
9	82.92	−0.3997	80.23	0.0324
10	87.51	−0.4067	85.69	0.0208

Mean relative error = 0.0144

as shown in (2) and (3):

$$\mathrm{MC} = 15873 * |\Gamma|^2 - 29576 * |\Gamma| + 13814 \tag{2}$$
$$\mathrm{MC} = -779.94 * \Delta\Phi - 231.51 \tag{3}$$

where MC is predicted moisture content, $|\Gamma|$ and $\Delta\Phi$ is measured magnitude of reflection coefficient and phase shift at 0.52 GHz, respectively.

The validation of empirical Equations (2) and (3) at 0.52 GHz can be observed particularly in Tables 1 and 2 in predicting moisture content when compared to standard oven drying method. Both tables indicate that minimum mean relative error at 0.52 GHz were $\pm 5.05\%$ for magnitude and $\pm 1.44\%$ for phase shift to predict moisture content of rubber latex.

4. CONCLUSION

The values of magnitude and phase of reflection coefficient were significant in predicting moisture content of hevea rubber latex. Both results can be used to predict the moisture content of hevea rubber latex by taking into consideration the conductive losses due to dipole orientation in water molecules of latex samples at approximately below 3 GHz. However, the performance of insulated monopole antenna as a moisture sensor was suitable by using phase shift technique when compared to magnitude of reflection coefficient at 0.52 GHz. This is due to minimum mean relative error was obtained $\pm 1.44\%$ to predict mc range from 36.95% to 87.51%.

ACKNOWLEDGMENT

The authors gratefully acknowledge the Scholarship Division of Ministry of Higher Education, Malaysia for supporting this work.

REFERENCES

1. Khalid, K., J. Hassan, Z. Abbas, and M. Hamami, "Microwave dielectric properties of hevea rubber latex, oil palm fruit and timber and their application for quality assessment," *Electromagnetic Aquametry*, Springer, Germany, 2005.
2. Department of Statistic, Malaysia Rubber Board, Retrieved on 23 June 2011 from www.lgm.gov.my.
3. Hassan, J., K. Khalid, and W. M. D. W. Yusof, "Microwave dielectric properties of hevea rubber latex in the temperature range -30° to 50°," *Pertanika Journal Science* & *Technology*, Vol. 5, No. 2, 179–190, 1997.
4. Khalid, K., M. Ghretli, Z. Abbas, and I. V. Grozescu, "Development of planar microwave moisture hevea rubber latex and oil palm fruits," *International RF and Microwave Conference Proceedings*, Putrajaya, Malaysia, September 12–14, 2006.
5. Kupfer, K., *Electromagnetic Aquametry: Electromagnetic Wave Interaction with Water and Moist Substances*, Springer, Germany, 2005.
6. Karmas, E., "Techniques for measurement of moisture content of foods," *Journal of Food and Technology*, Vol. 52, 234–238, 1980.
7. Chen, L. F., C. K. Ong, C. P. Neo, V. V. Varadan, and V. K. Varadan, *Microwave Electronics: Measurement and Materials Characterization*, John Wiley & Sons Ltd., England, 2004.

MIMO Radar 3D Imaging with Improved Rotation Parameters Estimation

Changzheng Ma[1], **Tat-Soon Yeo**[1], **Chin Yuan Chong**[2], **and Tao Zhang**[3]

[1]Department of Electrical and Computer Engineering, National University of Singapore, Singapore
[2]DSO, Singapore
[3]Xi'an Electronic Engineering Research Institute, China

Abstract— Multiple Input Multiple Output (MIMO) radar provides wide aperture. In order to combine MIMO and Inverse Synthetic Aperture Radar (ISAR) and form three dimensional image of a target, the rotation parameters of the target relative to the radar should be obtained. The amplitudes of the scatterers are proposed to be the weight of a minimum mean square error (MMSE) estimation method. Simulation results show that the rotation parameter's precision are improved.

1. INTRODUCTION

Inverse Synthetic Aperture Radar (ISAR) imaging has received significant attention in the past three decades [1]. ISAR image is a projected image of the target on the Range-Doppler plane. The projected image is two-dimensional, thus could only deliver limited information in target recognition applications.

In order to provide more information, several three-dimensional imaging methods based on interferometry and antenna array technique have been proposed recently [2–5]. In these methods, the first step is to form the ISAR image, interferometry or array technique is then used to measure the 3-D positions of each separated scatterers.

MIMO radar transmits multiple independent signals from multiple antennas and receive the return signals using multiple receive antennas. One advantage of MIMO radar over conventional phased array is its higher angular resolution. For far field target imaging, a 2-D high resolution technique using narrow- and wide-band MIMO radar was proposed in [6]. A 3-D imaging technique using MIMO radar is discussed in [7]. In the above target imaging methods, only one snapshot is used to form the 3-D image. But it requires relatively high transmitting energy.

Combining MIMO radar and inverse synthetic aperture technique can reduce transmitting power as well as improve cross-range resolution when compared to mono-static ISAR imaging [8, 9]. In [10], two-dimensional MIMO radar and inverse synthetic aperture technique are combined to form a 3-D image. In order to coherently combine signal, the relative rotation parameters of the target should be known. Using the position information and the relative Doppler frequency information of some strong scatterers, the relative rotational parameters of the entire rigid-body target can be obtained by minimum mean square error method. Due to noise and interference, the estimate values of Doppler frequencies and positions may be wrong, which affect the estimation of rotation parameters. We know that the stronger a scatterer, the less probability of its parameters be wrongly estimated. So the amplitudes of the scatterers can be weight in the date fitting technique. This will improve the rotation parameters' estimation precision and then improve the 3D imaging quality.

2. MIMO RADAR SIGNAL MODEL AND IMAGING BASED ON ONE SNAPSHOT SIGNAL

For planar array MIMO radar, the transmit and receive array antennas form two uniform planar arrays. Let P_m, Q_n denote the positions of the mth transmit antenna and the nth receive antenna respectively. Let $\mathbf{c}_m$ denote the transmit code of the mth transmit antenna. The code can be phase-modulated signal. The baseband transmit waveform can be expressed as

$$\varphi_m(t') = \sum_{l=0}^{L-1} c_m(l)u(t' - lT_0), \tag{1}$$

where $u(t') = \begin{cases} 1 & \text{if } -T_0/2 < t' < T_0/2, \\ 0 & \text{others.} \end{cases}$, T_0 is the subpulse duration, L is the code length, t' is the fast time. Assume that the pre-transmitting time of the mth transmitting signal is T_m. The transmitting signal can be expressed as

$$\psi_m(t',t) = \sum_k \varphi_m(t + t' + T_m - kT)e^{j2\pi f(t+t')}, \tag{2}$$

where T is the pulse repetition duration, f is the carrier frequency, k is the pulse index, t is the slow time. After demodulation, the received back-scattered signal from scatterer A at receive antenna n can be expressed as

$$s_{nA}(t',t) = \alpha \sum_{m=0}^{M-1} \sum_k \varphi_m(t + t' + T_m - kT - \tau_{mA}(t) - \tau_{nA}(t)) \exp(-j2\pi f(\tau_{mA}(t) + \tau_{nA}(t))), \tag{3}$$

where $\tau_{mA}(t) = |P_m A(t)|/c$, $\tau_{nA}(t) = |Q_n A(t)|/c$, α is the signal amplitude, proportional to the square root of the RCS of scatterer A. Let the $M-1$th transmit antenna be the reference antenna, $\tau_{mA}(t) - \tau_{M-1,A}(t) \approx \overrightarrow{P_m P_{M-1}}^T \mathbf{n}_0/c$ is the relative delay, which is known *a prior* and independent of time. So we can define the pre-transmitting time T_m be $T_m = \overrightarrow{P_m P_{M-1}}^T \mathbf{n}_0/c$, then the different transmitting signals arrive at the target at the same time. The relative delay between the receive antennas is $\tau_{nA}(t) - \tau_{N-1,A}(t) \approx \overrightarrow{Q_n Q_{N-1}}^T \mathbf{n}_0/c$, which is also known. Generally speaking, the above two approximations are accurate enough when doing envelope alignment for far field and small angle imaging conditions. The receive signals from different antennas can be aligned and denoted as

$$\begin{aligned} \bar{s}_{nA}(t',t) &= s_{nA}(t' + \tau_{nA}(t) - \tau_{N-1,A}(t), t) \\ &= \alpha \sum_{m=0}^{M-1} \sum_k \varphi_m(t + t' - kT - \tau_{M-1,A}(t) - \tau_{N-1,A}(t)) e^{-j2\pi f(\tau_{mA}(t)+\tau_{nA}(t))}. \end{aligned} \tag{4}$$

Denote $\tilde{\varphi}_m(t')$ the receive filter corresponding to the nth transmitting code and satisfies $\varphi_n(t') \otimes \tilde{\varphi}_m(t') = \delta_{mn}\delta(t')$. After filtering with $\tilde{\varphi}_m$, the signal transmitted from P_m, back scattered from A and received at Q_n can be obtained as

$$\bar{s}_{mnA}(t',t) = \alpha \sum_k \delta\left(t + t' - kT - \tau_A(t)\right) e^{-j2\pi f(\tau_{mA}(t)+\tau_{nA}(t))}, \tag{5}$$

where we denote $\tau_A(t) = \tau_{M-1,A}(t) + \tau_{N-1,A}(t)$ for expression simplicity.

Let O_k be the space center for phase compensation at kth pulse, the corresponding phase is $2\pi f(\tau_{mO_k} + \tau_{nO_k})$. After phase compensation, the phase term is $2\pi f(\tau_{mO_k} + \tau_{nO_k} - \tau_{mA} - \tau_{nA}) = \frac{2\pi}{\lambda}(P_m O_k + Q_n O_k - P_m A - Q_n A)$. The distance term $P_m O_k + Q_n O_k - P_m A - Q_n A$ can be expressed as

$$P_m O_k + Q_n O_k - P_m A - Q_n A = -2(P_0 A - P_0 O_k) + (\mathbf{a}_k - (\mathbf{a}_k^T \mathbf{n}_0)\mathbf{n}_0)^T (\overrightarrow{P_0 Q_0} + \overrightarrow{P_0 P_m} + \overrightarrow{Q_0 Q_n})/r. \tag{6}$$

It can be seen that the phase term is determined by the cross-range vector of the scatterer $(\mathbf{a}_k - (\mathbf{a}_k^T \mathbf{n}_0)\mathbf{n}_0)$, the relative positions of the transmit antennas $(\overrightarrow{P_0 P_m})$ and the relative positions of the receive antennas $(\overrightarrow{Q_0 Q_n})$. In other words, the system can be equivalent to a two dimensional array with positions $\overrightarrow{P_0 P_m} + \overrightarrow{Q_0 Q_n}$.

We assume $M = M_1 \times M_2$ and $N = N_1 \times N_2$. The antenna index m and n can be expressed as $m = (m_1, m_2)$ and $n = (n_1, n_2)$. The positions of P_m and Q_n are $(m_1 d_{tx}, m_2 d_{ty}, 0) + P_X$ and $(n_1 d_{rx}, n_2 d_{ry}, 0) + Q_Y$, where d_{tx},d_{rx} and d_{ty}, d_{ry} are the inter-element distances of transmit array and receive array in X and Y directions, P_X and Q_Y are the positions of P_0 and Q_0 respectively. Then we have $\overrightarrow{P_0 P_m} = (m_1 d_{tx}, m_2 d_{ty}, 0)$, $\overrightarrow{Q_0 Q_n} = (n_1 d_{rx}, n_2 d_{ry}, 0)$ and $\overrightarrow{P_0 P_m} + \overrightarrow{Q_0 Q_n} = (m_1 d_{tx} + n_1 d_{rx}, m_2 d_{ty} + n_2 d_{ry}, 0)$.

When $N_1 \times d_{rx} = d_{tx}$ and $N_2 \times d_{ry} = d_{ty}$, denote $\tilde{m} = m_2 N_2 + n_2$ and $\tilde{n} = m_1 N_1 + n_1$, then $\overrightarrow{P_0 P_m} + \overrightarrow{Q_0 Q_n}$ can be expressed as $(m_1 N_1 d_{rx} + n_1 d_{rx}, m_2 N_2 d_{ry} + n_2 d_{ry}, 0) = (\tilde{n} d_{rx}, \tilde{m} d_{ry}, 0)$, $0 \le \tilde{m} < M_2 N_2, 0 \le \tilde{n} < M_1 N_1$. From here we can see that the positions of $\overrightarrow{P_0 P_m} + \overrightarrow{Q_0 Q_n}$ form a rectangular virtual array and the inter-element spacings are the same as that of MIMO receiving array. This is shown in Fig. 1.

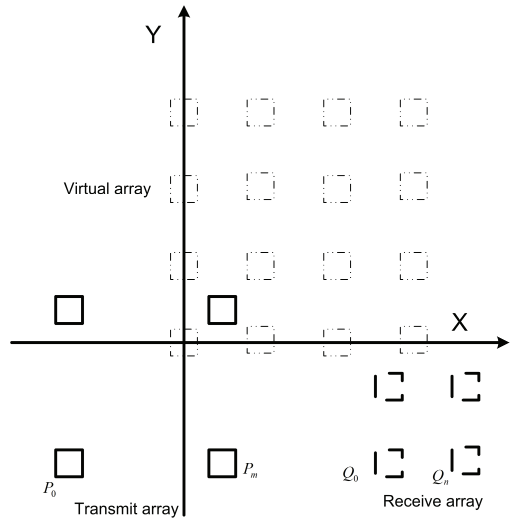

Figure 1: Geometry of a planar MIMO array.

The signal after phase compensation can be expressed as

$$\begin{aligned}\tilde{s}_{mnA}(t',t) &= \alpha\sum_k \delta\left(t+t'-kT-\tau_A(t)\right)e^{-j2\pi f(\tau_{mA}(t)+\tau_{nA}(t)-\tau_{mO_k}-\tau_{nO_k})}\\ &= \alpha\sum_k \delta\left(t+t'-kT-\tau_A(t)\right)e^{-j\frac{4\pi}{\lambda}(|P_0A|(t)-|P_0O_k|)}e^{j\frac{2\pi}{\lambda}\tilde{\mathbf{a}}_k^T(\overrightarrow{P_0Q_0}+\overrightarrow{P_0P_m}+\overrightarrow{Q_0Q_n})/r}\\ &= \alpha\sum_k \delta\left(t+t'-kT-\tau_A(t)\right)e^{-j\frac{4\pi}{\lambda}(|P_0A|(t)-|P_0O_k|)}e^{j\frac{2\pi}{\lambda}\tilde{\mathbf{a}}_k^T\overrightarrow{P_0Q_0}/r}e^{j\frac{2\pi}{\lambda}(\tilde{y}_kd_{ry}\tilde{m}+\tilde{x}_kd_{rx}\tilde{n})/r},\end{aligned} \tag{7}$$

where $\tilde{\mathbf{a}}_k=\mathbf{a}_k-(\mathbf{a}_k^T\mathbf{n}_0)\mathbf{n}_0$ with coordinate $(\tilde{x}_k,\tilde{y}_k,\tilde{z}_k)$.

Because the position of the virtual antenna is $\overrightarrow{P_0P_m}+\overrightarrow{Q_0Q_n}=(\tilde{n}d_{rx},\tilde{m}d_{ry},0)$, $0\le\tilde{n}\le M_1N_1, 0\le\tilde{m}\le M_2N_2$, the signal $\bar{s}_{mnA}(t',t)$ can be re-arranged and denoted as $\tilde{s}_{\tilde{m}\tilde{n}A}(t',t)$, where $\tilde{m}$ and $\tilde{n}$ are in ascending order.

The spatial domain two dimensional Fourier transform (on $\tilde{m},\tilde{n}$) of $\tilde{s}_{\tilde{m}\tilde{n}A}(t',t)$ can be expressed as

$$\begin{aligned}&\tilde{s}_A(f_x,f_y,t',t)=\alpha\sum_k e^{j\pi(M_1N_1-1)(\tilde{f}_{kx}-f_x)}e^{j\pi(M_2N_2-1)(\tilde{f}_{ky}-f_y)}e^{j\frac{2\pi}{\lambda r}\tilde{\mathbf{a}}_k^T\overrightarrow{P_0Q_0}}\\ &\times e^{-j\frac{4\pi}{\lambda}(|P_0A|(t)-|P_0O_k|)}\delta\left(t+t'-kT-\tau_A(t)\right)\frac{\sin(\pi M_1N_1(f_x-\tilde{f}_{kx}))}{\sin(\pi(f_x-\tilde{f}_{kx}))}\frac{\sin(\pi M_2N_2(f_y-\tilde{f}_{ky}))}{\sin(\pi(f_y-\tilde{f}_{ky}))}\\ =&\sum_k\tilde{\alpha}(f_x,f_y)e^{-j\frac{4\pi}{\lambda}(|P_0A|(t)-|P_0O_k|)}\delta\left(t+t'-kT-\tau_A(t)\right)\tilde{\delta}(f_x-\tilde{f}_{kx},f_y-\tilde{f}_{ky}),\end{aligned} \tag{8}$$

where we denote $\tilde{f}_{kx}=\frac{\tilde{x}_kd_{rx}}{\lambda r}$, $\tilde{f}_{ky}=\frac{\tilde{y}_kd_{ry}}{\lambda r}$, $f_x=\frac{n}{M_1N_1}$, $f_y=\frac{m}{M_2N_2}$, $\tilde{\delta}(x,y)=\frac{\sin(\pi M_1N_1x)}{\sin(\pi x)}\frac{\sin(\pi M_2N_2y)}{\sin(\pi y)}$ and $\tilde{\alpha}(f_x,f_y)=\alpha e^{j\pi(M_1N_1-1)(\tilde{f}_{kx}-f_x)}e^{j\pi(M_2N_2-1)(\tilde{f}_{ky}-f_y)}e^{j\frac{2\pi}{\lambda r}\tilde{\mathbf{a}}_k^T\overrightarrow{P_0Q_0}}$.

It can be seen that $\tilde{s}_A(f_x,f_y,t',kT)$ is actually the three dimensional image of the scatterer A at kth pulses. The peak is located at $(\frac{\tilde{x}_kd_{rx}}{\lambda r},\frac{\tilde{y}_kd_{ry}}{\lambda r},\tau_A(kT))$, where the cross-range and down-range information of A are obtained. If $\tilde{s}_{\tilde{m}\tilde{n}}(t',t)$ includes all scatterers' back scattered information, $\tilde{s}(f_x,f_y,t',t)$ is then the three dimensional image of the target at slow time t.

Because the discrete frequency is limited to $[-\frac{1}{2},\frac{1}{2}]$, the $\tilde{x}_k$ and $\tilde{y}_k$ should be limited to $[-r\frac{\lambda}{2d_x}, r\frac{\lambda}{2d_x}]$ and $[-r\frac{\lambda}{2d_y}, r\frac{\lambda}{2d_y}]$.

3. 3-D IMAGES ALIGNMENT, MOTION COMPENSATION AND COHERENT COMBINATION

The center of the three dimensional image at kth pulse is O_k and the O_k for different k may be different, so the 3-D images are not aligned. Even though the O_k can be chosen as the same, because the target is moving during different pulses, the 3-D images are also not aligned. Correlation criterion can also be used to align the 3-D images.The width of the unambiguous window is $\frac{\lambda r}{d_x}$ ($\frac{\lambda r}{d_y}$). In order to increase the cross-range resolution, the radar parameters are usually designed such that the width of the unambiguous window is as small as possible. However, during the coherent processing period, the target may move through multiple unambiguous windows. But in the range direction, there is no wrap. Based on this observation, the correlation of the images in the cross-range direction should be cyclic correlation, but in the range direction, the correlation is the conventional correlation.

After alignment, the 3-D images should be coherently combined to increase the SNR and mitigate the cross-range sidelobes. We consider the case that there is an isolated scatterer. Denote O as an isolated scatterer on the target, the phase of $\tilde{s}_A$ can be compensated using the phase of scatterer O. Denote $\tilde{s}_A(f_x, f_y, t', kT)$ the image at kth pulse after alignment. The image after alignment and motion compensation is (omit $\tilde{\alpha}(f_x, f_y)$ for simplicity):

$$\tilde{s}_A(f_x, f_y, t', kT) \times e^{j\frac{4\pi}{\lambda}(|P_0O|(kT)-|P_0O_k|)} = e^{-j\frac{4\pi}{\lambda}(\mathbf{w}^T\tilde{\mathbf{a}}kT)}\delta\left(t' - \tau_A(0)\right)\tilde{\delta}(f_x - \tilde{f}_{0x}, f_y - \tilde{f}_{0y}), \quad (9)$$

where $\mathbf{w} = (\mathbf{v} - \mathbf{n}_0^T\mathbf{v}\mathbf{n}_0)/r - \Omega\hat{\omega}\mathbf{n}_0$, Ω is the rotation speed of the target around its self axis, $\hat{\omega}$ is a skew symmetric matrix, $\mathbf{v}$ is the speed of the target, $\tilde{\mathbf{a}} = \overrightarrow{OA} - (\overrightarrow{OA}^T\mathbf{n}_0)\mathbf{n}_0$. It should be noted that the $\tilde{f}_{0x}$, $\tilde{f}_{0y}$ and $\tau_A(0)$ are now time independent or O_0 can be thought of as the origin of the 3-D images. The candidate isolated scatterer O can be chosen as the scatterer with a high amplitude and low variance.

From (9) it can be seen that the 3-D images in different instants can be combined coherently if the $\mathbf{w}$ is known. After coherent combination, the 3-D image can be expressed as

$$\begin{aligned}\tilde{s}_A(f_x, f_y, t') &= \sum_k \tilde{\alpha}(f_x, f_y)e^{-j\frac{4\pi}{\lambda}(\mathbf{w}^T(\tilde{\mathbf{a}}-\mathbf{a})kT)}\delta\left(t' - \tau_A(0)\right)\tilde{\delta}(f_x - \tilde{f}_{0x}, f_y - \tilde{f}_{0y}) \\ &= \tilde{\alpha}(f_x, f_y)\delta\left(t' - \tau_A\right)\tilde{\delta}(f_x - \tilde{f}_{0x}, f_y - \tilde{f}_{0y})\frac{\sin(\frac{2\pi}{\lambda}\mathbf{w}^T(\tilde{\mathbf{a}}-\mathbf{a})KT)}{\sin(\frac{2\pi}{\lambda}\mathbf{w}^T(\tilde{\mathbf{a}}-\mathbf{a})T)}. \quad (10)\end{aligned}$$

4. COMPUTATION OF W

According to (9), $\mathbf{w}^T\tilde{\mathbf{a}}_0$ can be obtained by Fourier transform of $\tilde{s}_A(\tilde{f}_{0x}, \tilde{f}_{0y}, \tau_A(0), kT)$ on k variable and denoted as f_d. At the same time, $\tilde{\mathbf{a}}_0$ can be obtained according to the information contained in $(\tilde{f}_{0x}, \tilde{f}_{0y}, \tau_A(0))$. It should be noted that $\tilde{\mathbf{a}}_0$ is relative to O (ISAR focusing point), ($\tilde{f}_{0x}$,$\tilde{f}_{0y}$, $\tau_A(0)$) is relative to O_0. O and O_0 may not be same. So in order to obtain $\tilde{\mathbf{a}}_0$, we should shift the 3-D images such that O is the origin. We use $\tilde{\mathbf{a}}$ to replace $\tilde{\mathbf{a}}_0$ for simplicity in the following derivation. Then $\mathbf{w}$ can be estimated by minimum mean square error method:

$$\begin{array}{rl}\min_{\mathbf{w}} & E\ \ |f_d + \frac{2\mathbf{w}^T\tilde{\mathbf{a}}}{\lambda}|^2 \\ s.t. & \mathbf{w}^T\mathbf{n}_0 = 0.\end{array} \quad (11)$$

The solution is

$$\mathbf{w} = -\frac{\lambda}{2}\mathbf{R}^{-1}\left(\mathbf{r}_{f_d\tilde{a}} - \frac{\mathbf{r}_{f_d\tilde{a}}^T\mathbf{R}^{-1}\mathbf{n}_0}{\mathbf{n}_0^T\mathbf{R}^{-1}\mathbf{n}_0}\mathbf{n}_0\right), \quad (12)$$

where $\mathbf{R} = E(\tilde{\mathbf{a}}\tilde{\mathbf{a}}^T)$, $\mathbf{r}_{f_d\tilde{a}} = E(f_d\tilde{\mathbf{a}})$, E expresses expectation operator.

If isolated scatterer does not exist, some other motion compensation methods such as Rank One Phase Estimation (ROPE) algorithm, entropy minimization method and subspace method can be used. But the phase obtained by ROPE and entropy minimization method is the estimation of the phase of one scatterer plus a linear phase term. A linear phase term changes the position of the image in cross-range direction, although it does not change the entropy of the image. The above $\mathbf{w}$

estimation method cannot be used in this case. It should be revised as the following optimization procedure, where $\tilde{f}$ is the unknown frequency shift.

$$\begin{array}{rl} \min_{\mathbf{w},\tilde{f}} & E|f_d - \tilde{f} + \frac{2\mathbf{w}^T\tilde{\mathbf{a}}}{\lambda}|^2 \\ s.t. & \mathbf{w}^T\mathbf{n}_0 = 0. \end{array} \tag{13}$$

Denote $\bar{\mathbf{R}} = E(\tilde{\mathbf{a}}\tilde{\mathbf{a}}^T) - E(\tilde{\mathbf{a}})E(\tilde{\mathbf{a}})^T$, $\bar{\mathbf{a}} = E(\tilde{\mathbf{a}})$, $\bar{f}_d = E(f_d)$, we have

$$\mathbf{w} = \frac{\lambda}{2}\bar{\mathbf{R}}^{-1}\left(\bar{\mathbf{a}}\bar{f}_d - \mathbf{r}_{f_d\tilde{a}} - \frac{\lambda}{4}\mu\mathbf{n}_0\right). \tag{14}$$

Using $\mathbf{n}_0^T\mathbf{w} = 0$, we have

$$\mu = \frac{4\mathbf{n}_0^T\bar{\mathbf{R}}^{-1}\left(\bar{\mathbf{a}}\bar{f}_d - \mathbf{r}_{f_d\tilde{a}}\right)}{\lambda\mathbf{n}_0^T\bar{\mathbf{R}}^{-1}\mathbf{n}_0}. \tag{15}$$

Due to noise and interference, the estimated Doppler frequencies and scatterer positions may be error. When data with errors are used, the estimate precision of $\mathbf{w}$ will be affected. We know that the stronger a scatterer, the less probability of its parameters be wrongly estimated. So the amplitudes of the scatterers can be used as weight in the date fitting technique. The new estimation method can be described as

$$\begin{array}{rl} \min_{\mathbf{w},\tilde{f}} & E\left(g^2(\alpha)|f_d - \tilde{f} + \frac{2\mathbf{w}^T\tilde{\mathbf{a}}}{\lambda}|^2\right) \\ s.t. & \mathbf{w}^T\mathbf{n}_0 = 0, \end{array} \tag{16}$$

where α is the amplitude of a scatterer, $g^2(\alpha)$ is the weighting function. Similarly, denote $\bar{\bar{\mathbf{r}}}_{f_d\tilde{a}} = E(f_d\tilde{\mathbf{a}}g^2(\alpha))$ $\bar{\bar{\mathbf{a}}} = E(\tilde{\mathbf{a}}g^2(\alpha))$, $\bar{\bar{f}}_d = E(f_dg^2(\alpha))$, $\bar{\bar{\mathbf{R}}} = E(\tilde{\mathbf{a}}\tilde{\mathbf{a}}^Tg^2(\alpha)) - \bar{\bar{\mathbf{a}}}\bar{\bar{\mathbf{a}}}^T/E(g^2(\alpha))$, we have

$$\mathbf{w} = \frac{\lambda}{2}\bar{\bar{\mathbf{R}}}^{-1}\left(\bar{\bar{\mathbf{a}}}\bar{\bar{f}}_d - \bar{\bar{\mathbf{r}}}_{f_d\tilde{a}} - \frac{\lambda}{4}\bar{\mu}\mathbf{n}_0\right), \tag{17}$$

$$\bar{\mu} = \frac{4\mathbf{n}_0^T\bar{\bar{\mathbf{R}}}^{-1}\left(\bar{\bar{\mathbf{a}}}\bar{\bar{f}}_d - \bar{\bar{\mathbf{r}}}_{f_d\tilde{a}}\right)}{\lambda\mathbf{n}_0^T\bar{\bar{\mathbf{R}}}^{-1}\mathbf{n}_0}. \tag{18}$$

5. SIMULATION RESULTS

5.1. Simulation A

In this simulation, we check the relationship between parameter's estimation precision and the number of errors occurred when estimating scatterer parameters. We assume $\mathbf{n}_0 = [0, 0, 1]$ and

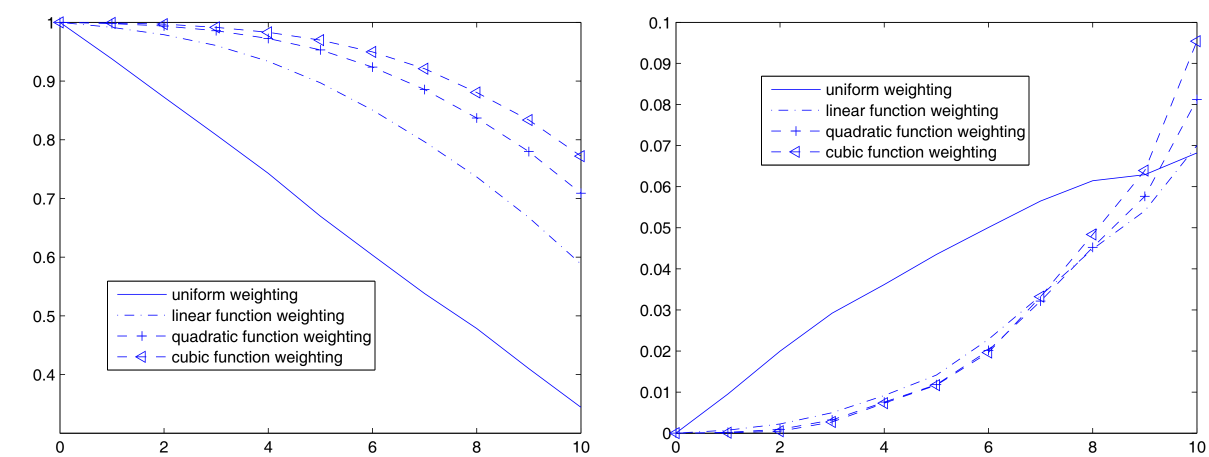

(a) (b)

Figure 2: The relationship between mean (a), variance (b) and error number.

$\mathbf{w} = [1, 0, 0]$. 15 scatterers are randomly distributed in a cubic of $[-50, 50] \times [-50, 50] \times [-50, 50]\,\mathrm{m}^3$. We assume the cross range resolution is 1 m. The wavelength λ is absorbed in $\mathbf{w}$ or we assume $\lambda = 2$. The frequency resolution is also assumed 1 Hz. The estimated positions and frequencies are uniformly distributed around their real values. We assume the amplitudes of the scatterers are from 1 to 10 uniformly. The probability of errors satisfies $p_e = 0.5 + (Amp - 1) * (0.05 - 0.5)/9$, that is for scatterers with amplitudes 1, error occurs with probability 0.5, but for scatterers with amplitudes 10, error occurs with probability 0.05. Simulations with error number from 0 to 10 are done. For each case, 1000 times simulations are performed. The estimated $\mathbf{w}$ is denoted as $\hat{\mathbf{w}}$. We chose $g(\alpha) = \alpha^k$ for $k = 0, 1, 2, 3$. The estimated $\hat{\mathbf{w}}(1)$ and the variance of $\hat{\mathbf{w}}(1)$ with error number are shown in Fig. 2(a) and Fig. 2(b). We can see that with the increase of the number of errors, the estimation precision decreases and the variance increases gradually. At the same time, with the increase of the order k, the performance increase. So generally, we should chose a larger order.

5.2. Simulation B

In this simulation we check the 3D imaging performance when using the rotation parameters estimation method proposed in this paper. The carrier frequency is 35 GHz. The transmitting code is random BPSK modulated signal with length $L = 512$ and bandwidth $B_s = 150M$ Hz. The MIMO radar under consideration contains a 8×8 square transmitting array with inter-element spacing of 107.1429 m and a 8×8 square receiving array with inter-element spacing of 13.3929 m. The target with 11 scatterers is located in the $\mathbf{n}_0 = [0.4402, 0.1761, 0.8805]$ direction and is 100 km from the radar. It moves uniformly in the X axis direction with speed $[133.9286, 0, 0]$ m/s. The unambiguous distance at 100 km is 64 m. The square roots of the RCS of the 11 scatterers are 1, 2, 3, …, and 11 m. Fig. 3 shows the original 3-D image of the target. We choose $g(\alpha) = \alpha^2$ when we estimate $\mathbf{w}$ using weighting MMES method. The relative error of the estimated $\mathbf{w}$ using conventional method and the weighting method are 0.022 and 0.02 respectively. The reconstructed image using the weighting method is shown in Fig. 4. It can be seen that the reconstructed images are similar to the original images.

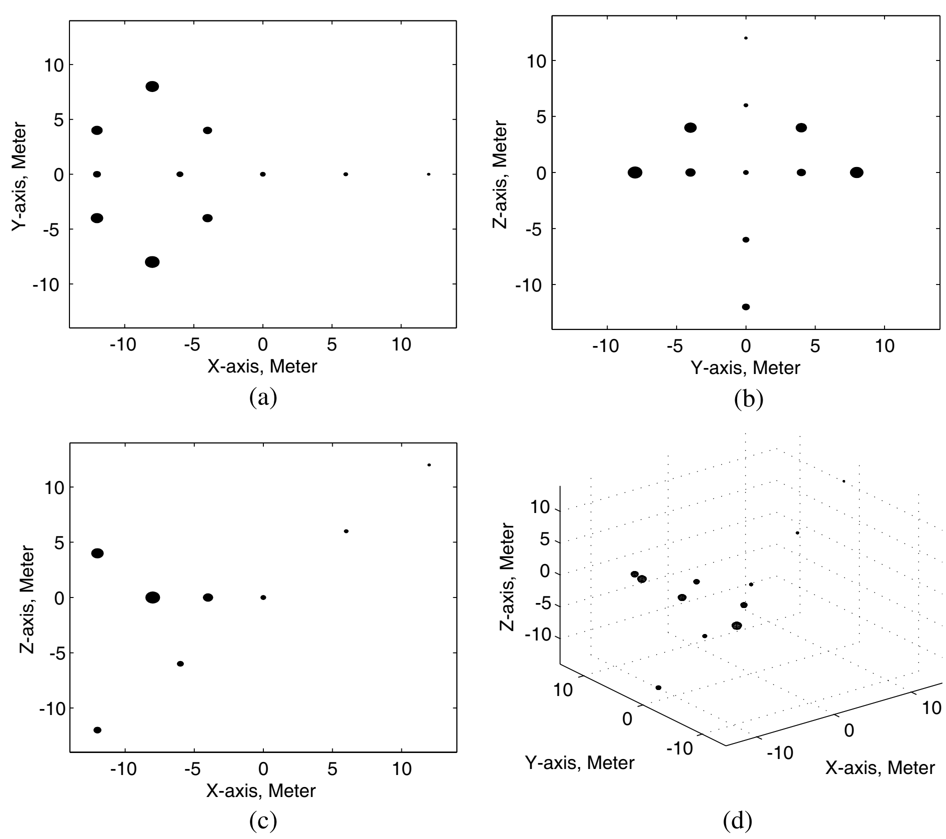

Figure 3: Three different projections and 3-D view of the target model (simulation B).

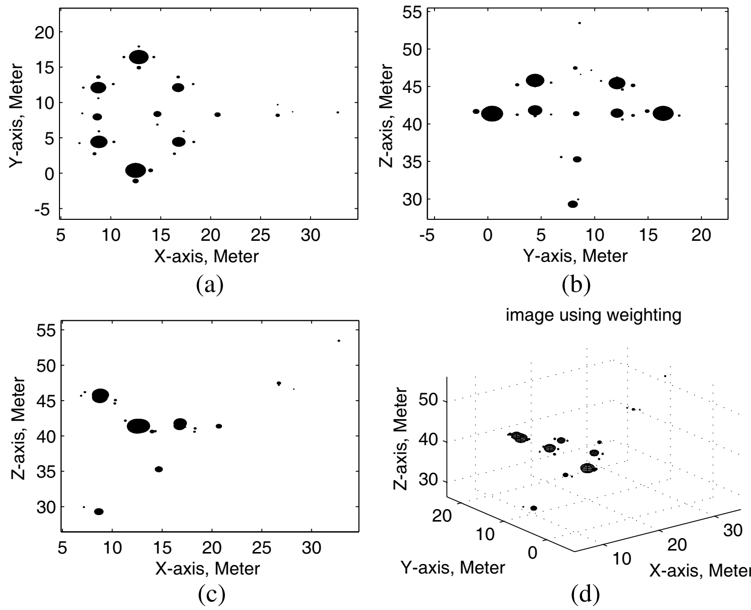

Figure 4: Three different projections and 3-D view of the reconstructed image.

6. CONCLUSION

Colocated MIMO radar provides wide aperture. Combining MIMO radar and ISAR technique can form 3D image with a higher SNR. A weighting MMSE estimation method is proposed to estimate the rotation vector of the target relative to the radar. The estimation precision is improved using the weighting method compared with the conventional method.

ACKNOWLEDGMENT

This work is supported by TDSI/11-008/1A Singapore and National Natural Science Foundation of China under Grant No. 61071175.

REFERENCES

1. Chen, C. C. and H. C. Andrews, "Target-motion-induced radar imaging," *IEEE Trans. Aerosp. Electron. Syst.*, Vol. 16, No. 1, 2–14, 1980.
2. Wang, G. Y., X. G. Xia, and V. C. Chen, "Three-dimensional ISAR imaging of maneuvering targets using three receivers," *IEEE Trans. Image Process.*, Vol. 10, No. 3, 436–447, 2001.
3. Zhang, Q, T. S. Yeo, G. Du, and S. H. Zhang, "Estimation of three-dimensional motion parameters in interferometric ISAR imaging," *IEEE Trans. Geosci. Remote Sens.*, Vol. 42, No. 2, 292–300, 2004.
4. Ma, C., T. S. Yeo, Q. Zhang, H. S. Tan, and J. Wang, "Three-dimensional interferometry ISAR imaging based on antenna array," *IEEE Trans. Geosci. Remote Sens.*, Vol. 46, No. 2, 504–515, 2008.
5. Ma, C., T. S. Yeo, C. S. Tan, and H. S. Tan, "Sparse array 3D ISAR imaging based on maximum likelihood estimation and CLEAN technique," *IEEE Trans. Image Process.*, Vol. 19, No. 8, 2127–2142, 2010.
6. Wang, D. W, X. Y. Ma, A. L. Chen, and Y. Su, "High-resolution imaging using a wideband MIMO radar system with two distributed arrays," *IEEE Trans. Image Process.*, Vol. 19, No. 5, 1280–1289, 2010.
7. Ma, C., T. S. Yeo, C. S. Tan, and Z. F. Liu, "Three-dimensional imaging of targets using colocated MIMO radar," *IEEE Trans. Geosci. Remote Sens.*, Vol. 49, No. 8, 3009–3021, 2011.
8. Zhu, Y., Y. Su, and W. Yu, "An ISAR imaging method based on MIMO technique," *IEEE Trans. Geosci. Remote Sens.*, Vol. 48, No. 8, 3290–3299, 2010.
9. Pastina, D., M. Bucciarelli, and P. Lombardo, "Multistatic and MIMO distributed ISAR for enhanced cross-range resolution of rotating targets," *IEEE Trans. Geosci. Remote Sens.*, Vol. 48, No. 8, 3300–3317, 2010.
10. Ma, C., T. S. Yeo, C. S. Tan, et al., "Three dimensional imaging using colocated MIMO radar and ISAR technique," *IEEE Trans. Geosci. Remote Sens.*, accepted.

High Performance Parallel Implementation of Compressive Sensing SAR Imaging

Jihua Tian, **Jinping Sun**, **Yuxi Zhang**, **and Najeeb Ahmad**
School of Electronic and Information Engineering, Beihang University, Beijing, China

Abstract— The compressive sensing (CS) theory has been applied to SAR imaging systems in many ways. And it shows a significant reduction in the amount of sampling data at the cost of much longer reconstruction time. In this paper, we investigate the development and optimization of Iterative Shrinkage/Thresholding (IST) algorithm applying to CS reconstruction of SAR images on two parallel architectures, standard vectorized multi-core processors (e.g., quad-core CPUs) and graphics processing units (GPUs). Meanwhile, we modify the IST algorithm according to the characteristic of SAR images to obtain a faster recovery speed. The experiment results show that CS reconstruction of SAR images on parallel architecture has a significant speedup in comparison with implemented on conventional serial architectures.

1. INTRODUCTION

As a major remote sensing sensor, synthetic aperture radar (SAR) can produce high resolution images from a moving platform, such as an airplane or a satellite. A SAR system produces 2D (range and azimuth) terrain reflectivity images by emitting a sequence of closely spaced radio frequency pulses and by sampling the echoes scattered from the ground targets [1]. Modern airborne and spaceborne SAR systems can produce very high resolution images and are being widely used in many civilian and military applications [1, 2]. Compressive sensing (CS) is a new developing novel theory that proclaims that an unknown sparse (or sparse under certain basis) signal can be exactly recovered with high probability from very limited number of measurements by solving a convex l_1 optimization problem [3–5]. Based on rigid mathematics, CS has attracted many attentions in image processing, data fusion of multiple sensors, radar applications and so on. Up to now, many literatures have addressed adopting CS in some radar applications including SAR and inverse synthetic aperture radar (ISAR) [6–8].

However, the computational complexity of the reconstruction of sparse signals is quite high. Meanwhile, the computation of CS based SAR imaging technique becomes larger and larger along with the increasing demand on high resolution SAR images. Recently, the graphics processing unit (GPU) and multi-core CPUs have shown great potential for accelerating computations in many application areas, which offer an alternative for fast reconstruction of sparse signals. This paper realized the fast reconstruction of CS based SAR images, taking advantage of the efficient parallel computing capabilities of GPU and CPUs.

2. THEORY OF COMPRESSIVE SENSING

The theory of CS reveals that exact recovery of an unknown sparse signal is possible from very limited samples by solving an inverse problem through either a linear program or a greedy pursuit. Suppose that signal $s \in R^N$ is K-sparse on an orthonormal basis Ψ, i.e., $s = \Psi x$, with $\Psi = \{\psi_1, \psi_2, \ldots, \psi_N\}$ is an $N \times N$ matrix, and x is a vector with all except K of its entries are zeros. In order to reconstruct signal s, a set of M measurements is acquired ($M < N$). We do this through non-adaptive linear projection in the form of $y = \Phi s = \Phi\Psi x$ where Φ is an $M \times N$ matrix. Since $M < N$, recovery of the signal s from the measurements y is ill-posed. The CS theory reveals that when the matrix $\mathbf{A} = \Phi\Psi$ has the restricted isometry property (RIP) [3–5], the signal s or x can be recovered from a similarly sized set of $M = O(K \log(N/K))$ measurements y with high probability. Formally, with high probability, x is the unique solution to

$$\min \|x\|_1 \quad \text{s.t.} \quad y = \Phi\Psi x \tag{1}$$

which can be solved efficiently with linear programming techniques.

3. ITERATIVE SHRINKAGE/THRESHOLDING ALGORITHM

Taking noise into account, we generally solve the problem by transforming the constraint convex optimization problem into the following unconstraint convex optimization problem

$$\min_x \frac{1}{2} \|y - \mathbf{A}x\|_2^2 + \tau \|x\|_1 \tag{2}$$

where $\|\cdot\|_2$ denotes the Euclidean norm and τ is the regularization parameter which provides a trade-off between fidelity to the measurements and the noise sensitivity. Iterative shrinkage/thresholding (IST) [9] is a state-of-the-art algorithm in solving the unconstraint convex optimization problem, with the following iterative scheme

$$x_{k+1} = soft(x_k + \mathbf{A}^H(y - \mathbf{A}x_k), \tau) \tag{3}$$

where $soft(x, \tau) = \mathrm{sign}(x)\max(|x| - \tau, 0)$ is the shrinkage operator.

In IST algorithm, the most computation prohibitive portion is the matrix-vector multiplication involving $\mathbf{A}$ and $\mathbf{A}^H$, with computational complexity of $O(MN)$, which is very large, especially when the matrix is a large dense one. Besides, there are two such multiplications per iteration. However, if we convert (3) to (4), where $\mathbf{B} = \mathbf{A}^H\mathbf{A}$, we can find that, the two multiplications reduce to one only involving $\mathbf{B}$ in each iteration. Although the computation complexity of $\mathbf{B}x_k$ is $O(N^2)$ larger than $O(MN)$, it really can reduce the whole computation when implemented in parallel.

$$x_{k+1} = soft\left(x_k + \mathbf{A}^H y - \mathrm{B}x_k, \tau\right) \tag{4}$$

So we proposed a new scheme based on the above analysis, precomputing $\mathbf{B}$ and $\mathbf{A}^H y$ before the iteration. In this way, it not only reduces the cost of matrix-vector multiplication, but also reduces the time cost by data transmission between two multiplications. In addition, we noticed that the residual vector $r_k = y - \mathbf{A}x_k$ should be available when compute the objective function value. However, r_k is dependent on $\mathbf{A}$, which is against the proposed method requiring only $\mathbf{B}$ and $\mathbf{A}^H y$. So we need some changes to the calculation of objective function value to meet with the proposal. Fortunately, we find that if we replace $f = 0.5\|r_k\|^2 + \tau\|x\|_1$ with (5), the two different methods show the same effect when judging whether the termination criterion is satisfied based on the relative change of two contiguous objective function values, although $\tilde{f}$ is different from f. In addition, as we know, SAR images are not sparse over all range bins, so we add some constraints to escape from recovering the unsparse ones. If the objective function value in one iteration is no less than the one got in the former iteration, then we can say the scene is not sparse and terminate the recovery.

$$\tilde{f} = 0.5\left\|\mathbf{A}^H y - \mathrm{B}x\right\|^2 + \tau\left\|x\right\|_1 \tag{5}$$

The basic procedure of the modified version of IST algorithm is

1. Initialize $x_1 = 0$, compute $\mathbf{A}^H y$ and $\mathbf{B}$, set iteration step $k = 1$;
   (a) Compute the correlation of $\mathbf{A}$ with the current residual: $x_{temp} = \mathbf{A}^H y - \mathbf{B}x_k$;
   (b) Compute the new estimate: $x_{k+1} = soft(x_k + x_{temp}, \tau)$;
   (c) Compute $\tilde{f}_{k+1} = 0.5\|x_{temp}\|^2 + \tau\|x_{k+1}\|_1$ and $\Delta\tilde{f} = |\tilde{f}_{k+1} - \tilde{f}_k|/\tilde{f}_k$, if $\tilde{f}_{k+1} > \tilde{f}_k$ for $k > 2$ or $\Delta\tilde{f} < \delta$, then terminate the iteration. Otherwise, go to step 2 for the next iteration.

4. PARALLEL IMPLEMENTATION OF CS SAR IMAGING

4.1. GPU Implementation

In CUDA framework, communication between host CPU and GPU device often costs lots of time, so we should use such communication as few as possible. In this paper, data communication between host CPU and GPU device only occurs at the start and end of the algorithm. At the start phase, the precomputed $\mathbf{A}^H y$ and $\mathbf{B}$, regularization parameter τ and other necessary parameters are transmitted to GPU, while the reconstructed results are transmitted back to CPU at the end of the recovery [10].

GPU device begins to execute the recovery once it receives the data. Note that in the matrix-vector multiplication, row vectors of the matrix are mutually independent, which is fit to be implemented in parallel. The matrix-vector multiplication is realized with coarse-grained parallelism blocks that can not communication with each other, together with the fine-grained parallelism threads. In detail, multiplications between row vectors of $\mathbf{B}$ with x_k are realized in coarse-grained parallelism, while elements and elements products inside the vector multiplication are realized in fine-grained parallelism. We store the matrix $\mathbf{B}$ in global memory, so we have to access the global memory to fetch it when it is needed. To limit the memory latency, we utilize the shared memory that is accessed as fast as register. For instance, row vectors of $\mathbf{B}$ and x_k are all stored in the shared memory that lies in each thread block.

In the IST recovery, we have to transform some multidimensional data to one dimension, such as the calculation of Euclidean norm and l_1 norm. Take the calculation of l_1 norm for instance, normally we add all the elements step by step. But on GPU, so we split such task into parallel accumulation involving multiple thread blocks, where each block is responsible for addition of part data and the partial sum got in each thread are summed up at last.

During the vector multiplication realization in fine-grained parallelism and computation of multidimensional data to one dimension, each thread block will complete summation of many data. This paper adopts the parallel summation reduction method to make most efficient of the parallel performance of GPU, Figure 1 shows the procedure of parallel summation reduction with 8 elements. The traditional serial summation method requires n steps to sum up n elements, while the parallel summation reduction method only requires $\log n$ steps. Meanwhile, the parallel summation reduction works with sequential addressing which is bank conflict free, avoiding the reduction in efficient access bandwidth. In addition, the threads in each warp will either execute the summation or not, which will avoid the performance degradation caused by divergence.

4.2. CPUs Implementation via OpenMP

OpenMP is a shared-memory application programming interface (API), whose features are based on prior efforts to facilitate shared-memory parallel programming [11]. OpenMP provides a fork-and-join execution model shown in Figure 2, which supports an incremental approach to realize parallel programs. It is easy to apply the OpenMP into the standard sequential code, only by placing parallel directives around time-consuming loops that do not contain data dependences and leaving the most part of the program unchanged.

On implementation of IST algorithm on CPUs via OpenMP, we should first identify the parts which can be implemented in parallelism. Based on the above analysis, we know that matrix-vector multiplication, calculation of Euclidean norm and l_1 norm are the ones we are looking for. By placing directives around these loops, we can apply the parallelism to the modified IST algorithm. In OpenMP model, all threads have access to the same globally shared memory. And the data being processed can be shared or private, where shared data is accessible by all threads, while private data can be accessed only by the thread that owns it. Therefore, we should identify the data in the loops is shared or private to make sure they will be handled properly.

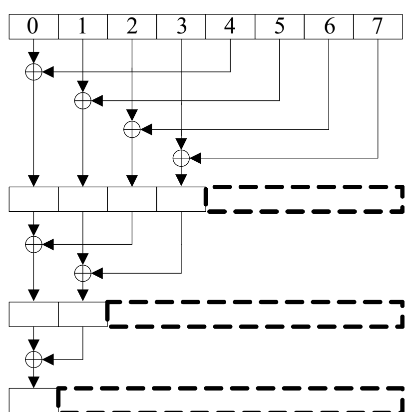

Figure 1: Parallel summation reduction with 8 elements.

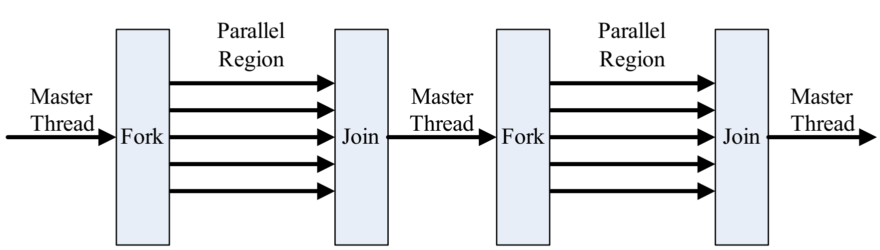

Figure 2: The Fork-Join model of OpenMP.

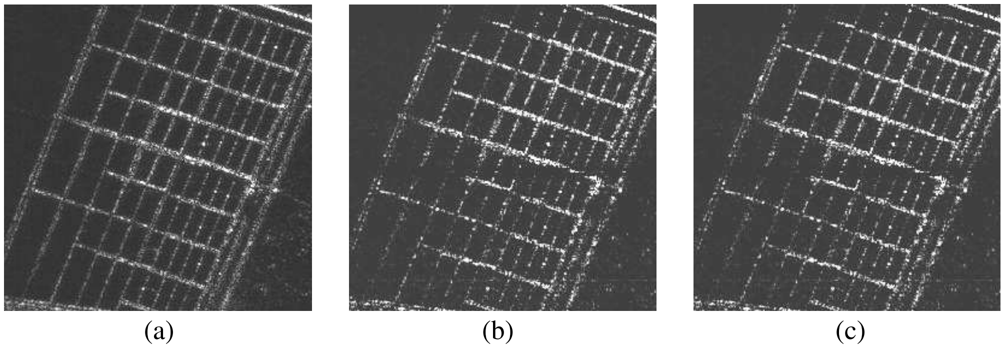

Figure 3: (a) Conventional SAR imaging result with full samples. (b) CS based SAR imaging result with 50% samples implemented on CPUs. (c) CS based SAR imaging result with 50% samples implemented on GPU.

Table 1: The average execution times on CPU and GPU.

CPU	**CPUs**		**GPU**	
time/s	time/s	speedup	time/s	speedup
8.995	4.09	2.2	0.258	35

5. EXPERIMENT

To validate the speedup of parallel realization of compressive sensing based SAR imaging on GPU, we reconstructed the same SAR image with IST algorithm on CPU and GPU, respectively. The configuration of the CPU used in this paper is Intel Core2 Quad 8400, 2.66 GHz, and the GPU is Tesla C1060. And the data used in the experiment are real airborne SAR data which have been collected by an X-band SAR with the resolution of 2 m. We implemented the CPU and GPU code in single precision float and computed the average processing time over 100 repeated executions on CPU and GPU separately. Figure 3 shows SAR imaging results via conventional method and CS method on CPU and GPU, respectively. We see that performance of CS based SAR imaging is comparable to that of conventional SAR imaging method. Meanwhile, the parallel implementation on CPUs and GPU get the same result. The time cost by CPUs and GPU are shown in Table 1. From Table 1, we can see that multi-core CPUs speeds up 2.2 times than single core CPU, while GPU reach a speedup of 35.

6. CONCLUSIONS

The paper realized the parallel implementation of compressive sensing based SAR imaging on GPU, and iterative shrinkage/thresholding algorithm is adopted to reconstruct the SAR images. To make the most efficient use of parallel architecture, we modified the conventional IST algorithm structure, and realized the fast implementation on multi-core CPUs and GPU device. The experiment result shows that parallel computing capabilities of CPUs and GPU have a significant speedup in comparison with computing capability of CPU.

ACKNOWLEDGMENT

This work is supported by the National Basic Research Program of China (2010CB731903) and in part by the National Natural Science Foundation of China (60901056, 61072112).

REFERENCES

1. Carrara, W. G., R. S. Goodman, and R. M. Majewaki, *Spotlight Synthetic Aperture Radar: Signal Processing Algorithms*, Artech House, Norwood, MA, 1995.
2. Cumming, I. G. and F. Wong, *Digital Processing of Synthetic Aperture Radar*, Artech House, Norwood, MA, 2005.
3. Donoho, D. L., "Compressed sensing," *IEEE Trans. Info. Theory*, Vol. 52, No. 4, 1289–1306, 2006.

4. Candès, E., J. Romberg, and T. Tao, "Robust uncertainty principles: exact signal reconstruction from highly incomplete frequency information," *IEEE Trans. Info. Theory*, Vol. 52, No. 2, 489–509, 2006.
5. Elad, M., "Optimized projections for compressed sensing," *IEEE Trans. Signal Process.*, Vol. 55, No. 12, 5695–5702, 2007.
6. Baraniuk, R. and P. Steeghs, "Compressive radar imaging," *IEEE Radar Conference*, 128–133, 2007.
7. Patel, V. M., G. R. Easley, D. M. Healy, and R. Chellappa, "Compressed synthetic aperture radar," *IEEE Journal of Selected Topics in Signal Processing*, Vol. 4, No. 2, 244–254, 2010.
8. Ender, J. H. G., "On compressive sensing applied to radar," *Signal Processing*, Vol. 90, No. 5, 1402–1414, 2010.
9. Figueiredo, M. A. T. and R. D. Nowak, "An EM algorithm for wavelet-based image restoration," *IEEE Trans. Image Process.*, Vol. 12, No. 8, 906–916, 2003.
10. Lee, S. and S. J. Wright, "Implementing algorithms for signal and image reconstruction on graphical processing units," Tech. Rep., Computer Sciences Department, University of Wisconsin-Madison, November 2008.
11. Barbara, C., J. Gabriele, and V. P. Ruud, *Using OpenMP: Portable Shared Memory Parallel Programming*, The MIT Press, 2007.

Spaceborne SAR Wide-swath Imaging Based on Poisson Disk-like Sampling and Compressive Sensing

Jinping Sun[1], **Yuxi Zhang**[1], **Jihua Tian**[1], **and Bingchen Zhang**[2]

[1]School of Electronic and Information Engineering, Beihang University, Beijing, China
[2]National Key Lab of MW Imaging Tech., Institute of Electronics, CAS, Beijing, China

Abstract— A novel spaceborne synthetic aperture radar (SAR) wide-swath imaging scheme based on compressive sensing (CS) for the sparse scene is presented. The proposed method designs a Poisson disk-like nonuniform sampling pattern along the azimuth direction, which meets the demand of wider swath by restricting the smallest time interval between any two azimuth samples. Experiment results validate the effectiveness of the proposed method via the Radarsat-1 raw data in F2 mode.

1. INTRODUCTION

Due to the range swath width in the conventional single channel spaceborne SAR is restricted by the system parameters, there is a trade-off between the azimuth resolution and the swath width in order to satisfy the Nyquist sampling criterion [1]. And the modern spaceborne SAR wide-swath imaging systems generally adopt the flexible digital beamforming (DBF) or waveform coding techniques of phased array radars, both of which increase the system complexity in various degrees and are still realized under Nyquist sampling criterion [1, 2]. However, the new concept of compressive sensing (CS) states that an unknown sparse (or sparse under transform-domain) signal can be recovered even from what appear to be highly sub-Nyquist-rate samples by solving a ℓ_1-optimization problem [3], which offers the possibility to realize wider swath for conventional single channel spaceborne SAR system. CS theory can effectively reduce the system complexity in acquiring image technique and has been already applied into the SAR imaging [4, 5]. In existing literatures, the realization of azimuth under sampling in SAR imaging based on CS is typically designed as the random selection strategy, but this method cannot be applied to wide-swath imaging in spaceborne SAR since it is unable to assure that the time interval between any two adjacent samples is smaller than the one under the Nyquist limitation. At this point, this article proposes a Poisson disk-like nonuniform sampling pattern along the azimuth direction, which satisfies the demand of wider swath with the constraint of the smallest interval between any two azimuth samples, and also presents the processing procedure and experiment results with raw data.

2. SPACEBORNE SAR RANGE SWATH RESTRICTIONS DUE TO SAMPLING

For a given conventional single channel spaceborne SAR system, the relation between azimuth resolution and Doppler bandwidth caused by platform motion can be expressed as $\rho_a = \kappa_a V_g / B_a$, where V_g denotes the ground speed of satellite, B_a represents the Doppler bandwidth, and a κ_a refers to the broaden factor. The Doppler bandwidth is approximately $B_a = 2 \times 0.8859 V_s/d$, where V_s being the speed of satellite, and d the size of radar antenna along azimuth direction. In order to meet Nyquist sampling criterion, the azimuth sampling rate of SAR system, which refers to the pulse repetition frequency (PRF), must be higher than Doppler bandwidth, i.e.,

$$\mathrm{PRF} \geq (1 + \kappa) B_a \tag{1}$$

where κ is oversampling factor required to suppress azimuth ambiguities. Hence, the slant range swath width is restricted to

$$R_w \leq (1/\mathrm{PRF} - 2T_p) \cdot c/2 \tag{2}$$

where T_p is the pulse duration, and c denotes the speed of light. Considering that the high resolution needs wider Doppler bandwidth, and then requires higher PRF according to (1), so the increasing PRF will inevitably decrease the range swath. However, the new CS theory provides the possibility to break the restriction of (1), and accordingly makes it possible to obtain a wider range swath than the conventional operation.

3. DESIGN OF POISSON DISK-LIKE RANDOM SAMPLING

Poisson disk sampling is commonly used in computer graphics, and it can simply and mathematically be defined as a set of samples (points) in a certain distance space such that every pair of samples are at least certain distance away from each other [6]. Poisson disk sampling has already been applied to compressed MRI as an optimal CS sampling pattern [7]. For the wide-swath imaging, to make sure no aliasing appears in the range direction, the smallest time interval between two adjacent pulses must follow $\Delta t_{\min} \geq (2R_w/c + 2T_p)$, as a result, the azimuth random sampling instant can be designed as

$$t_i = t_{i-1} + (2R_w/c + 2T_p) + \delta_t \tag{3}$$

where R_w is the desired swath width, δ_t is a random variable uniformly distributed in the interval $[0\ \ T_R]$, and $T_R = 1/\mathrm{PRF}$ is pulse repetition period that meets Nyquist sampling criterion. Here, we stack the M azimuth sampling instants as a vector $\mathbf{t} = [t_0\ \ t_1 \ldots\ \ t_{M-1}]^T$.

4. SPACEBORNE SAR DATA PROCESSING BASED ON CS

Since the random CS sampling will reduce the signal-to-noise ratio (SNR) in practice, therefore we still adopt the conventional sampling pattern along the range direction. Moreover, we employ range-azimuth decoupling method, which can meet the demand for focusing with middle level resolution. By the similar way as the processing procedure of spectral analysis (SPECAN) algorithm, we can realize the linear range migration correction (RMC) while carrying out range compression by utilizing the pre-designed sampling pattern, when the Doppler centroid is nonzero. For the detailed realization, please refer to [8, Chap. 9]. After range compression and the linear RMC, the azimuth signal of kth range bin is the convolution of target scene with the azimuth response

$$y_k(t) = \int S_k(t - t')x_k(t')dt' \tag{4}$$

The corresponding discrete form of observation model is

$$\mathbf{y}_k = \mathbf{\Phi}_k \mathbf{x}_k. \tag{5}$$

where the echo samples and desired scene samples are defined by $\mathbf{y}_k = [y_k(t_0)\ y_k(t_1) \ldots y_k(t_{M-1})]^T$ and $\mathbf{x}_k = [x_k(0)\ x_k(T_R) \ldots x_k((N-1) \cdot T_R)]^T$, and $\mathbf{x}_k$ with the uniform space interval $\Delta_x = V_g \cdot T_R$ satisfying the Nyquist limitation. $\mathbf{\Phi}_k$ is an $M \times N$ measurement matrix, whose element in the ith row and the nth column under the require of middle resolution can be written as

$$\phi_k(i, n) = w(t_i - nT_R)\exp(j2\pi f_{dc}(t_i - nT_R) + j\pi f_{dr}(k)(t_i - nT_R)^2) \tag{6}$$

where f_{dc} is Doppler centroid, $f_{dr}(k)$ is Doppler rate of kth range bin, and $w(t)$ is a weighting function related with radar beam footprint. Since $M < N$, (5) are underdetermined equation. Fortunately, according to the CS theory, $\mathbf{x}_k$ can be reconstructed by solving the following optimization problem with its characteristic of sparsity

$$\hat{\mathbf{x}}_k = \arg\min(\|\mathbf{x}_k\|_1)\ \text{ s.t. }\ \mathbf{y}_k = \mathbf{\Phi}_k \mathbf{x}_k \tag{7}$$

where $\|\cdot\|_1$ denotes ℓ_1 norm. Up to now, there are many state-of-art recovery algorithms that can be used to solve (7) in the field of CS.

5. RESULTS WITH RADARSAT-1 RAW DATA

The Radarsat-1 raw data in F2 mode used in our experiment are obtained from the CD provided by Reference [8], and the corresponding parameters can be referred to [8, Appendix A]. The azimuth sampling rate is PRF $= 1256.98$ Hz, and the azimuth sample number of picked block data is $M_0 = 3072$. In order to implement the proposed nonuniform sampling pattern, we firstly interpolate the raw data along azimuth direction to increase the sampling rate with $q = 30$ times, and then resample the interpolated data by the Poisson disk-like nonuniform random sampling pattern, where the slow time of the new azimuth samples can be calculated by

$$t_i = t_{i-1} + 2/\mathrm{PRF} + m_i/(q \cdot \mathrm{PRF}) \tag{8}$$

where m_i is a random integer uniformly distributed in the interval $[0\ q]$.

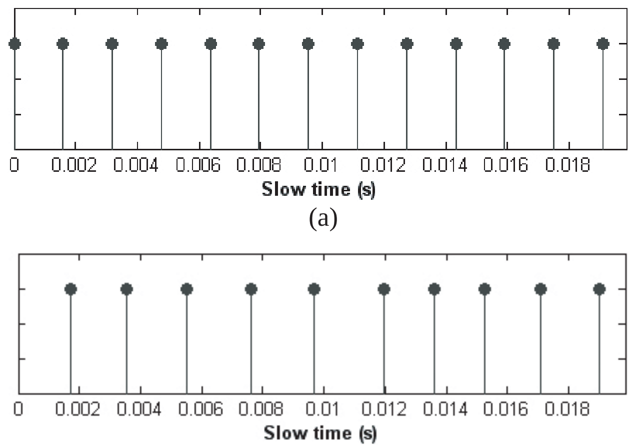

(b)

Figure 1: Comparision of different sampling patterns. (a) Uniform sampling pattern with a down sampling rate PRF/2. (b) Poisson disk-like nonuniform random sampling pattern.

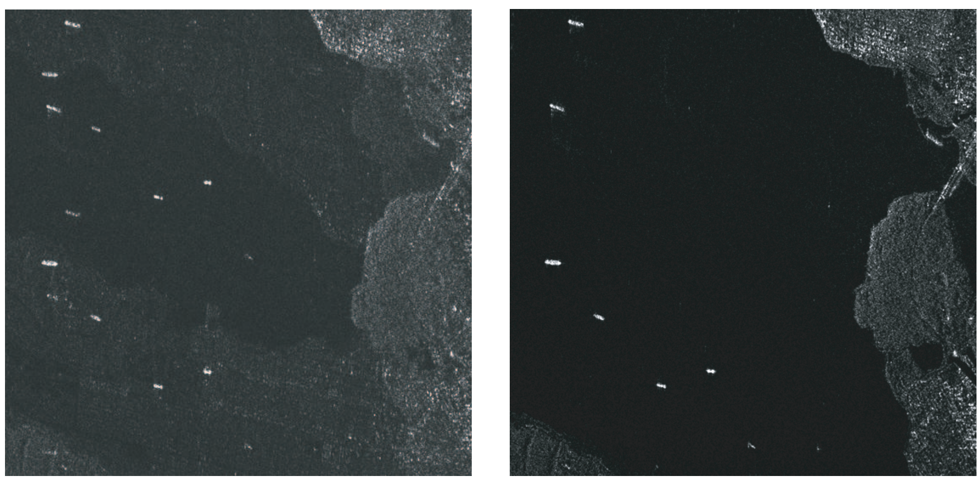

(a) (b)

Figure 2: Imaging results with Radarsat-1 raw data. (a) Image obtained by conventional SAR imaging with a down sampling rate PRF/2. (b) Image obtained by proposed technique.

The sampling pattern defined by (8) can make sure that the interval between any two adjacent samples is no longer than 2/PRF, which means the swath width can be increased one time. Fig. 1(b) shows the first 10 sampling instants, as a comparison, Fig. 1(a) shows the uniform sampling instants with a down sampling rate PRF/2.

The imaging result of conventional method with data sampled at a down sampling rate PRF/2 is shown in Fig. 2(a), where the azimuth samples number is 1536. Fig. 2(b) shows the imaging result based on CS with the Poisson disk-like nonuniform samples mentioned above, and the corresponding azimuth samples number is 1238. As shown in Fig. 2, there exists obvious azimuth aliasing in Fig. 2(a), while no such effect happens in Fig. 2(b) even the samples used in Fig. 2(b) are less than that used in Fig. 2(a).

6. CONCLUSIONS

The new CS theory provides the possibility to increase the swath width of conventional single channel spaceborne SAR system, the proposed Poisson disk-like nonuniform random sampling method allows wider swath by restricting the smallest time interval between any two azimuth samples. The experiment results validate the feasibility of the method in the application of sparse scene surveillance.

ACKNOWLEDGMENT

This work is supported by the National Basic Research Program of China (2010CB731903) and in part by the National Natural Science Foundation of China (60901056, 61072112).

REFERENCES

1. Currie, A. and M. A. Brown, "Wide-swath SAR," *IEE Proc.-F*, Vol. 139, No. 2, 122–135, 1992.
2. Gebert, N., G. Krieger, and A. Moreira, "Digital beamforming on receive: Techniques and optimization strategies for high-resolution wide-swath SAR imaging," *IEEE Trans. Aerosp. Electron. Syst.*, Vol. 45, No. 2, 564–592, 2009.
3. Donoho, D. L., "Compressed sensing," *IEEE Trans. Inf. Theory*, Vol. 52, No. 4, 1289–1306, 2006.
4. Herman., M. A. and T. Strohmer, "High-resolution radar via compressed sensing," *IEEE Trans. Signal Process.*, Vol. 57, No. 6, 2275–2284, 2009.
5. Alonso, M. T., P. López-Dekker, and J. J. Mallorqui, "A novel strategy for radar imaging based on compressive sensing," *IEEE Trans. Geosci. Remote Sens.*, Vol. 48, No. 12, 4285–4295, 2010.
6. Cook, R. L., "Stochastic sampling in computer graphics," *ACM Trans. Graph.*, Vol. 5, No. 1, 51–72, 1986.
7. Vasanawala, S. S., M. T. Alley, B. A. Hargreaves, R. A. Barth, J. M. Pauly, and M. Lustig, "Improved pediatric MR imaging with compressed sensing," *Radiology*, Vol. 256, No. 2, 607–616, 2010.
8. Cumming, I. G. and F. Wong, *Digital Processing of Synthetic Aperture Radar Data: Algorithms and Implementation,* Artech House, Norwood, MA, 2005.

High-resolution ISAR Imaging with Sparse-spectrum OFDM-LFM Waveforms

Ying Luo[1], **Qun Zhang**[1,2], **You-qing Bai**[3], and **Yan-Li Duan**[1]

[1]Telecommunication Engineering Institute, Air Force Engineering University, Xi'an 710077, China
[2]Key Laboratory of Wave Scattering and Remote Sensing Information
Fudan University, Shanghai 200433, China
[3]Science Institute, Air Force Engineering University, Xi'an 710051, China

Abstract— Based on the compressive sensing (CS) theory, an algorithm for high-resolution inverse synthetic aperture radar (ISAR) imaging with sparse-spectrum OFDM-LFM (orthogonal frequency division multiplexing — linear frequency modulation) waveforms is proposed, which achieves high resolution of radar target and also much lower data rate of radar system. In the approach, the OFDM technique is utilized to overcome the velocity sensitivity in traditional broad-bandwidth radar waveforms such as stepped-frequency signals and stepped-frequency chirp signals, and greatly reduce the acquisition time for high resolution range profile (HRRP) synthesis. The simulations validate the effectiveness of the proposed algorithm.

1. INTRODUCTION

High range resolution is achieved by transmitting broad-bandwidth waveforms in ISAR imaging techniques. Usually, bandwidth with several GHz is necessary to obtain a range resolution at centimeter level, where such a broad bandwidth may bring many difficulties to the A/D converter. For reducing the instantaneous bandwidth of radar system, the stepped-frequency signal (SFS) and stepped-frequency chirp signal (SFCS) were proposed and have been in wide applications [1, 2]. By means of concatenation of the individual pulses either in the time domain [3] or in the frequency domain [4], large total bandwidth of transmitted signal is achieved. However, due to the frequency-stepped processing, both the SFS and SFCS are sensitive to the radial velocity of the target. Another disadvantage of this kind of signals is the relatively much long acquisition time for high resolution range profile (HRRP) synthesis, which maybe intolerable in certain applications such as multi-target imaging.

Recently, a new approach based on the orthogonal frequency division multiplexing (OFDM) technique is presented in [5] for improving target detection of radar systems. With the application in radar imaging, OFDM-LFM waveform is a kind of potential broad-bandwidth radar signals, due to the following reasons: 1) by taking the chirp signals as subpulses, many existing imaging algorithm can be easily extended to OFDM-LFM radar imaging; 2) insensitive to radial velocity between radar and target because all subpulses are transmitted at the same time; 3) much shorter acquisition time for HRRP synthesis compared with SFS and SFCS.

However, different from SFCS, long enough frequency interval between each two subpulses is necessary to ensure perfect orthogonal performance of them. That's to say, the OFDM-LFM waveform is sparse-spectrum indeed, which brings difficulties to synthesize a total broad bandwidth. Fortunately, the emerging compressive sensing (CS) theory [6] indicates an effective approach to reconstruct full information from sparse signals. The CS theory suggests that, if a signal has sparse representations in a certain space, it can be sampled at a rate much lower than Nyquist rate and reconstructed with overwhelming probability by solving an inverse problem either through a linear program or a greedy pursuit [7]. It is well known that, in ISAR imaging, dominate scatterers contribute much to image formation but taking up only a fraction of whole bins of the range-Doppler (RD) plane, i.e., ISAR image is spatially sparse. Therefore, from the CS theory, it's possible to reconstruct ISAR images with sparsity from sparse-spectrum OFDM-LFM echoes.

The paper is organized as follows. For better comprehension, we first assume the OFDM-LFM waveform is full-spectrum and deduce the bandwidth synthesis method in Section 2, then introduce the ISAR imaging algorithm with sparse-spectrum waveforms in Section 3. Conclusions are presented in Section 4.

2. BANDWIDTH SYNTHESIS WITH FULL-SPECTRUM OFDM-LFM WAVEFORMS

Figure 1 shows the time-frequency relationship in a burst of OFDM-LFM waveforms. The waveform is consists of a group of chirp subpulses with stepped carrier frequencies, and the subpulses are

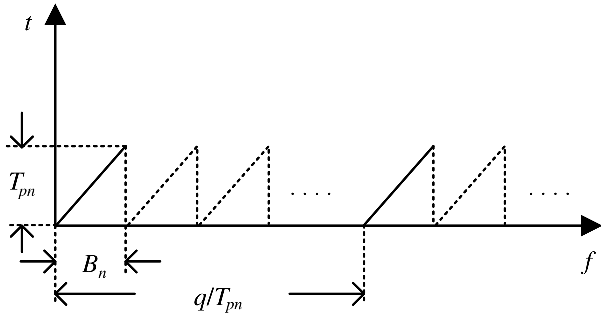

Figure 1: Frequency variance of OFDM-LFM waveform.

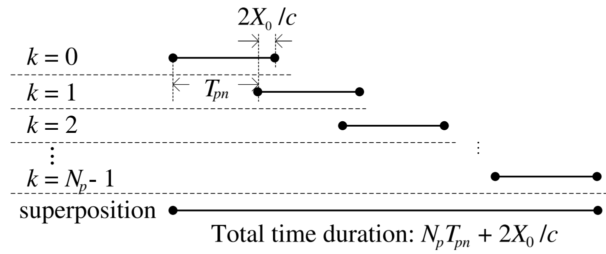

Figure 2: Diagram of the superposition of subpulses.

transmitted by the radar at the same time. Assume all subpulses have the same time duration T_{pn} and bandwidth B_n, to guarantee the perfect orthogonal performance between each two subpulses, the stepped frequency value Δf should be equal to q/T_{pn}, where $q \in \mathbb{N}$ is a appropriate number to ensure long enough frequency interval between each two adjacent subpulses (shown in Figure 1 using solid slanting straight lines). In the following, we assume each two subpulses are ideal orthogonal for simplicity.

In this section, we consider the OFDM-LFM waveform is full-spectrum, i.e., assume there are additional subpulses (shown in Figure 1 using dashed slanting straight lines) filled in the interval between each two adjacent subpulses, where the stepped frequency value Δf is changed to B_n. To make all subpulses end to end, it should be satisfied that $pB_n = q/T_{pn}$, where $p \in \mathbb{N}$ and $\mathbb{N}$ is the set of all natural numbers.

Assume the number of subpulses is N_p, the total synthetic bandwidth is $B = N_pB_n$, and the center carrier frequency of the synthetic signal is f_c, then the initial frequency of kth subpulse is given by

$$f_c(k) = f_c + (k - N_p/2)B_n, \quad k = 0, 1, \ldots, N_p - 1 \tag{1}$$

The subpulse can be expressed as $s(t, k) = \mathrm{rect}(t/T_{pn}) \exp(j2\pi f_c(k)t) \exp(j\pi\mu t^2)$, where $\mu = B_n/T_{pn}$ is the chirp rate. Assuming a target of a point-scatterer with unit scattering coefficient, the echo of the kth subpulse from the target is

$$s_r(t, k) = \mathrm{rect}((t - 2r_t/c)/T_{pn}) \exp(j2\pi f_c(k)(t - 2r_t/c)) \exp(j\pi\mu(t - 2r_t/c)^2) \tag{2}$$

where r_t is the distance between the target and the radar, and c is the wave propagation velocity.

Inspired by the bandwidth synthesis algorithm proposed in [4], the processing steps of bandwidth synthesis algorithm for OFDM-LFM waveforms are as follows.

Mixing the echoes and reference signal: the reference signal is given by $s_{ref}(t, k) = \exp(j2\pi f_c(k)$ $(t - 2r_s/c))$, where r_s is the distance between radar and the center of target. Mixing the received signal and the complex conjugate of reference signal, it yields

$$s_m(t, k) = \mathrm{rect}\left((t - 2r_t/c)/T_{pn}\right) \exp\left(j4\pi f_c(k)(r_s - r_t)/c\right) \exp\left(j\pi\mu(t - 2r_t/c)^2\right) \tag{3}$$

Sampling: generally, the sampling rate f_s of the synthetic signal must larger than the Nyquist rate B (for complex signals). However, because the dechirp processing instead of match filtering is utilized to form HRRP, the sampling rate f_s is just needed to be larger than $2\mu X_0/c$ when the radial length of target is X_0.

Frequency shift and phase correction: after sampling, the subpulses at baseband described by (3) need to be shifted in frequency before being combined. The frequency shift is carried out by multiplying (3) with

$$\phi_1(t, k) = \exp\left(j2\pi(f'_c + (k - N_p/2)B_n)(t - 2r_s/c)\right) \tag{4}$$

where f'_c can be set as a certain value making $f'_c + f_c$ is several times of B to satisfy the narrowband assumption. Then the phase correction term $\phi_2(k) = \exp(j\pi\mu(kT_{pn})^2)$ is added to each subpulse in order for phase continuous at the boundaries of subpulses. Therefore it yields

$$\begin{aligned} s_{m1}(t, k) = s_m(t, k) \cdot \phi_1(t, k) \cdot \phi_2(k) &= \mathrm{rect}\left((t - 2r_t/c)/T_{pn}\right) \exp\left(j4\pi f_c(r_s - r_t)/c\right) \\ &\cdot \exp\left(j2\pi\left(f'_c + (k - N_p/2)B_n\right)(t - 2r_t/c)\right) \exp\left(j\pi\mu(t - 2r_t/c)^2\right) \exp\left(j\pi\mu(kT_{pn})^2\right) \end{aligned} \tag{5}$$

Dechirp processing: the reference signal for dechirp processing is a chirp signal with initial frequency $f_c' + (k - N_p/2)B_n$ and time duration T_{pn} intercepted from a chirp signal with long time duration $T_p = N_p T_{pn}$, chirp rate μ and time delay $2r_s/c$:

$$\begin{aligned} s_{ref}'(t,k) &= \mathrm{rect}\left(\frac{t-kT_{pn}}{T_{pn}}\right)\mathrm{rect}\left(\frac{t-2r_s/c}{N_pT_{pn}}\right)\exp\left(j2\pi\left(f_c'+\left(-\frac{N_p}{2}\right)B_n\right)\left(t-\frac{2r_s}{c}\right)\right) \\ &\quad \exp\left(j\pi\mu\left(t-\frac{2r_s}{c}\right)^2\right) \\ &= \mathrm{rect}\left(\frac{t-2r_s/c}{T_{pn}}\right)\exp\left(j2\pi\left(f_c'+\left(k-\frac{N_p}{2}\right)B_n\right)\left(t-\frac{2r_s}{c}\right)\right) \\ &\quad \exp\left(j\pi\mu\left(t-\frac{2r_s}{c}\right)^2\right)\exp\left(j\pi\mu(kT_{pn})^2\right) \end{aligned} \tag{6}$$

The "dechirp" is performed by multiplying (5) with the complex conjugate of the reference signal (6). After removing the RVP (residual video phase), let $\lambda_c' = c/(f_c + f_c')$, and then one can obtain

$$\begin{aligned} s_c(t,k) &= \mathrm{rect}\left((t-2r_t/c)/T_{pn}\right)\exp\left(j4\pi\left(f_c+f_c'+(k-N_p/2)B_n/c\right)(r_s-r_t)\right)\exp\left(j4\pi\mu(r_s-r_t)t/c\right) \\ &\approx \mathrm{rect}\left((t-2r_t/c)/T_{pn}\right)\exp\left(j4\pi(r_s-r_t)/\lambda_c'\right)\exp\left(j4\pi\mu(r_s-r_t)t/c\right) \end{aligned} \tag{7}$$

Time shift and superposition of subpulses: the subpulses need to be shift in the time domain with the time-shift given by $\Delta t(k) = kT_{pn}$. It needs to be noticed that the time-shift should be an integer number of the discrete sample spaces to avoid errors because the unit of time-shift is $1/f_s$ in digital signal processing, namely, $T_{pn}f_s$ should be an integer. Then concatenating all the subpulses and it yields

$$s_c'(t) = \mathrm{rect}\left((t-2r_t/c)/T_p\right)\exp\left(j4\pi(r_s-r_t)/\lambda_c'\right)\exp\left(j4\pi\mu(r_s-r_t)t/c\right) \tag{8}$$

It is equivalent to the dechirp result of a chirp signal with time duration $T_p = N_pT_{pn}$ and chirp rate μ, namely, the N_p subpulses are synthesized as one broad-bandwidth signal, as shown in Figure 2. The total time duration of the synthetic waveform is $N_pT_{pn} + 2X_0/c$, where X_0 is the radial size of target or scene.

HRRP synthesis by FFT: taking FFT to (8) in terms of t and removing the sideling envelope term, it yields

$$S_c(f) = \exp\left(j\frac{4\pi}{\lambda_c'}(r_s-r_t)\right)\mathrm{psf}\left(f-\frac{2\mu}{c}(r_s-r_t)\right) \tag{9}$$

where $\mathrm{psf}(f) = \mathrm{FT}[\mathrm{rect}(t/T_p)]$. $S_c(f)$ is the complex HRRP, and $|S_c(f)|$ peaks at $f = 2\mu(r_s-r_t)/c$.

Furthermore, by transmitting a group of OFDM-LFM bursts and taking the Fourier transform to the HRRPs with respect to the slow-time and migration through resolution cell (MTRC) correction after motion compensation, the ISAR image of the target is achieved.

3. ISAR IMAGING WITH SPARSE-SPECTRUM OFDM-LFM WAVEFORMS

The bandwidth synthesis algorithm presented in last section is suitable for full-spectrum OFDM-LFM waveforms; however, as we known, the OFDM-LFM waveforms are in fact sparse in frequency domain. Therefore, the algorithm is further studied based on the CS theory in this section.

As all we known, the ISAR image of a target is usually sparse because it is mainly determined by the dominated scatterers, therefore, the HRRP $S_c(f)$ of target can be considered as sparse naturally. Namely, $s_c'(t)$ in (8) is sparse in frequency domain. Let $\mathbf{x} = s_c'(t)$, $\theta_x = S_c(f)$, we have

$$\mathbf{x} = \Psi\theta_x = \mathbf{D}_N^{-1}\theta_x, \quad \Psi = \mathbf{D}_N^{-1} \tag{10}$$

where $\mathbf{D}_N^{-1}$ is the N-dimensional inverse DFT matrix.

Assume the indices of subpulses in a burst of full-spectrum OFDM-LFM waveform are $1, 2, \ldots, N_p$. p_r subpulses indexed with $m_0, m_1, \ldots, m_{p_r-1}$ are chosen randomly from the N_p subpulses for forming a sparse-spectrum OFDM-LFM waveform, where $m_0 = 0$, $m_{p_r-1} = N_p - 1$, and the

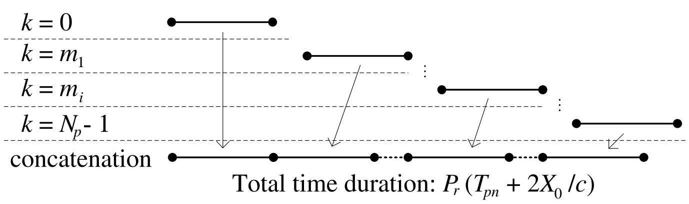

Figure 3: Diagram of concatenation of sparse-spectrum subpulses.

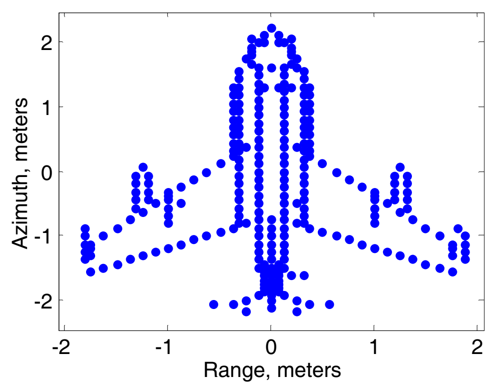

Figure 4: The target model.

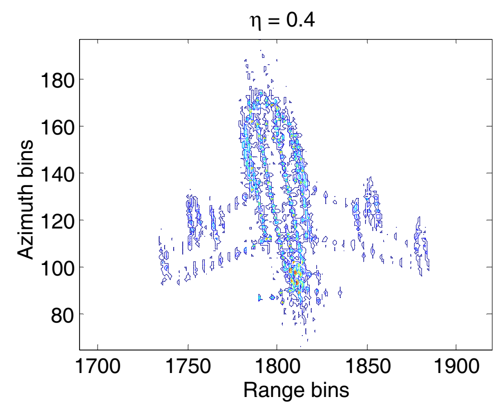

Figure 5: The ISAR image.

frequency interval between each two subpulses must be long enough to ensure perfect orthogonal performance of them. Therefore the sparsity of transmitted signal can be defined as $\eta = p_r/N_p$. The echoes of p_r subpulses are processed according to (3) $\sim$ (9), and then concatenated as an integrated signal $\mathbf{y}$ with length $M = (T_{pn} + 2X_0/c)p_r f_s$, as shown in Figure 3. The relationship between $\mathbf{y}$ and $\mathbf{x}$ is $\mathbf{y} = \Phi\mathbf{x}$, where $\Phi = \{\phi_{a,b}\}$ and $\phi_{a,b}$ given by (assuming the element at top left corner of Φ is $\phi_{0,0}$)

$$\phi_{a,b} = \begin{cases} 1, & b = m_i n_p + \mathrm{mod}(a, n_p),\ i = \lfloor a/n_p \rfloor,\ i \in [0, p_r - 1] \\ 0, & \text{Others} \end{cases} \tag{11}$$

where $n_p = (T_{pn} + 2X_0/c)f_s$, $a = 0, 1, \dots, M-1$, $b = 0, 1, \dots, N-1$.

It is obvious that the process of recovering $\mathbf{x}$ from the measurements $\mathbf{y}$ is ill-posed. However, the CS theory demonstrates that if $\Phi\Psi$ has the *Restricted Isometry Property* (RIP), then it is indeed possible to recover θ_x with high probability via solving the l_1 optimization problem as follows

$$\theta_x = \arg\min \|\theta_x\|_1, \quad \text{s.t.} \quad \mathbf{y} = \Phi\Psi\theta_x \tag{12}$$

It can be proved that $\Phi\mathbf{D}_N^{-1}$ satisfies the RIP, therefore, θ_x can be reconstructed by using the CS theory. There are many methods for CS reconstruction such as basis pursuit (BP), orthogonal matching pursuit (OMP), and so on. The recovered θ_x is the synthetic HRRP of target; after the compression in slow-time domain as same to conventional imaging algorithm, the ISAR image can be obtained.

4. SIMULATION

The target model is shown in Figure 4 and the parameters of transmitted waveforms are as follows: $f_c = 12\,\text{GHz}$, $N_p = 300$, $B = 6\,\text{GHz}$, $B_n = 20\,\text{MHz}$, $T_{pn} = 1\,\mu\text{s}$ and $f_s = 12\,\text{MHz}$. The range resolution of subpulses and synthetic broad-bandwidth waveform is 7.5 m and 0.025 m respectively. 256 bursts are transmitted during the imaging time and the azimuth resolution is 0.05 m. Figure 5 shows the imaging result in condition of $\eta = 0.4$, where the subpulses' indexes are randomly chosen from $[1, N_p]$ and the frequency intervals between each two subpulses are larger than B_n. It can be found that the quality of the ISAR image is quite high. Therefore, the simulation demonstrates the effectiveness of the proposed algorithm.

ACKNOWLEDGMENT

This work was supported by the "973" program of China under grant 2010CB731905 and the National Natural Science Foundation of China under Grant 61172169 and Grant 60971100.

REFERENCES

1. Freedman, A., R. Bose, and B. D. Steinberg, "Thinned stepped frequency waveforms to furnish existing radars with imaging capability," *IEEE Aerospace and Electronic Systems*, Vol. 11, No. 11, 39–43, 1996.
2. Levanon, N. and E. Mozeson, "Nullifying ACF grating lobes in stepped-frequency train of LFM pulses," *IEEE Transactions on Aerospace and Electronic Systems*, Vol. 39, No. 2, 694–703, 2003.
3. McGroary, F. and K. Lindell, "A stepped chirp technique for range resolution enhancement," *Proceedings of National Telesystems Conference*, Vol. 1, 121–126, Atlanta, GA, USA, Mar. 1991.
4. Lord, R. T. and M. R. Inggs, "High resolution SAR processing using stepped-frequencies," *Proceedings of IGARSS'97*, Vol. 1, 490–492, Singapore, Republic of Singapore, Aug. 1997.
5. Prasad, N. N. S. S. R. K., V. Shameem, U. B. Desai, and S. N. Merchant, "Improvement in target detection performance of pulse coded Doppler radar based on multicarrier modulation with fast Fourier transform (FFT)," *IEE Proc. Radar Sonar Navig.*, Vol. 151, No. 1, 11–17, 2004.
6. Donoho, D. L., "Compressed sensing," *IEEE Transcations on Information Theory*, Vol. 52, No. 4, 1289–1306, 2006.
7. Baraniuk, R. and P. Steeghs, "Compressive radar imaging," *IEEE Radar Conference*, 128–133, Boston, MA, 2007.

SAR Imagery Compressing and Reconstruction Method Based on Compressed Sensing

F. Zhu, Q. Zhang, J.-B. Yan, F. F. Gu, and M. Zhu
Institute of Telecommunication Engineering, AFEU, Xi'an, Shaanxi 710077, China

Abstract— In this paper, a SAR imagery compressing and reconstruction method based on Compressed Sensing (CS) theory is proposed. In the method, the SAR imagery can be divided to several sub-imageries firstly. Discrete Wavelet Transform (DWT) can be utilized to make SAR imagery sparse and the random Gauss matrix after approximate Orthogonal-matrix and Right-matrix (QR) decomposition can be employed to complete the low-dimension measurement for sparse results. For reconstructing SAR imagery, a modified Orthogonal Matching Pursuit (OMP) algorithm is proposed to perform better. On condition of the same reconstruction precision, the search burden is reduced and convergency speed is enhanced by using the proposed modified OMP algorithm. At the same time, the sparsity estimation can be avoided. Furthermore, some processing containing IDWT can be engaged to achieve the final reconstructed SAR imagery. The effectiveness of the proposed method can be validated by simulation results.

1. INTRODUCTION

As the development of Synthetic Aperture Radar (SAR) imaging technology, the dimension of SAR imagery will become larger and larger [1, 2]. Thus some problems such as data processing and transmission in real time would occur. Hence, how to compress and reconstruct these SAR imagery data is an important problem, which is necessary to solve for the time being. Compressive Sensing (CS), which is proposed by D L Donoho in 2006, is a new method of obtaining, compressing and reconstructing signals in Signal Processing field [3–5]. Because of its special advantages, it will be applied in many different kinds of fields. It will provide a new idea and approach for many different kinds of data compressing and reconstruction.

In this paper, we intent to study SAR imagery data compressing and reconstruction based on CS theory. From the related references, we can see that there are not many reports about researches on these related contents. The contents of most of these references are about SAR imagery and raw data compressing and reconstruction based on CS theory [6–9]. Reference [6] proposes a new method of fast encoding for SAR raw data by using CS theory to complete SAR raw data compressing and reconstruction. Reference [7] gives a framework to compress and reconstruct SAR imagery data simply. In order to suggest the sparsity feature of the SAR imagery, the contour transform based on wavelet analysis, block Walsh-Hadamard transform and block discrete cosine transform can be used [8, 9]. At the same time, random Gauss matrix can be utilized to complete the low-dimension measurement. According to CS theory, there are three main steps should be carried out. One is the sparsity expression of the original signal. Second is the low-dimension measurement for the original signal. And third is effective reconstruction algorithm for recovering the original signal. In this paper, our research according to these three steps in CS theory can be revealed as follows. For the poor sparsity feature of SAR imagery data, the Discrete Wavelet Transform (DWT) [10], which has a well time-frequency energy assembly character can be utilized to make SAR imagery data sparse. For the low-dimension measurement, the random Gauss matrix after approximate Orthogonal-matrix and Right-matrix (QR) decomposition can be employed [11], which perform better than the conventional random Gauss matrix. For the original data reconstruction, the modified Orthogonal Matching Pursuit (OMP) [12, 13] algorithm can be engaged for avoiding the sparsity degree estimation. In addition, compared with the traditional OMP algorithm, the convergency speed of the modified OMP algorithm is enhanced effectively.

2. SAR IMAGERY COMPRESSING AND RECONSTRUCTION BASED ON CS

For a $A \times B$ dimension SAR imagery, $\sigma^*(a, b)$, $a = 1, 2, \ldots, A$, $b = 1, 2, \ldots, B$, where A, B represents the discrete pixel number in the range and cross-range, respectively. $\sigma^*(a, b)$ can be expressed as a matrix format

$$\sigma^*_{A\times B} = \begin{bmatrix} \sigma^*_{11} & \ldots & \sigma^*_{1B} \\ \vdots & \ddots & \vdots \\ \sigma^*_{A1} & \ldots & \sigma^*_{AB} \end{bmatrix}_{A\times B} \tag{1}$$

$\sigma^*(a,b)$ can be divided to kk sub-imagery. For simplicity, kk is a square number. Each sub-imagery is $\sigma(u,v)$, $u = 1, 2, \ldots, U$, $v = 1, 2, \ldots, V$.

$$\begin{cases} U = A/\sqrt{kk} \\ V = B/\sqrt{kk} \end{cases} \tag{2}$$

Thus, the original SAR imagery and each sub-imagery $\sigma(u,v)$ can be written as, respectively

$$\sigma^*_{A\times B} = \begin{bmatrix} \sigma_{U\times V_{1,1}} & \cdots & \sigma_{U\times V_{1,\sqrt{kk}}} \\ \vdots & \ddots & \vdots \\ \sigma_{U\times V_{\sqrt{kk},1}} & \cdots & \sigma_{U\times V_{\sqrt{kk},\sqrt{kk}}} \end{bmatrix}_{A\times B}, \quad \sigma_{U\times V} = \begin{bmatrix} \sigma_{11} & \cdots & \sigma_{1V} \\ \vdots & \ddots & \vdots \\ \sigma_{U1} & \cdots & \sigma_{UV} \end{bmatrix}_{U\times V} \tag{3}$$

In order to obtain the sparsity express of SAR imagery, the $\sigma(u,v)$ is turned to a column $\sigma' = \{\sigma'_{uv}\}^H$, $uv = 1, 2, \ldots, U, U+1, U+2, \ldots, U\cdot V$. Let $U \cdot V = N$, and σ' is a N-dimension column, i.e., $\sigma'_{N\times 1}$.

Next, we intend to compress and reconstruct SAR imagery by using the CS theory. According to CS theory, let $x = \sigma'_{N\times 1}$, and take DWT of $\sigma'_{N\times 1}$ to obtain the sparsity results

$$\sigma'_{N\times 1} = \Psi_{DWT}\xi_{N\times 1} \tag{4}$$

where $\xi_{N\times 1}$ is a sparse column. Let $\Theta = \xi_{N\times 1}$ from CS theory.

For low-dimension measurement matrix, take QR decomposition for conventional random Gauss matrix,

$$\Phi = \mathbf{Q} \cdot \mathbf{R} \tag{5}$$

where $\mathbf{Q}$ is a $N \times N$ dimension orthogonal-matrix and $\mathbf{R}$ is a $M \times N$ $(M < N)$ dimension right-matrix (QR). We define the compressing rate as $\eta = M/N$. Because the elements in the dominant diagonal are comparatively large, these elements can be remained and other elements can be set to zeros. Suppose $\mathbf{R}' = \{r'_{i,j}\}$, $\mathbf{R} = \{r_{i,j}\}$, $i = 1, 2, \ldots, M$, $j = 1, 2, \ldots, N$, and this processing can be expressed as

$$\mathbf{R}' = \{r'_{i,j}\} = \begin{cases} r_{i,j}, & i = j \\ 0, & i \neq j \end{cases} \tag{6}$$

Φ' can be reconstructed, which not only still satisfies RIP [14, 15], but also has a better character, i.e.,

$$\sigma_{\min}(\Phi') > \sigma_{\min}(\Phi), \quad \sigma_{\max}(\Phi') < \sigma_{\max}(\Phi) \tag{7}$$

where $\sigma_{\min}(\Phi)$, $\sigma_{\max}(\Phi)$ and $\sigma_{\min}(\Phi')$, $\sigma_{\max}(\Phi')$, represent the minimum, maximum eigenvalue of random Gauss matrix and the matrix after approximately QR decomposition, respectively. From these Equations, the distance between the minimum and the maximum eigenvalue is shorten. And the measurement matrix will has a better non-correlation character, which is benefit for SAR imagery reconstruction.

Thus the measurement result can be written as

$$\zeta_{M\times 1} = \Phi'\xi_{N\times 1} \tag{8}$$

We can see that the dimension of measurement result is lower than the original column. According to CS theory, let $\mathbf{y} = \zeta_{M\times 1}$. On the basis of these processing, the optimal problem can be established

$$\hat{\xi} = \arg\ \min \|\xi\|_1, \qquad \text{s.t.} \qquad \zeta = \mathbf{\Phi}\mathbf{\Psi}^H_{DWT}\sigma' \tag{9}$$

The optimal problem can be solve to obtain $\hat{\xi}$, which is the reconstructed original column.

For the original imagery reconstruction, the modified OMP algorithm can be utilized. The steps are stated.

Step (1) Let $\mathbf{TT} = \Phi\Psi^H_{DWT}$. Design an initial zero column vector $rr_{N\times 1}$. Design a terminal threshold g.

Step (2) $PP(n) = \mathbf{TT} \cdot \zeta(m)$, $n = 1, 2, \ldots, N$, $m = 1, 2, \ldots, M$, $qq = \max PP(n)$. n is written as $n_{\max}$ at the moment.

Step (3) The $n_{\max}$th column of $\mathbf{TT}$ is written as $\mathbf{TT}_{\max}$. Let $qq_{\max} = (\mathbf{TT}^H_{\max}\mathbf{TT}_{\max})^{-1} \cdot qq$.

Step (4) Let $rr(n_{\max}) = qq_{\max}$.

Step (5) Let $\zeta(m) = \zeta(m) - \mathbf{TT}_{\max} \cdot qq_{\max}$, and let $\mathbf{TT}_{\max} = 0$ in $\mathbf{TT}$.

Step (6) Judge if $\|\zeta(m)\|_2 \geq g$, turn to Step (2), and if $\|\zeta(m)\|_2 < g$, stop, and $rr_{N\times 1}$ is the result, i.e., $\hat{\xi}$.

From this concrete step flow, we can see that the modified OMP algorithm can avoid the sparsity estimation. And generally, the threshold g can be designed according to the original $\|\zeta(m)\|_2$, that is

$$g = \alpha \cdot \|\zeta\,(m)\|_2 \tag{10}$$

where $0 \leq \alpha \leq 0.5$, generally.

Take IDWT of $\hat{\xi}_{N\times 1}$, the $\hat{\sigma}'$ which is the estimation result of the original column σ'.

$$\hat{\xi}_{N\times 1} = \Psi_{DWT}^{H} \hat{\sigma}'_{N\times 1} \tag{11}$$

The obtained result $\hat{\sigma}'$ as a matrix and the SAR imagery reconstructed result are expressed, respectively,

$$\begin{aligned} \hat{\sigma}_{U\times V} &= \begin{bmatrix} \hat{\sigma}_{11} & \dots & \hat{\sigma}_{1V} \\ \vdots & \ddots & \vdots \\ \hat{\sigma}_{U1} & \dots & \hat{\sigma}_{UV} \end{bmatrix}_{U\times V}, \\ \hat{\sigma}^{*}_{A\times B} &= \begin{bmatrix} \hat{\sigma}_{U\times V_{1,1}} & \dots & \hat{\sigma}_{U\times V_{1,\sqrt{kk}}} \\ \vdots & \ddots & \vdots \\ \hat{\sigma}_{U\times V_{\sqrt{kk},1}} & \dots & \hat{\sigma}_{U\times V_{\sqrt{kk},\sqrt{kk}}} \end{bmatrix} = \begin{bmatrix} \hat{\sigma}^{*}_{11} & \dots & \hat{\sigma}^{*}_{1B} \\ \vdots & \ddots & \vdots \\ \hat{\sigma}^{*}_{A1} & \dots & \hat{\sigma}^{*}_{AB} \end{bmatrix}_{A\times B} \end{aligned} \tag{12}$$

3. SIMULATIONS

In order to evaluate the quality of the reconstructed results, the mean square error (MSE) and peak signal noise ratio (PSNR) can be utilized. Their definition can be stated as follows, respectively,

$$MSE = \frac{1}{UV} \sum_{u=0}^{U-1} \sum_{v=0}^{V-1} [\sigma(u,v) - \hat{\sigma}(u,v)]^2, \quad PSNR = -10 \lg \left[\frac{255^2}{MSE}\right] \tag{13}$$

where $\sigma(u,v)$ and $\hat{\sigma}(u,v)$ represent the pixel-value of the original and reconstructed imagery.

Figure 1(a) shows a 128×128 dimension SAR imagery. Suppose $kk = 4$, the original SAR imagery can be divided to four sub-imageries. The dimension of each sub-imagery is 64×64. Next, the first sub-imagery will be processed by the proposed method. Fig. 1(b) shows that the column of the pixel-value of first sub-imagery, and its sparsity expressing result is shown in Fig. 1(c).

Figure 2 shows that the comparison results in the different case, where the compressing rate $\eta = 25\%$ and the terminal threshold $g = 0.3 \cdot \|\zeta(m)\|_2$, i.e., $\alpha = 0.3$. The quantization comparison of reconstructed results is revealed in Table 1. And the final reconstructed result of original SAR imagery is shown in Fig. 1(d).

From Fig. 2 and Table 1, we can see that MSE and PSNR of the reconstructed results and the original sub-imagery can be reduced and be increased, respectively by using the random Gauss matrix after approximately QR decomposition. What's more, the run time can be shorten apparently

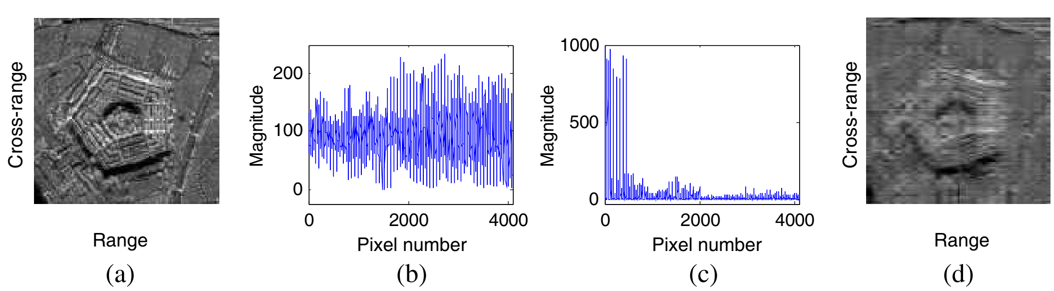

Figure 1: Related results (a) Original SAR imagery (b) Column of pixel-value. (c) Sparsity expressing of pixel-value (d) Reconstructed imagery.

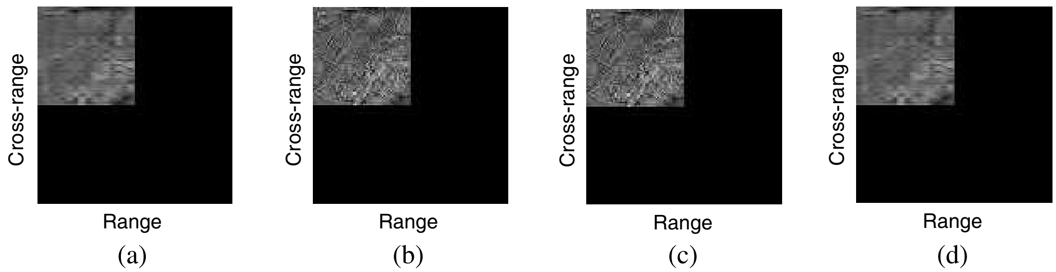

Figure 2: Reconstructed results of first sub-imagery by using the different method. (a) Result by random Gauss matrix and OMP algorithm. (b) Result by random Gauss matrix after approximately QR decomposition and OMP algorithm. (c) Result by random Gauss matrix and modified OMP algorithm. (d) Result by random Gauss matrix after approximately QR decomposition and modified OMP algorithm.

Table 1: Quantization comparison of reconstructed results.

	Fig. 2(a)	Fig. 2(b)	Fig. 2(c)	Fig. 2(d)
MSE	1.2431×10^8	1.2278×10^8	1.2431×10^8	1.2278×10^8
PSNR	3.3093	3.3631	3.3093	3.3631
Run time	388.62 s	384.27 s	218.14 s	52.17 s

by using the modified OMP algorithm and the sparsity estimation can be avoided. Comparing Fig. 1(d) with Fig. 1(a), we can see that the reconstructed result at compressing rate $\eta = 25\%$ is not the same as the original SAR imagery completely, because of some information has been compressed. But this result is still acceptable. These simulation results can prove the effectiveness of the proposed method.

4. CONCLUSIONS

SAR imagery compressing and reconstruction is an important issue, which is necessary to study. In this paper, a SAR imagery compressing and reconstruction method based on Compressed Sensing (CS) theory is proposed. On the basis of the original SAR imagery is divided to several sub-imageries, according to CS theory, DWT can be utilized to make SAR imagery sparse and the random Gauss matrix after approximate QR decomposition can be employed to complete the low-dimension measurement for sparse results. Furthermore, a modified OMP algorithm can be employed to reconstruct SAR imagery sparse data. By using this algorithm, the search burden is reduced and convergency speed is enhanced. At the same time, the sparsity estimation can be avoided. Next, IDWT can be engaged to achieve reconstructed SAR imagery. Simulations prove the validity of the method. This work can provide an effective approach for SAR imagery compressing and reconstruction.

ACKNOWLEDGMENT

This work was supported by the State Major Basic Research Development Program of China under grant 2010CB731905.

REFERENCES

1. Khwaja, A. S. and J. W. Ma, "Applications of compressed sensing for SAR Moving-target velocity estimation and image compression," *IEEE Transactions on Instrumentation and Measurement*, Vol. 60, No. 8, 2848–2860, 2011.
2. Witzgall, H. E. and J. S. Goldstein, "Exploiting fundamental properties of SAR data for compression of tactical SAR imagery," *IEEE Aerospace Conference*, 1354–1362, 2005.
3. Donoho, D. L., "Compressed sensing," *IEEE Transactions on Information Theory*, Vol. 52, No. 4, 1289–1306, 2006.
4. Baraniuk, R., "A lecture on compressive sensing," *IEEE Signal Processing Magazine*, Vol. 24, No. 4, 118–121, 2007.
5. Candès, E. J. and M. B. Wakin, "An introduction to compressive sampling," *IEEE Signal Processing Magazine*, Vol. 25, No. 2, 21–30, 2008.

6. Bhattacharya, S., T. Blumensath, B. Mulgrew, et al., "Fast encoding of synthetic aperture radar raw data using compressed sensing," *SSP*, 448–452, 2007.
7. Zhang, L., M. S. Chen, L. Xu, et al., "A novel random sampling method for radar image compression," *Wireless Communications Networking and Mobile Computing*, 1–4, 2010.
8. Si, X. Y., L. C. Jiao, H. Yu, et al., "SAR images reconstruction based on compressive sensing," *APSAR*, 1056–1059, Xi'an, China, Oct. 2009.
9. Wang, M., "Raw SAR data compression by structurally random matrix based compressive sampling," *APSAR*, 1119–1122, Xi'an, China, Oct. 2009.
10. Zeng, Z. and I. G. Cumming, "SAR image data compression using a tree structured wavelet transform," *IEEE Transactions on Geoscience and Remote Sensing*, Vol. 39, No. 3, 546–552, 2001.
11. Golub, G. and C. Loan, *Matrix Computations*, Johns Hopkins, Baltimore, 1996.
12. Tropp, J. A. and A. C. Gilbert, "Signal recovery from random measurements via orthogonal matching pursuit," *IEEE Transactions on Information Theory*, Vol. 53, No. 12, 4655–4666, 2007.
13. Kunis, S. and H. Rauhut, "Random sampling of sparse trigonometric polynomials II: Orthogonal matching pursuit versus basis pursuit," *Foundations of Computational Mathematics*, Vol. 8, No. 6, 737–763, 2007.
14. Candès, E., J. Romberg, and T. Tao, "Robust uncertainty principles: Exact signal reconstruction from highly incomplete frequency information," *IEEE Transactions on Information Theory*, Vol. 52, No. 2, 489–509, 2006.
15. Candès, E. and T. Tao, "Decoding by linear programming," *IEEE Transactions on Information Theory*, Vol. 51, No. 12, 4203–4215, 2005.

Health Recovery Effect of Physiological Magnetic Stimulation on Elder Person's Immunity Source Area with Transition of ECG and EEG

K. Mohri[1], **Y. Inden**[2], **M. Yamada**[3], **and Y. Mohri**[4]

[1]Nagoya Industrial Science Research Institute (NISRI), Nagoya 464-0819, Japan
[2]Graduate School of Med., Nagoya University, Nagoya 466-0065, Japan
[3]Faculty of Sci. and Tech., Meijo University, Nagoya 468-8502, Japan
[4]Yamazaki Mazak Co., Oguchi, Aichi 480-0197, Japan

Abstract— A remarkable health recovery effect of the physiological magnetic stimulation (PMS) for an elder person suffered from the angina pectoris is presented, in which four conditions out of five indices of the metabolic syndrome were normalized through two months. The PMS is carried out using a magnetized fayalite crushed stones crammed vinyl pipe with vibrating on the immunity source area of the thymus, the pit of the stomach, and the intestinal flora ("san jiao" in Chinese medicine). Mechanisms for the PMS effect are discussed with the magneto-protonics principle considering transition of the measured electro-encephalogram (EEG) and the electro-cardiogram (ECG) before and during the PMS.

1. INTRODUCTION

We have found a safe and remarkable arousal effect of a physiological magnetic stimulation (PMS) putting a magnetized fayalite crushed stones crammed vinyl pipe to spine position of elder persons during car driving [1]. The arousal effect is confirmed for two elder men subjects using a driving simulator and measurements of the electro-encephalogram (EEG) at four points on the subject's head with increase of FFT frequency spectrum components $\beta/(\theta + \delta)$ [2]. Mechanisms for arousal are explained with the magneto-protonics principle [3–5], in which the serotonin generated from the medulla in the central nervous system using increased ATP with the PMS activates the cerebral limbic system [1, 2, 6]. On the contrary, we tried to apply the PMS to the immunity source area of the human body on which the magnetic pipe is vibrated by a hand for health recovery to improve the Health-Related Quality of Life in aging society. For the purpose, we selected three areas of the thymus, the pit of the stomach, and the intestinal flora because that these areas are traditionally well known as the functional metabolic organ; san jiao, triple heater in Chinese medicine [7].

2. EXPERIMENTAL PROCEDURE

Figure 1 illustrates magnetized fayalite crushed stones crammed vinyl pipes with three kinds of length of 20 cm, 30 cm, and 40 cm and their surface magnetic field distribution measured using a MI magnetic sensor [8]. The pulse distributed magnetic field having steep change in around 10 mm is effective to generate the magneto-protonics principle for bio cells such as the blood cells and the nervous transmission cells at the san jiao area, in which free protons generated in transmitting bio-cell water with an extremely low frequency (ELF) magnetic field activates ATP synthase in the mitochondria. Patients oscillate the magnetic pipe by their hands on the san jiao area with around 2 Hz during around 1 min. time to time per day mainly after each eating. Patients do not need any specific guidance by a medical doctor on the diet and/or the exercise except the PMS.

3. EXPERIMENTAL RESULTS

3.1. Blood Pressures and Body Weight

Figure 2 represents recorded results of the systolic blood pressure (systolic BP), the diastolic blood pressure (diastolic BP), and the body weight of a patient (70 age man with 176 cm in height) through one year (October 1st, 2010 to September end, 2011) who has suffered from the angina pectoris and been operated a stent placement for his coronary artery stenosis at 6 years ago in the Nagoya University Hospital and then in the metabolic syndrome. A large fluctuation in blood pressure with between 120 and 200 mm Hg in the systolic BP and 70 and 115 mm Hg in the diastolic BP before applying the PMS has been normalized to between 80 and 120 mm Hg in the systolic BP and between 55 and 75 mm Hg in the diastolic BP after two months under the PMS. The

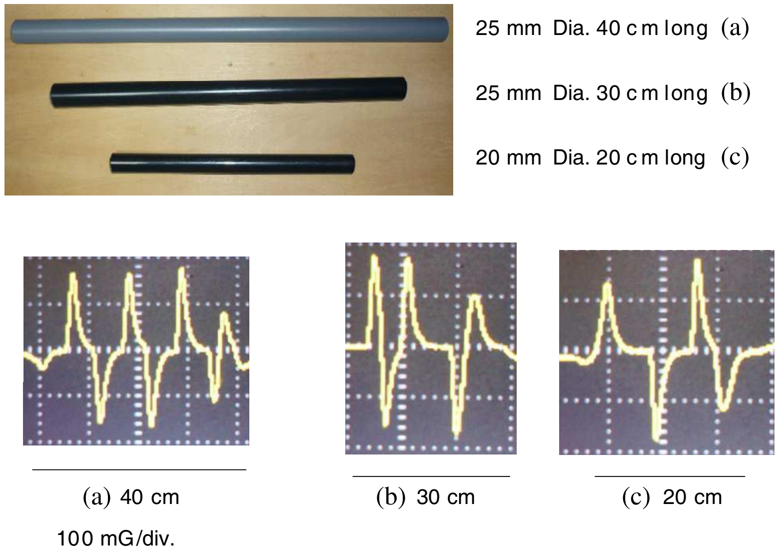

Figure 1: Pulse distributed surface magnetic field generated from magnetized fayalite crushed stones crammed vinyl pipe of three length.

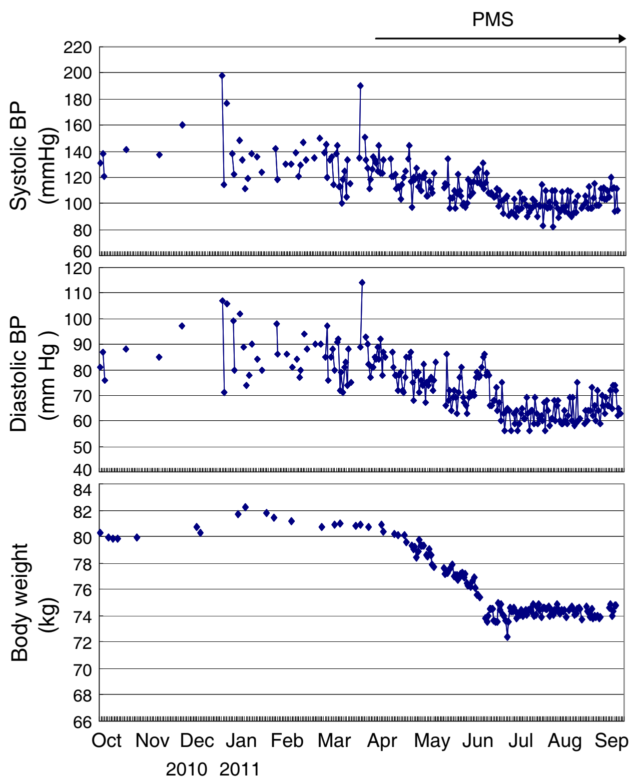

Figure 2: Transition of the systolic blood pressure, the diastolic blood pressure, and the body weight of 70 age man through one year with applying the PMS.

BP amount is an average of each successive three times measured values in the morning and the evening. Simultaneously, the body weight has linearly reduced from around 82 kg to around 74 kg during the two months without any specific guidance by a medical doctor on increase of exercise rate accompanied with a reduction of the waist circumference.

3.2. Blood Test Data and Metabolic Syndrome Indices

Transition of the blood test data concerning the metabolic syndrome defined by the American Heart Association (2004) [9] is listed in Table 1. The blood test by the Nagoya University Hospital has represented normalization of the HDL cholesterol and the glucose after 4 months with the PMS although the Triglycerides is still in abnormal. The four indices out of the five indices of defined

Table 1: Transition of five indices of the metabolic syndrome with the PMS for 70 age man patient of angina pectoris.

Metabolic syndrome measurements

70 age man angina pectoris (Standard value)*	4 months before PMS** 2011, Jan.	1 month before PMS 2011, April	PMS 2 months 2011, July	PMS 4 months 2011. Sept.	PMS 6 months 2011, Nov.
Waist Circumference ($\leq 102\,\text{cm}$)	104 **H**	105 **H**	94	92	90
Triglycerides ($\leq 150\,\text{mg/dL}$)	219 **H**	155 **H**	172 **H**	185 **H**	185 **H**
HDL cholesterol ($\geq 40\,\text{mg/dL}$) (men)	38 **L**	38 **L**	35 **L**	41	132
Blood pressure ($\leq 130/85\,\text{mmHg}$)	(130–200) /(80–110) **H**	($140 \sim 190$) /($85 \sim 130$) **H**	($80 \sim 110$) /($60 \sim 70$)	($80 \sim 110$) /($60 \sim 70$)	($80 \sim 110$) /($60 \sim 70$)
Glucose ($\leq 100\,\text{mg/dL}$)	127 **H**	115 **H**	113 **H**	85	85

* American Heart Association (2004)
** Physiological Magnetic Stimulation on san-jiao. Blood Test Data are authorized by Nagoya University Hospital

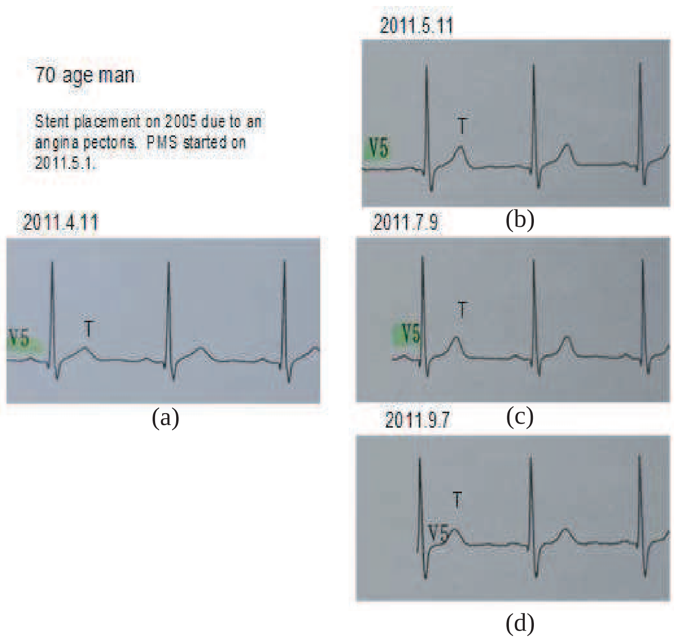

Figure 3: Transition of 12-lead ECG V5 waveform, in which a flat T waveform before the PMS as in (a) recovered to steeper T waveform during the PMS in (b), (c), and (d).

metabolic syndrome has been normalized with the san-jiao PMS.

3.3. Transition of Electrocardiogram (ECG)

The damaged electro-cardiogram (ECG) waveform due to the angina pectoris and the metabolic syndrome has also been recovered with the PMS as illustrated in Figure 3. The twelve-lead resting ECG has been regularly recorded by Nagoya University Hospital every two month since 6 years ago for the patient. A flatness of the T wave reflects declination of the left ventricular diastolic function due to heart diseases and aging. The ECG system diagnosis changed from "suspicion of the inferior wall infarction, and loading impossible" before application of the san-jiao PMS to "boundary area,

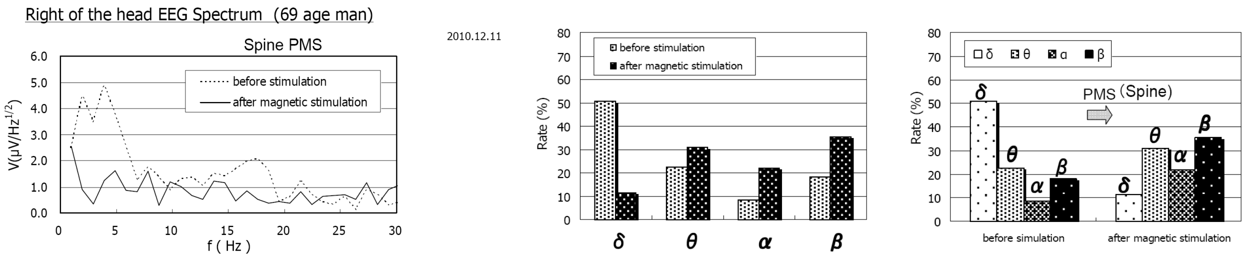

(a)

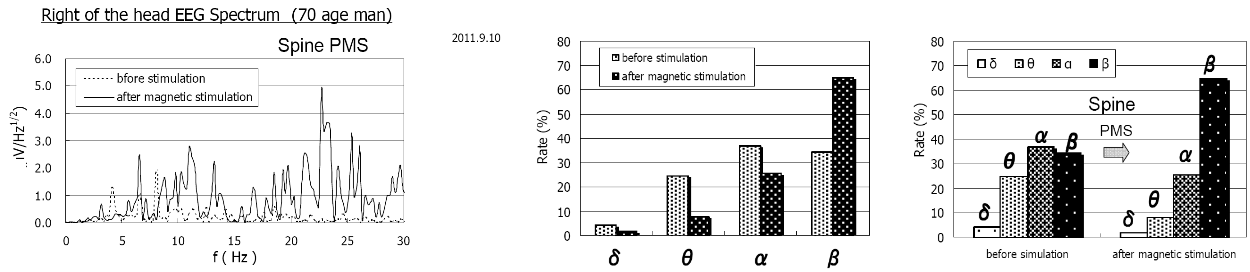

(b)

Figure 4: EEG FFT spectrum of an elder man patient suffered from the angina pectoris : (a) without san-jiao PMS, and (b) with san-jiao PMS.

and loading possible" during two months with the san-jiao PMS due to recovery of the T wave.

3.4. Transition of Electroencephalogram (EEG) FFT Spectrum

The electro-encephalogram (EEG) FFT frequency spectrum of the angina pectoris patient is also recovered as illustrated in Figure 4.

The EEG FFT spectrum at patient's right of the head before the san-jiao PMS [1] is illustrated in (a). The spectrum pattern before the spine PMS shows δ wave (0.2–3 Hz; sleepiness) component plus θ wave (4–7 Hz; drowsiness) component rich pattern due to an old age and angina pectoris, which is activated with the spine PMS to β wave (14– 40 Hz; active arousal) component rich pattern with the magnetoprotonics effect.

On the contrary, the EEG FFT spectrum shows already β (14–40 Hz; active arousal) rich pattern during the san-jiao PMS after four months even before the spine PMS as in (b). The β rich spectrum is further reinforced with the spine PMS. Similar remarkable effect of the san-jiao effect was observed at the top of head, the left of head, and the back of head.

4. DISCUSSION AND CONCLUSIONS

Remarkable health recovery effect of the san-jiao PMS using a magnetized fayalite crushed stones crammed vinyl pipe is found for an elder man patient suffered from the angina pectoris with normalization of four indices out of the five indices defined for the metabolic syndrome. The health recovery is also confirmed with transition of the ECG and the EEG. These systematic health recovery is considered to be due to the adjustment of the blood circulation with activated production of the blood cells and the nervous transmission material cells, the cardio muscle activation and vascular smooth muscle activation using the ATP which production is reinforced with the magneto-protonics. The systematic investigation and evaluation of experimental (diagnosis) results including the blood test data authorized by Nagoya University Hospital for an angina pectoris elder patient would be a standpoint for progression of a project of normalization of the metabolic syndrome for elder persons with the san-jiao PMS.

ACKNOWLEDGMENT

The authors wish to express their gratitude to Mr. T. Uemura of Tsuruta Sekizai Co., Japan for his presentation of the magnetized fayalite crushed stones produced in Sugashima, Japan.

REFERENCES

1. Mohri, K., T. Uchiyama, M. Yamada, T. Watanabe, Y. Inden, T. Kato, and S. Iwata, "Arousal effect of physiological magnetic stimulation on elder person's spine for prevention of drowsiness

during car driving," *IEEE Trans. Magn.*, Vol. 47, No. 10, 3066–3069, 2011.
2. Mohri, Y., M. Yamada, K. Endo, T. Suzuki, and K. Mohri, "Arousal effect of physiological magnetic stimulation on car driver's spine evaluated with electroencephalogram using driving simulator," *PIERS Proceeding*, 2012, Submitted.
3. Mohri, K. and M. Fukushima, "Milligauss magnetic field triggering reliable self-organization of water with long range ordered proton transport through cyclotron resonance," *IEEE Trans. Magn.,* Vol. 39, No. 5, 3328–3330, 2003.
4. Fukushima, M., T. Kataoka, N. Sugiyama, and K. Mohri, "Milligauss magnetic field applied water exert and induce firefly luciferine-luciferase luminescence and induce intracellular calcium elevation of CHO cells without ATP," *IEEE Trans. Magn.*, Vol. 41, No. 10, 4188–4190, 2005.
5. Fukushima, M., K. Mohri, T. Kataoka, and M. Matsumoto, "Milli Gauss pulsed magnetic field applied phosphate buffered saline solution elevates intracellular Ca^{2+} level and stimulates phagocytic activity in human neutrophils," *Trans. Mag. Soc. Jpn.*, Vol. 2, No. 2, 15–18, 2002.
6. Sugi, H., *Physiology of Human Body Function*, 3rd Edition, 143–157, Nankodo, Tokyo, Japan, 1999 (in Japanese).
7. Tan, S., K. Tillisch, and E. Mayer, "Functional somatic syndromes: Emerging biomedical models and traditional chinese medicine," *eCAM*, Vol. I, No. 1, 35–40, 2004.
8. Mohri, K. and Y. Honkura, "Amorphous wire and CMOS IC based magneto-impedance sensors — Origin, topics, and future," *Sensor Letters*, Vol. 5, 267–270, 2007.
9. Grundy, S. M., "Diagnosis and management of the metabolic syndrome," *Circulationaha*, AHA Scientific Statement, Sep. 12, 2005.

Arousal Effect of Physiological Magnetic Stimulation on Car Driver's Spine Evaluated with Electroencephalogram Using Driving Simulator

Y. Mohri[1], **M. Yamada**[2], **K. Endo**[2], **T. Suzuki**[2], **and K. Mohri**[3]

[1]Yamazaki Mazak Co., Oguchi, Aichi 480-0197, Japan
[2]Faculty of Science and Technology, Meijo University, Nagoya 468-8502, Japan
[3]Nagoya Industrial Science Research Institute (NISRI), Nagoya 464-0819, Japan

Abstract— Newly found arousal effect with application of a physiological magnetic stimulation (PMS) using a magnetized fayalite crashed stone crammed vinyl pipe put on the spine position for elder persons preventing drowsiness during car driving is evaluated measuring four-point electroencephalogram (EEG) at operation of the driving simulator. Both the ratio of the β wave component and the $\delta+\theta$ wave components ($\beta/(\delta+\theta)$; arousal index) in a FFT frequency spectrum of the measured EEG and a cross correlation among four point EEG remarkably increased using the spine PMS.

1. INTRODUCTION

We have found and presented an effective and safe method of arousal for elder persons using a physiological magnetic stimulation (PMS) with putting a magnetized fayalite crushed stone crammed vinyl pipe on the spine position, which would be expected to prevent drowsiness of elder persons during car driving for decreasing of the number of recent rapid increasing traffic accidents [1]. On the basis of these results we measured four-point EEG of elder persons using a driving simulator having a large screen system [2] in order to make further evaluation of the spine PMS in a very similar situation to car driving behavior on the real road. Remarkable transition of the ratio of β-wave (arousal) component and θ-wave (drowsiness) plus δ-wave (sleep) components ($\beta/(\theta+\delta)$; defined as an arousal index) and the cross correlation among four point EEG were obtained as both increasing with the PMS for both two elder men subjects. Possible mechanisms of these results are discussed with the Magneto-Protonics principle [3–5], in which production of the arousal neurotransmitter serotonin is reinforced with increase of the ATP production due to free protons in bio cells magnetized by an extremely low frequency magnetic field.

2. EXPERIMENTAL PROCEDURES

2.1. EEG Measurement Method Concerning Car Driving Behavior

According to the purpose to detect EEG as reflection of car driving behavior concerning the arousal, we adopted a method to measure the EEG at four points of a top head close to the forehead, a right head, a left head, and a back head of a subject with closing eyes due to detect bio signal of both consciousness and unconsciousness just after a driving behavior using the driving simulator considering the afterimage combined with the kinesthetic memory.

Table 1 shows a sequence for each set of driving task followed with EEG measurement for each subject without and under PMS. We set a 10 min. city driving for finding a change in EEG through a careful driving behavior. We also set three time highway night driving through simple curved road with each 10 min. in which almost all subjects tend to feel sleepy.

Table 1: Sequence for driving task followed with EEG measurements.

I	II		III		IV		V	
EEG- (5 min) (Before driving)	City driving (10 min)	EEG-2 (5 min)	Highway night driving 1 (10 min)	EEG-3 (5 min)	Highway night driving 2 (10 min)	EEG-4 (5 min)	Highway night driving 3 (10 min)	EEG-5 (5 min)

2.2. Physiological Magnetic Stimulation Method for Arousal at the Central Nervous System

There are two main requisite conditions of stimulation for car drivers with effectiveness and safety not to disturb any normal driving ability. Car drivers are simultaneously supported and controlled with two different nervous systems of the cerebral cortex nervous system which operates information processing gathering signals from five sense organs and simultaneously generates command signal for four limbs muscles (consciousness control), while instincts including sleep, arousal, respiration, body temperature, and blood flow are controlled with the central nervous system (CNS; unconsciousness control system) affecting the cerebral cortex function as peripheral nerves. Therefore, effective stimulation for arousal should be applied to the CNS including the spine on the basis of the physiology rather than stimulation for the cerebral cortex with alarm signals such as electronic sound, flash light, and strong smelling perfume spray that often result in dangerous so-called "rebound sleepiness" during car driving [6]. We adopted the PMS on the spine position same to the former experiment [1] showing a remarkable arousal effect by setting a magnetized fayalite crushed stone crammed vinyl pipe of 51 cm long generating pulse distributed magnetic field as illustrated in Figure 1 along the spine.

2.3. Driving Simulator

Figure 2 represents a driving simulator having a large display showing realistic driving environment with two small displays of a room mirror and a side mirror made by Mitsubishi Precision Co., Japan and set in Meijo University. Driver's face is monitored by an infrared micro camera system. Four EEG electrode positions are selected considering the relation between driving motion and cerebral functional area such as the motor area, the motor association area, the somatosensory area and the visual association area.

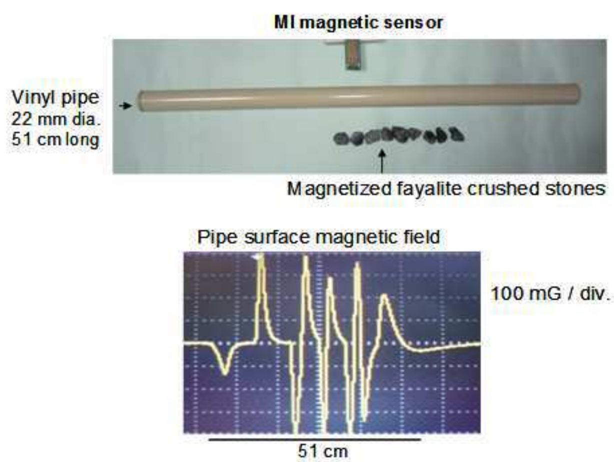

Figure 1: Pulse distribution surface magnetic field of a PMS pipe.

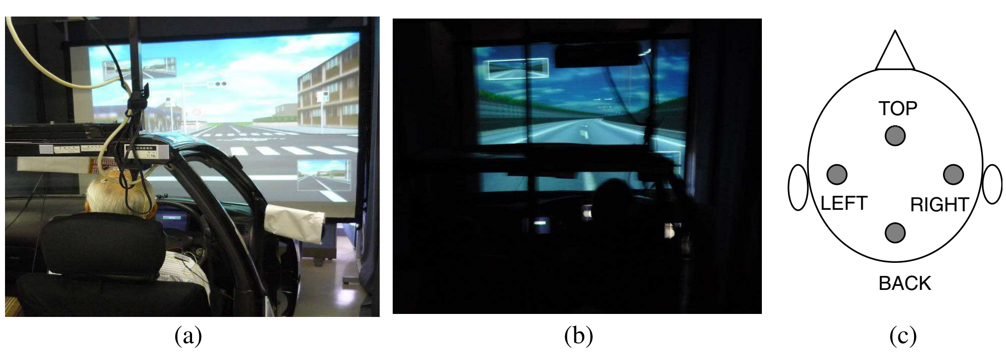

Figure 2: Two photos of driving simulator (Mitubishi Precision Co., Ltd., D3sim.): (a) City driving, and (b) Highway night time driving, and (c) Four electrode positions for EEG measurements.

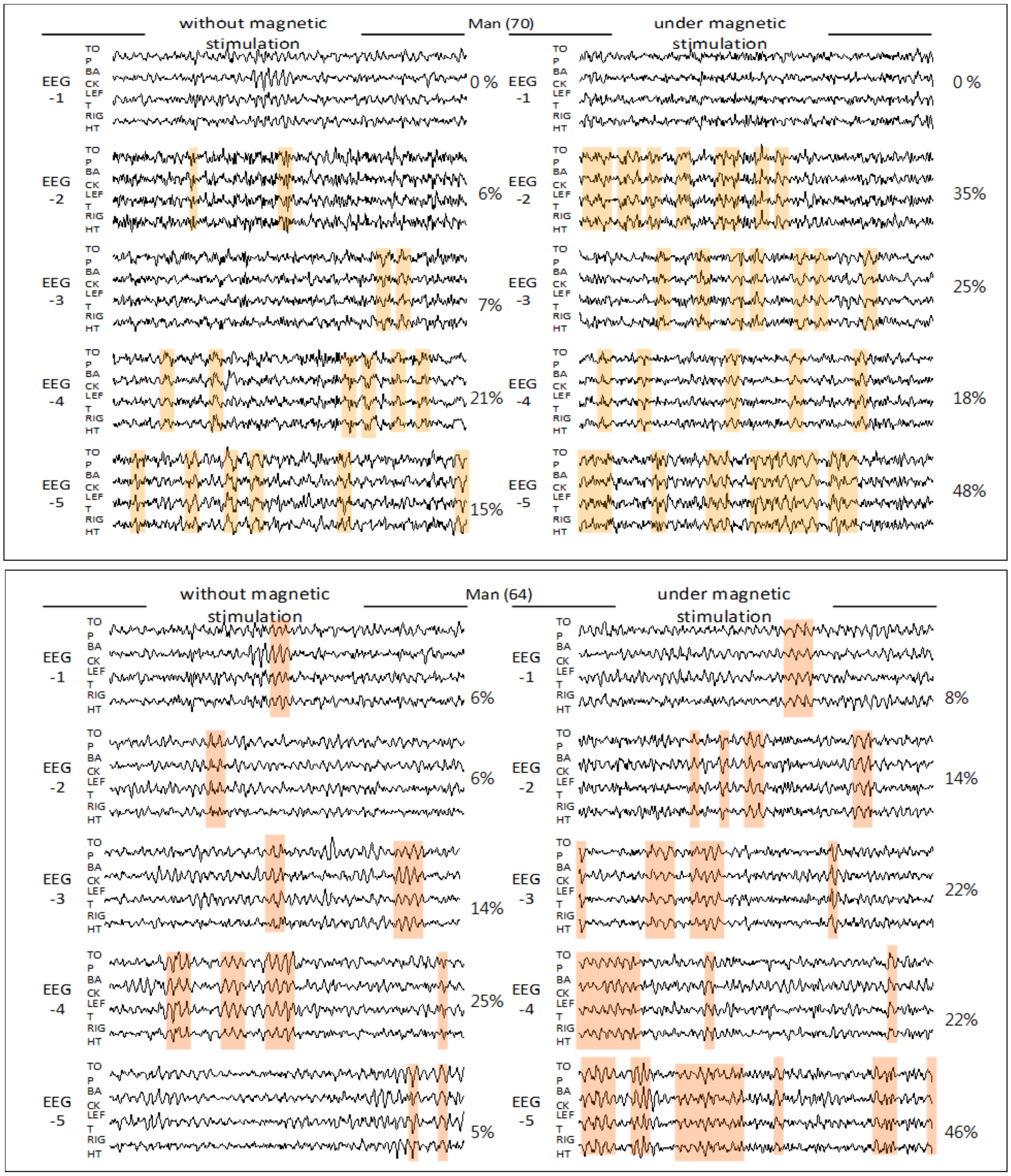

Figure 3: EEG time series at four points during 4 second. Colored blocks illustrate each time duration with strong correlation among four point time series. Each rate of time duration of strong correlation is indicated.

3. EXPERIMENTAL RESULTS

We found a feature of car driving motion in four points EEG measurement for both two elder men subjects as illustrated in Figure 3. Summation of time duration of strong correlation among four point EEG time series increased with increasing the driving time, which was reinforced with the PMS at spine position. It is considered that consciousness level is elevated with increasing driving time and the PMS at spine position. We used a EEG meter made by Inter Cross Co., Japan; inter cross-410, sampling frequency 1000 Hz, and amplifier gain of 100.

Transition of the FFT frequency spectrum with the PMS for two elder men of 70 age and 64 age in EEG-5 measurements is represented in Figure 4, which suggests that a car driver's arousal index should be $\beta/(\delta+\theta)$ matching with subjective estimation by the two subjects.

4. DISCUSSIONS

We tried to define an arousal index as $\beta/(\delta+\theta)$ considering measured results as shown in Figure 4. Table 2 illustrates calculated value of $\beta/(\delta+\theta)$ at four point EEG of the two subjects in EEG-5, which supported validity of the definition showing values less than 1.0 for sleepy state and more than 1.0 for arousal state.

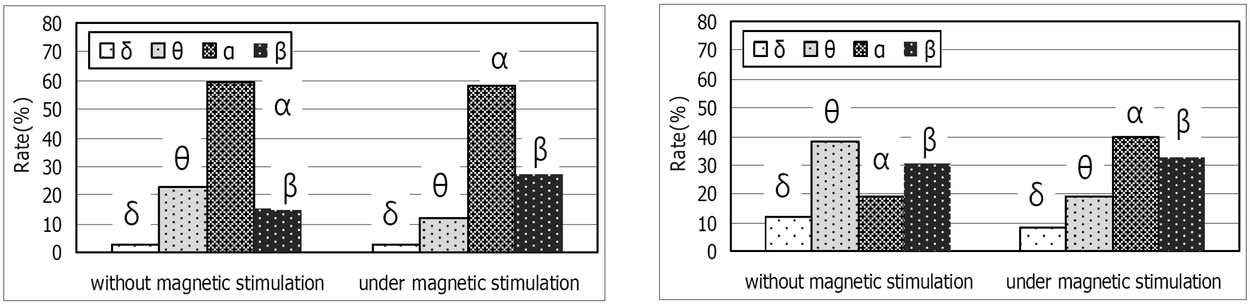

Figure 4: Bar graph for rate of EEG-5 FFT frequency spectrum component δ (0.2–3 Hz: sleep), θ (4–7 Hz: drowsiness), α (8–13 Hz: quiet arousal), and β (14–40 Hz: active arousal) at the top of head of two elder subjects without and under PMS.

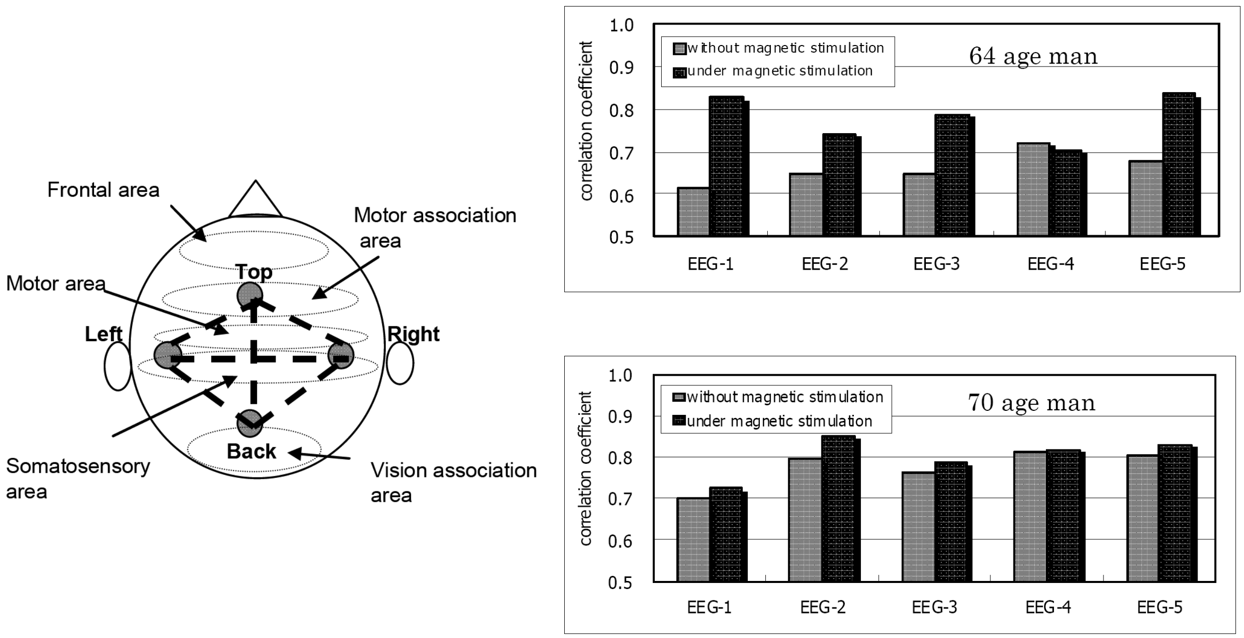

Figure 5: Cross correlation among EEG time series at four positions of subject's head.

Table 2: Car driver's arousal index $\beta/(\delta+\theta)$.

$\beta/(\delta+\theta)$	64 age man		70 age man	
EEG-5		With PMS		With PMS
Top of head	0.58	1.86	0.58	1.23
Back of head	0.40	1.48	0.61	1.50
Left of head	0.72	2.67	0.64	1.82
Right of head	0.83	2.00	0.68	1.45
Average	0.63	2.00	0.63	1.50
Subjective sleepy arousal sleepy arousal evaluation				

We also analyzed the cross correlation of EEG time series among the four positions of the subject's head as illustrated in Figure 5, in which an average values of the 6 pair of cross correlations among four electrode position EEG are illustrated as a correlation coefficient although not showing contents as shown in Figure 3. The correlation coefficient increased with the PMS for both two subjects at almost all stages.

Increasing of the correlation coefficient is considered an elevation of the brain activity for car driving behavior increasing the association (the synchronization or the resonance as in Figure 3) among the four positions reflecting brain functions at the motor area and the somatosensory area, the motor association area, and the vision association area. The magnitude of the correlation coefficient is higher for the 70 age man subject even without the PMS, which is considered due to his almost daily use of the san-jiao PMS [7]. We also found a transition of maximum cross correlation among four points from the Top-Left correlation of averaged value through 5 stages 0.796 without the PMS to the Top-Right correlation of 0.843 with the PMS. This is considered due to elevation of dynamic pattern recognition function at the right brain area useful for careful car driving.

Effects of elevation of the arousal and the brain function association with the PMS at the spine position in the central nervous system are considered due to the magneto-protonics principle in which circulating bio cells such as the blood cells and neural transmission material cells pass through the pulse distributed magnetic field generated from the magnetized fayalite stones and are reinforced to produce the ATP at mitochondria due to the reinforced proton flow in cell water [1]. Reinforced production of the serotonin at the medulla using the ATP activates the arousal system through stimulation for the cerebral limbic system.

5. CONCLUSION

(1) It is considered that a definition of car driver's arousal index using a form $\beta/(\delta+\theta)$ is reasonable, which matches measured results of four point EEG FFT frequency spectrum to the subjective evaluation of both two elder men subjects.

(2) A PMS using magnetized fayalite crushed stone crammed vinyl pipe set on the spine position of car driver is considered to be highly effective and safe to prevent drowsiness during driving.

(3) A new measurement method for the EEG of car drivers with eyes closing and rest just after stopping a car utilizing the afterimage and the kinesthetic memory which produces valuable information of car driver's EEG signal.

(4) A high cross correlation among four points EEG time series which increases with increasing driving time and with the PMS was found. These results suggest a physiological feature of car driving behavior and PMS effect.

ACKNOWLEDGMENT

The authors wish to express their gratitude to Mr. T. Uemura of Tsuruta Sekizai Co., Japan and Mr. N. Hirata of Famil Tsuruta Shokusan Ltd., Japan for their presentation of Sugashima's magnetized fayalite crushed stone and cooperation for the experiments.

REFERENCES

1. Mohri, K., T. Uchiyama, M. Yamada, T. Watanabe, Y. Inden, T. Kato, and S. Iwata, "Arousal effect of physiological magnetic stimulation on elder person's spine for prevention of drowsiness during car driving," *IEEE Trans. Magn.*, Vol. 47, No. 10, 3066–3069, 2011.
2. Ito, T., S. Mita, K. Kozuka, T. Nakano, and S. Yamamoto, "Driver blink measurement by the motion picture processing and its application to drowsiness detection," *Proc. IEEE 5th Int. Conf. on ITS*, 81–91, 2002.
3. Mohri, K. and M. Fukushima, "Milligauss magnetic field triggering reliable self-organization of water with long range ordered proton transport through cyclotron resonance," *IEEE Trans. Magn.,* Vol. 39, No. 5, 3328–3330, 2003.
4. Fukushima, M., T. Kataoka, N. Sugiyama, and K. Mohri, "Milligauss magnetic field applied water exert and induce firefly luciferine-luciferase luminescence and induce intracellular calcium elevation of CHO cells without ATP," *IEEE Trans. Magn.*, Vol. 41, No. 10, 4188–4190, 2005.
5. Fukushima, M., K. Mohri, T. Kataoka, and M. Matsumoto, "Milli Gauss pulsed magnetic field applied phosphate buffered saline solution elevates intracellular Ca^{2+} level and stimulates phagocytic activity in human neutrophils," *Trans. Mag. Soc. Jpn.*, Vol. 2, No. 2, 15–18, 2002.
6. Johns, M. W., "A new method for measuring daytime sleepiness: The Epworth sleepiness scale, sleep," Vol.14, 540–545, 1991.
7. Mohri, K., Y. Inden, M. Yamada, and Y. Mohri, "Health recovery effect of physiological magnetic stimulation on elder person's immunity source area with transition of ECG and EEG," *PIERS Proceedings*, 27–30, Kuala Lumpur, Malaysia, March 2012, Submitted.

Characteristic of Human Arm Frequency Radiation

Siti Zura A. Jalil[1,2], **Mohd Nasir Taib**[2], **Hasnain Abdullah**[2], **and Megawati Mohd Yunos**[2]

[1]Razak School of Engineering, Universiti Teknologi Malaysia, Malaysia
[2]Faculty of Electrical Engineering, Universiti Teknologi MARA, Malaysia

Abstract— Many studies have indicated that there are endogenous electromagnetic fields generated by the human body. All the living body, especially the human being is believed to have their own radiation which the field radiates into space around on the body. With the advancement of science and technology, this radiation field can be described as the vibration of electromagnetic (EM) field generated by the human body. The field penetrates the physical body and emits their characteristics radiations of frequency. This work discusses the analysis of frequency radiation on human arm and classifies the characteristic of human arm radiation based on gender. The human radiation frequency is experimentally studied from 33 healthy human subjects of 17 males and 16 females. The frequency radiation is obtained from 6 points of human arm on left-side and right-side of human body. The statistical technique is used to examine the characteristic of radiation frequency. The multivariate analysis of variance (MANOVA) is employed to compare the characteristic of radiation frequency differences between genders. Prior to MANOVA analysis, several preliminary assumptions testing were performed, which it is confirmed that no serious violations noted in the tests and met the MANOVA assumptions. The results of MANOVA indicate there is statistically significant difference among gender of males and females on a linear combination of human arm frequencies radiation. It is confirmed that the population means on a set of human arm frequencies varies across gender. Then, k-nearest neighbor (k-NN) technique is employed for classification. The default neighborhood setting of Euclidean Distance is used to find nearest neighbors. The results show that the k-NN produced 89% of correctly classified, which suggested that the k-NN classifier is able to classify human arm radiation frequency.

1. INTRODUCTION

Nowadays, with emerging application of physical field in biological objects has encourages the scientific studies of radiation wave in living body. All living bodies, particularly human is show have their own radiations that radiate into space on their surrounding body [1]. The radiation field emitted by human body can be identified as endogenous electromagnetic field, since it generated and contained within the biological system of body [2].

The electromagnetic radiation of human body is produced due to the electrical design of human body [3]. The electrical system is operated in the nervous system which responsible for sensing stimuli and transmitting signals to and from different parts of the body. As a biological system, the radiation is emitted around the physical body at various intensities, according to activity and health of the body. In essence, the human radiation is vibrates at their own frequencies which known as frequency radiation of the human body.

The unique characteristics of frequency radiation of human body are detected at a distance using special tuned antenna, as non-invasive technique using a body radiation wave detector. The frequency of human radiation is captured on 6 points of arm segment. In anatomical measurement, the arm is basically refers as the entire upper limb from shoulder to hand including upper arm, forearm, wrist and hand. A number of studies have been focused on human hand, which the information of human hand is extract based on its physical dimensions and shape [4, 5]. In [6], the dimension of hand length has been used to predict stature, and significant result is found in left hand length in both genders. Nonetheless, this research also shows that a characteristic of gender difference in anthropometric measures, which males having higher means values than females. Some other studies also have agreed that males and females differ significantly, which the results indicates that gender differences is relative to lengths of index and ring fingers [7]. Moreover, in gait analysis studies also show that all body segments including arm have their contribution for gender classification [8].

Based on the evidence described above, motivates to experimental studying a new technique that can distinguish between males and females subject using the frequency radiation of the human body. Initial analysis of extracting information from frequency radiation has shown that the human body has a different body radiation relationship between males and females [9]. Based from this study, a thorough analysis is performed to confirm the characteristic difference of human body radiation. This study focuses to examine frequency radiation characteristic in arm segment.

2. METHODOLOGY

2.1. Data Acquisition

The frequency radiation of human arm is obtained from 33 healthy participants of 17 males and 16 females between the ages of 19–26 years. The frequency is captured through body radiation wave detector that equipped with telescoping whip antenna used to detect a broad range of electromagnetic waves of human radiation fields. The frequency radiation is taken from 6 points of human arm on upper arm, forearm and palm, consisting 3 points on the left-side (L4, L5, L6) and 3 points on the right-side (R4, R5, R6).

The frequency for each subject was collected under controlled environment in anechoic chamber to ensure consistency and accuracy of frequency reading. During measurement, the chamber temperature is controlled to maintain at $23 \pm 2°$C, and the ambient conditions are measured immediately before and after experiment [10]. Throughout measurement, the antenna is set on the 6th segment length and placed on horizontal position to the human body. The frequencies are obtained remotely at a distances of 1 to 5 cm from body to antenna [11]. The procedure of the experiment involves capturing frequencies of all 6 points on human arm is shown in Figure 1.

2.2. Comparison of Characteristic Differences

The characteristic difference of frequency radiation on human arm is explored using multivariate analysis of variance (MANOVA), which has been previously shown to be capable to compare group for differences [12]. It is used to establish significant genders differences among linear combination of variables. The Pillai's trace is selected due to the robustness of the tests with small samples and unequal sample sizes [13]. Subsequently, the individual characteristic of frequency radiation is determined by the tests of between-subjects effect of univariate analysis (ANOVA). A Bonferroni adjustment is employed to compute adjusted probability in multiple-comparison procedures. The new alpha level is calculated by taking into account the number of comparison performed. The effect size is estimated with partial eta squared value, which interpreted within Cohen's criteria [14].

2.3. Classification of Frequency Radiation

The frequency radiation of human arm is classified into gender using K-nearest neighbor (kNN) algorithm. The kNN is one of the most fundamental, simple and robust classification methods. Applications of kNN have been successful in many areas including gene expression classification [15]. Basically, the kNN classification is performed by classifying samples based on closest distance of the feature space, which samples are classified according to majority vote of its neighbor. The default neighborhood setting of Euclidean is used to find closest neighbors. The Euclidean distance between two samples of x and y is computed as Equation (1),

$$d(x, y) = \sum_{k=1}^{n} \sqrt{(x_k - y_k)^2} \tag{1}$$

The distance between two samples is estimate using some distance function $d(x, y)$, where x, y are samples composed of n features, such that $x = \{x_1, \dots, x_n\}$, $y = \{y_1, \dots, y_n\}$. The value of k determines the desired number of nearest neighbor, and typically $k = 1$ is considered as nearest neighbor. The frequency data is divided into training and test sets. For each training set, different values of k are used to train to determine the optimal value of k that gives the best classification result. One of the techniques is performed algorithm with different values of k and chooses who has the best performance. In this study, the value of k varies from 1 to 10 is used to find a class match

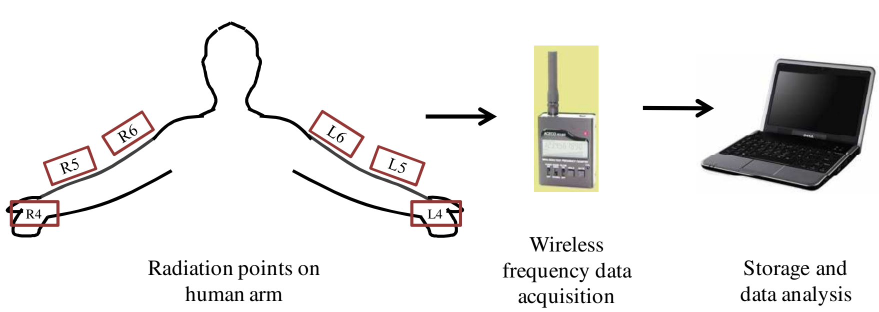

Figure 1: Frequency data acquisition procedure.

between training data and test data. In addition to the accuracy, the performance of classification could also determine by calculating of sensitivity and specificity.

3. RESULTS AND DISCUSSION

The frequency radiation of human arm has been studied from 33 healthy human subjects. All frequencies were taken in the anechoic chamber in order to obtain reliable data, and also seek to eliminate the influence of interference in the environment. In addition, ambient frequency is also taken before and after measurements. It is observed that the frequency of the ambient is constant, confirming the stability of the measurement system.

The characteristic of frequency radiation on human arm has been examined using statistical analysis of multivariate analysis of variance (MANOVA). Prior to MANOVA analysis, preliminary tests were conducted to examine several assumptions included normality, linearity, univariate and multivariate outliers, multicollinearity, and homogeneity of variance-covariance matrices, with no serious violations noted in the tests and met the MANOVA assumptions. The multivariate test of MANOVA indicates there is statistically significant differences among gender of males and females on linear combination of frequency radiation on human arm which the Pillai's trace obtained the significant value of $\rho < 0.05$ (Pillai's trace = 0.643, $F(6,26) = 7.795$). The results also show the power to detect the effect is 0.999 and therefore confirming the population means of human arm frequencies on left-side and right-side varies between genders. Further examination for gender differences on individual characteristic of six frequency radiation on left-side and right-side arm was studied from ANOVA. New level of alpha value using Bonferroni adjusted was computed ($\rho = 0.05/6$) to determine statistical significant difference among gender. The results indicate that all frequencies obtained the significant value after Bonferroni adjusted new alpha level ($\rho < 0.008$), which suggests the difference is significant. The effect sizes of these differences were in the range of large effect (Table 1).

For the purpose of classification, the classifier is train for the best value of k-nearest neighbor. Different values of k are used to compare the result which ranging from 1 to 10. The accuracy of each value of k is computed. Finally, the value of k is selected based on best classification performance [16]. The classification results are given in Figure 2. Note that each point in the graph represents a value of k ranging from 1 to 10. As shown in the graph, it is observed that the kNN classification achieves its best performance when $k = 3$, which yields an accuracy of about 89 percent. Therefore, the results suggested the kNN classifier is suitable to classify gender and capable to achieve a sensitivity and specificity of about 100 percent and 80 percent, respectively (Table 2).

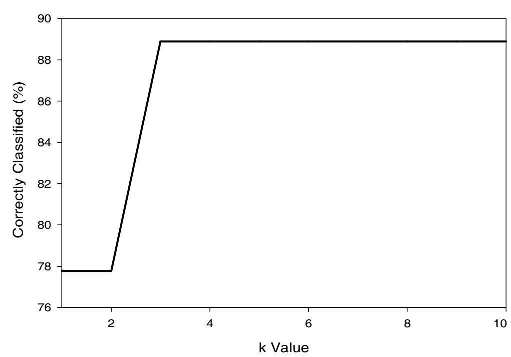

Figure 2: Accuracy plot using kNN classifier to train and test algorithm.

Table 1: Between-subjects effects.

Source	GENDER					
Dependent Variable	**L4**	**L5**	**L6**	**R4**	**R5**	**R6**
F	19.768	36.776	21.565	9.451	28.547	23.179
Significance (ρ)	0.000	0.000	0.000	0.004	0.000	0.000
Effect size (η_p^2)	0.389	0.543	0.410	0.234	0.479	0.428

Table 2: Performance characteristics of kNN classification.

k	**1**	**2**	**3**	**4**	**5**	**6**	**7**	**8**	**9**	**10**
Sensitivity (%)	80	80	100	100	100	100	100	100	100	100
Specificity (%)	75	75	80	80	80	80	80	80	80	80

4. CONCLUSION

The characteristic of frequency radiation of the human arm was experimentally studied from 33 healthy human subjects on 6 points of left-side and right-side. The results of the experiments have shown the characteristics different of frequency radiation among gender, which both analysis of MANOVA and ANOVA produced a significant results. Further analysis on gender classification suggested the kNN classifier correctly classify gender for about 89 percent and achieve the sensitivity and specificity of 100 percent and 80 percent, respectively. These results confirm that human has different characteristic of frequency radiation between gender and it is possible to classify the human gender based on frequency radiation analysis of human body, particularly in arm segment.

ACKNOWLEDGMENT

The authors wish to express their appreciation to Advanced Signal Processing Research Group, Faculty of Electrical Engineering, Universiti Teknologi MARA and Universiti Teknologi Malaysia for supporting the research.

REFERENCES

1. Tart, C. T., "Concerning the scientific study of the human aura," *Journal of the Society for Psychical Research*, Vol. 46, 1–21, 1972.
2. Movaffaghi, Z. and M. Farsi, "Biofield threrapies: Biophysical basis and biological regulations?," *Complementary Therapies in Clinical Practice*, Vol. 15, 35–37, 2009.
3. Geselowitz, D. B. and M. N. Geselowitz, "The bioelectrical century: bioelectrical engineering and the 'inside story' of the electrical century," *Proceedings of the IEEE*, Vol. 87, 1842–1846, 1999.
4. Amayeh, G., G. Bebis, and M. Nicolescu, "Gender classification from hand shape," *IEEE Computer Society Conference on Computer Vision and Pattern Recognition Workshops*, 1–7, Anchorage, AK, 2008.
5. Komandur, S., P. W. Johnson, R. L. Storch, and M. G. Yost, "Relation between index finger width and hand width anthropometric measures," *Annual International Conference of the IEEE Engineering in Medicine and Biology Society*, 823–826, 2009.
6. Agnihotri, A. K., S. Agnihotri, N. Jeebun, and K. Googoolye, "Prediction of stature using hand dimensions," *Journal of Forensic and Legal Medicine*, Vol. 15, 479–482, 2008.
7. McFadden, D. and E. Shubel, "Relative lengths of fingers and toes in human males and females," *Hormones and Behavior*, Vol. 42, 492–500, 2002.
8. Xuelong, L., S. J. Maybank, Y. Shuicheng, T. Dacheng, and X. Dong, "Gait components and their application to gender recognition," *IEEE Transactions on Systems, Man, and Cybernetics, Part C: Applications and Reviews*, Vol. 38, 145–155, 2008.
9. Jalil, S. Z. A., M. N. Taib, and H. Abdullah, "Investigation of frequency radiations of the human body," *IEEE EMBS Conference on Biomedical Engineering and Sciences (IECBES)*, 377–380, 2010.
10. Hintz, K. J., G. L. Yount, I. Kadar, G. Schwartz, R. Hammerschlag, and S. Lin, "Bioenergy definitions and research guidelines," *Alternative Therapies in Health and Medicine*, Vol. 9, 13–30, 2003.
11. Jalil, S. Z. A., M. Y. M. A. Karim, H. Abdullah, and M. N. Taib, "Instrument system setup for human radiation waves measurement," *2009 IEEE Student Conference on Research and Development (SCOReD)*, 523–525, 2009.
12. Sungur, S. and C. Tekkaya, "Students' achievement in human circulatory system unit: The effect of reasoning ability and gender," *Journal of Science Education and Technology*, Vol. 12, 59–64, 2003.
13. Tabachnick, B. G. and L. S. Fidell, *Using Multivariate Statistics*, 5th Edition, Pearson Eduacation, Boston, 2007.

14. Cohen, J., *Statistical Power Analysis for the Behavioral Sciences*, 2nd Edition, Lawrence Erlbaum Assosiates, Hilldate, NJ, 1988.
15. Dudoit, S., J. Friidlyand, and T. P. Speed, "Comparison of discrimination methods for the classifiacation of tumors using gene expression data," *Journal of the American Statistical Association*, Vol. 97, 77–87, 2002.
16. Guo, G., H. Wang, D. Bell, Y. Bi, and K. Greer, "KNN model-based approach in classification," *Lecture Notes in Computer Science*, 986–996, Vol. 2888, 2003.

Influence of Shield Distance on RF Transmit Performance for a 7T Multi-channel MRI Loop Array

M. Kozlov and R. Turner
Max Planck Institute for Human Cognitive and Brain Sciences, Leipzig, Germany

Abstract— We present numerical investigations, using RF circuit and frequency domain 3-D EM co-simulation, of loop-based RF arrays closely coupled to the load, with different distances to the local shield. We applied inductor-based decoupling networks, or alternatively we tuned the arrays by minimization of the power reflected by the entire array, with no dedicated decoupling network. In the circular polarization (CP) excitation mode, the transmit performance of a loop array closely coupled to a load is only weakly dependent on shield distance when this distance is greater than 20 mm, especially for tuning by reflected power minimization. The performance is only strongly affected by the shield position if the distance is less than 20 mm.

1. INTRODUCTION

The use of an RF shield is often proposed for the minimization of RF coil array inter-element coupling and the improvement of transmit performance. It is well known, nevertheless, that some unshielded 7T MRI coils still provide good transmit performance. There are no reliable transmit performance data for a loop-based array, loaded by a realistic head model, as a function of shield distance. Furthermore, it is difficult to compare literature values for transmit performance, since data for $\mathbf{B}_1+$ field versus array input power are rarely reported, and there are no reports concerning the power budget.

2. METHOD

In the simulation, eight resonance coil elements were mounted on rectangular acrylic supports, assembled to give an octagonal cross section with extreme dimensions of 230 mm by 255 mm, as in our previous research [1]. The planar single loop elements were simulated for a range of sizes: width 85 mm; length 85, 150 mm. The realistic 3-D EM model included all coil construction details for the resonance elements, simulated with precise dimensions and material electrical properties. The loads utilized were the Ansoft human body models with different scaling factors: head #1 with scaling $X = 0.9$, $Y = 0.9$, $Z = 0.9$ simulating a small head, and head #2 with scaling $X = 0.95$, $Y = 0.975$, $Z = 0.9$ simulating a large head, which practically fully occupied the coil volume.

The scanner gradient shield (with diameter of 683 mm and length 1200 mm) was always included in the numerical domain for the simulation of unshielded and shielded arrays. The distance between the shielded array and a 300 mm long local shield was varied between 10 mm and 80 mm.

Our investigation was performed using RF circuit and 3-D EM co-simulation [2]. The RF circuit simulator was Agilent ADS software, and Ansoft HFSS was chosen as the 3-D EM tool for its robustness in handling complex coil geometry. For all geometries the array was either tuned, matched and decoupled using capacitive and inductive decoupling networks, or alternatively tuned by minimization of the power reflected by the entire array with no dedicated decoupling network [3]. The results reported were obtained under the following array design conditions: a) the values of the fixed capacitors were not limited to the commercially available range, b) zero tolerance in component values was assumed, c) all tuning, matching and decoupling optimizations reached their global minima. The optimization criteria were a) for decoupled arrays: the impedance matching ($\mathbf{S}_{xx}$) for each element was required to be less than -30 dB, and the inter-element coupling ($\mathbf{S}_{xy}$) for each adjacent element pair to be decoupled was required to be less than -18 dB, at the Larmor frequency ($\mathbf{F}_{MRI}$) (thus there were 16 criteria for 8-element arrays); b) for arrays with no dedicated decoupling network, the reflected power $\mathbf{P}_{array\_refl}$ was required to be zero (a single criterion). This latter approach is not concerned with minimization of $\mathbf{S}_{xx}$ and $\mathbf{S}_{xy}$. Instead, in most cases this optimization yielded highly coupled array elements and pure $\mathbf{S}_{xx}$ matching [3].

The array was excited in circular polarization mode, applying 1 W power to each port (array transmit power, $\mathbf{P}_{transmit} = 8$ W), with a sequential 45 degree phase increment. We analyzed the quantities related to the power budget, obtained by direct calculation from volume and surface loss densities or wave quantities: a) $\mathbf{P}_{array\_refl}$, the power reflected by the entire array; b) $\mathbf{P}_{radiated}$ the radiated power; c) $\mathbf{P}_{array\_internal}$, the inherent coil losses produced by lossy capacitors, dielectrics, and conductors; and d) $\mathbf{P}_{load}$ the power absorbed by the load. One volume of interest (**VOI**) was defined as the entire human brain. The array transmit properties were evaluated by considering the values of a) $\mathbf{B}_1+_V$, the value of $\mathbf{B}_1+$ averaged over **VOI**, and its root-mean-square inhomogeneity (evaluated as a percentage "%"); b) $\mathbf{B}_1+_s$, the mean $\mathbf{B}_1+$ averaged over the transverse central slice through the **VOI**, and its root-mean-square inhomogeneity (evaluated as a percentage "%"); c) $\mathbf{P}_V$, the power deposited in the **VOI**; d) $\mathbf{E}_V = \mathbf{B}_1 +_V /\sqrt{\boldsymbol{P}_V}$, the **VOI** excitation efficiency; e) $\mathbf{SAR}_{10g}$, the peak SAR averaged over 10 gram; and f) $\mathbf{B}_1 +_V /\sqrt{\mathbf{SAR}_{10g}}$, the safety excitation efficiency. Parameters also evaluated were the **S** parameter matrix; $\mathbf{Q}_{loaded}$, the quality factor for the first array element; $\mathbf{maxS}_{21}$, the maximum value of coupling between adjacent elements; and $\mathbf{maxS}_{31}$, the maximum value between the second adjacent elements.

Although widely used for indirect evaluation of $\mathbf{P}_{array\_internal}$ and $\mathbf{P}_{load}$, the $\mathbf{Q}_{load}/\mathbf{Q}_{unload}$ ratios are not tabulated here, since $\mathbf{P}_{array\_internal}$ and $\mathbf{P}_{load}$ were directly evaluated and also because the use of $\mathbf{Q}_{load}/\mathbf{Q}_{unload}$ can mislead the array power budget analysis at 300 MHz. The reasons for this are as follows: a) both for unloaded and loaded coils, radiation losses and the coupling between array elements differ significantly; b) the coupling between power supply and coil is altered by coil loading, which can invalidate the general requirement of critical coupling that enables calculation of the **Q**-factor; and c) the reflected power $\mathbf{P}_{array\_refl}$ is not taken into account.

3. RESULT AND DISCUSSION

An obvious approach to improve array performance is to find a way to increase $\mathbf{P}_V$ for a given array length and load geometry. Taking into account the knowledge that $\mathbf{P}_V$, $\mathbf{P}_{load}$, $\mathbf{P}_{radiated}$ and $\mathbf{P}_{array\_internal}$ are all closely interrelated, increasing $\mathbf{P}_V$ requires: a) minimization of $\mathbf{P}_{array\_refl}$, $\mathbf{P}_{radiated}$ and $\mathbf{P}_{array\_internal}$; and b) maximization of the ratio $\mathbf{P}_V/\mathbf{P}_{load}$. The influence of shield distance on these quantities depends on the array tuning and decoupling approach, and for capacitor-based decoupling it also depends on the decoupling capacitor position relative to the array feed point. The latter dependencies, which are quite complicated, are reported separately.

For CP mode excitation, after minimization of $\mathbf{P}_{array\_refl}$, only $\mathbf{P}_{radiated}$ and $\mathbf{P}_{array\_internal}$ decrease $\mathbf{P}_V$, because this approach always resulted in $\mathbf{P}_{array\_refl} = 0$, independent of the distance to the shield and the size of the head model. For a decoupled array, $\mathbf{P}_{array\_refl}$ is larger for a smaller head model (#1) positioned in an array without shield with the largest (150 mm) length, because for this geometry $\mathbf{maxS}_{31}$ is the largest. The closer the shield to an array the smaller both $\mathbf{maxS}_{21}$ and $\mathbf{maxS}_{31}$. This resulted in reduced $\mathbf{P}_{array\_refl}$.

Reduction of $\mathbf{maxS}_{21}$, $\mathbf{maxS}_{31}$, and $\mathbf{P}_{radiated}$ to a negligible level was already achieved by a shield offset by 60 mm to the array. However the positive influence of the shield on the array element coupling, $\mathbf{P}_{radiated}$, and $\mathbf{P}_{array\_refl}$, was cancelled by a rapidly increased $\mathbf{P}_{array\_internal}$ when the distance between the array and the shield was decreased, especially for decoupled arrays. This resulted in reduced $\mathbf{P}_V$ and $\mathbf{B}_1+_V$ (consequently degradation of the absolute array transmit performance $\mathbf{B}_1+_V/\sqrt{\mathbf{P}_{transmit}}$ and $\mathbf{B}_1+_{slice}/\sqrt{\mathbf{P}_{transmit}}$) as soon as the distance between the array and the shield became less than 60 mm. It should be noted that $\mathbf{B}_1+_V/\sqrt{\mathbf{P}_V}$ - **VOI** related transmit performance remained practically unaffected in the entire range of shield distances, with a peak-to-peak variation of less than 5%. Also the safety excitation efficiency remained within 5% variation in a range of shield distances from "no shield" to 30 mm. Only when the distance is less than 30 mm, a significant gradient in the B field close to the tissue-air boundary resulted in

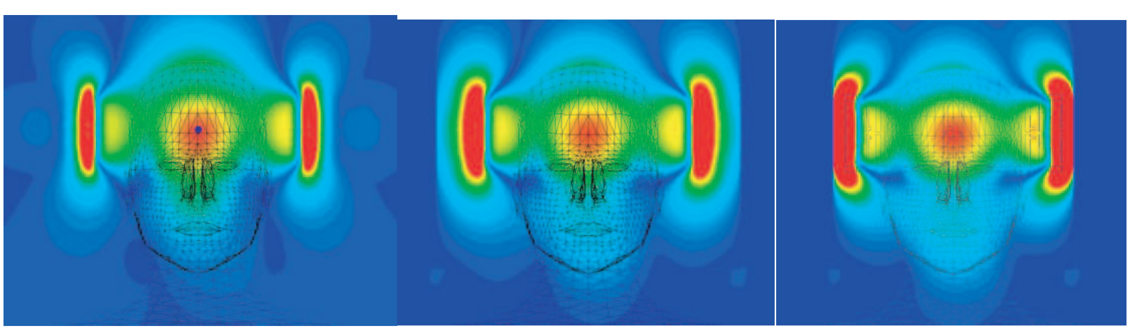

(a) (b) (c)

Figure 1: $\mathbf{B}_1+$ slices, (a) 85 mm length coil, no shield, (b) distance to shield 40 mm and (c) 10 mm.

significantly decreased safety excitation efficiency, especially for a large head that was closer to the array elements. For the same head, the $\mathbf{B}_1+$ brain inhomogeneity varied little with coil length and distance to the shield, when the shield distance is more than 20 mm. For smaller shield distances, inhomogeneity increased, especially for arrays of 85 mm length (Tables 1 to 4).

The results obtained provided no support for the commonly used array design criterion: "the higher the $\mathbf{Q}_{load}$ the better the transmit performance" at least for CP excitation mode. If tuning, matching and decoupling optimization reached their global minima, the shorter distance to the shield resulted in rapidly increased $\mathbf{Q}_{load}$ and $\mathbf{P}_{array\_internal}$. For the same array geometry and load, $\mathbf{Q}_{load}$ was always significantly smaller for arrays with no dedicated decoupling network compared with the arrays with a decoupling network. However, the decoupled arrays always generated a smaller $\mathbf{B}_1+_V$, since $\mathbf{P}_{array\_internal}$ is higher for these arrays. In addition, if the tuning was not perfect and there was a small offset between the array resonance frequency and $\mathbf{F}_{MRI}$ (array operating frequency), the higher quality factor resulted in a large reduction of current (relative to optimal tuning) in the array elements, and consequently a decrease in $\mathbf{B}_1+_V$.

The loop-based elements of the array investigated were closely coupled to the load as usual for transceiver design. When a transmit-only receive-only (TORO) array design is preferred, for

Table 1: Data for coil length 85 mm. Minimization of power reflected back for CP excitation mode.

Distance to local shield	no		60		40		20		15		10	
head	1	2	1	2	1	2	1	2	1	2	1	2
$\mathbf{P}_{array\_refl}$, W	0	0	0	0	0	0	0	0	0	0	0	0
$\mathbf{P}_{radiated}$, W	0.42	0.26	0.04	0.03	0.02	0.02	0.01	0.01	0.01	0.01	0.01	0.01
$\mathbf{P}_{array\_internal}$, W	0.36	0.31	0.49	0.41	0.62	0.51	1.07	0.84	1.42	1.11	2.1	1.68
$\mathbf{P}_{load}$, W	7.22	7.43	7.47	7.56	7.36	7.47	6.92	7.15	6.57	6.88	5.89	6.31
$\mathbf{P}_V$, W	2.54	2.52	2.57	2.50	2.50	2.43	2.28	2.23	2.14	2.11	1.90	1.92
$\mathbf{B}_1+_{brain}$, μT	1.59	1.47	1.62	1.48	1.60	1.46	1.54	1.41	1.50	1.37	1.41	1.31
Inhomogeneity brain, %	25	25	26	27	27	28	29	28	30	31	31	32
$\mathbf{B}_1+_{slice}$, μT	1.90	1.78	1.98	1.83	1.98	1.83	1.94	1.79	1.90	1.76	1.80	1.69
Inhomogeneity slice, %	18	17	18	17	18	17	17	16	16	16	16	17
$\mathbf{SAR}_{10g}$, W/kg	4.60	4.37	4.51	4.21	4.44	4.33	4.40	5.12	4.35	5.47	4.93	4.30
$\mathbf{B}_1+_V/\sqrt{\mathbf{SAR}_{10g}}$, μT/$\sqrt{}$(W/kg)	0.74	0.70	0.76	0.72	0.76	0.70	0.73	0.62	0.72	0.58	0.63	0.63
$\mathbf{Q}_{loaded}$ for 1st element	13	11	18	14	23	18	38	31	51	40	73	56

Table 2: Data for coil length 85 mm. Inductive decoupling for CP excitation mode.

Distance to local shield	no		60		40		20		15		10	
head	1	2	1	2	1	2	1	2	1	2	1	2
$\mathbf{P}_{array\_refl}$, W	0.48	0.29	0.32	0.19	0.29	0.16	0.22	0.12	0.19	0.10	0.13	0.08
$\mathbf{P}_{radiated}$, W	0.41	0.26	0.05	0.03	0.02	0.02	0.01	0.01	0.01	0.01	0.01	0.01
$\mathbf{P}_{array\_internal}$, W	0.39	0.35	0.65	0.46	0.71	0.58	1.2	0.97	1.57	1.25	2.1	1.85
$\mathbf{P}_{load}$, W	6.72	7.10	7.30	7.32	7.00	7.24	6.57	6.90	6.23	6.64	5.89	6.06
$\mathbf{P}_V$, W	2.33	2.38	2.72	2.38	2.34	2.32	2.16	2.13	2.03	2.02	1.90	1.84
$\mathbf{B}_1+_{brain}$, μT	1.53	1.43	1.61	1.44	1.55	1.43	1.50	1.36	1.46	1.33	1.41	1.28
Inhomogeneity brain, %	25	25	26	27	27	28	29	30	30	31	31	31
$\mathbf{B}_1+_{slice}$, μT	1.83	1.73	1.96	1.78	1.92	1.78	1.89	1.75	1.85	1.72	1.80	1.66
Inhomogeneity slice, %	18	17	18	16	17	16	16	15	15	15	16	14
$\mathbf{SAR}_{10g}$, W/kg	4.27	4.18	4.91	4.31	4.33	4.64	4.63	5.33	4.61	5.44	4.93	5.23
$\mathbf{B}_1+_V/\sqrt{\mathbf{SAR}_{10g}}$, μT/$\sqrt{}$(W/kg)	0.74	0.70	0.72	0.70	0.75	0.66	0.69	0.59	0.68	0.57	0.64	0.56
$\mathbf{Q}_{loaded}$ for 1st element	22	19	29	25	38	31	61	51	79	63	105	87
$\mathbf{maxS}_{21}$	−14.7	−15.8	−15.5	−16.6	−15.8	−17.1	−17.1	−18.2	−18.1	−18.6	−19.6	−20.0
$\mathbf{maxS}_{31}$	−11.7	−13.2	−12.8	−14.5	−14.0	−15.7	−17.0	−18.3	−19.0	−19.5	−21.3	−21.6

Table 3: Data for coil length 150 mm. Minimization of power reflected back.

Distance to local shield	no		60		40		20		15		10	
head	1	2	1	2	1	2	1	2	1	2	1	2
$\mathbf{P}_{array\_refl}$, W	0	0	0	0	0	0	0	0	0	0	0	0
$\mathbf{P}_{radiated}$, W	0.63	0.43	0.08	0.06	0.05	0.04	0.02	0.02	0.02	0.02	0.02	0.02
$\mathbf{P}_{array\_internal}$, W	0.21	0.2	0.33	0.3	0.44	0.39	0.9	0.78	1.26	1.09	2.0	1.74
$\mathbf{P}_{load}$, W	7.16	7.37	7.59	7.64	7.51	7.57	7.08	7.20	6.72	6.89	5.98	6.24
$\mathbf{P}_V$, W	2.67	2.73	2.78	2.74	2.71	2.67	2.53	2.51	2.39	2.38	2.12	2.13
$\mathbf{B}_1+_{brain}$, μT	1.57	1.47	1.62	1.50	1.61	1.48	1.56	1.44	1.52	1.40	1.43	1.33
Inhomogeneity brain, %	23	24	24	24	25	24	25	24	25	24	25	25
$\mathbf{B}_1+_{slice}$, μT	1.77	1.67	1.85	1.72	1.85	1.71	1.80	1.66	1.75	1.62	1.64	1.53
Inhomogeneity slice, %	23	23	24	23	24	23	24	23	24	23	24	24
$\mathbf{SAR}_{10g}$, W/kg	4.08	4.29	4.54	4.21	4.41	4.11	4.15	3.86	3.92	3.82	3.49	3.69
$\mathbf{B}_1+_V/\sqrt{\mathbf{SAR}_{10g}}$, μT/$\sqrt{}$ (W/kg)	0.78	0.71	0.77	0.73	0.77	0.73	0.77	0.73	0.77	0.72	0.76	0.69
$\mathbf{Q}_{loaded}$ for 1st element	8	7	13	11	17	15	33	29	47	41	70	61

Table 4: Data for coil length 150 mm. Inductive decoupling.

Distance to local shield	no		60		40		20		15		10	
head	1	2	1	2	1	2	1	2	1	2	1	2
$\mathbf{P}_{array\_refl}$, W	0.56	0.29	0.25	0.13	0.20	0.10	0.14	0.13	0.14	0.12	0.12	0.11
$\mathbf{P}_{radiated}$, W	0.82	0.59	0.08	0.06	0.04	0.04	0.02	0.02	0.02	0.02	0.02	0.02
$\mathbf{P}_{array\_internal}$, W	0.24	0.24	0.42	0.38	0.57	0.50	1.08	0.94	1.46	1.27	2.21	1.92
$\mathbf{P}_{load}$, W	6.38	6.88	7.25	7.43	7.19	7.36	6.76	6.91	6.38	6.59	5.65	5.95
$\mathbf{P}_V$, W	2.40	2.59	2.64	2.66	2.60	2.59	2.41	2.40	2.27	2.27	1.98	2.00
$\mathbf{B}_1+_{brain}$, μT	1.48	1.43	1.58	1.47	1.57	1.46	1.52	1.41	1.48	1.37	1.38	1.29
Inhomogeneity brain, %	23	23	24	24	25	24	25	24	25	24	25	25
$\mathbf{B}_1+_{slice}$, μT	1.66	1.61	1.80	1.68	1.80	1.67	1.75	1.62	1.69	1.62	1.64	1.48
Inhomogeneity slice, %	23	23	24	23	24	23	24	23	24	24	25	25
$\mathbf{SAR}_{10g}$, W/kg	4.09	4.25	4.43	4.45	4.24	4.12	4.23	3.84	4.08	3.61	3.68	3.57
$\mathbf{B}_1+_V/\sqrt{\mathbf{SAR}_{10g}}$, μT/$\sqrt{}$(W/kg)	0.73	0.69	0.75	0.70	0.75	0.72	0.74	0.72	0.73	0.72	0.72	0.68
$\mathbf{Q}_{loaded}$ for 1st element	13	12	21	18	29	22	48	44	58	52	80	80
$\mathbf{maxS}_{21}$	−16.2	−18.2	−18.1	−20.7	−18.4	−21.0	−19.6	−21.8	−20.5	−21.6	−21.9	−21.9
$\mathbf{maxS}_{31}$	−10.3	−11.5	−11.4	−12.8	−12.2	−13.8	−14.7	−15.6	−16.2	−17.2	−18.4	−19.6

whatever reason, the transmit- only components of the arrays should be separated by a larger distance from a load than in the current study. Thus additional investigation would need to be performed to be able to project the results obtained to the behaviour of a transmit-only array.

If higher (than first circular polarization) modes are required to be used for the optimization of array geometry and tuning condition all required modes should be taken into account.

4. CONCLUSION

Consideration of the parameters $\mathbf{Q}_{load}$ and coupling only is insufficient to understand, compare and optimize array transmit performance for CP mode excitation. Analysis of the array power balance should be regarded as the key for understanding the relative improvement or degradation of the array performance. In the CP excitation mode, the transmit performance of a loop array closely coupled to a load is only weakly dependent on shield distance when this distance is greater than 20 mm, especially when tuning by reflected power minimization is employed. For the array investigated the performance is strongly affected by this distance only if it is less than 20 mm.

REFERENCES

1. Kozlov, M. and R. Turner, "Comprehensive analysis of transmit performance for an 8-element loop MRI RF coil at 300 MHz," *Proceedings of the 40th European Microwave Conference*, 328–331, Paris, France, Sep. 2010.
2. Kozlov, M. and R. Turner, "Fast MRI coil analysis based on 3-D electromagnetic and RF circuit co-simulation," *Journal of Magnetic Resonance*, No. 200, 147–152, 2009.
3. Kozlov, M. and R. Turner, "Analysis of transmit performance optimization strategies for multi channel MRI array," *PIERS Proceedings*, 1622–1626, Marrakesh, Morocco, Mar. 2011.

Estimation of Electromagnetic Exposure Level Based on a Multilayered Model of the Pelvic-hip Region

M. Macedo and M. Yarlequé
Pontificia Universidad Católica del Perú, Sección Telecomunicaciones
Av. Universitaria 1801, Lima-32, Lima, Perú

Abstract— Intensive research has been addressed to determine the effect of nonionizing radiation on head and human body. In this paper, a specific model for analyzing the EM exposure within the pelvic-hip region is proposed and simulated by FDTD method. This model includes seven layer and vital organs of the male and female anatomy. It is observed the most of the radiation is located within the outer layer, and minimum exposure in vital organs.

1. INTRODUCTION

Within the last years, mobile phones and wireless devices usage has been rapidly spread globally. When these devices are used in close proximity to any part of the human body, the electromagnetic (EM) interaction with the body could be complex and affected by many factors. One figure to evaluate this interaction is the specific absorption rate (SAR), which measure the power absorbed by a biological tissue.

SAR can be determined through numerical calculation or simulations on 3D Maxwell solvers or alternatively by employing phantoms [1]. SAR studies at the head [2, 3] were developed in the last years considering mobile phones as a source of radiation, whereas SAR full body calculation has been developed as well, but this analysis considers a base station as radiation source [4, 5].

Nowadays, there is a trend to place wireless device close to the hip-pelvic region, for instance, mobile phones inside the pants pockets, laptop computers on the lap, and so forth. The electromagnetic emission of this device is likely to make an impact on vital organs and other tissues that are around the hip. Then, it is important to assess the effect of this radiation. To our best knowledge, SAR determination on the pelvic region of the body has not been developed yet, and then the main aim of this paper is to determine SAR (W/kg) for the pelvic region and hip area through simulation software. Knowing hip anatomy, we propose a seven-layer model for the pelvic and hip tissues plus internal organs. Based on this new model, the EM exposure level is determined.

2. NUMERICAL METHOD AND MODELLING

2.1. General Characteristics

Basic models for power absorption of tissue layer are based on the interaction of an EM wave impinging on multiple layers interface, as it can be observed in Fig. 1. Elemental equations can be established to determine the propagation of this wave throughout the different layers [6]. The fundamental property in this interaction is the complex propagation constant.

The propagation constant of the wave depends on the electrical properties of each interface. The amount of energy transmitted to another interface depends on the type of the material in each layer. Fig. 2 shows the behavior of electrical properties in biological tissues.

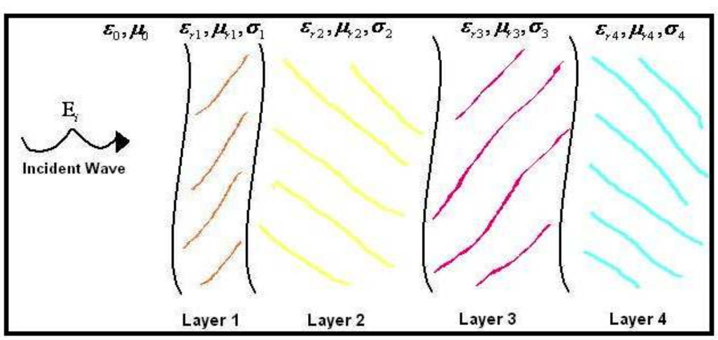

Figure 1: EM wave impinging on multiple layers.

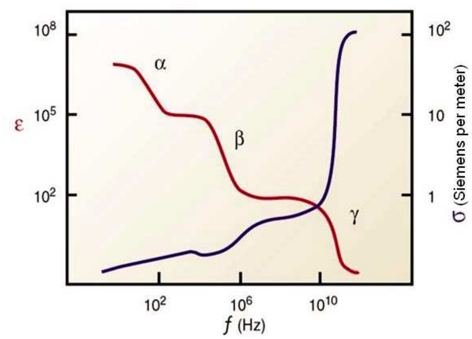

Figure 2: Electrical properties of biological tissues [12].

The conductivity (σ) at low frequencies largely depends on the fraction occupied by the extracellular fluid in the tissues. Over 100 MHz, conductivity has dissimilar properties in tissues; and exists a relaxation at frequencies below 1 GHz. Moreover, conductivity increases directly with respect to frequency [7]. On the other hand, the permittivity (ε) decreases with frequency increment. α dispersion at low frequencies is due to several physical processes, meanwhile β dispersion is notable for the frequency range from 0.1 to 10 MHz. γ dispersion takes place at 25 GHz at body temperature, in which water is distributed in 80% of the volume of most tissues [7].

Considering the tissue layer model and their electrical properties, the electromagnetic fields can be solved. Then, the specific absorption rate could be defined as in (1).

$$SAR = \frac{\sigma}{2\rho}\left|E_{tiss}\right|^2 = \frac{2\pi f \varepsilon_0 \varepsilon"}{2\rho}\left|E_{tiss}\right|^2 \tag{1}$$

where ρ is the volume density and E_{tiss} is the peak value of electric field present in that portion of tissue. SAR units are then watts per kilogram (W/kg). Actually, (1) defines the local SAR, the average SAR could be determined as in (2)

$$AverageSAR = \frac{(\int SARdv)}{V} \tag{2}$$

where V is the volume of the model and dv the volume of each cell. The integral could be calculated over the whole exposed object, as well as, over samples of 1 gram or 10 grams, which determine the volume of each sample. The average values for 1 gram and 10 grams mass are employed in this work. The concept of SAR is very useful to quantify the interaction of RF radiation on living tissues and extends up to 10 GHz.

2.2. Male and Female Model Structure

The pelvic-hip region has been modeled in different ways. For instance, a planar distribution of tissues was developed in [7] while, a three-layer cylindrical structure was employed in [8]. The developed model consists of seven layers, which represent all the tissues between the organs and the skin surface, plus five organs. These layers are modeled as a cylindrical structure (see Figs. 3(a). and 3(b).).

The cylindrical structure consists of an elliptical base with diameter ratio of 1.6 for male and female 7-layer model. Skin tissue (including penis only for male model), adipose tissue, muscle tissue, bone tissue, nervous system, blood, body fluid are considered for the structure. The following organs are considered for male model: colon (1) bladder (2), prostate (3), kidney (4), and testis (5) as shown in Fig. 3(a) Similarly, the following organs are considered for female model: colon (1), uterus (2), bladder (3), kidney (4), and ovaries (5), as shown in Fig. 3(b).

The thickness values of each layer of the model are detailed in Table 1(a) [7]. The organs shapes are modeled as a flattened ellipsoid and spheres, and the sizes of these are according in proportion to the cylindrical structure, and are reported in Table 1(a). Density values of tissues and organs are established as is described in [5], and are reported in Table 1(b) Colon, prostates, ovaries and uterus are not specified in [5]; nevertheless these organs have similarly characteristics with the

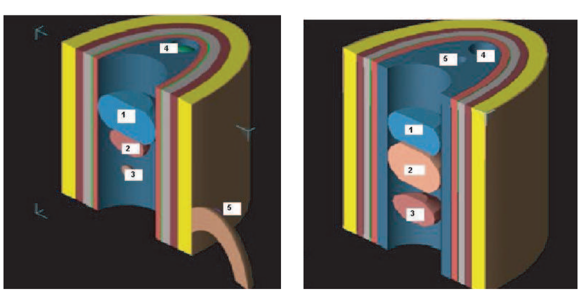

(a) (b)

Figure 3: (a) Male model on EMPro agilent. (b) Female model on EMPro agilent.

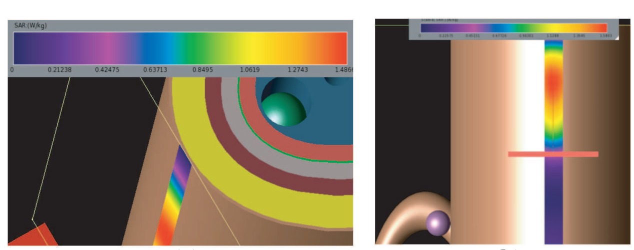

(a) (b)

Figure 4: SAR distribution over tissues at 900 MHz. (a) View of slice where the maximum SAR is located. (b) Monopole antenna tuned at 900 MHz radiates over the whole model.

Table 1: (a) Thickness values for biological tissues. (b) Volume density values for biological tissues.

	Male	Female
Tissue	Thickness (mm)	Thickness (mm)
Skin	2	2
Fat	25	20
Muscle	15	10
Bone	15	15
Nerve	3	3
Blood	10	10

(a)

	Male		Female
Organ Tissue	Diameter (mm)	Organ Tissue	Diameter (mm)
Colon	110	Colon	80
Bladder	65	Bladder	65
Kidney	40	Kidney	30
Prostate	20	Uterus	80
Testis	30	Ovaries	16

(b)

Table 2: Permittivity and conductivity values for biological tissues [10].

Frequency	900MHz		1800MHz		2.4GHz		150MHz		450MHz	
Tissue	Conductivity [S/m]	Relative permittivit	Conductivity [S/m]	Relative permittivity	Conductivity [S/m]	Relative permittivity	Conductivity [S/m]	Relative permittivity	Conductivity [S/m]	Relative permittivity
Air	0	1	0	1	0	1	0	1	0	1
Bladder	0.38308	18.936	0.53516	18.341	0.67265	18.026	0.30085	21.432	0.3316	19.58
Blood	1.5379	61.36	2.0435	59.372	2.5024	58.347	1.2592	71.252	1.3664	63.675
Fluid	1.6362	68.902	2.0325	68.573	2.4392	68.24	1.5064	69.052	1.5363	68.993
Bone	0.14331	12.454	0.27522	11.781	0.38459	11.41	0.069522	14.412	0.095834	13.039
Colon	1.0799	57.94	1.5762	55.148	1.9997	53.969	0.7223	73.753	0.88023	61.748
Fat	0.051043	5.462	0.078388	5.3494	0.10235	5.2853	0.037263	5.8453	0.041938	5.5606
Kidney	1.3921	58.675	1.9495	54.426	2.3901	52.856	0.88053	85.002	1.1274	65.001
Muscle	0.94294	55.032	1.341	53.549	1.705	52.791	0.72719	62.179	0.80926	56.754
Nerve	0.57369	32.531	0.8429	30.867	1.0681	30.196	0.36439	42.33	0.45992	34.882
Ovary	1.2904	50.471	1.8178	46.396	2.2277	44.817	0.81639	74.815	1.0424	56.279
Prostate	1.2096	60.553	1.6915	58.605	2.1273	57.629	0.93698	70.301	1.0434	62.871
SkinWet	0.84465	46.08	1.232	43.85	1.5618	42.923	0.55841	59.22	0.68689	49.196
Testis	1.2096	60.553	1.6915	58.605	2.1273	57.629	0.93698	70.301	1.0434	62.871
Uterus	1.2699	61.115	1.7641	58.937	2.2058	57.897	0.97343	73.081	1.0934	63.855

muscular layer, as it is explained in [9]. The electrical properties of the tissues layers and organs are shown in Table 2. These conductivity (S/m) and relative permittivity values for each tissue of human body are calculated from [10].

3. RESULTS AND DISCUSSION

To evaluate the SAR in the pelvic-hip region, the following sceneries will be analyzed:

Mobile phone radiation in the 900 and 1800 MHz bands.

Laptop radiation in 2.4 GHz, through Wi-Fi and Bluetooth wireless connection. Mobile phones also can establish connections through these technologies.

Two-way radio handheld radiation in 150 MHz (VHF) and 450 MHz (UHF) band.

The devices operating at these frequencies commonly cause EM radiation over the regions that are analyzed in this work. The simulation is executed in Agilent EMPro with the following parameter: FDTD solver, perfectly matched layer (PML) absorbing boundaries, base cell size of 1.3 mm and 1 GB of memory required for the simulations.

3.1. Mobile Phones Band Radiation

A quarter-wavelength monopole antenna is used as radiator for both 900 MHz and 1800 MHz, with different sizes at each frequency (8.16 and 4.07 cm respectively). It is provided at the antenna output a radiation power of 0.25 W at 900 MHz and 0.125 W at 1800 MHz. The distance between the antenna and the object in radiation exposure is 3 cms. Once the simulation is executed, the distribution of specific absorption rate, at 900 MHz, is obtained and is shown in Fig. 4. The small red objects observed in Fig. 4 and Fig. 5 corresponds to the ground plane of the monopole. The monopole can not be observed because is very thin SAR peak of 1.1 W/Kg is located at the first

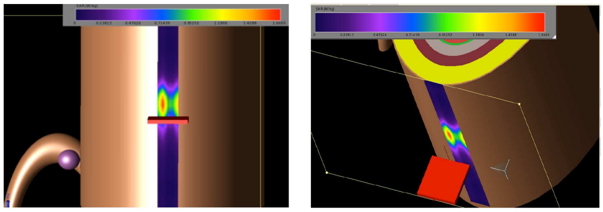

(a) (b)

Figure 5: SAR distribution over tissues at 1800 MHz. (a) Monopole antenna tuned at 1800 MHz radiates over the whole model. (b) View of slice where the maximum SAR is located.

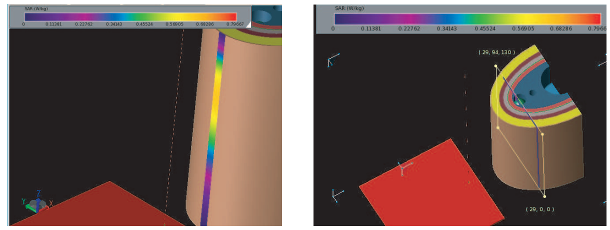

(a) (b)

Figure 6: SAR distribution over tissues at 150 MHz. (a) Monopole antenna tuned at 150 MHz radiates over the whole model. (b) View of slice where the maximum SAR is located.

Table 3: Final results.

Radiation Emitter	Frequency (MHz)	Transm. Power (W)	Type	SAR(W/kg) max	Location	SAR(W/kg) aver.	SAR(W/kg) 10g.	SAR(W/kg)1g.
Antenna GSM	900	0.2433	Male	1.1	Skin	0.00633	0.1777	0.3632
Antenna GSM	900	0.2447	Female	1.3	Skin	0.00925	0.1888	0.4049
Antenna GSM	1800	0.1245	Male	0.3893	Fat	0.001	0.0544	0.1028
Antenna GSM	1800	0.1243	Female	0.4934	Fat	0.0013	0.07	0.175
Antenna Wi-Fi	2400	0.44	Male	0.147	Skin	0.0026	0.0352	0.0525
Antenna Wi-Fi	2400	0.45	Female	0.217	Skin	0.00276	0.033	0.06
Antenna Bluetooth	2400	0.12	Male	0.0586	Skin	0.00074	0.0089	0.00162
Antenna Bluetooth	2400	0.121	Female	0.0392	Skin	0.00069	0.0094	0.014
Two-Way Radio VHF	150	3.98	Male	0.37	Skin	0.02263	0.1849	0.2598
Two-Way Radio VHF	150	4	Female	0.678	Kidney	0.0321	0.2915	0.353
Two-Way Radio UHF	450	3	Male	0.797	Skin	0.02541	0.2791	0.387
Two-Way Radio UHF	450	2.98	Female	0.6014	Skin	0.03506	0.2039	0.3622

outer layer, i.e., within the skin. It is observed that radiation attenuates rapidly, passed the skin layer. These results are obtained from the male model; similar results are obtained for the female model (see Table 3).

At 1800 MHz, the characteristics of permittivity and conductivity of the model layers and organs change, with higher conductivity and lower relative permittivity (see Fig. 2 and Table 2). The model was updated with these new values and the simulation output is presented in Fig. 5. In this case, a SAR maximum of 0.38 W/Kg is observed in the second outer layer (adipose tissue). Likewise, the radiation attenuates rapidly, passed this adipose layer. These results, obtained from the male model, are approximately similar to the ones obtained for the female model (see Table 3).

3.2. Wi-Fi and Bluetooth Radiation

At 2.4 GHz, a half-wave dipole antenna is commonly used for Wi-Fi technologies and Bluetooth connections, and it is employed as a radiator (5.4 cm of length) for SAR calculation in this case. A radiation power of 0.45 W for WiFi antenna, and 0.12 W for Bluetooth, is provided for the analysis. The distance between the radiator and the object is of 10 cms. From the Wi-Fi simulation, a maximum SAR value of 0.147 W/kg is obtained, and is located within the skin layer. In the case of Bluetooth radiation, a maximum SAR of 0.058 W/kg is determined, which is lower than Wi-Fi value, as expected. The values for male and female are similar (see Table 3).

3.3. Two-way Radio Handheld Radiation

There are two frequency bands to be analyzed. At VHF, two-way radios operate at frequencies around 150 MHz, while at UHF, these devices can be tuned from 410 to 450 MHz, being the frequency of 450 MHz chosen for the analysis. Larger monopole antennas (50 and 16.66 cm respectively) were designed. The distance between the antenna and the object is 9 cms. A radiation power of 4 W and 3 W is provided for the VHF and UHF simulation.

At 150 MHz, it is observed that the maximum SAR of 0.678 W/kg is located in the kidney tissue for the female model (this can be visualized in Fig. 6), while in the male model is located in the first outer layer. The small red object observed in Fig. 6 corresponds to the ground plane of the monopole. Definitely the wavelength at 150 MHz is larger than the structure of simulation; and the layer and interfaces of the skin, fat, muscle, bone and so forth, are not large enough to mitigate this long wave.

At 450 MHz a maximum SAR value of 0.797 W/kg is calculated from the male model. This maximum is within the skin layer, the first outer layer, which absorbs a large amount of power. Similar values are obtained for the female model (see Table 3). The SAR values obtained are greater than in the case of 150 MHz, and this is consequence of the shorter wavelength and the interaction with the different layers sizes and conductivity.

Finally, a summary of the results obtained for all cases is reported in Table 3.

All these simulations and results are obtained by employing short EM pulses (for instance 0,0001 μs). This pulse contains several harmonics components; however only the harmonic component at which the antenna is tuned will be radiated to the object. As part of the radiation is absorbed and converted into heat, the authors considers that temperature may increase slightly in the body and the dielectric properties may vary, as a result the exposure time may affect the analysis of the SAR value.

The results of the specific absorption rate (SAR) averaged for the pelvic region and hip area are lower than the value recommended in the standards of ICNIRP [11]. In addition the maximum SAR value was always lower than the exposure limit value specified by the ICNIRP (2 W/kg).

4. CONCLUSION

In this paper, a model of seven layers and vital organs of the pelvic-region for the male and female has been proposed and simulated. The EM exposure within the pelvis is calculated from different radiation devices. The maximum and average SAR value are obtained and it is observed that most of the radiation is localized in the outer tissue layer, with minimum exposure within vital organs, except for a particular case (at 150 MHz and in the female model). The latter will be further analyzed in a following research.

REFERENCES

1. Pokovic, K., M. Burkhardt, T. Schmid, and N. Kuster "Experimental and numerical near-field evaluation of RF transmitters," *Radiofrequency radiation dosimetry*, B. J. Klauenberg, D. Miklavcic, Eds., 159–186, Kluwer Academic Publishers, Netherlands, 2000.
2. Ghandi, O. P., G. Lazzi, and C. M. Furse, "Electromagnetic absorption in the human head and neck for mobile telephones at 835 and 1900 MHz," *IEEE Transactions on Microwave Theory and Techniques*, Vol. 44, 1884–1897, 1996.
3. Dimbylow, P. J. and S. M. Mann, "SAR calculations in an anatomically realistic model of the head for mobile communication transceivers at 900 MHz and 1.8 GHz," *Physics in Medicine and Biology*, Vol. 39, 1537–1553, 1994.
4. Bernardi, P., M Cavagnaro, S. Piza, and E. Piuzzi, "Human exposure to radio base-station antennas in urban environment," *IEEE Transactions on Microwave Theory and Techniques*, Vol 48, 1996–2003, 2000.
5. Martínez-Búrdalo, M., A. Martín, M. Anguiano, and R. Villar, "On the safety assessment of human exposure in the proximity of cellular communications base-station antennas at 900, 1800, 2170 MHz," *Physics in Medicine and Biology*, Vol. 50, 4125–4137, 2003.
6. Hayt, W., *Electromagnetic Theory*, 7th Edition, McGraw Hill, 2006.
7. Polk, C. and P. Elliot, *Handbook of Biological Effects of Electromagnetic Fields*, 2nd Edition, CRC Press, 1996.
8. Nishizawa, S. and O. Hashimoto, "Effectiveness analysis of lossy dielectric shields for a three-layered human model," *IEEE Transactions on Microwave Theory*, Vol. 4, 277–283, 1999.
9. Carpi, A., "Basic anatomy — Tissues and organs," John Jay College of Criminal Justice, 1999, http://web.jjay.cuny.edu/∼acarpi/NSC/14-anatomy.htm.
10. Gabriel, C., "Compilation of the dielectric properties of body tissues at RF and microwave frequencies," Report N.AL/OE-TR- 1996-0037, Occupational and Environmental Health Directorate, Radiofrequency Radiation Division, Brooks Air Force Base, Texas, USA, June 1996.
11. ICNIRP, "Guidelines for limiting exposure to time-varying electric, magnetic and electromagnetic fields," *International Commission of Non-ionizing Radiation Protection*, 1998.
12. Sebastián, J., "Medición en radiación de seres vivos," *Investigación y Ciencia*, Madrid, 2006.

Comments on Some Radio Wave Propagation Mechanisms in the Amazon Region

Mauro S. Assis
Brazilian Committee of URSI, Brazil

Abstract— This paper deals with radio wave propagation in the Amazon region. Three different propagation problems are commented: a) Radio wave attenuation in a forest environment; b) VHF and UHF long distance propagation; c) Rain effects in satellite communications.

1. INTRODUCTION

The Amazon region is covered by a dense rain forest, crossed by a large number of rivers and characterized by a hot and humid climate. The annual precipitation is of the order or higher than 2000 mm and the median temperature along the year is approximately constant between 25 and 28°C. In this scenario, depending on the frequency of operation, different propagation phenomena should be considered in the performance evaluation of a radio system. For instance, the following aspects can be pointed out: a) Signal attenuation due to vegetation is higher as the frequency increases; b) The knowledge of meteorological conditions of troposphere (turbulence and stratification), including super refraction and ducting, are quite important in the analysis of terrestrial VHF and UHF radio links covering long distances in this region; c) Rain attenuation is a critical issue when using frequencies above 10 GHz, being particularly relevant for satellite communication in the Ku band. Based on theoretical considerations and experimental results, some of these problems are commented in this paper.

2. RADIO WAVE PROPAGATION IN A FOREST ENVIRONMENT

Radio wave attenuation due to vegetation is the major constraint to the path range of a communication system operating within a jungle. The signal attenuation depends critically on the operating frequency and on the values of the electrical parameters of vegetation. The optimum frequency is chosen as the best compromise between low signal attenuation, an acceptable level of atmospheric noise and the physical dimension of a portable transceiver compatible with the mobility required for operation within the forest. According to these considerations, the HF band appears to be the best choice, the optimum frequency being around 10 MHz [1]. On the other hand, the electrical characteristics of vegetation were estimated through an experimental procedure which involves the comparison of direct measurement of field strength decay versus distance with numerical values derived from the theoretical model of the lateral wave. The best fit were achieved for $\varepsilon_f = 1.2$ and $\sigma_f = 0.2\,\text{mS/m}$ [2]. Based on measurements carried out in the Amazon region, two different aspects of the problem are described in this Section: (a) Both stations immersed in the jungle; (b) A radio link between a ground station located within the forest and other in an airplane or an helicopter (ground-to-air link).

2.1. Lateral Wave

Radio wave propagation characteristics in a forest environment are usually predicted by the plane conducting slab model shown in Fig. 1 [1]. At a first glance, the plane geometry seems to constitute a limitation to this model. However, as this section deals with radio paths of a few kilometers, the effect of the earth curvature can be disregarded. Theoretically, there are three propagation mechanisms in the transmitting-receiving path depicted in Fig. 1: (a) the forest geometric-optical components (direct and reflected rays); (b) the sky-wave component; (c) the lateral wave component. For distances larger than 0.5 km the forest geometric-optical components are highly attenuated. On the other hand, the sky-wave component can be neglected for distances lesser than about $10 \sim 20$ km. Consequently, within the range of interest here, the lateral wave represents the predominant mechanism.

As a check to the lateral wave model the following propagation test was carried out. A 15 W transmitter and a receiver were located inside the forest. The receiver was fixed while the transmitter was moved along a 3000 meters path. Several measurements were made from 50 to 3000 m. The frequency was 10.25 MHz. As depicted in Fig. 2, the comparison between theoretical results derived from the lateral wave model with experimental data shows a very good agreement.

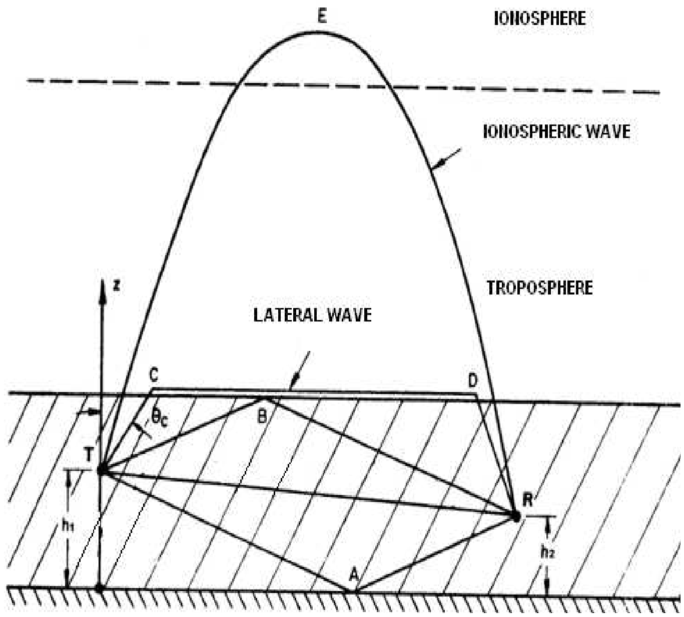

Figure 1: Propagation mechanisms.

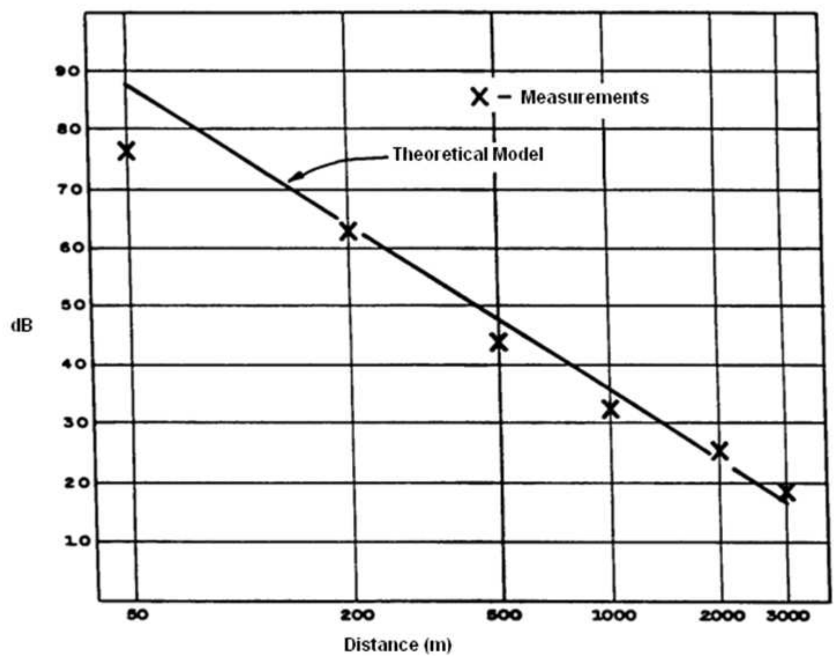

Figure 2: Variation of field strength with distance.

2.2. Ground-to-air Link

People engaged in a military or a scientific mission in a forest environment normally dispose of radio sets to be used for communication between them. In the case of a dense jungle, sometimes it happens that the all group or part of it may become lost in this environment. It should be pointed out that even the GPS signal can suffer a very strong attenuation due to the vegetation and a precise localization of this group becomes unfeasible. In this context, the availability of radio sets is of paramount importance to carry out a successfully search and rescue operation. A similar situation is the case of an airplane crash in the jungle. In such scenario, the radio equipment to be localized must be capable to operate with a voice channel or emitting a help radio signal put in action by some automatic device. The unknown position of the radio station can be settled by air with the aid of search equipment mounted in a plane or helicopter.

A crucial problem in the above scenario is the evaluation of the coverage area of the equipment to be localized. In a dense jungle, this coverage is limited by the high signal attenuation due to vegetation. Table 1 shows a comparison between theoretical results and experimental data. Measurements were carried out in the Brazilian Amazon jungle in the frequency of 10 MHz with a helicopter flying at an average height of 150 m, i.e., 120 m above the forest top. Taking as reference the position of the radio terminal inside the jungle, these measurements have covered a maximum horizontal distance of 16 km. The ground terminal was 1.5 m above the earth.

3. RADIO WAVE PROPAGATION IN VHF AND UHF BANDS

Based on measurements carried out in a 113 km long VHF radio link, the diurnal variation of troposphere in the Amazon region is described in this Section. The analysis of the experimental data has shown that the behavior of the troposphere follows two different conditions. During the day, due to troposphere turbulence, the scatter propagation is dominant and the received power

Table 1: Comparison between theoretical results* and experimental data.

Distance (km)	Full solution (dB)		Refracted wave (dB)		Measurements** (dB)
	Hor. Pol.	Vert. Pol.	Hor. Pol.	Vert. Pol.	
1	26.5	27.0	26.9	27.3	36.1
2	32.0	32.4	32.3	32.6	38.8
4	37.7	37.9	38.0	38.1	38.6
8	43.1	43.3	43.4	43.4	41.5
16	50.0	50.0	50.3	50.3	46.5

* Attenuation relative to free-space

**Average values for several measurements around the reference distance.

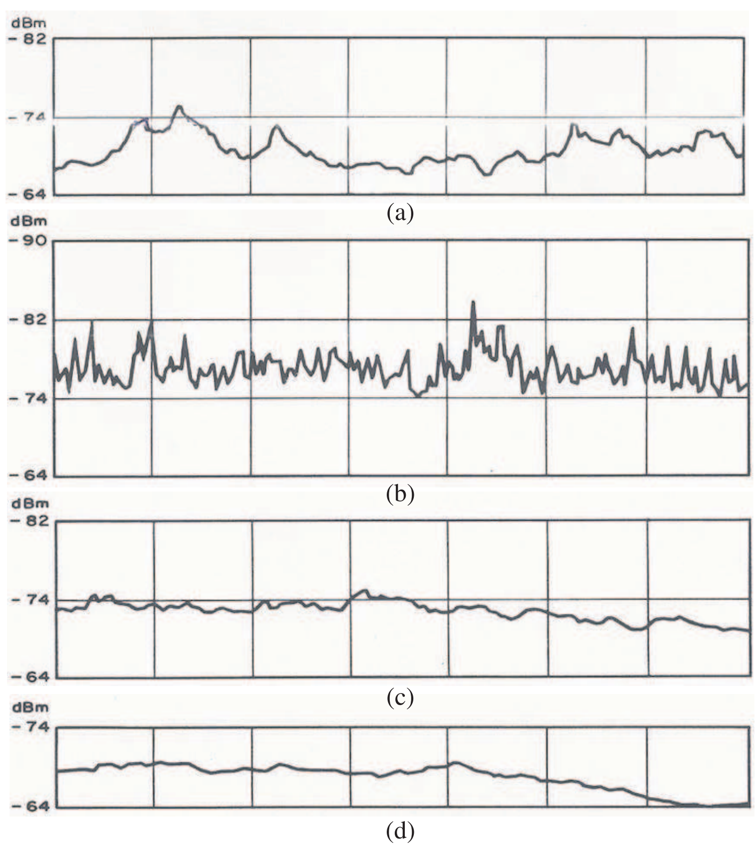

Figure 3: Samples of the received power. (a) Transition from stratification to turbulence (07:00 a.m.). (b) Turbulent troposphere — scatter propagation (02:00 p.m.). (c) Transition from turbulence to stratification (06:00 p.m.). (d) Stratified troposphere — diffraction propagation (08:00 p.m.).

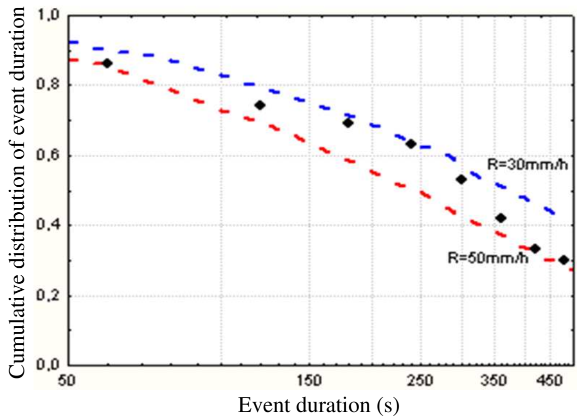

Figure 4: Comparison between the duration of rain and fade events.

fluctuates in a range of about 10 dB. In night hours, the troposphere becomes stratified and the diffraction mechanism predominates. This behaviour is shown in Fig. 3 for different hours along the day [4].

4. SATELLITE COMMUNICATIONS IN THE KU BAND

In the planning of low availability satellite systems an outage of 1 to 0.1% in the worst month is normally acceptable. In these systems the temporal variability of fading has a strong impact on system design. Consequently, the knowledge of rain dynamics is of fundamental relevance. It is recognized that the conversion of rain rate duration to slant path duration statistics is not an easy task. The main problems are the vertical non homogeneity of rain structure and the possibility of having more than one rain cell along the propagation path. However, according to Timothy et al. [5], if the vertical distribution of rain is uniform from the earth surface to a height near the 0° isotherm level and the elevation angle is higher than 30°, the measured rainfall rate threshold at a given probability level may be used to obtain information on the dynamics associated to the attenuation in slant path.

Based on measurements carried out in a rain gauge with 8 pluviographs, the problem of precipitation event duration was investigated in the Amazon region [6]. The experimental data have allowed the analysis of the following items: a) The statistical behavior of the rain event duration; b) The use of the two variables Weibull function as mathematical model to characterize such events; c) The mathematical representation, by a power function, of the rain event duration in terms of the precipitation rate and the time percentage that this precipitation is exceeded; d) The average event duration of interest for designing improvements techniques to satellite systems (1 to 3 minutes); e) The evidence of a correlation between the duration of rain and fade events. This last item is quite important in the analysis of a satellite link when there is no information about fade event duration. An example of this correlation is given in Fig. 4. The curves in this figure correspond to precipitation rates exceeded for 30 and 50 mm/h, respectively (broken lines). The isolated points refer to fade durations higher than 7 dB observed in a 12 GHz beacon receiver [7]. It is clear that the events of fade duration are well in agreement with the rain events.

REFERENCES

1. Assis, M. S., "HF tactical communication in the Amazon region," *International Conference on Communication Systems (ICCS)*, Singapore, 1990.
2. Assis, M. S. and R. C. Pinto Filho, "Measurements of the electrical characteristics of vegetation in a dense jungle," *European Conference on Antennas and Propagation (EUCAP)*, Barcelona, Spain, 2010.
3. Assis, M. S., "Ground-to-air propagation in a dense jungle," *International Symposium on Antennas and Propagation (ISAP)*, Macao, China, 2010.
4. Assis, M. S., "Diurnal variation in a long distance VHF tropospheric path in the brazilian amazon region," *International Symposium on Antennas, Propagation, and EM Theory (ISAPE)*, Guangzhou, China, 2010.

5. Timothy, K. I., N. C. Mondal, and S. K. Sarkar, "Dynamical properties of rainfall for performance assessment of earth/space communication links at Ku and Ka bands," *International Journal of Satellite Communications*, No. 16, 53–57, 1998.
6. Cerqueira, J. L. and M. S. Assis, "Rainfall rate duration study for performance assessment of satellite communication links," (Abstract), *Asia-Pacific Radio Science Conference (AP-RASC'10)*, Toyama, Japan, 2010.
7. ITU-R, "Dynamic statistics of slant path attenuation in Brazil," WP 3J, Doc. 3J/75, Geneva, October 2004.

Negative Power Law Attenuation Estimation for Rainy Earth-Space Radio Links

P. O. Akuon and T. J. O. Afullo
School of Electrical, Electronic and Computer Engineering
University of Kwa-Zulu Natal (UKZN), Durban 4041, South Africa

Abstract— A model is proposed to estimate the non-uniformity of attenuation along a rainy satellite path. The growth of rain attenuation is described by a power law model that is derived from rain cell diameter distribution (RCDD). The RCDD is determined from 1-minute integration time point rain rate data. To validate the proposed factor, the method of moments is used to evaluate the fractional area occupied by rain cells. Consequently, by the use of the given attenuation prediction equation, the expected attenuation values at 0.01% of the time for 15 satellite links situated in tropical sites are obtained. The sampled links have varying elevation angles, frequencies and they experience different rainfall types. This procedure is repeated for other two models used in attenuation prediction for satellite links: the ITU-R P.618-9 and Bryant et al. models. Comparison tests are then carried out using the RMS test variable, and the proposed model results in the lowest RMS value for the sites.

1. INTRODUCTION

Higher frequency bands are desirable for Earth-Space communication systems because they provide higher bandwidths. However, these bands experience undesired signal degradation through propagation impairments. The worst contribution comes from the effects of rainfall [1–3]. To date, many rain attenuation approaches have been suggested to model the effect of rainfall in the propagation path. In all the methods, the specific attenuation is derived physically from the rain drop size distribution modelling [3, 4]. Some models assume a uniform rainfall rate effect while other attempts include modelling rain in the form of various rain cell shapes [5–8]. Other rain models are based on "Synthetic Storm" technique [9–11]. However, accuracy of the models needs to be increased especially for tropical regions. In this attempt, we model the non-uniformity in rain-induced attenuation to follow the decay in rain cell diameter distribution.

The population of individual drop sizes vary for each rain rate [4]. In the same way, a rain event consists of different rain rate thresholds (or rain cells). We postulate that given equal rain drop sizes, the continuity in attenuation due to high packing density of rain drops along a path will be more prominent than sparsely populated rain drops. This way we define specific attenuation as the contribution of attenuation on a given signal by a given rain rate where the rain rate is dependent on the drop-size distribution, thus specific attenuation increases with rain rate.

Conversely, we propose that there is more growth in attenuation along the path by densely populated cells than sparsely populated ones. The basic assumption is that rain-drops with smaller diameters (majority form low rain rates) as they propagate along a path coalesce more closely than larger drop sizes (majority form high rain rates). Thus, the path reduction factor within a rain cell for low rain rates is higher than that of higher rain rates which are characterized by sparsely distributed rain drops. The problem is how to resolve this difficulty.

Therefore, the objective of this paper is to evaluate the hypothesis that the decay in rain cell diameter distribution, RCDD represents the same decay in path reduction factor experienced by the radio signal intersecting through densely populated rain drops to less populated rain drops. This is done by developing a slant path attenuation analysis and applying the mathematical results in predicting measured data from various sites.

2. DEVELOPING RAIN CELL DIAMETER DISTRIBUTION, RCDD

Today, the diameter distributions of rain cells have been modelled by many authors with circular shape assumption for the rain cells. However, most analyses have been based on rain field measurements from radar observations in [12–14]. Here, the model is processed from probability distribution function, PDF of rain cells in Durban, South Africa. The measurements are obtained from 2-year rainfall rate data collected from disdrometer that computes the rain rate values after every minute. The details of these rainfall rate measurements and the development of the rain cell sizes have been published elsewhere [15, 16].

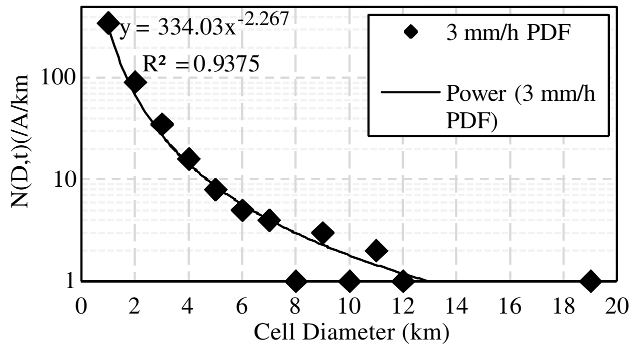

Figure 1: Measured RCDD plot for Durban, South Africa.

The equivalent rain rate-dependent rain cell size was developed by the use of "Synthetic Storm" technique and the model is described by $D = 51R^{-0.46}$. The assumptions of velocity of rainfall movements for stratiform and convective structures were catered for. Since numerous rain cells occur for lower rain rates that are likely to skew the data, only rain cells of 3 mm/h and above are considered in this work. Consequently, all the cells with equal diameters are grouped together and the PDF is then produced. Fig. 1 represents the plot of the rain cell diameter distribution. From the analysis, there are 518 rain cells within 1 km in diameter and only a single cell is seen to extend up to 19 km. The plot consists of all the cells from a rain rate threshold value of 3 mm/h and above. We observe that the population of rain cells decays from those cells with small diameters to those cells with larger diameters.

2.1. Power Law Model of Distribution

The general power law model is expressed as [17, 18]:

$$N(D, R_\tau) = N_0(R_\tau) D^{-\lambda(R_\tau)} \tag{1}$$

where D is the equivalent rain cell diameter bound by a given rain rate threshold, R_τ, $N(D, R_\tau)$ is the total number of cells having a diameter D per unit area of observation, A (km^2), $N_0(R_\tau)$ is considered as the intercept parameter and λ is the slope factor of the distribution.

The raw moment functions of the power law expressions are given in (2) and (3):

$$m_n(R_\tau) = N_0(R_\tau) \int_0^\infty D^n D^{-\lambda(R_\tau)} dD \tag{2}$$

$$= \frac{N_0(R_\tau)}{n - \lambda + 1} \left[D_{\max}^{n-\lambda+1} - D_{\min}^{n-\lambda+1} \right] \tag{3}$$

where n $(= 1, 2, 3 \ldots)$ depicts the moment value.

The fractal area that can possibly be measured by the point rain rate equipment is analyzed through statistical evaluation. The fractal area is defined as the total region covered by all cells that pass through the point rain rate equipment. For circular assumption of rain cells, this area has a value in length (F_D) that is twice the maximum rain cell diameter, D_m. This means that the largest rain cell with its edge radially D_m km away from the equipment will be detected.

The fractal area, F_A occupied by the cells (km^2) can be found from (4) while the fractal length is given by (5):

$$F_A = \frac{\pi}{4} \int_0^\infty D^2 \cdot N(D, R_\tau) dD = \frac{\pi}{4} m_2 \tag{4}$$

$$F_D = \sqrt{\int_0^\infty D^2 \cdot N(D, R_\tau) dD} = \sqrt{m_2} \tag{5}$$

From the measurement fitting in Fig. 1, the slope power factor is found to be $\lambda = -2.267$ with correlation coefficient, $R^2 = 0.9375$. The next step is to estimate the maximum fractal area of rain cells that can be captured by the disdrometer in order to test the exactness of the proposed factor. We therefore use the raw moment functions described in (4) and (5) and the results are listed in Table 1.

Table 1: Error analysis in the prediction of the fractal cell area.

Parameter	Value
λ	2.267
D_m	30.16
F_A	2740.208
F_D	59.0648
$e_m(\%)$	1.2639

The percentage error, e_m in predicting the fractal area or simply the fractal diameter by the use of power law is computed by:

$$e_m = \frac{|F_{Dp}/2 - D_m|}{D_m} * 100 \tag{6}$$

where F_{Dp} is the value of the predicted length and D_m is the expected value. D_m is computed from $D = 51R^{-0.46}$ when $R = 3\,\mathrm{mm/h}$.

From the error analysis, the slope factor underestimates the measured diameter only by a small margin of 1.2639%. From rainfall studies around the world [17, 18], the value of λ is found to vary from -1.91 to -2.51. The proposed power factor falls within this range and is applied in the next section to estimate the slant path reduction factor and the effective slant path length.

3. SLANT PATH ANALYSIS

Some tropical regions that experience high rainfall rates have been shown to have rain heights that increase with rain rates up to about 10 km as suggested by [19] among others. This implies that the cumulative distribution of rain rate alone is not sufficient to estimate the attenuation; knowledge of rainfall distribution beyond the 0°C isotherm height is also vital. Bryant et al. through empirical analysis deduced a formula for the rain height that increases as the rain rate increases. A relationship for the change in value for the rain freezing height at high rain rates in tropical regions was deduced to be of the form [19]:

$$H_{fr} = 4.5 + 0.0005R^{1.65} \tag{7}$$

The effects of the melting layer and the changing rain height are accounted for in this discussion by the use of rain height model proposed by Bryant et al..

3.1. Path Reduction Factor

With the onset of a rainfall event, a rain cell is set up whose contribution leads to attenuation. As the rain rates change due to the changes is the rain drop sizes, attenuation along a path is proposed to decay due to the changes in packing density or simply the path reduction factor reduces. At the same time, the specific attenuation per rain rate increases. This decaying growth (ς) in path reduction factor in the cell can therefore be estimated by:

$$\varsigma = 1 + R^{-\frac{1}{\lambda}} \tag{8}$$

where 1 represents the existence of the rain cell, $R \geq R_{0.01}$ is the rain rate (mm/h) and λ is the decay factor.

It has been established that rain varies in its vertical structure. Also, in tropical sites, there is a break point in rain rate profiles where an abrupt increase occurs in measured attenuation [19]. It is further suggested that there exist multiple rain cell structures that occur at the break-point which contribute to these changes in attenuation. We therefore modify the expression in (8) to include this multiplicity of rain cells above the break point, thus:

$$\varsigma_{0.01} = 1 + nR^{-\frac{1}{\lambda}} \tag{9}$$

where $n \geq 2$ is the number of rain cells after the break point in a given tropical site.

Another observation indicates that in tropical zones, rain attenuation increases with higher elevation angles at high rain rates due to the changing rain height. To cater for this, we introduce a factor in the growth of the second cell structure (after the break point) to compensate for this variation. The growth is modified by the sine of the elevation angle to account for the vertical variability in the second rain cell with respect to the path inclination as the second cell develops from the frozen precipitation (this is a logical approach). Thus:

$$\varsigma_{0.01} = 1 + nR^{-\frac{1}{\lambda \sin\theta}}; \quad \lambda = 2.267 \tag{10}$$

where R is the rainfall rate (mm/h) and θ is the link elevation angle

The slant path attenuation at any given rain rate is the product of the specific attenuation (dB/km) and the effective path length, L_e (the rain cell growth factor and the mean intercepted length). From our earlier work, the path parameters were derived and used to produce rain-induced attenuation equation. These parameters include the size of the rain cell, the ellipsoidal signal path, the mean intercept of path through rain and the effects of elevation angle. The set of equations are described as [16, 20]:

$$A = \left(\gamma \frac{rL_G}{\cos\theta}\right) \tag{11a}$$

$$A = \left(\gamma \frac{L_G}{\cos\theta}\right) \varsigma \frac{2}{\pi}\left(1 + \frac{1.047}{\bar{\xi}_\theta}\right)\left(\frac{1}{\bar{\xi}_\theta L_G/D + 1}\right) \tag{11b}$$

$$\bar{\xi} = 1/\eta; \quad \eta = 1.0175 - 0.0029\theta - 0.0001\theta^2 \tag{12}$$

where A (dB) denotes the attenuation, γ is the specific attenuation (dB/km), D (km) is the diameter of the rain cell which is a function of rain rate, L_G (km) is the horizontally projected path length and θ, the elevation angle. $\bar{\xi}_\theta$ is the elevation coefficient, and ς is the factor of growth in rain attenuation within the cell.

By definition of the path reduction factor by ITU-R [2], the overall slant path reduction factor, $r_{0.01}$ is deduced from (11b) as:

$$r_{0.01} = \varsigma_{0.01} \frac{2}{\pi}\left(1 + \frac{1.047}{\bar{\xi}_\theta}\right)\left(\frac{1}{\bar{\xi}_\theta L_G/D + 1}\right) \tag{13}$$

4. RESULTS AND DISCUSSIONS

The sampled satellite links are situated in equatorial sites which include: Lae (Papua New Guinea) [19], Nigeria [21], Bangkok and Indonesia [22]. Nairobi (Kenya) [23], Suva (Fiji) [24], Bangladesh [25], Spinno d'Adda in Italy [19, 26], Rio de Jeneiro and Belem in Brazil [27], USM [28] and Johor Bahru

Table 2: Link parameter used in the calculations.

Station	Frequency (GHz)	Pol.	Elevation angle (°)	$R_{0.01}$ (mm/h)	α	β
Malaysia, UTM-Johor [29]	12.594	V	70	125	0.028605	1.10585
Malaysia, USM [28]	12.255	V	40.1	130	0.02455	1.1216
Lae, PNG [19]	12.749	V	72.8	110	0.03063	1.12000
Suva, Fiji [24]	11.61	C	68.7	63	0.02093	1.14165
Surabaya [19]	11.2	C	20.2	120	0.01752	1.18820
Bangkok [22]	12.75	V	54.8	137	0.0300	1.12000
Nairobi [23]	11.6	C	56.9	75	0.02093	1.14165
Indonesia [22]	12.32	V	64.7	125	0.02455	1.1216
Nigeria [21]	11.6	C	48.3	135	0.02093	1.14165
Spinno d'Adda [19, 26]	39.6	C	37.7	38	0.3304	0.9346
	18.7	V	37.7	38	0.05978	1.08221
Bangladesh [25]	12	V	61.8	132	0.0168	1.1218
	20	V	61.8	132	0.0691	1.065
Brazil Rio de Jeneiro Belem [27]	11.452	C	62.8	80	0.02093	1.17602
	11.452	C	89	125	0.02093	1.17602

(Malaysia) [29]. Though, Italy is sub-tropical, the Spinno d'Adda site is included to test the high frequency used of 39.6 GHz. The frequencies used in these sites range from 11 GHz to 40 GHz with elevation angles being between 20.2° in Surabaya and 89° in Belem, Brazil. The link parameters listed in Table 2 are used to compute attenuation at 0.01% of the time, $A_{0.01}$. Where unavailable, the break point rain rate is assumed to be the same as $R_{0.01}$ mm/h [19]. The three models ITU-R P.618, Bryant et al. model and the proposed model are then used to compute $A_{0.01}$ and the results are shown in Table 3. The ITU-R model was applied using the height model in (7) of Bryant et al. for uniformity and improvements in the results. The multiplicity of cells is noted in high rainfall areas like in Indonesia and Johor, Malaysia where $n = 5$ in (10) is used. The performance of the proposed model where low elevation angles are used like in Surabaya (20.2°) and USM, Malaysia (40.1°) is quite good whereas in sites with higher elevation angles, all the three models give good estimations for attenuation.

5. ERROR ESTIMATIONS

Some sites whose polarizations were not obtained were assumed to be circular or vertical. This assumption and the interpolations made to determine the coefficients for the different frequencies may introduce some errors. The values of the rain rates at 0.01% of time $R_{0.01}$ were adopted from the ITU-R maps [30] while others were available from measured statistics. The station height above the sea level was assumed to be minimal in all the sites. ITU-R P.311-13 [31] stipulates the error analysis method used to determine the percentage errors in the prediction results. It also stipulates that the best model has the lowest standard deviation and RMS for the points analyzed. The error results from the measured attenuation for all the three models are given in Table 4. From the mean error values for all the 15 sites, the proposed model overestimates the measured values by

Table 3: Measured and calculated attenuation values at 0.01% of the time.

<table>
<tr><th>Station</th><th>$A_{0.01}$ (dB) Measured</th><th>$A_{0.01}$ Proposed Model (dB)</th><th>$A_{0.01}$ ITU-R Model (dB)</th><th>$A_{0.01}$ Bryant et al. Model</th></tr>
<tr><td>Malaysia, UTM-Johor [29]</td><td>25</td><td>22.393</td><td>17.053</td><td>17.702</td></tr>
<tr><td>Malaysia, USM [28]</td><td>23.5</td><td>22.717</td><td>19.696</td><td>18.66</td></tr>
<tr><td>Lae, PNG [19]</td><td>17.1</td><td>16.958</td><td>16.758</td><td>17.34</td></tr>
<tr><td>Suva, Fiji [24]</td><td>9.7</td><td>10.205</td><td>8.636</td><td>7.93</td></tr>
<tr><td>Surabaya [19]</td><td>28.5</td><td>27.00</td><td>28.12</td><td>15.86</td></tr>
<tr><td>Bangkok [22]</td><td>23.4</td><td>25.02</td><td>20.78</td><td>22.98</td></tr>
<tr><td>Nairobi [23]</td><td>8.1</td><td>10.737</td><td>10.89</td><td>9.41</td></tr>
<tr><td>Indonesia [22]</td><td>21.9</td><td>20.822</td><td>17.15</td><td>16.74</td></tr>
<tr><td>Nigeria [21]</td><td>20.8</td><td>20.45</td><td>17.49</td><td>18.41</td></tr>
<tr><td rowspan="2">Spinno d'Adda [19, 26]</td><td>37.2</td><td>43.37</td><td>51.047</td><td>38.67</td></tr>
<tr><td>14.4</td><td>16.75</td><td>14.63</td><td>11.97</td></tr>
<tr><td>Bangladesh [25]</td><td>13.8</td><td>12.59</td><td>11.3</td><td>12.96</td></tr>
<tr><td></td><td>39.2</td><td>39.26</td><td>32.3</td><td>40.4</td></tr>
<tr><td rowspan="2">Brazil Rio de Jeneiro Belem [27]</td><td>13.1</td><td>12.40</td><td>10.905</td><td>12.109</td></tr>
<tr><td>20.1</td><td>17.90</td><td>18.30</td><td>17.387</td></tr>
</table>

Table 4: Error tests for the models.

Parameters	Models	Percentage of time (0.01%)
μ_{ei}	Proposed Model	8.33
	ITU-R Model	−14.52
	Bryant et al. Model	−15.72
σ_{ei}	Proposed Model	7.96
	ITU-R Model	10.00
	Bryant et al. Model	12.47
δ_{ei}	Proposed Model	0.6
	ITU-R Model	10.52
	Bryant et al. Model	9.58

8.33%, however the ITU-R model results in an underestimation with 14.52% in error followed by the Bryant et al. model with 15.72% in error. The standard deviations for the error distribution are 7.96, 10 and 12.47 respectively. The proposed model has the least RMS error of 0.6 for the sites sampled for this study.

6. CONCLUSION

The assumption of rain-induced attenuation statistics along a path to take the form of rain cell size distribution for all rain rates within a cell is validated by the proposed model with minimal error. This is achieved by using the proposed attenuation model to estimate the expected attenuation levels from the sites. However, the occurrence of rainfall event is random in form and therefore more stochastic methods can be applied to reduce the error encountered in the current approach. Other forms of mathematical estimation of the rain cell distribution may also be used to estimate the attenuation decay factor along satellite path links and the results compared with the current form so as to obtain the best model. Also, the current rain cell diameter was generated from point rainfall measurements; further analogy with spatial information from RADAR data on rain fields will give a better conclusion. Nevertheless, the postulation that path attenuation follows the decay in rain cell diameter distribution has been proved to be accurate. The model takes into account the break point at the melting layer, multiplicity of cells and the increase of attenuation with elevation angles at high rain rates as observed in tropical sites.

REFERENCES

1. Crane, R. K., *Electromagnetic Wave Propagation through Rain*, Wiley, New York, 1996.
2. International Telecommunications Union, "Propagation data and prediction methods required for the design of earth-space telecommunication systems," Recommendation. P.618-9, ITU-R Recommendation, 2007.
3. International Telecommunications Union, "Specific attenuation model for rain for use in prediction models," Recommendation P. 838-5, ITU-R Recommendation, 2005.
4. Afullo, T. J. O., "Raindrop size distribution modeling for radio link design along the eastern coast of South Africa," *Progress In Electromagnetics Research B*, Vol. 34, 345–366, 2011.
5. Capsoni, C., F. Fedi, C. Magistroni, A. Paraboni, and A. Pawlina, "Data and theory for a new model of the horizontal structure of rain cells for propagation applications," *Radio Science*, Vol. 22, No. 3, 395–404, 1987.
6. Féral, L., F. Mesnard, H. Sauvageot, L. Castanet, and J. Lemorton, "Rain cells shape and orientation distribution in south-west of France," *Phys. Chem. Earth (B)*, Vol. 25, No. 10–12, 1073–1078, 2000.
7. Paraboni, A., G. Masini, and C. Riva, "The spatial structure of rain and its impact on the design of advanced TLC systems," *Proc. Fourth Ka Band Utilization Conf.*, 169–172, Venice, Italy, Nov. 2–4, 1998.
8. Assis Mauro, S., L. A. R. da Silva Mello, and J. L. Cerqueira, "Rain attenuation research in Brazil," URSI GA, 2005.
9. Fontan, F. P., A. Nunez, A. Valcare, and U. C. Fiebig, "Converting simulated rain-rate series into attenuation series using the synthetic storm technique," *Propagation Impairment Mitigation for Millimetre Wave Radio Systems, COST Action*, 280, Jun. 2005.
10. Kanellopoulos, D. and P. Kafetzis, "Comparison of the synthetic Storm technique with a conventional rain attenuation prediction model," *IEEE Transaction on Antennas and Propagation*, Vol. 34, 713–715, 1985.
11. Matricciani, E. and C. Riva, "Concurrency of rain rate attenuation statistics in slant paths: Test with the synthetic storm technique," *EuCAP 2007*, Edinburgh, Nov. 11–16, 2007.
12. Dennis, A. S. and F. G. Fernald, "Frequency distributions of shower sizes," *J. Appl. Meteor.*, Vol. 2, 767–769, 1963.
13. Konrad, T. G., "Statistical models of summer rain showers derived from fine-scale radar observations," *J. Appl. Meteor.*, Vol. 17, 171–188, 1978.
14. Tenório, R. S., H. Sauvageot, and S. Ramos-Buarque, "Statistical studies of rain cell size distribution using radar data during squall line episodes in West Africa," *Proc. Third Int. Symp. on Hydrological Applications of Weather Radar*, 518–526, Sao Paulo, Brazil, 1995.

15. Akuon, P. O. and T. J. O. Afullo, "Rain cell size statistics from rain gauge data for site diversity planning and attenuation prediction," *Proceedings of Southern Africa Telecommunication Networks and Applications Conference (SATNAC)*, 213–216, East London, South Africa, Sep. 4–7, 2011, ISBN: 978-0-620-50893-3.
16. Akuon, P. O. and T. J. O. Afullo, "Rain cell sizing for the design of high capacity radio link systems in South Africa," *Progress In Electromagnetics Research B*, Vol. 35, 263–285, 2011.
17. Kuo, K. S., R. M. Welch, and S. K. Sengupta, "Structural and textural characteristics of cirrus clouds observed using high spatial resolution LANDSAT imagery," *J. Appl. Meteor.*, Vol. 27, 1242–1260, 1988.
18. Machado, L. A. T. and W. B. Rossow, "Structural characteristics and irradiative properties of tropical cloud clusters," *Mon. Wea. Rev.*, Vol. 121, 3234–3260, 1993.
19. Bryant, G. H., I. Adimula, C. Riva, and G. Brussard, "Rain attenuation statistics from rain column diameters and heights," *International Journal of Satellite Communications*, Vol. 19, No. 3, 263–283, 2001.
20. Akuon, P. O. and T. J. O. Afullo, "Path reduction factor modeling for terrestrial links based on rain cell growth," *Proceedings of IEEE Africon 2011 Conference*, Livingstone, Zambia, Sep. 12–15, 2011, ISBN:978-1-61284-991-1.
21. McCarthy, D. K., J. E. Allnutt, W. Salazar, E. C. Omeata, B. R. Owolabi, T. Oladiran, G. O. Ajayi, T. I. Raj, and C. Zaks, "Results of 11.6 GHz radiometric experiment in Nigeria," *Electronics Letters*, Vol. 28, No. 3, 316–317, 1992.
22. Igarashi, K., H. Minakoshi, S. Watari, M. Kawamura, T. Ojima, N. Hemmakorn, A. Sang-in, W. Srisupasitanon, U. Sastrokusmo, S. I. S. Hassan, R. Reyes, K. Maitava, M. Sasaki, T. Minode, and Y. Yoshimura, "Satellite signal propagation experiments in the equatorial region and a development of satellite communication network in Asian pacific region," *Forum on the Results of the POST-PARTNERS Experiments*, Tokyo, Japan, 2002.
23. McCarthy, D. K., J. E. Allnutt, W. E. Salazar, W. Sitati, M. Okoth, J. Mutungi, C. D. Odhiambo, and C. Zarks, "Results of 11.6 GHz radiometric experiment in Kenya," *Electronics Letters*, Vol. 28, No. 3, 316–317, 1992.
24. Kumar, V. and V. Ramachandran, "Rain attenuation measurement at 11.6 GHz in Suva Fiji," *Electronics Letters*, Vol. 40, No. 22, 1429–1431, 2004.
25. Islam, M. R , M. A. Rahman, F. Anwar, and M. M. Rashid, "Performance investigation of earth-to-satellite microwave link due to rain fade in Bangladesh," *Computer and Information Technology, ICCIT 2008, 11th International Conference*, 773–778, 2008.
26. Paraboni, A., C. Riva, C. Capsoni, G. Codispoti, L. Zuliani, et al., "Propagation and Radar measurements performed in Spinno d'Adda and the Italian planning for the Alphasat TDP5 scientific experiment," *Proceedings of the Institute of Electrical and Electronic, Antennas and Propagation*, Berlin EuCAP, 911–915, 2009.
27. Couto de Miranda, E., M. S. Pontes, and M. L. A. R da Silva, "Rainfall induced satellite beacon attenuation on three 12 GHz links in equatorial and tropical Brazil," *IEEE Ant. & Propagation Society International Symposium*, Vol. 4, 1892–1895, 1998.
28. Mandeep, J. S. and J. E. Allnut, "Rain attenuation predictions at KU-band in south east Asia," *Progress In Electromagnetics Research*, Vol. 76, 65–74, 2007.
29. Abdulrahman, A. Y., T. A. Rahman, A. S. K. Rahim, and M. R. Ul Islam, "A new rain attenuation conversion technique for tropical regions," *Progress In Electromagnetic Research B*, Vol. 26, 53–67, 2010.
30. International Telecommunications Union, "Characteristics of precipitation for propagation modeling," *Recommendation*, ITU-R P.837-5, ITU-R P Sers., 2007.
31. International Telecommunications Union, "Acquisition, presentation and analysis of data in studies of tropospheric propagation," *Recommendation*, ITU-R P.311-13, ITU-R P Sers., Oct. 2009.

A Simple Forwarding Technique for Two-way Relay Channels

Md Anisul Karim[1,2], **Jinhong Yuan**[1], **Jun Li**[1], **and Zhuo Chen**[2]

[1]Wireless Communications Laboratory (WCL)
School of Electrical Engineering and Telecommunications
The University of New South Wales, NSW 2052, Australia
[2]Wireless and Networking Technologies Laboratory
CSIRO ICT Center, Marsfield, NSW 2122, Australia

Abstract— In this paper, we focus on soft forwarding schemes for two-way relay channels (TWRC). In specific, we propose a new soft information forwarding (SIF) scheme for TWRC, referred to as mutual information based forwarding with network coding (MIF-NC). In MIF-NC, the relay broadcasts the MIF based soft information to the sources using network coding. Simulation results reveal that when both the source-relay (S-R) channels are symmetric, the proposed MIF-NC scheme yields about 0.4–0.7 dB signal-to-noise ratio (SNR) gains compared to the existing schemes such as amplify-forward with network coding (AF-NC) and soft bit forwarding with network coding (SBF-NC). All these results are verified by the simulation.

1. INTRODUCTION

Recently a new class of relay protocol based on soft information forwarding (SIF) from relay has been emerged as efficient and effective one. Among the SIF schemes studied for one way relay channels (OWRC), in [1], a soft forwarding method, namely estimate-forward (EF), has been proposed for memoryless relay networks. It is shown that EF maximizes the generalized signal-to-noise ratio (GSNR) at the destination. A BER optimal solution for the scenario with one relay and no link between source and destination is described in [2]. The approach, however, does not generalize to more than one relay.

Recently a novel soft forwarding technique based on symbol-wise mutual information, referred to as mutual information based forwarding (MIF), has been proposed for parallel relay networks in AWGN channels [3, 4]. In MIF scheme, each relay node calculates the log-likelihood ratio (LLR) and a corresponding symbol-wise mutual information (SMI) [5] of the received symbols. The sign of the soft decision is determined by the sign of LLR values, and the SMI conditioned on the absolute value of the LLR is used as a reliability measure in generating the soft forwarding symbols. It was shown in [3] that MIF scheme achieves the superior bit error rate (BER) performance compared with other memoryless soft forwarding schemes.

In this paper, we consider a two-way relay channel (TWRC), first introduced by Shannon in 1961 [6]. Recently, the TWRC has gained renewed attention from both academia and industry [7–12] due to its promising application to contemporary wireless systems. Here, we focus on a memoryless TWRC where two source nodes, S_1 and S_2, communicate with each other with the assistance of an intermediate relay node. The data exchange between two source nodes can be accomplished with a three-phase communication protocol, in which the relay node R is allowed to perform algebraic operations on the data received from node S_1 and S_2, and broadcast those packets to S_1 and S_2, simultaneously. In this paper, the algebraic operation involves modulo-2 or XOR of the packets received from S_1 and S_2, we term it as *network coding (NC)*.

Related soft forwarding techniques in TWRC have been reported in [13–15]. A soft network coding has been proposed, namely, AF-NC in [13, **?**], where relay forwards a scaled version of the LLR of the network coded bits to the two source nodes. In [15], another method of soft network coding, namely soft bit forwarding (SBF) has been proposed for TWRC, where a minimum mean square error (MMSE) estimation of the XOR-ed bit is broadcasted to the two source nodes.

In this paper, we consider a symmetric TWRC, where both the source-relay (S-R) links have similar path loss coefficients. We propose a MIF based soft forwarding technique for TWRC using network coding. The proposed MIF technique is shown to outperform the SBF and AF-NC schemes by 0.4 and 0.7 dB signal-to-noise ratio (SNR) gains, respectively.

An outline of the remainder of this paper is as follows. In Section 2, we present the system model. In Section 3, calculation of soft information for TWRC is given. Numerical results and discussions are provided in Section 4. Some concluding remarks are presented in Section 5.

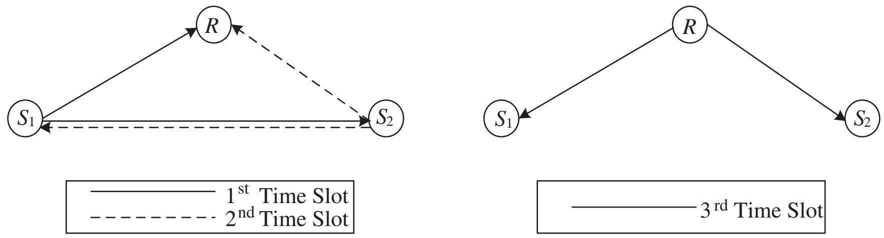

Figure 1: A two-way relay network.

2. SYSTEM MODEL

We consider a TWRC as shown in Fig. 1, where a relay R is located in between the two sources, namely S_1 and S_2. The relay node R assists S_1 and S_2 to exchange their information. We assume that all the three nodes operate in half duplex mode, i.e., each node can either transmits or receives at a particular time. The total transmission period is divided into two phases, namely, orthogonal phase and the broadcast phase.

2.1. Orthogonal Phase

In this phase, each source transmits its respective information to the relay and to the other source through orthogonal channels. In the first time slot, the source node S_1 sends its information to the source node S_2 and to the relay node R. In the second time slot, the source node S_2 sends its information to the source node S_1 and to the relay node R. The received symbols at the both sources and at the relay can be expressed as

$$\begin{aligned} r_{S_iR} &= \sqrt{P_S} h_{S_iR} x_{S_i} + n_{S_iR}, &(1)\\ r_{S_iS_j} &= \sqrt{P_S} h_{S_iS_j} x_{S_i} + n_{S_iS_j}, &(2) \end{aligned}$$

where r_{S_iR} and $r_{S_iS_j}$ are the received symbols at the relay from S_i, and the received symbols at S_j from S_i, respectively, for $i, j \in \{1, 2\}, i \neq j$. h_{S_iR} and $h_{S_iS_j}$ denote the path loss coefficients between each source to the relay, and one source to other, respectively, P_S denotes the transmitted symbol energy, and x_{S_i} are the information symbols transmitted by S_i. n_{S_iR} and $n_{S_iS_j}$, are complex additive white Gaussian noise (AWGN), with variance $\sigma_n^2 = N_0/2$ per dimension, for the S-R links and the inter-source links, respectively. We assume that the binary information streams at the sources are mapped into BPSK symbols, $x_{S_i} \in \{\pm 1\}$.

2.2. Broadcast Phase

In this phase, the relay broadcasts the soft information of the network coded symbols of the received symbols from two sources to the both source nodes. Next, we will derive soft information of network coded symbols for two soft forwarding techniques, namely, soft bit forwarding (SBF) and mutual information based forwarding (MIF) schemes.

3. CALCULATION OF SOFT INFORMATION WITH NETWORK CODING

3.1. Soft Bit Forwarding (SBF-NC)

The soft information in TWRC for SBF scheme with network coding can be calculated as [15]

$$\begin{aligned} \tilde{x}_{\mathrm{SBF-NC}} &= E[x_{\oplus} | r_{S_1R} r_{S_2R}] \\ &= E[x_{S_1} x_{S_2} | r_{S_1R} r_{S_2R}] \\ &= E[x_{S_1} | r_{S_1R}] E[x_{S_2} | r_{S_2R}] \\ &= \tanh\left(\frac{l_{S_1R}}{2}\right) \tanh\left(\frac{l_{S_2R}}{2}\right), \qquad (3) \end{aligned}$$

where $x_{\oplus} = x_{S_1} \oplus x_{S_2}$, the symbol $\oplus$ denotes the modulo-2 operator, and l_{S_iR} denotes the log-likelihood ratio (LLR) of the received symbols at the relay in first two orthogonal time slots which is given by

$$l_{S_iR} = \log \frac{p(r_{S_iR} | x_{S_i} = 1, h_{S_iR})}{p(r_{S_iR} | x_{S_i} = -1, h_{S_iR})}. \qquad (4)$$

In the broadcast stage, the received symbols at the source node S_i is given by

$$r_{RS_i,\text{SBF-NC}} = \beta_{\text{SBF-NC}} h_{RS_i} \tilde{x}_{\text{SBF-NC}} + n_{RS_i}, \tag{5}$$

where P_R denotes the relay symbol energy, $\beta_{\text{SBF-NC}} = \sqrt{\frac{P_R}{E[(\tilde{x}_{\text{SBF-NC}})^2]}}$ is the normalization factor, h_{RS_i} are the path loss coefficients between relay to source links, and n_{S_iR}, is the complex AWGN, with variance $\sigma_n^2 = N_0/2$ per dimension, for the R-S_i links.

3.2. Mutual Information Based Soft Forwarding (MIF-NC)

The soft information in MIF scheme consists of the hard decisions of the symbol estimates and a reliability measure. The reliability measure is determined by SMI computed from the absolute value of the LLR at the relay. The LLR of network coded symbols $x_\oplus$, denoted by $l_{x_{S_1} \oplus x_{S_2}}$, can be computed as

$$l_{x_{S_1} \oplus x_{S_2}} = \log \frac{1 + e^{l_{S_1R} l_{S_2R}}}{e^{l_{S_1R}} + e^{l_{S_2R}}}. \tag{6}$$

The symbol-wise mutual information (SMI) between $X_\oplus$ and its corresponding LLR $L_{x_{S_1} \oplus x_{S_2}}$ conditioned on $\lambda_{x_{S_1} \oplus x_{S_2}} \triangleq |L_{x_{S_1} \oplus x_{S_2}}|$ can be computed as

$$\begin{aligned} \Theta(\lambda_{x_{S_1} \oplus x_{S_2}}) &= I(X_\oplus; L_{x_{S_1} \oplus x_{S_2}} | \lambda_{x_{S_1} \oplus x_{S_2}}) \\ &= \sum_{l_{x_{S_1} \oplus x_{S_2}} = \pm \lambda_{x_{S_1} \oplus x_{S_2}}} p(l_{x_{S_1} \oplus x_{S_2}} | \lambda_{x_{S_1} \oplus x_{S_2}}) I(X_\oplus; l_{x_{S_1} \oplus x_{S_2}} | \lambda_{x_{S_1} \oplus x_{S_2}}) \\ &= \frac{1}{1 + e^{\lambda_{x_{S_1} \oplus x_{S_2}}}} \log_2 \frac{2}{1 + e^{\lambda_{x_{S_1} \oplus x_{S_2}}}} + \frac{1}{1 + e^{-\lambda_{x_{S_1} \oplus x_{S_2}}}} \log_2 \frac{2}{1 + e^{-\lambda_{x_{S_1} \oplus x_{S_2}}}}, \end{aligned} \tag{7}$$

where

$$p(x_\oplus | l_{x_{S_1} \oplus x_{S_2}}, \lambda_{x_{S_1} \oplus x_{S_2}}) = \frac{1}{1 + e^{-l_{x_{S_1} \oplus x_{S_2}} x_\oplus}}. \tag{8}$$

The network coded MIF based soft information can then be given by

$$\tilde{x}_{\text{MIF-NC}} = \text{sign}(l_{x_{S_1} \oplus x_{S_2}}) \Theta(\lambda_{x_{S_1} \oplus x_{S_2}}). \tag{9}$$

In the broadcast stage, the received symbols at S_i is given by

$$r_{RS_i,\text{MIF-NC}} = \beta_{\text{MIF-NC}} h_{RS_i} \tilde{x}_{\text{MIF-NC}} + n_{RS_i}, \tag{10}$$

where $\beta_{\text{MIF-NC}} = \sqrt{\frac{P_R}{E[(\tilde{x}_{\text{MIF-NC}})^2]}}$ is the normalization factor.

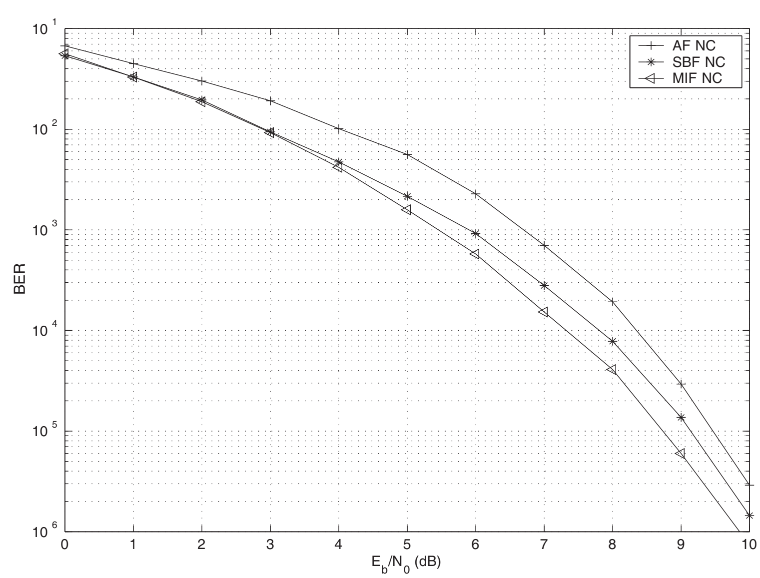

Figure 2: BER performance comparison for various soft forwarding schemes with network coding in TWRC.

4. NUMERICAL RESULTS AND DISCUSSION

In this section, we provide Monte Carlo simulation results to compare the proposed MIF schemes in TWRC with AF-NC and SBF-NC schemes for different transmit SNRs. We adopt BPSK modulation and set $P_S = P_R = 1$. The SNR is defined as

$$\frac{E_b}{N_0} = \frac{P_S}{2\sigma_n^2}. \tag{11}$$

Fig. 2 shows the BER performance versus SNR for various soft forwarding schemes in symmetric S-R channels with network coding, where we set $h_{S_1R} = h_{S_2R} = 1$. We can see that, MIF-NC achieves around 0.4 dB, and 0.7 dB SNR gain over AF-NC and SBF-NC, respectively. The improved BER performance of MIF-NC scheme is attributed to the MIF relay function that preserves reliability avoiding making hard decision at the relay.

5. CONCLUSION

This paper presented new mutual information based soft forwarding techniques for two-way relay channels. We focused symmetric source-relay channels. In particular, we proposed a new scheme, namely, MIF-NC. We found that MIF-NC scheme outperforms other existing techniques. These results were supported by simulations.

REFERENCES

1. Gomadam, K. S. and S. A. Jafar, "Optimal relay functionality for SNR maximization in memoryless relay networks," *IEEE J. Select. Areas Commun.*, Vol. 25, No. 2, 390–400, Feb. 2007.
2. Abou-Faycal, I. and M. Medard "Optimal uncoded regeneration for binary antipodal signaling," *Proc. IEEE ICC*, Paris, France, Jun. 2004.
3. Karim, M. A., T. Yang, J. Yuan, Z. Chen, and I. Land, "A novel soft forwarding technique for memoryless relay channels based on symbol-wise mutual information," *IEEE Commun. Lett.*, Vol. 14, No. 10, 927–929, Oct. 2010.
4. Karim, M. A., J. Yuan, J. Li, and Z. Chen, "Performance analysis of mutual information based soft forwarding relay network," *Proc. IEEE Global Communications Conference*, Texas, USA, Dec. 2011.
5. Land, I., P. A. Hoeher, and S. Gligorevic, "Computation of symbol-wise mutual information in transmission systems with LogAPP decoders and application to EXIT charts," *Proc. 5th ITG Conf. on Source and Channel Coding*, Jan. 2004.
6. Shannon, C. E., "Two-way communication channels," *Proc. 4th Berkeley Symp. Math. Stat. Prob.*, 611–644, 1961.
7. Larsson, P., N. Johansson, and K. E. Sunell, "Coded bi-directional relaying," *IEEE 63rd Vehicular Technology Conference, VTC 2006-Spring*, 851–855, May 2006.
8. Rankov, B. and A. Wittneben, "Achievable rate regions for the two-way relay channel," *Proc. of IEEE ISIT*, 1668–1672, Jul. 2006.
9. Rankov, B. and A. Wittneben, "Spectral efficient protocols for half-duplex fading relay channels," *IEEE J. Select. Areas Commun.*, Vol. 25, No. 2, 379–389, Feb. 2007.
10. Hausl, C. and J. Hagenauer, "Iterative network and channel decoding for the two-way relay channel," *Proc. of IEEE ICC*, 1568–1573, Jun. 2006.
11. Zhang, S., S. C. Liew, and P. P. Lam, "Hot topic: Physical-layer network coding," *Proc. of ACM Mobicom*, 358–365, 2006.
12. Popovski, P. and H. Yomo, "Physical network coding in two-way wireless relay channels," *Proc. of IEEE ICC*, 707–712, Jun. 2007.
13. Zhang, S., Y. Zhu, S. C. Liew, and K. B. Letaief, "Joint design of network coding and channel decoding for wireless networks," *Proc. of WCNC*, Hong Kong, 2007.
14. Yang, S. and R. Koetter, "Network coding over a noisy relay: A belief propagation approach," *Proc. IEEE Int. Symp. Inf. Theory*, Nice, France, Jul. 24–29, 2007.
15. Zhang, S., Y. Zhu, and S. C. Liew, "Soft network coding in wireless two-way relay channels," *J. of Commun. and Networks*, Vol. 10, No. 4, 371–383, Dec. 2008.

BICM-ID for Relay System Allowing Intra-link Errors and a Similarity Constellation to ARQ Schemes

Meng Cheng[1], **Ade Irawan**[1], **Khoirul Anwar**[1], **and Tad Matsumoto**[1,2]

[1]Japan Advanced Institute of Science and Technology (JAIST), Japan
[2]Center for Wireless Communication (CWC), University of Oulu, Finland

Abstract— In this paper, we propose an accumulator-assisted (ACC) relay system with bit-interleaved coded modulation using iterative decoding (BICM-ID) technique and apply the network topology to an Automatic Repeat Request (ARQ) scheme. Our code design is based on the analysis of the extrinsic information transfer (EXIT) chart. The ACC enables the convergence tunnel of the EXIT curves opening until almost the (1, 1) point of the mutual information, which avoids the error floor. The most advantageous point of the proposed technique is that even though errors may happen in the intra-link (source-relay), they can be corrected at the destination by exploiting the correlation knowledge between the source and the relay nodes. This technique significantly reduces the complexity of the relay where the source bits are simply extracted, even though errors may occur due to the imperfect channel. The error rate of the intra-link can be estimated at the destination node by using the a-posteriori Log likelihood Ratios (LLRs) of the two decoders. Then, it can be further utilised in the iterative processing. Since the relay location directly influences the quality of the intra-link, we change the relay locations, and provide the analysis of the performances corresponding to different relay locations. The theoretical background of this technique is the Slepian-Wolf/Shannon theorem for correlated source coding. The simulation results show that the bit-error-rate (BER) performances of the proposed system are very close to theoretical limits supported by the Slepian-Wolf/Shannon theorem. In this paper, it is also shown that if the intra-link is error free, the topology of the relay network is equivalent to an ARQ scheme that exploits Shannon's random coding theorem by utilising an interleaver in the framework of ARQ. Based on this observation, results of simulations conducted to evaluate the throughput of an ARQ scheme are presented.

1. INTRODUCTION

General relay systems usually consist of three basic components, source, relay nodes and a common destination node. Specifically, the transmitter is able to broadcast the information to both the relay and the destination nodes. The relay receives signals from the source and re-transmits them to the destination, by using different strategies. The signals from both the source and the relay sides can be received at the destination, while in different time slots.

Since the intra-link (source-relay link) of relay systems is always intractable to deal with, it is assumed to be error free in most of the works so far. In [1], an LLR updating function is used at the receiver by exploiting the source-relay correlation, represented by the intra-link error rate, in order to enhance the system performances. Based on this contribution, we adopt the Bit-Interleaved Coded Modulation using Iterative Decoding (BICM-ID) technique [4] for higher order modulation schemes. Moreover, we also show that if the intra-link is error free, the topology of the relay network is equivalent to an Automatic Repeat Request (ARQ) scheme, where the relay re-transmits the incorrectly-detected frame of the prior transmission. Here we exploit Shannon's random coding theorem to achieve the best performance by utilising an interleaver between the first and second transmissions in order.

This paper is organised as follows. The relay system mode is introduced in Section 2. The proposed decoding method and the BICM-ID technique are described in Section 3. In Section 4, the EXIT Chart analysis and the results of the BER simulations are provided. Based on above, a simple ARQ scheme is presented in Section 5. Finally, the conclusions are given in Section 6. All the channels are assumed to suffer from the Additive White Gaussian Noise (AWGN) through our discussions. The subscripts $\bullet_{sr}$, $\bullet_{sd}$, and $\bullet_{rd}$ are used to indicate the source-relay, source-destination and relay-destination links, respectively.

2. SYSTEM MODEL

There is one simple relay in the proposed system, operating in a half-duplex mode. During the first time slot, the transmitter broadcasts the signals to both the relay and the destination nodes. After receiving signals from the source, the relay only extracts the data in a simple way while containing some errors. In the second time slot, the relay re-encodes the extracted data and re-transmits them to the destination.

Three scenarios of different relay locations are considered in this paper, as shown in Fig. 1(a). The relay can be allocated closer to the source or to the destination, or three nodes keep a same distance, d, with each other. The geometric-gain of the source-relay link with regard to the source-destination link can be defined as:

$$G_{sr} = \left(\frac{d_{sd}}{d_{sr}}\right)^{\alpha}, \tag{1}$$

where the path loss exponent α is assumed to be 3.52 [8] in our simulations. It is straightforward to derive the geometric-gain of the relay-destination link G_{rd} in the same way. Moreover, the geometric-gain of the source-destination link, G_{sd}, is fixed to one. Therefore the received signals y_{ij} $(ij \in \{sr, sd, rd\})$ at the relay and the destination node can be expressed as [8]:

$$y_{sr} = \sqrt{G_{sr}} \cdot h_{sr} \cdot s + n_r, \tag{2}$$
$$y_{sd} = \sqrt{G_{sd}} \cdot h_{sd} \cdot s + n_d, \tag{3}$$
$$y_{rd} = \sqrt{G_{rd}} \cdot h_{rd} \cdot s_r + n_d, \tag{4}$$

where s and s_r represent the symbols transmitted from the source and the relay, respectively. The fading channel gains, h_{ij} $(ij \in \{sr, sd, rd\})$, are equal to one in AWGN channel. Notations n_r and n_d represent the zero-mean AWGN noise vectors at the relay and the destination with variances σ_r^2 and σ_d^2, respectively. The signal to noise ratio (SNR) of source-relay and relay-destination links at each location scenario are evaluated as follows: given the path loss parameter α equal to 3.52, we have $\mathrm{SNR}_{sr} = \mathrm{SNR}_{sd} + 21.19\,\mathrm{dB}$ and $\mathrm{SNR}_{rd} = \mathrm{SNR}_{sd} + 4.4\,\mathrm{dB}$ in the location A; $\mathrm{SNR}_{sr} = \mathrm{SNR}_{sd} + 4.4\,\mathrm{dB}$ and $\mathrm{SNR}_{rd} = \mathrm{SNR}_{sd} + 21.19\,\mathrm{dB}$ in location B; $\mathrm{SNR}_{sd} = \mathrm{SNR}_{rd} = \mathrm{SNR}_{sr}$ in location C. The SNR without subscripts is with regard to the direct link (source-destination) in the following discussions.

3. PROPOSED DECODING SCHEME

The diagram of the proposed relay system is illustrated in Fig. 1(b). In this paper, memory-1 half rate ($R = 1/2$) systematic non-recursive convolutional code (SNRCC) is adopted for both encoders C_1 and C_2. The original information bits at the source node are first encoded by the C_1, interleaved by Π_1, doped-accumulated by ACC with a doping rate P_{d1} and modulated using BICM. We use 4PSK and 8PSK for the modulation. The ACC has the same structure with the memory-1 half rate systematic recursive convolutional code (SRCC). The output of the ACC is a systematic bit sequence, where every P_{d1}-th bit is replaced by the corresponding coded bit [1] within that frame. The code rate does not change after passing through it. The modulated symbols s are transmitted to both the relay and the destination in phase one.

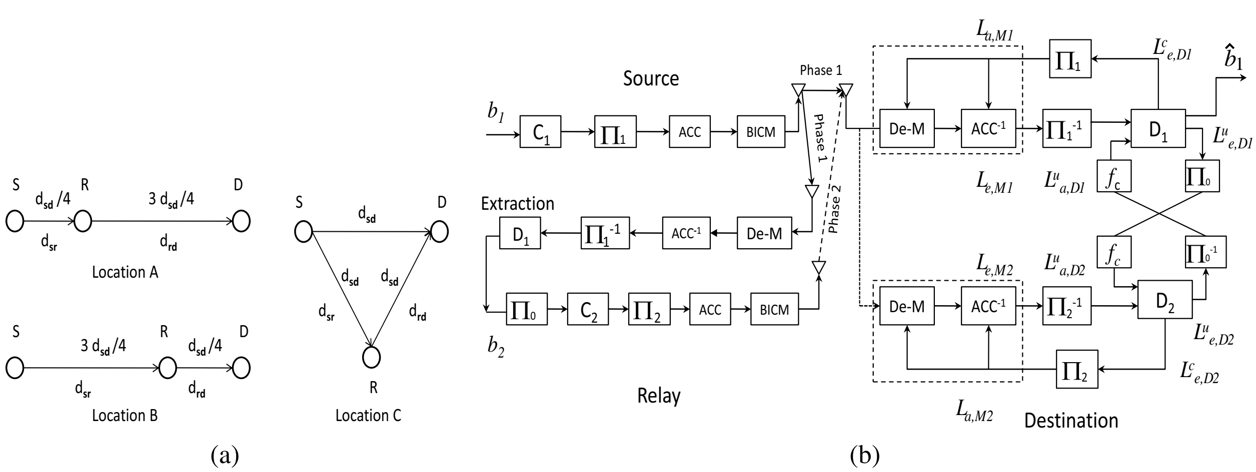

Figure 1: (a) Proposed relay system with different relay location scenarios, (b) the system structure.

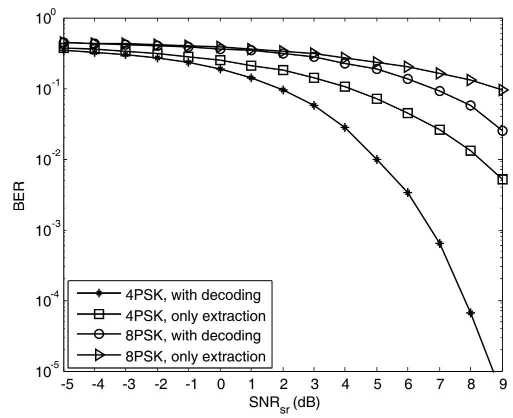

Figure 2: BER comparisons of the intra-link link in AWGN channel.

The received signals at the relay firstly go through the BICM demapper, ACC^{-1} and de-interleaver Π_1^{-1}. Then hard decisions of the source bits are made by the decoder D_1. The Maximum A-Posteriori (MAP) algorithm proposed by Bahl, Cocke, Jelinek, and Raviv (BCJR) is used for decoding convolutional codes and the ACC. It's noticeable that the relay does not perform iterative channel decoding in our proposed system. After that, the recovered bits are interleaved by Π_0 and forwarded to C_2 encoder, Π_2, and then ACC (with doping rate P_{d2}). Then the data are modulated into s_r, and transmitted to the destination during the second time slot.

At the destination node, the received signals y_{sd} and y_{rd} are firstly decoded via horizontal iterations (HI) according to Fig. 1(b). Independently, the extrinsic LLRs obtained from the two decoders D_1 and D_2 in HI are exchanged by several vertical iterations (VI) through an LLR updating function f_c [1]. Finally, hard decisions of the original information can be made based on the a posteriori LLRs from D_1.

When the relay is closer to the source, signals going through the intra-link suffer from noises with less distortions. Errors at the relay node, with the probability $P_r(b_1 \neq b_2)$, may occur as shown in Fig. 2. Obviously, for both 4PSK and 8PSK cases, channel decoding at the relay node can achieve better BER performances. However, this advantage is not significant for low SNR_{sr} scenarios. In this case, the systematic bits are simply extracted instead of performing channel decoding. Consequently, the relay complexity can be further reduced without decreasing the system performances.

3.1. BICM-ID Demapper

The extrinsic information at the receiver is exchanged between the demapper and the decoder, through the HI. Further improvement of demapping can be achieved using the BICM-ID technique by invoking the soft-decision feedbacks from the decoder's outputs [2]. The extrinsic LLRs of v-th bit of symbol s after the demapper in AWGN channel can be expressed as

$$L_e(s_v) = \ln \frac{P(s_v = 1 \mid y)}{P(s_v = 0 \mid y)} = \ln \frac{\sum_{s \epsilon S1} \left\{ \exp\left\{ -\frac{|y-s|^2}{2\sigma_N^2} \right\} \prod_{w \neq v}^{M} \exp\left(s_w L_a(s_w)\right) \right\}}{\sum_{s \epsilon S0} \left\{ \exp\left\{ -\frac{|y-s|^2}{2\sigma_N^2} \right\} \prod_{w \neq v}^{M} \exp\left(s_w L_a(s_w)\right) \right\}}, \tag{5}$$

where S_1 and S_0 denote the set of labeling have v-th bit being zero or one, respectively. M represents the number of bits per symbol and $L_a(s_w)$ is the LLR fed back from the decoder corresponding to the w-th position of the labeling patterns. The output LLRs of the demapper are then forwarded to the ACC decoder.

3.2. LLR Updating Function

First of all, given the a posteriori LLRs of the uncoded bits, $L_{p,D1}^u$ and $L_{p,D2}^u$, from the decoders D_1 and D_2, the intra-link error probability P_r can be estimated as [1]:

$$P_r = \frac{1}{N} \sum_{n=1}^{N} \frac{e^{L_{p,D1}^u} + e^{L_{p,D2}^u}}{\left(1 + e^{L_{p,D1}^u}\right)\left(1 + e^{L_{p,D2}^u}\right)}, \tag{6}$$

where N denotes the number of the a posteriori LLR pairs from the two decoders with sufficient reliability. Only the LLRs with absolute values greater than a given threshold can be chosen. The threshold is set to one in our simulations. Based on the estimated error probability P_r given by Eq. (6), the LLR updating function f_c shown in Fig. 1(b) can be defined as follows [5]:

$$f_c(x) = \ln \frac{(1 - P_r) \cdot \exp(x) + P_r}{(1 - P_r) + P_r \cdot \exp(x)}, \tag{7}$$

where x denotes the input LLRs. The output of f_c is the updated LLRs by exploiting P_r as the correlation knowledge of the intra-link. The VI operations at the receiver can be expressed as [6]:

$$L^u_{a,D1} = f_c\left\{\Pi_0^{-1}\left(L^u_{e,D2}\right)\right\} \tag{8}$$

$$L^u_{a,D2} = f_c\left\{\Pi_0\left(L^u_{e,D1}\right)\right\} \tag{9}$$

4. EXIT CHART AND BER ANALYSIS

The EXIT curves [3] of the HI loop with regards to the source-destination link's BICM-ID detector using 4PSK and 8PSK are shown in Fig. 3(a) and Fig. 3(b), where HI was performed 50 times in the simulations. During each HI, 5 times of VI take place between D_1 and D_2, which pushes down the EXIT curves of the decoder towards the lower right side [1]. For the combined EXIT curves of the demapper and the ACC^{-1}, the x-axis represents the a priori mutual information (MI) $I_a(DeM + ACC^{-1})$, while the y-axis represents the extrinsic MI $I_e(DeM + ACC^{-1})$. While for the decoder's EXIT curves, the y-axis denotes the a priori MI $I^c_a(D1)$ and x-axis denotes the extrinsic MI $I^c_e(D1)$. Each SNR value corresponds to a certain intra-link error probability P_r according to Fig. 2. The ACC's doping rate P_{d1} was properly chosen in order to get the best matching among those tested values between the demapper's and decoder's EXIT curves, as shown in Fig. 3. In our simulations, the doping rate P_{d1} for the source-destination link and the P_{d2} for the relay-destination were set at 5, 3, 3 for the scenarios A, B and C, respectively, for 4PSK. They are set at 4, 2, 8 for 8PSK.

Figure 4 shows the BER performances of the proposed system with 4PSK and 8PSK modulations. The frame length is 10000 in our simulations. Obviously, less SNR is needed to achieve the turbo cliff when the relay is getting closer to the source node. It's noticeable that in location A, the BER performances are almost the same when the relay either extracts the systematic bits or performs the channel decoding.

As can be seen in Fig. 4(a) and Fig. 4(b), the SNR threshold happens at low energy values for both the 4PSK and 8PSK modulations. Therefore, it is reasonable to rely on the Shannon/SW limit calculation using the Gaussian codebook. According to [7], the Shannon/SW limit with Gaussian codebook is -1.55 dB for 4PSK and 1.61 dB for 8PSK cases, both with the coding rate being 1/2. Therefore, the gaps of our proposed system are 2.75 dB and 2.89 dB for 4PSK and 8PSK, respectively.

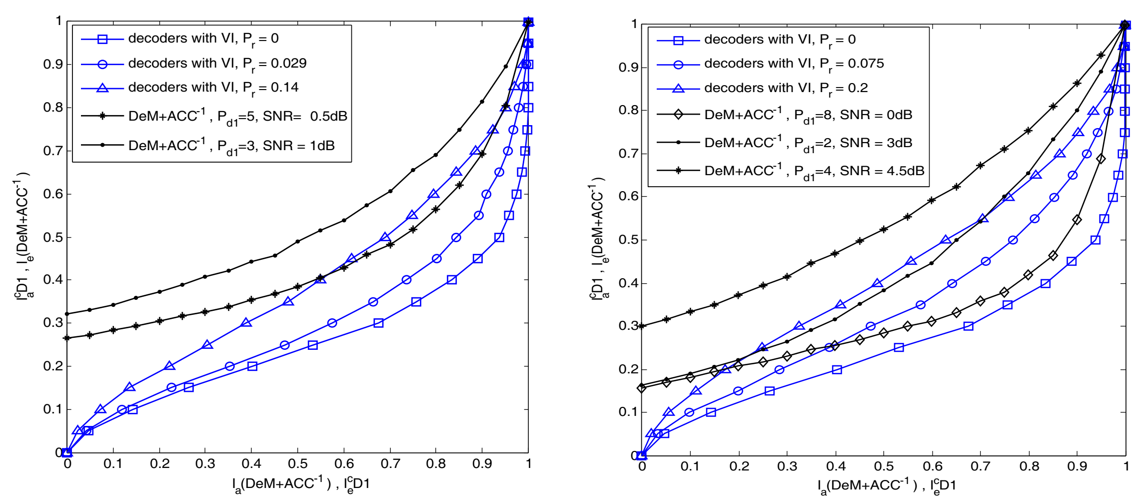

(a) (b)

Figure 3: EXIT curves of HI for (a) 4PSK and (b) 8PSK in AWGN channel.

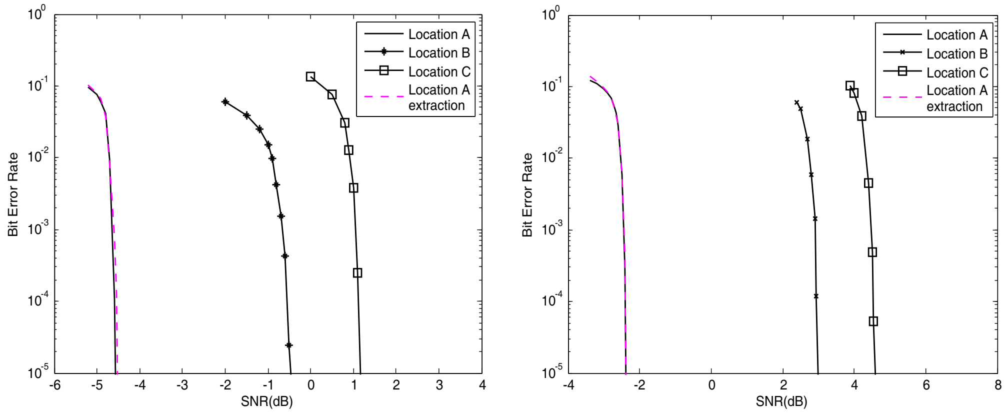

(a) (b)

Figure 4: BER of the proposed relay system for (a) 4PSK and (b) 8PSK in AWGN channel.

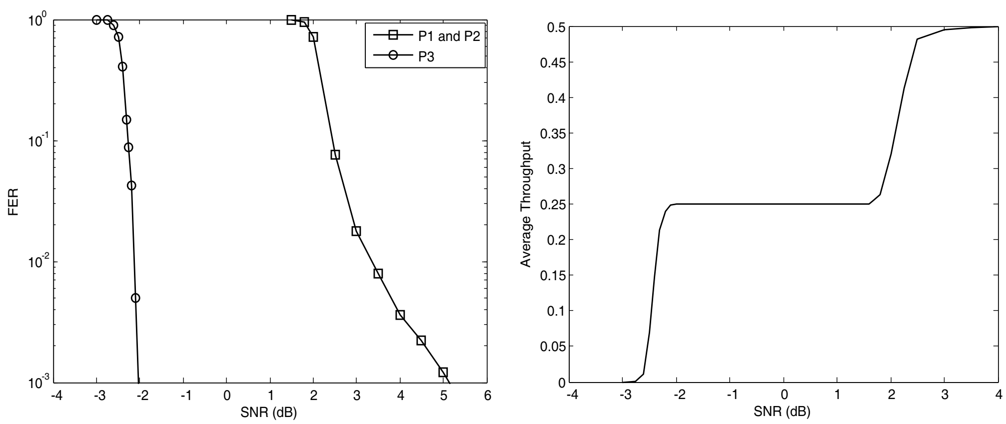

(a) (b)

Figure 5: (a) FER and (b) the average throughput of the ARQ scheme using 4PSK in AWGN channel.

5. PROPOSED ARQ SCHEME

If the intra-link of our previous system is assumed to be error free, a similarity constellation of a simple Automatic Repeat Request (ARQ) scheme can be developed: initially, the data frame is sent from the source to the destination and the receiver only performs HI for detecting. If the transmitter is acknowledged that the frame is correctly detected, it continues to transmit the next data frame. However, if error happens in this frame, with frame error rate (FER) denoted by P_1, second transmission takes place. Unlike the conventional ARQ scheme, with our proposed scheme, the frame should first be forwarded to a random interleaver before being re-transmitted, which is equivalent to the case when relay perfectly recovers the source bits and interleaves them before re-encoding. The FER for the second transmission is represented by P_2. Finally, if both transmissions fail, the receiver works exactly the same as our proposed relay system, which combines VI and HI, based on the received signals. Therefore, the FER P_3, which is the result of the collaboration of HI and VI decoding, can be significantly reduced. Assigning selective repeat ARQ, the average system throughput T_{ave} is given by Eq. (10). The frame length is 4000 in our simulations and 10000 frames are tested. The results using 4PSK are shown in Fig. 5; Fig. 5(a) shows SNR versus P_1, P_2 and P_3 and Fig. 5(b) shows SNR versus the average throughput.

$$\begin{aligned} T_{ave} &= R\left[(1-P_1)+0.5P_1(1-P_2)+0.5P_1P_2(1-P_1P_2P_3)\right] \\ &= R\left[1-0.5P_1(1+P_2P_3)\right] \end{aligned} \tag{10}$$

where R denotes the coding rate, which is 1/2 in our simulations.

6. CONCLUSIONS

In this paper, we have proposed a novel technique that combines the BICM-ID with our proposed relay scheme for higher order modulations, which allows the intra-link errors. The intra-link error probability is regarded as the correlation knowledge between source and relay nodes, which can be estimated and further exploited at the receiver by the LLR updating function f_c due to the error functions in the VI. Thereby, close-limit BER performances can be achieved without requiring high complexity at the relay. In addition, a simple ARQ strategy has been proposed based on the structure.

REFERENCES

1. Anwar, K. and T. Matsumoto, "Accumulator-assisted distributed Turbo codes for relay system exploiting source-relay correlation," *IEEE Trans. on Communications*, May 2011, submitted.
2. Zhao, D., A. Dauch, and T. Matsumoto, "BICM-ID using extented mapping and repetition code with irregular node degree allocation," *IEEE Vehicular Tech. Conf.-Spring, Barcelona*, 1–5, Sep. 2009.
3. Ten Brink, S., "Convergence behavior of iteratively decoded parallel concatenated codes," *IEEE Trans. Communications*, Vol. 49, 1727–1737, Oct. 2001.
4. Hanzo, L., T. H. Liew, and B. L. Yeap, *Turbo Coding, Turbo Equalisation and Space-time Coding for Transmission over Fading Channels*, John Wiley IEEE Press, New York, USA, 2002.
5. Lu, P.-S., V. Tervo, K. Anwar, and T. Matsumoto,, "Low-complexity strategies for multiple access relaying," *Vehicular Technology Conference (VTC Spring), 2011 IEEE 73rd*, 1–6, May 2011.
6. Anwar, K. and T. Matsumoto, "Spatially concatenated coded with Turbo equalization for correlated sources," *IEEE Trans. on Signal Processing*, Feb. 2011, submitted.
7. Cristescu, R., B. Beferull-Lozano, and M. Vetterli, "Networked Slepian-Wolf: Theory, algorithm and scalling laws," *IEEE Trans. on Information Theory*, Vol. 51, No. 12, 4057–4073, Dec. 2005.
8. Youssef, R. and A. Graell, and I. Amat, "Distributed serially concatenated codes for multi-source cooperative relay networks," *IEEE Trans. on Wireless Communications*, Vol. 10, No. 1, 253–263, Jan. 2011.

Turbo-coded CDMA-based Two-way Relaying

Soon Xin Ng and Sha Sha Liao
School of Electronics and Computer Science, University of Southampton, UK

Abstract— In this contribution, we have studied the performance of a Turbo-Coded (TC) Code Division Multiple Access (CDMA) based two-way relaying scheme. More explicitly, we employ a seven-user CDMA model, where two of the CDMA users are communicating with each other with the aid of an additional relay node, while the other five CDMA users are interferers. More explicitly, two CDMA users exchange their information frames within two timeslots. Note that the conventional one-way relaying system can only transmit one information frame within two timeslots because the relay node is half-duplex, where it cannot listen and transmit simultaneously. We found that our proposed TC-CDMA two-way relaying scheme is capable of attaining over 4 dB of SNR gain at a Bit Error Rate (BER) of 10^{-6} when compared to a conventional non-cooperative TC-CDMA system. We also found that there is about two dB of SNR loss at a BER of 10^{-6}, due to the error propagation from the relay node. The proposed scheme exploits the benefits of TC and CDMA schemes in order to assist the two-way relaying system to operate with a reduced transmit power. The reduction of the transmit power can also be exploited for increasing the coverage area of a cellular cell. Hence, the TC-CDMA two-way relaying scheme is a good candidate for future generation mobile systems.

1. INTRODUCTION

We proposed a Turbo-coded Code-Division Multiple Access (CDMA) based two-way relaying scheme for cooperative communications with the aid of a relay node. More specifically, Turbo Codes (TCs) [1] are power-efficient channel coding schemes that can perform near channel capacity, while CDMA [2] is an attractive multiple access scheme that allows multiple users to access the same frequency band at the same time. Both TC and CDMA schemes have been adopted in the current 3G mobile standard. By contrast, cooperative communications [3–5] is a new paradigm where each mobile unit collaborates with one partner or a few partners for the sake of reliably transmitting its own information and of its partners jointly. More specifically, source nodes can transmit their signals to their destination nodes via relay nodes. Cooperative communications can increase the capacity, transmission reliability, energy efficiency and coverage area of the overall system. Due to these advantages, cooperative communication schemes based on relaying have been considered in the recent LTE-Advance standard [6].

In this contribution, we studied the performance of the TC-CDMA scheme under the two-way relaying system [7] based on the Decode-And-Forward (DAF) protocol. More explicitly, we employ a seven-user CDMA model, where two of the CDMA users are communicating with each other with the aid of an additional relay node, while the other five CDMA users are interferers. In a conventional one-way relaying schemes [5, 8], two timeslots are required for the transmission of one information frame from the source node to the destination node, via a half-duplex relay node. Four timeslots would be required for the transmission of two information frames according to the conventional one-way relaying technique. In our system, only two timeslots are required for two CDMA users to exchange two information frames. This is because in a CDMA system, each user is equipped with a unique spreading code for enabling an effective multiuser detection at the destination node or relay node. Hence, time-orthogonality is not required to separate the two user signals. Our proposed TC-CDMA two-way relaying scheme is capable of attaining over 4 dB of SNR gain at a Bit Error Rate (BER) of 10^{-6} when compared to a conventional non-cooperative TC-CDMA system. We also found that there is about two dB of SNR loss at a BER of 10^{-6}, due to the error propagation from the relay node. The proposed scheme exploits the benefits of TC and CDMA schemes in order to assist the two-way relaying system to operate with a reduced transmit power. The reduction of the transmit power can also be exploited for increasing the coverage area of a cellular cell.

The paper is organised as follows. The system model is described in Section 2 while the performance of the proposed scheme is evaluated in Section 3. Our conclusion is offered in Section 4.

2. SYSTEM MODEL

We assume that each user unit is equipped with a single-antenna and the channel is constant during a symbol period. The received signal vector of a CDMA system supporting K users using P-chip

CDMA sequences can be represented by [9]:

$$\mathbf{y} = \mathbf{C}\widetilde{\mathbf{H}}\mathbf{x} + \mathbf{n}, \tag{1}$$

where the received signal $\mathbf{y}$ is a $(P \times 1)$-dimensional vector, the spreading code matrix $\mathbf{C}$ is $(P \times K)$-dimensional, the channel matrix $\widetilde{\mathbf{H}}$ is $(K \times K)$-dimensional, the user signal $\mathbf{x} = [x_1\, x_2\, \ldots\, x_K]^T$ is a $(K \times 1)$-dimensional vector and the noise vector $\mathbf{n}$ is $(P \times 1)$-dimensional. We consider a frequency-flat uncorrelated Rayleigh fading channel, which can be conveniently represented by the following diagonal matrix:

$$\widetilde{H} = \begin{bmatrix} \sqrt{G_{u_1 d}} h_{u_1 d} & \ldots & 0 \\ \vdots & \ddots & \vdots \\ 0 & \ldots & \sqrt{G_{u_K d}} h_{u_K d} \end{bmatrix},$$

where $G_{u_k d}$ and $h_{u_k d}$ are the corresponding reduced-pathloss-induced geometrical gains [8] and the Rayleigh fading coefficient between the kth user node and the destination node, respectively. When considering a free-space path loss model, the geometrical gain between the kth user node and the destination node is given by [8]:

$$G_{u_k d} = \left(\frac{d_{u_k u_l}}{d_{u_k d}} \right)^2, \tag{2}$$

where $d_{u_k u_l}$ is the distance between the kth and lth users, who are the two users that want to exchange their information frames, while $d_{u_k d}$ is the distance between the kth user and the destination node (in our two-way relaying scheme, this is the relay node because the lth user node is the destination node for the kth user and vice versa). Equation (1) can be more conveniently rewritten as:

$$\mathbf{y} = \mathbf{H}\mathbf{x} + \mathbf{n}, \tag{3}$$

where $\mathbf{H} = \mathbf{C}\widetilde{\mathbf{H}}$. Minimum Mean-Square Error (MMSE) based multiuser detection is considered and the MMSE weight matrix is given by:

$$\mathbf{W} = \mathbf{H} \left(\mathbf{H}\mathbf{H}^H + N_0 \mathbf{I}_P \right)^{-1}, \tag{4}$$

where $\mathbf{I}_P$ is a $(P \times P)$-element matrix having ones on its diagonal, $N_0/2$ is the noise variance per dimension and $\mathbf{H}^H$ is the Hermitian transpose of $\mathbf{H}$. The MMSE-detected signal is given by:

$$\mathbf{z} = \mathbf{W}^H \mathbf{y} = \left(\mathbf{H}^H \mathbf{H} + N_0 \mathbf{I}_P \right)^{-1} \mathbf{H}^H \mathbf{H} \mathbf{x} + \left(\mathbf{H}^H \mathbf{H} + N_0 \mathbf{I}_P \right)^{-1} \mathbf{H}^H \mathbf{n} = \mathbf{A}\mathbf{x} + \mathbf{v}, \tag{5}$$

where $\mathbf{z}$ is a $(K \times 1)$-dimensional vector, $\mathbf{A} = (\mathbf{H}^H \mathbf{H} + N_0 \mathbf{I}_P)^{-1} \mathbf{H}^H \mathbf{H}$ is the $(K \times K)$-dimensional equivalent channel matrix and $\mathbf{v} = (\mathbf{H}^H \mathbf{H} + N_0 \mathbf{I}_P)^{-1} \mathbf{H}^H \mathbf{n}$ is the $(K \times 1)$-dimensional equivalent noise vector. More specifically, Equation (5) can be written as:

$$\begin{bmatrix} z_1 \\ \vdots \\ z_K \end{bmatrix} = \begin{bmatrix} a_{11} & \ldots & a_{1K} \\ \vdots & \ddots & \vdots \\ a_{K1} & \ldots & a_{KK} \end{bmatrix} \begin{bmatrix} x_1 \\ \vdots \\ x_K \end{bmatrix} + \begin{bmatrix} v_1 \\ \vdots \\ v_K \end{bmatrix}, \tag{6}$$

where it can be shown that the noise variance for the kth noise v_k is given by the multiplication of the kth diagonal element of $\mathbf{W}^H \mathbf{W}$ and N_0, i.e., $N_{0,k} = \mathrm{diag}_k\{\mathbf{W}^H \mathbf{W}\} N_0$. Hence, the kth MMSE signal can be written as:

$$z_k = a_{kk} x_k + \sum_{i \neq k}^{\mathrm{all}\, i} a_{ik} x_i + v_k = a_{kk} x_k + w_k + v_k, \tag{7}$$

where $w_k = \sum_{i \neq k}^{\mathrm{all}\, i} a_{ik} x_i$ is the interference term which equals zero when orthogonal spreading sequence is employed. Note that $\mathbf{A}$ is a diagonal matrix if orthogonal spreading code is used. We employ the m-sequence spreading code [9], where the off-diagonal elements in $\mathbf{A}$ is very small when the number of users supported is not greater than the number of chips, i.e., $K \leq P$. Hence, we

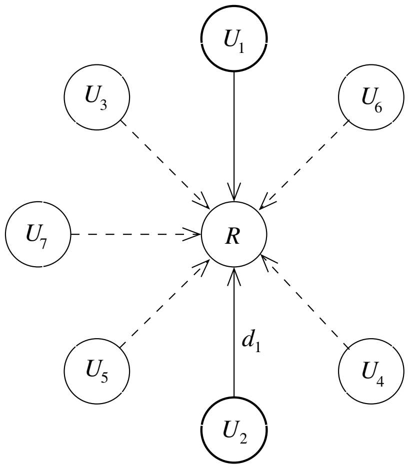

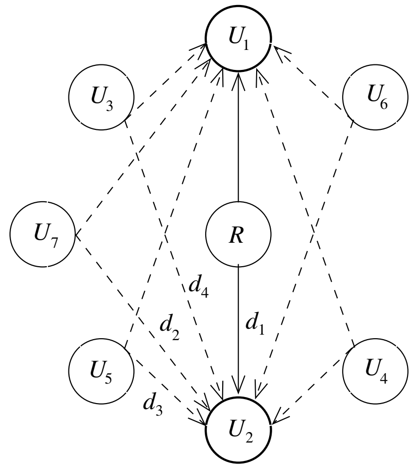

Figure 1: Two-way relaying transmission for users U_1 and U_2, in the presence of five interfering users, with the aid of a relay node, in the **circular model (m1)**. The corresponding normalized distances (and geometrical gains) are given by: $d_1 = 0.5\,(G_1 = 4)$, $d_2 = 0.7071\,(G_2 = 2)$, $d_3 = 0.3827\,(G_3 = 6.8283)$ and $d_4 = 0.9239\,(G_4 = 1.1716)$.

ignore the w_k term in Equation (7), when computing the probability of receiving z_k given that x_k was transmitted as:

$$P(z_k|x_k) = \frac{1}{\pi N_{0,k}} \exp\left(-\frac{|z_k - a_{kk}x_k|^2}{N_{0,k}}\right). \tag{8}$$

The probability $P(z_k|x_k)$ is computed for each symbol in a transmission frame and then fed to the Turbo decoder for computing the information bit sequence. A more complicated interference-cancelation technique can be employed to remove the w_k term in Equation (7) but we opted for a lower complexity detection, which can still provide a good performance despite ignoring the presence of the inference term w_k in the calculation of Equation (8).

2.1. Network Topology

Figure 1 shows the network topology of the circular model (m1) where seven CDMA users are located in a circular arrangement and a relay node is located in the center. Seven-chip m-sequences are considered in our system to support seven users. The Relay Node (R) helps the first user (U_1) and the second user (U_2) to exchanging their information frames, in the presence of five interfering CDMA users (U_3, U_4, U_5, U_6 and U_7). During the first timeslot, U_1 and U_2 transmit their information frames to R, where R detects the two information frames. Then, R re-encodes and broadcasts the two information frames to U_1 and U_2 during the second timeslot. The detection of the wanted information frame at U_1 (or U_2) is also interfered by the other five CDMA users. By contrast, Figure 2 depicts the network topology of the triangular model (m2) where the five interfering CDMA users are located at the two sides in the network topology. Again the detection of the wanted signals at R, U_1 and U_2 are in the presence of the five interfering users. Assuming that the distance between U_1 and U_2 is normalized to unity, the various normalized distances can be calculated according to the trigonometry rules. The normalized distances and the corresponding geometrical gains are shown in the captions of Figures 1 and 2.

At each user node, a half-rate Turbo encoder and a four-level Phase-Shift Keying (4PSK) modulation is employed. At the relay node R, the two decoded information sequences $\mathbf{b}_1$ (from U_1) and $\mathbf{b}_2$ (from U_2) are modulo-two added to produce a new information sequence $\mathbf{b}_0 = \mathbf{b}_1 \oplus \mathbf{b}_2$. Then $\mathbf{b}_0$ is encoded by the same half-rate Turbo encoder into a coded sequence $\mathbf{c}_0$. The same 4PSK modulation is employed to map $\mathbf{c}_0$ into 4PSK sequence $\mathbf{x}_0$, which is then spread by either the spreading sequence of U_1 (or U_2), before it is broadcast to both users. A frame length of $N = 12000$ 4PSK symbols is used. In this study, we add the two user-frames at the information bit level. However, it is also possible to add the two user-frames at the chip-level after the two 4PSK sequences are properly spread by each corresponding CDMA codes. We found that these two approaches give similar performance in our two-way relaying scheme. On one hand, the complexity in using the information bit level addition is lower because only one encoder, one 4PSK mapper and one spreader

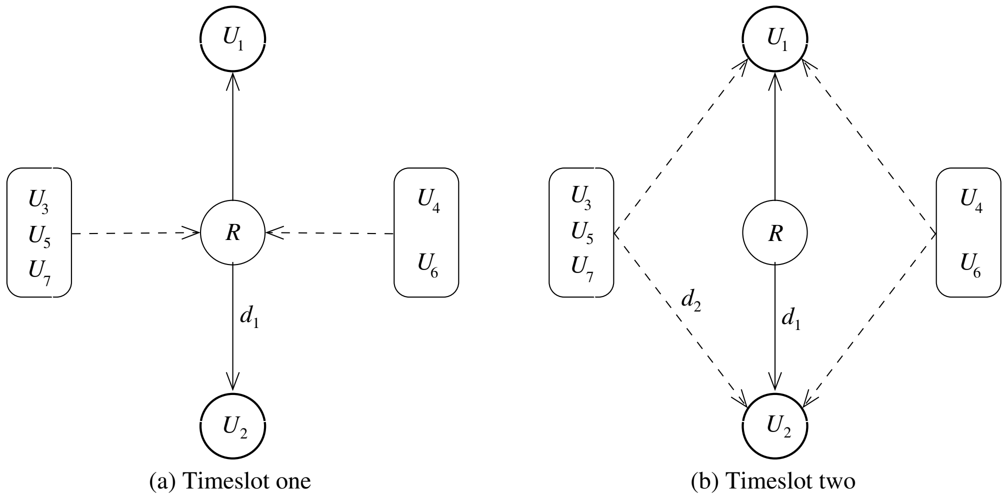

Figure 2: Two-way relaying transmission for users U_1 and U_2, in the presence of five interfering users, with the aid of a relay node, in the **triangular model (m2)**. The corresponding normalized distances (and geometrical gains) are given by: $d_1 = 0.5\,(G_1 = 4)$ and $d_2 = 0.7071\,(G_2 = 2)$.

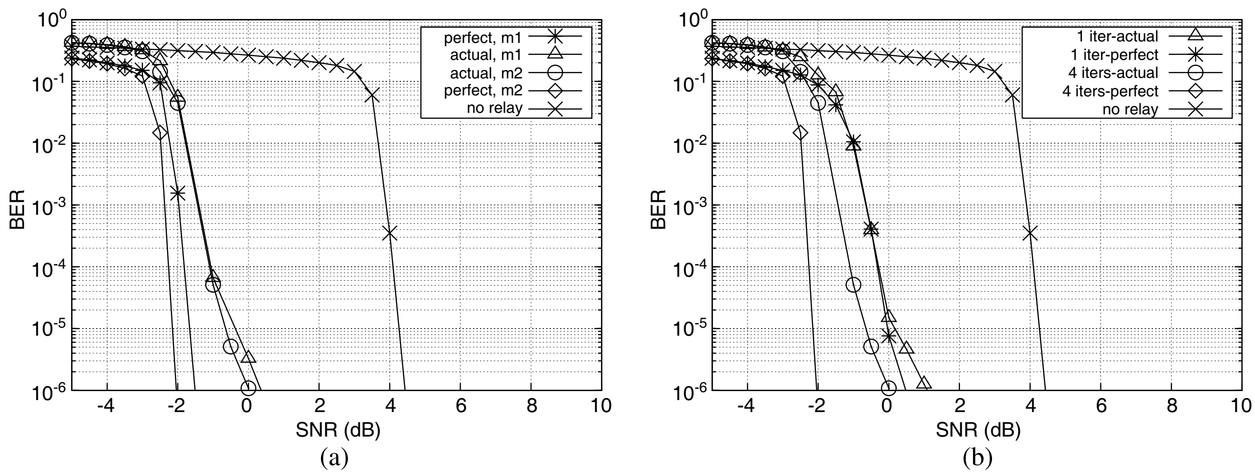

Figure 3: BER versus transmit SNR performance of the Turbo-coded CDMA-based two-way relaying system. MMSE detection is used in conjunction with $P = 7$-chip m-sequences in a $K = 7$-user CDMA system. A frame length of 12000 symbols is employed. (a) Performance comparison between the m1 and m2 models. (b) Effect of employing one and four Turbo decoding iterations.

is required. One the other hand, if our scheme is extended to multiple-way relaying system, then all user frames have to be added at the chip-level.

3. PERFORMANCE EVALUATION

The received Signal to Noise power Ratio (SNR) of our relay model is given by [8]:

$$\mathrm{SNR}_r = \mathrm{SNR}_t + 10\log_{10} G, \tag{9}$$

where $\mathrm{SNR}_t = 10\log_{10}(1/N_0)$ is the *transmit* SNR and G is the corresponding geometrical gain. The SNR per information bit is given by:

$$E_b/N_0 = \mathrm{SNR}_t - 10\log_{10}(R\log_2(M)), \tag{10}$$

where R is the coding rate and $\log_2(M)$ is the number of bits per modulated symbol. In our case we have $R\log_2(M) = 0.5\log_2(M) = 1$, hence $E_b/N_0 = \mathrm{SNR}_t$.

The BER versus transmit SNR performance of the Turbo-coded CDMA-based two-way relaying schemes are shown in Figure 3. More specifically, as shown in Figure 3(a), a 7-user CDMA system without using a relay node would require approximately 4.3 dB in order to achieve a BER of 10^{-6}.

However, the relay-aided scheme in the m2 model can achieve the same BER at -2 dB if a perfect relay is assumed. A perfect relay is an idealistic relay where it is capable of detecting all wanted signals without error. However, the scheme using an actual relay in the m2 model is 2 dB away from this upper bound performance. Nonetheless, the relay aided scheme in the m2 model is still approximately 4.3 dB better than that of the non-relay aided scheme. On the other hand, the relay-aided schemes in the m1 model perform approximately 0.5 dB worse than that of their counterparts in the m2 model. This is because in the m1 model, as shown in Figure 1, there exists two strong interferers for either U_1 or U_2 where the normalized distance is given by $d_3 = 0.3827$. By contrast, in the m2 model of Figure 2, all interferers have the same distance d_2 away from U_1 or U_2, where $d_2 > d_3$. A longer distance would inflict a stronger path loss (or a smaller geometrical gain), making the interfering signals to be weaker.

Figure 3(b) shows the effect of the number of Turbo decoding iterations based on the m2 model. The performance of the perfect-relay aided scheme becomes approximately 2.5 dB worse, at a BER of 10^{-6}, when the number of Turbo decoding iterations is reduced from four to one. However, increasing the number of Turbo iterations from one to four, for the scheme employing the actual relay, only provides a gain of approximately one dB, at a BER of 10^{-6}. Hence, the iteration gain at the destination node is limited by the error propagation effects from the relay node.

4. CONCLUSION

Turbo-coded CDMA-based two-way relaying scheme has been studied. It was found that the orthogonality of the spreading code of each CDMA user can be beneficially utilized for enabling a two-way relaying based cooperative communication system, without the need for time/frequency orthogonality as in the conventional one-way relaying system. The proposed two-way relaying scheme is capable of attaining 4.3 dB of SNR gain at a BER of 10^{-6}, when compared to a non-relaying scheme. The proposed scheme can be extended to multiple-way relay scheme with the aid of a relay node that can perform multiuser detection. Powerful channel coding schemes, such as Turbo codes, should be used in order to minimize the detection error at the relay node and consequently to reduce the effects of error-propagation to the destination node.

REFERENCES

1. Hanzo, L., T. H. Liew, B. L. Yeap, R. Y. S. Tee, and S. X. Ng, *Turbo Coding, Turbo Equalisation and Space-Time Coding: EXIT-Chart-Aided Near-Capacity Designs for Wireless Channels*, 2nd Edition, John Wiley, IEEE Press, New York, USA, Mar. 2011.
2. Hanzo, L., L.-L. Yang, E. L. Kuan, and K. Yen, *Single- and Multi-Carrier CDMA*, John Wiley, IEEE Press, New York, USA, 2003.
3. Sendonaris, A., E. Erkip, and B. Aazhang, "User cooperation diversity part I: System description," *IEEE Transactions on Communications*, Vol. 51, No. 11, 1927–1938, 2003.
4. Laneman, N., D. N. C. Tse, and G. W. Wornell, "Cooperative diversity in wireless networks: Efficient protocols and outage behavior," *IEEE Trans. on Information Theory*, Vol. 50, No. 12, 3062–3080, 2004.
5. Dohler, M. and Y. Li, *Cooperative Communications: Hardware, Channel and PHY*, John Wiley and Sons, 2010.
6. Sesia, S., I. Toufik, and M. Baker, *LTE: The UMTS Long Term Evolution, from Theory to Practice*, 2nd Edition, John Wiley, 2011.
7. Chen, M. and A. Yener, "Multiuser two-way relaying: Detection and interference management strategies," *IEEE Transactions on Wireless Communications*, Vol. 8, No. 8, 4296–4305, Aug. 2009.
8. Ochiai, H., P. Mitran, and V. Tarokh, "Design and analysis of collaborative diversity protocols for wireless sensor networks," *Proceedings of IEEE VTC Fall*, 4645–4649, Los Angeles, USA, Sep. 26–29, 2004.
9. Hanzo, L., L.-L. Yang, E. L. Kuan, and K. Yen, *Single- and Multi-Carrier DS-CDMA: Multi-User Detection, Space-Time Spreading, Synchronisation and Standards*, John Wiley, IEEE Press, New York, USA, 2003.

Differential Distributed Space-time Block Code for Two-way Relay Channel with Physical-layer Network Coding

Kai Zhu and Alister G. Burr
Communications Research Group, Department of Electronics
University of York, YO10 5DD, United Kingdom

Abstract— In this contribution, we present a low-complexity differential cooperation scheme for communications over two-way relay channels. More specifically, a frame of Differential Phase-Shift Keying (DPSK) symbols is generated at the source nodes, while differential distributed space-time block coding (DDSTBC) scheme is invoked at each cooperating relay node. Since non-coherent detection can be carried out to recover the transmitted signals at both relay and destination nodes, it is not necessary to incorporate any channel estimation components in our proposed system. A selection relaying protocol based on CRC is utilized at the relay nodes to counteract the negative effects of error propagation. It is shown that full diversity order is still attainable at the destination nodes, even when the source-to-relay link is not protected by powerful channel codes with high computational complexity.

1. INTRODUCTION

New applications of wireless communications in networked devices such as wireless sensor networks, body area networks, and the smart grid will result in networks containing much larger numbers of low powered communication nodes than current wireless networks. Networks of this sort are more likely to form a peer-to-peer or heterogeneous mesh topology, rather than the star topology more common today, and hence require data to be forwarded by relaying from node to node through the network. However, since links in the network may be unreliable due to fading or node failure, diversity provided by cooperation between multiple relay nodes is very desirable to improve network robustness [1].

Distributed space-time block coding (DSTBC) [2] is one of the most popular cooperative MIMO techniques developed for multi-user communication environments. DSTBC is capable of offering similar temporal and spatial diversity gain as conventional MIMO systems employing multiple co-located antennas. However, DSTBC requires accurate estimation of the channel state information (CSI) for reliable detection at the receiver. As a remedy, a differentially encoded non-coherently decodable STBC scheme was proposed in [3]. By taking full advantage of the relationship between two successive transmitted symbols, the information conveyed by differential STBC signals can be recovered without the knowledge of CSI. Hence, compared with its coherently detected counterpart, differential STBC is appealing in saving power and bandwidth otherwise required for training symbols, as well as reducing implementation complexity.

The classic unidirectional cooperative communication has been recently extended to bidirectional or two-way relaying [4] with the assistance of physical-layer network coding (PNC) [5]. Unlike other superposition coding techniques, the primary interest of PNC is to directly extract the network coded symbols from superimposed received signals at the relay nodes instead of explicitly detecting the individual symbols separately and independently. Therefore, the spectral efficiency as well as the achievable channel capacity is significantly increased by deploying PNC in the relaying protocol. In this contribution we combine the benefits of differential and distributed STBC with two-way relaying, and propose a differential distributed STBC (DDSTBC) scheme for the physical-layer network coded two-way relay channel using a "decode-and-forward" cooperative protocol. More specifically, our investigation first concentrates on the performance of unidirectional two-hop cooperative differential STBC system. Similar to the strategy used in [6], the problem of error propagation induced in the decoding and re-encoding stage can be effectively circumvented by incorporating an appropriately-designed frame-by-frame (or packet-by-packet) based selection relaying protocol [7] at each relay node. Hence, although the antenna array is constructed in a distributed fashion, full diversity order is still achievable at the destination. Subsequently, we extend the selection relaying aided differential DSTBC scheme to two-way relaying scenario and propose a simple method to directly extract the network coded symbols from two superimposed differentially encoded signals without any assistance of CSI.

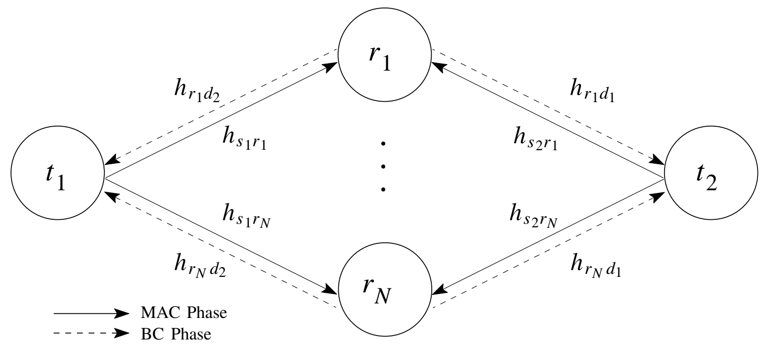

Figure 1: The schematic of a classic multi-relay aided two-way cooperative communication system.

2. SYSTEM MODEL

The symmetric structure of a classic multi-relay aided two-way cooperative communication network is depicted by Fig. 1, where two ordinary time-division half-duplex wireless terminals (t_1, t_2) simultaneously exchange information with the assistance of N number of parallel cooperating relay nodes ($r_1, r_2, \ldots, r_N$). Note that each terminal node acts as a source node (s) as well as a destination node (d). Furthermore, each terminal and relay node as seen in Fig. 1 is equipped with a single antenna for the consideration of balancing the trade-off between the implementation complexity and system robustness. A transmission session consists of two stages: the multiple access (MAC) phase as well as the broadcast (BC) phase. In the MAC phase, a frame of uniformly-distributed information bits x_{s_i} are encoded using Differential $\mathcal{M}$-ary Phase-Shift Keying (DPSK) modulation and transmitted by the two source nodes simultaneously. If the DPSK symbols are denoted as v_{s_i}, the received signal at the jth relay node, which is basically a noisy version of the superposition of two differentially-encoded and channel-corrupted $\mathcal{M}$-PSK signals, is formulated by:

$$y_{r_j} = \sum_{i=1}^{2} \left(h_{s_i r_j} v_{s_i} \right) + n_{r_j}, \tag{1}$$

where $j \in \{1, 2, \ldots, N\}$ and $h_{s_i r_j}$ is the quasi-static Rayleigh fading coefficient of the transmission link between the ith source node and the jth relay node, which is constant for all symbols within a frame. And n_{r_j} is the complex-valued Additive White Gaussian Noise (AWGN) introduced at the jth relay node having a zero mean and a variance $\sigma_I^2 = \sigma_Q^2 = N_0/2$.

Next, PNC is employed to decode this superimposed signal y_{r_j} and extract the network coded (exclusive or-ed) symbols u_{r_j} without the knowledge of CSI. Assuming the notation $\hat{x}_{s_i}^{(r_j)}$ represents the information sequences estimated by the jth relay node, the network coded symbols are defined as:

$$u_{r_j} = \hat{x}_{s_1}^{(r_j)} \oplus \ \hat{x}_{s_2}^{(r_j)}, \tag{2}$$

where $\oplus$ indicates an element-by-element modulo-two addition performed in the Galois Field GF(2^m), which can be simplified to the exclusive or arithmetic when $m = 1$. The principle of acquiring the network coded symbols using differential PNC will be elaborated further in the next section.

In order to enhance the error-resilience against potential error propagation, after obtaining the network coded symbol frame, an error-detecting process is carried out to calculate its Cyclic Redundancy Check (CRC) value. Owing to the linearity of the CRC encoders[1], each relay node is capable of distinguishing whether one specific frame of network coded symbols is generated correctly by comparing its CRC with the 'modulo-two sum' of two CRCs corresponding to the information streams at two source nodes. More specifically, if two uncoded information sequences pass the same CRC check using identical CRC generator polynomial, their modulo-two sum will also pass. On the other hand, when one is in error, or both are in error but in different positions, the check will fail. Depending on the results of CRC checks, each cooperating node can decide whether to become active during next transmission period or just keep silent.

[1]The generator polynomial used here is $\Gamma = [x^8 + x^7 + x^4 + x^3 + x + 1]$, which corresponds to the 9-bit string {110011011}.

During the BC phase, only correctly estimated network coded symbols are re-encoded into differential DSTBC symbols w_{r_j} and broadcasted to the destination nodes. Although each cooperating relay node only constitutes one row of the differential STBC code matrix, a frame of virtual differential STBC codewords is received at the destination nodes. The received signal at the ith destination node can be expressed as:

$$y_{d_i} = \sum_{j=1}^{N} \left(h_{r_j d_i} w_{r_j} \right) + n_{d_i}, \tag{3}$$

where $i \in \{1, 2\}$ and $h_{r_j d_i}$ denotes the complex-valued quasi-static Rayleigh fading coefficient of the channel between the jth relay node and the ith destination node, while n_{d_i} is the AWGN induced at the ith destination node with a zero mean and a variance $\sigma_I^2 = \sigma_Q^2 = N_0/2$. Note that the transmit power of each source, relay node is normalized to unity; therefore, the overall power of differential DSTBC codewords is $\sum_{j=1}^{N} |w_{r_j}|^2 = 1$.

At the destination node, a conventional differential STBC decoder followed by a $\mathcal{M}$-PSK demapper are deployed to recover the network coded symbols $\hat{u}_{r_j}$. Eventually, each destination node is capable of retrieving the information bits transmitted from corresponding source node by applying the exclusive or between the estimated network coded symbols and their local information as follows:

$$\hat{x}_{s_1} = \hat{u}_{r_j} \oplus \; x_{s_2}. \tag{4}$$

Similarly, for the information bits transmitted from s_2, we have:

$$\hat{x}_{s_2} = \hat{u}_{r_j} \oplus \; x_{s_1}, \tag{5}$$

where $j \in \{1, 2, \ldots, N\}$.

3. PRINCIPLE OF DIFFERENTIAL PNC MAPPING

In this section, we will introduce the principle of differential PNC mapping, which is employed at each receiving relay node to extract the network coded symbols from the superimposed signal y_{r_j}. For ease of analysis, we assume that a 2-level differential PSK modulation scheme, namely differential BPSK, is used at the source nodes to modulate the information bits. Furthermore, we consider $N = 2$ relay nodes located in the middle of the direct line-of-sight path between t_1 and t_2 in the following discussion. If '+1' is chosen as the reference symbol for the DBPSK modulators at both source nodes, the mapping rule of this novel differential PNC can be generalized in Table 1.

Similar to the conventional DPSK demodulation, the differential PNC mapping is designed to successively process the received signal by taking advantage of the relationship between two adjacent

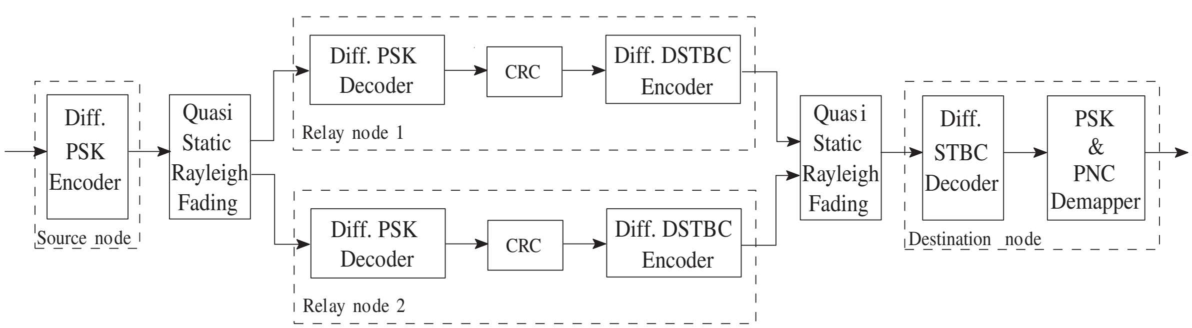

Figure 2: The schematic of the proposed DPSK-DDSTBC scheme for one-way relaying case.

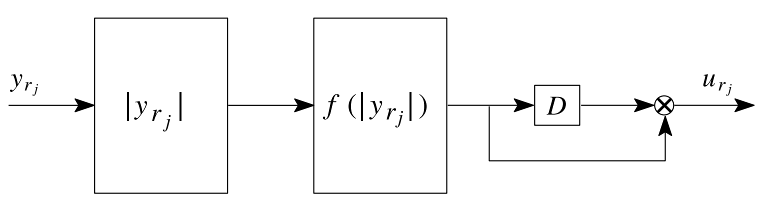

Figure 3: The schematic of the novel differential PNC mapper used at the relay nodes.

Table 1: An example of PNC mapping using two differential BPSK symbols. The reference symbols for v_{s_1} and v_{s_2} are assumed to be $[+1, +1]$.

	Info. Bit x_{s_1}	x_{s_2}	**Diff. Symbol** v_{s_1}	v_{s_2}	**Superimposed Symbol at Relay** m	**PNC Codeword**	**New Diff. Symbol** $f(m)$
Time T	**0**	**0**	**+1**	**+1**	**+2**	**0**	**+1**
Time $T+1$	0	0	+1	+1	+2	0	+1
	0	1	+1	−1	0	1	−1
	1	0	−1	+1	0	1	−1
	1	1	−1	−1	−2	0	+1
Time T	**0**	**1**	**+1**	**−1**	**0**	**1**	**−1**
Time $T+1$	0	0	+1	−1	0	0	+1
	0	1	+1	+1	+2	1	−1
	1	0	−1	−1	−2	1	−1
	1	1	−1	+1	0	0	+1
Time T	**1**	**0**	**−1**	**+1**	**0**	**1**	**−1**
Time $T+1$	0	0	−1	+1	0	0	+1
	0	1	−1	−1	−2	1	−1
	1	0	+1	+1	+2	1	−1
	1	1	+1	−1	0	0	+1
Time T	**1**	**1**	**−1**	**−1**	**−2**	**0**	**+1**
Time $T+1$	0	0	−1	−1	−2	0	+1
	0	1	−1	+1	0	1	−1
	1	0	+1	−1	0	1	−1
	1	1	+1	+1	+2	0	+1

symbols. Hence, accurate estimation of CSI is unnecessary. When the received signal at each relay node is the superposition of two differential BPSK modulated symbol sequences, the schematic of the differential PNC mapper is illustrated in Fig. 3. As shown in Fig. 3, the amplitude of the received signal y_{r_j} is first acquired by calculating its absolute value. Subsequently, the resultant output is fed into a function $f(m)$, which is defined as:

$$f(m) = \frac{m^2}{2} - 1, \quad m \geqslant 0. \tag{6}$$

Finally, a classic differential decoder is invoked to produce the network coded symbols.

4. PERFORMANCE EVALUATION

The Bit Error Ratio (BER) performance of the proposed DPSK-DDSTBC scheme with a straightforward CRC-based selection relaying strategy for the one-way relaying case is evaluated and quantified using Monte-Carlo simulation shown in Fig. 4. It is assumed that the quasi-static Rayleigh fading channel model is invoked in the simulation. Furthermore, the frame length used at both source and relay nodes is defined as $N_s = N_r = 50, 100, 300$ DPSK/DDSTBC symbols with BPSK modulation.

As illustrated in Fig. 4, the BER of the DDSTBC with selection relaying (DDSTBC-SR) shares the same slope with the conventional non-cooperative differential STBC scheme having two co-located transmit antennas and a single receive antenna, which is chosen as the benchmark. This indicates our proposed DDSTBC scheme achieves second order diversity. By contrast, although the cooperation stage is assisted by multiple relay nodes, the DDSTBC scheme without selection relaying strategy (DDSTBC-NO-SR) is only capable of providing a diversity order of one due to the lack of an efficient countermeasure to alleviate the detrimental effect of error propagation, which degrades the system BER performance by more than 5 dBs at BER $= 10^{-3}$.

It is also worth noticing the effects of different frame length shown in Fig. 4. When the frame length increases from 50 to 300, the BER performance has a slight degradation. This is caused by

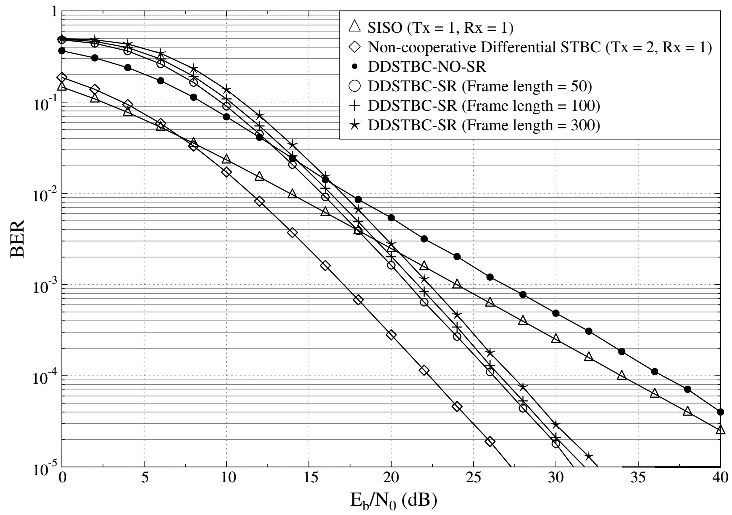

Figure 4: BER versus E_b/N_0 performance of the proposed novel DPSK-DDSTBC scheme with selection relaying strategy.

the fact that it becomes difficult to ensure the whole frame is decoded correctly when the frame length is relatively long. Therefore, as mentioned before, the number of valid differential STBC codewords constructed by two relay nodes will decline in such circumstances.

5. CONCLUSION

A novel relay selection assisted differential distributed space-time block coding (DDSTBC) scheme for two-way cooperative communications was proposed and investigated in this paper. We have shown that, with the assistance of CRC-based selection relaying protocol, the proposed virtual differential STBC system was capable of approaching full transmit diversity order. On the other hand, the complexity of such system is lower than conventional MIMO system, since the distributed antenna array is constructed by a group of single antenna aided cooperating nodes. The signal detection is performed non-coherently at the relay and destination nodes so that the system complexity can be further reduced. Hence, our proposed scheme is practical and easy to implement.

ACKNOWLEDGMENT

The financial support of the EPSRC UK and British Telecom (BT) is gratefully acknowledged.

REFERENCES

1. Laneman, J. N., D. N. C. Tse, and G. W. Wornell, "Cooperative diversity in wireless networks: Efficient protocols and outage behavior," *IEEE Transactions on Information Theory*, Vol. 50, 3062–3080, 2004.
2. Laneman, J. N. and G. W. Wornell, "Distributed space-time-coded protocols for exploiting cooperative diversity in wireless networks," *IEEE Transactions on Information Theory*, Vol. 49, 2415–2425, 2003.
3. Tarokh, V. and H. Jafarkhani, "A differential detection scheme for transmit diversity," *IEEE Journal on Selected Areas in Communications*, Vol. 18, No. 7, 1169–1174, 2000.
4. Tian, S., Y. Li, and B. Vucetic, "A near optimal amplify and forward relaying in two-way relay networks," *Proceedings of IEEE International Conference on Communications (ICC)*, 1–5, Kyoto, Japan, Jun. 2011.
5. Zhang, S., S. C. Liew, and P. P. Lam, "Physical layer network coding," *Proceedings of MobiCom'06: The 12th Annual International Conference on Mobile Computing and Networking*, 358–365, New York, USA, 2006.
6. Zhu, K. and A. G. Burr, "Relay selection aided distributed space-time block code for two-way relay channel with physical-layer network coding," *Proceedings of IEEE Vehicular Technology Conference (VTC)*, 1–5, Budapest, Hungary, May 2011.
7. Bastami, A. H. and A. Olfat, "Optimal SNR-based selection relaying scheme in multi-relay cooperative networks with distributed space-time coding," *IET Communications*, Vol. 4, No. 6, 619–630, 2010.

Distributed Algorithm for Multiple Antenna Cooperative Cognitive Radio Networks with Multiple Primary and Secondary Users

S. Bayat[1], **R. H. Y. Louie**[1], **Y. Li**[1], **S. X. Ng**[2], **and B. Vucetic**[1]

[1]Centre of Excellence in Telecommunications, School of Electrical and Information Engineering
University of Sydney, Australia
[2]School of Electronics and Computer Science, University of Southampton, UK

Abstract— We propose a distributed spectrum access algorithm for cognitive radio relay networks with multiple primary users (PU) and multiple secondary users (SU) utilizing multiple antennas at their transmitter. The overlay model is considered, where the PUs allow spectrum access opportunities for the SUs, in exchange for the SUs cooperatively relaying the PUs' data in exchange for both spectrum access and monetary compensation. We show that the PUs which utilize the SUs for cooperative relaying achieves a rate greater than what it would achieve without cooperative relaying, i.e., direct transmission, and thus motivates their participation in the proposed algorithm.

1. INTRODUCTION

Cognitive radio has been proposed as a promising technology to improve the spectral efficiency. This is achieved by allowing unlicensed secondary users (SU) to coexist with licensed primary users (PU) in the same spectrum. This coexistence is facilitated by spectrum access techniques, such as those involving an agreement between the PUs and SUs on an acceptable spectrum access strategy. The key idea is that the PUs are motivated to lease spectrum bands to the SUs in exchange for some form of compensation.

Monetary compensation have been well studied (see e.g., [1–3]), with the predominant approach for spectrum access and performance analysis involving the use of tools from game theory. For these monetary payment schemes, the PUs are assumed to have sufficient spectrum for leasing to the SUs, such that their own performance requirements are not affected. In practice, however, the PUs may desire higher data rates than what its current spectrum can provide.

Multiple antenna technology is well known as a powerful technique to enhance performance, due to their ability to provide diversity, high reliability and capacity in wireless networks. To allow for higher data rates, the use of cooperative relaying has emerged as a powerful technique due to its ability to exploit user diversity and provide high reliability and capacity in wireless networks [4]. This is achieved by the use of intermediate relay nodes to aid transmission between the source and destination nodes. The use of cooperative relaying is particularly advantageous when the direct link between the source and destination is weak, due to, for example, high shadowing.

This paper is organized as follows. In Section 2, we first describe our system model. We then formulate the problem we are trying to solve in Section 3, and present a distributed solution to this problem in Section 4. Finally, we analyze the performance and the implementation aspects of our proposed algorithm in Section 5.

2. SYSTEM MODEL AND UTILITY SETTING

We consider an overlay cognitive radio wireless network, comprising of L_{PU} PU transmitter $\{\mathrm{PT}_i\}_{i=1}^{L_{\mathrm{PU}}}$ -PU receiver $\{\mathrm{PR}_i\}_{i=1}^{L_{\mathrm{PU}}}$ pairs, with the ℓth pair having a rate requirement of $R_{\mathrm{PU}_\ell,\mathrm{req}}$, and with each pair occupying a unique spectrum band of constant size. In the same network, there are L_{SU} SU transmitter $\{\mathrm{ST}_i\}_{i=1}^{L_{\mathrm{SU}}}$–SU receiver $\{\mathrm{SR}_i\}_{i=1}^{L_{\mathrm{SU}}}$ pairs, with the qth pair having a rate requirement of $R_{\mathrm{SU}_q,\mathrm{req}}$, and seeking to obtain access to one spectrum band occupied by a (PT, PR) pair. The secondary transmitters all are equipped with N antennas and the other transmitters and receivers are equipped with single antenna. We assume that there are T time slots per transmission frame, and each (ST, SR) pair has access to a monetary value C.

Each PT attempts to grant spectrum access to a unique (ST, SR) pair, as determined by the various matching algorithms, in exchange for (i) the ST cooperatively relaying the PT's data to the corresponding PR, and (ii) monetary compensation. In particular, without loss of generality (w.l.o.g), let us consider $(\mathrm{PT}_\ell, \mathrm{PR}_\ell)$, whose transmission is relayed by ST_q during a fraction $\beta_{\ell,q}$ $(0 \leq \beta_{\ell,q} \leq 1)$ of T, whilst also receiving a fraction $\zeta_{\ell,q}$ $(0 \leq \zeta_{\ell,q} \leq 1)$ of C from ST_q, as depicted

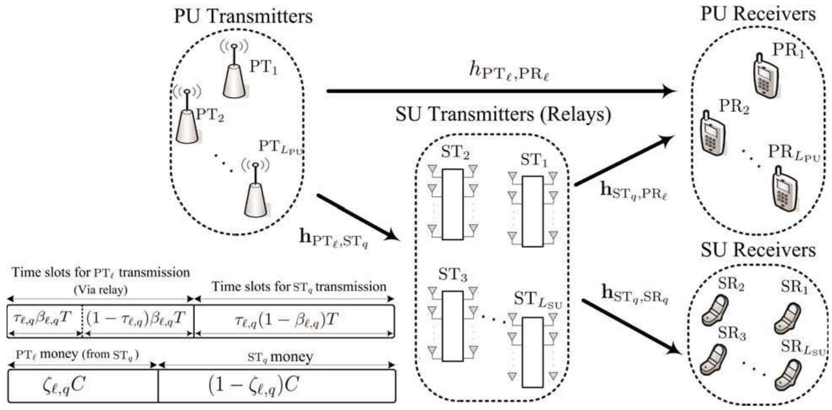

Figure 1: Secondary user and primary user spectrum-access model. The channel and price and time slot allocation numbers are indicated for $(\text{PT}_\ell, \text{PR}_\ell)$ and $(\text{ST}_q, \text{SR}_q)$.

in Fig. 1. We will refer to $\zeta_{\ell,q}$ and $\beta_{\ell,q}$ as the price and time slot allocation numbers respectively, whose exact values will be determined by the matching algorithms described in Section 3.

During the cooperative relaying stage in the initial $\beta_{\ell,q}T$ time slots, a fraction $\tau_{\ell,q}$ $(0 < \tau_{\ell,q} < 1)$ is first allocated for PT_ℓ to broadcast its signal to ST_q and PR_ℓ, thus occurring in the first $\beta_{\ell,q}\tau_{\ell,q}T$ time slots. In the subsequent $\beta_{\ell,q}(1-\tau_{\ell,q})T$ time slots, ST_q will beamforming the PT_ℓ's signal using maximum ratio transmission (MRT) and cooperatively relays the signal from ST_q to PR_ℓ.

PR_ℓ then applies maximum ratio combining (MRC) to the signal received from PT_ℓ in the first $\beta_{\ell,q}\tau_{\ell,q}T$ time slots, and the signal received from ST_q in the subsequent $\beta_{\ell,q}(1-\tau_{\ell,q})T$ time slots. After this cooperative relaying stage, PT_ℓ ceases transmission, allowing ST_q to beamform to SR_q over the spectrum occupied by (PT_ℓ, PR_ℓ) in the final $(1-\beta_{\ell,q})T$ time slots. The ST_q will beamforming its signal using maximum ratio transmission (MRT) and transmit the signal from ST_q to SR_q.

In particular, the received scalar signal from the PT_ℓ at the PR_ℓ in the time slot $\beta_{\ell,q}\tau_{\ell,q}T$ can be written as

$$y_{\text{PR}_{\ell,1}} = \sqrt{P_{\text{PT}_\ell}}\, h_{\text{PT}_\ell,\text{PR}_\ell} x_{\text{PT}_\ell} + n_{\text{PR}_{\ell,1}} \tag{1}$$

where P_{PT_ℓ} is the transmission power at PT_ℓ, $h_{\text{PT}_\ell,\text{PR}_\ell} \sim \mathcal{CN}(0, d^{-\alpha}_{\text{PT}_\ell,\text{PR}_\ell})$ is the Rayleigh channel from PT_ℓ to PR_ℓ, α is the path loss exponent, $d_{\text{PT}_\ell,\text{PR}_\ell}$ is the distance from PT_ℓ to PR_ℓ, x_{PT_ℓ} is the transmitted scalar symbol from the PT_ℓ with $\text{E}[|x_{\text{PT}_\ell}|] = 1$, $n_{\text{PR}_{\ell,1}} \sim \mathcal{CN}(0, \sigma^2)$ is additive white Gaussian noise (AWGN) at the PR_ℓ and σ^2 is the noise variance.

At the ST_q, after applying a $1 \times N$ weight vector $\mathbf{w}_r^\dagger$ to the received signal from the PT_ℓ, the resultant scalar signal at the ST_q in the $\beta_{\ell,q}\tau_{\ell,q}T$ time slot can be written as

$$y_{\text{ST}_q} = \sqrt{P_{\text{PT}_\ell}}\, \mathbf{w}_r^\dagger \mathbf{h}_{\text{PT}_\ell,\text{ST}_q} x_{\text{PT}_\ell} + \mathbf{w}_r^\dagger \mathbf{n}_{\text{ST}_q} \tag{2}$$

where $\mathbf{h}_{\text{PT}_\ell,\text{ST}_q} \sim \mathcal{CN}_{N\times 1}(0, d^{-\alpha}_{\text{PT}_\ell,\text{ST}_q}\mathbf{I}_N)$ is the Rayleigh channel vector from the PT_ℓ to ST_q, $d_{\text{PT}_\ell,\text{ST}_q}$ is the distance from PT_ℓ to ST_q, $\mathbf{n}_{\text{ST}_q}$ is additive white Gaussian noise (AWGN) at the ST_q and $(.)^\dagger$ denotes conjugate transpose.

In the subsequent $\beta_{\ell,q}(1-\tau_{\ell,q})T$ time slot, the ST_q first normalizes the received PT_ℓ's signal by multiplying (2) by the normalization constant $g^{\ell,q}_{\text{ST}} = 1/\sqrt{\mathbf{w}_r^\dagger (P_{\text{PT}_\ell}\mathbf{h}_{\text{PT}_\ell,\text{ST}_q}\mathbf{h}^\dagger_{\text{PT}_\ell,\text{ST}_q} + \sigma^2\mathbf{I}_N)\mathbf{w}_r}$.

The ST_q then amplifies and forwards the normalized signal $g^{\ell,q}_{\text{ST}} y_{\text{ST}_q}$. ST then applies a $N \times 1$ transmit weight vector $\mathbf{w}_{\text{PU}}$ to the normalized PT's signal. The received scalar signal at the PR_ℓ from the ST_q can thus be written as

$$y_{\text{PR}_{\ell,2}} = g^{\ell,q}_{\text{ST-PR}} g^{\ell,q}_{\text{ST}} \mathbf{h}^\dagger{}_{\text{ST}_q,\text{PR}_\ell} \mathbf{w}_{\text{PU}} \mathbf{w}_r^\dagger \mathbf{h}_{\text{PT}_\ell,\text{ST}_q} x_{\text{PT}_\ell} + g^{\ell,q}_{\text{ST-PR}} g^{\ell,q}_{\text{ST}} \mathbf{h}^\dagger{}_{\text{ST}_q,\text{PR}_\ell} \mathbf{w}_{\text{PU}} \mathbf{w}_r^\dagger \mathbf{n}_{\text{ST}_q} + n_{\text{PR}_{\ell,2}} \tag{3}$$

where $\mathbf{h}_{\text{ST}_q,\text{PR}_\ell} \sim \mathcal{CN}_{N\times 1}(\mathbf{0}, d^{-\alpha}_{\text{ST}_q,\text{PR}_\ell}\mathbf{I}_N)$ is the Rayleigh channel vector from ST_q to PR_ℓ, $d_{\text{ST}_q,\text{PR}_\ell}$ is the distance from ST_q to PR_ℓ, and $n_{\text{PR}_{\ell,2}} \sim \mathcal{CN}(0, \sigma^2)$ is additive white Gaussian noise (AWGN) at the PR_ℓ. $g^{\ell,q}_{\text{ST-PR}}$ is the normalization constant, designed to ensure that the total transmit power at the ST_q is constrained, and is given by $g_{\text{ST-PR}}^{\ell,q}=\sqrt{P_{\mathrm{ST}_q}/\mathrm{Trace}(\mathbf{w}_{\mathrm{PU}}\mathbf{w}_{\mathrm{PU}}^{\dagger})}$ where P_{ST_q} is the transmission power at ST_q.

In the time slot $\beta_{\ell,q}\tau_{\ell,q}T$ of the proposed scheme, the ST receives only the PT's signal, and thus the optimal linear weight design is MRC. The received weight $\mathbf{w}_r$ at the ST is thus chosen as $\mathbf{w}_r = \frac{\mathbf{h}_{\mathrm{PT}_\ell,\mathrm{ST}_q}}{\|\mathbf{h}_{\mathrm{PT}_\ell,\mathrm{ST}_q}\|}$ where $\|.\|$ denotes the Frobenius norm. In the time slot $\beta_{\ell,q}(1-\tau_{\ell,q})T$, the ST amplifies and forwards the PT's signal. The transmit weight $\mathbf{w}_{\mathrm{PU}}$ at the ST is chosen according to the principles of MRT as $\mathbf{w}_{\mathrm{PU}} = \frac{\mathbf{h}_{\mathrm{ST}_q,\mathrm{PR}_\ell}}{\|\mathbf{h}_{\mathrm{ST}_q,\mathrm{PR}_\ell}\|}$.

The received scalar signal at the SR_q from the ST_q in the $(1-\beta_{\ell,q})T$ time slot can be written as

$$y_{\mathrm{SR}_q} = g_{\text{ST-SR}}^{\ell,q}\mathbf{h}^{\dagger}{}_{\mathrm{ST}_q,\mathrm{SR}_q,\ell}\mathbf{w}_{\mathrm{SU}}x_{\mathrm{ST}_q} + n_{\mathrm{SR}_q} \tag{4}$$

where $\mathbf{w}_{\mathrm{SU}}$ is the $N\times 1$ transmit weight vector, $\mathbf{h}_{\mathrm{ST}_q,\mathrm{SR}_q,\ell} \sim \mathcal{CN}_{N\times 1}(\mathbf{0}, d_{\mathrm{ST}_q,\mathrm{SR}_q}^{-\alpha}\mathbf{I}_N)$ is the Rayleigh channel vector from ST_q to SR_q while using the PT_ℓ's spectrum, $d_{\mathrm{ST}_q,\mathrm{SR}_q}$ is the distance from ST_q to SR_q, and $n_{\mathrm{SR}_q} \sim \mathcal{CN}(0,\sigma^2)$ is additive white Gaussian noise (AWGN) at the SR_q. $g_{\text{ST-SR}}^{\ell,q}$ is the normalization constant, designed to ensure that the total transmit power at the ST_q is constrained, and is given by $g_{\text{ST-SR}}^{\ell,q}=\sqrt{P_{\mathrm{ST}_q}/\mathrm{Trace}(\mathbf{w}_{\mathrm{SU}}\mathbf{w}_{\mathrm{SU}}^{\dagger})}$.

The transmit weight $\mathbf{w}_{\mathrm{SU}}$ at the ST is chosen according to MRT as $\mathbf{w}_{\mathrm{SU}} = \frac{\mathbf{h}_{\mathrm{ST}_q,\mathrm{SR}_q}}{\|\mathbf{h}_{\mathrm{ST}_q,\mathrm{SR}_q}\|}$. The PR_ℓ then applies MRC to the two received signals, given in (1) and (4) in the first and second time slot respectively, resulting in a received signal to interference noise ratio (SINR) at the PR_ℓ given by

$$\gamma_{\mathrm{PR}_{\ell,q}} = \frac{P_{\mathrm{PT}_\ell}|h_{\mathrm{PT}_\ell,\mathrm{PR}_\ell}|^2}{\sigma^2} + \frac{\gamma_1\gamma_2}{\gamma_1+\gamma_2+1} \tag{5}$$

where $\gamma_1 = \frac{P_{\mathrm{PT}_\ell}|\mathbf{h}_{\mathrm{PT}_\ell,\mathrm{ST}_q}|^2}{\sigma^2}$ and $\gamma_2 = \frac{{g_{\text{ST-PR}}^{\ell,q}}^2 {g_{\mathrm{ST}}^{\ell,q}}^2\|\mathbf{h}_{\mathrm{ST}_q,\mathrm{PR}_\ell}\|^4\|\mathbf{h}_{\mathrm{PT}_\ell,\mathrm{ST}_q}\|^4}{{g_{\text{ST-PR}}^{\ell,q}}^2 {g_{\mathrm{ST}}^{\ell,q}}^2\|\mathbf{h}_{\mathrm{ST}_q,\mathrm{PR}_\ell}\|^4|\mathbf{h}_{\mathrm{PT}_\ell,\mathrm{ST}_q}^{\dagger}|^2+\sigma^2}$ and the received signal to interference noise ratio (SINR) at the SR_q given by $\gamma_{\mathrm{SR}_{\ell,q}} = \frac{{g_{\text{ST-SR}}^{\ell,q}}^2\|\mathbf{h}_{\mathrm{ST}_q,\mathrm{SR}_q,\ell}\|^2}{\sigma^2}$.

Note that the PRs requires $h_{\mathrm{PT}_\ell,\mathrm{PR}_\ell}$ and $g_{\text{ST-PR}}^{\ell,q}g_{\mathrm{ST}}^{\ell,q}\mathbf{h}^{\dagger}{}_{\mathrm{ST}_q,\mathrm{PR}_\ell}\mathbf{w}_{\mathrm{PU}}\mathbf{w}_r^{\dagger}\mathbf{h}_{\mathrm{PT}_\ell,\mathrm{ST}_q}x_{\mathrm{PT}_\ell}$ to perform MRC at PR. $h_{\mathrm{PT}_\ell,\mathrm{PR}_\ell}$ can be obtained via pilot training symbols [5], and the complex scalar $g_{\text{ST-PR}}^{\ell,q}g_{\mathrm{ST}}^{\ell,q}\mathbf{h}^{\dagger}{}_{\mathrm{ST}_q,\mathrm{PR}_\ell}\mathbf{w}_{\mathrm{PU}}\mathbf{w}_r^{\dagger}\mathbf{h}_{\mathrm{PT}_\ell,\mathrm{ST}_q}x_{\mathrm{PT}_\ell}$, is initially transmitted from the ST before the transmission procedure.

In practice, channel state information (CSI) between the ST and SR can be obtained by the classic channel training, estimation, and feedback mechanisms as in [5], while the CSI between the PT and ST and the ST and PR can be obtained as in [6], as we assume that the PU and SU systems cooperate with each other. Finally, in a fading environment, there might be cases where it is difficult for the ST to perfectly estimate instantaneous channels. In such cases,the results obtained in this paper provide upper-bounds for the performance of the proposed scheme in a CR network.

In this paper, we consider the amplify-and-forward (AF) relaying protocol, due to its simple and practical operation, and thus set $\tau_{\ell,q} = \frac{1}{2}$. We note, however, that the proposed algorithm is applicable to any relaying protocol, such as the decode-and-forward or compress-and-forward protocol. The AF gain at ST_q is chosen such that its instantaneous transmission power is constrained to P_{SU_q}.

To evaluate the performance of each (PT, PR) and (ST, SR) pair, we consider the utility function, which comprises of both rate and monetary factors. Specifically, for $(\mathrm{PT}_\ell, \mathrm{PR}_\ell)$, the achievable instantaneous rate is given by [4]

$$R_{\mathrm{PU}_{\ell,q}}(\beta_{\ell,q}) = \frac{\beta_{\ell,q}T}{2}\log_2\left(1+\frac{P_{\mathrm{PT}_\ell}|h_{\mathrm{PT}_\ell,\mathrm{PR}_\ell}|^2}{\sigma^2}+\frac{\gamma_1\gamma_2}{\gamma_1+\gamma_2+1}\right) \tag{6}$$

To allow for both the rate and monetary value to be combined into one utility function, we introduce a variable $\bar{c} \in \mathbb{R}^+$, with unit defined as: rate per unit monetary value. We can thus express the utility for $(\mathrm{PT}_\ell, \mathrm{PR}_\ell)$ as

$$U_{\mathrm{PU}_{\ell,q}}(\beta_{\ell,q}, \zeta_{\ell,q}) = R_{\mathrm{PU}_{\ell,q}}(\beta_{\ell,q}) + \bar{c}\,\zeta_{\ell,q}C\ . \tag{7}$$

For $(\mathrm{ST}_q, \mathrm{SR}_q)$, the achievable instantaneous rate is given by

$$R_{\mathrm{SU}_{q,\ell}}(\beta_{\ell,q}) = (1-\beta_{\ell,q})T\log_2\left(1+\frac{{g^{\ell,q}_{\text{ST-SR}}}^2|\mathbf{h}_{\mathrm{ST}_q,\mathrm{SR}_q,\ell}|^4}{\|\mathbf{h}_{\mathrm{ST}_q,\mathrm{SR}_q,\ell}\|\sigma^2}\right) \tag{8}$$

The utility for $(\mathrm{ST}_q, \mathrm{SR}_q)$ is thus given by

$$U_{\mathrm{SU}_{q,\ell}}(\beta_{\ell,q},\zeta_{\ell,q}) = R_{\mathrm{SU}_{q,\ell}}(\beta_{\ell,q}) - \bar{k}\zeta_{\ell,q}C \tag{9}$$

where $\bar{k} \in \mathbb{R}^+$ is a variable which is defined to allow for both the rate and monetary value to be combined into one utility function, with unit defined as:rate per unit monetary value.

3. PROBLEM FORMULATION

In this section, we describe the optimization problem we aim to address. To proceed, we introduce some notation. We first define the primary and secondary user sets respectively as $\mathcal{P} = \{\mathrm{PU}_\ell = (\mathrm{PT}_\ell, \mathrm{PR}_\ell)\}_{\ell=1}^{L_{\mathrm{PU}}}$ and $\mathcal{S} = \{\mathrm{SU}_q = (\mathrm{ST}_q, \mathrm{SR}_q)\}_{q=1}^{L_{\mathrm{SU}}}$. Moreover, we define a $L_{\mathrm{PU}} \times L_{\mathrm{SU}}$ matching matrix $\mathbf{M}$, with $m_{i,j} = 1$ if PU_i is matched with SU_j, and $m_{i,j} = 0$ otherwise, where the notation $x_{i,j}$ denotes the (i,j)th entry of matrix $\mathbf{X}$. From this matrix, we introduce an injective function $\mu : (\mathcal{P} \cup \mathcal{S}) \to (\mathcal{P} \cup \mathcal{S} \cup \{\varnothing\})$, such that (a) $\mu(\mathrm{PU}_\ell) \in (\mathcal{S} \cup \{\varnothing\})$, (b) $\mu(\mathrm{SU}_q) \in (\mathcal{P} \cup \{\varnothing\})$, and (c) $\mu(\mathrm{SU}_q) = \mathrm{PU}_\ell$ and $\mu(\mathrm{PU}_\ell) = \mathrm{SU}_q$ if $m_{\ell,q} = 1$, for $\ell = 1,\ldots,L_{\mathrm{PU}}$ and $q = 1,\ldots,L_{\mathrm{SU}}$, (d) $\mu(\mathrm{SU}_q) = \varnothing$ if $m_{\ell,q} = 0$, for $\ell = 1,\ldots,L_{\mathrm{PU}}$, and (e) $\mu(\mathrm{PU}_\ell) = \varnothing$ if $m_{\ell,q} = 0$, for $q = 1,\ldots,L_{\mathrm{SU}}$.

We also define an $L_{\mathrm{PU}} \times L_{\mathrm{SU}}$ price allocation matrix $\mathbf{G}$ with $g_{i,j} = \zeta_{i,j}$, and an $L_{\mathrm{PU}} \times L_{\mathrm{SU}}$ time-slot allocation matrix $\mathbf{B}$ with $b_{i,j} = \beta_{i,j}$, and where $g_{i,j} = b_{i,j} = 0$ if $m_{i,j} = 0$. We denote the price and time-slot allocation matrices with continuous elements as $\mathbf{G}^{\mathrm{cont}}$ and $\mathbf{B}^{\mathrm{cont}}$ respectively. Mathematically, this implies that the elements of $\mathbf{G}^{\mathrm{cont}}$ and $\mathbf{B}^{\mathrm{cont}}$ respectively take values from the sets $\{g^{\mathrm{cont}}_{i,j} = \zeta_{i,j} \in \mathbb{R} : 0 \le \zeta_{i,j} \le 1\}$ and $\{b^{\mathrm{cont}}_{i,j} = \beta_{i,j} \in \mathbb{R} : 0 \le \beta_{i,j} \le 1\}$. So our problem here is a matching between $\mathcal{P}$ and $\mathcal{S}$ such that for each primary and secondary user is to ensure their minimum rate requirements are satisfied. When this is achieved, the secondary goal is to maximize their utility functions. To address these issues, we propose a distributed low-complexity algorithm which accounts for selfish users.

4. PROPOSED DISTRIBUTED MATCHING ALGORITHM

In this section, we describe the proposed algorithm which determines spectrum access for each $(\mathrm{PT}, \mathrm{PR})$ and $(\mathrm{ST}, \mathrm{SR})$ pair.

We first describe two scenarios we will be considering in the proposed algorithm, characterized by different assumptions on the received SNR at the transmitters and receivers.

4.1. Complete Received SNR

In the first scenario, PT_ℓ has perfect knowledge of the instantaneous receivedSNRs in $\{\frac{\gamma_{\mathrm{PT}_\ell}|h_{\mathrm{PT}_\ell,\mathrm{PR}_\ell}|^2}{d^\alpha_{\mathrm{PT}_\ell,\mathrm{PR}_\ell}}\}$, $\{\frac{\gamma_{\mathrm{PT}_\ell}|\mathbf{h}_{\mathrm{PT}_\ell,\mathrm{ST}_q}|^2}{d^\alpha_{\mathrm{PT}_\ell,\mathrm{ST}_q}}\}$, $\{\frac{\gamma_{\mathrm{ST}_q}|\mathbf{h}_{\mathrm{ST}_q,\mathrm{PR}_\ell}|^2}{d^\alpha_{\mathrm{ST}_q,\mathrm{PR}_\ell}}\}_{q=1}^{L_{\mathrm{SU}}}$. Moreover, ST_q has perfect knowledge of the instantaneous received SNRs in the expressions $\{\frac{\gamma_{\mathrm{ST}_q}|\mathbf{h}_{\mathrm{ST}_q,\mathrm{SR}_q,\ell}|^2}{d^\alpha_{\mathrm{ST}_q,\mathrm{SR}_q}}\}_{\ell=1}^{L_{\mathrm{PU}}}$. As such, PT_ℓ and ST_q are able to respectively calculate their *instantaneous* rate in (6) and (8).

4.2. Partial Received SNR

In the second scenario, PT_ℓ has knowledge of the average received SNRs in the term $\{\frac{\gamma_{\mathrm{ST}_q}}{d^\alpha_{\mathrm{ST}_q,\mathrm{PR}_\ell}}\}_{q=1}^{L_{\mathrm{SU}}}$ and the instantaneous received SNRs in the terms $\{\frac{\gamma_{\mathrm{PT}_\ell}|h_{\mathrm{PT}_\ell,\mathrm{PR}_\ell}|^2}{d^\alpha_{\mathrm{PT}_\ell,\mathrm{PR}_\ell}}, \frac{\gamma_{\mathrm{PT}_\ell}|\mathbf{h}_{\mathrm{PT}_\ell,\mathrm{ST}_q}|^2}{d^\alpha_{\mathrm{PT}_\ell,\mathrm{ST}_q}}\}_{q=1}^{L_{\mathrm{SU}}}$. Moreover, ST_q has perfect knowledge of the instantaneous received SNRs in the term $\{\frac{\gamma_{\mathrm{ST}_q}|\mathbf{h}_{\mathrm{ST}_q,\mathrm{SR}_q,\ell}|^2}{d^\alpha_{\mathrm{ST}_q,\mathrm{SR}_q}}\}_{\ell=1}^{L_{\mathrm{PU}}}$. As such, PT_ℓ is able to calculate its instantaneous conditional rate, given by the expectation of the rate in (6) with respect to $\{\mathbf{h}_{\mathrm{PT}_\ell,\mathrm{ST}_q}\}_{q=1}^{L_{\mathrm{SU}}}$, while ST_q is able to calculate its *instantaneous* rate in (8).

4.3. Users Preference Lists

Each PT has a preference list of STs which can cooperatively relay the PT's message such that it obtains a rate greater than its minimum rate requirement.

Similarly, each ST has a preference list of PTs which, if it transmits in the spectrum band occupied by the (PT, PR) pair in the list, obtains a rate greater than its minimum rate requirement and a utility greater or equal to zero.

4.4. Proposed Algorithm

The key idea of the proposed algorithm is that each (PT, PR) pair trades with the (ST, SR) pair which provides the highest utility, through both cooperative relaying and monetary payment. This trading will be done by negotiating on the price and time-slot allocation numbers $\{\zeta_{\ell,q}, \beta_{\ell,q}\}_{\ell=1}^{L_{\rm PU}} {}_{q=1}^{L_{\rm SU}}$. We say PT_ℓ makes an *offer* of $(\zeta_{\ell,q}, \beta_{\ell,q})$ to ST_q to imply that PT_ℓ is willing to allow ST_q to transmit, in exchange for ST_q (i) cooperatively relaying PT_ℓ's message with time slot allocation number $\beta_{\ell,q}$ and, (ii) providing a monetary payment with price allocation number $\zeta_{\ell,q}$.

To summarize the main algorithm (MA), each PT will first make an offer to the ST which is first in its preference list. The ST will then check if the offering PT is in it's preference list. If it is, and the ST is already matched with another PT, the ST has two choices: (a) if the offering PT can provide a better utility than the ST's current matching, then the ST will reject its current matching in favor of the new matching,or (b) if the offering PT can not provide a better utility than the ST's current matching, the ST will reject the PT's offer. If the ST is not matched, then the ST will be matched with the offering PT. If the offering PT is not in the ST's preference list, the ST will reject the offering PT. The algorithm will then repeat this procedure with each PT until no more matchings are possible.

Note that if the ST rejects a PT, then PT updates its proposal, and the PT will either (i) decrease its price allocation number by a price step number δ, or (ii) decrease its time slot allocation number by a time slot-step number ϵ, depending on which option maximizes the PT's utility, and assuming a positive price and time-slot allocation number and the minimum data rate requirement for the PT is satisfied.

5. PERFORMANCE AND IMPLEMENTATION ANALYSIS

We now analyze the performance of the proposed algorithm, and consider related implementation issues. We first present some assumptions we will be considering in the analysis. To demonstrate that the (PT, PR) pairs are motivated to participate in the proposed algorithm, we set the minimum rate requirement of each (PT, PR) pair to be the rate of the direct PT to PR link. This is given for $(\mathrm{PT}_\ell, \mathrm{PR}_\ell)$ by $R_{\mathrm{PT}_\ell,\mathrm{PR}_\ell} = T\log_2(1+\frac{\gamma_{\mathrm{PT}_\ell}|h_{\mathrm{PT}_\ell,\mathrm{PR}_\ell}|^2}{d^{\alpha}_{\mathrm{PT}_\ell,\mathrm{PR}_\ell}})$ where $h_{\mathrm{PT}_\ell,\mathrm{PR}_\ell}$ and $d_{\mathrm{PT}_\ell,\mathrm{PR}_\ell}$ denote respectively the channel coefficient and distance from PT_ℓ to PR_ℓ. In this paper, we thus set $R_{\mathrm{PU}_\ell,\mathrm{req}} = R_{\mathrm{PT}_\ell,\mathrm{PR}_\ell}$.

5.1. Utility Performance

In fact, the proposed algorithm can achieve a utility for every matched (PT, PR) pair very close to the centralized optimal algorithm. This can be observed in Fig. 2(a), which plots the average sum-utility of all matched (PT, PR) pairs vs. time-slot step number ϵ for the proposed algorithm, the centralized algorithm, and the random algorithm. Note that the average sum-utility corresponds to the sum over all utilities achieved by the matched (PT, PR) pairs, averaged over the channel realizations, and given by $U_{\mathrm{PU}_\Sigma,\mu} = \sum_{\ell\in\mathcal{P}_\mu} \mathrm{E}[U_{\ell,\mu-\mathrm{ind}(\ell)}(\zeta_{\ell,\mu-\mathrm{ind}(\ell)}, \beta_{\ell,\mu-\mathrm{ind}(\ell)})]$, where $\mathcal{P}_\mu$ corresponds to all the (PT, PR) pairs matched under μ.

We first observe in Fig. 2(b) that for the proposed algorithm, the complete and partial received SNR scenarios achieve very similar performance, despite the different channel assumptions. We next observe that the proposed algorithm (i) achieves a sum-utility comparable with the sum-utility of the centralized algorithm for sufficiently small ϵ, and (ii) performs significantly better than the random matching algorithm.

In practice, the unmatched PTs will transmit directly to their corresponding PRs and thus (PT_ℓ, PR_ℓ) will achieve the rate $R_{\mathrm{PT}_\ell,\mathrm{PR}_\ell}$. However, the unmatched STs will not be able to transmit at all. To remedy this, various modifications to the proposed algorithm can be made, such as integrating a fairness mechanism into the algorithm so each ST has a turn transmitting, though at different times.

5.2. Overhead and Complexity

The proposed algorithm is distributed, and thus incurs significantly less overhead and complexity compared to centralized algorithms. It can be observed from the proposed algorithm that the total number of times the PTs communicates with the STs scales as

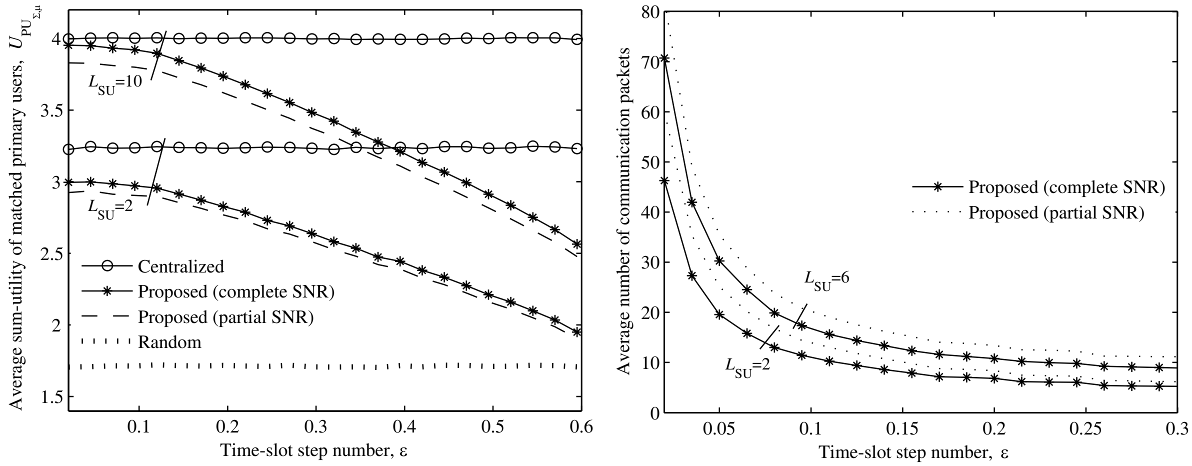

(a) (b)

Figure 2: (a) Average sum-utility of all matched (PT, PR) pairs vs. time slot step-number ϵ. (b) Total number of communication packets vs. ϵ for the complete instantaneous received SNR scenario with $\zeta_{\mathrm{init}} = 0.99$, $\beta_{\mathrm{init}} = 0.99$, $\delta = \epsilon$, $\gamma_{\mathrm{SU}_1} = \dots \gamma_{\mathrm{SU}_{L_{\mathrm{SU}}}} = 25\,\mathrm{dB}$, $L_{\mathrm{PU}} = 2$, $\gamma_{\mathrm{PU}_1} = \gamma_{\mathrm{PU}_2} = 5\,\mathrm{dB}$, $R_{\mathrm{SU,req}} = 0.1$, $\{R_{\mathrm{PU}_\ell,\mathrm{req}} = R_{\mathrm{PT}_\ell,\mathrm{PR}_\ell}\}_{\ell=1}^{L_{\mathrm{PU}}}$, $N = 2$, $\bar{c} = 1$, $\bar{k} = 1$ and $\alpha = 4$.

$$Q \sim L_{\mathrm{PU}} L_{\mathrm{SU}} \left(a \left\lfloor \frac{\zeta_{\mathrm{init}}}{\delta} \right\rfloor + b \left\lfloor \frac{\beta_{\mathrm{init}}}{\epsilon} \right\rfloor \right) \tag{10}$$

where $a, b \in \mathbb{R}^+$. We observe in (10) that the amount of overhead, and thus the number of iterations, decreases with ϵ and δ. We see that the total number of communication packets converge to a constant at sufficiently high ϵ. This is because if ϵ is sufficiently large, the time-slot allocation numbers are updated in the algorithm in such a way that the preference lists for each (PT, PR) and (ST, SR) pair remain unchanged.

We note that the packet length required for communication between the PTs and the STs is very short. In particular, assuming that ζ_{init}, β_{init}, δ and ϵ are initially known to all users, each PT is only required to send *one bit* to the first ST in its preference list indicating an offer, and the corresponding ST only needs to send *one bit* back to the offering PT indicating either acceptance or rejection. As demonstrated in Fig. 2(b), the total number of communication packets for each PT can be designed to be reasonably small, and thus given the short packet lengths, the total running time and amount of overhead from the proposed algorithm can be quite small.

6. CONCLUSION

We proposed a distributed algorithm for spectrum access which guarantees that the PUs' and SUs' rate requirement are satisfied. Numerical analysis also revealed that the distributed algorithm achieves a performance comparable to an optimal centralized algorithm, but with significantly less overhead and complexity.

REFERENCES

1. Niyato, D., E. Hossain, and Z. Han, "Dynamics of multiple-seller and multiple-buyer spectrum trading in cognitive radio networks: A game-theoretic modeling approach," *IEEE Trans. Mobile Comput.*, Vol. 8, No. 4, 1009–1022, Aug. 2009.
2. Ji, Z. and R. Liu, "Multi-stage pricing game for collusion-resistant dynamic spectrum allocation," *IEEE J. Select. Areas Commun.*, Vol. 26, No. 1, 182–191, Jan. 2008.
3. Jayaweera, S. K. and T. Li, "Dynamic spectrum leasing in cognitive radio networks via primarysecondary user power control games," *IEEE Trans. Wireless Commun.*, Vol. 8, No. 6, 3300–3310, Jun. 2009.
4. Laneman, J. N., D. N. C. Tse, and G. W. Wornell, "Cooperative diversity in wireless networks: Efficient protocols and outage behavior," *IEEE Trans. Inform. Theory*, Vol. 50, No. 12, 3062–3080, Dec. 2004.
5. Tong, B. S. L. and M. Dong, "Pilot-assisted wireless transmissions: general model, design criteria, and signal processing," *IEEE Signal Processing Mag.*, Vol. 21, No. 6, 12–25, Nov. 2004.
6. Jovicic, A. and P. Viswanath, "Cognitive radio: An information-theoretic perspective," *IEEE Trans. Inform. Theory*, Vol. 55, No. 9, 3945–3958, Sep. 2009.

Distributed Allocation of the Spectrum Sensing Durations for Cooperative Cognitive Radios

O. van den Biggelaar, **J.-M. Dricot**, **P. de Doncker**, **and F. Horlin**
Université Libre de Bruxelles, Belgium

Abstract— In cognitive radio systems, the sparse assigned frequency bands are opened to secondary users. We consider the sensing of the frequency spectrum for cognitive radios, based on energy detection. It has been shown that the sensing reliability can be improved by using several cooperating cognitive radios that exchange their individual sensing information to a coordinator node. The coordinator node combines the received information in order to make a decision about the primary network presence. In this paper, we propose a decentralized Q-learning algorithm to share the sensing time among the cognitive radios in a way that maximizes the throughputs of the radios. Numerical results show that the algorithm converges faster to the same throughputs as those obtained with a reference algorithm.

1. INTRODUCTION

The scarcity of available radio spectrum frequencies, densely allocated by the regulators, represents a major bottleneck in the deployment of new wireless services. Cognitive radios have been proposed as a new technology to overcome this issue [1]. For cognitive radio use, the assigned frequency bands are opened to secondary users, provided that interference induced on the primary licensees is negligible. Cognitive radios are established in two steps: the radios firstly sense the available frequency bands and secondly communicate using these bands.

To tackle the fading phenomenon — typical in wireless propagation — when sensing the frequency spectrum, cooperative spectrum sensing has been proposed to take advantage of the spatial diversity in wireless channels [2, 3].

In cooperative spectrum sensing, the secondary cognitive nodes send the results of their individual observations of the primary signal to a coordinator node through specific control channels. The coordinator node then combines the received information in order to make a decision about the primary network presence. Each cognitive node observes the primary signal during a certain sensing time, which should be chosen high enough to ensure the correct detection of the primary emitter but low enough so that the node has still enough time to communicate. In literature [4, 5], the sensing times used by the cognitive nodes are generally assumed to be identical and allocated by a central authority.

In this paper, a decentralized Q-learning algorithm is proposed to share the sensing time among the cognitive radios in a way that maximizes the throughputs of the radios. The multiple cognitive radios (the agents) self-adapt by directly interacting with the environment in real time and by properly utilizing their past experience. They aim to distributively learn an optimal strategy to maximize their throughputs.

The rest of this paper is organized as follows: in Section 2, we formulate the problem of sensing time allocation in the secondary network. In Section 3, we present the decentralized Q-learning algorithm used to solve the sensing time allocation problem. In Section 4, we present numerical results allowing to compare its performances with those of a reference algorithm.

2. PROBLEM FORMULATION

2.1. Cooperative Spectrum Sensing

We consider a cognitive radio cell made of $N + 1$ nodes including a central base station. Each node j performs an energy detection of the received primary signal in additive white Gaussian noise, using M_j samples [6].

It is shown in [7] that if the M_j are large enough, then the local probability of false alarm (i.e., the probability that the locally received energy is superior to a threshold λ when no primary signal is present) is given by:

$$P_{F_j} = Q\left(\frac{\lambda - M_j}{\sqrt{2M_j}}\right) \forall j, \tag{1}$$

where $Q(x) = \int_x^{+\infty} \frac{1}{\sqrt{2\pi}} e^{-\frac{t^2}{2}} \mathrm{d}t$. The local detection probability (i.e., the probability that the locally received energy is superior to a threshold λ when the primary signal is present) is given by:

$$P_{D_j} = Q\left(\frac{\lambda - M_j(1+\gamma_j)}{\sqrt{2M_j(1+2\gamma_j)}}\right) \ \forall j, \tag{2}$$

where γ_j is the local signal-to-noise ratio (SNR).

By combining Equations (1) and (2), the false alarm probability can be expressed with respect to the detection probability:

$$P_{F_j} = Q\left(Q^{-1}(P_{D_j})\sqrt{(1+2\gamma_j)} + \gamma_j\sqrt{\frac{M_j}{2}}\right). \tag{3}$$

where $Q^{-1}(x)$ is the inverse function of $Q(x)$.

As illustrated on Figure 1, we consider that every T_H seconds, each node sends a one bit value representing the local hard decision about the primary network presence to the base station. The base station combines the received bits in order to make a global decision for the nodes. The base station decision is sent back to the node as a one bit value. The duration of the communication with the base station is assumed to be negligible compared to the duration T_H of a time slot. In this paper, we focus on the logical-OR fusion rule at the base station but the other fusion rules could be similarly analyzed. Under the logical-OR fusion rule, the global detection probability P_D and the global false alarm probability P_F depend respectively on the local detection probabilities P_{D_j} and false alarm probabilities P_{F_j} [4]:

$$P_D = 1 - \prod_{j=1}^{N}(1 - P_{D_j}), \tag{4}$$

and

$$P_F = 1 - \prod_{j=1}^{N}(1 - P_{F_j}). \tag{5}$$

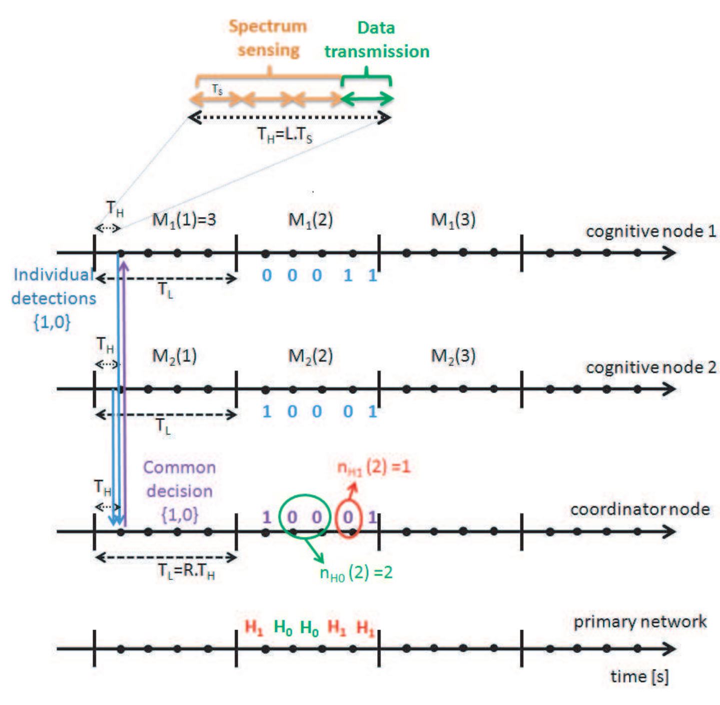

Figure 1: Time diagram of the sensing time allocation algorithm.

Given a target global detection probability $\bar{P}_D$, we thus have:

$$P_{D_j} = 1 - (1 - \bar{P}_D)^{1/N}, \tag{6}$$

and Equation (3) can be rewritten as:

$$P_{\mathrm{F_j}} = Q\left(Q^{-1}\left(1 - (1 - \bar{P}_D)^{1/N}\right)\sqrt{(1 + 2\gamma_j)} + \gamma_j\sqrt{\frac{M_j}{2}}\right). \tag{7}$$

2.2. Throughput of a Secondary User

A secondary user performs data transmission during the time slots that have been identified as free by the base station. In each of these time slots, $M_j T_S$ seconds are used by the secondary user to sense the spectrum, where T_S denote the sampling period. The remaining $T_H - M_j T_S$ seconds are used for data transmission. The secondary user average throughput R_j is given by the sum of the throughput obtained when the primary network is absent and no false alarm has been generated by the base station plus the throughput obtained when the primary network is present but has not been detected by the base station [8]:

$$R_j = \frac{T_H - M_j T_S}{T_H} P_{H_0}(1 - P_F) C_{H_0,j} + \frac{T_H - M_j T_S}{T_H}(1 - P_{H_0})(1 - P_D) C_{H_1,j} \tag{8}$$

where P_{H_0} denotes the probability that the primary network is absent, $C_{H_0,j}$ represents the data rate of the secondary user when the primary network is absent and $C_{H_1,j}$ represents the data rate of the secondary user when the primary network is present. The target detection probability $\bar{P}_D$ is required to be close to 1 since the cognitive radios should not interfere with the primary network; moreover, P_{H_0} is usually close to 1 and $C_{H_1,j} < C_{H_0,j}$ due to the interference from the primary network [8]. Therefore, (8) can be approximated by:

$$R_j \approx \frac{T_H - M_j T_S}{T_H} P_{H_0}(1 - P_F) C_{H_0,j} \tag{9}$$

Equation (9) shows that there is a trade-off for the choice of the sensing window length M_j: on the one hand, if M_j is high then user j will not have much time to perform his data transmission and R_j will be low. On the other hand, if all the users use low M_j values, then the global false alarm probability in (9) will be high and all the average throughputs will be low. In this paper we rely on the secondary users themselves to determine their individual best sensing window lengths.

3. *Q*-LEARNING ALGORITHM

In this paper, we use a multi-agent Q-Learning algorithm to allocate the sensing times of the secondary users. Each secondary user is an agent that aims to learn an optimal sensing time allocation policy by interacting with the environment.

The Q-Learning algorithm keeps a quality information (the Q-value) for every state-action couple (s, k) it has tried. The Q-value $Q^s_{jk}(t)$ represents how high the expected quality of an action k is for user j when the environment is in state s, at iteration t of the algorithm [9].

Each learning iteration $t \in \{1, \ldots, K\}$ consists of the following sequence:

1. The agent senses the state $s(t) = s \in \mathcal{S}$ of the environment. In our problem, the state $s(t)$ of the environment is defined by the number $n_{H_0}(t-1)$ of time slots that have been identified as free by the base station during the $(t-1)$th learning period.
2. Based on s and its accumulated knowledge, the agent chooses and performs an action $a(t) = k \in \mathcal{A}$. In our problem, the action $a(t)$ selected by secondary user j is the duration $M_j(t)$ of the sensing window to be used during the T_L seconds of the learning iteration t.
3. Because of the performed action, the state of the environment is modified. The new state is denoted $s(t+1) = s' \in \mathcal{S}$. The transition from s to s' generates a reward $r_j(t) = r \in \mathbb{R}$ for the agent. In our problem, the reward function used by is the throughput $R_j(t)$ realized by node j during the learning period t. In this paper, Boltzmann distribution [10] is used for the selection of action k by agent j when the environment is in state s:

$$P\,(\text{user } j \text{ chooses action } k \mid \text{state } s) = \frac{e^{\frac{Q^s_{jk}(t)}{\epsilon}}}{\sum\limits_{l \in \mathcal{A}} e^{\frac{Q^s_{jl}(t)}{\epsilon}}} \tag{10}$$

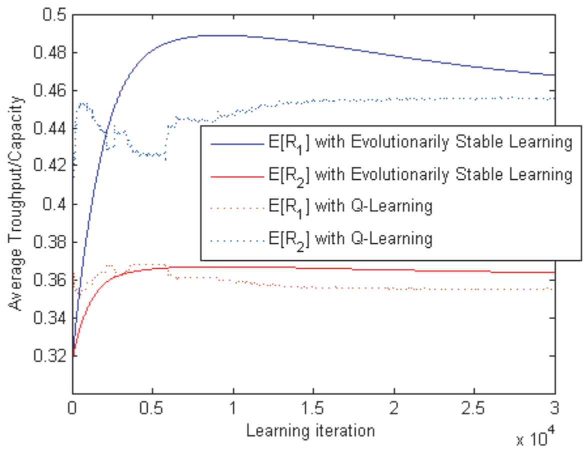

Figure 2: Evolution of the average normalized throughputs obtained with the Q-learning and Evolutionary Stable Learning algorithms.

where ϵ is a parameter called *temperature*, which controls the randomness for exploration of the learning algorithm, i.e., how often the algorithm should take a random action instead of the best action it knows. A high value of ϵ favours exploration of new good actions over exploitation of existing knowledge, while a low value of ϵ reinforces what the algorithm already knows instead of trying to find new better actions. The exploration-exploitation trade-off is typical for learning algorithms. In this paper, we consider online learning (i.e., at every time step the agents should display intelligent behaviors) which requires a low ϵ value.

4. The agent uses r and s' to update the accumulated knowledge that made him choose action k when the environment was in state s. The update is handled by the rule $Q_{jk}^{s}(t+1) = (1-\alpha)Q_{jk}^{s}(t) + \alpha(r + \delta \max_{l \in \mathcal{A}} Q_{jl}^{s'}(t))$ where α is the learning rate and δ is the discount rate of the algorithm. The learning rate $\alpha \in [0,1]$ is used to control the linear blend between the previously accumulated knowledge and the newly received quality information. The discount rate $\delta \in [0,1]$ is used to control how much the success of a later action l should be brought back to the earlier action k that led to the choice of l.

4. NUMERICAL RESULTS

Unless otherwise specified, we consider $N = 2$ nodes able to transmit at the same maximum data rates $C_{H_0,1} = C_{H_0,2}$. Their sensing channel gains are $\gamma_1 = 0\,\text{dB}$ and $\gamma_2 = -10\,\text{dB}$. This scenario could represent an outdoor primary network sensed by a first outdoor node and a second indoor node subject to stronger signal fading than the first node.

It is assumed that the primary network transition probabilities are $p_{00} = 0.9$, $p_{01} = 0.1$, $p_{10} = 0.1$ and $p_{11} = 0.9$. The target detection probability is $\bar{P}_D = 0.95$.

We consider $L = 10$ samples per time slot and $R = 10$ time slots per learning periods. The Q-Learning algorithm runs during $K = 30000$ iterations which is the typical number of iterations required for the convergence of the algorithm. It is implemented with a learning rate $\alpha = 0.5$, a discount rate $\delta = 0.7$ and a temperature $\epsilon = 0.1$.

Figure 2 shows the evolution of the normalized throughputs of the radios obtained with the proposed Q-Learning (QL) algorithm and compares this evolution with the one obtained with the Evolutionarily Stable Learning (ESL) algorithm proposed in [8] for the distributed allocation of the sensing times.

It is observed that the algorithms give the same normalized throughputs asymptotically when $t \to \infty$. It is also observed that the QL algorithm converges faster toward its final throughputs than the ESL algorithm: in average, the QL algorithm requires 20 times less iterations to reach its asymptotic throughputs with a $\pm 10\%$ error margin than the ESL algorithm.

5. CONCLUSION

In this paper, we have proposed a decentralized Q-Learning algorithm to solve the problem of the allocation of the sensing times in a cooperative cognitive network in a way that maximizes the throughputs of the cognitive radios. Compared to a centralized allocation algorithm, the proposed allocation technique minimizes the need for exchange of control information between the cognitive nodes and the coordinator node. Numerical results have shown that the algorithm converges faster to the same throughputs as those obtained with a reference algorithm.

REFERENCES

1. Weiss, T. A. and F. K. Jondral, "Spectrum pooling: An innovative strategy for the enhancement of spectrum efficiency," *IEEE Radio Communications*, Vol. 42, No. 3, S8–S14, 2004.
2. Sendonaris, A., E. Erkip, and B. Aazhang, "User cooperation diversity. Part I. System description," *IEEE Transactions on Communications*, Vol. 51, No. 11, 1927–1938, Nov. 2003.
3. Bazerque, J. A. and G. B. Giannakis, "Distributed spectrum sensing for cognitive radio networks by exploiting sparsity," *IEEE Transactions on Signal Processing*, Vol. 58, No. 3, 1847–1862, Mar. 2010.
4. Liang, Y.-C., Y. Zeng, E. Peh, and A. T. Hoang, "Sensing-throughput tradeoff for cognitive radio networks," *IEEE International Conference on Communications*, Jun. 2007.
5. Stotas, S. and A. Nallanathan, "Sensing time and power allocation optimization in wideband cognitive radio networks," *GLOBECOM 2010, 2010 IEEE Global Telecommunications Conference*, 1–5, Dec. 2010.
6. Alouini, M. S., F. F. Digham, and M. K. Simon, "On the energy detection of unknown signals over fading channels," *Proceedings of the IEEE International Conference on Communications*, Vol. 5, 3575–3579, May 2003.
7. Ma, J., G. Zhao, and Y. Li, "Soft combination and detection for cooperative spectrum sensing in cognitive radio networks," *IEEE Transactions on Wireless Communications*, Vol. 7, No. 11, 4502–4507, Nov. 2008.
8. Wang, B., K. J. R. Liu, and T. C. Clancy, "Evolutionary cooperative spectrum sensing game: How to collaborate?," *IEEE Transactions on Communications*, Vol. 58, No. 3, 890–900, Mar. 2010.
9. Millington, I., *Artificial Intelligence for Games*, 612–628, Morgan Kaufmann Publishers, 2006.
10. Sutton, R. S. and A. G. Barto, *Introduction to Reinforcement Learning*, 1st Edition, MIT Press, Cambridge, MA, USA, 1998.
11. Li, M., Y. Xu, and J. Hu, "A Q-learning based sensing task selection scheme for cognitive radio networks," *International Conference on Wireless Communications and Signal Processing*, Nov. 2009.

Collaborative Data Dissemination in Opportunistic Vehicular Networks

Yong Li[1], **Zhaocheng Wang**[1], **Depeng Jin**[1], **Lieguang Zeng**[1], **and Sheng Chen**[2,3]

[1]Tsinghua National Laboratory for Information Science and Technology
Department of Electronic Engineering, Tsinghua University, Beijing 100084, China
[2]Electronics and Computer Science, Faculty of Physical and Applied Sciences
University of Southampton, Southampton SO17 1BJ, UK
[3]Faculty of Engineering, King Abdulaziz University, Jeddah 21589, Saudi Arabia

Abstract— Future opportunistic vehicular networks offers viable means for collaborative data dissemination by high-capacity device-to-device communication. This is a highly challenging problem because a) mobile data items are heterogeneous in size and lifetime; b) mobile users have different interests to different data; and c) dissemination participants have limited storages. We study collaborative data dissemination under these realistic opportunistic vehicular network conditions and formulate the optimal data dissemination as a submodular function maximisation problem with multiple linear storage constraints. We then propose a heuristic algorithm to solve this challenging problem, and provide its theoretical performance bound. The effectiveness of our approach is demonstrated through simulation using real vehicular traces.

1. INTRODUCTION

Mobile Internet access is getting increasingly popular for providing various services and applications including video, audio and images. Cisco forecasts that mobile traffic will be growing at an annual rate of 131% in 2011, and will reach over 6.3 exabytes per month in 2015 [1]. Two-thirds of the world's mobile data traffic will be video by 2015. Mobile cellular networks provide the most popular method of mobile access today. With the increase of mobile services and user demands, however, cellular networks will very likely be overloaded and congested in the near future. To cope with this explosive growth in traffic demands, offloading mobile data from the overloaded cellular networks to WiFi networks is currently considered [2, 3]. The development of opportunistic vehicular networks offers a viable alternative to mobile data offloading. With an increasing number of vehicles equipped with devices to provide device-to-device communication capacities, large scale vehicular ad hoc networks will soon be available. Many applications in vehicular networks will then appear, including high speed Internet access and multimedia content sharing [4]. Since a vehicular network is highly mobile and sometimes sparse, it is hard to maintain a connected network to distribute the content. However, opportunistic contact between vehicles offers high bandwidth communication capacity for content dissemination, known as opportunistic vehicular content dissemination [5].

Collaborative data dissemination in opportunistic vehicular networks is highly challenging for several reasons: 1) the network contains heterogeneous vehicles, in terms of data preference, 2) the data items are multi-types of different delay sensitivities and sizes, and 3) the data dissemination participants' storages are limited in size. The existing works [6–8] did not consider these realistic conditions. We study collaborative data dissemination in realistic opportunistic vehicular networks, and our contribution is threefold: a) formulate the optimal data dissemination with heterogeneous data items and vehicles of limited storage as a submodular function maximisation with linear constraints; b) propose a heuristic algorithm to solve this NP-hard problem and derive the performance bound of this algorithm; and c) demonstrate the effectiveness of our algorithm in challenging opportunistic vehicular network environments through real trace-driven simulations.

2. PROBLEM FORMULATION

In an opportunistic data dissemination system, the service provider chooses some vehicles that are willing to participate in data dissemination, and transmit data to the chosen vehicles. These vehicles then further propagate the data to other users that subscribe the data by device-to-device opportunistic communication. As illustrated in Figure 1, there are two types of vehicles in the system, data dissemination *participator* and data *subscriber*. A participator may store more than one data item, depending on the buffer and data sizes, and a subscriber may be interested in different data items. In general, there are $N + H$ vehicles in the system, labelled as $i \in \{1, 2, \ldots, N + H\}$,

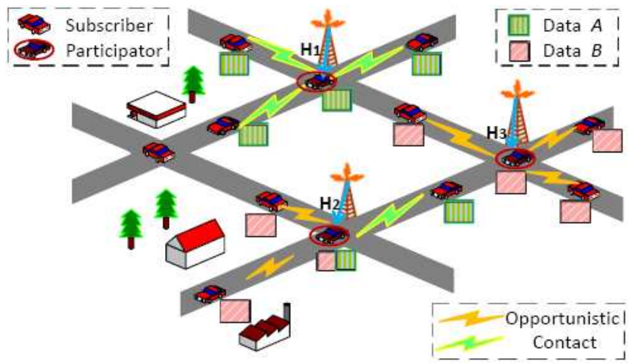

Figure 1: Collaborative data dissemination in the opportunistic vehicular network.

while the traffics of I different data items are labelled as $\mathcal{I}$. For any $k \in \mathcal{I}$, its data length is l_k. As the storage in each vehicle is limited, user s can at most buffer L_s size of data items. We use $\mathcal{H}$ to denote the set of vehicles that are willing to participate the data dissemination, and $\mathcal{N}$ for the other subscriber vehicles, where $|\mathcal{H}| = H$ and $|\mathcal{N}| = N$. Any subscriber in $\mathcal{N}$ may be interested in a data item, and obtains it through device-to-device communication from the participators. Thus, we associate subscriber i is with a vector $\mathbf{w}_i = [w_{i,1}\ w_{i,2} \ldots w_{i,I}]^{\mathrm{T}}$, where $w_{i,k}$ defines the user's interest in data item k and $w_{i,k} = 0$ means that user i is completely not interested in data k. Without loss of generality, $\sum_{k=0}^{I} w_{i,k} = 1$ for $\forall i$. Vehicles can communicate with each other only when they move to within the transmission range, which is called a communication contact. The communication contact between vehicles i and j is assumed to obey the Poisson process with a contact rate $\gamma_{i,j}$. Poisson distributed contact rate has been validated to fit well to real vehicular traces and is widely used to model opportunistic vehicular systems [9–11].

Let $\mathbf{X} = (x_{s,k})$, $s \in \mathcal{H}$, $k \in \mathcal{I}$, be the storage allocation policy, in which $x_{s,k} \in \{0, 1\}$ and $x_{s,k} = 1$ indicates that participator s stores item k in its buffer. A lifetime T_k is assigned to each item k, and all the users will discard this data at deadline T_k. If subscribers do not receive a required item from dissemination participators after the lifetime is expired, they will try to get it directly from the service provider. Therefore, we should maximise the expectation of the disseminated data size in all the subscribers, and this objective function can be expressed as $U(\mathbf{X}) = \sum_{k\in\mathcal{I}} l_k \sum_{i\in\mathcal{N}} d_{i,k}$, where $d_{i,k}$ is the probability that user i receives data k before deadline T_k. As more than one participator may store item k, we define the *dissemination opportunity* metric for $s \in \mathcal{H}$, $i \in \mathcal{N}$ and $k \in \mathcal{I}$, as $t_{s,i,k}$, which is the probability that user i obtains content k from participator s. Because the contact rate between s and i follows the Poisson distribution with rate $\gamma_{s,i}$ and the contact event is independent of user interests, we model the dissemination opportunity as the Poisson process with rate $\gamma_{s,i} w_{i,k}$. Hence, $t_{s,i,k} = 1 - e^{-x_{s,k}\gamma_{s,i} w_{i,k} T_k}$ and $d_{i,k} = 1 - \prod_{s\in\mathcal{H}} (1 - t_{s,i,k})$. The expectation of the total disseminated data size can then be written as:

$$U(\mathbf{X}) = \sum\nolimits_{k\in\mathcal{I}} l_k \sum_{i\in\mathcal{N}} \left(1 - e^{-w_{i,k} T_k \sum_{s\in\mathcal{H}} x_{s,k}\gamma_{s,i}}\right). \tag{1}$$

For the subset of $\mathcal{H} \times \mathcal{I}$, $\mathbf{A} \subseteq \mathcal{H} \times \mathcal{I}$, we define the storage allocation policy $\mathbf{X}$ as

$$\mathbf{X} = F(\mathbf{A}),\ \text{s.t.}\ x_{s,k} = 1 \quad \text{if} \quad (s, k) \in \mathbf{A} \quad \text{and} \quad x_{s,k} = 0 \quad \text{if} \quad (s, k) \notin \mathbf{A}.$$

Since $F(\mathbf{A})$ is a bijection, the utility function $U(\mathbf{X})$ over the subset $\mathbf{A} \subseteq \mathcal{H} \times \mathcal{I}$ is

$$\widehat{U}(\mathbf{A}) = U(F(\mathbf{A})) = \sum\nolimits_{k\in\mathcal{I}} l_k \sum\nolimits_{i\in\mathcal{N}} \left(1 - e^{-w_{i,k} T_k \sum_{s:(s,k)\in\mathbf{A}} \gamma_{s,i}}\right). \tag{2}$$

Thus, maximising the system's expected disseminated data size for all the items and over all the subscribers can be specified as the following optimisation problem

$$\max U(\mathbf{X})\ \text{ or }\ \max \widehat{U}(\mathbf{A}),\ \text{s.t.}\ x_{s,k} \in \{0, 1\}, \forall s \in \mathcal{H},\ k \in \mathcal{I},\ \text{ and }\ \sum\nolimits_{k\in\mathcal{I}} l_k x_{s,k} \le L_s,\ \forall s \in \mathcal{H},\ \tag{3}$$

where $\sum_{k\in\mathcal{I}} x_{s,k} l_k \le L_s$ is the buffer size constraint of dissemination participator s.

3. DATA DISSEMINATION ALGORITHM

Submodularity is found in various problems [12–14]. A function f defined on subsets of the universe $\mathbf{C}$ is called *submodular*, if and only if $f(\mathbf{A} \cup x) - f(\mathbf{A}) \geq f(\mathbf{B} \cup x) - f(\mathbf{B})$ holds for $\forall \mathbf{A} \subseteq \mathbf{B} \subseteq \mathbf{C}$ and $\forall x \in \mathbf{C} \backslash \mathbf{B}$. Due to space limitation, we offer the following theorem without proof.

Theorem 1. The system utility function $\widehat{U}(\mathbf{A})$ is a submodular function on $2^{\mathcal{H} \times \mathcal{I}}$, and the problem (3) is NP-complete.

Thus, the problem (3) is an NP-hard submodular function maximisation with multiple linear constraints (MLCs). The computer science community has studied this type of optimisation [12–15]. In [12], an algorithm is proposed to solve this problem by an approximation, but it has a very high complexity. Taking the system with 5 participators and 10 data items as an example, the computation time for the first step of Rounding Procedure in [12] is more than 10^{15}. We propose a greedy based heuristic algorithm to solve this problem by allocating storage one by one.

When one more copy of an item is stored in a participator, which meets the constraints, the objective function is enhanced. The gain in the objective function is generally different for different choices of item and participator. As our first greedy strategy, we select the items and participators that maximise the gain on the objective function at each stage, that is, select (s_0, k_0) as

$$(s_0, k_0) = \arg \max_{(s,k) \in \mathbf{P}} \left(\widehat{U}(\mathbf{A} \cup (s,k)) - \widehat{U}(\mathbf{A}) \right), \tag{4}$$

where $\mathbf{A}$ is the set of chosen data items and participators, and $\mathbf{P}$ is the set of possible solutions that satisfy the storage constraint. The length of each data is also important because, although an item may offer a large gain, it may also have a huge length such that other items cannot be stored. Our second greedy strategy is to calculate the gain per unit data length for each choice of item and participator, and select the pair that maximises this per-unit-length gain, that is, select

$$(s_0, k_0) = \arg \max_{(s,k) \in \mathbf{P}} \frac{\widehat{U}(\mathbf{A} \cup (s,k)) - \widehat{U}(\mathbf{A})}{l_k}. \tag{5}$$

Our heuristic algorithm, listed in Algorithm 1, performs both these two greedy strategies and chooses the better result from the two solutions. Algorithm 1 is a pseudo-polynomial-time algorithm with the complexity $O(H^3 I^2 N)$, which is acceptable in practice. We analyse the performance bound of this algorithm in the following theorem. Space limitation precludes the proof.

Theorem 2. Denote the optimal solution of the problem (3) by $\mathbf{OPT} = \arg \max_{\mathbf{A} \in \mathbf{Q}} \widehat{U}(\mathbf{A})$, where $\mathbf{Q} \subseteq 2^{\mathcal{H} \times \mathcal{I}}$ is the feasible solution set. The solution obtained by Algorithm 1, $\mathbf{OPT}^*$, satisfies

$$\widehat{U}(\mathbf{OPT}^*) \geq \frac{1}{2}\left(1 - e^{-\frac{L-\mu}{L}}\right)\widehat{U}(\mathbf{OPT}), \text{ where } L = \sum\nolimits_{s \in \mathcal{H}} L_s \text{ and } \mu = (H-1) \cdot \max_{k \in \mathcal{I}} l_k.$$

Algorithm 1 Heuristic algorithm for data dissemination.

Initialise $m = 0$ and $\mathbf{A}_0 = \emptyset$;
while $m = 0$ or $\widehat{U}(\mathbf{A}_m) - \widehat{U}(\mathbf{A}_{m-1}) > 0$ **do**
$m = m + 1$; $(s_m, k_m) = \arg \max_{(s,k) \in \mathbf{P}} \left(\widehat{U}(\mathbf{A}_{m-1} \cup \{(s,k)\}) - \widehat{U}(\mathbf{A}_{m-1}) \right)$; $\mathbf{A}_m = \mathbf{A}_{m-1} \cup \{(s_m, k_m)\}$;
end while
Initialise $j = 0$ and $\mathbf{B}_0 = \emptyset$;
while $j = 0$ or $\widehat{U}(\mathbf{B}_j) - \widehat{U}(\mathbf{B}_{j-1}) > 0$ **do**
$j = j + 1$; $(s_j, k_j) = \arg \max_{(s,k) \in \mathbf{P}} \frac{\widehat{U}(\mathbf{B}_{j-1} \cup \{(s,k)\}) - \widehat{U}(\mathbf{B}_{j-1})}{l_k}$; $\mathbf{B}_j = \mathbf{B}_{j-1} \cup \{(s_j, k_j)\}$;
end while
if $\widehat{U}(\mathbf{A}_m) > \widehat{U}(\mathbf{B}_j)$ **then**
$\mathbf{OPT}^* = \mathbf{A}_m$;
else
$\mathbf{OPT}^* = \mathbf{B}_j$;
end if
Return $\mathbf{OPT}^*$ and $\widehat{U}(\mathbf{OPT}^*)$;

4. SIMULATION RESULTS

The performance of our **Heuristic Algorithm** is compared with the following schemes: 1) **Random Algorithm**, in which each participator chooses the data items randomly to fill its buffer until no more item can be stored; 2) **Homogeneous Algorithm** [8], where the system allocates the buffer based on the assumption that all participators have the same storage size and the lengths of all data items are identical; and 3) **SFM Algorithm** [12], which uses some approximation algorithms to maximise a submodular set function subject to MLCs. Our evaluation was conducted on two realistic vehicular mobility traces, *Shanghai* trace [16] and *Beijing* trace, which record the positions of vehicles carrying GPS devices. In *Beijing* trace, we utilised the GPS devices to collect the taxi locations and timestamps of 2700 participating taxis, and used GPRS modules to report the records every one minute for moving taxis. In the simulation, a node updated its contact rates with other nodes in real-time, based on the up-to-date contact counts since the network started, and we used halftime of the trace to obtain the contact rates of each node pairs. We randomly chose 10% of the vehicles as the participators and used the rest as the subscribers. We set the number of data items as 35 in *Shanghai* trace and 50 in *Beijing* trace. The sizes of data items were generated randomly and uniformly in the range of [50 kB, 150 kB], while the data lifetimes followed the uniform distribution in [0, $2T_a$ s], where T_a is the average data lifetime. The participator buffer sizes were randomly and uniformly generated in [0, $2l_a$ kB], where l_a is the average buffer size. User interests to different data items followed the exponential distribution with an expectation of 20.

The results for *Shanghai* trace are shown in Figure 2, where the dashed curve indicates the

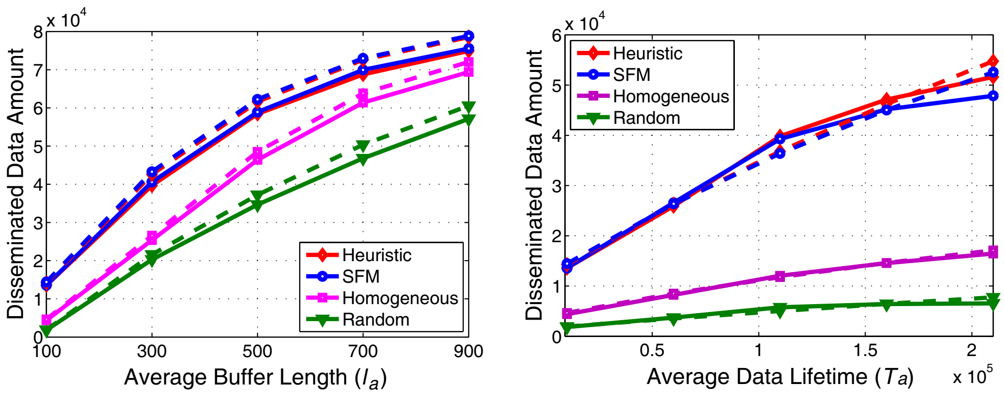

(a) (b)

Figure 2: Results of different algorithms for *Shanghai* trace with (a) the fixed average data lifetime of 10000 s and variable average buffer size, and (b) the fixed buffer size of 100 kB and variable average data lifetime, where dashed curves are theoretical results and solid curves are simulation results.

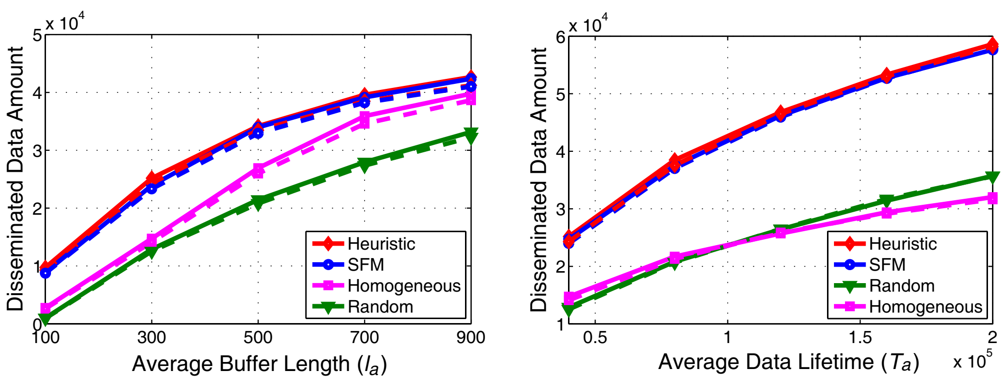

(a) (b)

Figure 3: Results of different algorithms for *Beijing* trace with (a) the fixed average data lifetime of 40000 s and variable average buffer size, and (b) the fixed average buffer size of 300 kB and variable average data lifetime, where dashed curves are theoretical results and solid curves are simulation results.

theoretical disseminated data size calculated by each algorithm and the solid curve is obtained by simulating the system with the buffer allocation strategy of each algorithm. The accuracy of our formulated problem is validated by the fact that the theoretical and simulation results are very close. Figure 2(a) shows that, with a fixed average data lifetime and different average buffer sizes, our Heuristic algorithm achieves almost the same performance of the SFM algorithm, and it outperforms the Random and Homogeneous algorithms considerably. The results under a fixed average buffer size and different average data lifetimes are shown in Figure 2(b). It can be seen that, for the average lifetime larger than 10000 s, our Heuristic algorithm even achieves about 2% to 9% higher data amount than the SFM algorithm. Moreover, our Heuristic algorithm dramatically outperforms the Random and Homogeneous algorithms. The results using *Beijing* trace are shown in Figure 3. Again, the simulation results agree with the theoretical results, and similar observations to those for *Shanghai* trace can be drawn. For *Beijing* trace, our Heuristic algorithm achieves a slightly better performance than the SFM algorithm.

The above results confirm that our Heuristic algorithm performs much better than the Homogeneous algorithm, which does not consider the heterogeneous features of data length and buffer size, and the Random algorithm. Most significantly, our Heuristic algorithm achieves almost the same or slightly better performance in comparison with the SFM algorithm, which is not very piratical due to its very high computational complexity. This demonstrates the effectiveness of our approach.

5. CONCLUSIONS

We have studied the collaborative mobile data dissemination in a realistic opportunistic vehicular network environment, where the network is heterogeneous, in terms of the disseminated data being multi types with different delay sensitivities and lengths as well as the participators' storages being limited with difference sizes. By formulating this challenging problem as a submodular function maximisation, we have designed an efficient heuristic algorithm to allocate the buffer. Simulation results have demonstrated that our algorithm achieves almost the same performance as the very high-complexity SFM algorithm, traditionally used to solve this type of challenging problems.

REFERENCES

1. Cisco visual networking index: Global mobile data traffic forecast update, 2010–2015, Feb. 2011. http://www.cisco.com/en/US/solutions/collateral/ns341/ns525/ns537/ns705/ns827/white_paper_c11-520862.html.
2. Lee, K., I. Rhee, J. Lee, Y. Yi, and S. Chong, "Mobile data offloading: How much can WiFi deliver?" *ACM SIGCOMM Computer Communication Review*, Vol. 40, No. 4, 425–426, 2010.
3. Balasubramanian, A., R. Mahajan, and A. Venkataramani, "Augmenting mobile 3G using WiFi," *Proc. 8th Int. Conf. Mobile Systems, Applications, and Services*, 209–222, June 15–18, San Francisco, CA, 2010.
4. Johnson, M., L. De Nardis, and K. Ramchandran, "Collaborative content distribution for vehicular ad hoc networks," *Proc. 44th Allerton Conf. Communication, Control, and Computing*, 751–760, Monticello, IL, Sept. 27–29, 2006.
5. Câmara, D., N. Frangiadakis, F. Filali, and C. Bonnet, "Vehicular delay tolerant networks," M. M. Cruz-Cunha and F. Moreira, Eds., *Handbook of Research on Mobility and Computing: Evolving Technologies and Ubiquitous Impacts*, 356–367, IGI Global, 2011.
6. Hu, L., J.-Y. Le Boudec, and M. Vojnoviae, "Optimal channel choice for collaborative ad-hoc dissemination," *Proc. 29th IEEE INFOCOM*, 1–9, San Diego, CA, Mar. 14–19, 2010.
7. Han, B., P. Hui, V. S. Ali Kumar, M. V. Marathe, G. Pei, and A. Srinivasan, "Cellular traffic offloading through opportunistic communications: A case study," *Proc. 5th ACM Workshop Challenged Networks*, 31–38, Chicago, IL, Sept. 20–24, 2010.
8. Reich, J. and A. Chaintreau, "The age of impatience: Optimal replication schemes for opportunistic networks," *Proc. 5th Int. Conf. Emerging Networking Experiments and Technologies*, 85–96, Rome, Italy, Dec. 1–4, 2009.
9. Lee, K., Y. Yi, J. Jeong, H. Won, I. Rhee, and S. Chong, "Max-contribution: On optimal resource allocation in delay tolerant networks," *Proc. 29th IEEE INFOCOM*, 1–9, San Diego, CA, Mar. 14–19, 2010.
10. Gao, W. and G. Cao, "User-centric data dissemination in disruption tolerant networks," *Proc. 30th IEEE INFOCOM*, 3119–3127, Shanghai, China, Apr. 10–15, 2011.
11. Khouzani, M. H. R., S. Sarkar, and E. Altman, "Maximum damage malware attack in mobile wireless networks," *Proc. 29th IEEE INFOCOM*, 1–9, San Diego, CA, Mar. 14–19, 2010.

12. Kulik, A., H. Shachnai, and T. Tamir, "Maximizing submodular set functions subject to multiple linear constraints," *Proc. 20th Annual ACM-SIAM Symp. Discrete Algorithms*, 545–554, New York, Jan. 4–6, 2009.
13. Leskovec, J., A. Krause, C. Guestrin, C. Faloutsos, J. VanBriesen, and N. Glance, "Cost-effective outbreak detection in networks," *Proc. 13th ACM SIGKDD Int. Conf. Knowledge Discovery and Data Mining*, 420–429, San Jose, CA, Aug. 12–15, 2007.
14. Sviridenko, M., "A note on maximizing a submodular set function subject to a knapsack constraint," *Operations Research Letters*, Vol. 32, No. 1, 41–43, 2004.
15. Vondrák, J., "Optimal approximation for the submodular welfare problem in the value oracle model," *Proc. 40th Annual ACM Symp. Theory of Computing*, 67–74, Victoria, Canada, May 17–20, 2008.
16. Zhu, H., L. Fu, G. Xue, Y. Zhu, M. Li, and L. Ni, "Recognizing exponential inter-contact time in VANETs," *Proc. 29th IEEE INFOCOM*, 1–5, San Diego, CA, Mar. 14–19, 2010.

Ultra Thin Metamaterial Absorbers Using Electric Field Driven LC (ELC) Resonator Structure

Somak Bhattacharyya and Kumar Vaibhav Srivastava
Department of Electrical Engineering, Indian Institute of Technology, Kanpur, India

Abstract— The aim of this paper is to construct ultra thin absorbers using metamaterials in C-band. An Electric Field Driven LC (ELC) structure has been proposed and its equivalent LC circuit combination has been shown. The simulation of the proposed structure using Ansoft HFSS shows that absorption occurs at 6.46 GHz with absorbance of 98.24% with S_{11} of -17.55 dB. The frequency where absorption occurs is reduced significantly as compared to previously reported structure. The proposed structure can be further reduced in area to provide a more compact structure which reduces the extra metallic strip in the outer side. The capacitor value can be changed by incorporating changes in the proposed structure which shows the absorbance of 99.2% at 6.70 GHz. Thus, the size reduction of the ELC element is possible with slight increase of frequency where the absorption occurs.

1. INTRODUCTION

Microwave absorbers play a crucial role in stealth technology [1], where reduction of Radar Cross-Section [2] is one of the major challenges. To make thin absorber at microwave frequencies, metamaterials [3] have been used where the thickness as well as size can be reduced significantly. SRR-based metamaterials are first used as absorbers [4], but the wave has to travel all along the length of the elements. Later, by using periodic metallic wires and SRRs, Landy et al. [5] proposed a structure where the wave has to travel much shorter distance. Li et al. [6] has suggested metamaterial absorbers using the Electric Field Driven LC (ELC) resonator structure, which is explained in [7].

In this paper, an ELC driven metamateral absorber structure has been proposed, where the capacitance value has been increased and hence the resonance frequency reduces to 6.46 GHz from 9.92 GHz [6]. This structure suffers from fabrication point of view, where more area is needed; but the difficulty can be overcome if one uses the modified structure as discussed in this paper. The modification leads to the absorbance of 99.2% at 6.70 GHz. Thus, the frequency at which absorbance occurs is increasing slightly at the cost of compactness.

2. DESIGN OF THE STRUCTURE

The front view of the basic unit cell structure of the proposed structure is shown in Fig. 1(a). The direction of electric field, magnetic field and wave propagation in the structure is also shown. The absorbance can be found out as shown in Equation (1) [5], where $A(\omega)$, $|S_{11}(\omega)|^2$ and $|S_{21}(\omega)|^2$ are the absorbance, reflected power and transmitted power respectively at an angular frequency ω.

$$A(\omega) = 1 - |S_{11}|^2 - |S_{21}|^2 \tag{1}$$

The structure consists of two layers [6], with the upper layer consisting of an array of ELC resonators [7] which are responsible for electric resonance and the back layer made up of copper sheet. These two layers are separated by a dielectric substrate FR-4 (relative permittivity of 4.4 and dielectric loss tangent of 0.02) with thickness of 1 mm. The metal used in this structure is copper with conductivity of 5.8×10^7 S/m. The dimension of the cell is $a = 5$ mm, $d = 3.6$ mm, $l = 1.5$ mm, $w = 0.4$ mm, and $g = 0.2$ mm with the thickness of the copper film of 0.035 mm. Since the structure is backed by copper sheet, $|S_{21}| = 0$ and thus $A(\omega) = 1 - |S_{11}|^2$. Thus, by reducing the reflection from the structure, absorbance can be maximized.

The equivalent L-C circuit of the proposed structure is shown in Fig. 1(b). In the equivalent structure, there are two identical capacitances C are in parallel with each other and hence the net capacitance value increases as compared to the ELC resonator structure as discussed in [7]. However, at the same time the effective inductance value slightly comes down than [7]. So, this leads to the reduction in the frequency at which absorption occurs.

The simulation of the structure is carried out in the FEM-based solver Ansoft HFSS software where proper boundary conditions are given. The top and bottom side of the structure in Fig. 1(a) have been assigned as PEC boundary while the right and left side of the structure have been

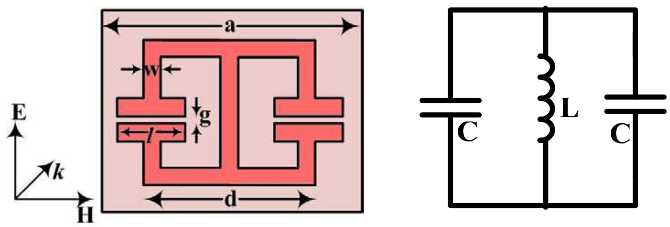

Figure 1: (a) Proposed ELC resonator structure. (b) Equivalent L-C circuit.

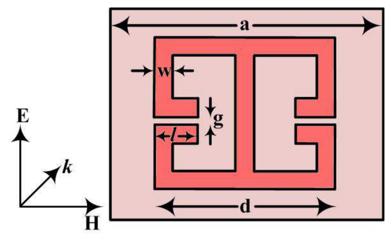

Figure 2: Proposed modified ELC structure.

assigned as PMC boundary. This enables the simulation of array structure of the unit cell. The waveports are suitably defined in the structure at the front and back side respectively to evaluate the reflected power from the structure. Due to the metal backing, $|S_{21}| = 0$.

The value of capacitance in Fig. 1(a) can be modified where the extra metallic patches are removed and hence the structure size is becoming compact in nature as shown in Fig. 2. The other dimensions remain constant while $l = 0.95$ mm is taken. This leads to decrease of the effective area of the metal patch and hence the decrease of capacitance value. But, this also leads to a slight increase of the resonance frequency as compared to the structure defined in Fig. 1(a). The same boundary condition is used to simulate the new structure in HFSS.

3. SIMULATED RESULTS

The simulation of the first proposed structure shows a dip in the plot of S_{11} to -17.56 dB at 6.46 GHz as shown in Fig. 3(a). This corresponds to absorbance value $A(\omega)$ of 98.24% at 6.46 GHz as shown in Fig. 3(b) as calculated from Equation (1). Thus, the structure will behave as absorber at frequency of 6.46 GHz.

The simulation in the modified structure shows that the minima of S_{11} and maxima of $A(\omega)$ take place at 6.70 GHz, where these values are -19.6 dB and 99.2% respectively as shown in Fig. 4(a) and Fig. 4(b) respectively.

The normalized input impedance z of the structure is given as [8] in Equation (2a). Since $|S_{21}| = 0$, this equation is reduced to the form as shown in Equation (2b). So, the real part of the normalized impedance should be unity and the imaginary part of the impedance should be null at the frequency where the absorption takes place. The plot in Fig. 5 shows that the real and imaginary parts are unity and null respectively at 6.70 GHz to ensure absorption at this frequency.

$$z = \sqrt{\frac{(1+S_{11})^2 - S_{21}^2}{(1-S_{11})^2 - S_{21}^2}} \tag{2a}$$

$$z = \frac{1+S_{11}}{1-S_{11}} \tag{2b}$$

The size of the unit cell is scaled to change the frequency of absorption varying in C-band. The dimensions of the metallic patches of the unit cell can be scaled by a factor k so that the frequency of absorption can vary from the obtained one. A scaling factor k of 0.8 and 1.2 respectively yields absorption at 7.9 GHz and 5.74 GHz respectively with absorbance of 85.64% and 95.34% respectively as shown in Fig. 6.

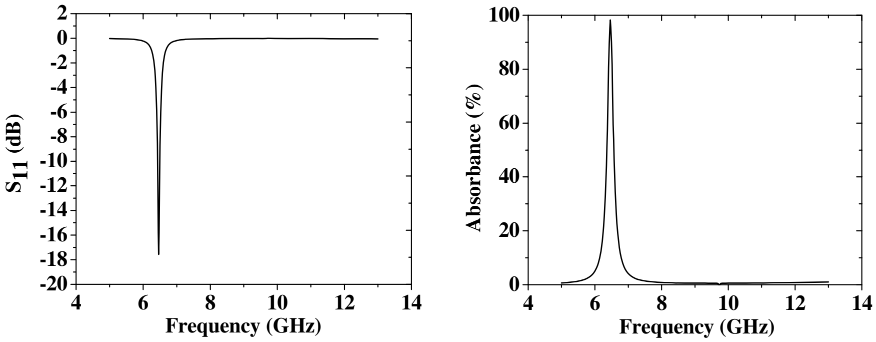

(a) (b)

Figure 3: (a) S_{11} plot and (b) absorbance plot for the proposed structure shown in Fig. 1(a).

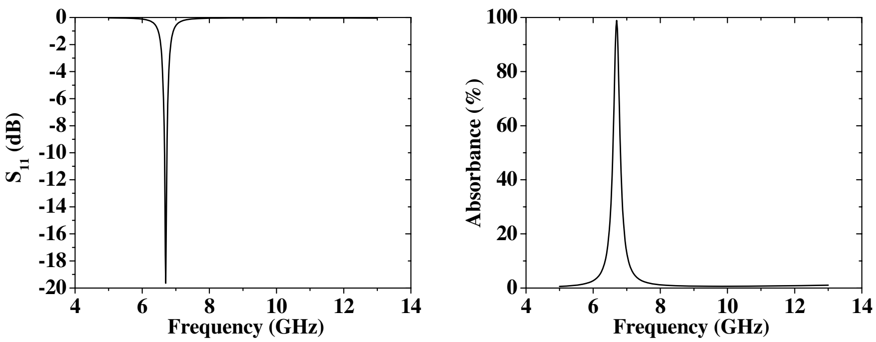

(a) (b)

Figure 4: (a) S_{11} plot and (b) absorbance plot for the modified ELC Structure shown in Fig. 2.

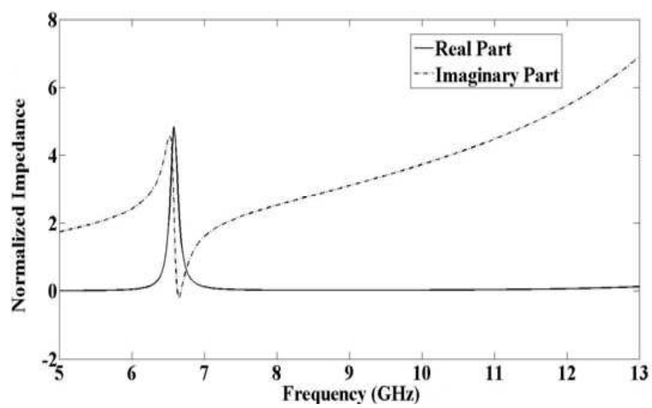

Figure 5: Impedance plot of the modified structure.

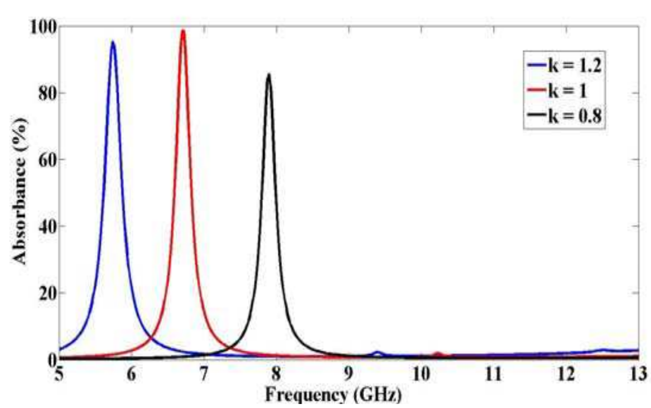

Figure 6: Absorbance as a function of frequency for different scale factors k.

4. CONCLUSIONS

The simulation result shows that microwave absorber can be made at C-band with ELC resonating structures, where the incident electromagnetic wave has to travel across the thickness of the FR-4 substrate; thus making advantage of using such structures instead of conventional metamaterials structure. The resonating frequency comes down to 6.46 GHz and 6.70 GHz respectively as compared to 9.92 GHz as mentioned in [6]. Also, the absorption criterion is supported by calculating input impedance which shows the matching of impedances at 6.70 GHz. The scaling of the unit cell leads to a shift of frequency where absorption occurs. Experiments should be carried out to validate the result obtained by using the simulations.

The structure can be used as a multiband absorber provided different scale factors of the dimensions of the metallic patches of the unit cell can be used in array. If a 3×3 array is used with dimensions scaled as 1.2, 1 and 0.8 respectively, the structure will resonate at 5.74 GHz, 6.7 GHz and 7.9 GHz respectively. So, in the C-band, the structure can be used as multiband absorber. If the resonant frequencies can be made closer to each other, then there will be broadband absorption by using the modified structure.

ACKNOWLEDGMENT

The authors want to acknowledge all the staffs of Microwave Circuit Laboratories for their continuous support and IIT Kanpur institute for the financial support.

REFERENCES

1. Bahret, W. F., "The beginning of stealth technology," *IEEE Transactions on Aerospace and Electronic Systems*, Vol. 29, No. 4, 1377–1385, Oct. 1993.
2. Skolnik, M., *RADAR Handbook*, McGraw Hill, 2nd Edition, Vol. 11, 1–30, 1990.
3. Smith, D. R., W. J. Padilla, D. C. Vier, S. C. Nemat-Nasser, and S. Schultz, "Composite medium with simultaneously negative permeability and permittivity," *Physical Review Letters*, Vol. 84, No. 18, 4184–4187, May 2000.
4. Bilotti, F., L. Nucci, and L. Vegni, "An SRR-based microwave absorber," *Microwave and Optical Technology Letters*, Vol. 48, No. 11, 2171–2175, Nov. 2006.
5. Landy, N. I., S. Sajuyigbe, J. J. Mock, D. R. Smith, and W. J. Padilla, "Perfect metamaterial absorber," *Physical Review Letters*, 207402, May 23, 2008.
6. Li, H., L. H. Yuan, B. Zhou, X. P. Shen, Q. Cheng, and T. J. Cui, "Ultrathin multiband gigahertz metamaterial absorbers," *Journal of Applied Physics*, Vol. 110, 014909, 2011.
7. Schurig, D., J. J. Mock, and D. R. Smith, "Electric-field-coupled resonators for negative permittivity metamaterials," *Applied Physics Letters*, Vol. 88, 041109, 2006.
8. Smith, D. R., D. C. Vier, T. Koschny, and C. M. Soukoulis, "Electromagnetic parameter retrieval from inhomogeneous metamaterials," *Physical Review E*, Vol. 71, 036617, 2005.

Comparison of Ultra-wideband Radar Target Classification Methods Based on Complex Natural Resonances

M. Khodjet-Kesba, K. Chahine, K. El Khamlichi Drissi, and K. Kerroum
LASMEA UMR 6602 UBP/CNRS, 24 Avenue des Landais, 63177 Aubière Cedex, France

Abstract— The principal objective of automatic target recognition (ATR) is to identify the target from UWB radar returns. In intelligent vehicles, ATR can be a solution to identify pedestrians, vehicles, traffic signs, etc. Typically radar ATR relies on classifying the characteristics of the target obtained from the backscattered signal. In this paper, we apply Matrix Pencil Method (MPM) to extract complex natural resonances (CNRs) from the late time part of the backscattered field, which is characteristic of the studied target and can be used for its recognition and identification. Next, we compare three classification methods of CNRs: support vector machine (SVM), K-nearest neighbor (KNN) and Naive Bayes classification.

1. INTRODUCTION

In intelligent vehicles, ATR can be a solution to identify pedestrians, vehicles, traffic signs, etc. When a target is illuminated by ultra-wideband signals, the scattered transient response in the time domain is composed from two successive parts [1]. First, an impulsive part, corresponding to the early time response, comes from the direct reflection of the incident wave on the object surface. Next, during the late time, the oscillating part arises from resonance phenomena of the target. In the case where targets are perfect conductors, resonances occur outside the object and correspond to surface creeping waves.

Currently, there exist several techniques based on the analysis of the late time impulse response to extract the poles of resonance such as: Fourier Transform, MUltiple Signal Classification (MUSIC), Estimation of Signal Parameters via Rotational Invariance Techniques (ESPRIT), Prony's method, etc. One of the most efficient and accurate extraction method of resonance poles is the Matrix Pencil Method [2].

Radar ATR relies on classifying the characteristics of the target obtained from the backscattered signal. In the literature we can find many algorithms used for classification [3]. In this paper, we examine three methods which are commonly used for classification: Naive Bayes, K-NN and SVM.

Simulations are conducted by using three metallic canonical objects: thin wire, sphere and cylinder.

A database containing the CNRs extracted from a noiseless signal is used to train the classifiers, we take different sizes of the canonical objects to construct this database. As test examples we use the CNRs extracted from a noisy signal. The comparison is made in terms of classification accuracy.

The reminder of the paper is organized as follows: Section 2 presents the Matrix Pencil Method. Section 3 introduces the classification methods used in this paper, and in Section 4 we present the simulation results and discussion of results. The last Section 5 gives the conclusions related to this study.

2. MATRIX PENCIL METHOD

The Singularity Expansion Method (SEM) introduced by Baum [4] provides a convenient technique that expresses the late time response of various scatterers in terms of a finite sum of exponentially attenuated sinusoids as:

$$h_r(t) = \sum\nolimits_r R_r e^{S_r t} \tag{1}$$

- R_r is the residue associated with each natural pole,
- S_r is the rth pole of the target: $S_r = \sigma_r + j\omega_r$,
- σ_r is the damping factor,
- $\omega_r = j2\pi f_r$ with f_r the natural frequency.

The MPM is applied to the impulse response in the late time instants $y_L(t)$ of a target illuminated by a broadband electromagnetic wave. After the sampling procedure, it can be written as follows:

$$y_r\left(kT_s\right) = h_r\left(kT_s\right) + b_r(kT_s) \approx \sum\nolimits_{n=1}^{N} R_n z_n^k + b_r(kT_s) \tag{2}$$

with

$$\begin{aligned} R_n &= |a_n|\, e^{j\varphi_n} \quad n = 1, 2, \ldots, N &(3)\\ z_n &= e^{S_n T_s} = e^{(\sigma_r + j\omega_r)T_s} \quad n = 1, 2, \ldots, N. &(4)\end{aligned}$$

The MPM is performed in two stages. The first stage consists in resolving Hankel's matrix using Singular Value Decomposition (SVD) in order to determine the number of poles N and the value of resonance poles z_n:

$$(Y_r) = \begin{pmatrix} y_r(0) & y_r(1) & \ldots & y_r(L) \\ y_r(1) & y_r(2) & \ldots & y_r(L+1) \\ \vdots & \vdots & \vdots & \vdots \\ y_r(K-L-1) & y_r(K-L) & \ldots & y_r(K-1) \end{pmatrix} \tag{5}$$

where Y_r is of dimensions $(K-L) \times (L+1)$ and L is the "Pencil" parameter.

Once N and z_n are known, the residues R_n are solved by using the following least square equation:

$$\begin{pmatrix} y(0) \\ y(1) \\ \vdots \\ y(K-1) \end{pmatrix} = \begin{pmatrix} 1 & 1 & \ldots & 1 \\ z_1 & z_2 & \ldots & z_N \\ \vdots & \vdots & \vdots & \vdots \\ z_1^{(K-1)} & z_2^{(K-1)} & \ldots & z_N^{(K-1)} \end{pmatrix} \begin{pmatrix} R_1 \\ R_2 \\ \vdots \\ R_N \end{pmatrix}. \tag{6}$$

Note that the impulse response is represented by N poles and residues.

3. SUPERVISED CLASSIFICATION

Supervised classification algorithms enable to assign a class label for each input example. Given a training data set of the form $(x_i,\, y_i)$, where $x_i \in \Re^n$ is the ith example and $y_i \in \{1, \ldots, K\}$ is the ith class label, the main objective is to find a learning model Λ that correspond to $\Lambda(x_i) = y_i$ for new unknown examples.

3.1. Naive Bayes

This classifier is based on the Bayes' theorem and the maximum a posteriori hypothesis [5].

Let $x = (x_1, \ldots, x_N)$ be an N-dimensional instance which has no class label. Our goal is to build a classifier to predict its unknown class label. Let $C = \{C_1, \ldots, C_K\}$ be the set of the class labels. $P(C_k)$ is the prior probability of $C_k (k = 1, \ldots, K)$; $P(x|C_k)$is the conditional probability of the evidence x if the hypothesis C_K is true. We have to find the class that maximizes $P(C_k|x)$. The class C_k for which $P(C_k|x)$ is maximized is called the maximum a posteriori hypothesis. By using the Bayes' theorem we obtain:

$$P(C_k \,|\, x) = \frac{P(x \,|\, C_k)\; P(C_k)}{P(x)} \tag{7}$$

A naive Bayes classifier assumes that the value of a particular feature of a class is unrelated to the value of any other feature, so that:

$$P(x \,|\, C_k) = \prod\nolimits_{j=1}^{N} P(x_j \,|\, C_k). \tag{8}$$

3.2. K-NN

K-Nearest Neighbor is based on the principle that the instances within a dataset will generally exist in close proximity to other instances that have similar properties. If the instances are tagged with a classification label, then the value of the label of an unclassified instance can be determined by observing the class of its nearest neighbors [6]. To classify an unknown example, the distance from that example to every other training example is measured. Usually the Euclidean distance criterion is used. A Euclidean distance between any pair $x_1 = (x_{1,1}, \ldots, x_{1,k})$ and $x_2 = (x_{2,1}, \ldots, x_{2,k})$ of instances is defined as:

$$d(x_1, x_2) = \sqrt{\sum\nolimits_{j=1}^{k} (x_{1,j} - x_{2,j})^2}. \tag{9}$$

3.3. Support Vector Machine

Support vector machine (SVM) maps the input vectors to a higher dimensional space where a maximal separating hyper plane is constructed [7]. Two parallel hyper planes are constructed on each side of the hyper plane separating the data. The maximum distance between the parallel planes is known as the margin. SVM maximizes the margin and thereby creates the largest possible distance between the separating hyper plane and the examples in the training set on either side of it.

Given a training set of sample-label pairs (x_i, y_i), with features x, labels y and $i = 1, \ldots, K$, the Support Vector Machines are constructed from the following mathematical optimization procedure:

$$\begin{aligned} &\text{minimize}_{w,b,\xi} \left[\frac{1}{2}\left(w^T w\right) + C \sum\nolimits_{i=1}^{K} \xi_i \right] \\ &\text{subject to } y_i \left(w^T \phi\left(x_i\right) + b \right) \geq 1 - \xi_i, \quad \xi_i \geq 0 \end{aligned} \tag{10}$$

where w is the decision plane orientation vector, b is the bias, ξ_i represents the margin slack variable, ϕ is the mapping function and C is the penalty parameter of the error term.

SVM were primarily designed for binary classification problems, but it can be used in multi classification problems, for that, we use the "one versus the rest" approach. In our work, we used a radial kernel, where the parameters γ and C are optimized by means of a grid search.

4. SIMULATION RESULTS

The backscattered fields of the targets are computed by using electromagnetic commercial simulation (TIME-FEKO). The field is obtained in the time domain and the incidence is normal. A Gaussian pulse with duration of 0.45 ns is used as an excitation plane wave, which corresponds to a wideband frequency.

Figure 1(a) shows the pairs of complex conjugate poles extracted from the late time response of the three canonical objects using the MPM.

Table 1: Classification accuracy of Naive Bayes, K-NN, and SVM.

Classifier	Naive Bayes	K-NN	SVM
SNR = 15 dB	**73.33%**	**73.33%**	**86.67%**
SNR = 20 dB	**73.33%**	**86.67%**	**93.33%**
SNR = 25 dB	**80%**	**93.33%**	**100%**

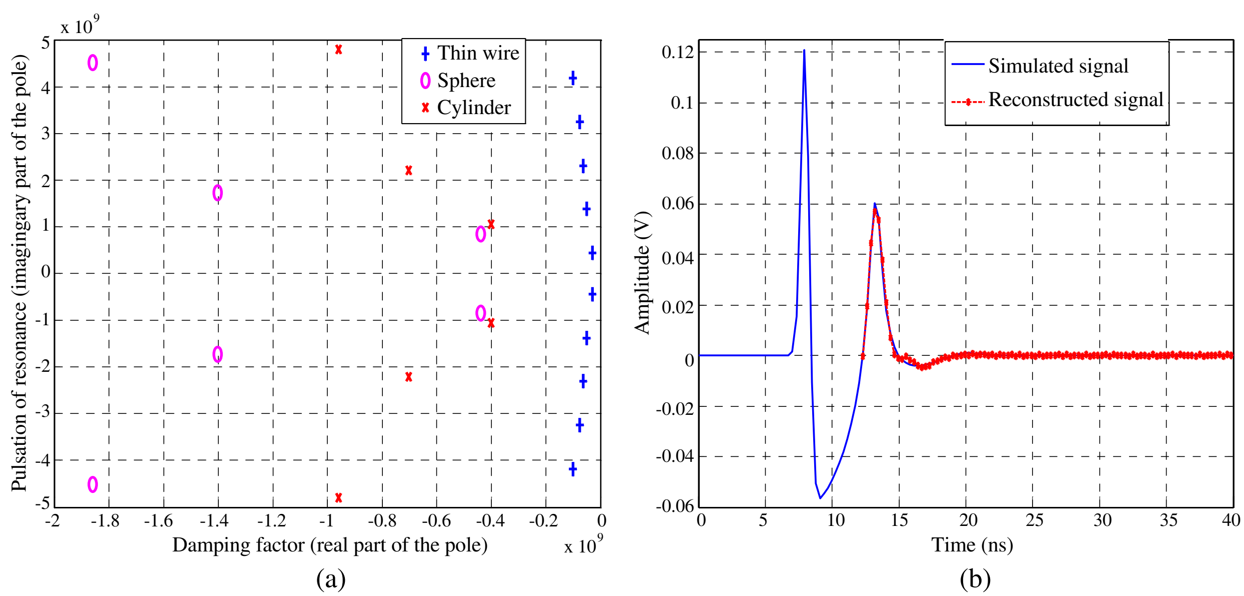

Figure 1: (a) Mapping of natural poles for the three canonical objects. (b) Simulated signal compared with reconstructed signal by MPM with SNR = 20 dB of a sphere (radius = 0.3 m).

To obtain the training data, we have used five examples of different sizes for each perfectly electric conducting target: thin wire (length: 1 m to 3 m), sphere (radius: 0.1 m to 0.5 m) and cylinder (length: 0.5 m to 1 m, radius: 0.1 m to 0.25 m). The database is filled in with damping factors (real part of poles) and positive pulsation of resonances (imaginary part of the poles).

To obtain the testing data, we have used the same targets, and we have added a noise to the temporal signal before applying the MPM, then we have taken only the dominant poles. A reconstructed signal by MPM with SNR = 20 dB of the late time part of the field scattered by a sphere (radius = 0.3 m) is shown in Figure 1(b).

Table 1 shows the results of the three classification methods: Naïve Bayes, K-NN and SVM. The results indicate that the three classification methods are successful in the identification procedure. SVM gives the best results, with accuracy up to 100% for SNR = 25 dB. K-NN performs well, the obtained results are found to be between the other methods. The Naive Bayes classifier is less accurate than the other methods, due to the fact that our database is not very large.

5. CONCLUSIONS

In this paper, the comparison of the classifiers is done on the basis of their classification accuracy. Results indicate that target discrimination based on the natural frequencies of ultra wideband radar targets represent a good solution to automatic target recognition.

The extrapolation related to real targets is expected to allow generation of unique signature associated to each target.

The application of the three classifiers Naïve Bayes, K-NN and SVM has given good results. The best accuracy is obtained by using SVM method. Also it requires only a dozen examples for training. K-NN is an easy technique to implement and it performs well. It is possible to improve the accuracy of Naive Bayes classifier by increasing the size of the database.

Future work will be devoted to increase the size of the database with new canonical objects (cube, strip, etc), complex objects (combination of canonical objects), and dielectric objects.

ACKNOWLEDGMENT

This work has been supported by Gyeonggi Technology Development Program by a grant (I09200) funded by Gyeonggi Province.

REFERENCES

1. Chauveau, J, N. de Beaucoudrey, and J. Saillard, "Characterization of perfectly conducting targets in resonance domain with their quality of resonance," *Progress In Electromagnetics Research,* Vol. 74, 69–84, 2007.
2. Sarkar, T. K. and O. Pereira, "Using the Matrix Pencil Method to estimate the parameters of a sum of complex exponentials," *IEEE Ant. and Prop. Mag.*, Vol. 37, No. 1, 48–55, 1995.
3. Wu, X., V. Kumar, J. R. Quinlan, J. Ghosh, Q. Yang, H. Motoda, G. J. McLachlan, A. Ng, B. Liu, P. S. Yu, Z.-H. Zhou, M. Steinbach, D. J. Hand, and D. Steinberg, "Top 10 algorithms in data mining," *Knowledge and Information Systems*, Vol. 14, No. 1, 1–37, December 2007.
4. Baum, C. E., "The singularity expansion method," *Transient Electromagnetic Field*, L. B. Felsen, 129–179, 1976.
5. Mitchell, T., *Machine Learning*, McGraw Hill, 1997.
6. Cover, T. and P. Hart, "Nearest neighbor pattern classification," *IEEE Transactions on Information Theory*, Vol. 13, 21–27, 1967.
7. Kecman, V., *Learning and Soft Computing*, MIT Press, Cambridge, MA, 2001.

Processing of COBRA FMCW SAR Data

M. Frioud[1], **A. Wahlen**[2], **H. Essen**[2], **and E. Meier**[1]

[1]Remote Sensing Laboratories, University of Zurich, Zurich, Switzerland
[2]Fraunhofer FHR, Wachtberg, Germany

Abstract— We present results from air-borne SAR campaigns using the FMCW SAR system COBRA operating at 35 GHz. Thanks to its large bandwidth the theoretical image resolution is below 10 cm in both the range and azimuth dimensions. Highly precise navigation data as well as very accurate synchronization of navigation and SAR data enables equally accurate absolute positioning. The SAR data were focused using a Frequency Scaling Algorithm (FSA) that accounts for the movement of the platform during the long ramp duration. The focusing chain integrates a two-step motion compensation scheme. The geometric and radiometric characteristics of the resulting single look complex (SLC) images were analyzed based on corner reflectors deployed within the test site. The scene was illuminated several times from two opposite directions in a standard strip-map mode. For each track, highly overlapping data segments were focused and geocoded individually. These products were subsequently mosaicked to generate a single geocoded image. Examples of change detection and moving target indication are also given.

1. INTRODUCTION

As reported in [1] and [2], the COBRA system is a modular FMCW SAR system with four front-end modules at 10 GHz, 35 GHz, 94 GHz and 220 GHz, coupled to a common data-acquisition unit. It was originally developed for high resolution imaging in ground-based applications, such as ISAR in a tower/turntable configuration or in a ground based SAR mode (rail-SAR).

In [3] and [4] results of COBRA operating in a standard air-borne strip-map SAR mode were reported. In [3] the data was used to exemplify a novel processing scheme in the wave-number domain while it was processed in the time domain in [4]. In [4] the focusing quality was assessed by looking at the signature of some strong scatterers.

In this paper we present the results obtained from two 35 GHz measurement campaigns that took place in May 2010 and May 2011 over a rural area in Switzerland. Nine and respectively fourteen linear tracks were flown over the same area. For both campaigns, the focusing quality as well as the geometric accuracy could be properly assessed thanks to the deployment of several corner reflectors in the scene. In 2010 the system was operated in two different modes corresponding to different chirp-rates as well as different nominal flight altitudes, while a single mode was used in 2011.

2. THE COBRA FMCW SAR SYSTEM

The COBRA system is well described in [2]. As a side-effect of its modular architecture sharing the same data-acquisition system as the pulsed-radar MEMPHIS[1], a full duty-cycle cannot be achieved. Although the data share the characteristics of a continuous wave system due to the extreme long pulses and the dechirp-on-receive technique used in the acquisition chain, the system is still a pulsed one, in the sense that no signal is transmitted between two consecutive ramps. The nominal measurement parameters used during the reported campaigns are shown in Table 1.

COBRA is carried by a Transall C-60. The navigation data are based on three units, namely the onboard INS/GPS units as well as a 20 Hz dGPS system. The synchronization between the navigation and the SAR data was considerably enhanced using a direct link and event markers.

3. PROCESSING METHOD

As is usually the case for FMCW SAR systems, the received data was de-ramped by mixing with the transmitted signal and this de-ramped data was subsequently demodulated to base-band. The demodulation brings the center of the range frequency interval of interest to zero. The frequency scale is directly associated with the slant range scale, while the mid-range is given by

$$R_m = \frac{c \cdot F_0 \cdot T_0}{2 \cdot B_w} \tag{1}$$

[1]The experimental pulsed radar system MEMPHIS is described in [3].

where F_0 is the demodulation frequency, T_0 is the nominal ramp duration, B_w is the nominal bandwidth and c is the speed of light. The mid-ranges corresponding to the nominal ramp durations in Table 1 are approximately 453 m and 798 m respectively. The corresponding maximum unambiguous ranges are half these values.

A FMCW Frequency Scaling Algorithm (FSA) as described in [6] was chosen to focus the data. This algorithm compensates very accurately the dilation in the received signal caused by the relative motion between radar and target during reception and between transmission and reception, while avoiding any interpolation. A two-step motion compensation scheme is integrated within this processing chain as described in [7]. The first step is a bulk correction performed prior to starting FSA while the second step is a differential correction performed in the time domain before the azimuth match filtering.

Highly overlapping data segments were focused with FSA and geocoded using a 2 m resolution lidar terrain model as reference height. The pixel size of the geocoded images is 10 cm. The resulting geocoded products were mosaicked to generate a single geo-referenced image.

4. RESULTS

4.1. Absolute Positioning

The position of the reflectors deployed in the scene was measured with a precision of a few centimeters. To check the absolute positioning the data were focused around positions of the reflector. For every possible match of the tracks with the reflectors, a point target analysis was performed. The absolute accuracy depends on the state vector of the antenna phase center which virtually follows

Table 1: Nominal measurement parameters of the COBRA system.

Carrier frequency	35.2 GHz
Azimuth antenna beamwidth	3.3°
Pulse repetition frequency	1600 Hz
System bandwidth	2 GHz
Sampling frequency	25 MHz
Demodulation frequency	50 MHz
Ramp duration	121 µs or 213 µs
Flying altitude	180 m or 330 m
Mean velocity	79 m/s
Look direction	left
Depression angle	23.5°

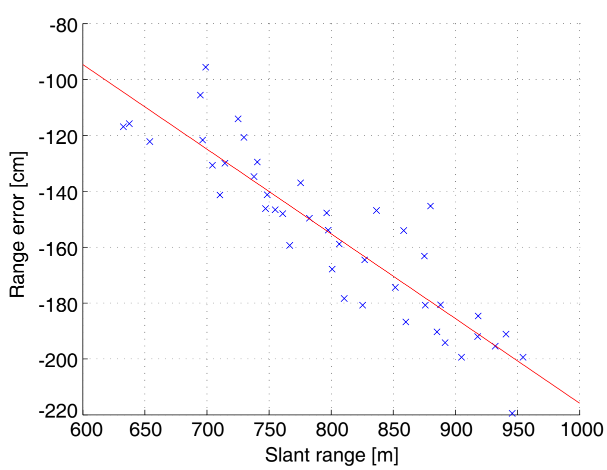

Figure 1: Distribution of the absolute errors in range versus slant range for all matches of the 14 data takes and 4 reflectors (44 cases) before calibration (see text).

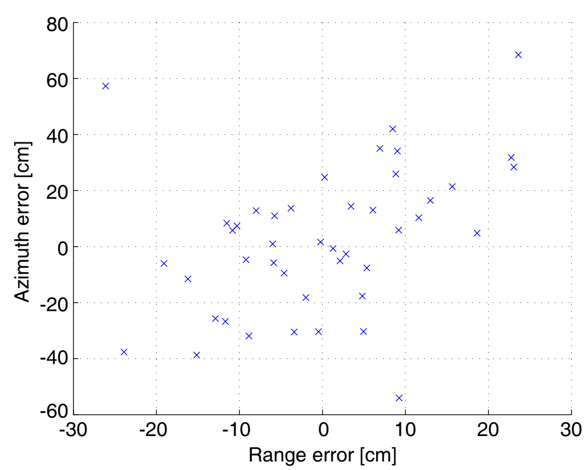

Figure 2: Distribution of the absolute errors for all matches of the 14 data takes and 4 reflectors (44 cases) after calibration (see text).

Figure 3: Mosaicked image from the data take 1 in 2011. The SAR image is superimposed over an orthophoto. The coordinate system is LV 95.

a linear track at constant velocity after the motion compensation.

Figure 1 presents the errors obtained in the range direction as a function of slant range for the four reflectors for all of the 2011 data takes, when using the nominal system parameters listed in Table 1. We can observe large systematic errors in range (average of −156.1 cm) as well as a significant linear trend of this error as a function of the slant range, leading to a standard deviation of 29.7 cm. Unlike the errors in the range direction, the errors in azimuth are almost independent on the slant range and average out to only 2.1 cm (standard deviation of 27.1 cm). Although an uncertainty in the lever arm could contribute efficiently to the systematic error in range, the most likely source of error is the uncertainties in the actual sampling and demodulation frequencies. In absence of independent estimates of these uncertainties, these values have been calibrated so as to cancel out the average range error as well as its slant range dependency. The resulting error distribution is shown in Figure 2. After calibration the standard deviations of the range and azimuth errors are 12.0 cm and 26.0 cm respectively.

The absolute positioning accuracy was also assessed by comparing the geocoded products with an orthophoto. Figure 3 presents an example of a mosaicked image from the data take 1 in 2011, where the geocoding process used a lidar terrain model. The SAR image geometry is seen to be very consistent with the orthophoto product from the Swiss Federal Office of Topography. The nominal standard deviation of the geolocation of this product is 25 cm.

4.2. Focusing Quality

From the parameters in Table 1, theoretical resolutions of about 7.5 cm in both range and azimuth are expected. One needs to bear in mind that the pixel spacings in range and azimuth are about

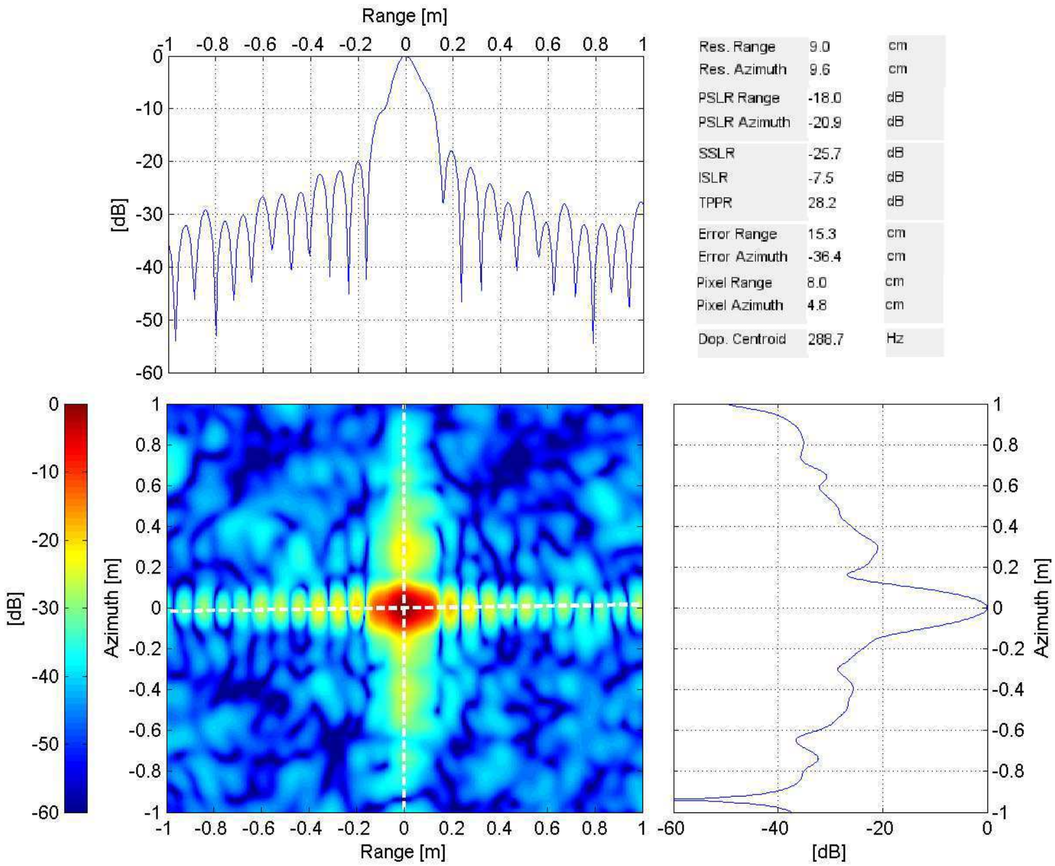

Figure 4: Example of point target analysis (data take 7 in 2010). The 2D plot presents the intensity distribution of the detected image 2 m × 2 m around the detected peak. The top and right panels present the corresponding sections along range and azimuth. The corresponding geometric and radiometric characteristics are listed.

Figure 5: Zoomed view of a geocoded product from the data take 1 in 2011.

Figure 6: Zoomed view of a geocoded product from the data take 3 in 2011.

Figure 7: Zoomed view of a geocoded product from the data take 1 in 2011, where the signatures of four moving vehicles are visible. The coordinate system is LV 95.

8 cm and 5 cm respectively. Figure 4 presents an example of point target analysis for a reflector located almost at mid-range of the data take 7 in 2010. We observe that the radiometric values obtained are close to the theoretical expectation.

4.3. Change Detection

The Figures 5 and 6 present the same zoomed area 25 m × 25 m in size from two different data takes in 2011, showing a group of people in two different configurations. The length of the shadows indicate that most of the people in Figure 5 are standing, while they're seated in Figure 6. Note that thanks to the small azimuth beamwidth, the aperture time is only about 0.35 s. As a consequence, the de-focusing due to possible movements of the people is relatively small.

4.4. Moving Target Indication

In 2011 a convoy of 4 vehicles was driving through the test site. Figure 7 shows an extract around the observed signatures in the geocoded image from the data take 1. The area is 180 m × 180 m in size. The aircraft is heading towards the SW while the vehicles are heading almost in the opposite direction. The shadows of the four vehicles are located to the SE of their actual position, while the signatures of the vehicles are seen to be notably shifted in azimuth.

5. CONCLUSION

This paper describes the COBRA FMCW millimetre-wave SAR system during two campaigns in May 2010 and 2011 over a rural area of Switzerland while it was operating in low-altitude strip-map mode. The data was focused using a frequency scaling algorithm that accounts for the platform movement during the long ramp duration. The geometric accuracy as well as the focusing quality was assessed by a point target analysis using corner reflectors. Resolutions below 10 cm as well as peak sidelobe ratios below −18 dB were achieved while the distribution of the positioning errors are characterized by standard deviations of about 12 cm and 26 cm in range and azimuth, respectively. Potential applications such as change detection and moving target indications were demonstrated.

ACKNOWLEDGMENT

This work was funded by ARMASUISSE. We are very grateful to all the collaborators of the involved institutions for their contributions during the measurement campaigns.

REFERENCES

1. Essen, H., et al., "Very high bandwidth millimetre-wave radar," *Electronic Letters '08*, Vol. 41, No. 22, 1247–1249, 2005.
2. Essen, H., et al., "High resolution millimetre wave measurement radars for ground based SAR ansd ISAR imaging," *Proceedings of the Radar Conference '08*, 1247–1249, Rome, Italy, May 2008.
3. Wang, R., et al., "Focus FMCW SAR data using the wavenumber domain algorithm," *IEEE Transactions on Geoscience and Remote Sensing*, Vol. 48, No. 4, 2109–2118, 2010.
4. Ribalta, A., et al., "High resolution FMCW-SAR image generation," *Proceedings of the 8th European Conference on SAR*, 1–4, Aachen, Germany, Jun. 2010.
5. Schimpf, H., et al., "MEMPHIS — A fully polarimetric experimental radar," *Proceedings of the International Geoscience and Remote Sensing Symposium*, Vol. 3, 1714–1716, Toronto, Canada, Jun. 2002.
6. Zhihong, J., et al., "Modified frequency scaling algorithm for FMCW SAR data processing," *Chinese Journal of Aeronautics*, Vol. 20, 339–345, 2007.
7. Zaugg, E. C. and D. G. Long, "Theory and application of motion compensation for LFM-CW SAR," *IEEE Transactions on Geoscience and Remote Sensing Symposium*, Vol. 46, No. 10, 2990–2998, 2008.

High Resolution MEMPHIS SAR Data Processing and Applications

C. Magnard[1], T. Brehm[2], H. Essen[2], and E. Meier[1]

[1]Remote Sensing Laboratories, University of Zurich, Switzerland
[2]Fraunhofer FHR, Wachtberg, Germany

Abstract— This paper focuses on MEMPHIS (Multi-frequency Experimental Monopulse High-resolution Interferometric SAR) data processing, possible applications using its various SAR modes and the results obtained. The processing chain used to focus MEMPHIS data is presented. To demonstrate the focusing quality, the signatures of corner reflectors were analyzed, revealing not only a high resolution, but also a very precise geometric positioning accuracy on the order of the resolution, in spite of MEMPHIS' experimental and portable design. Finally, applications and results using the various antennas are presented, such as the generation of digital surface models with the multi-baseline interferometric antenna along with a quality evaluation, as well as channel combinations of the polarimetric data.

1. INTRODUCTION

MEMPHIS is a millimeter-wave high-resolution SAR system, developed and operated by the German research institute Fraunhofer FHR [1]. It operates at the 35 GHz and 94 GHz radar bands (Ka and W-bands respectively). It is an experimental, modular and removable system, typically mounted on a C-160 Transall airplane. Various antenna shapes and configurations can be used, making the following SAR modes possible: single-path multi-baseline cross-track interferometry with a four horn antenna, dual-pol circular or linear polarimetry and monopulse for MTI applications.

MEMPHIS was introduced at the end of the 90's and has significantly improved over the years, including enhancement of the bandwidth using a stepped-frequency chirp, addition of dGPS and precise INS systems, as well as the determination of the lever arms. This has led to a dedicated processing chain, whose features include navigation data processing, SAR data extraction and synchronization with the navigation data, range compression of the separate stepped-frequency raw data, reconstruction of the full bandwidth from the range-compressed data of each chirp and azimuth focusing using an Extended Omega-k algorithm. MEMPHIS characteristics are summarized in Table 1.

2. PROCESSING CHAIN

2.1. Navigation Data

The quality of the aircraft navigation data is not sufficient for processing the SAR data with a high quality due to low GPS positioning precision, low sampling rates for the INS and GPS and inaccurate synchronization between the systems. To overcome these weaknesses, an additional dGPS antenna (AeroAntenna AT2775-41 with a Trimble R7 receiver) was used beginning in 2009 and a precise INS system (iMAR iNAV-RQH, provided by TU Munich) followed in 2011. These are synchronized with the SAR data using event and second markers. Using terrestrial surveillance method, the lever arms between the various systems were measured with a few centimeters accuracy.

Table 1: MEMPHIS SAR system parameters.

Carrier frequencies	35 GHz (Ka-band) and 94 GHz (W-band)
Bandwidth	900 MHz (stepped-frequency)
PRF	1500 Hz
Typical airplane velocity	77 m/s
Airplane altitude	300–1000 m a.g.l.
Depression angle	20°–35°
Theoretical range resolution	0.167 m
Theoretical azimuth resolution	0.082 m in Ka-band, 0.061 m in W-band

The navigation data from the additional dGPS and INS are processed together with the Novatel Inertial Explorer commercial software. This software directly combines the raw data from both sources to calculate the position, velocity and attitude information. The resulting navigation data may contain a few spikes, and are too noisy (in the mm range) for directly using them for the SAR processing. A post processing is therefore needed to remove the spikes and smooth the navigation data through a Kalman filter for the position and velocity and an average filter for the attitude data.

2.2. From Raw to Stepped-frequency Range Compressed Data

MEMPHIS uses stepped-frequency chirps to enhance its bandwidth. It transmits successively 8 chirps with 200 MHz bandwidth and 100 MHz overlap between each successive chirp, forming a 900 MHz full bandwidth. The raw SAR data corresponding to each chirp part are extracted and synchronized with the navigation data using the event markers. Each of the raw data files is range-compressed using either chirp replicas when available or synthetic chirps, using a conventional matched filtering technique.

The full bandwidth is then reconstructed through a stepped-frequency algorithm based on [2]. A range FFT is first applied to the range-compressed data from each chirp, their spectra arranged side by side in a new array, and overlapping frequencies averaged through a weighted average function. An inverse FFT is then finally applied to obtain the range-compressed data of the full bandwidth. In case of range artifacts, the phases of the overlapping frequencies are compared and corrected before the full bandwidth is reconstructed.

2.3. Azimuth Compression

The azimuth focusing is performed using an Extended Omega-k algorithm [3]. This algorithm extends the conventional Omega-k algorithm to airborne SAR systems with large antenna beam widths in both directions. The block diagram in Figure 1 shows the algorithm processing chain.

It includes a two-step motion compensation. The motion compensation is first prepared: the navigation data are transformed into Cartesian coordinates, they are linearized with a constant velocity, the distances between the real and linearized tracks are calculated and projected onto the depression angles corresponding to each range position. In the first order motion compensation, the SAR data are interpolated in the azimuth direction to correspond to the constant velocity. A range-independent pixel shift and phase correction is applied, corresponding to the mid-range depression angle. The second order motion compensation is performed after the range cell migration, and consists of a range-dependent phase and pixel shift correction.

The modified Stolt mapping performs the range cell migration. An approximation is often used for the conventional Stolt mapping to avoid interpolating the data and using a phase shift in time domain instead [4]. This approximation cannot be used with our implementation as the shift is not constant in the ω direction, thus the interpolation is made separately for the real and imaginary parts with a B-spline interpolation method ([5] and [6]).

In Ka- and especially W-bands, the Doppler centroid can vary extremely: it is not uncommon to have ~ 1 PRF variation within a few seconds. It also varies strongly along the range direction. A variable Doppler centroid can be handled through the combination of zero interleaving [7] and a windowing of the azimuth spectrum. In the range direction, the filtering window is defined for each range line. In the azimuth direction, a block processing with overlapping blocks is needed to handle the varying Doppler centroid, at the expense of a longer processing time. A downsampling corresponding to the zero interleaving can be applied at the end of the azimuth compression.

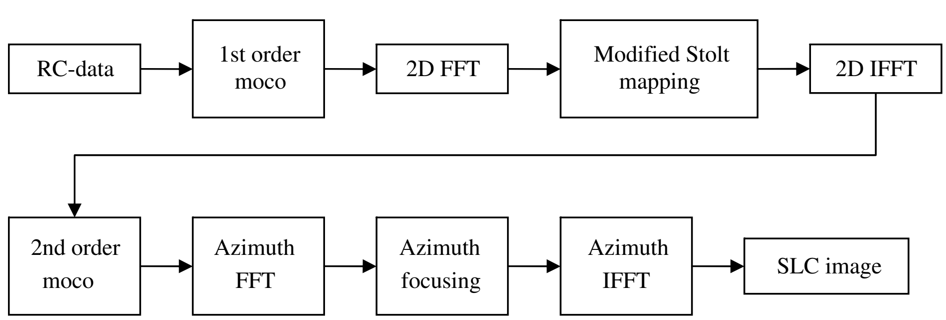

Figure 1: Block diagram of the extended Omega-k algorithm.

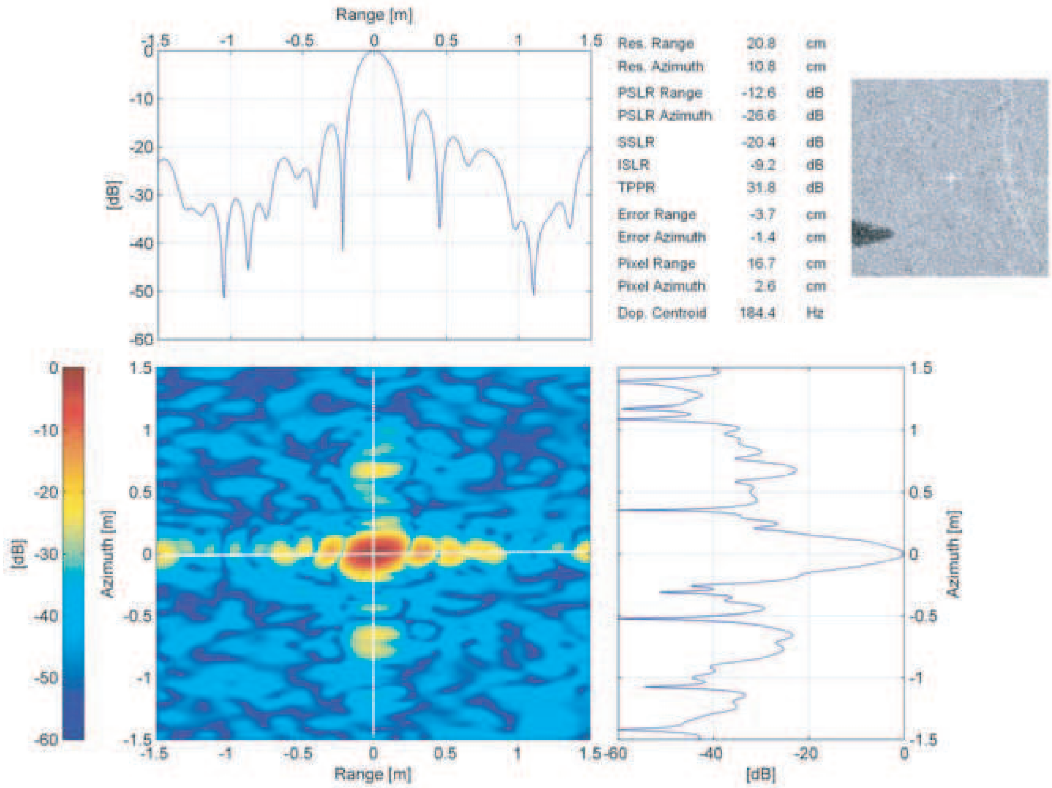

Figure 2: Point target analysis of a reflector signature in Feldberg.

Table 2: Summary of the point target analysis over the reflectors in Feldberg and Memmingen. Fourteen samples were analyzed in Feldberg and eight in Memmingen.

	Feldberg		Memmingen	
	Average	Std. dev.	Average	Std. dev.
Range resolution [cm]	19.4	2.11	18.35	1.64
Azimuth resolution [cm]	10.69	1.97	9.29	0.59
Range PSLR [dB]	−14.27	1.62	−11.09	1.13
Azimuth PSLR [dB]	−19.69	7.56	−24.38	4.03
Range position error [cm]	−4.05	7.93	1.18	12.98
Azimuth position error [cm]	−0.41	13.93	−12.15	9.18

3. RESULTS

The Ka-band results from two areas surveyed during a May 2011 campaign, namely the Feldberg in the Black Forest, Germany and Memmingen in Bavaria, Germany, were analyzed. Reflectors were deployed on the ground and their positions were measured with a few centimeters accuracy using dGPS. The signatures of these reflectors were then analyzed as shown in Figure 2. The average and standard deviation of the results are summarized in Table 2.

The experimental values obtained for both range and azimuth resolutions are close to the theoretical expectations (see Table 1). Moreover, the positioning accuracy is also very high, despite the experimental setup. This confirms the accuracy of many hard- and software parameters: navigation data acquisition and processing, lever arm measurements, SAR system parameters like the sampling window start time, PRF and sampling rate accuracies, SAR data processing including the motion compensation steps, speed of light in the atmosphere.

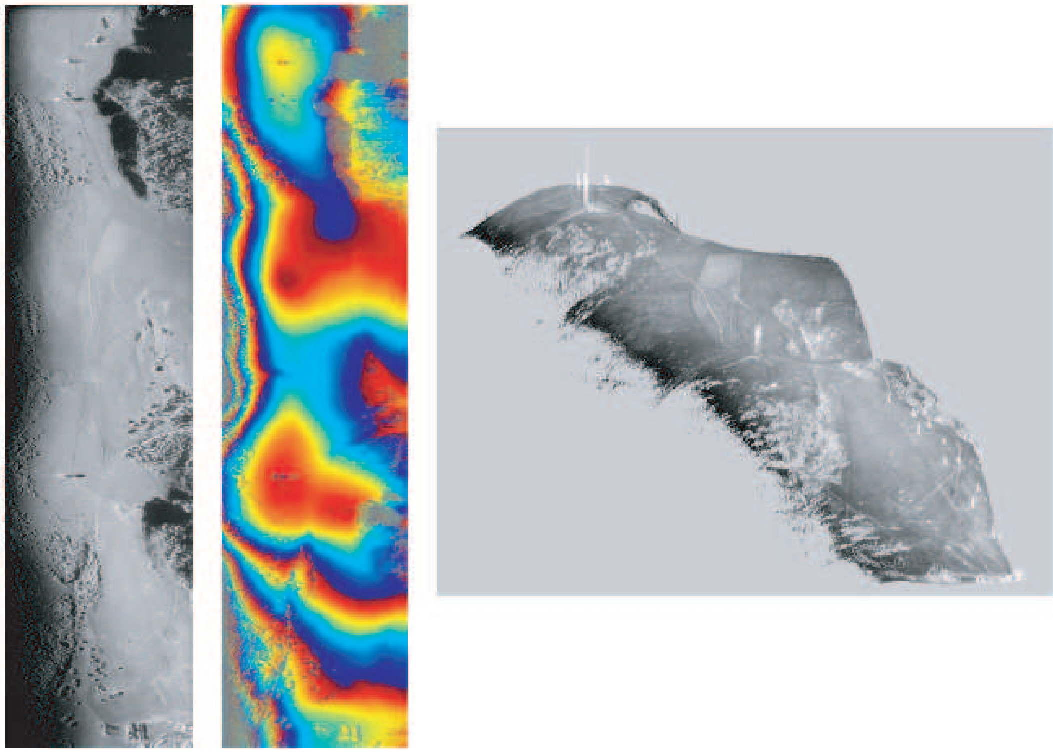

Figure 3: Results of the interferometric processing of a Ka-band data take over Feldberg, acquired in May 2011. One of the four SAR images is shown on the left. The interferogram in the middle was generated with a baseline of 0.165 m, resulting in a 2π ambiguity of ~ 68 m. The image on the right is a 3D visualization of the reconstructed digital surface model, overlaid with the geocoded SAR image. The two towers on top of the ridge as well as the pylons of the cable car and chairlift on the right are clearly visible.

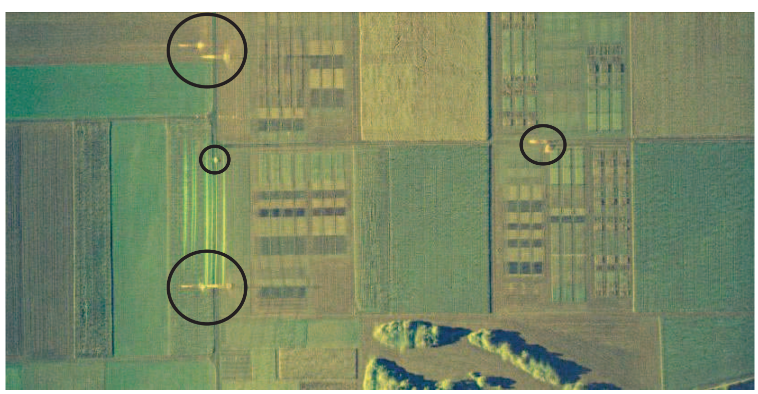

Figure 4: Circular dual-polarization Ka-band composite image of an agricultural area near Oensingen, Switzerland acquired in June 2010. The RR and RL polarizations are respectively represented as red and green channels. Man-made objects appear yellow/red, since they contain more RR scattering due to double-bounce scattering. The electric lines are only reflected once and appear pure green.

4. APPLICATIONS

MEMPHIS is a versatile system that can be used for various applications. Two of them are briefly presented in the following sections, including some image examples.

4.1. Multi-baseline Cross-track Interferometry

Interferometric antennas can be used with MEMPHIS sensor. Both 35 and 94 GHz antennas consist of one emitter and four receivers placed vertically, allowing multi-baseline cross-track interferometry. Interferometric processing of MEMPHIS data and its results are presented in [8]. The new INS and the implementation of the Extended Omega-k algorithm have further improved the quality of the digital surface models generated. Figure 3 shows a result of the interferometric processing. The accuracy of the generated height model is in the order of 0.5 m RMSE, when compared to LIDAR measurements.

4.2. Dual-pol Circular Polarimetry

One emitter and two receivers for each frequency can be used at a time, allowing dual-pol polarimetry. Using only dual-pol instead of full-pol data and the properties of millimeter waves (almost no vegetation penetration) suggest the use of circular-polarized waves. Odd and even reflection numbers are then visible on the composite image, emphasizing for example the scattering of man-made objects. An example is shown on Figure 4.

5. CONCLUSIONS

In this paper we described the current status of the MEMPHIS SAR system and its data processing. Despite its experimental and portable design, we obtained a resolution near the theoretical best case and high positioning accuracy through the use of accurate navigation data, precise characterization of the hardware parameters and a robust processing chain. We demonstrated two applications, multi-baseline interferometry and circular polarimetry, which have become feasible thanks to MEMPHIS modular design. The digital surface models generated with the multi-baseline interferometric data are also highly accurate.

ACKNOWLEDGMENT

The authors would like to thank the TU Munich for lending us their INS system and Christian Ackermann for supporting its integration with the SAR and GPS systems.

REFERENCES

1. Schimpf, H., H. Essen, S. Boehmsdorff, and T. Brehm, "MEMPHIS — A fully polarimetric experimental radar," *Proceedings of the IEEE International Geoscience and Remote Sensing Symposium IGARSS*, Vol. 3, 1714–1716, Toronto, Canada, Jun. 2002.
2. Wilkinson, A. J., R. T. Lord, and M. R. Inggs, "Stepped-frequency processing by reconstruction of target reflectivity spectrum," *Proceedings of the 1998 South African Symposium on Communications and Signal Processing, 1998, COMSIG'98*, 101–104, Rondebosch, South Africa, Sep. 7–8, 1998.
3. Reigber, A., E. Alivizatos, A. Potsis, and A. Moreira, "Extended wavenumber-domain synthetic aperture radar focusing with integrated motion compensation," *IEE Proceedings Radar, Sonar and Navigation*, Vol. 153, No. 3, 301–310, Jun. 2006.
4. Cafforio, C., C. Prati, and F. Rocca, "SAR data focusing using seismic migration techniques," *IEEE Transactions on Aerospace and Electronic Systems*, Vol. 27, No. 2, 194–207, Mar. 1991.
5. Unser, M., A. Aldroubi, and M. Eden, "B-spline signal processing: Part I — Theory," *IEEE Transactions on Signal Processing*, Vol. 41, No. 2, 821–832, Feb. 1993.
6. Unser, M., A. Aldroubi, and M. Eden, "B-spline signal processing: Part II — Efficient design and aplications," *IEEE Transactions on Signal Processing*, Vol. 41, No. 2, 834–848, Feb. 1993.
7. Prati, C. and F. Rocca, "Focusing SAR data with time-varying Doppler centroid," *IEEE Transactions on Geoscience and Remote Sensing*, Vol. 30, No. 3, 550–559, May 1992.
8. Magnard, C., E. Meier, D. Small, H. Essen, and T. Brehm, "Processing of MEMPHIS millimeter wave multi-baseline InSAR data," *IEEE International Geoscience and Remote Sensing Symposium (IGARSS)*, 4302–4305, Honolulu, Hawaii, USA, Jul. 25–30, 2010.

A Highly-linear Low-power Down-conversion Mixer for Monostatic Broadband 80 GHz FMCW-radar Transceivers

Christian Bredendiek[1], **Nils Pohl**[1], **Timo Jaeschke**[1], **Klaus Aufinger**[2], **and Attila Bilgic**[3]

[1]Institute of Integrated Systems, Ruhr-Universität-Bochum, Germany
[2]Infineon Technologies AG, Germany
[3]KROHNE Messtechnik, Germany

Abstract— This paper investigates on simulation level three techniques, the multi-tanh technique, resistive, and inductive emitter degeneration, to improve the linearity of double-balanced Gilbert-Cell mixers and proposes a mixer-design with inductive degeneration. Using this technique the highest dynamic range is obtained at the expense of a slightly degenerated noise figure and an increased compression point. The developed direct-down-conversion mixer is fabricated in a SiGe:C bipolar production technology with an f_{T} of 170 GHz and $f_{\max}$ of 250 GHz. The mixer achieves a 1 dB-input-referred compression point of -1.2 dBm with a low current consumption of 13 mA from a 5 V supply. The noise figure is approximately 12 dB in a wide frequency band around 80 GHz.

1. INTRODUCTION

Recently, radar transmitters [1], VCOs [2], and frequency multiplier chains in silicon-based circuits, which are well suited for mm-Wave applications have been published. This paper focuses on the design of highly-linear broadband mm-Wave down-conversion mixers for FMCW-Radar-Systems. The intended application is a single-channel monostatic transceiver with a high bandwidth of approximately 20 GHz.

While an output power of more than 10 dBm can easily be attained with VCOs [6] and PAs [1] around 80 GHz in SiGe-Technologies, a sufficient linearity of mixers can not be achieved that easily. Particularly in monostatic applications this is one of the most important requirements for SiGe-Radar-Frontends, due to possible strong reflections for instance at the antenna which could drive the frontend into saturation. Mixers with a 1-dB input referred compression point of around zero dBm in silicon technologies have been reported [3], while compromising with current-consumption and exhibiting higher noise. This compromise may not lead to an increase in dynamic range of the mixer depending on the amount of excess noise.

2. LINEARIZATION-TECHNIQUES

To discuss the linearization techniques for the Gilbert-Cell mixer we first have to take a glance at the Gilbert-Cell [4] itself which is shown in Fig. 1(a). Its simplified differential output current is given as

$$\Delta I_{\mathrm{Out}} = I_{\mathrm{Core}} \cdot \left[\tanh\left(\frac{V_{\mathrm{RF}}}{2 \cdot V_{\mathrm{T}}}\right)\right] \left[\tanh\left(\frac{V_{\mathrm{LO}}}{2 \cdot V_{\mathrm{T}}}\right)\right]. \tag{1}$$

For input voltages V_{RF} and V_{LO}, which are small compared to the thermal voltage V_{T}, the hyperbolic tangent functions can be approximated as linear and the Gilbert-Cell functions as an analog multiplier. In another and more interesting case for mixers where one signal is large compared to V_{T} these transistors behave like switches. This effectively causes the other small signal to be multiplied by a square wave and allows it to function as a mixer. In the typical case of a mixer the large signal is applied to the LO-Port of a Gilbert-Cell which simplifies (1) to

$$\Delta I_{\mathrm{Out}} = I_{\mathrm{Core}} \cdot \mathrm{sgn}\left(V_{\mathrm{LO}}\right) \cdot \left[\tanh\left(\frac{V_{\mathrm{RF}}}{2 \cdot V_{\mathrm{T}}}\right)\right]. \tag{2}$$

Equation (2) shows that the output current of the mixer is independent of the amplitude of the LO-signal, as long as the signal is large enough. This is called the LO overdrive. This leads to the assumption that the linearity of a Gilbert-Cell mixer is mainly dependent on the linearity of the input transconductance stage consisting of transistors T_{5-6}.

While designing the proposed mixer, three linearization techniques for the transconductance stage of the Gilbert-Cell have been investigated. The three techniques used are shown in Figs. 1(a)–(d), the multi-tanh technique, resistive emitter-degeneration, and inductive emitter-degeneration.

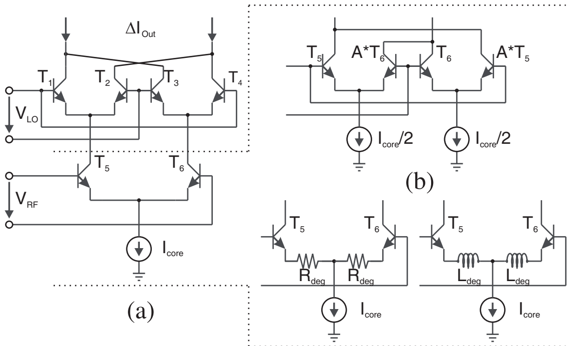

(a) (b) (c) (d)

	NF_{SSB} [dB]	ICP [dBm]	Complexity
standard Gilbert-Cell	11.6	–6	-
multi-tanh (A = 4)	12.7	–3.79	high
multi-tanh (A = 9)	15.4	–0.16	high
$R_{\mathrm{deg}} = 25\ \Omega$	14.1	–2.52	simple
$R_{\mathrm{deg}} = 50\ \Omega$	15.8	+0.25	simple
$L_{\mathrm{deg}} = 15$ pH	11.65	–3.65	moderate
$L_{\mathrm{deg}} = 60$ pH	11.8	–0.85	moderate
$L_{\mathrm{deg}} = 75$ pH	14.4	+1.62	moderate

(e)

Figure 1: (a) Circuit diagram of a standard Gilbert-Cell, (b) first linearization technique for the transconductance stage of a Gilbert-Cell the multi-tanh technique, (c) second technique the resistive degeneration, (d) third technique the inductive degeneration, (e) comparison of linearization techniques.

All investigated linearizaition techniques have the reduction of the transconductance of a differential pair in common.

In Fig. 1(b) the multi-tanh technique as described in [5] for a basic doublet is shown. The multi-tanh-technique uses differential pairs with different offset voltages in parallel. The linearity is increased due to a more constant transconductance over the input voltage range. For multi-tanh systems with a low order of differential pairs the offset voltage can simply be generated using emitter-area ratios. The doublet, where only two differential pairs are used, is one of these systems.

The second technique, the simplest and probably most adopted one, is shown in Fig. 1(c). It is based on resistive emitter degeneration. This technique uses resistors to decrease the transconductance of the differential pair thus increasing its linearity.

The third investigated technique is the emitter degeneration with the use of inductors instead of resistors, which is shown in Fig. 1(d). This technique has the advantage of avoiding the voltage drop at the inductors and has a better noise performance due to the low parasitic ohmic resistance of the inductors.

Figure 1(e) shows the comparison of the three investigated linearization techniques for a standard Gilbert-Cell mixer. A core current of 9 mA was used for all techniques and the simulations where kept as ideal as possible. Fig. 1(e) clearly shows that all investigated linearization techniques can be used to increase the linearity of a mixer, but not all can be used to increase the dynamic range. The dynamic range is limited on the upper end by the transmitted power and the linearity of the radar-frontend while on the lower end it is limited by the smallest signal which is still detectable, which is dependent on the noise figure and the transmitted power. With this retrospect, the dynamic range of a radar-frontend in a monostatic application becomes the most important requirement.

In this comparison the inductive emitter degeneration with $L_{\mathrm{deg}} = 60$ pH stands out as the best choice. It introduces only a small amount of excess noise and greatly increases the linearity of the mixer, which offers the highest dynamic range of the investigated techniques. The assessment made for the complexity was done with the number of used components, additional needed wiring and additional design overhead. The complexity for the inductive degeneration is slightly higher than the resistive degeneration due to the need of additional EM-simulations for the design of the emitter coils. The doublet has the worst complexity due to the additional two transistors and the additional wiring needed. Higher order multi-tanh systems are not investigated because of their increased wiring overhead and thus increased unwanted parasitic capacitances and inductances which are very important in the design of mm-Wave circuits.

3. CIRCUIT DESIGN

Figure 2(a) shows the schematic of the proposed mixer. The transmission lines L_{RF} and L_{LO} are microstrip lines with inductive behavior. In contrast to the inductor L_{deg} which is a symmetrical planar spiral inductor with a center tap for the emitter degeneration of the transconductance stage. The capacitances $C_{\mathrm{LO,RF}}$ provide the DC-decoupling in the RF- and LO-paths of the mixer. The bias voltages of the switching-quad and the transconductance stage are generated on-chip with diodes and resistors in the kilo ohm region. The current consumption of the complete mixer is 12.6 mA from a 5 V supply. The core current of 9.2 mA is delivered by a transistor current source. The biasing circuits consume the remaining 3.4 mA.

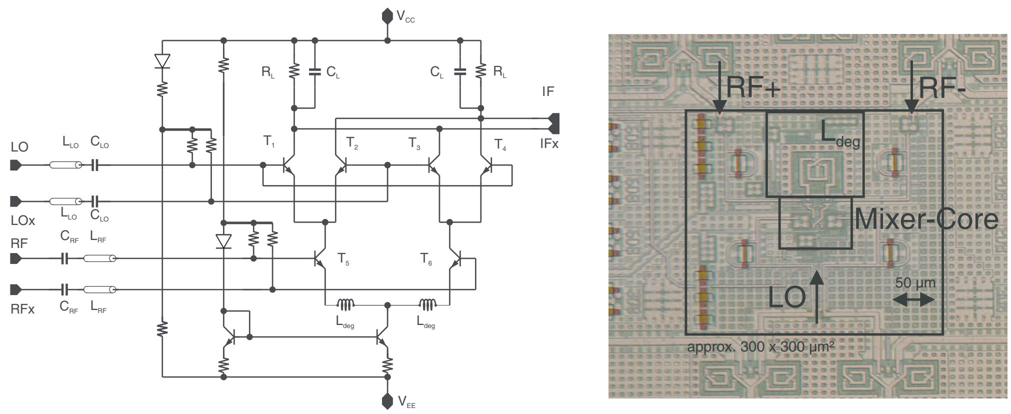

(a) (b)

Figure 2: (a) Schematic of the proposed Gilbert-Cell mixer with inductive degeneration inductors L_{deg}, biasing circuits, and matching structures $L_{RF;LO}$. (b) Chip photo of the proposed mixer with the center tapped spiral inductor L_{deg} in the top center and the microstrip lines for the RF- and LO-path.

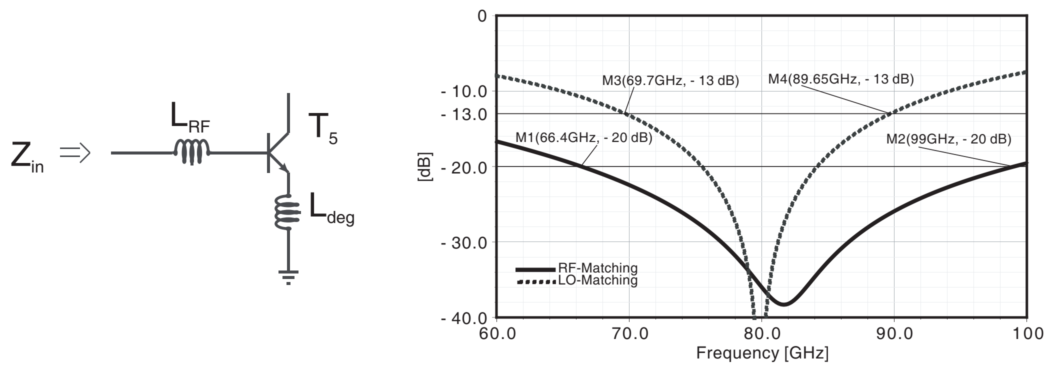

(a) (b)

Figure 3: (a) Simplified section for the calculation of the input impedance. For symmetry reasons, only half of the transconductance stage is shown. (b) S-Parameter simulation for the input matching of the RF- and the LO-Stage.

The switching-quad, consisting of transistors T_{1-4}, itself is biased at the current density for maximum f_T to keep the transistors switching capabilities as fast as possible. The transistors T_{5-6} are four times larger than the transistors of the switching-quad. This method keeps the transconductance stage biased below the current density for maximum f_T which improves the noise performance of the mixer. The load of the switching-quad is a low pass RC filter with R_L and C_L. The corner frequency of the load is 2 GHz which is low enough to filter out unwanted signals on-chip like the 80 GHz LO-signal. Further filtering can be done off-chip.

The simulations and designs for the used inductor were done with the 3D planar electromagnetic field solver Sonnet. The center tapped planar spiral inductor which is used for the inductive degeneration has an inductance of about two times 65 pH and a quality factor of about 20 at 80 GHz. In addition to the increased linearity the inductive degeneration is used to achieve a good input matching as well. Fig. 3(a) shows the simplified schematic for the calculation of the input impedance. For symmetry reasons only one half of the fully-differential transconductance stage is shown. The simplified[1] input impedance can be expressed as

$$Z_{\text{in}}(\omega) = r_{\text{B}} + \frac{g_{\text{m}} \cdot L_{\text{deg}}}{C_{\text{BE}}} + j\omega\left(L_{\text{deg}} + L_{\text{RF}}\right) - \frac{j}{\omega \cdot C_{\text{BE}}}, \tag{3}$$

where r_B is the base resistance, C_{BE} is the base-emitter-capacitance of the input transistor T_5, L_{deg} is one part of the center-tapped spiral inductor and L_{RF} is the input transmission line. The expression for the input impedance has a frequency dependent imaginary part and a frequency

[1]Only C_{BE} and r_B were considered, whereas especially C_{BC} and r_E have been neglected to keep the calculation simple. The simulation were done without these simplifications.

independent real part with two effective degrees of freedom L_{deg} and L_{RF} which can be used for input matching. With the proper choice of L_{deg} the frequency independent part can be tuned to 50 Ohm to achieve a perfect match at the center frequency. A compromise between good matching and linearity has to be found. Higher L_{deg} would result in higher linearity but at the cost of matching and vice versa. The second degree of freedom L_{RF} can be used to achieve a series resonance at the center frequency to cancel out the frequency dependent imaginary part of the input impedance.

Figure 3(b) shows the simulated input matching of the mixer for the LO- and the RF-path with an optimized L_{deg} for matching and linearity. The input matching for the RF-path is better than -20 dB in the frequency range from 66.4 GHz to 99 GHz. The considerable advantages of the inductive degeneration can be seen in this broadband matching, which results in a robust and tolerance invariant input matching. An LO matching of -13 dB, with a bandwidth of approximately 20 GHz, is achieved. In comparison to the RF-path it also shows the benefit of the inductive degeneration regarding matching.

4. EXPERIMENTAL RESULTS

In Fig. 2(b) a chip photo of the mixer is shown. In the top center of the photo the center tapped spiral inductor can be seen which occupies an area of only $80 \times 70\,\mu\text{m}^2$ including the guard ring, which results in a quite small total area of about $300 \times 300\,\mu\text{m}^2$.

The source to drive the LO-input of the mixer is a PLL-stabilized VCO based on [6] and is integrated with the mixer on-chip. The integrated VCO offers a high tuning bandwidth of 24.5 GHz and is designed to deliver a maximum output power at the LO-port of 6 dBm at the center frequency. The RF-path is driven by a commercial waveguide frequency quadrupler. The chip is mounted on a Rogers 5880 substrate where the fully differential input is connected to a rat-race coupler which is connected to a rectangular waveguide flange for the quadrupler. All measurements and simulations were done with an IF-frequency of 10 MHz.

The simulated and measured conversion gain fits well at the center frequency of 80 GHz and are shown in Fig. 4(a). The difference between the simulation and measurement is below 1 dB. The higher deviations below the center frequency can be explained with the frequency dependency of the rat-race coupler and waveguide flange on the Rogers substrate. The frequency range of the conversion gain measurement is limited to 68 GHz and to 87 GHz by the LO- and RF-source,

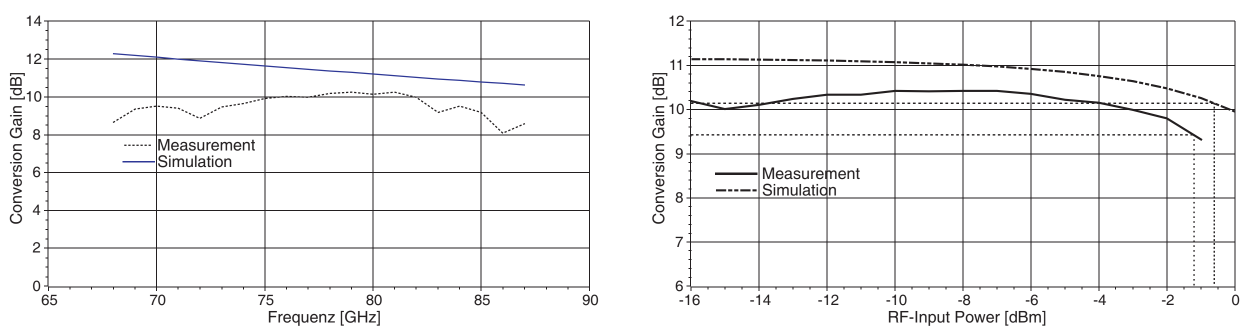

(a) (b)

Figure 4: (a) Measured and simulated conversion gain versus frequency. (b) Measured and simulated conversion gain versus the input power at the center frequency of 80 GHz.

Table 1: Performance of 80 GHz Gilbert down-conversion mixer.

	NF_{SSB}	ICP	CG	3-dB BW	P_{DC}
	[dB]	[dBm]	[dB]	[GHz]	[mW]
[7]	14	-30	24	≈ 25.8	300
[3]	16.5	0	11	≈ 18	413
[8]	11.2	2.5	15	-	335
[9]	10.8	-5	21.5	-	70
This Work	12	-1.2	11	> 20	65

respectively. Nevertheless, this results in a measured bandwidth of more than 19 GHz with a flatness of 2 dB. Although the conversion gain is only around 10 dB it is sufficient for a monostatic application. Further amplification can be done off chip with an IF-Amplifier. A simulated noise figure of 11.8 dB is achieved at the center frequency. The noise figure shows anti-proportional characteristics to the conversion gain and is below 13 dB in the same frequency range.

The input referred compression point (ICP) is measured at the center frequency of 80 GHz with an IF-frequency of 10 MHz. The results of the measurement and simulation are shown in Fig. 4(b). The mixer achieves an ICP at −1.2 dBm which is around −0.6 dB lower than the simulated.

5. CONCLUSION

In this paper, a low-power, highly linear mixer with an inductive degenerated Gilbert-Cell structure is presented. The measurement results agree reasonably well with the simulated ones. The presented mixer is well suited for an operation in a broadband monostatic FMCW-Radar with a high dynamic range. A comparison to published Gilbert-Cell type down-conversion mixers around a center frequency of 80 GHz is given in Table 1. The compression point of the mixer at this low power consumption is state-of-the-art. Furthermore the mixer offers the best compromise between power consumption and dynamic range, due to its high linearity and only slightly degenerated noise figure.

ACKNOWLEDGMENT

This work was supported by the German Bundesministerium für Bildung und Forschung within the project RoCC (FKZ 13N9822). The authors would like to thank Infineon Technologies AG and its staff members for fabricating the chips.

REFERENCES

1. Starzer, F., A. Fischer, H.-P. Forstner, et al., "A fully integrated 77-GHz radar transmitter based on a low phase-noise 19.25-GHz fundamental VCO," *Proc. IEEE Bipolar/BiCMOS Circuits and Technology Meeting BCTM 2010*, 65–68, Oct. 4–6, 2010.
2. Pohl, N., H.-M. Rein, T. Musch, et al., "Investigation and reduction of frequency pulling in SiGe mm-wave VCOs at limited power consumption," *Proc. IEEE Bipolar/BiCMOS Circuits and Technology Meeting BCTM 2010*, 69–72, Oct. 4–6, 2010.
3. Dehlink, B., H.-D. Wohlmuth, H.-P. Forstner, et al., "A highly-linear SiGe double-balanced mixer for 77 GHz automotive radar applications," *IEEE RFIC Digest*, 205–208, Jun. 2006.
4. Gilbert, B., "A precise four-quadrant multiplier with subnanosecond response," *IEEE J. Solid-State Circ.*, Vol. 3, No. 4, 365–373, Dec. 1968.
5. Gilbert, B., "The multi-tanh principle: A tutorial overview," *IEEE J. Solid-State Circ.*, Vol. 33, No. 1, 2–17, Jan. 1998.
6. Pohl, N., H.-M. Rein, T. Musch, et al., "SiGe bipolar VCO with ultra-wide tuning range at 80 GHz center frequency," *IEEE J. Solid-State Circ.*, Vol. 44, No. 10, 2655–2662, Oct. 2009.
7. Perndl, W., H. Knapp, M. Wurzer, et al., "A low-noise and high-gain double balanced mixer for 77 GHz automotive radar front-ends in SiGe bipolar technology," *IEEE RFIC Digest*, 47–50, Jun. 2004.
8. Trotta, S., B. Dehlink, H. Knapp, et al., "Design considerations for low-noise, highly-linear millimeter-wave mixers in SiGe bipolar technology," *33rd European Solid State Circuits Conference*, 356–359, Sep. 2007.
9. Yang, S. J., H. P. Forstner, G. Haider, et al., "A low noise, high gain, highly linear mixer for 77 GHz automotive radar applications in SiGe:C bipolar technology," *Proc. of ESSCIRC'09*, 312–315, Sep. 14–18, 2009.

Electromagnetic and Gravitational Equations of Rotational Objects

Zi-Hua Weng
School of Physics and Mechanical & Electrical Engineering
Xiamen University, Xiamen 361005, China

Abstract— The paper studies the electromagnetic equations of the rotational charged object in the electromagnetic field in the presence of the gravitational field. In the description with the algebra of octonions, there exist some weightlessness states in the two fields to cause the motions similar to the planetary revolution or the planetary rotation. The study claims that the field potential has an influence on the field strength, and results in the waggle of electromagnetic strength, and impacts finally the movement states of the rotational charged object.

1. INTRODUCTION

The validity of Maxwell's equations [1] and the correctness of Newton's law of gravitation [2] are being doubted all the time, especially when the charged objects rotate in the case for coexistence of the electromagnetic field and the gravitational field. This validity remains as puzzling as ever. The existing theories do not explain why the charged particles possess the spin and why the planets keep rotating, and then do not offer compelling reason for those special situations.

The quaternion was invented by W. R. Hamilton [3], and was first used by J. C. Maxwell to represent the physical properties of electromagnetic fields. Recently the quaternion can also be used to rephrase the features of gravitational fields. The quaternion space for the gravitational field is independent to that for the electromagnetic field. Those two quaternion spaces can be combined together to become one octonion space [4]. The latter can be used to depict the gravitational field and electromagnetic field simultaneously.

Further the radius vector can be combined with the integral of field potential to become one compounding physical quantity in the octonion space, which is one kind of function space. With the algebra of octonions, the results claim that there exist some kinds of weightlessness states in the two fields [5]. The field potential will impact the weightlessness states, and the variation of field potential may shift the rotational velocity or the spin velocity.

2. GRAVITATIONAL FIELD

The physical characteristics about the gravitational field of the rotational object can be described by the quaternion space, including the weightlessness state and angular velocity etc.

In the quaternion space for the gravitational field, the basis vector is $\mathbb{E}_g = (\mathbf{i}_0, \mathbf{i}_1, \mathbf{i}_2, \mathbf{i}_3)$, and the coordinates is r_i, while the radius vector is $\mathbb{R}_g = \Sigma(r_i \mathbf{i}_i)$. The latter can be combined with the quaternion physical quantity $\mathbb{X}_g = \Sigma(x_i \mathbf{i}_i)$ to become the compounding radius vector $\overline{\mathbb{R}}_g$,

$$\overline{\mathbb{R}}_g = \mathbb{R}_g + k_{rx} \mathbb{X}_g, \tag{1}$$

where r_i and x_i are all real; $r_0 = v_0 t$; $x_0 = a_0 t$; v_0 is the speed of light; a_0 is the scalar potential of gravitational field; t denotes the time; $\mathbb{X}_g$ is the integral of gravitational potential; $k_{rx} = 1/v_0$ is the coefficient for dimensional homogeneity [6]; $i = 0, 1, 2, 3$, with $\mathbf{i}_0 = 1$.

Further the $\overline{\mathbb{R}}_g$ can be considered as the radius vector in the quaternion compounding space, which is one kind of function space with the quaternion basis vector $(\mathbf{i}_0, \mathbf{i}_1, \mathbf{i}_2, \mathbf{i}_3)$. In the quaternion compounding space, the velocity $\mathbb{V}_g(v_0, v_1, v_2, v_3)$ is combined with the gravitational potential $\mathbb{A}_g(a_0, a_1, a_2, a_3)$ to become the compounding velocity $\overline{\mathbb{V}}_g(\overline{v}_0, \overline{v}_1, \overline{v}_2, \overline{v}_3)$,

$$\overline{\mathbb{V}}_g = \mathbb{V}_g + k_{rx} \mathbb{A}_g. \tag{2}$$

In the quaternion compounding space, the compounding field potential $\overline{\mathbb{A}}_g(\overline{a}_0, \overline{a}_1, \overline{a}_2, \overline{a}_3)$ is

$$\overline{\mathbb{A}}_g = \mathbb{A}_g + K_{rx} \mathbb{V}_g, \tag{3}$$

and the compounding field strength $\overline{\mathbb{B}}_g(\overline{b}_0, \overline{b}_1, \overline{b}_2, \overline{b}_3)$ is

$$\overline{\mathbb{B}}_g = \lozenge \circ \overline{\mathbb{A}}_g = \mathbb{B}_g + K_{rx} \mathbb{U}_g, \tag{4}$$

where the symbol $\circ$ denotes the octonion multiplication, the operator $\lozenge = \Sigma(\mathbf{i}_i \partial_i)$, $\nabla = \Sigma(\mathbf{i}_j \partial_j)$, $\partial_i = \partial/\partial r_i$; The velocity $\mathbb{V}_g = v_0[\lozenge \circ \mathbb{R}_g - \nabla \cdot \{\Sigma(r_j \mathbf{i}_j)\}]$, the velocity curl $\mathbb{U}_g = \lozenge \circ \mathbb{V}_g$. The field potential $\mathbb{A}_g = \lozenge \circ \mathbb{X}_g$, the field strength $\mathbb{B}_g = \lozenge \circ \mathbb{A}_g$. $K_{rx} = 1/k_{rx}$. $j = 1, 2, 3$.

The field strength, $\overline{\mathbb{B}}_g = \overline{\mathbf{g}}/v_0 + \overline{\mathbf{b}}$, includes two components,

$$\overline{\mathbf{g}}/v_0 = \partial_0 \overline{\mathbf{a}} + \nabla \overline{a}_0, \tag{5}$$

$$\overline{\mathbf{b}} = \nabla \times \overline{\mathbf{a}}, \tag{6}$$

where the gauge equation is, $\overline{b}_0 = \partial_0 \overline{a}_0 + \nabla \cdot \overline{\mathbf{a}} = 0$. $\overline{\mathbf{a}} = \Sigma(\overline{a}_j \mathbf{i}_j)$. $\mathbf{a} = \Sigma(a_j \mathbf{i}_j)$.

The linear momentum density, $\overline{\mathbb{P}} = m\overline{\mathbb{V}}_g$, is the source density $\overline{\mathbb{S}}_g$ of gravitational field. The latter one is defined from the gravitational strength $\overline{\mathbb{B}}_g$ and the operator $\lozenge$.

$$\lozenge^* \circ \overline{\mathbb{B}}_g = -\mu_g \overline{\mathbb{S}}_g, \tag{7}$$

where m is the mass density. $*$ denotes the octonion conjugate. $\mu_g = 4\pi G/v_0^2$ is a coefficient, and G is the gravitational constant.

In the quaternion space, the linear motion and the rotational motion of an object can produce the gravitational strength $\mathbb{B}_g$, which includes two components, $\mathbf{g}/v_0 = \partial_0 \mathbf{a} + \nabla a_0$, and $\mathbf{b} = \nabla \times \mathbf{a}$. It requires that the object possesses two kinds of motions to counteract the effects of two components of gravitational strength, and keeps the weightlessness state of the object.

When $\overline{\mathbf{g}} = 0$, the object stays on one kind of weightlessness state, and it can explain the planetary revolution about the sun. When $\overline{\mathbf{b}} = 0$, the object may stay on other kind of 'weightlessness' state, while it can offer reasons for the planetary rotation. And this may be one cause for the celestial body possessing the rotational angular velocity.

2.1. Newton's Law of Gravitation

In the gravitational field, the scalar part $\overline{s}_0$ of source $\overline{\mathbb{S}}_g$ in Eq. (7) is rewritten as follows

$$\nabla^* \cdot \overline{\mathbf{h}} = -\mu_g \overline{s}_0, \tag{8}$$

where $\overline{\mathbf{h}} = \Sigma(\overline{b}_j \mathbf{i}_j)$. $\overline{s}_0 = \overline{p}_0 = m\overline{v}_0$.

Further, the above is reduced to

$$\nabla^* \cdot (\overline{\mathbf{g}}/v_0 + \overline{\mathbf{b}}) = -\mu_g m \overline{v}_0. \tag{9}$$

Equations (3) and (6) yield the equation

$$\nabla \cdot \overline{\mathbf{b}} = 0, \tag{10}$$

and Eqs. (9) and (10) deduce the Newton's law of gravitation for the rotational object,

$$\nabla^* \cdot \overline{\mathbf{g}} = -m/\varepsilon_g, \tag{11}$$

where the coefficient $\varepsilon_g = 1/(\mu_g v_0 \overline{v}_0)$.

Table 1: The octonion multiplication table.

	1	$\mathbf{i}_1$	$\mathbf{i}_2$	$\mathbf{i}_3$	$\mathbf{I}_0$	$\mathbf{I}_1$	$\mathbf{I}_2$	$\mathbf{I}_3$
1	1	$\mathbf{i}_1$	$\mathbf{i}_2$	$\mathbf{i}_3$	$\mathbf{I}_0$	$\mathbf{I}_1$	$\mathbf{I}_2$	$\mathbf{I}_3$
$\mathbf{i}_1$	$\mathbf{i}_1$	-1	$\mathbf{i}_3$	$-\mathbf{i}_2$	$\mathbf{I}_1$	$-\mathbf{I}_0$	$-\mathbf{I}_3$	$\mathbf{I}_2$
$\mathbf{i}_2$	$\mathbf{i}_2$	$-\mathbf{i}_3$	-1	$\mathbf{i}_1$	$\mathbf{I}_2$	$\mathbf{I}_3$	$-\mathbf{I}_0$	$-\mathbf{I}_1$
$\mathbf{i}_3$	$\mathbf{i}_3$	$\mathbf{i}_2$	$-\mathbf{i}_1$	-1	$\mathbf{I}_3$	$-\mathbf{I}_2$	$\mathbf{I}_1$	$-\mathbf{I}_0$
$\mathbf{I}_0$	$\mathbf{I}_0$	$-\mathbf{I}_1$	$-\mathbf{I}_2$	$-\mathbf{I}_3$	-1	$\mathbf{i}_1$	$\mathbf{i}_2$	$\mathbf{i}_3$
$\mathbf{I}_1$	$\mathbf{I}_1$	$\mathbf{I}_0$	$-\mathbf{I}_3$	$\mathbf{I}_2$	$-\mathbf{i}_1$	-1	$-\mathbf{i}_3$	$\mathbf{i}_2$
$\mathbf{I}_2$	$\mathbf{I}_2$	$\mathbf{I}_3$	$\mathbf{I}_0$	$-\mathbf{I}_1$	$-\mathbf{i}_2$	$\mathbf{i}_3$	-1	$-\mathbf{i}_1$
$\mathbf{I}_3$	$\mathbf{I}_3$	$-\mathbf{I}_2$	$\mathbf{I}_1$	$\mathbf{I}_0$	$-\mathbf{i}_3$	$-\mathbf{i}_2$	$\mathbf{i}_1$	-1

The above states that the gravitational potential $\mathbb{A}_g$ affects the field strength $\overline{\mathbf{g}}$ as well as $\overline{\mathbf{b}}$, and impacts finally the movement states of the rotational object, although it is unknown how to measure directly the influences of the gravitational potential at present.

When $\overline{\mathbf{g}} \neq 0$, the object's motion will deviate from the weightlessness state or the prediction deducing from Newton's gravitational theory, such as the orbital receding of the moon [7]. When $\overline{\mathbf{b}} \neq 0$, the object's rotation may depart from the anticipation deriving from the 'weightlessness' state in the above. And the weightlessness state, $\overline{\mathbf{h}} = 0$, is only the extreme case theoretically.

2.2. Ampere's Law of Gravitation

In the quaternion compounding space, the vectorial part $\overline{\mathbf{s}}$ of linear momentum density $\overline{\mathbb{S}}_g$ can be decomposed from Eq. (7).

$$\partial_0 \overline{\mathbf{h}} + \nabla^* \times \overline{\mathbf{h}} = -\mu_g \overline{\mathbf{s}}, \tag{12}$$

where $\overline{\mathbf{s}} = \Sigma(\overline{s}_j \mathbf{i}_j)$. $\overline{s}_j = \overline{p}_j = m\overline{v}_j$.

The above can be rewritten as follows

$$\partial_0(\overline{\mathbf{g}}/v_0 + \overline{\mathbf{b}}) + \nabla^* \times (\overline{\mathbf{g}}/v_0 + \overline{\mathbf{b}}) = -\mu_g \overline{\mathbf{s}}. \tag{13}$$

Equations (3), (5), (6) yield the equation

$$\partial_0 \overline{\mathbf{b}} + \nabla^* \times \overline{\mathbf{g}}/v_0 = 0, \tag{14}$$

and we obtain the Ampere's law of gravitation for the rotational object from the above,

$$\partial_0 \overline{\mathbf{g}}/v_0 + \nabla^* \times \overline{\mathbf{b}} = -\mu_g \overline{\mathbf{s}} \ . \tag{15}$$

The above means that the gravitational field theory in the quaternion compounding space is similar to the classical gravitational theory in form. And it may be used to describe the nonstable movement state of rotational objects in the gravitational field when $\overline{v}_i \neq 0$.

3. ELECTROMAGNETIC FIELD AND GRAVITATIONAL FIELD

The physical feature about the gravitational field and the electromagnetic field of rotational objects can be depicted simultaneously by the octonion space, including the weightlessness state, velocity curl, and spin etc. And the octonion space consists of two perpendicular quaternion spaces.

In the quaternion space for the electromagnetic field, the basis vector is $\mathbb{E}_e = (\mathbf{I}_0, \mathbf{I}_1, \mathbf{I}_2, \mathbf{I}_3)$, the radius vector is $\mathbb{R}_e = \Sigma(R_i \mathbf{I}_i)$, and the velocity is $\mathbb{V}_e = \Sigma(V_i \mathbf{I}_i)$. The $\mathbb{E}_e$ is independent of the $\mathbb{E}_g$, with $\mathbb{E}_e = \mathbb{E}_g \circ \mathbf{I}_0$. These two basis vectors can be combined together to become the basis vector, $\mathbb{E} = (1, \mathbf{i}_1, \mathbf{i}_2, \mathbf{i}_3, \mathbf{I}_0, \mathbf{I}_1, \mathbf{I}_2, \mathbf{I}_3)$, for the octonion space.

In the octonion space for the gravitational field and the electromagnetic field, the radius vector, $\mathbb{R} = \Sigma(r_i \mathbf{i}_i) + k_{eg}\Sigma(R_i \mathbf{I}_i)$, can be combined with the octonion quantity, $\mathbb{X} = \Sigma(x_i \mathbf{i}_i) + k_{eg}\Sigma(X_i \mathbf{I}_i)$, to become the compounding radius vector $\overline{\mathbb{R}}$,

$$\overline{\mathbb{R}} = \mathbb{R} + k_{rx}\mathbb{X}, \tag{16}$$

where k_{eg} is the coefficient. The $\mathbb{X}_e = \Sigma(X_i \mathbf{I}_i)$ is the integral of electromagnetic potential.

Similarly the $\overline{\mathbb{R}}$ can be considered as the radius vector in the octonion compounding space with the basis vector $\mathbb{E}$. While the velocity, $\mathbb{V} = \Sigma(v_i \mathbf{i}_i) + k_{eg}\Sigma(V_i \mathbf{I}_i)$, can be combined with the field potential, $\mathbb{A} = \Sigma(a_i \mathbf{i}_i) + k_{eg}\Sigma(A_i \mathbf{I}_i)$, to become the compounding velocity, $\overline{\mathbb{V}} = \Sigma(\overline{v}_i \mathbf{i}_i) + k_{eg}\Sigma(\overline{V}_i \mathbf{I}_i)$, in the octonion compounding space,

$$\overline{\mathbb{V}} = \mathbb{V} + k_{rx}\mathbb{A}, \tag{17}$$

where $\overline{v}_i = v_i + k_{rx} a_i$; $\overline{V}_i = V_i + k_{rx} A_i$. And the field potential $\mathbb{A}$ consists of the gravitational potential, $\mathbb{A}_g = \Sigma(a_i \mathbf{i}_i)$, and the electromagnetic potential, $\mathbb{A}_e = \Sigma(A_i \mathbf{I}_i)$. $\mathbf{A} = \Sigma(A_j \mathbf{I}_j)$.

In the octonion compounding space, the potential $\overline{\mathbb{A}} = \Sigma(\overline{a}_i \mathbf{i}_i) + k_{eg}\Sigma(\overline{A}_i \mathbf{I}_i)$ is defined as,

$$\overline{\mathbb{A}} = \mathbb{A} + K_{rx}\mathbb{V}, \tag{18}$$

where $\overline{a}_i = a_i + K_{rx} v_i$; $\overline{A}_i = A_i + K_{rx} V_i$. The velocity is $\mathbb{V} = v_0[\lozenge \circ \mathbb{R} - \nabla \cdot \{\Sigma(r_j \mathbf{i}_j)\}]$, the field potential is $\mathbb{A} = \lozenge \circ \mathbb{X}$. A_0 is the scalar potential of electromagnetic field, with $\mathbf{A}_0 = A_0 \mathbf{I}_0$.

The compounding strength $\overline{\mathbb{B}} = \Sigma(\bar{b}_i \mathbf{i}_i) + k_{eg}\Sigma(\overline{B}_i \mathbf{I}_i)$ is defined from the field potential $\overline{\mathbb{A}}$,

$$\overline{\mathbb{B}} = \lozenge \circ \overline{\mathbb{A}} = \mathbb{B} + K_{rx}\mathbb{U}, \tag{19}$$

where $\bar{b}_i = b_i + K_{rx}u_i$, $\overline{B}_i = B_i + K_{rx}U_i$; The velocity curl is $\mathbb{U} = \lozenge \circ \mathbb{V}$, while the field strength is $\mathbb{B} = \lozenge \circ \mathbb{A}$. The compounding strength, $\mathbb{B} = \mathbb{B}_g + k_{eg}\mathbb{B}_e$, consists of the gravitational strength, $\mathbb{B}_g = \Sigma(b_i \mathbf{i}_i)$, and the electromagnetic strength, $\mathbb{B}_e = \Sigma(B_i \mathbf{I}_i)$.

The electromagnetic strength, $\overline{\mathbb{B}}_e = \overline{\mathbf{E}}/v_0 + \overline{\mathbf{B}}$, covers two components,

$$\overline{\mathbf{E}}/v_0 = \partial_0 \overline{\mathbf{A}} + \nabla \circ \overline{\mathbf{A}}_0, \tag{20}$$

$$\overline{\mathbf{B}} = \nabla \times \overline{\mathbf{A}}, \tag{21}$$

where $\overline{\mathbf{A}}_0 = \overline{A}_0 \mathbf{I}_0$, $\overline{\mathbf{A}} = \Sigma(\overline{A}_j \mathbf{I}_j)$. The gauge conditions are $\bar{b}_0 = 0$ and $\overline{B}_0 = 0$.

The electric current density, $\overline{\mathbb{S}}_e = q\overline{\mathbb{V}}_e$, is the source density of electromagnetic field in the octonion compounding space. And $\overline{\mathbb{S}}_e$ and $\overline{\mathbb{S}}_g$ can be combined together to become the compounding field source density, $\mu\overline{\mathbb{S}} = \mu_g \overline{\mathbb{S}}_g + k_{eg}\mu_e \overline{\mathbb{S}}_e$. While the source density $\overline{\mathbb{S}}$ is defined as

$$\lozenge^* \circ \overline{\mathbb{B}} = -\mu\overline{\mathbb{S}}, \tag{22}$$

where μ is a coefficient, and μ_e is the electromagnetic constant. q is the electric charge density.

From the above, we have

$$\lozenge^* \circ \overline{\mathbb{B}}_g + k_{eg}\lozenge^* \circ \overline{\mathbb{B}}_e = -(\mu_g \overline{\mathbb{S}}_g + k_{eg}\mu_e \overline{\mathbb{S}}_e), \tag{23}$$

According to the basis vector and k_{eg}, the above can be decomposed further as follows,

$$\lozenge^* \circ \overline{\mathbb{B}}_g = -\mu_g \overline{\mathbb{S}}_g, \quad \lozenge^* \circ \overline{\mathbb{B}}_e = -\mu_e \overline{\mathbb{S}}_e, \tag{24}$$

where the former equation is the same as Eq. (7) for the gravitational field, while the latter one is the electromagnetic field equation. The coefficient $k_{eg}^2 = \mu_g/\mu_e$.

In the octonion space, the linear motion and rotational motion of one charged object can generate the electromagnetic strength $\mathbb{B}_e$, which has two parts, $\mathbf{E}/v_0 = \partial_0 \mathbf{A} + \nabla \circ \mathbf{A}_0$, and $\mathbf{B} = \nabla \times \mathbf{A}$. Similarly it requires that the charged object possesses two kinds of motions to counteract the effects of two components of electromagnetic strength.

When $\overline{\mathbf{E}} = 0$, the charged object stays on one kind of 'weightlessness' state, and it can cause the motion similar to the planetary revolution. When $\overline{\mathbf{B}} = 0$, the charged object will stay on other kind of 'weightlessness' state, while it may result in the motion similar to the planetary rotation. And this may explain why the charged object owns the spin angular momentum.

3.1. Gauss's Law

In the electromagnetic field, the part $\overline{\mathbf{S}}_0$ of the source $\overline{\mathbb{S}}_e$ in Eq. (24) is rewritten as,

$$\nabla^* \cdot \overline{\mathbf{H}} = -\mu_e \overline{\mathbf{S}}_0, \tag{25}$$

where $\overline{\mathbf{S}}_0 = \overline{S}_0 \mathbf{I}_0$, $\overline{S}_0 = q\overline{V}_0$, $\overline{\mathbf{H}} = \Sigma(\overline{B}_j \mathbf{I}_j)$.

Further, the above is reduced to

$$\nabla^* \cdot (\overline{\mathbf{E}}/v_0 + \overline{\mathbf{B}}) = -\mu_e q\overline{V}_0 \mathbf{I}_0. \tag{26}$$

Equations (18) and (21) yield the Gauss's law of magnetism

$$\nabla \cdot \overline{\mathbf{B}} = 0, \tag{27}$$

and then, we have the Gauss's law from Eqs. (26) and (27),

$$\nabla^* \cdot \overline{\mathbf{E}} = -(q/\varepsilon_e)\mathbf{I}_0, \tag{28}$$

where the coefficient $\varepsilon_e = 1/(\mu_e \overline{V}_0 v_0)$.

The above means that the electromagnetic potential $\mathbb{A}_e$ impacts the field strength $\overline{\mathbf{E}}$ and $\overline{\mathbf{B}}$, and affects finally the movement states of the rotational charged object, although we do not how to survey directly the influences of the electromagnetic potential until to now.

When $\overline{\mathbf{E}} \neq 0$, the movement of the charged object will deviate from the 'weightlessness' state or the prediction deducing from classical Coulomb's law. When $\overline{\mathbf{B}} \neq 0$, the charged object's rotation may depart from the anticipation deriving from the 'weightlessness' state in the above. And the 'weightlessness' state, $\overline{\mathbf{H}} = 0$, is only the extreme case theoretically too.

3.2. Ampere-Maxwell Law

The vectorial part $\overline{\mathbf{S}}$ of electromagnetic source $\overline{\mathbb{S}}_e$ can be decomposed from Eq. (24),

$$\partial_0 \overline{\mathbf{H}} + \nabla^* \times \overline{\mathbf{H}} = -\mu_e \overline{\mathbf{S}}, \tag{29}$$

where $\overline{\mathbf{S}} = \Sigma(\overline{S}_j \mathbf{I}_j)$, $\overline{S}_j = q\overline{V}_j$.

The above can be rewritten as follows

$$\partial_0 (\overline{\mathbf{E}}/v_0 + \overline{\mathbf{B}}) + \nabla^* \times (\overline{\mathbf{E}}/v_0 + \overline{\mathbf{B}}) = -\mu_e \overline{\mathbf{S}} \ . \tag{30}$$

Equations (18), (20), and (21) yield the Faraday's law

$$\partial_0 \overline{\mathbf{B}} + \nabla^* \times \overline{\mathbf{E}}/v_0 = 0, \tag{31}$$

and then, we obtain Ampere-Maxwell law in the electromagnetic field from Eqs. (30) and(31),

$$\partial_0 \overline{\mathbf{E}}/v_0 + \nabla^* \times \overline{\mathbf{B}} = -\mu_e \overline{\mathbf{S}}. \tag{32}$$

The above means that the electromagnetic theory in the octonion compounding space is similar to the classical electromagnetic theory in form also. And it may be used to describe the nonstable movement state of rotational charged objects in the electromagnetic field when $\overline{V}_i \neq 0$.

4. CONCLUSIONS

In the quaternion compounding space, the $\overline{\mathbf{g}}$ and $\overline{\mathbf{b}}$ can be transformed into each other, and may spur the swing of gravitational strength, and then to impact the celestial body's orbital motion and rotational motion. In a similar way, in the octonion compounding space, the $\overline{\mathbf{E}}$ and $\overline{\mathbf{B}}$ can be transformed into each other, and may result in the waggle of electromagnetic strength, and then to impact the movement state of rotational charged objects.

It should be noted that the study for the influences of the field potential to the weightlessness states and the movement states of the rotational object examined only some simple cases in octonion compounding spaces. Despite its preliminary characteristics, this study can clearly indicate that the field potential impacts the weightlessness states and movement states. For the future studies, the research will concentrate on only some predictions about the weightlessness states.

ACKNOWLEDGMENT

This project was supported partially by the National Natural Science Foundation of China under grant number 60677039.

REFERENCES

1. Maxwell, J. C., *A Treatise on Electricity and Magnetism*, Dover Publications Inc., New York, 1954.
2. Newton, I., *The Mathematical Principles of Natural Philosophy*, Dawsons of Pall Mall, London, 1968.
3. Hamilton, W. R., *Elements of Quaternions*, Longmans, Green & Co., London, 1866.
4. Cayley, A., *The Collected Mathematical Papers*, Johnson Reprint Co., New York, 1963.
5. Weng, Z.-H., "Velocity curl and spin in electromagnetic fields," *PIERS Proceedings*, 352–356, Marrakesh, Morocco, March 20–23, 2011.
6. Weng, Z.-H., "Electromagnetic field equation described with the octonions," *Modern Physics*, Vol. 1, No. 1, 17–22, 2011 (in Chinese).
7. Murray, C. D. and S. F. Dermott, *Solar System Dynamics*, Cambridge University Press, Cambridge, 1999.

The Active Filter for Use in Measurement of the Fast Moving Object

Martin Friedl, **Lubomír Fröhlich**, and **Jiří Sedláček**
Department of Theoretical and Experimental Electrical Engineering
Faculty of Electrical Engineering and Communication
Brno University of Technology, Kolejní 2906/4, 612 00 Brno, Czech Republic

Abstract— In the field of a measurement of the fast one shot processes there is necessary to use special frequency filters. This article deals about the synthesis and optimization of the ARC ladder filters with transmission zeros based on frequency dependent negative resistors (FDNR). Frequency filters designed using approximation functions with transfer zeros (like Inverse Chebyshev or Cauer functions) exhibit in comparison to approximation functions with monotonic magnitude response in stop band essential higher steepness of magnitude response in area of transitive band of filter. Active RC filters synthesized using modern active elements grown from passive RLC filter prototypes with very small sensitivity on passive elements can be in comparison to their RLC prototypes realized relative easily. These filters designed using active FDNR blocks as LP (low pass) filters or using SI (Simulated inductors) active blocks in case of HP (high pass) filters can be designed with minimum active and passive elements. During resulting optimization filter design process must be an influence of real lossy active blocks (FNDR, SI) on resulting filter response respected. In contribution here are presented some possibilities of filter optimization from this point of view. There are also discussed and in some examples prescribed ways of filter synthesis with account of influence of lossy active blocks on resulting filter magnitude response in case of Inverse Chebyshev and Cauer filter of LP and HP filters higher (from 3rd to 7th) filter orders.

1. INTRODUCTION

The presented paper describes ARC filter, which is used as LP filter in block diagram for measurement of the fast moving objects. This measurement is based on the eddy currents. Principle of the measurement is draws in Fig. 1. The moving object affects the coil sensor and thus amplitude of the oscillator. The peak detector monitors this change of the signal and next steps are filtering and comparing. The last block is used control unit for signal processing.

Synthesis of the filters was worked out for filter with transmission zeros, where are used lossy FDNR elements. The realization of filters with transmission zeros requires only a small increasing in complexity. However it enables to obtained essential increasing of filter steepness in transition band of filter characteristics and significantly suppress the specific frequency area (zero transmission) [1]. The zero transfer in the transmission function of the filter is obtained by insertion an additional resonant circuit into the classical ladder filter structure.

There are advisedly used lossy FDNR elements, by reason that by useful optimization the value of the filter element can be achieved almost the same filter transfer response as by filters with lossless blocks, however using only half number of OAs. In this paper influence of the quality factor Q (corresponding with lossy of the real elements) is analysed, depending on the filter parameters.

2. PRINCIPLE OF THE LOSSY FDNR BLOCKS

In area of passive filter design are well-known problems with realization of passive elements namely inductors. Consequently, for low and medium frequencies, passive RLC filters are preferably replaced by active filters RC (ARC). For the following simulations was chosen ladder filter with

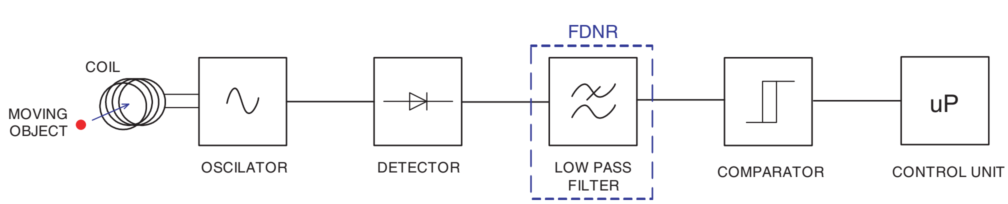

Figure 1: Block diagram of the measurement of the fast moving objects.

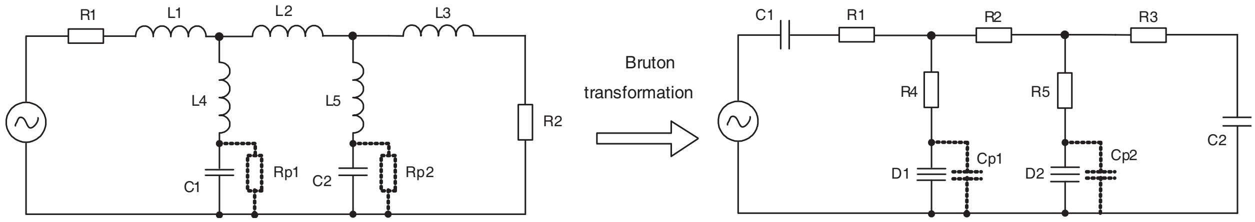

Figure 2: Design principle of active LP filter of the 5th order with transfer zero (Inverse Chebyschev filter).

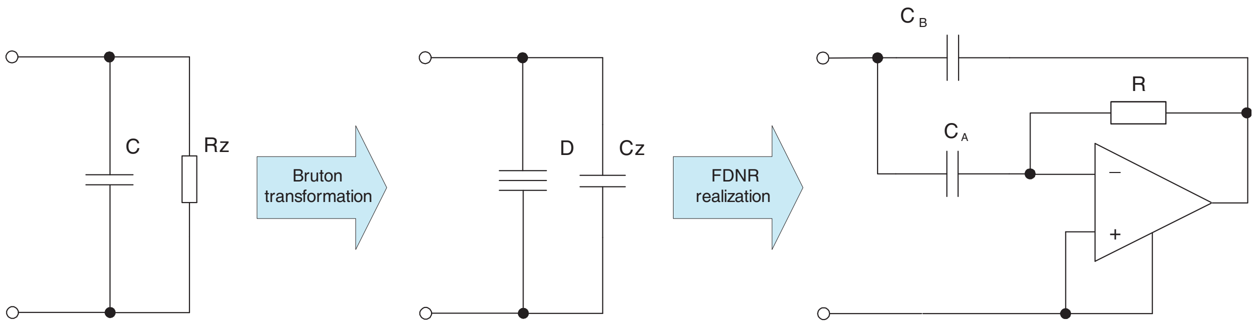

Figure 3: The parallel equivalent lossy circuits and their realization using grounded lossy FDNR.

T-configuration, where can be used FDNR elements. By design of these active filters using Bruton's transformation [2], the initial RLC structure is transformed into equivalent circuit of the CRD structure (Fig. 2). This new structure does not contain an element of inductive character, but uses the properties of the synthetic element named as FDNR (Frequency Depended Negative Rezistor).

The active circuits realized of the FDNR elements can be divided into different types according to their basic circuit characteristics and parameters [3]. The lossy FDNR grounded circuit (Fig. 3) can be realized by the use one active element (OA) [4]. In this circuit the losses are represented by a parallel capacitor. These losses correspond to resistors R_{p1} and R_{p2} parallel connected to capacitors in the original circuit of the RLC filter (Fig. 2). Thus it is very easy these lossy to simulate and change of the quality factor Q of the resonant circuit (which represents transmission zero) and investigate filter response due to these variations of lossy.

3. OPTIMIZATION OF THE QUALITY FACTOR FOR LOSSY FDNR BLOCK

The resonant circuits in the transverse branches of the ladder filter determine the frequency of transmission zero of the filter. The resonant frequency and Q-factor of these circuit are given very known formulas:

$$f = \frac{1}{2 \cdot \pi \cdot \sqrt{L \cdot C}}, \tag{1}$$

$$Q = \omega \cdot C \cdot R_Z. \tag{2}$$

Losses caused by resistor R_Z in Fig. 3, respectively capacitor C_Z directly related to the quality factor Q. It is evident that the resonant frequency is not affected by the lossy resistor R_Z (Fig. 3) connected to the circuit, but the whole filter cutoff frequency yes, as will be shown later. Inserted losses represent lossy in the resonant circuit of original RLC filter prototype. In the active CRD circuit realization these losses are modeled with lossy capacitors $C_{p1,}$ C_{p2} (see Fig. 2).

Losses caused by resistor R_Z in Fig. 2, respectively capacitor C_Z directly determined the quality factor Q of resonant circuits, which realize transfer zero of filter. Investigation of influence the Q-factor on resulting filter parameters is very important and enables the optimization by filter design using active lossy elements (FDNR).

Table 1: The parameter p for different quality factor.

Q	1	2	3	4	5	6	7	8	9	10	20	30	40	50
p	0.1592	0.3183	0.4775	0.6366	0.7958	0.9549	1.1141	1.2732	1.4324	1.5915	3.1831	4.7746	6.3662	7.9577

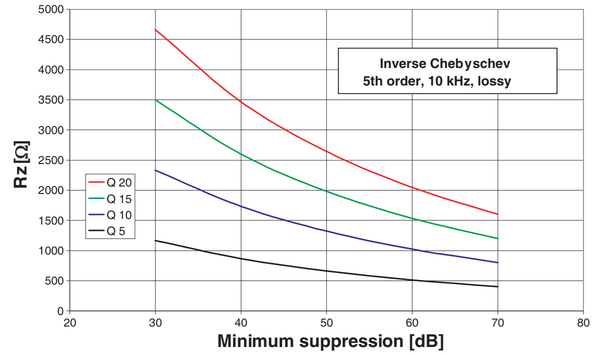

Figure 4: The dependence of the minimal suppress filter on lossy resistor for diferent quality factor Q.

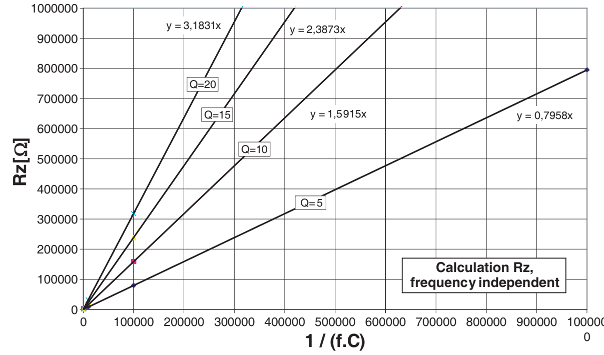

Figure 5: The dependence of lossy rezistor R_z on the coefficient k.

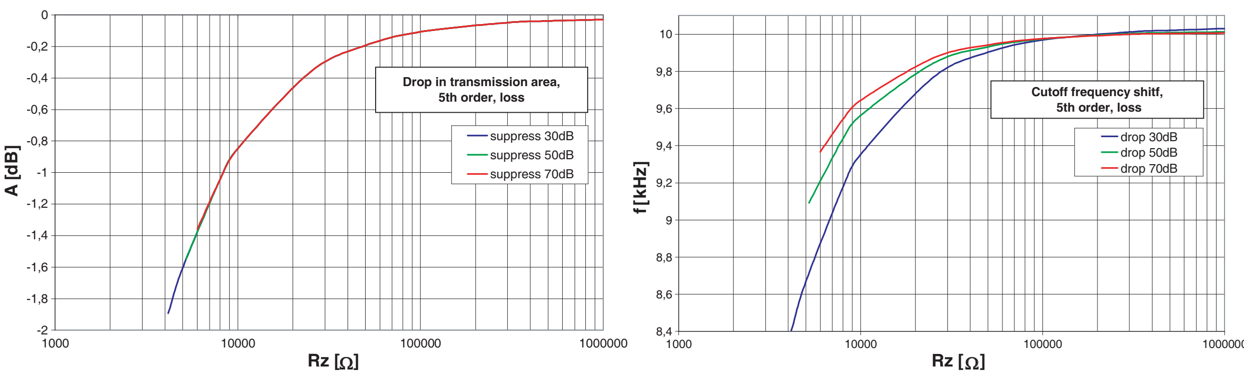

Figure 6: The dependence of the drop in the transfer of the filter and cutoff frequency shift of the filter on lossy resistor R_Z (5th order, LP, Chebyshev).

The following chart (Fig. 4) express for example (in case of the 5th order filter LP, inverse Chebyshev) the dependence of the minimum suppress of the resulting filter on value of lossy resistors for different quality factor Q.

There is evident from the relation (1) that for a resonant frequency can be used a lot of combinations of L and C value parameters thus the chart (Fig. 4) is valid only for one of the ratios of elements L and C in the resonant circuit. In case of the frequency change by constant ratio of elements L and C, the chart will be frequency independent. However, there is dependence on the frequency for different ratio of elements L and C. Therefore, the chart drawn in Fig. 5 has been normalized for all frequencies using the coefficient $k = 1/(C \cdot f)$ (3), where C is the capacitor of the resonant circuit and f is the resonant frequency for the for quality factor 5, 10, 15 and 20:

$$k = \frac{1}{C \cdot f}, \tag{3}$$

$$R_Z = p \cdot k. \tag{4}$$

Thus the chart in Fig. 5 can be easily used also for calculation of the required slope of the line for other different quality factors. In next step it can be determined lossy resistor R_Z according to Equation (4), where p is the slope parameter of the line just for the individual quality factor and k is the coefficient according to Equation (3). The following table shows the various parameters p for quality factor $Q = 1 \div 30$.

The following charts in Fig. 6 draw the dependence of the resulting parameters for the filter of 5th order (Inverse Chebyshev, LP) on losses (loss resistor R_Z from Fig. 3). The left chart shows the dependence of the drop of filter transfer and the right chart shows the dependence of the cutoff frequency shift of the filter on lossy resistors.

All the charts enable by the process of active filter optimization to get an idea about the influence of the losses on the resulting filter parameters (Inverse Chebyshev, LP). The chart on Fig. 4 shows, for the required minimum suppress of the filter, minimum loss resistor R_Z which must be used for required quality factor of the resonant circuit (realized zero of the transmission). The loss resistor R_Z in this chart represents the total losses in the whole ladder filter which for the 5th filter order

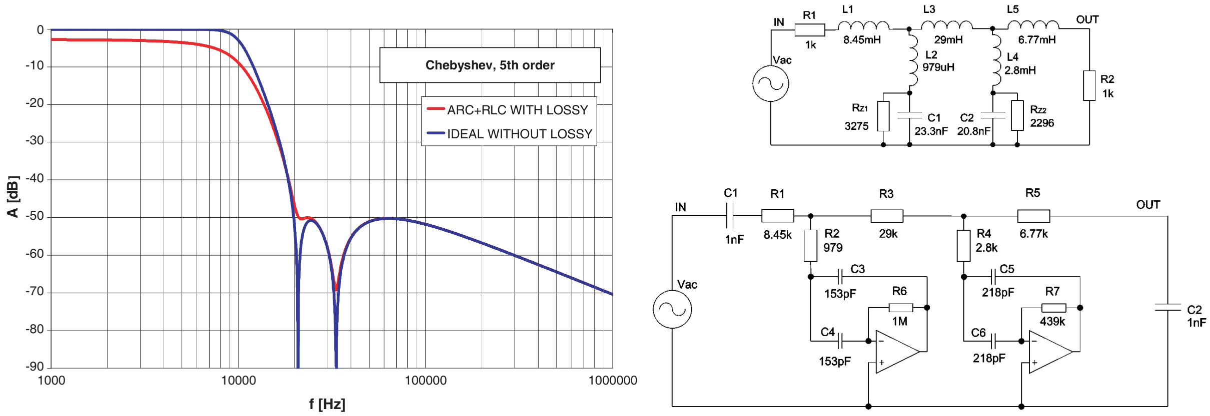

Figure 7: The RLC filter with lossy and corresponding filter with lossy FDNR elements (5th, LP, Chebyshev) and their corresponding transfer characteristic.

is the parallel sum of the resistors R_{p1} and R_{P2} in Fig. 2. The normalized chart from the Fig. 5 achieves more universal validity, because it is frequency independent for the all combinations of the parallel connection of the capacitor C and loss resistor R_Z from Fig. 3. With substituting the calculated parameter p and after putting it into Equation (4) we obtain the value of loss resistor for the required quality factor Q. This loss resistor correspond only to parallel combination of the capacitance C and loss resistor R_Z and therefore losses will be larger because there are two loss resistors in filter of the 5th order (total losses can be calculated simply by the parallel sum of the loss resistors R_{p1} and R_{p2}). The influence of the calculated lossy resistor R_Z on the resulting filter parameters can be found from the charts on the Fig. 6.

The filter which is shown on the Fig. 7 was designed according above prescribed procedure. On the left of the Fig. 7 is transfer characteristic of the ARC and RLC filters with lossy and for comparison there is showed the ideal characteristic without lossy. There is suppressed influence of the voltage divider — the termination resistors R_1 and R_2. The both characteristic are shifted up 6 dB. The circuit diagram of the original RLC filter with lossy resistors and the correspond active filter with lossy FDNR elements are drawn on the right. The filter was designed for frequency 10 kHz and quality factor $Q = 10$ for each resonant circuit (corresponding to two transmission zeros).

According to charts on the Fig. 5 and according to Equations (3) and (4) loss resistors $R_{Z1} = 3257\,\Omega$ and $R_{Z2} = 2296\,\Omega$ correspond to quality factor $Q = 10$ for each resonant circuit. After application of the Bruton transformation and calculation of the lossy FDNR elements with an operational amplifiers we obtain according to Fig. 2 the final circuit, see in Fig. 7 on the right.

The difference of the filter parameters in comparison with designed filter it can be obtained from the PC simulations. The drop in the transmission area of the filter is 2.77 dB and drop by cutoff frequency of the filter is 8.5 dB. The lossy of the designed filter we can read for higher values of Q from the curve on Fig. 6.

4. CONCLUSIONS

The contribution prescribed optimization process by filter design of active ARC filters with transfer zeros, where active filters are based on RLC ladder prototypes. As active blocks of designed filters here are used simple and economical lossy FDNR active elements. The prescribed process of filter optimization has been grown from wide analysis and investigations of filter response by influence of lossy in resonant circuits. In this analysis the quality factor Q was chosen as the basic attitude, which determines the starting point in calculations of possible losses. The resulting influence of the losses on the filter parameters can be determined from the derived charts.

Active RC filters with transfer zeros based on passive RLC filter prototypes exhibit higher steepness of magnitude response in area of transitive band of filter by very small sensitivity on passive elements and can be realized relative easily. These filters designed using active lossy FDNR blocks can be realized with minimum active and passive elements, therefore can be in process of active filter optimization successfully used.

ACKNOWLEDGMENT

The research described in the paper was financially supported by grant of Czech ministry of industry and trade no. FR-TI1/001, GACR 102/09/0314 and project of the BUT Grant Agency FEKT-S-11-5/1012.

REFERENCES

1. Pactitis, S., *Active Filters: Theory and Design*, CRC Press, USA, 2008, 274 str. ISBN 978-1-4200-5476-7.
2. Bruton L. T., *RC-Active Circuits Theory and Design*, Prentice-Hall, Inc., Englewood Cliffs, New Jersey, 1980, ISBN 0-13-753467-1.
3. Friedl, M., *Synthesis of Modern Structures Frequency Filters*, Brno, 2010, 21 s. Pojednáník disertační práci. Brno university of technology Faculty of Electrical Engineering and Communication, Department of Theoretical and Experimental Electrical Engineering.
4. Hájek, K., V. Michal, J. SedláceK, M. Steinbauer, "A simple method of goal — Directed lossy synthesis and network optimization," *Advances in Electrical and Electronic Engineering*, 249–253, Zilinapp, 2006, ISSN 1336-1376.
5. Massara, R. E., "FDNR realisation of all-pole lowpass filters," *IEEE Proceedings*, No. 4, 195–197, 1981, 4 s.

Electromagnetic Force and Velocity Curl

Zi-Hua Weng
School of Physics and Mechanical & Electrical Engineering
Xiamen University, Xiamen 361005, China

Abstract— The paper studies the electromagnetic force of the rotational charged object in the electromagnetic field in the presence of the gravitational field. In the description with the algebra of octonions, there exist some equilibrium states in the two fields to cause the motions similar to the stable overspeed movement of the stars on the fringe of a galaxy. The study claims that the field potential has an influence on the force, the torque, and the equilibrium state, and impacts finally the movement states of the rotational charged object.

1. INTRODUCTION

The validity of Newton's law of gravitation [1] and of electromagnetic force are being doubted all the time, especially in the overspeed movement of stars on the fringe of a galaxy [2]. This uncertainty remains as puzzling as ever. The existing theories do not expound the star's overspeed movement, and then do not offer compelling reason for the physical phenomenon.

The algebra of quaternions [3] was first used by J. C. Maxwell [4] to depict the electromagnetic theory. At present the gravitational field can be described with the quaternion also. The quaternion space for gravitational field can combine with that for electromagnetic field to become an octonion space. Therefore the two fields can be represented with the octonion [5] simultaneously, including the electromagnetic force in the presence of the gravitational field and the velocity curl.

With the algebra of octonions, the results claim that there exist some kinds of equilibrium states in the two fields. The field potential will impact the equilibrium states, and the variation of field potential may shift the force or the torque.

2. LINEAR MOMENTUM

The linear momentum in the gravitational field and the electromagnetic field can be described by the algebra of octonions. In other words, the physical features of the gravitational field and of the electromagnetic field can be depicted in the octonion space simultaneously [6].

2.1. Gravitational Field

In the quaternion space for the gravitational field, the coordinate r_i is real, and the radius vector is $\mathbb{R}_g = \Sigma(r_i \mathbf{i}_i)$, with the basis vector is $\mathbb{E}_g = (\mathbf{i}_0, \mathbf{i}_1, \mathbf{i}_2, \mathbf{i}_3)$. The radius vector can be combined with the physical quantity $\mathbb{X}_g = \Sigma(x_i \mathbf{i}_i)$ to become the compounding radius vector $\overline{\mathbb{R}}_g = \Sigma(\overline{r}_i \mathbf{i}_i)$,

$$\overline{\mathbb{R}}_g = \mathbb{R}_g + k_{rx}\mathbb{X}_g, \quad (1)$$

where $r_0 = v_0 t$; v_0 is the speed of light; t denotes the time. The derivation of $\mathbb{X}_g$ will yield the gravitational potential $\mathbb{A}_g$. $k_{rx} = 1/v_0$ is the coefficient. $\mathbf{i}_0 = 1$. $j = 1, 2, 3$; $i = 0, 1, 2, 3$.

The $\overline{\mathbb{R}}_g$ can be considered as the radius vector in the quaternion compounding space, which is one kind of function space with the basis vector $\mathbb{E}_g$. In this space, the velocity $\mathbb{V}_g = \Sigma(v_i \mathbf{i}_i)$ and the $\mathbb{A}_g = \Sigma(a_i \mathbf{i}_i)$ will combine together to become the compounding velocity $\overline{\mathbb{V}}_g = \Sigma(\overline{v}_i \mathbf{i}_i)$,

$$\overline{\mathbb{V}}_g = \mathbb{V}_g + k_{rx}\mathbb{A}_g, \quad (2)$$

or the gravitational compounding potential $\overline{\mathbb{A}}_g = \Sigma(\overline{a}_i \mathbf{i}_i)$,

$$\overline{\mathbb{A}}_g = \mathbb{A}_g + (1/k_{rx})\mathbb{V}_g. \quad (3)$$

In the quaternion compounding space, the gravitational compounding strength $\overline{\mathbb{B}}_g = \Sigma(\overline{b}_i \mathbf{i}_i)$ is defined from the gravitational compounding potential $\overline{\mathbb{A}}_g$,

$$\overline{\mathbb{B}}_g = \lozenge \circ \overline{\mathbb{A}}_g = \mathbb{B}_g + K_{rx}\mathbb{U}_g, \quad (4)$$

Table 1: The octonion multiplication table.

	1	$\mathbf{i}_1$	$\mathbf{i}_2$	$\mathbf{i}_3$	$\mathbf{I}_0$	$\mathbf{I}_1$	$\mathbf{I}_2$	$\mathbf{I}_3$
1	1	$\mathbf{i}_1$	$\mathbf{i}_2$	$\mathbf{i}_3$	$\mathbf{I}_0$	$\mathbf{I}_1$	$\mathbf{I}_2$	$\mathbf{I}_3$
$\mathbf{i}_1$	$\mathbf{i}_1$	-1	$\mathbf{i}_3$	$-\mathbf{i}_2$	$\mathbf{I}_1$	$-\mathbf{I}_0$	$-\mathbf{I}_3$	$\mathbf{I}_2$
$\mathbf{i}_2$	$\mathbf{i}_2$	$-\mathbf{i}_3$	-1	$\mathbf{i}_1$	$\mathbf{I}_2$	$\mathbf{I}_3$	$-\mathbf{I}_0$	$-\mathbf{I}_1$
$\mathbf{i}_3$	$\mathbf{i}_3$	$\mathbf{i}_2$	$-\mathbf{i}_1$	-1	$\mathbf{I}_3$	$-\mathbf{I}_2$	$\mathbf{I}_1$	$-\mathbf{I}_0$
$\mathbf{I}_0$	$\mathbf{I}_0$	$-\mathbf{I}_1$	$-\mathbf{I}_2$	$-\mathbf{I}_3$	-1	$\mathbf{i}_1$	$\mathbf{i}_2$	$\mathbf{i}_3$
$\mathbf{I}_1$	$\mathbf{I}_1$	$\mathbf{I}_0$	$-\mathbf{I}_3$	$\mathbf{I}_2$	$-\mathbf{i}_1$	-1	$-\mathbf{i}_3$	$\mathbf{i}_2$
$\mathbf{I}_2$	$\mathbf{I}_2$	$\mathbf{I}_3$	$\mathbf{I}_0$	$-\mathbf{I}_1$	$-\mathbf{i}_2$	$\mathbf{i}_3$	-1	$-\mathbf{i}_1$
$\mathbf{I}_3$	$\mathbf{I}_3$	$-\mathbf{I}_2$	$\mathbf{I}_1$	$\mathbf{I}_0$	$-\mathbf{i}_3$	$-\mathbf{i}_2$	$\mathbf{i}_1$	-1

where $\lozenge = \Sigma(\mathbf{i}_i\partial_i)$, $\nabla = \Sigma(\mathbf{i}_j\partial_j)$, with $\partial_i = \partial/\partial r_i$; $\mathbb{V}_g = v_0[\lozenge \circ \mathbb{R}_g - \nabla \cdot \{\Sigma(r_j\mathbf{i}_j)\}]$; The velocity curl $\mathbb{U}_g = \lozenge \circ \mathbb{V}_g$; $\mathbb{A}_g = v_0\lozenge \circ \mathbb{X}_g$; $\mathbb{B}_g = \lozenge \circ \mathbb{A}_g = \Sigma(b_i\mathbf{i}_i)$. The symbol $\circ$ denotes the octonion multiplication. φ is the scalar potential, while $\mathbf{a}$ is the vectorial potential. $a_0 = \varphi/v_0$ is the scalar. $\mathbf{a} = \Sigma(a_j\mathbf{i}_j)$, $\overline{\mathbf{a}} = \Sigma(\overline{a}_j\mathbf{i}_j)$. The gauge equation is $\overline{b}_0 = \partial_0\overline{a}_0 + \nabla \cdot \overline{\mathbf{a}} = 0$. $K_{rx} = 1/k_{rx}$.

The field source density $\overline{\mathbb{S}}$ is defined from the compounding strength $\overline{\mathbb{B}}_g$,

$$(\overline{\mathbb{B}}_g/v_0 + \lozenge)^* \circ \overline{\mathbb{B}}_g = -\mu\overline{\mathbb{S}} = -\mu_g\overline{\mathbb{S}}_g + \overline{\mathbb{B}}_g^* \circ \overline{\mathbb{B}}_g/v_0, \tag{5}$$

where μ and μ_g are the constants. $*$ denotes the octonion conjugate. $\overline{\mathbb{B}}_g^* \circ \overline{\mathbb{B}}_g/(2\mu_g)$ is the energy density of gravitational field, and is similar to that of electromagnetic field.

The linear momentum density $\overline{\mathbb{P}}_g = \Sigma(\overline{p}_i\mathbf{i}_i)$ is the extension of $\overline{\mathbb{S}}_g$, and is defined as

$$\overline{\mathbb{P}}_g = \mu\overline{\mathbb{S}}/\mu_g, \tag{6}$$

where $\overline{p}_0 = \widehat{m}\overline{v}_0$, $\overline{p}_j = m\overline{v}_j$; $\widehat{m} = m + \triangle m$. The $\widehat{m}$ is the gravitational mass density, and the m is the inertial mass density; $\triangle m = -\overline{\mathbb{B}}_g^* \circ \overline{\mathbb{B}}_g/(\overline{v}_0 v_0 \mu_g)$. For a single particle, $\overline{\mathbb{S}}_g = m\overline{\mathbb{V}}_g$.

The above means that the linear momentum of the rotational object includes the linear momentum $\overline{\mathbb{S}}_g$ from the object, and the extra part, $\overline{\mathbb{B}}_g^* \circ \overline{\mathbb{B}}_g/(\mu_g v_0)$, from the gravitational field, although the latter is often neglected in the weak gravitational field.

2.2. Electromagnetic Field

The gravitational field and the electromagnetic field both can be described by the quaternion space. Their quaternion spaces are orthogonal to each other, and can be combined together to become the octonion space. In the octonion space, the basis vector $\mathbb{E} = (\mathbf{i}_0, \mathbf{i}_1, \mathbf{i}_2, \mathbf{i}_3, \mathbf{I}_0, \mathbf{I}_1, \mathbf{I}_2, \mathbf{I}_3)$ consists of the quaternion basis vectors $\mathbb{E}_g$ and $\mathbb{E}_e$. The $\mathbb{E}_e$ is independent of the $\mathbb{E}_g$, with $\mathbb{E}_e = \mathbb{E}_g \circ \mathbf{I}_0$.

In the quaternion space for the electromagnetic field, the coordinate R_i is real, the basis vector is $\mathbb{E}_e = (\mathbf{I}_0, \mathbf{I}_1, \mathbf{I}_2, \mathbf{I}_3)$, and the radius vector is $\mathbb{R}_e = \Sigma(R_i\mathbf{I}_i)$. The latter can be combined with the physical quantity $\mathbb{X}_e = \Sigma(X_i\mathbf{I}_i)$ to become the compounding radius vector,

$$\overline{\mathbb{R}}_e = \mathbb{R}_e + k_{rx}\mathbb{X}_e, \tag{7}$$

where $\mathbb{X} = \mathbb{X}_g + k_{eg}\mathbb{X}_e$, and the derivation of $\mathbb{X}_e$ will yield the electromagnetic potential $\mathbb{A}_e$.

In the octonion space for the gravitational field and the electromagnetic field, the $\overline{\mathbb{R}}_e$ and the $\overline{\mathbb{R}}_g$ can be combined together to become the compounding radius vector,

$$\overline{\mathbb{R}} = \overline{\mathbb{R}}_g + k_{eg}\overline{\mathbb{R}}_e, \tag{8}$$

where the k_{eg} is the coefficient, with $k_{eg}^2 = \mu_g/\mu_e$. $\overline{\mathbb{R}}_e = \Sigma(\overline{R}_i\mathbf{I}_i)$, and $\overline{\mathbb{R}} = \Sigma(\overline{r}_i\mathbf{i}_i + k_{eg}\overline{R}_i\mathbf{I}_i)$.

Similarly $\overline{\mathbb{R}}$ is considered as the radius vector in the octonion compounding space, which is one function space with the basis vector $\mathbb{E}$. In this space, the octonion velocity, $\mathbb{V} = \Sigma(v_i\mathbf{i}_i + k_{eg}V_i\mathbf{I}_i)$, is combined with the octonion potential, $\mathbb{A} = \Sigma(a_i\mathbf{i}_i + k_{eg}A_i\mathbf{I}_i)$, to become the octonion compounding velocity, $\overline{\mathbb{V}} = \Sigma(\overline{v}_i\mathbf{i}_i + k_{eg}\overline{V}_i\mathbf{I}_i)$,

$$\overline{\mathbb{V}} = \mathbb{V} + k_{rx}\mathbb{A}, \tag{9}$$

or the octonion compounding potential, $\overline{\mathbb{A}} = \Sigma(\overline{a}_i \mathbf{i}_i + k_{eg}\overline{A}_i \mathbf{I}_i)$,

$$\overline{\mathbb{A}} = \mathbb{A} + K_{rx}\mathbb{V}, \tag{10}$$

where $\mathbb{V}_e = \Sigma(V_i \mathbf{I}_i)$, $\mathbb{A}_e = \Sigma(A_i \mathbf{I}_i)$, $\overline{\mathbb{V}}_e = \Sigma(\overline{V}_i \mathbf{I}_i)$, $\overline{\mathbb{A}}_e = \Sigma(\overline{A}_i \mathbf{I}_i)$, and $\mathbb{R} = \mathbb{R}_g + k_{eg}\mathbb{R}_e$.

In the octonion compounding space, the compounding strength $\overline{\mathbb{B}} = \Sigma(\bar{b}_i \mathbf{i}_i + k_{eg}\overline{B}_i \mathbf{I}_i)$ is defined from the compounding potential $\overline{\mathbb{A}}$,

$$\overline{\mathbb{B}} = \lozenge \circ \overline{\mathbb{A}} = \mathbb{B} + K_{rx}\mathbb{U}, \tag{11}$$

where $\mathbb{V}_e = v_0 \lozenge \circ \mathbb{R}_e$; $\mathbb{B}_e = \lozenge \circ \mathbb{A}_e = \Sigma(B_i \mathbf{I}_i)$. $\mathbb{U} = \lozenge \circ \mathbb{V}$; $\mathbb{B} = \lozenge \circ \mathbb{A} = \Sigma(b_i \mathbf{i}_i + k_{eg} B_i \mathbf{I}_i)$. ϕ is the scalar potential, and $\mathbf{A} = \Sigma(A_j \mathbf{I}_j)$ is the vectorial potential. $\mathbb{A} = v_0 \lozenge \circ \mathbb{X}$; $\mathbf{A}_0 = A_0 \mathbf{I}_0$, with $A_0 = \phi / v_0$. $\overline{\mathbf{A}}_0 = \overline{A}_0 \mathbf{I}_0$, $\overline{\mathbf{A}} = \Sigma(\overline{A}_j \mathbf{I}_j)$. The gauge equation is $\overline{B}_0 = \partial_0 \overline{A}_0 + \nabla \cdot \overline{\mathbf{A}} = 0$.

The octonion field source density $\overline{\mathbb{S}}$ is defined from the compounding strength $\overline{\mathbb{B}}$,

$$(\overline{\mathbb{B}}/v_0 + \lozenge)^* \circ \overline{\mathbb{B}} = -\mu \overline{\mathbb{S}} = -(\mu_g \overline{\mathbb{S}}_g + k_{eg}\mu_e \overline{\mathbb{S}}_e) + \overline{\mathbb{B}}^* \circ \overline{\mathbb{B}}/v_0, \tag{12}$$

where μ_e is the constant. q is the electric charge density. $\overline{\mathbb{B}}_e^* \circ \overline{\mathbb{B}}_e/(2\mu_e)$ is the energy density of the electromagnetic field. For a single charged particle, $\overline{\mathbb{S}}_e = q\overline{\mathbb{V}}_e$. Meanwhile

$$\overline{\mathbb{B}}^* \circ \overline{\mathbb{B}}/\mu_g = \overline{\mathbb{B}}_g^* \circ \overline{\mathbb{B}}_g/\mu_g + \overline{\mathbb{B}}_e^* \circ \overline{\mathbb{B}}_e/\mu_e. \tag{13}$$

The linear momentum density $\overline{\mathbb{P}} = \Sigma(\overline{p}_i \mathbf{i}_i + k_{eg}\overline{P}_i \mathbf{I}_i)$ is defined as

$$\overline{\mathbb{P}} = \mu \overline{\mathbb{S}}/\mu_g, \tag{14}$$

where $\overline{P}_0 = M\overline{V}_0$, $\overline{P}_j = M\overline{V}_j$; $M = q\mu_e/\mu_g$; $\overline{p}_0 = (m + \triangle m)\overline{v}_0$, $\triangle m = -\overline{\mathbb{B}}^* \circ \overline{\mathbb{B}}/(\overline{v}_0 v_0 \mu_g)$.

The above means that the linear momentum of the rotational charged object includes the linear momentum $\overline{\mathbb{S}}_g$ from the object, the $k_{eg}\mu_e\overline{\mathbb{S}}_e/\mu_g$ from the charged particle, the $\overline{\mathbb{B}}_g^* \circ \overline{\mathbb{B}}_g/(\mu_g v_0)$ from the gravitational field, and the $\overline{\mathbb{B}}_e^* \circ \overline{\mathbb{B}}_e/(\mu_e v_0)$ from the electromagnetic field, although the last two parts are often neglected in the weak fields.

3. GRAVITATIONAL FORCE

We introduce the force's definition from the energy and the torque, so as to encompass various forces regarding gravitational fields, including the inertial force and the gravity etc.

The angular momentum density $\overline{\mathbb{L}}_g = \Sigma(\bar{l}_i \mathbf{i}_i)$ is defined from the linear momentum density $\overline{\mathbb{P}}_g$ and the radius vector $\overline{\mathbb{R}}_g$, and can be written as follows,

$$\overline{\mathbb{L}}_g = \overline{\mathbb{R}}_g \circ \overline{\mathbb{P}}_g, \tag{15}$$

where $\bar{\mathbf{l}} = \Sigma(\bar{l}_j \mathbf{i}_j)$; $\overline{\mathbf{p}} = \Sigma(\overline{p}_j \mathbf{i}_j)$; $\overline{\mathbf{r}} = \Sigma(\overline{r}_j \mathbf{i}_j)$; The $\overline{\mathbb{L}}_g$ includes the scalar $\bar{l}_0$ and the orbital angular momentum density $\overline{\mathbf{r}} \times \overline{\mathbf{p}}$ etc. $\mathbb{L}_g = \overline{\mathbb{R}}_g \circ \mathbb{P}_g = \Sigma(l_i \mathbf{i}_i)$, and $\mathbf{l} = \Sigma(l_j \mathbf{i}_j)$.

3.1. Energy and Torque

We choose the following definition of energy to include various energies in the gravitational field. In the quaternion compounding space, the quaternion energy-torque density $\overline{\mathbb{W}}_g = \Sigma(\overline{w}_i \mathbf{i}_i)$ is defined from the angular momentum density $\overline{\mathbb{L}}_g$,

$$\overline{\mathbb{W}}_g = v_0(\overline{\mathbb{B}}_g/v_0 + \lozenge) \circ \overline{\mathbb{L}}_g, \tag{16}$$

where the $-\overline{w}_0/2$ is the compounding energy density, and the $\overline{\mathbf{w}}/2 = \Sigma(\overline{w}_j \mathbf{i}_j)/2$ is the compounding torque density. The energy includes the kinetic energy, the potential energy, and the work etc.

Expressing the compounding energy density as

$$\overline{w}_0 = v_0 \partial_0 \bar{l}_0 + v_0 \nabla \cdot \bar{\mathbf{l}} + \overline{\mathbf{h}} \cdot \bar{\mathbf{l}}, \tag{17}$$

where $\mathbf{x} = \Sigma(x_j \mathbf{i}_j)$. $\mathbf{h} = \Sigma(b_j \mathbf{i}_j)$. $\overline{\mathbf{h}} = \Sigma(\bar{b}_j \mathbf{i}_j)$. $\mathbf{a} = \partial_0 \mathbf{x} + \nabla x_0 + \nabla \times \mathbf{x}$; $a_0 = \partial_0 x_0 + \nabla \cdot \mathbf{x}$.

In a similar way, expressing the compounding torque density as

$$\overline{\mathbf{w}} = v_0 \partial_0 \bar{\mathbf{l}} + v_0 \nabla \bar{l}_0 + v_0 \nabla \times \bar{\mathbf{l}} + \bar{l}_0 \overline{\mathbf{h}} + \overline{\mathbf{h}} \times \bar{\mathbf{l}}, \tag{18}$$

where the above covers the gyroscopic torque and the torque terms caused by the gravity and the inertial force etc. $\mathbb{W}_g = v_0(\mathbb{B}_g/v_0 + \lozenge) \circ \mathbb{L}_g = \Sigma(w_i \mathbf{i}_i)$, and $\mathbf{w} = \Sigma(w_j \mathbf{i}_j)$.

3.2. Power and Force

We introduce the force definition to incorporate various kinds of force terms within a single formula. In the quaternion compounding space, the quaternion power-force density $\overline{\mathbb{N}}_g = \Sigma(\overline{n}_i \mathbf{i}_i)$ is defined from the energy-torque density $\overline{\mathbb{W}}_g$,

$$\overline{\mathbb{N}}_g = v_0(\overline{\mathbb{B}}_g/v_0 + \lozenge)^* \circ \overline{\mathbb{W}}_g, \tag{19}$$

where the $\overline{f}_0 = -\overline{n}_0/(2v_0)$ is the power density, while the vectorial part $\overline{\mathbf{n}} = \Sigma(\overline{n}_j \mathbf{i}_j)$ is the function of force density. $\mathbb{N}_g = v_0(\mathbb{B}_g/v_0 + \lozenge)^* \circ \mathbb{W}_g = \Sigma(n_i \mathbf{i}_i)$, and $\mathbf{n} = \Sigma(n_j \mathbf{i}_j)$.

Expressing the scalar part $\overline{n}_0$ as

$$\overline{n}_0 = v_0 \partial_0 \overline{w}_0 + v_0 \nabla^* \cdot \overline{\mathbf{w}} + \overline{\mathbf{h}}^* \cdot \overline{\mathbf{w}}. \tag{20}$$

In a similar way, the compounding force density $\overline{\mathbf{f}} = -\overline{\mathbf{n}}/(2v_0)$ in the gravitational field can be defined from the vectorial part $\overline{\mathbf{n}}$,

$$-2\overline{\mathbf{f}} = \nabla^* \overline{w}_0 + \partial_0 \overline{\mathbf{w}} + \overline{\mathbf{h}}^* \times \overline{\mathbf{w}}/v_0 + \nabla^* \times \overline{\mathbf{w}} + \overline{w}_0 \overline{\mathbf{h}}^*/v_0, \tag{21}$$

where the above encompasses the gravity, the inertial force, and the gradient of energy etc.

In the quaternion space, when the $\mathbf{w} = 0$ and the $\mathbf{n} = 0$, the object stays on one kind of equilibrium state, which is similar to that in the Newton's gravitational theory, and is correspondent with the $\mathbf{h} = 0$. In the quaternion compounding space, when the $\overline{\mathbf{w}} = 0$ and the $\overline{\mathbf{n}} = 0$, the rotational object stays on the other kind of 'equilibrium' state, although there may be $\mathbf{w} \neq 0$ and $\mathbf{n} \neq 0$, and it is correspondent with the $\overline{\mathbf{h}} = 0$ (weightlessness state) [7] and the $\mathbf{h} \neq 0$. And it can be used to explain the stable overspeed movement of the rotational stars on the fringe of a galaxy.

4. ELECTROMAGNETIC FORCE

Defining from the energy and torque in the electromagnetic and gravitational fields, the force covers the inertial force, the gravity, the Coulomb force, the Lorentz force, the gradient of energy, and the interacting force between the magnetic strength with the magnetic moment, etc.

In the case for coexistence of electromagnetic field and gravitational field, the angular momentum density $\overline{\mathbb{L}} = \Sigma(\overline{l}_i \mathbf{i}_i + k_{eg} \overline{L}_i \mathbf{I}_i)$ is defined from the $\overline{\mathbb{P}}$ and the $\overline{\mathbb{R}}$,

$$\overline{\mathbb{L}} = \overline{\mathbb{R}} \circ \overline{\mathbb{P}}, \tag{22}$$

where $\overline{\mathbf{L}}_0 = \overline{L}_0 \mathbf{I}_0$; $\overline{\mathbf{L}} = \Sigma(\overline{L}_j \mathbf{I}_j)$. $\overline{\mathbf{P}}_0 = \overline{P}_0 \mathbf{I}_0$; $\overline{\mathbf{P}} = \Sigma(\overline{P}_j \mathbf{I}_j)$. The $\overline{\mathbb{L}}$ includes the part $\overline{\mathbb{L}}_g = \Sigma(\overline{l}_i \mathbf{i}_i)$ from the gravitational field, and the part $\overline{\mathbb{L}}_e = \Sigma(\overline{L}_i \mathbf{I}_i)$ from the electromagnetic field. $\mathbb{L} = \overline{\mathbb{R}} \circ \mathbb{P} = \Sigma(l_i \mathbf{i}_i + k_{eg} L_i \mathbf{I}_i)$, $\mathbf{L}_0 = L_0 \mathbf{I}_0$, $\mathbf{L} = \Sigma(L_j \mathbf{I}_j)$. $\mathbf{X}_0 = X_0 \mathbf{I}_0$, $\mathbf{X} = \Sigma(X_j \mathbf{I}_j)$.

4.1. Energy and Torque

In the electromagnetic and gravitational fields, the energy-torque density $\overline{\mathbb{W}} = \Sigma(\overline{w}_i \mathbf{i}_i + k_{eg} \overline{W}_i \mathbf{I}_i)$ is defined from the angular momentum density $\overline{\mathbb{L}}$ and the field strength $\overline{\mathbb{B}}$,

$$\overline{\mathbb{W}} = v_0(\overline{\mathbb{B}}/v_0 + \lozenge) \circ \overline{\mathbb{L}}, \tag{23}$$

where the $-\overline{w}_0/2$ is the compounding energy density, and the $\overline{\mathbf{w}}/2 = \Sigma(\overline{w}_j \mathbf{i}_j)/2$ is the compounding torque density. The energy includes the kinetic energy, the work, the gravitational potential energy, the electromagnetic potential energy, the gravitational field energy, the electromagnetic field energy, and the interacting energy between the dipole moment with the electromagnetic strength etc.

Expressing the compounding energy density as

$$\overline{w}_0 = v_0 \partial_0 \overline{l}_0 + v_0 \nabla \cdot \overline{\mathbf{l}} + \overline{\mathbf{h}} \cdot \overline{\mathbf{l}} + k_{eg}^2 \overline{\mathbf{H}} \cdot \overline{\mathbf{L}}, \tag{24}$$

where $\mathbf{A} = \partial_0 \mathbf{X} + \nabla \circ \mathbf{X}_0 + \nabla \times \mathbf{X}$; $\mathbf{A}_0 = \partial_0 \mathbf{X}_0 + \nabla \cdot \mathbf{X}$. $\mathbf{H} = \Sigma(B_j \mathbf{I}_j)$. $\overline{\mathbf{H}} = \Sigma(\overline{B}_j \mathbf{I}_j)$.

In a similar way, expressing the compounding torque density as

$$\overline{\mathbf{w}} = v_0 \partial_0 \overline{\mathbf{l}} + v_0 \nabla \overline{l}_0 + v_0 \nabla \times \overline{\mathbf{l}} + \overline{l}_0 \overline{\mathbf{h}} + \overline{\mathbf{h}} \times \overline{\mathbf{l}} + k_{eg}^2 (\overline{\mathbf{H}} \times \overline{\mathbf{L}} + \overline{\mathbf{H}} \circ \overline{\mathbf{L}}_0), \tag{25}$$

where the above includes the gyroscopic torque and the torque caused by the gravity, the inertial force, the Coulomb force, the Lorentz force, and other force terms etc. $\overline{\mathbf{W}}_0 = \overline{W}_0 \mathbf{I}_0$, $\overline{\mathbf{W}} = \Sigma(\overline{W}_j \mathbf{I}_j)$. $\mathbb{W} = v_0(\mathbb{B}/v_0 + \lozenge) \circ \mathbb{L} = \Sigma(w_i \mathbf{i}_i + k_{eg} W_i \mathbf{I}_i)$, and $\mathbf{w} = \Sigma(w_j \mathbf{i}_j)$.

In the electromagnetic field and the gravitational field, the torque $\overline{\mathbf{w}}/2$ of the rotational charged object can be detected in the quaternion space $\mathbb{E}_g$, but the other vectorial part $\Sigma(\overline{W}_i \mathbf{I}_i)$ can not be yet currently, although the latter has still an effect on the power and the force.

4.2. Power and Force

In the octonion compounding space, the power-force density $\overline{\mathbb{N}} = \Sigma(\overline{n}_i \mathbf{i}_i) + k_{eg}\Sigma(\overline{N}_i \mathbf{I}_i)$ is defined from the energy-torque density $\overline{\mathbb{W}}$ and the field strength $\overline{\mathbb{B}}$,

$$\overline{\mathbb{N}} = v_0(\overline{\mathbb{B}}/v_0 + \lozenge)^* \circ \overline{\mathbb{W}}, \tag{26}$$

where $\overline{f}_0 = -\overline{n}_0/(2v_0)$ is the power density, while one vectorial part $\overline{\mathbf{n}} = \Sigma(\overline{n}_j \mathbf{i}_j)$ is the function of force density. $\mathbb{N} = v_0(\mathbb{B}/v_0 + \lozenge)^* \circ \mathbb{W} = \Sigma(n_i \mathbf{i}_i + k_{eg} N_i \mathbf{I}_i)$, and $\mathbf{n} = \Sigma(n_j \mathbf{i}_j)$.

Further expressing the scalar part $\overline{n}_0$ as

$$\overline{n}_0 = v_0 \partial_0 \overline{w}_0 + v_0 \nabla^* \cdot \overline{\mathbf{w}} + \overline{\mathbf{h}}^* \cdot \overline{\mathbf{w}} + k_{eg}^2 \overline{\mathbf{H}}^* \cdot \overline{\mathbf{W}}. \tag{27}$$

In a similar way, the force density $\overline{\mathbf{f}} = -\overline{\mathbf{n}}/(2v_0)$ in the gravitational field and the electromagnetic field can be defined from the vectorial part $\overline{\mathbf{n}}$,

$$-2\overline{\mathbf{f}} = \nabla^* \overline{w}_0 + \partial_0 \overline{\mathbf{w}} + \overline{\mathbf{h}}^* \times \overline{\mathbf{w}}/v_0 + \nabla^* \times \overline{\mathbf{w}} + \overline{w}_0 \overline{\mathbf{h}}^*/v_0 + k_{eg}^2(\overline{\mathbf{H}}^* \times \overline{\mathbf{W}} + \overline{\mathbf{H}}^* \circ \overline{\mathbf{W}}_0)/v_0, \tag{28}$$

where the above includes the inertial force, the gravity, the electromagnetic force, the gradient of energy, and the interacting force between the dipole moment with the magnetic strength etc.

In the octonion space, when the $\mathbf{w} = 0$ and the $\mathbf{n} = 0$, the charged object stays on one kind of equilibrium state, which is similar to that in the Maxwell's electromagnetic field theory, and is correspondent with the $\mathbf{h} = 0$. In the octonion compounding space, when the $\overline{\mathbf{w}} = 0$ and the $\overline{\mathbf{n}} = 0$, the rotational charged object stays on the other kind of 'equilibrium' state, although there may be $\mathbf{w} \neq 0$ and $\mathbf{n} \neq 0$, and it is correspondent with the $\overline{\mathbf{h}} = 0$ and the $\mathbf{h} \neq 0$. And it can be used to explain the stable overspeed movement of the rotational charged objects.

5. CONCLUSIONS

In the octonion compounding space, the field potential affects the field strength, the field source, the angular momentum, the energy, the torque, the power, and the force etc. The force's definition incorporates various forces regarding the electromagnetic field and the gravitational field within a single formula, which covers the inertial force, the gravity, the Coulomb force, the Lorentz force, the gradient of energy, interacting force between the field strength with the magnetic moment etc. When $\overline{\mathbf{w}} \neq 0$ and $\overline{\mathbf{n}} \neq 0$, the rotational charged object departs from the equilibrium state and the anticipation deriving from the Newton's law of gravitation and the classical Coulomb's law.

It should be noted that the study for the influences of the field potential to the equilibrium state and electromagnetic force of the rotational charged object examined only some simple cases. Despite its preliminary characteristics, this study can clearly indicate that the field potential impacts the equilibrium state and the electromagnetic force etc. For the future studies, the research will focus on some predictions about the equilibrium states of the rotational charged objects.

ACKNOWLEDGMENT

This project was supported partially by the National Natural Science Foundation of China under grant number 60677039.

REFERENCES

1. Newton, I., *The Mathematical Principles of Natural Philosophy*, Dawsons of Pall Mall, London, 1968.
2. Zwicky, F., "On the masses of nebulae and of clusters of nebulae," *Astrophysical Journal*, Vol. 86, No. 3, 217–246, 1937.
3. Hamilton, W. R., *Elements of Quaternions*, Longmans, Green & Co., London, 1866.
4. Maxwell, J. C., *A Treatise on Electricity and Magnetism*, Dover Publications Inc., New York, 1954.
5. Cayley, A., *The Collected Mathematical Papers*, Johnson Reprint Co., New York, 1963.
6. Weng, Z.-H., "Electromagnetic field equation described with the octonions," *Modern Physics*, Vol. 1, No. 1, 17–22, 2011 (in Chinese).
7. Weng, Z.-H., "Velocity curl and spin in electromagnetic fields," *PIERS Proceedings*, 352–356, Marrakesh, Morocco, March 20–23, 2011.

Limiting Effects in the Application of Inductive Sensors for Measuring of Non-harmonic High-level Current Pulses

R. Myška, and P. Drexler
Department of Theoretical and Experimental Electrical Engineering
Brno University of Technology, Kolejni 2906/4, Brno 612 00, Czech Republic

Abstract— This article deals with description of limiting effects occurring by measurement of non-harmonical high-level current pulses by means of inductive sensors. These effects will be described for the case of Rogowski coil application in current pulses measurement. The first is a fact that the sensor must be considered as a circuit with distributed parameters. For measuring of non-harmonic waveforms is necessary to ensure the Heaviside's condition for distortionless transmission line. The second factor is the Gibbs's effect which causes overshoots on the edges of a rectangular pulse. The third factor is the influence of wire position in the sensor on the character of output waveform. All of these factors which have been mentioned above cause a serious limitation of induction sensor application for non-harmonic current pulses measurement. Special precautions have to be ensured in order to attain of distortion-free measurement. The influence of precaution violation on the measured waveform will be shown.

1. INTRODUCTION

During development of measuring system for high-level current source, which is able to create pulses of several tens as far as thousands of amperes, a inductive sensor in design of Rogowski coil has been tested. Three limiting effect occurring by the measurement of non-harmonical high-level current pulses were discovered during the experimental measurement. The description of these effects is presented in this paper and some possibilities of suppression of these effects are proposed.

2. ROGOWSKI COIL

Rogowski coil is a type of inductive sensor, Figure 1. It eliminates the dependence of induced voltage on wire position toward the sensor in this design. The base of sensor is a coil in toroidal form with N turns. Core of the coil is air, therefore it cannot come to saturation. For output voltage holds

$$u_i(t) = -\mu_r \mu_0 N S \frac{di(t)}{dt}. \tag{1}$$

Output voltage from the sensor is proportional to derivation of the measured current therefore it must be integrated. A self-integrating property of the sensor was chosen for integration. This approach utilizes a low resistance as terminating impedance [1, 2].

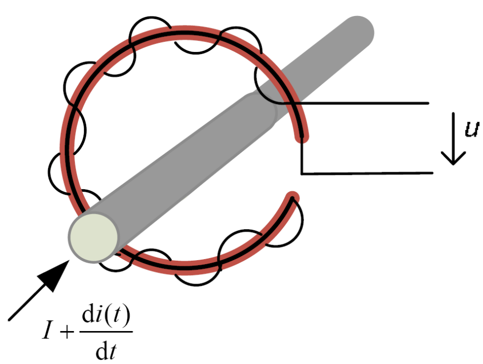

Figure 1: Rogowski coil.

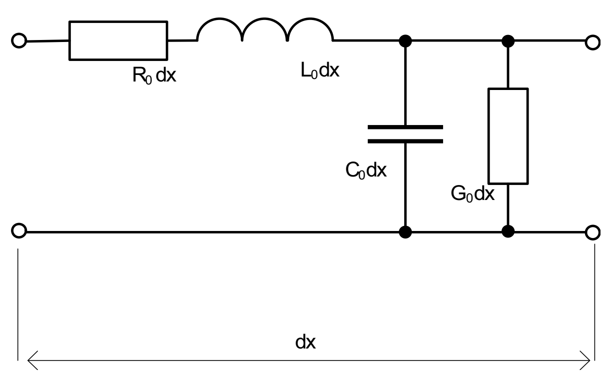

Figure 2: Equivalent circuit of Rogowski coil — transmission line with distributed parameters.

3. DESCRIPTION OF LIMITING EFFECTS

In case when the inductive sensor is realized as a Rogowski coil it is possible to consider sensor as a transmission line with distributed parameters (Figure 2).

For distortionless signal output from the sensor the Heaviside's condition for distortionless transmission line must be ensured

$$\frac{R_0}{L_0} = \frac{G_0}{C_0}. \tag{2}$$

Since the wire resistivity R_0 is frequency dependent because of the skin effect, it is difficult to preserve this condition in selected frequency range. In case when condition (2) isn't satisfied the measured current waveform may be hard distorted. This effect may be identified as a first important factor in application of inductive sensors for non-harmonic high frequency current measurement. The transmission line parameters G_0, L_0, C_0 can be considered as frequency invariant with some simplifications. Hence, the main source of Heaviside's condition violation is frequency dependent R_0. In order to suppress the R_0 frequency dependency, which is caused by the skin effect, the stranded wire has to be used.

A second important effect is the influence of wire position in sensor for high-frequency current measurement. In this case a fast varying magnetic field with different phase shifts in different parts of sensors occurs due to high frequency current flowing through the wire. Voltage signals from various parts of sensor come to output with different time delay. Hence the wire position in the sensor coil is not insignificant. In order to verify the influence of wire position in the sensor coil on the character of output waveform, a series of measurements has been made. The wire has been placed in three different positions in toroidal coil, Figure 3. The positions are marked in Figure 4. Rectangular current pulse with amplitude $I = 24\,\mathrm{A}$ and width $t = 40\,\mathrm{ns}$ has been used for measured.

Output waveforms are shown in Figure 6 to Figure 8. Amplitude oscillation is evident in the waveforms behind the voltage pulse. Their level is dependent on the position of wire in the coil. is The relation between length of the sensor and the rate of change of magnetic field for position 2 is

Figure 3: Realized Rogowski coil in form of toroidal coil.

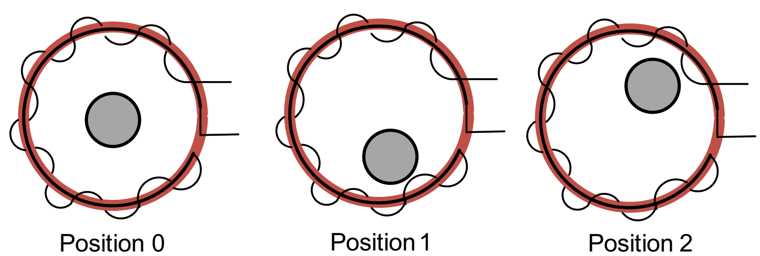

Figure 4: Position of wire in the Rogowski coil.

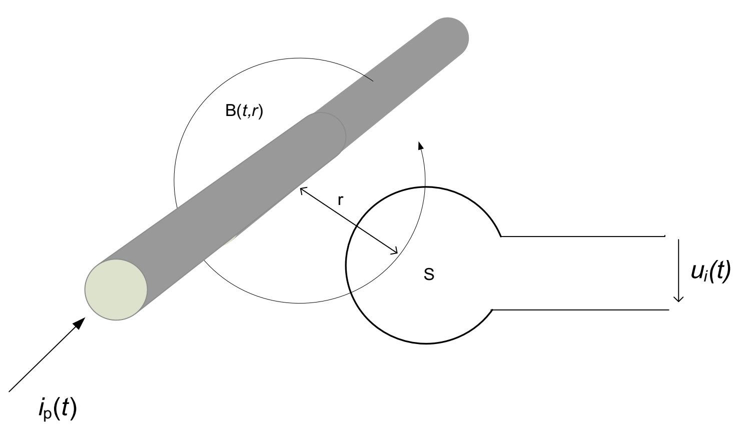

Figure 5: B-dot sensor arrangement for suppress of wire position induced distortion.

suitably adjusted that oscillation is significantly suppressed. In order to avoid the signal distortion the suitable position of wire in sensor has to be chosen. However this is very difficult to achieve for non-harmonic currents, because of different phase shifts of the frequency components. A sensor coil with very small diameter should be used to reduced the position induced distortion or we have to constrain the measurement for current waveforms with limited content of high frequency components (with slower rising and falling edges). A different approach is to utilize a B-dot sensor, which principle is shown in Figure 5. This sensor arrangement solves the problem with correct wire position in respect to sensing coil.

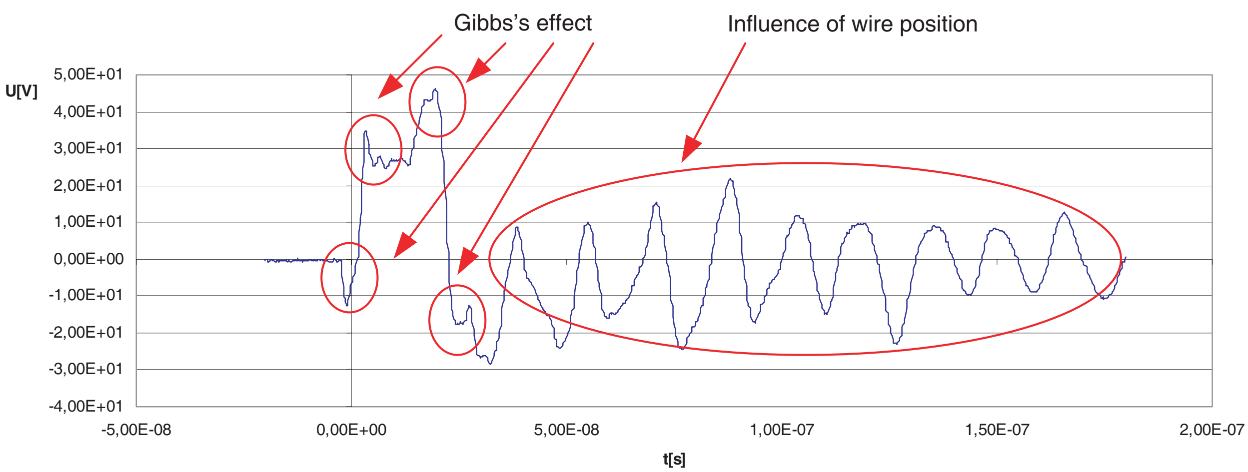

Figure 6: Output waveform Rogowski coil for position 0 of wire.

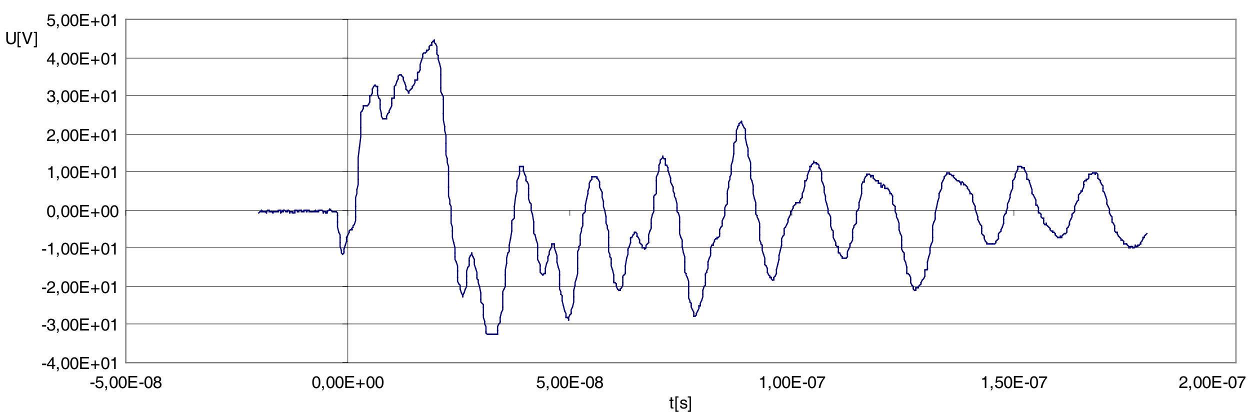

Figure 7: Output waveform Rogowski coil for position 1 of wire.

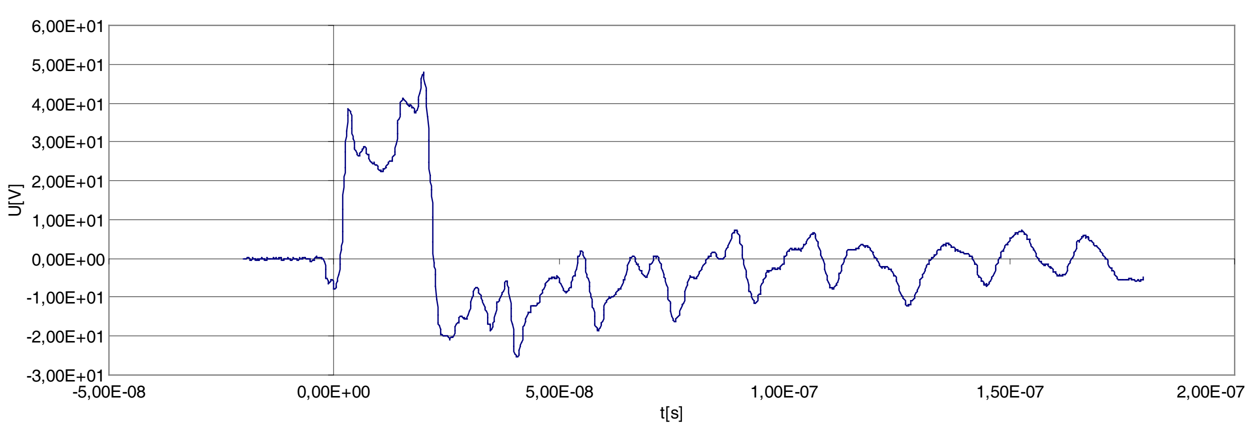

Figure 8: Output waveform Rogowski coil for position 2 of wire.

For output voltage holds

$$u_i(t) = -\frac{d}{dt} \cdot \left(\mathbf{B}(r,t) \oint_S d\mathbf{S} \right) = -\mu_0 \cdot S \frac{d}{dt} \cdot H(r,t) = -\frac{\mu_0 \cdot S}{2\pi r} \frac{di(t)}{dt}, \tag{3}$$

where r determines loop position with area S, referring to source of magnetic field (conductor). From this reason, the geometry of sensor arrangement must be known. This is a disadvantage in comparisson to Rogowski coil.

The third restricting effect is caused by the limited frequency range of the sensor. Rogowski coil had a low-pass filter character. Hence its transmission bandwidth is reduced on high frequencies. Due to this fact, overshoots are present on the edges of output waveforms. This can be mathematically described by Gibbs's effect. This effect describes properties of Fourier series for rectangular function $f(t)$. For infinite number of harmonic components there are overshoots about 9% of amplitude function $f(t)$. For final number of harmonic component overshoots will be bigger. In order to suppress the influence of Gibb's effect, the bandwidth of the sensor has to be increased. This can be achieve with reduction of sensor inductance utilizing less turns count. However this approach causes a decrease in the sensor sensitivity and we have to confine to large current pulses measurement.

4. CONCLUSION

In this paper, three limiting effects has been presented. These effect were observed by non-harmonical high-level current pulses measurements by inductive sensors. Theoretical description of these effect has been given and their influence on output voltage waveforms has been shown. First effect is associated with Heaviside's condition. Resistivity of the sensor isn't equal for low and high frequency because of the skin effect. Therefore, it is hard to ensure this condition. A second effect is the influence of wire position in sensor for high-frequency current measurement. The third effect can be describe by the influence of Gibbs's effect. This effect causes overshoots on the edges of a rectangular pulse. The approaches to avoiding of distortions, which are caused by above mentioned effects, has been outlined in the paper.

ACKNOWLEDGMENT

The research described in the paper was financially supported by project of the BUT Grant Agency FEKT-S-10-13, by research plan No. MSM 0021630513 ELCOM and the grant of Czech ministry of industry and trade No. FR-TI1/001.

REFERENCES

1. Drexler, P., "Measurement methods of ultra-short non-periodical electromagnetic pulses," 92, Ph.D. thesis, Brno University of Technology, Brno, 2007.
2. Myška, R. , "Measurement system for pulsed current source," 79, Master thesis, Brno, Brno University of Technology, 2011.

Temperature Dependencies Measurement, Proposal and Preparing

J. Hrozek[1], **D. Nespor**[1], **and K. Bartusek**[2]

[1]Deptartment of Theoretical and Experimental Electrical Engineering
Brno University of Technology, Kolejni 2906/4, 612 00 Brno, Czech Republic
[2]Institute of Scientific Instruments, Academy of Sciences of the Czech Republic
Kralovopolska 147, 612 64 Brno, Czech Republic

Abstract— This paper contains two parts. The first one deals with proposal and preparing of temperature dependencies measurement of bio-material thermal properties. The thermal properties of each matter are dependent on its own temperature. The measurement of heat conduction and specific heat of bio-material is described in this paper. Knowledge of these parameters is very important for the thermal processes computer simulation. However, these properties are very bad to find out. The bio-material will be used for a real experiment of the cryosurgery optimization. The second part of this paper deals with computer simulation of prepared measurement. Real measurement will be provided in close future and measured thermal dependencies of bio-material thermal properties will be used in next one simulation of cryosurgery. The main aim of this simulation is to find optimized parameters of cryosurgery. Results of simulation will be used in real experiment of cryosurgery optimization.

1. INTRODUCTION

The thermal conduction and the specific heat are two most important thermal properties of each matter for computer simulation. However these parameters could be very different in whole temperature range. Knowledge of these temperature dependencies is very important for correct results obtaining. For example see Figures 1(a) and (c) where temperature dependencies of stainless steel AISI 302 are shown.

We need to know temperature dependencies of the bio-material thermal properties. These properties will be used for real experiment of cryosurgery optimization. We have to use two physical approaches for obtaining of all important data. The first one is calculation of thermal conductivity from known parameters of system, see equation (1) and figure 1 b). It's necessary to have only small temperature gradient $T_1 - T_2$ about 1 K for exact determination of the thermal conductivity by the temperature in $\frac{1}{2}$ of Δx.

$$Q = k \cdot A \cdot \frac{T_1 - T_2}{\Delta x} \quad \Rightarrow \quad k = \frac{Q \cdot \Delta x}{A \cdot (T_1 - T_2)}, \tag{1}$$

where Q is heat transfer [W], k is thermal conductivity [W/(m · K)], A is area [m^2], T_1, T_2 are temperatures on both sides of material [K], Δx is thickness [m].

The second physical approach is the calorimetry. The main principle of the calorimetry is in heat transferring from first matter of known weight to second matter of known weight. We need

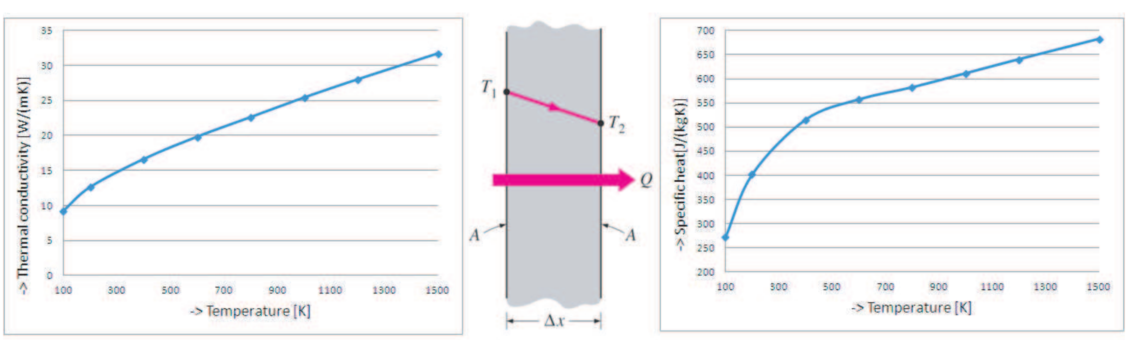

(a) (b) (c)

Figure 1: (a) Thermal conductivity. (b) Heat transfer scheme. (c) Specific heat.

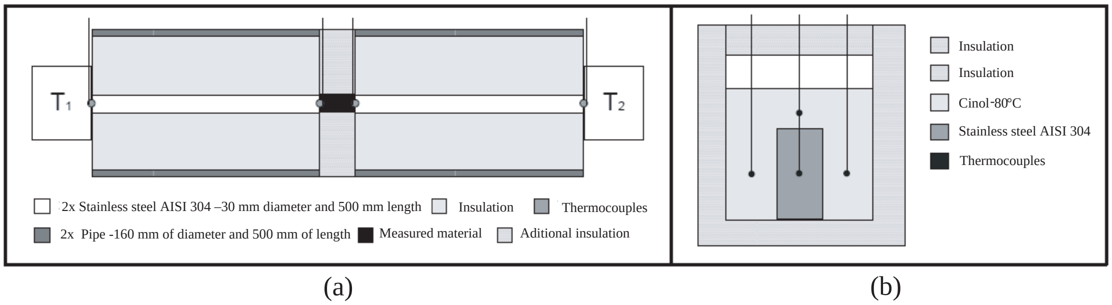

Figure 2: Principle scheme of (a) thermal conductivity measurement, (b) calorimetry.

temperature stable state for reading of specific heat by this temperature. The principle of the calorimetry is obvious from the Equation (2).

$$Q_1 = Q_2 \quad \Rightarrow \quad C_1 \cdot m_1 (T_1 - T) = C_2 \cdot m_2 (T - T_2) \quad \Rightarrow \quad C_2 = \frac{C_1 \cdot m_1 (T_1 - T)}{m_2 (T - T_2)}, \tag{2}$$

where C_1, C_2 are specific heats of both matters [kJ/(kg $\cdot$ K)], m_1,m_1 are weights [kg], T_1, T_2 are initial temperatures [K], T is the final stable temperature [K].

2. EXPERIMENTS

Two laboratory preparations will be realized for measuring of thermal conductivities and specific heats. The scheme of the first one is displayed on Figure 2(a).

Two stainless steel AISI 304 rods of 30 mm in diameter and 500 mm in length will be surrounded with thermal insulation and finally covered with waste pipe of 160 mm in diameter. The measured matter is situated between these two parts. Heat stable sources are realized like two radiators cooled with liquid nitrogen and heated with electric power heating. Power of cooling is regulated with depth of immerse into container of liquid nitrogen. Electric power heating is realized with heating coil. We need adjust temperatures in range 76 K to body temperature about 310 K. The thermocouples are placed on boundaries of matter. The main idea of realized experiment corresponds with Equation (1). We know thermal conductivity of stainless steel but we don't know the thermal conductivity of measured material a heat transfer thru it. Therefore we have to set up 10 K temperature gradient with two stable heat sources. Then we can read temperatures on ends of two steel rods and assume the same heat transfer is thru the preparation. These temperatures may be used in left side of Equation (1). We obtain heat transfer which can be used in right side of Equation (1). The result is then the thermal conductivity of measured material.

The scheme of second experiment is displayed on Figure 2(b). The calorimetry is based on law of energy continue and correspond with Equation (2). Unknown specific heat of one matter is calculates from known specific heat of second matter and other parameters. But we have problem in this case. We don't know thermal dependencies of specific heat of non freezing liquid CINOL $-80°$C based on ethanol. Therefore we have to measure specific heats of SINOL $-80°$C. So the prism of stainless steel AISI 304 with temperature T_1 is inserted to the SINOL $-80°$C with temperature T_2. Temperature gradient must be small about 10 K. We can stop measurement when the temperature T will be stable. Then we can substitute three temperatures to the left side of Equation 2 and obtain temperature dependence of specific heat of SINOL $-80°$C. Temperature dependence of specific heat of bio-material can be measure finally.

3. MEASUREMENT OF LIQUID NITROGEN HEATING POWER

The first part of real experiment is focused on finding of liquid nitrogen heating power. This experiment is displayed in Figure 3(a). Square prism of stainless steel AISI 304 of dimensions $25 \times 25 \times 86$ mm is immersed 30 mm in liquid nitrogen. The temperature is measured with the time simultaneously. We can stop time measurement when the temperature on non cooled end of the prism come stable close the temperature of liquid nitrogen. The temperature rate is displayed in Figure 4 compared with calculated results. Now we can calculate the cooling power per immersed prism surface. We suppose next parameters of the steel prism and measurement like specific heat $C_p = 400$ J/(kg $\cdot$ K), density $\rho =$7900 kg/m^3 and weight of steel prism $m = 0.425$ kg. The necessary

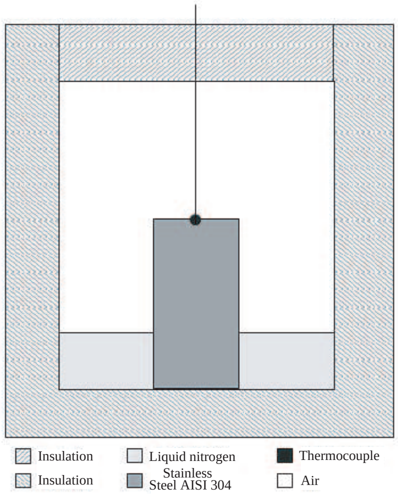

(a)

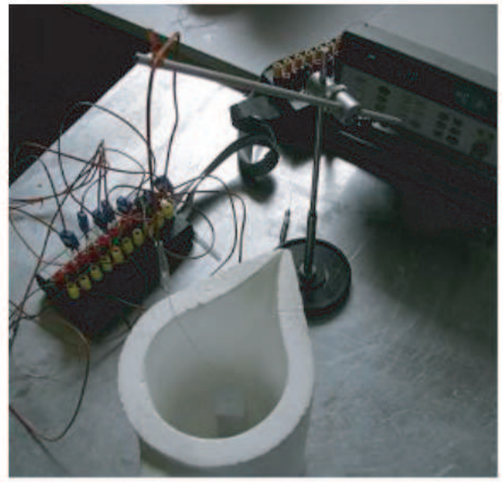

(b)

Figure 3: (a) Principle scheme of calorimetry. (b) Real experiment.

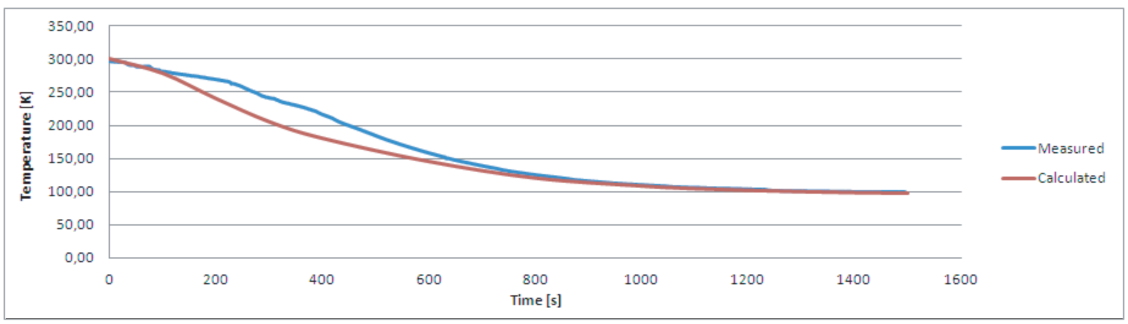

Figure 4: Measured temperature in opposite end of 86 mm AISI 304 rod during the time compared with calculated.

energy for heating our steel prism up 1 K is then 169 J. So temperature change about 200 K needs 33970 J. Applied cooling power is then 22 W or J/s per immersed surface $S = 0.003625\,\mathrm{m}^2$ because we know the necessary time for stable temperature state about 1500 s. Latent cooling power of liquid nitrogen is about $6068\,\mathrm{W/m}^2 \Rightarrow 75.85\,\mathrm{W/m}^2 \cdot K$.

4. COMPUTER DESIGN AND PREPARING OF MEASUREMENT

We have to design the laboratory preparation with enough heat power for setting the temperature gradients about 10 K in whole temperature range from 100 K to 310 K corresponds with Figure 2(a). We have to add from 1536 J to 2910 J per 1 K change of temperature. Because one meter length of stainless steel AISI 304 rod weights about 5,65 kg and specific heat is in range from 272 to 515 J/(kg · K). Latent heat of vaporization of liquid nitrogen is about 199 KJ/kg and cooling power is about $6068\,\mathrm{W/m}^2$. If we suppose the cooling power of our system about $76\,\mathrm{W/m}^2 \cdot \mathrm{K}$ then it would take approximately 22 s per 1 K temperature change. The 200 K change needs then about $4400\,\mathrm{s} \cong 1$ hour and 13 minutes. But the cooling rate is dependent on many factors. The main factor is surface on which is applied cooling power is applied. The temperature rate in opposite end of 0.5 m AISI 304 rod is displayed in Figure 5(a). The cooling power was setup coordinate with counted cooling power of liquid nitrogen. Three centimetres of the rod is immersed in liquid nitrogen and other part of the rod is insulated. Whole temperature distribution in whole steel prism is shown bellow in Figure 5(b) after 1500 s.

5. RESULTS

Real experiment with square prism of stainless steel AISI 304 of dimensions $25 \times 25 \times 86$ mm and liquid nitrogen gave us latent cooling power of liquid nitrogen about $6068\,\mathrm{W/m}^2 \Rightarrow 75.85\,\mathrm{W/m}^2 \cdot \mathrm{K}$. Time for stable temperature state in 0.5 m steel rod is then estimated over 4 hours.

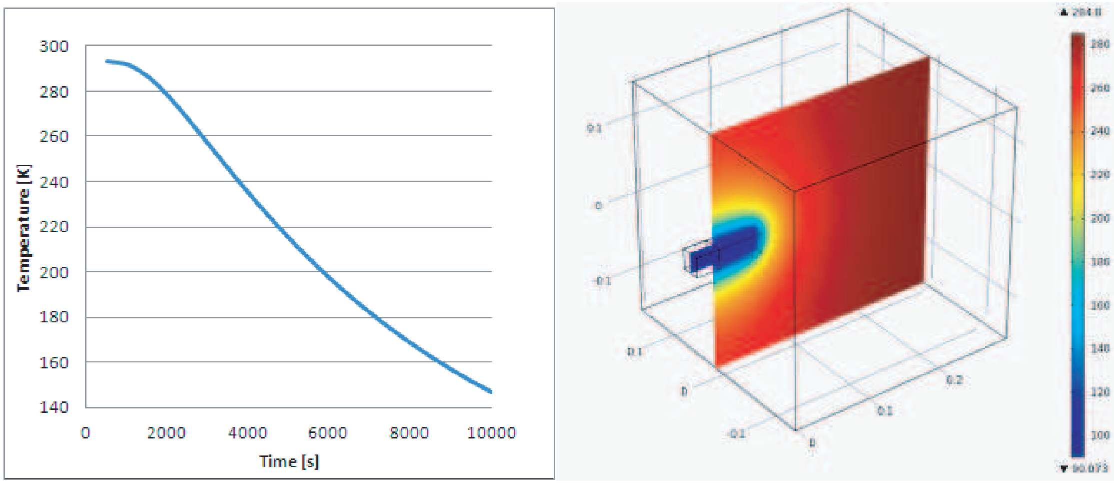

(a) (b)

Figure 5: (a) Temperature rate in opposite end of 0.5 m AISI 304 rod. (b) Temper temperature distribution in whole steel prism after 1500 s.

6. CONCLUSIONS

The main goal of research discrabed in this paper is temeperature dependecies meeasurement of bio-material thermal properties. This properties are very important for next computer simulation for optimization of cryosurgery. The stainless steel AISI 304 is used because its temperature dependecies of thermal properties are known and closer to bio-material then other known metal materials. Assumtion of bio-material thermal conductivity is about 0.5 W/m and specific heat is about 3600 J/(kg · K) insteed of thermal conductivity of AISI 304 about 12 W/m and specific heat is about 400 J/(kg · K). Next part of research will be focused on real measurement of temperature dependencies of bio-material thermal properties. Final part of this research will be focused on cryosurgery optimization.

ACKNOWLEDGMENT

The research described in the paper was financially supported by FRVS (a fund of university development), by research plan No. MSM 0021630513 ELCOM, No. MSM 0021630516, and project of the BUT Grant Agency FEKT-S-10-13.

REFERENCES

1. Incropera, F., et al., *Fundamentals of Heat and Mass Transfer,* Vol. 6, 1024, Wiley, 2006, ISBN: 978-0-471-45728-2.
2. Cho, Y., *Bioengineering Heat Transfer: Advances in Heat Transfer,* 443, Academis Press Limited, London, 1992, ISBN: 0-12-020022-8.
3. Zhmakin, A. I., *Fundamentals of Cryobiology : Physical Phenomena and Mathematical Models,* 280, Springer, Berlin, 2009, ISBN: 978-3-540-88784-3.
4. Akay, M., *Biomedical Engineering,* Vol. 1–5, John Wiley and Sons, Hoboken, New Jersey, 2006, ISBN-13: 978-0-471-24967-2.

NMR Lens — Technological Limits

D. Nespor, P. Drexler, K. Bartusek, and P. Fiala
Department of Theoretical and Experimental Electrical Engineering
Brno University of Technology, Kolejni 2906/4, Brno 612 00, Czech Republic

Abstract— The paper presents a numerical analysis, calculations and measuring of the basic resonators parameters for the planar technological processes. Further, it describes specifically technological problems with spirals resonators made by high resolution technology. The main problems are inaccuracies of the spirals due to chemical etching during manufacturing. The final step is to find optimal technological parameters for the best resonator accuracy.

1. INTRODUCTION

Electromagnetic field is possible to manipulate by means of dielectric materials. Electromagnetic field will be affected due to values of dielectric constant ε_r and permeability μ_r. The lens was constructed as periodic structure of single split ring resonators [1, 2]. A negative effective permeability μ_r can be imposed on this structure. The main problem is to set up the resonance frequencies of the resonators [3]. The demand for the metamaterial structure is that the resonators size has to be much smaller than the length of electromagnetic wave. The intended application of the designed structure is the increasing of the magnetic resonance (MR) system sensitivity. The frequency of the MR system is 198.75 MHz. The resonator working frequency must be slightly higher than the frequency of the MR system because the effective permeability μ_r is negative in this area. But single split resonators for that frequency would be too big. That is why the constructed resonators with resonant frequency about 6 GHz has been modified by means of chip capacitors. Therefore, the ceramic chip capacitors have been assembled over the interspaces [1, 3]. But this solution is inconvenient in many aspects. The main inconveniency is the inaccuracy of capacitors and soldered pads. Next inconveniency is the need for the surface mount. Another solution is the spiral resonator [3]. Spiral resonators are possible to manufacture as a planar types without the external component assembly. That is the main advantage of these resonators. But the problem of this solution is very high sensitivity on the technological accuracy of manufacturing. For example: resonant frequency of the particular resonators has very high scattering due to under-etching.

2. FUNDAMENTAL PROBLEMS OF INACCURACY

In principle the spiral resonator is a classical resonant circuit which consists of capacitive, inductive and resistive elements [3]. Course of the impedance Z of this resonant circuit shows Figure 1(a). A magnetic induction flux Φ corresponds with the impedance Z. Course of the magnetic induction flux Φ is shown in Figure 1(b). From the Figure 1(b), it is obvious that the magnetic induction flux Φ is very sensitive to the resonant frequency because the change of this parameter is really sharp near the resonant frequency. It means that the slight change of the resonant frequency causes large change of the magnetic induction flux Φ Figure 2(a) shows the computed magnetic field of the resonator matrix with the same resonant frequency and Figure 2(b) shows computed magnetic field of the resonator matrix with slightly different resonant frequencies.

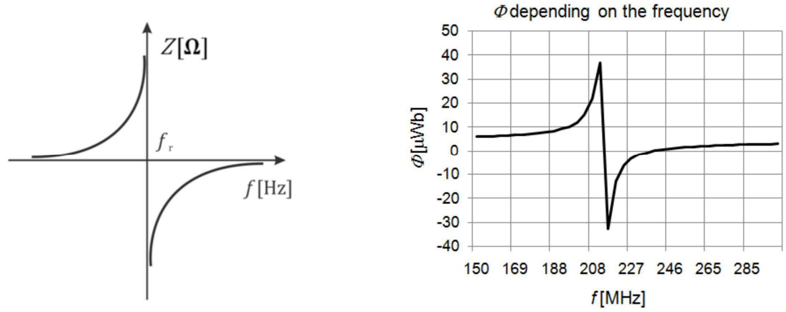

(a) (b)

Figure 1: (a) Impedance Z of the resonant circuit. (b) Course of the magnetic induction flux Φ.

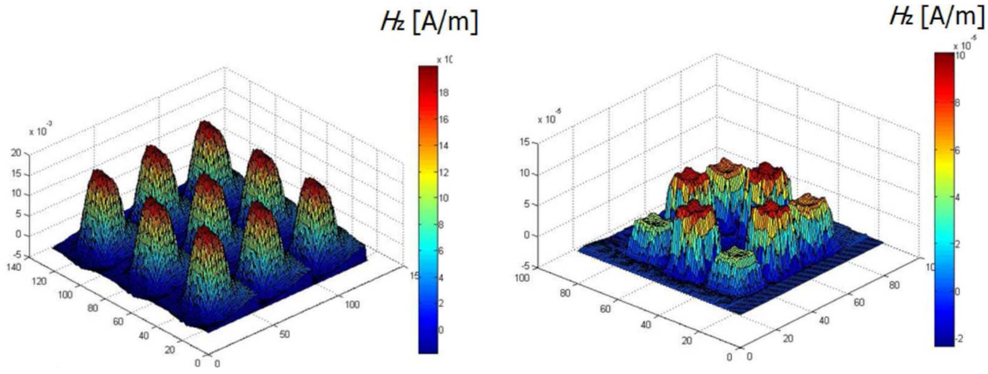

(a) (b)

Figure 2: (a) Computed magnetic field of the resonator matrix with the same resonant frequency. (b) Computed magnetic field of the resonator matrix with the slightly different resonant frequencies.

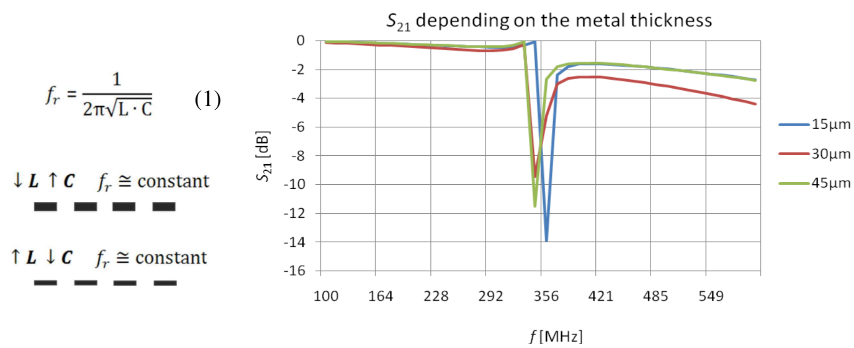

(a) (b)

Figure 3: (a) Dependance the resonant frequency f_r on the spiral thickness. (b) Numerical analysis of the resonant frequency of spiral resonator with different thickness.

In case of correctly working NMR lens it is necessary that the lens must create homogeneous magnetic field. In opposite case this lens seriously influences or totally distorts homogeneity of the magnetic field in the NMR system.

3. THIN LAYERS

The first version of the spiral resonators was designed for classical PCB technology. In principle, the resonators can be manufactured with thin-layer technology utilization. A first problem is resonant frequency shift due to the change of the spiral thickness. Numerical analysis was performed for 35 μm spiral thickness. The standard thin layer has thickness of 100 nm, the special thin layers has even 1 μm. But there is still a huge difference. The limitation of a numerical analysis is number of elements. It is necessary to have extremely high number of elements for spiral with 8 mm length and 100 nm thickness. Therefore, the problem is to perform the analysis for this size. Hence, another experiment was made.

Actually the resonant frequency of the spiral resonators should not depend on the spiral thickness. Resonant frequency f_r is depend on the capacitance and inductance of structure [4]. If the spiral thickness is higher the capacitance is higher also but the inductance is lower and conversely. This is shown in Figure 3(a). In Figure 3(b) is a result of numerical analysis of the resonant frequency of spiral resonator with different thickness. This proves that the resonant frequency is almost independent on the thickness of the spirals.

A second problem is the resistivity of the spirals. The resonator gain is reduced due to internal resistance of the resonator. It is not a problem for a simple resonator shape like SSR for example. But for spiral resonator, which is created from thin and long wire, it could be a problem. In Figure 4(a) is shown the scattering parameter S_{21} which depends on the resistivity of the simple shape resonator. In Figure 4(b), is shown the magnetic induction flux Φ which depends on the resistivity of the simple shape resonators. Analysis was performed for basic frequency of these resonators.

It is obvious that the acceptable spiral resistivity is from $R = 1\,\Omega$ to $R = 10\,\Omega$ from Figures 4(a) and 4(b). Table 1 shows values of the spiral resonator resistivity for different layer thickness. The wire width was 0.1 mm and the spiral length was 140 mm. The computed and the measured values are different. It is caused by under-etching, surface roughness and materials impurity. The graphs and table shows that the thin layer technology is not suitable for spiral resonators because the resistance of the spiral is too high when the thin layer technology is used.

4. CLASSICAL PCB TECHNOLOGY

The main problem of the classical PCB is under-etching of the copper film. Wire made by this technology has never shape of a rectangle but it has trapezoid shape. But this is not a problem if it is included in the numerical model. Basically, the under-etching is not so big problem if it is uniform for all samples. One spiral resonator made by the classical PCB technology with use FR4 and 35 μm thick copper film shows Figure 5 on the left side. Detail of acceptable wires is in Figure 5 in the middle. Detail of unacceptable wires is in Figure 5 on the right side. One spiral resonator made by the classical PCB technology with use FR4 and 18 μm thick copper film shows Figure 6 on the left side. Detail of acceptable wires is in Figure 6 in the middle. Detail of unacceptable wires is in Figure 6 on the right side. The wire and the spacing widths are 0.1 mm for both thickness of the copper.

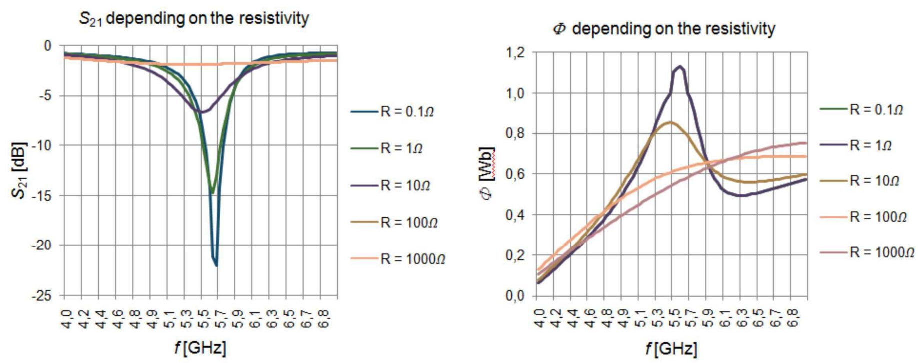

(a) (b)

Figure 4: (a) S_{21} dependance on the resistivity of the basic shape resonator. (b) Φ dependance on the resistivity of the basic shape resonator.

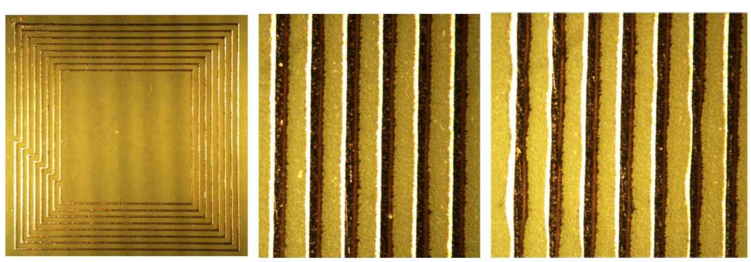

Figure 5: One spiral resonator made by the classical PCB technology with use FR4 and 35 μm thick copper film.

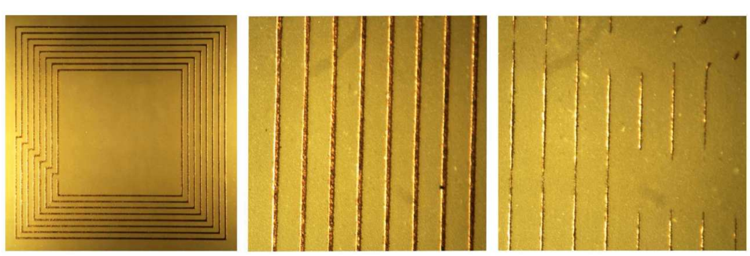

Figure 6: One spiral resonator made by the classical PCB technology with use FR4 and 18 μm thick copper film.

Table 1: S_{21} dependance on the resistivity of the basic shape resonator.

material thickness	computed resistivity	measured resistivity
Cu 35 µm	0.67 Ω	2–3 Ω
Cu 18 µm	1.3 Ω	3–3.5 Ω
Ag 1 µm	24 Ω	31 Ω

5. SUMMARY OF THE RESULTS

As is evident from above the thin layers is not suitable for long spirals manufacture because these spirals have very high resistance. The classical PCB technology is sufficient for this spirals but the main problem is under-etching. If the under-etching is constant for all spirals the problem is less severe. But the biggest problem is if the under-etching is different on each spiral. This causes a change in frequency of each spiral. The final step is to find optimal process parameters for uniformity of the all spirals.

ACKNOWLEDGMENT

The work described in the paper was financially supported by the research project GA102/09/0314, research plan MSM 0021630513 and project of the BUT Grant Agency FEKT-S-10-13.

REFERENCES

1. Freire, M. J., L. Jelinak, and R. Marques, "On the applications of $\mu = -1$ metamaterial lenses for magnetic resonance imaging," Departamento de Electronica y Electromagnetismo, Facultad de Fisica, Universidad de Sevilla, Avda. Reina Mercedes s/n. 41012 Sevilla, Spain.
2. Pendry, J. B., "Negative refraction makes a perfect lens," *Phys. Rev. Lett.*, Vol. 85, No. 18, 3966–3969, Oct. 2000.
3. Nespor, D., P. Drexler, P. Fiala, and K. Bartusek, "Using metamaterials as electromagnetic lens for mr tomograph," *PIERS Proceedings*, 1158–1161, Marrakesh, Morocco, Mar. 20–23, 2011.
4. Stratton, J. A., "Teorie elektromagnetického pole," Státní nakladatelství technické literatury v Praze, Tipe number L25a-D-5III/5397, 1961.

The Correction of B_1 Errors in Magnetization Transfer Ratio Measurements

M. Alkhaddour and P. Fiala
Department of Theoretical and Experimental Electrical Engineering
Brno University of Technology, Kolejni 2906/4, Brno 612 00, Czech Republic

Abstract— The paper presents the assessment and correction of B_1-induced errors in magnetization transfer ratio measurements, where new method is presented for fast and accurate large volumetric radio frequency (RF) field. This method is a modification of the Double Angle Method (DAM), which accelerates imaging speed and applies 3D imaging.

The aims of this Paper are to describe B_1 errors in Magnetization Transfer Ratio (MTR) and to reduce MTR histogram dispersion using B_1 field mapping. The proposed B_1 field mapping sequence for the study is the DAM. In order to reduce acquisition time, an FSE sequence was used in this study. The FSE sequence was performed twice, with the excitation stage of the sequence altered.

1. INTRODUCTION

Magnetization transfer is based on the assumption that protons in tissue can be founded in two pools where the free water pool A has a high ability of spins and the other particles which is semi-solid pool (B) are immobile which are pool invisible using classical MRI methods because the immobile spins occur in very short T_2 relaxation times ($\sim$ 10–15 µs) Where the relaxation behavior of tissue is important to obtain contrast in MRI using Magnetization transfer (MT) imaging method. The exchange of magnetization between the two pools via dipolar interactions and diffusion is Magnetization transfer [3].

2. METHOD

Flip angle α is defined between magnetization vectors before and after excitation by RF impulse. An extension of the flip angle depends on the energy, which the excited nuclei obtain, it means on magnetic induction of B_1 field, on the duration of RF impulse (t_{RF}), and on gyromagnetic ratio of the nuclei γ. For a general, amplitude-modulated RF impulse is:

$$\alpha = \gamma \int_0^{t_{\mathrm{RF}}} B_1 dt. \tag{1}$$

In the case of RF impulse with rectangular envelope we can the flip angle express by simple expression

$$\alpha = \gamma B_1 t_{\mathrm{RF}}. \tag{2}$$

In MR tomography the flip angle $\alpha = 90^\circ$ is interesting, for which the transversal component of magnetization M_{xy} is maximum (corresponds to amplitude of scanned signal). The size of xy part of flip angle is after end of excitation given by [4].

$$M_{xy} = M_0 \sin\alpha. \tag{3}$$

where the Equation (4) gives the the MT ratio (MTR) to obtain the amount of MT, where radio frequency (RF) is applied to the immobile pool slightly off resonance for the free pool, where the MT ratio is between MT saturation (M_S) and without saturation (M_0).

$$\mathrm{MTR} = 100 \left[\frac{M_0 - M_S}{M_0}\right] \tag{4}$$

The MR images of dimension 60×60 mm (256×256 pixels) were measured by the spin echo (SE) method with the different flip angles. The variations of the flip angles form $\beta = 135^\circ$ to $\beta = 30^\circ$ were reached by the RF transmitter power changing with attenuation from 6 dB to -9 dB. The obtained images were normalized to the image maximum amplitude, corresponding to 90°

exciting impulse. The amplitudes of the normalized images were converted into the RF magnetic field induction B_1 by use of

$$B_1 = B_{1,90} \arcsin\left(\frac{M}{M_0}\right). \tag{5}$$

The obtained maps of field B_1 are depicted in Fig. 1. The optimum map is obtained for RF power attenuation -6 dB, in which the contrast k is maximal and the noise is minimal.

From the Fig. 1 it is obvious that for the plain orthogonal to axis and in the middle of the RF coil the field inductions are $B\text{max} = 13$ mT a $B\text{min} = 5$ mT. From this fact follows that the flip angle can for the optimum configuration rise up to 150°.

Using the method described above, the influence of the eddy current induced in the conducting specimens under measurement on the MR image deformation was examined. The MR images of 60×60 mm in dimension (256×256 pixels) were measured by the spin echo (SE) method with 66° flip angles. The specimen was a rod of Au-Pt-Ag alloy, used for dental implants. The alloy is produced by the Safina Company under the trade mark Safibond Bio. Electrical conductivity and susceptibility of this alloy were measured and established, the results are $\rho = 5.37\,\text{Sm/m}^2$, $\chi = -24 \cdot 10^{-6}$.

Tissue parameters are related with MTR, if the fraction of immobile spins has a little value, that means the MTR also will be reduce, where the fraction of immobile spinsin the tissue is given by the following equation $f = M_0^B/(M_0^A + M_0^B)$ normal-appearing white matter (NAWM) shows the effects of diffuse abnormalities in the Volumetric MTR histogram analyses. errors of the measured MTR depend on the errors in RF. B_1 errors ealeted with intrinsic nonuniformity of the transmitter coil, and olso with the skin depth, or the RF penetration effect, which attenuates the RF field inside an electrically conducting object, where B_1 errors realeted with dielectric resonance which increases the RF field inside an object.

The effects of nonuniformity of transmitter amplitude are very important for MTR histograms because the nonuniformity is often more obvious in the z-direction (i.e., along B).

Theoretical method for correcting B_1 errors is based on the collection of a B_1 map, where B_1 errors are very important in MTR. To measure how much pulsed MTR is basedon B_1 for different tissue types in control subjects and MS patients using double spin bath MT. It be used B_1 field mapping to obtain B_1 errors in MTR and reduce MTR histogram dispersion [3].

The FSE sequence is done twice, with the excitation stage of the sequence altered to reduce acquisition time.The flip angle (FA) of the first pulse in the sequence is changed from 90 to $a = 60$ in the first acquisition, and in the second acquisition, FA is changed to $2a = 120$ to reduce acquisition time.

Two main factors are related with the B_1 errors, magnetization transfer ratio (MTR) measurements, and radio frequency (RF) nonuniformity, where MTR value is based on the amplitude of the magnetization transfer (MT) pulse.Non-uniform B_1 transmission (B_{1+}) produces spatially varying flip-angles, causing intensity and contrast to be non-uniform, and complicating quantitative imaging. Thus (RF) causes MTR histograms to be broadened. B_1 non-uniformity causes changes in intensity and contrast across MR images [3].

RF field B_1 nonuniformity is the largest resource of error in the quantitative measurement of many relevant parameters in MR images. Radio frequency nonuniformity may cause MTR histograms to be broadened. The field strength B_1 of the of the saturation pulse affect on the magnetization transfer ratio histogram analysis, particularly if data from a large volume of interest are included.

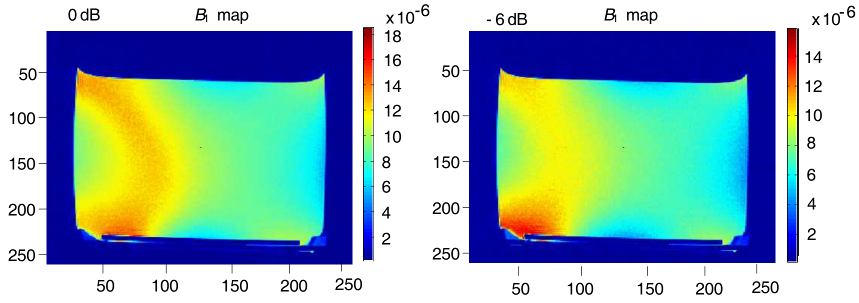

Figure 1: Maps of field B_1.

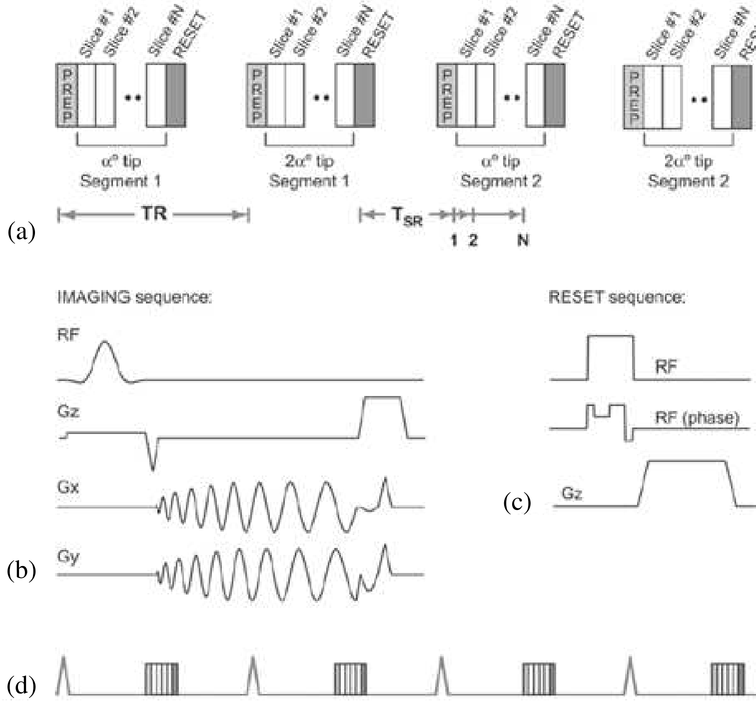

Figure 2: Spiral distribution of B_{1+} mapping pluse sequence.

The double angle method (DAM), with fast spin-echo (FSE) readout, are used in B_1 field mapping technique to quantify B_1 errors and correct MTR maps and histograms [3].

The double angle method (DAM) can be used to measure the B_1 field by calculating a flip-angle map. Two images are acquired l_1 with prescribed tip angle α_1 and l_2 with prescribed tip angle $\alpha_2 = 2\alpha_1$. All other signal-affecting sequence parameters are constant [1].

The first and the second acquisitions were used to calculated the effective FA distribution by obtain the ratio of the signal intensities. To image all tissue types a sequence is sufficient for complete longitudinal relaxation of TR. The effective FA a can be calculated using the simple relation 3. Where the ratio of signals then depends only on the FAs of the first and the second acquisitions the transverse magnetization after the first pulse depends on $\sin\alpha$. Therefore $I_2/I_1 = \sin(2a)/\sin(a) = 2\cos(a)$ (where I_1 and I_2 are the signal intensities resulting from the first and second acquisitions, respectively.

$$\alpha = \cos^{-1}(I_1/2I_2) \tag{6}$$

A new method is applied for magnitude mapping of highly rapid B_1, it is important the homogeneity of the active B_1 field (B_{1+}), specifically if surface coils are used for RF transmission, when the field is high ($>= 3\,\mathrm{T}$) for in-vivo magnetic resonance imaging MRI. to obtain volumetric coverage with high spatial resolution in a few seconds a new method from the double angle method with a B_1-insensitive magnetization-reset sequence,where the repetition time (TR) is independent of T_1.

At two flip angles a flip angle can be mapped to compute the inverse cosine, in using map of flip angle with modest supposition of the action of the excitation pulse, it is possible to measured the spatial distribution of B_{1+}, where different flip angles a short TR sequence is often used.

Figure 2 shows the spiral distribution for B_{1+} mapping pluse sequence, the acquisition of multiple slices and imaging sequence of a simple slice-selective excitation and reset sequence consists of a B_1 insensitive and non-spatially selective saturation pulse followed by a dephaser [1].

Flip angles prescribed are 60 and 120 degrees, the imaging sequence has a tip pulse, readout, and gradient spoiler, while the reset sequence has a composite 90-degree pulse (which is insensitive to both B_1 variations and off-resonance) and a gradient spoiler and short echo time. A linear transmit/receive extremity coil was used to produce a B_{1+} map in the leg of a normal volunteer, both with the new method and the reference double-angle method with a long TR (3 s).

3. CONCLUSIONS

The aim of this paper was to report a modifying method of DAM. This method has the purpose of accelerating 3D imaging speed. The B_1-induced errors in magnetization transfer ratio measurements were presented by means of B_1 field mapping. We also mentioned the principles which are related to B_1 errors, which are MTR measures and RF nonuniformity.

REFERENCES

1. Cunningham, C. H., J. M. Pauly, and K. S. Nayak, "Saturated double-angle method for rapid B_1 mapping," *Magnetic Resonance in Medicine*, Vol. 55, 1326–1333, 2006.
2. Wang, D. X., S. Zuehlsdorff, and A. C. Larson, "Rapid 3D radiofrequency field mapping using catalyzed double-angle method," *NMR Biomed*, Vol. 22, 882–890, 2009.
3. Samson, R. S., C. A. Wheeler-Kingshott, M. R. Symms, D. J. Tozer, and P. S. Tofts, "A simple correction for B_1 field errors in magnetization transfer ratio measurements," *Magnetic Resonance Imaging*, Vol. 24, No. 3, 255–263, 2006.
4. Bartusek, K. and E. Gescheidtova, "Measurement of radio frequency magnetic field," *PIERS Online*, Vol. 2, No. 6, 555–558, 2006.

Measurement of DWI and DTI Images of Isotropic and Anisotropic Materials by Using NMR Methods

P. Marcon[1], **K. Bartusek**[2], **and M. Cap**[1]

[1]Department of Theoretical and Experimental Electrical Engineering
Brno University of Technology, Kolejni 2906/4, 612 00 Brno, Czech Republic
[2]Institute of Scientific Instruments, Academy of Sciences of the Czech Republic
Kralovopolska 147, 612 64 Brno, Czech Republic

Abstract— The paper deals with measurement of Diffusion Weighted Imaging (DWI) and Diffusion Tensor Imaging (DTI) images of images of isotropic and anisotropic materials by using NMR methods. We studied differences between the tensor determined from the sample of an isotropic and an anisotropic material; we compared the results with the theoretical knowledge. As a sample of isotropic material, we used a physiological solution (saline). As a sample of anisotropic material we used plants-cabbage. For measurement of DWI and DTI images, we applied a widely used method of measuring — the Pulse Filed Gradient Spin Echo (PFGSE). The experiments were carried out on an MR tomograph system 4.7 T/120 mm (i.e., 200 MHz for 1 H nuclei). Actively shielded gradient coils yield a maximum gradient field magnitude of 180 mT/m. The data measured were processed in the MAREVISI and MATLAB programs.

1. INTRODUCTION

Diffusion is a mass transport process arising in nature, which results in molecular or particle mixing without requiring bulk motion. Diffusion should not be confused with convection or dispersion, which are other transport mechanisms that require bulk motion to carry particles from one place to another [1]. In the nature the substances can be divided into two groups: isotropic and anisotropic. For example in the isotropic tissues, such as brain gray matter, where the measured apparent diffusivity is largely independent of the orientation of the tissue at the voxel length scale, it is usually sufficient to describe the diffusion characteristics with a single (scalar) apparent diffusion coefficient (ADC or D). However, in anisotropic media, such as white matter or skeletal and cardiac muscle, where the measured diffusivity is how to depend upon the orientation of the tissue, a single D does not adequately characterize the orientation-dependent water mobility. The next most complex model that describes anisotropic diffusion replaces the scalar D with a symmetric effective or apparent diffusion tensor of water, $\mathbf{D}$. This article examines the dependences size of diffusion coefficient in different directions of coordinate axes. We compare the relative error of the diffusion coefficient of real isotropic materials in different coordinate axes.

2. METHOD

MRI method is suitable method of research of particles transport in various substances. This motion is according to Stokes-Einstein's equation depended on temperature and on diffusion coefficient D of measured substance [1]. The most widely used method for diffusion measurement Pulsed Feiled Gradient Spin Echo (PFGSE) is [2]. The data obtained by the PFGSE method are used to calculate D *(diffusion coefficient)*. One D value represents one pixel in the DWI image. In the calculation of D the following calculation is used:

$$\frac{S}{S_0} = e^{-bD}, \tag{1}$$

where b is the so-called b-factor, which is calculated from the properties of gradient pulses that are used in the PFGSE sequence [3, 4]. The quantity S describes an image weighted by the signal intensity from a specimen that was obtained using the PFGSE sequence with gradient pulses in a certain direction of the coordinate system. The quantity S_0 denotes an image weighted by the signal intensity without the application of gradient fields. Equation (1) is correct only for isotropic materials or for measuring diffusion along one coordinate axis. To measure diffusion in anisotropic substances, it is necessary to use the following relation (2).

$$\frac{S}{S_0} = e^{-\mathbf{b}\cdot\mathbf{D}\cdot\mathbf{b}^T}, \tag{2}$$

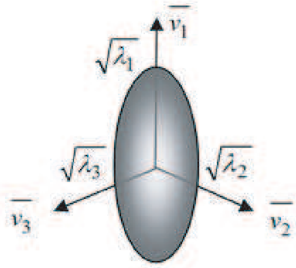

Figure 1: Ellipsoid which depicts the diffusion tensor according to relation (3).

Figure 2: NMR probe with specimen (cabbage and saline solution).

where **b** is a vector containing information not only about the size of the gradient but also about its orientation. Matrix **D** represents a symmetrical tensor that contains diffusion coefficients D calculated from the measurement along six independent coordinate directions. For the calculation of diffusion it is also necessary to measure a seventh image, and this time without using gradient pulses. When imaging a diffusion tensor, one voxel is in our case imaged by means of an ellipsoid. To form the ellipsoid it is necessary to know the eigenvalues λ and eigenvectors $\mathbf{v}$. These are obtained from tensor **D** by means of the "diagonalization" process, as can be seen in Equation (3).

$$\mathbf{D} = \begin{bmatrix} D_{xx} & D_{xy} & D_{xz} \\ D_{yz} & D_{yy} & D_{yz} \\ D_{zx} & D_{zy} & D_{zz} \end{bmatrix} \quad \xrightarrow{\textit{diagonalization}} \quad \lambda_1, \lambda_2, \lambda_3, \mathbf{v}_1, \mathbf{v}_2, \mathbf{v}_3. \tag{3}$$

One **D** value represents one pixel in the DTI image. Fig. 1 shows imaging the ellipsoid on the basis of the knowledge of eigenvectors and eigenvalues. The eigenvalues determine the ellipsoid magnitude in individual directions, which are given by eigenvectors $\mathbf{v}$.

3. EXPERIMENTS

To verify the Equations (1) and (2) we made measurements for two samples (isotropic — saline solution; anisotropic — a piece of cabbage). And then we calculated for both samples the DWI and DTI images. For isotropic material we compared the size of the diffusion in individual coordinates (according to theory, we should get the sphere; therefore diffusion coefficient should be the same in all directions). The experiment was conducted on an MR tomograph system with the magnetic field $B_0 = 4.7\,\mathrm{T}/120\,\mathrm{mm}$ (i.e., 200 MHz for 1 H nuclei) [5–7]. From measurement we obtain an image. Each image voxel has an intensity that reflects a single best measurement of the rate of water diffusion at that location. The measurement was conducted without and with gradients in axes x, y, z. However, the direction of fibres that nourish the plant cannot be seen from these DWI images. The data measured were therefore added up with the data measured with gradients in axes *xy, yz* and *xz* and the diffusion tensor was calculated according to relations (2) and (3). The diffusion tensor was imaged with the aid of small ellipsoids. Each image point, called voxel, is thus formed by an ellipsoid.

Rewriting relation (3) led to the following equation, which was used to calculate individual diffusion coefficients:

$$\mathbf{b}\cdot\mathbf{D}\cdot\mathbf{b}^T=\left[\sqrt{b_\mathrm{X}},\sqrt{b_\mathrm{Y}},\sqrt{b_\mathrm{Z}}\right]\cdot\begin{bmatrix}D_{xx} & D_{xy} & D_{xz}\\ D_{yz} & D_{yy} & D_{yz}\\ D_{zx} & D_{zy} & D_{zz}\end{bmatrix}\cdot\begin{bmatrix}\sqrt{b_\mathrm{X}}\\ \sqrt{b_\mathrm{Y}}\\ \sqrt{b_\mathrm{Z}}\end{bmatrix}. \tag{4}$$

In the experiment, the following combination of gradients was used: [0, 0, 0], [1, 0, 0], [0, 1, 0], [1, 0, 1], $[\frac{1}{\sqrt{2}}, \frac{1}{\sqrt{2}}, 0]$, $[\frac{1}{\sqrt{2}}, 0, \frac{1}{\sqrt{2}}]$, $[0, \frac{1}{\sqrt{2}}, \frac{1}{\sqrt{2}}]$. The magnitudes of gradients were set such that $b_\mathrm{x}=b_\mathrm{y}=b_\mathrm{z}=\sqrt{b_\mathrm{X}}\cdot\sqrt{b_\mathrm{Y}}=\sqrt{b_\mathrm{X}}\cdot\sqrt{b_\mathrm{Z}}=\sqrt{b_\mathrm{Y}}\cdot\sqrt{b_\mathrm{Z}}=221.5\,\mathrm{mm}^2/\mathrm{s}$. This makes the calculation of diffusion coefficients D simpler.

4. RESULTS AND DISCUSSION

The procedure of processing the data measured is indicated in Fig. 3. By the application of PFGSE, measurement data were obtained that represented the intensity of images in the so-called k-space. These data represent a matrix of 64 × 64 pixels and to obtain a resultant image, they must be transformed using the Fourier transform as, for example, in Fig. 3 (here the measurement was performed without gradients). The data are then filtered for pulse noise and the images are calculated by the DWI and DTI methods [8, 9].

In the Fig. 4 you can see results from our measurement of isotropic sample-saline solution. From the left is DWI image of saline solution obtained from the calculation of the three measurement method [8]; DTI image of saline solution, which consists of nearly equal ellipsoids DTI image of saline solution (the size of the ellipsoid is determined by their eigenvalues λ and inclination of ellipsoid is determined by eigenvectors $\mathbf{v}$). According to the theory represent spheres each voxel in DTI image of isotropic materials. In Table 1 is drawn shape of the selected tensor $\mathbf{D}$, also calculated eigenvectors v and eigenvalues l according to Equation (3).

In the Fig. 5 you can see results from our measurement of anisotropic sample-cabbage. Left: DWI image of sample of cabbage obtained from the calculation of the Three measurement method [8]; DTI image. There are not all ellipsoids the same size as in the case of isotropic material, but the ellipsoids have the different size and different inclination according to the growth of fibers within sample of the cabbage.

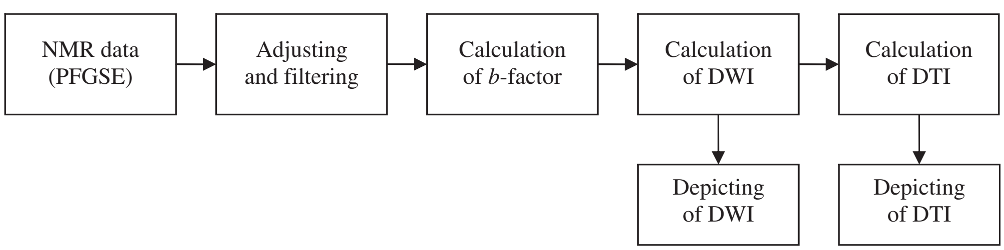

Figure 3: Algorithm for processing the data measured.

Table 1: Example of tensor obtained from isotropic sample (saline solution).

Tensor [m^2/s]	Eigen vector	Eigen values
$\mathbf{D}=\begin{pmatrix}0.2340 & -0.0241 & -0.0233\\ -0.0241 & 0.2340 & -0.0073\\ -0.0233 & -0.0073 & 0.2410\end{pmatrix}\cdot 10^{-8}$	$\mathbf{v}_1=\begin{pmatrix}-0.6843\\ -0.5580\\ -0.4694\end{pmatrix}$, $\mathbf{v}_2=\begin{pmatrix}-0.1129\\ 0.7171\\ -0.6877\end{pmatrix}$, $\mathbf{v}_3=\begin{pmatrix}0.7204\\ 0.4176\\ -0.5538\end{pmatrix}$	$\lambda_1=0.1983\cdot 10^{-8}$ $\lambda_2=0.2447\cdot 10^{-8}$ $\lambda_3=0.2659\cdot 10^{-8}$

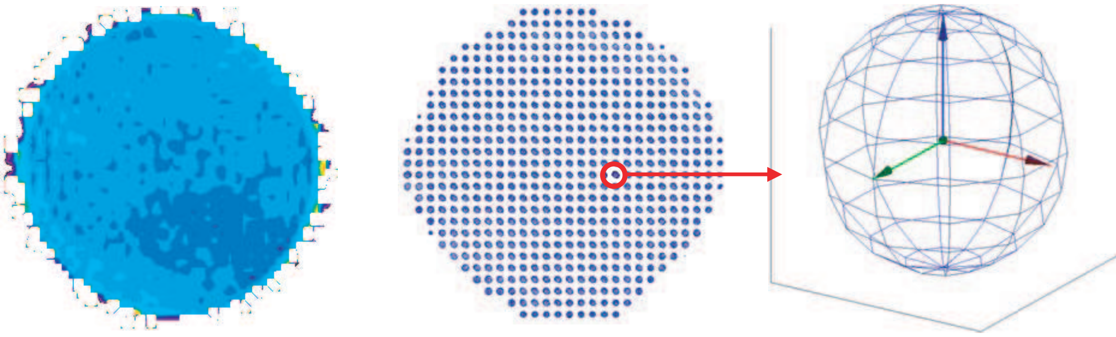

Figure 4: The results of measurement and calculation of isotropic sample. Left: DWI image of saline solution sample, DTI image of saline solution sample, selected sample of ellipsoid whose direction is determined by its eigenvectors and the size of its eigenvalues.

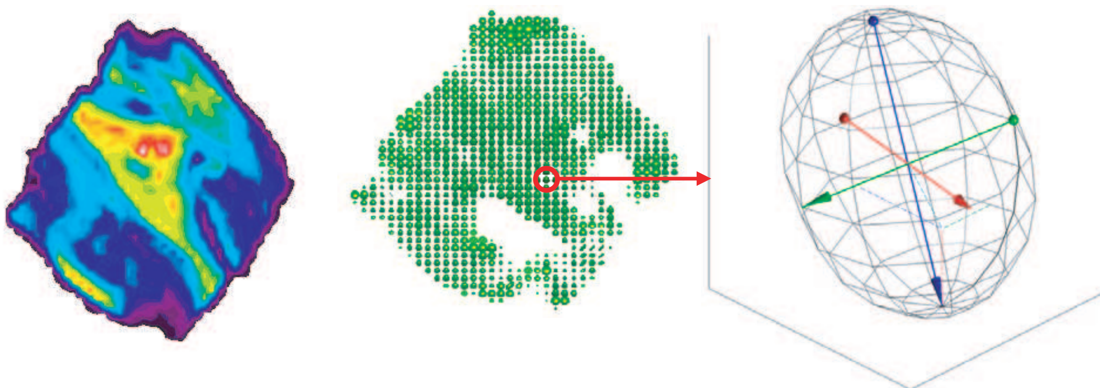

Figure 5: The results of measurement and calculation of anisotropic sample. Left: DWI image of cabbage sample, DTI image of cabbage sample, selected sample of ellipsoid whose direction is determined by its eigenvectors and the size of its eigenvalues.

Table 2: Tensor obtained from isotropic sample (saline solution).

	D [m^2/s]	D average [m^2/s]	δD [%]
Axis x	0.234	0.233	−0.99
Axis y	0.234		−0.99
Axis z	0.241		1.97

5. CONCLUSIONS

In this paper we focus on the differences between DWI and DTI images of isotropic and anisotropic samples. For anisotropic sample it is clear that we obtain by using the DTI method more information about the sample than if we use the DWI method. Therefore we obtain information not only about the size of the voxel, but also the information about direction (everything is encoded in shape of ellipsoid).

In contrast, a sample of anisotropic material (saline solution), we obtain the DTI image ellipsoids that approached the shape of the ball, so it is not necessary to evaluate the image tensor $\mathbf{D}$, but only a scalar variable diffusion coefficient D and make a DWI image. In the Table 2 is an example of the diffusion coefficient difference in directions of coordinate axes (x, y and z). The difference of the size of diffusion coefficient from the mean value is small, less than 2 %.

ACKNOWLEDGMENT

This work was supported within GACR 102/11/0318, project CZ.1.05/2.1.00/01.0017 (ED0017/01/01) and FEKT-S-11-5/1012.

REFERENCES

1. Johansen-Berg, H. and T. E. J. Behrens, *Diffusion MRI: From Quantitative Measurement to in Vivo Neuroanatomy*, Elsevier, China, 2009, ISBN 978-0-12-374709-9.
2. Bartusek, K. and E. Gescheidtova, "MR Measurement technique of rapidly switched gradient magnetic fields in MR tomography," *Applied Magnetic Resonance* (IF 0,665), Vol. 29, No. 12, 675–686, 2006, ISSN 0937-9347.
3. Mansfield, P. and B. Chapman, "Active magnetic screening of gradient coils in NMR imaging," *Journal of Magnetic Resonance*, Vol. 66, 1986.
4. Bartusek, K., "Special Methods of diffusion coefficients measurement by use of nuclear magnetic resonance," Inaugural Thesis, Brno Univeristy of Technology, Brno, 2007, ISSN 1213-418X.
5. Bartusek, K. and E. Gescheidtova, "MRI method of diffusion measurement in heterogeneous materials," *Measurement Science and Technology* (IF 1,297), Vol. 19, 2008, ISSN 0957-0233.
6. Gescheidtova, E., R. Kubasek, Z. Smekal, and K. Bartusek, "Digital filter banks in MR measurement of gradient magnetic fields," *Applied Magnetic Resonance* (IF 0,706), Vol. 33, 399–417, 2008, ISSN 0937-9347.
7. Bartusek, K. and E. Gescheidtova, "Testing the quality of magnetic gradient fields for studying self-diffusion processes in biological specimens by magnetic resonance methods," *Measurement Science and Technology* (IF1,118), Vol. 17, 2256–2262, 2006, ISSN 0957-0233.
8. Mikulka, J., E. Gescheidtova, and K. Bartusek, "Perimeter measurement of spruce needles profile using MRI," *PIERS Proceedings*, 1128–1131, Beijing, China, March 23–27, 2009.
9. Marcon, P. and K. Bartusek, "Errors in diffusion coefficients measurement," *PIERS Proceedings*, 1035–1039, Cambridge, USA, July 5–8, 2010.

The Determination of Function G and Air Ion Mobility Spectrum in an Aspiration Condenser with Segmented Inner Electrode

Z. Roubal[1] **and K. Bartušek**[2]

[1]Department of Theoretical and Experimental Electrical Engineering, Brno University of Technology
Kolejní 2906/4, Brno 612 00, Czech Republic
[2]Institute of Scientific Instruments, Academy of Sciences of the Czech Republic
Kralovopolska 147, Brno 612 64, Czech Republic

Abstract— It was confirmed that light air ions have positive influence on human health. For its appraisal it is necessary to know the concentration of air ions and air ion mobility spectrum. When we measure spectrum of air ions by the standard type of the Gerdien tube with non-segmented electrode we must change voltage in the time. The disadvantage of this method is impossibility of real-time measurement air ion mobility spectrum because it is time-consuming. If we use aspiration condenser with segmented inner electrode it is possible determination air ion mobility spectrum from current individual segments inner electrode. This is problem because it is necessary numeric modeling of the electrostatic field inside the aspiration condenser using FEM and in the next step the determination trajectory of air ion in aspiration condenser. From this result is possible to determine function G. This function is used for determination of air ion mobility spectrum. This algorithm is showed in this paper.

1. INTRODUCTION

In industrial zones, where the environment air is often polluted with dust and smog, the concentration of air ions can be regulated or measured only with difficulty. Any thus impaired area shows an inherent deficiency of negative ions and, conversely, an abundance of positive ions complementing the nano and microscopic dust particles. Significantly, the described aspects have a markedly negative effect on the overall degree of fatigue and professional performance of a human being [1, 2]. The impact of environment on a human organism has been analyzed in studies [1, 2]. In the DTEEE laboratories, the methodology supporting the measurement of air ions concentration and mobility spectrum utilizes an aspiration condenser [3, 4], this method is dependent upon a suitable approximation of saturation characteristics. In a simple aspiration condenser — gerdien tube the internal electrode is not divided into several segments. This method will be modeled saturation characteristics for the natural spectrum of negative air ions measured in [3]. Here, the disadvantage consists in considerable time consumption inherent with the measurement of air ions spectrum. However, if an aspiration condenser with a segmented inner electrode is applied, the pace of measurement can be substantially accelerated. We will obtain an estimation of the air ions spectrum in the given interval, whose accuracy can be further advanced by measurement at several voltages.

2. ASPIRATION CONDENSER

An aspiration condenser (Gerdien tube, AC) is instrumental towards the measurement of air ions concentration assuming that the volume of tested air has not been limited or the ions are continuously generated. In the time domain, it is possible to measure by means of an AC only ions of one polarity; then, following a certain interval, ions of the other polarity can be measured. Ionized air is sucked into the AC by a ventilator. There is a homogeneous electric field set between the inner and the outer electrode. If an electric ion shows a negative electric charge and the collecting inner electrode has a positive electric potential, the ion is progressively attracted to the inner electrode. Provided that the ion impinges upon the electrode, it will induce an electric current that is measured by the help of a sensitive electrometric picoampermeter [4]. The velocity of the ions motion in the electric field can be described by mobility k [$\mathrm{m^2 \cdot V^{-1} s^{-1}}$].

It is possible to determine boundary mobility k_m for every AC configuration.

All ions showing an index of mobility greater than k_m will impinge upon the inner electrode; however, only a proportionate part will impinge in ions whose mobility is smaller than km. Based on the aspiration condenser parameters, the air flow volume rate is defined as

$$M = \left(r_2^2 - r_1^2\right) \cdot \pi \cdot v_x, \tag{1}$$

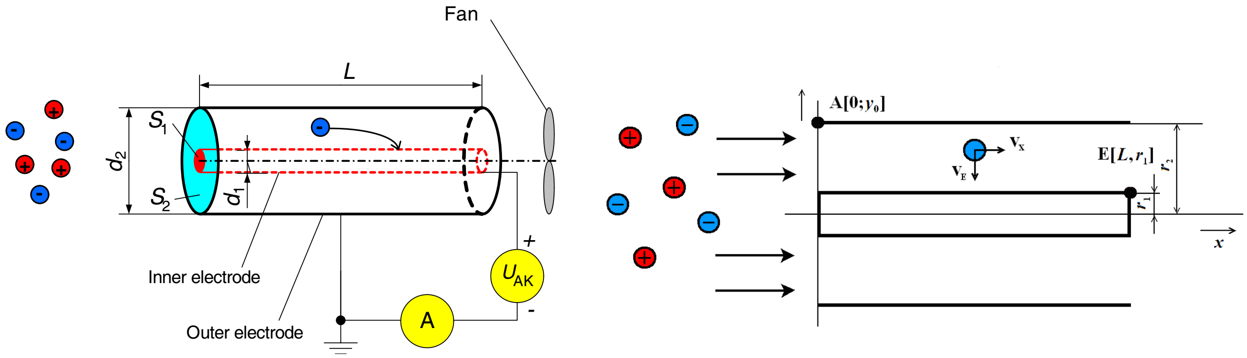

Figure 1: The basic principle of an aspiration condenser.

where M, r_2, r_1, v_x ... are the air flow volume rate, the outer electrode radius, the inner electrode radius, and the air flow velocity, respectively.

The main parameter applied for the definition of air ions mobility consists in boundary mobility k_m,

$$k_m = \frac{\varepsilon_0 \cdot \varepsilon_r \cdot M}{C_{\mathrm{AK}} \cdot U_{\mathrm{AK}}}, \tag{2}$$

where $\tilde{\varepsilon_0}$, ε_r, C_{AK}, U_{AK} ... are the vacuum permittivity, the relative permittivity, the AC capacity, and the AC polarization voltage, respectively. Then, for current I measured by the electrometric picoampermeter, we can define

$$I_{k<k_m} = \frac{k}{k_m} \cdot n \cdot q \cdot M, \quad I_{k \geq k_m} = n \cdot q \cdot M, \tag{3}$$

where n, q ... are the volume concentration of ions and the elementary charge, respectively.

2.1. Concentration of the Volume Density of Ions

The condition of equivalence between an ion charge and an electron elementary charge is satisfied only in light ions, which implies that the condition is not valid in heavy ions that contain several charges of the described type. Then, the relevant situation is referred to as relative number of ions per volume unit. The starting point for the determination of an ion mobility consists in the quantity of charge q and volume concentration of electric charge ρ [3, 4].

$$n_{+-}(k_1, k_2) = \frac{\rho_{+-}(k_1, k_2)}{q}. \tag{4}$$

Now, electric current in the circuit can be written in the form of

$$I = M \cdot \frac{1}{k_m} \int_0^{k_m} k \cdot \rho(k)\, dk + M \cdot \int_{k_m}^{\infty} k \cdot \rho(k)\, dk. \tag{5}$$

It is advantageous [4] to express the characteristics of the aspiration condenser by the help of function G. Equation (5) can be modified to the form

$$I = \int_0^{\infty} G(k) \cdot \rho(k) \cdot dk, \tag{6}$$

for the gerdien tube, function G is given

$$G = \begin{cases} \dfrac{C \cdot U \cdot k}{\varepsilon_0} & k < k_m \\ M & k \geq k_m \end{cases} \tag{7}$$

3. ELECTROSTATIC FIELD IN AC AND EQUATION TRAJECTORY OF ION IN AC

The electric field intensity inside cylindrical capacitor is described by equation

$$E = \frac{U_{AK}}{y \cdot \ln\left(\frac{r_2}{r_1}\right)}. \tag{8}$$

The dependence of electric field intensity for gerdien tube DTEEE [5–8] and UAK = 25 V between inner and outer electrode is in Fig. 2. From this dependence implies that gradient electric field increases to inner electrode. In the Fig. 3 electric potential around the AC using FEM method is simulated.

Because of gradient electric field intensity increase to inner electrode is advantageous use inner electrode as collector electrode. The angle impact ion to inner electrode is higher than the angle impact ion to outer electrode. Potential disturbance air flow near the inner electrode is less important than possible disturbance near the outer electrode.

The equation of motion was derived for a ion entered to gerdien tube with inner collector electrode for initial point A $[0, y_0]$. The y coordinates of ion is given by a solution equation

$$\begin{aligned} &-3y^4 + 4\left(2r_1 + 2r\right) \cdot y^3 + 6\left(r^2 - \left(-r_1 - r\right)^2\right) y^2 + 12x \cdot k \cdot \frac{U_{AK}}{P \cdot \ln\left(\frac{r_2}{r_1}\right)} \\ &+3y_0^4 - 4\left(2r_1 + 2r\right) \cdot y_0^3 - 6\left(r^2 - \left(-r_1 - r\right)^2\right) y_0^2 = 0, \end{aligned} \tag{9}$$

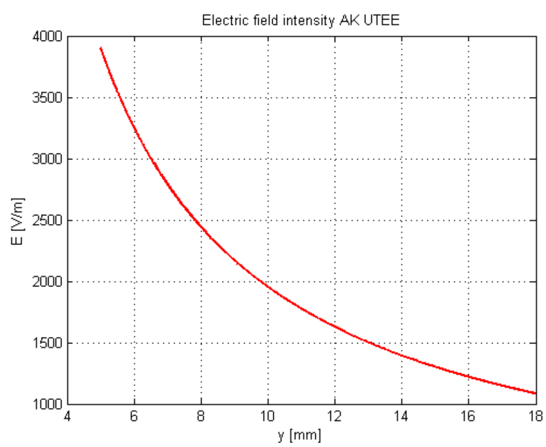

Figure 2: The ideal dependence of electric field intensity between inner and outer electrode.

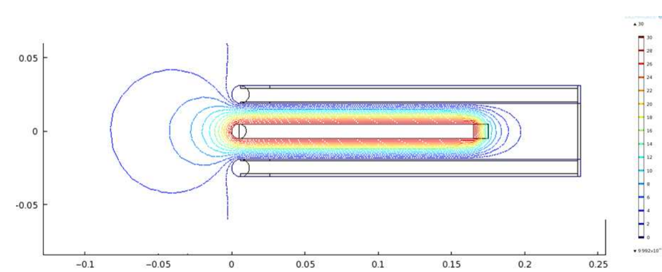

Figure 3: The simulated electric potential using FEM.

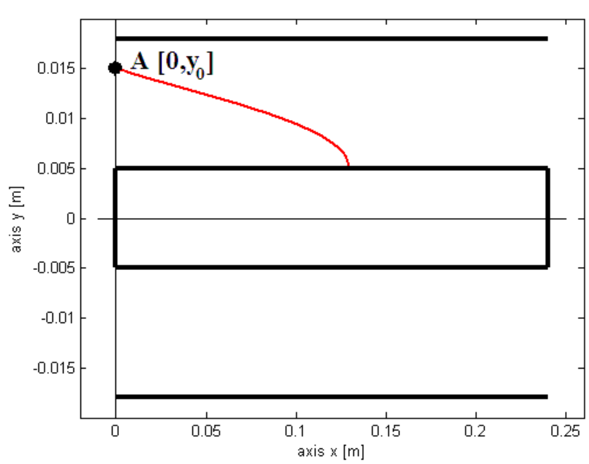

Figure 4: Trajectory of ion for inner collector electrode.

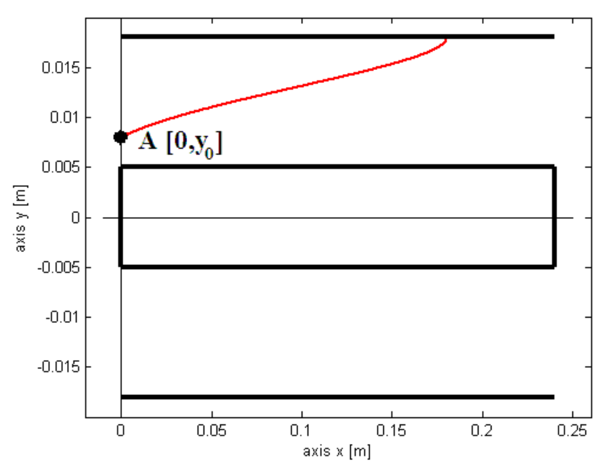

Figure 5: Trajectory of ion for outer collector electrode.

where $r = (r_2 - r_1)/2$ and parameter P is

$$P = \frac{\frac{\Delta p}{\Delta l}}{4 \cdot \eta}, \tag{10}$$

where $\Delta p/\Delta l$ is pressure drop inside AC and η is dynamic viscosity of air. In the Fig. 4 is trajectory of negative ion for inner collector electrode. This equation is valid for the laminar flow.

4. AC WITH SEGMENTED INNER ELECTRODE AND ESTIMATION OF AIR ION SPECTRUM

For the motion equation pertaining to the aspiration condenser with a segmented inner electrode there holds Equation (9). With that said, it should also be noted that it is necessary to establish a new initiatory distance y_0 for each segment. The measuring connection of electrometers and polarization voltage for an aspiration condenser with four segments of the inner electrode is described in Fig. 6.

The G_i functions for the individual segments are modeled (for the voltages of 30 V and 25 V) in Figs. 7 and 8. Function G_1 of the first segment is highlighted in red, while for the second segment it is depicted in green, for the third in blue, and for the fourth in black.

Function G for individual segment electrode overlap and begin in heavy ions. It is advantageous measurement current from I_1 to I_n for to two voltages U_1 and U_2. If we multiply function G by voltage ratio $a = U_2/U_1$ and deducted (Fig. 9) suitably this function G, we give for individual segment inner electrode new function G (show in the Fig. 11) which formulates numbers of ions between two limitation mobility. The new type of the electrometric amplifiers designed in DTEEE [7] allows to measure current in order fA. Due to the fact is possible choice small voltage ratio $a = U_2/U_1$ and the new functions have trapezoid shape.

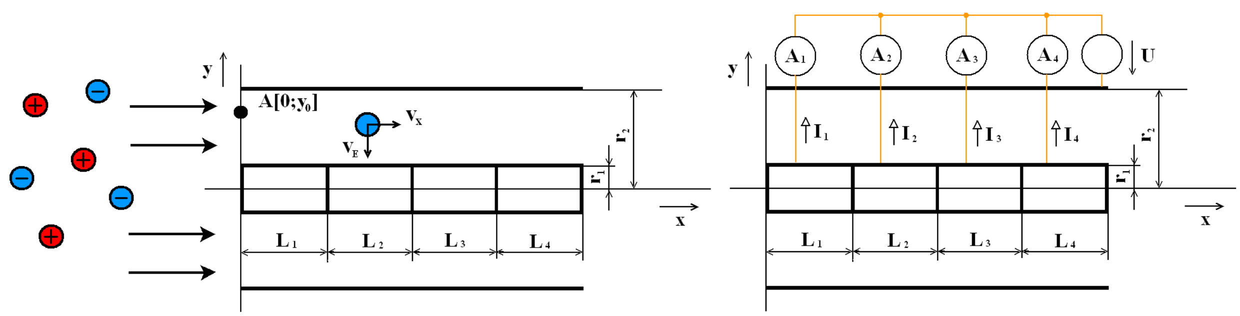

Figure 6: The trajectory of air ions in the gerdien tube is shown on the left, whereas the measurement of individual segment currents of the inner electrode and the applied polarization voltage are shown on the right.

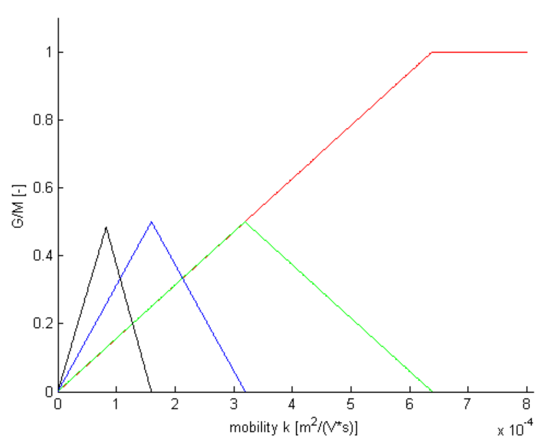

Figure 7: Function G_i for individual segments of the inner electrode and polarization voltage of 30 V.

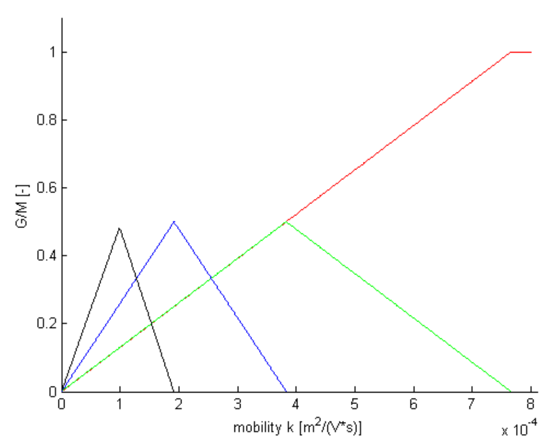

Figure 8: Function G_i for individual segments of the inner electrode and polarization voltage of 25 V.

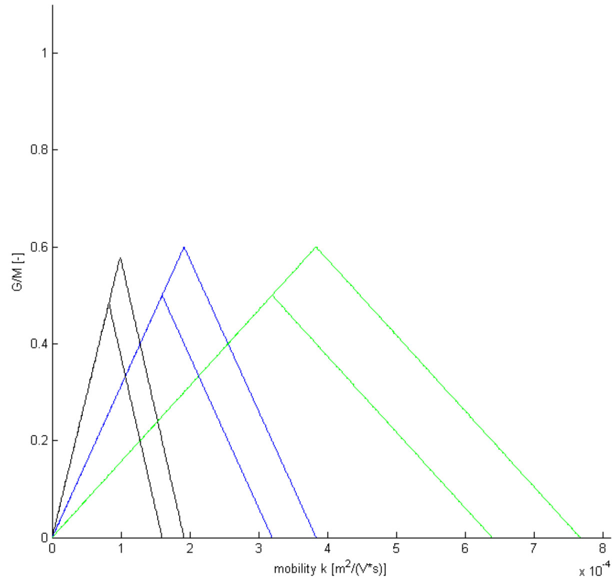

Figure 9: The diagram multiple and deduction for functions G_i.

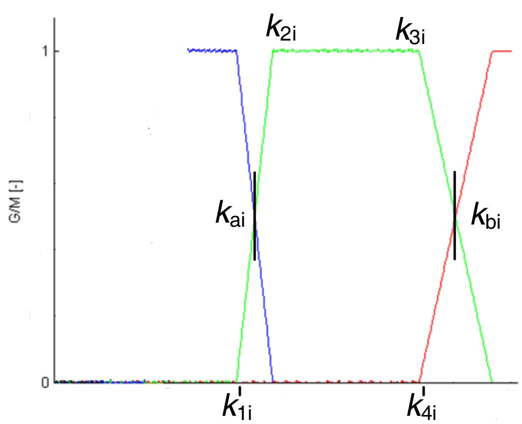

Figure 10: The graphic explanation Equations (12)–(14).

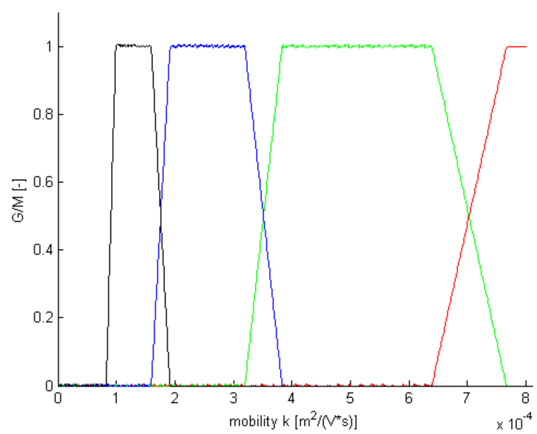

Figure 11: The new functions G_i. $U_1 = 30\,\mathrm{V}$ and $U_2 = 25\,\mathrm{V}$.

For determination of air ion mobility spectrum was derived equation for four limitation mobility (Fig. 10 and Equation (12)). Mean value of air ions concentration between two mean limitation mobility (Equations (13), (14)) is give Equation (15). The graphic significance of individual mobility limitation is shown in the Fig. 10.

$$C_n = \frac{L_n}{2 \cdot \ln\left(\frac{r_2}{r_1}\right)}, \tag{11}$$

$$\begin{aligned}
k_{1j} &= \frac{\frac{3}{4} a \cdot M}{8\pi \left(\sum\limits_{n=1}^{n=j-1} C_n + C_n\right) U_2}, \quad k_{2j} = \frac{a \cdot M}{8\pi \left(\sum\limits_{n=1}^{n=j-1} C_n + C_n\right) U_2}, \\
k_{3j} &= \frac{\frac{5}{4} a \cdot M}{8\pi \sum\limits_{n=1}^{n=j-1} C_n U_2}, \quad k_{4j} = \frac{\frac{3}{2} a \cdot M}{8\pi \sum\limits_{n=1}^{n=j-1} C_n U_2},
\end{aligned} \tag{12}$$

$$k_{aj} = \frac{(a+1)\cdot M}{8\pi\left(\sum\limits_{n=1}^{n=j-1} C_n + C_n\right)U_2}, \tag{13}$$

$$k_{bj} = \frac{(a+1)\cdot M}{8\pi\sum\limits_{n=1}^{n=j-1} C_n U_2}, \tag{14}$$

$$\rho\left(k_{aj}, k_{bj}\right) = \frac{aI_{j(U_1)} - I_{j(U_2)}}{(a-1)\,M}. \tag{15}$$

5. CONCLUSION

If we used a small ratio of voltages U_1 and U_2, the function G shape is trapezoid and determination of air ion mobility spectrum is similar to aspiration condenser with segmented inner electrode and electrostatic filter in the entrance tube. The advantage of this construction is simplier construction and greater measure current than the construction with electrostatic filter. The construction with the segmented inner collector electrode is better than the usually construction with the segmented output collector electrode for greater gradient electrostatic field near inner electrode. The new electrometric amplifier will be used to integrator for the elimination of the white noise. The noise $1/f$ of the operational amplifier will be eliminated by use modulated amplifier for compensation offset voltage. The electrometric amplifier will be used as a cooling peltier element to decrease of the input current operational amplifier and of the input noise current.

ACKNOWLEDGMENT

The research described in the paper was financially supported by grant of Czech ministry of industry and trade No. FR-TI1/001, GACR 102/09/0314 and project of the BUT Grant Agency FEKT-S-11-15.

REFERENCES

1. Tikhonov, V. P., A. A. Temnov, V. A. Kushnir, T. V. Sirota, E. G. Litvinova, M. V. Zakharchenko, and M. N. Kondrashova, "Complex therapeutical effect of ionized air:stimulation of the immune system and decrease in excessive serotonin. H_2O_2 as a Link between the two counterparts," *IEEE Trans. Plasma Scien.*, Vol. 32, No. 4, 1661–1667, 2004.
2. Kondrashova, M. N., E. V. Grigigorreko, A. N. Tikhonov, T. V. Sirota, A. V. Temnov, I. G. Stavrovskaya, N. I. Kosyakova, N. V. Lange, and V. P. Tikonov, "The primary physicochemical mechanism for the beneficia biological/medical effects of negative air ions," *IEEE Trans. Plasma Scien.*, Vol. 28, No. 1, 230–237, 2000.
3. Roubal, Z., M. Steinbauer, and Z. Szabó, "Modeling of saturation characteristic of an aspiration condenser," *PIERS Proceedings*, 216–220, Xi'an, China, Mar. 22–26, 2010.
4. Tammet, H. F., *The Aspiration Method for Determination of Atmospheric-ion Spectra*, IPST, Jerusalem, 1970.
5. Bartusek, K., P. Fiala, T. Bachorec, and E. Kadlecová, "Numerical modeling of accuracy of air ion field measurement," *PIERS Proceedings*, 578–581, Beijing, China, Mar. 26–30, 2007.
6. Bartusek, K., "Merení spektrálních charakteristik iontových polí," *Elektrorevue*, 2001 (online), http://www.elektro- revue.cz/clanky/01038/index.html.
7. Roubal, Z. and M. Steinbauer, "Design of electrometric amplifier for aspiration condenser measurement," *PIERS Proceedings*, 1430–1434, Xian, China, Mar. 22–26, 2010.
8. Steinbauer, M., P. Fiala, K. Bartusek, and Z. Szabó, "Experiments with accuracy of air ion field measurement," *PIERS Proceedings*, 1062–1066, Hangzhou, China, Mar. 24–28, 2008.

MR Perfusion Visualization in 3D Image

M. Cap[1], **E. Gescheidtova**[1], **P. Marcon**[1], **K. Bartusek**[2], **and E. Kroutilova**[1]

[1]Department of Theoretical and Experimental Electrical Engineering
Brno University of Technology, Kolejni 2906/4, 612 00 Brno, Czech Republic
[2]Institute of Scientific Instruments, Academy of Sciences of the Czech Republic
Kralovopolska 147, 612 64 Brno, Czech Republic

Abstract— MRI is a constantly developing region of medicine, which is suitable for the study of soft tissues. The current methodologies for obtaining images weighted by relaxation times give only an idea of the distribution of soft tissues. Differential diagnosis of a high-grade glioms and solitary metastases is in some cases inconclusive. Investigators in several studies have demonstrated that in perfusion MRI (magnetic resonance imaging) of high-grade glioms and solitary metastases are differences. Analysis of the peritumoral region could be more useful than the analysis of the tumor itself. Precise evaluation of mentioned differences in peritumoral region gives a hopeful chance for tumor diagnosis.

This article describes image processing and fusion of the MR images. T_2 weighted (T2W) images and perfusion weighted images are processed for creating a 3 dimensional image. System is designed for calculating slice from 3D image in any direction and position defined by user. Consequently, T2W and PWI are used for image fusion and to image perfusion in structural image in defined direction and position.

1. INTRODUCTION

This article deals with fusion of the perfusion weighted images with T_1, T_2 weighted image and its imaging in 3D images. The aim of this work is to create system for tumor and peritumoral region detection, image registration and fusion of the T_2 and perfusion weighted images. The importance of the perfusion imaging method lies in its ability to describe anatomy and physiology of the tumor and peritumoral region microvasculature [1]. Several studies have demonstrated that in perfusion MRI of high-grade glioms and solitary metastases are differences [2–4]. In this article, we are focused on the differences in perfusion weighted images in the peritumoral region.

Three sets of images were processed. T_1 and T_2 weighted images are used for detection of the tumor and peritumoral region size and position. These two image sets contain 22 images. Resolution of the T_1 weighted images is 256×256 px ($0.9\,\mathrm{mm} \times 0.9\,\mathrm{mm}$ pixel size), resolution of the T_2 weighted images is 512×512 px ($0.45\,\mathrm{mm} \times 0.45\,\mathrm{mm}$ pixel size). Fig. 1 gives as examples of the processed images. Perfusion images are acquired each $1.22\,\mathrm{s}$ with space resolution 64×64 px (pixel size $3.4\,\mathrm{mm} \times 3.4\,\mathrm{mm}$).

Image fusion requires precise image registration. In an effort to obtain the most accurate diagnosis is the image registration the key part of the image fusion algorithm. Hence, the PWI images are processed wit accuracy of ± 1 pixel. With the aim of image fusion the structural image is processed for tumor and peritumoral region detection.

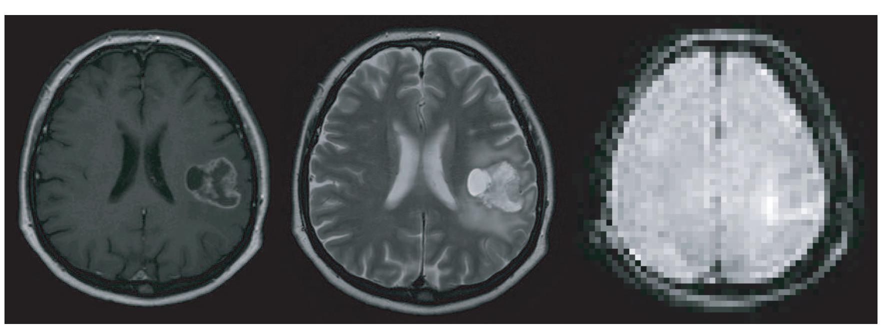

Figure 1: T_1 weighted image, T_2 weighted image and perfusion weighted image of the same slice.

2. METHODS

2.1. Image Registration

Image sets are acquired in different resolutions and slice positions. DICOM standard tags used for image positioning in 3D space are shown in Table 1.

Precise position detection in both images is necessary for right perfusion evaluation in peritumoral region. T1W, T2W and PWI images has the same Image orientation (patient) tag so all images are parallel. Slice thickness and spacing between slices tags for structural and PWI images are different. Image registration and consequent image fusion is provided in T2W image and in PWI image which are in the same volume.

Detection of the size and position of the patient's brain is based on the interhemispheric fissure position as can be seen in Fig. 2. Position of the interhemispheric fissure is detected from the local minimum in the frontal and occipital lobe. Each value is calculated as an average of 10 positions of the local minimum in surrounded rows. For size adjustment the bilinear method is used. Pixel is calculated as a weighted average of pixels in the nearest 2-by-2 neighborhood.

2.2. Segmentation

Most important part of the work is the segmentation of the regions of interest. T2W image was chosen for higher contrast in peritumoral region as you can see in Fig. 1. The goal of segmentation is to find position of the tumor and peritumoral region. Segmentation method is based on the detection of the high intensity of the tumor region [6]. At first, the high contrast area of the tumor

Table 1: Used tags for image positioning in 3D space.

Tag	Atribute name
0018/0050	Slice Thickness
0018/0050	Spacin Between Slices
0020/0032	Image Position (IP)
0020/0037	Image Orientation (Patient) (IOP)
0028/0030	Pixel Spacing

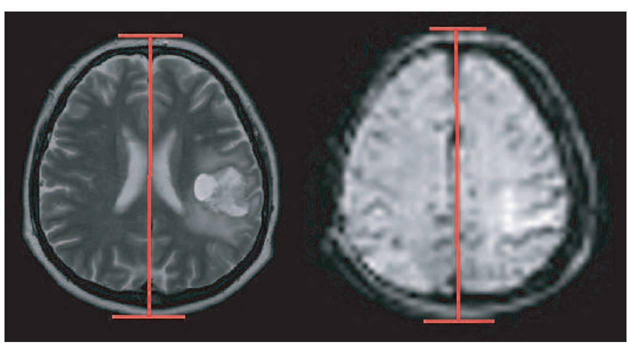

Figure 2: Results of the interhemispheric fissure detection. T2W image left, PWI image right.

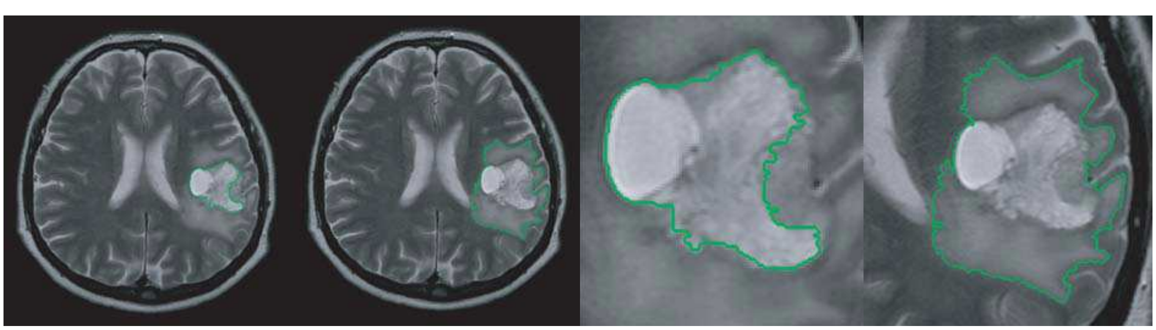

Figure 3: On the top the detected tumor, on bottom the detected peritumoral region in T2W image.

is detected. Tumor area intensity exceeds a threshold which is adjusted according to whole image intensity. In the second step the incorrectly detected areas are removed or added. Results of the tumor and peritumoral region detection are in Fig. 3.

Signal intensity in peritumoral region is not so significantly higher as is in tumor area. Algorithm detects higher signal intensity close to the tumor and signal loss on the peritumoral region boundaries.

2.3. Image fusion

Detection of the tumor and peritumoral region gave as a position of these objects. These positions are used for a mask creating. By multiplying the mask with PWI image the perfusion in peritumoral region is obtained. Results of the image fusion you can see in Fig. 5.

3. RESULTS

Results of the tumor and peritumoral region detection algorithms are masks shown in Fig. 3. Resulting mask is obtained as the peritumoral region mask reduced about the tumor mask in size of whole image. By multiplying this mask and PWI image is obtained perfusion only in peritumoral region.

Position of the T2W images in the space of tomograph is in Fig. 4. Zero position is defined as

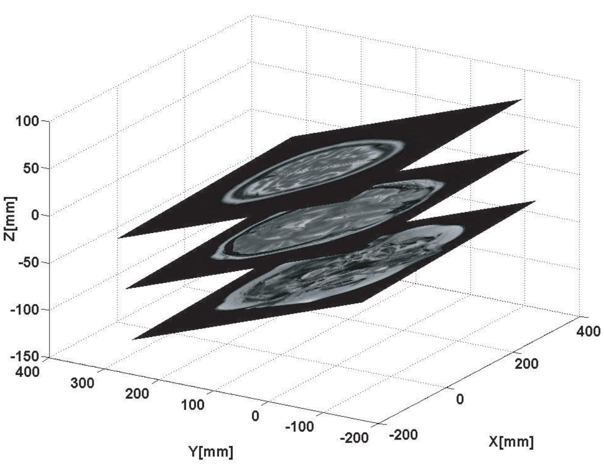

Figure 4: Position of the T2W images in the space of tomograph.

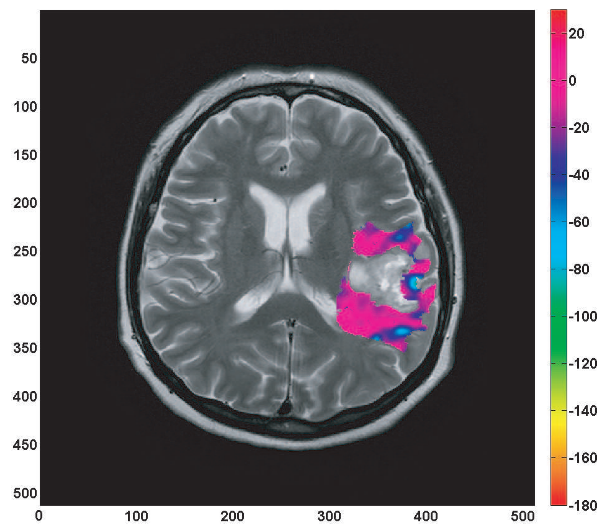

Figure 5: Fusion of the T1W and PWI image in peritumoral region.

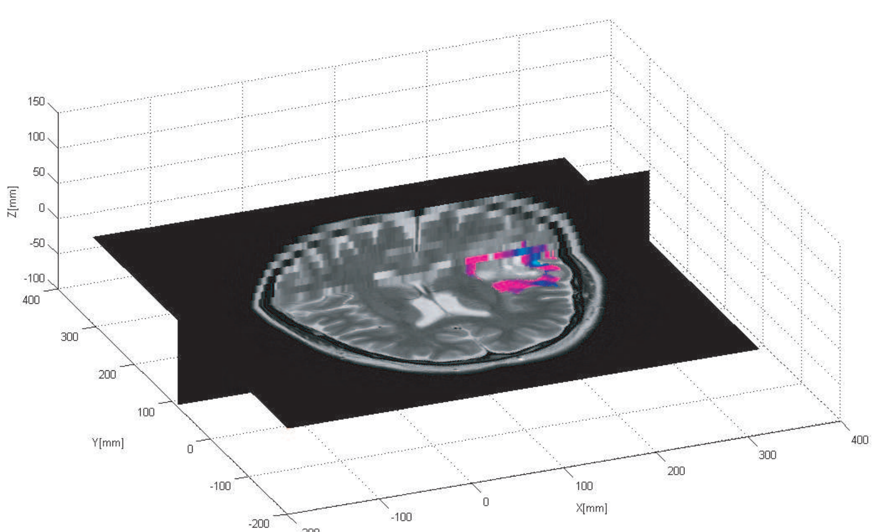

Figure 6: Perfusion in the transversal and coronal plane.

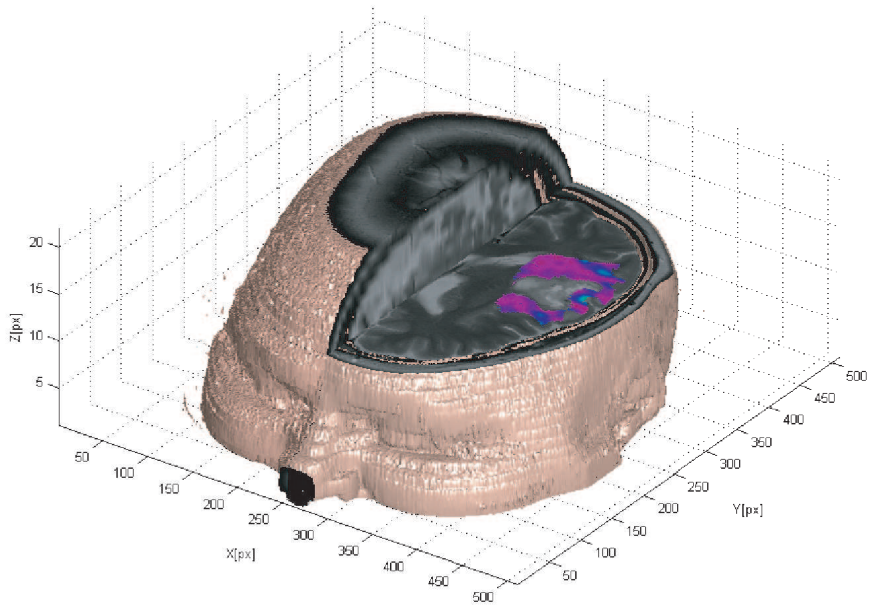

Figure 7: Perfusion visualization in structural 3D image.

center of the tomograph. Directional cosines of the Image orientation tag for this images are (0, 9946; −0, 0831; 0, 0657; 0, 0935; 0, 971; 0, 2167).

In this work designed system is based on fusion of perfusion images to the 2D structural data as is shown in Fig. 5. Gadolinium based contrast cause in image signal loss depending on the content of the contrast in volume of the voxel. Perfusion data are always imaged in peritumoral region and in always the same color scale from 30 to −180 units.

Goal of this work is to realize system for visualizing perfusion in more than one slice and in 3D image. System use IP a IOP DICOM tags as a information about requested slice. Voxel value is used from the nearest voxel to the calculated position of the new slice voxel. Example for the perfusion on the transversal and coronal plane you can see in Fig. 6.

Perfusion visualization in three dimensions could be useful for understanding of structure of tissue microvasculature, example of the cut throw the human brain with brain tumor you can see in Fig. 7. User is able to define in which plane (defined by IOP) will be made a cut throw the analyzed volume and how many cuts is necessary to image requested part of the analyzed tissue.

4. CONCLUSION

The paper presents registration, segmentation and fusion of the T2W and PWI images and its visualization in two defined planes and in 3D structural image. Interhemispheric fissure were localized and used for image registration. All PWI images were processed for registration wit corresponding T2W images. Perfusion imaging is possible to provide in two or more by user defined planes. This is possible to provide in defined number of slices or in 3D structural image. Presented result hold possibility to be useful for more precise tumor diagnosis.

ACKNOWLEDGMENT

This work was supported within GACR 102/11/0318 and CZ.1.05/2.1.00/01.0017 (ED0017/01/01) and GA FEKT-S-11-5/1012.

REFERENCES

1. Jackson, A., D. L. Buckley, and G. J. M. Parker, "Dynamic contrast-enhanced marnetic," *Resonance Imaging in Oncology*, Vol. XII, 311, Elsevier, 2005.
2. Law, M., S. Cha, E. Knopp, G. Johnson, J. Arnett, and A. Litt, "High-grade gliomas and solitary metastases: Differentiation by using perfusion and proton spectroscopic MR imaging," *Radiology*, 715–21, 2002.
3. Hakyemez, B., C. Erdogan, N. Bolca, N. Yildirim, G. Gokalp, and M. Parlak, "Evaluation of different cerebral mass lesions by perfusion-weighted MR imaging," *J. Magn. Reson. Imaging*, 817–24, 2006.

4. Rollin, N., J. Guyotat, N. Streichenberger, J. Honnorat, V. T. Minh, and F. Cotton. "Clinical relevance of diffusion and perfusion magnetic resonance imaging in assessing intra-axial brain tumors," *Neuroradiology*, 150–9, 2006.
5. Cianfoni, A., R. Calandrelli, P. De Bonis, A. Pompucci, L. Lauriola, and C. Colosimo, "Nocardia brain abscess mimicking high-grade necrotic tumor on perfusion MRI," *Journal of Clinical Neuroscience*, Vol. 17, No. 8, 1080–1082, 2010.
6. Mikulka, J., E. Gescheidtova, and K. Bartusek, "Modem edge-based and region-based segmentation methods," *32nd International Conference on Telecommunications and Signal Processing*, 89–91, Dunakiliti, Hungary, 2009.
7. Matlab, Help, Sections: Visualizing MRI data: Volume Visualization Techniques (3-D Visualization); Image Processing Toolbox; Creating Graphical User Interface.

Calibration of the Apparatus for 3D Magnetic Measurement for EIT

Z. Roubal and T. Kříž
Department of Theoretical and Experimental Electrical Engineering, Brno University of Technology
Kolejní 2906/4, Brno 612 00, Czech Republic

Abstract— The paper deals with result measurement of designed apparatus 3D Teslameter magnetic field. This apparatus allows measure direct or alternating magnetic field in environment with strong electromagnetic disturbance. In the case of measure alternating magnetic field it is possible measure signal with lower amplitude than electromagnetic disturbance, concreted S/N < 0.01. The measurement was perform in workplace for mapping magnetic field. In the designed 3D magnetic field meter, Hall probes are used for the measurement of magnetic flux density; also, the influence of Earth's magnetic field is compensated. The measurement result was compared with simulation results in program MATLAB. In this paper differences between measurement and by simulation results and determine source systematic error are discuss. The magnetic field map is measured using the calibrated 3D meter used for the reconstruction of material properties of the measured sample.

1. INTRODUCTION

The MIT (Magnetic field tomography) problem [1, 2] recovers conductivity distribution satisfying the continuity equation

$$\mathrm{div}\mathbf{J} = 0. \tag{1}$$

Current density $\mathbf{J}$ in a linear medium with interior conductivity σ can be obtained from electric field $\mathbf{E}$ or the corresponding potential distribution Φ

$$\mathbf{J} = \sigma \cdot \mathbf{E} = -\sigma \cdot \mathrm{grad}\Phi \tag{2}$$

Further, we assume the electric field in a very thin layer of an electrically conductive medium which can be described by the surface current density $\mathbf{K}$. Magnetic flux density $\mathbf{B}$ corresponding to $\mathbf{K}$ can be obtained according to the Biot-Savart Law

$$\mathbf{B} = \frac{\mu_0}{4\pi} \int\limits_S \frac{\mathbf{K} \times \mathbf{R}}{R^3} dS \tag{3}$$

For further numerical simulations, we divided the geometrical model into $NE = 22\ 394$ triangle elements with centers $[x_\mathrm{t},\ y_\mathrm{t},\ z_\mathrm{t}]$. The electrodes were placed on y axis outer diameter of sample elements. There was created air surround in the sample neighborhood. The source current was adjusted to 5 A. The conductivity of copper was adjusted to $\sigma = 59.59\,\mathrm{MS/m}$. Direction of current corresponded to negative y ax. Electrical potential was solved by finite element method. The surface current density was calculated on each element. We suppose that the surface current density $\mathbf{K}$ is constant on each element. These current values were used for calculation of magnetic field components. For magnetic flux density components evaluation Biot-Savart'law was used. Component of magnetic flux density was calculated in 0.65 mm distance above sample. The z-component of magnetic flux density in examined point, which is given by coordinates $[x_\mathrm{i},\ y_\mathrm{i},\ z_\mathrm{i}]$, it can be calculated by means of a superposition principle.

$$B_{iz} = \frac{\mu_0}{4\pi} \sum_{j=1}^{NE} \left(\frac{R_{ijy}\Delta S_j}{R_{ij}^3} K_{jx} - \frac{R_{ijx}\Delta S_j}{R_{ij}^3} K_{jy} \right),\quad i = 1, ...,\ 2 \cdot NE \tag{4}$$

where ΔS is element area, K is surface current density component, x, y, z are element center coordinates and R is distance between centers of elements.

$$\begin{bmatrix} B_{\mathrm{koef}zx} & B_{\mathrm{koef}zy} \\ B_{\mathrm{koef}zx} & B_{\mathrm{koef}zy} \end{bmatrix} \cdot \begin{bmatrix} K_x \\ K_y \end{bmatrix} = \begin{bmatrix} B_z \\ B_z \end{bmatrix} \quad \Leftrightarrow \quad \mathbf{B}_{\mathrm{koef}} \cdot \mathbf{K} = \mathbf{B}. \tag{5}$$

From system (5) we can obtain very easily the required current density distribution

$$\mathbf{K} = \mathbf{B}_{koef}^{-1} \mathbf{B}. \tag{6}$$

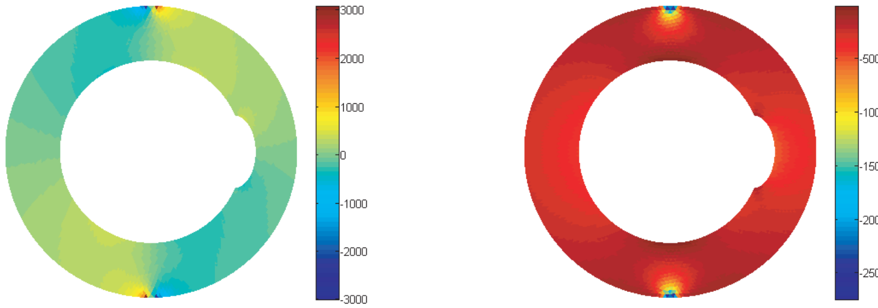

Figure 1: Simulation surface current density K_x and K_y in the measure sample.

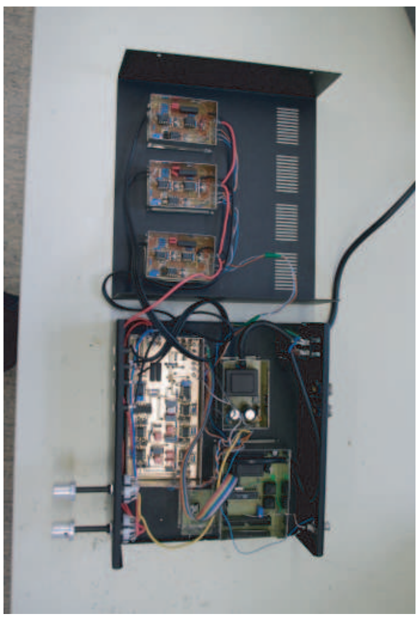

Figure 2: The 3D Teslameter.

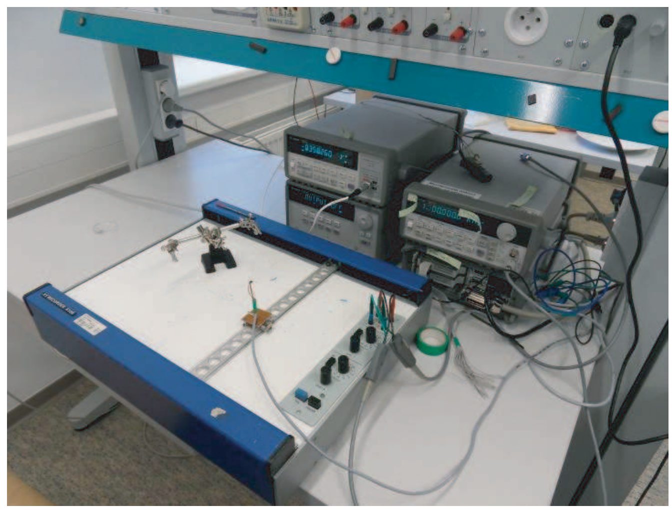

Figure 3: The measuring workplace.

2. THE DETERMINATION OF PROPERTIES OF MEASURING APPARATURE

In the work [3] was of 3D magnetic field meter for the mapping of the magnetic field described design. In Fig. 2 designed 3D Teslameter is showed. In the Fig. 3 there is measuring workplace for the measure data use the MIT.

In the start calibration we determined constant measuring of designed 3D Teslameter. For the calibration Helmholtz coils and accuary Teslameter were used F. W. BELL 9550. This organization of the calibration is in the Fig. 4. In the first step the DC magnetic field generated Helmholtz coils was measured by Teslameter F. W. BELL 9550. In the second step was measured voltage in the output 3D Teslameter for the equal magnetic fiedl. The value of measuring constant was 18.79 μT/V. This measuring constant coresponded to magnetic sensitivity for A1302 1.064 mV/100 μT. For the confirmation of the method MIT only DC source currrent was possible to use. For this measurement the most is significant influence of noise 1/f Hall probe and input amplfier. This noise isn't guaranteed by manufacturer of the Hall probe. The magnetic Hall probe A1302 with input amplifier was measured in spectral analyzer HP 35660. This spectral analyzer is industrially used for a determine input noise [4].

The principle diagram get of noise measure is in Fig. 6. During the measure Hall probe was in the sheilding preparation (Fig. 5).

The high-pass RC filter R_1C_1 and R_2C_2 decrease influence of their own noise 1/f pre-amplifier and the fluctuation offsets voltage the all operational amplifiers. The high-pass filter is set to 0.2 Hz. The operational amplifier OPA211 have extreme low input voltage noise, $1.1\,\mathrm{nV}/\sqrt{\mathrm{Hz}}$ in frequency 1 kHz. We gave the value amplitude spectrum $S_{\mathrm{UO,TOT}}$ from spectral analyzer. In the next step

Figure 4: The calibration using Helmholtz coil.

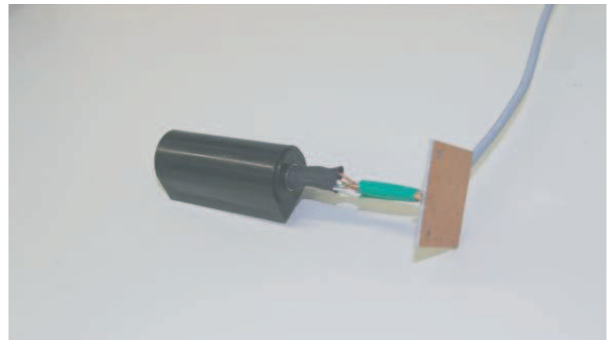

Figure 5: The shielding preparation.

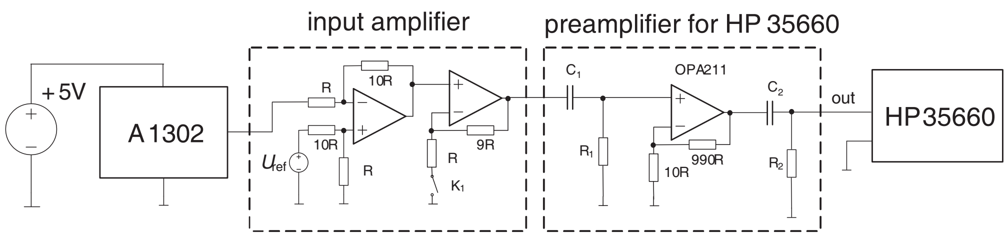

Figure 6: Principial diagram for measure input noise Hall probe with input aplifier.

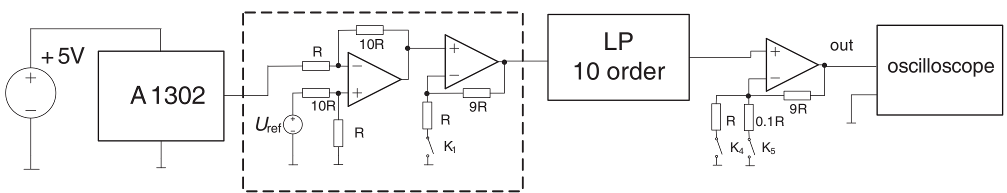

Figure 7: Measuring configuration with LP filter for determine output noise voltage.

we used Equation (7) [4–6] and recalculated to input voltage noise u_{NI},

$$u_{\mathrm{NI}} = 10^{\left(\frac{1}{20}(S_{\mathrm{UO,TOT}})-G_1-G_2\right)}. \tag{7}$$

where G_1 is gain input amplifier Teslameter and G_2 is gain preamplifier for the spectral analyzer. By using of the sensitivity S Hall probe A1302 input voltage noise was recalculated to input noise density magnetic flux density B_{NI}.

$$B_{\mathrm{NI}} = \frac{u_{\mathrm{NI}}}{S}. \tag{8}$$

The result from this measurement with gain input amplifier in the Teslameter 20 dB and 40 dB is showed in the Fig. 8. The noise bandwidth was 20 kHz. In the gain 40 dB the measured input noise was lower.

In the 3D Teslameter LP filter 10 order with noise was used to a bandwidth 20 Hz [4, 7]. This LP filter reduced noise in the output 3D Teslameter, the time of dependence of the output noise is in the Fig. 8. The measuring configuration is in the Fig. 7. In the output 3D Teslameter there is noise signal 1 μT.

3. THE COMPARING OF SIMULATED AND MEASURED VALUE

In the measuring workplace (Fig. 3) there was mapping magnetic field 0.65 mm distance above sample printed circuits board with defined conductance motive. This distance was calculated with comparing simulated and measured value. The measured sample is in the Fig. 9, the measured magnetic flux density B_{z} is in the Fig. 10.

In Fig. 11 simulated magnetic flux density B_z (using program Matlab) is and in Fig. 12 measured B_z is. The measured characteristic was influenced by fluctuations of Earth magnetic field and very low frequency interference generated near enviroment.

Throught the center mapping magnetic field B_z was made slice for $y = 0$. The simulation incision is shown in the Fig. 13 and the measured incision is shown in the Fig. 14.

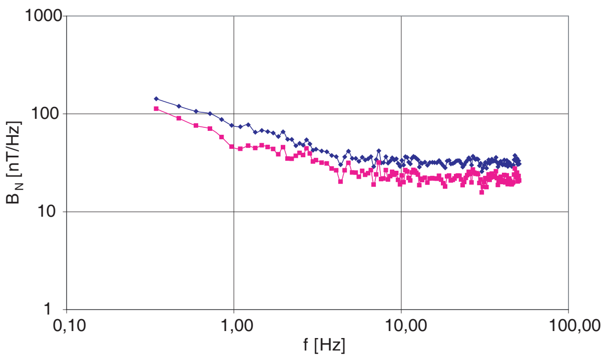

Figure 8: The Input noise of Hall probe and input amplifier 3D Teslameter recalculated to input noise magnetic flux density B_{NI} (pink 40 dB, blue 20 dB).

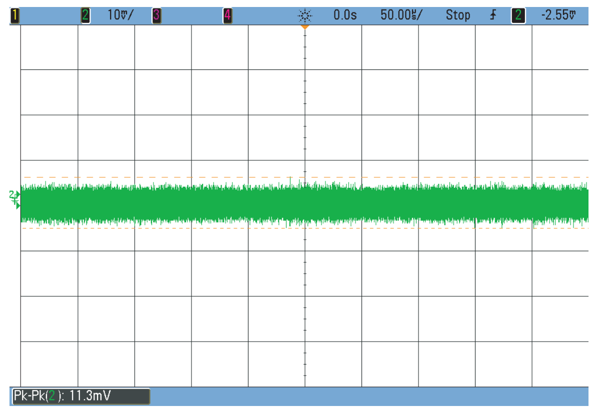

Figure 9: Time depence of output voltage noise.

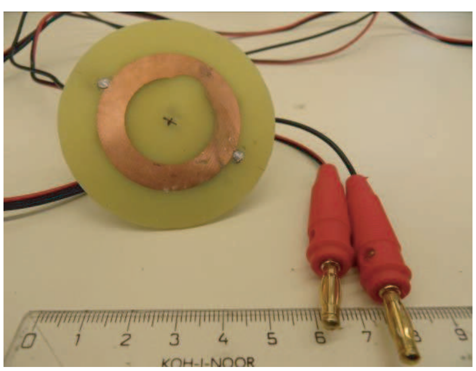

Figure 10: The measured sample.

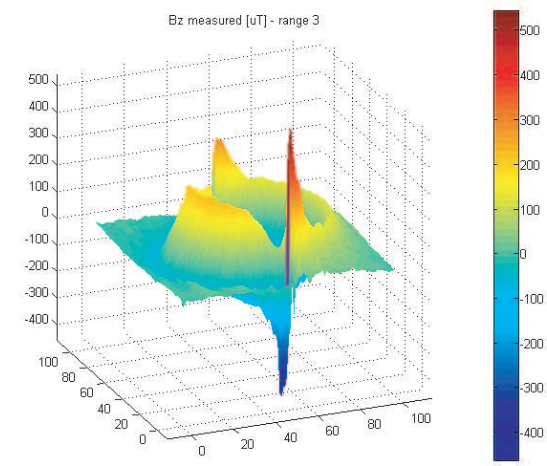

Figure 11: The measured magnetic flux density (B_z).

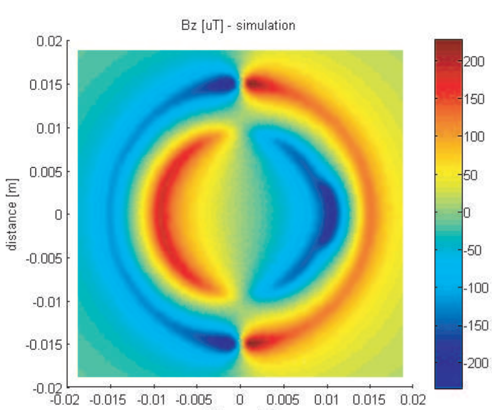

Figure 12: The simulated B_z in Matlab.

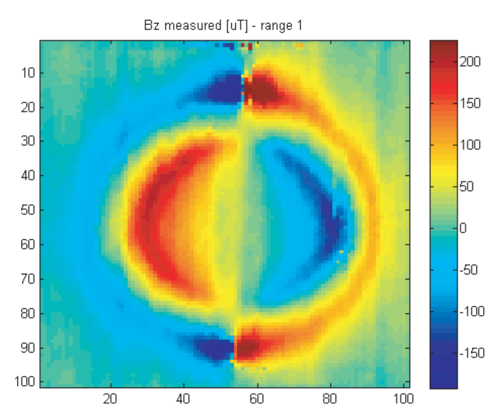

Figure 13: The mesured B_z.

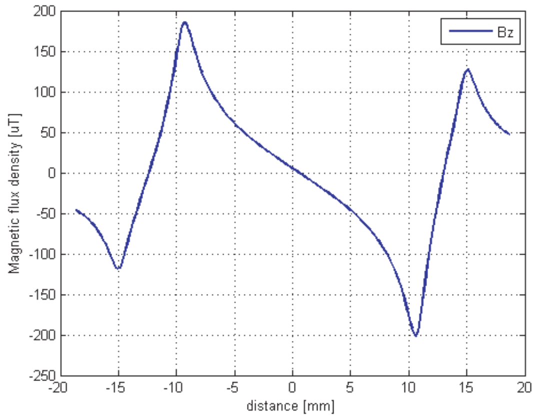

Figure 14: The simulated B_z in Matlab.

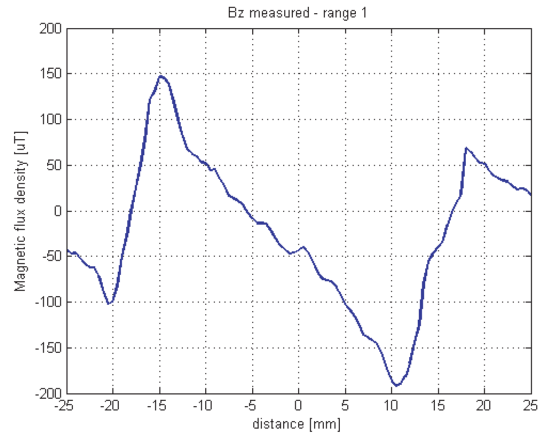

Figure 15: The mesured B_z.

4. CONCLUSION

From this result is obvious that in the next work it is necessary using AC source current. If we use this source, it is possible to use lock-in amplifier in the 3D Teslameter [3]. Influence of fluctuation earth magnetic field and noise 1/f Hall probe is suppressed in lock-in amplifier. The application MIT method is in the non-destrocted materiology of conductance material [2]. By using this method is possible to find fissures and conductance changes in the testing device.

ACKNOWLEDGMENT

The research described in the paper was financially supported by grant of Czech ministry of industry and trade No. FR-TI1/001, GACR 102/09/0314 and project of the BUT Grant Agency FEKT-S-11-15.

REFERENCES

1. Kříž, T., J. Dědková, and K. Bartušek, "Image reconstruction by EIT with usage NMR," *PIERS Proceedings*, 657–660, Marrakesh, Morocco, March 20–23, 2011.
2. Kříž, T., R. Kořınek, and K. Bartušek, "NMR magnetic field measurement for EIT," *Advanced Numerical Modelling*, 37–38, EI Warsaw, 2011, ISBN: 978-83-61956-02-0.
3. Roubal, Z. and T. Kříž, "A 3D magnetic measurement for S/N < 0.01," *PIERS Proceedings*, 981–985, Suzhou, China, September 12–16, 2011.
4. LaFontaine, D., "Making accurate voltage noise and current noise measurements on operational amplifiers down to 0.1 Hz," Application Note 1560, Intersil, January 19, 2011.
5. De Marcellis, A., G. Ferri, and E. Palange, "A novel analog autocalibrating phase-voltage converter for signal phase-shifting detection," *IEEE Sensors Journal*, Vol. 11, No. 2, 259–266, February 2011.
6. Roubal, Z. and M. Steinbauer, "Design of electrometric amplifier for aspiration condenser measurement," *PIERS Proceedings*, 1430–1434, Xi'an, China, March 22–26, 2010.
7. Hájek, K., J. Sedláček, and F. Kmitočtové,. Vydavatelství BEN, Praha, 2002.

Detection of Skull Trauma Using Resistance Tomography

K. Ostanina and J. Dedkova
Department of Theoretical and Experimental Electrical Engineering
Brno University of Technology, Kolejni 2906/4, 612 00 Brno, Czech Republic

Abstract— In the article, the non-invasive way for images reconstruction of an internal conductivity distribution of the human head tissue is described. This approach is based on the use of the current density distribution obtained from measurements of external magnetic flux density by using magnetic field measurement with the principles of conventional EIT imaging technique. The proposed algorithm enables the detection of biological tissue changes in a head with a high spatial resolution.

The algorithm was applied to the several computer simulations representing the detection of skull trauma to demonstrate its feasibility, and to assess the performance of reconstruction process in estimation head tissue conductivity values. The obtained results were presented and compared with the images of conductivity distribution reconstructed by the EIT algorithm. All reconstruction process properties were also discussed.

1. INTRODUCTION

At the present time there are a large number of different non-invasive methods of the biological tissues imaging in the human body. One of them is the method of Electrical Impedance Tomography (EIT). The principle of EIT image reconstruction is based on the evaluation of physical properties of the investigated object, namely on assessing the distribution of electrical conductivity inside the object [1, 2]. The internal conductivity distribution is recalculated from the measured voltages on the electrodes attached to the surface of the object by injecting small amounts of electric current within the range 1–10 mA. However, this method of the conductivity distribution imaging has relatively low spatial resolution and accuracy due to the ill-posed nature of the non-linear inverse problem.

To solve this problem the principle of Magnetic Resonance Imaging (MRI) — the so-called technique of Magnetic Resonance Current Density Imaging (MRCDI) — is introduced into the conventional EIT. This new method is called Magnetic Resonance Electrical Impedance Tomography (MREIT) [3, 4]. In the case of MREIT a current is applied to the investigate object by a pair of electrodes placed on its surface and the induced magnetic flux density inside the object is measured by an MRI system. This approach enables to determine the current density data directly from measurements inside the object (measurements of the magnetic flux density), rather than on its surface as in EIT, namely from measurements of the surface potential. As a result, MREIT method ensures the image reconstruction of an internal structure of the object by using its spatial conductivity distribution with a relative high spatial resolution and accuracy.

In previous studies on MREIT the principle of imaging was based mainly on minimization of the difference between the current density measured by MRI system and the current density representing a function of the conductivity. Thereby, it is necessary to measure all three components of the magnetic flux density to calculate the current density. In this paper, MREIT reconstruction algorithm is presented to obtain conductivity images with using only one component of the magnetic flux density — B_z. It simplifies the reconstruction process of images, because the z-component is parallel to the main magnetic field of MRI scanner; and so it is not necessary to rotate of the object.

2. BASIC THEORY

In the mathematical terms, the image reconstruction algorithm based on MREIT can be represented as the minimization of suitable objective functions $\Psi(\boldsymbol{\sigma})$ to $\boldsymbol{\sigma}$. In order to minimize function, a deterministic approach based on the Least Squares method with using the standard Tikhonov Regularization method, which ensures the improvement of the reconstruction process stability, was used. Thereby, the objective function $\Psi(\boldsymbol{\sigma})$ can by described by the following equation

$$\Psi(\boldsymbol{\sigma}) = \frac{1}{2}\sum \left\|\mathbf{J}_{\mathrm{M}} - \mathbf{J}_{\mathrm{FEM}}(\boldsymbol{\sigma})\right\|^2 + \frac{1}{2}\alpha \left\|\mathbf{L}\boldsymbol{\sigma}\right\|^2, \tag{1}$$

here $\boldsymbol{\sigma}$ is the volume conductivity distribution vector in the object, $\mathbf{J}_{\mathrm{M}}$ is the current density vector calculated from the measurement of a magnetic flux density $\mathbf{B}$, and $\mathbf{J}_{\mathrm{FEM}}(\boldsymbol{\sigma})$ is the vector of computed current density relative to $\boldsymbol{\sigma}$ obtained by using the Finite Element Method; α is the regularization parameter and $\boldsymbol{L}$ is a regularization matrix.

As it was mentioned before, the current density vector can be calculated from measured magnetic flux density into the object by MRI system. The components of $\mathbf{J}$ on elements are obtained from the Biot-Savart's law

$$\frac{\mu_0}{4\pi}\left[\frac{R_{\mathrm{y}}\Delta V}{R^3} \quad \frac{-R_{\mathrm{x}}\Delta V}{R^3}\right]\cdot\left[\begin{array}{c} J_{\mathrm{x}} \\ J_{\mathrm{y}} \end{array}\right]=\left[B_{\mathrm{z}}\right], \tag{2}$$

here J_{x}, J_{y} are the current density components on elements, ΔV represent volumes of elements and R are the distances between the centers of elements and arbitrarily points. The current density can be obtained also from the potential distribution by using the appropriate linear approximation on element

$$\mathbf{J}(x,y)\approx-\sigma\sum_{\mathrm{j}=1}^{3}U_{\mathrm{j}}\,\mathrm{grad}N_{\mathrm{j}}(x,y). \tag{3}$$

The details of the proposed reconstruction algorithm are presented in [5].

3. SIMULATION OF SKULL TRAUMA DETECTION

A series of computer simulations was conducted to assess the performance of the proposed algorithm in the case of skull trauma detection, namely a skull crack. The numerical simulation results are obtained using a 2D FEM model which represents a simplified horizontal slice of the human head. This FEM model consisting of 2360 elements and 1237 nodes is shown in Fig. 1(a). The model of 2D arrangement with the original conductivity distribution is presented in Fig. 1(b). This is a simplified model of the head, which consists of just four homogeneous isotropic layers: scalp, skull, brain (gray and white matters). The conductivity of the homogeneous region representing scalp (brown color) is 0.435 S/m, the conductivity of the skull region (dark blue color) corresponds to 0.087 S/m, the conductivity of the region representing grey matter (orange color) is 0.352 S/m, and the conductivity of the two regions representing white matter (blue color) is 0.147 S/m. These values were adopted from literature previously published [6, 7].

The original conductivity distributions demonstrating various cases of a skull cracks are shown in Figs. 2(a) to 2(d). Figs. 2(a) to 2(c) present the numerical models with different location and size of cracks. The size of defect is given by the area of elements. And the last case (Fig. 2(d)) is case, where the fragment of skull penetrated inside the region of gray matter. The conductivity of the skull crack corresponds to the zero value of conductivity.

The simulation results, illustrated reconstruction of conductivity distribution by applying the proposed algorithm, are identical with the original distribution for each case of skull trauma. And besides, an evaluation of the electrical conductivity changes of human head tissue caused by these traumas was realized by the conventional EIT algorithm based on the Tikhonov Regularization method. The theoretical background of this algorithm is presented in [8]. The conductivity images reconstructed using the EIT algorithm are shown in Figs. 3(a) to 3(d).

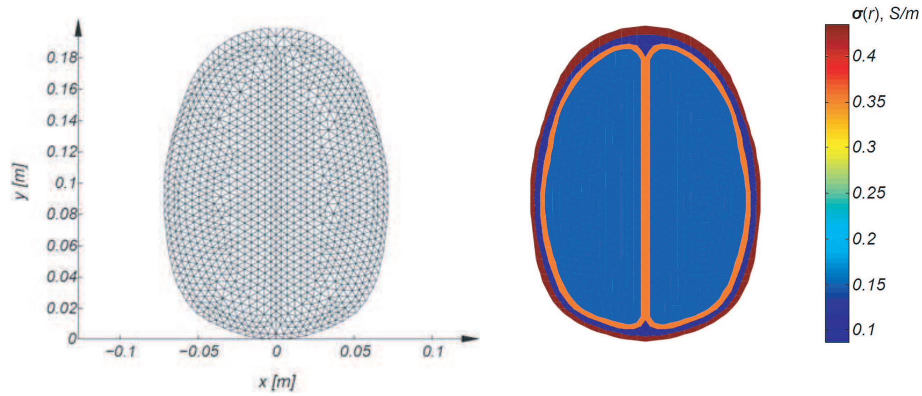

(a) (b)

Figure 1: (a) A 2D FEM model for the modeling of human head tissue and (b) the arrangement of health tissue.

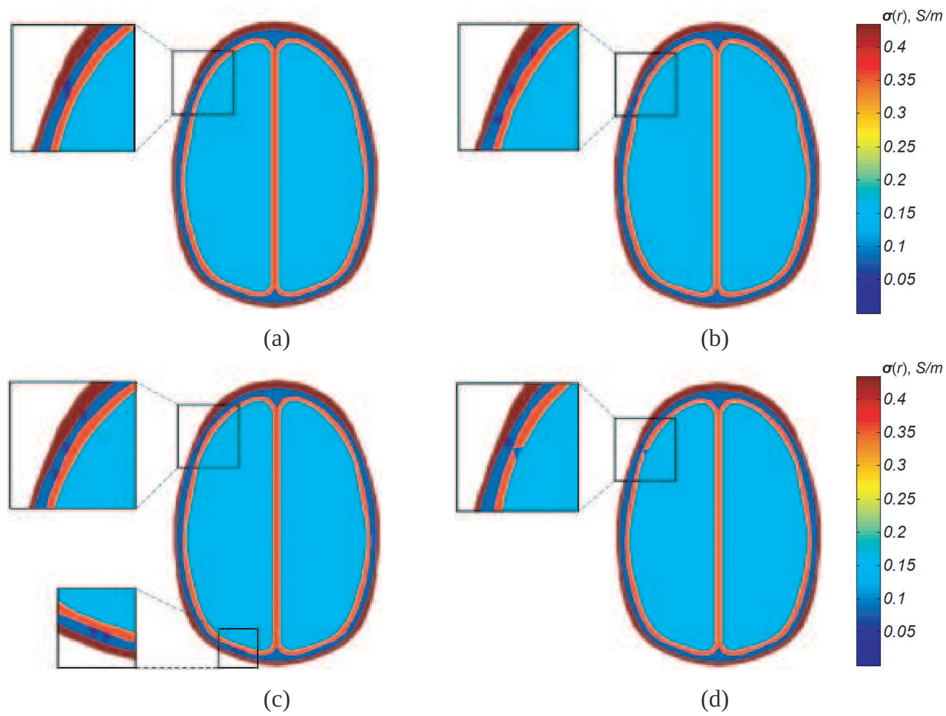

Figure 2: The original conductivity distributions of head tissue for four cases of a skull trauma.

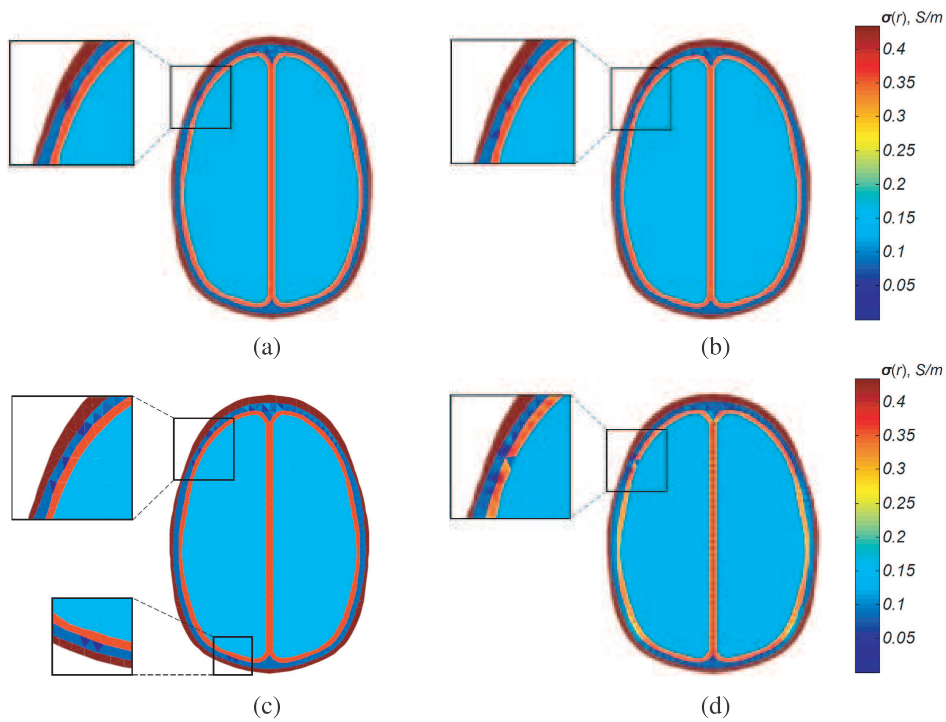

Figure 3: The reconstruction results of four cases of the skull trauma detection by using the EIT algorithm.

These two algorithms were used under the condition that the geometry and the conductivity values of healthy tissue were known. Furthermore, the conductivity value of skull trauma was known too. All parameters of these reconstruction processes are given in Table 1.

The proposed MREIT algorithm successfully reconstructs the conductivity distribution for above-presented cases of the skull trauma. The unknown conductivity distributions were obtained with relative error less than 0.5% in the a- to c-cases and 1% in the d-case. This imaging process is absolutely stable and convergent in contrast to the process based on the EIT, which starts to be unstable, after the 6-th iteration for a- to c-cases and 7-th for d-cases. This means after these iterations the change in the reconstructed conductivity distribution is not very small.

Table 1: The parameters of reconstruction process.

Parameters	a-case		b-case		c-case		d-case	
	MREIT	EIT	MREIT	EIT	MREIT	EIT	MREIT	EIT
Regularization parameter, α	5.e-8	5.e-8	5.e-8	5.e-6	5.e-8	5.e-6	5.e-10	5.e-10
Change of reg. parameter, $d\alpha$*	0.7	0.7	0.7	0.7	0.7	0.7	0.7	0.7
Objective function, $\Psi(\boldsymbol{\sigma})$	4.92e-5	9.83e-8	5.19e-5	8.76e-6	5.35e-5	7.90e-7	2.01e-4	2.49e-16
Number of iteration	2	6	2	6	2	6	7	7
Time**, [min]	3	4	3	4	3	5	7	4
Stability	yes	no	yes	no	yes	no	yes	no

Note: *$d\alpha$ ensures dynamically change of regularization parameter within the duration of the iteration process.
** Time of the reconstruction process depends on the parameters of hardware.

4. CONCLUSIONS

In the article, the feasibility of the image reconstruction method — the so-called method of Magnetic Resonance Electrical Impedance Tomography — and effectivity of its reconstruction process was demonstrated in the various cases of skull trauma detection. The proposed approach makes possible to reconstruct the conductivity images using only one component of the magnetic flux density, namely z-component.

The realized simulations showed that this way of imaging enables to obtain the conductivity distribution of human head tissue with a relative high spatial resolution and accuracy. The reconstruction process is stable and not more time consuming comparing with the conventional EIT.

ACKNOWLEDGMENT

The research described in the paper was financially supported by fund of university development, grant No. GACR 102/09/0314 and the project of the BUT Grant Agency FEKT-S-11-5.

REFERENCES

1. Sikora, J. and S. Wójtowicz, *Industrial and Biological Tomography. Theoretical Basis and Applications*, Electro-Technical Institute, Warsaw, 2010.
2. Sankowski, D. and J. Sikora, *Electrical Capacitance Tomography. Theoretical Basis and Applications*, Electro-Technical Institute, Warsaw, 2010.
3. Lee, T. H., H. S. Nam, M. Lee, Y. J. Kim, E. J. Woo, and O. Kwon, "Reconstruction of conductivity using the dual-loop method with one injection current in MREIT," *Physics in Medicine and Biology*, No. 55, 7523–7539, 2010.
4. Seo, J. K., O. Kwon, and E. J. Woo, "Magnetic resonance electrical impedance measurement tomography (MREIT): Conductivity and current density imaging," *Journal of Physics: Conference Series*, No. 12, 140–155, 2005.
5. Ostanina, K., J. Dedkova, and T. Kriz, "Utilization of boundary conditions in MR image reconstruction," *PIERS Proceedings*, 661–664, Marrakesh, Morocco, March 20–23, 2011.
6. Barber, D. C. and B. H. Brown, "Applied potential tomography," *Journal of Physics E: Scientific Instruments*, Vol. 17, No. 9, 723–733, 1984.
7. Ramon, C., P. H. Schimpf, and J. Haueisen, "Influence of head models on EEG simulations and inverse source localizations," *BioMedical Engineering Online*, Vol. 5, No. 10, 2006.
8. Ostanina, K. and J. Dedkova, "Significant parameters of image reconstruction convergence," *ELEKTRO 2010 8th International Conference*, 41–44, Žilina, Slovak Republic, May 2010.

NMR Diagnostic and Brain Cancer Treatment

P. Fiala[1], **K. Bartusek**[1, 2], **and M. Cap**[1]

[1]Department of Theoretical and Experimental Electrical Engineering
Brno University of Technology, Kolejni 2906/4, Brno 612 00, Czech Republic
[2]Institute of Scientific Instruments, Academy of the Czech Republic
Kralovopolska 147, Brno 61264, Czech Republic

Abstract— Brain cancer can be treated by several therapies. One of the methods available is the elimination of cancer cells in the tumor targeted volume through the influence of heat. In the case of this technique, it is necessary to know the location and distribution of the tumor volume in the surrounding tissue. Correct and precise tumor localization is one of the crucial parts of the brain tumor local hyperthermia, which is necessary for the corresponding adjustment of the local hyperthermia system. This method of cancer treatment requires the observance of temperature distribution in the treated tissue.

In this article, the authors focus on local hyperthermia for local increase of the tumor tissue temperature and on the minimization of the treatment influence on the healthy tissue. The paper includes simulations of the tumor tissue heating method based on the utilization of the complex permeability and complex permittivity of the heated tissue. The authors also discuss the adjustment of the local hyperthermia system, mainly the time of exposition needed to achieve the required temperature distribution in the tumor volume.

1. INTRODUCTION

This article analyzes the possibilities of use of local hyperthermia as a method of cancer treatment. Local hyperthermia is used together with other methods of cancer treatment. This technique is based on the effect of temperatures up to 42°C, which cause elimination of the cells in the targeted volume [1]. Effect of the heat is also shown in radiation therapy and chemotherapeutic drugs [2, 3].

Systems for local hyperthermia of non-surface tumors are based on arrays of antennas emitting microwaves or radiowaves delivering the required power density in W/kg. Commercially used antennas are designed with regard to the size of the heated area. These antennas could be designed as a whole body, regional or local, in dependence on the size of the heated area and the required therapeutic depth. All hyperthermia system also require a system for the heated area temperature monitoring.

Whole body hyperthermia

This method is used in the case of metastatic malignant tumors where the use of local or regional hyperthermia is not feasible because of a higher number of tumors in different areas of the body. The whole body hyperthermia utilizes lower temperatures (less than 42°C) to prevent any damage to the healthy tissue.

Regional hyperthermia

The method of regional hyperthermia is used for deep localized tumors or in the case of a higher number of tumors in the same area. This method requires a sophisticated system for the planning of the heating process. Three-dimensional antenna systems are used for the controlling of power distribution in the heated area.

Local hyperthermia

If the tumor is close to the body surface, it is possible to use the local hyperthermia system. In this way, the adjustment of the local hyperthermia system is crucial for achieving a high temperature only in the tumor volume.

2. MR METHODS OF BRAIN CANCER LOCALIZATION

MRI is a constantly developing field of medicine suitable for the study of soft tissues. The current methodologies for obtaining images weighted by relaxation times provide us not only with information about the distribution of soft tissues, but also with an image insight into the function of the tissue. The localization of brain cancer is a necessary precondition for further treatment. In the case of radiation therapy, precise localization of the tumor and the surrounding tissues constitutes a crucial element.

Many MR sequences are used for imaging the tumor and the peritumoral region area with the aim to achieve an image with a higher contrast. Figure 1 shows an example of the T1 weighted (T1W), T2 weighted (T2W), and perfusion weighted (PWI) images. The T1W and T2W images show anatomical information about the tissue in the slice volume. These images are acquired in a higher spatial resolution, such as 512×512, pixel size 0.4×0.4 mm. PWI images are used for investigation into the function of the tissue. A PWI image could be a T1 or T2 weighted. Spatial resolution is 64×64 and pixel size 3.4×3.4 mm, Figure 1(c).

3. OPTIMUM MODE OF THE HYPERTHERMIC METHOD

Optimal progress of the hyperthermic process depends on the method of heating the target material group [1]. In this paper, the authors describe the method of tissue heating by the help of an antenna and tissue temperature monitoring, Figure 2.

According to the applied source, a patient can participate in NM tomography diagnostics while the therapy is in progress. Here, the proposed method of electromagnetic heating can be affected by problems related to the stability and accuracy of an NM tomograph as a diagnostic instrument for the monitoring of tissue heating. The frequency of an electromagnetic wave excitation ranges within 100–150 MHz. As a rule, there occurs the heating of surrounding tissue that is not being/not to be subject to therapy; in this tissue, contrariwise, non-reversible damage may be incurred. Using

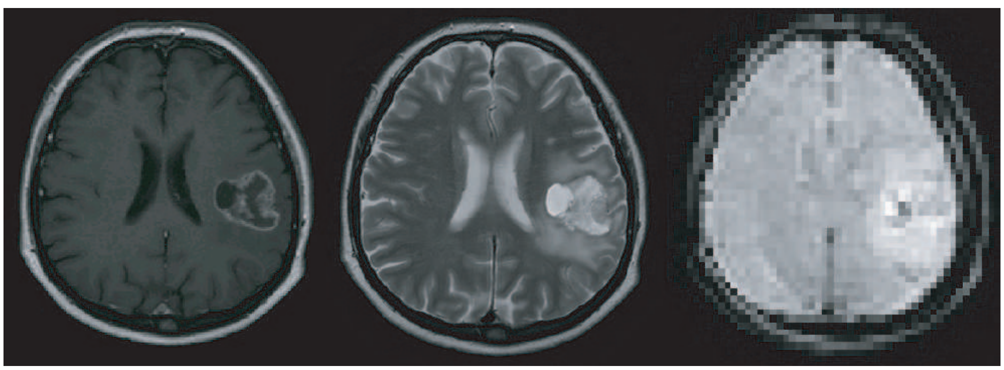

(a) (b) (c)

Figure 1: Imaging examples: Tumor and the peritumoral region area.

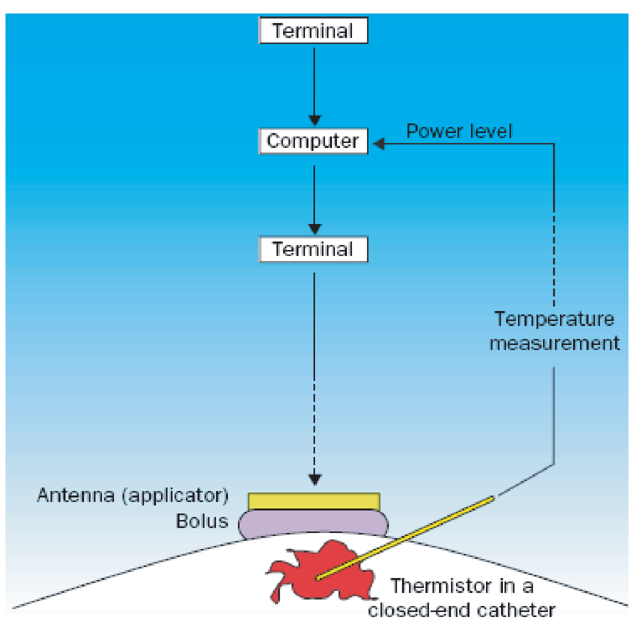

Figure 2: Scheme of a system for local hyperthermia. The applicator position and power output may vary until a clinically satisfactory adjustment is achieved [1].

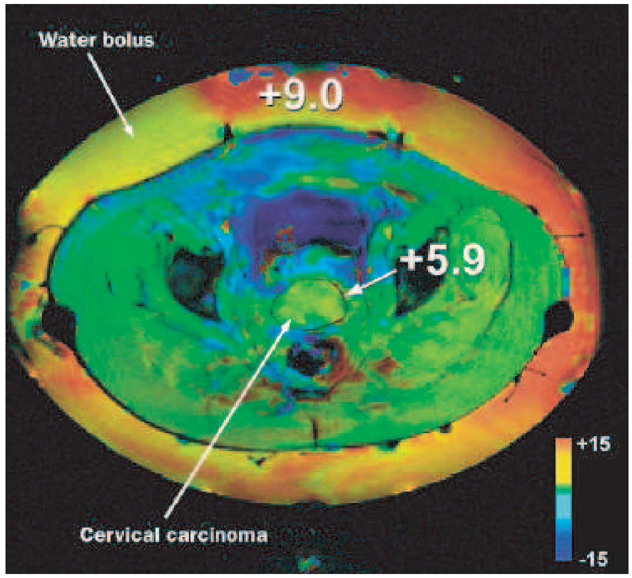

Figure 3: Non-invasive measurement of temperature distribution in the hybrid hyperthermia applicator [1].

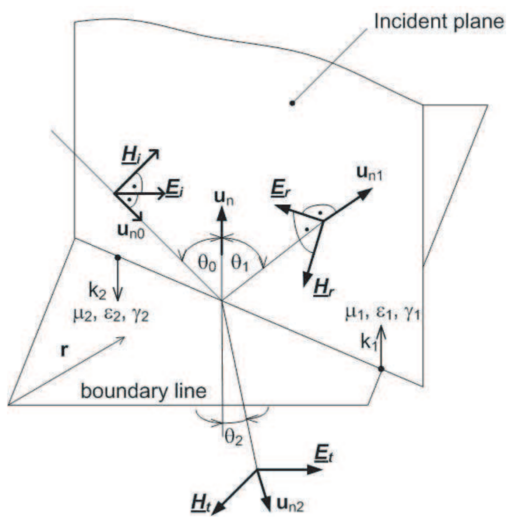

Figure 4: The reflection and refraction of light [9].

the MRT, we can nevertheless arrive at another progressive solution.

Viewed from macroscopic description of the electromagnetic field, the tissue of carcinomes shows peculiar characteristics, which holds true even in respect of the dependence on temperature and frequency. In the case of the described model of heating by means of an electromagnetic wave, it is possible to formulate the electromagnetic wave in this environment using the diffusion equation for function u and parameters C [9].

$$\Delta u = C_{t0}\frac{\partial^2 u}{\partial t^2} + C_{t1}\frac{\partial u}{\partial t} + C_{t2}u + C_{t3} \tag{1}$$

The electric component incident wave, according to Figure 4, is according to Formula (1):

$$E_i = E_0 e^{-j\,k_1\,u_{n0}\cdot r}, \tag{2}$$

where k is the complex wave number

$$k = \sqrt{j\omega\mu\cdot(\gamma + j\omega\varepsilon)}, \tag{3}$$

where γ is the conductivity, ε the permittivity and μ the permeability. Relation (1) is defining for the boundary line between the dielectrics medium. Generally, k_1 and k_2 is complex; then angle

θ_2 is complex. The propagation of the electromagnetic wave is understood as the propagation of electric field strength and magnetic field strength.

$$E_r = E_1 e^{-j\,k_1\,u_{n1}\cdot r}, \quad E_t = E_2 e^{-j\,k_2\,u_{n2}\cdot r}, \tag{4}$$

where E_0 is the amplitude of electric field strength on the boundary line, r is the positional vector and u_{no} is the unit vector of the direction of propagation. For numerical modelling, there is a suitable relation in the form of

$$\begin{aligned} E_r &= \frac{\mu_2 k_1 \cos\theta_0 - \mu_1\sqrt{k_2^2 - k_1^2 \sin^2\theta_0}}{\mu_2 k_1 \cos\theta_0 + \mu_1\sqrt{k_2^2 - k_1^2 \sin^2\theta_0}} E_0 \cdot e^{-j\,k_1\,u_{n1}\cdot r}, \\ E_t &= \frac{2\mu_2 k_1 \cos\theta_0}{\mu_2 k_1 \cos\theta_0 + \mu_1\sqrt{k_2^2 - k_1^2 \sin^2\theta_0}} E_0 \cdot e^{-j\,k_2\,u_{n2}\cdot r}. \end{aligned} \tag{5}$$

In view of the given problem, it is important to remain within the model of electromagnetic wave propagation (5) respecting the complex character of magnetic permeability μ and electric permittivity ε. However, these material parameters of the environment are the functions of temperature and frequency [4–6].

$$\varepsilon = \varepsilon(T, f), \quad \mu = \mu(T, f) \tag{6}$$

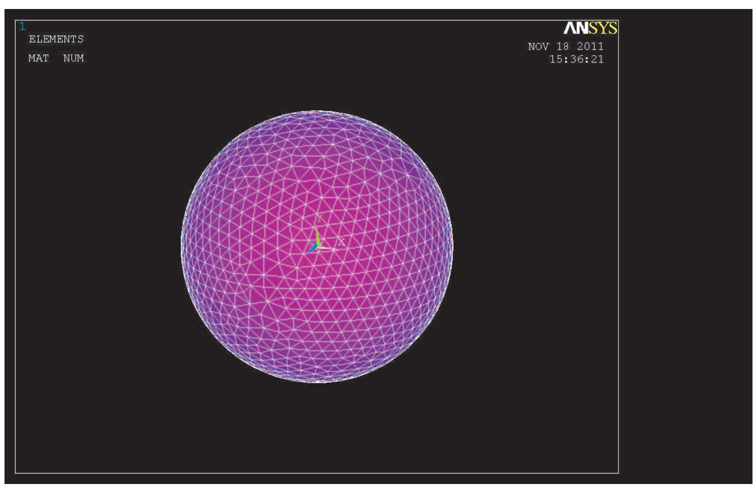

Figure 5: A phantom of the human head.

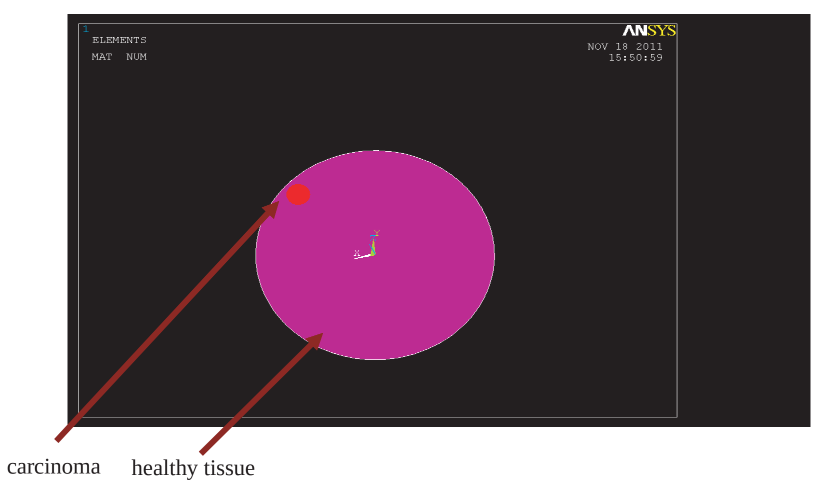

Figure 6: A phantom of the human head — the non-homogeneity position.

In respect of these forms of material characteristics, an optimum heating method can be proposed for a small increase in temperatur as already applied in the field of hyperthermic therapy. These characteristics were respected in the emulsion microwave heating with a phase change of materials [8].

4. HEATING TEST IN THE NUMERICAL MODEL

The described Model (1) having the given characteristics (6) was tested in the numerical model using the finite element method. The geometrical model was simplified to a phantom according to Figure 5.

5. CONCLUSION

Using the inversion problem method, the numerical model reconstructs such signal and electromagnetic pulse shape that will only provide for local heating of the carcinoma tissue, with the surrounding tissue not subject to heating by the source of the electromagnetic wave. This shape of the electromagnetic field can be applied, without any spurious effects resulting from hyperthermia, to specific conditions of individual tissue disorder cases.

ACKNOWLEDGMENT

The research described in the paper was financially supported by a grant of the Czech Science Foundation GACR 102/09/0314, a project of the BUT Foundation Agency FEKT-S-10-13, and EC and MEYS CR (project No. CZ.1.05/2.1.00/01.0017).

REFERENCES

1. Wust, P, B. Hildebrandt, et al, "Hyperthermia in combined treatment of cancer," *Lancet Oncol.*,Vol. 3, No. 8, 487–497, Aug. 2002
2. Bull, J. M. C., "An update on the anticancer effects of a combination of chemotherapy and hyperthermia," *Cancer Res.*, Vol. 44, 4853–4856, 1984.
3. Urano, M., M. Kuroda, and Y. Nishimura, "For the clinical application of thermochemotherapy given at mild temperatures," *Int. J. Hyperthermia*, Vol. 15, 79–107, 1999.
4. Kubásek, R., K. Bartušek, and P. Fiala, "Determination of pre-emphasis constants for eddy current reduction," *Measurement Science and Technology*, Vol. 21, 1–9, 2010. ISSN: 0957-0233.
5. Marcoň, P., K. Bartušek, and M. Čáp, "Modeling and measuring of the changes of the magnetic field next to non-ferromagnetic substances for magnetic susceptibility calculation," *Measurement 2011*, 213–216, Institute of Measurement Sciences, Bratislava, 2011, ISBN: 978-80-969672-4-7.
6. Marcon, P., K. Bartusek, M. Burdková, and Z. Dokoupil, "Magnetic susceptibility measurement using 2D magnetic resonance imaging," *Measurement Science and Technology*, Vol. 22, 1–8, 2011. ISSN: 0957-0233
7. Mikulka, J., E. Gescheidtová, and K. Bartušek, "Interpolation of 3D magnetic resonance data," *PIERS Online*, Vol. 7, No. 1, 31–34, 2011. ISSN: 1931-7360.
8. Drexler, P., T. Jirku, Z. Szabo, and P. Fiala, "Model of a reactor chamber with microwave heating," *PIERS Online*, Vol. 2, No. 6, 681–684, 2006.
9. Kadlec, R., E. Kroutilová, D. Nešpor, and P. Fiala, "Propagation of electromagnetic wave in layered heterogeneous medium," *PIERS Proceedings*, 1149–1152, Marrakesh, Morocco, Mar. 20–23, 2011.

X-ray Diagnostics of Non-homogeneous Material by Means of 2D Plane Transformation

P. Fiala[1], P. Koňas[1], M. Friedl[1], E. Kroutilová[1], and P. Šmíra[2]

[1]Department of Theoretical and Experimental Electrical Engineering
Brno University of Technology, Kolejni 2906/4, 612 00 Brno, Czech Republic
[2]Thermo Sanace s.r.o., Chamrádova 475/23, 718 00 Ostrava-Kunčičky, Czech Republic

Abstract— The problem of finding a suitable diagnostic procedure for the examination of structural elements has been closely analyzed in recent years. In this connection, the main material of interest is wood as a sort of heterogeneous matter, and the diagnostic procedure is directed towards enabling industrial application in the future. A new diagnostic method based on X-ray imaging has been proposed and tested; the technique utilizes the reduction of imaging information into 2D planar projection. It allows us to image clearly the rate of material damage through displaying the weighted damage rate.

1. INTRODUCTION

Currently, the protection of structural elements made of wood against decay fungi and wood-destroying insects is widely realized through the thermal treatment technique, which has been known and used in Germany since 1930. The principle of this method consists in heating the related wooden structures, by means of hot air whose temperature does not exceed 120°C, for a period of 4 –10 hours. Heat is accumulated inside wooden components of the structure under treatment, and the temperature of these components may reach as high as 60°C within the cross-section, Fig. 1.

At the temperature of 55°C, all viable forms (including the ova, worm, nymph, and beetle) of wood-destroying insects perish; this temperature is the boundary value for the coagulation of proteins that nurture wood-destroying insects such as old-house borer (Hylotrupes bajulus), common house borer (Anobium punctatum), the death watch beetle (Xestobium rufovillosum), or the powder post beetle (Lyctus brunneus).

A necessary preconditon for any sensible application of the method (Fig. 2) consists in diagnostics performed on damaged portions of structural elements. The diagnostics can be realized by means of non-destructive techniques or, alternatively, through destructive methods resulting in partial disruption of the examined element. This paper contains the proposal and analysis of a mobile non-destructive diagnostic method suitable for use with a damaged or disrupted structural element (Fig. 3). In connection with non-destructive diagnostics, the thermal treatment method constitutes a well-suited approach to be applied in artefacts and buildings of great historic value.

2. TREATMENT METHODS

The group of basic treatment methods includes the liquidation of insect foetus, fungus, or rot through the use of hot air or chemical preparations. In all application cases, these techniques are further modified or combined, and the extent of their use is usually determined from the diagnostic results.

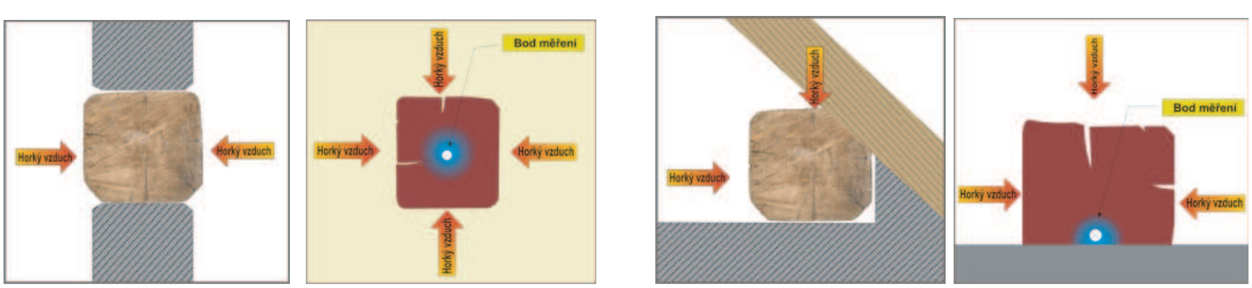

Figure 1: Heat propagation and detection in a non-homogeneous material: wood.

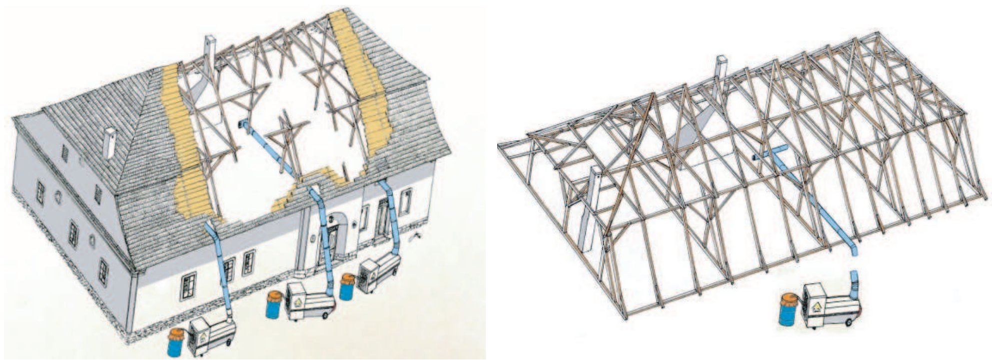

Figure 2: The removal and treatment of wood invaded by wood-destroying insects and fungi.

Figure 3: Examples of wood invaded by decay-fungi and wood-destroying insects.

Figure 4: Temperature diagnostics in a section of a wooden structural element.

3. DIAGNOSTICS

The diagnostics in buildings or in the applied structural elements containing wood are performed both visually and acoustically within the range of audible frequencies, or within the ultrasonic band. The application of acoustic methods frequently results in partial damage of the material. Suitable types of approach to the diagnostics of temperature distribution status include optical measurement methods or destructive methods utilizing probes introduced into a section through the material, Fig. 4.

4. DESTRUCTIVE DIAGNOSTICS

The rate of a material damage in 3D imaging can be determined by means of the acoustic diagnostic method (FAKOP [2]), whose application (Fig. 5) nevertheless poses certain risks; generally, there are two problems involved. In this respect, the first point of interest is related to erroneous interpretation of diagnostics by the employed software, whereby a mere 10% damage may be rendered as a large-scale problem within the material volume; this fact follows from the characteristics of acoustic waves propagation through a heterogeneous material as well as from its reconstructions and interpretations of the damaged region. The other problem as mentioned above consists in destructive character of the applied diagnostics together with certain limitations to the use of sensors (namely its repeatability). Further, the situation is made somewhat more difficult by the fact that, owing to the rate of wood heterogeneity, every diagnosed component constitutes a unique entity having no identical counterpart.

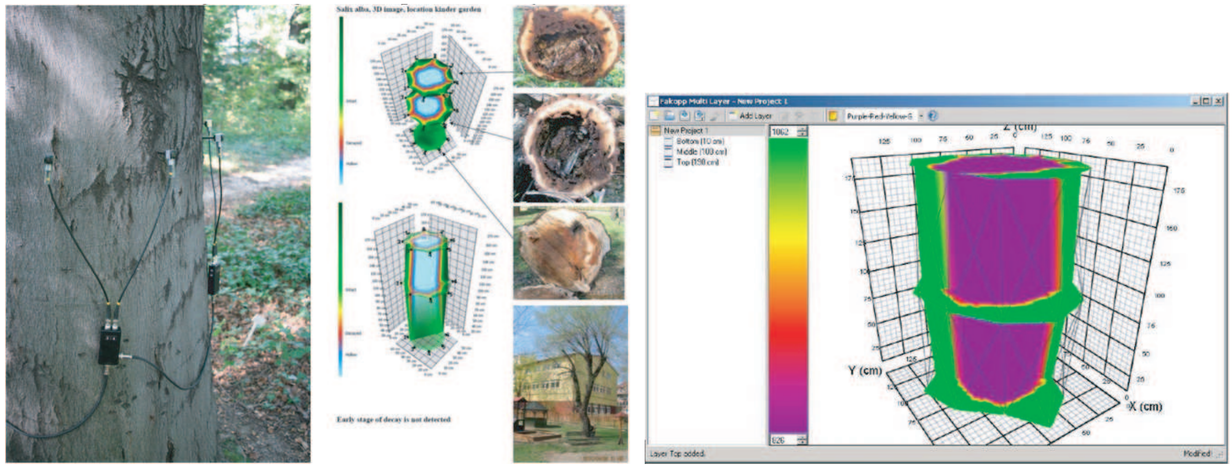

Figure 5: Temperature diagnostics in a section of a wooden structural element.

5. NON-DESTRUCTIVE DIAGNOSTICS

The group of non-destructive methods classifying the rate and extent of damage or inhomogeneity in wood includes various techniques that utilize, as a source of the active system, an electromagnetic wave with a wavelength shorter than 3000 m. Thus, wood treatment processes may involve the use of antenna systems applied in the diagnostics of breast carcinoma [3] or utilization of the X-ray diagnostic method known in the fields of human or veterinary medicine. With this technique, however, there occurs certain difficulty related to the evaluation of damage to the material volume. In spite of the fact, a cycle of tests using damaged material samples (Fig. 3) has led to an alternative apporach; this solution is based on the evaluation of the obtained shot image through a transparent X-ray method having a high rate of image resolution.

6. SOLUTION PROPOSAL

The described method utilizes a high-quality X-ray shot of the diagnosed material as well as a very effective image processing technique. The image was segmented, with subsequent evaluation of the required mapping of damage rate realized through filtration. Fig. 6 shows the diagram of an image processing obtained primarily by means of an X-ray shot.

At this point, for example, the evaluation of shot No. 1 (Fig. 3) is represented in the resolution of damage probability shown is Fig. 7. For image processing, we applied the Otsu filter, the binary filter, and the mean filter. These filters were implemented by the help of convolution techniques (1) [4].

$$P_{x,y} \otimes Q_{x,y} = \sum_{i=-m}^{m} \sum_{j=-m}^{m} P_{x-i,y-j} \cdot Q_{i,j} \tag{1}$$

While the Otsu filter [4] automatically calculates the threshold value by the scatter maximization in Eq. (2), the binary filter enables the user to define user value for sensitive separation of the structure from the image background.

$$\sigma_b^2\left(Th\right) = p_1\left(Th\right) p_2\left(Th\right) \left(\mu_1\left(Th\right) - \mu_2\left(Th\right)\right)^2 \tag{2}$$

$p_1(Th)$ is the probability of the first interval defined by threshold values lower than Th, $p_2(Th)$ is the probability of the second interval with a boundary value higher than Th, μ_1 or μ_2 are the mean value of the first (second) interval, Th is the threshold value. Threshold values of the binary filter can be manually set by the user; alternatively, it is possible to use suitable approximation derived from the mean value (Eq. (3)) and the image covariance (Eq. (4)).

$$\mu = \frac{1}{X_{\max} \cdot Y_{\max} \cdot (Z_{\max})} \sum_{i,j,(k)=1}^{X_{\max},Y_{\max},(Z_{\max})} w_{i,j,(k)} \tag{3}$$

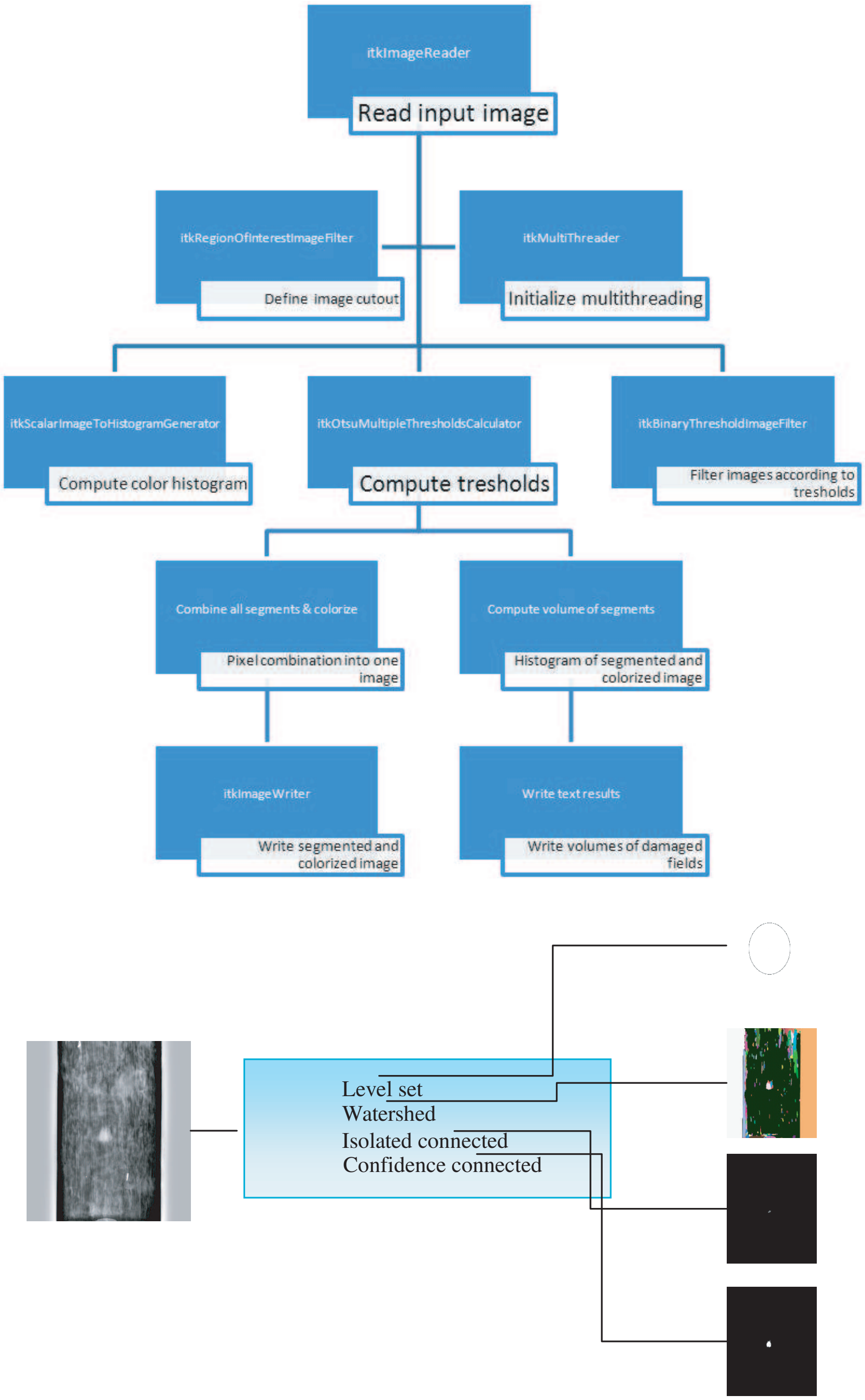

Figure 6: The process of X-ray shot filtration.

$X_{\max}$, $Y_{\max}$, $Z_{\max}$ are max. pixel values in the direction of $x, (z)$

$$\sigma^2 = \sum_{i,j,(k)=1}^{X_{\max},Y_{\max},(Z_{\max})} \left(w_{i,j,(k)} - \mu\right)^2 \tag{4}$$

$w_{x,y,(z)}$ is the output pixel at the position of $x, y, (z)$.

The multiple Otsu filter is based on an algorithm [5], and it is capable of determining multiple threshold values in such a manner that the mutual scatter of intervals determined by these threshold

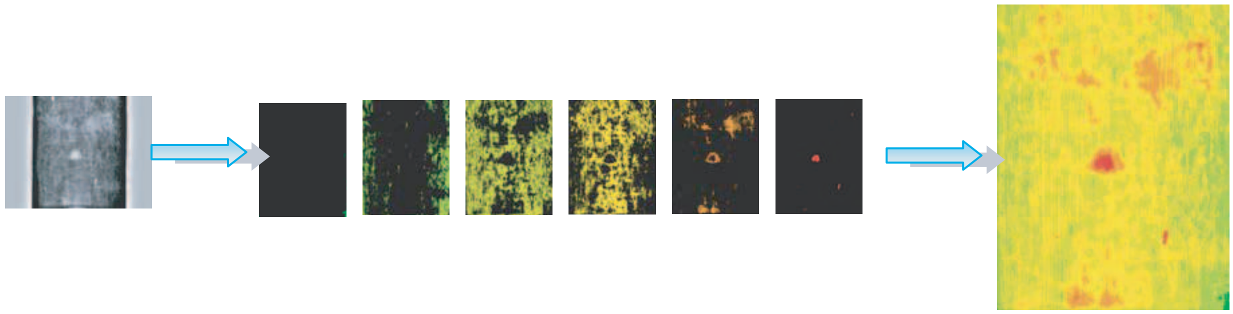

Figure 7: The progress of filtration in X-ray images and the 3D evaluation.

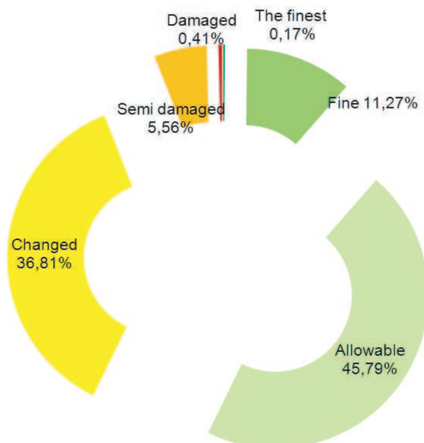

Figure 8: The segmented image resulting interpretation.

values is the maximum (5)

$$\frac{\partial \sigma_B}{\partial t_i} = \max \approx \sum_{k=1}^{M} \omega_k - \mu_k^2 - \mu_T^2 \ \omega_k = \sum_{i \in C_k} p_i \ \mu_k = \sum_{i \in C_k} i \cdot p_i / \omega_k \ \mu_T = \sum_{k=1}^{M} \omega_k \cdot \mu_k,$$

$$p_i = \frac{f_i^{(C_i)}}{N}, \ C_1 \in \{1, 2, \ldots, t_1\}, \ C_2 \in \{t_1 + 1, \ldots, t_2\}, \ldots, C_M \in \{t_{M-1} + 1, \ldots, L\} \tag{5}$$

t_i threshold value of the i-th group, f_i number of points on the i-th threshold, N total number of points, L total number of colour pigments, M total number of threshold groups.

The stages of processing (Fig. 7) represent individual steps of progressive filtration including the identification of main threshold values from the input x-ray image to the resulting interpretation composite together with the quantification of the individual image segments (Fig. 8).

The algorithm for the above-described segmentation was created in the ITK environment [6].

7. CONCLUSION

We designed and tested an X-ray transparent diagnostic method for 2-D imaging and 3-D quality evaluation with respect to the assigned image parameters. The parameters were set in such a manner as to enable the imaging of shot sections showing the rate of damage to the heterogeneous structure building.

ACKNOWLEDGMENT

The research described in the paper was financially supported by a grant of the Czech ministry of industry and trade No. FR-TI1/368, a project of the BUT Foundation Agency FEKT-S-11-5, and the Thermosanace Company Czech Republic. This paper also benefited from the use of the Insight Segmentation and Registration Toolkit (ITK), an open source software developed as an initiative of the U.S. National Library of Medicine.

REFERENCES

1. Prosser, V., *Experimentální Metody Biofyziky*, Academia Praha, 1989.
2. http://www.fakopp.com/site/fakopp-3d.
3. O'Halloran, M., M. Glavin, and E. Jones, "Channel-ranked beamformer for the early detection of breast cancer," *Progress In Electromagnetics Research*, Vol. 103, 153–168, 2010.
4. Yoo, T. S., *Insight into Images — Principles and Practice for Segmentation, Registration, and Image Analysis*, 393, A. K. Peters, Ltd., Wellesey, 2004.
5. Liao, P. S., T. S. Chen, and P. C. Chung, "A fast algorithm for multilevel thresholding," *Journal of Information Science and Engineering*, Vol. 17, No. 5, 713–728, Institute of Information Science Academia Sinica, 2001.
6. Ibáñez, L., W. Schroeder, L. Ng, and J. Cates, *The ITK Software Guide — Second Edition Updated for ITK Version 2.4*, 804, Kitware, Inc., 2005, ISBN 1-930934-15-7.

Analysis of SRR Metamaterials with Controllable Resonance Frequency

Shi-Quan Zhang[1], **Li-Jie Wang**[1], **Hui Zhang**[1], **and Bing Wei**[2]

[1]Physics Teaching and Research Office, Engineering University of CAPF
Xi'an, Shaanxi 710086, China
[2]Department of Physics, Xidian University, Xi'an, Shaanxi 710071, China

Abstract— Simulations are made to three types of symmetric SRRs including double-ring SRR, symmetric single-ring SRR and modified SSR by CST software. Comparison and analysis indicate that SRR with short metal rod can adjust the resonance frequency of the conventional SRR. It is also verified that the transmission zero points of the new type of SRR-based filter can be controlled by changing the distance between the short metal rod and the side of SRR with mouth. The above properties of the modified SRR are used to design a filter unit which shows an improved transmission characteristic and compact size.

1. INTRODUCTION

In recent years, there has been a growing interest for the study of the special properties of left-handed metamaterials and their applications. Metamaterials are also referred to as double-negative media which behave as an effective medium with negative values of permittivity and permeability. In 1968 Soviet scientist Veselago V. G. indicated that media with negative permittivity ε and permeability μ would have distinct electromagnetic characteristics, such as negative refraction. Since Smith D. R. et al. fabricated metamaterials whose ε and μ are negative by using Pendry J. B. et al.'s theoretical results for the first time in 2001 [1–3]. The discovery of metamaterials was considered as one of the ten greatest scientific and technological breakthroughs in 2003 by the famous American Journal, *science*. It was once again regarded as one of the ten greatest scientific and technological achievements in 2006 by *science* due to its application in electromagnetic stealth [4–6]. The study of metamaterials has become a hot topic in the international science field. Pendry J. B. and Koschny T. [7, 8] pointed out that both the effective permittivity and the effective permeability of split ring resonator (SRR for short) array of metamaterials can be negative, that is

$$\varepsilon_{\text{eff}}^{\text{SRR}}(\omega) = 1 - \frac{\omega_p^2 - \omega_0^2}{\omega^2 - \omega_0^2 + \mathrm{i}\omega\gamma}; \tag{1}$$

$$\mu_{\text{eff}}^{\text{SRR}}(\omega) = 1 - \frac{\omega_m' - \omega_m^2}{\omega^2 - \omega_m^2 + \mathrm{i}\omega\gamma}. \tag{2}$$

In this paper, simulations are made to three types of symmetric SRR including double-ring SRR, symmetric single-ring SRR and modified SSR by CST software. Comparison and analysis indicate that SRR with short metal rod can adjust the resonance frequency of the conventional SRR. It is also verified that the transmission zero points of the new type of SRR-based filter can be controlled by changing the distance between the short metal rod and the side of SRR with mouth. The above properties of the modified SRR are used to design a filter unit which shows an improved transmission characteristic and compact size.

2. SIMULATION ANALYSIS TO THE THREE TYPES OF SRR

The geometries for the traditional double-ring and single-ring SRR are shown in Figures 1(a) and (b), respectively. The width, distance between the rings, the width of the open mouth and the thickness of the rings are all equal to 0.2 mm, the side length a of the ring is 1.8 mm. For the controllable SRR the length l of the inserted short metallic rod is 1.0 mm, its width w and the distance d away from the mouth-contained side are all equal to 0.2 mm [see Figure 1(c)]. Suppose that the rings and wires are placed inside a unit box in the vacuum and the computation region is $3.8 \times 3.8 \times 3.2\,\text{mm}^3$ truncated by absorbing boundary, PEC and PMC boundaries along x, y and z axes, respectively. That is, the wave vector, the electric field strength and the magnetic field strength are along x, y, z directions, respectively. In this situation, the magnetic field which is perpendicular to xy plane has the strongest impact on SRR. We numerically study the transmission

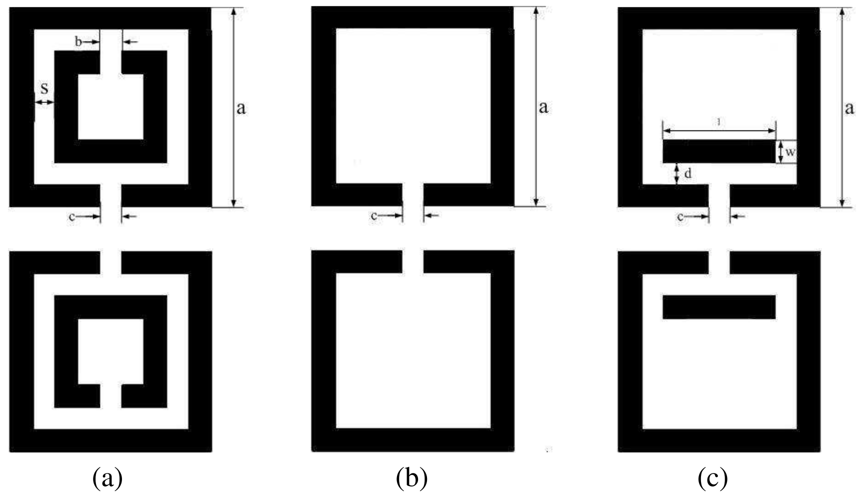

Figure 1: (a) Symmetric double SSR with square mouth. (b) Symmetric single SSR with square mouth. (c) New type of SSR.

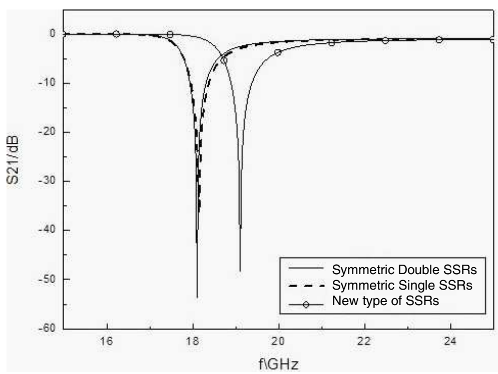

Figure 2: Transmission coefficients for three types of SRR.

properties of three types of SRR by using CST software. The simulation results are given in Figure 2 in which the solid, dash and circle lines indicate the transmission through the double-ring SRR, the single-ring SRR, and the new type of SRR, respectively.

It can be observed from Figure 2 that the resonance frequency of the double-ring SRR is at 18.09 GHz, in which the magnetic permeability of it will be negative, and the symmetric single-ring SRR is resonant at 19.11 GHz, experiencing an increase of 1.02 GHz comparing with that of the double-ring SRR. The resonance frequency of a double-ring SRR appears at lower frequency, which increases the possibility that the magnetic response is located in the region of $\varepsilon < 0$ for the combined SRR and metallic arrays structure. Since the resonance frequency of double-ring SRR is unchangeable, we replace it by a tunable SRR, which is capable of tuning its magnetic resonance frequency by adjusting the short rod. The transmission of the tunable SRR is quite similar with that of the double-ring SRR except that the magnetic resonance frequency is controllable.

3. FILTER APPLICATION OF THE NEW TYPE OF SRR

The influence of transmission coefficients by the distance d between the short rod and SRR is shown in Figure 3. It can be observed that the magnetic resonance frequency rises from 18.15 GHz to 19.01 GHz when d increases from 0.1 mm to 0.7 mm. That is, the magnetic resonance frequency of tunable SRR increases with d. This can be attributed to the increased capacitance. The additional capacitance is inversely proportional to the distance d, increasing d means reducing the capacitance and thus increasing the magnetic resonance frequency. Continuing increasing d, we can see from simulation that the resonance frequency of tunable SRR is greater than that of the single-ring SRR if $d > 0.7$ mm.

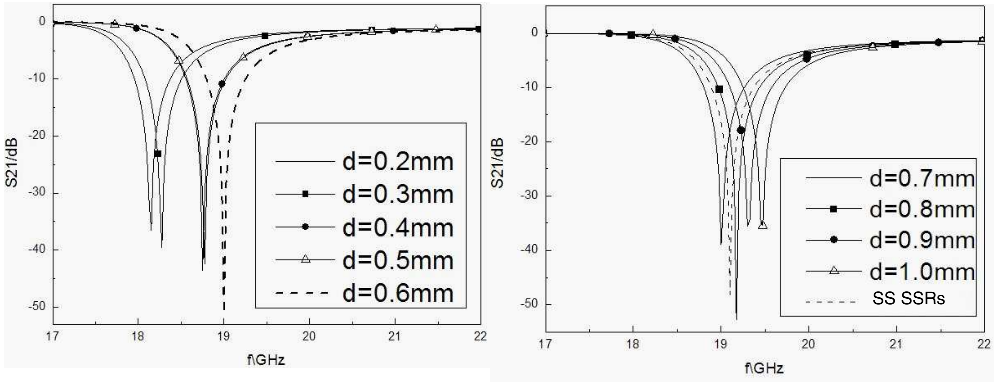

Figure 3: The relationship between transmission coefficients and frequency.

4. CONCLUSION

Simulations for three types of SRR are conducted. It is indicated that the resonance frequency of the new type of SRR can be controlled by adjusting the distance between the short metal rod and the side of SRR with mouth. The above properties of the modified SRR can also be used to design a filter unit with an improved transmission characteristics and compact size.

ACKNOWLEDGMENT

This project is supported by the National Natural Science Foundation of China (Grant No. 61072034) and the Basic Research Project of Engineering University of CAPF (Grant No. WJY201008).

REFERENCES

1. Pendry, J. B., A. J. Holden, W. J. Stewart, et al., "Extremely low frequency plasmas in metallic structure," *Phys. Rev. Lett.*, Vol. 76, No. 25, 4773–4776, 1996.
2. Pendry, J. B., A. J. Holden, D. J. Robbins, et al., "Magnetism from conductors and enhanced nonlinear phenomena," *IEEE Trans. Microwave Theory and Tech.*, Vol. 47, No. 11, 2075–2084, 1999.
3. Smith, D. R., W. J. Padilla, D. C. Vier, et al., "Composite medium with simultaneously negative permeability and permittivity," *Phys. Rev. Lett.*, Vol. 84, No. 18, 4184–4187, 2000.
4. Schurig, D., J. J. Mock, B. J. Justice, et al., "Metamaterial electromagnetic cloak at microwave frequencies," *Science*, Vol. 314, No. 5801, 977–980, 2006.
5. Lezec, H. J., J. A. Dionne, and H. A. Atwater, "Negative refraction at visible frequencies," *Science*, Vol. 316, No. 5823, 430–432, 2007.
6. Cai, W. S., U. K. Chettiar, A. V. Kildishev, et al., "Optical cloaking with metamaterials," *Nature Photonics*, Vol. 1, No. 4, 224–227, 2007.
7. Koschny, T. and M. Kafesaki, "Effective medium theory of left-handed materials," *Phys. Rev. Lett.*, Vol. 93, No. 10, 107402-1–4, 2004.
8. Cui, W. Z., W. Ma, L. D. Qiu, and H. T. Zhang, *Electromagnetic Metamaterials and Application*, The National Defense Industry Publishing House, Beijing, 2008.

Measurement of High Frequency Magnetic Radiation in Kuwait

Fuad Alkoot[1] **and Rabie K. Dib**[2]

[1]HITN, PAAET, P. O. Box 4575, Alsalmia 22046, Kuwait
[2]EE Department, CTS, PAAET, P. O. Box 4196, Hawalli 32072, Kuwait

Abstract— Due to the possible harmful effects of magnetic radiation countries have set limits on transmitted power density. Therefore, many have conducted field surveys to measure its levels, especially around mobile base stations. We present the initial results on our field survey to measure magnetic radiation between 75 MHz and 3 GHz in Kuwait. Presented results of four locations show that other sources are as high as GSM sources. However, all are below ICNIRP limits.

1. INTRODUCTION

There has been an increase of mobile users accompanied by an expansion of mobile telephone networks. This has resulted in mounting community concern about health effects caused by radiation emissions from the mobile antennas mounted on base station towers. Whether this concern is justified or not depends on the level of radiation emitted from the towers. We aim to find the level of radiation emitted by all sources emitting at frequencies between 75 MHz to 3 GHz.

Based on the surveyed literature [1–8] we believe there is a health hazard associated with EMF and RF radiation. However, studies were not able to find and confirm the exact dangerous levels due to the complex nature of the problem. Many organizations [9, 10] have set limits for each frequency of the RF band. The limit changes with the change in the frequency.

This study aims at finding the degree of radiation available and compares it to the standard levels. Our aim is to find the sum of all radiation existing due to many sources at one point covering the RF range of 100 MHz to 3 GHz. We aim to find radiation due to the GSM base station transmitters and G3 transmitters in addition to all other high frequency sources such as TV, radio, satellite paging systems and private networks. The recorded levels are compared to limits set by ICNIRP. Based on this comparison we may conclude whether the radiation levels in Kuwait pose any health hazard, and which source is the main contributor to this sum.

2. METHODOLOGY

For each surveyed area we record location, position, meter readings, and time of measurement. Considering the sensitivity of this type of readings, and in order to incorporate any undesired enormous range of response that depend on the angle and direction in which the measurement device is held, many redundant readings are taken to consolidate our measurements. A selective radiation meter made by Narda is used to find the magnetic radiation level in units of power density and in percentage of the ICNIRP limit. The nature of the device used and the special characteristics of the tri-axial antenna provided by the manufacturer were of great help in providing a more clear indication of the radiation measurement.

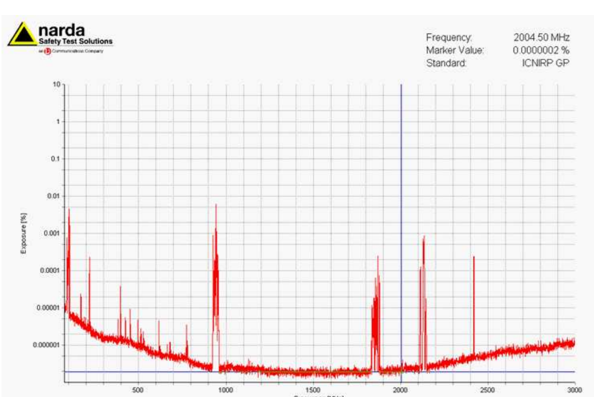

Figure 1: Radiation sources in percentage of ICNIRP limit at Shuwaikh-PAAET.

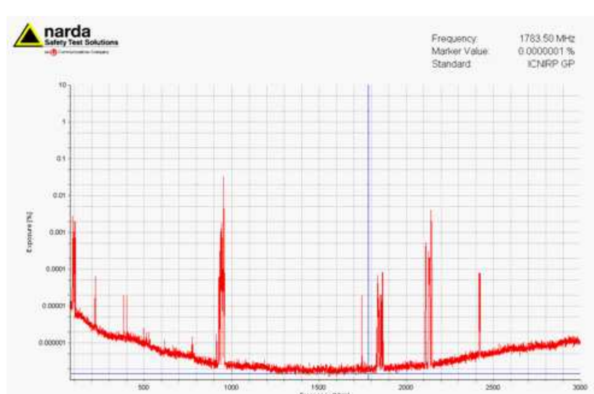

Figure 2: Radiation sources in percentage of ICNIRP limit at Ibn Sina Hospital.

3. RESULTS

We present results for four surveyed areas; Shuwaikh at location coordinates N29 20.016 E47 54.754, Ibin Sina Hospital at N29 19.521 E47 54.116, Jabriya at N29 19.018 E48 02.034 and Bayan at: N29 17.858 E48 03.209. As can be gleaned from the figures and tables presented below many radiation sources that pose a hazard exist in the surveyed areas. Figure 4 and colomns 2 and 4 of Table 1 present results in units of power density, while the rest present results in percentage of ICNIRP limit for the public. At Shuwaikh-PAAET area Figure 1 we find GSM 900 is the highest source, however GSM1800, UMTS at 2.15 GHz, and FM 100 MHz in addition to many sources between it and GSM900 exist. Surprisingly WLAN at 2.4 GHz was high reaching GSM1800. The same scenario appeared at IbnSina Hospital, although there were less private sources between the FM and GSM 900. Again WLAN was surprisingly high. At Jabria we found a light difference were the FM was weaker but a private source around 350 MHz existed. UMTS was higher than GSM1800. Although lower than the previous two areas WLAN sources existed from multiple sources at different frequencies. Finally, at Bayan, in addition to GSM 900, GSM1800 and UMTS we find many other sources of which the strongest were at 1.2 GHz and 400 MHz. As in the previously discussed areas sources between FM and GSM900 exist, however they were found to be stronger here, at Bayan. Figure 4 shows the source at 400 MHz is as strong as the GSM900.

Table 1 provide us with detailed radiation levels. Detailed levels at Shuwaikh-PAAET shown in Table 1, indicate that GSM 900 and FM sources are the highest contributors to the total radiation. UMTS is also a strong contributor although it appears at a lower level. WLAN also appears at the top 20 list of Shuwaikh sources. The total percentage sum due to the highest 100 frequencies at

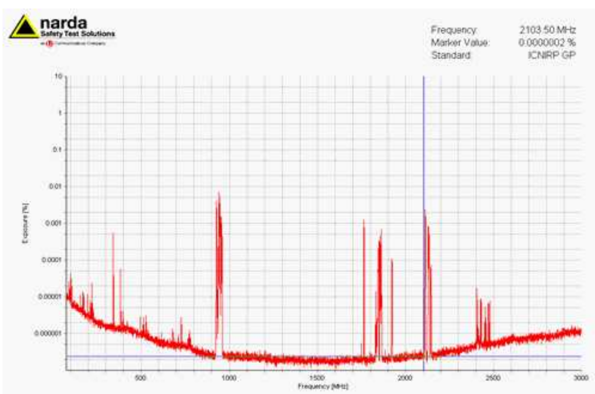

Figure 3: Radiation sources in percentage of ICNIRP limit at Jabria.

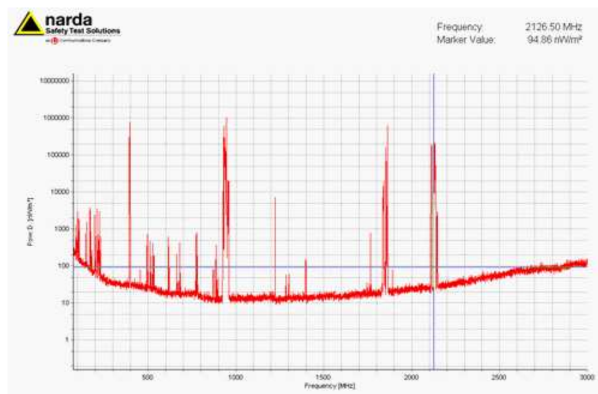

Figure 4: Power density of radiation sources at Bayan.

Table 1: Highest radiation levels in percentage of ICNIRP limit and in unit of power density for the four surveyed areas.

	Shuwaikh-PAAET		Ibin Sina Hospital		Jabria		Bayan	
Index	Frequency	Index	Frequency	Level in mW/m^2	Frequency	Level in %	Frequency	Level in mW/m^2
1	943.6	0.006	906.1	6.637	940.8	0.008	914.5	2.224
2	103.6	0.005	98.9	0.516	946.3	0.005	939.4	1.507
3	99.6	0.003	944.6	0.342	926.6	0.004	945.2	0.552
4	938.9	0.001	97.5	0.312	927.3	0.003	930.6	0.302
5	947.6	0.001	103.6	0.216	2111.6	0.003	1859.8	0.253
6	926.2	0.001	953.4	0.165	948.3	0.002	2111.5	0.171
7	2134.3	0.001	87.8	0.124	2113.0	0.002	2129.1	0.125
8	2135.6	0.001	938.2	0.116	954.9	0.002	2113.4	0.123
9	89.4	0.001	93.2	0.113	1764.4	0.001	2130.9	0.111
10	2130.0	0.001	2129.5	0.098	2113.9	0.001	948.2	0.105

Shuwaikh-PAAET is 0.026%. This is much below the ICNIRP limit. However, caution warrants that we don't view the level to be totally safe, due to the recent calls to reduce the exiting limits.

As in the previous area, table of results of IbnSina Hospital show the strongest radiation sources are GSM900, then Fm followed by UMTS. At Jabria GSM900 followed by UMTS then GSM1800 are the highest sources. Although FM and WLAN are strong contributors at Jabria, however, they do not appear at the top of the list. The total percentage sum due to the top 100 sources is 0.040%. At Bayan the three main sources are GSM900, GSM1800 and UMTS. GSM900 is much stronger than the rest reaching 2.224 mW/m^2, while the rest are in units of μW/m^2

4. CONCLUSION

We have conducted a survey of four locations at the state of Kuwait to measure levels of magnetic radiation from sources transmitting between 75 MHz and 3 GHz. This study is essential to confirm that existing levels are below the standard limits. Additionally results made available to the scientific community for possible future use. Results are presented in units of power density and in percentage of ICNIRP limit for the public. We have confirmed that none of the sources exceeds the maximum limit nor did the sum of the highest 100 sources. The main contributors at all four areas were GSM900, UMTS and GSM1800. FM existed close to GSM900 at all areas except at Jabria, while WLAN existed at all areas except for Bayan. Also many private sources between FM and GSM900 exist in all areas, however stronger at Bayan.

REFERENCES

1. Roosli, M., et al., "Symptoms of ill health ascribed to electromagnetic field exposure — A questionnaire survey," *International Journal of Hygiene and Environmental Health*, Vol. 207, No. 2, 141–150, 2004.
2. Navarro, E. A., et al., "The microwave syndrome: A preliminary study in Spain," *Electromagn. Biol. Med.*, Vol. 22, No. 2–3, 161–169, 2003.
3. Santini, R., et al., "Symptoms experienced by people in vicinity of base stations: II/Incidences of age, duration of exposure, location of subjects in relation to the antennas and other electromagnetic factors," *Pathol. Biol.*, Vol. 51, No. 7, 412–415, Paris, 2003.
4. Santini, R., et al., "Investigation on the health of people living near mobile telephone relay stations: I/Incidence according to distance and sex," *Pathol. Biol.*, Vol. 50, No. 6, 369–373, Paris, 2002.
5. Ahlbom, A., A. Green, L. Kheifets, D. Savitz, and A. Swerdlow, "Epidemiology of health effects of radiofrequency exposure," Standing Committee on Epidemiology, International Commission for Non-Ionizing Radiation Protection. Available at http://www.ncbi.nlm.nih.gov/pmc/articles/pmc1253668/.
6. Wolf, R. and D. Wolf, *Increased Incidence of Cancer Near a Cell-phone Transmitter Station*, *International Journal of Cancer Prevention*, Vol. 1, No. 2, 2004.
7. Eger, H., et al., "The influence of being physically near to a cell phone transmission mast on the incidence of cancer," *Umwelt Medizin Gesellschaft*, Vol. 17, No. 4, 2004.
8. Carpenter, D. and C. Sage, "A rationale for a biologically-based public exposure standard for electromagnetic fields (ELF and RF)," BioInitiative Report, Aug. 2007, http://www.bioinitiative.org.
9. International Commission on Non-Ionizing Radiation Protection, "Guidelines for limiting exposure to time-varying electric, magnetic, and electromagnetic fields (UP to 300 GHz)," *Health Physics*, Vol. 74, No. 4, 494–522, 1998.
10. F.C.C., "A local government official's guide to transmitting antenna RF emission safety: Rules, procedures, and practical guidance," Jun. 2, 2000, Available at http://wireless.fcc.gov/siting/FCC_LSGAC_RF_Guide.pdf.

Relative Cellular Energy Balance and Biometric Interaction

K. F. Kaspareck
CTE, Italy

Abstract— This paper attempts to describe basic cellular energy exchanges for biometric interactions by combining redox information and thermodynamics along a texture model acting for signal/feedback transport. The model was adopted from the processing of Nuclear Magnetic Resonance images.

Cellular balance is set as a function of energy intake and metabolic output, baseline energy, electrochemical/magnetization gradients. Cellular energy reciprocally controls electrochemical exchanges. Differences in pH reflect on temperature over a thermodynamic/chemical loop, and vice versa.

Entropy shifts during the process as temperature, pH, potential and water gradients modify and interrelate with molecular/cell bound water. The shape of interaction surfaces, differential electromagnetic forces and gravitation participate to the process. Cellular vibration states, feedback quality also modify.

Elements with asymmetric bonds such as aromatics, NOxs, interfere with glycoprotein receptors and ATP-ADPs cycles by interacting with Sulfur and Phosphorous molecular bridges. Strong electropositive trace elements provide extra inertia and catalysis contributions.

Biometric energy unbalance seems to coincide with a yield point of cellular equilibrium, making free energy available for additional thermo-electrochemical reactions and, or displacement of resident cellular energy. The physics of reaction, linear over a wider internal loop, may be non-linear in the very near field, ending with anisotropic cellular polarization. The progression appears inertial along sequential rebalancing or cumulative unbalancing, independent from path.

1. INTRODUCTION

The human body has a mean requirement of c.a. 100 Kcal/hr, corresponding to about 3 kWh of energy over the 24 hrs or 6×10^{25} ev. Cellular balance is function of energy intake and metabolic output, baseline energy, electrochemical/magnetization induced gradients.

Cellular energy controls pH and internal electrochemical exchanges, and vice versa, where differences in pH reflects on T over a thermodynamic loop. Changes in pH and, or T affect cellular energy balance and internal biometric gradients, including intracellular radiation re-radiation.

Entropy shifts during the process as T, pH and electrochemical potential modifies ($\varepsilon = hv^2/4\pi - U$) and interrelate with molecular water. The shapes of interaction surfaces, differential electromagnetic attenuation condition the process.

Biometric energy unbalance coincides with a yield point of cellular equilibrium, creating free energy available for additional thermo-electrochemical reactions and, or displacement of resident cellular energy. Protein acids are less than two orders of magnitude than cell size and activate/synthesize with relatively small free energy. Cellular vibration frequencies and feedback quality (RNA-ATPs) are also affected, so is the glycolic process.

The physics of reaction, linear over a wider internal loop, may be non-linear in the very near field. The process is inertial and progresses along sequential rebalancing or cumulative unbalancing. Trace elements with double asymmetric bonds such as aromatics contribute to unbalance, strongly electropositive elements provide inertial contribution.

This paper attempts to provide an integrated, perhaps viable, chemical and thermodynamic model for cellular energies and exchanges that drives biometric interactions.

2. MODEL FRAME OF REFERENCE

Nuclear magnetic resonance, NMR, can provide comprehensive information on the base dynamics of the body, as this is made by over 80% water. Indicative Hydrogen relaxation times after excitation by a toroidal magnetic field indicate that bound water resonant intensity decreases asymptotically by nearly 18 dB in 10 ms, free water, linearly in 120 ms.

The sequence of images above shows an NMR reverse image (negative), imaginary (phase) and real (amplitude) parts computed over a 9×9 pixels sliding window. Square roots of phase and real parts were auto scaled and displayed using the same colors range, the input image is in grey scale.

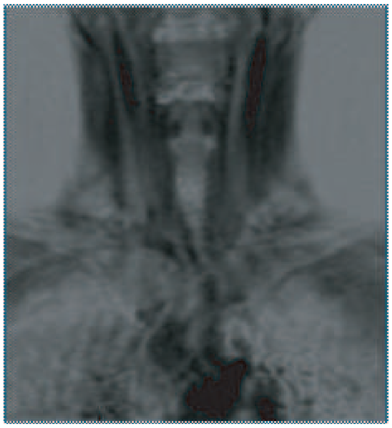

Figure 1: Input image −180 degrees.

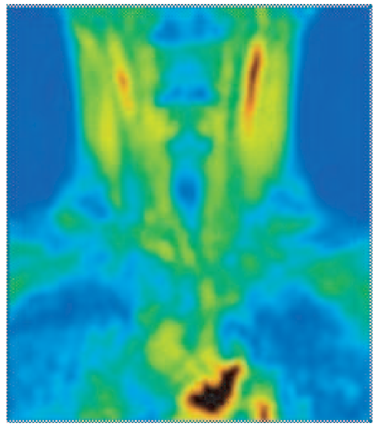

Figure 2: Square root real part of signal.

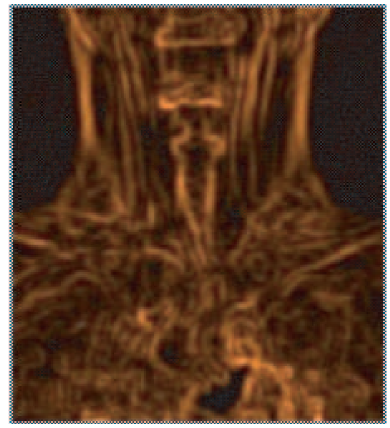

Figure 3: Square root imaginary part.

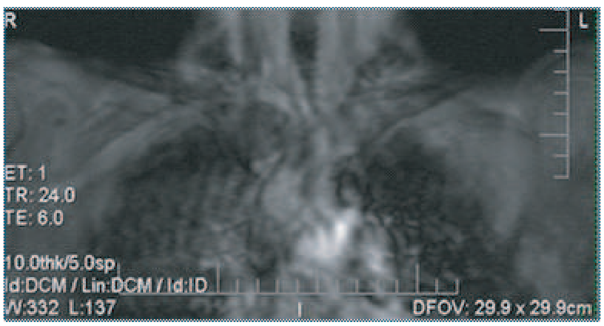

Figure 4: Input image (Merge Healthcare Instrumentation).

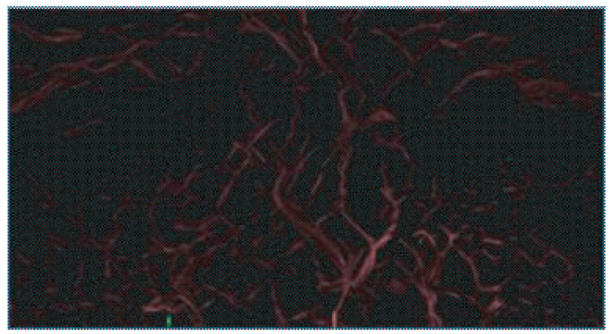

Figure 5: Imaginary root of filtered output.

The original purpose was to improve definition of a hemangioma, considerably clearer on the centre bottom of processed images.

Wideband deconvolution of a wider portion of the input image was then performed, imaginary roots derived linearly and threshold to an arbitrary value coinciding with the highest visual signal-to-noise ratio.

The result is shown below. The imaginary root image to the right appears very useful for base model structure reference over a mean body surface, which can be assumed c.a. 20 sqft. The image shows what can perhaps be interpreted as macro texture "bond" Hydrogen isotropic network frame, along which the cellular framework and signal transmission develop, path independently.

Hydrogen bond energy is 4 ev or 10^{-22} Kcal. Nevertheless, free water inertia should be considered. This was empirically derived as $p = kC_{p(T)} + k\Delta T - gk/\mu$ from a slowly heated water solar panel.

Electromagnetically, cells' energy interconnects to cell's vibration periods and probably to structural frame envelope and frame clusters' frequencies.

3. ELECTROCHEMICAL/MAGNETIC BALANCE

Homeostasis links closely to cellular energy, where the body's gross energy resident value is some orders of magnitude daily energy intake. Apparent cellular hydrated rest energy, calculated from general anesthetic requirements vs. body weight, is close to 0.15 Kcal/mol, which seems a realistic value, within the order of magnitude of damaging external radiation energy.

Thermodynamics/electrochemical balance could be simplified and associated to four base parameters, namely T, water, pH and cellular frequency. Increasing T draws water and reduces pH, but also influences vibration states. A change of internal energy and, or an energy gradient, connect to a change in pH, where T is driving at the onset and ΔT correlates closely to the difference of pH cubic roots. Lower pH would generally weaken molecular bonds, higher pH, tighten bonds, where mean plasma pH is 7.3.

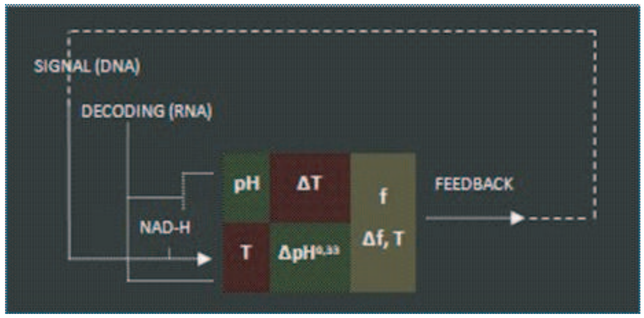

Figure 6: T, pH, f hypothetical loop.

Enzyme/peptide links connect with amino acids formation/break down as for enzyme-peptide-water interaction. Since proteins' synthesis generates water and a pH change draws water, water-soluble vitamins' increase should follow increasing T, if pH, water and amino acids availability conditions were satisfied. Fat-soluble vitamins' increase should instead follow decreasing T, resulting in tighter molecular bonding because of greater availability of hydroxyl bridges. Bond weakening will occur in the first case, stretching of bonds concern both cases.

Conflicting base parameters combinations may give way to cellular energy range/derange reactions as cellular and clusters' vibration frequencies interconnect with T. Interaction of vibration frequency differences could perhaps be described according to $4k\Delta f$. Cellular unbalance would coincide with a yield point of cellular equilibrium. Root causes could be linked to wrong decoding and feedback along the model framework, replicating and further impairing coding over the hypothetical T and pH loop flow scheme of Figure 6, sustained by rapid adiabatic cellular dynamics.

4. TEMPERATURE AND PH LOOPS

Signal transmission and biochemical reactions may privilege thermodynamic balance with respect to chemical balance. Geometrically and physically the reference model is compatible with the simplified flow scheme proposed, the main question the existence and satisfaction of boundaries.

Near red or equivalent coded frequency signal feeds as T and is decoded. Information, passed through NAD-H, acts on pH, in turn acting on resident/reradiating T and leaving a core residual ΔT. Feedback is ΔT, frequency coded with intensity related to $T/\Delta T$.

Wrong coding/decoding may be induced by "non-linear" thermodynamics/electrochemistry, where the base relation $T = (\varepsilon + U - H)/S$ might not be satisfied and the nucleotide NAD-H output wrong redox information. A sequential chains of errors could then result from a sort of thermal runaway and, or back EMF, leading to extended wrong feedback.

Persistent endothermic conditions would lead to cell nucleic depletion or meta-stability. Re-radiation would be according to Planks' re-radiation fifth power exponent for a black body, adding non-linearity to the process. Energy flows across the cell would occur with the partaking of cellular bound water, which may result at later stage in a shift from multi-polar to prevalently dipolar cells/cellular aggregations.

At larger scale, textural frame flow may converge or diverge, involving electromagnetic coincidence/de-coincidence(s) in the overall field. This would in turn induce localised extra ΔUs and cells' groups/clusters polarisation.

Aromatics and other complex molecules may impair coding/decoding of primary signal by interacting with Sulfur/Phosphorous-Oxygen molecular bridges and affecting tri/diphosphate nucleoside (ATP/ADP) cycle. Wrong feedback for base protein (i.e., insulin) may also occur. Kynase polyphosphate-RTK (RNA) receptor is blood distributed and given its base molecular structure shape, if modified, could further impair clusters through hybrid bonding.

Strong electropositive trace elements may provide extra inertia and unnecessary catalytic potential. Nitrogen Oxide compounds-NOXs, strong nucleophiles, may tend weakening bonds of, for instance, glycoprotein receptor polymers, freeing oxygen, with possible differential impairment of hydrogen and hydroxyl bonds. Natural body potassium equilibrium, thus overall pH, would also be affected.

5. CONCLUSIVE REMARKS

The model chosen appears compatible with the physical and chemical exchanges described, it is isotropic along the textural framework and could perhaps have no electromagnetic boundaries. Because of its textural framework, it seems reasonable to assume that information conveys through frequency and temperature, path independently, and that coding anomalies relate to erroneous feedback (distortion) and, or initial wrong decoding.

In the first case, the imaginary portion of signal is changed, transports insufficient or amplifies wrong information. In the second case, the entire feedback signal may be false.

As a result of non-linearity, spectral information aliasing may occur, altering this way also immune system feedback, which relies on a wider and balanced spectrum, especially at lower frequencies.

Given the very low value of intracellular energy exchanges and the textural model frame extending over a large surface, the near/far gravity field too appears to play a critical homeostatic role. Gravitational differences/gradients in the Northern Hemisphere can attain 110 mG, which seems significant also given the cellular regeneration cycle.

As a result of the analysis performed and hypotheses brought forward, we could say that passive and forward imaging, for instance time lapses at constant conditions, with far larger dynamic range, would improve quantitative understanding in the field and aid both diagnosis and prevention. Red and near-infrared information could be critical for identifying and calibrating localised and general temperature gradients, variations or anomalies, possibly in conjunction with thin needles. As well, differential electromagnetic applications could prove very valuable in related therapy.

6. SYMBOLS

Cp: heat specific capacity	hr: hour	ms: millisecond
ev: electron volt	K: Boltzmann constant	pH: oxidation index
ε: charge	k: thermal conductivity	sqft: square foot
sqft: square foot	Kcal: Kilocalorie	S: entropy
g: gravity	kWh: kilowatt per hour	T: temperature
H: enthalpy	μ: viscosity	U: potential
h: Plank constant	mG: milligal	v: velocity

REFERENCES

1. *7th Eutech Seminar*, Cellular Chemistry Presentation, Borellini, 2006.
2. Rapport de Recherché n.5187, INRIA Sophia Antipolis, Apr. 2004.
3. Lai, H. and N. P. Singh, "Single and double-strand DNA breaks after acute exposure to radiofrequency radiation," *Int. J. Radiation Biology*, 1996.
4. Briischweiler, R., C. Griesinger, and R. R. Ernst, "Correlated motion monitored by NMR relaxation in the rotating frame, a source of structural and dynamic information on macromolecules," Laboratorium Fur Physikalische Chemie Eidgenossische Technische Hochschule, Zurich, Apr. 1989.
5. McKinney, G., "Applicability of Kundt's rule to chlorophyll," *Brief Papers*, University of Berkley, Undated.

Influence of Variations of Near Earth Electromagnetic Fields on Cerebrovascular System of the Person in Time of Heliogophysical Disturbances

Yu. Ya. Varakin[1], **V. G. Ionova**[1], **G. V. Gornostaeva**[1],
E. A. Sazanova[2,3], **and N. P. Sergeenko**[2]

[1]Scientific Center of Neurology RAMS, Moscow, Russia
[2]Pushkov Institute of Terrestrial Magnetism
Ionosphere and Radio Wave Propagation RAS, Troitsk, Moscow Region, Russia
[3]Clinical Hospital of Russian Academy of Sciences, Troitsk, Moscow Region, Russia

Abstract— Problems of adaptation of the person to influence heliogeophysical disturbances are actual at its life-support, both on the Earth, and in space. In work properties cross-correlation between variations of number of the hospitalised people with defeats of vessels of a brain and indexes of heliogeophysical disturbances characterising various physical processes in a near Earth space are analyzed. The hypothesis is checked, that one of the internal reasons of observed effects are increases of catecholamins levels and variations of deformative and aggregative ability of erythrocytes of blood. The found out effects are statistically authentic and specify on direct influences of electromagnetic fields variation during disturbances on blood cells.

1. INTRODUCTION

During disturbances of near the Earth electromagnetic field in time of heliogeophysical storms and substorms of solar and magnetosphere origins, during other natural and manmade influences many diseases (especially cardio-cerebrovascular, psychological, etc.) are aggravated up to lethal outcomes. Professional reliability of functioning of persons, labile to influence heliogeophysical disturbances (especially in systems and situations of extreme risk) decreases. Problems of adaptation of the person to influence heliogeophysical disturbances are actual at its life-support, both on the Earth, and in space.

In the last decades, considerable evidence has been accumulated to reliably indicate that fluctuations of physical fields in the near-Earth space during heliogeophysical disturbances affect on biological processes to cause a failure in the functioning of various physiological systems [1–3].

In this work, we considered a temporal correlation between the heliogeophysical indices, which describe the physical processes in the Sun-Earth system during geomagnetic storms, and indices characterizing cerebrovascular deseases of people.

2. MATERIAL AND METHODS

We analyzed the time series of the 10.7-cm solar flux — index (R), the auroral electrojet index (AE), and the geomagnetic activity index at Moscow (?) [4]. These indices describe the development of the heliogeophysical processes during a magnetic storm. The consequences of the burst begin to affect the near-Earth space environment almost simultaneously with the events on the Sun: the UV, X-ray, and radio radiation intensities increase. Near the boundary of the magnetosphere and the solar wind, substorms emerge because of fluctuations of the solar wind power. In this time, in the magnetosphere, electromagnetic waves with frequencies in range of 0.001–10.0 Hz are generated, which reach the Earth. The intensity of this low-frequency radiation increases during magnetic storms by a factor of 10–100. It is occurred ionospheric substorms. Approximately in 2 days on the Earth variations of intensity of a geomagnetic field in a range of ultralow frequencies amplify, there is actually geomagnetic storm.

As indices of the state of health, we used the 1979–1980 and 1983–1984 Moscow Ambulance Service data on the number of hospitalized patients with damage to brain vessels. This indicator-integrated. To study the reasons of deterioration of state of health, have been investigated variation of catecholamins of plasma: noradrenalin (NA), adrenalin (A), dofamin (DA). These parameters were measured in 73 health men and 93 patients in different heliogeomagnetic conditions.

Also character of changes by erythrocytes component of haemorheological properties at healthy people and patients with cerebrovascular shifts according to screening of the population of Moscow was studied. At 261 men at the age of 40–64 years were studied a condition agregative and deformative properties of erythrocytes in quiet days and during of heliogeophysical disturbances. Among them there was a group healthy ($n = 115$) and a group of persons with signs of initial clinical displays ($n = 146$). At all observable persons defined ability erythrocytes to aggregation (AE), their deformation properties (?E) and filtration time (TF).

At mathematical processing the Student criterion was used, reliable considered differences at $p < 0.05$. Results are summarised and analysed depending on heliogeophysical conditions.

3. THE RESULTS OF EXAMINATION

These data were used for cross-correlation analysis between the heliogeophysical and medical samples, which allows one to determine not only the degree of relationship of one sequence of events with another, but also the time delay of one process with respect to another. All the regular rhythms (at -3.5, 7, 14, and 27 days) were subtracted from the time variations of both heliogeophysical and medical data. A total of 23 disturbances were considered. The Fig. 1 shows how the time shift affects the correlation coefficients between the variations of the numbers of hospitalized patients from both groups and the indices R, AE, and K during periods of weak, moderate, and strong disturbances, which follow one another and in began on October 15, 18, and 23, 1984. The dashed lines present the significance levels of the correlation coefficients. The Fig. 1 shows that patients with cerebrovascular pathology began to respond to a disturbance almost at the moment of the beginning of the events on the Sun and the development of wave disturbances in the auroral atmosphere: a significant correlation between the impairment of the patients' health and the increase in the variations of the R and AE indexes was observed virtually without time delay. A correlation with the increase in the ? index in these patients takes place with a delay of ~ 2 days, i.e., at the moment of the beginning of the increase in the geomagnetic activity in Moscow.

For finding-out of the answer to a question on the reason of observable functional shifts it is reversible to the analysis of indicators of catecholamins of blood during the various periods heliogeomagnetic disturbances. "Stress hormones" — catecholamins directly or indirectly influence on activation of curtailing system, increase of aggregation of cellular elements and vasospasm of microvasculature.The viewing of changes of catecholamins in a blood of the healthy people has revealed detrusions of investigated parameters in periods of heliogeomagnetic paroxysms in comparison with quiet days (Fig. 2). Consideration of behaviour catecholamins of blood has shown, that at healthy people during of disturbances level NA authentically raises 2 days prior to a storm, remains raised in a storm and again raises on a phase of restoration of a storm (in 2 days after a storm). Also adrenaline level similarly behaves. At the same time concentration DA 2 days prior to a storm and in a storm falls, and in 2 days after a storm grows more than in 2 times.

At patients with chronic cerebrovascularic pathology NA concentration grows during of geomagnetic paroxysms. Greatest increase passes at the moment of a storm and 2 days prior to it, the raised level is marked in 2 days after a storm also. The average indicator of level of adrenaline of blood in the disturbance conditions at patients also authentically increases 2 days prior to a storm and at the moment of a storm. DA concentration of blood plasmas in quiet days was low: 2.7 pg/ml. During the heliogeophysical disturbances it increases, especially at the moment of a storm to 23.5 pg/ml ($p < 0.05$).

Liberated catecholamins promote maintenance of an adequate homeostasis, including influence on rheological and curtailing properties of blood. They influence on activity of formation ?? ?? on ?? by erythrocytes of blood, and their deformation properties. There is a direct communication

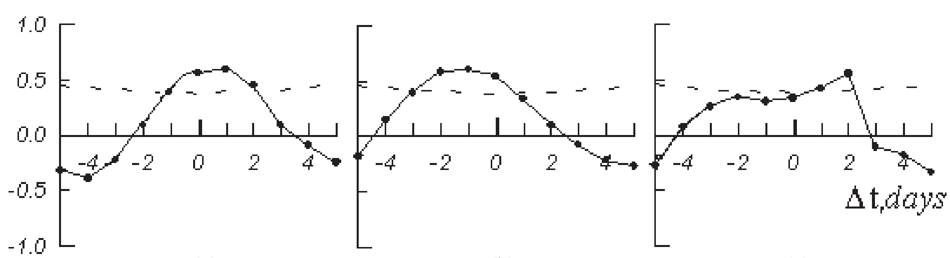

(a) (b) (c)

Figure 1: Correlation coefficients between the time series of the daily numbers of hospitalized patients and (a) the R index, (b) the AE index, and (c) the ? index. The dashed lines present the significance levels of the correlation coefficients. The abscissa is the time before and after a magnetic storm.

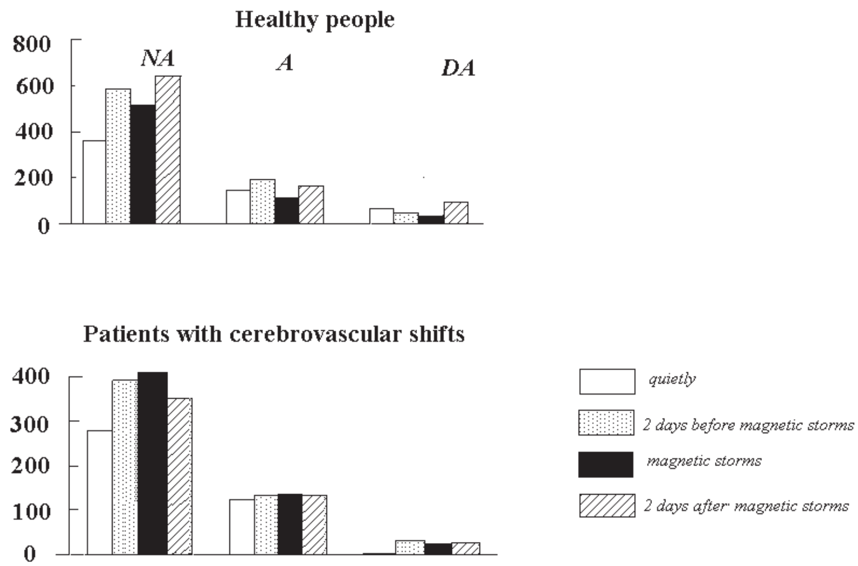

Figure 2: Dynamics of changes of concentrations of catecholamins of a blood plasma at the healthy people and patients at various times of heliogeophysical activity.

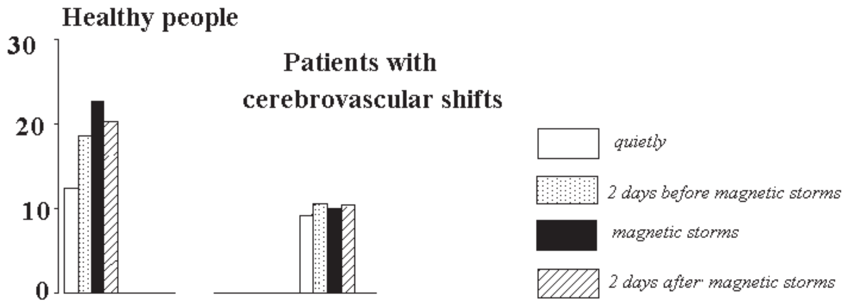

Figure 3: Dynamics of changes of concentrations of erythrocytes aggregation of a blood at the healthy people and patients at various times of heliogeophysical activity.

between deformation properties of erythrocytes and level noradrenalin of blood. It is necessary to assume, that regular influence of storms on an organism which is accompanied by noradrenalin and adrenalin emission, can become one of risk factors at this category of patients.

The analysis of dynamics of changes of values of erythrocytes aggregation at healthy men has been carried out (Fig. 3) which has revealed essential shifts of a studied indicator in days heliogeophysical disturbances. In quiet days indicator erythrocytes aggregation did not overstep the bounds of normal fluctuations, 12.4 ± 2.4 %, but 2 days prior to a storm, at the moment of a storm and after it its growth is noted. Maximum increase erythrocytes aggregation in 1.6 times was observed at the moment of a storm, in these cases considerable excess of the top parametre of norm of erythrocytes aggregation is accompanied by double increase in a root-mean-square deviation (19.1 in comparison with 8.1). It specifies in increase of intraordinary individual variability of functional activity of blood cells at healthy people in conditions of heliogeophysical disturbances.

A little bit other picture of aggregative activity of erythrocytes has been found out in patients with cerebrovascular desease. It has appeared, that at the given category of patients in quiet days average erythrocytes aggregation below control values ($7.8 \pm 1.6\%$). The same is noted and at the moment of a storm. But the tendency to increase erythrocytes aggregation during disturbances (before, during and after disturbances) also is noted at them.

Thus, at healthy men and at patients with cerebrovascular shifts at the age of 40–64 years in conditions heliogeophysical indignations are observed growth of number of cases with raised erythrocytes aggregation, though and with different amplitude.

Let's notice, that deformative properties erythrocytes at healthy faces essentially did not change at various heliogeophysical conditions and have made accordingly: percent of filtration $97 \pm 0.2\%$, time of filtration 79 ± 1.0 sec. At patients with cerebrovascular shifts in quiet days average values of indicators of erythrocytes deformability did not differ from norm. During the period heliogeophysical paroxysms at patients deformative properties of erythrocytes worsen. So percent of filtration at the moment of a storm has decreased to $90.8\% \pm 3,4$ ($p < 0.02$), and time of filtration has increased to $97.2\,\mathrm{sec} \pm 5.5$ ($p < 0.01$).

4. DISCUSSION

From spent above the analysis it is visible, that the majority of considered characteristics starts to change already before the beginning of a magnetic storm. Changes of concentration neurotransmitters and erythrocytes aggregation in the blood, connected with strengthening heliogeophysical activity, allow to assume, that in these conditions physical factors which are connected with processes in system the Sun — the Earth operate on a human organism. The above described physiological shifts occur prior to the beginning actually magnetic storm. Thus it is obvious, that at initial stages of storms changes of amplitude of a geomagnetic field don't operate on an organism. It has to be the other physical factors. It is possible to assume, that the stochastic resonance can be such physical mechanism.

The exterior oscillations can synchronize or desynchronize rhythms of humoral systems of a human organism. The development of the resonant phenomena probably may lead a stress reaction with activation sympathoadrenal system, that can result in increased aggregation of cell elements of a blood and increased of intensity of processes hemocoagulation.

From all spectrum of an electromagnetic field on a surface of the Earth, the biologically effective factor is in that frequency rang, where a level of a field is greatest, and the differences of its intensity from quiet conditions to disturbances are great enough. To such requirements satisfies a range of superlow frequencies, in which low-frequency "transparency window" of an ionosphere is situated. The electromagnetic waves with such frequencies freely reach the Earth, and the intensity of this low-frequency radiation increases 10–100-fold during disturbances [4, 5].

In a low-frequency range, beside for micropulsations generated by processes in a magnetosphere of the Earth, and Shuman resonances, in a region of the Earth — the ionosphere is formed the resonator for Alfven waves. The resonancet structure of a spectrum of an atmospheric noise phon is regularly apparent feature of background electromagnetic noise within the frequency range 0.1–10 Htz. The Alfen's ionospheric resonancet structure of a spectrum is the fundamental characteristic of an electromagnetic field in a region of the Earth — ionosphere. The parameters of resonancet structure are controlled by a structure and degree of disturbance of an ionosphere in a point of observation. Good quality of the resonator is great at initial stages of disturbance and during a regenerative phase of a storm. This fact explains the raised concentration of catecholamins at healthy people already before a storm and after a storm. Neurotransmitters, activating curtailing system of blood, increase agregative effect of erythrocytes.

5. CONCLUSION

Results of the carried out research allow to assume, that, apparently, one of leading mechanisms of influence of variations of near the Earth electromagnetic field, capable to influence haemocirculation of the person are both direct influences, and indirect (in particular, through catecholamins). It is obvious, that ambiguity of reaction of complex nonlinear systems what the human organism is, on weak external electromagnetic influences depends not only on properties of the influencing factor, but also from a state of the system. Practically healthy and sick organisms differently react on external stress-factors. Conditions during disturbances are much heavier even for a healthy organism: in the indisturbed conditions protection of cellular membranes and many other things is required for its normal functioning. The organism makes active the reserve mechanisms of adaptation to new conditions. The sick organism do not be able to managee with this problem of adaptation as its reserve possibilities are exhausted. Therefore the condition of a sick organism during storms is characterised by oppression cellular immunity.

REFERENCES

1. Komarov, F. I., T. K. Breus, S. I. Rapoport, V. N. Oraevskii, Yu. L. Gurfinkel, F. Halberg, G. Cornelissen, and S. I. Chibisov, "Medicobiological effects of solar activity," *Vestn. Ross. Akad. Med. Nauk*, No. 11, 37–49, 1994.
2. Ionova, V. G., E. A. Sazanova, and N. P. Sergeenko, "Influence of heliogeophysical disturbances on the haemorheological characteristics of the people," *Aerospace and Ecological Medicine*, Vol. 38, No. 2, 33–37, 2004, in Russian.

3. Baluda, V. P., M. V. Baluda, I. I. Deyanov, and I. K. Tlepshukov, "Fiziologiya sistemy gomeostaza," *Physiology of Homeostasis System*, 243, Moscow, 1995.
4. Akasofu, S.-I. and S. Chapman, *Solar-Terrestrial Physics: An Account of the Wave and Particle Radiations from the Quiet and the Active Sun, and of the Consequent Terrestrial Phenomena*, 509, Oxford, Clarendon, 1972.
5. Rodionov, Y. Y., A. A. Yaknovets, A. A. Naumenko, and V. I. Shebeko, "Electromagnetic fields in hemodynamics physical mechanisms of interrelationship," *Proceeding of the 2 international conference on Problems of Electromagnetic Safety of the Human Being. Fundamental and Applied Research*, 40–41, Moscow, 1999.

Overview of Methods for Magnetic Susceptibility Measurement

P. Marcon and K. Ostanina
Department of Theoretical and Experimental Electrical Engineering
Brno University of Technology, Kolejni 2906/4, 612 00 Brno, Czech Republic

Abstract— In this paper, an overview of methods for magnetic susceptibility measurement is described. Older methods — Faraday's scale and Guoy's scale are based on force effects of magnetic filed to magnetized specimen. Another methods — Inductive methods, use change of coil inductance, when magnetically conductive specimen is embedded. Modern methods (SQUID magnetometer) benefits from quantum interference device, allowing such sensitive magnetic measurement, that magnetic quantum can be detected. Magnetic resonance is another modern way, how to measure susceptibility and some of MR based methods were introduced. The authors of this article mainly focus on the measurement of magnetic susceptibility of non-ferromagnetic material by means of MRI methods. In this respect, three basic measurement techniques are known and covered in this article.

1. INTRODUCTION

Magnetic susceptibility is the physical quantity describing material properties in the external magnetic field [1]. Magnetic susceptibility is defined as ratio between magnetization $\mathbf{M}$ of the material in the magnetic field and the field intensity $\mathbf{H}$:

$$\mathbf{M} = \chi_{\mathrm{m}} \mathbf{H}. \tag{1}$$

All materials can be classified by value of magnetic susceptibility into three groups:

- diamagnetic materials: $-1 < \chi_{\mathrm{m}} < 0$,
- paramagnetic materials: $0 < \chi_{\mathrm{m}} \ll 1$,
- ferromagnetic materials: $\chi_{\mathrm{m}} \gg 1$.

Several methods are used for magnetic susceptibility measuring such as Faraday's scale, Guoy's scale or inductive method with SQUID magnetometer. For detailed description of these methods see [2]. The MR based method for susceptibility measurement makes also this measurement possible [3, 4].

2. FARADAY'S SCALE

The Faraday's scale (Fig. 1(a)) is suitable for susceptibility measurement of a small specimen made from paramagnetic, diamagnetic or even ferromagnetic materials. When inserting the specimen of volume V with total magnetic moment

$$\mathbf{M}_{\mathrm{C}} = \mathbf{M} \cdot V \tag{2}$$

into magnetic field, energy change occurs

$$E = -\frac{1}{2}\mu_0 \mathbf{M}_{\mathrm{C}}\mathbf{H}. \tag{3}$$

Force acting on the sample in magnetic field with gradient in direction x is [5]

$$F = -\frac{dE}{dx} = \frac{1}{2}\mu_0 V \frac{\mathrm{d}\left(\mathbf{M}_{\mathrm{C}}\mathbf{H}\right)}{\mathrm{d}x} = \mu_0 \chi_{\mathrm{m}} V H \frac{\mathrm{d}H}{\mathrm{d}x}, \tag{4}$$

for linear dependence of this force on susceptibility value we need gradient field meeting the condition:

$$H\frac{dH}{dx} = konst. \tag{5}$$

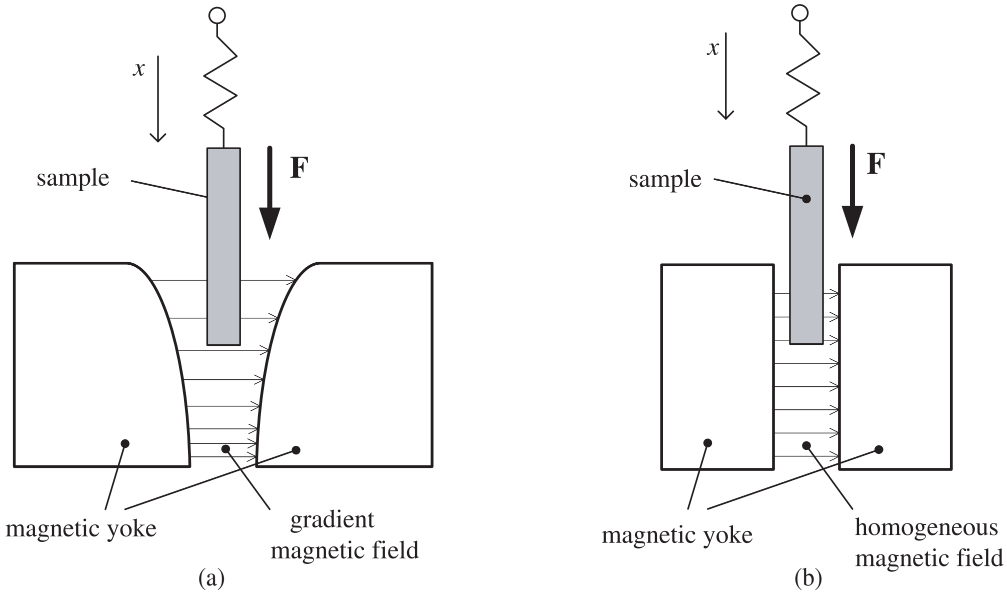

Figure 1: Principle draft of (a) Faraday's scale and (b) Gouy's scale used for susceptibility measurement.

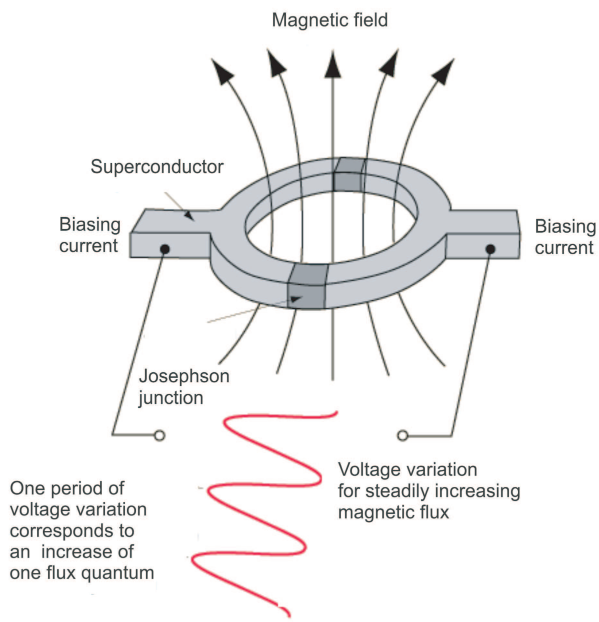

Figure 2: Principle of SQUID magnetometer.

3. GUOY'S SCALE

This scale uses slightly modified principle compared to Faraday's scale. Homogenous magnetic field is used instead of the gradient one (Fig. 1(b)). Axial force acting on the sample in magnetic field is

$$F = \frac{1}{2}\mu_0 \chi_\mathrm{m} S \left(H_1^2 - H_2^2\right), \tag{6}$$

where S is cross-section of sample in x direction and H_1, H_2 are magnetic field intensities in inner and outer end of the sample. The achieved sensitivity of magnetic susceptibility measurement is 10^{-9} with accuracy of 1%.

4. INDUCTIVE METHOD

Induction method is based on change of coil inductance invoked by embedded specimen. Unbalanced bridge of two identical coils powered by stable harmonic current generator is used, where one coil has reference yoke and specimen is inserted into the second one. This kind of susceptibility evaluation methods is obviously used in geology measurement.

5. SQUID MAGNETOMETER

The superconducting quantum interference device (SQUID) can be used as an extremely sensitive detector of magnetic flux. It consists of two parallel Josephson junctions — Fig. 2. The great sensitivity of the SQUID devices is associated with measuring changes in magnetic field related to one flux quantum

$$\Phi_0 = \frac{h}{2e} = 2,068 \cdot 10^{-15}\,(\mathrm{T} \cdot \mathrm{m}^2). \tag{7}$$

If a constant biasing current is maintained in DC SQUID, the measured voltage oscillates with change in the magnetic flux. Counting the oscillations allows evaluating the flux change which has occurred. Because of the necessary superconductive state, this device works only at low temperatures (4.2 K, liquid helium).

6. MR METHOD

The authors of this article mainly focus on the measurement of magnetic susceptibility of non-ferromagnetic material by means of MRI methods [1]. In this respect, three basic measurement techniques are known. The first was described by Wang [6], who characterized an MRI susceptibility measurement method which utilizes a resonant frequency discontinuity at the interface between two materials, each having an observable MR signal. The susceptibility difference between the two materials can be obtained using the data acquired from the vicinity of the interface without knowing all details of the geometry of a sample.

The second method of magnetic susceptibility measurement in samples either assumes a uniform susceptibility distribution or further requires a well-defined geometric shape [7, 8]. A voxel-based inversion requiring a sufficient number of measurement points was proposed [9, 10]. However, the inversion is computationally intensive and no experimental work applying this technique has been published to date. The numerical difficulty may be sidestepped by recasting the inverse problem as an iterative model fitting problem, but such a solution underestimates the susceptibility by 50%. The magnetic field map interpolation as a means for image correction is also utilized by Sumanaweera [11]. The inverse problem is further complicated by the nonuniform noise in the field measurement and by the high phase noise in regions with strong susceptibility due to signal voids caused by T_2^* effects. Another disadvantage of this method consists in the necessity to have a sufficiently large number of measured points. Here, it is important to note that these techniques are based on the knowledge of the map of magnetic field inside a sample (thus, the sample must be magnetically compatible).

The third (and a very interesting) approach to magnetic susceptibility measurement was described in [1, 2]. In these papers, the authors inquire into the calculation of magnetic susceptibility. A sample of a weakly magnetic material embedded in a magnetic field causes a distortion of the static magnetic field. The susceptibility of a sample material can be computed from the shape of this reaction field in the vicinity of the sample. In contrast to the method described above, in this way it is possible to measure materials which do not provide any MR signal. In [1], an analytical calculation of the reaction field is derived using a numerical model and the method of boundary elements. The susceptibility of a sample is calculated from this reaction field. The calculation of magnetic susceptibility is limited to the infinitely large plane of a sample.

6.1. Magnetic Susceptibility Measurement from 3D Map of Reaction Field

This method of susceptibility measurement is based on the assumption of constant magnetic flux in the working space of superconducting magnet. Inserting a specimen with magnetic susceptibility χ_s causes local deformation of previously homogeneous magnetic field — for illustration see Fig. 3.

The magnitude of these deformations depends on the difference of magnetic susceptibility of the specimen χ_s and of its vicinity χ_v, on the volume and shape of the specimen, and on the magnitude of basic field B_0.

Let there be a static magnetic field described by B_0, both in the z direction. Assume that a cylindrical specimen of diameter d and length l ($l_\mathrm{s} \gg d$) is inserted into the magnetic field, parallel to the direction of B_0. The behaviour of magnetic induction $B_\mathrm{z}(x)$ in the position $y = 0$ and $z = 0$ on a straight line is shown in Fig. 3. The difference between the change in the magnetic field in the specimen vicinity and the value of static magnetic field B_0 is called the reaction field ΔB.

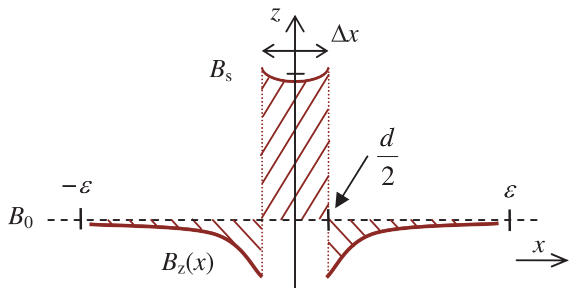

Figure 3: Idealized shape of magnetic flux density $Bz(x)$ in paramagnetic specimen and its vicinity.

As can be seen, the specimen affects the field not only in its volume but also in its vicinity. Magnetic flux density inside the specimen will, according to [1], be equal to:

$$B_{\mathrm{s}} = B_0\left(1 + \chi_{\mathrm{s}}\right). \tag{8}$$

Assume a constant magnetic flux Φ through the normal area of cross-section S_{z} of the magnet working space [8]:

$$\Phi = \iint_{S_{\mathrm{z}}} B \cdot \mathrm{d}S = \mathrm{const.} \tag{9}$$

from which it is evident that magnetic flux density outside the specimen is changed, resulting in a shape that can be considered the superposition of homogeneous field B_0 and reaction field ΔB.

From Eqs. (8) and (9) we derived the following relations for the calculation of magnetic susceptibility from a 3D map of the reaction field being measured [1]:

$$\chi = -\frac{\iiint_{\Omega} \Delta B_{\mathrm{v}} \mathrm{d}x\mathrm{d}y\mathrm{d}z}{V_{\mathrm{s}} \cdot B_0}, \tag{10}$$

where ΔB_{v} is reaction field in the vicinity of specimen, V_{s} is volume of the specimen and B_0 is a static magnetic field.

7. CONCLUSIONS

The methods of magnetic susceptibility measurement are clearly described in this article. The authors of this articles focus on the magnetic susceptibility measurement from the 3D reaction field. This reaction field was measured by the NMR tomograph. The methods of NMR magnetic susceptibility measurement are more detail in references [1].

ACKNOWLEDGMENT

The work described in the paper was financially supported by the projects GA102/1/0318, CZ.1.05/2.1.00/01.0017 (ED0017/01/01) and FEKT-S-11-5/1012.

REFERENCES

1. Marcon, P., K. Bartusek, M. Budrkova, and Z. Dokoupil, “Magnetic susceptibility measurement using 2D magnetic resonance paging,” *Measurement Science and Technology*, Vol. 22, 2011.
2. Steibauer, M. and K. Bartusek, “Magnetic susceptibility measurement using magnetic resonance tomography,” *Acta Technica ČSAV*, Vol. 53, 2008.
3. Bartusek, K., M. Cap, P. Marcon, and J. Mikulka, “Magnetic susceptibility modelling using ANSYS,” *PIERS Proceedings*, 190–193, Marrakesh, Morocco, March 20–23, 2011.
4. Bartusek, K., Z. Dokoupil, and E. Gescheidtova, “Mapping of magnetic field around small coils using the magnetic resonance method,” *Measurement Science and Technology*, Vol. 18, 2223–2230, 2007.
5. Steinbauer, M. “Magnetic susceptibility measurement by means o MRI technice,” Ph.D. Thesis, Faculty of Electrical Enginering and Communication, Brno University of Technology, Brno, 2005.

6. Wang, Z. J., S. Li, and J. C. Haselgrove, "Magnetic resonance imaging measurement of volume magnetic susceptibility using a boundary condition," *Journal of Magnetic Resonance*, Vol. 140, 477–481, 1999.
7. Tian, L., P. Spincemaille, L. Rochefort, B. Kresssler, and Y. Wang, "Calculation of susceptibility through multiple orientation sambpling (COSMOS): A method for conditioning the inverse problem from measured magnetic field map to susceptibility source image in MRI," *Magnetic Resonance in Medicine*, Vol. 61, 196–204, 2009.
8. Chu, Z., A. R. Cohen, R. Muthupillai, T. Chung, and Z. J. Wang, "MRI measurement of hepatic magnetic susceptibility-phantom validation and normal subject studies," *Magnetic Resonance in Medicine*, Vol. 52, 1318–1327, 2004.
9. Li, L., "Magnetic susceptibility quantification for arbitrarily shaped objects in inhomogeneous fields," *Magnetic Resonance in Medicine*, Vol. 46, 907–916, 2001.
10. Li, L. and J. S. Leigh, "Quantifying arbitrary magnetic susceptibility distributions with MR," *Magnetic Resonance in Medicine*, Vol. 51, 1077–1082, 2004.
11. Sumanaweera, T. S., G. H. Glover, T. O. Binford, and J. R. Adler, "MR susceptibility misregistration correction," *IEEE Transactions on Medical Imaging*, Vol. 12, 251–259, 1993.

Algorithms for Electromagnetic Waves on Interface

R. Kadlec, Z. Roubal, E. Kroutilová, and P. Fiala
Department of Theoretical and Experimental Electrical Engineering
Brno University of Technology, Kolejní 2906/4, Brno 612 00, Czech Republic

Abstract— The paper presents the problem of algorithm design of propagation, reflection and refraction of the electromagnetic waves on a layered medium. The analytic solution of this issue is very intricate and time demanding. This method is suitable for specific purposes of the detailed analysis of the general issue. Numerical methods are more suitable for analysis of the reflection and refraction of electromagnetic waves on layered heterogeneous medium. Fundamental law for analysis of the reflection and the refraction of electromagnetic waves on the boundary line between two materials are Snell's law for electromagnetic waves. In some cases, the form of transfer matrices and wave impedances for perpendicular incidence is same as for oblique incidence. By selection transverse and longitudinal fields with respect to the direction the dielectrics are vertical. We show that the transverse components satisfy the identical transfer matrix relationships as in the case of perpendicular incidence. The paper deals with the problem of complex angle of refraction in the losing medium. In non-lossy environment, interpretation of Fresnel relations and Snell's law is simple. This phenomenon is occur in metamaterial. These materials with negative parameters constitute a group of media that possesses a negative value, relative permittivity or relative permeability or both.

1. INTRODUCTION

Generally, inhomogeneities and regions with different parameters appear even in the cleanest materials. During the electromagnetic wave passage through a material there occur an amplitude decrease and a wave phase shift, owing to the material characteristics such as conductivity, permittivity, or permeability. If a wave impinges on an inhomogeneity, a change of its propagation there occurs. This change materializes in two forms, namely in reflection and refraction. In addition to this process, polarization and interference may appear in the waves.

2. ELECTROMAGNETIC WAVES IN ISOTROPIC DIELECTRICS MATERIALS

Algorithms were generated in the Matlab program environment that simulates reflection and refraction in a lossy environment on the interface between two dielectrics. The reflection and refraction is in accordance with Snell's law for electromagnetic waves as shown in Figures 1 and 2. The form of Snell's law is

$$\frac{\sin\theta_0}{\sin\theta_2} = \frac{k_2}{k_1} = \frac{\sqrt{j\omega\mu_2\cdot(\gamma_2 + j\omega\varepsilon_2)}}{\sqrt{j\omega\mu_1\cdot(\gamma_1 + j\omega\varepsilon_1)}}, \tag{1}$$

where k is the wave number, γ is the conductivity, ε the permittivity and μ the permeability. Relation (1) is defining for the boundary line between the dielectrics medium. Generally, k_1 and k_2 are complex; then angle θ_2 is also complex. An electromagnetic wave is understood as the electric field strength and the magnetic field strength. The electric component and magnetic component incident wave according to Figure 1 follows the formula:

$$\mathbf{E}_i = \mathbf{E}_0 e^{-j\mathbf{k}_1\mathbf{u}_{n0}\cdot\mathbf{r}}, \quad \mathbf{H}_i = \frac{\mathbf{u}_{n0}\times\mathbf{E}_i}{\mathbf{Z}_{v1}} \tag{2}$$

where $\mathbf{E}_0$ is the amplitude electric field strength on the boundary line, $\mathbf{r}$ is the positional vector, and $\mathbf{u}_{n0}$ is the unit vector of propagation direction.

For simplicity, we will analyze separately the $\mathbf{E}$ vector parallel to the interface (also known as TE wave) as shown in Figure 1 and $\mathbf{H}$ vector parallel to the interface (also known as TM wave) as shown in Figure 2. For TE wave and electric intensity of reflection beams and the intensity of refraction beams are expressed according to the formula:

$$\mathbf{E_r} = \mathbf{E}_1 e^{-jk_1\mathbf{u}_{n1}\times\mathbf{r}}, \quad \mathbf{E_t} = \mathbf{E}_2 e^{-jk_2\mathbf{u}_{n2}\times\mathbf{r}}, \tag{3}$$

where $\mathbf{E}_1$ is calculated from the intensity on boundary line $\mathbf{E}_0$ and reflection coefficient ρ_E, and $\mathbf{E}_2$ is calculated from the intensity on boundary line $\mathbf{E}_0$ and transmission factor τ_E:

$$\mathbf{E}_1 = \rho_E\cdot\mathbf{E}_0, \quad \mathbf{E}_2 = \tau_E\cdot\mathbf{E}_0, \tag{4}$$

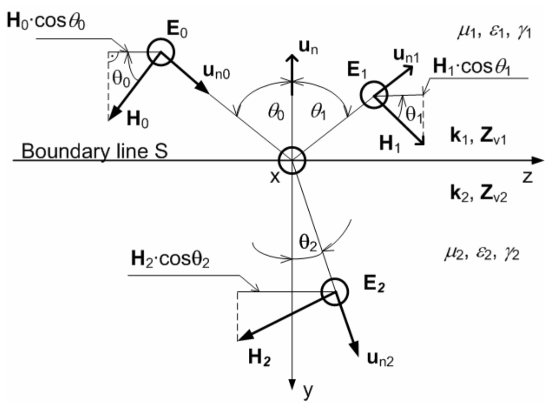

Figure 1: Reflection and refraction of TE wave [1].

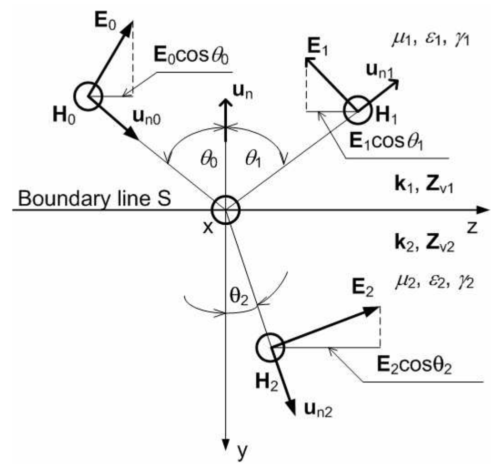

Figure 2: Reflection and refraction of TM wave [1].

magnetic component is calculated from electric component and wave impedance:

$$\mathbf{H}_0 = \frac{\mathbf{E}_0}{\mathbf{Z}_{v1}}, \quad \mathbf{H}_1 = \frac{\mathbf{E}_1}{\mathbf{Z}_{v1}}, \quad \mathbf{H}_2 = \frac{\mathbf{E}_2}{\mathbf{Z}_{v2}}. \tag{5}$$

The calculation of reflection coefficient ρ_E and transmission factor τ_E with utilization of wave impedance Z_v is according to these relations:

$$\rho_E = \frac{\mathbf{E}_1}{\mathbf{E}_0} = \frac{Z_{v2}\cos\theta_1 - Z_{v1}\cos\theta_2}{Z_{v2}\cos\theta_1 + Z_{v1}\cos\theta_2}, \quad \tau_E = \frac{\mathbf{E}_2}{\mathbf{E}_0} = \frac{2Z_{v2}\cos\theta_1}{Z_{v2}\cos\theta_1 + Z_{v1}\cos\theta_2}. \tag{6}$$

For numerical modelling, there is a suitable relation in the form of

$$\begin{aligned} \mathbf{E_r} &= \frac{\mu_2 k_1\cos\theta_0 - \mu_1\sqrt{k_2^2 - k_1^2\sin^2\theta_0}}{\mu_2 k_1\cos\theta_0 + \mu_1\sqrt{k_2^2 - k_1^2\sin^2\theta_0}}\mathbf{E}_0 \cdot e^{-jk_1\mathbf{u_{n1}}\times\mathbf{r}}, \\ \mathbf{E_t} &= \frac{2\mu_2 k_1\cos\theta_0}{\mu_2 k_1\cos\theta_0 + \mu_1\sqrt{k_2^2 - k_1^2\sin^2\theta_0}}\mathbf{E}_0 \cdot e^{-jk_2\mathbf{u_{n2}}\times\mathbf{r}}. \end{aligned} \tag{7}$$

These relations are calculated from the basic variable and they facilitate an acceleration of the calculation process. Relationships for calculating the magnetic components usually express by the relationship (2). Using the basic variables we obtain these formulas:

$$\begin{aligned} \mathbf{H}_r &= \frac{\mathbf{u}_{n1} \times \frac{\mu_2\mathbf{k}_1\cos\theta_0 - \mu_1\sqrt{\mathbf{k}_2^2 - \mathbf{k}_1^2\sin^2\theta_0}}{\mu_2\mathbf{k}_1\cos\theta_0 + \mu_1\sqrt{\mathbf{k}_2^2 - \mathbf{k}_1^2\sin^2\theta_0}}\mathbf{E}_0 \cdot e^{-j\mathbf{k}_1\mathbf{u}_{n1}\cdot\mathbf{r}}}{\frac{\omega\mu_1}{\mathbf{k}_1}} \\ \mathbf{H}_t &= \frac{\mathbf{u}_{n2} \times \frac{2\mu_2\mathbf{k}_1\cos\theta_0}{\mu_2\mathbf{k}_1\cos\theta_0 + \mu_1\sqrt{\mathbf{k}_2^2 - \mathbf{k}_1^2\sin^2\theta_0}}\mathbf{E}_0 \cdot e^{-j\mathbf{k}_2\mathbf{u}_{n2}\cdot\mathbf{r}}}{\frac{\omega\mu_2}{\mathbf{k}_2}} \end{aligned} \tag{8}$$

These relations are intricate, and therefore it is better to use atypical formulas expressed by the relationship (10):

$$\begin{aligned} \mathbf{H}_r &= -\frac{\frac{\mu_2}{\mu_1}\mathbf{k}_1\cos\theta_0 - \sqrt{\mathbf{k}_2^2 - \mathbf{k}_1^2\sin^2\theta_0}}{\mu_2\cos\theta_0 + \frac{\mu_1}{\mathbf{k}_1}\sqrt{\mathbf{k}_2^2 - \mathbf{k}_1^2\sin^2\theta_0}}\frac{\mathbf{E}_0}{\omega} \cdot e^{-j\mathbf{k}_1\mathbf{u}_{n1}\cdot\mathbf{r}} \\ \mathbf{H}_t &= -\frac{2\mathbf{k}_2\cos\theta_0}{\mu_2\cos\theta_0 + \frac{\mu_1}{\mathbf{k}_1}\sqrt{\mathbf{k}_2^2 - \mathbf{k}_1^2\sin^2\theta_0}}\frac{\mathbf{E}_0}{\omega} \cdot e^{-j\mathbf{k}_2\mathbf{u}_{n2}\cdot\mathbf{r}} \end{aligned} \tag{9}$$

Sometimes it is easier to deduce the magnetic component from the electrical component, according to these formulas:

$$\mathbf{H}_r = \frac{\mathbf{u}_{n1} \times \mathbf{E}_r}{\mathbf{Z}_{v1}}, \quad \mathbf{H}_t = \frac{\mathbf{u}_{n2} \times \mathbf{E}_t}{\mathbf{Z}_{v2}}. \tag{10}$$

Situation of incident of TM wave is shown in Figure 2. For TM wave and magnetic intensity of reflection beams and the intensity of refraction beams are expressed according to the formula:

$$\mathbf{H}_r = -\mathbf{H}_1 e^{-j\mathbf{k}_1 \mathbf{u}_{n1} \cdot \mathbf{r}}, \quad \mathbf{H}_t = -\mathbf{H}_2 e^{-j\mathbf{k}_2 \mathbf{u}_{n2} \cdot \mathbf{r}} \tag{11}$$

where $\mathbf{H}_1$ is calculated from the intensity on boundary line $\mathbf{H}_0$ and reflection coefficient ρ_H, and $\mathbf{H}_2$ is calculated from the intensity on boundary line $\mathbf{H}_0$ and transmission factor τ_H:

$$\mathbf{H}_1 = \rho_H \mathbf{H}_0, \quad \mathbf{H}_2 = \tau_H \mathbf{H}_0. \tag{12}$$

The calculation of reflection coefficient ρ_H and transmission factor τ_H with utilization of wave impedance Z_v is according to these formulas:

$$\rho_H = \frac{\mathbf{H}_1}{\mathbf{H}_0} = \frac{\mathbf{Z}_{v2}\cos\theta_2 - \mathbf{Z}_{v1}\cos\theta_1}{\mathbf{Z}_{v2}\cos\theta_2 + \mathbf{Z}_{v1}\cos\theta_1}, \quad \tau_H = \frac{\mathbf{H}_2}{\mathbf{H}_0} = \frac{2\mathbf{Z}_{v1}\cos\theta_1}{\mathbf{Z}_{v2}\cos\theta_2 + \mathbf{Z}_{v1}\cos\theta_1} \tag{13}$$

For numerical modelling, there is a suitable relation in the form:

$$\begin{aligned} \mathbf{H}_r &= -\frac{\mu_2 \mathbf{k}_1 \sqrt{\mathbf{k}_2^2 - \mathbf{k}_1^2 \sin\theta_0} - \mu_1 \mathbf{k}_2^2 \cos\theta_0}{\mu_2 \mathbf{k}_1 \sqrt{\mathbf{k}_2^2 - \mathbf{k}_1^2 \sin\theta_0} + \mu_1 \mathbf{k}_2^2 \cos\theta_0} \mathbf{H}_0 \cdot e^{-j\mathbf{k}_1 \mathbf{u}_{n1} \cdot \mathbf{r}} \\ \mathbf{H}_t &= -\frac{2\mu_1 \cos\theta_0}{\mu_2 \mathbf{k}_1 \sqrt{\mathbf{k}_2^2 - \mathbf{k}_1^2 \sin\theta_0} + \mu_1 \mathbf{k}_2^2 \cos\theta_0} \mathbf{E}_0 \cdot e^{-j\mathbf{k}_2 \mathbf{u}_{n2} \cdot \mathbf{r}} \end{aligned} \tag{14}$$

These relations are calculated from the basic variable and they facilitate an acceleration of the calculation process. Relationships for calculating the electric components from magnetic components are according to these relations:

$$\mathbf{E}_r = \mathbf{Z}_{v1} \left(\mathbf{H}_r \times \mathbf{u}_{n1} \right), \quad \mathbf{E}_t = \mathbf{Z}_{v2} \left(\mathbf{H}_t \times \mathbf{u}_{n2} \right) \tag{15}$$

Relationships for calculating the electric components of TM wave from basic variables we can expressed as in the relationship (8) and (9), and therefore it is easier to deduce the magnetic components from the electrical components.

Interpretation of the Fresnel equations and Snell's laws is simple in the case of the refraction on boundary line between the dielectrics medium. In case of refraction in a lossy medium, angle θ_2 is complex. According to relation (1), angle θ_2 depends on wave numbers k_1 a k_2, which are generally complex; then, in medium 2 an inhomogeneous wave is propagated.

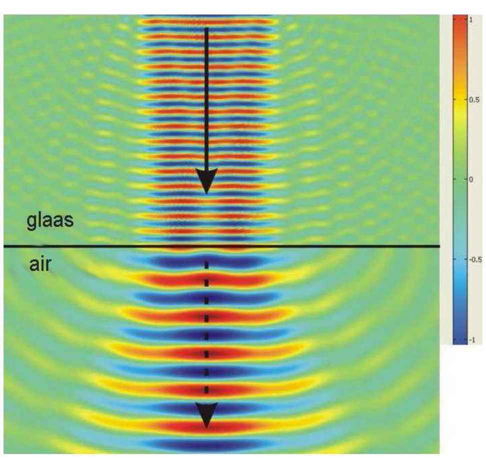

Figure 3: Reflection and refraction on a planar boundary line [2].

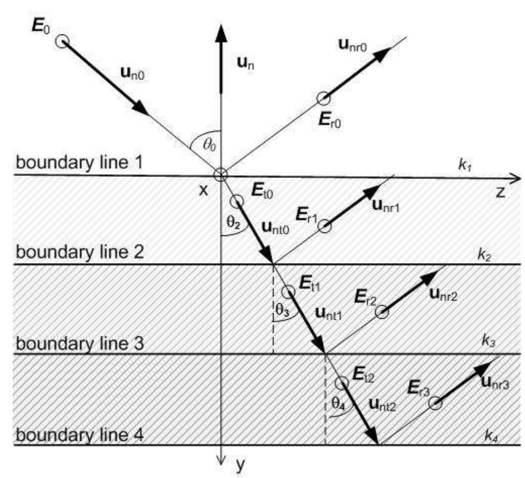

Figure 4: Reflection and refraction on a layered heterogenous material.

Example of reflection and refraction on a planar boundary line in COMSOL program is shown in Figure 3 (at perpendicular incidence of the wave on the interface).

For a layered heterogeneous medium, an algorithm is deduced for the reflection on several layers, according to Figure 4. The interpretation of propagation of electromagnetic waves on a layered heterogeneous medium is according to relation:

$$\mathbf{E_{rl}} = \mathbf{E_{il}}\rho_{E\lambda} \cdot e^{-jk_l \mathbf{u_{nrl}} \times \mathbf{r_l}}, \quad \mathbf{E_{tl}} = \mathbf{E_{il}}\tau_{E\lambda} \cdot e^{-jk_l \mathbf{u_{ntl}} \times \mathbf{r_l}}, \tag{16}$$

where $\mathbf{E}_{rl}$ a $\mathbf{E}_{tl}$ are the reflection and refraction electromagnetic waves on the boundary line ($l = 1, \ldots, \max$) according to Figure 4, $\mathbf{E}_{il}$ is the amplitude electric field strength on boundary line l, ρ_{El} a τ_{El} are the reflection coefficient and transmission factor on boundary line l, k_l is the wave number of layer, $\mathbf{r}_l$ is the electromagnetic wave positional vector on boundary line l, $\mathbf{u}_{ntl}$ and $\mathbf{u}_{nrl}$ are the unit vectors of propagation direction.

3. CONCLUSIONS

The paper includes a theoretical analysis and references to the generated algorithms, which are verified using numerical models. For simple cases (such as a planar interface), the behavior of an impinging wave can be calculated analytically by the help of Snell's refraction/reflection law and the Fresnel equations, which are fundamental law for analysis of the reflection and the refraction of electromagnetic waves on boundary line between two materials.

Analytic solution of propagation, reflection and refraction of wideband electromagnetic signals on field of multilayer optical materials in Matlab program is very time demanding. This method is suitable for specific purposes of detail analysis of general issue. Therefore, numerical methods are applied to facilitate the calculation process, and a wide range of programs like ANSYS, Comsol, or Matlab can be utilized in the realization of numerical modelling. Algorithms created in the Matlab environment are verified by the help of programs based on the finite element method, namely programs such as Comsol and ANSYS.

Methods describe in this paper are suitable for analysis of beam refraction to the other side from the perpendicular line during the passage through the interface. This phenomenon is occur in metamaterials.

ACKNOWLEDGMENT

The research described in the paper was financially supported by the research program MSM 0021630516 and research plan MSM 0021630513, Ministry of Defence of the CR, Ministry of Industry and Trade of the CR (Diagnostics of Superfast Objects for Safety Testing, FR-TI1/368), Czech Science Foundation (102/09/0314) and project of the BUT Grant Agency FEKT-S-11-5.

REFERENCES

1. Dedek, L. and J. Dedková, *Elektromagnetismus*, Vol. 2, 232, VITIUM, Brno, 2000, ISBN 80-214-1548-7.
2. Nešpor, D., "Electromagnetic wave propagation study in heterogeneous structures," Ph.D. Thesis, 20, Supervisor Doc. Ing. Pavel Fiala, 2009.
3. Fiala, P., "Finite element method analysis of a magnetic field inside a microwave pulsed generator," *2nd European Symposium on Non-Lethal Weapons*, Ettlingen, SRN, May 13–15, 2003.
4. Fiala, P., R. Kadlec, P. Drexler, and P. Dohnal, "Tuned periodical structures — Model, experiments in THz band applied in safety application," *PIERS Proceedings*, 1022–1026, Cambridge, USA, July 5–8, 2010.
5. Orfanidis, S., *Electromagnetic Waves and Antennas*, 1031, 2008. Available from WWW: ⟨www.ece.rutgers.edu/∼ orfanidi/ewa⟩.

Comparison of Segmentation Methods in MR Image Processing

J. Mikulka[1], **E. Gescheidtová**[1], **K. Bartušek**[2], **and D. Nešpor**[1]

[1]Department of Theoretical and Experimental Electrical Engineering
Brno University of Technology, Czech Republic
[2]Institute of Scientific Instruments
Academy of Sciences of the Czech Republic, Czech Republic

Abstract— Image processing in biomedical applications is strongly developing issue. There were described many methods and approaches for image preprocessing, segmentation and visualization. It is necessary to choose suitable segmentation method to create a correct three-dimensional model. The accuracy of reconstruction depends on precision of regions boundary determining in MR slices. The very often application is sensing of soft tissues. To imaging mentioned soft tissues is usually used tomography by magnetic resonance. Ideally, several tissue slices in three orthogonal planes (sagittal, coronal, transverse) are acquired. With slices in three planes is following reconstruction of shape of examined tissues most accurate. In case of acquired slices only in one plane the high spatial information lost occurs by image acquisition. Then it is necessary the shape of tissue appropriately reconstruct. At first the images are segmented and with use of particular segments the three dimensional model is composed. This article compares several segmentation approaches of MR images and their results. The results of segmentation by active contour, thresholding, edge analysis by Sobel mask, and watershed segmentation methods are compared. The results for different values of parameters of segmentation methods are compared. As the test image was chosen MR slice of human liver tumour.

1. INTRODUCTION

Image processing in biomedical applications is strongly developing issue. There were described many methods and approaches for image preprocessing, segmentation and visualizing. In many cases it is useful to evaluate volume of examined objects and monitor its development in time. Typical example of examined object are tumors in human organs and monitoring their development depending on time and efficiency of treatment. To imaging mentioned soft tissues is usually used tomography by magnetic resonance. It is necessary the shape of tissue appropriately reconstruct. At first the images are segmented and with use of particular segments the three dimensional model is composed. The reconstructed model has step-surface. There are several methods for smoothing the shape. In this article the methodology for shape smoothing are discussed. The results of volumetry with use of several smoothing levels are compared. Impact of shape smoothing to quality of reconstruction is discussed. It is shown that high level of smoothing suppress the step-surface but the edge information is lost. Conversely the low smoothnig level leads to poor reconstruction with visible slicing.

Real medical image processing application is presented in this article. It is focused at human liver tumour segmentation — the problem is in unclosed tumor areas, which should be segmented. The article presents methods which allows processing (noise suppression/segmentation) of noisy low contrast signals in 1D and even 2D signal processing.

2. MATHEMATICAL MODELS

The mentioned level set methods known as active contours are based on partial differential equation solution. The deformable model of active contour with initial shape and location in the image and by iterative solution of equation(s) the contour can change own shape, topology and location is defined. In the steady state the active contour bounds the found objects in their real boundaries. The problem of searching the tumour boundaries in the image is in unclosed area of the tumour. The tumours are situated in many cases on the edge of liver, so the boundary of tumour disappears in the image background. The solution is just in use the edge-based level set approach, which can complete the real boundary of tumour, as well.

The edge-based segmentation is described by this energy functional [1]:

$$F(\phi) = \lambda \int_{\Omega} g\delta(\phi) |\nabla \phi| \, \mathrm{d}x\mathrm{d}y + \nu \int_{\Omega} gH(-\phi) \, \mathrm{d}x\mathrm{d}y, \tag{1}$$

where the first term means the length of the zero level curve of Φ (level set distance function) and the second term is called weighted area of Ω_Φ^-. λ and ν are the weighted coefficients of the mentioned terms, $\delta(\phi)$ is the Dirac function and H is the Heaviside function. The g function is the edge indicator defined by

$$g = \frac{1}{1 + |\nabla G_\sigma * I|^2}, \tag{2}$$

where I is the original image and G_σ is the Gaussian kernel with standard deviation σ. By calculus of variation, the first variation of the functional in (2) can be written as

$$\frac{\mathrm{d}\phi}{\mathrm{d}t} = \mu\left[\Delta\phi - \operatorname{div}\left(\frac{\nabla\phi}{|\nabla\phi|}\right)\right] + \lambda\delta(\phi)\operatorname{div}\left(g\frac{\nabla\phi}{|\nabla\phi|}\right) + \upsilon g\delta(\phi). \tag{3}$$

This gradient flow is the evolution equation of the level set function Φ. The second and third term in the Equation (3) correspond to the length and area energy functional. The first term penalizes the deviation of the level set function from a signed distance function during its evolution.

In some cases region-based segmentation approach is better. It means that the image is not segmented with regard to object edges but only with regard to mean region intensities. This segmentation is in general described by

$$F_n(\mathbf{c}, \mathbf{\Phi}) = \sum_{1\le I\le n=2^m} \int_\Omega (u_0(x,y) - c_I)^2 \chi_I \mathrm{d}x\mathrm{d}y + \sum_{1\le i\le m} \nu \int_\Omega |\nabla H(\Phi_i)|, \tag{4}$$

and for the two-phases result the general energy functional (4) is in shape:

$$F(c_1,c_2,\phi) = \int_\Omega (u_0(x,y) - c_1)^2 H(\phi)\, dx\mathrm{d}y + \int_\Omega (u_0(x,y) - c_2)^2 (1 - H(\phi))\mathrm{d}x\mathrm{d}y + \nu\int_\Omega |\nabla H(\phi)|, \tag{5}$$

where the first two terms divide the area Ω of the original image u_0 to two subareas with the mean values of intensity c_1 and c_2. The third term minimizes the length of the resultant contour. It can be used for suppression of noise in the image and the final contour is smoother. This term is weighted by the coefficient ν. H is the Heaviside function. This function recognizes where the level set function φ is positive, respectively negative.

$$\frac{\partial\Phi}{\partial t} = \delta_\varepsilon(\Phi)\left[\nu\operatorname{div}\left(\frac{\nabla\Phi}{|\nabla\Phi|}\right) - (u_0 - c_1)^2 + (u_0 - c_2)^2\right]. \tag{6}$$

This gradient flow is the evolution equation of the level set function Φ. The first term in (6) in the brackets corresponds to the length functional.

Thresholding — the simplest segmentation method is defined as:

$$g(i,j) = \begin{cases} 1 & \text{pro}\, f(i,j) \ge T \\ 0 & \text{pro}\, f(i,j) < T \end{cases}. \tag{7}$$

The biggest disadvantage of this method is that it is very noise sensitive, but it is very often used in medical praxis in manual processing, it's very simple and fast.

Image segmentation based on Sobel mask convolution is defined by convolution kernel:

$$S_x = \begin{pmatrix} 1 & 0 & -1 \\ 2 & 0 & -2 \\ 1 & 0 & -1 \end{pmatrix}, \qquad S_y = \begin{pmatrix} -1 & -2 & -1 \\ 0 & 0 & 0 \\ 1 & 2 & 1 \end{pmatrix}. \tag{8}$$

3. IMPLEMENTATION

The algorithm was implemented in Matlab 7.0. The Equation (3) was approximated by central and forward difference schemes and solved by iterative process. The Dirac function was approximated by:

$$\delta_\varepsilon(x) = \begin{cases} 0, & |x| > \varepsilon \\ \frac{1}{2\varepsilon}\left[1 + \cos\left(\frac{\pi x}{\varepsilon}\right)\right], & |x| \le \varepsilon \end{cases} \tag{9}$$

4. RESULTS, LIVER TUMOR SEGMENTATION

The aim of this work is 3D model creation of tumors in the human liver (Fig. 1). It is useful for diagnosis and decision about the treatment success. In traditional way it consists of many steps of MR image processing — preprocessing the images (noise suppression, contrast and edge enhancement), edge analysis and segmentation, segmented images processing. The goal of the proposed processing method is elimination of needful steps of processing and its simplification. The modern segmentation method was found and tested. The MR slices with visible tumors in human livers were segmented by edge-based level set segmentation method [1, 2]. This level set approach gives very good results in segmentation of noised MR images with low contrast and smooth edges so that it is not necessary to preprocess the image before the segmentation of image. The second step is calculation of the tumour volume from known pixel dimensions. The number of pixels in each bounded tumour will be numbered and multiplied by the slice thickness. We get the resultant volume of tumour by normalizing the number of all tumour subarea pixels with the one pixel dimensions.

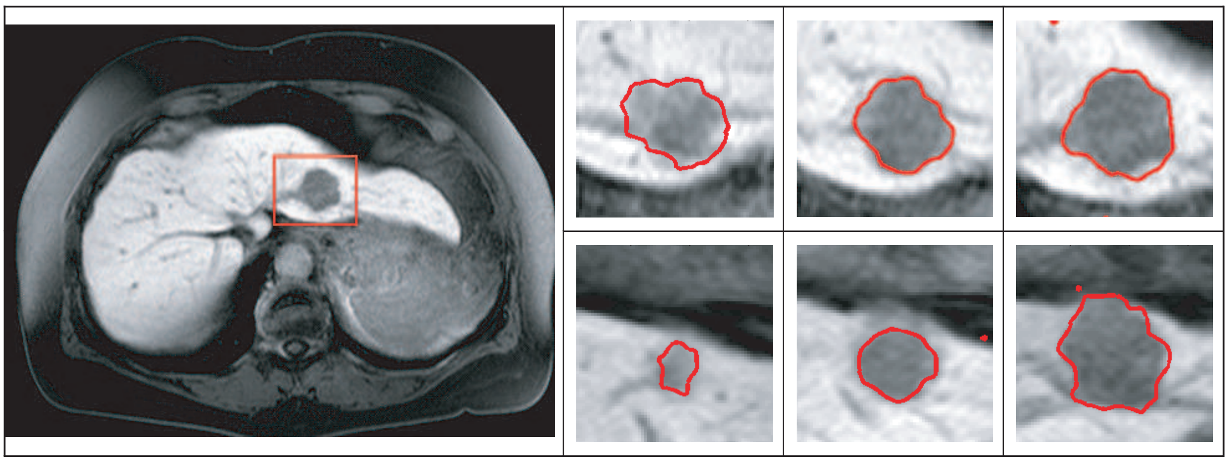

Figure 1: Example of one slice of the human liver, segmentation results of the edge-based level set method, the red contour bounds the liver tumour in 6 chosen slices.

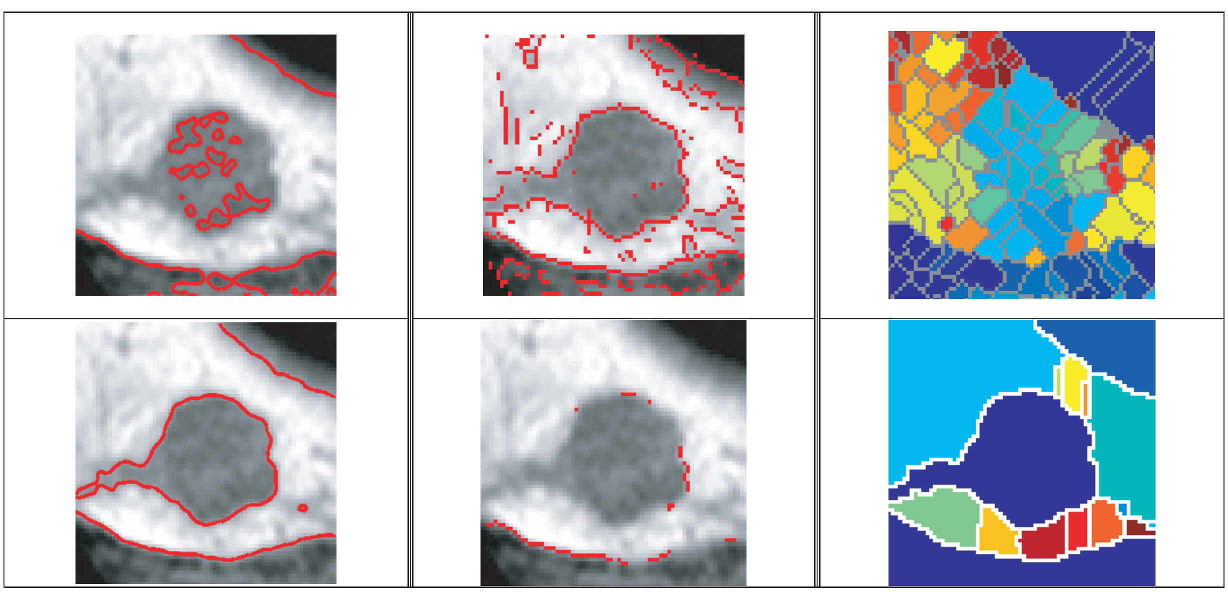

(a) (b) (c)

Figure 2: Segmentation result of the method (a) thresholding (levels 100 and 150), (b) Sobel mask convolution (levels 0.05 and 0.15), (c) watershed (without and after preprocessing).

5. COMPARISON OF RESULTS WITH OTHER METHODS

The images of human livers were selected for compare of results of proposed methods and other commonly used methods for image segmentation (Sobel mask segmentation, thresholding, watershed). In Fig. 2 is shown segmentation results of human liver tumour by thresholding (on the left) with 2 chosen levels (100, 150). It's clear that the result of segmentation depends of chosen level. If the level is low, this method gives noisy results. If the level is higher, some darker regions are incorrectly jointed to segmented area. In the middle of Fig. 2 is shown segmentation results of human liver tumour area processing by edge analysis with use of Sobel mask convolution. There were used two thresh levels to segment the image. It's clear that the results of image convolution by Sobel mask are noised or it gives incomplete edges of segmented object.

The last one tested methods for image segmentation was watershed method. The results of watershed segmentation is shown on the right of Fig. 2. Watershed method gives similar results as simple thresholding. It is important to preprocess the image because of over-segmentation, which is the biggest known disadvantage of watershed segmentation.

6. CONCLUSIONS

The image segmentation methods were mentioned and their results were compared. The proposed image segmentation methods called level set or active contour gives very good results not only in medical application. The main advantage of active contour segmentation methods is low sensitivity to noise and unclosed edges of segmented object. The partially solved disadvantage is that the segmentation is little bit time and computationally demanding.

ACKNOWLEDGMENT

This work was supported within GACR 102/11/0318 and CZ.1.05/2.1.00/01.0017 (ED0017/01/01) and GA FEKT-S-11-5/1012.

REFERENCES

1. Li, C., C. Xu, C. Gui, and M. D. Fox, "Level set evolution without re-initialization: A new variational formulation," *Proceedings of the 2005 IEEE Computer Society Conference on Computer Vision and Pattern Recognition CVPR'05*, IEEE Computer Society, Washington, DC, San Diego, USA, 430–436, 2005, ISBN 0-7695-2372-2.
2. Aubert, G. and P. Kornprobst, *Mathematical Problems in Image Processing: Partial Differential Equations and the Calculus of Variations*, 2nd Edition, Springer Science + Business Media, LLC, New York, 2006, ISBN 0-387-32200-0.
3. Mikulka, J., E. Gescheidtová, and K. Bartušek, "Processing of MR slices of human liver for volumetry," *PIERS Proceedings*, 202–204, Xi'an, China, March 22–26, 2010.

Simulation and Experimental Measurements for Near Field Imaging

S. Adnan[1], **R. A. Abd-Alhameed**[1], **M. Usman**[2], **C. H. See**[1], **J. M. Noras**[1], **and M. B. Child**[1]

[1]Mobile and Satellite Communications Research Centre
University of Bradford, Bradford, UK
[2]Department of Electrical Engineering, University of Hai'l, KSA

Abstract— Near field imaging using microwaves in medical applications has gained much attention recently as various researchers have shown its capability and accuracy in identifying features of interest compared to better known screening tools. This paper documents the development of system primarily for microwave imaging applications such as breast cancer detection. When the performance of the prototype is tested and analyzed experimentally it exhibits reasonable agreement with simulations.

1. INTRODUCTION

Breast cancer is the most common non-skin related malignancy and the second leading cause of cancer death among women in the world every year thousands of women die from the disease [1, 2]. Until research uncovers a way to prevent breast cancer, early detection will be the best hope for reducing mortality from this disease. X-ray mammography has proved to be a most effective tool and plays an important role in early breast cancer detection, but despite providing a high percentage of successful detection compare to other screening tools, X-ray mammography has limitations. The uncomfortable breast compression associated with this diagnosis method mitigates against patients undergoing early stage examination and both false positive and negative rates have been reported [2, 3] which suggests a need for alternative screening. Exposure to ionizing radiation from X-rays is also a concern.

These factors have motivated a search for a better solution and one possibility under investigation is microwave imaging, a technology whose applications for diagnostic purposes in the field of biomedical engineering are increasing. Based on variation in dielectric properties, this technique promises non-destructive evaluation of biological tissue, and the creation of images related to the electrical properties of the breast tissue. The tissue of a malignant tumor has higher water content than normal breast tissue and hence markedly different dielectric properties [4]. As result, strong scattering take place when the microwaves hit the tumor. Several applications of microwave imaging in the medical field have been recorded and implemented for breast cancer detection [3–8].

In this paper we present an experimental system with time domain microwave imaging. First we discuss the breast phantom used to mimic the conductivity and relative permittivity of actual breast tissue. A previously designed microstrip patch antenna with air as dielectric with a rectangular patch mounted on two vertical plates, with the ground size $40 \times 40\,\mathrm{mm}^2$ [9] used. Simulations and experiments are described using the phantom with various sizes and locations of tumors, and with different antenna array layouts.

2. METHODOLOGY

In the simulation the interaction of the antenna with a tissue model is investigated. The electromagnetic model used to simulate the breast contains two layers: the first layer is the skin layer with thickness = 4 mm, dielectric constant = 36 and conductivity = $4.0\,\mathrm{Sm}^{-1}$. The second layer models the breast tissue, with a width of 10 cm, dielectric constant = 9 and conductivity = $0.4\,\mathrm{Sm}^{-1}$ [10, 11].

We have compared the performance of the antenna locating on different position on the container wall in order to gain insight into the relationship between antenna performances and ability of the system.

We present three distinct cases.

- Case 1 Antenna apart by 0°.
- Case 2 Antenna apart by 90°.
- Case 3 Antenna apart by 180°.

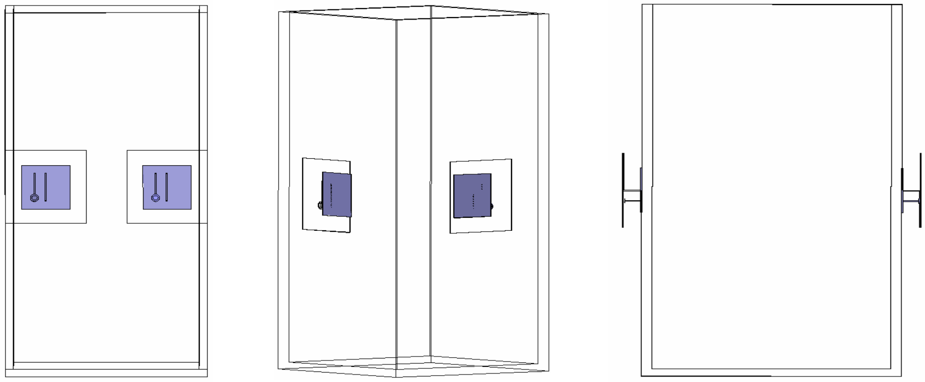

Figure 1: Model of the imaging system.

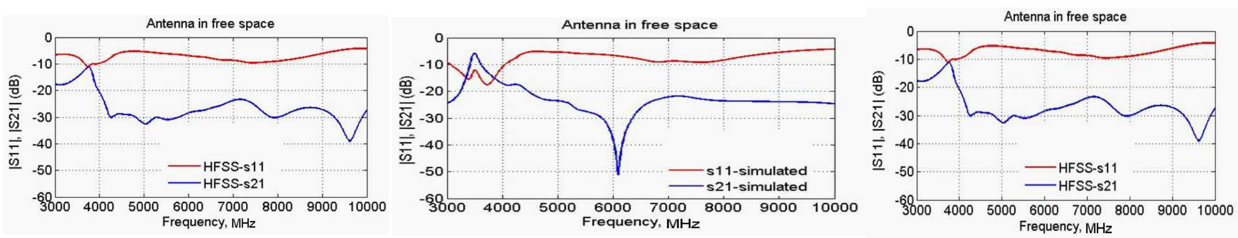

(a) (b) (c)

Figure 2: Scattering parameters for two element sensor array in free space. (a) Antenna apart 0°. (b) Antenna apart 90°. (c) Antenna apart 180°.

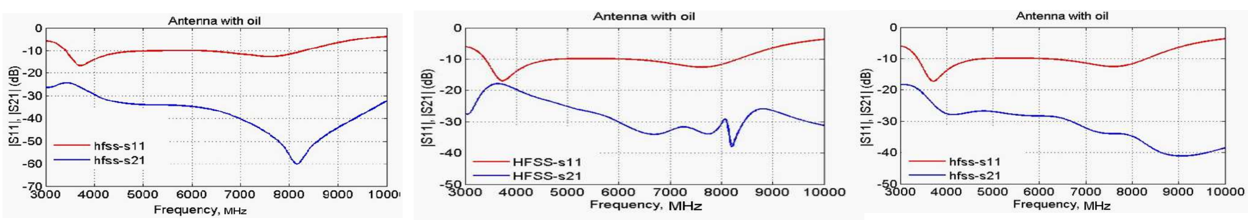

(a) (b) (c)

Figure 3: Scattering parameters for two element sensor array attached to the wall of container filled with oil. (a) Antenna apart 0°. (b) Antenna apart 90°. (c) Antenna apart 180°.

Figure 4: Photograph of the prototypes.

A photograph of the phantom is shown in Figure 1. the simulated return loss S_{11} and transmission coefficient for the antenna in air and with the phantom are shown in Figures 2 and 3. All the simulations were performed using the software tool HFSS [12]. We note that antenna has poor behavior in air however it exhibits an improved S_{11} when attached to the phantom.

In order to validate the results obtained from the simulated model; an experimental model is setup, as shown in Figure 2. In the measurement, vegetable oil is used as its dielectric properties closely match the actual tissue. The simulated and measured return loss from 4 to 8 GHz in free space, with the antenna connected to the wall of the container filled with vegetable oil show good agreement as shown in Figure 5. Both the commercial software simulation and measurement results are in acceptable agreement. The measured S_{21} showed best agreement with the simulated result.

3. DISCUSSION

The specific goal of this part is to prove the measurement of scattered waves due to the transmitted ultra-wideband microwave signal traveling through a tissue mimicking environment like phantom and tumor. The task now is to integrate the system components with a vector network analyser and perform measurements with various scattering objects. Photographs of the measurements system are shown in Figure 6. For each design option a pair of antenna was tested: one antenna designated as transmitter and the other as receiver. The propagated signals S_{21} were measured with

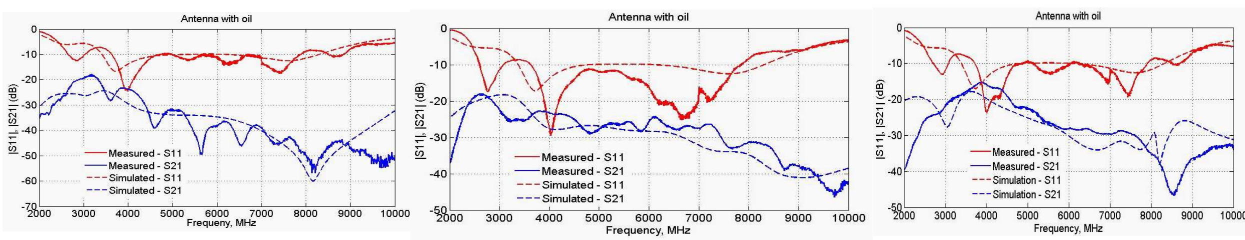

Figure 5: Simulated and measured scattering parameters for two element sensor array attached to the wall of container filled with oil.

(a) (b) (c)

Figure 6: (a) Measurement setup. (b) 4.1 mm tumor. (c) Simple model for breast tumor detection.

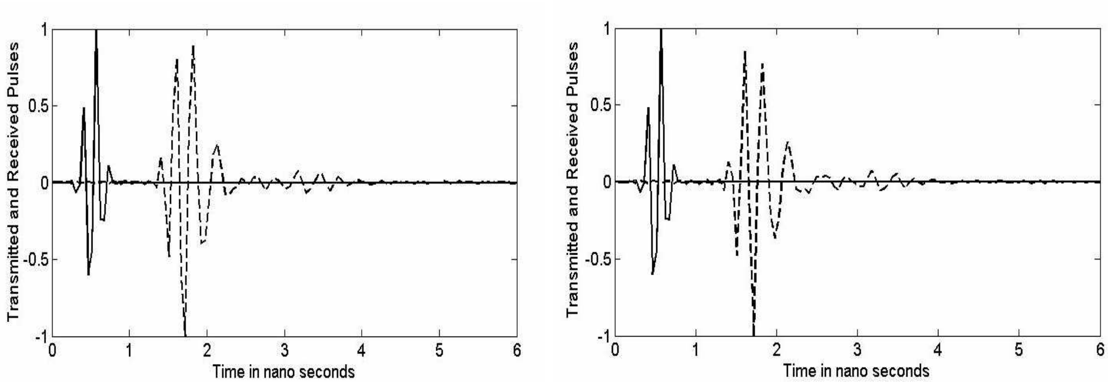

(a) (b)

Figure 7: (a) Measured transmitted and received pulse with no target. (b) Measured transmitted and received pulse with target.

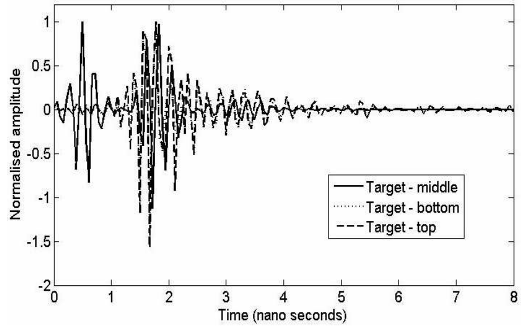

(a)

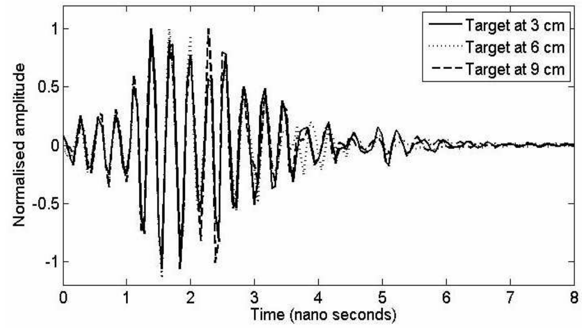

(b)

Figure 8: (a) Tumor responses of three different depths. (b) Tumor position responses at 3 mm, 6 mm, and 9 mm.

the network analyser. In all cases S_{21} transmission parameter was first measured with no scattering objects present between the antennas. S_{21} transmission was measured again with the scattering object placed at different location between the antennas. The scattering object includes 10 g of wheat flour mixed with 5.5 g of water This mixture has a relative permittivity 23 and conductivity of 2.57 (S/M) at frequency of 4.7 GHz [13]. This mixture is used to construct tumor for various sizes and inserted in the breast phantom for experimental detection. In testing system with the first pair of antennas and the 4 mm tumor used as scattering object. The first set of data show measurements when antennas were placed 10 cm apart in a straight path facing each other with and without the scattering object. Figure 7 shows the time-domain reconstructed pulses with and without presence of target respectively. The scattered field shown in Figure 8(a) shows sensitivity of the imaging system to this small object. The scattering object is placed in the middle, bottom and top of the cubical container keeping the antenna spacing 10 cm and record the reflection from the target.

Next are the time domain behavior of the propagated signal with the two antenna are at 0° degree apart as shown in Figure 8(b), measurement with the scattering object for this pair of antenna at 3 cm, 6 cm and 9 cm. In all the cases 4 mm sphere, i.e., mixture of flour and water as a scattering object, for time domain analysis a 4 GHz bandwidth pulse was used. The time domain plots show the scattering plot for the microstrip antenna with a rectangular radiating patch.

4. CONCLUSION

The experimental microwave imaging measurement was constructed using small ultra-wideband antennas, breast phantom, target and a vector network analyser. The measurement results showed that this system is capable of detecting electrically small targets as required for early detection of breast cancer. Even though irregular shaped objects were not tested, it is expected that the scattering from such objects would be even more pronounced than from a spherical target and it might be possible to detect even smaller targets. Over all this experiment confirm the choice of antenna design and the overall system design parameter. No actual images were formed, however the successful measurements carried out here prepare the way for the next step of using these measurements in the time domain to show the super-resolution concept experimentally.

REFERENCES

1. "Breast cancer key facts," *Cancer Research*, UK, Mar. 2008.
2. Blanks, R. G., S. M. Moss, C. E. McGahan, M. J. Quinn, and P. J. Babb, "Effect of NHS breast screening programme on mortality from breast cancer in England and Wales, 1990-8: Comparison of observed with predicted mortality," 665–669, 2000.
3. Yun, X., E. C. Fear, and R. H. Johnston, "Compact antenna for radar-based breast cancer detection," *IEEE Trans. Antennas Propagat.*, Vol. 53, 2374–2380, Aug. 2005.
4. Meaney, P. M., M. W. Fanning, D. Li, S. P. Poplack, and K. D. Paulsen, "A clinical prototype of active microwave imaging of the breast," *IEEE Transactions on Microwave Theory and Techniques*, Vol. 48, 1841–1853, Nov. 2000.

5. Meaney, P. M., K. D. Paulsen, A. Hartov, and R. K. Crane, "An active microwave imaging system for reconstruction of 2-D electrical property distributions," *IEEE Transactions on Biomedical Engineering*, Vol. 42, 1017–1026, 1995.
6. Li, D., P. M. Meaney, T. Raynolds, S. Pendergrass, M. Fanning, and K. D. Paulsen, "A parallel-detection microwave spectroscopy system for breast imaging," *Review of Scientific Instruments*, Vol. 75, 2305–2313, 2004.
7. Semenov, S. Y., R. H. Svenson, A. E. Boulyshev, A. E. Souvorov, V. Y. Borisov, A. N. Starostin, K. R. Dezen, G. P. Tatsis, and V. Y. Baranov, "Microwave tomography: Two dimensional system for biological imaging," *IEEE Transcations on Microwave Theory and Techniques*, Vol. 43, 869–877, 1996.
8. Semenov, S. Y., R. H. Svenson, A. E. Boulyshev, A. E. Souvorov, A. G. Nazarov, Y. E. Sizov, A. V. Faviovsky, V. Y. Borisov, B. A. Voinov, G. I. Simonova, A. N. Staostin, V. G. Posukh, G. P. Tatsis, and V. Y. Baranov, "Three dimensional microwave tomography: Experimental prototype of the system and vector born reconstruction method," *IEEE Transactions on Biomedical Engineering*, Vol. 46, 937–945, 1999.
9. Adnan, S., R. A. Abd-Alhameed, H. I. Hraga, I. T. E. Elfergani, and M. B. Child, "Compact microstrip antenna design for microwave imaging," *Loughborough Antennas* & *Propagation Conference*, Loughborough, UK, Nov. 8–9, 2010.
10. Fear, E. C. and M. A. Stuchly, "Confocal microwave imaging for breast tumor detection: Comparison of immersion liquids," *IEEE APS*, 250–253, 2001.
11. Sill, J. M. and E. C. Fear, "Tissue sensing adaptive radar for breast cancer detection: Study of immersion liquids," *Electronics Letters*, Vol. 41, 113–115, 2005.
12. Ansoft High Frequency Structure Simulator Corporation, V11, 2007.
13. Alshehri, S. A., S. Khatun, A. B. Jantan, R. S. A. Raja Abdullah, R. Mahmood, and Z. Awang, "Experimental breast tumor detection using NN-based UWB imaging," *Progress In Electromagnetics Research*, Vol. 111, 447–465, 2011.

The Measurement of Diffusion in Plants Tissue Culture

M. Burdková, P. Marcon, E. Gescheidtová, and M. Cap
Department of Theoretical and Experimental Electrical Engineering
Brno University of Technology, Kolejni 4, 612 00 Brno, Czech Republic

Abstract— For monitoring of tissue structures of Euphorbia plants is used magnetic resonance imaging (MRI). In contrast with CT the MRI does not emit any harmful radiation. The images are obtained without any deformation or destruction of the plant. The principle of MRI technique is based on the measurement of the interaction of the electromagnetic waves with nuclei placed in the strong magnetic fields. Diffusion is random translational motion of molecules from a place of higher concentration to a location with lower concentrations, arising due to their thermal energy. The diffusion coefficients measured by MRI method are describing the degrees of mobility of nuclei. Measurements of these coefficients is performed by measuring the PFGSE sequence, it is a normal spin-echo sequence extended by two identical rectangular diffusion gradients. During measurements there are distinguished three time intervals. In the first interval the nuclei are dephased, in the next interval the nuclei diffuse (relaxation time). In the last interval the nuclei are phased in by gradient pulses. When not all magnetization vectors are phased, diffusion is non-zero, otherwise diffusion is zero and the maximum MRI signal is obtained. During the measurement of the diffusion coefficient the static gradient is manifested as a result of magnetic properties of the substance. There are four gradients used for measurement for each axis. Evaluation of acquired images was performed in the program Marevisi. The images were evaluated separately for positive gradient ones and negative gradient ones. To obtain more accurate values in all directions averaged values were calculated.

1. INTRODUCTION

Currently, for the monitoring of the structure of Euphorbia plant tissues are used methods of imaging techniques based on the principle of magnetic resonance imaging (MRI). The principle of MRI technique is based on the measurement of the interaction of the electromagnetic waves with nuclei placed in the strong magnetic fields [1]. Amongst the specialized MRI scans belongs the diffusion MRI. Diffusion is a mass transport process arising in nature, which results in molecular or particle mixing without requiring bulk motion. The degree of mobility during the diffusional motion of nuclei is characterized by the diffusion coefficient (constant). The coefficients for each substance other reason other motion of nuclei in different substances [2].

Amongst the most widely used basic sequences for measuring diffusion measurements belongs the Pulsed Field Gradient Spin Echo (PFGSE). Two-interval PFGSE is the simplest sequence utilising spin-echo under the influence of a constant gradient g. Six-PFGSE interval measurement sequence is the most common method for measuring diffusion. This sequence usually uses two identical rectangular gradient pulse with length δ called diffusion gradients G. Other sequence for measuring diffusion is the six-interval PFGFE, which is using two gradient pulses of different polarities instead of the two radio frequency pulses [3].

2. SIX-INTERVAL PULSED FIELD GRADIENT SPIN ECHO

The measuring sequence is extended by two diffusion gradients, the first, which is applied between the two radio frequency pulses, is used for re-phasing spins in defined way. The second pulse is used for consequent phasing. The advantage of this method is to reduce the relaxation time for the same timing as the gradient method PFGSE and higher ratio signal to noise ratio in MRI signal. The measuring sequences can be applied to both isotropic (homogeneous) and heterogeneous materials (Fig. 1), which are characterized by their internal inhomogeneous structure. Therefore, the diffusion of nuclei in the different directions is different. Due to variations in magnetic susceptibility of the material in the different areas the magnetic field in the material is deformed. When measuring the diffusion coefficients the accuracy and sensitivity of the measurements is influenced by internal static gradient magnetic field caused by magnetic susceptibility of measured substances [4].

Mathematical derivation of the b factor and diffusion coefficients for measuring PFGSE sequence in heterogeneous materials is given in the article of Bartuska and Gesheidtove [5].

3. EXPERIMENTAL MEASUREMENTS

MRI images were recorded at 4.7 T MRI system (200 MHz) at temperature of 20 ± 0.2°C at ÚPT AV CR in Brno. Scanned images were 256×256 pixels large and the size of the operation point was 26×26 mm. System resolution was 0.1 mm per pixel. For measurements were used six-interval sequence PFGSE. Sequence parameters were set to $d = 4.72$ ms, $D = 15.4$ ms, static gradient (DAC) was set in the range from 0 to ± 25 k. MRI images were measured perpendicular to the axis of the stem of Euphorbia succulent in several slices, which were at different heights from the root to the upper part of the plant.

The evaluation of pictures taken by the PFGSE method with measurements of the diffusion is done manually in the program Marevisi. Measurements in different axes were carried with different values of gradient. In the Fig. 2 are diffusion images of examined succulent Euphorbia, measured successively in the different axes (x, y and z) with the same gradient $DAC = -25$ k. The color in the image corresponds to the intensity that is proportional to the number of proton nuclei in the place of the succulent stem.

Values of the diffusion coefficient obtained from defined areas (Fig. 1) of examined succulent are listed in Table 1.

In the Fig. 3 are shown diffusion images of examined succulent using PFGSE sequence at different positive values of gradient in the z-axis.

Evaluation of acquired diffusion images went as follows, first were used the images with a positive gradient and the resulting diffusion image was generated. Subsequently were evaluated the images with a negative gradient. The Table 2 shows diffusion coefficients obtained from the areas listed in the Fig. 4.

To obtain more accurate values in all directions the images with positive and negative gradient were averaged. D_{prum} value is the average value of diffusion coefficient obtained from the individual averages obtained for each coordinate separately. Individual relative errors are related to this value. In the Table 3 are listed all the averaged values and their relative errors.

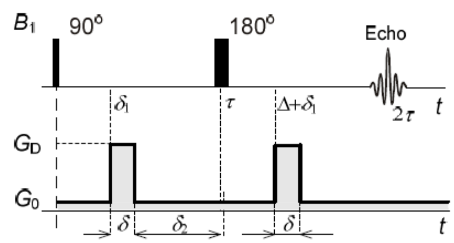

Figure 1: PFGSE sequence for measuring diffusion.

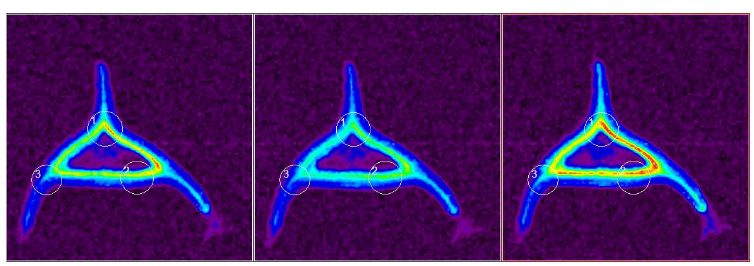

Figure 2: Diffusion images of succulent Euphorbia (gradient x, y, z).

Table 1: Diffusion coefficient from defined areas.

Area	Gradient in axis x Coefficient [ms]	Gradient in axis y Coefficient [ms]	Gradient in axis z Coefficient [ms]
1	1,853e-9	1,834e-9	1,774e-9
2	3,549e-9	3,526e-9	3,498e-9
3	2,340e-9	2,329e-9	2,356e-9

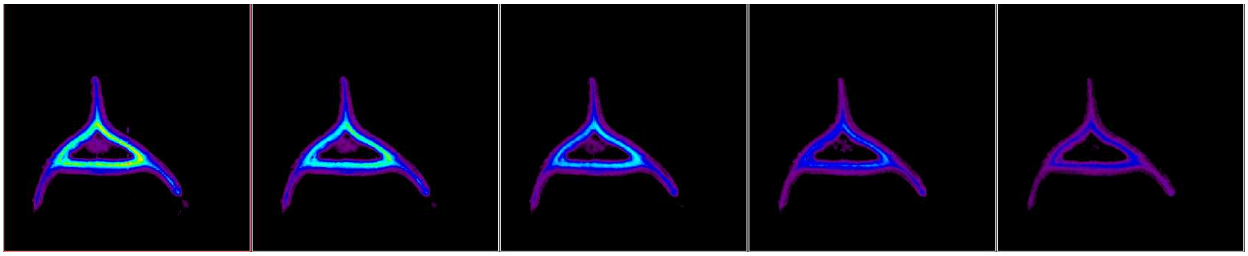

(a) 0k	10k	15k	20k	25k
(b) 0 mT/m	7,14e - 2 mT/m	1,071e - 1 mT/m	1,428e - 1 mT/m	1,785e - 1 mT/m

Figure 3: Diffusion images of succulent Euphorbia at different values of gradient in the z-axis [(a) DAC, (b) G_D].

Table 2: Diffusion coefficients obtained from diffusion images.

Area	$\mathrm{G_{DXplus}}[\mathrm{m^2/s}]$	$\mathrm{G_{DXminus}}[\mathrm{m^2/s}]$	$\mathrm{G_{DYplus}}[\mathrm{m^2/s}]$	$\mathrm{G_{DYminus}}[\mathrm{m^2/s}]$	$\mathrm{G_{DZplus}}[\mathrm{m^2/s}]$	$\mathrm{G_{DZminus}}[\mathrm{m^2/s}]$
1	2,823e-9	1,898e-9	2,017e-9	2,221e-9	2,107e-9	2,295e-9
2	3,333e-9	2,108e-9	2,575e-9	2,573e-9	2,410e-9	2,174e-9
3	2,728e-9	1,947e-9	2,241e-9	2,228e-9	2,482e-9	2,385e-9
4	2,019e-9	1,505e-9	1,689e-9	1,762e-9	1,915e-9	1,674e-9

Table 3: Averaged diffusion coefficients and their relative errors.

Area	G_{DXprum} $[\mathrm{m^2/s}]$	δ [%]	G_{DYprum} $[\mathrm{m^2/s}]$	δ [%]	G_{DZprum} $[\mathrm{m^2/s}]$	δ [%]	$D_{\mathrm{prum}}[\mathrm{m^2/s}]$
1	2.36e-09	6.0	2.12e-09	−4.8	2.20e-09	−1.2	2.23e-09
2	2.72e-09	7.6	2.57e-09	1.8	2.29e-09	−9.4	2.53e-09
3	2.34e-09	0.1	2.23e-09	−4.3	2.43e-09	4.2	2.34e-09
4	1.76e-09	0.1	1.73e-09	−2.0	1.79e-09	1.9	1.76e-09

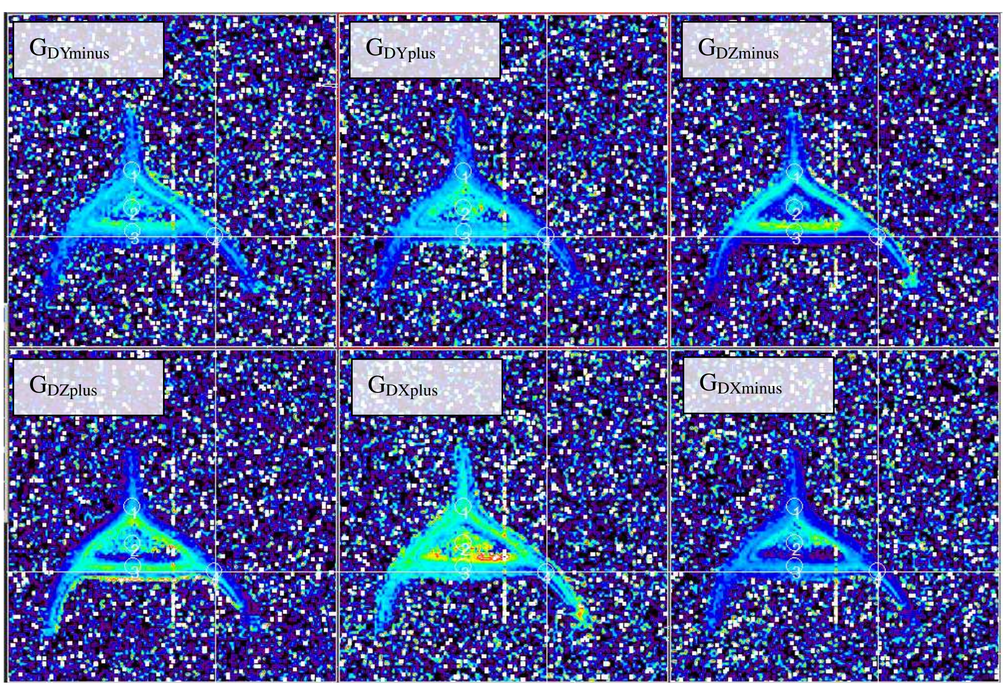

Figure 4: Diffusion images of succulent Euphorbia at different values of gradient.

4. CONCLUSIONS

The MRI methods are mostly used in medicine for obtaining patterns of tissue cultures. Amongst the specialized MRI scans belongs the diffusion MRI. The aim of this work was to display diffuse pattern of tissue culture of succulent Euphorbia using diffusion MRI and obtain diffusion coefficients. Exploring of the succulent was conducted on an experimental 4.7 T tomograph at the Institute of Scientific Instruments, Academy of Sciences ČR in Brno. For measurements on MRI tomograph was chosen the PFGSE measurement sequence using diffusion gradients. Values were measured for zero gradient echo and then for positive and negative values greater than zero. Measurement and subsequent evaluation took place gradually for all three axes. The resulting value for the diffusion succulent after averaging was around $2e^{-9}m^2/m$ with relative error to 7%. Comparing the resulting values of diffusion coefficient for all three axes the values comes nearly identical.

ACKNOWLEDGMENT

This work was supported within the framework of the research plan MSM 0021630513 and project GACR 102/11/0318 and project of the BUT Grant Agency FEKT-S-11-5/1012.

REFERENCES

1. Vlaardingerbroek, M. T. and J. A. Den Boer, *Magnetic Resonance Imaging Springer*, Verlag, Berlin, 1999, ISBN 3-540-64877-1.
2. Berg, H. J. and E. J. T. Behrens, *Diffusion MRI*, China, 2009, ISBN 978-0-12-374709-9.
3. Bartusek, K., *Speciální Metody Merení Difúzních Koeficientu Metodami Nukleární Rezonance*, VUTIUM, 2007, ISBN 978-80-214-3379-3.
4. Král, J., "Merení difúzních koeficientu technikami magnetické resonance," Bachelor Thesis, Vysoké Ucení Technické v Brne, Fakulta Elektrotechniky a Komunikacních Technologií, Brno, 2007.
5. Bartusek, K. and E. Gescheidtová, "Kompenzace vlivu statického magnetického pole pri mr merení difúze," *Elektrorevue*, Vol. 29, 1–6, 2008, ISSN 1213-1539.

Waves and Signals

S. L. Vesely[1], A. A. Vesely[2], and C. A. Dolci[3]

[1]I.T.B. — C.N.R., Italy
[2]Via L. Anelli 13, Milano, Italy
[3]Politecnico, Milano, Italy

Abstract— It is commonly retained that the celebrated Heinrich Hertz's experiments validated Mawell's theory by proving the existence of electromagnetic waves for the first time. Nowadays, the existence of electromagnetic signals is established. Indeed, telecommunications devised techniques to transmit and receive encoded electromagnetic signals efficiently and reliably. A wide number of technical problems about signals were solved relying upon purposely conceived theories of communication and information. There are interesting interrelations between the latter approaches and electromagnetism. However, it is not clear what relationship is to be assumed between the elementary solutions of Maxwell's equations (waves) and the means for conveying messages (signals). Commonly, electromagnetic signals are held to be wave packets, bearing an energetic connotation to which the information-theoretical point of view has to adhere. In this paper, instead, we consider signals to be the only experimental evidence, starting with that experimental validation of Maxwell's theory. That is, the technique by which Hertz revealed waves does not conceptually differ from modern telecommunications techniques. To give a visual account of this position, we describe the experiment carried out by Otto Wiener to reveal light waves, and compare his classical interpretation versus interpreting such waves as images.

1. INTRODUCTION

Nowadays, on the one hand information tends to be codified so as to make it independent of the kind of channel or medium that is used to transfer or convey it. On the other hand, electromagnetic waves, as information carriers, are credited with physical characteristics both of their own as well as of the bodies that interacted with them [1]. The distinction between messages encoded for telecommunications purposes and those obtained from probing samples is essentially a question of locating the relevant theoretical layer. In the former case, a message is considered a communication theoretical entity, while for the latter one electrodynamical considerations seem to be appropriate. Both theories indissolubly attribute to electromagnetic fields a universal encoding according to amplitude, frequency, and phase. This habit may somehow limit the ability to interpret signals received from non-compliant sources.

In facts, electromagnetism did not evolve from telecommunications needs, but from a series of failed attempts at explaining electrical and magnetic phenomena by taking recourse to mechanic-theoretical conceptions. Hendrik A. Lorentz extended dynamics to electrodynamics by introducing the (aethereous) electromagnetic fields as physical entities, besides their sources. In his theory, all of the interactions among conductors, dielectrics, and magnets happen through the fields. Therefore, in telecommunications' parlance, monitoring the fields provides a means to track electromagnetic responses of electrodynamical systems. That position implies the assumption that the dynamic behavior of such systems encompasses all the information that can be obtained about them. For complex systems, recourse to statistics can be taken by analyzing space and time correlations [2]. Although different kinds of information about a system can be treated through approaches different from the dynamical one, all physical theories are compelled to present dynamical variables. From a mathematical point of view, restricting to dynamical variables allows to have a definite, unified sample space for all physical concepts, expressing any newly found property in terms of the existing ones. However, that part of electromagnetism that concerns the human visual experience, either naturally or through specific instruments, can be approached independently of dynamics without losing objectivity.

Reducing bodies to sets of points and radiations to waves hinders seizing the relationship between material bodies and their electrical/optical responses. For example, an electric susceptibility curve can be interpreted as a polarization of a dielectric material, or as a response of an electric circuit. In facts, harmonic analysis[1] determines a linear electric circuit that gives an electric response

[1]Harmonic analysis corresponds to the usual way to analyze a circuit's response. In probability theory, the basis must be chosen so as to satisfy Parseval's theorem. Otherwise, under suitable conditions, any experimental graph can be mathematically represented by an analytic function.

equivalent to that given by the dielectric. Both a circuital scheme and a microscopic description of the polarization are possible interpretations of the signal received. The model that involves the circuital scheme can be implemented by building a circuit that gives the same linear response as the sample. Such modeling works as long as responses are linear. That shows the limit of modeling. Indeed, behavior of real bodies is not linear, in general. The equivalence between the responses of the circuit and the sample is meant to be modulo the receiver. If the receiving or measuring circuit work linearly, the dielectric sample can be interpreted as the equivalent circuit. On the other hand, signals themselves, like any phenomenon, tend to be unrepeatable, and information can result from the way they vary. Hence, the experience derived from received signals involves more than what current model-based interpretations can reach.

In the following, we analyze the experiment in which O. Wiener, by analogy with experiments on acoustic waves, photographed light waves. We try and interpret his experiment's waves as a signal (i.e., as an encoded radiation).

2. WIENER'S EXPERIMENT ON STANDING WAVES

Methods developed in the 1890's in conjunction with experiments aiming at unraveling the propagation of sound or light perturbations belong to the history of antenna configurations and techniques. However, the interpretation of O. Wiener's experiment [3] remained outside telecommunications interests. Phenomena used to be understood as purely luminous if light featured as an effect of some kind of transduction. Furthermore, the notions of light and signal were related to the observed facts in peculiar ways. For example, almost any image of a material body, from bodies observed by eye to images detected using sophisticated optical instruments, was ascribed in category "bodies" rather than "signals". On the opposite, properties of bodies that involved dispersing, reflecting, or however diffusing light were specifically referred to light. That attitude is prone to introduce problems when the theoretical question of the representation of electromagnetic waves is tackled in a communication-theoretic framework, where the aim is obviously to treat signals. In short, although preferred referrals didn't impede to appreciate mirrors for the vividness of the "ethereal images" they reproduce, they impeded to appreciate them as signal detectors specifically. It has to be said that specular reflection as such is susceptible to several equally valid explanations, according to the context. An epoch may be notable for being plenty of good reasons for delving into mechanical reduction of light, while another may be more interested in optical channels for the amount of information that they can transmit.

To recall the context of O. Wiener's experiment [4], we touch on the related problem of visualizing acoustic waves. The dynamical reduction of sound propagation dates back to Newton, even if thermodynamical adjustments were necessary for comparing measured data against calculated values. Helmholtz's experiments (circa 1850) contributed to substantiate harmonic analysis of sound, and eventually, in 1866, A. Kundt made sound waves visible. His purpose was to measure the speed of sound indirectly; that is, simultaneously evaluating the length λ and the frequency ν of a supposedly synchronous sound wave, and then compute the speed as $c = \lambda\nu$. To that end, he generated sounds and made them visible. In particular, he studied the patterns formed by lycopodium seeds when the air column between the sealed ends of a tube gets a slight elastic excitation. It seems to be useful in view of what follows, to distinguish acoustic amplification from the motions that involve the air mass inside the tube. The air exerts an amplifying function on the sound produced while the walls of a soundboard are being stimulated. As the acoustic power increases, further effects can be observed, including air streaming. In such circumstance, Kundt says that lycopodium seeds levitate as a consequence of the air motion and eventually settle on the tube's walls forming a pattern, in a way similar to how they arrange themselves on vibrating plates or membranes, forming Chladni patterns. In this specific case, however, the formation of air streams appears to be a higher order effect with respect to sound amplification. In other words, and just because visual analysis and encoding of sounds are common nowadays, it's appropriate to clarify that Kundt's patterns do not constitute an unambiguous encoding of sounds; that is, sounds cannot be linearly reproduced based on them.

O. Wiener considered Kundt's merit to consist in visualizing sounds, which are perceivable as such to the ears anyway, unveiling their true time-independent form. On his part, he aimed at making standing light waves perceivable to the eyes as well. We are not going to delve into details of how mechanical vibrations may become audible. However, we note that, although eyes are the best light-sensing organs we have, it was already known at those times that light is not directly perceivable with eyes. Some argued that luminous fields could not be seen because light travels too fast to be fixed on the retina. White light, in particular, was thought to possibly consist of random wave trains, whose root mean squared (rms) values in normal conditions would cancel out. That's why Wiener associated visualization of light with monochromatic standing waves. We think that a modern take of that experiment's interpretation may be interesting, as then even electricians retained that thermocouple or moving-vane ammeters measured rms values of alternating currents. Later experience with radiophonic transmissions taught that to ease fruition of radiofrequency transmissions it is convenient to use heterodyne receivers [5]. Moreover, it taught that both detection and modulation/demodulation are the result of non-linear effects. Thus, before we even start to describe Wiener's experiment, we warn that the interpretative difference between him and us is about this point, that the perception of light intensity as diffused by bodies may also be the result of some mixing process.

In essence, Wiener's experiment is designed so as to intercept a standing wave system with a very thin film [6–8]. The film was prepared using a variation of the wet collodion process that makes it very transparent. Wiener sensitized it with diluted silver chloride, taking care that both the film and the thin glass plate that served as support had the same refraction index. The mirror consisted of a flat, polished surface of chemically deposited silver. The plate was fastened to it with rosin, at a small dihedral angle[2] whose gap was filled with either air or benzene. The standing waves system was obtained by illumination directed orthogonally toward the mirror. For that purpose, Wiener used an arc lamp's beam dispersed by a Flint's prism so as to expose the film to a small radiation range about Fraunhofer line H ($\approx 380\,\mathrm{nm}$), which the film was sensible to. After development, the film showed by transparency a series of alternated light and dark bands. Wiener interpreted them as a cut across the wave system, excluding the possibility of interferences, such as Selényi fringes[3]. According to his mechanical interpretation, aether waves are similar to capillary waves[4], except that the former ones are uniformly distributed *throughout the volume* in front of the mirror. His concept of interference refers to the pattern observed when two waves originating from different points propagate in the same region. "Standing wave", instead, refers to the pattern observed when a wave hits perpendicularly the planar surface between two media, the second of which has a much higher density, so that the wave gets reflected upon itself completely[5]. Wiener reported that fringes across the film could not form, because it was too thin. He also excluded Newton's interference fringes, as no fringes were seen in case the plate glass side of the film was facing the mirror, while in case the mirror was replaced with glass they were almost unnoticeable. For standing waves, H. Hertz measurements had established that UHF waves form a node against the zinc cylindrical parabolic surface that they reflect themselves on, and subsequent nodes at distances $1/2n\lambda$, $n = 1, 2, \ldots$ from it. Wiener's observations confirmed that illumination is minimal along the margin of the film that touches the mirror. However, that explanation of why the incident wave gets out of phase by π upon reflection becomes invalid when the *optical density* of silver is considered, instead of its *mass density*[6]. Indeed, the former is associated with the relative refractive index, which is about 0.15 for silver to air at 380 nm, with possible variations according to surface conditions. Hence, silver is optically less dense than air. Nowadays, the vanishing of the transverse component of the electric field on the surface of a perfect electric conductor (PEC) replaces that mechanical condition[7]. Under normal incidence conditions, the reflection coefficient for silver results to be $\Gamma = -1$, independently

[2]The angle was judged by observing Newton's fringes of the Na D-line.

[3]He called "interferences" the systems of fringes formed at infinity, according to the current criterion. Such systems are out of focus on the film, but contribute to the irradiance. The waves he called "stationary", instead, are sharply on focus.

[4]Capillary waves are called the crumples that form on the surface between two immiscible liquids in response to a perturbation. They are usually ascribed to surface tension.

[5]This representation is borrowed from the dynamics of transverse waves on a rope tied to a fixed point at one end.

[6]To be precise, Wiener referred to the "optical density" of silver. However, he meant the inertia of the aether contained in the unit volume of this substance.

[7]The so called pillbox boundary conditions for the electromagnetic fields, at the interface $1-2$, are $\widehat{\mathbf{n}}\times(\mathbf{E}_1 - \mathbf{E}_2) = 0$ and $\widehat{\mathbf{n}}\times(\mathbf{H}_1 - \mathbf{H}_2) = \mathbf{J}$, where $\widehat{\mathbf{n}}$ is the outward normal from medium 2 (the PEC). As they follow from Gauss' and Stokes' theorems, they don't really specify the current density distribution $\mathbf{J}$ on the conductor's surface. In facts, the boundary is the whole surface, and $\mathbf{J}$ has to be evaluated on it –say by having recourse to the method of images– to perform the integral and yield the radiation characteristics of the reflector. Besides the current distribution method, many other theoretical issues, from whom the reflection mechanism is still being deduced, such as the Eikonal (after the Hamilton-Jacobi equation), or the method of characteristics of Levi Civita, are taken over directly from ray or wave theories. All those issues make some assumptions on the structure of radiation, and on its behavior upon reflection. We are stressing this point in order to put forward that some kind of encoding is enforced by mirror reflection, even of solar radiation. Hence, as an alternative to specifying geometric boundary conditions, one could assume that the mirror's response function determines the output radiation field. A mirror reflection is not a pointwise mapping of bounces, but involves a detection, although this can be treated according to the small-signal model. That's the reason why we consider it a limitation to theorize that signals can be unconditionally decomposed into waves or rays.

of reference impedance. Wiener associates a chemical energy to his traveling monochromatic waves, so that when they oscillate steadily in front of the mirror, the exposed film blackens proportionally to $|\sin Kx|^2$, on average, at positions x[8]. Nowadays, the emissions of thermal sources, like that carbon arc lamp, are considered to be due to Gaussian random processes, and thus the radiometric energy associated with them is fully described by a second order theory. To derive a small-signal interpretation, let's note that Wiener's experiment can be considered a technique for transforming a lamp's emission into an encoded signal, where the encoding is the one shown by the developed film frame. That is an application of the typical property of mirrors of rendering incident light as images. Wiener discarded the interpretation of the bands shown on focus in his photographs as equal-thickness Fizeau fringes. He thought that beams reflected from two interfaces only cancel at the nodes, when they are of equal amplitudes, which happens in case of two air-glass reflections. An air-metal interface would produce a reduced visibility of the fringes. In actual facts, however, those Fizeau bands appear much enhanced by substitution of the lower glass lame by a silvered scattering surface. Silvered mirrors are renown for the high quality of the images they render of any illuminated body. There are two implications. 1) Can Wiener's standing waves be interpreted as images? If the transparent film faces the mirror directly, with only air or benzene in between, the image of the lamp illuminates it exactly in the same way as the lamp itself. Hence, the air-or-benzene wedge behaves as a phase object. The image results from a beat that varies with the thickness of the gap proportionally to $1 + \cos(2Kx + \pi) = 1 - \cos 2Kx$, where K is a constant that also depends on the film's slant, and x is the distance from the pointed end of the wedge. Mathematically, the simple band-pattern obtained by Wiener is described equally well by each of the two trigonometric expressions above, which equal one another because of the double-angle formulae $\cos 2A = 1 - 2\sin^2 A$. Physically, however, the interpretation that associated an energy flux with the electromagnetic waves is substituted by a new interpretation in which the mirror performs a "demodulation", whereby the latter is the usual way to receive radio signals; 2) We presume that such functioning holds in general, whenever metallic surfaces detect the images of illuminated bodies. In this sense, mirrors can be thought of as antennas' reflectors that transform[9] their inputs in reflected images of the usual kind. Although the bands in Wiener's experiment can be viewed as a decoding of partially coded light (the Fraunhofer H-line), and reflector antennas certainly do receive even fully coded light, we are accustomed to interpret mirror detection just when the carrier is diffused solar light. That is, detectors receiving "wild" illumination sources can form images recognizable by humans. As far as the carried information is concerned, this restates that unencoded signals are equivalent to small signals, modulo the mirror receiver.

3. CONCLUSIONS

In this paper, we hint that a metallic mirror showing an image is working as a signal detector, implying that the image can be assumed to be the optical field associated with the mirror, without the need to provide any additional characterization of the incoming radiation in this range. To give a visual account of that, we reinterpreted the historically first experiment that revealed standing light waves, so as to compare the functioning of a mirror to homodyne detection. A polished silver surface gives a good signal, which carries information, which in turn human observers can get if they have adequate visual experience. If the same optical field is surveyed with a bolometer, say, it supplies a different kind of information. It seems to be a question of convenience whether or not to admit that any revealed radiation corresponds to a signal, even if the signal is bad or incomprehensible. From a theoretical point of view, it would be opportune to consider a signal-centric alternative to theories hinged on energetic concepts. In this respect, electromagnetism, as validated by experiments such as Hertz's and Wiener's, can do all received signals, also those with no priorly established encoding, but information theory presently cannot.

[8]The final part of Wiener's paper mulls over the reasons why that latent image forms on the film. We would decompose such problem into 1) why exposed films have a latent image in general (a photochemical issue), and 2) why that film shows those particular bands (a reception issue). Instead, Wiener tackled it as one united issue of standing aether vibrations. In mechanical terms, blackening of the negative could be attributed to either the steady motion of the wave on the film, or the force exerted by such motion on its molecules. Assuming it is legitimate to disregard longitudinal components of elastic waves in the mathematical treatment of reflection, Wiener concentrates on the position of the vibration plane relative to the incident and polarization planes. For a wave to leave a sharp mark on the film, with linearly polarized light coming at an incident angle of 45°, the vibration plane must be perpendicular to the incident plane. By taking up this as the polarization plane, he agrees with Fresnel's theory and dissents from Neumann's one. As Wiener considers the film a geometric section of the standing field, he ultimately identifies the vibrational component with the mean electric component of the Poynting vector.

[9]For comparison, an optically polished white surface, used as a mirror, may allow to distinguish the bodies that diffuse light upon it, but it always appears lighted. The aperture also plays a role in the transform.

REFERENCES

1. Gabor, D., "Communication theory and physics," *Transactions of the IRE*, Vol. 1, No. 1, 48–59, 1953.
2. Walther, A., "Radiometry and coherence," *JOSA*, Vol. 58, No. 9, 1256–1259, 1968.
3. Wiener, O., "Stehende lichtewellen und die schwingungsrichtung polarisierten lichtes," *Wied. Ann.*, Vol. 40, 203–243, 1890.
4. Connes, P., "Silver salts and standing waves: The history of interference colour photography," *J. Opt.*, Vol. 18, No. 4, 147–165, 1987.
5. Smith, D. W., D. Cotter, and R. Wyatt, "Optical homodyne detection," *U. S. Patent Doc.*, No. 4977620, 1990.
6. Cotton, A., "Sur les ondes lumineuses stationnaires," *J. de Phys.*, 4e série, Vol. 1, 689–708, 1902.
7. Leistner, K., "Über stehende lichtwellen in grosser entfernung von reflektierenden flächen," *Ann. d. Phys.*, Vol. 74, 325–345, 1924.
8. Schult, E., "Intensitätsmessungen an interferenzerscheinungen (nebst untersuchungen stehender lichtwellen)," *Ann. d. Phys.*, Vol. 82, 1025–1050, 1927.

Effects of Multipath Propagation and Measurement Noise in IEEE 802.11g WLAN Beacon for Indoor Localization

C. Sapumohotti, M. Y. Alias, and S. W. Tan
Multimedia University, Malaysia

Abstract— IEEE 802.11 Wireless Local Area Network (WLAN) beacon based indoor localization has gained much attention. However, there has been little investigation relating the beacon measurement to the underlying physical process. The WLAN beacon is usable for indoor location due to the correlation that it has with large scale phenomenon such as distance and obstacles such as walls. Random variations which do not correlate with the environment introduce uncertainty into location predictions. This paper analyzes the effect of two such random processes, namely multipath propagation and measurement noise.

1. INTRODUCTION

Global Positioning System (GPS) technology has become the de-facto standard for outdoor localization. However, GPS requires line of sight satellite signal which does not function well in indoor environment due to multipath signals. Indoor location information is highly useful for context aware applications. Recent proliferation of Wireless Local Area Network (WLAN) devices gives an opportunity to provide indoor localization by using radio maps generated from WLAN access point (AP) beacons.

Indoor localization based on IEEE 802.11 WLAN beacon measurement was first introduced in radio frequency (RF) based location and tracking (RADAR) system [1]. In RADAR, the information about the propagation environment was not considered and localization was done by matching the online measurements with offline calibration data using a variant of nearest neighbour classification. The evolution of this approach, which is named as location fingerprinting, was done by considering probabilistic models [2] for the radio fingerprint measurements and by considering motion models [2, 3] to capture user movement in a constrained map.

The usefulness of WLAN beacon based localization techniques depends on the correlation of beacon strength with the propagation environment. Apart from the propagation related issues, measurement noise may present in WLAN beacon measurement as well. Therefore, it is necessary to identify random processes that affect the beacon measurement and to determine how the propagation environment affects the beacon measurement.

In this paper, we simulate beacons in IEEE 802.11g network and evaluate how the multipath propagation effects the beacon measurement. We also present results from experimental data collected in an anechoic chamber for modelling the noise process in an IEEE 802.11g network due to beacon measurement noise. Understanding the effects of measurement noise and multipath propagation on WLAN beacon measurement will significantly improve the efficiency of indoor localization systems.

2. EFFECTS OF MULTIPATH PROPAGATION

The simulation scenario given in Figure 1 is a large room with dimensions of $10\,\mathrm{m} \times 20\,\mathrm{m}$. The AP is placed in a fixed location and the client is moved in a straight line away from the AP with an increment of 5 cm. The AP has a transmit power of 17 dBm. The direct path and reflections from the four walls creates the multipath channel. The reflections from the ceiling and the floor have been ignored as the dipole antennas considered will significantly attenuate the signal paths that highly deviate from the antenna broadside.

In Figure 1, path d_0 represents the direct path and paths d_1 to d_4 represent reflections from wall w_1 to w_4. The power of each path is calculated using the free space path loss equation. The arrival time relative to the direct path is calculated by taking the distance difference from direct path and dividing it by speed of light.

In order to calculate the power of multipath signal, it is necessary to convert individual paths into voltage signals with magnitude related to their power before summing them up. The voltage magnitudes of the individual multipath are expressed relative to the direct path. The power of the multipath signal is calculated relative to the direct path signal and the power of the direct path is

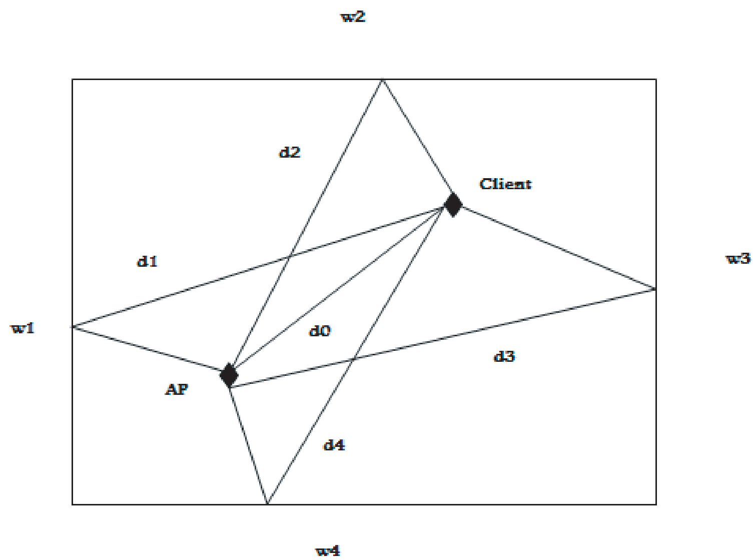

Figure 1: The simulation scenario and multipath signals.

added to get the absolute value. The steps for calculating the power of multipath signal is given below.

Let V_i, P_i, PL_i, r_i, L_i, α_i and τ_i represent the voltage, power, path loss, length, other losses (reflection loss, body loss, antenna pattern), normalized voltage factor relative to direct path and time delay relative to direct path at the receiver due to path i, respectively. The multipath voltage is given by V_{mp}. The transmit power of the AP is P_{ap}. Power X expressed in dBm is given as $X_{,\text{dBm}}$.

$$P_{i,\text{dBm}} = P_{ap,\text{dBm}} - (PL_{i,\text{dBm}} + \sum L_{i,\text{dBm}}) \tag{1}$$

$$PL_{i,\text{dBm}} = 32.4 + 20\log_{10}(2400) + 20\log_{10}(r_i/1000) \tag{2}$$

Assuming L_i is negligible for the 4 reflections and direct path, the power of path i can be given as

$$P_{i,\text{dBm}} = P_{ap,\text{dBm}} - PL_{i,\text{dBm}} \tag{3}$$

From Equation (3), we can calculate the power of path i relative to direct path as

$$\frac{P_i}{P_0} = 10^{(PL_{0,\text{dBm}} - PL_{i,\text{dBm}})/10} \tag{4}$$

Let the normalized voltage factor (voltage of path i relative to the direct path) is given as

$$\alpha_i = \frac{V_i}{V_0} \tag{5}$$

Since power is proportional to the square of voltage, combining Equations (4) and (5) gives

$$\alpha_i = \sqrt{10^{PL_{0,\text{dBm}} - PL_{i,\text{dBm}}/10}} \tag{6}$$

Using the normalized voltage factor, α_i and path delay τ_i, all the multipath components can be described relative to the direct path. Multipath signal and direct path signal are given by S_{mp} and S_0, respectively.

$$S_{mp} = \sum_{i=0}^{4} \alpha_i S_0(t - \tau_i) \tag{7}$$

The AP sends beacon frame advertising information about the AP with a period of 100 ms. The start of the frame includes a short preamble which is used for frequency and timing synchronization and a long preamble. The beacon Receive Signal Strength Indicator (RSSI) is computed using the long preamble. The IEEE 802.11g Extended Rate Physical-Layer Orthogonal Frequency Division Multiplexing (ERP-OFDM) mode uses 64 subcarriers with 48 data subcarriers and 4 pilot subcarriers. The power of multipath signal relative to direct path signal P_r is calculated in discrete time domain by simulating the OFDM long preamble and the multipath channel.

The long preamble is a Binary Phase Shift Keying (BPSK) modulated signal. The baseband time domain representation of this signal, $S_{bb}(t)$ is obtained by performing Inverse Fast Fourier Transform (IFFT) of length 64 on the frequency domain representation of this signal $P(f)$ and adding a cyclic prefix which is 1/4 of the IFFT sequence. $I_{pb}(t)$ is the in phase pass band signal, $Q_{pb(t)}$ is the quadrature pass band signal. Pass band signals are obtained by modulating carrier at frequency f_c using $S_{bb}(t)$ [4, 5].

$$I_{pb}(t) = \mathrm{real}(S_{bb}(t)) \times \cos(2\pi f_c t) \tag{8}$$
$$Q_{pb}(t) = \mathrm{imag}(S_{bb}(t)) \times \sin(2\pi f_c t) \tag{9}$$

P_r is calculated as a ratio of 2 summations carried out in discrete time. t_s is the OFDM symbol time including the cyclic prefix = 4 µs, t_{cp} = duration of the cyclic prefix = 0.8µs, t_1 = direct path arrival time. I and Q are orthogonal signals. I_{mp} and Q_{mp} are calculated by combing individual paths using Equation (7).

$$P_r = \frac{P_{mp}}{P_0} = \frac{\sum_{t=t_1+t_{cp}}^{t=t_1+t_s} I_{mp}^2(t) + Q_{mp}^2}{\sum_{t=t_1+t_{cp}}^{t=t_1+t_s} I_0^2(t) + Q_0^2} \tag{10}$$

P_r expresses the power of multipath signal P_{mp} relative to direct path. In order to obtain absolute power of multipath signal, power of direct path (P_0) is added to P_r. This is given in Equation (11).

$$P_{mp,\mathrm{dBm}} = P_{0,\mathrm{dBm}} + 10\log_{10}(P_r) \tag{11}$$

The simulation results given in Figure 2 shows that multipath variance significantly increases after the distance between AP and client increases beyond 5 m. At close proximity, the direct path power is significantly higher compared to reflections. At large distances the power of reflection paths approach the power of direct path creating significant multipath fading.

3. CHARACTERIZATION OF BEACON MEASUREMENT NOISE

To isolate beacon measurement noise, it is necessary to remove any propagation related factors. This is particularly necessary since there are quite a lot of interference sources at 2.4 GHz. For example, other wireless APs and devices such as microwave ovens. The following experiment was conducted in an anechoic chamber. An anechoic chamber is able to remove multipath propagation and unwanted interference from any outside signal source. Two APs: one Cisco WAG160N wireless

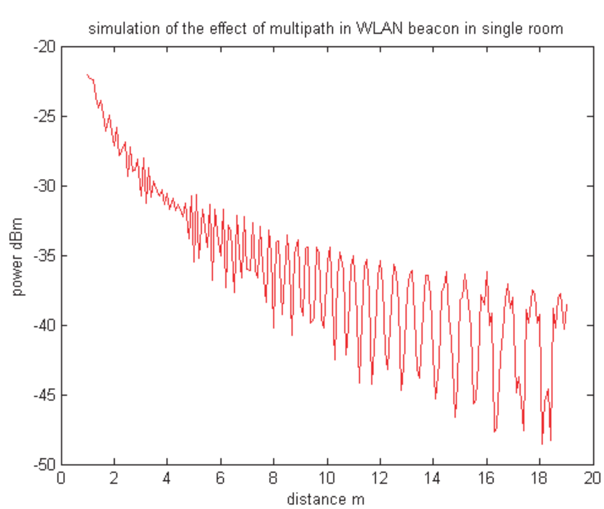

Figure 2: power of multipath signal vs. distance from AP.

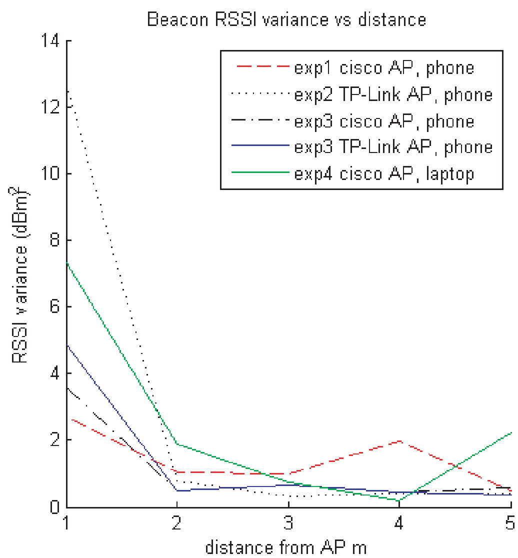

Figure 3: Beacon RSSI variance versus distance.

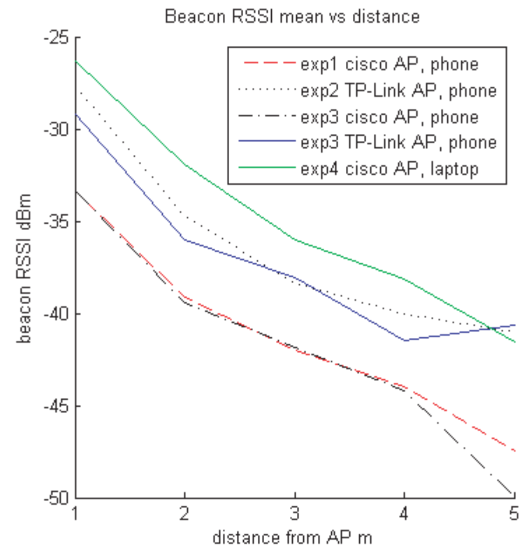

Figure 4: Beacon RSSI mean versus distance.

router operating in 802.11g mode and one TP-Link TL-WR340G wireless router were used. Two client devices, namely an LG optimus1 P500 Android phone and a Dell laptop with Intel wireless 3945 G card were used. The android phone and the Dell laptop are able to collect unique beacon reading at every 1 s. The APs were placed 6 m from each other.

The following experiments were conducted. 150 beacons were captured by client device for each point.

1. exp1, Turn on only the Cisco AP and collect beacons using the phone.
2. exp2, Turn on only the TP-Link AP and collect beacons using the phone.
3. exp3, Turn on both Cisco AP and TP-Link AP and collect beacon using the phone.
4. exp4, Turn on only the Cisco AP and collect beacons using the laptop.

Four sets of data at distances of 1 m, 2 m, 3 m, 4 m and 5 m away from the AP were collected to identify the dependency of measurement noise due to receiver power, AP type, client devices and interference level. The variance of the beacon signal strength is a good representation of the measurement noise process.

Figure 3 indicates that the variance is very high at a distance of 1 m from the AP for all data sets. This might be due to receiver saturation at high power levels. The variance levels off to less than 1 dBm for almost all cases when the distance increases above 2 m, a noise variance of 2 dBm could be a very general value to model the measurement noise variance for all cases in which distance separation is above 1 m. According to Figure 4, different combinations of devices have different mean RSSI, this can be explained by considering the fact that AP are transmitting at different power levels and the equipment use antennas of different gains. There is no relationship of the measurement noise with interference. The 802.11g physical layer protocol will not transmit a beacon if it senses a transmission. Thus, it is very unlikely that two APs which can hear each other would transmit at the same time. However, interference might come in to play in a hidden node scenario, where a client can hear two beacons but the AP cannot hear each other. Even in such a scenario a collision is unlikely since the preamble only lasts for 16 µs while the beacon transmission rate is done every 100 ms.

4. CONCLUSIONS

The paper identifies the main contributors for uncertainty in WLAN beacon when used for indoor localization. The random power variation due to multipath propagation has a low variance up to 5 m from the access point when multipath signal power is much less compared to the direct path, but increase significantly with distance when the power of reflection paths approaches the power of direct path. The random variation due to measurement noise has a very high variance near the AP at 1 m range; but decrease below 2 dBm as the power level decreases. These parameters are useful for modeling the random noise process in beacons and in building more effective indoor localization systems in the future.

ACKNOWLEDGMENT

The authors would like to thank Ministry of Science, Technology & Innovation (MOSTI) for supporting this work.

REFERENCES

1. Bahl, P. and V. N. Padmanabhan, ”RADAR: An in-building RF-based user location and tracking system,” *Proc. IEEE Conf. Comput. Commun.*, 775–784, 2000.
2. Honkavirta, V., T. Perala, S. Ali-Loytty, and R. Piche, “A comparative survey of WLAN location fingerprinting methods,” *6th Workshop on Positioning, Navigation and Communication, WPNC*, 243–251, March 19–19, 2009.
3. Lim, Y.-X., “Efficient wireless location estimation through simultaneous localization and mapping,” Ph.D. Thesis, Georgia Institute of Technology, May 2009.
4. IEEE WLAN standard, “IEEE 802.11-2007,” http://standards.ieee.org/getieee802/download/802.11-2007.pdf.
5. Heiskala, J. and J. Terry, *OFDM Wireless LANs: A Theoretical and Practical Guide*, Sams Publishing, 2002.
6. Ulaby, F. T., *Fundamentals of Applied Electromagnetics*, Prentice-Hall, 2001.
7. Proakis, J. G. and M. Salehi, *Digital Communications*, McGraw-Hill, 2008.
8. Rappaport, T. S., *Wireless Communications: Principles and Practice*, Prentice-Hall, 2002.

Correlation Analysis on the Specific Absorption Rate (SAR) between Metallic Spectacle and Pins Exposed from Radiation Sources

M. H. Mat, M. F. B. A. Malek, S. I. Syed Hassan, M. S. Zulkefli, and S. H. Ronald
School of Electrical Systems Engineering
Universiti Malaysia Perlis, Kangar, Perlis 01000, Malaysia

Abstract— In this paper, the Specific Absorption Rate (SAR) inside the head due to metallic straight pins and spectacles is investigated. The finite integration in time domain technique (FIT) computer simulation using CST Microwave Studio was used in this investigation. Two sets of dipole antennas operated at 900 MHz and 1800 MHz for GSM application were used in the simulation model represent as radiation sources from MCE. In parametric studies the optimum dipole location is selected for all simulations and only varying both of the pin length and its horizontal separation distance between the head. The results compared with the head worn metallic spectacle.

1. INTRODUCTION

Nowadays, with more open source for mobile applications listed in market, mobile communication equipment (MCE) used in frontal of the face is becoming increasing significantly. Numerous studies have examined the interaction between the electromagnetic fields radiated by the antenna that may also couples with metallic objects and the results seem to suggest that metallic objects could increase the SAR [1–4]. Nowadays, high demand of the mobile communications equipment (MCE) that adopting a larger touch screen has become increasingly. Thus, it brings a new impact for scientists and researchers to study specific absorption rate (SAR) and antenna performances in details. With the latest and free applications in markets, usages of the MCE lead the users to spent most of their time by holding it in front of the face rather than holding it near to the ear. Even though it was reported that specific absorption rate was below the safe limits, however these value can change. Hence, it is needed to study consistently on changes of SAR since many reported that the metallic objects can alter the SAR in the head and in particularly in the eyes [1].

Bernardi [5] considered the eyes to be particularly sensitive organs due to their proximity to the surface of the head and the relatively low levels of blood flow when compared to other regions of the body. Dimbylow [6] also stresses the vulnerability of the eyes as they have a tendency to accumulate damage and cellular debris. In the same area Cooper [7], modeled a geometric head, and Bernardi [8] investigated an anatomical head, irradiated by simple dipoles positioned near metallic walls. Both found that metallic walls could increase the power absorbed in the head. Similarly Cooper [9] considered metal implantations inside the head and found that they increased the SAR in the surrounding region. These papers show that metal objects close to biological matter may increase SAR in that matter.

The RF radiation is incident on the user face. In order to minimize the heating caused in the head while operating the MCE by RF energy absorption, all MCE must meet maximum transmit power regulations. SAR is used as the method of evaluating energy absorption rates in tissue and spatially averaged SAR limits have been adopted worldwide, For example, the SAR limit specified in IEEE C95.1 : 1999 is 1.6 W/kg in a 1 g averaging mass while that specified in ICNIRP guidelines is 2 W/kg in a 10 g averaging mass [10]. In general, there are various parameters such as radiation patterns of the antenna, antenna positions relative to the human body, radiated power, and antenna types can influenced the SAR value [11].

2. MODEL AND METHODOLOGY

To evaluate SAR in frontal of the face, SAM (Specific Anthropomorphic Mannequin) head phantom provided by CST Microwave Studio® (CST MWS) employed in simulation. In this simulation the dipole antenna was used as a radiation source. The antennas carefully chose to operate at 900 MHz and 1800 MHz. Theory and practice have proven that the transmitting and receiving of antenna achieved the highest conversion efficiency when the antenna length is approximately 1/4 of the wavelength of radio signals. Therefore, the antenna length is set to $\lambda/4$ in this study. In order to

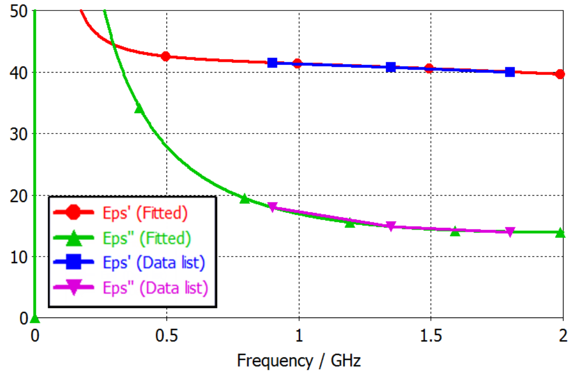

Figure 1: Dispersive permittivity of the liquid in SAM phantom head for simulation.

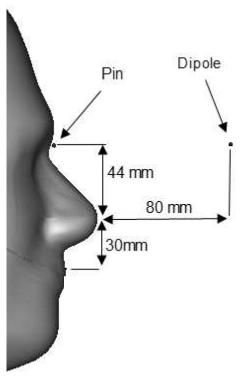

(a)

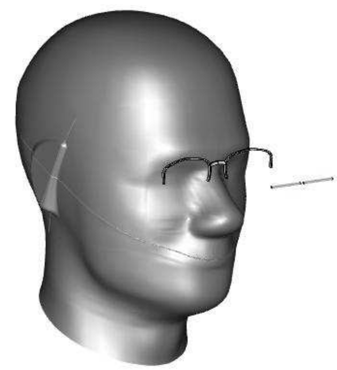

(b)

Figure 2: Diagram of (a) pin and dipole location in parametric study. (b) SAM phantom head with spectacle.

accurately characterize the performance over broad frequency range, dispersive models for all the dielectrics were adopted during the simulation. Fig. 1 shows the dispersive permittivity of the HSL in SAM phantom head for simulation.

Specific absorption (SA) is defined as the quotient of the increment energy (dE) absorbed by an incremental mass (dm) contained in a volume (dV) of a given density (rho). The SA is express in units of joules per kilogram (J/kg). However, SAR is defined as the rate of energy (dE) absorbed or dissipated in an incremental mass (dm) contained in an incremental volume (dV) of a given density (rho). Mathematically, SAR can be expressed in watt per kilogram (W/kg) as

$$SAR = \frac{d}{dt}\left(\frac{dE}{dm}\right) = \frac{d}{dt}\left(\frac{dE}{\rho dV}\right) \tag{1}$$

The interaction of energy from communications enabled device (MCE) into the head is a topical area of research. In order to allow meaningful comparisons to be made between different types of devices, a set of international standards have evolved that suggest maximum levels of radio frequency energy into humans and experimental techniques for modeling and measurement. A typical example is that of the IEEE head phantom that is commonly used to benchmark levels of energy delivered by mobile phones to the ear of a representative phantom.

3. RESULTS

Parametric studies were conducted to find the optimum pin length and location for causing maximum SAR in the head at both 900 MHz and 1800 MHz. The results from parametric studies over 1 gram of the maximum SAR at 900 MHz and 1800 MHz are given in Fig. 3.

The results for all simulations were normalized to 1 Watt transmitted power and assumed in worst case scenario where the mobile phone antenna require more power when operated at longer distance from base stations. The results were agreed without the pin, maximum SAR_{1g} was located inside the nose and with the pin it was located directly behind the wire. The maximum $\mathrm{SAR}_{1\mathrm{g}}$

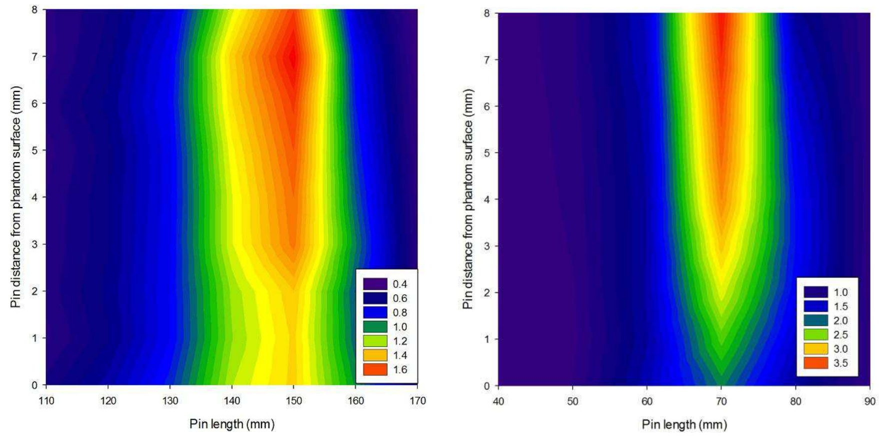

(a) (b)

Figure 3: Simulated SAR_{1g} at (a) 900 MHz and (b) 1800 MHz with increasing pin length and distance from shell.

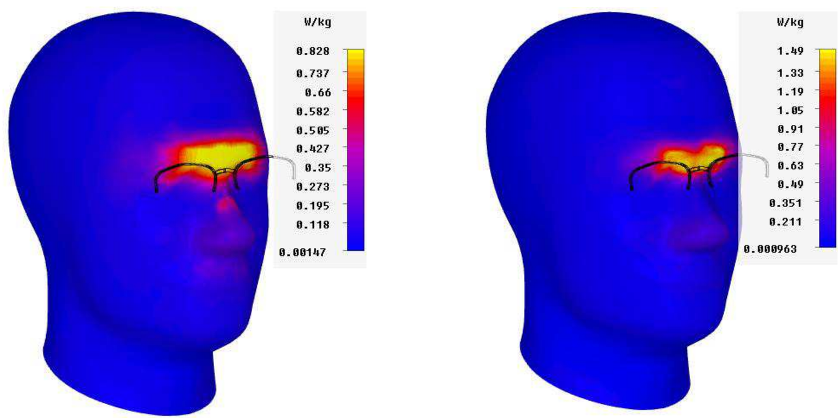

(a) (b)

Figure 4: Simulated (a) SAR_{1g} and (b) SAR_{10g} at 900 MHz.

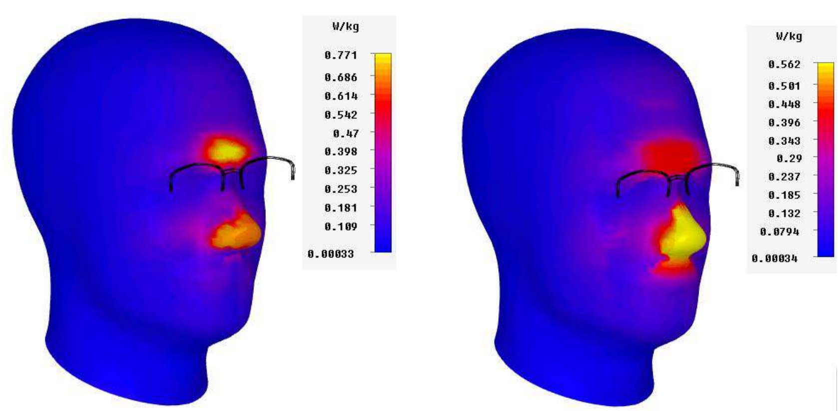

(a) (b)

Figure 5: Simulated (a) SAR_{1g} and (b) SAR_{10g} at 1800 MHz.

generally occurs at the tip of the nose and it was also found that the metallic objects orientated perpendicular to the dipole had negligible effect over the entire frequency range considered. Therefore, in these studies, dipoles and metallic objects were aligned in parallel.

The simulated values of maximum SAR_{1g}, so as the maximum SAR_{10g} values, in both frequencies, are shown in Figs. 4 and 5. It can be appreciated that maximum SAR_{10g} at 1800 MHz values are far few compare to the SAR_{10g} at 900 MHz. Moreover at 900 MHz, maximum plot of averaging SAR was located behind the spectacle.

4. CONCLUSION

The FIT method was used to investigate the relation of the metallic spectacle and metallic pin on SAR in SAM phantom head with. The frontal radiation of 900 MHz and 1800 MHz couple with metallic objects and resonate. When the length of metallic pin is approximately equal to the length of dipole, the largest SAR was plotted behind the pin around eye brow and nose. The optimum pin length for dipole antenna operated 900 MHz and 1800 MHz are from 135 mm to 160 mm and from 65 mm to 80 mm respectively. Authors suggest using a straight metallic pin as configured in present paper to investigate the energy absorption in human eye from frontal radiation sources. This strongly agreed as results found the length of half rim metallic spectacle could act as amplifier if its length is approximately same to the antenna length at resonate frequency. The SAR expected could be higher if the spectacle length is reduces around 65 mm to 75 mm. However this is not possible since the spectacle size must match with SAM phantom head as in present paper.

The results presented here may find potential application in wireless communication field in evaluating the power absorption in a bio-medium and an anatomical study for evaluating SAR in the human face for the consumer awareness.

REFERENCES

1. Panagamuwa, C. J., et al., "A study of the effects of metallic pins on SAR using a specific anthropomorphic mannequin (SAM) head phantom, in antennas and propagation," *The Second European Conference on EuCAP*, 2007.
2. Whittow, W. G. and R. M. Edwards, "A study of changes to specific absorption rates in the human eye close to perfectly conducting spectacles within the radio frequency range 1.5 to 3.0 GHz," *IEEE Transactions on Antennas and Propagation*, Vol. 52, No. 12, 3207–3212, 2004.
3. Stergiou, K., et al., "Effects of metallic semi-rimmed spectacles on SAR in the head from a 900 MHz frontal dipole source," *Antennas & Propagation Conference LAPC*, Loughborough, 2009.
4. Whittow, W. G., et al., "Effect of tongue jewellery and orthodontist metallic braces on the SAR due to mobile phones in different anatomical human head models including children," *Antennas and Propagation Conference*, Loughborough, 2008.
5. Bernardi, P., M. Cavagnaro, S. Pisa, and E. Piuzzi, "SAR distribution and temperature increase in an anatomical model of the human eye exposed to the field radiated by the user antenna in a wireless LAN," *IEEE Trans. Microwave Theory Tech.*, Vol. 46, No. 12, 2074–2082, Dec. 1998.
6. Dimbylow, P. J. and S. M. Mann, "SAR calculations in an anatomically realistic model of the head for mobile communication transceivers at 900-MHz and 1.8-GHz," *Phys. Med. Biol.*, Vol. 39, No. 10, 1537–1553, 1994.
7. Cooper, J. and V. Hombach, "The specific absorption rate in a spherical head model from dipole with metallic walls nearby," *IEEE Trans. Electromagnet. Compat.*, Vol. 40, No. 4, 377–382, Nov. 1998.
8. Bernardi, P., M. Cavagnaro, and S. Pisa, "Evaluation of the SAR distribution in the human head for cellular phones used in a partially closedenvironment," *IEEE Trans. Electromagn. Compat.*, Vol. 38, No. 3, 357–366, Aug. 1996.
9. Cooper, J. and V. Hombach, "Increase in specific absorption rate in humans from implantations," *Electron. Lett.*, Vol. 32, No. 24, 1996.
10. Fung, L. C., S. W. Leung, and K. H. Chan, "An investigationof the SAR reduction methods in mobile phone applications," *2002 IEEE International Symposium on EMC*, Vol. 2, 656–660, Aug. 2002.
11. Jung, M. and B. Lee, "SAR reduction for mobile phones based on analysis of EM absorbing material characteristics," *2003 IEEE International Symposium on Antennas and Propagation*, Vol. 2, 1017–1020, Jun. 2003.

A Internal Planar Antenna Design for WiMAX Mobile Handset

Cheng-Hung Lin[1], **Wei-Hung Liu**[1], **Kwong-Kau Tiong**[1], **and Guan-Yu Chen**[2]

[1]Department of Electrical Engineering, National Taiwan Ocean University, Taiwan
[2]Department of Electronic Engineering, National Taipei University of Technology, Taiwan

Abstract— In recent years, the MIMO (Multiple Input, Multiple Output) is utilized to enhance the performance of wireless communication systems. To design several antennas in the same ground plane for getting the benefit of MIMO system is required to have high isolation property. Moreover, the antennas are strongly coupled with each other. It is quite challenge for antennas to obtain good isolation when the two antennas are located closely due to the limited antenna space in a mobile handset.

In this paper, we propose the compact antennas design for WiMAX mobile handset application. The proposed antennas are using the inverted F antennas (IFAs) structure [1] In the first study, the locations of two antennas are at the difference corners on the top of the mobile handset. The compact area of the proposed antenna is 20 mm × 10 mm × 6 mm. And the PCB is FR4 substrate and the dimension is 120 mm × 60 mm × 0.8 mm. The two antennas show the operating bandwidth of about 200 MHz in 2.6 GHz respectively for covering the WiMAX bands.

To miniaturize the antenna area in a mobile handset, the two antennas are placed closely on the top of the mobile handset In these circumstances, the two antennas have poor isolation with each other. In order to enhance the performance, the two IFAs with a common grounding pad structure are studied.

The L-type area of the proposed antenna is used on the top side of the mobile handset. The antenna with a common shorting pad is capable of covering the bandwidth of 2.5–2.7 GHz for WiMAX operation The common shorting pad design effectively reduces the mutual coupling between the two antennas. A good isolation and low correlation coefficient between the antennas are obtained by utilizing the common shorting pad design. All of the performances including return loss, antenna gain, and current distribution tell that the proposed antenna is proper to applied in the MIMO system of WiMAX operation.

1. INTRODUCTION

WiMAX (Worldwide Interoperability for Microwave Access) is developed by the IEEE 802.16 standard which wireless communication technology can support high data rate and reliability of the connection and wide coverage area. The standard frequency for WiMAX operation is allocated at 2.5–2.7 GHz. In order to increase the data rates required in the communication and reduce the deep fading caused by the multi-path propagating environment, the MIMO (Multiple Input, Multiple Output) system which consist in increasing the number of antennas in the design [2] The integration of several antennas in a limited space of the mobile handset while keeping a good isolation between radiators is a challenge [3].

A compact antenna design is required for mobile handset. However, the antenna with compact feature still has to achieve good performances. The Inverted F Antenna (IFA) is a structure with a shorting pad to minimize the size of the antenna and to achieve matching impedance [4]. In addition, by changing and adjusting the position of feed point and shorting pad, the impedance matching can be achieved [5]. The purpose of this research is to design a compact antenna that can be used for 2.5–2.7 GHz of WiMAX operation.

To achieve a MIMO system, a multi-antenna structure is developed by increasing the number of antennas. A miniature IFA (Inverted-F Antenna) is at first designed and positioned at the corner of a 60 mm × 120 mm PCB (Printed Circuit Board) [6]. Then, another identical IFA is placed at the other corner of the first antenna. To keep a good isolation between the antennas the common shorting technique is used and then adjusted the radiator to the WiMAX operation. The antenna design of MIMO system is simulated, fabricated and measured.

2. ANTENNA DESIGN

In this paper, the design of a MIMO system operated bands of 2.5–2.7 GHz is proposed. A second identical IFA is placed closely to the first IFA (Fig. 1(a)). The left side is the antenna 1; the right side is the antenna 2. The distance between the two antennas is adjusted. The measured

S-parameters of this structure are presented in Fig. 1(b). It shows that the system exhibits a return loss better than -6 dB in the entire band. The maximum mutual coupling is about -8.5 dB. This performance is not sufficient to achieve a good MIMO system because the total efficiency and the independence of the signals received by each of the antennas also rely on this scattering parameter. This is why we used the common shorting technique to increase isolation at the required frequency.

The proposed design was fabricated and tested. A photo of the fabricated prototype is also shown in the Fig. 2(a). By using common shorting pad structure to obtain the good isolation is proposed. The associated simulated measured S-parameters of two antennas are presented in the Fig. 2(b). The common shorting structure gives the good isolation at the frequency OF 2.5–2.7 GHz. The advantage is that the new system covers the WiMAX bands. This structure has been fabricated and simulated in the Fig. 3. The IFA is connected to a feeding system using coaxial probe. The antenna is made of copper and placed on the plastic carrier.

3. MEASURED RESULTS

By adjusting the gap between two antennas more close, the gain and isolation are getting worse. In the 20 mm gap, the isolation between two antennas is 8.5. the gain of antenna 1 is 1.5 dBi and antenna 2 is 1.4 dBi; the efficiency of antenna 1 is 57% and antenna 2 is 56%. The result is shown in the Table 1. The current distribution is shown is the Fig. 3. Referring to the geometry of the proposed antenna in Fig. 2(a), the most current is located on the a1 and a2. The lengths of the planar antenna from g1 to a1 and g2 to a2 are about 25 mm which are corresponded to 0.25

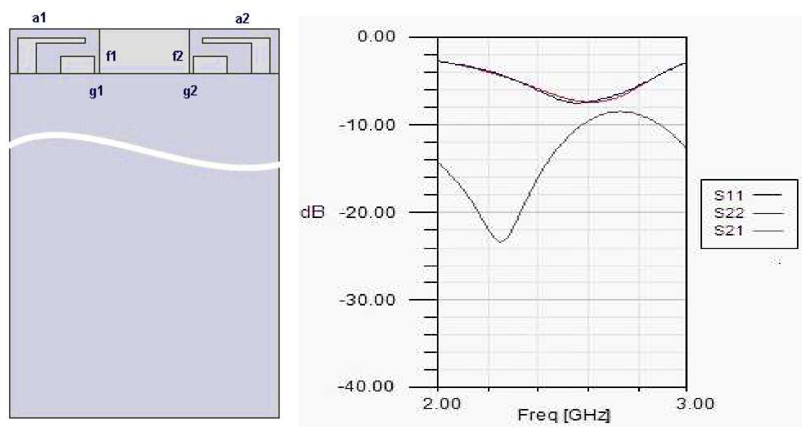

(a) (b)

Figure 1: (a) Geometry of the proposed antennas. (b) Measured S-parameters of the proposed antennas.

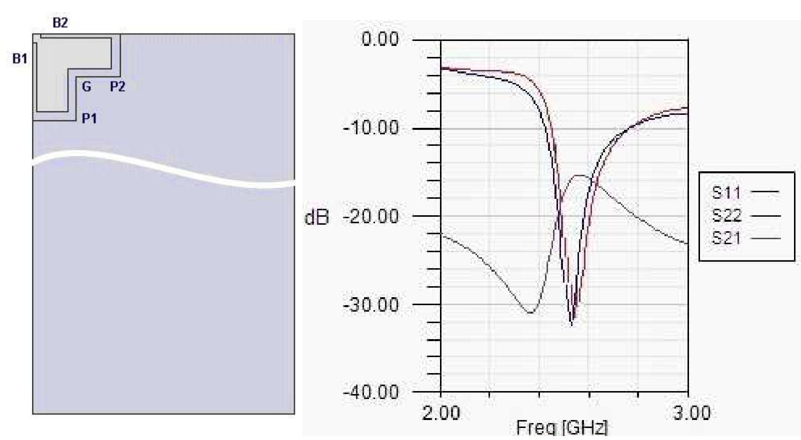

(a) (b)

Figure 2: (a) Geometry of the proposed common feeding pad antenna. (b) Measured S-parameters of the proposed common feeding pad antenna.

Table 1: Measured antenna gain of antenna 1 and antenna 2.

Frequency (GHz)	2.6	2.6	2.6
Gap (mm)	20	15	10
Measured Antenna 1 Gain (dBi)	1.5	1.4	1.1
Measured Antenna 1 Efficiency (%)	57	55	52
Measured Antenna 2 Gain (dBi)	1.4	1,2	0.9
Measured Antenna 2 Efficiency (%)	56	52	50
Isolation	8.5	7.9	7.2

Table 2: Measured antenna gain of antenna 1 and antenna 2.

Frequency (GHz)	2.6
Antenna 1 Gain (dBi)	2.1
Antenna 1 Efficiency (%)	61
Antenna 2 Gain (dBi)	2.3
Antenna 2 Efficiency (%)	64
Isolation	15.5

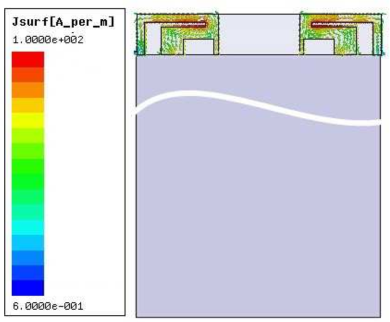

Figure 3: The current distributions excited on the surface of the antennas in the 2.6 GHz.

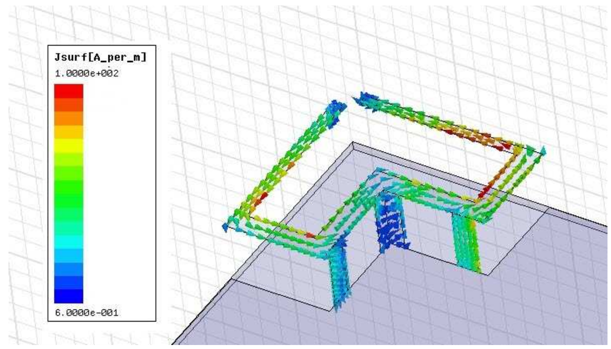

Figure 4: The current distributions excited on the surface of the antennas in the 2.6 GHz.

wavelength of the 2.5 GHz.

By adjusting the two arms of the antenna the gain and isolation of the required frequency are measured. The antenna has a bandwidth of about 200 MHz (6-dB return loss). The bandwidth can be easily to cover WiMAX operation. The measured antenna gain and radiation efficiency are shown in Table 2. The antenna gain in the band is about 2 dBi and the efficiency is about 60%, and is easily covers WiMAX operation. The current distribution is shown is the Fig. 4. Referring to the geometry of the proposed antenna in Fig. 2(a), the most current is located on the B1 and B2. And the lengths of the planar antenna from G to P1 to B1 and G to P2 to B2 are about 25 mm which are corresponded to 0.25 wavelength of the 2.6 GHz. The simulated results are evaluated by using Ansoft HFSS [7]. From the experiments, there is a good agreement between the measurement and simulation.

4. CONCLUSION

In this paper, a compact multi-antenna system antenna for WiMAX mobile handset having low isolation has been presented. The miniaturized antenna is consisted of the antenna placed in the corner of the PCB with a common shorting pad for the MIMO system of WiMAX operation. The common shorting pad structure is used to achieve a good isolation between the two antenna ports. This method allows achieving an isolation better than 15 dB in the WiMAX operation. This system is suitable for the MIMO system WiMAX operation.

ACKNOWLEDGMENT

The authors acknowledge the Antenna and EMC Department of HTC, Taiwan, for sport the wireless technique and measurement environment.

REFERENCES

1. Balanis, C. A., *Antenna Theory*, John Wiley & Sons, Inc., 2005.
2. Gao, V., X. D. Chen, Z. N. Ying, and C. Parini, "Design and performance investigation of a dual-element PIFA array at 2.5 GHz for MIMO terminal," *IEEE Trans. Antennas Propag.*, Vol. 55, No. 12, 3433–3441, Dec. 2007.
3. Wu, T.-Y., S.-T. Fang, and K.-L. Wong, "Printed diversity monopole antenna for WLAN operation," *Electronics Letters*, Vol. 38, No. 25, 1625–1626, Dec. 2002.

4. Wong, K. L., *Planar Antennas for Wireless Communication*, John Wiley & Sons, Inc., 2003.
5. Ying, Z. and D. Zhang, "Study of the mutual coupling, correlations and efficiency of two PIFA antennas on a small ground plane," *IEEE Antennas and Propagation Society International Symposium*, Washington, USA, Jul. 2005.
6. Kuo, Y., T. Chiou, and K. Wong, "A novel dual-band printed inverted-F antenna," *Microwave and Optical Technology Letters*, Vol. 31, No. 5, 353–355, Dec. 5, 2001.
7. Ansoft Corporation HFSS, available at: http://www.ansoft.com/.

A New Proof of the Non-constancy of Speed of Light in Vacuum and a Simple Solution for the Damped Wave Equation with a Moving Mirror Boundary (Part I)

Namık Yener
Technical Education Faculty, Kocaeli University, Izmit, Kocaeli 41380, Turkey

Abstract— A new proof of the non-constancy of speed of light in vacuum is obtained in the process of solving the damped wave equation with a mirror boundary in uniform rectilinear motion with respect to a simple, lossy medium and with specific conditions for the other boundary, using Laplace transform. Lorentz transformation is also needed in the proof. However because of the need to assign different speeds of light in vacuum to the two moving media, the resulting solution has further to be stretched in time, in addition to the hyperbolic rotation of the Lorentz transformation. The existing methods in literature to solve the involved damped wave equation are employed and a simple solution is proposed when the boundary conditions are of a special class. In the solution Laplace transform technique is used to convert the partial differential equation into an ordinary one. The uniform rectilinear motion of the mirror boundary and the particular type of conditions treated for the other boundary, permit a solution by this technique. The presentation of the work is organized as a series of three papers with the same title but with an extension in the title as Part (I), Part (II) and Part (III). In Part (I) which is the present paper, the moving mirror boundary condition is imposed and the new proof for the non-constancy of speed of light in vacuum is introduced. In Part (II) different speeds of light in vacuum for K and K' are incorporated in the differential equation. In Part (III), an example is worked out that illustrates the ideas developed in the first two parts.

1. INTRODUCTION

Analytical methods to solve the wave equation and the damped wave equation both with a moving boundary have been studied [1, 2]. In the present work Laplace transform technique is used to solve the latter one of the two problems, but we implement the boundary condition of vanishing tangential electric field on the moving mirror. For this condition we must obtain the tangential electric field vector in the moving coordinate system of the boundary. This requires determination of the magnetic flux density and hence solution of a second differential equation coupled to the damped wave equation. This distinguishes the problem at hand for this work from similar ones studied in the literature.

It has been proved by the author in a series of articles that the principle of the constancy of speed of light in vacuum which is one of the two postulates of Special Relativity Theory [3] is false. The first of these articles was based on the phase invariance principle, boundary conditions on surface of a perfect electric conductor moving half space (to which is attached the rest frame K') and Lorentz transformation (between K' and the laboratory frame K which is attached to a simple lossy medium) [4]. The present work was motivated by the need to obtain a proof for the same fact for the same media using a differential equation (the damped wave equation stemming from Maxwell's equations), the boundary conditions on surface of the perfect electric conductor moving half space, Lorentz transformation and covariance of Maxwell's equations. The Laplace transformation technique has been employed to convert the partial differential equation into an ordinary one. The uniform rectilinear motion of the mirror boundary and the particular type of conditions treated for the other boundary, permit a solution by this technique. It is demonstrated that the said problem transforms into a problem that is for fixed boundaries. The solution to this problem is known [5] with a simple method existing for a special class of boundary value functions [6]. A by-product of the solution procedure is the new proof of the non-constancy of speed of light in vacuum.

However in this work this solution is modified because of the need to assign different speeds of light in vacuum for K and K'. It is shown in [7], that this change amounts to a stretching of time additional to the hyperbolic rotation of the Lorentz transformation.

In [8] an example is presented to illustrate the ideas in this paper and [7].

2. IMPOSITION OF THE MOVING MIRROR BOUNDARY CONDITION AND A NEW PROOF FOR THE NON-CONSTANCY OF SPEED OF LIGHT IN VACUUM

The two dimensional damped wave equation that can be obtained from Maxwell's equations for an electric field vector of one component E_x is:

$$-\frac{1}{\mu\varepsilon}\frac{\partial^2 E_x}{\partial z^2}-\frac{1}{\mu\varepsilon}\frac{\partial^2 E_x}{\partial y^2}+\frac{\sigma}{\varepsilon}\frac{\partial E_x}{\partial t}+\frac{\partial^2 E_x}{\partial t^2}=0. \tag{1}$$

On the other hand the first Maxwell's equation is

$$\nabla\times\vec{E}=-\frac{\partial\vec{B}}{\partial t}. \tag{2}$$

For a velocity boost along Oz under the Lorentz transformation, the following chain differentiation rules apply. (Here we have adopted the notation $r=-v/c$, $\alpha=1/\sqrt{1-r^2}$ with v as the relative speed of K' with respect to K and c as the speed of light in vacuum. Also throughout the paper, primed quantities pertain to K' whereas unprimed ones to K.):

$$\frac{\partial}{\partial z}=\alpha\frac{\partial}{\partial z'}+\alpha\frac{r}{c}\frac{\partial}{\partial t'}, \tag{3a}$$

$$\frac{\partial^2}{\partial z^2}=\alpha^2\frac{\partial^2}{\partial z'^2}+(\alpha\frac{r}{c})^2\frac{\partial^2}{\partial t'^2}+2\alpha^2\frac{r}{c}\frac{\partial^2}{\partial z'\partial t'}, \tag{3b}$$

$$\frac{\partial}{\partial t}=\alpha rc\frac{\partial}{\partial z'}+\alpha\frac{\partial}{\partial t'}, \tag{3c}$$

$$\frac{\partial^2}{\partial t^2}=(\alpha rc)^2\frac{\partial^2}{\partial z'^2}+\alpha^2\frac{\partial^2}{\partial t'^2}+2\alpha^2 rc\frac{\partial^2}{\partial z'\partial t'}, \tag{3d}$$

$$\frac{\partial}{\partial y}=\frac{\partial}{\partial y'}. \tag{3e}$$

Then Equation (1) when observed from K' reads:

$$\begin{aligned}&-\frac{1}{\mu\varepsilon}\frac{\partial^2 E_x}{\partial y'^2}-\frac{\alpha^2}{\mu\varepsilon}\left[\frac{\partial^2 E_x}{\partial z'^2}+\left(\frac{r}{c}\right)^2\frac{\partial E_x}{\partial t'^2}+2\frac{r}{c}\frac{\partial^2 E_x}{\partial z'\partial t'}\right]+\frac{\sigma}{\varepsilon}\left(\alpha rc\frac{\partial E_x}{\partial z'}+\alpha\frac{\partial E_x}{\partial t'}\right)\\&+\alpha^2\left[(rc)^2\frac{\partial^2 E_x}{\partial z'^2}+\frac{\partial^2 E_x}{\partial t'^2}+2rc\frac{\partial^2 E_x}{\partial z'\partial t'}\right]=0.\end{aligned} \tag{4}$$

Setting $n^2=\mu\varepsilon c^2$ and taking the Laplace transform of (4) with respect to t' we obtain

$$\begin{aligned}&\frac{1}{\alpha^2}\frac{\partial^2 E_x}{\partial y'^2}+\left(1-n^2r^2\right)\frac{\partial^2 E_x}{\partial z'^2}+\left(\frac{s'}{c}\right)^2\left(r^2-n^2\right)E_x+2s'\left(\frac{r}{c}\right)\left(1-n^2\right)\frac{\partial E_x}{\partial z'}-rc\frac{\mu\sigma}{\alpha}\frac{\partial E_x}{\partial z'}-s'\frac{\mu\sigma}{\alpha}E_x\\&=\left(\frac{1}{c}\right)^2\left(r^2-n^2\right)\left[s'E_x(z',0)+\frac{\partial}{\partial t'}E_x(z',0)\right]+2\left(\frac{r}{c}\right)\left(1-n^2\right)\frac{\partial E_x(z',0)}{\partial z'}-\frac{\mu\sigma}{\alpha}E_x(z',0).\end{aligned} \tag{5}$$

Here we have used the same letter symbol for both the function and its Laplace transform. The same convention will be used throughout the paper. The Laplace transform on the other hand is defined as:

$$E_x(z',\,s')=\int_0^\infty E_x(z',\,t')\cdot\exp(-s't')dt'. \tag{6}$$

The general solution of (5) which is obtained by setting the right hand side of (5) equal to zero, is as below:

$$E_x=\sum_{p=1}^{2}A'_p(s')\exp(k'_{pz'}z'+k'_{py'}y'). \tag{7}$$

θ'_p being the angle of the wave vector with the Oz' axis, here $k'_{pz'} = k'_p \cos\theta'_p$, $k'_{py'} = k'_p \sin\theta'_p$ with $p = 1, 2$ are the roots of the characteristic equation associated with (5), namely the equation,

$$\begin{aligned}&\left(1-n^2r^2\right)\left(k'_p\cos\theta'_p\right)^2+\frac{s'^2}{c^2}\left(r^2-n^2\right)+2s'k'_p\cos\theta'_p\frac{r}{c}\left(1-n^2\right)\\&-rc\frac{\mu\sigma}{\alpha}k'_p\cos\theta'_p-s'\frac{\mu\sigma}{\alpha}+\frac{1}{\alpha^2}\left(k'_p\sin\theta'_p\right)^2=0.\end{aligned}\qquad(8)$$

This equation has the same form given in [9] for a moving lossy medium for an arbitrary value of θ'_p.

On the other hand from (2) we obtain,

$$-\frac{\partial\vec{B}}{\partial t}=\vec{j}\frac{\partial E_x}{\partial z}-\vec{k}\frac{\partial E_x}{\partial y}.\qquad(9)$$

Here $\vec{j}$ and $\vec{k}$ are the unit vectors of the Cartesian coordinate system of K. Using (3), from (9) we get:

$$-\frac{\partial\vec{B}}{\partial t}=-\left(\alpha rc\frac{\partial\vec{B}}{\partial z'}+\alpha\frac{\partial\vec{B}}{\partial t'}\right)=\vec{j}\left(\alpha\frac{\partial E_x}{\partial z'}+\alpha\frac{r}{c}\frac{\partial E_x}{\partial t'}\right)-\vec{k}\frac{\partial E_x}{\partial y'}.\qquad(10)$$

The $\vec{j}$ component of (10) reads:

$$-\alpha rc\frac{\partial B_y}{\partial z'}-\alpha\frac{\partial B_y}{\partial t'}=\alpha\frac{\partial E_x}{\partial z'}+\alpha\frac{r}{c}\frac{\partial E_x}{\partial t'}.\qquad(11)$$

Taking the Laplace transform of this equation with respect to t' and in it substituting (7) we get:

$$\begin{aligned}-\alpha rc\frac{dB_y}{dz'}-\alpha s'B_y\;=\;&\alpha k'_{pz'}\sum_{p=1}^{2}A'_p(s')\exp(k'_{pz'}z'+k'_{py'}y')\\&+\alpha\frac{r}{c}s'\sum_{p=1}^{2}A'_p(s')\exp(k'_{pz'}z'+k'_{py'}y')-\alpha\frac{r}{c}E_x(z',0)-\alpha B_y(z',0).\end{aligned}\qquad(12)$$

In (12) if we set the initial conditions equal to zero we find the following solution for the resulting differential equation:

$$B_y=\sum_{p=1}^{2}B'_p(s')\exp(k'_{pz'}z'+k'_{py'}y')+B'_3(s')\exp\left(-\frac{s'}{rc}z'\right).\qquad(13)$$

Here we disregard the last term because it involves a translation in time to the left on the time axis which is not acceptable for causal functions [10]. (Recall $r < 0$). The terms due to initial conditions in (12) also possess the same character when the associated non-homogeneous differential equation is considered. So they are disregarded as well. Also:

$$B'_1=-\frac{(k'_{1z'}+s'r/c)}{rck'_{1z'}+s'}A'_1,\qquad B'_2=-\frac{(k'_{2z'}+s'r/c)}{rck'_{2z'}+s'}A'_2.\qquad(14)$$

holds. Under the Lorentz transformation we also have,

$$E'_x=\alpha(E_x-vB_y).\qquad(15)$$

Using (7), (13), (14) and (15) one obtains:

$$\begin{aligned}E'_x\;=\;&\alpha\left[A'_1\left(1+v\frac{k'_{1z'}+s'r/c}{rck'_{1z'}+s'}\right)\exp\left(k'_{1z'}z'+k'_{1y'}y'\right)\right.\\&\left.+A'_2\left(1+v\frac{k'_{2z'}+s'r/c}{rck'_{21z'}+s'}\right)\exp\left(k'_{2z'}z'+k'_{2y'}y'\right)\right].\end{aligned}\qquad(16)$$

The boundary condition $E'_{x'}|_{z'=0} = 0$ on the surface of the perfectly conducting half space can now be expressed as:

$$A'_1 \left(1 + v\frac{k'_{1z'} + s'r/c}{s' + rck'_{1z'}}\right) = -A'_2 \left(1 + v\frac{k'_{2z'} + s'r/c}{s' + rck'_{2z'}}\right). \tag{17a}$$

This can be re-expressed as:

$$A'_1(s' + rck'_{2z'}) = -A'_2(s' + rck'_{1z'}). \tag{17b}$$

The two roots of (8) for k'_p must constitute the incident and reflected waves in the medium of incidence. We need the reflected wave along with the incident wave in order to be able to satisfy the boundary condition of vanishing tangential electric field component on the surface of the perfectly conducting moving half space.

Now owing to the boundary condition on the surface of the perfect electric conductor, the incident and reflected waves must have equal $k'_{py'}$ and same frequency s'. Otherwise the tangential components of incident and reflected wave electric field vectors cannot cancel each other on the boundary for all y' and for all t'. However the reflected wave must be such as to travel in opposite Oz' direction with the incident wave [11]. Hence

$$k'_1 \cos\theta'_1 = -k'_2 \cos\theta'_2, \tag{18}$$

has to hold. Then we have two solution sets stemming from each solution p of (8). First is the incident wave with ($k'_1 \cos\theta'_1$, $k'_1 \sin\theta'_1$, s') and the second is the reflected wave with ($-k'_1 \cos\theta'_1, k'_1 \sin\theta'_1$, s') in view of the above requirement of equality of $k'_{py'}$ and s' and (18). Both these sets yield the same squared wave number $k'^2_1 = k'^2_2$ as it is seen from the following equations.

$$(k'_1 \cos\theta'_1)^2 + (k'_1 \sin\theta'_1)^2 = k_1^{'2}, \tag{19a}$$

$$(-k'_1 \cos\theta'_1)^2 + (k'_1 \sin\theta'_1)^2 = k_2^{'2}. \tag{19b}$$

On the other hand because incident and reflected waves must satisfy the same dispersion Equation (8), Equation (19) can also be expressed as:

$$\begin{aligned}(k'_1 \cos\theta'_1)^2 + (k'_1 \sin\theta'_1)^2 &= -(r\alpha)^2(1-n^2)(k'_1\cos\theta'_1)^2 - \alpha^2\left(\frac{s'}{c}\right)^2(r^2-n^2)\\ &\quad -2\alpha^2 s'\frac{r}{c}k'_1\cos\theta'_1(1-n^2) - \alpha rc\mu\sigma k'_1\cos\theta'_1 + \alpha s'\mu\sigma = k_1^{'2}, \end{aligned}\tag{20a}$$

$$\begin{aligned}(-k'_1 \cos\theta'_1)^2 + (k'_1 \sin\theta'_1)^2 &= -(r\alpha)^2(1-n^2)(-k'_1\cos\theta'_1)^2 - \alpha^2\left(\frac{s'}{c}\right)^2(r^2-n^2)\\ &\quad +2\alpha^2 s'\frac{r}{c}k'_1\cos\theta'_1(1-n^2) + \alpha rc\mu\sigma k'_1\cos\theta'_1 + \alpha s'\mu\sigma = k_2^{'2}. \end{aligned}\tag{20b}$$

By virtue of the equality $k'^2_1 = k'^2_2$ one concludes in the light of (20), that $2\alpha^2 s'\frac{r}{c}k'_1\cos\theta'_1(1-n^2) + \alpha rc\mu\sigma k'_1\cos\theta'_1 = 0$, has to hold. In the case $k'_1\cos\theta'_1 \neq 0$ one then has,

$$\frac{2\alpha s'}{c^2}(1-\mu\varepsilon c^2) = -\mu\sigma, \tag{21}$$

which is equivalent to Equation (40) of [4]. Therefore one can argue that because s' is a free parameter, c appearing in (21) must necessarily depend on v. This is sufficient to conclude that the Special Relativity Theory is false because its postulate of the constancy of speed of light in vacuum (c) for different Galilean reference systems, fails. Therefore we have to choose different speeds of light in vacuum for K and K'.

3. CONCLUSION

A new proof has been proposed for the non-constancy of speed of light in vacuum. The first part of the solution method of the damped wave equation involved is given using techniques existing in the literature, namely the Laplace transform method and application of the boundary condition on the moving mirror boundary. The other steps are presented in [7]. A by-product of the solution procedure is the new proof of the non-constancy of speed of light in vacuum.

REFERENCES

1. Gaffour, L., "Analytical method for solving the one dimensional wave equation with moving boundary," *Progress In Electromagnetics Research*, Vol. 20, 63–73, 1998.
2. D'acunto, B., "Hyperbolic, parabolic singular perturbations in general regions," *Le Mathematiche*, Vol. XLVI, No. 1, 117–126, 1991.
3. Einstein, A., "On the electrodynamics of moving bodies," *The Principle of Relativity*, Dover, New York, 1952.
4. Yener, N., "On the non-constancy of speed of light in vacuum for different Galilean reference systems," *Journal of Electromagnetic Waves and Applications*, Vol. 21, No. 15, 2241–2255, 2007.
5. Stratton, J. A., *Electromagnetic Theory*, McGraw Hill, New York, 1941.
6. Yener, N., "A simple solution for the damped wave equation with a special class of boundary conditions using the Laplace transform," *Progress In Electromagnetics Research B*, Vol. 33, 69–82, 2011.
7. Yener, N., "A new proof of the non-constancy of speed of light in vacuum and a simple solution for the damped wave equation with a moving mirror boundary (Part II)," *Progress In Electromagnetics Research Symposium*, Kuala Lumpur, Malaysia, March 27–30, 2012.
8. Yener, N., "A new proof of the non-constancy of speed of light in vacuum and a simple solution for the damped wave equation with a moving mirror boundary (Part III)," *Progress In Electromagnetics Research Symposium*, Kuala Lumpur, Malaysia, March 27–30, 2012.
9. Ko, H. C., "On the relativistic invariance of the complex phase of plane waves," *Radio Science*, Vol. 12, No. 1, 151–155, 1977.
10. Abramowitz, M. and I. A. Stegun, *Handbook of Mathematical Functions*, Dover, New York, 1977.
11. Kong, J. A., "Reflection and transmission of electromagnetic waves by stratified moving media," *Canadian J. of Physics*, Vol. 49, 2785–2792, 1971.

A New Proof of the Non-constancy of Speed of Light in Vacuum and a Simple Solution for the Damped Wave Equation with a Moving Mirror Boundary (Part II)

Namık Yener
Technical Education Faculty, Kocaeli University, Izmit, Kocaeli 41380, Turkey

Abstract— A new proof of the non-constancy of speed of light in vacuum is obtained in the process of solving the damped wave equation with a mirror boundary in uniform rectilinear motion with respect to a simple, lossy medium and with specific conditions for the other boundary, using Laplace transform. Lorentz transformation is also needed in the proof. However because of the need to assign different speeds of light in vacuum to the two moving media, the resulting solution has further to be stretched in time, in addition to the hyperbolic rotation of the Lorentz transformation. The existing methods in literature to solve the involved damped wave equation are employed and a simple solution is proposed when the boundary conditions are of a special class. In the solution Laplace transform technique is used to convert the partial differential equation into an ordinary one. The uniform rectilinear motion of the mirror boundary and the particular type of conditions treated for the other boundary, permit a solution by this technique. The presentation of the work is organized as a series of three papers with the same title but with an extension in the title as Part (I), Part (II) and Part (III). In Part (I) the moving mirror boundary condition is imposed and the new proof for the non-constancy of speed of light in vacuum is introduced. In Part (II) which is the present paper, different speeds of light in vacuum for K and K' are incorporated in the differential equation. In Part (III), an example is worked out that illustrates the ideas developed in the first two parts. In the present paper we discuss a simple general solution of the differential equation involved making use of a simplification that applies when the boundary conditions for the non-moving boundary are of a special class. In particular we assume $E_x|_{z'=0}$ and $\frac{\partial E_x}{\partial z'}|_{z'=0}$ have no essential singularities or branch points and furthermore the former tends to zero while the latter remains bounded as s' tends to infinity. $E_x(z', t')$ is the unknown function of the differential equation, s' is the complex frequency, z' is the space coordinate and t' is the time variable, the last three of which are measured in K'.

1. INCORPORATION OF DIFFERENT SPEEDS OF LIGHT IN VACUUM FOR K AND K' IN THE DIFFERENTIAL EQUATION

It must be also noted that (5) of [1] takes the following form when the condition (21) of [1] is imposed on it:

$$\frac{1}{\alpha^2}\frac{\partial^2 E_x}{\partial y'^2} + \left(1 - n^2 r^2\right)\frac{\partial^2 E_x}{\partial z'^2} + \left(\frac{s'}{c}\right)^2 (r^2 - n^2)E_x - s'\frac{\mu\sigma}{\alpha}E_x$$
$$= \left(\frac{1}{c}\right)^2 \left(r^2 - n^2\right)\left[s' E_x(z', 0) + E'_x(z', 0)\right] + \mu\sigma E_x(z', 0). \tag{1}$$

In the remaining part of this work we shall assume

$$\theta'_1 = \theta'_2 = 0. \tag{2}$$

This will eliminate the y' dependence of E_x and allow simpler dispersion relations. Then we shall be able to state

$$k'_1 = -k'_2. \tag{3}$$

Solution (7) of [1] subject to (21) of [1] will still be a solution of (1) and this solution can be computed using an inverse Laplace transformation procedure. Observing (21) of [1] and (3), the dispersion (characteristic) equation in (20) of [1] can be written as follows when $\theta'_1 = \theta'_2 = 0$ and $k' = k'_1 = -k'_2$:

$$\left(1 - n^2 r^2\right) k'^2 = -\left(\frac{s'}{c}\right)^2 \left(r^2 - n^2\right) + \frac{s'}{\alpha}\mu\sigma, \tag{4}$$

Notice (4) follows from the homogeneous form of (1) as well. This can also be cast into the form:

$$k'^2 = -\frac{1}{c^2}\left(\frac{r^2-n^2}{1-n^2r^2}\right)s'\left(s'+\frac{\mu\sigma}{\alpha}\frac{c^2}{n^2-r^2}\right). \tag{5}$$

Adhering to (17b) of [1] and using $k' = k'_1 = -k'_2$, we can write

$$E_x(z', s') = \frac{A'_1}{s'-vk}[(s'-vk')\exp(kz') - (s'+vk)\exp(-k'z')]. \tag{6}$$

Assume further that

$$E_x|_{z'=0} = f(s'), \tag{7a}$$

$$\frac{\partial E_x}{\partial z'}|_{z'=0} = F(s'), \tag{7b}$$

are given functions which provide the boundary conditions on E_x in frame K'. Then because of (6), (7) will mean

$$f(s') = -A'_1\frac{2vk'}{s'-vk'}, \tag{8a}$$

$$F(s') = A'_1\frac{2s'k}{s'-vk'}. \tag{8b}$$

In this case $f(s')$ and $F(s')$ have to be interrelated as follows:

$$s'f(s') = -vF(s'). \tag{8c}$$

I.e., the boundary conditions in (7) cannot be selected independently of each other.

Summarizing,

$$E_x(z', s') = -\frac{f(s')}{v}\left[\frac{s'}{k}\sinh(k'z') - v\cosh(k'z')\right], \tag{9a}$$

or,

$$E_x(z', s') = \frac{1}{2}\left[f(s') + \frac{F(s')}{k'}\right]\exp(k'z') + \frac{1}{2}\left[f(s') - \frac{F(s')}{k'}\right]\exp(-k'z'), \tag{9b}$$

can be found. This is the same structure as Equation (12) of [2]. Therefore the entire analysis in that paper could be employed here, to compute the inverse Laplace transform of $E_x(z', s')$, if of course Equation (21) of [1] were not true.

Because of (21) of [1] we have inferred that the speed of light in vacuum for different Galilean reference systems has to be different. To incorporate this difference we have proposed the following modified Lorentz transformation in [3]:

$$z = \alpha(z' - c'rt'), \tag{10a}$$

$$t = \alpha\left(-\frac{r}{c}z' + \frac{c'}{c}t'\right), \tag{10b}$$

$$z' = \alpha(z + crt), \tag{11a}$$

$$t' = \alpha\left(\frac{r}{c'}z + \frac{c}{c'}t\right). \tag{11b}$$

Note that (10) and (11) are mathematical inverses of one another and at the same time they preserve the invariance of transformation structure as entailed by the principle of relativity [3]. Under this transform (3) of [1] takes the following form:

$$\frac{\partial}{\partial z} = \alpha\frac{\partial}{\partial z'} + \alpha\frac{r}{c'}\frac{\partial}{\partial t'}, \tag{12a}$$

$$\frac{\partial^2}{\partial z^2} = \alpha^2\frac{\partial^2}{\partial z'^2} + \left(\alpha\frac{r}{c'}\right)^2\frac{\partial^2}{\partial t'^2} + 2\alpha^2\frac{r}{c'}\frac{\partial^2}{\partial z'\partial t'}, \tag{12b}$$

$$\frac{\partial}{\partial t}=\alpha rc\frac{\partial}{\partial z'}+\alpha\frac{c}{c'}\frac{\partial}{\partial t'},\tag{12c}$$

$$\frac{\partial^2}{\partial t^2}=(\alpha rc)^2\frac{\partial^2}{\partial z'^2}+\left(\alpha\frac{c}{c'}\right)^2\frac{\partial^2}{\partial t'^2}+2\alpha^2 r\frac{c^2}{c'}\frac{\partial^2}{\partial z'\partial t'}.\tag{12d}$$

When $\theta_1'=\theta_2'=0$, Equation (1) of [1] observed from K' now reads:

$$-\frac{\alpha^2}{\mu\varepsilon}\left[\frac{\partial^2 E_x}{\partial z'^2}+\left(\frac{r}{c'}\right)^2\frac{\partial E_x}{\partial t'^2}+2\frac{r}{c'}\frac{\partial^2 E_x}{\partial z'\partial t'}\right]+\frac{\sigma}{\varepsilon}\left(\alpha rc\frac{\partial E_x}{\partial z'}+\alpha\frac{c}{c'}\frac{\partial E_x}{\partial t'}\right)$$
$$+\alpha^2[(rc)^2\frac{\partial^2 E_x}{\partial z'^2}+(\frac{c}{c'})^2\frac{\partial^2 E_x}{\partial t'^2}+2r\frac{c^2}{c'}\frac{\partial^2 E_x}{\partial z'\partial t'}]=0.\tag{13}$$

Taking the Laplace transform of (13) with respect to t' we obtain:

$$\left(1-n^2r^2\right)\frac{d^2E_x}{dz'^2}+\left(\frac{s'}{c'}\right)^2\left(r^2-n^2\right)E_x+2s'\left(\frac{r}{c'}\right)\left(1-n^2\right)\frac{dE_x}{dz'}-rc\frac{\mu\sigma}{\alpha}\frac{dE_x}{dz'}-s'\left(\frac{c}{c'}\right)\frac{\mu\sigma}{\alpha}E_x$$
$$=\left(\frac{1}{c'}\right)^2\left(r^2-n^2\right)\left[s'E_x(z',0)+E_x'(z',0)\right]+2\left(\frac{r}{c'}\right)\left(1-n^2\right)\frac{dE_x(z',0)}{dz'}-\frac{\mu\sigma}{\alpha}\left(\frac{c}{c'}\right)E_x(z',0).\tag{14}$$

Comparison of the homogeneous version of (14) with the homogeneous version of (5) of [1] reveals that this version of (14) can be obtained by substituting $\frac{c}{c'}s'$ for s' in this said version of (5) of [1]. In turn this implies a stretching of the time t' by a multiplication of t' by a factor of $\frac{c'}{c}$ when the inverse Laplace transform is taken.

In other words the modified Lorentz transformation in (10) and (11) amounts to the hyperbolic rotation provided by the Lorentz transformation plus a stretching of the time t' by a multiplicative factor of $\frac{c'}{c}$. This fact can also be proven without recourse to any differential equation, but simply utilizing (10), (11) and the similar equations for the classical Lorentz transformation.

Now following the same steps as was done to get (21) of [1] (or employing the mentioned stretching in s' in (22) of [1]), we arrive at

$$\frac{2\alpha s'}{cc'}(1-n^2)=\mu\sigma.\tag{15}$$

When this condition is applied to (14) we get:

$$\left(1-n^2r^2\right)\frac{d^2E_x}{dz'^2}+\left(\frac{s'}{c'}\right)^2\left(r^2-n^2\right)E_x-s'\left(\frac{c}{c'}\right)\frac{\mu\sigma}{\alpha}E_x$$
$$=\left(\frac{1}{c'}\right)^2\left(r^2-n^2\right)\left[s'E_x(z',0)+E_x'(z',0)\right]-\frac{\mu\sigma}{\alpha}\left(\frac{c}{c'}\right)E_x(z',0).\tag{16}$$

Notice that on the right hand side we have also deleted the relevant initial conditions when we have deleted a derivative on the left hand side while (15) is applied to (14). In order to solve (16), which has the structure observant of (15), we can obtain the inverse Laplace transform of (9b) and in it, effect the said stretching in time t', because (9b) takes into account (21) of [1] already.

We can write (16) in the following form as well:

$$\frac{d^2E_x}{dz'^2}-k'^2E_x=-\frac{k'^2}{s'}f_1(z')+af_2(z')=Z(z',s'),\tag{17}$$

where

$$f_1(z')=\lim_{t'\to 0}E_x(z',t'),\tag{18a}$$

$$f_2(z')=\lim_{t'\to 0}\frac{\partial E_x}{\partial t'},\tag{18b}$$

represent the initial sate of the solution [2, 4], k'^2 is defined in (5) and $a=\frac{1}{c^2}(\frac{r^2-n^2}{1-n^2r^2})$ holds. The general solution of (17) is a solution of the homogeneous equation

$$\frac{\partial^2 E_x}{\partial z'^2}-k'^2E_x=0.\tag{19}$$

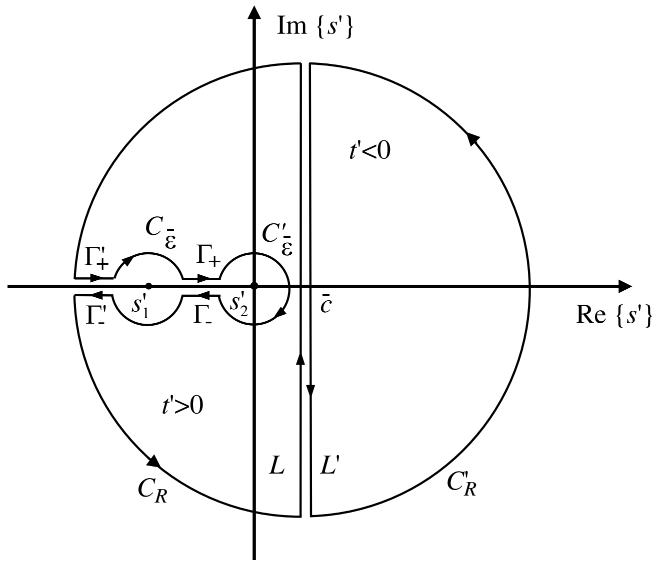

Figure 1: Integration paths for the inverse Laplace transform.

The particular solution of (17) will then be [4]:

$$E_{xp}(z', s') = \frac{\exp(k'z)}{2k'} \int \exp(-k'z')Z(z', s')dz' - \frac{\exp(-k'z)}{2k'} \int \exp(k'z')Z(z', s')dz'. \tag{20}$$

2. A SIMPLE GENERAL SOLUTION OF (16) WITH A SPECIAL CLASS OF BOUNDARY CONDITIONS

The inverse Laplace transform of (9b) was found in Section 2 of [2] for a special class of boundary conditions with a simplified procedure. (Figure 1 depicts the integration paths for this inversion. In this figure $\bar{c}$ replaces c of Figure 1 in [2]). We shall herewith assume $f(s')$ and $F(s')$ are in the same class of functions, with no essential singularities and no branch points. Distinct from [2] though we shall assume additionally $\lim_{s'\to\infty} f(s') = 0$ and that $F(s')$ remains bounded as s' tends to infinity. Also in this case k' that is in place of h of [2] has the form given by (5). Then $s'_1 = -\frac{\mu\sigma}{\alpha}\frac{c^2}{n^2-r^2}$ and $s'_2 = 0$ will hold true with $a = \frac{1}{c^2}(\frac{r^2-n^2}{1-n^2r^2})$ if (5) is written in the form:

$$k' = \sqrt{-as'(s' - s'_1))}. \tag{21}$$

In our case we can assume

$$r^2 - n^2 < 0, \tag{22a}$$

$$1 - n^2r^2 < 0, \tag{22b}$$

at least for a r value for relativistic speeds v of the Galilean reference systems. Because then r^2 will be close to one while n can be assumed greater than one. Then $a > 0$ and $s'_1 < 0$ will be true. Furthermore under (23),

$$s'_1 < -a < 0 = s'_2, \tag{23}$$

will hold also. As in Figure 1 the branch cut will be between s'_1 and s'_2.

This requires

$$-\pi < \arg(s' - s'_1) < \pi, \quad -\pi < \arg(s' - s'_2) < \pi.$$

Hence $-a$ will be on the branch cut. Because of the square root, this will require the choice of the value of $-a$ as $a\exp(i\pi)$ or $a\exp(-i\pi)$ depending on whether it is on the segment Γ_+ or Γ_-. Then again as in reference [2] the integrals along the segments Γ_+ and Γ_- will add to zero always. The remainder of the analysis in Section 2 of [2] will apply in our case as well. Here the only difference will be the assumption that $\lim_{s'\to\infty} f(s') = 0$ and that $F(s')$ remains bounded as s' tends to infinity. This is to ensure vanishing of the second integral in (14a) of [2]. Because then one can apply

Jordan's theorem for this integral despite the $-a$ factor in (21), which makes the corresponding steps in [2] inapplicable. Indeed the factors $[f(s') \pm \frac{F(s')}{k'}]$ in (9b) now will tend to zero as $|s'|$ approaches infinity, while the exponential factors remain bounded because an exponential function is entire and because the only singularities of these exponential factors which are due to the branch points of k' remain in a bounded region in the s' plane. Hence (9b) will approach zero as $|s'|$ approaches infinity. Therefore by Jordan's theorem, the said integral will be zero.

3. CONCLUSION

Different speeds of light in vacuum for K and K' are incorporated into the damped wave equation observed from K'. A simplified solution is pointed out when the boundary condition functions for the non-moving boundary are of a special class.

REFERENCES

1. Yener, N., "A new proof of the constancy of speed of light in vacuum and a simple solution for the damped wave equation with a moving mirror boundary (Part I)," *Progress in Electromagnetics Research Symposium*, Kuala Lumpur, Malaysia, March 27–30, 2012.
2. Yener, N., "A simple solution for the damped wave equation with a special class of boundary conditions using the Laplace transform," *Progress In Electromagnetics Research B*, Vol. 33, 69–82, 2011.
3. Yener, N., "On the non-constancy of speed of light in vacuum for different Galilean reference systems," *Journal of Electromagnetic Waves and Applications*, Vol. 21, No. 15, 2241–2255, 2007.
4. Stratton, J. A., *Electromagnetic Theory*, McGraw Hill, New York, 1941.

A New Proof of the Non-constancy of Speed of Light in Vacuum and a Simple Solution for the Damped Wave Equation with a Moving Mirror Boundary (Part III)

Namik Yener
Technical Education Faculty, Kocaeli University, Izmit, Kocaeli 41380, Turkey

Abstract— A new proof of the non-constancy of speed of light in vacuum is obtained in the process of solving the damped wave equation with a mirror boundary in uniform rectilinear motion with respect to a simple, lossy medium and with specific conditions for the other boundary, using Laplace transform. Lorentz transformation is also needed in the proof. However because of the need to assign different speeds of light in vacuum to the two moving media, the resulting solution has further to be stretched in time, in addition to the hyperbolic rotation of the Lorentz transformation. The existing methods in literature to solve the involved damped wave equation are employed and a simple solution is proposed when the boundary conditions are of a special class. In the solution Laplace transform technique is used to convert the partial differential equation into an ordinary one. The uniform rectilinear motion of the mirror boundary and the particular type of conditions treated for the other boundary, permit a solution by this technique. The presentation of the work is organized as a series of three papers with the same title but with an extension in the title as Part (I), Part (II) and Part (III). In Part (I), the moving mirror boundary condition is imposed and the new proof for the non-constancy of speed of light in vacuum is introduced. In Part (II) different speeds of light in vacuum for K and K' are incorporated in the differential equation. In Part (III), which is the present paper, an example is worked out that illustrates the ideas developed in the first two parts. The result of the solution takes into account different speeds of light for the two reference frames involved.

1. EXAMPLE

As an example we take up the case

$$f(s') = \frac{1}{(s'-s'_1)^2}. \tag{1a}$$

Then

$$F(s') = -\frac{s'}{v(s'-s'_1)^2}, \tag{1b}$$

as per (8c) of [1]. We assume that (1) are valid after a Lorenz transformation of K into K'. We shall apply a time stretching on the resulting $E_x(z',t')$ to have taken into account that the speeds of light in vacuum for K and K' are different.

Then in our case we only have to evaluate the integrals about s'_1. If we use the same technique as in [2] and make the change of variables $s'-s'_1 = \bar{\varepsilon}\exp(i\varphi)$, then ds' becomes $ds' = i\bar{\varepsilon}\exp(i\varphi)d\varphi$. If the integrations about s'_1 between $\varphi = 2\pi$ and $\varphi = 0$ are performed then taking the limit $\bar{\varepsilon} \to 0$

$$E_x(z',t') = \left(t' - \frac{1}{v}z' - \frac{s'_1}{v}zt' - as'_1\frac{z'^2}{2} + as'_1 2\frac{z'^3}{6v}\right) \times \exp\left(s'_1 t'\right), \tag{2}$$

can be found. It can easily be verified that this solution satisfies the form of Equation (4) of [3], when the y' dependence is not considered and (21) of [3] is observed, i.e., that it satisfies the differential equation

$$-\frac{\alpha^2}{\mu\varepsilon}\left[\frac{\partial^2 E_x}{\partial z'^2} + \left(\frac{r}{c}\right)^2\frac{\partial E_x}{\partial t'^2}\right] + \alpha\frac{\sigma}{\varepsilon}\frac{\partial E_x}{\partial t'} + \alpha^2\left[(rc)^2\frac{\partial^2 E_x}{\partial z'^2} + \frac{\partial^2 E_x}{\partial t'^2}\right] = 0, \tag{3}$$

and the boundary conditions (7) of [1]. Figure 1 is a plot of the function in (2).

Equation (2) is the inverse transform of the solution (9b) of [1] that takes into account (21) of [3] by assuming (5) of [1] holds, but it supposes the speeds of light in vacuum for K and K' are the

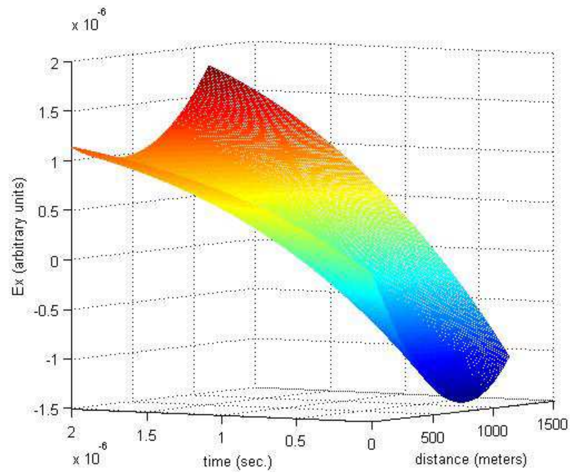

Figure 1: Solution in Equation (2) with $n^2 = 81,\ c = 3 \times 10^8$ (m/s), $v = 0.98c$ (m/s), $1/\sqrt{\mu\varepsilon} = 1/3 \times 10^8$ (m/s), $\sigma/(2\varepsilon) = 1.4 \times 10^5$ (s^{-1}).

same. To obtain a solution that also takes into account the different speeds of light for K and K' we must stretch the time terms in (2) by the multiplicative factor $\frac{c'}{c}$. Then one gets:

$$E_x(z', t') = \left(\frac{c'}{c}t' - \frac{1}{v}z' - \frac{s_1'}{v}\frac{c'}{c}zt' - as_1'\frac{z'^2}{2} + as_1'^2\frac{z'^3}{6v}\right) \times \exp\left(s_1'\frac{c'}{c}t'\right), \tag{4}$$

This solution must satisfy (13) of [1] subject to the time domain version of (15) of [1]. Indeed this also can be verified to be true. On the other hand (1a) when considered in the stretched time domain will now have to read

$$E_x(0, t') = \frac{c'}{c}t' \exp\left(s_1'\frac{c'}{c}t'\right). \tag{5a}$$

It is seen that (4) satisfies this condition. (1b) when considered in the stretched time domain will now have to read

$$\frac{\partial E_x(0, t')}{\partial z'} = -\frac{1}{v}\left(\frac{c'}{c}s_1't' + 1\right)\exp\left(s_1'\frac{c'}{c}t'\right). \tag{5b}$$

(4) satisfies this boundary condition too.

Now we are in a position compute the 'particular solution' given by (20) of [1]. Indeed if the functions $f_1(z)$ and $f_2(z)$ given by (18) of [1] are generated such that (2) is used as the function $E_x(z', t')$, one finds that the 'particular solution' obtained by evaluating (20) of [1] for this choice, is naturally equal to (2) itself. So the solution of (4) of [3] for the case $f(s') = \frac{1}{(s'-s_1')^2}$ and $F(s') = -\frac{s'}{v(s'-s_1')^2}$ will be equal to (2) and this result also satisfies (18) of [1] because of the coalescence of (2) with the 'particular solution' (20) of [1].

2. CONCLUSION

In a series of three articles [1, 3] a new proof has been proposed for the non-constancy of speed of light in vacuum based on Maxwell's partial differential equations, Lorentz transform and the boundary condition on a moving mirror. The solution method of the differential equation involved is given using techniques existing in the literature. A simplified solution is pointed out when the boundary condition functions for the non-moving boundary are of a special class. A by-product of the solution procedure is the new proof of the non-constancy of speed of light in vacuum. In this last part of the three-parts series of papers we have presented an example in order to illustrate the ideas developed in the first two parts.

REFERENCES

1. Yener, N., "A new proof of the constancy of speed of light in vacuum and a simple solution for the damped wave equation with a moving mirror boundary and a special class of conditions for the other boundary (Part II)," *Progress In Electromagnetics Research Symposium*, Kuala Lumpur, Malaysia, March 27–30, 2012.

2. Yener, N., "A simple solution for the damped wave equation with a special class of boundary conditions using the Laplace transform," *Progress In Electromagnetics Research B*, Vol. 33, 69–82, 2011.
3. Yener, N., "A new proof of the constancy of speed of light in vacuum and a simple solution for the damped wave equation with a moving mirror boundary and a special class of conditions for the other boundary (Part I)," *Progress In Electromagnetics Research Symposium*, Kuala Lumpur, Malaysia, March 27–30, 2012.

Indoor Positioning Based on IEEE 802.15.4a Standard Using Trilateration Technique and UWB Signal

Jirapat Sangthong[1], **Prakaidao Dokpikul**[2], **and Sathaporn Promwong**[2]

[1]Department of Electrical Engineering, Faculty of Engineering
King Mongkut's Institute of Technology Ladkrabang, Bangkok 10520, Thailand
[2]Department of Telecommunication Engineering, Faculty of Engineering
King Mongkut's Institute of Technology Ladkrabang, Bangkok 10520, Thailand

Abstract— Nowadays, precision and accurate positioning in an indoor environment could provide widely researched because of its variety services. There have been many position estimation techniques that can be proposed such as geometric technique, statistical technique, mapping technique and many others. Trilateration technique is the one technique of geometric technique. This technique can be estimate the target position by using the intersection of circle that can be obtained from a set of reference positions. For low-rate communication, the IEEE 802.15.4a standard is proposed. This paper studies on indoor positioning based on IEEE 802.15.4a standard in IR-UWB option. All of measurements using vector network analyzer (VNA) to measure the channel frequency transfer functions. The biconical antennas were used as both transmitter (Tx) antenna and receiver (Rx) antenna with vertical polarization. Trilateration technique will be use to estimate position related parameter RSS and TOA. From the results, TOA has the higher accuracy than RSS both low band and high band cases.

1. INTRODUCTION

In recent years, the positioning system is based on technologies such as wireless local area network (WLAN), ZigBee, Bluetooth, ultrasonic, radio frequency identification (RFID) and ultra wideband (UWB). Precision and accurate positioning in an indoor environment could provide widely researched because of its variety services [1, 2] including position detection people such as miner in mine [3, 4], medical instrumentation, industrial sensors and many others. This system requires high accuracy in an indoor environments which dense multipath. This leads to use UWB for indoor positioning [5].

There have been many position estimation techniques that can be proposed. These position estimation techniques is related on signal parameters: received signal strength (RSS), angle of arrival (AOA), time of arrival (TOA) and time difference of arrival (TDOA) [6, 7]. Trilateration technique is the one technique of geometric technique. This technique can be estimate the target position by using the intersection of circle that can be obtained from a set of reference positions.

Nowadays, IEEE 802.15.4a has developed an UWB based on MAC and physical layer standards for wireless personal area network (WPAN). The IEEE 802.15.4a had two signal formats based on impulse radio (IR) and chirp spread spectrum (CSS). The IR-UWB signal have three bands: sub-gigahertz band uses frequencies ranging between 250–750 MHz, the low band uses frequencies ranging between 3.244–4.742 GHZ and the high band uses frequencies ranging between 5.944–10.234 GHz; whereas the CSS signal use frequencies ranging between 2.400–2.4835 GHz [8].

The remainder of this paper is organized as follows. Trilateration technique is described in Section 2. After that, the measurement setup of this paper is explained in Sections 3. Finally, the results and conclusion is given in Sections 4 and 5, respectively.

2. TRILATERATION TECHNIQUE

Trilateration technique uses at least three reference nodes to find positions that related parameter (RSS or TOA). The parameter of measurement is specified the range between each reference node and a target node. Consequently, the position of target node can be estimated by the intersections of three circles can be shown in Fig. 1.

2.1. Received Signal Strength: RSS

RSS is considered the changed energy of signal along the distance. A main factor that affected signal energy is path loss. The path loss model can be represented by using

$$\bar{P}(d) = P_0 - 10n\log_{10}\left(\frac{d}{d_0}\right) \tag{1}$$

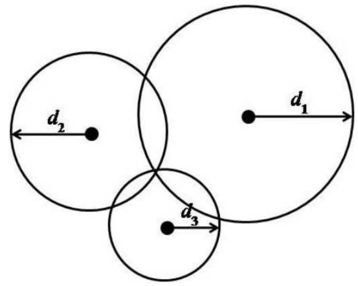

Figure 1: Positioning based on trilateration technique.

where $\bar{P}$ is the average received power in at a distance d, P_0 is the received power at a reference distance d_0 and n is path-loss exponent, respectively.

Therefore, the distance from each reference node to target node by considering from RSS parameter d_{RSS} can be calculated by

$$d_{\mathrm{RSS}} = d_0 \cdot 10^{\left[\frac{|P_0 - \bar{P}|}{10 \cdot n}\right]} \tag{2}$$

2.2. Time of Arrival: TOA

TOA is considering a time of flight that the signal is travelled from one node to another. The delay time τ can be represented by

$$\tau = {}^{\arg\min_{\tau}} P(\tau) \tag{3}$$

where τ is the delay time of maximum received power.

So, the distance from each reference node to target node by considering from TOA parameter d_{TOA} can be calculated by

$$d_{\mathrm{TOA}} = c \cdot \tau \tag{4}$$

where c is the velocity of radio wave (3×10^8 m/s) and τ is delay time, respectively.

For trilateration technique, the circle's equation that uses to find the position can be evaluated by

$$(x - h)^2 + (y - k)^2 = d_{\mathrm{RSS}}^2 \tag{5}$$

$$(x - h)^2 + (y - k)^2 = d_{\mathrm{TOA}}^2 \tag{6}$$

where (h, k) is the position coordinates (x, y) of each reference node. d_{RSS} and d_{TOA} are the distance of RSS parameter and TOA parameter, respectively.

3. MEASUREMENT SETUP

This section is described about measurement scheme that use to study the accuracy of trilateration techbique. The VNA is used to measure the UWB channel measurement in the frequency response mode at three frequencies ranged based on IEEE 802.15.4a standard. The minimum frequencies are 3.244 GHz for low band and 5.944 GHz for high band while maximum frequencies are 4.742 GHz for low band and 10.234 GHz for high band. The biconical antennas [9] with vertical polarization are used as both Tx and Rx antennas. The heights of Tx and Rx antennas are set to be 1 m. The measurements were done to collect the data from three transmitted antennas. A total of 30 positions with 1 m space are measured. The layouts of the room and the measurement setup are shown in Fig. 2.

4. RESULTS

For RSS, The received power is computed using Equation (1) and calculated the distance from reference node to target node by Equation (2). Then, the position can be estimated by Equation (5). For low band, the CDF of error in 'x' and error in y' are shown in Fig. 3 and Fig. 4, respectively. For high band, the CDF of error in 'x' and error in 'y' are shown in Fig. 5 and Fig. 6, respectively.

From low band, the average of error in 'x' is 0.47 m with the maximum error in 'x' is 1.71 m. Besides that, the average of error in 'y' is 0.34 m with the maximum error in 'y' is 1.28 m. For high band, the average of error in 'x' is 0.47 m with the maximum error in 'x' is 1.38 m. Besides that, the average of error in 'y' is 0.28 m with the maximum error in 'y' is 0.79 m.

For TOA, The delay time is calculated using Equation (3) and evaluated the distance from reference node to target node by Equation (4). Then, the position can be estimated by equation

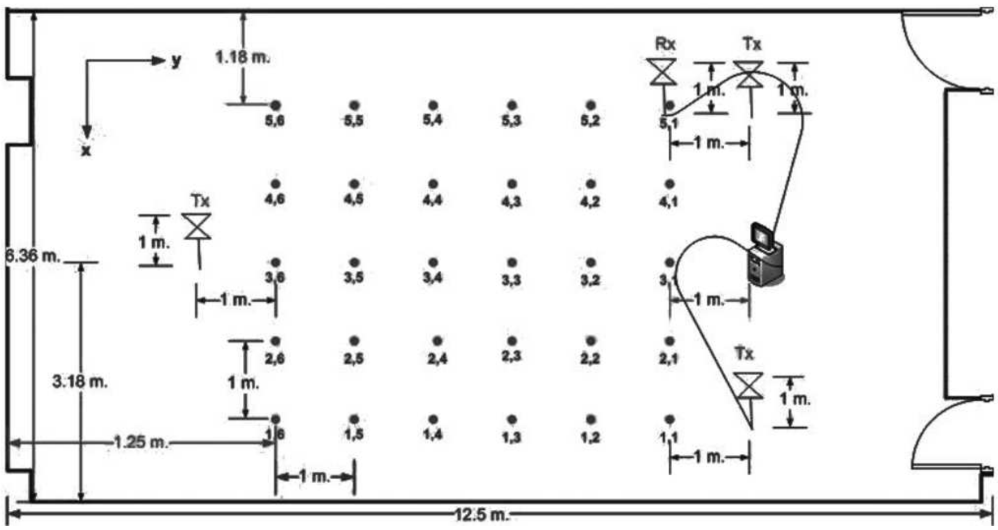

Figure 2: The layouts of the room and measurement setup.

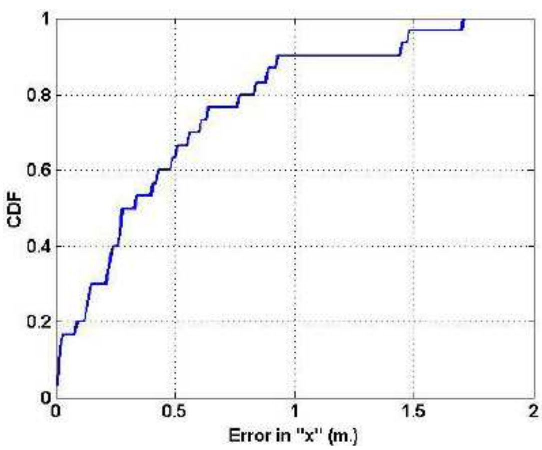

Figure 3: CDF for error in 'x', RSS, Low band.

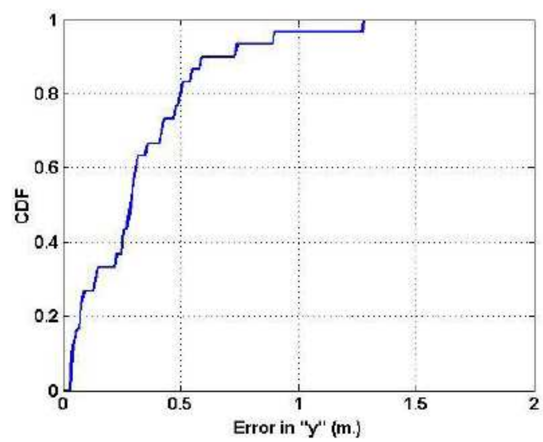

Figure 4: CDF for error in 'y', RSS, Low band.

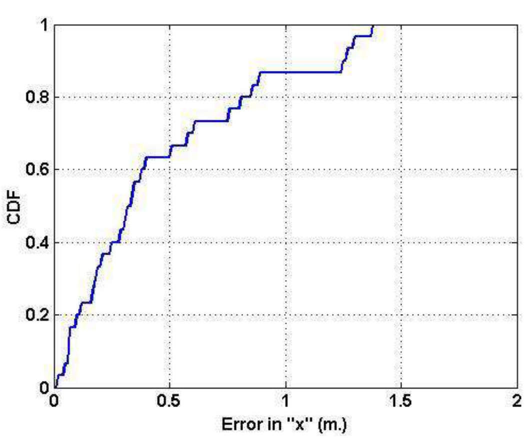

Figure 5: CDF for error in 'x', RSS, High band.

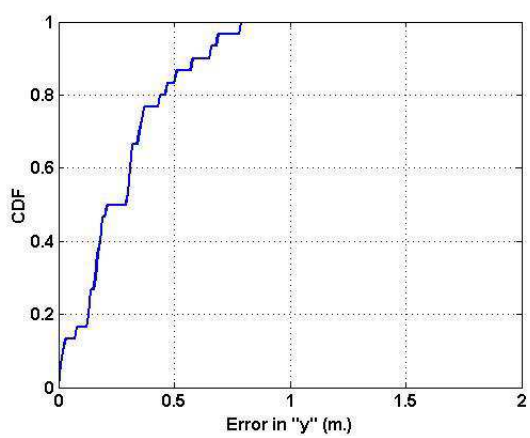

Figure 6: CDF for error in 'y', RSS, High band.

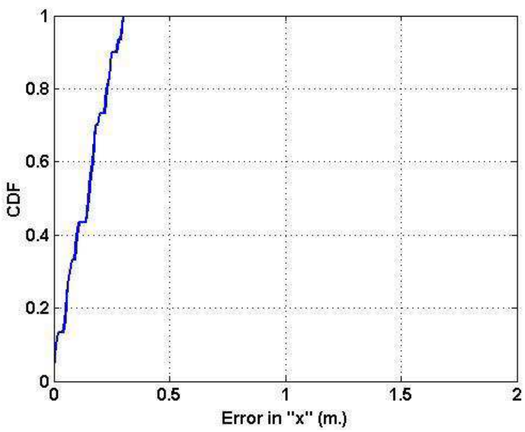

Figure 7: CDF for error in ‘x’, TOA, Low band.

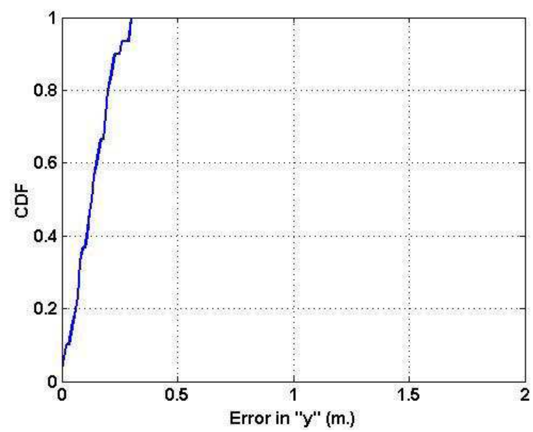

Figure 8: CDF for error in ‘y’, TOA, Low band.

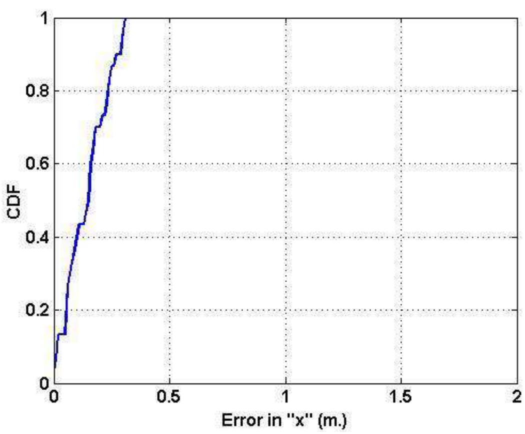

Figure 9: CDF for error in ‘x’, TOA, High band.

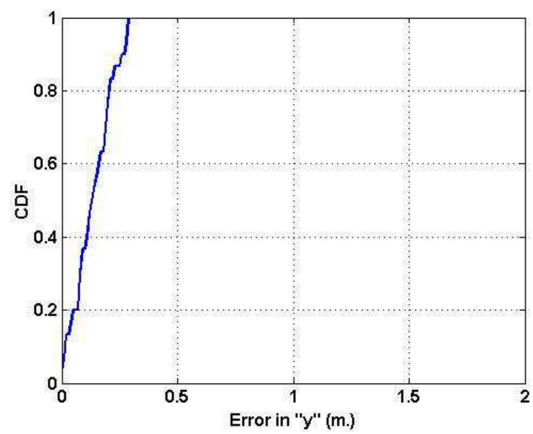

Figure 10: CDF for error in ‘y’, TOA, High band.

(6). For low band, the CDF of error in ‘x’ and error in ‘y’ are shown in Fig. 7 and Fig. 8, respectively. For high band, the CDF of error in ‘x’ and error in ‘y’ are shown in Fig. 9 and Fig. 10, respectively.

From the results, the average of error in ‘x’ is 0.14 m with the maximum error in ‘x’ is 0.3 m. Besides that, the average of error in ‘y’ is 0.14 m with the maximum error in ‘y’ is 0.3 m for low band. While high band, the average of error in ‘x’ is 0.15 m with the maximum error in ‘x’ is 0.31 m. Besides that, the average of error in ‘y’ is 0.14 m with the maximum error in ‘y’ is 0.29 m.

5. CONCLUSIONS

In this paper, we studied on indoor positioning based on IEEE 802.15.4a standard using trilateration technique and UWB signal. The channel frequency transfer functions were measured at the frequency ranged from 3 GHz to 5 GHz for low band and 5 GHz to 11 GHz for high band. From the results, high band case is better accuracy than low band in RSS case but small difference and the errors are equal in TOA case. Besides that, TOA has the better accuracy than RSS both low band and high band case.

For the future work, we will study the possibility of accuracy improvement by using another technique such as statistical technique and mapping technique.

REFERENCES

1. Fontana, R. J., E. Richley, and J. Barney, “Commercialization of an ultra wideband precision asset location system,” *2003 IEEE Conference on UWB Systems and Technologies*, 369–373, Nov. 2003.
2. Pahlavan, K., X. Li, and J. Makela, “Indoor geolocation science and technology,” *IEEE Communications Magazine*, Vol. 40, No. 2, 112–118, Feb. 2002.

3. Toak, A., N. Kandil, S. Affes, and S. Georges, "Fingerprinting localization using ultra-wideband and neural networks," *2007 International Symposium on Signals, Systems and Electronics*, 529–532, Jul.–Aug. 2007.
4. Toak, A., N. Kandil, and S. Affes, "Neural networks for fingerprinting-based indoor localization using ultra-wideband," *Journal of Communications*, Vol. 4, No. 4, 267–275, May 2009.
5. Mahfouz, M. R., A. E. Fathy, M. J. Kuhn, and Y. Wang, "Recent trends and advances in UWB positioning," *2009 IEEE MTT-S International Microwave Workshop on Wireless Sensing, Local Positioning, and RFID*, 1–4, Sep. 2009.
6. Liu, H., H. Darabi, P. Banerjee, and J. Liu, "Survey of wireless indoor positioning techniques and systems," *IEEE Transactions on Systems, Man, and Cybernetics Part C*, Vol. 37, No. 6, 1067–1080, Nov. 2007.
7. Gu, Y., A. Lo, and I. Niemegeers, "A survey of indoor positioning systems for wireless personal networks," *IEEE Communications Surveys and Tutorials*, Vol. 11, No. 1, 13–32, Jan.–Mar. 2009.
8. Karapistoli, E., F. Pavlidou, I. Gragopoulos, and I. Tsetsinas, "An overview of the IEEE 802.15.4a standard," *IEEE Communications Magazine*, Vol. 48, No. 1, 47–53, Jan. 2010.
9. Promwong, S., W. Hachitani, and J. Takada, "Experimental evaluation scheme of UWB antenna performance," *IEE Japan Tech. on Instrumentation and Measurements*, IM-03-35, Jun. 2003.

Design of Terahertz Quantum Cascade Lasers for High Temperature Operations Using Non-equilibrium Green's Function Method

Hiroaki Yasuda[1], **Tillmann Kubis**[2], **Iwao Hosako**[1], **and Kazuhiko Hirakawa**[3]

[1]National Institute of Information and Communications Technology, Japan
[2]Network for Computational Nanotechnology, Purdue University, USA
[3]Institute of Industrial Science and INQIE, University of Tokyo, Japan

Abstract— Suppression of thermally activated phonon scattering is crucial to realize room-temperature operations of terahertz quantum cascade lasers (THz-QCLs). We have investigated GaN-based resonant phonon THz-QCL structures for possible high-temperature operations using the non-equilibrium Green's function method. It is found that the GaN-based THz-QCL structures do not have a gain sufficient for lasing due to very strong electron-LO phonon interaction. We have also calculated the performances of new GaAs-based THz-QCL schemes for further improvement. Based on the findings, we proposed a novel and simple two-well THz-QCL structure that has the scattering injection and diagonal transition schemes.

1. INTRODUCTION

Remarkable progress on terahertz quantum cascade lasers (THz-QCLs) has been made since their first demonstration in 2002. However, operation temperatures of THz-QCLs tend to be limited by hf/k (h: the Planck constant, f: frequency, k: the Boltzmann constant). Room-temperature operation of THz-QCLs has not been realized yet.

Two degradation mechanisms of population inversions at high temperatures in the widely-used resonant-phonon depopulation scheme THz QCLs, where electrons in the lower lasing level are depopulated by longitudinal optical (LO) phonon scattering have been proposed [1]. One is thermal backfilling, in which electrons in the lasing levels 3, 2 are backfilled from the lower levels 1 by thermal excitation as shown in Figure 1(a). The other degradation mechanism is thermally activated LO phonon scattering, where electrons in the upper lasing level 3 acquire sufficient in-plane kinetic energy to emit LO phonons and relax to the lower lasing level 2 in a non-radiative manner as depicted in Figure 1(b). The thermal backfilling can be suppressed by using the double LO phonon depopulation scheme. Therefore, reduction of the thermally activated phonon scattering is important to realize high-temperature operations of THz-QCLs. In this paper, we present new THz-QCL schemes for higher temperature operations and clarify their performances using the non-equilibrium Green's function (NEGF) method.

2. GAN-BASED THZ-QCL FOR HIGH TEMPERATURE OPERATIONS

Use of a material system of a large LO phonon energy seems promising for roomtemperature operations of THz-QCLs, because large thermal energy is needed to induce the thermally-activated

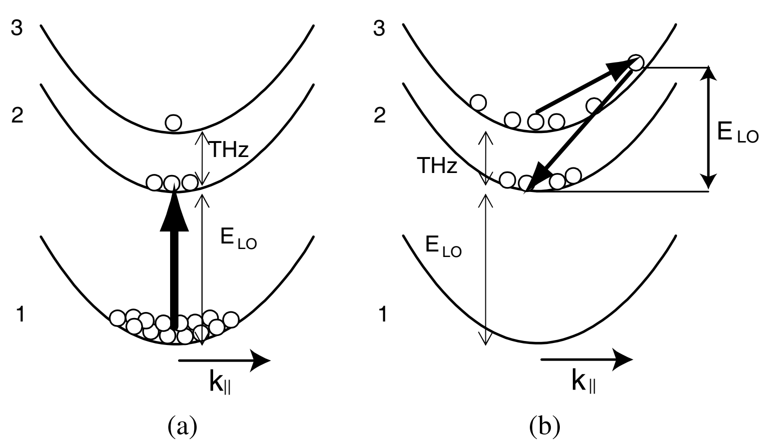

Figure 1: (a) Thermal backfilling. (b) Thermally-activated phonon scattering.

phonon scattering. GaN is one of the candidates, because the LO phonon energy in GaN is about 90 meV, which is much larger than that in GaAs (36 meV). However, no clear lasing of GaN-based QCLs has been reported so far.

In our NEGF calculation, a real-space eigenbasis was used. The Green's functions G and self-energies Σ are taken as functions of two spatial coordinates z, z', the lateral electron momentum $k_{\|}$, and the energy E [2]. The Fröhlich interaction Hamiltonian was used for the self-energy of the LO phonon-electron coupling. The acoustic phonon, optical phonon, and interface roughness are taken into account.

For the calculations of the GaN-based THz-QCLs, the conduction band discontinuity and the polarization at the interface between the barrier and the well were set to 0.25 eV and 0.0042 C/m^2. Figure 2 illustrates the calculated spectral function that is, the density of states at $k_{\|}, = 0$, for one period of the GaN-based THz-QCL structure The electric field is 80 kV/cm. The local optical gain is observed mainly in the two wells designated as the active region. The maximum local optical gain at 200 K is almost two orders of magnitude smaller than that of a typical GaAs-based THz-QCL. When averaged over one period of the QCL structure, the gain vanishes.

The reason for the poor performance of the GaN-based THz-QCL can be explained as follows; the interaction between the electrons and the LO phonons in GaN is very strong, that is, the Fröhlich coupling constant in GaN is more than 15-times larger than that in GaAs. Therefore, the broadening of the subband levels takes place as seen in Figure 2, leading to a small and broad gain. These facts suggest that GaN-based resonant phonon THz-QCL structures may not be suitable for high temperature operations.

3. NOVEL GAAS-BASED THZ-QCL SCHEMES

Another approach to reduce of the thermally-activated phonon scattering is to use the diagonal transition design of active regions [3]. The probability for the thermally-activated phonon scattering depends on the overlap of the wave-functions of the upper and lower lasing states. In contrast, the optical transition is proportional to the dipole element, which has a different dependence on

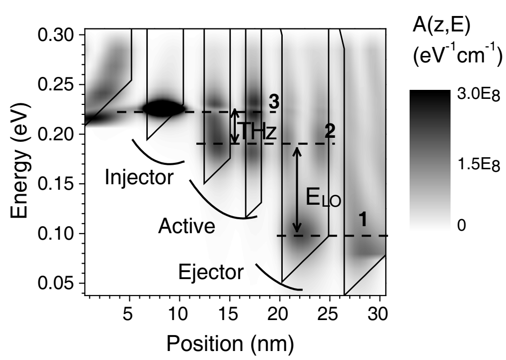

Figure 2: Spectral function for one period of the GaN-based THz QCL.

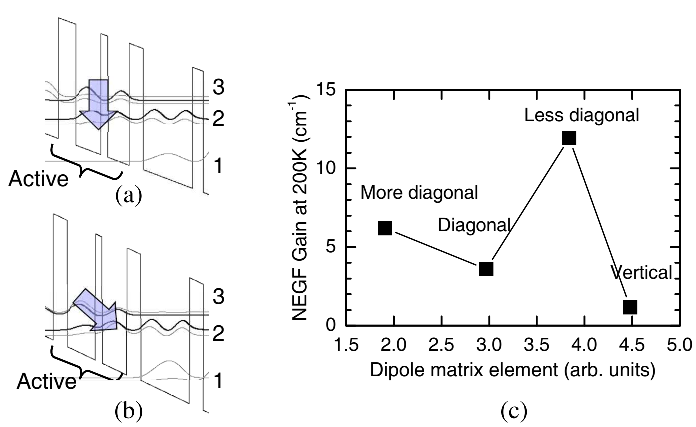

Figure 3: Schematics of (a) vertical transition, (b) diagonal transition designs. (c) Gain over one period of QCL at 200 K with different diagonality.

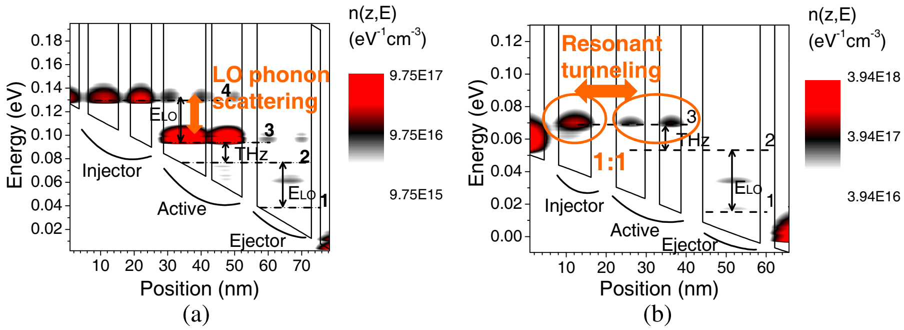

Figure 4: Electron distributions in (a) a resonant tunneling injection scheme, and (b) a scattering injection scheme THz QCLs at 40 K.

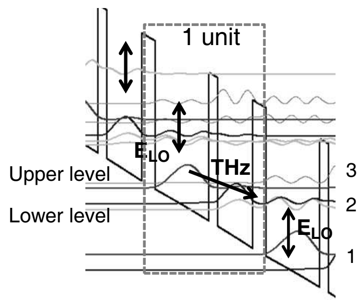

Figure 5: Conduction band diagram in the proposed two-well THz QCL.

the overlap of the wave-functions. Figure 3 illustrates the results of the NEGF calculations at 200 K with varying the diagonality. The gain at high temperatures was improved by optimizing the overlap of the wave-functions.

Furthermore, we calculated the performance of the novel indirect pump (scattering injection) scheme THz-QCLs where electrons are injected to the upper lasing level by LO phonon scattering as depicted in Figure 4(a) [4, 5]. The gain was larger than that of the conventional THz-QCLs at low temperatures [5]. This is mainly because a larger number of electrons accumulate in the upper lasing level 3 and contribute to lasing in the scattering injection scheme as illustrated in Figure 4(a). In contrast, a half of electrons contribute to lasing in the conventional THz-QCLs that use resonant tunneling for electron injections as shown in Figure 4(b).

Based on the findings, a novel and simple two-well THz-QCL structure that has the scattering injection and diagonal transition schemes was proposed as depicted in Figure 5(a) [6]. The NEGF calculations showed that the gain at high temperatures improved and the thermally-activated phonon scattering was suppressed. Furthermore, the undesirable electron injection to the lower lasing level 2 decreases because the upper and lower lasing levels are localized in different wells. Therefore, laser performance at lower-frequencies would be improved. Suppression of the continuum currents and confinement of electrons in the active region, which lead to increase of optical gains, are realized with setting the aluminum content in the barrier layers to more than 20%.

4. CONCLUSIONS

We have calculated performances of novel THz-QCL structures to realize room-temperature operations by using the NEGF method. It is found that the GaN-based THz-QCL structure, which seems promising due to the large LO phonon energy, does not have a gain sufficient for lasing due to very strong electron-LO phonon interaction. A novel and simple two-well THz-QCL structure that has the scattering injection and diagonal transition schemes was proposed and investigated.

ACKNOWLEDGMENT

We would like to thank P. Vogl and G. Klimeck for fruitful discussions and support.

REFERENCES

1. Williams, B. S. "Terahertz quantum-cascade lasers," *Nature Photonics*, Vol. 1, No. 9, 517–525, 2007.
2. Kubis, T., C. Yeh, P. Vogl, A. Benz, G. Fasching, and C. Deutsch, "Theory of non equilibrium quantum transport and energy dissipation in terahertz quantum cascade lasers," *Phys. Rev. B*, Vol. 79, No. 19, 195323, 2009.
3. Kumar, S., Q. Hu, and J. L. Reno, "186 K operation of terahertz quantum-cascade lasers based on a diagonal design," *Appl. Phys. Lett.*, Vol. 94, No. 13, 131105, 2009.
4. Yamanishi, M., K. Fujita, T. Edamura, and H. Kan, "Indirect pump scheme for quantum cascade lasers: dynamics of electron-transport and very high T-values," *Opt. Exp.*, Vol. 16, No. 25, 20748–20758, 2008.
5. Yasuda, H., T. Kubis, P. Vogl, N. Sekine, I. Hosako, and K. Hirakawa, "Non-equilibrium Green's function calculation for four-level scheme terahertz quantum cascade lasers," *Appl. Phys. Lett.*, Vol. 94, No. 15, 151109, 2009.
6. Wacker, A., "Extraction-controlled quantum cascade lasers," *Appl. Phys. Lett.*, Vol. 97, No. 8, 081105, 2010.

Mode-locked Yb-doped Fiber Ring-Laser for Use as a Pump Pulse Source of THz-TDS

J. Hamazaki, N. Sekine, and I. Hosako
National Institute of Information and Communications Technology, Japan

Abstract— We present characteristics of three types of mode-locking operation from our ring-type Yb-doped fiber laser oscillator. We clarified stretched-pulse operation is suitable for use as a pump source of THz-TDS, since it shows shortest pulse duration time of $\sim$ 100 fs. By using Yb-doped fiber amplifier system, output power of the stretched-pulse is amplified up to 150 mW without decreasing its operation stability.

1. INTRODUCTION

Many molecules show the characteristic finger-print absorption peaks in tera-hertz (THz) frequency region. Therefore, THz spectroscopy has attracted much attention to many applications. For example, to detect and identify explosive materials and/or to detect illicit drugs hidden in mail envelopes [1, 2]. Generally, THz spectrum is measured time-domain spectroscopy (TDS) by using a combination of a femtosecond pulsed-laser and photoconductive antennas (PCA) [3]. Normally, Second-harmonic-generation (SHG) of Er-doped mode-locked laser (EDFL) is used as a pump pulsed-laser source and low temperature grown GaAs (LT-GaAs) is used as a substrate of PCA, in present day [4]. Since the optical energy of EDFL (0.8 eV) is much lower than the bandgap energy of LT-GaAs (1.55 eV), SHG of EDFL is necessary to generate and/or detect THz spectrum, in this case.

To generate (detect) THz wave efficiently, avoiding the SHG process in a pump source is desired, to omit SHG conversion loss. Therefore, it is important to develop substrate semiconductor materials having bandgap energy smaller than 0.8 eV (corresponding to optical energy of EDFL). However, this is a tight constrained condition for substrate materials. Thus, pump pulsed-laser source having higher optical energy rather than EDFL is desired. Optical energy of Yb-doped fiber laser (YDFL) is about 1.2 eV (wavelength of $\sim 1\,\mu$m). It is 1.5 times larger than that of EDFL. Therefore, the constrained condition for the materials is well relaxed. Moreover, YDFL can produce shorter and more intense pulses than EDFL [5, 6] Thus, YDFL is expected to be a pump source for 1-μm-based THz-TDS. Note that, minimum requirements for pump source of THz-TDS are as follows: well stable operation, pulse duration time of < 100 fs, output power of > 100 mW.

In this paper, we present characteristics of our ring-type mode-locked YDFL. Depending on cavity condition, various types of mode-locked operation are observed. We present their optical spectrum, radio frequency (RF) spectrum, and autocorrelation waveform. Moreover, we demonstrate pulse amplification and obtained output power of 150 mW without decreasing pulse operation stability.

2. EXPERIMENTAL SETUP

Figure 1 shows schematic diagram of our experimental setup. YDF used in this experiment was highly doped fiber (Liekki Inc., YB1200-4/125). Its length, core and clad diameter were 150 cm, 4 μm and 125 μm, respectively. Our ring-type fiber laser cavity was composed of two wavelength-division multiplexing (WDM), two quarter-wave plates (QP), a half-wave plate (HP), a polarized beam splitter (PBS), two collimate lenses (CL), an isolator (ISO), a set of four gratings (4-Gs), and single mode fiber (SMF). The YDF was pumped by CW laser diodes (LDs) at 976 nm. The isolator was used for unidirectional ring laser oscillation. The 4-Gs were used to compensate dispersion of the ring cavity. Our oscillator was mode-locked by nonlinear-polarization rotation effect [7], by using combination of QPs, HP and PBS The PBS also works as an output coupler (output 1) The output 2 is used to monitor the optical spectrum of pulse in the cavity.

3. EXPERIMENTAL RESULTS AND DISCUSSION

Depending on net group velocity dispersion (GVD) of the cavity, various types of mode-locking pulses were produced. Figures 2–4 show characteristics of stretched-pulse, soliton, and chirped-pulse, respectively. Their net GVD were estimated to be +5, +15, and −15 fs/nm, respectively.

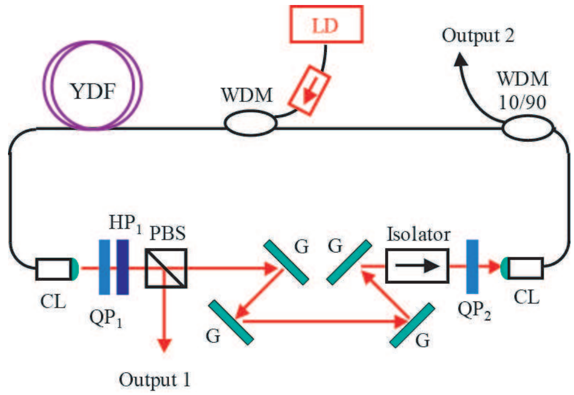

Figure 1: Setup of ring-cavity Yb-doped fiber laser. WDM: Wavelength division multiplexer; CL: Collimate lens; QP: Quarter-wave plate; HP: Half-wave plate; G: Grating.

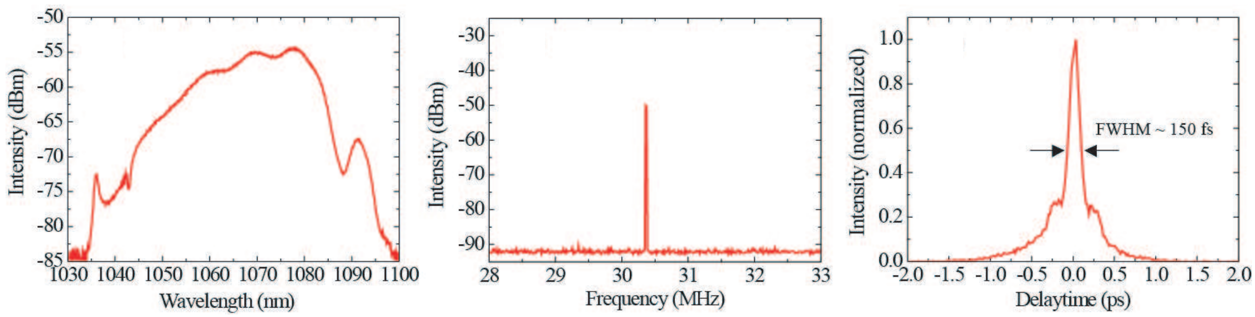

(a) (b) (c)

Figure 2: Characteristics of stretched-pulse: (a) optical spectrum, (b) RF spectrum, and (c) autocorrelation waveform.

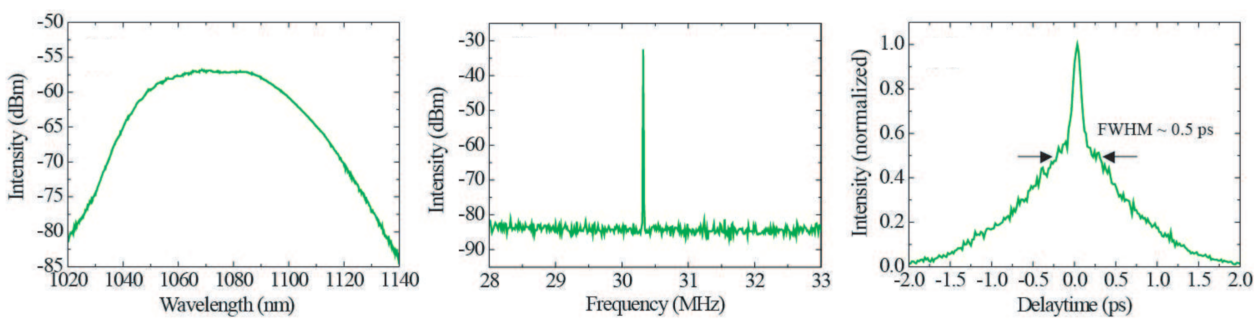

(a) (b) (c)

Figure 3: Characteristics of soliton: (a) optical spectrum, (b) RF spectrum, and (c) autocorrelation waveform.

Figure 2(a) shows optical spectrum of the stretched-pulse. The spectrum has two peak structures at 1035 nm and 1095 nm with steep spectral edges. This is a typical spectrum of stretched-pulse [8]. Figure 2(b) shows RF spectrum of the stretched-pulse. The frequency of ~ 30.35 MHz is corresponding to the repetition rate. The stable mode-locking operation is confirmed by this RF spectrum with a SNR (>40 dB). Figure 2(c) shows autocorrelation waveform of dechirped stretched-pulse. Its full width at half maximum (FWHM) was ~ 150 fs. Assuming sech^2 pulse shape, pulse duration is estimated to be ~ 100 fs. Figure 3(a) shows optical spectrum of the soliton. Gaussian-like spectrum with FWHM of ~ 50 nm was observed. The mode-locking operation is also stable, confirmed by its RF spectrum (Figure 3(b)). Figure 3(c) shows autocorrelation waveform of the dechirped soliton. Its FWHM was ~ 0.5 ps. Here, nonnegligible pedestal component was observed. This pedestal component could not be avoided by dechirping with a grating pair. Figure 4(a) shows optical spectrum of the chirped-pulse. The spectrum is as Gaussian-like, but it is asymmetric. Its RF spectrum indicated stable mode-locking operation (Figure 4(b)). However, its autocorrelation waveform was quite different from that of stretched-pulse and soliton (Figure 4(c)), i.e., the pedestal component was the main part of the waveform.

Since the stretched-pulse has few pedestal components and shows minimum pulse duration of 100 fs, the stretched-pulse operation is most suitable for pump source of THz-TDS. However, the stretched-pulse operation has a significant problem, *that is*, mode-locking operation becomes unstable when pump power is increased as shown in Figure 5. Above pump power of 350 mW, noise appears in RF spectra. The noise increases at higher pump power. Therefore, stable mode-locking operation was limited by pump LD power of 300 mW. In this case, maximum output power was limited to be ~ 25 mW. The output power of 25 mW is not enough for the pump source.

To obtain output power of > 100 mW, we constructed YDF amplified system as shown in Fig-

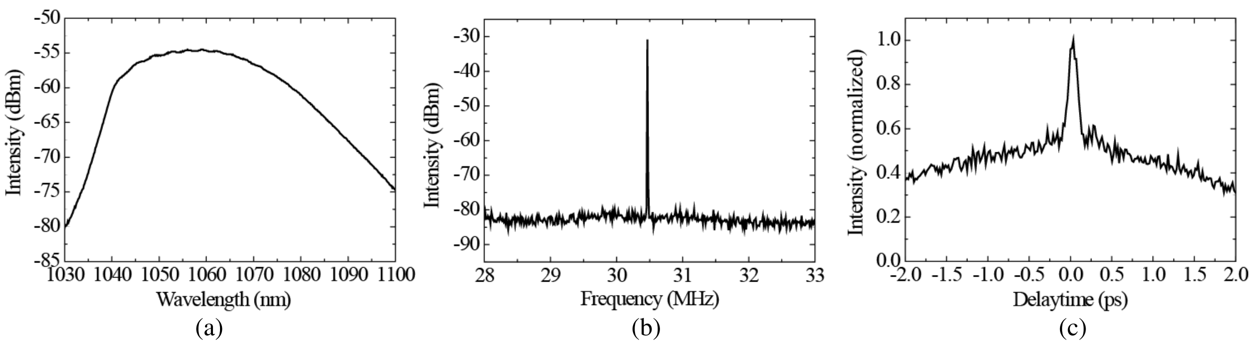

Figure 4: Characteristics of chirped pulse oscillation: (a) optical spectrum, (b) RF spectrum, and (c) autocorrelation waveform.

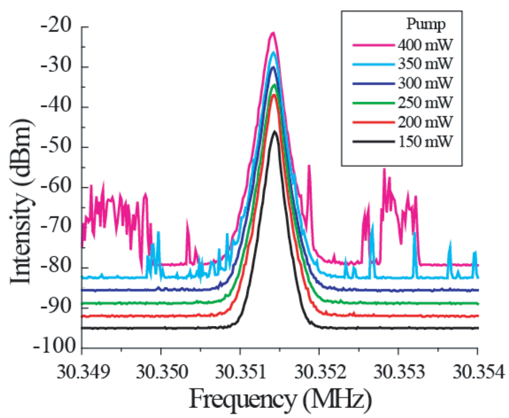

Figure 5: RF spectra of stretched-pulse operation with various pump LD power.

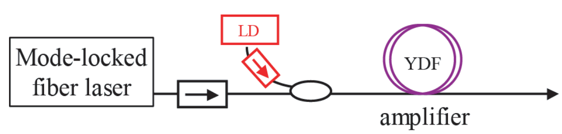

Figure 6: Configuration of Yb-doped fiber amplifier system.

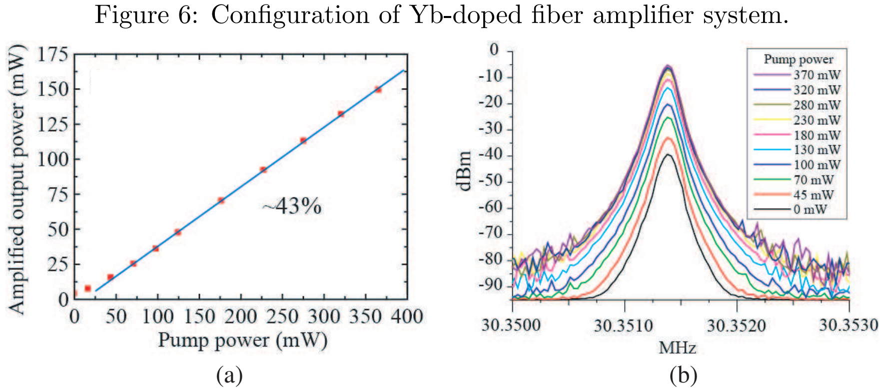

Figure 7: (a) Amplified output power as a function of pump power. (b) RF spectra of the amplified output with various pump power.

ure 6. Length of the YDF is 50 cm, which is the same YDF as used in our oscillator. Figure 7(a) shows amplified output power as a function of pump LD power. The corresponding extraction efficiency and the maximum output power were $\sim 43\%$ and ~ 150 mW, respectively. Figure 7(b) shows RF spectra of the amplified outputs. Noise was not appeared in the spectra even at high pump LD power. This indicates that output from the oscillator was well amplified without decreasing stability.

4. CONCLUSIONS

We presented characteristics of stretched-pulse, soliton, and chirped-pulse mode-locking operation. We clarified pulse waveform of stretched-pulse was better than the others and its pulse duration time was estimated to be ~ 100 fs. To obtain enough power of stretched-pulse, we constructed YDF amplifier system. We obtained amplified output power of 150 mW, without decreasing stretched-pulse operation stability. This amplified output is suitable for use as a pump source of 1-μm-based THz-TDS.

REFERENCES

1. Shen, Y. C., T. Lo, P. F. Taday, B. E. Cole, W. R. Tribe, and M. C. Kemp, "Detection and identification of explosives using terahertz pulsed spectroscopic imaging," *Appl. Phys. Lett.*, Vol. 86, 241116-1–3, 2005.
2. Kawase, K., Y. Ogawa, and Y. Watanabe, "Terahertz specroscopic imaging and its application to drug detection," *IEICE Transactions on Electronics*, Vol. E87-C, No. 7, 1186–1191, 2004.
3. Ashida, M., "Ultra-broadband Terahertz wave detection using photoconductive antenna," *Jpn. J. Appl. Phys.*, Vol. 47, 8221–8225, 2008.
4. Kitagishi, K., K. Sumida, Y. Kurata, S. Yoshida, and Y. Izutani, "A compact THz-TDS system for stable and quick measurements," *Infrared and Millimeter Waves, 2007 and the 2007 15th International Conference on Terahertz Electronics*, 220–221, 2007.
5. Zhou, X., D. Yoshitomi, Y. Kobayashi, and K. Torizuka, "Generation of 28-fs pulses from a mode-locked ytterbium fiber oscillator," *Opt. Express*, Vol. 14, 7055–7059, 2008.
6. Davydov, B. L. and A. A. Krylov, "30-W Yb^{3+}-pulsed fiber laser with wavelength tuning," *Laser Physics*, Vol. 17, 1404–1415, 2007.
7. Salhi, M., H. Leblond, and F. Sanchez, "Theoretical study of the stretched-pulse erbium-doped fiber laser," *Phys. Rev. A*, Vol. 68, 033815-1–7, 2003.
8. Lim, H., F. O. Ilday, and F. W. Wise, "Generation of 2-nJ pulses from a femtosecond ytterbium fiber laser," *Opt. Lett.*, Vol. 28, 660–662, 2003.

Terahertz Negative Dynamic Conductivity in Optically Pumped Graphene

A. Satou[1], **T. Otsuji**[1], **V. Ryzhii**[2], **and F. T. Vasko**[3]

[1]Research Institute of Electrical Communication, Tohoku University, Japan
[2]Computational Nanoelectronics Laboratory, University of Aizu, Japan
[3]Department of Electrical Engineering, University at Buffalo, USA

Abstract— We theoretically study the carrier relaxation dynamics in intrinsic graphene under pulse excitation taking into account optical-phonon (OP) scattering and carrier-carrier (CC) scattering. We consider the two limiting cases (a) where the CC scattering quasi-equilibrates carriers at all times, and (b) where the energy relaxation by intraband OP emission is dominant. We develop rate equations for the quasi-Fermi level and carrier temperature and calculate their time evolution. It is shown that in both cases the population inversion in the terahertz (THz) range can be achieved on the order of 10 ps after the pulse excitation. It is revealed that the threshold pumping intensity for the population inversion and negative dynamic conductivity in the case (a) is one order of magnitude smaller than that in the case (b) because of the thermal broadening of the carrier distribution by the CC scattering.

1. INTRODUCTION

Graphene has attracted much attention for wide variety of device applications due to its exceptional electronic and optical properties (see, for instance, Refs. [1–3]). Especially, THz devices such as lasers [4–6] and photodetectors [7] utilizing its high carrier mobility and gapless dispersion have been investigated. In Refs. [4], we demonstrated that the population inversion can occur in optically pumped graphene at THz/far-infrared range of frequency and hence the lasing at such a range is possible, utilizing the gapless linear energy spectrum and relatively high OP energy ($\sim 200\,\text{meV}$) in graphene. Due to the energy spectrum $\varepsilon = \pm v_F \hbar k$, where $v_F \simeq 10^8\,\text{cm/s}$ is the Fermi velocity and k is the wavenumber, the Fermi energy ε_F in equilibrium in intrinsic graphene is equal to zero. Hence, the electron and hole distribution functions at the bottom of the conduction band and the top of the valence band have values $f_e(0) = f_h(0) = 1/2$. This implies that at even weak photoexcitation, one might expect to make the values of the distribution functions at low energies greater than one half, i.e., $f_e(\varepsilon) = f_h(\varepsilon) > 1/2$, corresponding to the population inversion. Such a population inversion leads to the negative dynamic conductivity at relatively small frequency, and lasing in graphene is possible.

Recently, we measured the carrier relaxation and recombination dynamics in optically pumped epitaxial graphene on silicon [8] and exfoliated graphene [10] using THz time-domain spectroscopy based on an optical pump/THz&optical probe technique, and observed the amplification of THz radiation by stimulated emission from graphene under pulse excitation. To our knowledge, those are the first observation of the THz amplification using optically pumped graphene. Those results demonstrate the possibility of realizing THz lasers based on graphene.

The dynamics strongly depends on the initial temperature of carriers and the intensity of the optical pumping. With sufficiently low carrier concentration, i.e., at low temperature and upon weak pumping, photoexcited carriers are effectively accumulated near the Dirac point via cascade emission of OPs, and the achievement of the population inversion is expected to be efficient [4]. On the contrary, at room temperature or upon not so weak pumping where the carrier concentration is rather high, the CC scattering plays a crucial role in the dynamics after the pulse excitation, due to fast quasi-equilibration of carriers [9]. In fact, ultrafast optical pump-probe spectroscopy on graphene has indicated that the quasi-equilibration by the CC scattering takes place within the time on the order of 10 fs [11, 12], which is much faster than the process of single OP emission.

In this paper, we consider the relaxation and recombination dynamics at room temperature in two limiting cases (a) where the CC scattering quasi-equilibrates carriers at all times and the energy relaxation and recombination take place via OP emission, and (b) where the energy relaxation by intraband OP emission precedes the the quasi-equilibration. The latter case can be thought of as an ideal case where the threshold pumping intensity of the negative dynamic conductivity in the THz range is minimal. We develop the rate equations for the quasi-Fermi level and carrier temperature and calculate the time-dependent dynamic conductivity. On the contrary to the previous work [4], we take into account both the intraband and interband OP scattering with energy-dependent scattering rate and the Pauli exclusion principle. We show that the threshold intensity in the case (b) is much lower than the case (a). This demonstrates that the population inversion and, hence, the negative dynamic conductivity is degraded by the effect of the CC scattering.

2. RATE EQUATIONS AND DYNAMIC CONDUCTIVITY

Assuming the quasi-Fermi distribution of carriers due to the quasi-equilibration by the CC scattering, i.e., $f_\varepsilon = \{1 + \exp[(\varepsilon - \varepsilon_F)/k_B T_c]\}^{-1}$, the time evolution of the distribution is represented through the quasi-Fermi level $\varepsilon_F(t)$ and the carrier temperature $T_c(t)$. Here, both electron and hole distributions can be expressed by a single "carrier distribution" because we consider intrinsic graphene. The rate equations which determine the quasi-Fermi level and carrier temperature can be obtained from the Boltzmann equation [9]:

$$\frac{dn}{dt} = \frac{2}{\pi} \sum_{i=\Gamma,K} \int_0^\infty kdk \left[(1 - f_{\hbar\omega_i - \varepsilon})(1 - f_\varepsilon)/\tau_{i,\text{inter}}^{(+)} - f_\varepsilon f_{\hbar\omega_i - \varepsilon}/\tau_{i,\text{inter}}^{(-)} \right], \tag{1}$$

$$\begin{aligned} \frac{d\mathcal{E}}{dt} = & \frac{2}{\pi} \sum_{i=\Gamma,K} \int_0^\infty kdk \left\{ \hbar\omega_i \left[f_\varepsilon (1 - f_{\varepsilon+\hbar\omega_i})/\tau_{i,\text{intra}}^{(+)} - f_\varepsilon (1 - f_{\varepsilon-\hbar\omega_i})/\tau_{i,\text{intra}}^{(-)} \right] \right. \\ & \left. + \varepsilon \left[(1 - f_{\hbar\omega_i - \varepsilon})(1 - f_\varepsilon)/\tau_{i,\text{inter}}^{(+)} - f_\varepsilon f_{\hbar\omega_i - \varepsilon}/\tau_{i,\text{inter}}^{(-)} \right] \right\}, \end{aligned} \tag{2}$$

where $n = n(\varepsilon_F, T_c)$ and $\mathcal{E} = \mathcal{E}(\varepsilon_F, T_c)$ are the concentration and energy density of either type of carriers, which are found by integrating over $\boldsymbol{k}$ the distribution function multiplied by proper factors, the index i runs for types of OPs (long-wavelength Γ-OP and short-wavelength K-OP), and $\tau_{i,\text{intra}}^{(\pm)}$ and $\tau_{i,\text{inter}}^{(\pm)}$ are the intraband and interband scattering rates for OPs ($(+)$ for absorption and $(-)$ for emission). Those rates are on the order of sub-picoseconds for high-energy carriers. Here, we assume the equilibrium OPs and neglect the nonequilibrium population of OPs due to their emission via OP scattering of carriers.

Equations (1) and (2) together with initial conditions form a nonlinear system of equations for $\varepsilon_F(t)$ and $T_c(t)$, which can be solved numerically. Eqs. (1) and (2) are accompanied with the initial carrier concentration and energy density from which the initial quasi-Fermi level and carrier temperature can be found:

$$n|_{t=0} = n_0 + \Delta n, \quad \mathcal{E}|_{t=0} = \mathcal{E}_0 + \Delta\mathcal{E}, \tag{3}$$

where n_0 and $\mathcal{E}_0$ are the intrinsic carrier concentration and energy density, and Δn and $\Delta\mathcal{E}$ are contributions of photogenerated carriers determined differently in each case. In the case (a) where the CC scattering is dominant, those are just equal to the concentration and energy density of absorption of the pumping:

$$\Delta n = \frac{\pi\alpha I}{\sqrt{\epsilon}\hbar\Omega}\Delta t, \quad \Delta\mathcal{E} = \frac{\pi\alpha I}{2\sqrt{\epsilon}}\Delta t, \tag{4}$$

where $\alpha \sim 1/137$, ϵ is the dielectric constant surrounding graphene, $\hbar\Omega$, I, and Δt are the photon energy, peak intensity, and duration of the pump pulse assuming the square-shape pulse. Here we have neglected the Pauli blocking of the photon absorption. In this case, $t = 0$ corresponds to the time at which the quasi-equilibration of intrinsic and photo-carriers completes.

On the other hand, in the case (b) where the OP scattering is dominant, we assume that all the energy of photogenerated carriers is taken by intraband OP emission, and then the quasi-equilibration by the CC scattering and recombination by the interband OP emission follow. The latter assumption is rather inaccurate in the sense that the distribution function in a real situation can deviate from the quasi-Fermi distribution due to the interplay between CC and interband OP scattering. However, for qualitative understanding of the dynamics this assumption is sufficient. Taking these assumptions into account and setting $t = 0$ at the time of completion of all the possible OP emission, the initial conditions for the case (b) take the same form as Eq. (3) except the factor $\hbar\Omega_{cas}/\hbar\Omega$ is multiplied to $\Delta\mathcal{E}$ in Eq. (4), where $\hbar\Omega_{cas}$ is the average energy of a carrier after all the possible cascade OP emission and can be calculated from the photon energy of the pumping, $\hbar\Omega$, and the energy-dependent emission rates of Γ- and K-OPs, $\tau_{\Gamma,\text{intra}}^{(-)}$ and $\tau_{K,\text{intra}}^{(-)}$. It is worth mentioning that $\hbar\Omega_{cas}$ cannot be zero because of the energy difference between Γ- and

K-OPs as well as the energy dependences of the emission rates which go linearly down to zero when the carrier energy is equal to the OP energy. For instance, our calculation showed that $\hbar\Omega_{cas} \simeq 50\,\text{meV}$ for $\hbar\Omega = 800\,\text{meV}$. More general model with simplified rate equations taking into account the interplay between OP and CC scattering as $\hbar\Omega_{cas}/\hbar\Omega$ being an arbitrary parameter has been developed elsewhere [13].

The real part of dynamic conductivity of intrinsic graphene under optical pumping can be expressed as follows [14]:

$$Re\ \sigma_\omega \simeq \frac{e^2}{\hbar}(1 - 2f_{\hbar\omega/2}) + \frac{2e^2 v_F^2}{\pi}\frac{\tau}{1+(\omega\tau)^2}\int_0^\infty dkk\left(-\frac{df_\varepsilon}{d\varepsilon}\right), \tag{5}$$

where τ is the momentum relaxation time. The first term in Eq. (5) corresponds to the interband contribution which can be negative when the rate of stimulated emission exceeds the rate of absorption, i.e., when the population inversion takes place. Since the distribution function is the quasi-Fermi distribution, the condition of the population inversion for the photon energy $\hbar\omega$ is simply represented as $\varepsilon_F > \hbar\omega/2$. On the other hand, the second term corresponds to the intraband contribution (Drude conductivity) which is always positive in the system under consideration. When the real part of the dynamic conductivity becomes negative at some frequency, the electromagnetic wave at that frequency passing through optically pumped graphene is amplified and it serves as a gain medium. Note that from Eq. (5) one can say that the minimum value of the conductivity is $-e^2/\hbar$.

3. RESULTS AND DISCUSSION

Using the model developed above, we investigate the population inversion and the dynamic conductivity in intrinsic graphene under pulse excitation. In calculation, we assumed $\hbar\Omega = 800\,\text{meV}$ and $\Delta t = 80\,\text{fs}$, corresponding to the pulse excitation by a commercially available femtosecond laser with telecommunication wavelength $1.55\,\mu\text{m}$, and set $T_l = 300\,\text{K}$ and $\epsilon = 5.5$. The latter corresponds to the effective dielectric constant of the interface between the air and SiC, i.e., to a layer of exfoliated graphene on top of a SiC substrate.

Figure 1 illustrates the time evolution of the quasi-Fermi level and carrier temperature in the cases (a) and (b) with different pumping intensity. It is clearly demonstrated in Fig. 1 that the population inversion at THz frequencies, say, up to about 4 THz corresponding to $\hbar\omega/2 \sim 8\,\text{meV}$, can be achieved in either case, and that it lasts on the order of 10 ps. However, the time dependences of the quasi-Fermi level and carrier temperature as well as the threshold pumping intensity for each case are fundamentally different. First, in the case (b), the threshold intensity for the population inversion is about one order of magnitude larger than in the case (b), and the carrier temperature becomes negative. This cooling is due to the fact that the photogenerated carriers falling into near the Dirac point after the cascade OP emission have lower average energy than that of intrinsic carriers, resulting in the decrease in the total energy and, thus, in the temperature. On the other hand, in the case (a), the quasi-Fermi level is negative and the carrier temperature is much higher than the lattice temperature initially. These correspond to very hot carrier distribution created by the pulse excitation. After 5–20 ps, carriers having very high energy are accumulated near the Dirac point due to the intraband OP emission, forming the population inversion.

The rate of recombination via the interband OP emission strongly depends on the carrier distribution because the large fraction of interband transition can be prevented by the Pauli blocking.

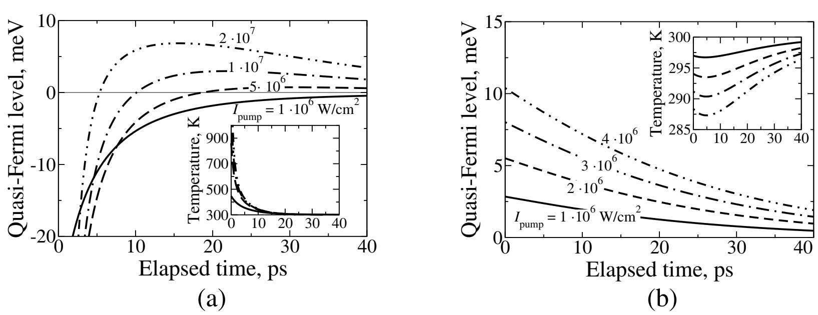

Figure 1: Time evolution of the quasi-Fermi level and carrier temperature in the cases (a) and (b) with different pumping intensities.

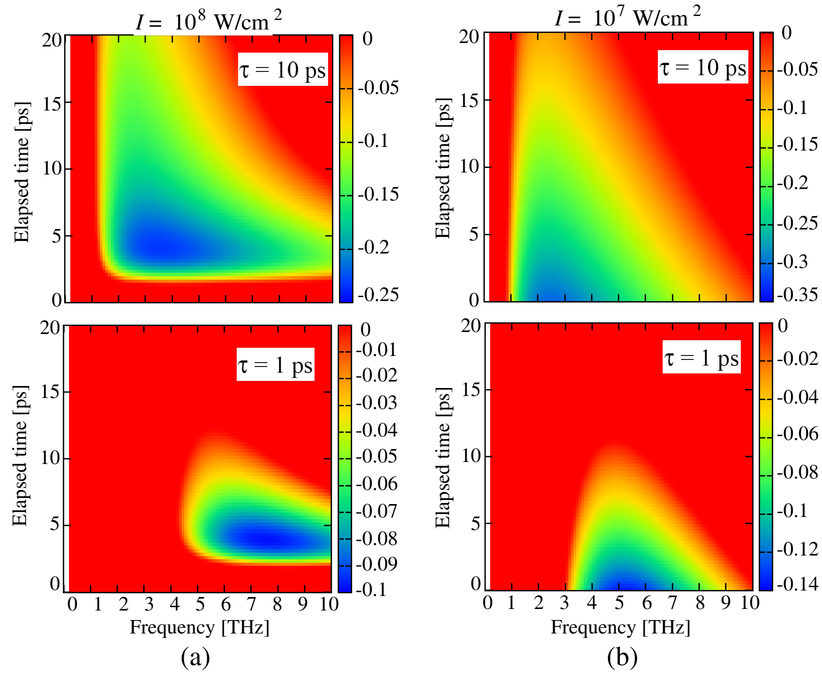

Figure 2: Normalized time-dependent dynamic conductivity in the cases (a) and (b) with the pumping intensities $I = 10^8\,\mathrm{W/cm}^2$ and $10^7\,\mathrm{W/cm}^2$, respectively, and with different momentum relaxation times $\tau = 10\,\mathrm{ps}$ (upper panels) and $\tau = 1\,\mathrm{ps}$ (lower panels).

Considering the linear energy dependences of the interband OP scattering rates and the linear density of states for the initial state of a carrier, the recombination only occurs for carriers with their energy lower than OP energies, and the recombination rates have maxima at half the OP energies ($\sim 100\,\mathrm{meV}$ for Γ-OP and $\sim 80\,\mathrm{meV}$ for K-OP). Moreover, the linear density of states indicates that the recombination, which takes place only in the lower-energy region, is less frequent than the energy relaxation, which takes place in the higher-energy region. With these reasons, it is expected that the rate of the recombination is slower than the rate of energy relaxation via the intraband OP emission. In fact, the achievement of the population inversion in the case (a) is attributed to this imbalance between intraband and interband OP emission.

Also, the larger threshold intensity in the case (a) is attributed to the fact that the recombination takes place from the beginning even before most of carriers are accumulated near the Dirac point, and therefore more carriers are lost before the population inversion.

Figure 2 shows the time-dependent dynamic conductivity in the cases (a) and (b) with the pumping intensities $I = 10^8\,\mathrm{W/cm}^2$ and $10^7\,\mathrm{W/cm}^2$, respectively, and with different momentum relaxation times, calculated from Eq. (5). In Fig. 2, we cut the positive value of $Re\ \sigma_\omega$ and normalized it by $e^2/\hbar$. and set it to zero. It is demonstrated that the negative dynamic conductivity is achieved at some frequency range in both cases. As can be seen in Fig. 2, the range of the negative dynamic conductivity extends from a few THz to above 10 THz. The threshold intensity of the negative dynamic conductivity and its minimum value depend on the value of the momentum relaxation time as well as which limitting case we assume. The threshold frequency is determined primarily by the rapid increase of the Drude conductivity below the THz region and thus by the momentum relaxation time. In principle, the threshold intensity of the negative dynamic conductivity is larger than that of the population inversion and their difference is larger in the case (a) than in the case (b) because the higher carrier concentration in the former means the larger Drude conductivity.

Qualitatively speaking, the effect of the CC scattering can be smeared by the introduction of high-k dielectric layer and/or substrate. This leads to the dielectric screening of the Coulomb potential of carriers and, hence, to slowing down the quasi-equilibration.

4. CONCLUSION

We investigated the carrier relaxation dynamics in intrinsic graphene under pulse excitation taking into account OP scattering and CC scattering. We considered the two limiting cases (a) where the CC scattering quasi-equilibrates carriers at all times, and (b) where the energy relaxation by intraband OP emission is dominant. We developed rate equations for the quasi-Fermi level and carrier temperature and calculate their time evolution. We showed that in both cases the population inversion in the THz range can be achieved on the order of 10 ps after the pulse excitation. We revealed that the threshold pumping intensity for the negative dynamic conductivity in the case (a) is one order of magnitude smaller than that in the case (b) because of the thermal broadening of the carrier distribution by the CC scattering.

ACKNOWLEDGMENT

This work has been financially supported in part by the JSPS Grant-in-Aid for Specially Promoted Research and JSPS Grant-in-Aid for Young Scientists (B).

REFERENCES

1. Berger, C., et al., "Ultrathin epitaxial graphite: 2D electron gas properties and a route toward graphene-based nanoelectronics," *J. Phys. Chem. B*, Vol. 108, No. 52, 19912–19916, 2004.
2. Novoselov, K. S., et al., "Two-dimensional gas of massless Dirac fermisons in graphene," *Nature*, Vol. 438, 197–200, 2005.
3. Geim, A. K. and A. H. MacDonald, "Graphene: Exploring carbon flatland," *Physics Today*, Vol. 60, No. 8, 35, 2007.
4. Ryzhii, V., M. Ryzhii, and T. Otsuji, "Negative dynamic conductivity of graphene with optical pumping," *J. Appl. Phys.*, Vol. 101, No. 8, 083114, 2007.
5. Ryzhii, V., et al., "Feasibility of terahertz lasing in optically pumped epitaxial multiple graphene layer structures," *J. Appl. Phys*, Vol. 106, No. 8, 084507, 2009.
6. Ryzhii, V., et al., "Terahertz lasers based on optically pumped multiple graphene structures with slot-line and dielectric waveguides," *J. Appl. Phys.*, Vol. 107, No. 5, 054505, 2010.
7. Ryzhii, V., et al., "Device model for graphene nanoribbon transistor," *Appl. Phys. Exp.*, Vol. 1, 063002, 2008.
8. Karasawa, H., et al., "Observation of amplified stimulated terahertz emission from optically pumped heteroepitaxial graphene-on-silicon materials," *J. Infrared Milli. Thrz. Waves*, Vol. 32, No. 5, 655–665, 2011.
9. Satou, A., T. Otsuji, and V. Ryzhii, "Theoretical study of population inversion in graphene under pulse excitation," *Jpn. J. Appl. Phys.*, Vol. 50, No. 7, 070116, 2011.
10. Otsuji, T., et al., "Terahertz light amplification by stimulated emission of radiation from optically pumped graphene," *Proc. SPIE*, Vol. 8023, 802304, 2011.
11. Sun, D., et al., "Ultrafast relaxation of excited Dirac fermions in epitaxial graphene using optical differential transmission spectroscopy," *Phys. Rev. Lett.*, Vol. 101, No. 15, 157402, 2008.
12. Dawlaty, J. M., et al., "Measurement of ultrafast carrier dynamics in epitaxial graphene," *Appl. Phys. Lett.*, Vol. 92, No. 4, 042116, 2008.
13. Ryzhii, V., et al., "Effect of heating and cooling of photogenerated electron-hole plasma in optically pumped graphene on population inversion," *Jpn. J. Appl. Phys.*, Vol. 50, No. 9, 094001, 2011.
14. Falkovsky, L. A. and A. A. Varlamov, "Space-time dispersion of graphene conductivity," *Eur. Phys. J.*, Vol. 56, 281–284, 2007.

RoF-DAS over WDM-PON Using Bandpass-sampling and Optical TDM Techniques as Universal Entrance Network for Broadband Wireless Access

Katsutoshi Tsukamoto[1], **Tatsuhiko Iwakuni**[1], **Kenji Miyamoto**[1], **Takeshi Higashino**[1], **Shozo Komaki**[1], **Takayoshi Tashiro**[2], **Youichi Fukada**[2], **Jun-Ichi Kani**[2], **Naoto Yoshimoto**[2], **and Katsumi Iwatsuki**[3]

[1]Graduate School of Engineering, Osaka University, Japan
[2]NTT Access Network Service Systems Laboratories, Japan
[3]NTT Service Integration Laboratories, Japan

Abstract— Under the situation of mobile traffic explosion, the air interface of mobile services is rapidly improved, and new ones are being provided in new radio frequency bands. Also in order to effectively use frequency or network resources and avoid their bottleneck, the use of femto-cell or pico-cell architectures has been started. Backhaul networks accommodating a huge number of these pico- and femto-cell stations become more important issue. Broadband fixed access networks like FTTH systems will play an important roll as an entrance network for broadband wireless access. Radio on Fiber (RoF) technologies are able to transparently transmit various types of radio services, and its operation as entrance networks realizes an effective universal platform for newly coming air interfaces. RoF-DAS over WDM-PON using bandpass-sampling and optical TDM techniques has been proposed as a universal entrance network for broadband wireless access. This paper introduces its proposed architecture and reports the latest results of experimental and theoretical investigation of the transmission performance.

1. INTRODUCTION

Mobile traffic is rapidly increasing to access variety of cloud services, and their access methods diversifies in various types of radio air interfaces, 3.5G, 3.9G, next coming 4G, commercial or private WLAN. This trend requires the more and more efficient use of radio frequency, and the reduction of radio cell size for heterogeneous wireless access. Then the distribution of a huge number of base stations (BSs) and the provision of more efficient and flexible mobile backhaul networks will be required in a wide area. As a broadband and flexible entrance network, we have proposed Radio on Fiber Distributed Antenna System (RoF-DAS) over WDM-PON (Passive Optical Network) architecture [1–3]. When implementing DAS on the WDM-PON architecture as shown in Fig. 1, RoF technologies enable efficient and economical antenna distributions for several different types of MIMO RF signals [4].

This paper introduces its proposed architecture, and as the latest results of experimental and theoretical investigation of the transmission performance, reports the experimental investigation of the EVM quality of MIMO RF signals in 2.4 GHz after 40 km RoF downlink transmission using optical time division multiplexing (OTDM) over WDM-PON system. Channel capacity in a wireless access zone is also investigated for different types of cell shapes easily provided by RoF-DAS over WDM-PON system.

2. MOBILE TRAFFIC ESTIMATION AND THEIR OFFLOAD

In Ref. [5], we have estimated traffic amount flowed into mobile networks from the Internet traffics via broadband fixed (wired) access networks by using the traffic amount data reported on 2007 white paper information and communications presented by Ministry of Internal Affairs and Communications, Japan [6]. We assumed following four types of scenario in the prediction model of traffic generated per a mobile user in nth year from 2007:

Type 1: $A_{\text{type1}} = 26.8 + 27 * 1.5^n$ [bps] predicted based on telephone traffic and mobile packet data communication with its annual increase rate of 50%.

Type 2: $A_{\text{type2}} = 134 + 464 * 1.5^n$ [bps] modified from type 1 model based on questionnaires results for mobile users.

Type 3: $A_{\text{type3}} = 3,940 * 1.465^n$ [bps] assumed that 10% of Internet traffic amount in fixed access networks will flow into mobile networks. Mobile packet data with its annual increase rate of 46.5%.

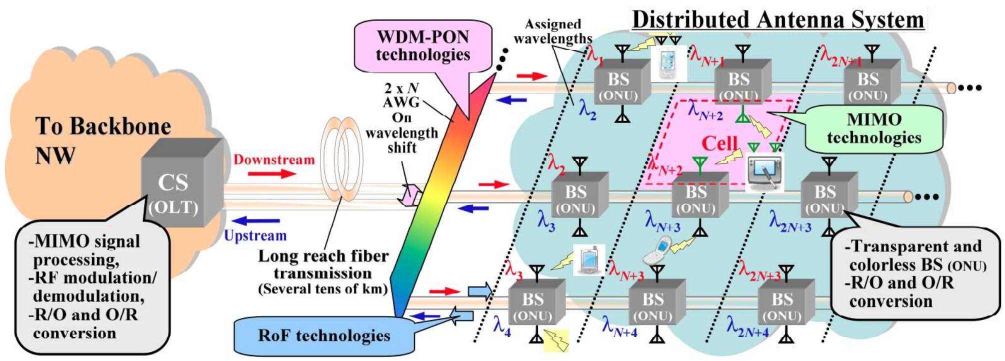

Figure 1: Configuration example of RoF-DAS over WDM-PON architecture.

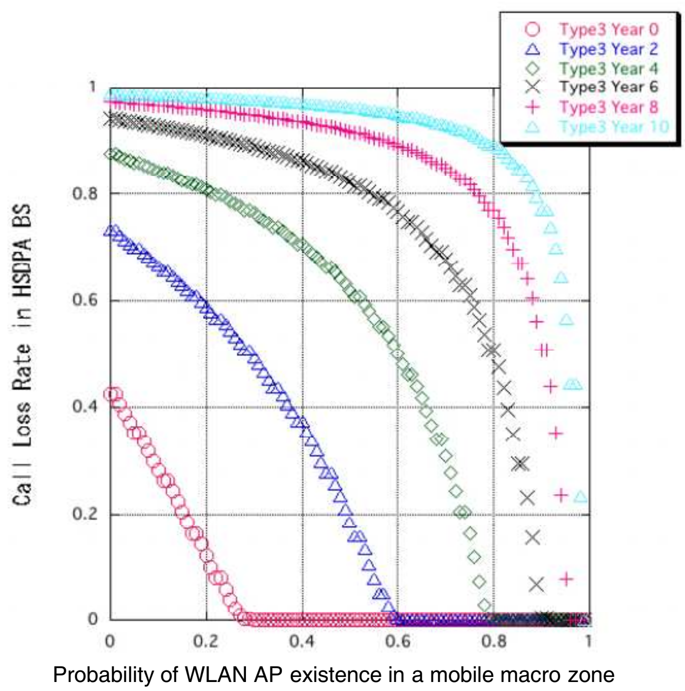

Figure 2: Calculation results of call (session) loss rate in 3.5G HSPA BS versus the existence probability of WLAN (11g) APs overlaid in a mobile macrocell.

Type 4: $A_{\text{type4}} = 3,940 * 1.465^n$ [bps] assumed that 100% of Internet traffic amount in fixed access networks flows in mobile networks.

For Type 3 traffic prediction model, Fig. 2 shows the calculation results of call (session) loss rate in 3.5G HSPA BS versus the existence probability of WLAN (11g) APs which are installed in a mobile macrocell. It is seen that the existence probability of WLAN (11g) of 80% will be required to offload the mobile Internet traffics in a macrocell after four years. These calculation results were obtained under the pessimistic assumption, and when next higher speed mobile access methods as LTE and LTE advance will be introduced in wide areas, these value can be eased. However, the rapid spread of smart phone terminals is extremely accelerating mobile Internet traffics, and the prediction of mobile traffic on the above assumption should be modified in upturn. Therefore, the rapid installation of a large number of 3.9G or 4G BS and their entrance networks will be strongly required, but the realization will also need a large investment and time. The above-mentioned overlaid WLAN AP will be still effective to offload mobile traffics and the trends must be more and more important. To realize the cost effective and rapid expansion of various types of wireless access, the broadband WDM-PON will play an important role as universal backhaul network for mobile access or wireless LAN hotspots.

3. ROF-DAS OVER WDM-PON ARCHITECTURE AND ITS EXPERIMENTAL SETUP

In the configuration shown in Fig. 1, WDM scheme is used to multiplex a large number of bidirectional RoF links between a center station (CS) and radio base stations (RBSs) [2, 3]. To multiplex different types of radio air-interfaces, each MIMO RF signal is simply bandpass-sampled [7], and multiplexed by optical TDM on a wavelength channel. This proposal is effective in achieving transparency in each wavelength channel, and has been experimentally confirmed [2].

Figure 3 shows the experimental setup to assess the downlink of RoF-DAS over WDM-PON. The amplified optical pulse with its width of 100 ps and its repetition rate of 1 GHz was divided into four streams, and each was modulated by a 802.11n signal with its mode of high-throughput mode (HT, modulation format: 64QAM), its bandwidth of 40 MHz realizing the channel bonding, and its centre frequencies of 2.422 GHz or 5.230 GHz. Four optical pulses conveying two types of bandpass-sampled RF signals and their two dummy signals for an adjacent other cell, were time-division-multiplexed by use of optical delay lines and 3 dB couplers. At the RBS, the dropped optical signal was received by a photodiode and demultiplexed in time domain by use of an electrical switch (SW) driven by the gating signals extracted from the received optical signals with a PLL. After passed through BPF, we obtained the regenerated the original 802.11n signals.

4. MEASURED EVM OF 64-QAM OFDM SIGNAL AFTER ROF TRANSMISSION

We examined back-to-back (B-B), 20 km (loss: 3.90 dB) and 40 km (loss: 7.82 dB) fiber transmission. In the experiment, clock signals recovered from received optical pulse trains by using PLL drove the electrical switch to perform TDM demultiplexing operation [8]. We evaluated RF signal quality in error vector magnitude (EVM) values of demodulated 64-QAM OFDM signals versus input optical power at a PD-TIA (P_{in}).

The measured results of the 2.4 GHz band regenerated RF signals showed no degradation in the EVM after the optical fiber transmission of up 40 km (at least). We obtained a clear constellation

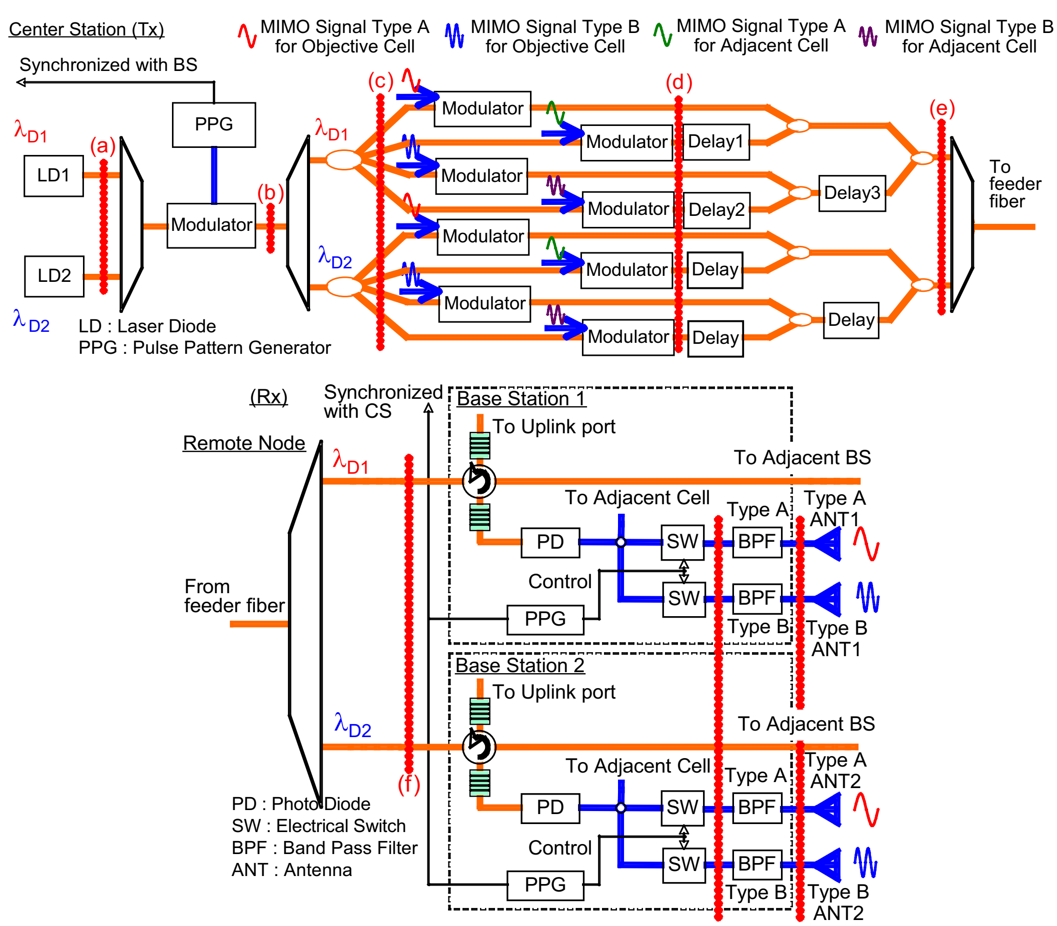

Figure 3: Experimental setup for down link of RoF-DAS over WDM-PON.

of 64-QAM achieving the minimum EVM value at the received optical power, P_{in} of about -8 dBm in 20 km transmission.

5. WIRELESS CELL DESIGN AND INVESTIGATION OF CHANNEL CAPACITY

We have examined some antenna architectures suitable for MIMO wireless transmission in RoF-DAS over WDM-PON. Fig. 4 shows considered four types of cell shapes, called type (1), (2), (3) and (4), each of which has 2, 3, 4, and 6 antennas covering one radio cell, respectively. To realize these cell shapes in the proposed system, each RBS has to equip 2, 6, 4, and 3 antennas to also cover neighboring 2, 6, 4 and 3 sector cells, respectively.

Channel capacity of the proposed system was analyzed by a computer simulation taking into

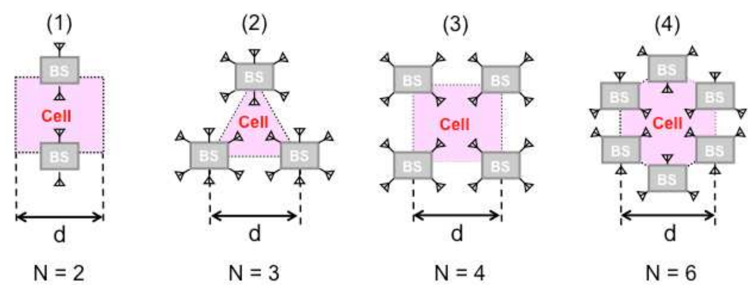

Figure 4: Considered four types of cell shapes, each of which is covered by 2, 3, 4, and 6 antennas for MIMO transmission, respectively.

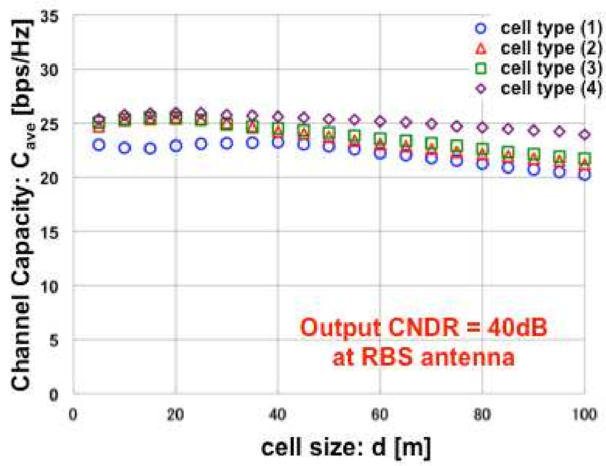

Figure 5: Simulation results of channel capacity achieved in a cell.

Table 1: Specification of simulation.

Radio Frequency	2.422 GHz
RF bandwidth	40 MHz
RF transmitted power per one antenna at RBS	10 dBm
Difference in High between RBS and MT	10 m
Boundary between Race fading Channel and Rayleigh Fading Channel	30 m from RBS
Transmitting Antenna Gain at RBS	14 dBi
HPBW (Half Power Beam Width) in Elevation	30 degree
SLL (Side Lobe Level) in Elevation	-20 dB
Antenna Duration at MT	0.06 m
Receiving Antenna Gain at MT	2.14 dBi
NF in Receiver at MT	5 dB

consideration noise components including 3rd order intermodulation distortions added in the RoF link, multipass fading distortions in wireless links, and additive noises at a MT. Table 1 summarizes the specification of simulation.

Figure 5 shows the simulation results of channel capacity achieved in a cell for four types of cell shapes as a function of cell size, d [m]. The CNDR on an OTDM channel of WDM RoF link was set up at 40 dB for any cell size and shape. It can be seen that in the range of smaller cell size, the fixed capacity of about 25 bps/Hz is obtained except for Type (1) case because the noise and distortion added in RoF link dominates the whole system. The capacity for Type (1) with two antennas is smaller because its MIMO effect is smaller than other types. As the cell size increases, the fading distortion and the additive noise at a MT decrease each capacity for each types of cell shapes. It can be found from Fig. 5 that in the larger cell size, Type (4) with six antennas can achieve the largest capacity in 4 types of cell shapes, and at the cell size of 100 m, Type (4) system has the advantage of about 2–3 bps/Hz in the capacity. These gains correspond to 80–120 Mbps for 802.11n WLAN access.

6. CONCLUSIONS

This paper has introduced the proposed RoF-DAS over WDM-PON system, and reported the experimental investigation for the EVM quality of MIMO RF signals in 2.4GHz after 40km RoF downlink transmission using OTDM over WDM-PON system. The investigation of channel capacity in a wireless access zone has shown the largest channel capacity is obtained in a hexagonal cell shape covered by 6 RBS with three antennas.

REFERENCES

1. Tsukamoto, K., T. Nishiumi, T. Yamagami, T. Higashino, S. Komaki, R. Kubo, T. Taniguchi, J. Kani, N. Yoshimoto, H. Kimura, and K. Iwatsuki, "Convergence of WDM access and ubiquitous antenna architecture for broadband wireless services," *PIERS Online*, Vol. 6, No. 4, 385–389, 2010.
2. Miyamoto, K., et al., "Experimental demonstration of MIMO RF signal transmission in RoF-DAS over WDM-PON," *MWP 2011*, paper 2122, Oct. 2011.
3. Tashiro, T., et al., "Experimental demonstration of RoF-DAS over WDM-PON with bandpass-sampling and optical TDM techniques," *IEICE Electronics Express*, Vol. 9, No. 3, 206–212, Feb. 2012.
4. Yamakami, T., et al., "An experimental investigation of applying MIMO to RoF ubiquitous antenna system," *Proc. IEEE Topical Meeting on MWP/APMP 2008*, 201–204, Sep. 2008.
5. Tsukamoto, K., et al., "Regional divide of wireless broadband system for ubiquitous networks — metropolitan area case —," *Journal of Japan Society of Information and Communication Research*, Vol. 27, No. 1, 1–10, May 2009 (in Japanese).
6. http://www.soumu.go.jp/johotsusintokei/english/.
7. Kohlenberg, "Exact interpolation of band-limited functions," *AIP J. of Applied Physics*, Vol. 24, No. 12, 1432–1436, Dec. 1953.
8. Tashiro, T., et al., "40 km fiber transmission of time domain multiplexed MIMO RF signals for RoF-DAS over WDM-PON," *OFC/NFOEC 2012*, OTu2H.4, Mar. 2012.

Development of Heterogeneous Radio Access Network Using Radio on Fiber and Its Field Trial

T. Higashino, S. Okumura, K. Hayasaka, K. Tsukamoto, and S. Komaki
Division of Electric, Electronic and Information Engineering
Graduate School of Engineering, Osaka University, Japan

Abstract— In this paper, we describe the convergence of broadcasting and heterogeneous communication RF signals over the radio-on-fiber network. One feature of this approach is that multiple RF signals are converged on the physical layer and they are transmitted to the remote site transparently. This paper focused on the intermodulation distortion when heterogeneous OFDM RF services are transmitted. Field trial experiment found that critical degradations were not found in multiple service transmission over RoF network.

1. INTRODUCTION

As for nationwide progressing the terrestrial digital broadcasting and high-speed Internet access services such as the Fiber-To-The-Home (FTTH) with the optical fiber network is rapidly spread in Japan. The equipments of the broadcasting and communication infrastructure is rapidly developed in recent years, and in Japan, various communication services like IP broadcasting, one segment broadcasting, and a high-speed mobile Internet communication are supplied in the urban area. On the other hand, the mountainous area and isolated islands where the equipments of the broadcasting and communication infrastructure are not rapidly condtructed. The rural area have a serious problem so called "digital divide". The strategy to constructing broadcasiting and communication infrastructure is planed, however, it is a current state that additional construction of infrastructure equipments are not promoted for rural regions and the isolated island because there is no hope for earnings in terms of a cost-effectiveness. Additionally, a various kind of wireless radio services appeared in a present wireless Internet access, such as 3G cellular and WiMAX, maintaining the infrastructure of each service (cable and base station installation) is attended to be difficult with respect of cost. It is preferable for such a digital divide region to install the general-purpose network infrastructure that doesn't depend on the waveform formats of radio signal. It is thought that "Radio on Fiber (In short, RoF)" technology that is capable of transferring multiple radio services to the remote site by using intensity modulated optical signal and direct detection [1–4]. But, the optical fiber constructed beforehand is needed. Since the technology-shift to the terrestrial digital broadcasting [5] from conventional analog broadcasting is conducted on July 2011, the optical fiber network is rapidly constructed by CATV operators. In order to provide digital TV broadcasting, pass-through DTV signal is transferred to residents living in the mountainous region. In addition to the digital TV, high-speed Internet access and wireless phone service such as WiFi [6, 7], WiMAX [8], and LTE are not push forwarder at rual region than urban region, because of low cost-effectiveness.

To establish a systematic design of heterogeneous radio access network, performance analysis before actual implementation is required. Some of required performance analysis are required carrier-to-noise power ratio (CNR) made from level diagram, and acceptable power loss of free space propagation. Figure 1 shows the overview of whole system. The target experimental site is located at the Nosegawa village in Nara prefecture in Japan. The system transfers digital TV RF signlas receiving from the Osaka broadcasting station relaying to the Nosegawa village with two hub station. Pass-through signals is transferred from Osaka broadcasting station to the Nosegawa village on existing FTTH link. At the Nosegawa hub, two RF services transmitted from WiFi Access Point (AP) and WiMAX base station (BS) is coupled with 10 ch DTV signals in electrical domain [9–11]. These RF services are converted to optical signal as subcarriers of optical light source. Optical RF signal is transferred to the remote site on new FTTH link. Thus, the WiMAX is capable of 2 by 2 multiple-input multiple-output (MIMO), plural antenna element must be constructed to achieve spatial division multiplexing or antenna diversity. At the remote site, three kind of RF services such as digital TV, WiFi and WiMAX are provided [12, 13].

This paper describes as follows. After the description of system configuration, acceptable path loss is evaluated in order to clarify the required carrier to noise power ratio (CNR) at the output of RoF link before re-radiation. Moreover, the CNR improvement due to the supurious suppression

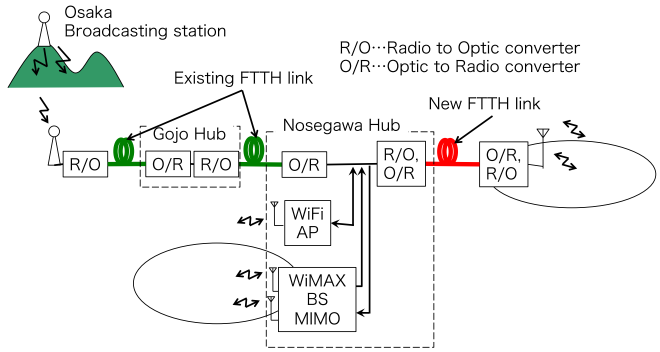

Figure 1: Overview of system configuration.

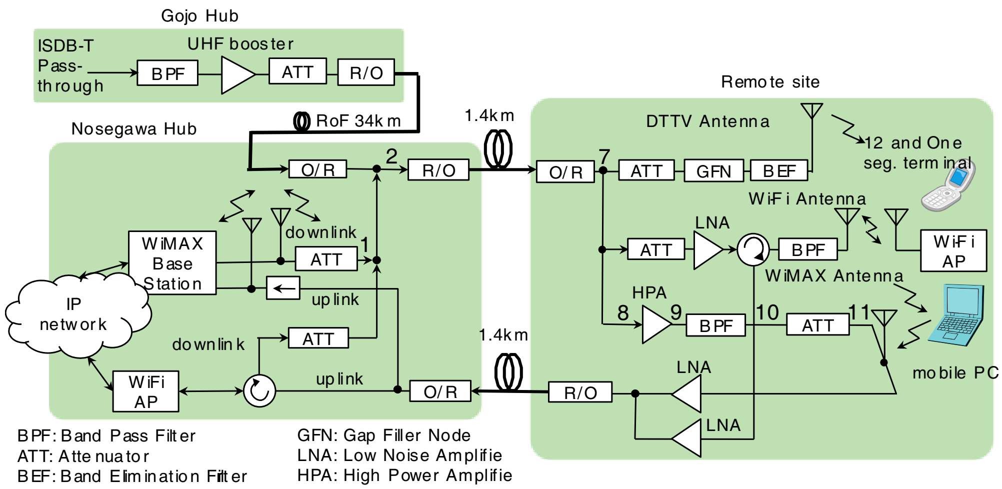

Figure 2: System configuration.

at the intermidiate node in tandem RoF link is described. Finally, throughput performance of WiMAX downlink UDP stream is shown as an example of field trial experiment.

2. SYSTEM CONFIGURATION

Figure 2 shows a block diagram. The pass-through signal of digital TV includes analog broadcasting signals and undesired TV channels, then they are input to the RoF transmitter module. It is amplified with the UHF booster (gain: 40 dB), and the band pass filter (470–550 MHz) is used to eliminate undesired TV channel. Filtered RF signals modulate the O/R converter, then optical RF signal is tranfered to the Nosegawa hub through the 34 km single mode fiber. Once their ISDB-T signal is converted to electrical signal, WiFi and WiMAX signals are coupled. At the remote site, every service is discriminated by a use of BPF. 10 ch ISDB-T signal is amplified and adjusted to 10 dBm/ch evenly by the use of Gap Filler Node (GFN). WiMAX and WiFi signals are amplified and duplexed uplink and downlink RF stream by the use of circulator. The 12 and one segment digital broadcasting, WiFi, and WiMAX services are provided at remote site. WiMAX is not capable of spatial division multiplexing, but is single antenna syetem.

3. ACCEPTABLE PATH LOSS EVALUATION

Figure 3 shows the model for acceptable path loss estimation. The RoF link is modeled as an additive white gaussian noise channel (AWGNC). The RF power amplifier boosts the output signals of O/R converter. Free space loss is assumed between trasmitting antenna and receiving antenna. The carrier-to-noise power ratio (CNR) before terminal input, γ_{ter}, is represented as,

$$\gamma_{ter} = \frac{\frac{P_{RF}}{L}}{N_R + \frac{P_{RF} \cdot F}{L \cdot \gamma_{rof}}}, \tag{1}$$

where P_{RF}, L, N_R, F, $\gamma_{\rm rof}$ are output RF power from antenna, path loss, receiver noise power over signal bandwidth, noise figure of amplifier, and CNR at the output of RoF link, respectively. If the $\gamma_{\rm ter}$ is considered as a required CNR at terminal, $\gamma_{\rm ter} = \gamma_{\rm req}$. If the Eq. (1) is solved to L, it stands for the acceptable path loss, L_{ac}, as

$$L_{ac} = \frac{P_{RF}}{N_R} \cdot \left(\frac{1}{\gamma_{req}} - \frac{F}{\gamma_{rof}} \right). \tag{2}$$

Figure 4 shows the numerical results of Eq. (2) for three RF services: DTV, WiFi, and WiMAX. $P_{\rm RF}$ of services are 10 dBm, −10 dBm and 3 dBm, respectively. The $\gamma_{\rm req}$ of three services are assumed to 20 dB, 30 dB and 20 dB, respectively. Noise figure, F, is assumed to 5 dB for every service. It is found that CNR at the RoF output must achieve required CNR at terminal plus F [dB]. $L_{\rm ac}$ is saturated in spite of increasing of CNR at RoF output. Saturation value of $L_{\rm ac}$ is limit by the $P_{\rm RF}$.

4. HETEROGENEOUS ROF LINK COUPLING

Figure 5 shows heterogeneous OFDM spectrum and a neccesity of supurious suppression at the output of O/R in the Nosegawa hub. This figure shows that surpurious emission noise degrades the CNR performance of R/O input port of WiFi and WiMAX, because the noise power of O/R output additively coupled with WiFi and WiMAX transmitter output line. This surpirous emittion suppression improves CNR performance of the antenna output at the remote site.

Figure 6 shows the level diagram and CNR performance of WiMAX RF signal transportation in cases of with surpurious suppresion and without suppression. Horizontal number indicates the measurement point in the block diagram. 20 dB suppression improves 20 dB CNR performance directly.

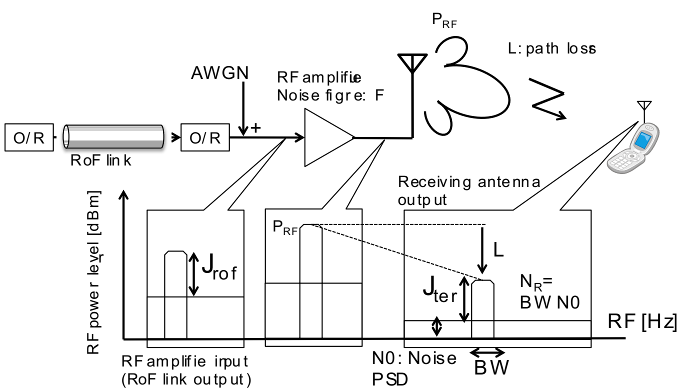

Figure 3: Analysis model.

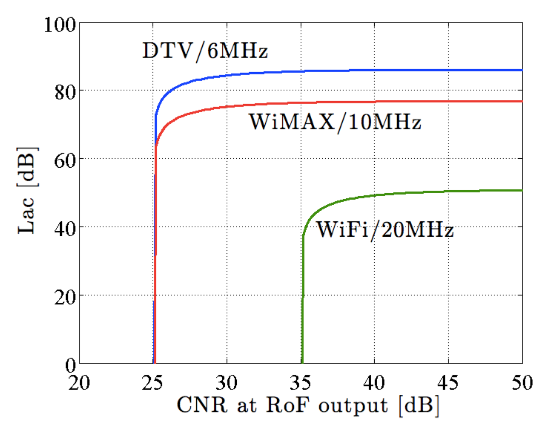

Figure 4: Relationship between $L_{\rm ac}$ and $\gamma_{\rm rof}$.

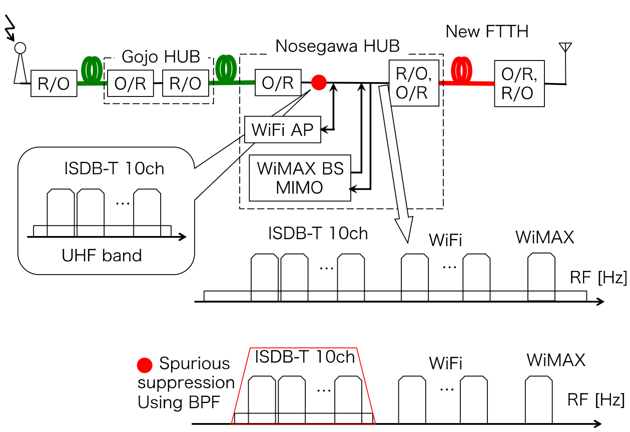

Figure 5: Heterogeneous RoF link coupling.

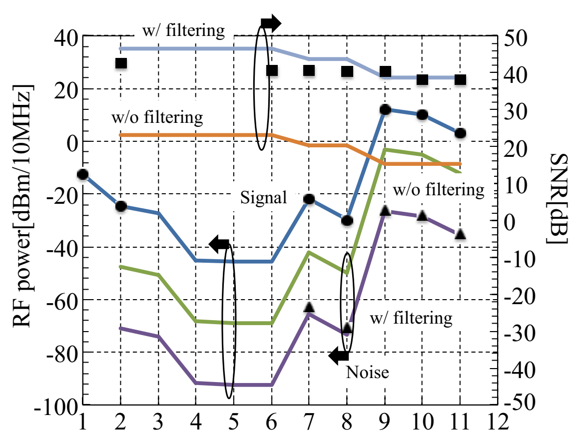

Figure 6: Level diagram of WiMAX transportation.

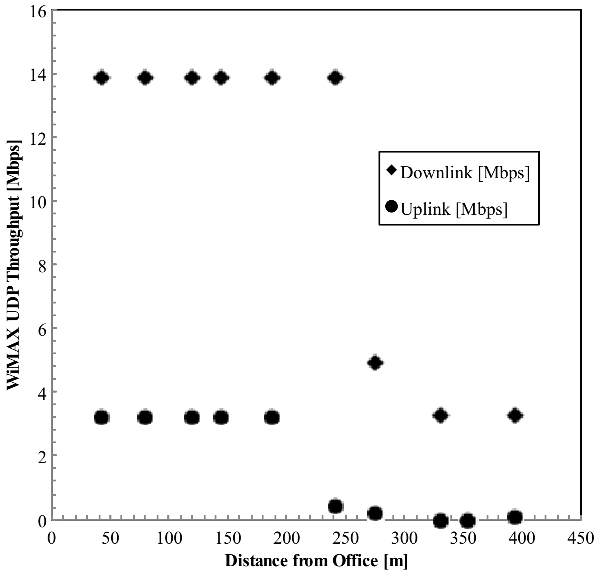

Figure 7: Throughput of WiMAX (distance).

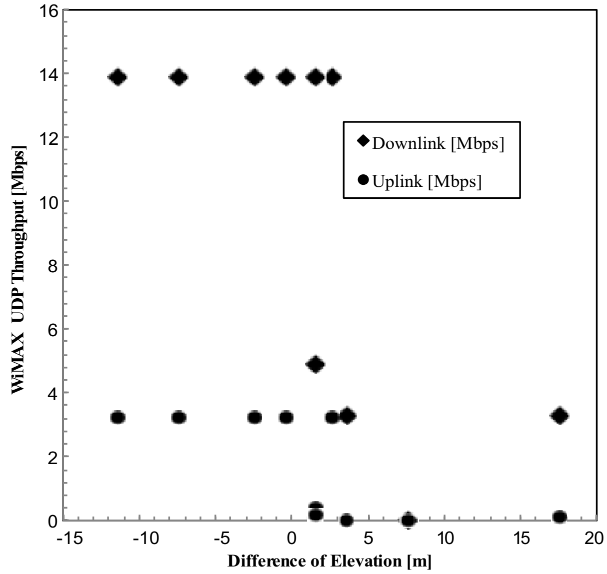

Figure 8: Throughput of WiMAX (elevation).

5. FIELD TRIAL EXPERIMENT

Figure 7 shows the throughput performance of WiMAX up/down link. Stable high performance is obtained, because transmitting antenna of WiMAX system have sharp directivity to north area. However, the difference altitude prevents the propagation of WiMAX RF signals then wireless coverage is limited up to about 220 m from the transmission point. In the coverage, throughput performance for downlink of 14 Mbps is obtained.

Figure 8 shows the throughput performance of WiMAX up/down link with related to difference of elevation between transmitting and receiving point. WiMAX antenna whose half value angle and absolute gain of 7 degree in the vertical plane and 17 dBi, respectively, is used in the trial. Stable high performance is obtained within a few difference of 5 m. However, WiMAX service cannot be provided the difference of eleveation over 5 m. As mentioned in Figure 4, high transmittion power is required in order to improve the acceptable path loss.

6. CONCLUSIONS

This paper described on the heterogeneous radio access network utilzing broadband radio on fiber link and its report of field trial experiment. This is the first practical trial of heterogeneous radio transferring using RoF technology. And it is found that required CNR at output of RoF link is enough to be required CNR at wireless terminal plus noise figure of RF amplifier before antenna feeder. Although strict high path loss due to the mountanous profile prevents the wide service coverage, critical degradation was not be found in the throughput performance of WiMAX system.

REFERENCES

1. Tsukamoto, K., H. Onodera, K. Kyung-Hwan, T. Nakamura, T. Higashino, Y. Aburakawa, S. Komaki, K. Wakamori, K. Takahashi, T. Suzuki, K. Kazaura, A. M. Shah, K. Omae, M. Matsumoto, and T. Satou, "Link design of radio on free space optic system for heterogeneous wireless services," *Technical Dig. of MWP'08*, Vol. 1, 232–5, 2008.

2. Uegaki, K., K. Kumamoto, K. Yasukawa, K. Inagaki, T. Higashino, K. Tsukamoto, and S. Komaki, "A novel nonlinear distortion suppression method in RoF systems using optical filter," *Technical Dig. of MWP'07*, Vol. 1, 33–6, 2007.

3. Higashino, T., K. Tsukamoto, S. Komaki, K. Kazaura, K. Wakamori, M. Matsumoto, and T. Satou, "A demonstrative link design of RoFSO and its optimum performance — indoor short range experiment and a new model of optical scintillation," *International Telecommunication Union, Proceedings of the 2009 ITU-T Kaleidoscope Academic Conference: Innovations for Digital Inclusions*, 7, 2009.

4. Kumamoto, K., K. Yasukawa, K. Inagaki, T. Higashino, K. Tsukamoto, and S. Komaki, "Convergence of broadcasting and communication utilizing CATV network," *Proc. of AP-RASC'10*, Vol. DC-2-3, 2010.
5. "Transmission system for digital terrestrial television broadcasting," ARIB STD-B31.
6. "Broadband mobile access communication system (CSMA)," ARIB STD-T77.
7. "Second generation low power data communication system/wireless LAN system," ARIB STD-T66.
8. "OFDMA broadband mobile wireless access system," ARIB STD-T94.
9. Maeda, M. and M. Yamamoto, "FM-FDM optical CATV transmission experiment and system design for HDTV signals," *IEEE J. Select. Areas Commun.*, Vol. 8, No. 7, 1257–1313, September 1990.
10. Darcie, T. and R. Tucker, "Intermodulation harmonic distortion in InGaAsP lasers," *Electron. Lett.*, Vol. 21, No. 12, 665–666, August 1985.
11. Hayasaka, K., T. Higashino, K. Tsukamoto, and S. Komaki, "A theoretical estimation of IMD on heterogeneous OFDM service over SCM RoF link," *International Topical Meeting on MWP*, Vol. 1, No. 1, 1–4, October 2011.
12. Higashino, T., K. Tsukamoto, and S. Komaki, "The convergence of broadcasting and heterogeneous wireless communications over fiber network — An experiment of field trial —," *2011 XXXth URSI General Assembly and Scientific Symposium*, 1–4, August 2011.
13. Higashino, T., K. Miyamoto, K. Tsukamoto, S. Komaki, T. Tashiro, K. Hara, J. Kani, N. Yoshimoto, and K. Iwatsuki, "A new configuration of broadband wireless access in heterogeneous ubiquitous antenna and its experimental investigation," *PIERS Online*, Vol. 7, No. 4, 311–315, 2011.

Next Generation Free-space Optical System by System Design Optimization and Performance Enhancement

Mitsuji Matsumoto
GITS/GITI, Waseda University, Japan

Abstract— Free Space Optical (FSO) system is being realized as an alternative means to compensate and/or replace the traditional optical communication in many applications where the fiber cable is not available. New generation FSO systems in which the optical signal after transmission over free-space is directly coupled into a single mode fiber have attracted considerable interest recently due to its remarkable advantages. This paper introduces the concept of FSO technology and reviews our recent achievements on development and demonstration of new generation free-space optical systems. The other aspects on the system design optimization and performance improvement are also clarified in this paper.

1. INTRODUCTION

Light-wave communication has become an attractive means for broadband access networks. Recently, free-space optical (FSO) communication is receiving considerable attention to provide broadband communications due to its remarkable advantages including flexibility, easy-to-install, and license-free. FSO systems can be categorized into 2 broad groups, i.e., conventional FSO based-systems, and new generation FSO based-systems. Conventional FSO systems operate at 800 nm wavelength band, and need to use O/E and E/O conversions before emitting/coupling optical signals from/into an optical fiber. They have been used for data transmission but due to power and bandwidth limitation of optical devices in this wavelength band, they are not possible to operate above 2.5 Gbps [1]. The use of 0.8 μm wavelength optical devices also makes it incompatible with current high capacity optical fiber systems. Because of this, it is not being considered as a suitable and practical solution for very high-speed communications.

New generation FSO technology has been developed in order to overcome the limitations of conventional FSO systems [2]. Unlike conventional FSO systems, in the new generation FSO systems the necessity of converting signal from electrical to optical and vice versa before transmitting or receiving through free-space is eliminated. In this configuration, the signal is emitted directly to the free-space from the fiber termination point and at the receiving end focused directly into the fiber core. Therefore, a protocol and data rate transparent FSO link is achieved. In this paper, we review our recent achievements on development of new generation FSO systems and introduce some experimentally evaluated results. Some prospects on system design optimization and performance enhancement will also be pointed out.

2. OVERVIEW OF FSO COMMUNICATION TECHNOLOGY

2.1. Conventional FSO Systems

Conventional FSO communication systems are considered to be those operating near the 800 nm wavelength. In conventional systems, a fiber transceiver converts an electrical signal to optical signal (E/O — conversion). The electrical signal is amplified by a laser driver providing enough current to drive the laser diode. Modulated light from the laser diode is directed through space to the corresponding receiver which focuses the beam onto a photo detector (PD). The PD converts the optical signal to electrical signal. After noise filtering and reshaping the electrical signal is converted at the fiber transceiver back to an optical signal. This type of FSO communication system is depicted in Figure 1. Because of the power and bandwidth limitations imposed on optical devices operating in the 800 nm wavelength, they cannot operate at data rates above 2.5 Gbps, and they are also incompatible with most current widely deployed optical fiber networks operating at 1550 nm wavelength.

2.2. New Generation FSO Systems

The so called new generation or full-optical FSO communication systems operate at the 1550 nm wavelength. In these systems, the technology that is widely used in fiber transmission like EDFAs and WDM technology is applied. In a full-optical FSO system an optical beam is emitted directly from a fiber termination to the atmosphere using an optical antenna. At the receiver, the

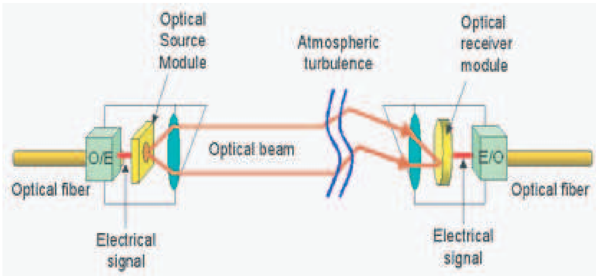

Figure 1: Conventional FSO system concept.

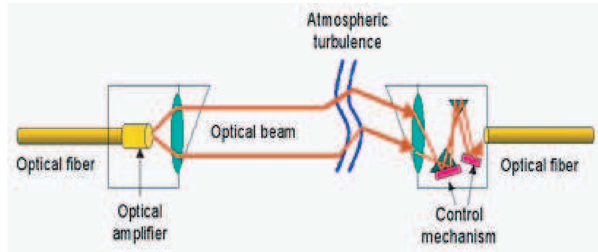

Figure 2: New generation FSO system concept.

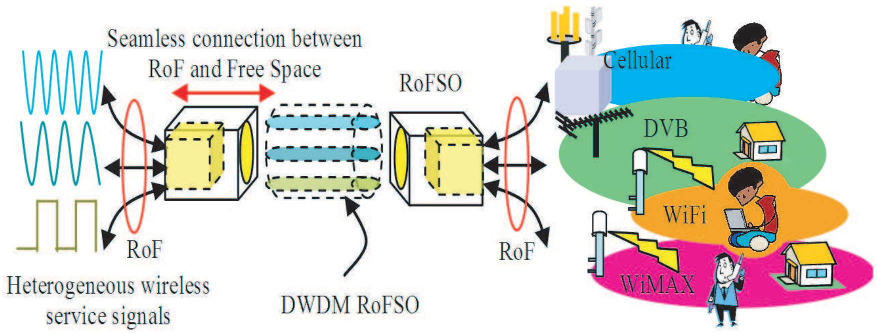

Figure 3: New generation FSO system concept.

transmitted optical beam is focused, using the receiver optics, directly to a fiber and then sent down the fiber for detection. Unlike conventional FSO communication system, in full-optical FSO communication systems the necessity of converting the signal from electrical to optical formats or vice versa for transmitting or receiving through the atmosphere is eliminated. This greatly enhances the system throughput. Also, a bandwidth and protocol transparent communication link is realized whereby the need for reconfiguring the transceiver is eliminated even when the nature of the transmitted signal changes due to varying bit-rate, signal format or wavelength channel. The merits of full-optical FSO communication system make it a strong candidate for access technology in the envisaged Next Generation Network. The concept of full-optical FSO communication system is shown in Figure 2.

2.3. Advanced DWDM RoFSO System

One attractive application area for the above described full-optical FSO communication system is deploying it as an access technology for providing broadband heterogeneous wireless services. In this scenario, various kinds of wireless signals such as terrestrial digital TV, 3G cellular signals like W-CDMA, WLAN or new innovative wireless services can be transmitted by using DWDM full-optical FSO links. Recently, we developed and experimentally evaluated an advanced DWDM full-optical FSO system link for multiple RF signal transmission [3]. The basic transceiver design concept is similar to the one we have developed for the full-optical FSO communication system but it was optimized for transmission of multiple RF signals using DWDM technology. The basic concept of the advanced full-optical FSO communication system using DWDM technology for multiple RF signal transmission is depicted in Figure 3.

3. EXPERIMENT EVALUATION RESULTS

3.1. High Speed Optical Signal Transmission

Based on the new generation FSO technology, a pair of new compact FSO antenna was developed and a world record high speed optical signal transmission was demonstrated recently. In the experiment, we placed two FSO terminals on rooftops of two buildings with a distance of about 210 m in Pisa, Italy. In both FSO antennas a collimator and a custom beam expander were used for bidirectional operation. At transmitting site, the FSO antenna emitted a collimated beam light directly from a single-mode fiber output to free-space, and at the receiving site another FSO antenna efficiently focused the free-space laser beam and coupled it into a single-mode fiber. WDM signals were produced and detected in the laboratory, using typical fiber communication equipment trans-

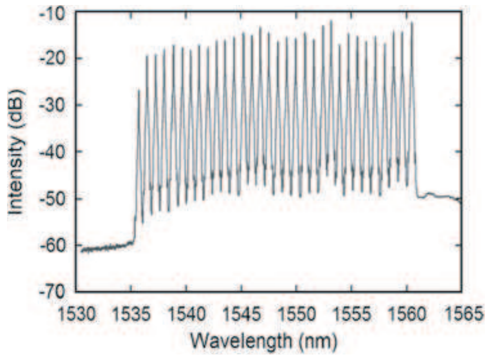

Figure 4: Optical spectrum measured at the receiving end (resolution bandwidth: 0.1 nm).

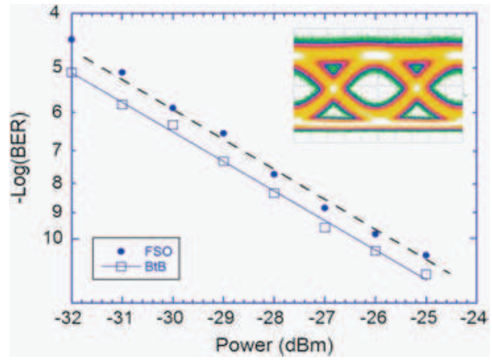

Figure 5: BER measured for channel at 1548.51 nm.

parently connected to the FSO antennas. 32 continuous-wave distributed-feedback (DFB) lasers were used with 100-GHz spacing (from 1535.7 to 1560.5 nm), aligned in polarization, combined by an arrayed waveguide grating, and modulated at 40 Gb/s. The total signal transmission capacity is 1.28 Tbps, a world record high speed signal transmission over a FSO link. Details of the experiment set up and results were presented in [4].

Figure 4 shows the output spectrum of the 32 channels. It can be seen that some side channels, particularly at the shorter wavelengths, suffered from the reduced gain of the EDFA, but overall the optical signal-to-noise ratio (OSNR) was quite acceptable. BER characteristic measurement was then measured for all WDM channels. An example is shown in Figure 5 for the BER curves in back-to-back (squares) and after transmission (dots) for the central channels. An eye diagram taken with 30-min persistence (x-axis timescale: 5 ps/div) is also inserted in the Figure. We can see that a penalty lower than 1 dB is obtained at BER.

3.2. Heterogeneous Wireless Signal Transmission

An advanced DWDM RoFSO system was developed based on a new generation FSO system for transmission of multiple heterogeneous wireless signals. We conducted a long term measurement under an actual operation environment to evaluate the system performance. In our experiment set up, two RoFSO transceivers were set up at two buildings in the Waseda University campus in Shinjuku Ward, Tokyo. The link span was 1 km. The system performance was evaluated using the specific quality metric parameters defined for transmission of the various wireless service signals, including 3G mobile cellular, terrestrial digital television broadcasting, and WLAN IEEE 802.11g/a services. WDM was used to simultaneously transmit the different wireless service signals independently over the same RoFSO link. The wireless service signals were placed on different wavelengths, which were separated using the ITU-T 100 GHz grid spacing.

For WLAN IEEE 802.11g experiment, the signal was generated at -20 dBm and fed into the RoF module with an OMI of 10 percent. A pass/fail judgment of the spectrum mask was used to evaluate quality of the transmitted WLAN signal. Figure 6 shows an example of received signal (at 2.4 GHz with 54 Mb/s, 64-QAM) with a spectrum mask after transmission over 1-km RoFSO link. In this case it is in compliance with the specified standard (i.e., spectrum mask test pass). A data transmission experiment using two laptop computers placed at the two sites and connected via a WLAN IEEE 802.11g access point to the RoFSO link was also conducted. A simple throughput measurement application was utilized to continuously transmit a 64-Mbyte file size in 8-kbyte packet size chunks. The result depicted in Figure 7 for a measurement over 24 hour period shows that the variation of the throughput characteristics was correlated to the measured mean received optical power. In this particular measurement the throughput (for both transmit [Tx] and receive [Rx]) was consistently above 12 Mb/s, and seemed to drop below this value around midday — a time usually characterized by increased transmission errors because of atmospheric turbulence. This result confirms that the RoFSO system is stable and can provide consistent TCP/IP data transmission, even when the link quality deteriorates due to atmospheric turbulence.

3.3. Connectivity Resilience during Massive Earthquake

Unfortunately, on March 11, 2011, a massive earthquake has struck off Japan's northeastern coast, shaking buildings in Tokyo for several minutes. At that moment, our RoFSO system had to maintain the automatic data measurement. Figure 8 shows the variation of the tracking status and

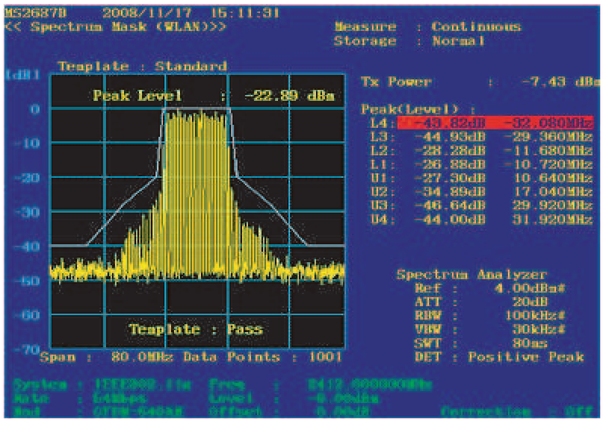

Figure 6: WLAN 802. 11g spectrum mask.

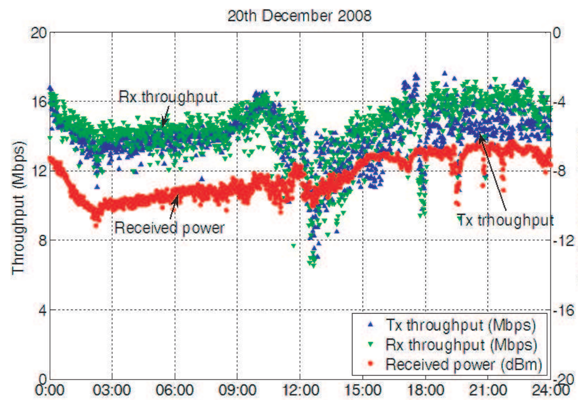

Figure 7: WLAN 802.11g throughput characteristics.

the optical received power at this time. The tracking data was measured at 10 second intervals and the received power is plotted as the average of one minute. When the Mainshock reaches the site, the error signal (Az & El_QER) of tracking system (2D-FPM: fine pointing mirror) increased significantly. It seems to be shaking out as a beacon light from the perspective of the position detection device. Nonetheless the RoFSO link was not shut down and the data shows that the tracking continued to work properly. Although there were at least three large aftershocks of magnitude 7 within one hour, high tracking error was recorded only once. Moreover, when the aftershock intensity was less than 5, the RoFSO system showed no abnormality Usually, after the earthquake, the main challenge that FSO communication is likely to face is the instability of the optical received power However, as shown in Figure 8, the new tracking scheme adopted in this innovative RoFSO system could help to maintain seamless communication connectivity even during such a massive earthquake. Therefore, based on the previous results, it has been shown that undoubtedly FSO technology turns to be very helpful in the emergency situations when other means of communication such as fiber cable or wireless networks are destroyed or temporarily unavailable.

4. SYSTEM DESIGN OPTIMIZATION AND PERFORMANCE ENHANCEMENT

4.1. System Modeling and Closed-form Expressions

To further optimize the system design, we theoretically investigated the transmission performance of the wireless signals over a turbulent FSO channel. We derived an analytical model for the optimization of the RoFSO link and closed-form expressions for BER and outage probability, taking into account the laser nonlinearity effect, system noises and atmospheric channel turbulence fading. We found that the system performance is highly sensitive to the atmospheric turbulence, received optical power, and the selection of a proper optical modulation index (OMI) for optimum performance. This work provides insight on the system design and performance characteristics relevant in implementing economical links for wireless services transmission, especially in areas lacking fiber infrastructure. Detail of the work can be referred to [5].

4.2. Reception Diversity System

To further improve FSO systems performance under effects of strong atmospheric turbulence or long transmission ranges, we introduced a spatial diversity scheme in which many receivers are used to receive the signal. In this scheme, the received optical signal is collected by multiple receiving apertures, optically combined, amplified by an optical pre-amplifier and finally detected by a photo-detector. This helps to reduce the receiver complexity, system cost and noises. Based on the model, optimal values of system parameters such as receiving aperture size, pre-amplifier gain, transmitting power are derived for different operation conditions and requirements. It is shown that a significant enhancement in system performance can be obtained by this proposed solution, especially when the atmospheric turbulence is strong. An example of the numerical results on performance of the proposed system is shown in Figure 9. In this analysis, we assume that the receivers are placed centimeters apart each other (same as coherence length of turbulence) so that the fading distribution of each receiver can be assumed to approximately independent. From the Figure it can be seen that the use of reception diversity helps to decrease significantly the receiver

Figure 8: The variation of the tracking status and the optical received power during massive earthquake (March 11 2011).

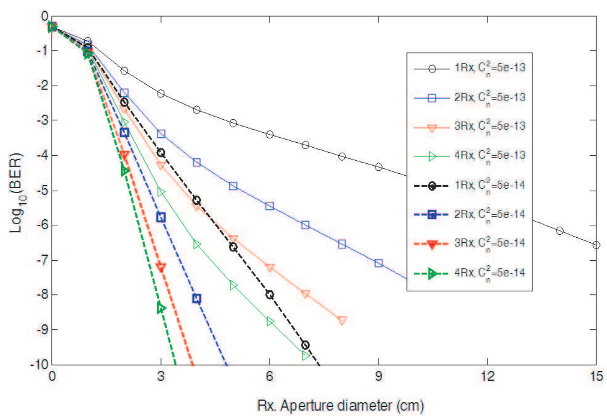

Figure 9: BER characteristics and receiver aperture diameter.

aperture size. The respective diameter of each receiver aperture when one, two, three and four receivers are used and for example a BER of 10^{-6} is required are 13 cm, 7 cm, 5 cm and 4 cm. This result may be useful to choose optimal values for new generation FSO system receiver aperture to operate under turbulence condition and other given requirements.

4.3. Advanced Tracking Mechanism

FSO systems experience fading due to the turbulent atmosphere. The random changes in the temperature gradient and pressure of atmosphere lead to the random variations of refractive index along the transmission path. These variations produce fluctuations in both intensity and phase of an optical wave propagating through this medium. Such fluctuations can lead to an increase in the link error probability, limiting the performance of the communication systems. In new generation FSO systems the impact of phase fluctuations is particularly severe due to the use of direct coupling the signal into a fiber cable at the receiver. The systems thus need specially designed terminals and precisely coupling techniques. Tracking subsystem is the most important key element in new generation FSO systems. Our developed system employing a novel tracking scheme thus could help to suppress most effects induced from atmospheric turbulence. However, under severe weather conditions such as heavy rain or strong atmospheric turbulence, the tracking capability was not enough due the limitation of the operation dynamic range. A system with improved tracking scheme and optimized system design would be necessary to provide better transmission availability for heterogeneous wireless services. Recently, an advanced tracking algorithm in the acquisition/tracking controller consisting of a pointing predictor was proposed [6]. This adaptive tracking controller can help to maintain communication link even under some severe weather conditions.

5. CONCLUSION

In this paper, we present an overview of FSO technology and some demonstration conducted recently based on a newly developed new generation FSO systems. It is confirmed that this technology can be used to transmit super high speed signal as well as heterogeneous wireless service. We also review some of our recent activities and proposals on the optimization and improvement of the developed system. It is believed that the system is suitable for application as a universal platform for providing convergence of fiber and free-space optical communication networks, extending broadband connectivity to underserved areas.

REFERENCES

1. Kim, I. I., M. Mitchel, and E. Korevaar, "Measurement of scintillation for free-space laser communication at 785 nm and 1550 nm," *Optical Wireless Communications II,* Vol. 3850, 49–62, SPIE, Sep. 1999.
2. Kazaura, K., et al., "Performance evaluation of next generation free-space optical communication system," *IEICE Transactions on Electronics*, E90-C, 381–388, 2007.
3. Tsukamoto, K., S. Komaki, and M. Matsumoto, "Development project of radio on free space optics," *Proc. SPIE*, 6788, Jan. 2007.
4. Ciaramella, E., Y. Arimoto, G. Contestabile, M. Presi, A. D'Errico, V. Guarino, and M. Matsumoto, "1.28 Terabit/s (32 × 40 Gbit/s) WDM transmission system for free space optical communications," *IEEE Journal on Selected Areas in Communications*, Vol. 27, No. 9, Dec. 2009.
5. Bekkali, A., C. B. Naila, K. Kazaura, K. Wakamori, and M. Matsumoto, "Transmission analysis of OFDM-based wireless services over turbulent radio-on-FSO links modeled by gamma — Gamma distribution," *IEEE Photonics Journal*, Vol. 2, No. 3, Jun. 2010.
6. Arimoto, Y., "Operational condition of direct single-mode-fiber coupled FSO terminal under strong atmospheric turbulence," *Proc. SPIE*, Vol. 7923, 79230O, 2011.

λ-tunable WDM/TDM-PON Using DWBA towards Flexible Next-generation Optical Access Networks

Hirotaka Nakamura
NTT Access Network Service Systems Laboratories, NTT Corporation, Japan

Abstract— This paper introduces requirements of next generation optical access network from the telecom operator's viewpoint and proposes λ-tunable WDM/TDM-PON using DWBA as a promising technological solution This paper demonstrates the feasibility of the proposed system by the transmission experiments emulating the λ-tunable ONU and OLT, and the DWBA operation.

1. INTRODUCTION

Broadband optical access systems based on passive optical network (PON) are rapidly being installed in the world. Gigabit Ethernet-PON (GE-PON) system has been first commercially installed in Japan in 2004 among the world and the number of subscribers of fiber-to-the-home (FTTH) is over 20 million in March, 2011. 10 Gbit/s-class PON systems, namely 10G-EPON and XG-PON systems, have already been standardized in IEEE in 2009 and ITU-T in 2010, respectively [1, 2]. Now, requirements of next-generation optical access networks (NGOAs), as next-generation PON2 (NG-PON2) over 40 Gbit/s as post 10-Gbit/s-class PON systems are being discussed in the Full-service access network (FSAN) Group [3, 4]. In NG-PON2, the target scope of requirements is in very broad area, e.g., the bandwidth, the accommodation number of users, the transmission distance, new functions, and new applications.

This paper introduces requirements from the telecom operator's viewpoint and proposes the best technological solution for NGOAs. This paper proposes the λ-tunable wavelength division multiplexing/time division multiplexing (WDM/TDM)-PON using dynamic wavelength and bandwidth assignment/allocation (DWBA). The WDM technology can incrementally and cost-effectively upgrade the total bandwidth of the system by adding the wavelength, because devices which are 40 Gbit/s-burst-mode transceivers and dispersion compensators used in the 40-Gbit/s-class TDM-PON are too expensive for access systems. This incremental upgradability can realize the smooth migration from the existing system. Moreover, the wavelength tunablity in the OLT and ONU can realize to change their sending and receiving wavelengths dynamically according to the utilization of the wavelength, so the bandwidth which the user demands can efficiently be allocated. This paper demonstrates the transmission experiment that uses 10 Gbit/s-class burst-mode receivers (B-Rxs), fast-switching tunable laser diode and fast-switching tunable filters (TFs) to emulate the DWBA operation.

2. REQUIREMENTS OF NEXT GENERATION OPTICAL ACCESS NETWORKS

Figure 1 shows the number of subscribers of broadband services in Japan. FTTH users are now rapidly increasing from 2004 in which GE-PON was installed, because GE-PON shares the optical fiber form the central office to the splitting point by some users and can provide cost effective broadband access system. The demand for the more broadband optical access system will be increasing and require over 10 Gbit/s bandwidth per system in the next generation.

There are many requirements from viewpoints of the user, the operator, and the society, and they will also drive future deployment of higher-capacity PON. Examples of the requirements are the capability to diversify the required bandwidth, to have incremental upgradeability of the total bandwidth, the flexible operability for the number of accommodated users, and the low power consumption To address these issues, multiple-level bandwidth allocation services with an appropriate price for each level will be required. However, the total bandwidth of TDM-PON is limited and the allocated bandwidths cannot be expanded. If we can actualize incremental upgradeability of the total bandwidth, it will greatly improve the capability to increase and diversify the required bandwidth. In the same way as with the total bandwidth, operators require flexible operability for the number of branches. After implementing this function, the power consumption of the OLT will become comparatively high. To decrease the power consumption further, we would need to decrease the number of OLTs by increasing the number of accommodated users

The main requirements of the NGOA from the viewpoint of operator are following.

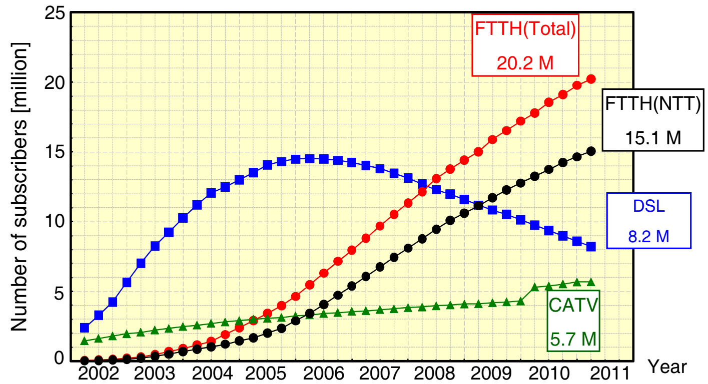

Figure 1: Number of subscribers of broadband services in Japan.

One is the incremental upgradeability of the bandwidth and the other is flexible operability for the number of branches without excess loss.

To realize these capabilities economically, we propose a hybrid multiplexing technology "λ-tunable WDM/TDM-PON using DWBA" which has a wavelength tunability in OLT and allocate the flexible bandwidth according to user demand.

3. λ-TUNABLE WDM/TDM-PON USING DWBA

Figure 2(a) shows the configuration of the proposed PON. The optical line terminal (OLT) is equipped with line cards (LCs) that output downstream signals and receive upstream signals at several wavelengths and a DWBA controller. A $1\times m$ coupler and a $1\times n$ arrayed wavelength grating (AWG) connect m-LCs to n-PON branches. An optical network unit (ONU) is equipped with a λ-tunable burst-mode transmitter (T-B-Tx) to realize a colorless function and a burst-mode receiver. Different wavelengths (λu1-λun/λd1-λdn) are assigned to each PON branch (1-n). The ONUs in the PON branch output the assigned wavelengths and their upstream signals are multiplexed in the time domain. Upstream signals with different wavelengths from those of each PON branch are multiplexed by the $1 \times n$ AWG, divided by the $1 \times m$ coupler, and input into the LCs. A tunable filter (TF) in each LC changes the transmitting wavelength according to the λ-switching signal from the DWBA controller, and the upstream signal is received by the burst-mode receiver (B-Rx).

The DWBA controller calculates the wavelength and bandwidth allocation that balances the load between LCs to satisfy requests from ONUs. It assigns a sending time to each ONU and a receiving wavelength and time to each LC. Figure 2(b) shows an example of DWBA operation with 2-LCs and 4-PON branches. DWBA observes the requests from the ONUs and sets the wavelength and time matrices of LC1 and LC2. After LC1 receives λ1 from PON branch1, in which the traffic demand is small, LC1 and LC2 receive λ2, λ3 and λ4 to meet requests from PON branch 2, PON branch 3, and PON branch 4 equally; these 3 PON branches have heavy data traffic demands.

In this system, the number of accommodated ONUs can be easily increased without any loss budget degradation, because the PON branches are bundled by the AWG. The number of LCs can be minimized due to the flexible load balance between the LCs achieved by the DWBA.

4. TRANSMISSION EXPERIMENT

4.1. Upstream Signal

Figure 3(a) shows our experimental setup, which emulates the case of 2-LCs and 4-PON branches to confirm the feasibility of realizing fast λ-switching/receiving characteristics for the upstream signal. The T-B-Tx consists of a tunable laser diode (TLD), an LN modulator for 10-Gbit/s-data signals, and an acousto-optic modulator (AOM) for the burst mode [5]. The extinction ratio (ER) of the upstream signal was 10 dB. The four wavelengths used in this experiment were 1546.9, 1547.3, 1547.7 and 1548.1 nm. Our 10-Gbit/s-class B-Rx has a high sensitivity, a wide dynamic range, and an instantaneous response [6]. The fast switching tunable filter consists of two AWGs and four SOAs. Burst-mode signals with wavelengths of λ1 and λ2 were input into LC1 in a 1-µs period, with a 15-ns guard time and a 6-dB difference in optical power. The λ-switching trigger was input into LC1 in the guard time. The λ-switching time was less than 20 ns and the amplitude of the output signal from the B-Rx was recovered within 40 ns. Figure 4(a) shows characteristics of the bit error rate (BER) of the payload of the received signal with λ1 and λ2. For the λ1-signal, the optical received power at BERs of 10^{-3} and 10^{-12} were -34.2 and -24.5 dBm, respectively. The slope of the BER curve with the TF was smaller than that without the TF, because the gain of the TF improved the BER of 10^{-3}, and the increasing NF around the -25 dBm input power degraded the BER.

4.2. Downstream Signal

Figure 3(b) shows the experimental setup for downstream signal [7]. A tunable transmitter (tunable-Tx1) with a fast-switching tunable laser diode (TLD), an LN modulator for 10-Gbit/s-data signal, and a λ controller was developed. The TLD uses a distributed Bragg reflector (DBR)-LD whose channel spacing is 50 GHz and number of the channel is 64 in the C-band. The λ controller commands the TLD to switch its output wavelength according to the programmed order for the

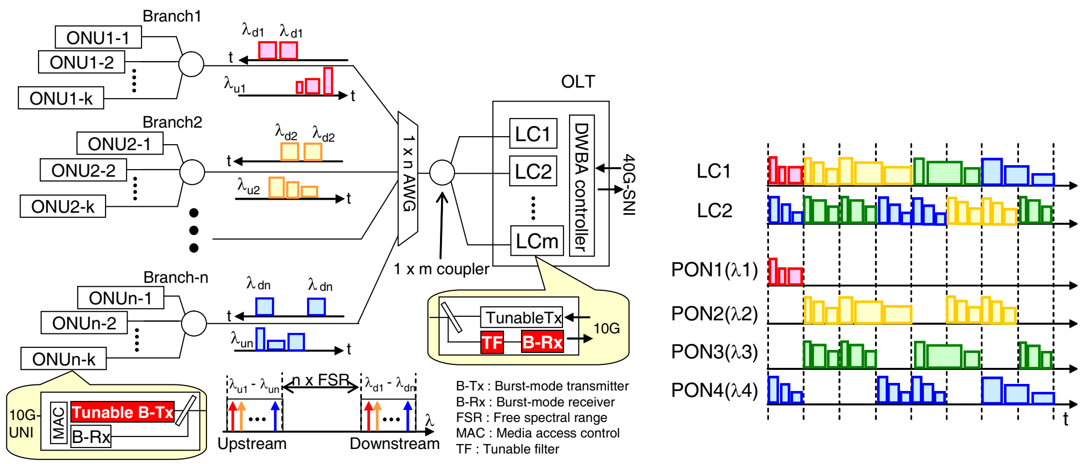

(a) (b)

Figure 2: (a) Configuration of λ-tunable WDM/TDM-PON. (b) DWBA operation.

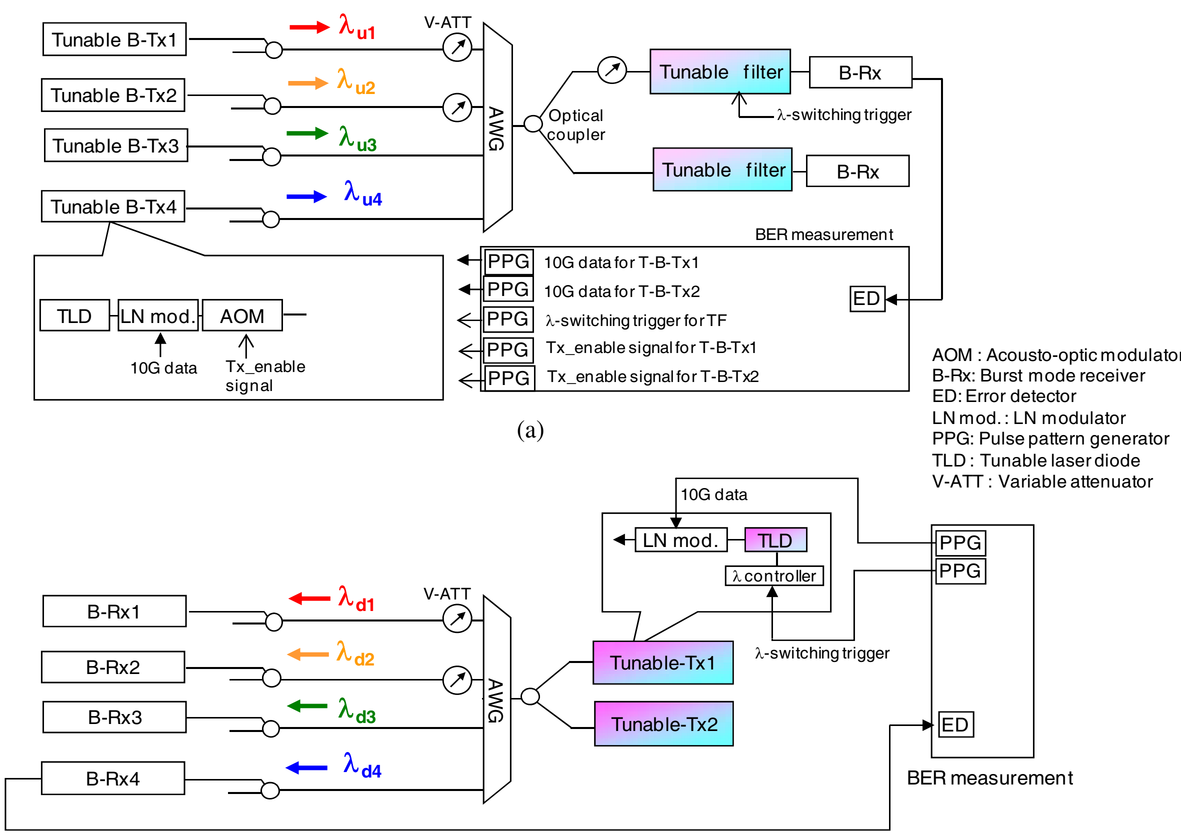

(b)

Figure 3: Experimental setups. (a) Experiment setup for upstream signals. (b) Experimental setup for downstream signals.

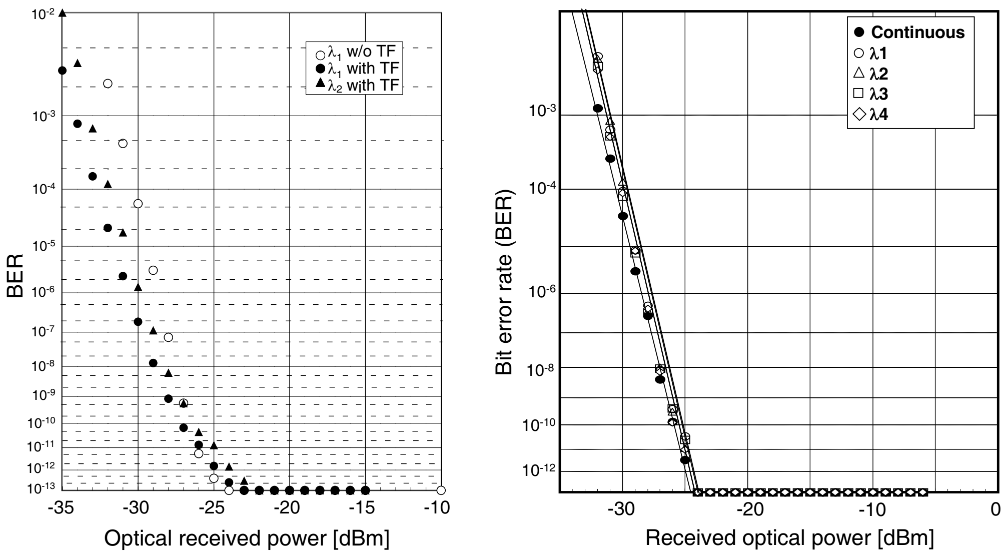

(a) (b)

Figure 4: (a) Characteristics of BER for upstream signals, (b) for downstream signals.

switching trigger. Its switching time was 50 ns. The four wavelengths used in this experiment were 1538.6, 1539.0, 1539.4, and 1539.8 nm. In the ONU, the B-Rx is required, because the downstream data is TDM signal among PON branches. Figure 4(b) shows characteristics of BER of the downstream signal received in each B-Rx. The received optical power at the BER of 10^{-3} and 10^{-12} were -31.3 dBm and -24.2 dBm, respectively. These results confirm the feasibility of high receiver sensitivity and fast response wavelength switching as realized by the DWBA algorithm.

5. CONCLUSIONS

This paper introduces requirements of NGOA from the telecom operator's viewpoint and proposes λ-tunable WDM/TDM-PON using DWBA as a promising technological solution The proposed PON can realize the incremental upgrade of the total bandwidth and allocate the flexible bandwidth according to users' demand by the wavelength tunability of the ONU and the OLT, and the DWBA algorithm. The transmission experiment λ-tunable ONU and OLT, and the DWBA operation confirmed the feasibility in proposed PON.

REFERENCES

1. ITU-T Recommendation G.987 series, "10-Gigabit-capable passive optical network (XG-PON) systems".
2. IEEE Std 802.3av-2009, "Physical layer specifications and management parameters for 10 Gb/s passive optical networks," 2009.
3. FSAN website, http://fsanweb.com/.
4. Kani, J.-I., F. Bourgart, A. Cui, A. Rafel, M. Campbell, R. Davey, and S. Rodrigues, "Next-generation PON-part I: Technology roadmap and general requirements," *IEEE Communications Magazine*, 43–49, 2009.
5. Nakamura, H., S. Tamaki, K. Hara, S. Kimura, and H. Hadama, "40 Gbit/s λ-tunable stacked-WDM/TDM-PON using dynamic wavelength and bandwidth allocation," *Proceedings of OFC*, OThT4, Los Angeles, USA, March 2011.
6. Hara, K., S. Kimura, H. Nakamura, N. Yoshimoto, and H. Hadama,, "New AC-coupled burst-mode optical receiver using transient-phenomena cancellation techniques for 10 Gbit/s-class high-speed TDM-PON systems," *J. Lightwave Technol.*, Vol. 28, 2775–2782, 2010.
7. Hara, K., H. Nakamura, S. Kimura, M. Yoshino, S. Nishihara, S. Tamaki, J. Kani, N. Yoshimoto, and H. Hadama, "Flexible load balancing technique using DWBA toward 100 Gbit/s-class-WDM/TDM-PON," *Proceedings of ECOC*, Tu.3.B.2, Torino, Italy, September 2010.

Reconstruction of a Layered Dielectric Cylinder Using a Split Particle Swarm Optimization

K. Ishida
Kyushu Sangyo University, Japan

Abstract— Reconstruction of a layered dielectric cylinder is formulated with cost functions, which are minimized by a split PSO. In the split PSO, particles are split into, for example, two groups. Particles of a group evaluate a cost function and those of the other group do another cost function. Particles change their positions according to experience of their own and both groups to search the common minimum point of both cost functions. Numerical examples show that the split PSO saves computational cost and tends to reduce traps at local minimum points.

1. INTRODUCTION

Electromagnetic inverse scattering problem of evaluating properties of an object from its scattered electromagnetic waves is interesting in a variety of application such as medical diagnostics, non-destructive testing, and underground prospecting. For a strongly scattering object the problem reduces an optimization problem to minimize a cost function that relates differences between the measured and the calculated scattered-waves. It is difficult in general to search for the minimum point of the cost function in terms of a gradient-based optimization method because of existence of local minimum points.

To avoid traps at local minimum points two strategies are being considered. One is use of a stochastic nonlinear optimization algorithm such as particle swarm optimization (PSO) [1–3]. In PSO, multiple particles (candidate points) change their positions (the coordinates) in solution space according to their own experience and experience of the swarm. PSO requires as many evaluation of the cost function at each iteration as the number of particles.

The other is use of multiple cost functions. In inverse scattering problems, it is likely that data of different measurements, such as multi-frequency data, is utilized in order to obtain detailed information of the object. In those cases it is natural that we should introduce a cost function as a sum of squared errors of the different measurements. Summing the cost functions would reduce rises and falls, emphasize its global minimum point, and facilitate the search for the global minimum point to some extent. There probably remain local minimum points, however, and evaluation time of the cost function is increased.

In the present study a split PSO, which is a blending of the above strategies and has been proposed by the author [4], is applied to reconstruction of a layered dielectric cylinder. In the split PSO, particles are split into, for example, two groups. Particles of a group evaluate a cost function and those of the other group do another cost function. Particles change their positions according to experience of their own and both groups to search the common minimum point of both cost functions. Solution might not be trapped at a local minimum point unless the minimum points lie at the same point.

In order to clarify effectiveness of the split PSO, we will apply PSO to a simple inverse scattering problem of evaluating a few parameters of a layered dielectric cylinder from scattered waves. Numerical examination will be done and comparison of the split PSO with the basic PSO will be presented.

2. SCATTERING BY A L-LAYER DIELECTRIC CIRCULAR CYLINDER

Let us begin with review of scattering problem of a layered circular cylinder located at the origin in free space under E-wave time-harmonic excitations of the time factor $\exp(\mathrm{j}\omega t)$. The geometry is shown in Figure 1. The relative dielectric constants and the radii of each layer are denoted by $\varepsilon_{\mathrm{r}1}, \ldots, \varepsilon_{\mathrm{r}L}$ and $r_1, \ldots, r_L$, respectively. When a plane wave propagating in the θ direction is incident to the cylinder, the scattered wave in the far-field is expressed as

$$u_{\mathrm{s}}(\rho, \phi) \simeq \sqrt{\frac{2}{\pi k \rho}} \mathrm{e}^{-\mathrm{j}k\rho + \frac{\mathrm{j}\pi}{4}} \bar{u}_{\mathrm{s}}(\phi) \tag{1}$$

where k is the wavenumber in free space and $\bar{u}_{\mathrm{s}}(\phi)$ is the far-field (complex) pattern of scattered wave, which is represented as

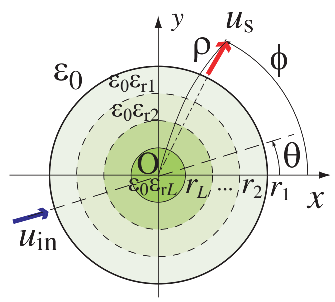

Figure 1: Geometry of the scattering problem.

$$\bar{u}_{\mathrm{s}}(\phi) = \sum_{m=-\infty}^{\infty} \beta_m \mathrm{j}^m \mathrm{e}^{\mathrm{j}m\phi}. \tag{2}$$

The coefficient β_m is calculated from $\varepsilon_{\mathrm{r}1}, \ldots, \varepsilon_{\mathrm{r}L}$ and $r_1, \ldots, r_L$ according to the following recurrence formula:

$$\beta_m = \xi_{0m}\mathrm{j}^{-m}\mathrm{e}^{-\mathrm{j}m\theta}, \tag{3}$$

$$\xi_{Lm} = 0, \tag{4}$$

$$\xi_{l-1m} = -\frac{\begin{array}{l} k_l \mathrm{J}_m(k_{l-1}r_l)\{\mathrm{J}_{m+1}(k_l r_l) + \xi_{lm}\mathrm{H}_{m+1}^{(2)}(k_l r_l)\} \\ -k_{l-1}\mathrm{J}_{m+1}(k_{l-1}r_l)\{\mathrm{J}_m(k_l r_l) + \xi_{lm}\mathrm{H}_m^{(2)}(k_l r_l)\} \end{array}}{\begin{array}{l} k_l \mathrm{H}_m^{(2)}(k_{l-1}r_l)\{\mathrm{J}_{m+1}(k_l r_l) + \xi_{lm}\mathrm{H}_{m+1}^{(2)}(k_l r_l)\} \\ -k_{l-1}\mathrm{H}_{m+1}^{(2)}(k_{l-1}r_l)\{\mathrm{J}_m(k_l r_l) + \xi_{lm}\mathrm{H}_m^{(2)}(k_l r_l)\} \end{array}}, \quad l = L, \ldots, 1 \tag{5}$$

where $k_l = \sqrt{\varepsilon_{\mathrm{r}l}}\,k$ indicates the wavenumber of lth layer and $k_0 = k$ is implied. The symbols J_m and $\mathrm{H}_m^{(2)}$ are the Bessel function and the Hankel function of the second kind, respectively.

3. INVERSE SCATTERING PROBLEM

Let us consider reconstruction of a layered dielectric circular cylinder from the scattered waves. The center of the circular cylinder is fixed to the origin for simplicity; i.e., $\theta = 0$ is used because of the symmetry.

In order to recast the inverse problem to an optimization problem let us introduce the mean square error as

$$\Omega^{(i)}(\mathbf{x}) = \frac{1}{2\pi}\int_0^{2\pi} \left| \bar{u}_{\mathrm{s}}^{(i)}(\phi; \mathbf{x}) - \tilde{\bar{u}}_{\mathrm{s}}^{(i)}(\phi) \right|^2 d\phi \tag{6}$$

where $\mathbf{x}$ is a vector which contains unknown parameters, $\bar{u}_{\mathrm{s}}$ and $\tilde{\bar{u}}_{\mathrm{s}}$ denote the calculated and the measured far-field patterns, respectively, and the superscript (i) means that the wavenumber $k = k_i$ is used. Substituting Equation (2) into Equation (6), we can obtain another form as

$$\Omega^{(i)}(\mathbf{x}) \simeq \sum_{m=-M}^{M} \left| \beta_m^{(i)}(\mathbf{x}) - \tilde{\beta}_m^{(i)} \right|^2, \qquad \tilde{\beta}_m^{(i)} = \frac{\mathrm{j}^{-m}}{2\pi}\int_0^{2\pi} \tilde{\bar{u}}_{\mathrm{s}}^{(i)}(\phi)\mathrm{e}^{-\mathrm{j}m\phi} d\phi \tag{7}$$

where M is a large number and β_m and $\tilde{\beta}_m$ denote the calculated and the measured coefficients of far-field patterns, respectively. Equation (7) is suitable for computation and is used as the cost function in the following numerical analysis.

4. APPLICATION OF PARTICLE SWARM OPTIMIZATION

In order to apply PSO to the inverse problem that minimizes the cost function indicated in Equation (7) let us set a swarm of P particles whose position is characterized as $\mathbf{x}_p$, $(p = 1, \ldots, P)$

In the basic PSO the velocity of pth particle is updated according to

$$\mathbf{v}_p^{(t+1)} = w\mathbf{v}_p^{(t)} + c_1 r_1 \left(\mathbf{p}_p^{(t)} - \mathbf{x}_p^{(t)}\right) + c_2 r_2 \left(\mathbf{g}^{(t)} - \mathbf{x}_p^{(t)}\right) \tag{8}$$

where t is the iteration number, $\mathbf{p}_p^{(t)}$, which is called *pbest*, is the best solution which pth particle personally encountered, $\mathbf{g}^{(t)}$, which is called *gbest*, is the best solution which the entire swarm encountered, w is called the inertial weight, c_1, c_2 are scaling factors, and r_1, r_2 are random numbers uniformly distributed in $[0, 1]$. The position of pth particle $\mathbf{x}_p$ is updated (assuming the unit time is elapsed per iteration) according to

$$\mathbf{x}_p^{(t+1)} = \mathbf{x}_p^{(t)} + \mathbf{v}_p^{(t+1)}. \tag{9}$$

Each particle moves along its original course to some extent and is stochastically pulled to *pbest* and *gbest*, as is depicted in Figure 2(a).

Let us consider the case that scattering data of two different frequencies is available. A method in this case is to minimize the cost function $\Omega^{(1)} + \Omega^{(2)}$. As another method we introduce a novel PSO, which we call a split PSO in this paper, where the particles are split into two groups. The particles of the first group evaluate $\Omega^{(1)}$ and those of the other group do $\Omega^{(2)}$, moving according to

$$\mathbf{v}_p^{(t+1)} = w\mathbf{v}_p^{(t)} + c_1 r_1 \left(\mathbf{p}_p^{(t)} - \mathbf{x}_p^{(t)}\right) + c_{21} r_{21} \left(\mathbf{g}_1^{(t)} - \mathbf{x}_p^{(t)}\right) + c_{22} r_{22} \left(\mathbf{g}_2^{(t)} - \mathbf{x}_p^{(t)}\right) \tag{10}$$

instead of Equation (8) where c_{21}, c_{22} are scaling factors, r_{21}, r_{22} are random numbers uniformly distributed in $[0, 1]$, and $\mathbf{g}_i^{(t)}$ is the best solution of $\Omega^{(i)}$ that the ith group encountered. In split PSO each particle moves along its original course to some extent and is stochastically pulled to *pbest* and two *gbests*, as is depicted in Figure 2(b). We may note, in passing, that we can easily apply idea of the split PSO to cases in which more than two cost functions are used.

The inverse algorithm is summarized as follows:

Step 1: Set the initial position of each particles by randomly selecting a value with uniform probability over the solution space. Similarly, set each dimension of the initial velocity of each particles by a random value in the range $[-V, V]$. Evaluate the cost function according to the position of particles and set *pbest* and *gbest*.

Step 2: Update the velocity of each particle by Equation (8) or (10) and update position by Equation (9). Evaluate the cost function at the updated positions and update the *pbest* and the *gbest*.

Though the particles are allowed to move out of the solution space, the particle outside the solution space are not evaluated for cost function; namely, invisible walls [1] are assumed as the boundary condition. This step is repeated until a termination criterion is satisfied.

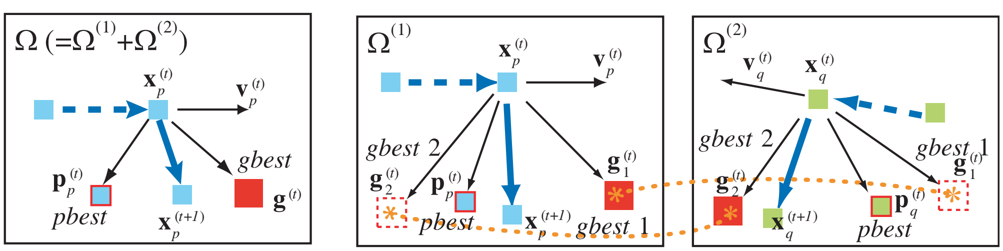

(a) basic PSO (b) split PSO

Figure 2: Behavior of a particle according to the basic and the split PSO.

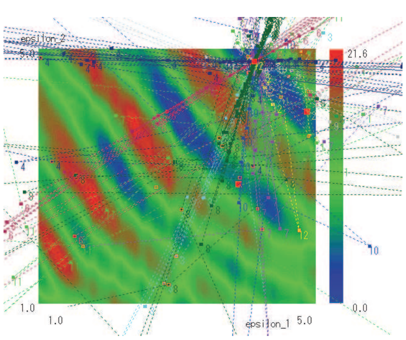

Figure 3: Cost function $\Omega^{(1)}$, whose minimum point is searched for by the basic PSO.

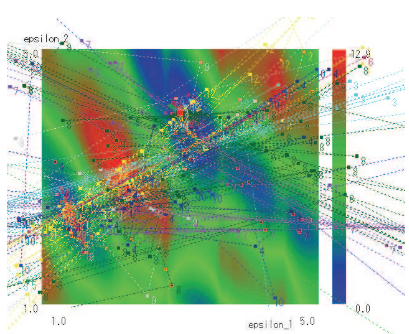

Figure 4: Cost function $\Omega^{(2)}$, whose minimum point is searched for by the basic PSO.

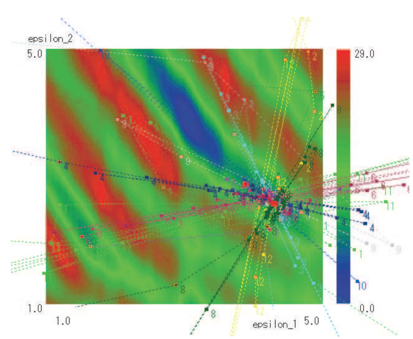

Figure 5: Cost function $\Omega^{(1)} + \Omega^{(2)}$, whose minimum point is searched for by the basic PSO.

5. NUMERICAL ANALYSIS

Let us examine reconstruction of a lossless two-layer cylinder whose parameters are $\varepsilon_{r1} = 3, \varepsilon_{r2} = 4$ and $r_1/\lambda = 2$, $r_1/\lambda = 1$ where λ is a wavelength in free space. The parameters r_1, r_2 are fixed and $\mathbf{x} = (\varepsilon_{r1},\ \varepsilon_{r2})$ shall be recovered. The solution space is set to $1 \leq \varepsilon_{r1},\ \varepsilon_{r2} \leq 5$ and V is set to be equal to the dynamic range of the solution space, i.e., 4. The parameters of PSO are set to $P = 12$, $w = 0.4$, $c_1 = c_2 = 2$ with reference to [2] and $c_{21} = c_{22} = 1$. If all the dimensions of the velocity of particles and of difference between the positions of particles and *gbest* are less than $\epsilon = 0.01$ or the iteration number becomes larger than $I_{\max} = 300$, the minimization process is terminated. The scattering data of $k_1 = 2\pi/\lambda$ and $k_2 = k_1/2$ is assumed to be available.

At first let us analysis the case that one frequency of k_1 or k_2 is available. Figures 3 and 4 show the contours of $\Omega^{(1)}$ and $\Omega^{(2)}$ and behaviors of particles searching for the minimum point according to the basic PSO, respectively. We see that the particles have gathered around $(4.1, 4.8)$, i.e., the search for the minimum point has failed in $\Omega^{(1)}$. On the other hand the search for the minimum point in $\Omega^{(2)}$ has succeeded.

Next let us examine the case that both frequencies are available. Figure 5 shows a movement of particles which have failed to search for the minimum point of $\Omega^{(1)} + \Omega^{(2)}$ according to the basic PSO. The particles have gathered around $(4.3, 2.6)$. Figure 5 shows that the summed cost function has a tendency to reduced rises and falls, however, to leave local minimum points.

Figure 6 shows a movement of particles according to the split PSO, where each half of particles has successfully searched for the minimum point of $\Omega^{(1)}$ or $\Omega^{(2)}$, respectively.

A hundred runs are similarly executed for three different cylinders. The numbers of successes in recovering the parameters for the cylinders are shown in Table 1. We see from the table that the split PSO is more successful than the basic one in searching for the global minimum point. Also note that the split PSO requires less computation time than the basic one using $\Omega^{(1)} + \Omega^{(2)}$ because the only one cost function of $\Omega^{(1)}$ or $\Omega^{(2)}$ is evaluated for each particle.

As the second example, let us consider reconstruction of a four-layer cylinder which is shown in Figure 7. In this reconstruction positions of layers are fixed, and four dielectric constants ε_{r1}, ε_{r2}, ε_{r3}, and ε_{r4} shall be recovered by particles $P = 24$ using two frequencies k_1 and k_2. Figure 8 shows the estimated parameters for the numbers of iterations. We can recover the parameters accurately in a trial (Figure 8(a)) and inaccurately in another trial (Figure 8(b)) through using basic or split PSO. A hundred runs are executed for reconstruction of the cylinder including the use of more particles $P = 36,\ 48$, and 96. The number of successes in recovering the parameters are shown in Figure 9. We see from the figure that the split PSO is more successful than the basic

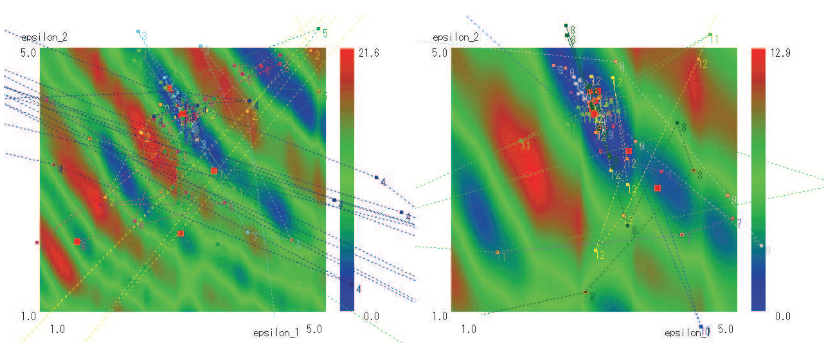

Figure 6: Cost functions $\Omega^{(1)}$ and $\Omega^{(2)}$, whose minimum points are simultaneously searched for by the split PSO.

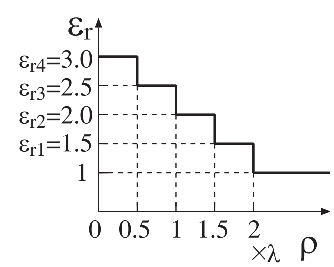

Figure 7: A four-layer cylinder.

Table 1: The number of successful estimation of 100 runs ($P = 12$).

PSO type	basic	basic	basic	split
cost function(s)	$\Omega^{(1)}$	$\Omega^{(2)}$	$\Omega^{(1)} + \Omega^{(2)}$	$\Omega^{(1)}$, $\Omega^{(2)}$
cylinder 1: $\varepsilon_{r1} = 3$, $\varepsilon_{r2} = 4$	66	100	90	97
cylinder 2: $\varepsilon_{r1} = 2$, $\varepsilon_{r2} = 3$	53	64	58	71
cylinder 3: $\varepsilon_{r1} = 4$, $\varepsilon_{r2} = 2$	54	83	72	93

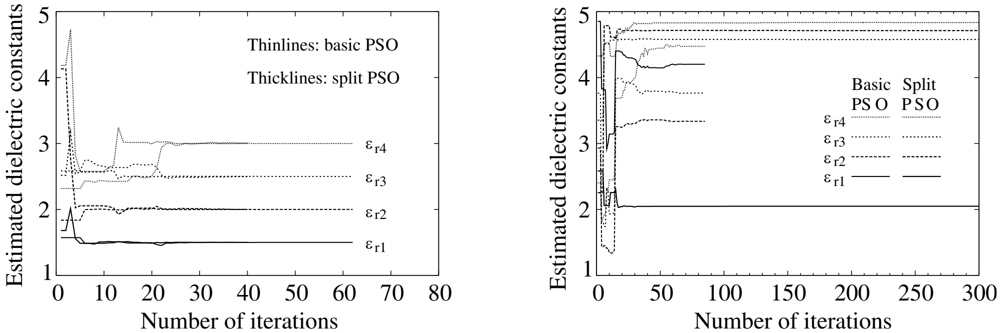

(a) These estimation succeeds (b) These estimation fails

Figure 8: Estimated dielectric constants versus the number of iterations.

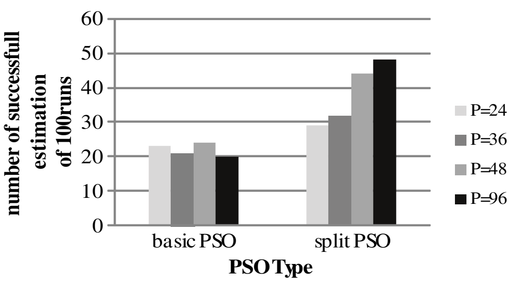

Figure 9: Number of successful estimation of 100 runs.

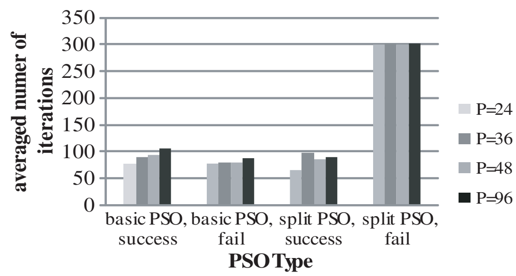

Figure 10: Averaged number of iterations.

one in searching for the global minimum point also in this example. Figure 10 separately shows the averaged number of iterations over the runs of successes or fails to search the global minimum point. When a search fails in the basic PSO the particles seem to gather at a local minimum point; on the other hand in the split PSO the particles seem to wander around two *gbests* which are likely in different points. We should presume that the search fails in the split PSO when the iteration number becomes large. A procedure that positions and velocities of particles are initialized every 100 times of iteration is added to the above algorithm of the split PSO, and another hundred runs are executed for reconstruction of the cylinder. The numbers of successes within 300 iterations have been increased to 58, 53, 62, and 62 for $P = 24$, 36, 48, and 96, respectively.

6. CONCLUSION

In this paper, we have considered a simple inverse scattering problem using the split PSO which simultaneously minimize two cost functions. The split PSO saves computational cost and tends to reduce traps at local minimum points. We also have found that there is difference in the behavior of particles between the split and the basic PSO when they fail to search the accurate solution. Adding an initialization procedure to the split PSO should make improvement in escape from traps at false solutions. Analysis of characteristics of the PSO in details and its application to more complex problems which have many unknown parameters are subjects for future studies.

REFERENCES

1. Robinson, J. and Y. Rahmat-Samii, “Particle swarm optimization in electromagnetics,” *IEEE Trans. Antennas & Propag.*, Vol. 52, No. 2, 397–407, 2004.
2. Donelli, M. and A. Massa, “Computational approach based on a particle swarm optimizer for microwave imaging of two-dimensional dielectric scatterers,” *IEEE Trans. Microwave Theory & Tech.*, Vol. 53, No. 5, 1761–1776, 2005.
3. Rocca, P., M. Benedetti, M. Donelli, D. Franceschini, and A. Massa, “Evolutionary optimization as applied to inverse scattering problems,” *Inverse Probl.*, Vol. 25, No. 12, 123003, 41 pages, 2009.
4. Ishida, K., “An application of particle swarm optimization to reconstruction of a homogeneous dielectric circular cylinder,” *Proceedings of 2011 International Symposium on Antennas and Propagation*, 4 pages, Jeju, Korea, October 2011.